

# 16. INTERNATIONAL CONFERENCE ON MACHINE DESIGN AND PRODUCTION

CONFERENCE PROCEEDINGS

VOLUME I

## **Editorial Board**

Metin AKKÖK  
Abdülkadir ERDEN  
S. Engin KILIÇ  
E. İlhan KONUKSEVEN

## **Machining Day Editorial Board**

Erhan BUDAĞ  
İsmail LAZOĞLU

umtik 2014

**30 June - 3 July 2014**

İZMİR- TURKEY

**MATIMAREN**  
**DEPARTMENT OF MECHANICAL ENGINEERING**  
**MIDDLE EAST TECHNICAL UNIVERSITY**  
**ANKARA – TURKEY**







All rights of this book are reserved by the Middle East Technical University. None of the papers printed in this book may be reproduced without the prior permission, in writing, from the Author(s) of the paper(s) and the editors of the book. The papers can however be cited by giving the source.

This book can be obtained from the following address:

**UMTIK**  
**Mechanical Engineering Department**  
**Middle East Technical University**  
**06800 Ankara – Turkey**

**Editorial Assistant:**

Bahram Lotfi Sadigh

**Cover Print:**

METU-Ankara

**Printing and Binding:**

METU-Ankara

**Printed by:**

Dereağzı Fotokopi

**ISBN            978-975-429-332-6 (1.c)**



### Organizing Committee

Metin AKKÖK (METU, Mechanical Eng. Dept.)  
Abdülkadir ERDEN (Atılım Univ. , Dept. of Mechatronics Eng.)  
S. Engin KILIÇ (Atılım Univ. , Mechanical Eng. Dept.)  
E. İlhan KONUKSEVEN (METU, Mechanical Eng. Dept.)  
Ali Oral (Balıkesir University, Mechanical Eng. Dept.)  
İbrahim E. SAKLAKOĞLU (Ege University, Mechanical Eng. Dept.)

[akkok@metu.edu.tr](mailto:akkok@metu.edu.tr)  
[aerden@atilim.edu.tr](mailto:aerden@atilim.edu.tr)  
[engin.kilic@atilim.edu.tr](mailto:engin.kilic@atilim.edu.tr)  
[konuk@metu.edu.tr](mailto:konuk@metu.edu.tr)  
[alioral@balikesir.edu.tr](mailto:alioral@balikesir.edu.tr)  
[i.e.saklakoglu@ege.edu.tr](mailto:i.e.saklakoglu@ege.edu.tr)

### Machining Day Organizers

Erhan Budak (Sabancı University, Mechanical Eng. Dept.)  
İsöail Lazoğlu (Koç University, Mechanical Eng. Dept.)

[ebudak@sabanciuniv.edu.tr](mailto:ebudak@sabanciuniv.edu.tr)  
[ilazoglu@ku.edu.tr](mailto:ilazoglu@ku.edu.tr)

**Contact :** [umtik@metu.edu.tr](mailto:umtik@metu.edu.tr) **Tel :** + 90 312 210 2570- 2589- 5242

### International Program Committee

Memiş	ACAR	UK
Serpil	ACAR	UK
M. Oktay	ALNIAK	TURKEY
Ahmet T.	ALPAS	CANADA
Yusuf	ALTINTAŞ	CANADA
Ömer	ANLAĞAN	TURKEY
Stuart	BARNES	UK
Adil	BAYKASOĞLU	TURKEY
Necip	CAMUŞCU	TURKEY
Fuh-Kuo	CHEN	TAIWAN
Tsung Chia	CHEN	TAIWAN
Hugi	CHRISTOPH	SWITZERLAND
Octavian	CIOBANU	ROMANIA
M. Cemal	ÇAKIR	TURKEY
Can	ÇOĞUN	TURKEY
Samad	DADVANDIPOUR	HUNGARY
Saied	DARWISH	SAUDI ARABIA
Türkay	DERELİ	TURKEY
Leo	De VIN	SWEDEN
László	DUDÁS	HUNGARY
Bülent	EKMEKÇİ	TURKEY
Ferenc	ERDELYI	HUNGARY
Kaan	ERKORKMAZ	CANADA
Hüseyin	FİLİZ	TURKEY
Necdet	GEREN	TURKEY
Francesco	JOVANE	ITALY
Yiğit	KARPAT	TURKEY
Zvi	KATZ	SOUTH AFRICA
Adnan Z.	KILANI	JORDAN
Bozidar	KRIZAN	CROATIA
Bing	LI	P. R. C.
Yangmin	LI	MACAO
Tzuo Liang	LUO	TAIWAN
Yoshiyuki	MATSUOKA	JAPAN
Laszlo	MONOSTORY	HUNGARY
Toshimichi	MORIWAKI	JAPAN
Jokin	MUNOA	SPAIN
Jun	NI	USA
Tuğrul	ÖZEL	USA
Naki	POLAT	TURKEY
Mustafizur	RAHMAN	SINGAPORE
Can	SAYGIN	USA
Eiji	SHAMOTO	JAPAN
R.	SIVASUBRAMANIAN	INDIA
Daizhong	SU	UK
Ulvi	ŞEKER	TURKEY
Uğur	ŞİMŞİR	TURKEY
Erman	TEKKAYA	GERMANY
Tibor	TOTH	HUNGARY
Ali	ÜNÜVAR	TURKEY
Hakkı Özgür	ÜNVER	TURKEY
Ivica	VEZA	CROATIA
Min	WAN	P. R. C.

## List of Referees

Ahmet Hakan	ARGEŞO	TURKIYE
Kutluk	B. ARIKAN	TURKIYE
Mustafa	BAKKAL	TURKIYE
Besim	BARANOĞLU	TURKIYE
Stuart	BARNES	UNITED KINGDOM
Hakan	ÇALIŞKAN	TURKIYE
Barbaros	ÇETİN	TURKIYE
Ender	CİĞEROĞLU	TURKIYE
Serkan	DAĞ	TURKIYE
Kemal	DAVUT	TURKIYE
Ali Gökhan	DEMİR	TURKIYE
Cem	DÖKMEN	TURKIYE
Merve	ERDAL	TURKIYE
Zuhal	ERDEN	TURKIYE
Seniz	ERTUĞRUL	TURKIYE
Fehmi	ERZİNCANLI	TURKIYE
Volkan	ESAT	TURKIYE
Kemal Efe	ESELLER	TURKIYE
Marcel	FEY	GERMANY
Kemal	İDER	TURKIYE
Celalettin	KARADOĞAN	TURKIYE
Zekai Murat	KILIÇ	TURKIYE
Aylin	KONEZ EROĞLU	TURKIYE
Bahram	LOTFISADIGH	TURKIYE
Cemal	MERAN	TURKIYE
Ömer	MUSIC	TURKIYE
Ahmet	ÖZDEMİR	TURKIYE
Bülent	ÖZER	TURKIYE
Gökhan	ÖZGEN	TURKIYE
M. Kemal	ÖZGÖREN	TURKIYE
Bülent	PLATİN	TURKIYE
Merih	ŞENGONUL	TURKIYE
Tayfun	SİĞİRTMAÇ	TURKIYE
Caner	ŞİMŞİR	TURKIYE
Ming-Yi	TSAI	TAIWAN
Kazim	TUR	TURKIYE
Y, Samim	ÜNLÜSOY	TURKIYE
Yusuf	USTA	TURKIYE
Orhan	YILDIRAN	TURKIYE
Orhan	YILDIRIM	TURKIYE
YANG	YUN	P.R.C.

## SPONSORS



ORS



MAIB



RENAULT



AES



SPINNER



USEL



TIAD



BIAS



TEKNODROM



İGREK



DİRİNLER

**Conference Secretariat**

**ORIGIN Event Management Company**

Kozyatağı Mahallesi, Forsa sok. No. 18/4, Şenesenevler- Kadıköy/ İstanbul  
TEL: +90 216 372 23 30 FAX:+90 216 372 23 31

**www.originemc.com.tr**  
**info@originemc.com.tr**

**Contact Adress**

**http://www.umtik.com**  
**umtik@metu.edu.tr**

## PREFACE

It was thirty years ago when six young professors of the Mechanical Engineering Department of the Middle East Technical University started UMTIK conferences as a national event. The Members of the Organizing Committee of the first UMTIK Conference will be with us on the 2<sup>nd</sup> July 2014 to bring us back to 1984 in a special session “From 1984 to 2014 30 Years of UMTIK Conferences” where the chronological development of UMTIK conferences until 2014 and the future of UMTIK will be discussed with all the participants.

Professor Yusuf Altıntaş is the Honorary Speaker of UMTIK 2014. He is the holder of 2013 special scientific award of TÜBİTAK (Scientific and Technological Research Council of Turkey) in Science and Engineering (2013). He will be delivering his speech on “University – Industry Research Partnership Models In Manufacturing Engineering” right after the opening session.

The first day program will continue by a Panel Discussion Session on “Realisation of Transformation in Manufacturing, Decreasing the Dependency on Import” organized by Professor Ulvi Şeker, Adviser to the Ministry of Science, Industry and Technology and to be moderated by Professor Ersan Aslan, Undersecretary to the Ministry of Science, Industry and Technology. There will be four panelists to represent the Ministries of Economy, Energy and Natural Resources, Development, Transport, Maritime Affairs and Communications at the level of undersecretaries or senior officers. The panel will be conducted in Turkish; but simultaneous translation to English will be provided to the audience.

There will be 49 (15 in Turkish) papers to be presented in 17 regular sessions (3 in Turkish) and 15 papers to be presented in four special sessions on three different topics: “Design Science and Timeaxis Design” organized by Professor Yoshiyuki Matsuoka, “Optimization of Mechanical Systems” organized by Dr. Erdem Acar and “Design for Transport Safety” by Professor Serpil Acar.

Two keynote speeches will be delivered: “Performance Prediction of Coated Tools based on Innovative Procedures to Detect Properties of the Compound Film-Interface Substrate” by Professor K. D. Bouzakis, and “Advances in Cryogenic and Ultrasonic Assisted Machining” by Professor Stuart Barnes in plenary sessions.

Three plenary sessions are reserved for the conference sponsors to make presentations about their companies/associations. We hope these sessions give an opportunity to the participants to learn the capabilities of the sponsoring companies for possible future partnerships.

UMTIK 2012 starts with “Machining Day”, UMTIK 2014 will close with “Machining Day”. “Machining Day” program has 20 papers to be presented in 5 plenary sessions.

We highly acknowledge the Honorary Chair Persons of the Conference: Presidents of the three universities, Professor Ahmet Acar of the Middle East Technical University, Professor Abdurrahim Özgenoğlu of Atılım University and Professor Candeğer Yılmaz of Ege University for their kind support. We also highly acknowledge Professor Ersan Aslan, Under Secretary of the Ministry of Science, Industry and Technology, Professor Ulvi Şeker, Adviser to the Ministry and Assoc. Prof. Dr. Rasim Akpınar, Director of İzmir Directorate, Ministry of Science, Industry and Technology for organizing the Panel Discussion and for their support. We would like to thank the panellists, the Honorary Speaker, Professor Yusuf Altıntaş, the keynote speakers, special session organizers, session chair persons, the authors and all participants for their valuable contributions. Bahram Lotfi Sadigh, a Ph.D. candidate in METU, is gratefully acknowledged for the tremendous time and effort he spent in every aspect of conference organization.

Last, but not the least, we would also like to thank our main sponsor TUBITAK, “The Scientific and Technological Research Council of Turkey”, sponsors, the International Program Committee Members, the referees, our conference secretariat, ORIGIN, and all those who contributed to the success of UMTİK 2014.

We wish all the participants a highly memorable time during their stay in İzmir.

The Organizing Committee

UMTIK 2014, 30<sup>th</sup> June – 3<sup>rd</sup> July 2014

İzmir, Türkiye



## **PREFACE TO MACHINING DAY IN UMTIK 2014**

This year we will have the second Machining Day in UMTIK Conferences. The first one was held in 2012 in Pamukkale as a tribute to Prof. Altintas of UBC for his achievements and contributions to manufacturing science and engineering. Not suprisingly, shortly after that Prof. Altintas received Special Award from TUBITAK in 2013 (The Scientific and Technological Research Council of Turkey) in addition to many others he has been awarded. We had interesting presentations and good discussions in the first Machining Day during and after the sessions. This year we have 20 interesting presentations grouped in 4 sessions: Experimental Methods, Multi Axis Machining, Machine Tool Dynamics and Process Modeling. We again hope that these presentations will create a dynamic atmosphere stimulating interaction among participants. We welcome all of you to İzmir and wish you a productive and pleasant stay.

“Machinin Day” Organizers

Prof. Dr. Erhan Budak

Prof. Dr. İsmail Lazoglu



# CONTENTS

## VOLUME I

<b>University– Industry Research Partnership Models in Manufacturing Engineering</b>	1
--------------------------------------------------------------------------------------	---

Yusuf ALTINTAŞ

<b>Performance Increase of Coated Cutting HM-Tools By Adapting the Cutting Conditions to the Film Properties</b>	13
------------------------------------------------------------------------------------------------------------------	----

K.-D. BOUZAKIS, G. SKORDARIS, E. BOUZAKIS, R. PARASKEVOPOULOU, G. KATIRTZOGLU, S. MAKRIMALLAKIS, P. CHARALAMPOUS

<b>Advances in Cryogenic and Ultrasonic Assisted Machining</b>	29
----------------------------------------------------------------	----

Stuart BARNES, Helen ASCROFT, Pipat BHUDWANNACHAI, Aishah Najiah DAHNEL, Aniruddha GUPTA

### Design Science and Time-axis Design

<b>Application of M Method and Consideration of Measures to Adapt for Diverse Users</b>	49
-----------------------------------------------------------------------------------------	----

Shuji KANAZAWA, Yuma SAKAE, Shuji TAKANO, Koichiro SATO, Yoshiyuki MATSUOKA

<b>Multispace Quality Function Deployment using Design Structure Matrix</b>	61
-----------------------------------------------------------------------------	----

T. KATO, T. SOGA, Y. HOSHINO

<b>Value Growth Mobility Based on Timeaxis Design</b>	75
-------------------------------------------------------	----

Yuma KUSUNOKI, Kei KAMIYA, Akira KITO, Koichiro SATO, Yoshiyuki MATSUOKA

<b>Conceptual Structuring of Modular Design Methodology for Mechatronic Systems: Behaviour Based Design Perspective</b>	87
-------------------------------------------------------------------------------------------------------------------------	----

Zuhal ERDEN

### Design for Transport Safety I

<b>Pregnant Occupant Model Design to Improve Safety</b>	101
---------------------------------------------------------	-----

B. Serpil ACAR, Moustafa MERIC, Memis ACAR

<b>A FEM-MB Mixed Methodology to Analyze the Passive Safety Performances of A Passenger Seat for Railway Use</b>	115
------------------------------------------------------------------------------------------------------------------	-----

Francesco CAPUTO, Giuseppe LAMANNA

<b>Optimization Study on Multi-Body Vehicle-Front Model for Pedestrian Safety</b>	131
-----------------------------------------------------------------------------------	-----

Hariharan S. SUBRAMANIAN, Anoop CHAWLA, Sudipto MUKHERJEE, Dietmar GOEHLICH

<b>Design Concept for an Integrated Whiplash Mitigating Headrests and Car Seat</b>	153
M. ACAR, S.R. BEWSHER	
 <u>Design for Transport Safety II</u>	
<b>Structural Crashworthiness Analysis of A Pickup Truck Subjected to Pole Side Impacts</b>	167
M. Ozan KOCABAŞ, Eren ÜNSAL, Volkan ESAT	
 <b>Crashworthiness of Guardrail Post Embedded in Cohesionless Soil</b>	181
Sassi ABDELMONAAM, Faouzi GHRIB	
 <b>Effects of Chassis Geometry on Structural Crashworthiness of A Pickup Truck in Full-Frontal Impacts</b>	199
Semih DAĞDEVİREN, Mecit YAVUZ, Volkan ESAT	
 <b>Hybrid RFID System for Driver Assistant and Active Road Accident Prevention</b>	215
Huanjia YANG, Shuang-Hua YANG	
 <u>Optimization of Mechanical Systems and/or Manufacturing</u>	
<b>Shape Optimization of 2D Rubber Bushing using Differential Evolution Algorithm</b>	235
Necmettin KAYA	
 <b>Structural Optimization of Blade – Disc Firtree Attachment of An Aero-Engine</b>	245
Erdem ACAR, Mutlu GÜNDÜZ	
 <b>Development of New Crash Boxes for Automotive Industry</b>	267
Emre DEMİRCİ, Ali Rıza YILDIZ, Fehim SEMERCİ	
 <u>Experimental Methods</u>	
<b>Investigating the Effects of Variable Feed Rate on Tool Life in Turning</b>	273
Ali ORAL, M. Cemal ÇAKIR, Demet GÖNEN, A. Deniz KARAOĞLAN	
 <b>Experimental Investigation of Double Point Angle Polycrystalline Diamond Drill Geometries</b>	283
Yiğit KARPAT, Onur BAHTİYAR	
 <b>Experimental Investigation of CGI Drilling Adapted with External MQL System</b>	297
A. Taner KUZU, U. Alican ALMA, Kaveh RAHIMZADEH BERENJI, Mustafa BAKKAL	

<b>Performance of Novel <math>\alpha/\beta</math>-SiAlON-TiN Ceramic Composites on High Speed Milling of Inconel 625</b>	309
Ali ÇELİK, Melike Sert ALAGAÇ, Uğur Evrensel YILMAZ, Alpagut KARA, Servet TURAN, Ferhat KARA	
<b>High Efficiency Elliptical Vibration Cutting of Hardened Steel with Large Nose Radius Single Crystal Diamond Tool</b>	321
Yilong WANG, Eiji SHAMOTO	
<u>Multi Axis Machining</u>	
<b>Verification of Cone Frustum Accuracy Test of Five-Axis Machining Center</b>	333
Toru TAJIMA, Tomohiro KUBO, Yukitoshi IHARA	
<b>Effect of Joint Stiffness on the Dynamic Performance of the Machine Tool</b>	345
Chih CHUNG, Faby FENG, Robert J. BENJAMIN	
<b>The Effect of Tool Orientation on Five Axis Ball End Milling of Ti6Al4V</b>	355
S. Ehsan LAYEGH K., İsmail LAZOĞLU	
<b>A Study of A Postprocessor System for A Hybrid Parallel serial Five-Axis Machine Tool</b>	365
Yuan-Lung LAI, Hsiao-Ying CHAN, Tzuo-Liang LO	
<b>Modelling of Turn Milling Processes for Increased Productivity</b>	381
Umut KARAGÜZEL, Emre UYSAL, Erhan BUDAK, Mustafa BAKKAL	
<u>Machine Tool Dynamics</u>	
<b>Mechatronic Spindle Head for Chatter Suppression in Heavy Duty Operations</b>	395
Iker MANCISIDOR, Jokin MUNOA, Rafael BARCENA, Xabier MENDIZABAL	
<b>Influence of the Spacer Clearance on the Dynamic Characteristics of A Spindle Tool</b>	415
Jui-Pin HUNG, Kung-Da WU, Chun-Wei LIN, Bing-Jie PENG	
<b>Comparison of Damping Properties of Spindle Bearings</b>	427
C. BRECHER, M. FEY, R. HABERMANN	
<b>Active Damping of Heavy Duty Milling Operations</b>	443
Robin KLEINWORT, Yusuf ALTINTAŞ, Michael F. ZAEH	
<b>A Model of Tool Point Dynamics Considering Effects of Bi-distributed Joint Interfaces</b>	459
Yun YANG, Min WAN, Weihong ZHANG	

## Process Modelling

### **Mechanics and Dynamics of Multi-Functional Tools** 469

Min WAN, Z. Murat KILIÇ, Yusuf ALTINTAŞ

### **The Mechanics of Double-Sided Milling Operation** 483

Z. Murat KILIÇ, Yusuf ALTINTAŞ

### **Workpiece Surface Burn Detection by Force and Temperature Modeling for Grinding Operations** 493

Deniz ASLAN, Erhan BUDAK

### **Force Model for Micro Milling of Free Form Surfaces** 515

Ali MAMEDOV, İ. E. YİĞİT, Ismail LAZOĞLU

### **Single Grit Scratch Tests to Explore the Material Removal Mechanism in Grinding at Micro Scale** 525

Tahsin T. ÖPÖZ, Xun CHEN

## Resource Management and Sustainability in Manufacturing

### **A Decision Support System for Selection of Bio-Materials** 541

M. Alper SOFUOĞLU, Sezan ORAK

### **Extended Models for Supporting CAPP- MES Integration in Discrete Production Systems** 555

Tibor TÓTH, Gyula KULCSÁR, Ferenc ERDÉLYI, Mónika Kulcsárné FORRAI, Péter BIKFALVI

### **Conceptualization of A Web-Based Software Platform that Enables Cleaner Production and Industrial Symbiosis** 571

Tuna Çağlar GÜMÜŞ, Christoph HUGİ, Dirk HENGVOSS, Sadık Engin KILIÇ, Murat ÖZBAYOĞLU, Hakkı Özgür ÜNVER

### **Investigation of Free-Form Surface Reconstruction Techniques for Reverse Engineering of Worn-Out Gas Turbine Blades: A Case Study** 579

Özgür POYRAZ, Oğuzhan YILMAZ, Evren YASA

## Smart and Intelligent Design, Design Models and Machines

### **Evaluation of A Scanning Technique used for Medical Design Applications** 595

Octavian CIOBANU, Gabriela CIOBANU

### **Bioinspired Transformation for Design of Biorobots** 605

Aylin Konez EROĞLU, Zuhail ERDEN, Abdulkadir ERDEN

<b>Development of An Autonomous Lawn Mower</b>	619
Serkan ÇİÇEK, E. İlhan KONUKSEVEN, A. Buğra KOKU	

<b>Design of A Humanoid Robot Spine Constructed of Asymmetric Parallel Mechanism Modules</b>	635
Ekim YURTSEVER, Şeniz ERTUĞRUL	

#### Industrial Applications

<b>Defects and Remedies in Advanced High Strength Steels Stamping</b>	647
Ilyas KACAR, Fahrettin OZTURK, Firas JARRAR	

<b>Recent Trends of Application of Advanced High-Strength Steels in Automotive Industry to Enhance Sustainability</b>	663
Suleyman KILIÇ, Fahrettin ÖZTÜRK	

<b>Noise in Hydraulic Systems and Prevention Methods</b>	675
H.Sevil ERGUR, Yasar PANCAR	

<b>Contamination Phenomena and Prevention Methods in Hydraulic Systems</b>	693
H.Sevil ERGUR	

### **VOLUME II**

#### Design for Machines and their Applications I

<b>Design and Validation of A Three-Axis High-Precision Positioning System from Mechatronically Modular Components</b>	711
Erva ULU, Nurcan GECER-ULU, Melih ÇAKMAKCI	

<b>Vibration and Bifurcation Analysis of Ultra Short Aero-lubricated Journal Bearing System</b>	726
C. C. WANG, H. T. YAU	

<b>Mechanical Structure Designs for Two Axis Solar Trackers</b>	736
H. Orhan YILDIRAN	

#### Machining

<b>The Tool-Chip Contact Length using A New Slip Line Solution for Orthogonal Cutting</b>	752
Shao-Hsien CHEN	

<b>Modelling of Cutting Forces in Face Milling Ti6Al4V Superalloy with a-CN/TiAlN Coated Carbide Tools</b>	762
Halil ÇALIŞKAN	

**The Effects of Cutting Parameters on Chip-Tool Interface Temperature and Surface Roughness in Turning of Waspaloy** 774  
M. Cemal CAKIR, Abdil KUŞ, Yahya IŞIK

Design for Machines and their Applications II

**A CPG Based Gait Generation for 12 dof Biped Robot (Birol) using ZMP Criteria** 788  
M.Hassan GOL.M.Z, Kutluk B. ARIKAN, Bülent İRFANOĞLU

**Innovative Virtual Machine Tool Design** 804  
Tzuo-Liang LUO, Chien-Chih LIAO, Z. Murat KILIÇ, Yusuf ALTINTAŞ

**Design and Analysis of A Parallel Mechanism for Kinematically Redundant Hybrid Planar Laser Cutting Machine** 810  
M. İ. CAN DEDE, Erkin GEZGİN, Gökhan KİPER, Ercan MASTAR, Tayfun SIĞIRTMAÇ, Emre UZUNOĞLU

Design for Production Processes

**Modelling Cone Angle Deformation of Microtubes in Flaring Process** 824  
Tsung-Chia CHEN, Wei-Kai CENG

**Fabrication of Microfluidic Devices for Dielectrophoretic and Acoustophoretic Applications using High-Precision Machining** 840  
Soheila ZEİNALİ, Barbaros ÇETİN, M. Bülent ÖZER, Süleyman BÜYÜKKOÇAK

**Micromachining with NS-Pulsed Fibre Lasers: Materials, Applications and Sectors** 850  
Ali Gökhan DEMİR, Barbara PREVITALI

**Experimental Investigation of the Process Parameters on the Forming Force for Single Point Incremental Forming** 860  
Barış ÖZGEN, İsmail LAZOĞLU, İsmail DURGUN

Design for Machines and their Applications III

**Contact Line Analysis of Worm Gearings Having Arched Profile** 874  
László DUDÁS

**Development of A Test System for Viscoelastic Material Characterization** 888  
Fulya EROL, Gökhan O. ÖZGEN, Halil ARDIÇ, Bilgehan ERDOĞAN, S. Samet ÖZKAN

**Robust Fuzzy-PID Control of An Unbalanced Quadrotor** 908  
Ahmed AKSAL, Kutluk Bilge ARIKAN, Fuad ALİEW



#### Advanced Materials in Manufacturing I

- Investigation of the Effect of Titanium (Ti) Addition to the Mg-Az31 Alloy in the Cast Condition and After Extrusion and Its Effect on Metallurgical and Mechanical Characteristics** 920

Adnan I. O. ZAİD, Raghad S. HEMEİMAT

- Effect of Molybdenum Addition to Zinc-Aluminum 22, Za22, Alloy on Grain Size and Mechanical Properties after Pressing by the Equal Channel Angular Pressing, ECAP** 934

Adnan I. O. ZAİD, Jihad A. S. ALKASASBEH, Safwan M. A. ALQAWABAH

- Effect of Zr Addition on the Mechanical Characteristics and Wear Resistance of Al Grain Refined by Ti after Extrusion** 948

Adnan I. O. ZAİD, Safwan M. A. ALQAWABAH

- The use of Superplastic TiN-Lead Alloy as A Solid Lubricant in Metal Forming Processes in General and in Forging in Particular** 962

Adnan I. O. ZAİD, Hebah B. MELHEM

#### Non-Traditional Machining Processes

- Copper Powder Reinforced Polyester Electrodes in Electric Discharge Machining** 976

Kemal YAMAN, Can ÇOĞUN

- Development and Analysis of Double-Faced with Radial and Cluster-arranged CMP Diamond Disk** 984

M. Y. TSAİ, C. H. CHEN, J. H. CHIANG

- Effects of Cutting Parameters on The Material Removal Rate and Surface Quality of Al 7075 in Turning Operation with Abrasive Waterjet Machine** 998

Muhammad A. HASAN, Mustafa DERE, İ. Hüseyin FİLİZ

#### Finite Element Analysis Applications in Design and manufacturing

- Finite Element Analysis of Finger Joint Implant** 1012

T. AZİZ, S. Saied DARWİSH, A. M. AL-AHMARİ, Hazem AL KHAWASHKİ

- Characterization of C67s Sheet Metal and Design of Manufacturing Steps with Finite Element Analysis** 1032

H. Onat TUĞRUL, D. Kivanç AKSUNGUR, Celalettin KARADOĞAN

- Implementation of Rate-and-State Friction Law in Finite Element Simulation of Sliding Motion using User-Defined Subroutine** 1049

Babak RAJİHAMED, Demirkan ÇÖKER

#### Advanced Materials in Manufacturing II

- Characteristics of Aluminum Foam Under Different Loading Rates** 1060  
A. A. HUSSEIN, W. M. CHAIRLADIES, A. A. KHALIL, A. A. NASSER

- Comparison Between the Effect of Zr Addition to Al Grain Refined by Ti or Ti+B on Its Mechanical Characteristics in the as Cast and After Extrusion** 1076  
Safwan M. A. ALQAWABAH, Adnan I. O. ZAID

- Particle Deposition in Resin Transfer Molding of Advanced Composites** 1094  
Tugce Aydil DALKIRAN, Hamed TANABI, Merve ERDAL

- Deformation of Super Alloys at Elevated Temperatures** 1104  
M. Oktay ALNIAK

#### Modeling and Analysis of Mechanical Systems

- Nonlinear Free Vibration Analysis of Nonuniform Rotating Double Walled Carbon Nanotubes** 1116  
Hamed SAMANDARI, Ender CİĞEROĞLU

- Characteristic of Anchor Embedded on Concrete Under Different Loading Rate** 1132  
Sh. M. ISMAEL, W. M. KHAIR-ALDIEN, A. A. KALIL, A. A. NASSR

- Contact and Bending Stress Analysis of Spur Gear Drives** 1150  
Sadık OLGUNER, İ. Hüseyin FİLİZ

#### Modeling and Analysis of Failure in Mechanical Systems

- A Study of Some Three-Dimensional Issues in Modified Arcan Loading Device Under Mixed-Mode Loading Conditions** 1162  
Abuzar ES'HAGİ OSKUI\*, Naghdali CHOUPANI, Morteza SOLTANPOUR KHAMNEH

- Dynamics Behavior Analysis of Cracked Shaft in Rotating Machinery** 1174  
Hamit SARUHAN, Fikret POLAT, Mert KILINÇEL

- Void Coalescence through Internal Necking: Thomason's Criterion Revisited** 1184  
Cihan TEKÖĞLU, Sanaz ATTARI, Jean-Baptiste LEBLOND, Thomas PARDOEN

- Experimental Vibration Analysis of Simulated Shaft Crack** 1196  
Hamit SARUHAN, Mert KILINÇEL, Fikret POLAT

## **TÜRKÇE BİLDİRİLER**

### **Endüstriyel Uygulamalar**

**Kalıp Değişimlerinde Hidrolik Sabitleyici Kullanılmasının Avantajları** 1212

Ersel ÖZDEN, Ebru TAŞKIN, Orçun YÖNTEM, R.Güçlü ARIKAN

**Otomotiv Endüstrisinde Kullanılan 3 Boyutlu Parçaların Kesimi için Lazer Kesim Tezgâhları** 1226

Hakan DEMİR, Tayfun SİĞİRTMAÇ

**Hotmelt Teknolojisi ile Enkapsülasyon Uygulaması ve Elektronik Donanım Gövdelendirme Örnek Proses İncelemesi** 1246

Burhan ÖZÜĞÜR, Serhat APAK

**Düze Ana Delik Çap Değerlerinin Hava Akımı ve İplik Tüylülüğü Üzerindeki Etkileri** 1258

D. YILMAZ, M.R. USAL

### **Mekanik Yapılar ve Analizleri**

**Takım Tezgâhlarındaki Bilyalı Vidalı Mil Hareket Sisteminin Eksenel ve Burulma Titreşimlerinin İncelenmesi** 1272

Muhammet ERDÖL, Hasan KURTARAN

**Petek Yapılı Sandviç Yapıların Dinamik Özelliklerinin İncelenmesi** 1284

M. Fatih ŞANSVEREN, Alparslan YİĞİT, Mustafa YAMAN

**Alüminyum Matrisli Fonksiyonel Derecelendirilmiş Malzemede Çatlak İlerleyişinin Deneysel Analizi** 1296

Arzum ULUKÖY, Muzaffer TOPÇU, Süleyman TAŞGETİREN

**Metal Şekillendirme Prosesi Üzerinden Geri Esneme Telafi Yöntemlerinin İncelenmesi** 1314

Emre ESENER, Mehmet FIRAT

### **Yeni ve Alışılmamış İmalat Yöntemleri**

**Elektrolitik ve Alaşım Bakır Elektrotların Elektro-Erozyon ile İşleme Performansına Etkisi** 1322

Ülke ŞİMŞEK, Can ÇOĞUN

**Saç Modelleme: Fonksiyonel Parçaların İmalatı İçin Eklemeli İmalat Yöntemi** 1338

Uğur ERKEN, Hasan Erdem HARMAN, Serdar SEÇKİN, Emin Faruk KEÇECİ

**Lazer Oyma İşleminin WC-Co Yüzey Özelliklerine Etkilerinin Araştırılması** 1354

Şefika KASMAN, İ.Etem SAKLAÇOĞLU

## Talaşlı İmalat

- Sert Malzemelerin Tornalaması İşlemlerinde Takım Aşınmasını Etkileyen Faktörlerin Tepki Yüzeyi Metodolojisi ile Belirlenmesi** 1368  
Dilek MURAT, M. Cemal ÇAKIR, Necmi GÜRSAKAL, Ali ORAL
- 55 HRC Sertlikteki AISI H13 Takım Çeliğinin Yüksek İlerleme ile Frezelenmesinde Oluşan Takım Aşınması - Kalıcı Gerilme İlişkisinin Araştırılması** 1380  
Selim KOCA, M. Cemal Çakır
- Farklı Soğutma Şartları İle Farklı Kesme Parametrelerinin AA7075 ve AA2024 Alüminyum Alaşımlarında Delik Delme İşlemlerine Etkisinin Deneysel Olarak İncelenmesi** 1396  
Ayşegül ÇAKIR, Onur BAHTİYAR, Ulvi ŞEKER
- AISI H13 Takım Çeliğini Yüksek Hızlı İşleme Parametrelerinin Taguchi Yöntemiyle Optimizasyonu ve Yapay Sınır Ağlarıyla Yüzey Pürüzlülüğü Tahmini** 1412  
Mustafa HAMAMCI, E. Sabri TOPAL

# PAPERS





## UNIVERSITY– INDUSTRY RESEARCH PARTNERSHIP MODELS IN MANUFACTURING ENGINEERING

**Yusuf ALTINTAŞ**, Professor, F-RSC, F-ASME, F-SME, F-CIRP, F-CAE, F-CE.

*altintas@mech.ubc.ca*, Manufacturing Automation Laboratory, University of British Columbia, V6T1Z4, Vancouver, Canada [www.mal.mech.ubc.ca](http://www.mal.mech.ubc.ca)

### ABSTRACT

This paper presents a survey of university – industry research models practiced in North America, Europe and Asia. While universities value scholarly research that leads to archival journal publications with high impact, industry considers only the development of innovative and practical methods which reduce the cost of producing the parts. The author believes that the university researcher cannot try to replicate the practices of engineers in industry. Instead the researcher must try to develop new, science-based methods which lead to archival journal articles, while transferring knowledge to industry by training highly- qualified specialists and packaging the scientific know-how in industry-friendly formats.

**Keywords:** University, Industry, Partnership, Research

### 1. INTRODUCTION

There have been constant arguments when describing the interaction between academics and industry. Industry desires quick solutions from academics for their daily production problems. Production managers often accuse academics of not being as experienced and as practical as their shop floor engineers. They expect to see magic fixes to their daily problems in a short time period. The measurement of success in industry is to solve the problem in a shortest time with minimum cost. On the other hand, academic success is measured by the number of high quality scientific papers written, and the number of graduate students trained. The solution to an industry problem is considered to be added bonus to their success; hence the contribution to industry plays a secondary role in academia. The perception is almost the same in production engineering worldwide except in pure scientific knowledge based industries, i.e., pharmaceutical, electronics, aerospace and instrumentation design disciplines. This paper will focus on various research infrastructure models world-wide, and production engineering laboratories are used as an example. The paper provides



the details of the author's research infrastructure and operating principles to reflect his experience as an academic with industrial interaction.

## 2. RESEARCH FUNDING CATEGORIES

Research funding schemes are almost the same in all countries, and can be classified as follows:

- A. Basic Research Funding from Government Science Foundations:** The research needs to be fundamental, pre-competitive and must contribute novel findings and discoveries proven by publishing in peer-reviewed archival journals. The grant application is confidentially reviewed by experts, and usually a panel recommends the approval or rejection of the application. The researchers must show the impact of the resulting research on industry and society in the long run, and the application needs to be supported by letters and in some cases, by minor cash contributions from industry. Such research grants are instrumental and essential to train doctoral students without constraining research freedom with industry pressure. The results are expected to be published in open literature, and all intellectual properties created would belong to the university. The researchers receive shares earned from the royalty income.
- B. University – Industry Partnership Grants:** The research is jointly funded by industry and government science foundations, usually with 50%-50% cash contributions. The grant application is prepared by the professor at the university but supported by a company or a group of companies with cash and in-kind support. The university and companies must have a legal agreement which covers the ownership of the intellectual properties to be created; the publication rules and confidentiality of company secrets need to be clarified in the legal agreement, a process which can be quite challenging and time consuming.
- C. Industrial Research Contracts:** The research project is designed completely to benefit the company which pays 100% of the project cost plus overhead to the university. The results are usually screened by the company which may delay or prevent the publications, and hence the professor must be very careful in assigning graduate research students to such fully company-supported projects. From the university point of view, the research must still lead to new knowledge which belongs to the academic institution, but privileged licensing conditions are usually granted to the company which paid for them.





**D. Service Contracts:** A university research laboratory may have the expertise and instruments to test and study engineering problems using existing knowledge. A company may wish to use the laboratory for testing to receive the results quickly, and these are non-research services offered by the laboratory. The company pays 100% of the cost plus university overhead, and the results are usually confidential for the company. Such activities do not lead to a master's or doctoral thesis, but usually brings income to the laboratory, and brings the company and researcher together for future research collaboration.

The following sections describe how these funding mechanisms are used by different countries and culture.

### 3. RESEARCH INSTITUTE MODEL OF GERMANY

Germany has a centuries-long engineering culture with the closest interaction between universities and industry. There are two forms of German research units at universities: Chairs and Institutes. The institute is the extended version of a chair. It has an managing board and a different financial and personal structure such as several professors can be part in an institute. Typically, a specialized field is managed by a research institute led by a senior Chair professor (i.e. Lehrstuhl). There can be additional professors in the institute with complimentary expertise. For example, Machine Tools and Production Engineering Institute (WZL) at Technical University of Aachen has four chair professors covering machine tools, processes, metrology and production management fields. In production engineering, the professor is desired to have a minimum of five years' industrial experience as an engineering manager. Once the professor is appointed, the position is permanent until retirement, hence the selection process must be handled very carefully to ensure a success. Recently, Germany introduced three yearlong "Junior Professor" positions to prepare them for larger academic roles while assisting the chair in research. The university provides a laboratory space, an operating budget, secretarial-staff, technicians and salaries for several research assistants. This basic university support is provided to ensure the teaching of subjects which are assigned to the institute as its core responsibility. The size of the operating budget depends on the number of students who need to be trained by the Chair in lectures, tutorials and laboratories. The Chair is expected to bring research and development funding from government agencies and industry, which will enable the institute to hire more research assistants and equip the laboratory with the state-of-the-art instruments. A Chair is expected to earn research funding that supports an average of several doctoral assistants in Germany. A highly successful Chair may have about fifty doctoral assistants, one hundred master's

students and paid undergraduate laboratory students. In such a scheme, the professor acts as a research manager. As the director of a research laboratory, the professor is expected to understand the field as an expert and give sound but high-level directions in research. Such a large operation and infrastructure requires a special management structure in the institute, as in **Error! Reference source not found.** Each major research field, such as machine tool structures and vibrations, automation and control and CAM divisions may be managed by dedicated chief engineers who either have doctoral degrees or senior doctoral assistants. Each chief engineer creates several research groups dedicated to different sub-disciplines, and led by group leaders who are also doctoral assistants. A number of research assistants, the doctoral students, report to group leader. Each assistant in the group is responsible for a specialized research topic which is usually her/his doctoral thesis. After one year of support, the assistants are expected to solicit research funds from grants and/or industry. Once the research proposal is established, the assistant asks for approval of the project upwards along the hierarchy: to the group leader, chief engineer and the professor. The doctoral assistants are called research scientists rather than graduate students in the German system, because they have to work on all projects which bring research funds to the institute. There are slight variations in each institute depending on the university policies and chair professor's style.

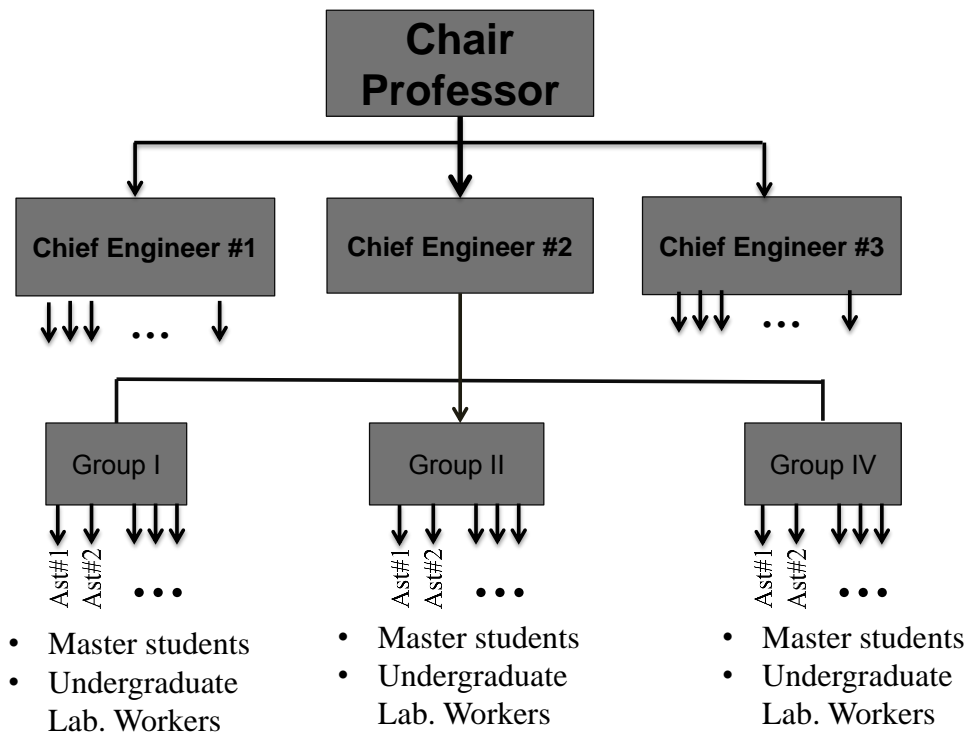


Figure 1 A general structure of a research laboratory in Germany.



Typically, senior doctoral assistants survey the best possible grant and/or contract sources, and start the initial investigation and contacts. The general expectation is that approximately 30% of the funds need to be raised from the government (**DFG: Deutsche Forschungsgemeinschaft**). DFG funds are used for fundamental research (**Category A**) without having to show a direct application in industry. The grant or research contract application is started by the research group leader and the chief engineer, and submitted to the professor for consultation and approval. DFG funds are highly competitive and are used for basic research, which must lead to archival publications with strong scientific content. The companies value high-level engineering and technology, and are heavily involved in collaborative research projects with the universities. The university assistants try to transfer the knowledge to collaborating companies as much and as efficiently as possible. The assistant hires master's and undergraduate students to conduct experiments, study algorithms, develop software and create charts/drawings. The junior students gain strong experience while earning an hourly income, and the assistant acts both as a research scientist and a manager by supervising the personnel and the research project, while handling all meetings, reports and financial matters with the company. The doctoral assistants do their best to transfer the technology to the company under the research contract with the institute. A doctoral assistant tries to find contracts which are related to their thesis topics. The assistants not only learn the research steps, but also gain significant experience in managing the projects with industry. When they graduate with doctoral degrees, they are usually hired as a leader or engineering manager in industry. They develop strong networks with companies who are involved with the specialized field of their projects.

German institutes also accept research and service contracts (**C,D**) regardless of the size of the funding. The assistants are not treated as graduate students, but as scientific staff with engineering salaries. They have to raise funds for the institute to earn their salaries. The assistants in Germany receive broader engineering training with strong project management skills, but their scientific depth is not as strong as their counterparts in North America.

#### 4. RESEARCH LABORATORY MODEL OF JAPAN

The Japanese research laboratory is the mini version of German Institute. The laboratory has a senior professor, a secretary, a technician and a junior assistant or associate professor, who are all paid by the university. The professorial appointments are life-time. The university gives a fixed budget to the laboratory to maintain the basic equipment, office expenses and to teach the basic courses which are assigned to the laboratory.



In the past, the research funding always used to come from the government (A), hence the research was always fundamental in nature, leading to journal publications in open literature. Industry used to donate equipment and help the laboratory with some research gifts and support, based on a personal relationship with the professor. However, Japan recently started to adopt a more North American style. The universities have to compete for industrial funds through university – industry partnership grants (B) and bring research contracts from companies to laboratories. Direct government funds are more attached to the university-industry partnership grants (C). The training of master's and doctoral assistants is similar to the training in North American Universities, and they are not involved in writing research grant and industrial contract proposals. Instead, the professor and junior professor are involved in bringing in research funds, and they supervise both the projects and students. As a result, Japanese laboratories do not work on service contracts or apply the research know-how for a company directly. Usually, the engineers in a company study for their master's and Ph.D.'s part-time with the professor, and hence learn and apply the knowledge directly in their company during the process.

## **5. RESEARCH LABORATORY MODEL OF NORTH AMERICA**

The North American laboratory system is totally different from the systems in Germany, Japan and elsewhere in the world. The professors are ranked as assistant, associate or full professors but each is totally independent with their own dedicated, and in a way personal, laboratory. An assistant or sometimes associate professor is hired with a “tenure-track” appointment. The performance of the tenure-track faculty member is monitored for the first three years, and if progress is satisfactory, an additional four-year appointment is granted. Otherwise, the tenure-track faculty member's appointment is terminated (i.e. fired!). If the appointment is renewed, the file is closed at the end of year six, and sent to the university and external committees for review and assessment. Tenure-track faculty must have a good teaching performance, and the teaching evaluations issued by the students must be better than the faculty average. Research success is measured by the number of graduate students trained, the number and quality of journal papers published, and the amount of research funds raised by the tenure-track faculty. Contributions to university administration and professional engineering societies, the awards received for teaching, papers and contributions to the profession are also considered in evaluating the candidate. The file of the candidate along with the four best journal papers is sent to at least four confidential referees for their independent academic evaluations. When all the data is collected about the candidate, the case is discussed within the department, followed by faculty and university committees in sequence. If the file is rejected, the academic appointment is terminated



permanently, and the faculty member is given a notice to leave the university. This is called “losing tenure”. If tenure is granted, the faculty member is promoted to an associate professorship with a permanent appointment in the university.

Professors must bring all of the research funds from outside the university, and must pay for all research costs as well as the salaries of their master’s and doctoral assistants. Expenses include shop, computer, technician, instrumentation, telephone, travel, repair and consumable materials (and even for paper in my department). Naturally, if the professor cannot raise any research funds, it is impossible to hire assistants and purchase instruments to conduct research. The university does not provide any research support, but deducts 25% to 60% of the funds as overhead for the use of laboratory space of the university. As a result, North American professors work desperately to win competitive research grants from the National Science Foundation (NSF) in the USA, and the Natural Sciences and Engineering Research Council of Canada (NSERC). NSF and NSERC grants are peer-reviewed and prestigious with about a 10-15% success rate, and each faculty member is expected to win these grants before they are granted tenure. The professors try their best to get NSF – NSERC grants for fundamental research (A), but also have to pursue university – industry partnership grants and research contracts from industry. Similar to Germany, American companies value the technology and do not mind investing in new research ideas at the university. Canadian industry tends to be more conservative and spend less cash on university research. An average professor is expected to support about five graduate students at a time, and closely supervise their theses. The laboratory is usually created by the professor, and when the professor retires or leaves for another university, the department may shut it down, or replace it with another field and professor. There is no institute culture in North America, and the laboratory is always associated with the professor who runs it.

## **6. MANUFACTURING AUTOMATION LABORATORY AT UBC**

The author is a professor in Canada, and hence he has to follow the North American system at his university. He joined the University of British Columbia (UBC) in 1986 with an \$8000 startup fund from the university, and a \$22,000 equipment grant and a \$19000 per year research grant from NSERC (the Canadian research granting agency for university researchers). The laboratory was completely empty except for a 25-year-old non-operational milling machine with a junk value of \$500. The author graduated one Ph.D. and five Master’s, and published 7 journal papers with his students in four years, and received both tenure and promotion at the end of year five (1991). In addition to the \$19000 per year general research grant from NSERC, he received one university – Pratt & Whitney Canada Inc. research



partnership grant for three years (\$150,000 in total). He also taught manufacturing processes, solid mechanics, vibrations, CAM and a graduate course in machine tool vibrations and control during this period. He spent eight months in Germany for his sabbatical study leave, and learned the German institute culture. However, it is impossible to have such a system in North America which has a totally different culture and mechanism as explained above.

The laboratory started to grow mainly by successfully winning NSERC grants for fundamental research which started to receive high recognition from international academic peers. He became a full professor in 1996 with 33 journal articles, two graduated Ph.D's and three in process, and about 15 Master's graduates. He started to receive more university – industry partnership grants from NSERC in collaboration with Boeing, Pratt & Whitney Canada and General Motors as of 1996. The laboratory now has a CMM and 5 CNC machines, two of which were donated to our laboratory based on our reputation. We built our own CNC (first out of poverty, and later for basic research), a high-speed CNC micro machining center built in-house, and four ball screw and linear motor driven tables. The laboratory has all basic research instruments such as a laser interferometer, a ball bar, a laser vibrometer, vibration and modal testing instruments, a profile-meter, a tool microscope and 7 stationary and rotating dynamometers.

Although the author has a wide network of large international companies from all parts of the world, he receives most of his research funds from NSERC through highly competitive peer reviewed grants. His success rate is very high because of the quality of the proposed projects with strong scientific focus and originality, and past history of successful results from the laboratory. The author has published 141 journal articles, 95 peer-reviewed conference papers and a widely-used textbook. His overall publications have received over 12300 citations (Google Scholar in April 2014) with an h index 60, and his journal publications alone have received 6700 citations with an h index of 46, which appears to be the highest in his field of expertise worldwide. In short, the author is trying to send the message that high quality basic research with industrial relevance can lead to a successful academic career. It is important to select excellent graduate students who can work in a team with a passion for the field, and close supervision of the students is the first requirement followed by the rigorous study of details in research.



The current research and laboratory structure of the Manufacturing Automation Laboratory is shown in Figure 2. The professor receives weekly progress reports from all members of the laboratory on Thursday evening, and holds weekly group meetings on Friday mornings. Research issues are discussed, and if there is substantial progress, the member involved gives a twenty minute research presentation to the group. The professor visits the laboratory

## MANUFACTURING AUTOMATION LABORATORY

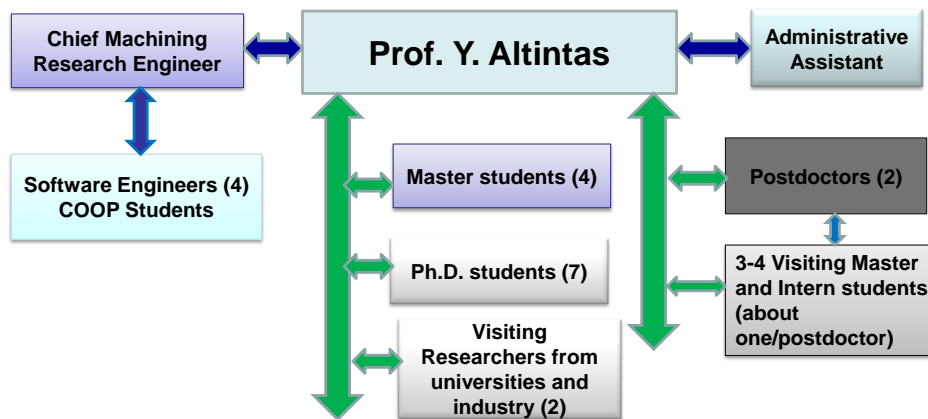


Figure 2. The structure of Manufacturing Automation Laboratory (MAL) at UBC. All students and staff are paid from research grants and contracts.

every day, and the students can walk into his office at any time to discuss the research.

The research proposals, grant applications, research contracts with industry and lecture notes are all prepared by the professor. The students work only on basic research related to their thesis, and do not have any obligation towards the companies, nor do they develop any industrial software during their thesis research. They draft the research paper, and the professor edits it with a number of back and forth revisions until it is submitted to a journal for review. Journal papers are always given priority, and conferences are attended only by invitation or through strong networking with other well-established researchers. MAL graduated 13 Ph.D. students from UBC directly, and 9 of them became professors: in Canada (3), Turkey (1), USA (3), Sweden (1) and Iran (1). Also, 10 Ph.D. students completed all of their research at MAL, but graduated from their home universities in Turkey (1) and China (9). All became professors except one who is in industry but who also works as an adjunct professor in Canada. MAL graduated 45 Master of Applied Science (research) and 37 project Master's students from UBC, and 24 visiting Master's from Europe who are the equivalent to UBC's project master's degrees. MAL has trained 28 Postdoctoral Fellows





and the majority were sent to UBC funded by their governments with little in the way of research contributions to MAL. There have been around 5 Postdoctoral Fellows from MAL who had the necessary expertise and contributed to supervision and publications. MAL has also trained 22 research engineers, 23 visiting engineers and fellows, and 45 visiting and undergraduate students since 1987. The laboratory currently has 7 Ph.D., 3 M.A.Sc. and 2 M.Eng. students; two postdoctoral fellows, and five research engineers. The chief engineer is in charge of maintaining laboratory equipment, and supervising research engineers and software engineers who package research algorithms for technology transfer to industry. The laboratory brings in approximately \$600,000 cash per year, with \$250,000 raised from industry through university – industry research partnership and technology transfer-based research contracts. Industry also donates approximately \$150,000 per year in equipment and tools. The administrative assistant supports the Canada wide machining research network ([www.nserc-canrimt.org](http://www.nserc-canrimt.org)). MAL has created several virtual machining, machine tool and CNC design software products which are used worldwide in industry and academia. CUTPRO<sup>™</sup> is an advanced machining process analysis, simulation and measurement tool kit. The measurement tool kit includes data acquisition, impact modal testing and experimental modal analysis modules. The machining modules include milling, turning, drilling and boring which predicts the chatter-free cutting conditions, forces, torque, power, vibrations and dimensional machining surface errors for a given tool geometry and the material and dynamics of the machine. CUTPRO concept is integrated to CAM systems for part machining process simulation and optimization using NC codes and part geometry (MACHPRO). SpindlePro is a non-linear Finite Element software which allows the designer to virtually test the conceptual spindle configurations for bearings in simulated cutting conditions. The Virtual CNC is a MATLAB Simulink based, 5-axis CNC design and analysis tool kit that works both in virtual and real time on the machine tool. The Virtual CNC is an open research platform to test trajectory generation, axis control, contouring error control and active damping of machine tool vibrations. The details can be found in [www.malinc.com](http://www.malinc.com).

## 7. CONCLUSION

The university – industry research partnership needs to be different from pure university-based research and also pure industrial development. When a graduate student is involved in any research project, the confidentiality and direct application of know-how on the company products should be avoided to ensure high quality, scholarly research. The company must understand that this is university-based research, and must treat the research project differently than their daily development activities. The university professor must be careful not to promise practical deliverables which can be applied directly and quickly by the





company. A fine balance must be kept in designing the university – industry partnership projects. The professor must always search for public funds to conduct basic, unconstrained research which leads to publications in the most prestigious journals in order to be recognized as a world class researcher. The balance must be always heavier on the side of academic contributions in university-based research, because that is the fundamental task of professors.

## **ACKNOWLEDGEMENT**

Prof. Erman Tekkaya, Chair Professor of Institute of Metal Forming and Lightweight Components at Technical University of Dortmund provided valuable feedback on German Institute System. The author also spent two sabbatical terms at RWTH Aachen, WZL.





## **PERFORMANCE INCREASE OF COATED CUTTING HM-TOOLS BY ADAPTING THE CUTTING CONDITIONS TO THE FILM PROPERTIES**

**K.-D. Bouzakis**, bouzakis@eng.auth.gr, Laboratory for Machine Tools and Manufacturing Engineering, Aristoteles University of Thessaloniki, Thessaloniki, Greece

**G. Skordaris**, gskor@eng.auth.gr, Laboratory for Machine Tools and Manufacturing Engineering, Aristoteles University of Thessaloniki, Thessaloniki, Greece

**E. Bouzakis**, e.bouzakis@certh.gr, Laboratory for Machine Tools and Manufacturing Engineering, Aristoteles University of Thessaloniki, Thessaloniki, Greece

**R. Paraskevopoulou**, paraskeu@auth.gr, Laboratory for Machine Tools and Manufacturing Engineering, Aristoteles University of Thessaloniki, Thessaloniki, Greece

**G. Katirtzoglou**, geokatir@gmail.com, Laboratory for Machine Tools and Manufacturing Engineering, Aristoteles University of Thessaloniki, Thessaloniki, Greece

**S. Makrimalakis**, makrimalakis\_s@eng.auth.gr, Laboratory for Machine Tools and Manufacturing Engineering, Aristoteles University of Thessaloniki, Thessaloniki, Greece

**P. Charalampous**, paschalischaralampous@gmail.com, Laboratory for Machine Tools and Manufacturing Engineering, Aristoteles University of Thessaloniki, Thessaloniki, Greece

### **ABSTRACT**

The optimization of cutting conditions, when using coated tools, is associated with not negligible experimentation cost. Sophisticated coatings' characterization procedures reduce this cost. In the paper, examples highlight such innovative procedures, facilitating the adaption of cutting conditions to the film properties. The heat resistance of the interfaces of Nano-Composite Diamond coatings is characterized by successive impacts at ambient and elevated temperatures. The fatigue strength of PVD-films at high strains and strain rates, an important parameter for milling operations, is evaluated by repetitive impacts of various durations. Furthermore, the coating brittleness, also pivotal for milling is assessed by nano-impact tests.

**Keywords:** PVD coatings, NCD films, fatigue, brittleness, wear



## 1. INTRODUCTION

In material removal processes with coated tools, the wear mechanisms may vary, depending on the properties of the film and its interface to the substrate, thus leading to potentially unexpected tool life deterioration, complicating the cutting conditions optimization [1,2,3,4,5,6]. In figure 1 methods for determining material, dimensional and functional data of coated tools are displayed [1]. Combinations of these procedures jointly with FEM

PROPERTIES		TEST METHODS																		
		EDX	SEM	XRD	TEM	...	NI	...	NIT	IT	ITMFS	BC	WLS	IIT	S	NS	RC	DiF	OX	TRM
Material	Structure	√	√	√	√															
	Residual stresses			√																
	Mechanical properties						√													
	Hardness						√													
	Brittleness								√											
	Fatigue									√										
	Fatigue at high strain rates										√									
Dimensional	Thickness											√								
	Thickness distribution on the cutting edge												√							
Functional	Friction																			√
	Adhesion													√	√	√	√			
	Diffusion																	√		
	Chemical stability																		√	

EDX: Energy-dispersive X-ray spectroscopy  
SEM: Scanning Electron Microscope  
XRD: X-ray Diffraction  
TEM: Transmission Electron Microscopy

NI: NanoIndentations  
NIT: Nano-Impact Test  
IT: Impact Test  
ITMFS: Impact Test with Modulated Force Signal  
BC: Ball Cratering Test  
WLS: White light scanning 3D measurements

IIT: Inclined Impact Test  
S: Scratch test  
NS: Nano-scratch test  
RC: Rockwell C  
DiF: DiFusion test  
OX: Oxidation test  
TRM: TRiBoMeter

Figure 1. Characteristic methods for determining coating material, dimensional and functional properties.

computations contribute to the explanation of the cutting tool films' failure mechanisms, thus restricting the experimental cost for optimizing cutting conditions. In the paper, characteristic examples of such innovative experimental-analytical test procedures are described for determining the interface fatigue strength of NanoCrystalline Diamond coatings (NCD) at ambient and elevated temperatures, the fatigue strength of PVD-films at high strains and strain rates and the brittleness of mono- and multi-layered PVD films. The developed procedures allow the prediction of the coated tool performance and the adaption of the cutting conditions to the film properties.

## **2. FATIGUE STRENGTH OF NCD COATINGS' INTERFACE AT AMBIENT AND ELEVATED TEMPERATURES**

The fatigue strength of nanocrystalline diamond coatings (NCD) deposited on cemented carbide inserts is a key factor for ensuring a long life-time of NCD coated tools in milling of non-ferrous materials like Al-Si alloys [7]. Prior the NCD coating deposition on cemented carbide substrates, appropriate treatments are conducted for reinforcing the bonding region of the film, thus possessing sufficient fatigue strength to withstand successfully the repetitive cutting loads [7,8,9]. NCD coatings on hardmetal tools are characterized by high residual stresses due to their significantly smaller thermal expansion coefficient compared to its cemented carbide substrate [2,10]. In this way, compressive stresses are developed in the film structure during cooling of NCD coated specimens from CVD process temperature to ambient one [2,10].

The temperature dependent fatigue strength of interface regions of NCD coatings with thickness of ca. 5  $\mu\text{m}$  were investigated by inclined impact tests at ambient temperature and at 300°C, as it is shown in figure 2. The employed impact tester device was designed and manufactured by the Laboratory for Machine Tools and Manufacturing Engineering of the Aristoteles University of Thessaloniki in conjunction with CemeCon AG (see figure 2a). The load signal duration  $t_d$  and impact time  $t_e$  are displayed in figure 2b. These were practically constant in all carried out experiments. The applied force increases progressively up to a set maximum value. As it can be observed, depending upon the applied load, after a certain number of impacts, damages in the film interface region develop resulting in coating detachment [2]. In this way, residual stresses of the film are released leading to its lifting (bulge formation). The bulges are destroyed by further repetitive impacts and the coating is totally removed. When the NCD coated tools are heated at a temperature of 300°C, the film interface damage is initiated at a comparably lower threshold load and number of impacts.

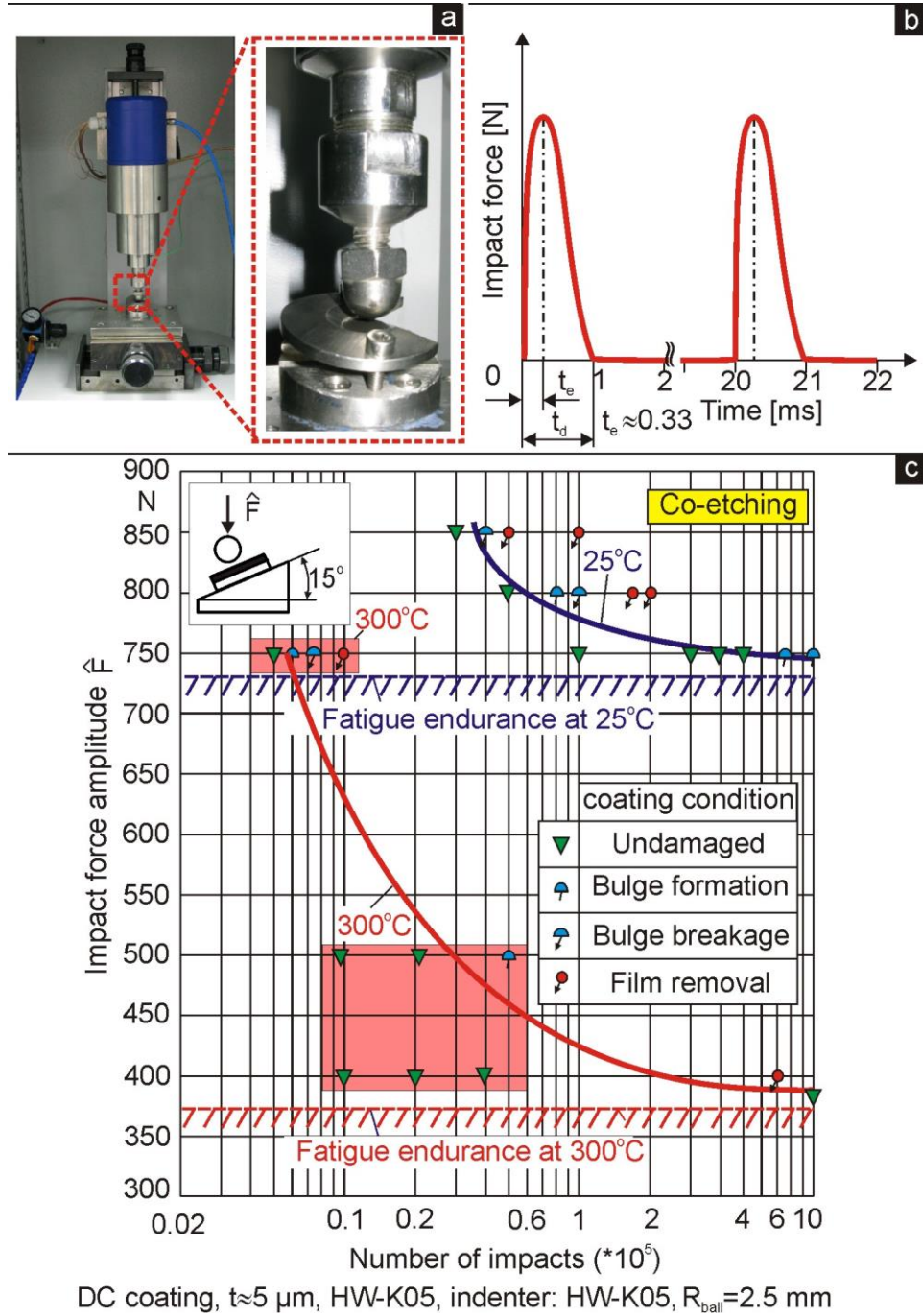


Figure 2. (a) The mechanical unit of the employed impact tester (b) Characteristic data of the applied force signals (c) NCD coating conditions after the inclined impact tests at various loads and number of impacts at ambient temperature and at 300°C.

Characteristic developed film bulges of the heated NCD coated inserts at an impact load of 750 N, after various numbers of impacts, which were scanned by white light via confocal measurements, are illustrated in figure 3. The graphs capture the surface topomorphies after the indicated number of impacts. Even at the limited number of 6000 impacts, a film bulge formation of 12  $\mu\text{m}$  height occurs due to the interface fatigue failure. Moreover, after 7500

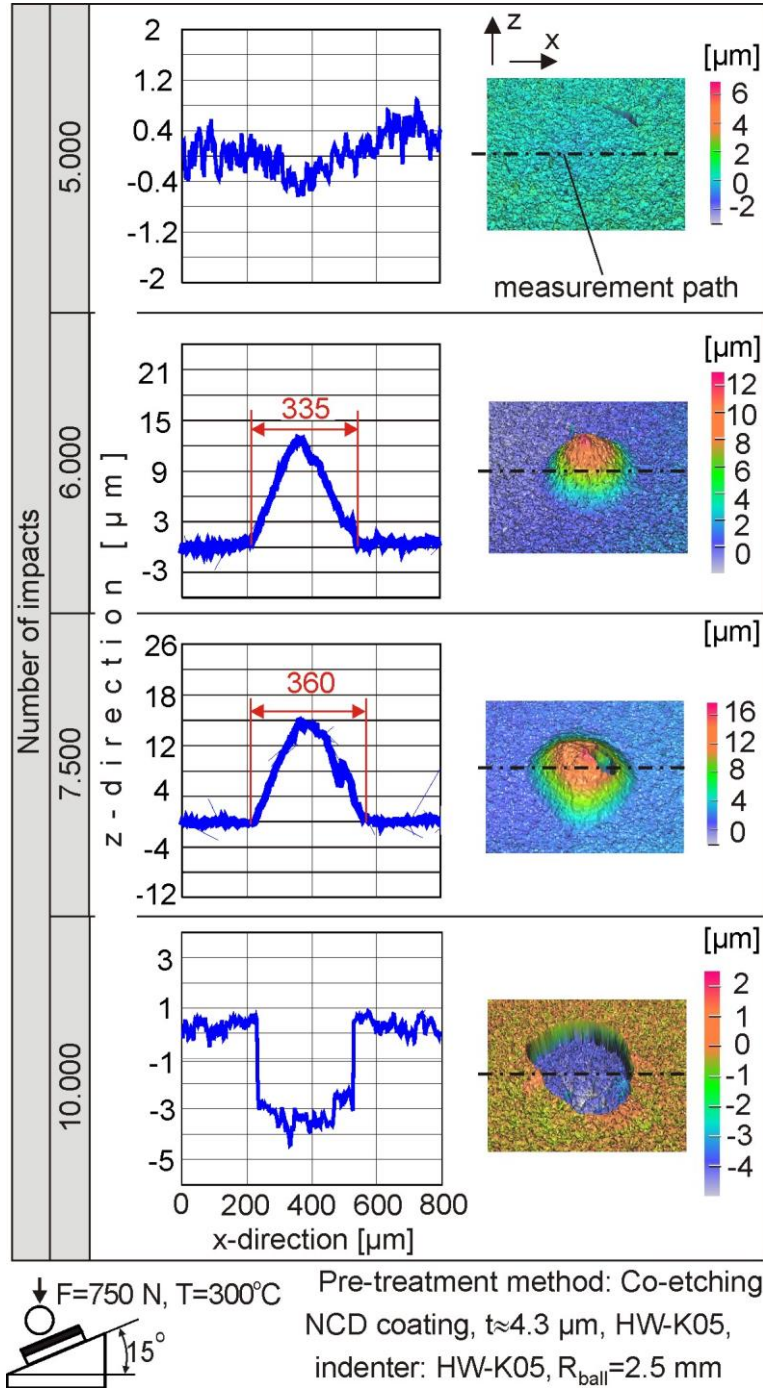


Figure 3. Impact test results at an impact load of 750 N after various numbers of impacts at 300°C.

impacts, the formed bugle is partially broken, whereas after 10000 impacts the entire bulge is removed. The consequence of this behavior is that on the one hand, such coated tools can be successfully applied in cutting operations of composite materials with hard fibers, whereas the cutting temperatures remain at a low level. On the other hand, in cutting aluminum alloys, the developed tool temperatures commonly reach 300°C. Thus, such tools become inappropriate for these operations.



### 3. FATIGUE STRENGTH OF PVD-FILMS AT HIGH STRAINS AND STRAIN RATES

In milling, impact loads with variable magnitudes and durations are subjected to coated cutting edge, which may lead to fatigue failure of the applied film and subsequently intensive tool wear [3,5,6]. Via impact tests with adjustable force signal characteristics, the applied loads can simulate the developed ones in milling when the cutting edge penetrates the workpiece. In this context, a novel impact tester which facilitates the modulation of the applied impact force versus the time was developed. The impact tester arrangement is exhibited in figure 4a and it is thoroughly described in [11]. The attained coated tool life in milling can be associated with the developed maximum strain and its rate in the film during milling. The latter factors can be correlated to the strain and strain rate dependent coating fatigue endurance. Based on these dependencies, the tool life can be sufficiently explained in various milling kinematic cases. A characteristic example is shown in up-and down-milling stainless steel [3].

The fatigue endurance strains of the applied TiAlN coating are monitored in figure 4b depending upon the impact time and the impact force amplitude. At constant impact force amplitude, the reduction of the impact time  $t_e$ , i.e. the strain rate increase, diminishes the resulting strain. This tendency is graphically presented at an impact force amplitude of 155 daN in the diagram at the bottom of figure 4b. The strain decreases, as the strain rate grows. At strain rates less than approximately  $3 \text{ s}^{-1}$ , the developed strain remains constant. Hence, in the considered case, this strain rate corresponds to the limit between static and dynamic film loading. With the aid of such diagrams, the strain rate effect of the resulting strains in a dynamically-loaded coating can be estimated. In this way, the film fatigue critical strain depends on the relevant strain rate. Based on the results exhibited in figure 4b, strain and strain rate combinations, leading to film fatigue damage after one million impacts can be determined analytically [11]. These fatigue critical strain and strain rate combinations are described for the applied coating by the almost straight line displayed in figure 4c.

Taking into account the previously described dependencies, the experimental results in milling stainless steel can be explained based on a correlation between the accumulated tool life and the cutting edge entry impact average duration (see figure 5) [3]. The latter parameter can be calculated considering the cutting time up to the maximum equivalent strain developed in the coating [3]. For determining the cutting edge entry impact duration in



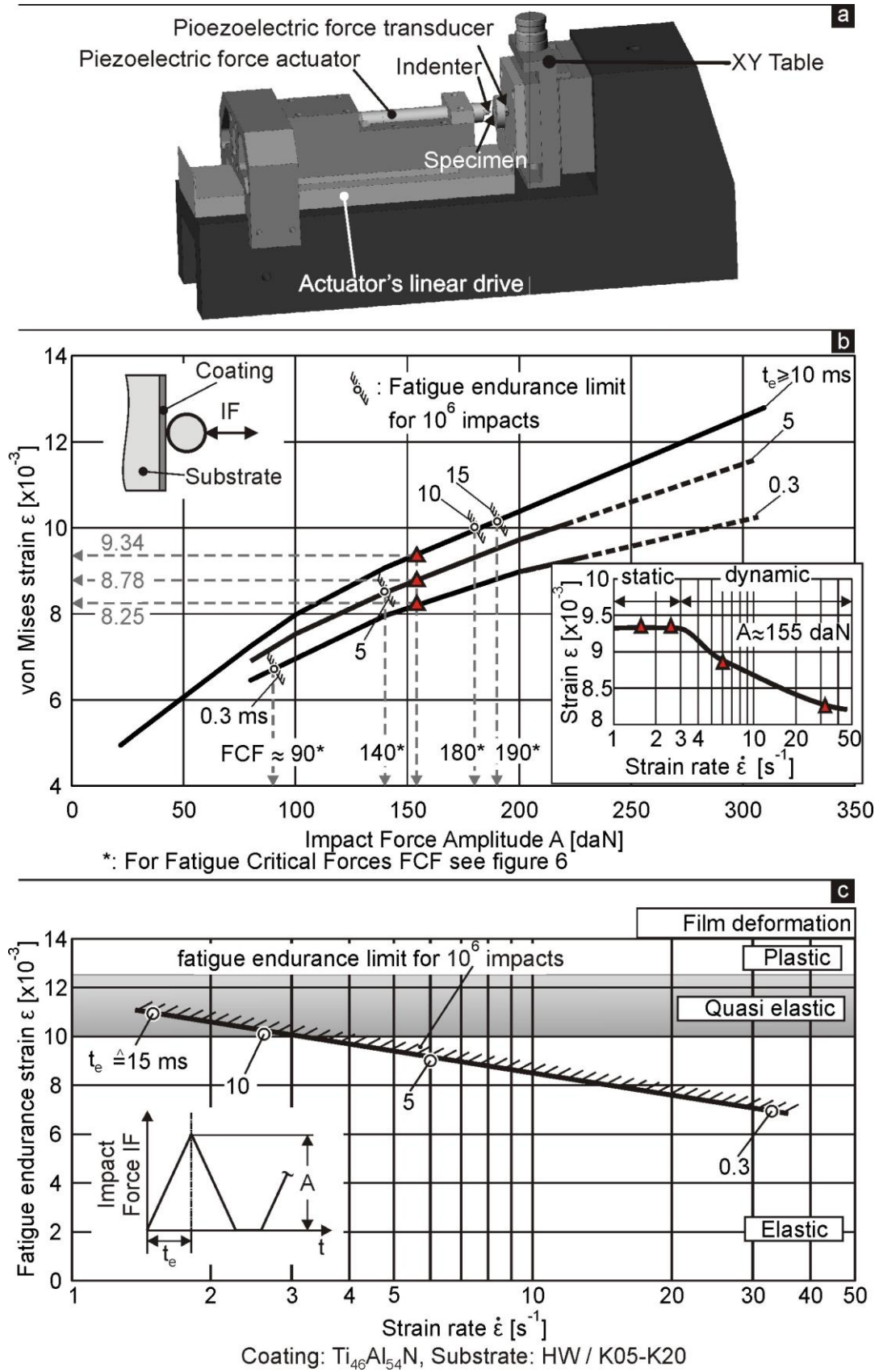


Figure 4. (a) The developed impact tester arrangement with adjustable force pattern (b) The developed von Mises strains at various impact force amplitudes and impact times  $t_e$  (c) Effect of the strain rate and impact times  $t_e$  on the film fatigue endurance limit.

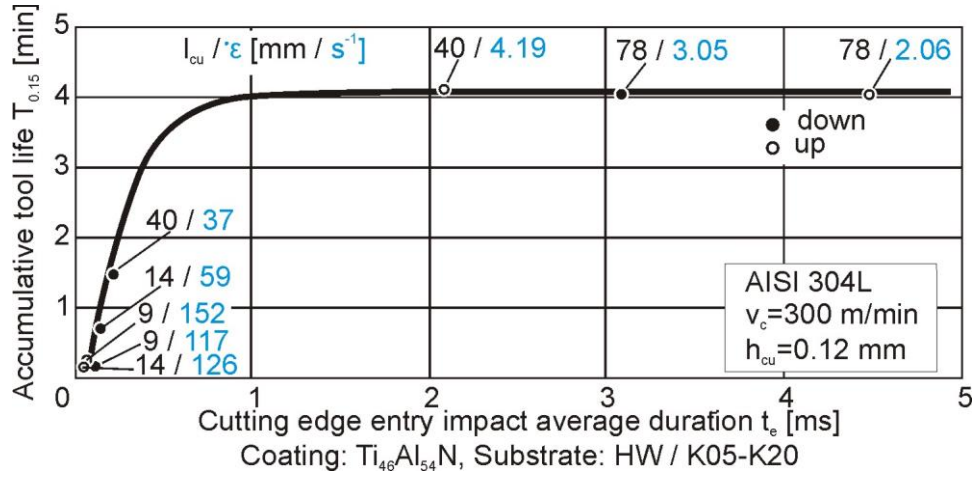


Figure 5. Effect of the cutting edge entry impact average duration on the accumulated coated tool life.

the conducted milling investigations, the contact between tool and workpiece was simulated by appropriate finite elements analysis (FEA) methods [3]. The correlation between the accumulated tool life and the cutting edge entry impact average duration is graphically shown in figure 5. Short entry impact average durations and, hence, higher strain rates correspond to comparably-lower coating fatigue strength. In contrast, longer entry durations improve the film fatigue behavior and, thus, they enhance the tool life. Over an entry impact average duration of around 1 ms, the tool life at constant cutting speed and feed rate is not practically affected by film fatigue mechanisms and, other wear phenomena are prevailing [3]. In this case, parameters, as for example the undeformed chip length, tool diameter and

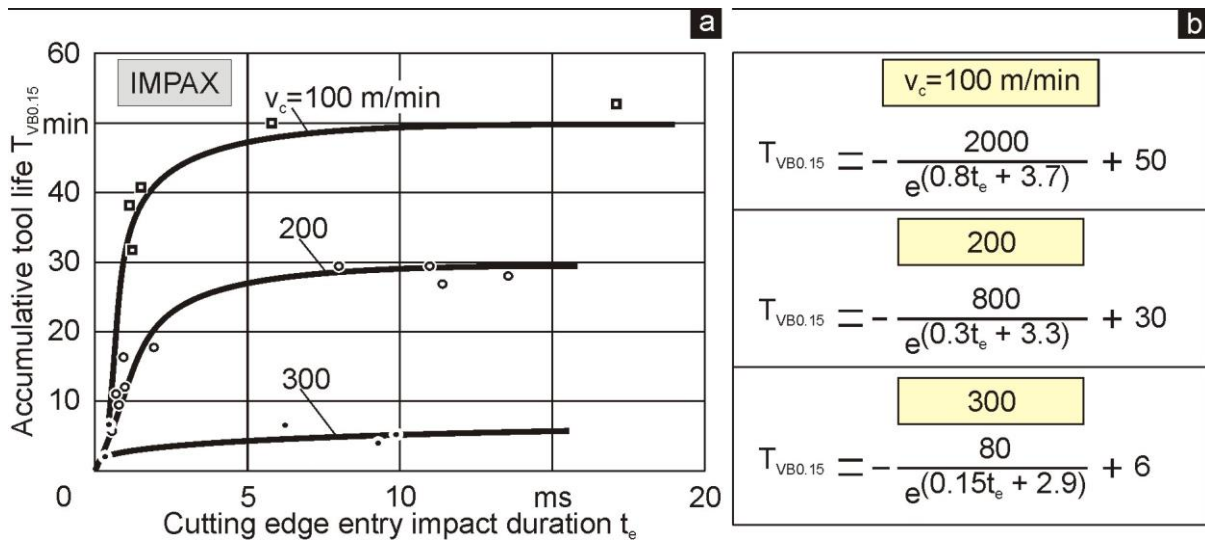


Figure 6. Accumulated tool life in milling of the employed hardened steel IMPAX versus the entry impact duration at various cutting speeds.

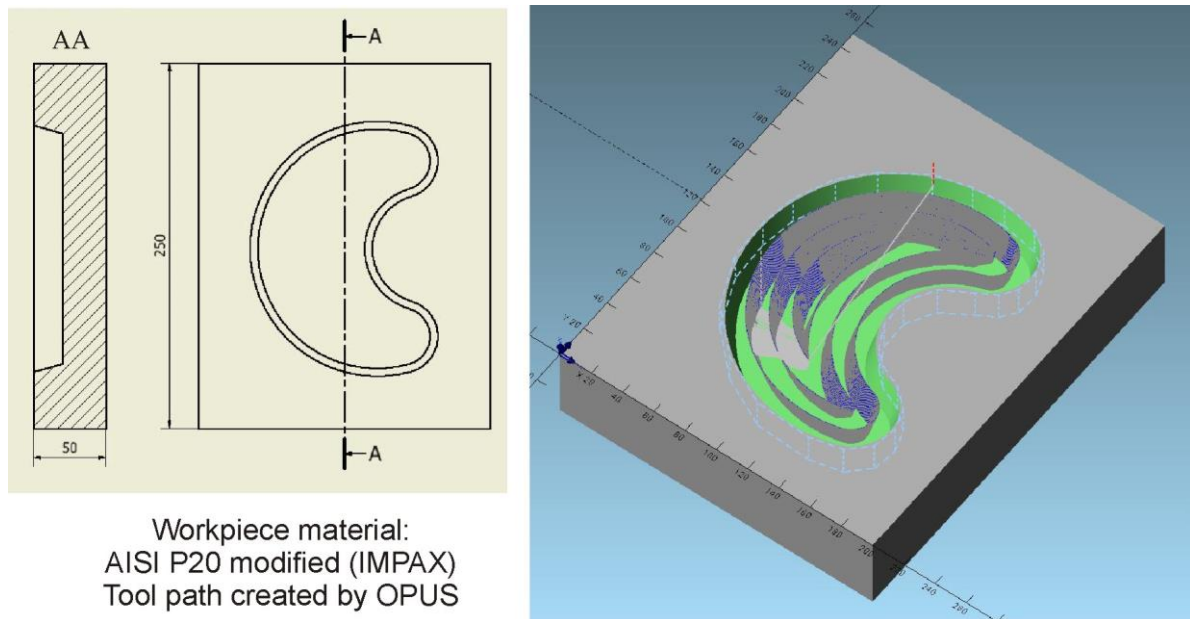


Figure 7. The employed test part and the tool paths required for the material removal.

milling kinematics do not influence the coated cutters wear evolution, which is associated with an almost constant accumulated tool life. Here, the prevailing film wear mechanisms are associated with film mechanical overstressing and abrasion and not with fatigue.

The accumulated tool life in milling of a further steel, of the hardened IMPAX, versus the entry impact duration at various cutting speeds is displayed in figure 6a. The accumulated tool life can be described by the equations, as displayed in figure 6b, for the cutting speeds of 100, 200 and 300 m/min.

Considering these data, a method was developed for calculating the coated tool wear evolution in milling [6]. An application example of this method, in the case of the part presented in figure 7, will be described in the following. Taking into account the initial and final workpiece's geometry, the tool paths required to remove the raw material volume were defined using the commercial "OPUS-CAM" system [12]. The determined tool paths are displayed in the right part of figure 7. The machining took place in forty z-levels. The raw material removal was accomplished using up milling and down milling as well. Both operations lead to the same final workpiece shape, but the tool wear behaviour in each case may be different.

After the tool paths have been determined, the "Schnitte.dat" file is generated by OPUS, as shown in figure 8. This file contains geometrical data related to the chips formed in each tool path. More specifically, the parameters illustrated in figure 8, determined at certain distances

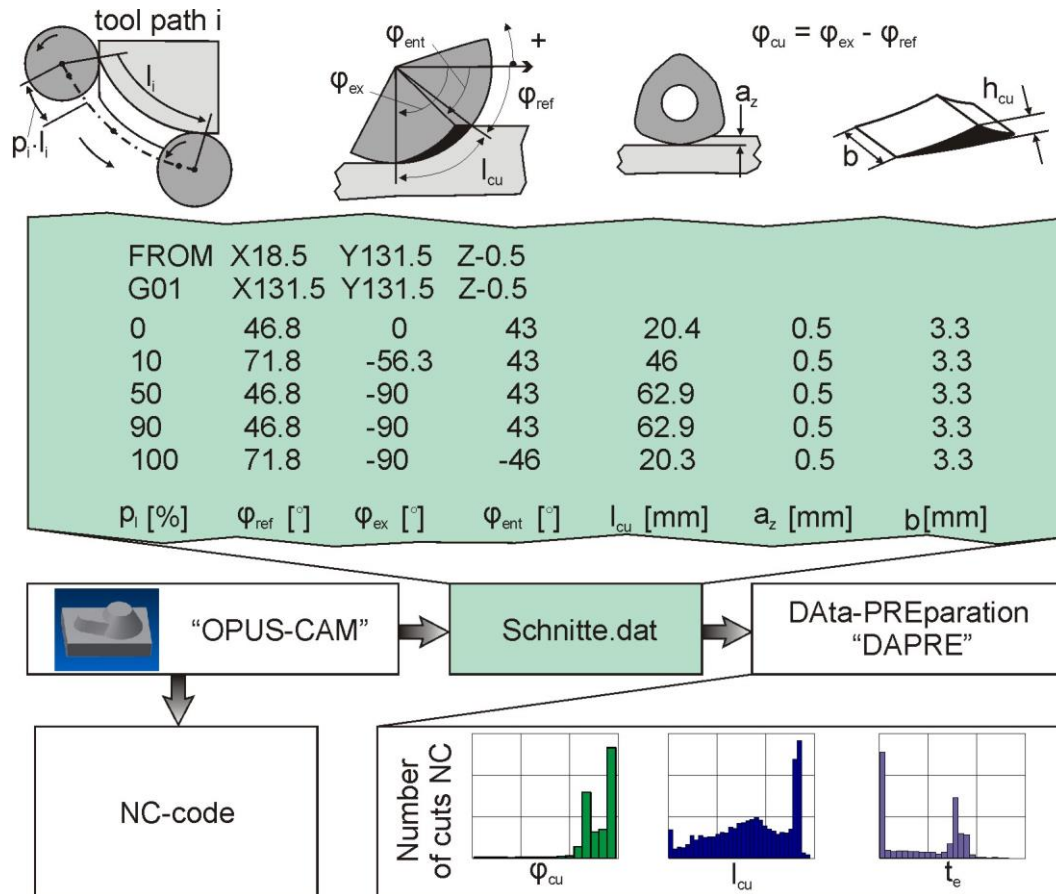


Figure 8. Determination of chip data along the tool paths by a CAD/ CAM system.

from every tool path initial point are stored into the "Schnitte.dat" file. In the first column of the file, the tool position is defined as a percentage  $p$  of the actual tool path length  $l_i$ , whereas  $i$  is the number of the tool path. At every tool position, the angle  $\varphi_{ref}$  of the first tool rake – workpiece contact, the corresponding entry angle  $\varphi_{ent}$  at the maximum cutting edge penetration into the part material and the exit angle  $\varphi_{ex}$  are stored. Moreover, in the following columns, the undeformed chip length  $l_{cu}$ , the axial depth of cut  $a_z$  and the chip width  $b$  are accumulated. The data of the "Schnitte.dat" file are further processed by the developed Data - PREparation (DAPRE) software. Thus, various data, as for instance the entry impact time per chip, the undeformed chip lengths, the tool–workpiece contact angle etc. can be provided. Considering these data the coated tool wear evolution versus the number of cuts is described and in this way, the conduct of algorithms for an analytical optimization of milling process towards attaining set targets is facilitated.

Characteristic results of this methodology are displayed in figure 9, where histograms of the entry impact time of the removed chips in both up and down milling kinematics are illustrated. In up milling almost all chips were cut at impact duration of approximately 4.8 ms. In contrary,

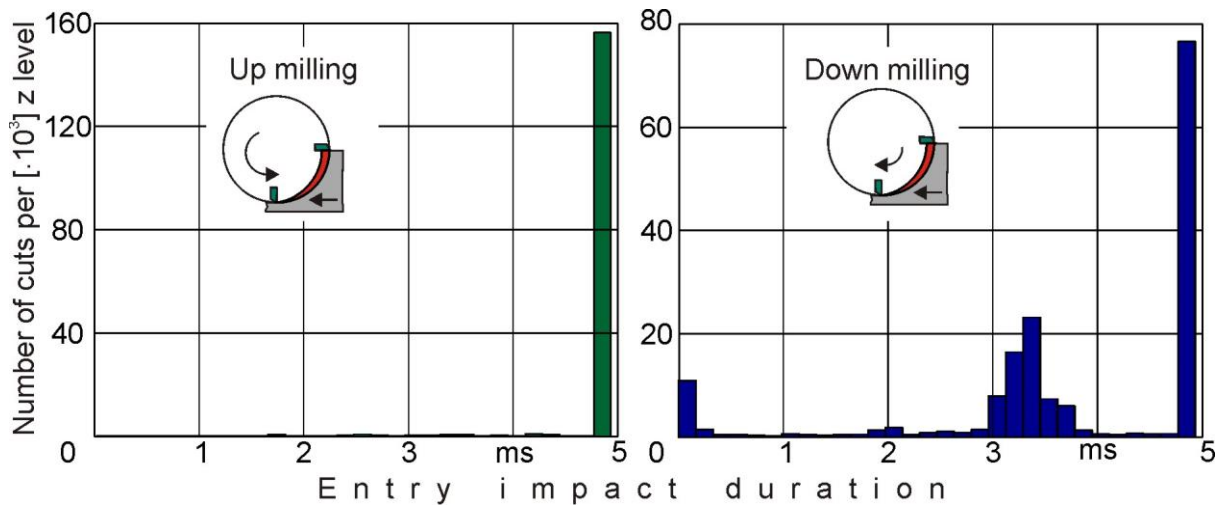


Figure 9. Histograms of the entry impact duration along the tool paths Determination of chip data along the tool paths by a CAD/ CAM system.

when down milling is applied almost half chips possess entry impact durations of less than 4 ms, while some of them are associated with impact durations less than 1 ms. In this way, it is expected a more intense wear evolution in down milling compared to up one. It is has to be pointed out, that the more intense tool wear evolution in down milling of this particular test part compared to the up one, cannot stand for every milling case and depends on the workpiece and the tool edge geometry and material data.. The measured and the calculated values of the tool wear evolution in both milling kinematics are presented in figure 10. The experimental results converge sufficiently with the calculated ones.

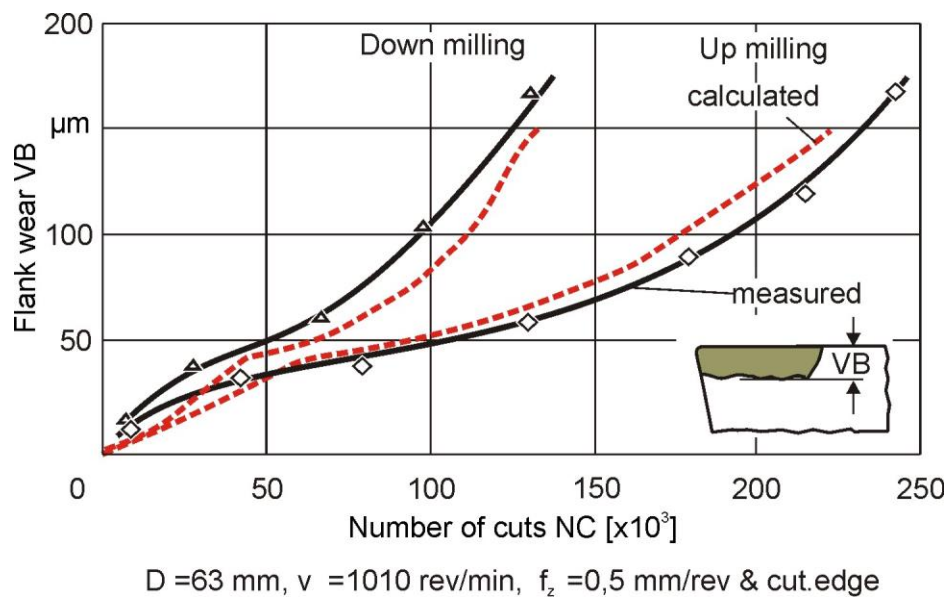


Figure 10. Calculated and measured flank wear development versus the number of cuts.



#### 4. BRITTLENESS OF MONO- AND MULTI-LAYERED PVD FILMS

The deposition of multilayer PVD (Ti,Al)N coating systems instead of monolayer ones has been approved as a very effective method for prolonging coated tool life [4,13]. The layer's interfaces obstruct the crack propagations. In this way, the cracking process has to start all over again in a certain location where the developed stresses concentration progressively overcomes a critical stress limit [14]. This is schematically shown in the upper part of figure 11. Multi-layered PVD films also possess increased fatigue strength [4]. For investigating the effect of the PVD film structures on their brittleness, nano-impact tests were carried out on the coated inserts by a sharp cube corner diamond indenter [15]. The applied load amounted to 100 mN and the maximum number of impacts was set equal to 1800. Related test results on coatings with mono- and multi-layered structures are displayed in figure 11. A comparably steeper depth augmentation occurs in the case of a mono-layer

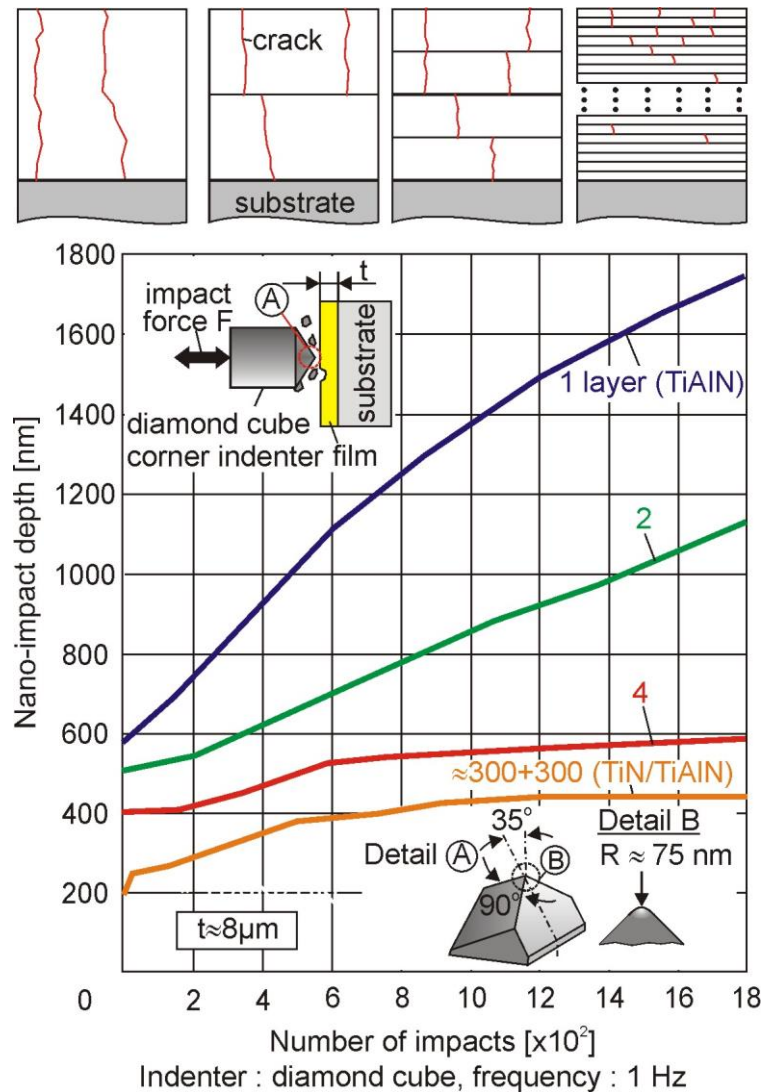


Figure 11. Nano-impact results on the investigated coatings with different structures

coating, whereas an improved behaviour is revealed when multilayer coatings, and especially nano-composite films, are used. All multilayered PVD film structures withstand more sufficiently the repetitive impacts compared to the mono-layers ones.

According to the attained cutting results in [4], as the number of film's layers increases, the tool life grows (see also figure 12). This improvement is associated with the higher film fatigue strength at short and long entry impact durations and the lower brittleness. A correlation among brittleness, film fatigue strength and the accumulated tool life is shown in figure 12a, 12b and 12c respectively. Moreover, the enhancement of the cutting performance of coated tools by applying multi-layer PVD film structures can be quantified at various cutting edge entry impact durations  $t_{ce}$ , as displayed in figure 12d. At a low  $t_{ce}$  of 0.3 ms, through the employment of multi-layer films, a tool life increase up to 75% can be achieved.

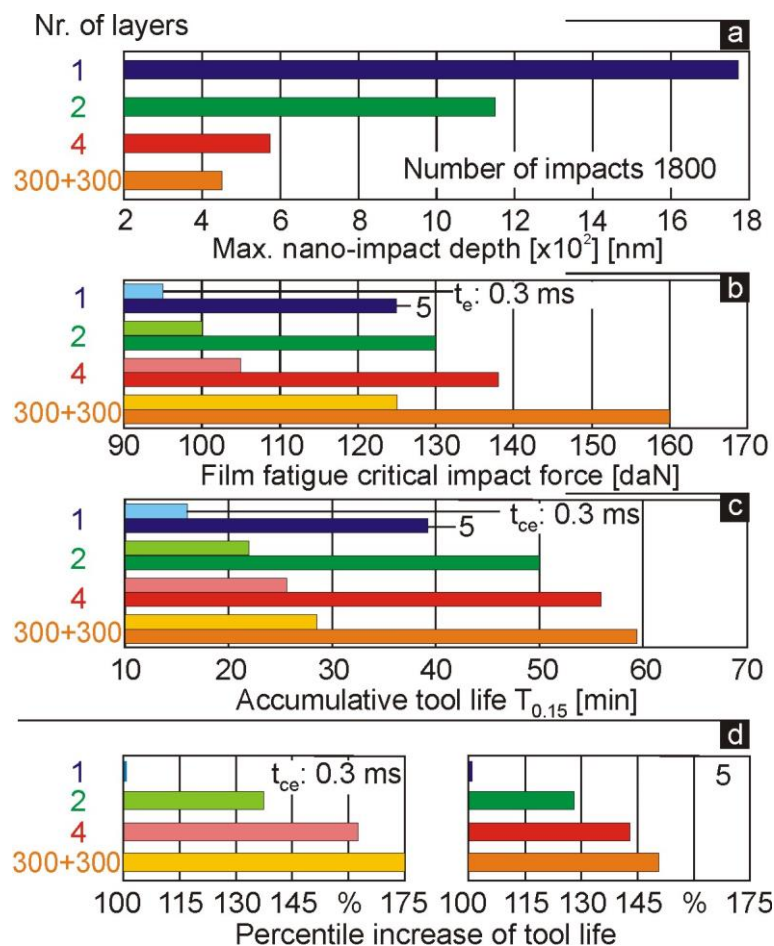


Figure 12. Correlation among (a) brittleness, (b) film fatigue strength and (c) the accumulated tool life coated tool life in milling. (d) Percentile increase of tool life, when multi-layered PVD films are employed at various  $t_{ce}$ .



This improvement is lower ( $\approx 50\%$ ) at a longer  $t_{ce}$  of 5 ms. It is worth mentioning that in the latter  $t_{ce}$  case the attained tool lives are significantly higher compared to the obtained ones at  $t_{ce} \approx 0.3$  ms (see figure 12c).

## 5. CONCLUSIONS

Innovative surface engineering techniques for determining the interface fatigue strength of NCD coatings, the fatigue strength of PVD films at high strain and strain rates and the brittleness of mono- and multi-layered PVD films are presented. These methods are supported by appropriate experimental results evaluation via convenient FEM algorithms. Based on the attained results, a thorough understanding of the coated tools wear mechanisms is achieved, thus restricting the experimental cost for optimizing cutting conditions.

## REFERENCES

1. **Bouzakis, K.-D., Michailidis, N., Skordaris, G., Bouzakis, E., Biermann, D. and M'Saoubi, R. (2012)**, "Cutting with coated tools: Coating technologies, characterization methods and performance optimization", *CIRP Annals - Manufacturing Technology*, Vol. 61, pp 703-723.
2. **Bouzakis, K.-D., Skordaris, G., Bouzakis, E., Makrimalakis, S., Kombogiannis, S. and Lemmer, O. (2013)**, "Fatigue strength of diamond coatings' interface assessed by inclined impact test", *Surface and Coatings Technology*, Vol. 237, pp 135-141.
3. **Bouzakis, K.D., Makrimalakis, S., Skordaris, G., Bouzakis, E., Kombogiannis, S., Katirtzoglou, G. and Maliaris, G. (2013)**, "Coated tools' performance in up and down milling stainless steel, explained by film mechanical and fatigue properties", *WEAR*, Vol. 203, pp 546-559.
4. **Skordaris, G., Bouzakis, K.-D., Charalampous, P., Bouzakis, E., Paraskevopoulou, R., Lemmer, O. and Bolz, S. (2014)**, "Brittleness and fatigue effect of mono- and multi-layer PVD films on the cutting performance of coated cemented carbide inserts", *CIRP Annals - Manufacturing Technology*, Vol. 62, in press.
5. **Bouzakis, K.-D., Makrimalakis, S., Katirtzoglou, G., Bouzakis, E., Skordaris, G., Maliaris, G., Gerardis, S. (2012)**, "Coated tools' wear description in down and up milling based on the cutting edge entry impact duration", *CIRP Annals - Manufacturing Technology*, Vol. 61, pp 115-118.





6. **Bouzakis, K.-D., Paraskevopoulou, R., Katirtzoglou, G., Makrimalakis, S., Bouzakis, E., Efstathiou, K (2013)**, "Predictive model of tool wear in milling with coated tools integrated into a CAM system", CIRP Annals - Manufacturing Technology, Vol. 62, pp. 71-74.
- [9] CemeCon AG. Website, [www.cemecon.de/index\\_eng.html](http://www.cemecon.de/index_eng.html) (2010)
7. **Haubner, R. and Kalss, W. (2014)**, "Diamond deposition on hardmetal substrates - Comparison of substrate pre-treatments and industrial applications", International Journal of Refractory Metals and Hard Materials, Vol. 28, pp 475–483.
8. **Liu, Y., Yin, L., Zhao, L. and Zheng, Y. (2012)**, "Influence of Co Removal for Improving Diamond Films Adhesive on WC-Co Substrates by DC-PCVD", Advanced Materials Research, Vol. 538-541, pp 7-11.
9. **Lee, Dong-Gu, Fitz-Gerald, James M. and Singh, Rajiv K. (1998)**, "Novel method for adherent diamond coatings on cemented carbide substrates", Surface and Coating Technology, Vol. 100-101, pp 1877191.
10. **Woehrl, N., Hirte, T., Posth, O. and Buck, V. (2009)**, "Investigation of the coefficient of thermal expansion in nanocrystalline diamond films", Diamond & Related Materials, Vol. 18, pp 224–228.
11. **Bouzakis, K.-D., Maliaris, G. and Makrimalakis, S. (2012)**, "Strain rate effect on the fatigue failure of thin PVD coatings: An investigation by a novel impact tester with adjustable repetitive force", Int. J. Fatigue, Vol. 44, pp 89–97.
12. Opus-CAM, 2012, User Manual.
13. **PalDey, S. and Deevi, S.C. (2003)**, "Single layer and multilayer wear resistant coatings of (Ti,Al)N: A review", Materials Science and Engineering A, Vol. 342, pp 58-79.
14. **Panjan, P., Čekada and M., Navinšek, B. (2003)**, "A new experimental method for studying the cracking behaviour of PVD multilayer coatings", Surface and Coatings Technology, Vol. 174-175, pp 55-62.
15. **Beake, B. D., Fox-Rabinovich, G. S., Veldhuis, S. C. and Goodes, S.R. (2009)**, "Coating optimisation for high speed machining with advanced nanomechanical test methods", Surface and Coatings Technology, Vol. 203, pp 1919-1925.





## ADVANCES IN CRYOGENIC AND ULTRASONIC ASSISTED MACHINING

**Stuart BARNES**, *s.barnes@warwick.ac.uk University of Warwick, Coventry, CV4 7AL, UK.*

**Helen ASCROFT**, *h.ascroft@warwick.ac.uk University of Warwick, Coventry, CV4 7AL, UK.*

**Pipat BHUDWANNACHAI**, *p.bhudwannachai@warwick.ac.uk University of Warwick, Coventry, CV4 7AL, UK.*

**Aishah Najiah DAHNEL**, *a.n.dahnel@warwick.ac.uk University of Warwick, Coventry, CV4 7AL, UK.*

**Aniruddha GUPTA**, *Aniruddha.Gupta@warwick.ac.uk University of Warwick, Coventry, CV4 7AL, UK.*

### ABSTRACT

This paper provides a brief overview of two techniques which have the potential to improve the machinability of difficult-to-machine materials; the use of cryogenic cutting fluids and ultrasonic assisted machining. Some of the work using these techniques which is taking place in WMG at the University of Warwick is discussed. The literature indicates their ability to reduce cutting forces, tool wear and machining damage. However, work performed at WMG has demonstrated that reductions in machining damage are in some cases associated with increased cutting forces and tool wear. Further research is needed to develop additional fundamental understanding of these techniques.

**Keywords:** Cryogenic, LN<sub>2</sub>, CO<sub>2</sub>, Ultrasonic, Machining, CFRP.

### 1. INTRODUCTION

This paper will provide a brief review of two aspects of machining technology which have recently experienced renewed interest: machining with cryogenic cooling and ultrasonic assisted machining. It will then present an overview of some of the work which is currently being performed in these areas within WMG at the University of Warwick, primarily with regard to the machining of carbon fibre reinforced plastic (CFRP).



## 2. CRYOGENIC MACHINING

Before considering cryogenic machining techniques, it is worth briefly considering why they are being considered and the challenges they are designed to address. In the early days of machine tool development it was recognized that the process of machining (especially metallic materials) generates heat. Metal cutting involves a significant amount of plastic deformation with shear strains of  $\gamma = 2 - 5$  regarded as typical in the primary shear zone and of  $\gamma = 10 - 50$  in the secondary shear zone [Wright, 2000]. Figure 1 illustrates such levels of deformation in a quick-stop section produced when turning a 0.4% carbon steel at 30 m/min. When metals are subjected to such high levels of strain, virtually all the deformation produced is plastic deformation and hence it is assumed that effectively all the energy which is expended during this deformation is converted into heat [Knight and Boothroyd, 2005]. The heat which is generated in the cutting zone will either be carried away with the chips (which is generally not a problem), transmitted into the workpiece (the temperature of which needs to be controlled), or into the cutting tool where it can have a significant effect on the tool life. The most serious (and most difficult to control) issue is that of the heat being generated in the secondary shear zone on the underside of the chip. This is where temperatures are highest with temperatures of 1150°C being measured during high speed machining of AISI/SAE 4140 at 925 m/min [Abukhshim, Mativenga and Sheikh, 2006]. Temperatures of this order have also been reported when machining more traditional engineering materials at conventional cutting speeds [Wright, 2000]. These maximum temperatures are generated in the secondary shear zone on the underside of the chip where the amount of deformation is greatest, Figure 1.

The fact that this heat source is in intimate contact with the rake face of the cutting tool provides for rapid and efficient transfer of the heat into the cutting tool. In fact, detailed examination of the chip / tool interface over the years has demonstrated that the underside of the chip is actually seized to the rake face of the cutting tool during machining [Barnes, 1988; Qi, (2000); Wright, 2000]. Within the range of cutting speeds normally applied in practice, it has been recognized for many years that the maximum temperature generated in this cutting zone, and therefore on the rake face of the tool, will increase with increasing cutting speed. This fact has to a great extent provided the impetus for cutting tool manufacturers to develop tool materials with higher temperature resistance capability, in response to the constant desire to machine faster in order to increase productivity.

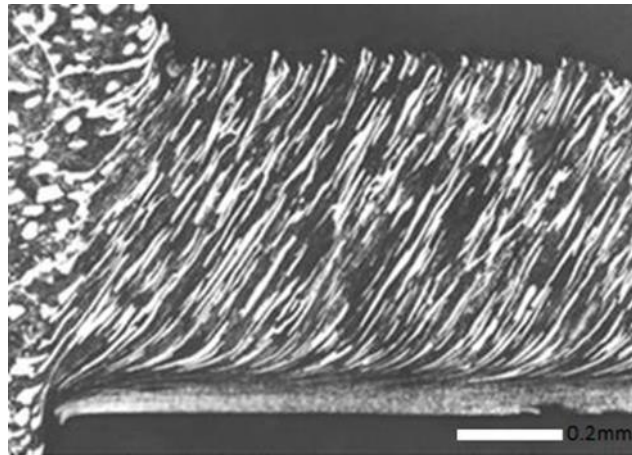


Figure 1. Quick-stop section during turning showing the flow zone on the underside of the chip (0.4%C steel, 30 m/min).

The removal of the heat generated in the cutting zone is one of the main reasons (amongst others) for the application of cutting fluids during most machining operations. These cutting fluids have been the subject of considerable development in their own right over the years, resulting in the complex and extremely effective offerings which are available today. Nevertheless, there has also been pressure in recent years from an economic and environmental perspective on the use of cutting fluids. Where it is technically possible, organisations are under pressure to stop using cutting fluids altogether, minimise their use and ensure that the fluids and their constituent parts have a minimal effect on operators and the environment. From an environmental point of view, the use of cryogenic cooling using carbon dioxide or nitrogen has the potential to be extremely attractive, if they can be demonstrated to be technically capable of fulfilling the role of cutting fluid at the same time as being a financially viable alternative.

**Previous Work on Cryogenic Machining:** Various techniques to reduce the temperature of the cutting tool and / or the cutting zone to cryogenic temperatures have been reported in the literature. These techniques use either liquid nitrogen (LN2) or carbon dioxide gas to achieve the cooling although their method of application varies considerably. Yildiz [2008] identifies four groups: a) Cryogenic pre-cooling; b) Injection of the cryogen into the cutting zone; c) Indirect cryogenic cooling of the cutting tool and d) Cryogenic cooling of the tool to improve properties (which as they note, is actually an extension of the heat treatment process and not applicable to modern cutting tool materials. The simple act of cooling the workpiece down to liquid nitrogen temperature by immersing the workpiece in LN2 prior to machining is one very simple option [Barnes, 1988]. However, while this has been shown to increase tool life and the maximum viable cutting speeds, it is not presented as a viable option for production machining of components for practical and economic reasons.



Other workers developed a system which directs a stream of LN2 into the cutting zone from a nozzle thus engulfing the cutting tool, the section of the workpiece about to be machined and the forming chips [Zurecki, 2003]. These workers reported that LN2 cooling of  $\text{Al}_2\text{O}_3$  based cutting tools could give “significantly longer” tool lives than conventionally cooled CBN tools. The application of LN2 to Ti-6Al-4V has been reported by Bermingham [2011] showing improvements to cutting forces and tool wear, while noting some detrimental effects associated with the chip no longer interacting with the chip breaker correctly. Such processes demonstrated improvements in cutting performance, however, there are issues with the use of liquid nitrogen from a health and safety point of view, in addition to the fact that many potential users would see this as an expensive option due to the amount of LN2 consumed. In some cases, there would also be concern about the effect that the extremely low temperature of LN2,  $-196^\circ\text{C}$ , would have on the component itself or the cutting tools / holders. Nevertheless in other cases an improvement in the surface properties of the machined part have been reported [Zurecki, 2003]. However, once the LN2 has vaporised and become an inert gas, there is no contamination to the workpiece or the machine tool (which in itself can be a significant advantage); the build-up of nitrogen gas would obviously need to be monitored and controlled. Advocates of nitrogen based systems also note that it is not a greenhouse gas and therefore release into the atmosphere does not present a problem.

In order to reduce the cost of the LN2 used in the process, Hong, Markus and Jeong (2001a) developed a system which used two “micro-nozzles” to direct smaller quantities of LN2 precisely along the rake face of the tool at the point where the chip lifted off the tool and up the flank face of the tool towards the cutting edge. They report that their technique represented an “economical system” due to the smaller quantities of LN2 used, with 0.65 kg/min of LN2 achieving a five times improvement in tool life when turning Ti-6Al-4V. The application of LN2 in this way has the effect of reducing friction between the chip and tool, thus reducing the feed force, at the same time the cutting force was found to increase due to the fact that the material in the primary shear zone retained more of its strength due to the cooling effect of the LN2 [Hong, 2001b; Venugopal, 2007]. Much of the work on the use of LN2, and cryogenic cooling in general, has been on difficult-to-machine materials such as titanium alloys. However, work has been performed on plain carbon mild steel, BS 970-080A15, (En32b) which has also demonstrated advantages in terms of reduced tool wear and cutting forces [Stanford, 2009]. Dhananchezian and Kumar (2011) reported on the development of a system which delivered the LN2 onto the rake face of the cutting tools which contained an electrical discharge machined hole, thus allowing the LN2 to pass

through the tool and out onto the two clearance faces. Reductions in cutting temperature, forces and tool wear were reported along with improvements in the surface finish of the machined surface when turning Ti-6Al-4V between 27 and 97 m/min. However, the authors did not comment on the amount of LN2 consumed. In contrast, Bermingham *et al.* (2011) also turned Ti-6Al-4V using LN2 delivered from a nozzle, but they reported an increase in the cutting force ( $F_c$ ) and no change in the feed force ( $F_f$ ) compared to dry machining, although they did report that cryogenic coolant extended the life of cutting tools compared to dry machining. Based on a detailed study of the microstructure in the chips, they found that this improvement was due to a combination of a reduction in the amount of deformation (and hence heat generation) associated with chip formation, and the more efficient removal of the heat which had been generated. They also report that the coefficient of friction between the rake face and the chip did not decrease with cryogenic application; in fact it actually increased in some instances. However, they found that at the optimum parameters, tool life could be improved by the application of cryogenic coolant, though it was not simply a case of more effective removal of heat from the cutting zone.

The delivery of LN2 through the cutting tools has been developed into commercial machine tools by MAG Industrial Automation Systems. It is reported that their system passes nitrogen through the spindle; tool holder and tool in “mostly the liquid state” prior to being “allowed to evaporate” near the cutting edge; this rapid expansion (x700) reportedly helping with chip removal [Zelinski, 2011]. It is argued that while other systems have delivered LN2 to the cutting area as if it were a conventional cutting fluid, this system uses less LN2 (flow rates of 0.04 and 0.24 l/min per cutting edge is quoted) and effectively makes the cutting tools a heat sink which assists in heat removal. A tenfold increase in tool life and a twofold increase in material removal rate were reported when milling titanium.

Another approach to using liquid nitrogen, which avoids the issue of having free-flowing LN2 in the machining area, has been developed. In this work, the researchers used a cutting tool and tool holder arrangement which was modified to allow the LN2 to pass through the holder and cool the cutting tool from underneath – the LN2 therefore never came in direct contact with either the workpiece or the outer surfaces of the tool [Wang, 1996; Wang 1997; Wang 2000]. The LN2 passed through a reservoir beneath the tool and tests showed that machinability was improved with the system being capable of maintaining a relatively constant tool temperature during cutting of -160 to -170°C, recognising that this was “2x1 mm from the cutting point” [Wang, 1996]. This arrangement appears to be far more suitable for





incorporation in a production environment, but it would no doubt still add a significant cost to the operation, for which the financial viability would need to be assessed.

Other systems based on the use of CO<sub>2</sub> as the “cutting fluid” have also been developed and the use of such techniques is generally referred to as *cryogenic machining*. However, they typically generate temperatures in the order of -77°C, whereas to be accurate, the definition of the cryogenic temperature range is from -150°C to absolute zero, (-273°C) [Britannica.com, 2014]. The use of carbon dioxide is the other approach which researchers have taken in order to achieve cryogenic cooling. It is regarded as a less expensive option than LN<sub>2</sub> and the temperatures achieved (often reported to be in the order of -77°C) are not considered as potentially harmful to operators, tools or equipment as the -196°C of LN<sub>2</sub>. The use of air which has been cooled to temperatures in the range of -15 to -45°C has also been shown to be beneficial when used in conjunction with minimum quantity lubrication (MQL) during the machining of Ti-6Al-4V alloy (also described as cryogenic machining) [Yuan, 2011]. The economics of using CO<sub>2</sub> are also reported to be more favorable and several workers have proposed that using CO<sub>2</sub> as a substitute for conventional metal cutting fluids can reduce the cost associated with the maintenance and disposal of conventional fluids, and reduce potential health problems as a result of exposure to the additives in conventional fluids [Davim, 2008; Jerold, 2011; Machai, 2011; Skerlos, 2008]. Since CO<sub>2</sub> can be obtained as a by-product from the chemical industry and power plants, the authors suggest that using CO<sub>2</sub> as a cutting fluid is regarded as more environmental friendly by reducing the energy and waste associated with the process for producing conventional cutting fluids, as well as liquid nitrogen which requires energy to be produced by cryogenic distillation. When liquid CO<sub>2</sub> expands to room temperature and air pressure, a mixture of solid and gaseous CO<sub>2</sub> is formed with the temperature as low as -80°C [Machai, 2011; Skerlos, 2008]. This low-temperature CO<sub>2</sub> cutting fluid is extremely effective at reducing the temperature in the cutting zone, as the heat from the cutting process is used in the sublimation of CO<sub>2</sub>. With the benefit of temperature reduction, it has been shown that the use of “CO<sub>2</sub> cutting fluid” could improve performance in the metal machining process compared to other cooling and lubricating methods [Çakır, 2004; Skerlos, 2008; Jerold, 2011; Machai, 2011; Clarens, 2006; Jerold, 2012]. It was reported in the work of Çakır, *et al.* [2004] that the use of CO<sub>2</sub> gas cooling resulted in lower cutting forces and better surface roughness compared to dry machining, the machining with conventional cutting fluid and machining with LN<sub>2</sub> during the turning of AISI 1040 steel. The effect of CO<sub>2</sub> cooling was shown to contribute to the decrease of the coefficient of friction at the tool/chip interface, which resulted in a shorter tool/chip contact length, an increase in the shear plane angle and hence lower cutting forces and better



surface finish. In the work of Jerold and Kumar [2011, 2012], it was demonstrated that the application of CO<sub>2</sub> cooling reduced the cutting temperature by 5-22% when compared to machining dry and with conventional fluids when turning AISI 1045 steel. The CO<sub>2</sub> cooling did not reduce the cutting temperature as much as the LN<sub>2</sub> cooling, nevertheless, it resulted in lower cutting forces, tool wear and better surface finish when compared to machining dry, with conventional fluids and with LN<sub>2</sub> cooling [Jerold, 2011 and 2012]. The authors reported this to be due to the reduction of cutting temperature and a decrease in friction at the tool/chip interface. In the work of Machai and Biermann [2011], it was also reported that the application of CO<sub>2</sub> cooling could improve tool life by reducing notch wear on the cutting edge during the turning of Ti-10V-2Fe-3Al titanium alloy, as compared to machining with an emulsion cutting fluid. Again, this was attributed to a reduction in cutting temperature. However, in this work it was shown that machining with CO<sub>2</sub> produced similar levels of cutting forces to the machining carried out with a conventional cutting fluids. It was suggested that while there was a benefit from the reduction in friction at the tool/chip interface, there was also an increase in the strength of the material in the primary cutting zone as a consequence of the reduced temperature during cutting [Machai, 2011]. This effect of increasing forces has been noted by other workers when comparing dry machining to conventional cutting fluids and is in line with expectations based on accepted metal cutting theory [Wright, 2000]. Although no reports were found which discussed the use of CO<sub>2</sub> cooling in the conventional drilling of carbon / epoxy composites in detail, the beneficial effects of machining with CO<sub>2</sub> reported above suggested that application of this technique to the drilling of these materials, as discussed later in this paper, may be beneficial.

**Cryogenic Machining of Carbon Fibre Reinforced Plastics (CFRP):** These materials are widely used as structural components in high performance applications within the aerospace industry due to their high specific strength and stiffness, improved fatigue performance, negative coefficient of thermal expansion (CTE) and the high specific thermal and electrical conductivity of the reinforcing carbon fibres [Soutis, 2005a and b; Campbell, 2010]. CFRP composites are manufactured into near-net-shape parts. Secondary machining processes are still required, however, in order to achieve the desired specification and tolerance in many of the final components. Among the secondary machining processes, the conventional drilling process is commonly applied to the CFRP parts in order to produce holes for mechanical joining, especially in the aerospace industry [Abrao, 2007; Liu, 2012; Sheikh-Ahmad, 2009]. However, machining defects induced from the conventional drilling process, which include delamination damage at the entry and exit laminates, fibre pull-out, matrix cracking and internal damage on the drilled surface of the hole in the form of material chip-

out, usually occur due to heterogeneity and anisotropic properties of CFRP composites [Abrao, 2007; Liu, 2012; Sheikh-Ahmad, 2009; Teti, 2002]. This drilling-induced damage degrades the mechanical properties and performance of the CFRP parts and components, which are critical to the high performance applications, and hence limit the application of such composites [Abrao, 2007; Isbilir, 2013; Liu, 2012; Teti, 2002]. The drilling-induced defect of most concern is delamination damage, which accounts for 60% of final part rejection in the aircraft industry [Abrao, 2007; Liu, 2012]. In addition, it was also shown that delamination damage significantly reduced static and fatigue properties of the CFRP parts [Persson, 1997]. For these reasons, there have been many attempts to minimise delamination damage induced from the conventional drilling process of CFRP composites.

Among the research work that has been performed on the conventional drilling of CFRP, attempts to minimise delamination damage have focused on the optimisation of tool material and geometry, and also cutting parameters [Davim, 2003a and b; Enemuoh, 2001; Hocheng, 2003, 2006 and 2007; Piquet, 2000; Sardinias, 2006; Tsao, 2007; Zhang, 2001]. In addition to the use of unsuitable machining parameters and drilling tools, heat being generated during dry drilling has also been shown to cause thermal damage and accuracy errors to the hole, due to the poor thermal conductivity of the epoxy matrix [Sheikh-Ahmad, 2009; Liu, 2012; Weinert, 2004]. Although cutting fluids and cryogenic cooling has been shown to improve the performance in metal machining processes [Ezugwu, 2005; Hong, 2001a and b; Shokrani, 2012; Yildiz, 2008; Wang, 2000], there has been little research published on their application to the conventional drilling of CFRP composites in order to improve their machinability. In industry, the drilling of CFRP parts is carried out either without a cutting fluid, primarily to avoid material degradation due to moisture absorption (it also reduces the cost of cleaning), or with a cutting fluid used only for dust suppression purposes rather than improving machining [Sheikh-Ahmad, 2009; Liu, 2012; Abrate, 1992; Teti, 2002; Weinert, 2004]. A cutting fluid which can reduce the cutting zone temperature without contaminating the CFRP components could therefore offer a real benefit.

**Cryogenic Machining of CFRP at WMG:** WMG has been working with SGS Carbide and DMG to investigate the effect of machining using CO<sub>2</sub> as the cutting fluid. The work discussed here relates to the application of this technique to the machining of CFRP, primarily carbon fibre-reinforced epoxy (carbon/epoxy) composites. What follows is an overview of some of the main findings from this work to date.

Some initial work was performed using a pre-cooling technique; the drill being cooled in LN2 prior to machining. While this is obviously not a viable production process, the work generated some interesting results and indicated the potential advantages that could be obtained from cryogenic machining [Barnes, 2013]. The main objective of this work was to reduce the damage caused to the CFRP material as a consequence of the drilling operation – the indications from the literature being that cutting forces must be kept low and the cutting edge sharp, therefore flank wear must be minimised. A comparison was made between drilling dry (at room temperature) with a conventional coolant and with a pre-cooled tool, using a 6 mm diameter Guhring DIN 6537 K, TiAlN coated, solid carbide twist drill to produce through-holes in an 18 mm thick woven carbon-fiber reinforced epoxy plaque with constant cutting speed and a feed rate of 94 m/min and 0.065 mm/rev respectively. Figures 2 to 5 show a summary of the results. It can be seen that cryogenic precooling resulted in higher cutting forces and tool wear than dry drilling, with conventional coolant being even worse than cryogenic cooling. However, when the damage associated with the drilling operation was measured it was found that the cryogenic cooled holes were superior to the holes produced with dry and conventional cutting fluid. The fact that the higher cutting forces had actually resulted in reduced damage was attributed to the fact that the cryogenic cooling had restricted the temperature rise during cutting and hence the epoxy matrix had retained more of its strength, thereby supporting the carbon fibres more effectively, thus reducing damage such as delamination and fibre pull-out. SEM images obtained from the cut surface of the holes also supported the suggestion of a lower cutting temperature, Figure 6.

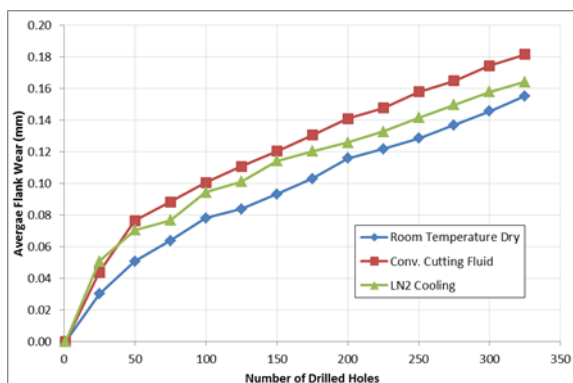


Figure 2. Average flank wear with number of holes drilled, machining dry, with conventional cutting fluid and with a tool pre-cooled in LN2.

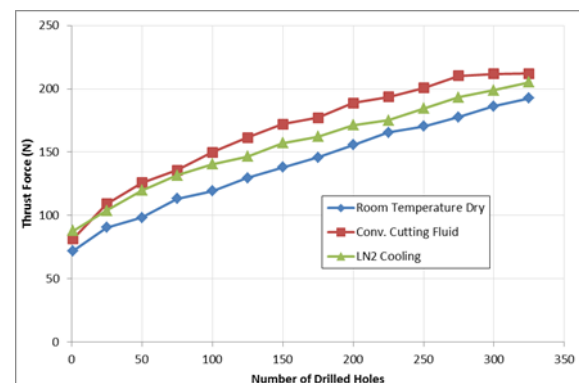


Figure 3. Average thrust force with number of holes drilled, machining dry, with conventional cutting fluid and with a tool pre-cooled in LN2.

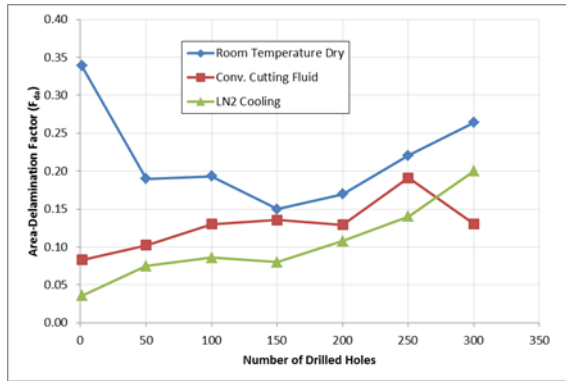


Figure 4. Average exit area delamination with number of holes drilled, machining dry, with conventional cutting fluid and with a tool pre-cooled in LN2.

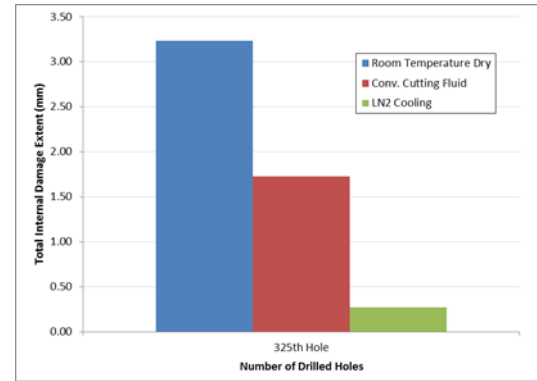


Figure 5. Total internal damage after drilling 325 holes, machining dry, with conventional cutting fluid and with a tool pre-cooled in LN2.

Following the pre-cooled tools work, research on the use of CO<sub>2</sub> cooling (external application) during the drilling of carbon/epoxy composites was performed in order to determine if the higher temperatures associated with CO<sub>2</sub> cooling would exhibit the same beneficial behavior. Two sets of drilling experiments were carried out to examine the effect of machining parameters (cutting speed and feed rate) and the effect of the CO<sub>2</sub> compared to dry drilling. For both sets of experiments, a SGS series 120 50017 DI-NAMITE (pure crystalline diamond) coated, solid carbide 8 facet double angle drill was used to produce 6 mm diameter through-holes in the carbon/epoxy plaques, which were manufactured from uni-directional carbon fibres reinforced in toughened epoxy matrix (IM 7/Hexply 8552 toughened epoxy) with a copper mesh layer on the entry side of the plaque. For the first set of experiments, the cutting speed was varied from 75-150 m/min and the feed rate was varied from 0.03-0.15 mm/rev. Drilling at each machining condition was carried out dry and with CO<sub>2</sub> cooling (flow rate was measured as 3.37 l/min, the maximum volume for the system). Evaluation of the drilling performance was based on the measurement of thrust force and exit delamination.

Similar results to the LN2 work were obtained in that the application of CO<sub>2</sub> cooling resulted in higher thrust force, combined with less exit delamination compared to dry drilling, Figure 7. Again, it is suggested that this is due to the higher strength and stiffness of the epoxy when drilling due to the cooling effect of the CO<sub>2</sub>. This was in contrast to the case of metal machining for which the application of CO<sub>2</sub> cooling was shown to provide a benefit in reducing friction at the tool/chip interface, hence decreasing cutting forces as discussed above [Çakır, 2004; Jerold, 2011; Machai, 2011]. However, the main cutting mechanism in

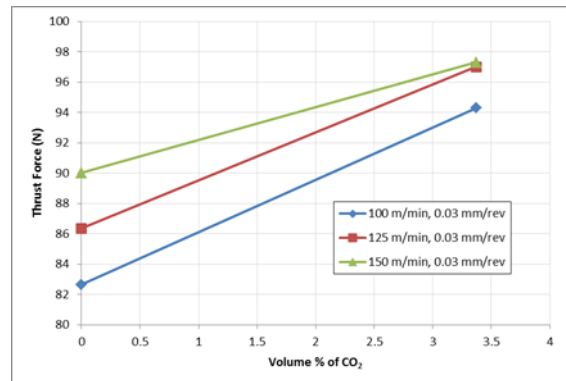


Figure 6. Maximum thrust force when drilling CFRP with CO<sub>2</sub> cooling at 100, 125 and 150 m/min with a feed rate of 0.03 mm/rev and 6 mm dia. carbide drill.

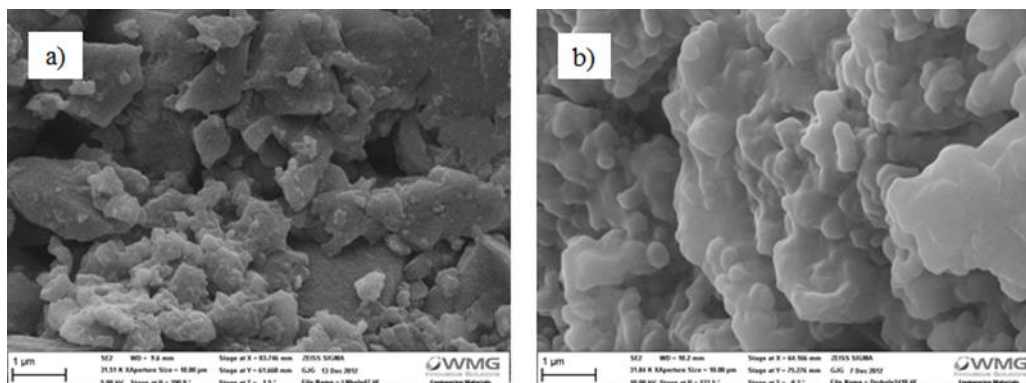


Figure 7. SEM images of machined surface produced by (a) drilling with a LN2 cooled tool and (b) dry drilling.

the drilling of carbon/epoxy composites involves a series of brittle fractures of the material and shearing at the fibre/matrix interface rather than shearing of the material within the secondary shear zone at the tool/chip interface [Konig, 1985; Koplev, 1983; Liu, 2012; Sheikh-Ahmad, 2009; Teti, 2002]. The application of CO<sub>2</sub> cooling did not provide the benefit of thrust force reduction with CFRP. Nevertheless, the retention of higher strength and stiffness in the epoxy again resulted in less delamination damage. In addition, it was shown that the difference between thrust force and delamination damage produced for dry drilling and CO<sub>2</sub> cooling was more significant at low cutting speeds and feeds compared to that at high cutting speeds and feeds. This is considered to be due to the method of CO<sub>2</sub> application used (a simple external nozzle) and this will be investigated in the next phase of work, which will deliver the CO<sub>2</sub> through the tool. Nevertheless, it was demonstrated that this simple application of CO<sub>2</sub> cooling reduced the cutting temperature by 27% as compared to dry drilling (85 to 62°C). While in the early stages of development, another research group at WMG is working on a technique to assess the damage associated with the drilling of holes in CFRP extremely accurately using the X-ray CT scanning.



### 3. ULTRASONIC ASSISTED MACHINING

Ultrasonic machining (USM) has been a well-known technique for machining hard and brittle materials for many years and the history of USM is reported to go back to a paper by Wood and Loomis in 1927 [Theo, 1998]. Traditionally, in USM a controlled static load is applied to a tool, which has no cutting edges, while abrasive slurry is pumped around the cutting zone. The ultrasonic vibration of the tool causes abrasive particles between the tool and workpiece to impact the workpiece thus removing material by a process of micro-chipping [Nath, 2012]. However, the use of diamond impregnated cutting tools has also been increasingly used in recent years in combination with non-abrasive slurry [Lv, 2013; Cong, 2014].

In contrast, ultrasonic assisted machining uses conventional cutting tools with cutting edges which are responsible for removing the workpiece material. The ultrasonic vibrations (typically in excess of 20 kHz) are applied *in addition* to the normal cutting parameters of cutting speed and feeds. As reported by Kadivar (2014), there has been a significant amount of interest in ultrasonic assisted machining in recent years with researchers reporting drilling and turning applications and investigating a range of workpiece materials from metal matrix composites [Kadivar, 2014], titanium alloys [Pujanaa, 2009], Inconel [Baghlani, 2013], aluminium alloys [Chang, 2010], carbon fibre composites [Phadnis, 2012; Wang, 2004] to bone [Alama, 2011]. In some research, workers have vibrated the workpiece while others the cutting tool; Kadivar *et al.* (2014) investigating both possibilities, the actuated tool system (ATS) and the activated work system (AWS) noting some differences in behaviour, e.g., the AWS increasing forces but reducing burr formation. There is general agreement in the literature that the application of such ultrasonic oscillations, which are in the order of 3 to 20  $\mu\text{m}$  in amplitude and 17 to 46 kHz frequency, have a beneficial influence on the machining process. Amongst the reported work, there is a consensus of opinion that the thrust and torque forces are reduced along with the tool wear [Babitsky, 2007; Pujanaa, 2009; Wang, 2004] and the burr formation when drilling [Kadivar, 2014]. For example, a thrust force of ~550 N during conventional drilling compared to ~150 N with ultrasonic assistance [Babitsky, 2007]. The surface finish is reported to be improved due to ultrasonic vibration, even though a rise in the cutting temperature is also reported which increased with increasing amplitude of oscillation [Pujanaa, 2009].

**Ultrasonic Assisted Drilling of Carbon Fibre Reinforced Plastics (CFRPs):** As has been noted in the previous section, other researchers have reported that when vibrations are induced during drilling, they result in a reduction in thrust force and an enhancement in tool-





life for CFRPs, as well as in metals [Brehl, 2008]. Sadek *et al.* [2013] have reported the attainment of zero exit delamination between 6000 rpm and 12000 rpm spindle speed, with a 6 mm diameter drill (113 to 226 m/min) and a feed rate of 0.025 mm/rev. However, they used oscillation frequencies of 30 to 60 Hz, below the ultrasonic range, and they presented no images of the holes to support the claim of having zero exit delamination. The research is still in its developing phase for the drilling of CFRPs using ultrasonic assisted drilling, with researchers striving to meet the challenges of minimizing the entrance and exit delamination, as well as the internal damage produced during drilling. Makhdum *et al.* [2012a and 2012b] conducted experiments on CFRP to develop an understanding of ultrasonic assisted drilling. They conducted the experiments on a lathe with an ultrasonic transducer mounted on the chuck, and drilled the holes horizontally at selected parameters. They found a reduction of 90% in the thrust force and the generation of longer chips during the UAD of CFRP as compared to that in conventional drilling. The authors suggested that the reason for the generation of longer chip was due to the “brittle-to-ductile transition of the composite material when subjected to ultrasonic vibration” but did not discuss possible mechanisms for this, or if it was related to the glass transition temperature of the matrix material. A reduction in the entrance and exit delamination in UAD was also reported in their work although the reason for the selection of the specific drilling parameters and the thrust force reduction was not discussed. Phadnis *et al.* [2012] have developed a finite element model for the prediction of thrust force in conventional and ultrasonic assisted drilling. They implemented Hashin’s criteria [1980] for fibre failure and Puck’s criteria [2002] for matrix failure and report that they could predict the thrust force in the error-range of 15%. A similar experimental study has also been conducted by Mehbudi *et al.* [2013] for glass fibre laminate (GFRP) material. They conducted the experiment at low cutting speeds (maximum cutting speed was 15.7 m/min) and 19 to 46 kHz oscillation frequency using Taguchi L9 orthogonal arrays and reported that UAD reduced thrust force and therefore drilling induced delamination “dramatically”.

**Ultrasonic Assisted Drilling of CFRPs at WMG:** While some good work has been reported on the use of ultrasonic assistance to the drilling process, such work has utilised experimental / laboratory set-ups to provide the ultrasonic aspect to the machining operation. Working in collaboration with DMG Mori Seiki, WMGs work is being carried out on a commercially available machine tool, the ULTRASONIC 65 monoBLOCK® with the actuator built into the tool holder. While still in the early stages of this research, the results being obtained are demonstrating benefits which are indicative of those reported by other workers using “laboratory scale” facilities. A pilot study using a Taguchi L9 orthogonal array has been conducted for a small range of cutting speeds (80 to 120 m/min) and feed rates (0.02 to 0.08

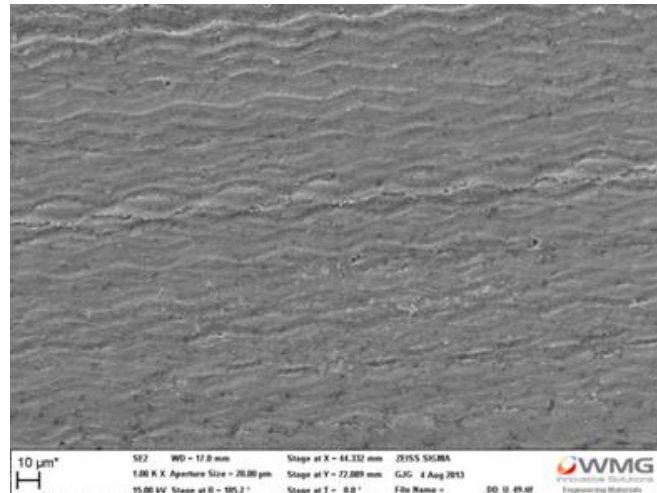


Figure 8. SEM image showing evidence of ultrasonic oscillation on machined CFRP surface.

mm/rev) with ultrasonic oscillation amplitudes of 0.98, 2.94 and 4.9  $\mu\text{m}$ . The UAD was found to reduce the thrust force by up to 10%, with the machined surface and the extent of entrance and exit delamination being reduced. Figure 8 shows an indication of the ultrasonic oscillation on the machined surface. Quantifying the drilling damage is an issue that all researchers in this field have encountered. While SEM images can give indications of improvements, an X-ray CT scanning approach is being developed with another research group in WMG which will allow far more accurate quantification and comparison of such holes. Work is continuing in order to quantify the improvements in machinability associated with the application, in addition to gaining a more fundamental understanding of the process and how these improvements are produced in terms of accepted machining theory.

### 3. CONCLUSIONS

Both cryogenic and ultrasonic assisted machining techniques have potential to improve the machining performance of difficult-to-machine materials. Some significant improvements have been demonstrated in the literature but it appears that there are further improvements to be gained as the technologies are developed, optimised and fully understood at a fundamental level. In the case of CFRPs, the more precise characterisation of machine induced damage promised by X-ray CT scanning will also help to drive process optimisation. An exciting additional option which is being investigated at WMG is the simultaneous use of cryogenic and ultrasonic assisted machining. Again, further research is needed to fully understand the possibilities of such a process.





#### 4. ACKNOWLEDGEMENTS

The authors would like to thank the WMG High Value Manufacturing Catapult for funding the ultrasonic enabled machine tool and the following companies for their support: BAE Systems, DMG Mori Seiki, Guhring, UK, SGS Carbide Tool UK.

#### 5. REFERENCES

- Abrate, S. & Walton, D.D., (1992),** "Machining of composite materials. Part I: Traditional methods," Composite Manufacturing, Vol. 3, pp.75-83.
- Abrao, A.M., Faria, P.E., Campos Rubio, J.C., Reis, P. & Davim, J.P., (2007),** "Drilling of fiber reinforced plastics: A review," J.of Materials Processing Technology, Vol. 186, pp.1-7.
- Abukhshim, N.A., Mativenga, P.T. & Sheikh, M.A., (2006),** "Heat generation and temperature prediction in metal cutting: A review and implications for high speed machining", International Journal of Machine Tools & Manufacture, Vol. 46, pp.782–800.
- Alama, K., Mitrofanov, A.V. & Silberschmidt, V.V., (2011),** "Experimental investigations of forces and torque in conventional and ultrasonically-assisted drilling of cortical bone", Medical Engineering & Physics, Vol. 33 pp.234-239.
- Babitsky, V.I., Astashev, V.K. & Meadows, A., (2007),** "Vibration excitation and energy transfer during ultrasonically assisted drilling", Journal of Sound and Vibration, Vol. 308, Issues 3-5, 4 Dec., pp.805-814.
- Baghlanian, V., Mehbudia, P., Akbarib, J. & Sohrabic, M., (2013),** "Ultrasonic assisted deep drilling of Inconel 738LC superalloy", Procedia CIRP, The Seventeenth CIRP Conference on Electro Physical & Chemical Machining (ISEM), 6, pp.571-576.
- Barnes, S., (1988),** "The machining Characteristics of Vanadium Microalloyed Forging Steels", PhD, The University of Birmingham, UK.
- Barnes, S., Bhudwannachai, P. & Dahnel, A. N., (2013),** "Drilling Performance of Carbon Fiber Reinforced Epoxy Composite when Machined Dry, with Conventional Cutting Fluid and with a Cryogenically Cooled Tool", Proc. of the ASME 2013 Int. Mechanical Engineering Congress & Exposition, IMECE 13, Nov. 15-21, San Diego, California, USA.
- Bermingham, M.J., Kirsch, J., Sun, S. Palanisamy, S. & Dargusch, M.S., (2011),** "New observations on tool life, cutting forces and chip morphology in cryogenic machining Ti-6Al-4V", Int. Journal of Machine Tools and Manufacture, Vol. 51, Issue 6, June, pp.500–511.



**Brehl, D.E. & Dow, T.A., (2008),** "Review of vibration-assisted machining," Precision Engineering-Journal of the International Societies for Precision Engineering & Nanotechnology, Vol. 32, July, pp.153-172.

**Britannica.com (2014),** <http://www.britannica.com/EBchecked/topic/144945/cryogenics>, accesses February 2014.

**Campbell, F.C., (2010),** Structural Composite Materials. Ohio, United States of America: ASM International.

**Çakır, O., Kiyak, M. & Altan, E., (2004),** "Comparison of gases applications to wet and dry cuttings in turning", Journal of materials processing technology, Vol. 153, pp.35-41.

**Chang, S.F.F. & Bone, G.M., (2010),** "Burr height model for vibration assisted drilling of aluminum 6061-T6", Precision Engineering, Vol. 34, Issue 3, July, pp.369-375.

**Clarens, A.F., Hayes, K.F. & Skerlos, S.J., (2006),** "Feasibility of metalworking fluids delivered in supercritical carbon dioxide", J. of Manufacturing Processes, Vol. 8, pp.47-53.

**Cong, W.L., Pei, Z.J., Sun, X. & Zhang, C.L., (2014),** "Rotary ultrasonic machining of CFRP: A mechanistic predictive model for cutting force", Ultrasonics, Vol.54, Issue 2, Feb., pp.663-675.

**Dhananchezian, M. & Kumar, M.P., (2011),** "Cryogenic turning of the Ti-6Al-4V alloy with modified cutting tool inserts", Cryogenics, Vol. 51, Issue 1, January, pp.34-40.

**Davim, J.P. & Reis, P., (2003a),** "Drilling carbon fiber reinforced plastics manufactured by autoclave - experimental and statistical study," Materials & Design, Vol. 24, pp.315-324.

**Davim J.P. & Reis, P., (2003b),** "Study of delamination in drilling carbon fiber reinforced plastics (CFRP) using design experiments," Composite Structures, Vol. 59, pp.481-487.

**Davim, J.P., (2008),** "Machining: Fundamentals and Recent Advances", London: Springer-Verlag London Limited, ISBN 10: 1848002122 / 1-84800-212-2, ISBN 13: 9781848002128.

**Enemuoh, E.U., El-Gizawy, A.S. & Okafor, A.C., (2001),** "An approach for development of damage-free drilling of carbon fiber reinforced thermosets," International Journal of Machine Tools & Manufacture, Vol. 41, Sept., pp.1795-1814.

**Ezugwu, E.O., (2005),** "Key improvements in the machining of difficult-to-cut aerospace superalloys", Int. Journal of Machine Tools & Manufacture, Vol. 45, Oct., pp.1353-1367.

**Jerold, B.D. & Kumar, M.P., (2011),** "Experimental investigation of turning AISI 1045 steel using cryogenic carbon dioxide as the cutting fluid," Journal of Manufacturing Processes, Vol. 13, pp.113-119.



**Jerold, B.D. & Kumar, M.P., (2012)**, "Experimental comparison of carbon-dioxide and liquid nitrogen cryogenic coolants in turning of AISI 1045 steel", *Cryogenics*, Vol. 52 pp.569-574.

**Hashin, Z., (1980)**, "Failure Criteria for Unidirectional Fiber Composites", *Journal of Applied Mechanics*, Vol. 47, pp.329-334.

**Hocheng, H. & Tsao, C.C., (2003)**, "Comprehensive analysis of delamination in drilling of composite materials with various drill bits," *Journal of Materials Processing Technology*, Vol. 140, pp.335-339.

**Hocheng, H & Tsao, C.C., (2006)**, "Effects of special drill bits on drilling-induced delamination of composite materials", *Int. Journal of Machine Tools & Manufacture*, Vol. 46, Oct., pp.1403-1416.

**Hocheng, H. & Tsao, C.C., (2007)**, "Computerized tomography and C-scan for measuring drilling-induced delamination in composite material using twist drill and core drill", *Progress of Precision Engineering and Nano Technology*, Vol. 339, pp.16-20.

**Hong, S. Y., Markus, I. & Jeong, W.C., (2001a)**, "New cooling approach and tool life improvement in cryogenic machining of titanium alloy Ti-6Al-4V", *Int. Journal of Machine Tools & Manufacture*, Vol. 41, pp.2245–2260.

**Hong, S.Y., Ding, Y. & Jeong, W.C., (2001b)**, "Friction and cutting forces in cryogenic machining of Ti–6Al–4V", *Int. Journal of Machine Tools and Manufacture*, Vol. 41, (12), pp.2271-2285.

**Isbilir, O., Ghassemieh, E., (2013)**, "Numerical investigation of the effects of drill geometry on drilling induced delamination of carbon fiber reinforced composites", *Composite Structures*, Vol. 105, pp.126-133.

**Kadivar, M.A., Akbari, J., Yousefi, R., Rahi, A. & Nick, M.G., (2014)**, "Investigating the effects of vibration method on ultrasonic-assisted drilling of Al/SiCp metal matrix composites", *Robotics and Computer-Integrated Manufacturing*, Vol. 30, pp.344-350.

**Knight, W.A. & Boothroyd, G., (2005)**, "Fundamentals of Metal Machining and Machine Tools", Third Ed., Taylor & Francis Ltd, ISBN 3: 9781574446593 ISBN 10: 1574446592.

**Konig, W., Wulf, C., Grab, P. & Willerscheid, H., (1985)**, "Machining of fibre reinforced plastics". *Annals of CIRP Manufacturing Technology*, Vol. 34, Issue 2, pp.537-548.

**Liu, D.F., Tang, Y.J. & Cong, W.L., (2012)**, "A review of mechanical drilling for composite laminates", *Composite Structures*, Vol. 94, pp.1265-1279.



**Lv, D., Huang, Y., Wang, H., Tang, Y. & Wu, X., (2013),** "Improvement effects of vibration on cutting force in rotary ultrasonic machining of BK7 glass", *Journal of Materials Processing Technology*, Vol. 213, Issue 9, Sept., pp.1548-1557.

**Machai, C. & Biermann, D., (2011),** "Machining of  $\beta$ -titanium-alloy Ti-10V-2Fe-3Al under cryogenic conditions: Cooling with carbon dioxide snow", *Journal of Materials Processing Technology*, Vol. 211, pp.1175-1183.

**Makhdum, F., Norddin, D.N.P., Roy, A & Silberschmidt, V.V., (2012a),** "Ultrasonically assisted drilling of carbon fibre reinforced plastics", *Advanced Materials and Structures IV*, Vol. 188, pp.170-175.

**Makhdum, F., Jennings, L.T., Roy, A. & Silberschmidt, V.V., (2012b),** "Cutting forces in ultrasonically assisted drilling of carbon fibre-reinforced plastics", *Journal of Physics: Conference Series*, Vol. 382, pp.1-6.

**Mehbudi, P., Baghlani, V., Akbari, J., Bushroa, A.R. & Mardi, N.A., (2013),** "Applying Ultrasonic Vibration to Decrease Drilling-Induced Delamination in GFRP Laminates", *Procedia CIRP*, Vol. 6, pp.578-583.

**Nath, C., Lim, G.C. & Zheng, H.Y., (2012),** "Influence of the material removal mechanisms on hole integrity in ultrasonic machining of structural ceramics", *Ultrasonics*, Vol. 52, Issue 5, July, pp.605-613.

**Persson, E., Eriksson, I. & Zackrisson, L., (1997),** "Effects of hole machining defects on strength and fatigue life of composite laminates," *Composites Part a-Applied Science and Manufacturing*, Vol. 28, pp.141-151.

**Phadnis, V.A., Makhdum, F., Roy, A. & Silberschmidt, V.V., (2012),** "Experimental and Numerical Investigations in Conventional and Ultrasonically Assisted Drilling of CFRP Laminate", *Procedia CIRP*, Vol. 1, pp.455-459.

**Piquet, R., Ferret, B., Lachaud, F. & Swider, P., (2000),** "Experimental analysis of drilling damage in thin carbon/epoxy plate using special drills," *Composites Part a-Applied Science & Manufacturing*, Vol. 31, pp.1107-1115.

**Puck, A. & Schürmann, H., (2002),** "Failure analysis of FRP laminates by means of physically based phenomenological models", *Composites Science and Technology*, Vol. 62, pp.1633-1662.

**Pujanaa, J., Riveroa, A., Celayab, A. & López de Lacalleb, L.N., (2009),** "Analysis of ultrasonic-assisted drilling of Ti6Al4V", *Int. Journal of Machine Tools & Manufacture*, Vol. 49, pp.500-508.



**Qi, H.S., Mills, B., (2000)**, "Formation of a transfer layer at the tool-chip interface during machining", *Wear*, Vol. 245, pp.136–147.

**Sadek, A., Attia, M.H., Meshreki, M. & Shi, B., (2013)**, "Characterization and optimization of vibration-assisted drilling of fibre reinforced epoxy laminates", *CIRP Annals, Manufacturing Technology*, Vol. 62, pp.91-94.

**Sardinas, R.Q., Reis, P. & Davim, J.P., (2006)**, "Multi-objective optimization of cutting parameters for drilling laminate composite materials by using genetic algorithms", *Composites Science and Technology*, Vol. 66, Dec., pp.3083-3088.

**Sheikh-Ahmad, J.Y., (2009)**, *Machining of Polymer Composites*. New York: Springer Science and Business Media.

**Shokrani, A., Dhokia, V. & Newman, S.T., (2012)**, "Environmentally conscious machining of difficult-to-machine materials with regard to cutting fluids", *Int. Journal of Machine Tools & Manufacture*, Vol. 57, June, pp.83-101.

**Skerlos, S.J, Hayes, K.F., Clarens, A.F. & Zhao, F., (2008)**, "Current advances in sustainable metalworking fluids research," *Int. Journal of Sustainable Manufacturing*, Vol. 1, pp.180-202.

**Stanford, M., Lister, P.M., Morgan, C. & Kibble, K.A., (2009)**, "Investigation into the use of gaseous and liquid nitrogen as a cutting fluid when turning BS 970-80A15 (En32b) plain carbon steel using WC–Co uncoated tooling", *Journal of Materials Processing Technology*, Vol. 209, Issue 2, January, pp.961-972.

**Soutis, C., (2005a)**, "Fibre reinforced composites in aircraft construction", *Progress in Aerospace Sciences*, Vol. 41, pp.143-151.

**Soutis, C., (2005b)**, "Carbon fiber reinforced plastics in aircraft construction", *Materials Science and Engineering (a)-Structural Materials Properties Microstructure and Processing*, Vol. 412, pp.171-176.

**Teti, R., (2002)**, *Machining of Composite Materials*, *CIRP Annals-Manufacturing Technology*.

**Theo, T.B., Aspinwall, D.K. & Wise, M.L.H., (1998)**, " Review on ultrasonic machining", *Int. Journal of Machine Tools and Manufacture*, Vol. 38, Issue 4, March, pp.239–255.

**Tsao, C.C. & Hocheng, H., (2007)**, "Parametric study on thrust force of core drill," *Journal of Materials Processing Technology*, Vol. 192, Oct., pp.37-40.

**Venugopal, K.A., Paul, S. & Chattopadhyay, A.B., (2007)**, "Growth of tool wear in turning of Ti-6Al-4V alloy under cryogenic cooling", *Wear*, Vol. 262, Issues 9-10, Apr., pp.1071-1078.



**Wang, X., Wang, L.J. & Tao, J.P., (2004),** “Investigation on thrust in vibration drilling of fiber-reinforced plastics”, Journal of Materials Processing Technology, Vol. 148, Issue 2, 15 May, pp.239-244.

**Wang, Z.Y., Rajurkar, K.P. & Murugappan, M., (1996),** “Cryogenic PCBN turning of ceramic ( $\text{Si}_3\text{N}_4$ )”, Wear, Vol. 195, Issues 1-2, July, pp.1-6.

**Wang, Z.Y. & Rajurkar, K.P., (1997),** “Wear of CBN tool in turning of silicon nitride with cryogenic cooling”, Int. Journal of Machine Tools & Manufacture, Vol. 37, Issue 3, March pp.319-326.

**Wang, Z.Y. & Rajurkar, K.P., (2000),** “Cryogenic machining of hard-to-cut materials”, Wear Vol. 239, pp.168-175.

**Weinert, K. & Kempmann, C., (2004),** "Cutting temperatures and their effects on the machining behaviour in drilling reinforced plastic composites", Advanced Engineering Materials, Vol. 6, Aug., pp.684-689.

**Wright, P.K. & Trent, E.M., (2000),** “Metal Cutting”, Fourth Ed., Butterworth-Heinemann, ISBN: 9780750670692.

**Yildiz, Y. & Nalbant, M., (2008),** “A review of cryogenic cooling in machining processes”, Int. Journal of Machine Tools and Manufacture, Vol. 48, Issue 9, July, pp.947–964.

**Yuan, S.M., Yan, L.T., Liu, W.D & Liu, Q., (2011),** “Effects of cooling air temperature on cryogenic machining of Ti–6Al–4V alloy”, Journal of Materials Processing Technology 211, pp.356-362.

**Zelinski, P., “The 400° Difference” (2011),** Modern Machine Shop; March, pp.67-72.

**Zhang, H.J., Chen, W.Y., Chen, D.C. & Zhang, L.C., (2001),** "Assessment of the exit defects in carbon fibre-reinforced plastic plates caused by drilling", Precision Machining of Advanced Materials, Vol. 196, pp.43-52.

**Zurecki, Z., Ghosh, R. & Frey, J.H., (2003),** “Finish-turning of hardened powder metallurgy steel using cryogenic cooling”, Proc. of the Int. Conf. on Powder Metallurgy and Particulate Materials, 8-12 June, Las Vegas, NV, USA.



## APPLICATION OF M METHOD AND CONSIDERATION OF MEASURES TO ADAPT FOR DIVERSE USERS

**Shuji KANAZAWA**, *kshuji747@gmail.com* Graduate School of Keio University, 3-14-1, Hiyoshi, Yokohama, Kanagawa, Japan

**Yuma SAKAE**, *yuma.sakae0831@gmail.com* Keio University, 3-14-1, Hiyoshi, Yokohama, Kanagawa, Japan

**Shuji TAKANO**, *takano@md.shonan-it.ac.jp* Shonan Institute of Technology, 1-1-25, Tsujido Nishi Kaigan, Fujisawa, Kanagawa, Japan

**Koichiro SATO**, *k.sato@mech.keio.ac.jp* Keio University, 3-14-1, Hiyoshi, Yokohama, Kanagawa, Japan

**Yoshiyuki MATSUOKA**, *matsuoka@mech.keio.ac.jp* Keio University, 3-14-1, Hiyoshi, Yokohama, Kanagawa, Japan

### ABSTRACT

This paper conducts an application of the M method in order to clarify issues needed to be improved. The M method is a design method which can realize both unrestricted thinking and logical thinking. By applying this method to varied users, such problems relating to the usability of the M method are extracted. Therefore, it is clarified that the M method needs to adapt to diverse users. Furthermore, measures to solve the clarified issues are discussed.

**Keywords:** M Method, Multispace Design Model

### 1. INTRODUCTION

To consider the increase in size and complication of design subjects, a comprehensive design method called the M method was proposed [Matsuoka, 2013]. First of all, the need of a comprehensive design method comes from the division of Industrial Design and Engineering design, which has triggered the intricacy and enlargement of artifacts. The division of labor started in the 19<sup>th</sup> century triggered by the arts and crafts movement of William Morris and others [Rosalind, 2006]. Moreover, in the 20<sup>th</sup> century each field of design continued to specialize within their field. Although the division and specialization have





enriched our lives, a new problem that artifacts are becoming larger and more complex have become conspicuous. Therefore, a design method to handle designing comprehensively was needed. The M method was proposed to solve such problems. This is a method based on the Multispace Design Model (M model), and enables users to realize both rational thinking and unrestricted idea generation. Furthermore, the M method is expected to being used in diverse circumstances considering the movement of design integration in recent years [Matsuoka, 2010].

In this paper, an application of the M method was conducted to 53 users to evaluate the usability of the M method and to extract issues of this method for further improvement. After the application, the testees were given a survey to confirm the usability and points of improvement. Analysis are conducted to the results of the survey, and issues are extracted from the results. After, specifics and means to overcome the issues are discussed.

## **2. A GENERAL DESCRIPTION OF THE M METHOD**

### **The Multispace Design Model**

Since the M method is a method based on the Multispace Design Model (M model), shown in figure 1, the M model will briefly described in this section.

The M model is a framework of design theory, which comprehensively acknowledges all kind of design procedures [Matsuoka, 2010]. The base of this model comes from the general design studies of Yoshikawa [Yoshikawa, 1979], and is expanded so the M model can consider the concept of value, meaning, state, attribute, and circumstance. This model enables logical reasoning of design practices through designing, and a novel design would be extracted.

As shown in the figure, the M model is composed a knowledge space, a Thinking space, and 4 outer systems. In the knowledge space, there are two types of knowledge: a Subjective knowledge, and an Objective knowledge. A subjective knowledge is knowledge consisting generality to everyone, whereas an objective knowledge is knowledge based on one's experience and characteristics. On the other hand, there are 4 spaces in the thinking space: a value space, meaning space, state space, and an attribute space. The value space



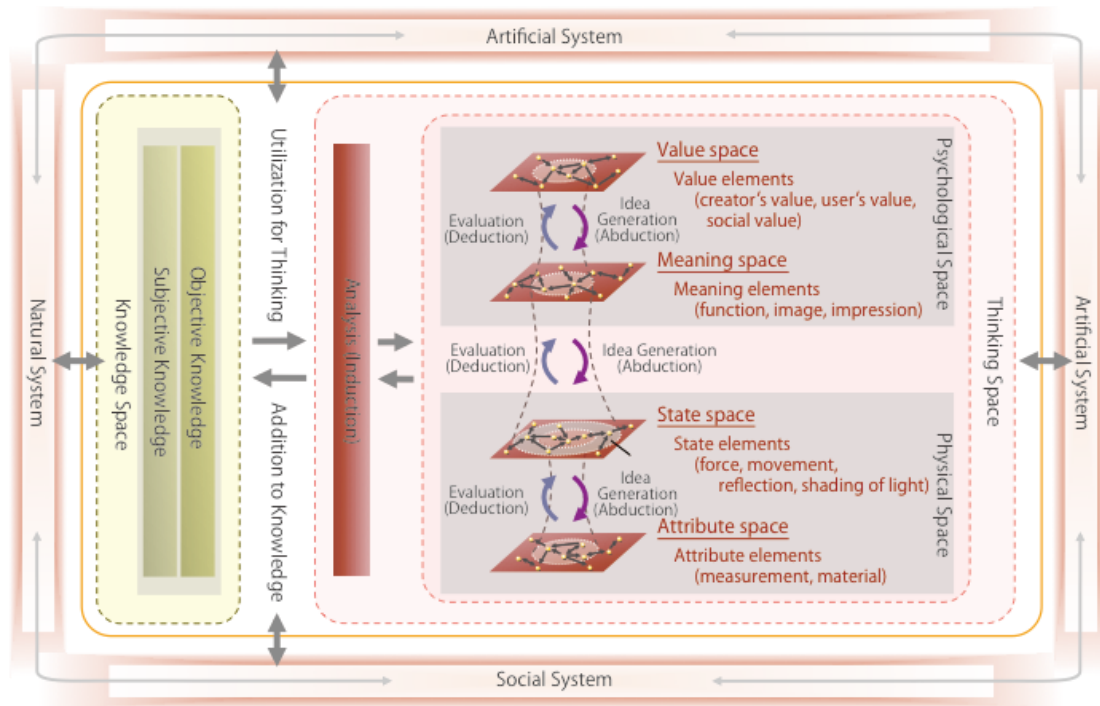


Figure 1. The Multispace Design Model (M model)

consists various values such as social value, cultural value, and personal values. The meaning space consists elements relating to the objects function and image. In the state space, the state of an object, which can be described by the relation of the object and its circumstance, exists. Finally, the attribute space holds elements expressing the objects traits that are not affected, by its surrounding circumstance. The two knowledge, four thinking spaces, and four outer systems comprises the M model, and these spaces are referred to as the Multispace.

The process of designing based on the M model, which is mainly divided into three processes, is expressed in figure 2. The concept design comes first in the design process in the viewpoint of the M model. In the concept design, psychological elements of the design object are considered. The basic design comes next, where meaning elements and physical elements are contemplated. The final process is the detail design, where physical elements are mainly comprehended and optimized.

### The M method

The M method is a design method based on the M model explained in the previous section. The M method is defined as

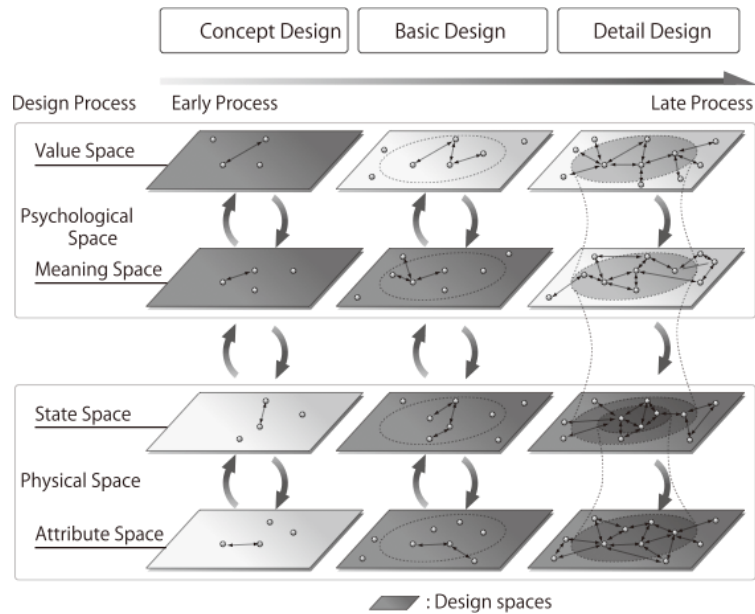


Figure 2. Design Process Expressed by the M model

"The "M method"(Multispace Design Method) is a new method of thinking that allows the user to conduct both unrestricted and rational thinking. It works by

- enabling the organization of ideas through the adoption of a Multispace perspective; and
- being adaptable to individual approaches(My way);
- to facilitate Modeling and idea generation through analysis." [Matsuoka, 2013]

The most substantial feature of this method is the point which this method incorporated the viewpoint of circumstance and Multispace. Herein, circumstance is defined as an environment of usage, and effects value, meaning, and state.

There are mainly four steps in the procedure of M method. First, sampling of design elements is done by extracting keywords, pictures, sketches and etc.. The design elements are distributed in the four spaces and circumstance. Then, classification of design elements is conducted by grouping the elements extracted. Third, design elements are structured by drawing correlations among the grouped design elements. Finally, design elements are broken down and added to re-examine design elements. Although these four steps are designated, one can freely work on any step when needed.



The M method is beneficial in the point of organization, usability, and ideation. When organizing, the M method enables the user to clarify the relationship between design elements, to clarify the differences of ideas, and to clarify the thinking process. In addition, from the point of usability, the M method is applicable to diverse domains, individual design approaches, and to collaboration with other people. Finally, considering the point of ideation, the M method can create new values, appropriate to new circumstances, and to use innovation seeds. Through these benefits, the M method enables to cope idea generation and logical thinking.

### **3. APPLICATION OF THE M METHOD**

In order to clarify the effectiveness and issues of the M method, application of the M method is conducted using testes of various backgrounds. The objective of this application is to confirm the effectiveness of the M method and to clarify the issues that needs to be improved. A total of 53 testes were given the same theme, “a bench under a sunset”, and used the M method to design such a bench. After designing, a survey based on the benefits of the M method was answered by each testes. Based on the answer on the survey, the effectiveness and issues of the M method are extracted. Finally, solutions to overcome the extracted issues are discussed.

The application was conducted by 53 testes, which were divided into 10 groups, each with 5 or 6 people. To ensure variety of testes, people from various fields were chosen and were divided equally as possible. These testes included people from the field of both Industrial Design and Engineering Design. At the beginning, every team were given the same concept; a beautiful bench under the sunset, and were given instructions to conduct their design using the M method. Before going on to the actual process of design, they were lectured how to use the M method. Everyone were given the same theme to exclude differences of the theme. Thus, every team had to include the keyword “sunset” in the circumstance to start with. However, no other restrictions were made. Examples of the final outcome of the designed bench are shown in figure 3.

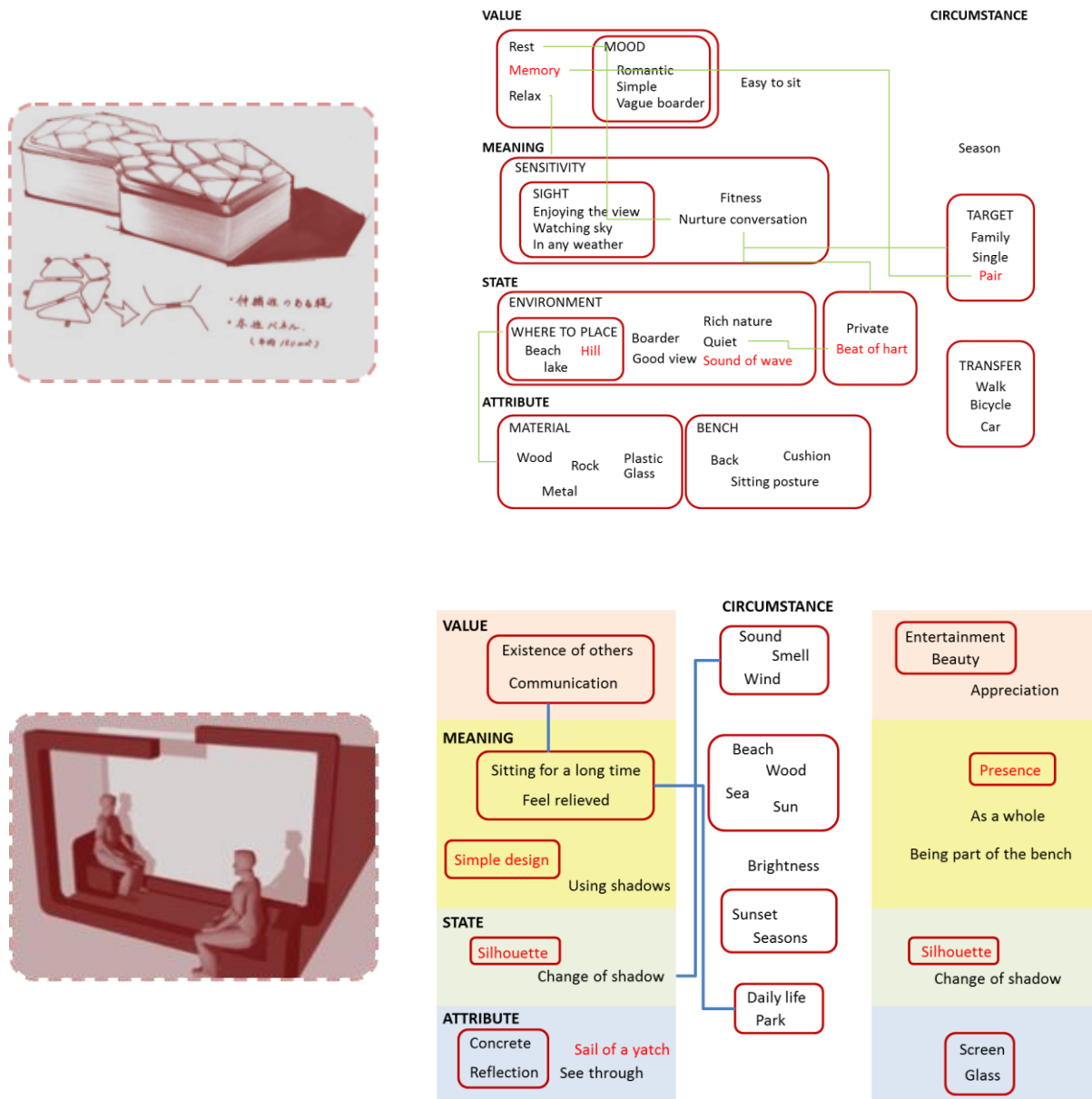


Figure 3. Examples of Design Solutions



#### 4. THE RESULTS OF THE APPLICATION

After finishing the design of the bench, each testee answered a survey based on the benefits of the M method. The survey had questions of the usefulness of the M method, and was answered with a five-grade evaluation. The evaluation items of the survey are as shown in table 1. The results of the survey is shown in table 2. In addition, the results of the analysis were executed through a factor analysis to examine what factors have effect on the evaluation of each items. The factor analysis was performed by first calculating basic statistics, calculating the factor score, deriving the contribution ratio, and plotting the evaluation items. When plotting the evaluation items, the factor axis was rotated using the varimax rotation. The final results of the factor analysis is shown in figure 4.

Table 1. Evaluation Items

1	Can clarify the relation of each design elements
2	Can compare ideas
3	Can clarify the process of design
4	Can create new values
5	Can create ideas adequate to the circumstance
6	Can create idea using innovation seeds
7	Applicable to individual users
8	Applicable to diverse fields
9	Applicable for collaboration

Table 2. Statistics of the survey

		average score	avarage of I.D	average of E.D	standard deviation
1	Can clarify the relation of each design elements	3.74	3.65	3.97	0.62
2	Can compare ideas	3.75	3.76	4.03	0.7
3	Can clarify the process of design	3.74	3.79	4.38	0.86
4	Can create new values	3.81	3.75	4.01	0.65
5	Can create ideas adequate to the circumstance	3.81	3.74	4.03	0.56
6	Can create idea using innovation seeds	3.57	3.56	4.13	0.72
7	Applicable to individual users	3.15	3.07	3.88	1.03
8	Applicable to diverse fields	3.55	3.5	3.8	0.77
9	Applicable for collaboration	3.79	3.83	4.41	0.86

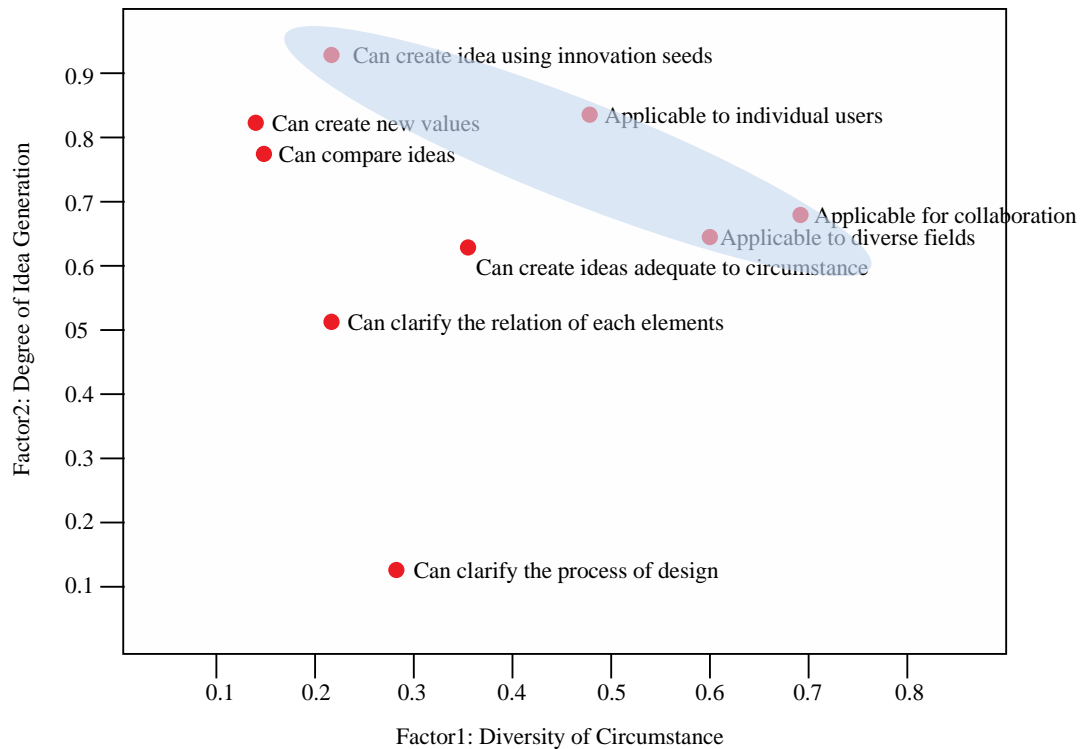


Figure 4. Results of the Factor Analysis

The statistics in table 2 show the average score of the whole testee, I.D testee, and E.D testee. In addition, the standard deviation is also shown in the table. From the result of table 2, it can be seen that the average of E.D. testees marked a high score overall. Furthermore, there were no items scoring below 3.00, which indicates that the M method is generally a useful design method. However, compared to other evaluation items, items 6, 7, and 8 had a low average, especially from I.D. testees. Therefore it was indicated that there is still room for improvement in these three items compared to other items.

Figure 4 illustrates the score of each evaluation items, which are the results of the factor analysis. Since items containing the word “create” are gathered at the top of the chart, and items including the word “clarify” are gathered at the bottom, it can be conceived that the vertical axis expresses the degree of idea generation. The evaluation items closer to the top of the chart includes elements relating to creating new ideas. In addition, since elements such as “Applicable for collaboration” and “Applicable to diverse fields”, it can be determined that the horizontal axis represents the diversity of circumstance. Evaluation items closer to the right of the figure considers the diversity of circumstance than items on the left side. Furthermore, evaluation items which showed a low average, especially “Applicable to individual users” and “Applicable to diverse fields” is gathered at the upper right corner of



figure 4, which is the circled area. Since evaluation items in the upper right corner has a low average compared to other items, it can be concluded that in both factors, “diversity of circumstance” and “Degree of Idea Generation”, the M method needs to be improved.

## 5. DISCUSSION TO IMPROVE THE M METHOD

From the results in chapter 4, it was indicated that the M method can be improved in the perspective of diverse circumstance and idea generation. Moreover, since the generation of ideas greatly depends on the skills and experience of the user, it is better to focus on improving the M method to adapt to diverse circumstance. By improving the M method so that it can adapt to diverse circumstance, the issue which it had can be overcome.

One means to make the M method adaptable to diverse circumstances, is to incorporate diverse design methods to the M method. Theoretically, if the M method included all design methods that exists, it would become adaptable to all situations. However, since covering all design methods is impracticable, covering wide areas of design methods is necessary. For example, based on the M model, design methods can be divided into 7 clusters, indicated in figure 5. This was extracted by conducting a cluster analysis to 80 design methods. If enough design methods were collected to fit these clusters, it may become possible that the M method will be able to adapt to diverse circumstances. Therefore, the next step in order to improve the M method is to collect enough design methods for each groups. By applying the collected design methods to the M method, it will become adaptable to diverse circumstance, and will overcome the issues extracted in this paper



		Design Process			
		Conceptual Design		Basic Design	Detail Design
		Thinking Space			
		Value, Meaning	Value, Meaning, State, Attribute	Meaning, State, Attribute	State, Attribute
Design Thinking	Extraction	extraction value and meaning elements in conceptual design	Extraction of value, meaning, state, and attribute elements through conceptual, basic design		
	Grouping		Grouping of each elements in conceptual and basic design		
	Qualitative Structuring		Qualitatively structures each elements in conceptual and basic design	Qualitatively structures meaning, state, and attribute elements in basic design	
	Quantitative Structuring			Quantitatively structures meaning, state, and attribute elements in basic design	Quantitatively structures state, and attribute elements in specific design

Figure 5. Grouping of Design Methods Based on the M Model

## 6. CONCLUSION

In this research, the need of adapting to diverse circumstances of the M method was clarified through application. To overcome this problem, design methods covering wide areas of design fields were incorporated to the M method enabling the M method to become adaptable for diverse circumstances. For future research, the extracted design methods need to be classified more specifically in order to verify if the methods cover enough areas of the field of design.

## ACKNOWLEDGEMENT

This work was supported in part by a Grant-in-Aid for the Global Center of Excellence Program for the Center for Education and Research of Symbiotic, Safe and Secure System Design from the Ministry of Education, Culture, Sports, Science and Technology of Japan.





## REFERENCES

1. **Matsuoka, Y. (2013)**, M method. Design Thinking on Multispace, Kindai Kagaku Sha, Tokyo, Japan
2. **Matsuoka, Y. (2006)**, Industrial Design and Engineering Design, HCD handbook, Maruzen, Tokyo, Japan
3. **Rosalind, P.B., (2006)**, The Arts and Crafts Movement, Phaidon, London
4. **Matsuoka, Y. (2010)**, Design Science, Maruzen, Tokyo, Japan
5. **Yoshikawa, H. (1979)**, “Introduction to General Design Theory”, The Japan Society for Precision Engineering, Vol.45, No.8, pp 906-912





## MULTISPACE QUALITY FUNCTION DEPLOYMENT USING DESIGN STRUCTURE MATRIX

**T. KATO**, *t.kato@tokai-u.jp* Tokai University, 4-1-1 Kitakaname, Hiratsuka, Japan

**T. SOGA**, *0bem2215@mail.tokai-u.jp* Tokai University, 4-1-1 Kitakaname, Hiratsuka, Japan

**Y. HOSHINO**, *y-hoshino@mail.nissan.co.jp* Nissan Motor Company Ltd., 560-2 Okatsukoku Atsugi, Japan

### ABSTRACT

Specialization and professionalization of design work make it difficult for members of a product development team to share product information each other. In the previous study, the Multispace Quality Function Deployment (M-QFD), which allows designers to extract design elements with respect to diverse requirements and enables them to understand their relationships, was proposed on the basis of the multispace design model and Interpretive Structural Modeling. This study improves the M-QFD using Design Structure Matrix. The proposed M-QFD enables them to construct a modular composition of the product components in the late process of design. Additionally, a design example (design of an automotive steering system) is presented to demonstrate the proposed M-QFD.

**Keywords:** Design theory and methodology, QFD, ISM, DSM

### 1. INTRODUCTION

Due to the diversity and complicity of the functions and mechanisms of products, the design work has become specialized and professionalized [Matsuoka, 2010]. Consequently, it is difficult for members of a product design team to share product information. In a previous study [Kato, 2013ab], we focused on Quality Function Deployment (QFD) [Akao, 1990] and proposed the QFD based on multi spaces (hereinafter called M-QFD) improved on the following two features (Figure 1):

1) Four deployment charts: value, meaning, state, and attribute based on Multispace design model [Matsuoka, 2010] are used in order to extract diverse design elements [Kato, 2013a];

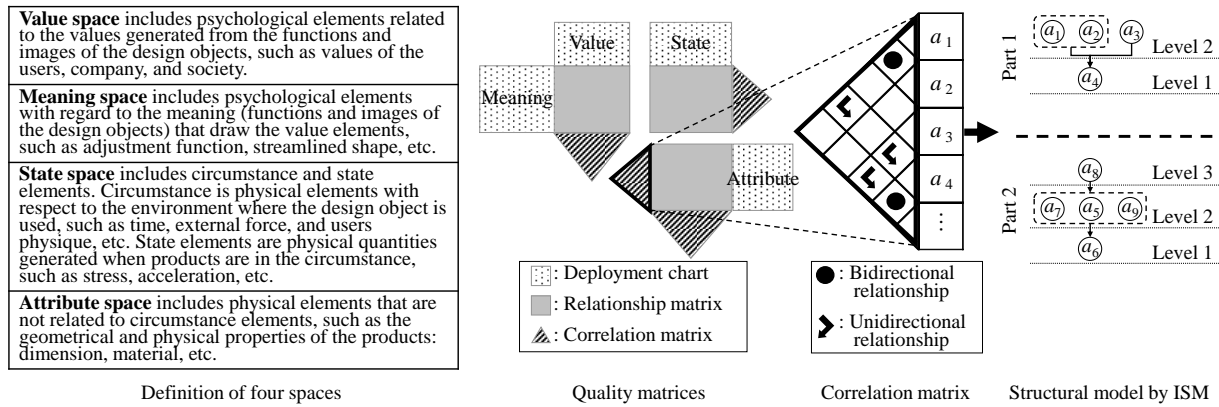


Figure 1. Conceptual drawing of M-QFD

2) Interpretive structural modeling (ISM) [Warfield, 1976 and Ansari et al., 2013] is applied in order to group and stratify the extracted design elements on the basis of their relationships. Additionally, the previous study applied the proposed M-QFD to the basic design of a head protection wear and confirmed the applicability of it.

ISM is suitable to generally analyze the relationships of the elements and to be used in the conceptual and basic design (the early process of design). However, it is not suitable to analyze them in detail and to be applied to the detail design (the late process of design). Therefore, the method which supports the designer in the late process of design in order to enables M-QFD to be applied in the entire process of design. This study focuses on the modularization of the product parts in the detail design and aims to construct M-QFD using a method alternative to ISM.

This paper is organized as follows. Section 2 clarifies the issue of ISM in modularization of the product parts and describes the outline of DSM (Design Structure Matrix) and the procedure of the proposed M-QFD using DSM. Section 3 illustrates an application of the proposed M-QFD to an automotive steering system, while Section 4 provides conclusions and the future research direction.

## 2. PROPOSITION OF M-QFD FOR MODULARIZATION

### Problem of ISM Related to Modularization

In the early process of design, the design elements are extracted and removed (i.e. idea generation and selection) repeatedly by the designers in order to clarify the design concept [Matsuoka, 2010]. This makes that the elements are not completely decided and their relationships are varied. In the situation, the method, which extracts whole the relationships and roughly and quickly analyzes them by grouping or stratifying them, is effective. ISM extracts indirect relationships between design elements by calculating the power of the direct

effective matrix, which expresses the direct relationships, to derive reachability matrix (Figure 2). On the basis of the extracted relationships, ISM conducts both grouping and stratifying the elements (part and level identification) automatically. Therefore, ISM is effective to be applied in the early process of design.

Whereas, in the late process of design, the design elements have been decided and their relationships are seldom varied in order to enable designers to decide the component parts or the process of product development and manufacture [Matsuoka, 2010]. Additionally, the relationships in the process are often complex and this makes it difficult to modularize the product components and construct the concurrent process of product development and manufacture. In the situation, the method, which explores the boundary between modules where the number of the relationships is low or deletes some of the relationships on the basis of the technical consideration by the designers, is effective. Therefore, extracting indirect relationships and automatically organizing the elements by ISM are not effective in the late process of design. Additionally, modularization of the elements requires not only the functional relationships of them but also some kinds of the relationships, such as cost and location. ISM, however, cannot deal with several types of the relationships and has a difficulty to be applied to the modularization.

Design Structure Matrix (DSM) is a method for the modularization and process management using the direct affective matrix same as ISM [Lindemann, 2009]. DSM has some different features from ISM: 1) DSM excludes indirect relationships; 2) DSM includes partitioning and clustering methods which can organize the relationships incorporating the designer's opinions; 3) Some kinds of DSM deal with several types of the relationships. This study, therefore, focused on DSM in order to improve M-QFD on behalf of ISM. The outline of the focused DSM and the proposed M-QFD using it are described in the next session.

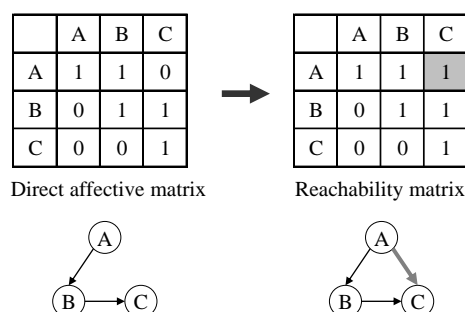


Figure 2. Indirect relationship derived by ISM

## Design Structure Matrix (DSM)

DSM is the matrix to express the relationships between the design elements considered in the product development, such as parts, design tasks and staff assignment. The lines and columns of DSM are reordered to simplify the relationships between them. DSM, therefore, enables designers to easily understand them and is useful to improve the efficiency in the late process of design, such as management of the development schedule, manufacturing, and parts. There are three typical methods for reordering the lines and columns of DSM as follows:

(1) Clustering: this method reorders the design elements in order to construct chunks (modules) of the elements which relate each other by transferring their relationships close to the diagonal position of the matrix. This groups the design elements on the basis of their relationships and enables the designers to comprehend the complex architecture of them. The method constructs the chunks whose number of the elements and relationships to other chunks should be as few as possible (Figure 3a).

(2) Partitioning: this method reorders the design elements in order to decrease the design feedback (relationships located in the upper triangular matrix) and to improve the design process by transferring their relationships to the upper triangular matrix (Figure 3b). However, it is impossible to delete it completely only by transferring in the case that the design object is complex. In this situation, the designer decides whether to accept some feedback or to delete it using the following tearing method.

(3) Tearing: this method deletes the effective feedback in order to improve the design process after the partitioning (Figure 3c).

There are some kinds of DSM, such as task DSM to describe the design task and parameter DSM to describe the relationships between design parameters. This study focused on

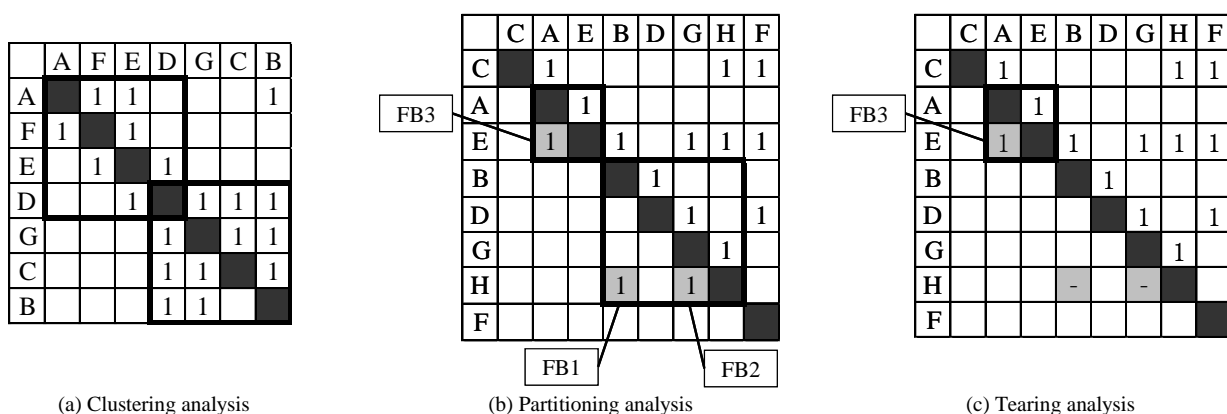


Figure 3. Conceptual drawing of DSM

Component-based DSM which constructs the modules of the components.

Component-based DSM decomposes the components or subsystems of the product system on the basis of some types of their relationships and was proposed by Eppinger [Pimm et al., 1994]. Eppinger defined four types of the relationships (spatial, energy, information, and material) and five-level evaluation of the relationships (2: required, 1: desired, 0: indifferent, -1: undesired, -2: detrimental). Note that this study focused on two-level evaluation (1: related, 0: unrelated) in order to handle the same data used in ISM. Transferring these relationships close to the diagonal position by clustering method for modularization (Figure 4), component-based DSM requires a particular clustering method to consider several types of the relationships. Ogawa [Ogawa et al., 2013] proposed the clustering method (four rules) to combine chunk swarms (Figure 5) derived from the direct affective matrices based on each type relationships using DSM cluster method. The following sentences illustrate the rules using an example of combining two chunk swarms:  $M_{(1)} = \{M_{(1)1}, M_{(1)2}, \dots, M_{(1)n}\}$  and  $M_{(2)} = \{M_{(2)1}, M_{(2)2}, \dots, M_{(2)m}\}$ , where  $M_{(a)b}$  is  $b$  th chunk included in  $a$  th chunk swarm, and  $n$  and  $m$  denote the numbers of chunks included  $M_{(1)}$  and  $M_{(2)}$ , respectively.

	B	A	D	E	C
B	1 1 1 1	1 0 1 1	1 0 0 1	0 0 0 0	0 0 0 0
A	1 1 0 1	1 1 0 1	1 1 1 0	0 0 1 1	0 0 0 0
D	0 0 0 0	1 1 1 1	1 1 1 1	1 1 0 1	0 1 1 1
E	1 1 0 1	0 0 0 0	1 1 1 0	1 1 1 1	1 1 1 0
C	0 0 0 0	0 0 0 0	0 0 0 0	0 1 1 1	1 1 1 1

Spatial      Energy  

S E  
I M

Information      Materials

Figure 4. Conceptual drawing of component **DSM**

	C	A	H	E	B	G	D	I	F
C	1	1				1	1		
A	1	1	1			1		1	
H			1	1	1				
E			1	1	1	1			
B	1		1	1	1	1	1	1	1
G		1				1	1	1	
D						1	1	1	
I						1	1	1	1
F	1			1					1

1<sup>st</sup> chunk:  $M_1 = \{A, C\}$   
 2<sup>nd</sup> chunk:  $M_2 = \{B, E, H\}$   
 3<sup>rd</sup> chunk:  $M_3 = \{D, G, I\}$   
 4<sup>th</sup> chunk:  $M_4 = \{F\}$

Figure 5. Conceptual drawing of chunk **swarm**



(1) Rule 1 for constructing a combined chunk swarm whose chunk includes as many elements as possible:

Step 1 Set  $i = 1$ .

Step 2 Set  $j_s = j$  to maximize the element number in the set expressed as the following equation:

$$M_{(1)i} \cup M_{(2)j} | \{M_{(1)i} \cap M_{(2)j}\} \neq \emptyset \quad (1)$$

Step 3 Derive  $i$  th chunk of the combined chunk swarm  $M'_i$  as the following equations:

$$M'_i = M_{(1)i} \cup M_{(2)j} \quad (2)$$

Step 4 Eliminate the elements included in the derived chunk as the following equation:

$$M_{(1)k} = M_{(1)k} - \{M_{(2)j_s} - (M_{(1)i} \cap M_{(2)j_s})\} \quad (k \neq i) \quad (3)$$

Step 5 Eliminate  $M_{(2)j_s}$  from  $M_{(2)}$  as the following equation:

$$M_{(2)} = M_{(2)} - M_{(2)j_s} \quad (4)$$

Step 6 If  $i \neq n$ , set  $n = n + 1$  and go to Step 2. Otherwise, quit the procedure.

(2) Rule 2 for constructing a combined chunk swarm whose chunk includes fewer elements:

Steps 1, 3, 4, 5, and 6 are same as those of Rule 1. In Step 2,  $j$  to minimize the element number is set to  $j_s$ .

(3) Rule 3 for improving Rule 1 by considering the information of the physical component connection:

Steps 1, 3, 4, 5, and 6 are same as those of Rule 1. In Step 2, the condition that all the elements in  $\{M_{(1)i} \cup M_{(2)j}\}$  are connected, i.e. an element relate to the others considering indirect relationships (Figure 6), is added.

(4) Rule 4 for improving Rule 1 by considering the Bills of material (BOM):

All steps are same as Rule 1. After the procedures of Rule 1, let an element, which is independent from the others according to BOM (Figure 7), be independent from the chunk. In Figure 7, "cable" and "ball" can be independent. Rule 3 and 4 improve rule 1 using the information of the component connection according to the designer's knowledge or BOM. This means they can be applied to the design problem in which the information is clarified.

The features of ISM and DSM are summarized in Table 1. This table indicates DSM is suitable for the modularization, compared to ISM.



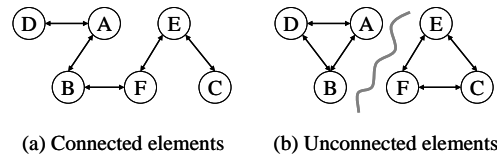


Figure 6. Connected and unconnected

### M-QFD based on DSM

This study applied DSM to M-QFD for the modularization. The process of the proposed M-QFD is shown in Figure 8. First, designers construct the deployment charts of value, meaning,

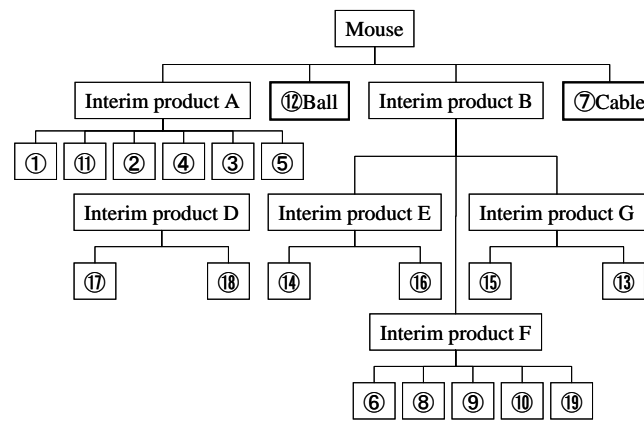


Figure 7. Conceptual drawing of BOM (Example: ball mouse)

Table 1. Feature comparison between ISM and DSM

	ISM	DSM		Component DSM
		Clustering	Partitioning & Tearing	Clustering
Adding subsidiary relationships	○	—		
Grouping	○	○	—	○
Stratifying	○	—	○	—
Evaluating several kinds of relationships	—	—	—	○
Organizing by designers (using designers' aim)	—	○		

state, and attribute space elements, i.e. extract design elements, (Step 1) and the relation and correlation matrices, i.e. clarify the relationships between them (Step 2, 3). Second, the designers extract and remove the design elements and the relationships between them using ISM. Where, Figure 6 describes this procedure using only attribute elements for simplification. If needed, designers apply ISM not only to the relationships in each space but also to those between spaces [Kato, 2013b] (Step 4). Until this process, proposed M-QFD is same as the conventional one. Finally, designers conduct the modularization of the attribute elements (product components) using DSM and decide the modular composition of the product (Step 5). If needed, designers derive several direct affective matrices in order to evaluate several types of the relationships. When they clarify the several types of the relationships, focusing the

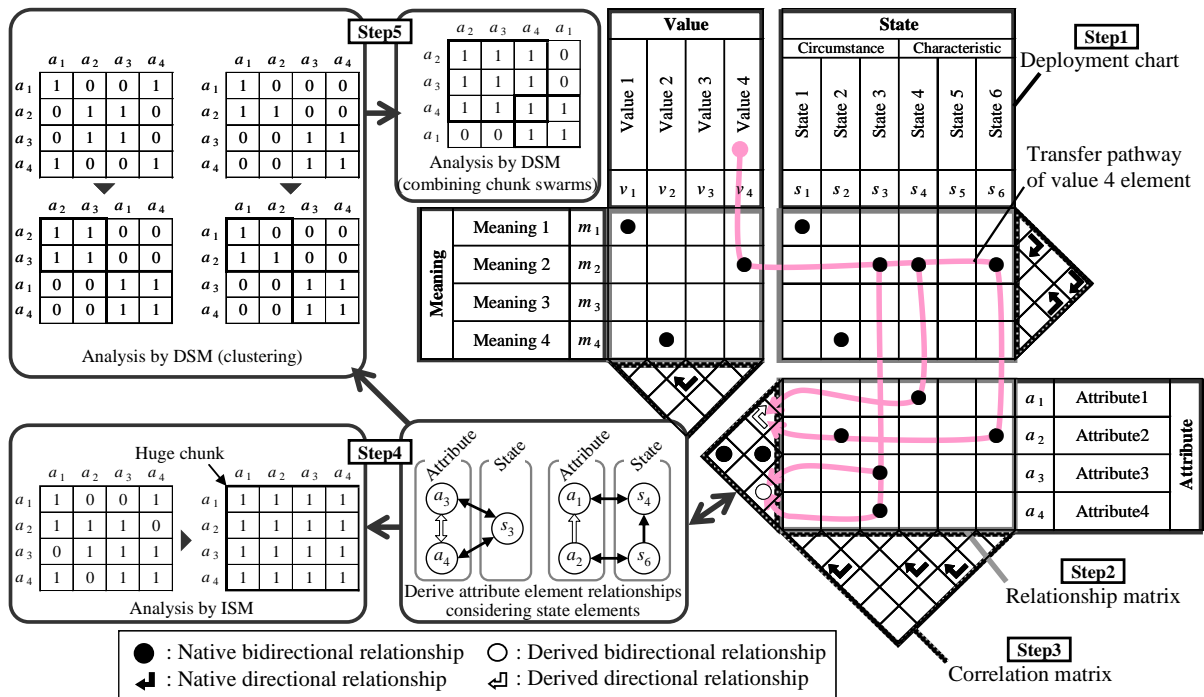


Figure 8. Conceptual drawing of M-QFD using DSM

value and meaning elements is useful. Figure 8 is an example that "value element 4" is transferred into the attribute space and derives the relationships (white colored arrow and circle). In this example, two direct affective matrices expressing native and the derived relationships are separately modularized by DSM clustering method and are combined. DSM finally derives two chunks of the elements and seems to be more useful for modularization, compared to ISM deriving one huge chunk.

### 3. ILLUSTRATIVE EXAMPLE

#### Design Object

To confirm the effectiveness, the proposed and conventional M-QFD (using DSM and ISM) were compared by applying them to the same design problem: an automotive steering system. The steering system turns a car according to a driver's steering action by changing the wheel angles. The mechanisms of the system are classified into two types: rack-and-pinion and ball screw. The former focused in this study conveys a rotary movement of steering by the driver to the "steering gear (rack-and-pinion)" through the "column shaft" and transfers it into the linear movement in the direction of the wheel axis to move the "tie-rod", which is a part of the linkage mechanism for changing the wheel angles (Figure 9). Most of the steering systems have an "assist motor" to decrease the driver's steering force, recently and are called electric power steering (EPS). Therefore, the number of the components, such as "electrical control

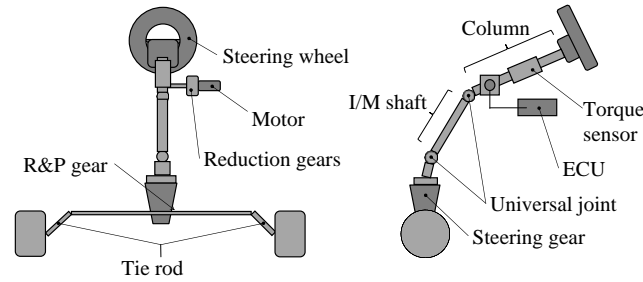


Figure 9. Conceptual drawing of steering

unit (ECU)" and "torque sensor", is increasing. Though most of the components have to be changed to meet the specifications of a vehicle type, such as vehicle weight and width, some components are generally modularized for mass production.

The steering system, however, is difficult to be modularized because it has several choices regarding the assist motor location (column shaft, rack and pinion gear) and a role of a user interface and requires to be considered not only cost and function but also component assignment and user's preference.

## Results and Discussion

Figure 10 shows the quality matrices of an automotive steering system constructed by an automotive engineer who belongs to a steering system development team. Using the matrices, this study carried out two types of the modularization evaluated on the basis of cost and functionality and compared the results. The former modularization transferred the relationships of the value elements related to the cost ("company profit ( $v_{14}$ )" and "better productivity ( $v_8$ )") into the attribute element ones, while the latter focused on the value elements related to the functionality ("better operability ( $v_1$ )" and "better robustness ( $v_3$ )"). The attribute elements of the two direct affective matrices (Figure 11) are modularized (grouped) using ISM and DSM. The results of applying ISM and DSM are shown in Figures 12 and 13, respectively. The comparison of them is shown in the following discussion:

Figure 12 indicates the matrix and its structural model obtained by ISM, and (a) and (b) show them for the modularization based on cost and functionality, respectively. This figure shows ISM derives a huge chunk (strong connection between all elements), and this makes it difficult for designers to proceed with the further modularization. Figure 13a shows the matrix obtained by DSM for the modularization based on cost. The matrix has a chunk including both the electronic components (e.g. "assist motor ( $a_2$ )" and "ECU main part ( $a_{16}$ )" ) and the column components (e.g. "column ( $a_1$ )" and "column mount ( $a_{21}$ )" ). This suggests for the designers to

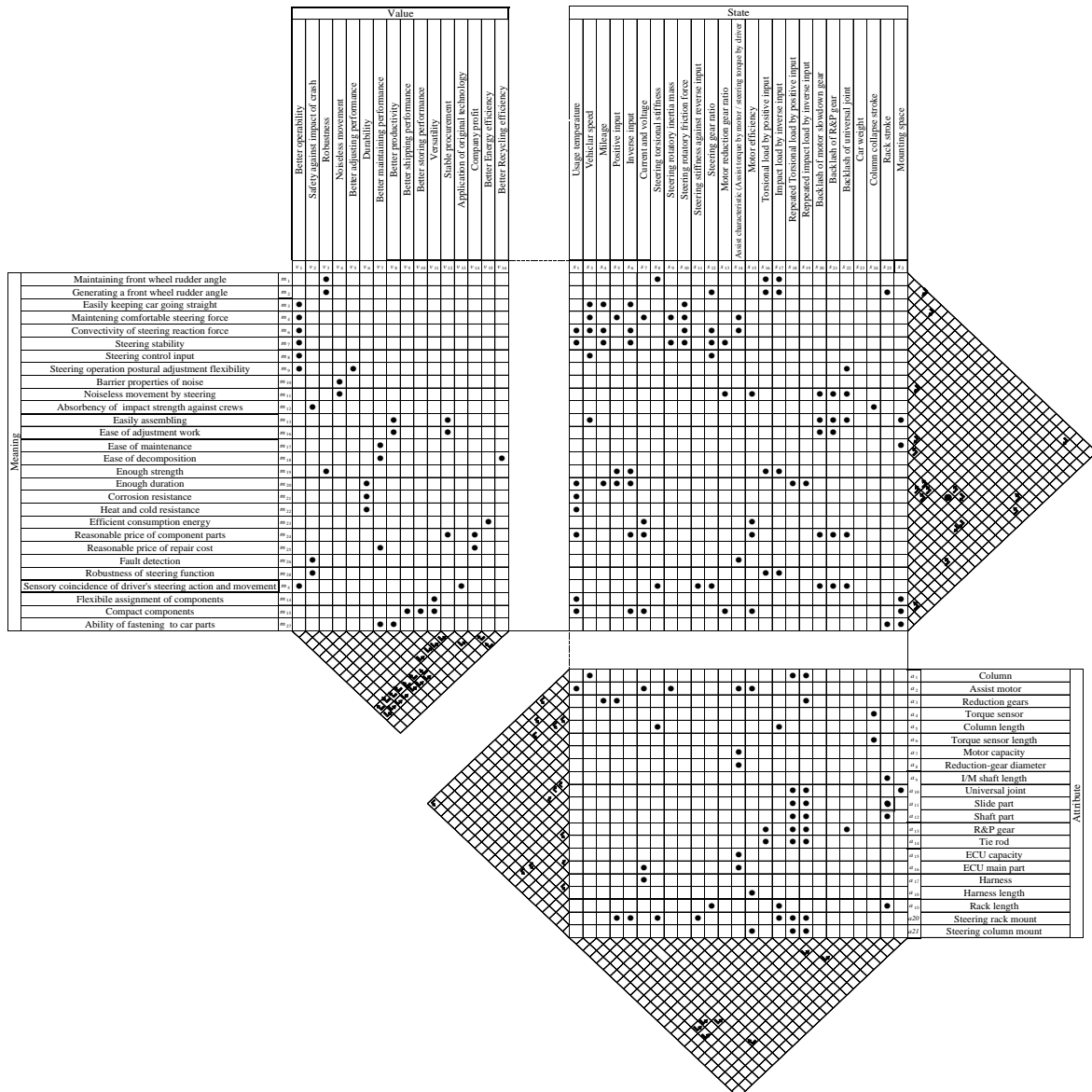


Figure 10. M-QFD of automotive steering

reduce the cost by locating the electronic components near the column (unwatered and less vibrant area), i.e. removing the water and vibration proof functions of the components.

Figure 13b describes the matrix obtained by DSM considering the functionality. The matrix has a chunk containing the "assist motor ( $a_2$ )" and the steering gear components (e.g. "tie rod ( $a_{14}$ )" and "rack mount ( $a_{20}$ )"). This indicates that setting the assist motor near the driving part (wheel axis) decreases the torque (mechanical transmission) and time loss and improves the feelings of the driver's operability.



	$a_1$	$a_2$	$a_3$	$a_4$	$a_5$	$a_6$	$a_7$	$a_8$	$a_9$	$a_{10}$	$a_{11}$	$a_{12}$	$a_{13}$	$a_{14}$	$a_{15}$	$a_{16}$	$a_{17}$	$a_{18}$	$a_{19}$	$a_{20}$	$a_{21}$
$a_1$	1	1	1	1	1	1	1	1	0	0	0	0	0	1	1	1	1	0	0	1	
$a_2$	1	1	1	0	1	0	1	1	0	0	0	0	0	1	1	1	1	0	0	1	
$a_3$	1	1	1	0	1	0	1	1	0	0	0	0	0	1	1	1	1	0	0	1	
$a_4$	1	0	0	1	1	1	0	0	0	0	0	0	0	0	0	0	0	0	0	1	
$a_5$	1	1	1	1	1	1	1	1	0	0	0	0	0	1	1	1	1	0	0	1	
$a_6$	1	0	0	1	1	1	0	0	0	0	0	0	0	0	0	0	0	0	0	1	
$a_7$	1	1	1	0	1	0	1	1	0	0	0	0	0	0	0	0	0	0	0	1	
$a_8$	1	1	1	0	1	0	1	1	0	0	0	0	0	0	0	0	0	0	0	1	
$a_9$	0	0	0	0	0	0	0	0	1	1	1	1	0	0	0	0	0	0	0	0	
$a_{10}$	1	0	0	0	0	0	0	0	1	1	1	1	1	0	0	0	0	0	0	0	
$a_{11}$	0	0	0	0	0	0	0	0	1	1	1	1	0	0	0	0	0	0	0	0	
$a_{12}$	0	0	0	0	0	0	0	0	1	1	1	0	0	0	0	0	0	0	0	0	
$a_{13}$	0	0	0	0	0	0	0	0	1	0	0	1	1	0	0	0	0	0	1	1	
$a_{14}$	0	0	0	0	0	0	0	0	0	0	0	1	1	0	0	0	0	1	1	0	
$a_{15}$	1	1	0	0	1	0	0	0	0	0	0	0	1	1	1	1	0	0	0	1	
$a_{16}$	1	1	0	0	1	0	0	0	0	0	0	0	0	1	1	1	1	0	0	1	
$a_{17}$	1	1	0	0	1	0	0	0	0	0	0	0	0	1	1	1	1	0	0	1	
$a_{18}$	1	1	0	0	1	0	0	0	0	0	0	0	0	1	1	1	1	0	0	1	
$a_{19}$	0	0	0	0	0	0	0	0	0	0	0	0	1	1	0	0	0	0	1	1	
$a_{20}$	0	0	0	0	0	0	0	0	0	0	0	0	1	1	0	0	0	0	1	1	
$a_{21}$	1	1	1	1	1	1	1	1	0	0	0	0	0	1	1	1	1	0	0	1	

(a) Modularization based on cost

	$a_1$	$a_2$	$a_3$	$a_4$	$a_5$	$a_6$	$a_7$	$a_8$	$a_9$	$a_{10}$	$a_{11}$	$a_{12}$	$a_{13}$	$a_{14}$	$a_{15}$	$a_{16}$	$a_{17}$	$a_{18}$	$a_{19}$	$a_{20}$	$a_{21}$
$a_1$	1	0	0	0	0	1	0	0	0	1	0	0	0	0	0	0	0	0	0	0	1
$a_2$	0	1	1	0	0	0	1	1	0	0	0	0	1	1	1	1	1	1	1	1	0
$a_3$	0	1	1	0	0	0	1	1	0	0	0	0	1	1	0	0	0	0	1	1	0
$a_4$	0	0	0	1	0	0	0	0	0	0	0	0	1	1	0	0	0	0	1	1	0
$a_5$	0	0	0	0	1	1	1	1	0	0	0	0	0	1	1	1	1	1	0	0	1
$a_6$	1	0	0	0	1	1	0	0	0	0	0	0	1	1	0	0	0	0	1	1	0
$a_7$	0	1	1	0	1	0	1	1	0	0	0	0	1	1	0	0	0	0	1	1	0
$a_8$	0	1	1	0	1	0	1	1	0	0	0	0	1	1	0	0	0	0	1	1	0
$a_9$	0	0	0	0	0	0	0	0	1	1	1	1	0	0	0	0	0	0	0	0	0
$a_{10}$	1	0	0	0	0	0	0	0	1	1	1	1	1	0	0	0	0	0	0	0	0
$a_{11}$	0	0	0	0	0	0	0	0	1	1	1	1	0	0	0	0	0	0	0	0	0
$a_{12}$	0	0	0	0	0	0	0	0	1	1	1	0	0	0	0	0	0	0	0	0	0
$a_{13}$	0	1	1	1	0	1	1	1	0	1	0	0	1	1	1	1	1	1	1	1	0
$a_{14}$	0	1	1	1	0	1	1	1	0	0	0	0	1	1	1	1	1	1	1	1	0
$a_{15}$	1	0	0	1	0	0	0	0	0	0	0	0	1	1	1	1	1	1	1	1	0
$a_{16}$	0	1	0	0	1	0	0	0	0	0	0	0	1	1	1	1	1	1	1	1	0
$a_{17}$	0	1	0	0	1	0	0	0	0	0	0	0	1	1	1	1	1	1	1	1	0
$a_{18}$	0	1	0	0	1	0	0	0	0	0	0	0	1	1	1	1	1	1	1	1	0
$a_{19}$	0	1	1	1	0	1	1	1	0	0	0	0	1	1	1	1	1	1	1	1	0
$a_{20}$	0	1	1	1	0	1	1	1	0	0	0	0	1	1	1	1	1	1	1	1	0
$a_{21}$	1	0	0	0	1	0	0	0	0	0	0	0	0	0	0	0	0	0	0	0	1

(b) Modularization based on functionality

Figure 11. Direct affective matrices

	$a_1$	$a_2$	$a_3$	$a_4$	$a_5$	$a_6$	$a_7$	$a_8$	$a_9$	$a_{10}$	$a_{11}$	$a_{12}$	$a_{13}$	$a_{14}$	$a_{15}$	$a_{16}$	$a_{17}$	$a_{18}$	$a_{19}$	$a_{20}$	$a_{21}$
$a_1$	1	1	1	1	1	1	1	0	0	0	0	0	0	1	1	1	1	0	0	1	
$a_2$	1	1	1	1	1	1	1	0	0	0	0	0	0	1	1	1	1	0	0	1	
$a_3$	1	1	1	1	1	1	1	0	0	0	0	0	0	1	1	1	1	0	0	1	
$a_4$	1	1	1	1	1	1	1	0	0	0	0	0	0	1	1	1	1	0	0	1	
$a_5$	1	1	1	1	1	1	1	0	0	0	0	0	0	1	1	1	1	0	0	1	
$a_6$	1	1	1	1	1	1	1	0	0	0	0	0	0	1	1	1	1	0	0	1	
$a_7$	1	1	1	1	1	1	1	0	0	0	0	0	0	1	1	1	1	0	0	1	
$a_8$	1	1	1	1	1	1	1	0	0	0	0	0	0	1	1	1	1	0	0	1	
$a_9$	0	0	0	0	0	0	0	1	0	0	0	0	0	0	0	0	0	0	0	0	
$a_{10}$	0	0	0	0	0	0	0	0	1	0	0	0	0	0	0	0	0	0	0	0	
$a_{11}$	0	0	0	0	0	0	0	0	0	1	0	0	0	0	0	0	0	0	0	0	
$a_{12}$	0	0	0	0	0	0	0	0	0	0	1	0	0	0	0	0	0	0	0	0	
$a_{13}$	0	0	0	0	0	0	0	0	0	0	0	1	0	0	0	0	0	0	0	0	
$a_{14}$	0	0	0	0	0	0	0	0	0	0	0	0	1	0	0	0	0	0	0	0	
$a_{15}$	1	1	1	1	1	1	1	0	0	0	0	0	0	1	1	1	1	0	0	1	
$a_{16}$	1	1	1	1	1	1	1	0	0	0	0	0	0	1	1	1	1	0	0	1	
$a_{17}$	1	1	1	1	1	1	1	0	0	0	0	0	0	1	1	1	1	0	0	1	
$a_{18}$	1	1	1	1	1	1	1	0	0	0	0	0	0	1	1	1	1	0	0	1	
$a_{19}$	0	0	0	0	0	0	0	0	0	0	0	0	0	0	0	0	0	0	1	0	
$a_{20}$	0	0	0	0	0	0	0	0	0	0	0	0	0	0	0	0	0	0	0	1	
$a_{21}$	1	1	1	1	1	1	1	0	0	0	0	0	0	1	1	1	1	0	0	1	

	$a_1$	$a_2$	$a_3$	$a_4$	$a_5$	$a_6$	$a_7$	$a_8$	$a_9$	$a_{10}$	$a_{11}$	$a_{12}$	$a_{13}$	$a_{14}$	$a_{15}$	$a_{16}$	$a_{17}$	$a_{18}$	$a_{19}$	$a_{20}$	$a_{21}$
$a_1$	1	0	0	0	0	0	0	0	0	0	0	0	0	0	0	0	0	0	0	0	0
$a_2$	0	1	1	1	0	1	1	1	0	0	0	0	0	1	1	1	1	1	1	1	0
$a_3$	0	1	1	1	0	1	1	1	0	0	0	0	0	1	1	1	1	1	1	1	0
$a_4$	0	0	0	1	0	0	0	0	0	0	0	0	0	0	0	0	0	0	0	0	0
$a_5$	0	0	0	0	1	0	0	0	0	0	0	0	0	0	0	0	0	0	0	0	0
$a_6$	0	1	1	1	0	1	1	1	0	0	0	0	0	1	1	1	1	1	1	1	0
$a_7$	0	1	1	1	0	1	1	1	0	0	0	0	0	1	1	1	1	1	1	1	0
$a_8$	0	1	1	1	0	1	1	1	0	0	0	0	0	1	1	1	1	1	1	1	0
$a_9$	0	0	0	0	0	0	0	0	1	0	0	0	0	0	0	0	0	0	0	0	0
$a_{10}$	0	0	0	0	0	0	0	0	0	1	0	0	0	0	0	0	0	0	0	0	0
$a_{11}$	0	0	0	0	0	0	0	0	0	0	1	0	0	0	0	0	0	0	0	0	0
$a_{12}$	0	0	0	0	0	0	0	0	0	0	0	1	0	0	0	0	0	0	0	0	0
$a_{13}$	0	1	1	1	0	1	1	1	0	0	0	0	0	1	1	1	1	1	1	1	0
$a_{14}$	0	1	1	1	0	1	1	1	0	0	0	0	0	1	1	1	1	1	1	1	0
$a_{15}$	0	1	1	1	0	1	1	1	0	0	0	0	0	1	1	1	1	1	1	1	0
$a_{16}$	0	1	1	1	0	1	1	1	0	0	0	0	0	1	1	1	1	1	1	1	0
$a_{17}$	0	1	1	1	0	1	1	1	0	0	0	0	0	1	1	1	1	1	1	1	0
$a_{18}$	0	1	1	1	0	1	1	1	0	0	0	0	0	1	1	1	1	1	1	1	0
$a_{19}$	0	1	1	1	0	1	1	1	0	0	0	0	0	1	1	1	1	1	1	1	0
$a_{20}$	0	1	1	1	0	1	1	1	0	0	0	0	0	1	1	1	1	1	1	1	0
$a_{21}$	0	0	0	0	0	0	0	0	0	0	0	0	0	0	0	0	0	0	0	0	1

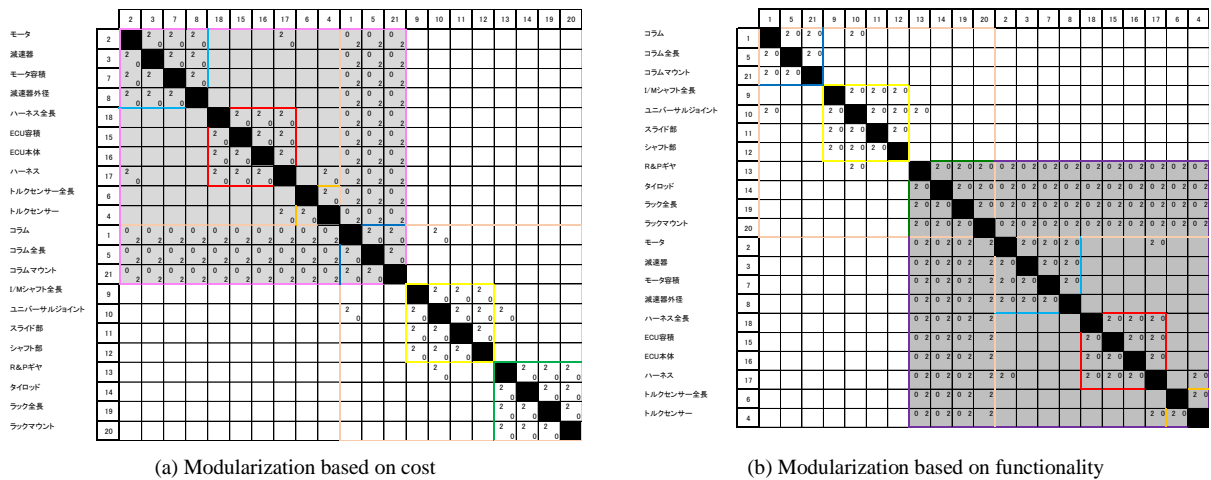


Figure 13. Result of DSM

(2) "Assist motor (a<sub>2</sub>)" corresponding to the required torque decided by the car weight;

(3) "Tie rod (a<sub>14</sub>)" and "rack length (a<sub>19</sub>)" corresponding to the car width (wheel axis length).

This study compared the two types of the modular composition (Figures 13a and 13b) regarding the three design changes as follows.

The modular composition for cost (Figures 13a) suggests corresponding to the space ("design change 1") using "I/M shaft length (a<sub>9</sub>)" on behalf of "Column length (a<sub>5</sub>)" combined with the electronic components to be a module. This enables the designers to standardize (i.e. unify the specifications of) the column components. Therefore, if "assist motor (a<sub>2</sub>)" regarding "design change 2" is standardized, whole of the electronic components and the column components can be standardized. This indicates the adoption of an assist motor having performance to generate enough torque for all car types. Whereas, modular composition for functionality (Figures 13b) does not suggest the standardized assist motor because a module of electronic components and steering gear components is difficult to be standardized, i.e. design change of "Tie rod (a<sub>14</sub>)" and "rack length (a<sub>19</sub>)" is inevitable. This means designers should select an assist motor suited to each car type in order to minimize its cost.

## 5. CONCLUSIONS

To support the modularization of design elements in the late process of design, this study introduced Design Structure Matrix (DSM) into Quality Function Deployment based on Multi spaces (M-QFD). DSM can modularize (group) the design elements on the basis of the relationships between them described in the correlation and relationship matrices of M-QFD and has the following benefits compared to ISM:

1) DSM excludes indirect relationships considered in ISM and prevents from making a huge chunk of the design elements (modularization failure);



- 2) DSM can organize the relationships incorporating the designer's opinions;
- 3) Some kinds of DSM deal with several types of the relationships.

The proposed M-QFD with DSM analyzes the relationships between design elements properly in the late process of design and indicates the information regarding modularization to the designers.

Additionally, the applicability of the proposed M-QFD was confirmed by applying it to a design problem of an automotive steering system. To confirm the versatility of the proposed M-QFD, future work will implement design applications.

## ACKNOWLEDGEMENT

This work was supported by the Japan Society for the Promotion of Science, Grant-in-Aid for Young Scientists (B) (26750005).

## REFERENCES

1. **Matsuoka Y., (2010)**, Design Science, Maruzen, Tokyo.
2. **Kato T, Shigehiro H, Sato K, and Matsuoka Y., (2013a)**, "Quality Function Deployment Based on the Multispace Design Model", The Science of Design, Vol.60, No.1, pp 77-86.
3. **Kato T., (2013b)**, "Quality Function Deployment Applying Structural Model " Proceedings of the International Conference on Advances in Mechanical and Robotics Engineering, Zurich, pp 31-36.
4. **Akao Y., (1990)**, Quality function deployment, Productivity Press, New York.
5. **Warfield J.N., (1976)**, Societal Systems: Planning, Policy and Complexity, Wiley, New York.
6. **Ansari M.F., Kharb R.K., Luthra S., Shimmi S.L., and Chatterji S., (2013)**, "Analysis of barriers to implement solar power installations in India using interpretive structural modeling technique", Renewable and Sustainable Energy Reviews, Vol.27, pp 163-174.
7. **Lindemann U., Maurer M., and Braun T., (2009)**, Structural Complexity Management: An Approach for the Field of Product Design, Springer, Berlin.
8. **Pimpler T.U. and Eppinger S.D., (1994)**, "Integration analysis of product decompositions", Proceedings of the ASME Design Theory and Methodology Conference, Minneapolis.
9. **Ogawa K. and Arakawa M., (2013)**, "A Method of Modular Design Involving Simultaneous Evaluation of Product Functions and Environmental Characteristics: Case Study of Modular Design for a Mouse Device Involving a Ball", Journal of JIMA, Vol. 62, No. 2, pp 205-218 (in Japanese).







## VALUE GROWTH MOBILITY BASED ON TIMEAXIS DESIGN

**Yuma. KUSUNOKI**, zond@z7.keio.jp Keio University, 3-14-1, Hiyoshi, Kohoku-ku, Yokohama, Japan

**Kei. KAMIYA**, k.kamiya.0123@gmail.com Keio University, 3-14-1, Hiyoshi, Kohoku-ku, Yokohama, Japan

**Akira. KITO**, fa0kitou@hotmail.co.jp Keio University, 3-14-1, Hiyoshi, Kohoku-ku, Yokohama, Japan

**Koichiro. SATO**, k.sato@mech.keio.ac.jp Keio University, 3-14-1, Hiyoshi, Kohoku-ku, Yokohama, Japan

**Yoshiyuki. MATSUOKA**, matsuoka@mech.keio.ac.jp Keio University, 3-14-1, Hiyoshi, Kohoku-ku, Yokohama, Japan

### ABSTRACT

This paper describes Value Growth Mobility based on Timeaxis Design. Timeaxis Design incorporates the viewpoint of time into the theory and methodology of design. We propose Value Growth Mobility including Core Module system and Service system which are realized by Timeaxis Design. Value Growth Mobility is able to adapt to users by Core Module system and Service system, and the value of the mobility grows as it is used. Finally, the effects by Value Growth Mobility to social problems such as global warming and energy problem are discussed.

**Keywords:** Value Growth Mobility, Timeaxis Design

### 1. INTRODUCTION

Recently, an integrated correspondence is demanded to solve problems such as environmental degradation, aging of the population and advancement of information society [Mitsubishi Research Institute, Inc., 2000, Tanaka, 2008, Aucnet Inc., 2013]. Then, in the society that carries these problems, the products which are sustainable and have design of robust are demanded. Moreover, the products that do not have only practical value but also spiritual value are wanted. To deal with these issues, Timeaxis Design has been proposed



[Asai, Hirata, Sato and Matsuoka, 2013]. Timeaxis Design incorporates the viewpoint of time into the theory and methodology of design. Using Timeaxis Design enables products to adapt to various circumstances as well as changing the two over time to be considered. Circumstances, in this report, mean operating environment such as usage of the products and users of the products. On the other hand, Value Growth Design is a concept of design growing values of products through usage embodied by Timeaxis design [Kanazawa, Sato and Matsuoka, 2012]. Perceived values of a Value Growth Design's products become higher as it is carried on using.

In this report, we propose the Value Growth Mobility and its configuring systems as a products applying Value Growth Design. When Value Growth Mobility's configuring systems are derived, M method which enables to design in emergent way with unfettered thought is used. Firstly we describe Timeaxis Design and Value Growth Design. Then, we describe Value Growth Mobility.

## **2. TIMEAXIS DESIGN**

### **The Outline of Timeaxis Design**

Timeaxis Design is the concept which incorporates the viewpoint of a time axis into the theory and methodology. Two technologies and three models for Timeaxis Design are described below.

Technologies Realizing Timeaxis Design: Timeaxis Design can be actualized by two technologies: Bio-inspired technology and service technology. Bio-inspired technology builds in learning functions, remembrance, and hereditary into an object. An object possessing these abilities may realize a steady performance and longer lifetime due to its high robustness, redundancy, and environmental sustainability found in a biological system. In contrast, service technology incorporates a service into the relationship between an object and its surrounding. Because of this service, an object can be customized to fit the user's preferences. In addition, conducting routine maintenance may extend the usable lifetime of an object under diverse conditions.

Models Realizing Timeaxis Design: Three models are used to realize Timeaxis Design: Unsteady Model, Plastic Model and Multi-time Scale Model. Multi-time Scale Model contains Unsteady Model and Plastic Model. These two models are described below.



Unsteady Model describes unsteady object. The word “unsteady” means that the object varies in process of time. Therefore time course have to be considered in Unsteady Model. On the other hand, it is not permitted to describe changes of the object with time course in order to simplify the model of the object.

Plastic Model describes plastic object. The word “plastic” means that the change of the object is preserved. This is common for human’s recognition. Thus, changes of values that are felt by users have to be considered in designing process.

Multi-time Scale Model is an integrated model of three different time scale model: Short time scale model, Medium time scale model and Long time scale model. In Short time scale model, change of the object is described by a second’s or a minute’s order. In Medium time scale model, change of the object is described by an hour’s or a day’s order. In Long time scale model, change of the object is described by a month’s or a year’s order. By using these different time scale models, the object can be expressed in changing circumstances in process of time.

### **Value Growth Design**

The idea that the value of an object or product based on Timeaxis Design may grow is novel. As shown in Figure 1(a), typical designs assume an object has the highest value when it is initially purchased, and as the object is used, which consequently decreases its ability to adapt to change, its value decreases. However in reality, the value of some objects increases over time. Examples include traditional handicrafts (lacquer wares and woodworks), sports equipment (baseball glove), and stationeries (writing brushes and fountain pens).

Consider a fountain pen where the head of the pen sharpens with use. Over time, the pen molds to the user’s hand. In addition, by repairing and maintaining the pen, it is possible to extend its life and increase its fitness and infinity, leading to an increased value. The design of such an object is called Value Growth Design. Unlike value decay design, Value Growth Design is a design concept where an object’s (or product’s) value increases over time [Figure 1(b)].

A design of value growth, as in the case of a fountain pen, can be achieved with Bio-inspired technology or service technology. Consequently, an object with a high affinity will be

designed and the value will increase. By developing practical applications of Value Growth Design, the robustness and safety of products will be improved. Thus, Value Growth Design may realize the design of more sustainable objects.

In the past study, Value Growth Model [Figure 2] is proposed as a model that expresses process of a product's Value Growth. Value Growth Model consists of five phases, the Value discovery phase, the Value realization phase, the Value growth phase, the Value establishment phase and the Value tradition phase. These five phases are sorted by features of practical value and mental value. Practical value indicates value of practical aspect such as functions. On the other hand, mental value indicates value of spiritual aspect such as attachment. This Value Growth Model is effective for realizing Value Growth Design products.

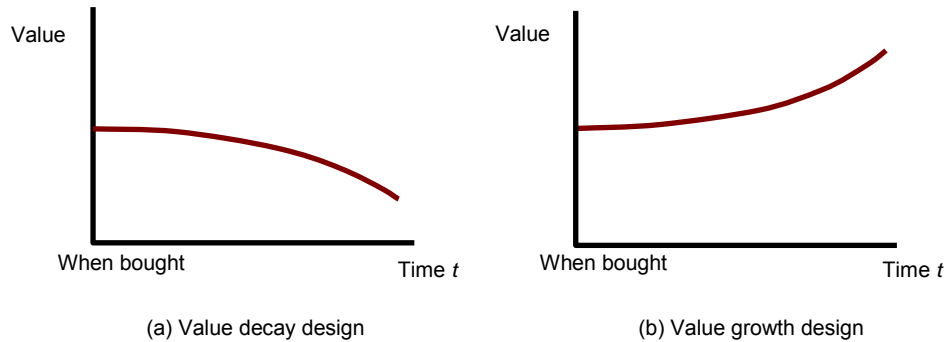


Figure 1. Value Decay Design and Value Growth Design.

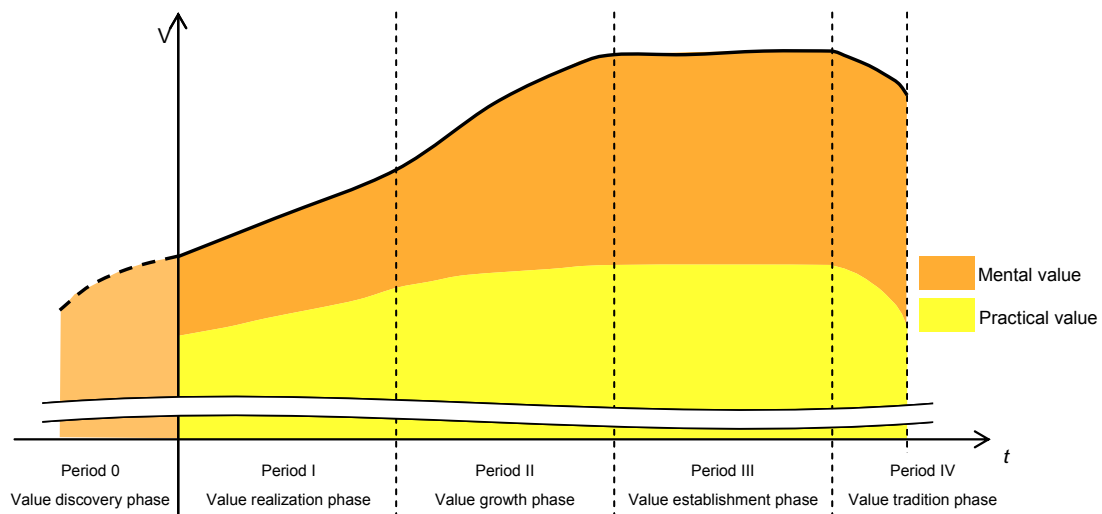


Figure 2. Value Growth Model.



#### Period 0: Value discovery phase

The value discovery phase occurs when one discovers the value of an object or product through brochure, advertisement, or trial period prior to purchasing. During this phase, both the practical value and mental value grow. However, since the object has not yet been purchased, mainly the mental value grows.

#### Period I: Value realization phase

The value realization phase is when a user uses an object or learns about different functions of an object. Since this is the phase when expectations and actual use of a product are reconciled, an object's value changes significantly. Although both practical and mental values grow during this phase, the practical value increases more.

#### Period II: Value growth phase

The value growth phase is when a user employs an object and develops a sense of attachment to it. Hence, the value changes the most during this phase. The mental value grows larger in proportion to practical value, and the differentiated value decreases as the user becomes accustomed to the object.

#### Period III: Value establishment phase

The value establishment phase is when a change in value on the whole decreases and the value stabilizes. Both the practical and mental values do not change much. In this phase, the value that has been built up is more significant than the growth.

#### Period IV: Value tradition phase

The value tradition phase is when the value begins to decrease due to decay and the object is replaced. An object (or product) is replaced, especially once it passes its life expectancy and the value decreases rapidly. In this case, it is possible to transfer the value of the former object to the replacement object due to data transfer.



### 3. VALUE GROWTH MOBILITY

#### Proposal of Value Growth Mobility

As an example of Value Growth Design products, we propose the Value Growth Mobility. Value Growth Mobility is a concept of next generation's mobility that user's perceived value to the mobility grows by operations of vehicle and surroundings such as dealers and infrastructures. Mobility in these days is demanded to solve the problems: increase of the environmental load because of exhaust gas and process of production and disposal, a trend that young people turn away from driving due to the diversification of the value, et al. Therefore applying Value Growth Design will be an answer to solve these problems.

M method and the Value Growth Model are used to design the Value Growth Mobility. M method is a design method in which M model (Multispace Design Model) is used[Matsuoka, 2010]. With M model, a design object is described by elements arranged in 4 spaces (Value space, Meaning space, State space, Attribute space) and circumstances. Spiritual elements are dealt in Value space and Meaning space, and physical elements are dealt in State space and Attribute space. Arrangement of design elements in each space, grouping elements and expressing relationships between elements are processes of the design. When designing based on M method, bottom-up generation of ideas caused by the extraction of elements and detection of relationships are supported. Thereby, it encourages emergent design which includes the bottom-up process. In addition, it promotes development that does not depend on apparent requirements. On the other hand, when designing based on Value Growth Model, extracting the mobility's value perceived by its users and designing of its process of value growth is supported.

Fig. 3 shows the element relationship diagram deprived from these design processes describing key elements of the value growth mobility led by M method. "Utility value", "experienced value", etc. are extracted in Value space, and "vehicle adapt to users", "Feel attachment", etc. are extracted in meaning space. Besides, "steering angle", "speed", etc. are extracted in State space, and "G sensor", "GPS", etc. are extracted in Attribute space. Users, road, etc. are described as circumstances. Those extracted elements are organized by inclusion relationship and lines between two elements. As a result, two main subsystems, Core Module system and Service system, are derived by the process of design that is described above. Core Module system that is an internal system of the vehicle improves control system of the vehicle by fitting to users and circumstances. Service system associated with internal and external system of vehicle makes mobility's value perceived by

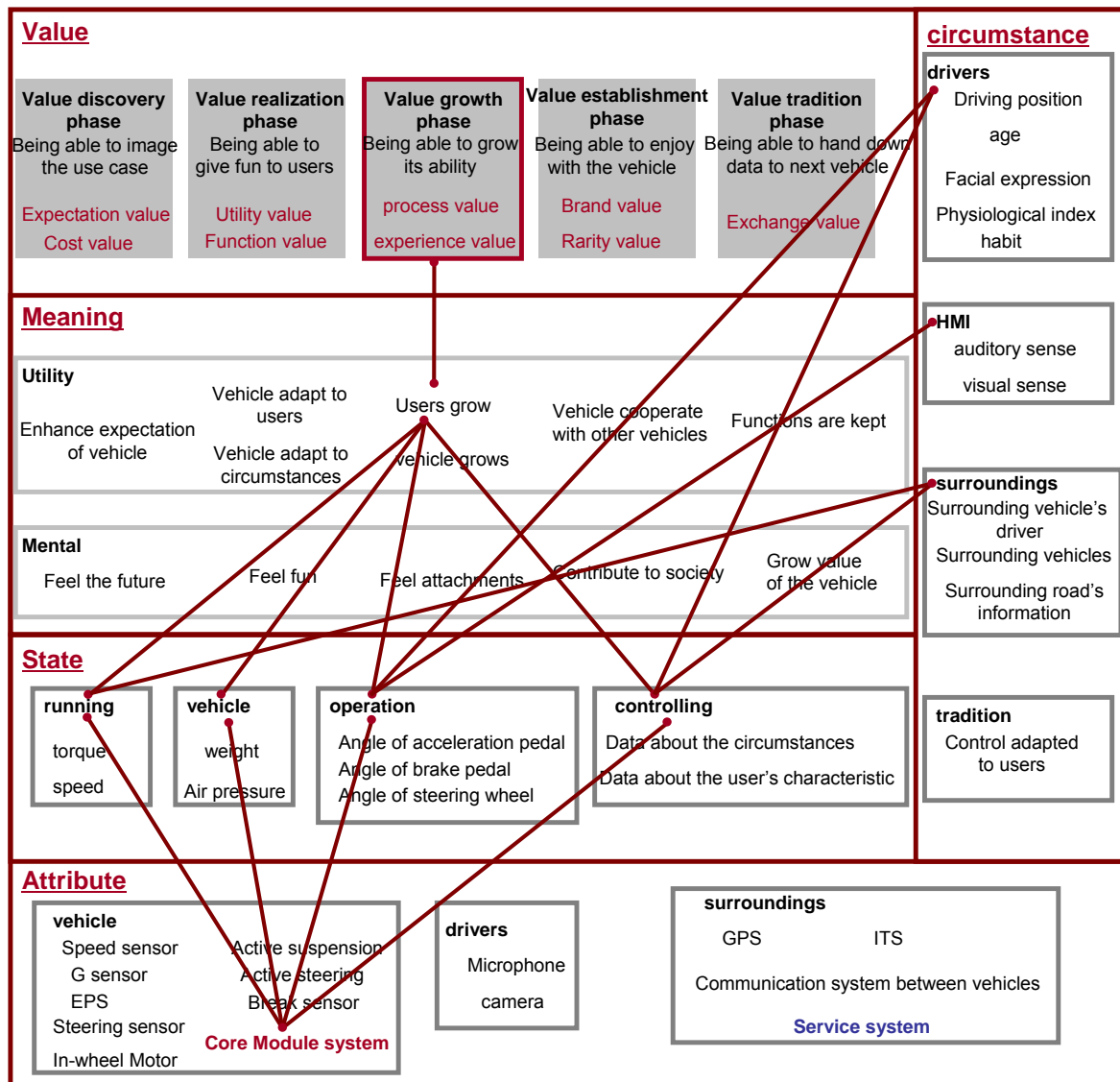


Figure 3. Elements relationship diagram

users better. The Value Growth Mobility realizes growth of its own value perceived by users with these two main subsystems. Value Growth process with these systems is described below.

### Concept of A Core Module System

Core Module system is the internal vehicle control system which enables the vehicle to adapt to various circumstances such as the users and the way it is used from the aspect of safety fuel economy, etc. In the process of time, the users of vehicle become to feel vehicle's value growth. This system has three features, learning, heredity and memorizing, and these features are realized by Bio-inspired technology.



## **Concept of A Service System**

A Service system encourages value growth of the vehicle by cooperation of the vehicle's external and internal systems. By the operation of a Service system, the users feel attachment to the vehicle, and this makes the vehicle's value for the users grow.

## **4. DEVELOPMENT OF THE CORE MODULE SYSTEM**

A Core Module system and a Service system described above are now under development in order to realize Value Growth Mobility. In regards to Core Module system, an example system called Emergent Control System has been developed. In this chapter, developed Core Module system is described.

### **Proposal of Emergent Control System As Core Module System**

To adapt to various circumstances and users, the Emergent Control System has been developed aiming to fit the vehicle individually [Furugori, et al, 2012]. Fig.4 shows the conceptual image of the Emergent Control System. The system controls the vehicle by presuming circumstances at all times. Data of circumstances and the optimum control algorithm that is fitted to those circumstances are saved to refer in a case of similar circumstance on the next time. If there is no data of similar circumstance, the Emergent Control System makes new control algorithm. Based on chosen control algorithm, the vehicle assists the driver, shows information and so on. This system becomes an example of the Core Module system of a value growth mobility.

### **Outline of The Emergent Control System**

We have made the vehicle that the more you drive the better its fuel economy become with an Emergent Control System. The vehicle with the Emergent Control System controls output power of the engine in order to make it better fuel economy by monitoring driver's input such as acceleration pedal angle, brake pedal angle, vehicle's speed et al.

Developed Emergent Control System consists of three subsystems: "the system estimating circumstances", "the system making emergent vehicle's control algorithm" and "the system saving data of circumstances and control algorithm fitted for there". The subsystems control the vehicle depending on a view point of the multi time scale model. "short time scale", "middle time scale" and "long time scale".





In short time scale, the systems estimate the circumstances from condition and environment of the vehicle. If they recognize the circumstances, the optimum control algorithm is chosen. The circumstances are judged from the driver's characteristic operations, weather, etc. If the systems do not know the circumstance, the circumstance is temporary recognized as a similar circumstance. The optimum algorithm fitted to a similar circumstance is selected, and the vehicle is controlled by it. The data on unknown circumstances is saved, these processes are treated in real time.

In medium time scale, new control algorithm is made for unknown circumstances from saved data by the Emergent Control System based on Genetic Network Programming (GNP). GNP is extension of Genetic Algorithm and Genetic Program.

In long time scale, new control algorithms that are made in medium time scale and thresholds about circumstances are updated. As updated data is adapted to presume circumstances and to control the vehicle, unknown circumstances become known. As a matter of fact, control of the vehicle is adapted to a driver and circumstances. That means the Emergent Control System enables the vehicle to adapt various circumstances and time variation.

The electric control unit with the Emergent Control System discussed above for a car was developed, and it was reported that the system made the vehicle better fuel economy and battery life[Ishikawa, et al, 2013].

## **5. THE REALIZATION OF THE VALUE GROWTH**

In this chapter, the cases of Value Growth realized by Value Growth Mobility with Core Module system and Service system are described.

### **The Case of Value Growth by Core Module System**

Core Module system is the vehicle control system that can adapt to users and various circumstances in terms of fuel economy, safety etc. Perceived value grows since the vehicle adapts to users in process of time by Core Module system. This system is realized by Bio-inspired Technology, and has three features of the technology, studying, heredity and storage. In this paragraph, process of value growth realized by Core Module system is described.



In the value discovery phase, a user feels value of the mobility by test ride at a dealer. The user feels the charm of it adapting to the user by Core Module system in terms of fuel economy, safety etc.

In the Value realization phase, the user feels value of the mobility by driving. In this phase, the user feels the vehicle practical and the vehicle memorizes act of the user while driving and studies characteristics of the user's driving. In process of time, the vehicle can adapt to various circumstances. Thus, usage of the vehicle for the user becomes better. Moreover, stored memories can be referred to not only for more comfortable driving, but also for dealing with something beyond expectations such as accident and traffic jam.

In the Value growth phase, control of the vehicle improves at anytime as the user drives it. That is because as the vehicle runs, more data about state of users and various circumstances memorize and the optimum control algorithm fitted to those circumstances is made from those data. On the other hand, the user can learn how to control the vehicle by using the vehicle adapted to the user efficiently. In this way, perceived value of the vehicle will grow.

In the Value establishment phase, the user nearly knows the vehicle's reaction to the control of the user and the vehicle can almost presume user's behavior. The user can ask to the vehicle what the user should act. As a relationship between the user and the vehicle is integral, it is easy to find the optimum correspondence against troubles beyond expectations.

In the Value tradition phase, value can be handed down to next vehicle by transferring the stored data when the user changes the vehicle due to its degradation. Thus the data is maintained along, for example, deletion of unnecessary data and recovery of the data.

### **The Case of Value Growth by Service System**

Value Growth Mobility's Service system associated with internal and external system of vehicle makes mobility's value perceived by users better. By the Service system, the user attaches to the mobility, and this makes the perceived mobility's value to grow. In this paragraph, value growth process of the mobility is described with value growth model. In addition, the Service system described below is composed of Social Networking Service



(SNS), motion recognition system, etc. By associating with these subsystems, the vehicle can share the memory of driving and propose services to the user with driver's motion.

In the Value discovery phase, though the user has not owned the vehicle, the user can register the SNS. Specifically, thorough the SNS, the user can know usage of other users; seeing the pictures taken by other users while driving. As a result, the user feels the vehicle's value.

In the Value realization phase, as the user practically drives the vehicle, perceived mobility's value grows. For example, the pictures and memories while driving can be shared by using SNS. Moreover, the vehicle proposes to stop along the way, a rest, etc. With these functions, the user feels the vehicle as practical. Information about favorites of the user are saved in a cloud by motion recognition system.

In the Value growth phase, the mobility's value perceived by the user grows by adapting vehicle to the user. The vehicle proposes services that the user tastes based on the user's favorites analyzed from information saved in cloud and SNS. Though these proposals include some unfavorable services at first, the vehicle adapt to the user by feeding back user's motion in process of time. Also, the number of friends who have similar tastes increases with SNS. Accordingly, as the user and the vehicle mature, the mobility's value perceived by the user grows.

In the Value establishment phase, the vehicle is capable of behavior according to the subtleties of the user's emotions. The mobility's value perceived by the user remains stable at high level. As the user's favor is thoroughly analyzed by this phase, the vehicle accurately gives proposals which are required by the user. Moreover, the connections between friends and communities become firm thorough the SNS, and off-line meetings are held.

In the Value tradition phase, although the user changes their vehicle due to degradation, the highly analyzed data about the user's favor can be taken over to the next vehicle. Therefore the value of the vehicle can be handed down to the next.



## 6. CONCLUSION

In this report, stages of progress of designing Value Growth Mobility based on Timeaxis Design are described. Moreover, two components of Value Growth Mobility, Core Module system and Service system are explained. And an example of mobility's value growth by realization of Core Module system and Service system is presented. Henceforth we continue to develop Value Growth Mobility's Service system.

## REFERENCES

1. **Mitsubishi Research Institute, Inc. (2000)**, The Grand Design for The New Century, Nikkei Inc.
2. **Tanaka, S. (2008)**, Mirai yosoku report 2009-2015, Nikkei Business Publications, Inc.
3. **Aucnet Inc. (2013)**, Jidousya to keitaidennwa no ijihi ni kannsuru ishiki tyousa syouhisya annke-to kekka.
4. **Asai, S. Hirata, Y. Sato, K. Matsuoka, Y. (2013)**, "Characteristic Analysis of Artifacts in Japan for the Application of Value Growth Design", Proceedings of the 5<sup>th</sup> International Congress of International Association of Societies of Design Research, pp 68-79.
5. **Kanazawa, S. Sato, K. Matsuoka, Y. (2012)**, "Value Growth Design Model Based on Design Science", 15<sup>th</sup> International Conference on Machine Design and Production.
6. **Matsuoka, Y. (2010)**, Design Science "Six Viewpoints" for the Creation of Future, Maruzen Co Ltd.
7. **Furugori, S. Yamazaki, T. Kuroda, Y. Suetomi, T. Nouzawa, T. Ujiie, Y. Kanazawa, K. Matsuoka, Y. (2012)**, "Value Growth Design in Next Generation Mobility", Oukan, Journal of Transdisciplinary Federation of science and Technology, Vol.6, No.1, pp 27-33.
8. **Ishikawa, K. Nakazawa, K. Yamazaki, T. Furugori, S. Suetomi, T. Matsuoka, Y. (2013)**, "Reduction of the Driving Cost for Capacitor-Battery Combined HEV by Using Genetic Network Programming", The Japan Society of Mechanical Engineers, Vol.79, No.803, pp 2259-2272.



## CONCEPTUAL STRUCTURING OF MODULAR DESIGN METHODOLOGY FOR MECHATRONIC SYSTEMS: BEHAVIOUR BASED DESIGN PERSPECTIVE

**Zuhal ERDEN**, *zuhal@atilim.edu.tr* Atılım University, 06836, Ankara, Turkey

### ABSTRACT

In an ever increasing global marketplace, it is often vital for companies to diversify their product ranges to meet customers' changing needs. This requirement leads companies to adopt their product development strategy for mass customization. An important strategy for this purpose is to develop product families (platform-based modular products) and there is considerable amount of research on modularity for mechanical products. On the other hand, research on the conceptual structuring of modular mechatronic products (mechatronic product families) is quite limited. This paper presents a conceptual scheme for systematic design of platform-based mechatronic product families for mass customization. The purpose of the conceptual scheme is to generate a formal structure for defining modules of a mechatronic product family to perform intended operational behaviours during conceptual design. A state-based behavioral representation framework for a mechatronic system has been developed and implemented on a physical structure in a previous research. This paper introduces a conceptual structure of the modular mechatronic design methodology based on that framework. The applicability of the developed conceptual scheme is also explained using a descriptive example.

**Keywords:** product platform, mechatronic product architecture, mechatronic product family, modular mechatronic design, modular behaviour

### 1. INTRODUCTION

Today's increasing and diversifying customer needs together with rapid technological developments have significantly influence the way that companies compete in the global market such that they are shifting towards adapting themselves to a new product development strategy known as "mass customization". Mass customization corresponds to



“the technologies and systems to deliver goods and services that meet the needs of individual customers with near mass production efficiency” [Tseng and Jiao, 2001]. The concept of mass customization forces companies to provide a variety of products satisfying individual desires and requirements of customers. An important way to accomplish the move to mass customization is to develop products with sufficient variety to meet customers’ demands.

Product variety in mass customization is provided by platform-based products which form product families. A product family refers to a set of similar products that are derived from a common platform and yet possesses specific features/functionality to meet particular customer requirements [Jiao et al., 2007]. Platform-based product development offers a multitude of benefits including reduced development time and system complexity, reduced development and production cost, and improved ability to upgrade products [Simpson, 2004]. Research on the modularity in relation to platform-based products has attracted much attention in the last decade and systematic methods for developing such products have been suggested. Most of these efforts are devoted towards mechanical products and they are generally component-dependent methods. Today, mechatronic products have become important for sustaining high living standards of people, as well as for increasing nations’ competitiveness in the global marketplace. Mechatronic products use integrated technologies to perceive environmental information that is used for decision-making through the control software and change the environment by producing motoric actions. Mechatronic products are under the effect of technological developments and they have the characteristics of dynamic needs, complexity in design, rapid responding and they are treated as typical kinds of engineering-to-order (ETO) products [Li et al., 2013]. Modularization and platform-based product family design is a widely recognized and effective method for mechatronic product development. Thus a research need arises towards development of systematic platform-based mechatronic product family design.

This paper presents an initial conceptual scheme for systematic design of platform-based mechatronic product families for mass customization, based on an event-driven operational behavior. The scheme articulates existing modular design methodologies for mechanical products and the state-based behavioural representation of a mechatronic system as a conceptual structure for the development of a modular mechatronic design methodology.

The remaining part of this paper is organized as follows; Section 2 provides a brief literature review on modular design methodology. Section 3 summarizes event-driven behavioural design approach for mechatronic systems. Section 4 introduces the initial conceptual scheme for assuring modularity using behavioural design approach and an example to



illustrate the applicability of the scheme. Finally, Section 5 concludes this work and describes future research directions.

## **2. MODULAR DESIGN METHODOLOGY**

In design engineering, concepts of modules and modularity are important to construct product architectures. A module refers to a physical or conceptual grouping of components that share some characteristics and it could be changed and replaced in a loose way and be produced independently [Jiao et al., 2007]. Modularity has been defined as the degree to which a product's architecture is composed of modules with minimal interactions [Gerherson et al., 2003]. Modularity is used for the expression of common and independent parts to create a variety of products [Huang and Kusiak, 1998] that are considered as a family of products. Development of product families provides an important opportunity for companies to increase their product variety with the scale and scope of the existing production systems [Simpson, 2004]. Development of product families is mainly based on modular design methodologies, which allows increase in the diversity of products, rapid designing, updating and manufacturing of new products in the family. Thus, changing customer expectations can be met in a timely manner and this will result in increasing customer satisfaction. This approach allows companies to adapt themselves for mass customization, thus responding and managing today's diversifying customer demand. Thus, research in design science towards the development of modular design methodologies is highly encouraged during the last decade [Jiao et al., 2007].

One of the important initial studies was the heuristic method for identifying modules from functional models [Stone et al., 2000]. This method has been extended with functional modeling of the products [Pahl and Beitz, 1996] and a systematic methodology for architecting a product portfolio has been suggested [Dahmus et al., 2001]. However, this study considers that modularization decisions are made after restricting the product portfolio to a physical principle and it does not consider modularity decisions needed to be done at a higher level of abstraction, where no physical principal is associated with the required functions and/or behaviours. Such modularity decisions are particularly critical for mechatronic products that need synergy at the upstream design stage. A knowledge management framework is proposed [Nanda et al., 2007] to capture, reorganize, and convert both linguistic and parametric product family design information into a unified network. The network called a networked bill of material (NBOM), uses formal concept analysis (FCA); encode the NBOM as a cyclic, labeled graph using the Web Ontology Language (OWL) that designers can use to explore, search, and aggregate design information across different



phases of product design as well as across multiple products in a product family; and analyzes the set of products in a product family based on both linguistic and parametric information. Since the development of modular products requires the identification of highly interactive groups of elements and arranging (i.e., clustering) them into modules, research has also been directed towards clustering techniques [Yu et al., 2007]. An adaptable design is proposed [Gu et al., 2009] aiming at creating designs and products that can be easily adapted for different requirements, as a generalization of modular design, product platform design, product family design and mass customization design. A modular product design methodology is developed as an integrated approach by combining several methods to allow designers to generate design solutions using modular concepts in a systematic manner. This new methodology contains four significant methods that form the integrated methodology; Generalisation, Modularisation, CUstomisation and REconfiguration (GeMoCURE) [Yan and Stewart, 2010].

As mechatronic products become important for sustaining high living standards of people, as well as for increasing nations' competitiveness in the global marketplace, mass customization and development of platform-based products are important for mechatronic product companies in order to be agile, so that they can develop new products in a very short period of time without changing the overall design of existing products. Therefore, companies need experience in applying systematic methods for the development of modular, platform-based mechatronic products. The above-mentioned requirements for mass customization in mechatronic product development need modular design methodologies for such products. Mechatronic products require integration of knowledge from various engineering disciplines starting from early design phases; particularly from the conceptual design stage. Thus, use of a top-down design methodology in mechatronic product development is necessary. This design methodology is based on generalization of the required overall function of the product, and then, dividing the overall function into simpler sub-functions by means of functional decomposition. Such a design methodology is a basis for the implementation of modular design methods that exist in the literature. Thus, mechatronic product design is considered to be useful for the implementation of existing modular design methods. In designing families of such products, flexible product platforms are required. An integrated product modularization scheme is proposed for the modular identification of a flexible platform based on flow analysis, design structure matrix (DSM) and fuzzy clustering [Li et al., 2013]. Recently, systematic methods for developing modularity of mechatronic products have been investigated by researchers. For example a modularization scheme has been developed for the modular design of mechatronics systems by integrating the DSM based modularization with the FBS(Function-behaviour-state) modeling [van Beek et al., 2010].



As a contribution to the development of a systematic modular design methodology, event-driven behavioural design approach [Araz and Erden, 2014] is used and an initial conceptual scheme is proposed in this study. The scheme is based on describing the operational behavior of a mechatronic system and generating its behavioural modules.

### **3. THEORETICAL BACKGROUND: BEHAVIOURAL DESIGN APPROACH FOR MECHATRONIC SYSTEMS**

In the engineering design process, conceptual design involves informal descriptions of functions and intended behaviours which will be elaborated towards a well-defined engineering system in terms of the physical components and corresponding physical behaviours at the end of the completed design cycle. These behaviours should be represented and simulated by a domain-independent approach in the mechatronic design. As a research contribution to this perspective, a systematic behaviour-based conceptual design and modelling approach has been developed [Araz and Erden, 2014] for mechatronic products with special implementations in laboratory-level robots for educational purposes. This approach is based on general characteristics of the operational behaviour of a mechatronic system at the highest level of abstraction, which is composed of three states as perception, cognition and motoric action. The system communicates its environment to collect and process data during the perception state. In the cognition state, the data is used with proper reasoning and decision-making to respond to changes in the environment. In the motoric action state, task execution is performed physically in accordance with decision-making and/or as a reflexive response to the changes in the environment. Perception is decided as the initial state, because once the system starts its operation, it is expected to collect data from the environment for processing and decision-making to create a motoric action. The environment outside a mechatronic system is defined as the physical medium which includes the physical world and other mechatronic/non-mechatronic systems. Based on this description, the operational behaviour of a mechatronic system is represented graphically using an event-driven model as illustrated in Figure 1.

As one can see in Figure 1, the system interacts with the environment in two ways; one of them is to change its behaviour in response to the changes in the environment and the other way is to affect the state of the environment by creating a change through its motoric actions after reflexive and/or cognitive initiators. The event-driven model is represented using Discrete Event System Specification (DEVS) formalism [Ziegler, 1989] and it has been used as a basis for developing a Petri Net [Murata, 1989] model of the operational behaviour for simulation, as it is detailed in [Araz and Erden, 2014].

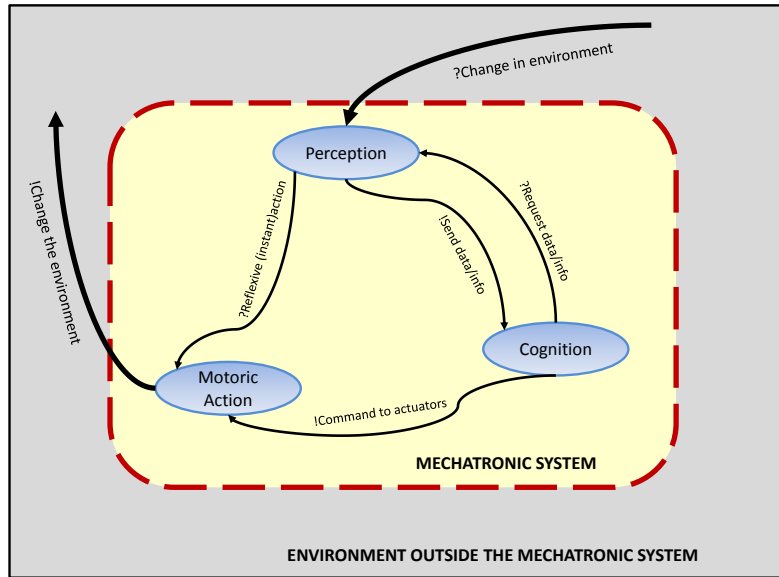


Figure 1. Event-driven model for a mechatronic system [Araz and Erden, 2014].

The two formal description techniques, namely DEVS and Petri Nets, have been articulated at a high level of abstraction, from the perspective of conceptual robot design as depicted in Figure 2. This articulation starts from a verbal description of the intended operational behaviour of the robot under conceptual design. The description is represented as a DEVS model, which is used as a basis for the Petri Net model of the operational behaviour. Then, the modelled behaviour is physically realized on a desktop design structure, which consists of necessary components/connections to obtain the behavior independent of the geometric and dynamic parameters of a real, physical robot model. The construction of the bridging links for this coupling has been performed both conceptually and manually with the inclusion of engineering intuition and creativity, as shown in Figure 2, and tested through various case studies. This form of coupling establishes an infrastructure for the development of complete formal specifications regarding the conversion of a DEVS model into a Petri Net model for a conceptual robot design.

Once the DEVS model for the operational behavior is constructed, it is used to develop the Petri Net model based on the relationships given in Figure 2. In the Petri Net model, the events are modelled by transitions which are considered as active components. The states, however, are modelled by markings, which denote the distribution of tokens over the places. In the behavioural design approach, the places represent conditions for sensorial information.

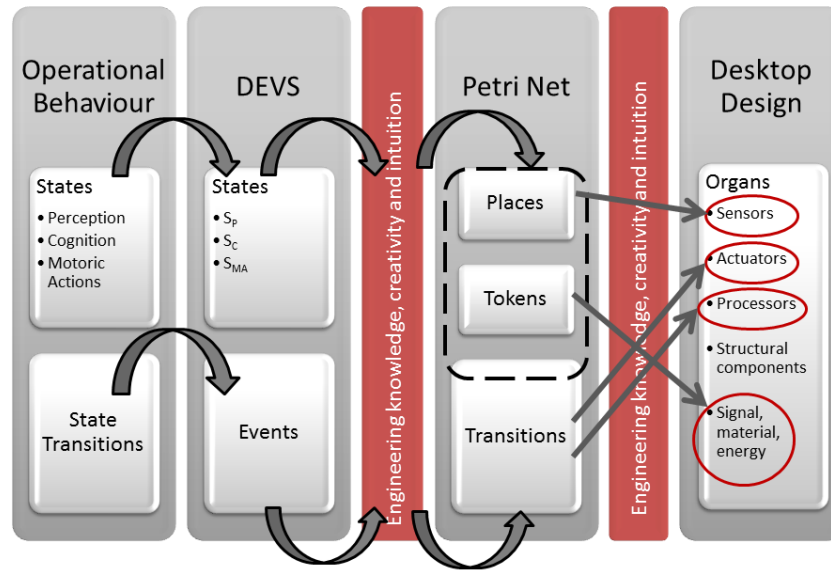


Figure 2. Relationship between operational behavior, DEVS, Petri Net model and desktop design [Araz and Erden, 2014].

In order to form a systematic connection from the DEVS model to the Petri Net model, we represent each organ ( $O_i$ ) at the top-level page of the Petri Net models. Then, each organ is modelled via a subnet. The Petri Net models of the organs are developed using engineering intuition. The general mapping is the following:

1. Organs ( $O_i$ ) – represented by nodes in the top-level Petri Net;
2. Organ behaviours – modelled by subnets;
3. Conditions (such as Start, Decision, etc.) and sensors – modelled by places in the Petri Nets of the organs; and
4. Events (such as 'request/receive\_data', 'sense', 'command\_to actuators', etc.) – modelled by transitions in the Petri Nets of the organs.

Since the desktop design is a physical structure, it is an easier and more straightforward engineering approach to select the required components in order to realize the modelled behaviour using engineering knowledge and creativity. Generally, broad mapping is the existence of compatibility between the places in the Petri Net and the sensors in the desktop

model. Similarly, the actuators and processors in the desktop design model are selected so as to achieve event occurrences modelled by transitions in the Petri Net (see Figure 2).

The behaviour-based modelling approach has been implemented on five design case studies, all of which have been assigned as laboratory-level educational robots, namely a 'curve-following robot', a 'dog robot', a 'cockroach robot', a 'frog robot' and a 'pick-packing automated guided vehicle'. The operational behaviours for these robots have been simulated using Artifex™ environment [Anon, 2004]. Then these behaviours are realized and tested on physical desktop design structures as illustrated in Figure 3.

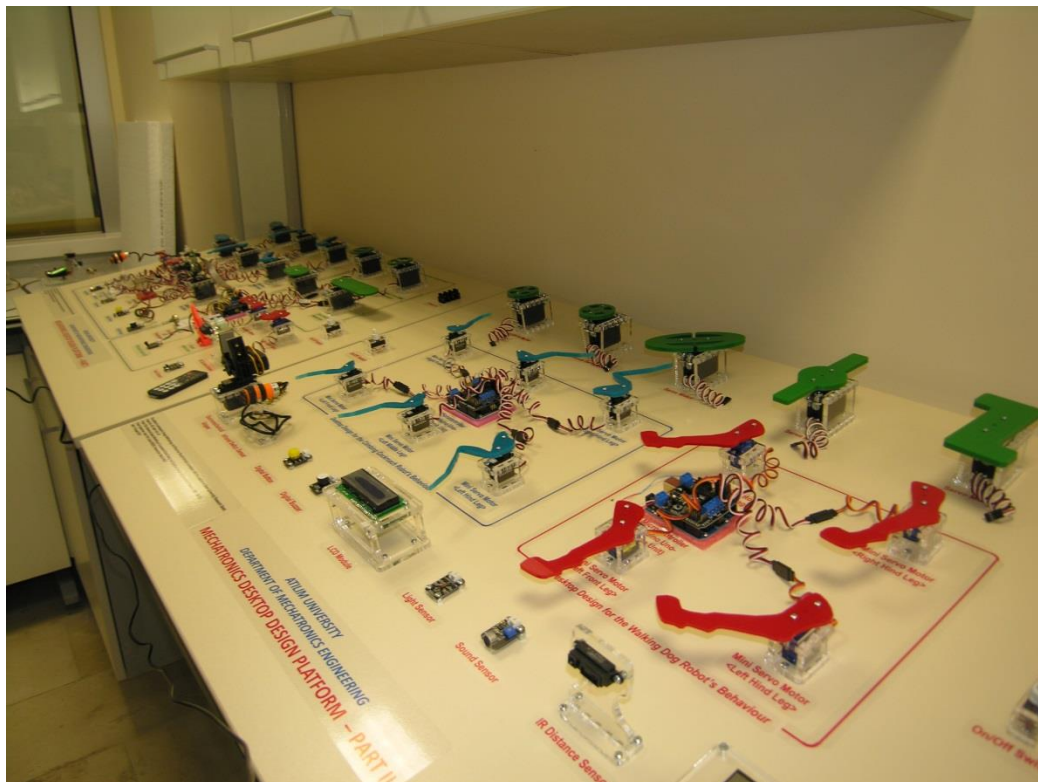


Figure 3. Desktop design models of laboratory-level educational robots.

#### 4. A CONCEPTUAL SCHEME FOR A MECHATRONIC PRODUCT FAMILY: BEHAVIOURAL MODULES

An important characteristic of the behavioural design approach is that the behavioural model is independent of physical subsystems and/or components. Thus, designers are allowed to consider various physical system alternatives to accomplish the required behaviors, while elaborating design at lower levels of abstraction. This characteristic is crucial for the design of mechatronic systems since these systems are differentiated by synergistic integration that can be achieved by domain independence. This domain-independent behavioural

representation is also used to develop an initial conceptual scheme for modular design of mechatronic products, namely robots. The scheme is based on defining behavioural modules by using the DEVS model of the robot's operational behaviour. In the DEVS model, the states are preserved, while their transitions are represented via event occurrences. The set of states in a DEVS model is defined as:

$$S = \{\text{Perception, Cognition, Motoric Action}\} = \{S_P, S_C, S_{MA}\} \quad (1)$$

In this approach, it is assumed that the robot exhibits  $n$  number of motoric action states that can be represented as a set  $S_{MA}$ :

$$S_{MA} = \{MA_1, MA_2, \dots, MA_n\} \quad (2)$$

where  $MA_i$  ( $i = 1, 2, \dots, n$ ) is a set whose elements denote the  $i^{th}$  motoric action state in terms of different configurations of mechatronic organs, such that:

$$MA_i = \{O_{jk} \mid O_{jk} \text{ is the } k^{th} \text{ configuration of the } j^{th} \text{ organ}\} \quad (3)$$

where,

$j = 1, 2, \dots, m$  ( $m$ : number of organs), and

$k = 1, 2, \dots, r$  ( $r$ : number of configurations for each organ)

As an example for the above definition, motoric action states for one of the case studies (frog robot) in [Araz and Erden, 2014] is given in Table 1. Motoric action states for the frog robot are defined as jumping, walking, happy, angry and frightened. Each of these states is represented by the related behaviours of virtual organs as a combination of various actions/effects. For example, in the 'Happy' state, the head turns left and right, eyes flash, sounds are produced, and forelegs and hind legs move back and forth.

States and state transitions of the DEVS model in Figure 1 represents the top level behavior of a mechatronic system. In this approach, the behaviour resembled by each state of the DEVS model is modularized conceptually, based on the characteristics of the top level state. Perception state represents "perception" behavior triggered via an input event "?change in environment", which resembles the occurrence of any change in the environment that needs perception. In general, the perception behavior is conceptually modularized considering various types of changes in environment caused by physical effects such as "change in temperature", "generation of heat", "generation of noise", "light emission", "existence of an object" etc. Perception behavior of a mechatronic system may differ based on the nature of these changes. Thus,  $S_P$  is defined as a set of behavioural elements which represent "modules for perception behavior", as follows:



Table 1. Representation of motoric action states for the frog robot [Araz and Erden, 2014].

Organ(O <sub>i</sub> )	Action Code (O <sub>jk</sub> )	Action Code Description	Motoric Action States of the Frog Robot (MA <sub>i</sub> )				
			Jumping (MA <sub>1</sub> )	Happy (MA <sub>2</sub> )	Walking (MA <sub>3</sub> )	Frightened (MA <sub>4</sub> )	Angry (MA <sub>5</sub> )
Head (O <sub>1</sub> )	O <sub>11</sub>	Without articular motion	√		√		
	O <sub>12</sub>	Shake					√
	O <sub>13</sub>	Right and left		√			
	O <sub>14</sub>	Fixed to flash point				√	
Eyes (O <sub>2</sub> )	O <sub>21</sub>	Fixed	√		√		
	O <sub>22</sub>	Fully open				√	√
	O <sub>23</sub>	Flashing		√			
Sound Organ (O <sub>3</sub> )	O <sub>31</sub>	Silent	√		√		
	O <sub>32</sub>	Roar					√
	O <sub>33</sub>	Happy sound		√			
	O <sub>34</sub>	Scream				√	
Forelegs (O <sub>4</sub> )	O <sub>41</sub>	Assault position					√
	O <sub>42</sub>	Guard position				√	
	O <sub>43</sub>	Back and forth		√			
	O <sub>44</sub>	Focus to maintain balance	√				
	O <sub>45</sub>	Stepping			√		
Hindlegs (O <sub>5</sub> )	O <sub>51</sub>	Assault position					√
	O <sub>52</sub>	Guard position				√	
	O <sub>53</sub>	Back and forth		√			
	O <sub>54</sub>	Springy function	√				
	O <sub>55</sub>	Stepping			√		

$$S_P = \{S_{P1}, S_{P2}, S_{P3}, \dots, S_{Pw}\} \quad (4)$$

where  $w$  is the number of environmental changes considered in describing the robot behaviour.

Motoric actions result in change(s) in the environment through different behaviours each of which can be represented by a “*motoric action behavior module*”. Motoric action behavior (MAB) modules are represented by a  $(p \times l)$  array as follows;

$$\begin{matrix} MA_{11} & MA_{21} & \cdot & \cdot & MA_{p1} \\ MA_{12} & MA_{22} & \cdot & \cdot & MA_{p2} \\ \cdot & \cdot & \cdot & \cdot & \cdot \\ \cdot & \cdot & \cdot & \cdot & \cdot \\ MA_{1l} & MA_{2l} & \cdot & \cdot & MA_{pl} \end{matrix}$$

where,

$p$ : the number of motoric action states for a motoric action behavior module, and

$l$ : the number of products in a mechatronic product (robot) family.

Cognition behavior represents the transformation of data/information provided by the perception behavior into commands to actuators via suitable decision making software. Cognition modules are defined as software modules to conduct such transformations.

$$S_C = \{S_{C1}, S_{C2}, S_{C3}, \dots, S_{Cg}\} \quad (5)$$

where  $g$  represents the number of software modules necessary for conducting cognitive behaviours.

The complete conceptual structure for the behavioural modules of a mechatronic system is depicted in Figure 4, where “?C\_in\_E” and “!C\_E” represents “?Change in environment” and “!Change the environment”, respectively.

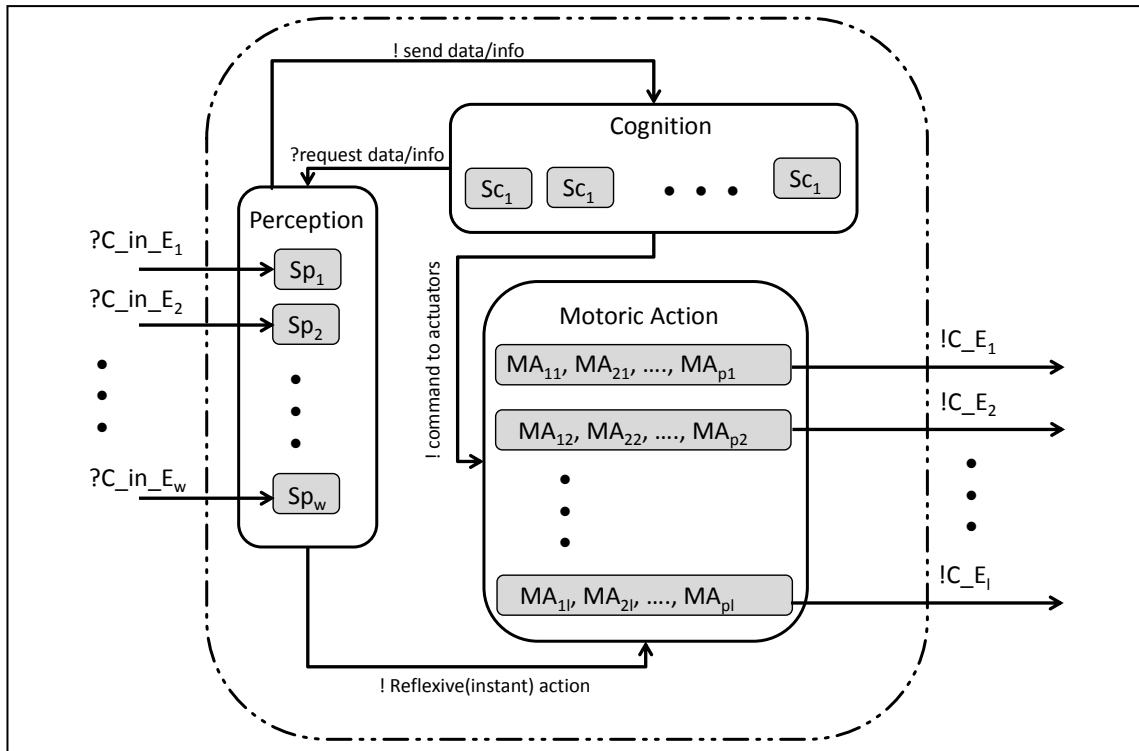


Figure 4. Conceptual structure for the behavioural modules of a mechatronic system.

As an example for using the above-mentioned conceptual scheme, one may consider generation of behavioral modules for a mechatronic product family, namely a robot family. It is assumed that a designer is required to design a robot product family composed of three robots as a frog robot, a packaging robot and a rescue robot. The designer will determine the required motoric action behavior for each robot as a set of motoric action states. These are already given in [Araz and Erden, 2014] for the frog robot. A packaging robot will be used to classify and separate various objects and collect them into various packages. Motoric action

states are defined as grasping object, classifying (separating) and packaging. This robot needs to detect the object, its color and geometry, which are selected as the perception behavior modules. Similarly, motoric action states for a rescue robot are defined as “grasping human” and “transporting human” for which the required perception behavior modules are “detect gas”, “detect fire”, “detect object” and “detect human”. By selecting the required perception behavior modules, related motoric action behavior module is activated and the corresponding robot’s behavior is obtained as it is shown in Figure 5. In this approach, physical modules are not specified and the modularity is only represented at the behavioural level.

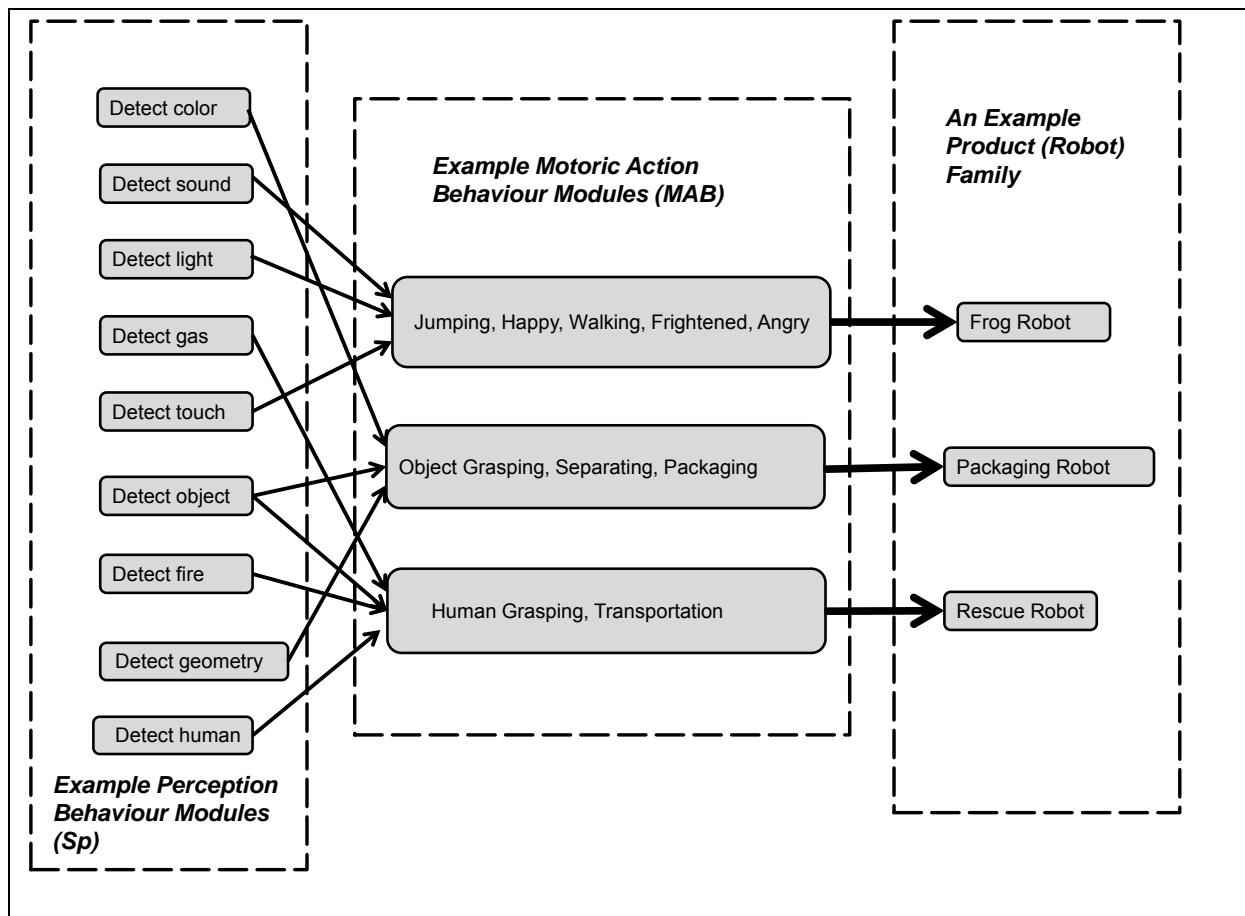


Figure 5. An example for using behavioural modules for a robot product family.

## 5. DISCUSSION AND CONCLUSIONS

Modularization is an important focus as a means for the design and development of product families by increasing the competitiveness of companies through the advantages of customization and flexibility. Implementing modular design methods for mechatronic products yields innovative design solutions that best fit changing customer requirements in this type of





products. This increases maneuverability of companies producing mechatronic products in mass customization. Domain-independent systematic methods for modularization are required in order to design and develop mechatronic product families, due to the integrated and multidisciplinary nature of such products. This paper presents an initial conceptual scheme for modular design methodology of mechatronic products using previously developed systematic behavioural representation framework. The scheme is based on *behavioral modules* for perception, cognition and motoric action required for an intended operational behavior of a mechatronic system. A formal structure for describing *behavioral modules* is proposed and an overall framework for the application of the scheme is presented by a descriptive example. This study is a first step for a systematic modular mechatronic design methodology. Future research will be directed towards the development and conceptual/physical implementation of a detailed formal structure to describe behavioral modules for mechatronic products.

## REFERENCES

1. **Anon, (2004)**, Artifex <sup>TM</sup> 4.4 Getting Started Handbook, New York: RSoft Design Group.
2. **Araz, M. and Erden, Z., (2014)**, "Behavioural representation and simulation of design concepts for systematic conceptual design of mechatronic systems using Petri Nets", *International Journal of Production Research*, Vol.52, No.2, pp. 563-583.
3. **Dahmus, J.B., Gonzales-Zugasti, J.P. and Otto, K.N., (2001)**, "Modular Product Architecture", *Design Studies*, Vol.22, No.5, pp.409-424.
4. **Gerherson, J.K., Prasad, G.J. and Zhang, Y., (2003)**, "Product Modularity: Definitions and Benefits", *Journal of Engineering Design*, Vol.14, No.3, pp.295-313.
5. **Gu, P., Xue, D. and Nee, A.Y.C., (2009)**, "Adaptable Design: Concepts, Methods, and Applications", *Proceedings of the IMechE, Part B: Journal of Engineering Manufacture*, Vol. 223, No.11., pp. 1367-1387.
6. **Huang, C.C. and Kusiak, A., (1998)**, "Modularity in Design of Products and Systems", *IEEE Transactions on Systems, Man and Cybernetics, Part-A: Systems and Humans*, 28(1), pp. 66–77.
7. **Jiao, J., Simpson, T. W. and Siddique, Z., (2007)**, "Product Family Design and Platform-Based Product Development: A State-of-the-Art Review", *Journal of Intelligent Manufacturing*, Vol.18, No.5, pp.5-29.



8. **Li, Z., Cheng, Z., Feng, Y. and Yang, J., (2013)**, “An Integrated Method for Flexible Platform Modular Architecture Design”, *Journal of Engineering Design*, Vol.24, No.1, pp.25-44.
9. **Murata, T., (1989)**, “Petri Nets: Properties, Analysis and Applications”, *Proceedings of the IEEE*, Vol.77, No.4, pp.541-580.
10. **Nanda, J., Thevenot, H.J., Simpson, T.W., Stone, R.B., Bohm, M. and Shhote, S.B., (2007)**, “Product Family Design Knowledge Representation, Aggregation, Reuse and Analysis”, *Artificial Intelligence for Engineering Design, Analysis and Manufacturing*, Vol.21, No.2, pp.173-192.
11. **Pahl, G. and Beitz, W., (1996)**, *Engineering Design-A Systematic Approach*, London: The Design Council.
12. **Simpson, T.W., (2004)**, “Product Platform Design and Customization: Status and Promise”, *Artificial Intelligence for Engineering Design, Analysis and Manufacturing*, Vol.18, No.1, pp.3-20.
13. **Stone, R.B., Wood, K.L. and Crawford, R.H., (2000)**, “A Heuristic Method for Identifying Modules for Product Architectures”, *Design Studies*, Vol.21, No.1, pp.5-31.
14. **Tseng, M. and Jiao, J., (2001)**, “Mass Customization”, *Handbook of Industrial Engineering*, Gaviel Salvendy (Ed.), Wiley, New York.
15. **van Beek, T.J., Erden, M.S. and Tomiyama, T., (2010)**, “Modular Design of Mechatronic Systems with Function Modeling”, *Mechatronics*, Vol.20, No.8, pp. 850-863.
16. **Yan, X. and Stewart, B., (2010)**, “Developing Modular Product Family Using GeMoCURE within an SME”, *International Journal of Manufacturing Research*, Vol.5 No.4, pp. 449-463.
17. **Yu, T., Yassine, A.A. and Goldberg, D.E., (2007)**, “An Information Theoretic Method for Developing Modular Architectures Using Genetic Algorithms”, *Research in Engineering Design*, Vol.18, pp.91-109.
18. **Ziegler, B.P., (1989)**, “DEVS Representation of Dynamic Systems: Event-Based Intelligent Control”, *Proceedings of the IEEE*, Vol.77, No.1, pp.72-80.



## **PREGNANT OCCUPANT MODEL DESIGN TO IMPROVE SAFETY**

**B. Serpil ACAR**, *B.S.Acar@Lboro.ac.uk*, Design School, Loughborough University, UK.

**Moustafa MERIC**, *M.Moustafa@Lboro.ac.uk*, Design School, Loughborough University, UK.

**Memis ACAR**, *M.Acar@Lboro.ac.uk*, Wolfson School of Mechanical and Manufacturing Engineering, Loughborough University, UK.

### **ABSTRACT**

Computational modelling is an effective way of estimating the risk of injuries and fatalities in road traffic accidents. Computational pregnant occupant modelling has an additional important role, that is the investigation of the risk of fetus mortality in crash test simulations. In this paper, the effect of including the fetus in the uterus of the pregnant occupant model is investigated using the computational pregnant occupant model 'Expecting' in crash test simulations. First, isolated drop test simulations with and without a fetus are used to show the effect of presence of fetus in the uterus model are conducted and compared with earlier researchers' findings. Then the pregnant occupant model, 'Expecting', with varying levels of restraint system use, such as fully restrained, 'seatbelt only', 'airbag only' and 'no restraint', is used in the simulations of frontal crashes representing five levels of impacts. Maximum strains developed in the utero-placental interface with and without a fetus are compared in both cases. Both experiments predict higher risks of placental abruption when the fetus is included in the model. Simulations with the pregnant occupant model, 'Expecting', with and without a fetus, provides an opportunity to explore the role of inclusion of fetus in the uterus of the model.

**Keywords:** Pregnant, Occupant, Fetus, Crash, Safety, Modelling, Simulations.

### **1. INTRODUCTION**

There are 131.5 Million pregnancies in the world which conclude with birth every year. It has been shown that 6-7% of all pregnancies are affected by trauma, with motor-vehicle accidents being the leading cause of accidental fetal mortality worldwide [1, 2]. According to Department of Transport National Travel Survey [3], from 1997 to 2012 the average number of car driver trips by women has increased by 12% and average distance travelled has

increased by 25%. During pregnancy, a woman's body changes significantly. Especially around the hip, abdominal and chest regions, a wide variety of physical changes occurs as detailed by Acar and Weekes [4]. Continuously changing anthropometry of pregnant women can create serious comfort and safety problems in motor vehicles which are normally designed for standard occupants. From this point of view, the transportation of pregnant occupants can be hazardous for the fetus.

The most common cause of fetal loss with known origins is placental abruption [5]. The injury occurs where the placenta becomes partially or completely detached from the inner surface of the uterus wall, the uteroplacental interface (UPI), disrupting the supply of oxygen and nutrients to the fetus.

One way of assessing the safety of occupants in motor vehicle accidents is using anthropometric test devices (ATD). The biofidelity of physical crash test dummies is limited. The only commercially available experimental pregnant crash test dummy is MAMA2B and no placenta or fetus is included in it. Its uterus is represented with water-filled bladder.

On the other hand computational human body modelling can offer good representation of the human body in detail if the models are realistic. Computational models have been increasingly used in crash simulation applications over the last decade. Finite element pregnant female models are developed to predict the safety of pregnant women and fetus in motor vehicle accidents. The computational pregnant occupant models usually include a finite element uterus and placenta models but either include no fetus as in Moorcroft et al [6] or include a lump mass representing the fetus as in Delotte et al [7]. None of the previous models incorporate detailed anthropometric changes of the whole body of pregnant women.

'Expecting', the computational pregnant occupant model developed by Acar and van Lopik [8] at Loughborough University represents 5<sup>th</sup> percentile female at 38-week pregnancy. 'Expecting' includes a finite element uterus and placenta models as well as a detailed multibody fetus model of Acar and van Lopik [9]. The model also incorporates the anthropometric changes to the female body during pregnancy [10].

## 2. METHODOLOGY

In this investigation, two sets of experiments were conducted:

1. Vertical drop test simulations of the isolated uterus model with and without the fetus model
2. Set of crash simulations with the 'Expecting' (with fetus) and a new version of 'Expecting' without a fetus

In order to demonstrate the difference between of strains at the utero-placental interface (UPI) caused by impacts when the fetus model is included and excluded.

But first the computational pregnant model 'Expecting' is described below:

### 2.1 The Pregnant Occupant Model: 'Expecting'

'Expecting', the computational pregnant occupant model, embodies the complexity of pregnant women's anatomy and anthropometric details based on 49 measurements sets of data from 107 pregnant women volunteers [4]. A detailed multi-body representation of a fetus within a finite element uterus model is also integrated into the model [8]. The model is placed within a typical vehicle interior model, consisting of a seat, vehicle floor, pedals, bolsters and steering wheel as shown in Figure 1(a), in the multi-body/finite-element software package MADYMO [11].

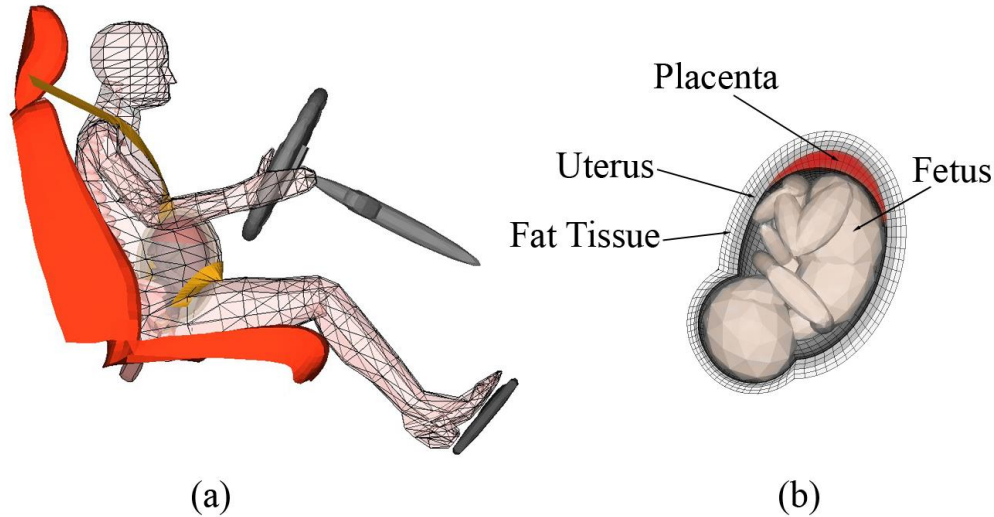


Fig. 1. The pregnant occupant model 'Expecting' (a); uterus, placenta and fetus in 'Expecting' (b).

The finite element uterus model is built in accordance with the fetus dimensions and configuration controlling the dimensions of the uterus to provide a snug fit around the fetus to represent the 38 weeks of pregnancy as shown in Figure 1(b). The multi-body fetus model is composed of 15 rigid bodies representing the various anatomical regions of the fetus interconnected by kinematic joints. Details of generating the fetus can be found in [9]. A finite element layer of fat encloses the outer surface of the uterus. A total fetal mass is 3.3kg and the resulting total mass of the uterus with the placenta and the fetus is nearly 4.6 kg. The pregnant occupant model 'Expecting' is validated against rigid-bar impact and belt loading tests performed by [12]. Further details of validation of the model can be found in [8].

### 2.2 Vertical Drop Tests with and without Fetus

A study by an earlier researchers simulated vertical drops of a uterus model, containing a simplified fetus geometry represented by two ellipsoids, onto a rigid flat surface [13] from 0.5m at angles of 0°, 30°, and 90° and concluded that the effect of an impact on uterus is independent of the fetus itself. This conclusion is questionable as there is no comparison of models with and without a fetus.

In this study, the drop tests of [13] are replicated with the uterus model of Expecting and an identical uterus model but without the fetus.

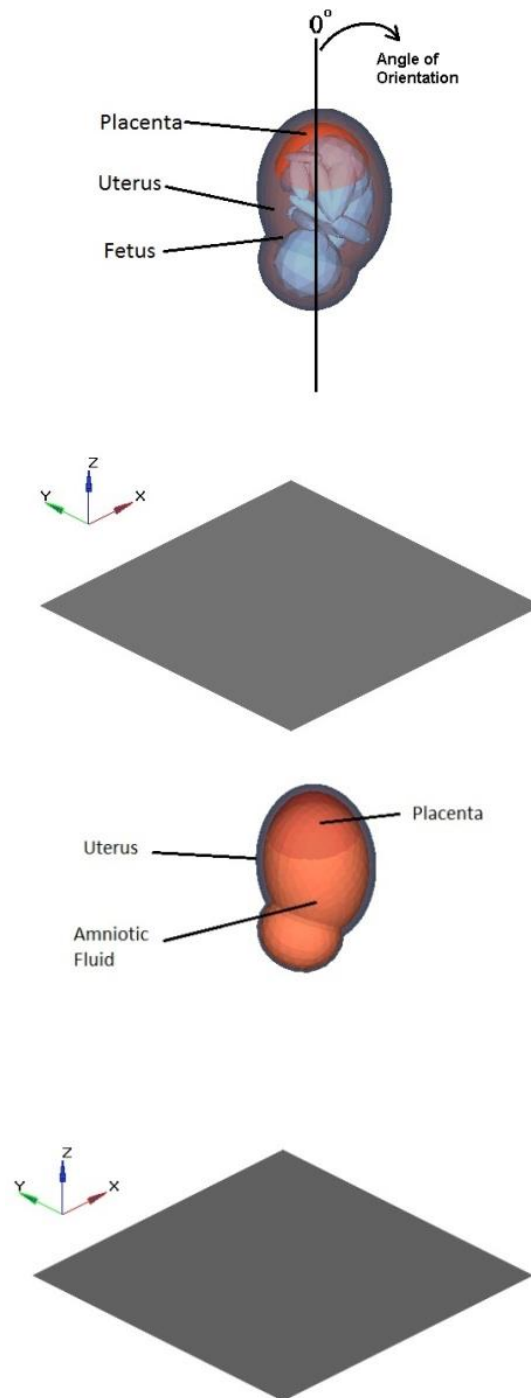


Fig. 2 Drop tests with and without fetus at 0° orientation

The FE uterus model of ‘Expecting’ contains a placenta and detailed multibody fetus model [9]. The second (identical) uterus model contains no fetus and the space was filled with amniotic fluid. With-fetus and without-fetus versions of FE uterus models are dropped vertically onto a rigid flat surface from 0.5m height, at angles of 0°, 30°, 90° and 180° in order to investigate the effect of the fetus on the strains on uterus. Figure 2 shows the vertical drop test of both models at 0° orientation. Figure 3 shows the with-fetus model at angles of 0°, 30°, 90°, and 180°. The maximum strains on uterus with and without fetus cases are compared.

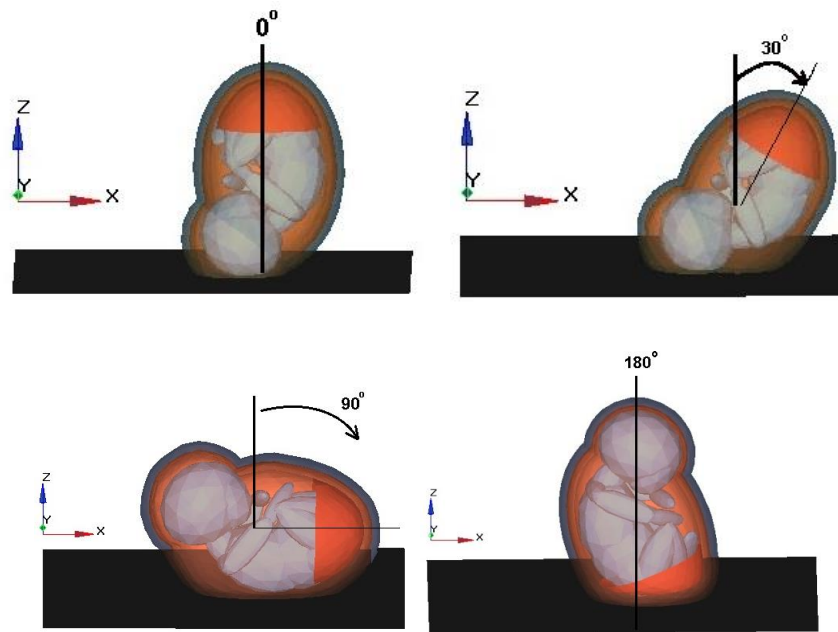


Fig. 3 Drop tests with fetus at 0°, 30°, 90°, and 180° orientation

### 2.3 Frontal Crash Simulations with and without Fetus

The research strategy adopted in this part of the study is to use the current ‘Expecting’ pregnant occupant model in order to represent a realistic pregnant occupant model. In addition a version of the ‘Expecting’ model without a fetus is developed (Figure 4). In the ‘Expecting’ without-fetus model, the entire uterus is filled with the amniotic fluid, which is 98-99% water and hence can be considered as incompressible. In the with-fetus model, the 38 weeks old fetus almost fills the entire volume of the uterus leaving minimal space for the amniotic fluid. The material properties of the uterus, placenta, fat tissue and amniotic fluid, as taken from the literature, are given in [8].



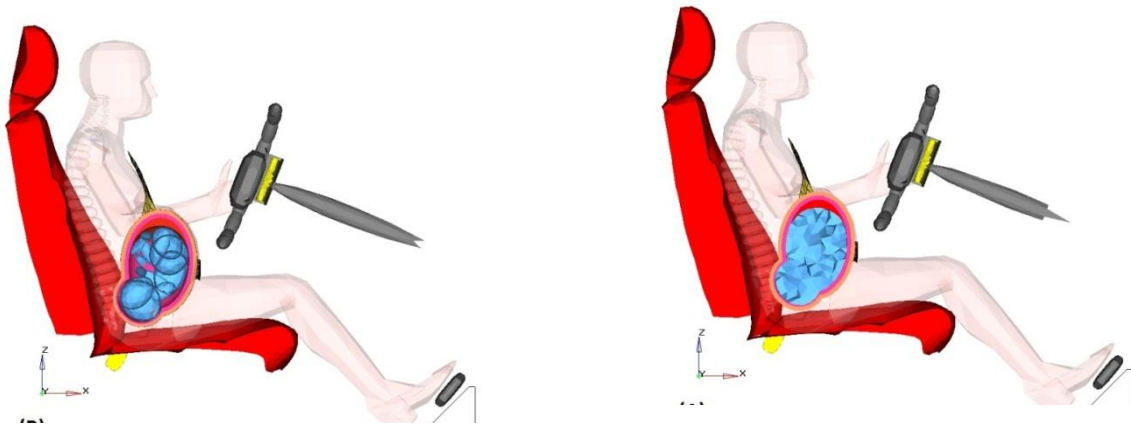


Figure 4. Computational pregnant occupant model ‘Expecting’ (with fetus) and modified ‘Expecting’ without a fetus

‘Expecting’, the pregnant occupant model and its without-fetus version are used in a number of frontal crash test simulations to investigate the contribution of the inclusion of a fetus on the strains generated at the UPI. The experiments include (a) ‘seatbelt & airbag’, representing a properly restrained pregnant driver; (b) ‘seatbelt only’ excludes the airbag; (c) ‘airbag only’ excludes the seatbelt, but yet the airbag is active; and finally (d) ‘no restraint’ excludes all restraints, in other words neither the seat belt is worn nor is the airbag deployed. For each case, tests are run with crash speeds of 15, 20, 25, 30 and 35 kph, and the acceleration pulses applied to the model are half-sine waves with 120 ms duration.

Maximum von Mises equivalent strain levels in uterus at the UPI are determined for with-fetus and without-fetus models to assess the possibility of placental abruption, which is the main cause of fetal and occasionally maternal fatalities. The threshold strain value of widely-accepted 60% is taken for the occurrence of placental abruption is at the UPI .

### 3. RESULTS AND DISCUSSION

#### 3.1 Vertical Drop Tests

Table 2 shows the strain levels on the uterus for simulations of vertical drop tests of the uterus with-fetus and without -fetus at angles of 0°, 30°, 90° and 180°.



Table 2 Von Mises strain levels at UPI with and without fetus drop tests

Drop Test	0°		30°		90°		180°	
	Whole Uterus	UPI	Whole Uterus	UPI	Whole Uterus	UPI	Whole Uterus	UPI
With Fetus	1.37	0.07	2.02	0.17	0.89	0.30	2.57	2.57
Without Fetus	0.72	0.01	0.66	0.02	0.86	0.24	0.66	0.66

At the angle of 0° orientation (Figure 5) the uterus model with the fetus ruptures when the model hits the impact plane, due to the compression of the uterus wall between the head of the fetus and impact surface. Without the fetus model, the highest strain is observed about the contact surface of the uterus with rigid floor and is much lower than the strain levels with-fetus model. Strain at UPI is almost the same for both cases with very slightly higher for with-fetus case.

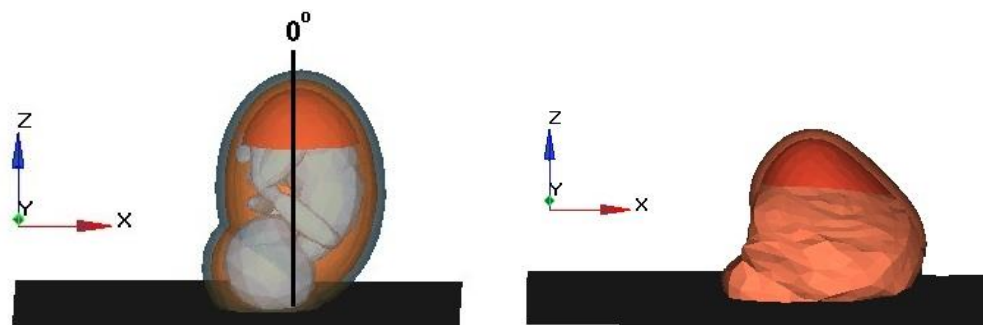


Figure 5 Vertical drop tests of the uterus with-fetus and without-fetus at angle of 0° orientation

In the 30° orientation drop test simulations, the maximum Von Mises strain anywhere in the uterus with-fetus is significantly higher than without-fetus model. Strain at UPI is also higher for the with-fetus case (Table 2).

For the 90° orientation angle, the maximum strain values at anywhere in the uterus are very similar for with-fetus and without-fetus cases.

In the 180° orientation, the placenta is at the leading end of the uterus in the impact simulations (Figure 6), hence the placenta is compressed between the fetus and the impact surface and the maximum strain on the uterus is generated at the UPI. A very high strain value of 2.57 is predicted in experiment with-fetus model. In the drop tests without-fetus the

strain value is predicted to be a much lower value of 0.66. The results clearly show that the fetus causes a sharp rise in the strain at angle of 180°

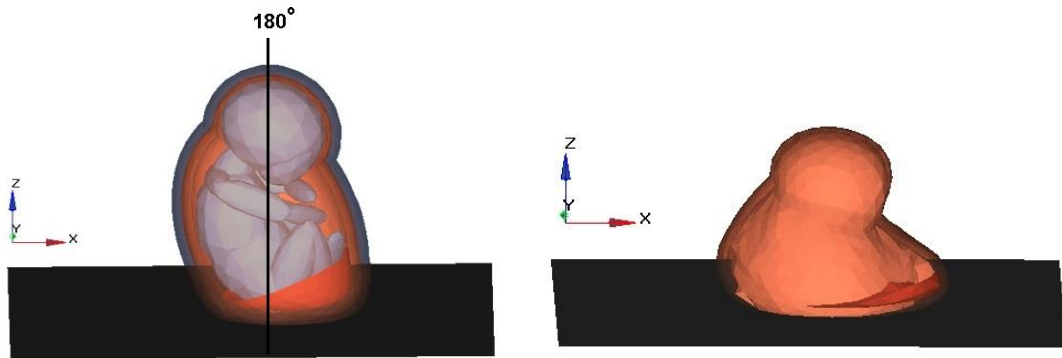


Figure 6 Vertical drop tests of the uterus with-fetus and without-fetus at angle of 180° orientation

### 3.2 Frontal Crash Simulations

In general, the maximum strain levels at the UPI increase with crash speed as expected. The maximum strain in the with-fetus model is typically higher than the strains in the without-fetus model, indicating a greater risk of placental abruption.

Strains in the uterus at placental location are investigated to highlight the placental abruption risk. Figures 7(a) and 7(b) depict visually a typical impact response at 30 kph for the fully restrained pregnant driver model with and without a fetus respectively.

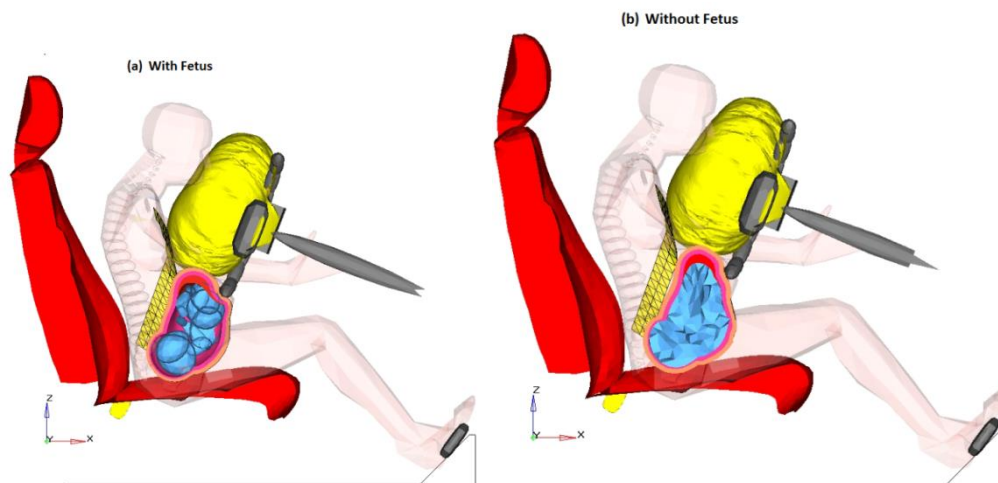


Figure 7. Typical frontal impact responses for 30 kph at 105ms of impact.

Figure 8 (a) compares the strain levels for the 'seatbelt & airbag' case for a crash speed range of 15-35 kph. The without-fetus model simulation results show lower strain levels than

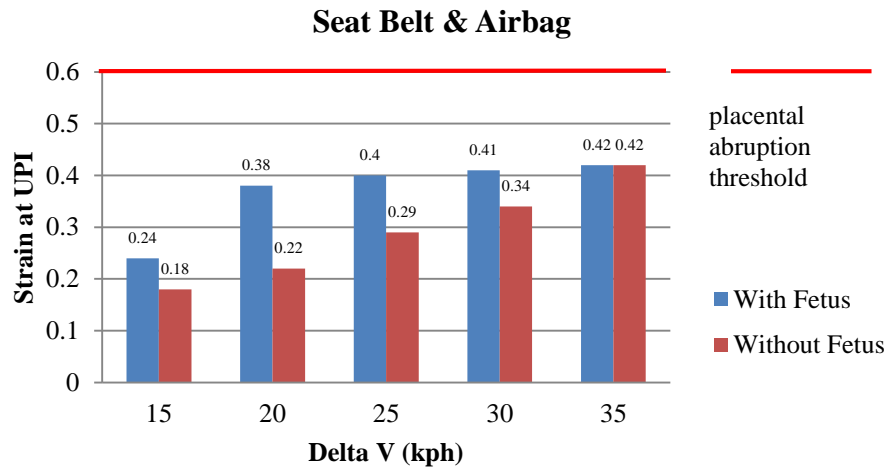
with-fetus model simulations up to the 35 kph. Figure 8 (a) shows that maximum strains at the UPI for the with- and without-fetus models vary between 0.24 to 0.42 and 0.18 to 0.42 respectively. The increase for without fetus case is gradual and almost linear, whereas for the with fetus case, there is a greater increase in strain from 15 to 20 kph. All strain values at the UPI are considerably below the injury threshold value, 60%.

The 'seatbelt only' case results for the maximum strains at the UPI are shown in Figure 8 (b), which follows a similar pattern to the strains in the 'seatbelt & airbag' case, but are generally higher. At 35-kph impact, the strain level approaches the placental abruption risk threshold of 60% for both cases. The higher strain levels could be attributed to the pressure that the steering wheel applies to the uterus at the anterior edge of the placental location forcing the fetus downwards. However, the lap portion of the three-point seatbelt prevents the occupant moving excessively forward. The placenta is also compressed between the fetus and steering wheel in the with-fetus model and this dynamic motion generates considerably higher strains at the UPI than in the without-fetus model.

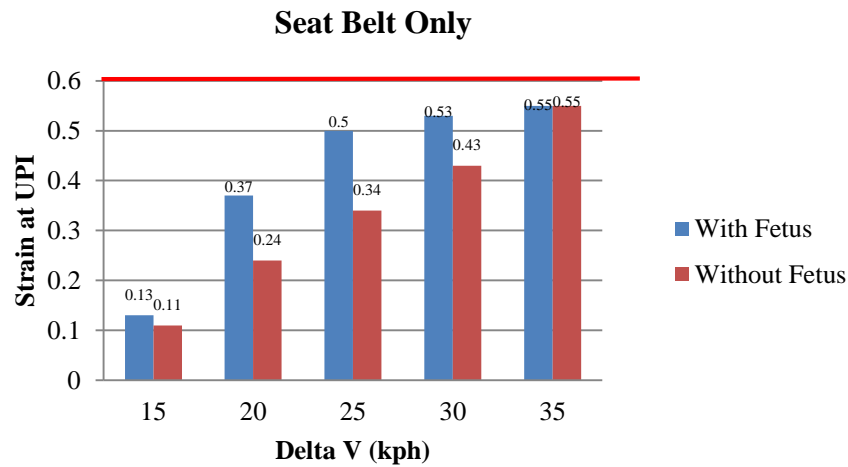
Figure 8 (c) shows the maximum strain levels at the UPI for the 'airbag only' case which demonstrates that when the fetus is included in the model, the placental abruption risk emerges at a crash speed of 20 kph, whereas the without-fetus model shows that the placental abruption risk begins at a higher crash speed of 30 kph. Without the seatbelt, it is clear that the contribution of the fetus on the maximum strains at the UPI is much more pronounced and the placental abruption risk is found to be higher. The mass of the fetus (3.3 kg) plays a significant role in the behavior of 'Expecting', the pregnant occupant model. These results clearly demonstrate that the fetus changes the entire dynamic response to impact.

For the 'no-restraint' case shown in Figure 8 (d), the with-fetus model, shows placental abruption risk at all speeds considered (15-35 kph), whereas in the without-fetus model, strains at the UPI are below the placental abruption threshold value of 60% for at 15, 20, and 25 kph.

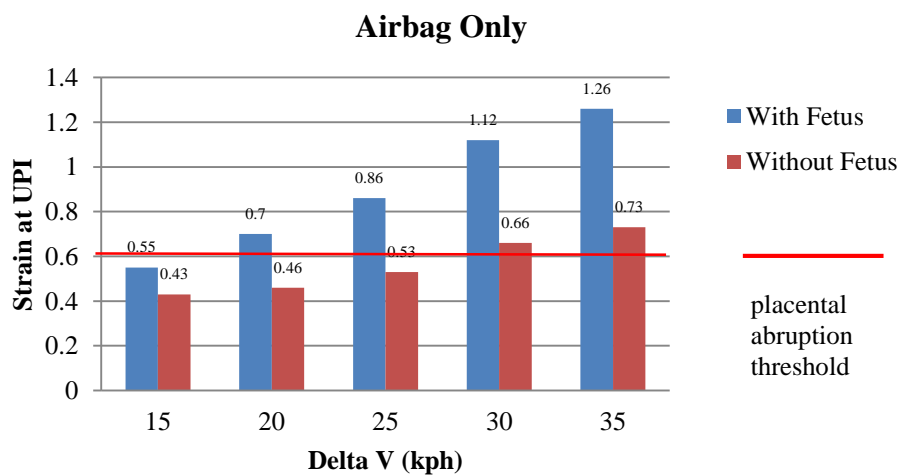
The simulation results suggest that the correct use of seatbelt in conjunction with the airbag is essential for the protection of the fetus in vehicle crashes.



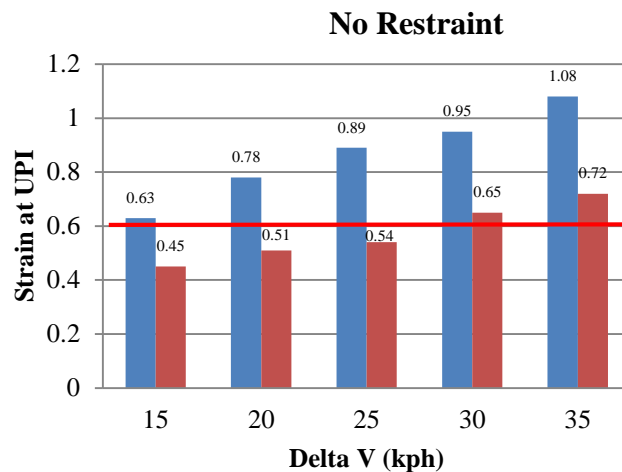
(a) Fully restraint (seatbelt and airbag) case



(b) seatbelt only case



(c) airbag only case



(d) No restraint case\_

Figure 8 Strain levels at UPI for four restraint cases and five crash speeds

#### 4. CONCLUSIONS AND DISCUSSION

In this research, implications of including the fetus model in the uterus of pregnant models are investigated. Vertical drops onto a rigid flat horizontal surface at angle of orientation of 0°, 30°, 90°, and 180° have been simulated for the isolated uterus model with and without the fetus. In addition, the computational pregnant occupant model 'Expecting' (with fetus) and its without fetus version are used to simulate a range of frontal impacts of increasing severity from 15 kph to 35 kph. Four cases of occupant restraint, seat belt and airbag, seat belt only, airbag only and completely unrestrained are investigated.

Contribution of the presence of a fetus on the maximum von Mises strains on the uterine wall has been determined. Drop test simulation results suggest that the existence of a fetus have a significant effect on the strain levels in the uterus. In all cases, the maximum strain levels are higher with the fetus than without the fetus model. This clearly demonstrates that the fetus changes the dynamics of the of the uterus and therefore the fetus should be included in the uterus in all pregnant woman models for realistic results in crash test simulations. The largest predicted strain difference between with-fetus and without-fetus appears to be at the angle of 180° orientation which represents a direct impact on the uterus where placenta is, similar to an impact through the steering wheel.

Contribution of the presence of a fetus on the maximum von Mises strains on the utero-placental interface in crashes has also been investigated. The loading from the seatbelt, steering wheel and airbag, causes strains to develop in the uterus. When the fetus model is included in the uterus, the inertial loading on the uterus due to the motion of the fetus occurs



too. Fetus' physical growth during the later stages of pregnancy is significant. The fetus is solid and moves during an impact and contribute to the deformation of its elastic environment. This significant mass in the uterus, characteristically different than the amniotic fluid, appears to have a significant effect on the dynamics of the pregnant woman.

Crash test simulation results from the 'Expecting' show that the inclusion of the fetus in the model creates a more realistic representation of the pregnant occupant, which changes the dynamic response of the model in crash simulations. Inertial effects on the fetus cause it to move forwards relative to the pregnant occupant. The fetus accelerates towards the anterior wall of the uterus. Consequently, this dynamic motion of fetus generates significantly higher strains at the UPI than without fetus model.

Therefore, fetus should be included in the uterus in pregnant woman models for realistic simulations and results in crash test simulations.

## 5. REFERENCES

1. **CEMD (1999)** Confidential Enquiry into Maternal Deaths Report, Publication of Department of Health, UK.
2. **El-Kady D, Gilbert W M, Anderson J, Danielsen B, Towner D and Smith L H (2004)** Trauma during pregnancy: an analysis of maternal and fetal outcomes in a large population. *Am J Obstet Gynecol* 2004;190: 1661-68
3. **Department for Transport. National Travel Survey (2013)** 2012 Statistical Release London.
4. **Acar B S and Weekes A, (2006)** Measurements for Pregnant Occupant Safety', *International Journal of Vehicle Design*, Vol. 42, No. 1-2, pp.101-118.
5. **Fildes J, Reed L, Jones N, Martin M, Barrett J. (1992)** Trauma: the leading cause of maternal death. *J Trauma* 1992;32:643–645
6. **Moorcroft, D., Duma, S., Stitzel, J., and Duma, G. (2003)** "A finite element and multi-body model of the pregnant female occupant for the analysis of restraint effectiveness." SAE paper 2003-01-0157.
7. **Delotte, J., Behr, M., Baque, P., Bourgeon, Andre, Peretti, F. and Brunet, C. (2006)** Modelling the pregnant woman in driving position, *Surgical and Radiologic Anatomy*, 28:359-263.
8. **Acar, B. S., and van Lopik, D., (2009)**, "Computational pregnant occupant model, 'Expecting', for crash simulations", *J. Automobile Engineering, Proc. IMechE Part D:*, 223, 891-902.



9. **Acar, B. S., and van Lopik, D., (2012)**, Modelling the fetus for pregnant occupant safety, Journal of multi-body dynamics, (Proc. IMechE Part K) 226 197-205.
10. **Acar, B. S., van Lopik, D. and Weekes A M (2009)** International Journal of Vehicle Design **51**((3)):375-385
11. MADYMO TNO Automotive BV, Delft, The Netherlands
12. **Hardy, W.N., Schneider, L.W., and Rouhana, S.W.(2001)** Abdominal impact response to rigid-bar, seatbelt, and airbag loading. *Stapp Car Crash J.*, 2001, **45**, 1-32.
13. **Rupp, J. D., Schneider, L. W., Klinich, K. D., Moss, S., Zhou, J., and Pearlman, M. D. (2001)**, "Design, development, and testing of a new pregnant abdomen for the Hybrid III small female crash test dummy", Report UMTRI-2001-07, University of Michigan Transportation Research Institute, Ann Arbor, Michigan, USA.







## **A FEM-MB MIXED METHODOLOGY TO ANALYZE THE PASSIVE SAFETY PERFORMANCES OF A PASSENGER SEAT FOR RAILWAY USE**

**Francesco CAPUTO**, *francesco.caputo@unina2.it* Second University of Naples, 81031, Aversa, Italy

**Giuseppe LAMANNA**, *giuseppe.lamanna@unina2.it* Second University of Naples, 81031, Aversa, Italy

### **ABSTRACT**

The research activity showed in the present paper aims to identify a FEM-MB mixed numerical procedure to support the structural design of a passenger seat in railway field, in order to make it compliant with passive safety requirements. The passive safety performances of the seat as a whole is understood here as its capability to minimize, or even to avoid, any damage to passengers seated on it or on adjacent seats, through the use of appropriate design features, which should allow to absorb large amounts of impact energy.

**Keywords:** Biomechanics, Passenger Seat, Multibody

### **1. INTRODUCTION**

The aim of the present paper is to define a numerical procedure such as to be used to modify and re-design a passenger seat of a railways convoy while considering passive safety as a main goal. In the first step of the described activity, the kinematics of a passenger has been numerically evaluated through the use of finite-element (FE) and multibody (MB) codes, as well as the damages which the same passenger may suffer in a frontal impact of the coach against a rigid obstacle. Subsequently, the corresponding indexes of biomechanical damages have been evaluated and compared with the extreme ones considered in the current regulations [1, 2]. The study of those subjects can be faced experimentally (sled-test) by using specific equipment (Fig. 1), which can assign to the seat the required speed and the corresponding acceleration/deceleration profile [3, 4]. During this kind of experiments anthropomorphic dummies can be also used, which are to be appropriately equipped with instruments such as to allow recording over the test the kinematical as well as dynamical parameters, which characterize the phenomenon under study. From those measurements



the damage indexes can be carried out, which correspond to the different parts of the body directly involved in the impact or just subjected to high inertia loads [5, 6].

It is of course evident that the fitting and the implementation of such tests is very demanding, because of the difficulties met to find the necessary equipment, the complexity of the adopted dummies, the availability of appropriate space and, at most, the required costs.

Furthermore, it has to be considered the limited possibility to examine in a test many different arrangements or lay-outs of the seats in the coach and various configurations of the dummy. For all those reasons, the numerical simulation of those phenomena is usually preferred, by using MB numerical models, which can be generally adopted to evaluate the kinematics of the dummy and its interactions with both the restraining systems, if available, and the seat cushion, with no possibility whatever to obtain any results about the structural behavior of the seat frame. Those models exhibit the priceless convenience to allow quick modifications of the analyzed configuration and to obtain reliable results, within the recalled limits, with very short runtimes.

Numerical FEM models are required to obtain information about the structural behaviour of the seat. Even if the developing time of those models is to be considered as acceptable for current design time scheduling, the same can't be said for runtimes, at most for applications of dynamical type and for the use of anthropomorphic dummies, whose models prove to be very complex and therefore require very accurate discretization and high mesh densities. Furthermore, those modes require an initial work to calibrate, correlate and validate the results by means of their comparison with similar results, whose accuracy is demonstrated. The high computational cost of those models is then limited to those cases where the designer is expecting to introduce some relevant structural modifications, which could be required to improve the passive safety performance of the components under study; such an evaluation could be carried out preferably by means of a MB analysis [7], even if the mentioned calibration problems would still be present. In this paper a numerical procedure has been adopted, which is founded on both methods of analysis, multibody and finite-element, and which is such as to profit opportunely by the peculiarities of both of them. At first, a MB model of an experimental sled-test has been calibrated; it allowed carrying out relevant information about the characteristics of the restraining systems, if existent, and also about the interactions of the dummy with the seat and the restraints. By using such information a FE model of the same sled-test has been prepared and it has been validated by means of experimental results and of those coming from the MB study.

Following some opportune analyses of that model, relevant information of structural type have been inferred about the seat components, on whose basis another MB model has been

prepared, which has been provided with elastic elements to connect the different components and with fictitious stiffness elements to simulate surface contacts. That model is such as to allow developing fast iterative procedures to improve the passive safety performance of the seat, by acting on the stiffness characteristics of those elements.

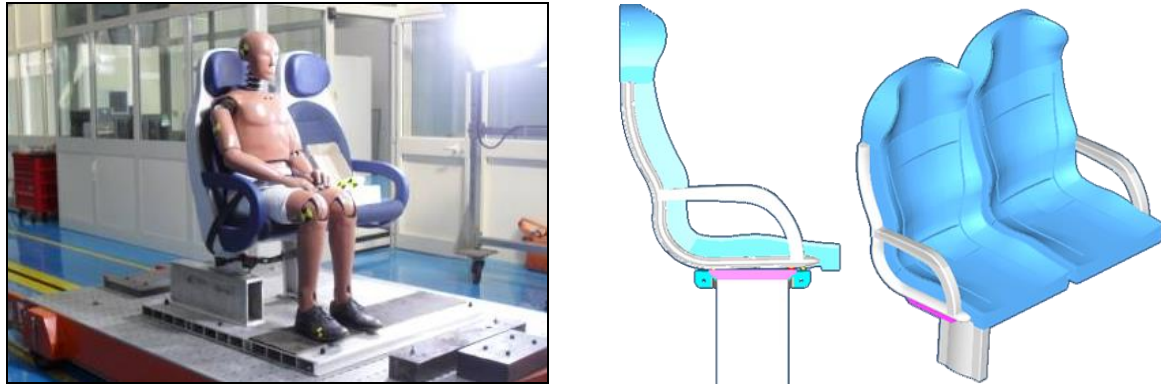


Figure 1. Implementation of a sled-test; geometry of a seat.

## 2. THE FINITE ELEMENT MODEL

The starting model adopted to develop the described work is a passenger seat mounted in a local and current circulating train (Fig. 1).

All metallic elements, which compose the seat, are made of aluminium AL2024-T3; following that hypothesis, the weight of the whole seat, as extracted from its geometry, turned out to be about 14 kg.

The lay-out adopted for this study considers the seats to be oriented in the direction of travel, with a 0.72 m pitch between two consecutive rows. The objective of the present activity is to prepare a computing method to carry out a new design of the passenger seat such as to improve the passive safety of the occupants [8, 9]. In order to attain the said objective, the most critical biomechanical parameters of the occupants have been identified; subsequently the necessary modifications have been introduced to allow those parameters to be within the boundary values imposed by the regulations.

Reference has been made to ECE94 regulations, which are used in the automotive field.

The analyzed seat model is made of a metallic support structure and of a foam cloth-covered layer, used for the cushion and the back (Fig. 2).

The whole support structure has been modelled by means of 4-noded shell-type elements (5 degrees of freedom per node) with a 10 mm average size for each element. The seat foam

has been modelled with 8-noded brick-type three-dimensional elements (3 degrees of freedom per node) with the same average size, obtaining a model composed by 38,209 nodes and 94,215 elements (among which 54,031 bricks) (Fig. 3). Several contact algorithms have been implemented in the model in order to avoid mutual penetrations [10] among the components.

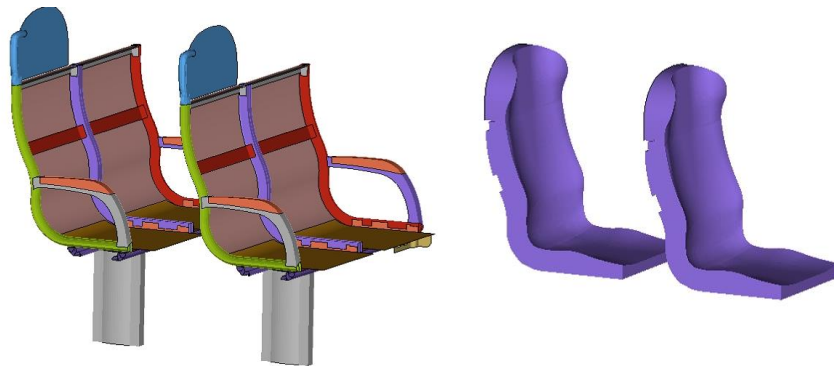


Figure 2. Structure and foam of the seat.

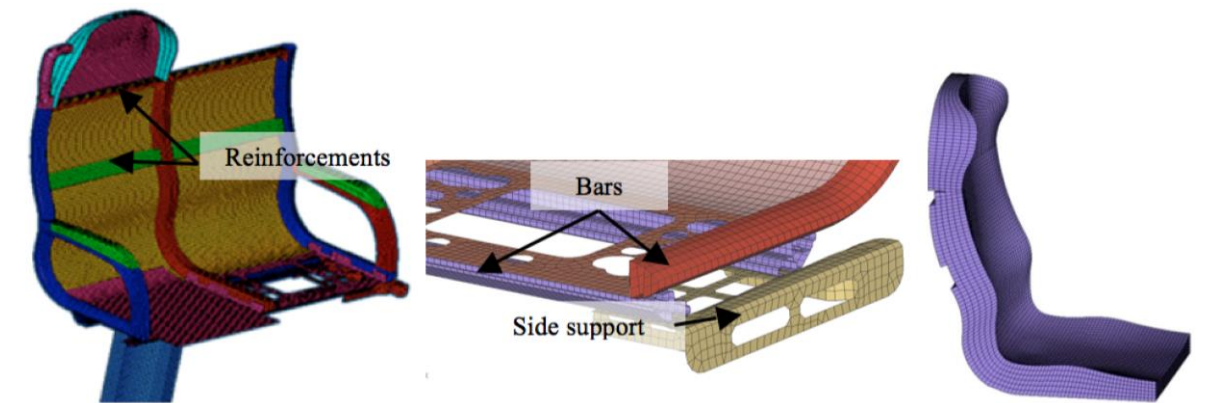


Figure 3. Discretization of the seat.

For what concerns the materials adopted in that model, they can be mentioned as follows:

- 2024-T3 aluminium for all the elements which compose the structure;
- plywood for the underseat panel;
- foam for the cushion and the back of the seat.

As no data were available for the characteristic stress-strain curve for the foam, specific experimental compression tests have been carried out at the Machine Design Test Facility of

the Department of Industrial and Information Engineering of the Second University of Naples according the UNI EN ISO 3386 regulation. Material properties are reported in Tab. 1.

Table 1. Mechanical properties.

Material	Elastic Modulus [GPa]	Poisson Ratio [-]	Yield Stress [MPa]	Elongation at Break [-]	Ultimate Stress [MPa]
Al 2024-T3	73.1	0.33	310	0.18	448
	Elastic Mod. [GPa]	Ult. Stress Ten. [MPa]	Ult. Stress Com. [MPa]	Density [kg/m3]	
Plywood	8.4	19.1	26.3	395	
Foam					
Strain [-]	0.2	0.4	0.5	0.6	0.7
Stress [kPa]	9.3	12.5	15.6	21.8	40.3

The foamy material, which composes the padding of the seat has been characterized through the n. 57 material model (MAT\_LOW\_DENSITY\_FOAM) from the materials library of Ls-Dyna® code.

Rigid connection elements have been used to fasten the structure to the floor of the coach; that floor has been subjected to the acceleration pulse that had been acquired through the experimental sled-test, which has been described and analyzed in [11, 12] (Fig. 4).

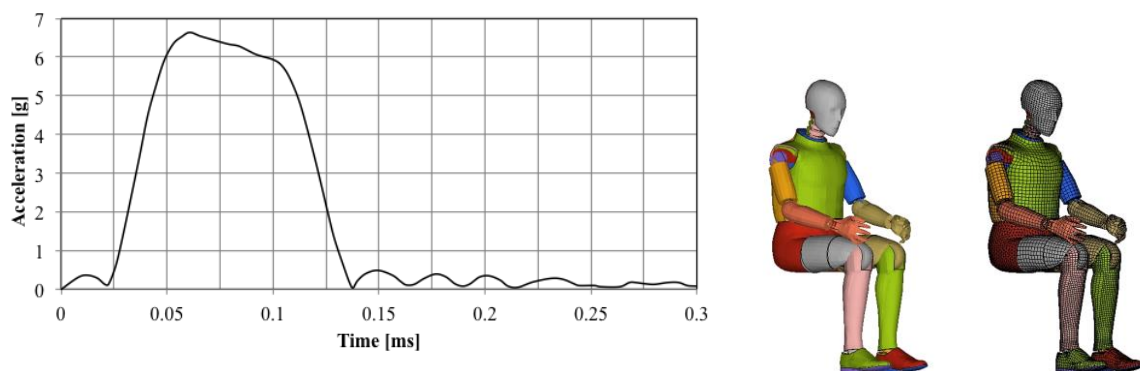


Figure 4. Deceleration pulse; FTSS 50% dummy.

To study the biomechanics of the occupant an anthropomorphic numerical model has been chosen, which is representative of a medium-built passenger, called FTSS 50%, which is



usually used in the automotive field; it represents an average people from USA: 1,68 m height, 77 kg weight (Fig. 4).

### 3. THE MULTIBODY MODEL

As we already pointed out, a MB model allows a relevant saving, for what concerns preparation and runtimes, because of the small number of components and of their moderate complexity (plane elements and rigid ellipsoids); those elements have been used to model the geometry of the seat, while the passenger has been simulated through a entirely multibody dummy.

In order to build a MB sled as near as possible to the FEM model, the contact stiffness, which have to be attributed to those parts of the back with which the passenger comes in contact in the impact, and the structural stiffness, which has to be attributed to the whole seat, have been gathered.

Those contact stiffness and the flexural one, which have to be assigned to different parts of the MB seat, have been deduced from both a FEM dynamical analysis carried out in Ls-Dyna® environment and some static simulation performed in Nastran® environment. In the following a comparison between the results obtained in those two different simulation environments has been reported.

#### Contact Stiffness Obtained from FEM Analyses

The contact stiffness to be attributed to the headrest and to the back panel of the seat have been evaluated by means of a dynamical analysis carried out through Ls-Dyna® code according to the following procedure:

1. identification of the impact zones;
2. identification of those nodes which are subjected to the largest displacements;
3. gathering of the largest displacements from Ls-Dyna® results;
4. gathering of the contact loads head/headrest (Fig. 5) and leg/front panel (Fig. 6) from Ls-Dyna® results;
5. making of the load/penetration curve (contact stiffness).

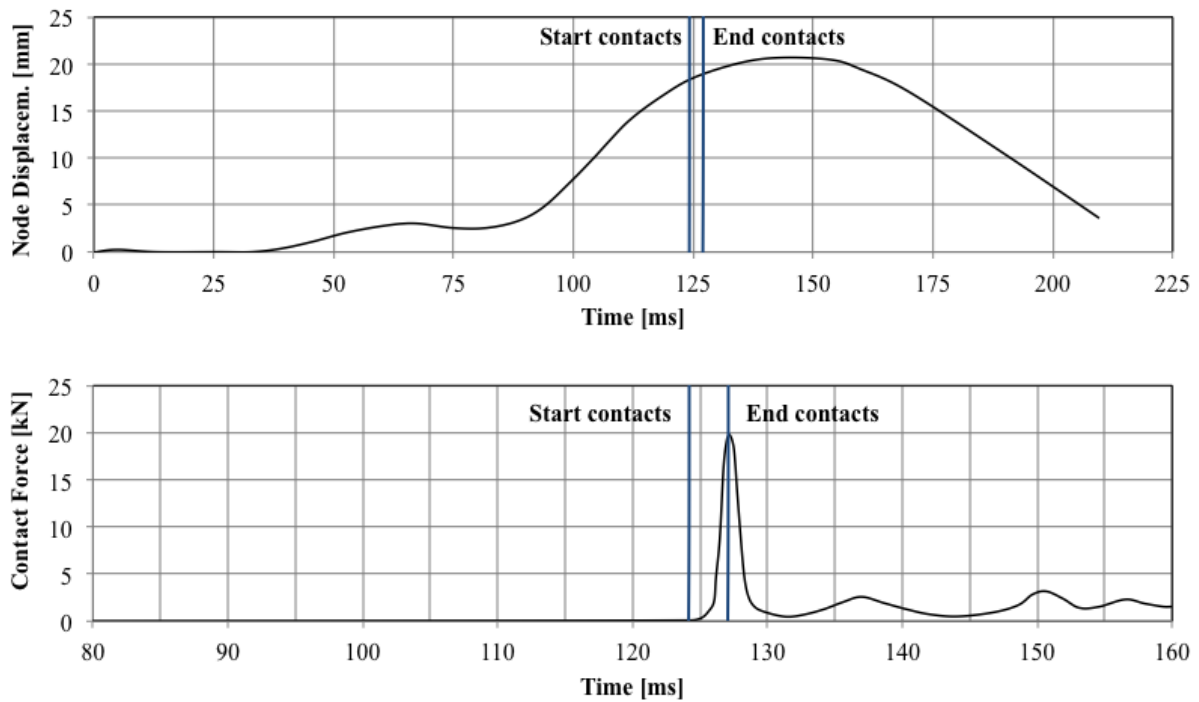


Figure 5. Largest deformation and contact load plots - Head.

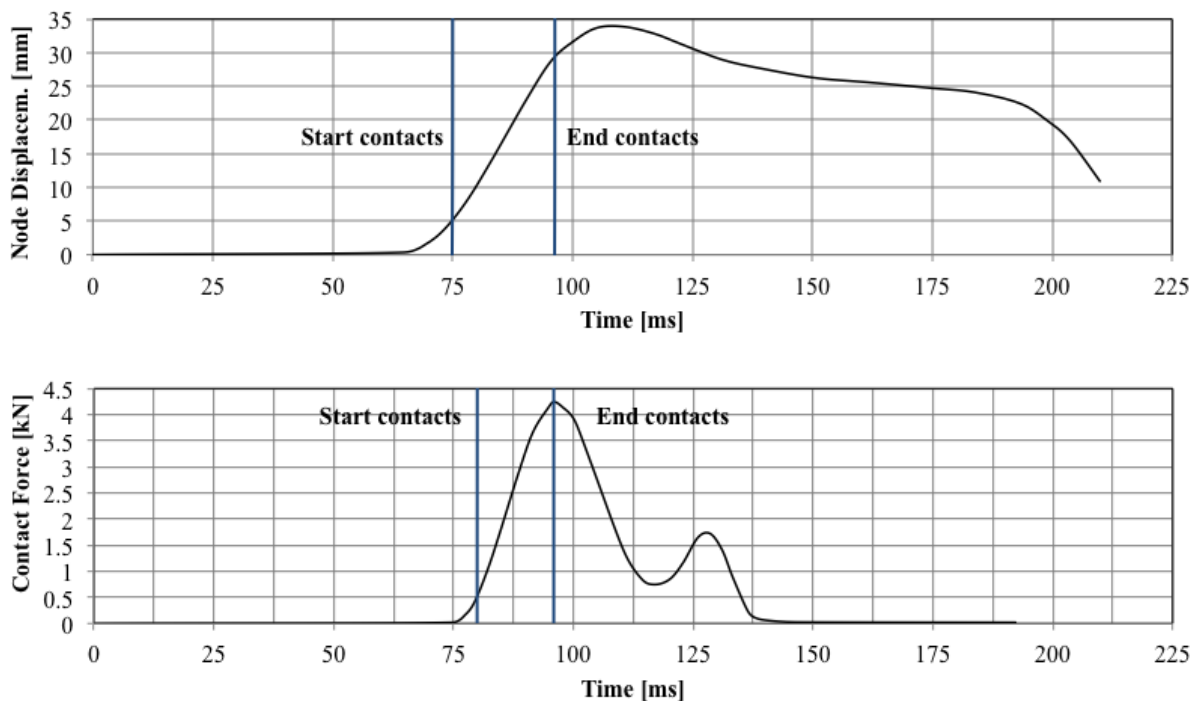


Figure 6. Largest deformation and contact load plots - Leg.

Strictly speaking, each leg which impacts on the back of the front-seat is characterized by an own stiffness, but, in presence of a mono dimensional pulse, the contact load is quite similar



for both legs; because of that reasoning our simulations have been developed using only one contact stiffness.

To investigate about different procedures to be used to evaluate the contact stiffness and to check the results obtained through the method above, the same stiffness have been evaluated by means of a static analysis carried out in Nastran® environment, according to the following procedure:

1. identification of the impact zones;
2. application of an assigned displacement to a node cloud near the impact zones;
3. evaluation of the resultant of the reaction forces in the points subjected to the displacement (Fig. 7);
4. making of the load/penetration curve (contact stiffness).

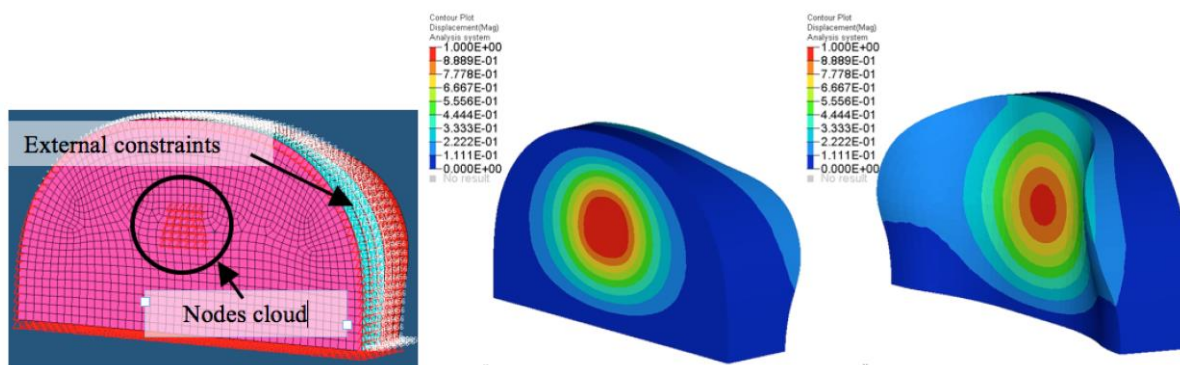


Figure 7. Constraints and displacements – contact stiffness of the headrest.

The whole frame of the headrest around the structure has been constrained, while a 1 mm displacement has been imposed to the nodes near the impact zone.

The contact stiffness of the back of the seat has been evaluated in an analogous way. The base of the seat, the back support bracket and the high part of the seat have been constrained to prevent any unwanted rotation and the displacement has been applied in proximity of the impact zone of the knee (Fig. 8).



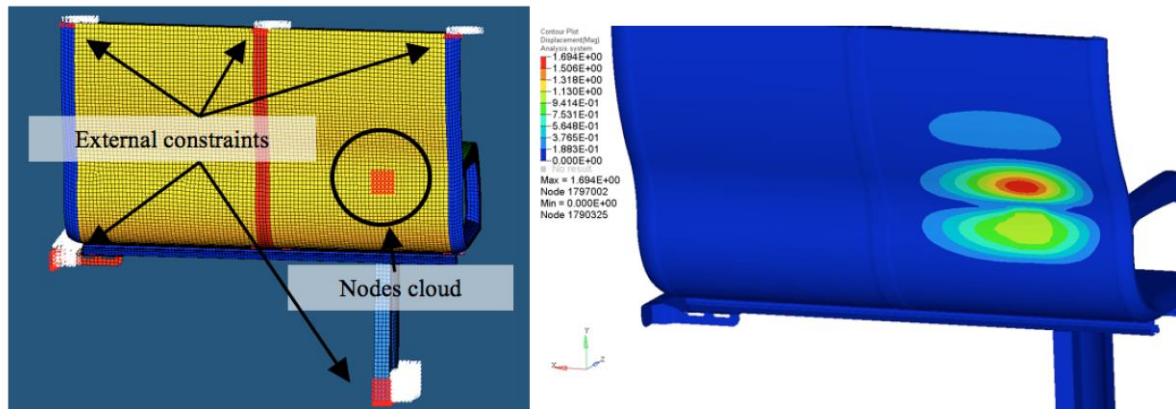


Figure 8. Constraints and displacements – contact stiffness of the back of the seat.

The stiffness values, gathered from the static analyses through the procedure above and evaluated in linear elastic conditions, resulted to be comparable to those obtained from the dynamical analysis.

### Structural stiffness

Following the impact of the legs of the dummy against the seatback, the front seat is subjected to a forward rotation, which can be thought to take place around an axis which passes through the mean point of the segment which connects the joints of the seat structure to the two support beams and therefore with the support base.

In order to introduce the same physical behaviour in the MB analysis it has been necessary to link the back of the front seat to its cushion by means of an elastic joint (called Joint Revolution in Madymo® library); that kind of joint allows a stiffness to be attributed to the rotational degree of freedom of the seatback.

To obtain that stiffness, thanks to the previous evaluations, another static analysis in Nastran® environment has been carried out, from which we extracted the rotation of the seatback because of the presence of a uniform load distributed on the headrest.

To that purpose, two different constraint conditions have been adopted: the first one is quite similar to that used to evaluate the contact stiffness, while in the second one the side of the seat attached to the wall of the coach frame has been replaced with a second frame support placed at the distance of the first one from the end of the seat; that arrangement has been adopted because it is rather similar to the constraint conditions used in the simplified MB model.

The rotation values obtained for the two arrangements are quite similar and therefore in the following they have been used that obtained for the constraint set up with two frame supports, which gives the flexural stiffness characteristic recorded in Tab. 2.

Table 2. Flexural stiffness of the seatback.

$\alpha$ [rad]	M [Nm]
0	0
0.046	681.66

#### 4. THE FINITE ELEMENT ANALYSIS

The two arrangements compared in FE environment are as follows (Fig. 9):

- model with one frame support constrained to the floor and the side plate connected to the wall;
- model with two frame supports constrained to the floor.

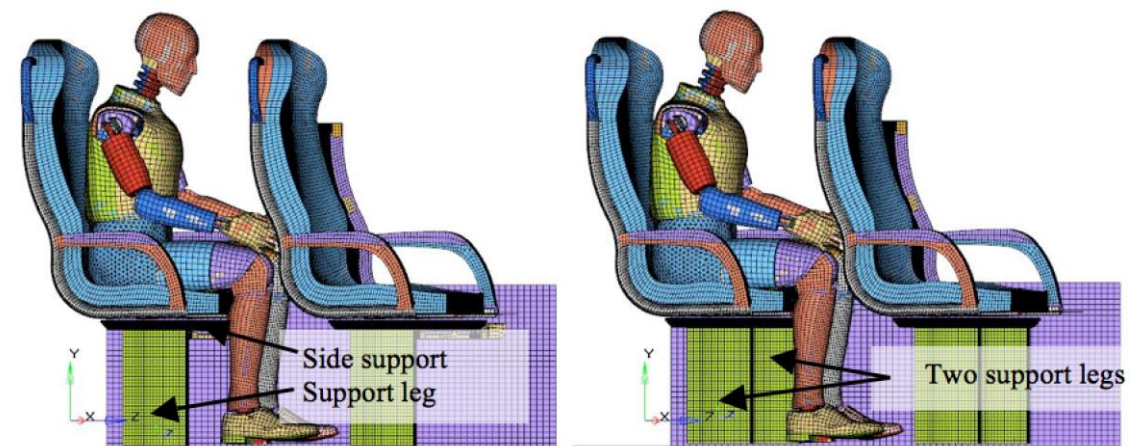


Figure 9. The FEM analyzed arrangements.

For what concerns von Mises' stresses obtained in the structure analysis, the highest values recorded for the two cases above are quite similar: 255 MPa for the first arrangement and 266 MPa for the second one (Fig. 10).

In what follows the behaviour of the main biomechanical parameters are compared, as recorded for the two analyzed arrangements of the seat structure (Fig. 11 and Fig. 12).

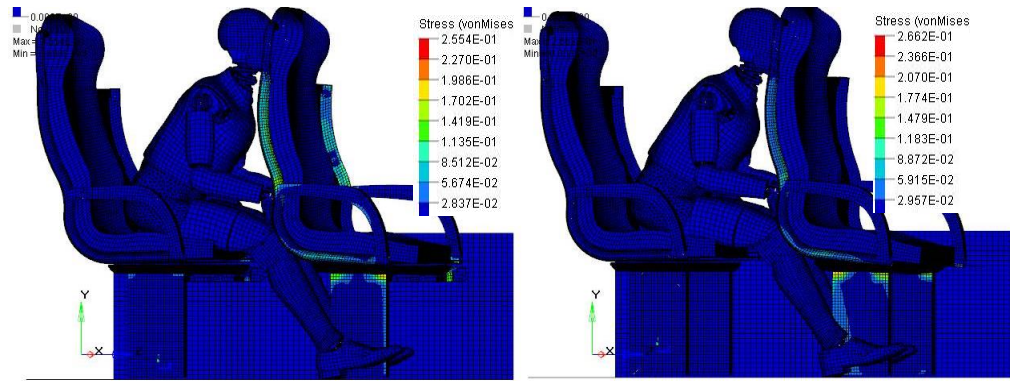


Figure 10. Comparison between Von Mises's stresses recorded in the seat structure.

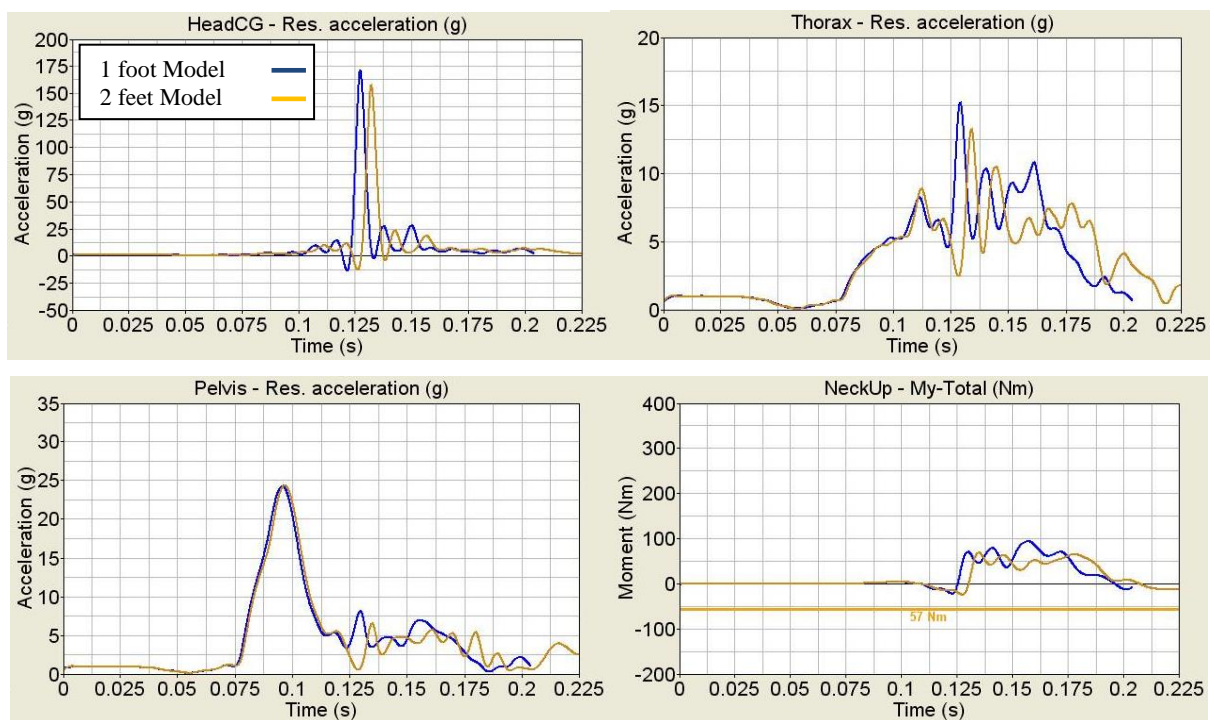


Figure 11. Comparison between accelerations (head, chest, hips, pelvis).

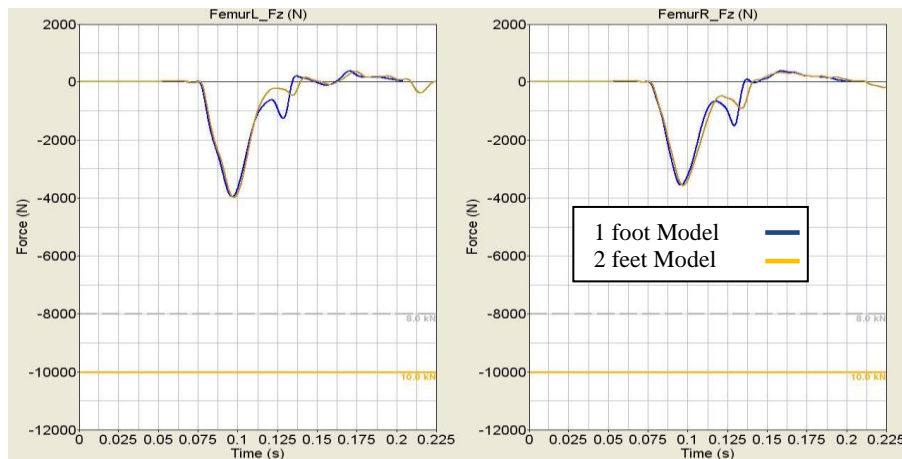


Figure 12. Comparison between forces on femurs.

It is possible to carry out from the showed results that the behaviour of the two analyzed arrangements are quite similar; the most remarkable difference refers to the time of the impact of the head against the back of the front seat, which is 4 ms delayed in the two-frame supports configuration. Therefore, it is possible to conclude that both arrangements can be used indifferently.

## 5. FEM/MB comparison

The comparison between the sled-test MB model and the FE one has been developed with reference to the arrangement with a two-frame supports seat, as that is also more expedite and easy in the case of an experimental test.

The adopted MB model takes into account the rotation of the seat, which occurs following the impact against the dummy. The contact stiffness used in the MB analysis are as follows (Fig. 13).

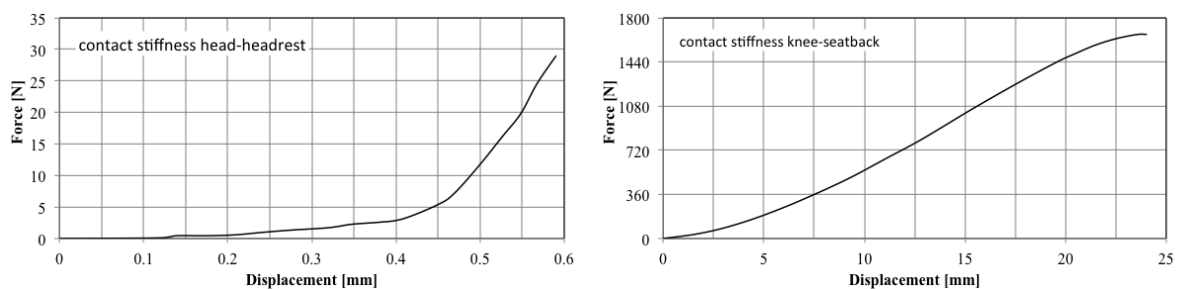


Figure 13. Calibrated contact stiffness head-headrest and knee-seatback.

The results obtained from the comparison between the two arrangements are shown in Fig. 14 and Fig. 15; such results can be considered satisfactory.

The acceleration values, calculated on the pelvis and head, are in good agreement; the peak acceleration of the head, in the numerical model, is achieved slightly earlier than the MB model, such effect occurs because of the greater bending stiffness observed in the neck area.

During the impact phenomenon, the chest does not enter directly into contact with the seat and therefore the values of the accelerations are more affected by the overall stiffness of the numerical model. For this reason, the accelerations measured on the thorax, although they show an overall good agreement, reveal different maximum values.



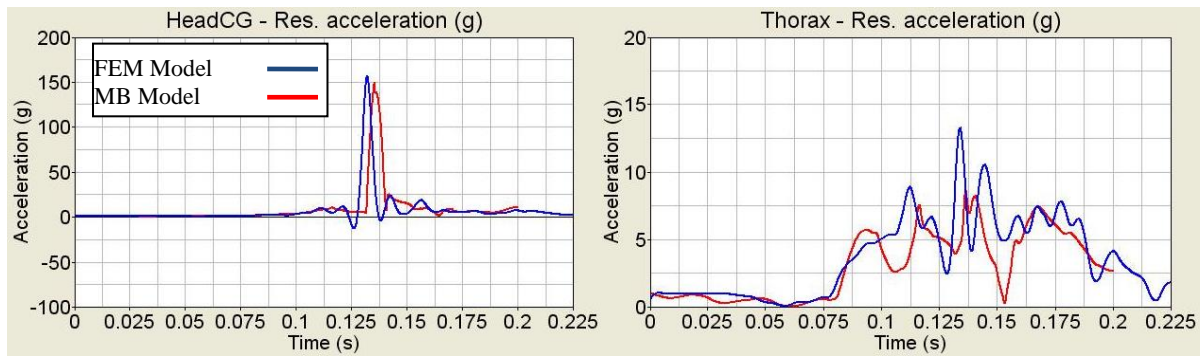


Figure 14. Comparison between some biomechanical parameters (head, chest).

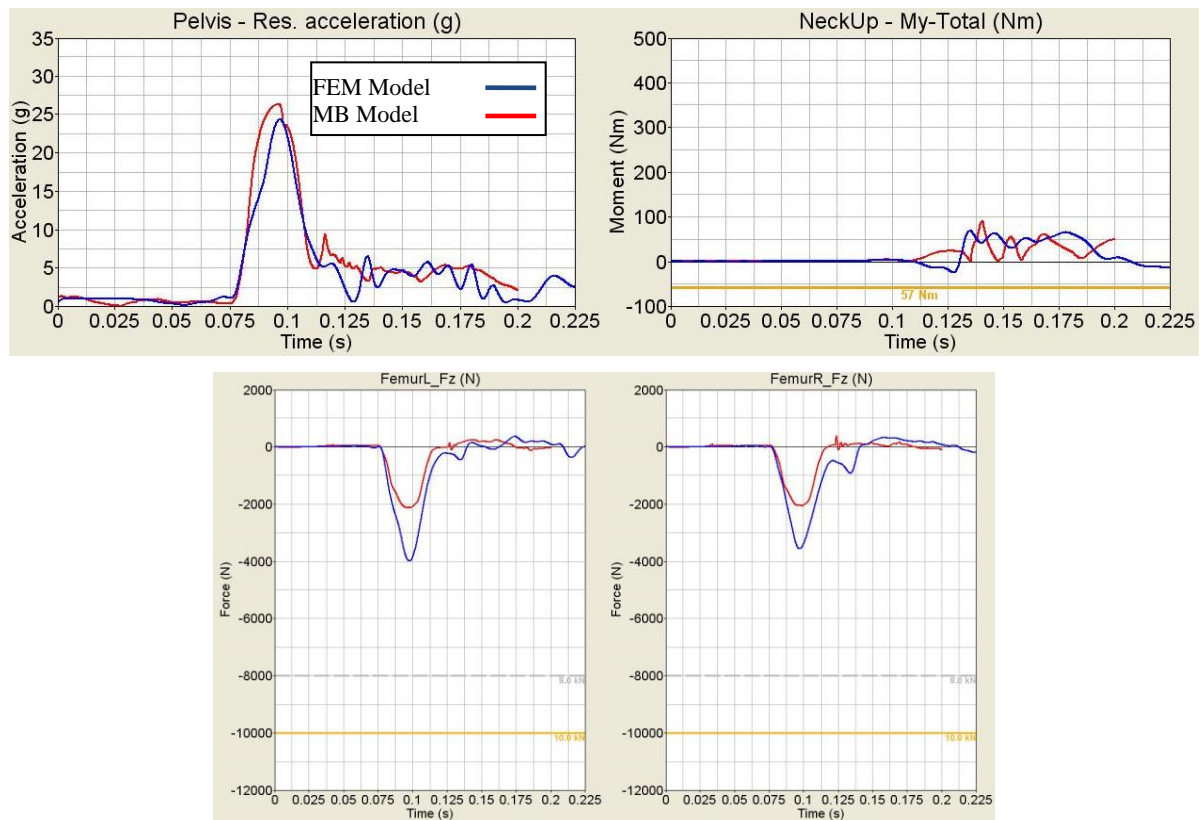


Figure 15. Comparison between some biomechanical parameters (pelvis, neck, femurs).

Load values recorded for femurs are more similar to those obtained by FEM; on the contrary, the largest acceleration for the pelvis is rather discordant between the two solutions, even if it is comparable in any case.

## 6. CONCLUSIONS

The proposed numerical methodology and its application to a complex industrial case study showed that it is possible, on the basis of robust FEM models, correlated to experimental



results, which are usually developed in the pre-design phase, to define simplified MB models, characterized by lumped stiffness, whose results, for what concerns the kinematics of the phenomenon and even more the biomechanical damage indexes, can be considered to be comparable with those obtained through the complete FEM model. Those MB models can be assumed as a very relevant tool in the phase of structural re-design of the seats, at most if it is necessary to carry out enhancement procedures based on probabilistic methods, which require, as it is well known, a large number of simulations.

## REFERENCES

1. **ECE R 80 (2001)**, Std Specifications for Approval of Seats in Motor Coaches and of These Vehicles with Respect to the Stability of the Seats and Their Anchoring.
2. **European Standard EN 12663 (2000)**, Railway applications – structural requirements of railway vehicle bodies.
3. **Bellucci, M., Caputo, F., Lamanna, G. and Soprano, A. (2010)**, “Multibody Evaluation of Interactions between the Coaches of a Train during an Impact”, Proceedings of the Seventh International Conference on Engineering Computational Technology, Paper 63.
4. **European Standard EN 15227 (2008)**, Railway applications - Crashworthiness requirements for railway vehicle bodies.
5. **Caputo, F., Lamanna, G. and Soprano, A. (2011)**, “Finite Element Dynamic Analysis of a Railway Seat Under Longitudinal Impact Condition”, ASME 2011 International Mechanical Engineering Congress and Exposition, code: 93919, Vol. 9, pp 413-420.
6. **ECE R94 (2007)**, Uniform Provisions Concerning the Approval of Vehicles with Regard to the protection of the Occupants in the Event of a Frontal Collision.
7. **Milho, J.F., Ambrósio, J.A.C. and Pereira, M.F.O.S. (2003)**, “Validated multibody model for train crash analysis”, International Journal of Crashworthiness, Vol. 8, No. 4, pp 339-352.
8. **Caputo, F., Lamanna, G. and Soprano, A. (2012)**, "On the evaluation of the overloads coming from the use of seat-belts on a passenger railway seat", International Journal of Mechanics and Materials in Design, Vol.8, pp 335-348.
9. **Kirkpatrick, S.W., Schroeder, M., Simons, J.W. (2001)**, “Evaluation of passenger rail vehicle crashworthiness”, International Journal of Crashworthiness, Vol. 6, No. 1, pp 95-106.
10. **Caputo, F., Lamanna, G. and Soprano, A. (2012)**, “Energy Absorption Capabilities of a Square Tube System”, Key Engineering Materials, Vol. 488-489, pp 561-564.



11. **Caputo, F., Fidanza, F. and Lamanna, G. (2010)**, “Multibody Investigation on the Passive Safety Performances of Seats in Railway Vehicles”, ASME 10th Biennial Conference on Engineering Systems Design and Analysis, code: 84828, Vol. 3, pp 195-202.
12. **Caputo, F., Fidanza, F. and Lamanna, G. (2008)**, “Interior's safety in a regional train unit”, 7th International Symposium on Passive Safety, pp. 129-140.







## OPTIMIZATION STUDY ON MULTI-BODY VEHICLE-FRONT MODEL FOR PEDESTRIAN SAFETY

**Hariharan S. SUBRAMANIAN**, [hariharan.s@mech.iitd.ac.in](mailto:hariharan.s@mech.iitd.ac.in) Indian Institute of Technology Delhi, 110016, New Delhi, India

**Anoop CHAWLA**, [achawla64@gmail.com](mailto:achawla64@gmail.com) Indian Institute of Technology Delhi, 110016, New Delhi, India

**Sudipto MUKHERJEE**, [sudipto@mech.iitd.ernet.in](mailto:sudipto@mech.iitd.ernet.in) Indian Institute of Technology Delhi, 110016, New Delhi, India

**Dietmar GOEHLICH**, [dietmar.goehlich@tu-berlin.de](mailto:dietmar.goehlich@tu-berlin.de) Technische Universitaet Berlin, 10623, Berlin, Germany

### ABSTRACT

The safety of vulnerable road users, namely pedestrians, in a road-crash scenario with automobiles remains as a vehicle design challenge. A multi-body simulation between pedestrian and vehicle in MADYMO was used to simulate a crash of vehicle front [14 parameters] against 4 different TNO pedestrian models [95th %le M, 50th %le M, 5th %le F, 6 Y.O. Child]. Pedestrian safety was measured using Weighted Injury Cost (WIC). A global optimization was performed using genetic algorithm in order to minimize WIC with geometric constraints on vehicle profile. Within known limitations, at least one pedestrian friendly vehicle shape not resembling any existing vehicle profile was found.

**Keywords:** Pedestrian safety, Injury Cost, vehicle front optimization, multi-body simulations, Genetic Algorithms

### 1. BACKGROUND

#### **Pedestrian Protection:**

Traffic injuries have been shown by World Health Organization (WHO) report (World Health Organization and WHO, 2004) to be one among the top ten causes of threat to human life around the world. The injuries related to vulnerable road users (VRU), more specifically pedestrian and vehicle collisions have remained higher in developing countries. Studies by (Mohan et al., 2009) has highlighted the importance of pedestrian fatalities from vehicles in urban regions of India. Studies on German In-Depth Accident Study (GIDAS) by (Otte et al., 2012) have provided specific comparison of injury causation on all three categories of VRU with vehicle. The study also points out role of vehicle shape on injuries. (Fredriksson et al., 2010; Peng et al., 2012) provide relationships between speed of crash to injury severity. A



speed of 40 kmph for pedestrian has been suggested and the same was indicated to be moderate level of threat from crash database analysis.

### **Injury threat measurement:**

Pedestrian injuries have been recorded in crash databases using Abbreviated Injury Score (AIS) developed by Association for the Advancement of Automotive Medicine (AAAM) with latest version 2005, revised in 2008 (Gennarelli et al., 2008). AIS consist of a scale of 1 to 6, with 6 representing an untreatable injury with existing medical facilities. AIS values are processed as maximum AIS (MAIS) or Injury Severity Score (ISS) to address multiple injuries to a subject.

A cost implication based measure for injury severity to a human was proposed by (Newman et al., 1994; Zeidler et al., 1993) . This methodology correlated severity of injury to a human by analysing various treatment cost factors involved like hospital and other related costs. (Adam and Untaroiu, 2011) used Whole Body Injury Metric (WBIM) as a measure to injury sustained for whole body of an occupant. A similar scale of “injury cost”(IC) as a measure of threat for whole pedestrian body injury was developed by the authors (Sankarasubramanian et al., 2013) based on cost estimates in (ISO, 2002) incorporating weighting factors taking to account for variation of population of pedestrians. Weighted IC was able to provide single unitary measure for threat severity to a pedestrian.

### **Multi-body Simulations of Vehicle with VRU Crash:**

Multi-body simulations to predict crash kinematics has been widely used in crash reconstruction studies. The TNO pedestrian models (TNO et al., 2012) have inputs of behaviour based on experimental results on PMHS and body segment experiments. Studies by (Elliott, Lyons, et al., 2012; Elliott, Simms, et al. 2012) indicated that head striking point along with injury severity could be predicted by the 50th percentile TNO pedestrian model.

Interactions between two multi-body models were modelled using a force-deformation characteristic. Force-deflection characteristics corridor for European fleet (Martinez et al. 2007; Martínez et al., 2008) based on pedestrian body-form tests conducted by Euro- NCAP, (EURO-NCAP, 2012) pedestrian safety rating tests has been used.

## **2. OPTIMIZATION PROBLEM DEFINITION:**

### **Crash simulation:**

A crash scenario involving simplified vehicle front profile and pedestrian model was modelled similar to simplified sketch shown in Figure 1. A VRU crash with vehicle front was set-up with crash initial velocity of 40 kmph. Scenarios with hard braking of vehicle [ 4.7 m/s<sup>2</sup> deceleration taken from autonomous braking trials by (Matsui et al., 2011) ] was considered for this study.

Pedestrian models are chosen from available TNO (TNO et al. 2012) pedestrian ellipsoid models. The kinematic predictive abilities of these models have been used for reconstructing pedestrian crashes (Rooij et al., 2003) and have also been validated for head impact velocity and location prediction based on PMHS tests data (Elliott, Lyons, et al., 2012). The gait position of pedestrian population (3 year old child [3C], 6 year old child [6C], 5th percentile female [5F], 50th percentile male [50M] and 95th percentile male [95M]) considered has been set to 0.25 radians at the hip joints (0.5 radians between the two legs) so as to simulate an approximate walking stance. The focus on this work was to use an approximate walking stance with struck leg forward although more detailed studies (Untaroiu et al., 2009) have been published on considering variations in gait.

### Problem formulation:

Threat to pedestrian has been measured using population Weighted

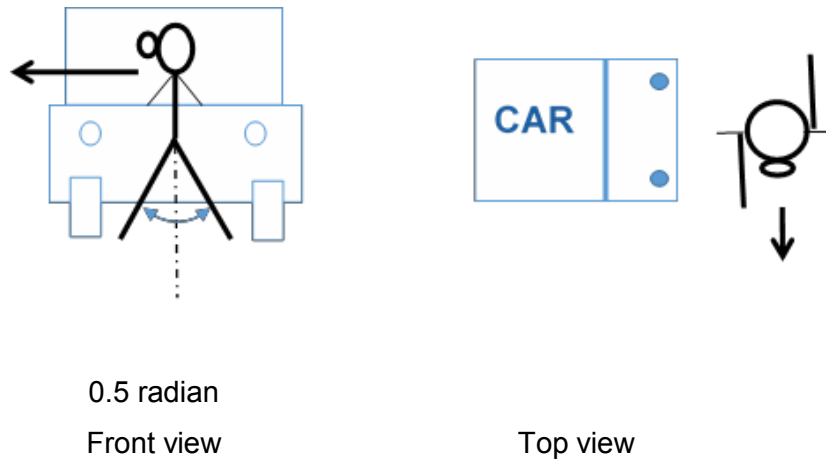


Figure 1. Simplified vehicle-pedestrian crash scenario

Injury Cost [WIC]. A higher cost would mean higher threat to pedestrian; hence problem was formulated as a minimization of WIC measure. WIC was calculated as threat measure to whole body; hence WIC was formulated as given below in (1) covering at least one injury measure from major regions of body being injured. An overview of the injury measures and their specific applications can be found in (Schmitt et al., 2007).

$$WIC = f(HIC, N_{ij}, (a_{sternum})_{3ms}, FFC, TI)_{pop} \quad (1)$$

Where,

WIC – Weighted injury cost (USD) for a pedestrian population

HIC – Head Injury Criterion



$(a_{sternum})_{3ms}$

– Linear peak acceleration at sternum for a window of 3 mS (m/S<sup>2</sup>)

FFC – Femur Force Criterion (N)

TI – Tibia Index

### Vehicle model:

Vehicle-front model was built as shown in Figure 2 with Bumper Lower (BL), Bumper Actual (BA), Bonnet Leading edge (BE1 and BE2), Bonnet ellipsoids (B1 and B2), Cowl region (C) and Windscreen (W). The model has specifications comparable to a typical Sedan vehicle in mass (1000kgs) and location of center of gravity. Tires to road interactions were modelled using dynamic tire models in MADYMO.

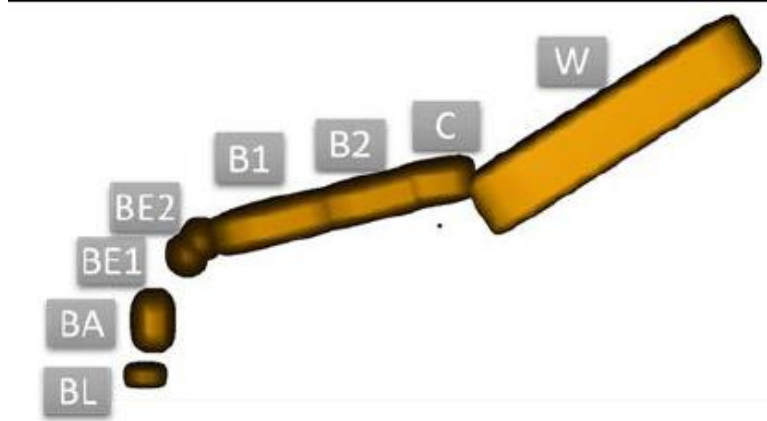


Figure 2 Vehicle Front model in MADYMO

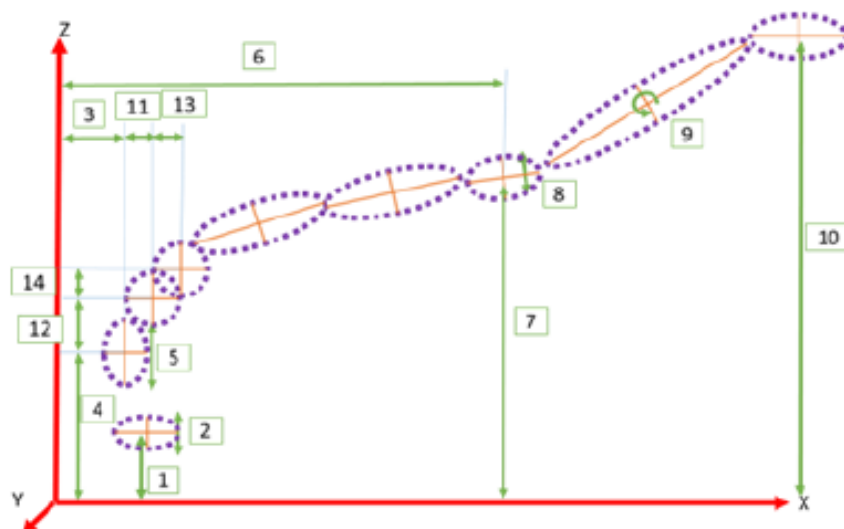


Figure 3 Parameterized vehicle front profile

To generate varied front-end shapes, positions and sizes of ellipsoids were modelled as 14 independent variables as shown in Table 1 and Figure 3. BL positions are assumed as the starting point with origins located at point indicated in Figure 3. For the different designs, positions of bumpers (BL and BA) are varied while the angle in bonnet leading edge and the location was varied for ellipsoids BE1 and BE2. Bonnet surface was approximated using two ellipsoids. Cowl region represents high stiffness region behind the bonnet and in front of the windscreen. Windscreen region was simplified to have similar characteristics across the whole area unlike the previous studies (Rooij et al., 2003).

Table 1 Parameters for vehicle front model

Parameter	Description
1	BL Ellipsoid CG location in Z direction
2	BL Ellipsoid width along Z direction
3	BA Ellipsoid CG location in X direction
4	BA Ellipsoid CG location in Z direction
5	BA Ellipsoid width along Z direction
6	C Ellipsoid CG location in X direction
7	C Ellipsoid CG location in Z direction
8	C Ellipsoid angle about Y axis
9	W Ellipsoid angle about Y axis
10	Location of point along Z direction on W ellipsoid along centre plane
11	BA Ellipsoid to BE1 Ellipsoid CG location distance in X direction
12	BA Ellipsoid to BE1 Ellipsoid CG location distance in Z direction
13	BE1 Ellipsoid to BE2 Ellipsoid CG location distance in X direction
14	BE1 Ellipsoid to BE2 Ellipsoid CG location distance in Z direction

### 3. OPTIMIZATION METHODOLOGY

WIC measure was calculated based on the outputs from multi-body simulations using MADYMO solver. Batch solver scripts were used in conjunction with OptiSlang<sup>TM</sup> to read the Ascii input files of Madymo and write back input files for it.

A Real Coded Genetic Algorithm [GA] optimization methodology was chosen. The problem was formulated with 14 input parameters from xml files and two outputs, namely WIC and EIC written by MATLAB in text file was read as output. The following constraint (2) was placed on the shape of the vehicle profile generated to maintain a regular looking bonnet shape as shown in Figure 6.

$$\text{Parameter\_6} - (\text{Parameter\_12} + \text{Parameter\_14} + \text{Parameter\_4}) \geq 0.01 \text{ [m]} \quad (2)$$

A constraint handling method based on cliff handling ratio of 10% was used which uses penalty based approach taking into consideration the previous values of the variables. Population size for every generation was chosen as 100. Ranking was selected as Linear and selection method of the best was through Roulette wheel method. The crossover operator selected was Simulated Binary with a probability of 50% and  $nc = 2$  to ensure a uniform distribution in variable values across the range. To prevent the algorithm from getting stuck in a local minimum, mutation was also modelled as constraint adaptive with 20% of the value (after previous trials) and a standard deviation of 0.1. GA process was repeated for 17 generations.

The theory behind the fine-tuning parameters like constraint handling, selection methods, crossovers and mutation along with overall implementation steps are described in (Dynardo GmbH, 2011). Figure 4 obtained from (Dynardo GmbH, 2011) shows the steps involved in GA bases optimization technique implementation procedure.

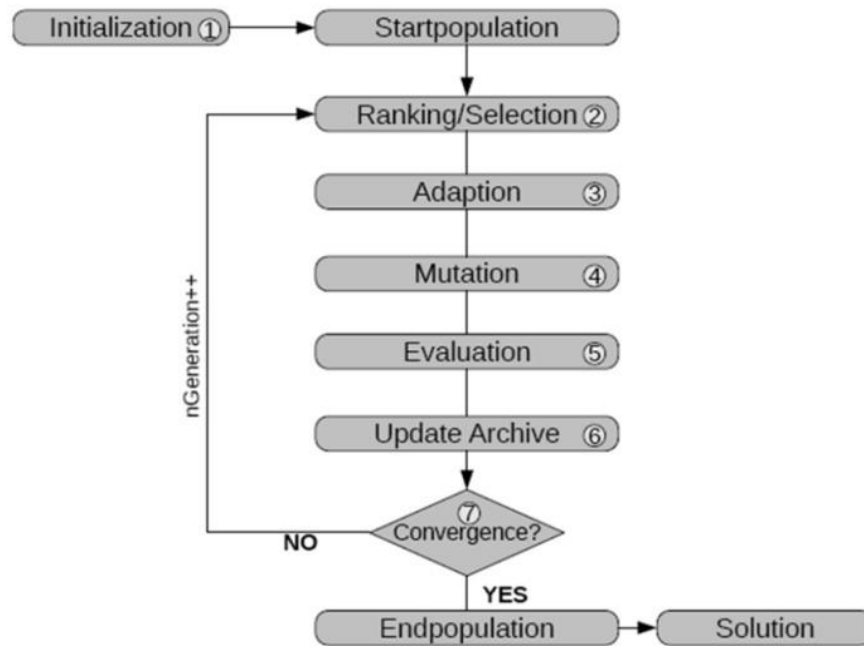


Figure 4. Methodology of optimization using Genetic Algorithms implemented in OptiSlangTM (Dynardo GmbH, 2011)

#### 4. RESULTS:

##### GA optimization process:

Genetic Algorithm process was monitored for samples generated in every generation for number of samples violating the constraint placed. A sample which violated the “constraint” was eliminated from the calculation of WIC/EIC values, hence monitoring was necessary to understand the working of GA process. The variation has been shown in Figure 5, which indicates that number of “in-feasible” samples (which violate the Constraints) reduced rapidly after 2 generations.

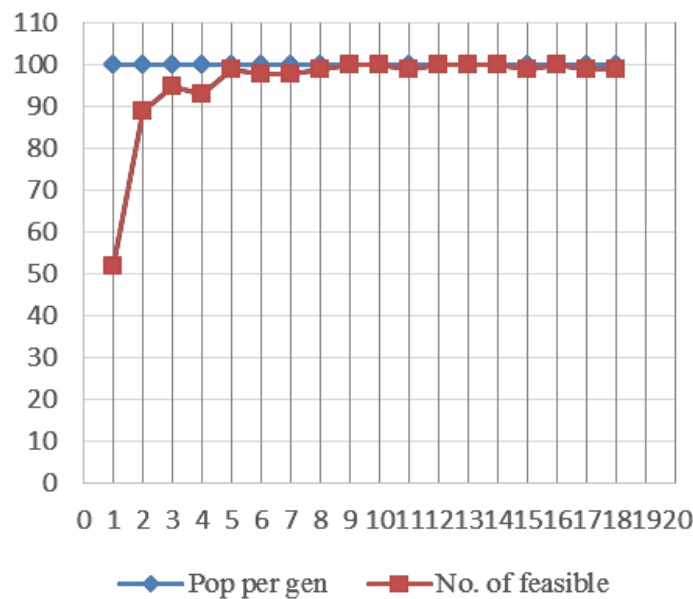


Figure 5. Variation in number of feasible designs across generations

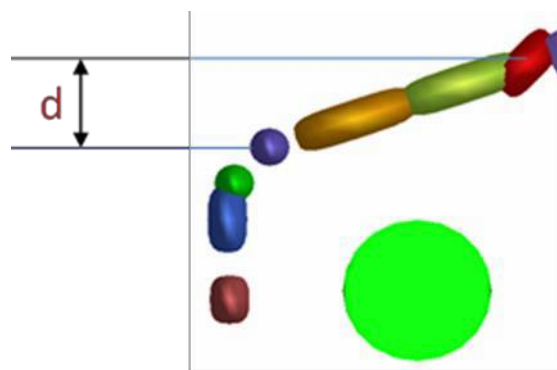


Figure 6. Constraint applied "d" to check for feasible design

##### Variation of parameters during GA process:

GA based optimization process was chosen to perform a global optimization over the entire design space. Variation of the parameter values across the generations shown in Figure A in Appendix. Initial population showed uniform distribution within the planned maximum and

minimum values, the convergence of parameters started beyond 5th generation. The parameters' range varied intermittently after 10th generation. The table also shows the variation of median of the values apart from maxima and minima for every generation. Every blue dot represents a single design parameter and the variation of dots indicates an almost uniform spread across the median value and less number of values at extremes. The spread of at least 10% of values near the extremes can be associated with the action of mutation operators in the GA process.

For every generation of designs generated during the GA optimization process, the minimum value showed an almost constant value till 10th generation and in 11th generation, least value was observed. The process was continued further to explore the design space further. In 17th generation two more minima were observed with value equal to the 11th generation value. Figure B in Appendix shows variation of minimum, median value in every generation to understand the convergence process towards the required minima.

#### **WIC measure for existing vehicle profiles:**

Front end designs generated by GA process were compared with simplified vehicle profiles for a sample of existing vehicle profiles in market. Figure 7 shows the WIC variation for a sample of 16 vehicle profiles from compact segment to SUV in Indian vehicle market along with 2 profiles, one each of SUV and sedan were simplified from shape observed in (Kerrigan et al., 2008). A sample size of 18 was assumed to be representative of existing vehicles. The maximum observed WIC was for "ALTO" simplified profile [0.48 Million USD] and simplified vehicle profile observed in (Kerrigan et al., 2008) [0.42 Million USD. The minimal WIC observed was for a simplified profile of "ACCORD" of 0.10 Million USD. "41", "1685", "17703" and "1772" represent four profiles extracted from GA optimization process. "41" and "1685" profiles have higher value of WIC of 0.55 and 0.39 Million USD as WIC. "1703" [shape "O1"] and "1772" [shape "O2"] profiles were observed minima with WIC value 0.08 Million, which was lesser than least observed WIC by around 20%.



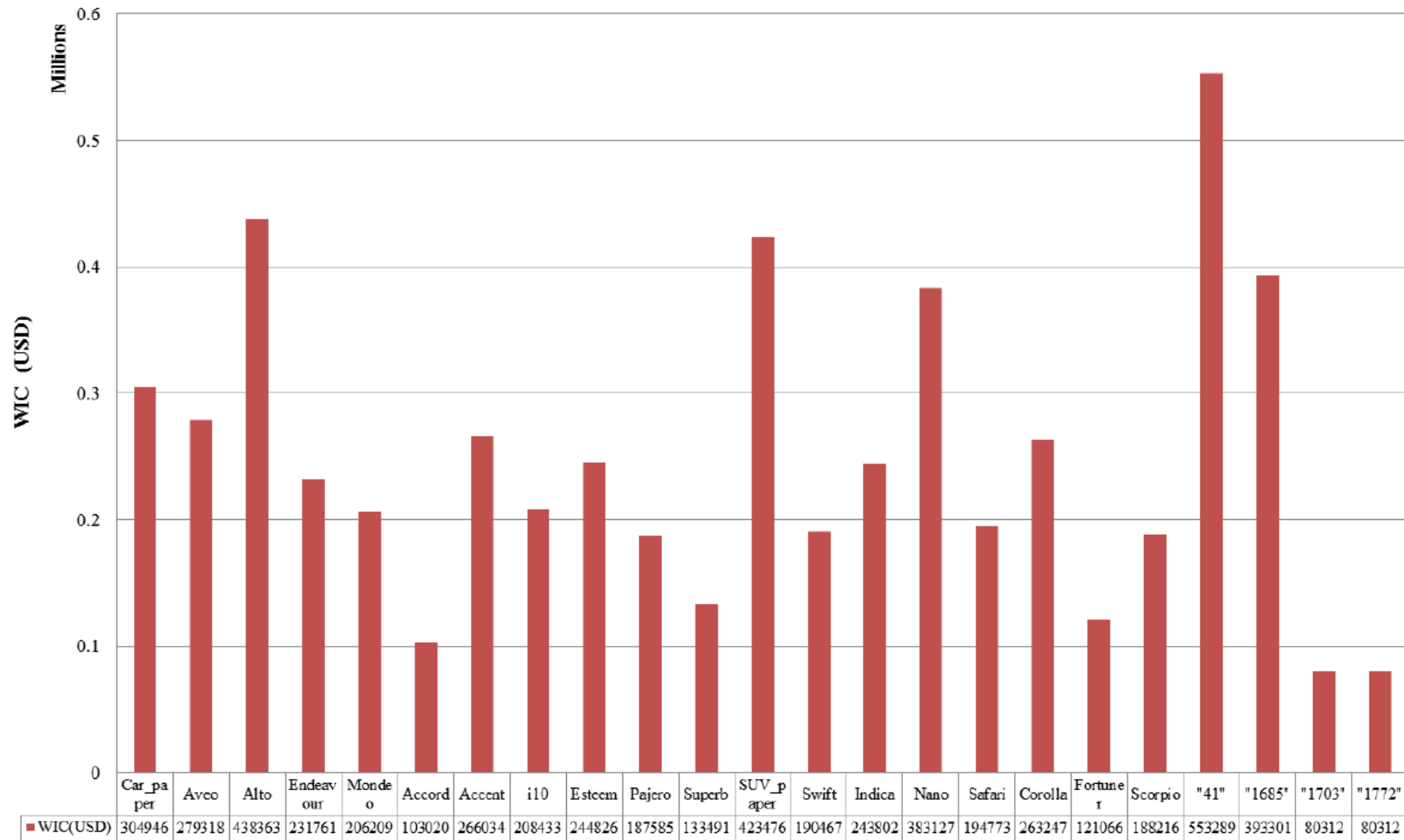


Figure 7. IC measures of simplified car profiles compared with "best" and "worst" profiles during GA optimization process

### Vehicle profile with minimal WIC:

Values in Table 1, Table 2 and Table 3 highlight the variation in injury measures to pedestrian models from the shapes O1 and O2. O1 and O2 profiles indicate that height of windscreen was not a significant factor the impact conditions for optimization study. Minimal differences were observed in the injury measures in lower extremities and VC measure for chest for both profiles. More differences were observed in HIC and sternum acceleration values. The differences were highlighted using IC measures calculated from AIS implication of these injury measures. Specific difference in IC values was observed in condition of 95M pedestrian model for sternum acceleration, but this difference was not reflected in WIC measure. WIC represents a weighted sum of IC values for 3 pedestrian models namely 6C, 5F and 50M.

Two shapes O1 and O2 had minimal WIC values at the 17th generation. The two profiles shown in Figure 8 are visually similar. A major difference in both profiles remained with the height of windscreen and location of cowl region. The bonnet leading edge height was to impact with a 5th percentile female and 50th percentile male above the hip region and also below the head height of a 6 year old pedestrian model. The bonnet length was similar to a compact to sedan type of vehicle front but the height of cowl region was in the category of a SUV or cross over SUV. A comparison of the shape with two simplified car profiles each in compact, sedan and SUV segments are shown in Figure 9. Variation of WIC values showed simplified compact segment vehicle profiles to have higher WIC values than sedans and SUV category. O2 shape indicates a cross-over SUV shape with bonnet leading edge height lower than the SUV category.

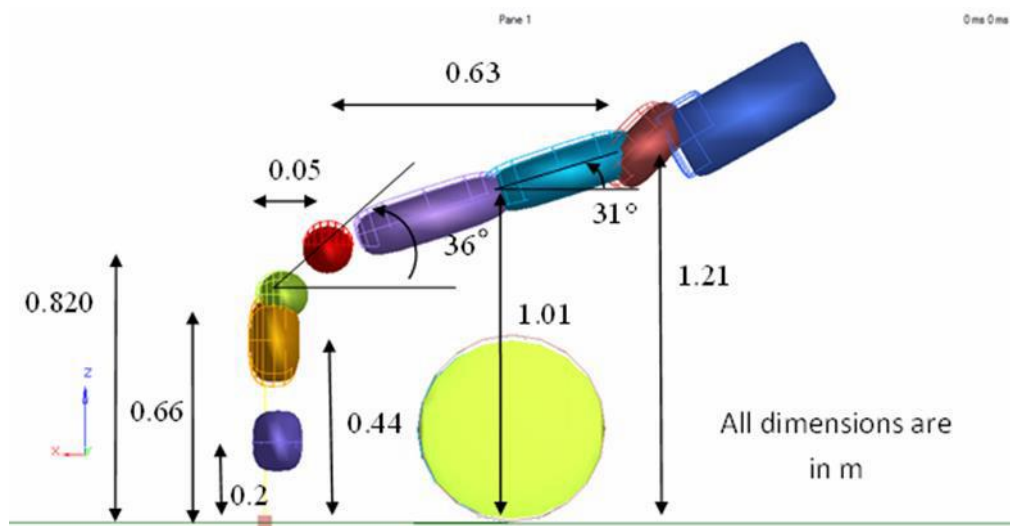


Figure 8. Two front end shapes [O1 and O2] shapes represented as multibody ellipsoid model



Table 2 Variation of IC measures for shape "O1"

<b>Pedestrian Model</b>	<b>HIC</b>	<b>H_cost</b>	<b>Nij</b>	<b>N_cost</b>	<b>VC</b>	<b>ST_3ms</b>	<b>T_cost</b>	<b>FFC</b>	<b>TI_L</b>	<b>L_cost</b>	<b>IC</b>
		<b>(USD)</b>		<b>(USD)</b>	<b>(s<sup>-1</sup>)</b>	<b>(m/s<sup>2</sup>)</b>	<b>(USD)</b>	<b>(N)</b>		<b>(USD)</b>	<b>(USD)</b>
3C	555	14625	0.182	0	0.007	2490.6	66430	1685	0.209	41656	122711
6C	515	3448	0.347	0	0.002	1173.7	66430	3488	0.401	41656	111534
5F	425	3448	0.482	0	0.005	469	66430	10974	0.817	41656	111534
50M	268	3448	0.316	0	0.004	256.5	0	13172	0.852	41656	45104
95M	1047	61988	1.39	96766	0.004	258.2	0	13042	1.279	51236	209990
										<b>WIC</b>	80312

Table 3. Variation of IC measures for shape "O2"

<b>Pedestrian Model</b>	<b>HIC</b>	<b>H_cost</b>	<b>Nii</b>	<b>N_cost</b>	<b>VC</b>	<b>ST_3ms</b>	<b>T_cost</b>	<b>FFC</b>	<b>TI_L</b>	<b>L_cost</b>	<b>IC</b>
		<b>(USD)</b>		<b>(USD)</b>	<b>(s<sup>-1</sup>)</b>	<b>(m/s<sup>2</sup>)</b>	<b>(USD)</b>	<b>(N)</b>		<b>(USD)</b>	<b>(USD)</b>
3C	529	14625	0.184	0	0.006	2535.9	66430	1474	0.207	41656	122711
6C	458	3448	0.551	0	0.004	1057.5	66430	3219	0.388	41656	111534
5F	391	3448	0.576	0	0.007	453.6	66430	11286	0.793	41656	111534
50M	262	3448	0.475	0	0.004	267.4	0	13238	0.775	41656	45104
95M	1053	61988	1.78	96766	0.005	291.9	66430	13280	1.366	51236	276420
										<b>WIC</b>	80312



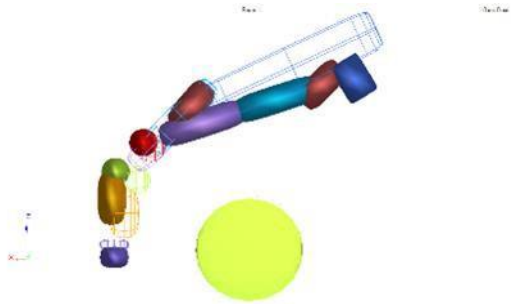
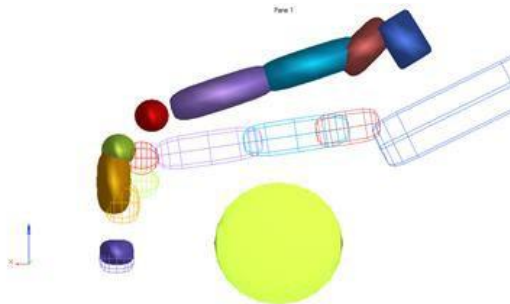
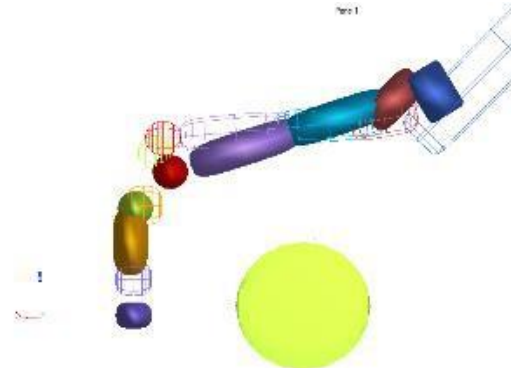
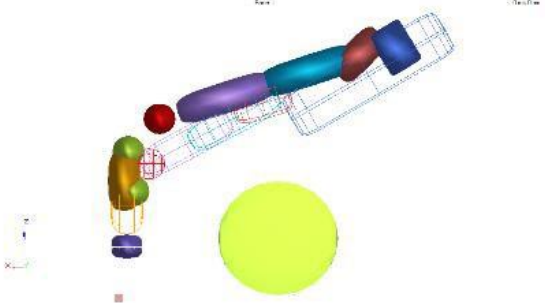
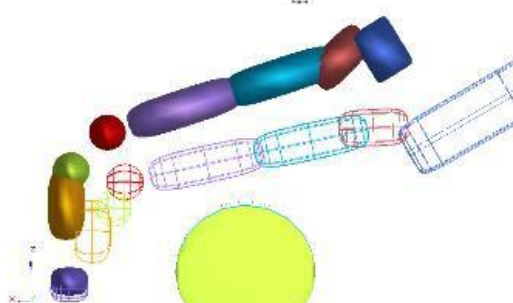
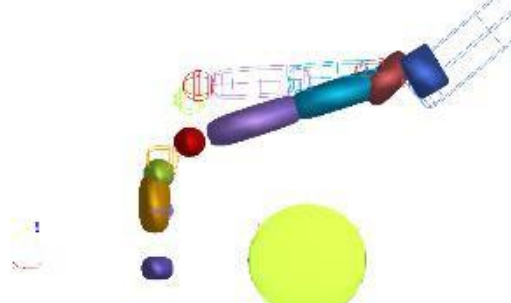
Compact / sub- compact	Sedan	SUV/ cross over
 <p>[Simplified Nano] WIC = 0.38 Million USD</p>	 <p>[Simplified Accord] WIC = 0.10 Million USD</p>	 <p>[Simplified Pajero] WIC = 0.187 Million USD</p>
 <p>[Simplified Alto] WIC = 0.43 Million USD</p>		 <p>[Simplified Pajero] WIC = 0.187 Million USD</p>

Figure 9. Comparison of optimal shape [O2] with some available simplified vehicle shapes – solid shape is O2 and wireframe shape denotes other vehicle compared

## 5. DISCUSSION

### Threat to pedestrian population:

WIC based optimization had resulted in front end shapes which had WIC measures 20% lesser than the least observed from simplified vehicle profiles. This reduction shows the existence of a shape with lower threat level implication to a pedestrian population.

### Injury measure in chest:

IC values in Table 2 and Table 3 are almost similar values for both O1 and O2, a notable difference was observed in 95M model. Kinematics of pedestrian vehicle crash for both O1 and O2 indicate similar characteristics at the point of initial crash and overall rotation of pedestrian. Figure C in Appendix shows crash kinematics observed at the significant points of impact indicated by peaks on Sternum acceleration (3mS window) on ordinate axis and time on abscissa. Two profiles are shown with O1 represented in solid and O2 in wireframe model. A shift in two pedestrian models was initiated in the time frame from 136 to 150mS after initial impact. During time frame 150 to 180mS, the offset in rotation was more clearly observed. The change in chest acceleration peak thus could directly be attributed to the impact conditions.

### Feasibility of the shape:

O1 and O2 shapes have been obtained from design space of compact cars to SUV shape. Since the profiles did not discuss on changes in longitudinal structural members of the vehicle, the high energy crash behaviour / safety would not be altered. Low energy crash testing for insurance tests involve crashes up to 15 kmph involve role of crash-boxes. Although they do not play essential role in safety of vehicle occupant directly, such characteristics are also not altered in this study.

The most direct question to address was under-bonnet packaging. Calculations were done to check if an internal combustion engine can be fitted inside the bonnet space enclosed. Engine dimensions have been taken from (Martin, 2005). Under-bonnet area calculations from vehicle FE models from (Opiela et al., 2011) have indicated approximately 90 mm clearance is required between bonnet outer surface and engine top surface. An approximate distance of 100mm would be required for slowing down a head form within 80g acceleration theoretically. The profile O1 had an under-bonnet space over 1 m, which was sufficient to fit a compact or sedan segment engine.

### Limitations:

The study has been conducted with an extended two dimensional profile of vehicle by projecting dimensions of central plane of the vehicle. The curvature of profile across the lateral



dimension of vehicle has not been included in this study which can significantly influence the rating of a vehicle during pedestrian safety tests.

The WIC measure has been approximated based on population census data and crash data available for Michigan in USA.

## 6. CONCLUSIONS

A GA based methodology using “real-coded” implementation provided better representation of the multi-disciplinary problem of vehicle design for pedestrian safety. Mutation operators with at least 10% standard deviation values were needed to prevent the algorithm from being caught in a local minimum.

The study showed that using a single measure for threat to pedestrians, a shape with lesser threat to a pedestrian population can be found.

It is concluded that for best pedestrian safety a vehicle front that can accommodate an internal combustion engine for urban applications should have:

- Bonnet leading edge located at a height of 0.82 m from ground
- The structural member for bonnet locking should be around 50 mm behind and 160 mm above the bumper leading edge.
- Bonnet is to have a length of 0.63m with bonnet rear end [bonnet hinges] at 1.21 m from ground.

The study assumes that the vehicle stiffness characteristics remain the same for the different designs. In the future, studies can be taken up to investigate effect of varying stiffness characteristics.

## 7. ACKNOWLEDGEMENT

We would wish to thank DAAD for providing a Sandwich model fellowship as financial support for the first author to work in TU, Berlin. The authors also wish to thank TRIPP, IIT Delhi for providing valuable support during the entire work.

## 8. REFERENCES

1. **Adam, T. and Untaroiu, C.D.** (2011), “Identification of occupant posture using a Bayesian classification methodology to reduce the risk of injury in a collision”, Transportation Research Part C: Emerging Technologies, Elsevier Ltd, Vol. 19 No. 6,



pp. 1078–1094.

2. **Dynardo Gmbh.** (2011), Dynardo Gmbh OPTISLANG - The optimizaing structural language v3.2.1, Dynardo Gmbh, Weimar, Luthergasse 1 D, Germany, p. 848.
3. **Elliott, J., Lyons, M., Kerrigan, J., Wood, D. and Simms, C.** (2012), "Predictive capabilities of the MADYMO multibody pedestrian model: Three-dimensional head translation and rotation, head impact time and head impact velocity", Proceedings of the Institution of Mechanical Engineers, Part K: Journal of Multi-body Dynamics, Vol. 226 No. 3, pp. 266–277.
4. **Elliott, J.R., Simms, C.K. and Wood, D.P.** (2012), "Pedestrian head translation, rotation and impact velocity: The influence of vehicle speed, pedestrian speed and pedestrian gait", Accident; analysis and prevention, Elsevier Ltd, Vol. 45 No. 2, pp. 342–53.
5. **EURO-NCAP.** (2012), European new car assessment programme ( Euro NCAP ) Pedestrian, available at: <http://www.euroncap.com/files/Euro-NCAP-Pedestrian-Protocol-v6.1---0-f2bd8d69-18e5-4779-9829-86a07299ae7e.pdf>.
6. **Fredriksson, R., Rosén, E. and Kullgren, A.** (2010), "Priorities of pedestrian protection--a real-life study of severe injuries and car sources.", Accident; analysis and prevention, Elsevier Ltd, Vol. 42 No. 6, pp. 1672–81.
7. **Gennarelli, T.A., Wodzin, E. and AAAM.** (2008), Abbreviated Injury Scale (AIS) 2005 – Update 2008, Association for the Advancement of Automative Medicine.
8. **ISO.** (2002), ISO: 13232 Motorcycles – Test and analysis procedures for research evaluation of rider crash protective devices fitted to motorcycles.
9. **Kerrigan, J.R.J., Subit, D., Untaroiu, C., Crandall, J. and Rudd, R.** (2008), "Pedestrian Lower Extremity Response and Injury: A Small Sedan vs . A Large Sport Utility Vehicle",
10. **SAE-2008-01-1245.**
11. **Martin, T.** (UTAC). (2005), D9 - Car geometrical/structural database and analysis of car to car geometric compatibility, p. 40.
12. **Martínez, L., Compigne, S. and Guerra, L.J.** (2008), "Influence of vehicle shape and stiffness on the pedestrian lower extremity injuries : Review of current pedestrian lower leg test procedure", IRCOBI.
13. **Martinez, L., Guerra, L.J. and Garcia, A.** (2007), "Stiffness corridors of the european fleet for pedestrian simulations", ESV -Paper no. 07-0267.
14. **Matsui, Y., Han, Y. and Mizuno, K.** (2011), "Performance of Collision Damage Mitigation Braking Systems and their Effects on Human Injury in the Event of Car-to-Pedestrian Accidents", Stapp car crash journal 2011-17, Vol. 55 No. November, pp.



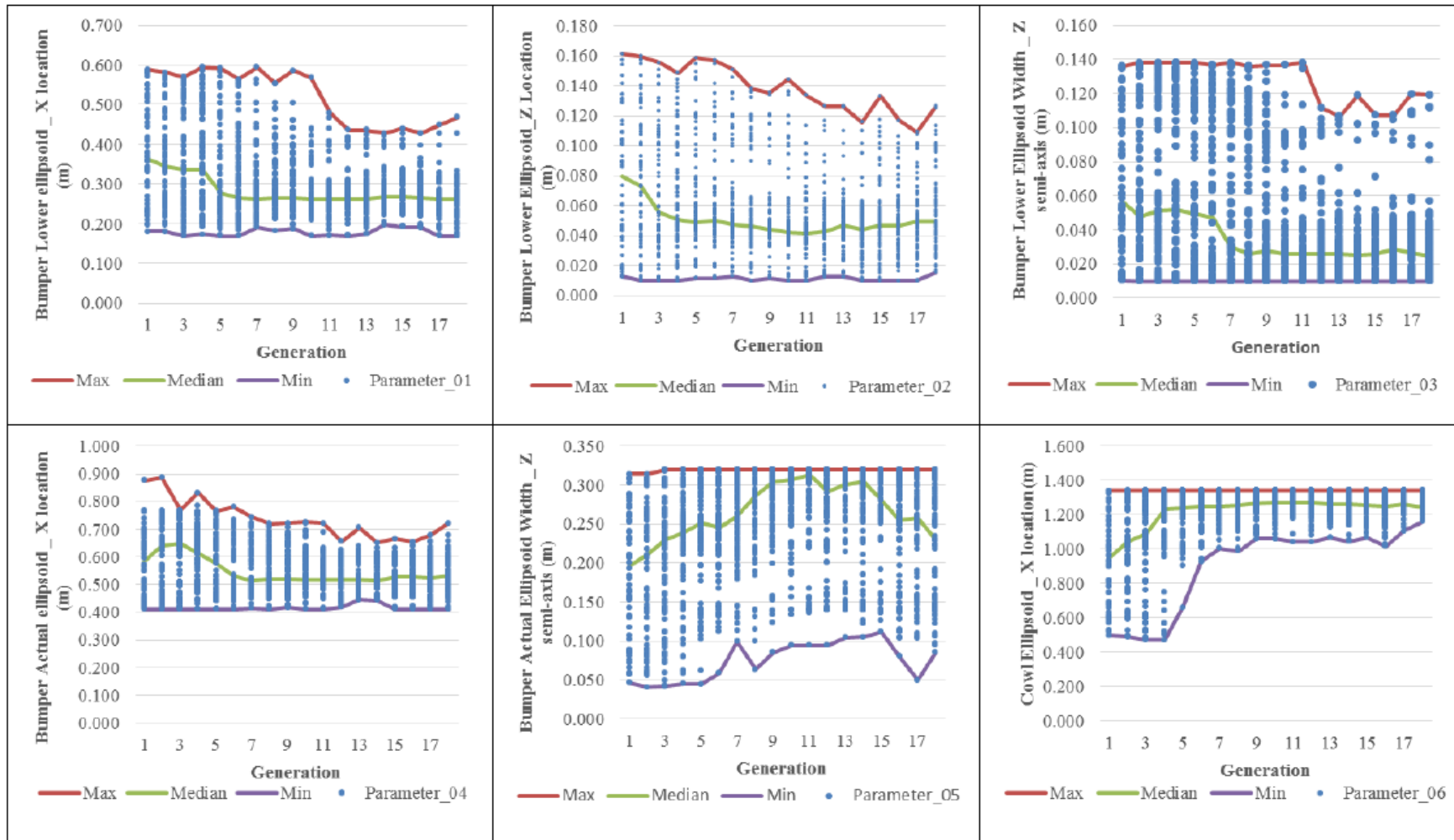
461–478.

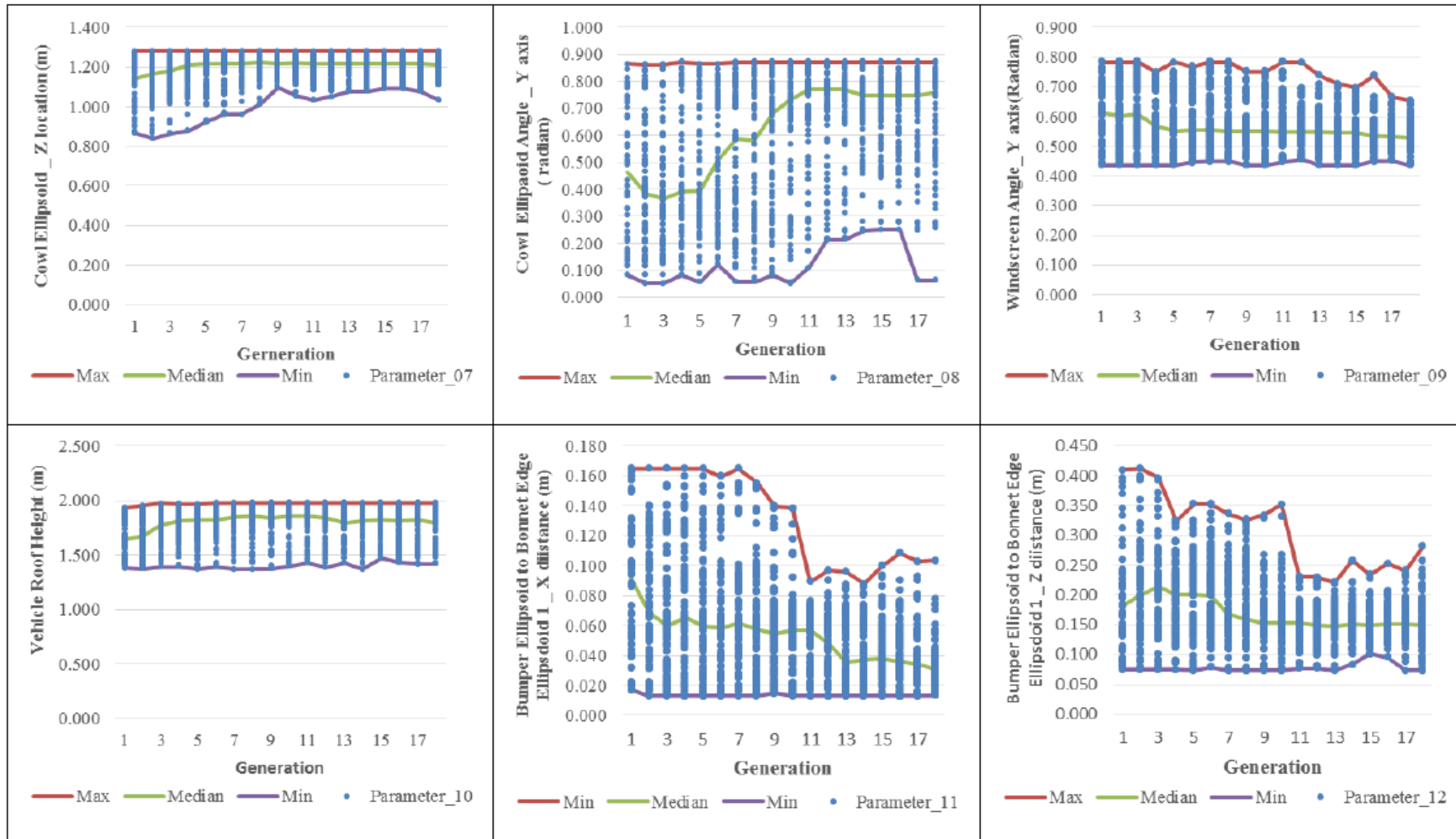
15. **Mohan, D., Tsimhoni, O., Sivak, M., J. Flannagan, M., Tshimoni, O. and Flannagan, M.J.** (2009), Road Safety in India: Challenges and Opportunities, Report No. UMTRI-2009-1.
16. **Newman, J.A., Tylko, S. and Miller, T.** (1994), "Toward a comprehensive biomechanical injury cost model", Accident Analysis & Prevention, Vol. 26 No. 3, pp. 305–314.
17. **Opiela, D.K., Kan, D.S. and Marzougui, D.D.** (2011), Development & Validation of a Finite element Model for the 2010 Toyota Yaris Passenger Sedan, available at: <http://www.ncac.gwu.edu/research/pubs/NCAC-2011-T-001.pdf>.
18. **Otte, D., Jänsch, M. and Haasper, C.** (2012), "Injury protection and accident causation parameters for vulnerable road users based on German In-Depth Accident Study GIDAS.", Accident; analysis and prevention, Elsevier Ltd, Vol. 44 No. 1, pp. 149–53.
19. **Peng, Y., Chen, Y., Yang, J., Otte, D. and Willinger, R.** (2012), "A study of pedestrian and bicyclist exposure to head injury in passenger car collisions based on accident data and simulations", Safety Science, Elsevier Ltd, Vol. 50 No. 9, pp. 1749–1759.
20. **Rooij, L. van, Bhalla, K., Meissner, M., Ivarsson, J., Crandall, J., Longhitano, D., Takashi, Y., et al.** (2003), "Pedestrian crash reconstruction using multi-body modeling with geometrically detailed, validated vehicle models and advanced pedestrian injury criteria", ESV -Paper no. 468.
21. **Sankarasubramanian, H., Mukherjee, S., Chawla, A. and Göhlich, D.** (2013), "A Method to Compare and Quantify Threat to Pedestrian Using Injury Cost Measure", Proceedings of IRCOBI 2013, Gothenburg, Sweden, IRCOBI.
22. **Schmitt, K., Niederer, P.F., Muser, M.H. and Walz, F.** (2007), Trauma Biomechanics Accidental injury in traffic and sports, Biomechanics, Springer-verlag Berlin Heidelberg, Second., p. 210.
23. **TNO, TassB.V. and TassBv.** (2012), Human Body Models Manual R 7.4.2, TNO, p. 122. Untaroiu, C.D., Meissner, M.U., Crandall, J.R., Takahashi, Y., Okamoto, M. and Ito, O. (2009), "Crash reconstruction of pedestrian accidents using optimization techniques", International Journal of Impact Engineering, Elsevier Ltd, Vol. 36 No. 2, pp. 210–219.
24. **World Health Organisation and WHO.** (2004), World report on road traffic injury prevention, World, p. 244.
25. **Zeidler, F., Pletschen, B., Scheunert, D., Mattern, B., Alt, B., Miksch, T., Eichendorf, W., et al.** (1993), "Development of a new injury cost scale.", Accident; analysis and prevention, Vol. 25 No. 6, pp. 675–87.





## Appendix





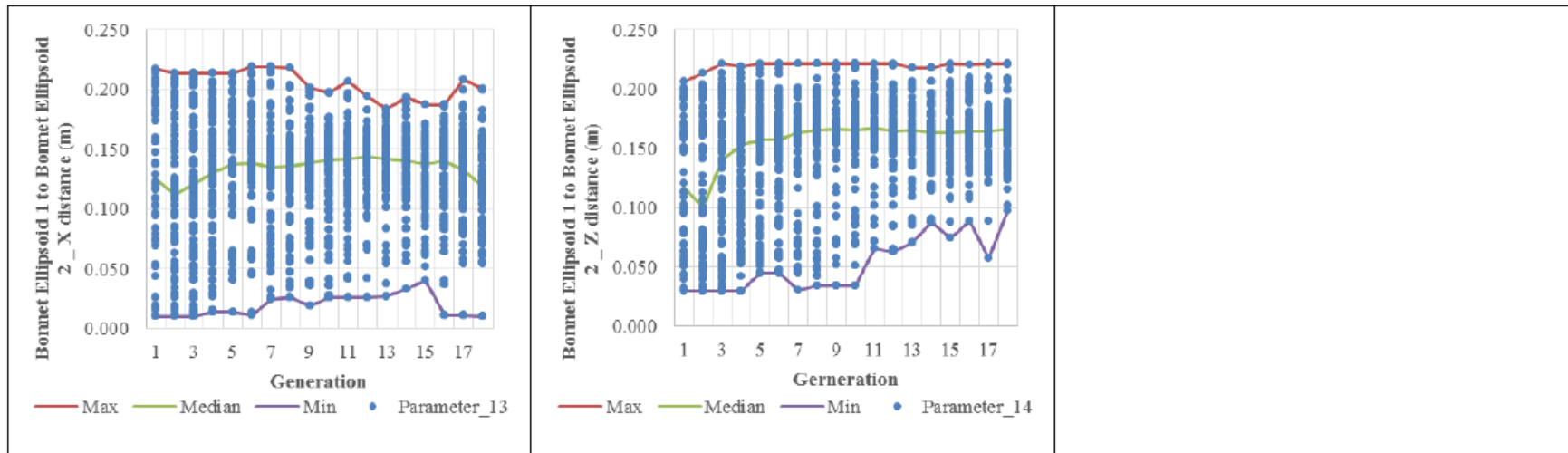


Figure A. Variation of 14 vehicle design parameter values during GA process

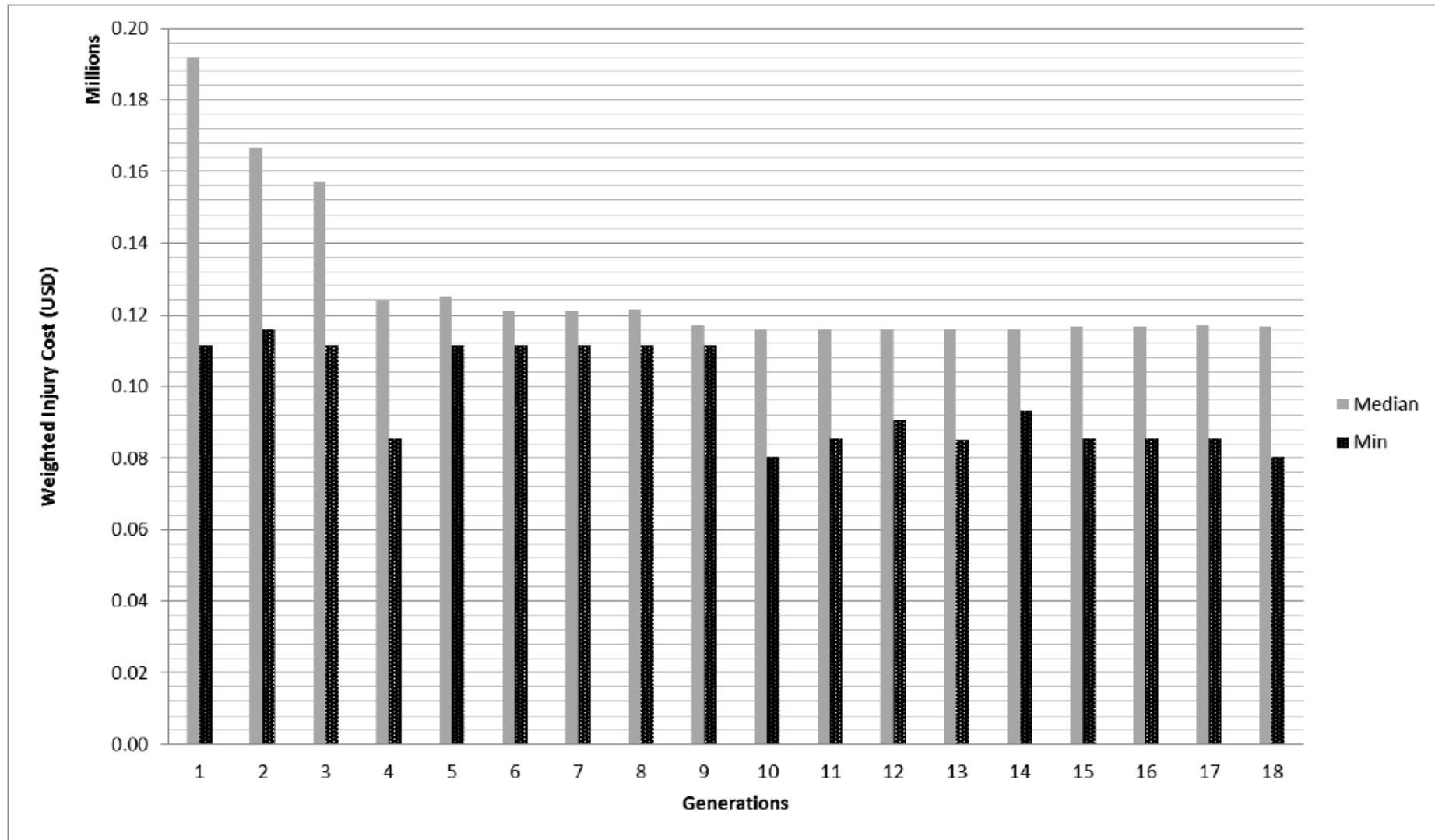


Figure B. Variation of Median and Minimum IC measure for every generation during GA process

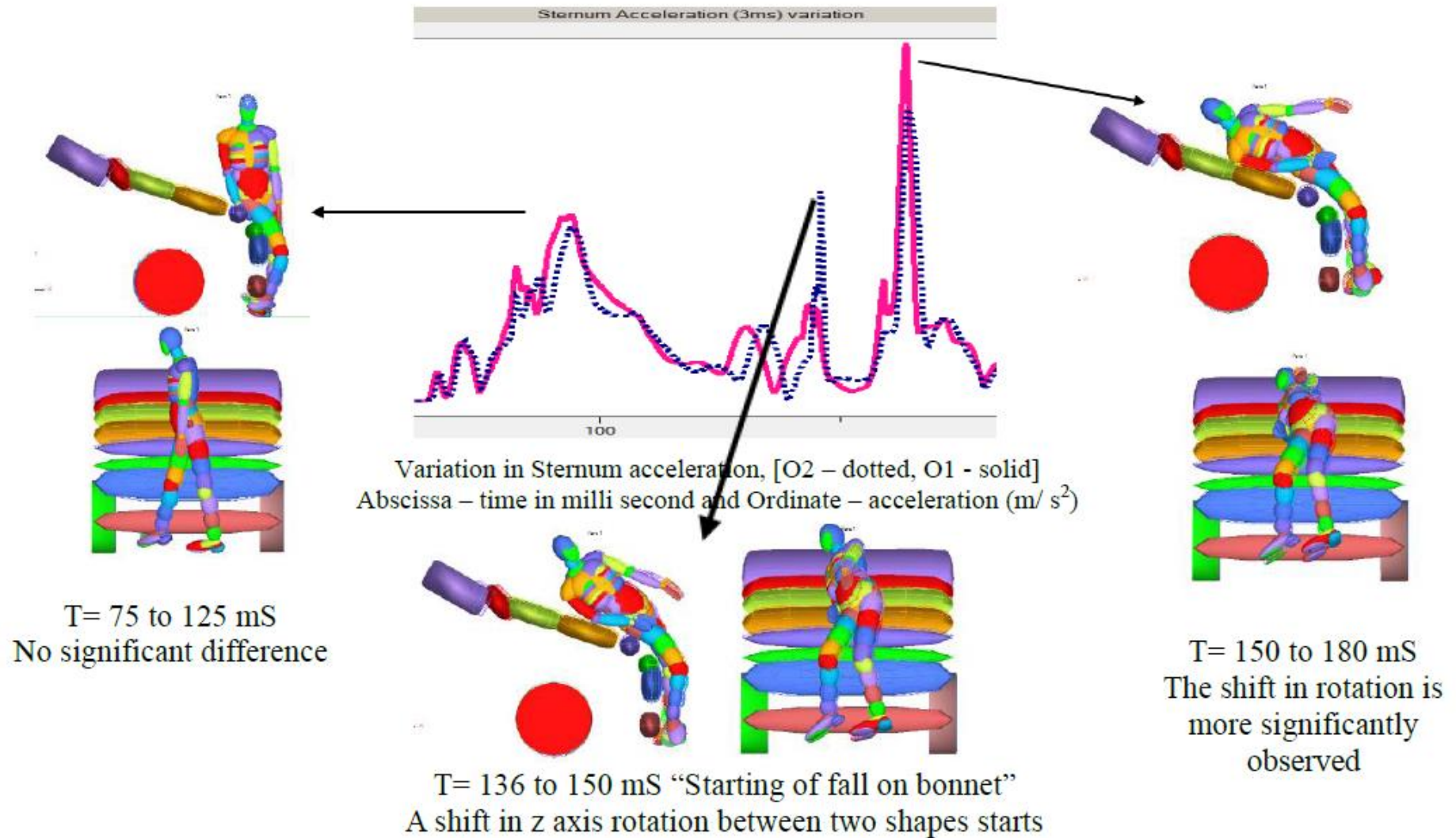


Figure C. Crash kinematics of a 95M pedestrian model against optimal profiles along with comparison of chest acceleration for O1 and O2 profiles





## DESIGN CONCEPT FOR AN INTEGRATED WHIPLASH MITIGATING HEADRESTRAINTS AND CAR SEAT

**M. ACAR**, *M.Acar@lboro.ac.uk*, Wolfson School of Mechanical and Manufacturing Engineering, Loughborough University, UK.

**S.R. BEWSHER**, *S.R.Bewsher-10@student.lboro.ac.uk*, Wolfson School of Mechanical and Manufacturing Engineering, Loughborough University, UK.

### ABSTRACT

This paper presents design of a concept for an integrated headrest and car seat system to mitigate whiplash in rear-end vehicle collisions. The main emphasis is a concept, which combines a reactive headrest with a reactive seat. The chosen concept is developed in the form of mechanical linkages using SAM 6.1. A human model positioned in a 'good' driving posture is used to show how the headrest and seat would operate using a typical crash pulse used for dynamic sled testing of automotive seats. The headrest system is capable of translating into an optimal position of 40 mm forwards and 60 mm upwards in 12 ms, before whiplash induced injuries start to take place. The reactive seat is also capable of reclining 15 degrees. The combination of reducing the backset and reclining the seat to reduce the relative motion between the head and torso has the potential to reduce the whiplash effect related injuries in rear-end collisions.

**Keywords:** whiplash, headrest, occupant seat

### 1. INTRODUCTION

Whiplash is the sudden differential movement between the head and torso which most often occurs as a result of motor vehicle collisions. Whiplash can result from impacts in all directions however, it most often occurs from low velocity rear impacts in car accidents. Although it is officially classed as a minor injury, whiplash has the potential to lead to many long lasting and uncomfortable symptoms. The aim of this project is to develop a more effective concept for a headrest and/or seat which is capable of significantly reducing the whiplash effect in rear-end collisions, as seat and headrest designs are known to have a significant influence on whiplash.

### **1.1 Whiplash Associated Disorder**

Whiplash injuries include muscle and ligamentous strain producing transient cervical pain, symptoms of headache and concussion, and injury to the intervertebral disks infrequently requiring cervical fusion (Prasad, et al., 1997). The Quebec Task Force created a system whereby whiplash associated disorder was split into four categories of severity; (Spitzer et al, 1995):

Grade 1; No sign of physical damage to the neck or upper back.

Grade 2; Signs of damage to the neck or upper back i.e. decreased range of motion and point tenderness.

Grade 3; Neurological damage to the neck or upper back i.e. decreased reflexes, sensation and strength.

Grade 4; Fracture or dislocation of the neck and upper back.

### **1.2 How Does Whiplash Occur**

Whiplash frequently occurs at low-speed rear-end car collisions with a delta-V up to 15.5km/h; anything higher than this value would result in more serious injuries. In a rear impact, the head and torso of an occupant move backwards relative to the seat (vehicle). The torso is supported by the seat back hence it will have a limited motion due to deformation of the seat padding and frame. The occupant body may also ramp up the seat as the seat back deforms backwards under the effect of the impact from the torso. The head sharply rotates backwards until it is stopped by a headrest. Finally, the head rotates forward and the torso rebounds. All this happens typically within 125 ms causing a whiplash disorder in the occupant's cervical spine.

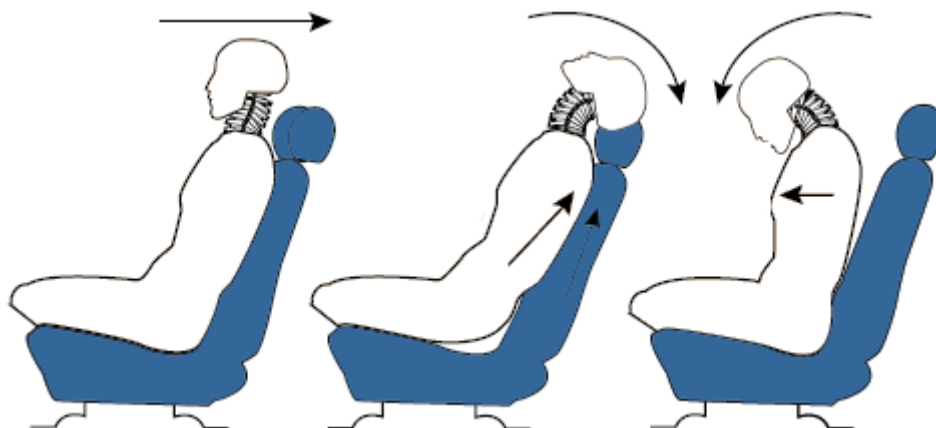


Figure 1: Whiplash injury is most commonly incurred during rear-end car collisions from motion of the spine and neck (Neck Solutions, 2014).

Analyses of high speed films have revealed a distinctive kinematic response of the cervical spine to whiplash trauma (Gunzburg & Szpalski, 1998). Figure 2 shows, within the 50 to



70ms time period, the initial phase of a developing S-shape curve in the cervical spine with extension at the spine's lower levels and flexion at upper levels. The 100 to 125ms time period represents the final phase with extension of the entire cervical spine.

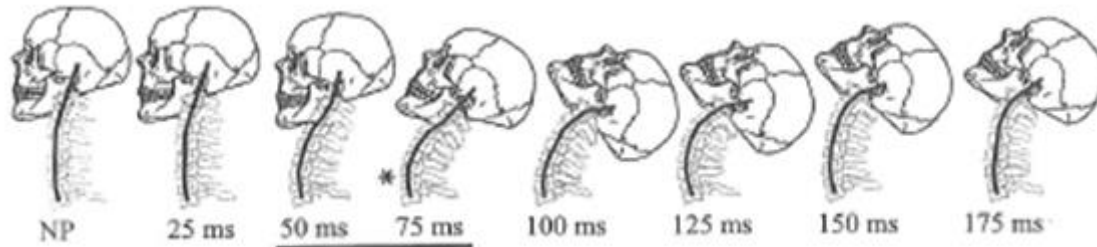


Figure 2: Schematic of a head and neck demonstrating time points during the occurrence of whiplash. A line is drawn through the vertebrae to highlight the curvature of the spine. A skull is shown for illustration only. NP, Neutral Posture. (Gunzburg & Szpalski, 1998)

## 2. HEADRESTRAINT PERFORMANCE

Design of seats and headrests has played a large part in the reduction of whiplash related injuries and claims, and has been a large area of research and product development. However, whiplash still continues to be the major source of insurance claims. Rating of headrests and seats of cars in the market by independent organisations such as IIHS in the USA and Thatcham in the UK, and making the results public played a significant role in the improvement of headrest designs. The automotive industry has found many effective ways of reducing the incidence of whiplash in rear-end collisions, with many unique and innovative designs for headrests and car seats.

Initially, ratings were based on static measurements of the geometry of the headrest. The 'backset' and 'topset' (Figure 5) of the headrests were measured and classified. Backset of less than 40 mm and 'zero' topset were classified as 'good' by Euro NCAP. Over the time, the number of headrests in the 'good' category increased as the manufacturers improved their designs. However, geometry alone was not sufficient to assess the ability of a headrest to mitigate whiplash. Standardised dynamic sled tests and crash pulses using rear impact test dummies, such as BioRID, were developed. The intention of a dynamic test is to simulate a rear-end collision in which the target vehicle is struck while stationary or moving very slowly. Neck injury criteria such as, NIC, were used to assess seats and headrests. Within Europe, Euro NCAP regulates sled tests and provides motoring consumers with a realistic and independent assessment of the safety performance of car seats sold in Europe.

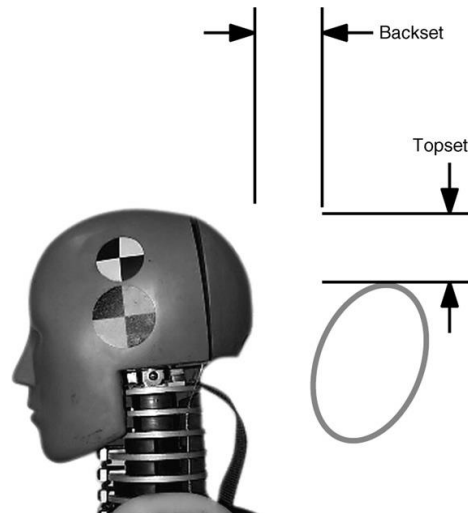


Figure 3: Diagram of geometric headrestrest 'backset' and 'topset' (Croft, 2007)

### 3. SEATS AND HEADRESTRAINTS

Anti-whiplash seat and headrestrest designs range from improved headrestrest geometry, automatic smart headrestrests, reactive head rests and seats, proactive headrestrests to new seat foams to absorb impact energy.

Different types of effective whiplash reducing headrestrests and car seat designs can be grouped in two main categories based upon the ways they attempt to protect the occupant from suffering whiplash during a collision. They are;

- (i) Reducing backset and topset
- (ii) Reducing relative motion between the head and torso

First group includes both reactive and proactive headrestrests. In a rear-end collision, a typical reactive headrestrest uses mechanical linkages to re-position the headrestrest up and forward in order to provide support to the vehicle occupant's head, triggered by the occupant's torso applying pressure to the seat back when it moves backwards during a rear-end crash. Hence the backset and topset are both reduced at the initial stages of the crash. A pro-active system typically consists of a headrestrest that automatically moves the up and forward at the onset of a collision, initiated by the vehicle's crash sensors, again aimed at reducing the backset and topset.

The second group requires the entire seat and headrestrest design to react to the impact to reduce the relative motion between the head and torso and also absorb the energy of a rear-end crash. This could include translation of the seat and tilting of the seatback backwards somehow absorbing energy during the process.

Typical seats in conjunction with traditional fixed or adjustable headrest with a good geometry but no specific anti-whiplash technology may still score 'good' in NCAP sled tests. Some use custom designed foam technology in the seat to absorb the energy of the crash whilst also allowing the occupant to engage the headrest without excessive neck distortion.

The European NCAP ratings for rear impact whiplash prevention show that reactive seats and headrests are the most effective solutions, consistently scoring higher than passive foam technologies and pro-active devices. However, seemingly no design combines a reactive seat with a reactive headrest.

### **3.1 Reactive Headrests**

In 1996 Saab pioneered reactive headrests and introduced the Saab Active Headrest (SAHR) system to the market. Such systems utilise a four-bar linkage or an inverted slider crank mechanism in conjunction with a pressure plate inside the seat-back. When the occupant moves rearward into the seat, their torso pushes against a plate that activates the linkage that moves the headrest upward and forward as shown in Figure 4, in order to reduce the distance to occupant's head, thus reducing the whiplash effect in a rear-end collision.

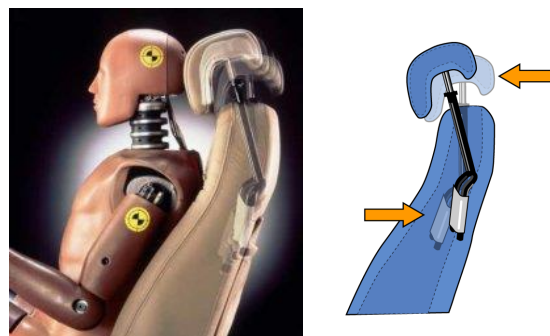


Figure 4: SAHR concept: as the occupant sinks into the seatback during a collision, their torso pushes against a plate and the mechanism is activated forcing the headrest up and forward (Memmolo, 2003).

### **3.2 Pro-Active Headrests**

Pro-Active Headrests (PAHRs) are designed with the aim of being able to prevent whiplash related neck injuries caused by the differential movement of the head and neck, by reducing the backset and topset. Both Mercedes Benz and BMW have applied different types of PAHRs.

The Mercedes Benz NECK-PRO was the first of its kind being sensor controlled, activated in the event of a rear-end collision (Figure 5). When the sensors detect a collision of this type

and above a pre-defined minimum level of severity, they release pre-compressed springs inside the headrests which, in turn, release a four-bar parallel linkage which swings the headrest 40 mm forward and 30 mm upward reducing the backset and topset. This provides the occupant's head the support required in a crash to prevent overextension of the cervical spine, thus reducing the risk of whiplash injury.



Figure 5: The movement of the NECK-PRO relative to the occupant's head (Daimler, n.d.).

The challenge was that, for successful operation of such headrests, the crash detection control systems must operate the linkage before the neck begins a whiplash action and S-shape formation.

In autumn 2007 BMW revealed its PAHRs which is designed to move the headrest up to 60 mm forward and up to 40 mm upward, activated and controlled by the car's airbag control unit, minimising the backwards movement of the head, to reduce the risk of neck injury. The headrest uses a spring-driven mechanism which is activated by a pyro-actuator. Once the pyro-actuator ignites, it propels a release mechanism to allow the springs to move freely adjusting the headrest in the forward and upward motion in order to protect the occupant from whiplash trauma.

### **3.3 Reactive Seat**

A reactive seat would aim to reduce the differential motion between the occupant's head and torso in a rear end collision whilst absorbing impact energy. It is important to note that the seat itself is not sufficient on its own; a suitable headrest must also be applied.

Volvo has designed a unique device (WHIPS) to mitigate whiplash injuries made up of two main parts. The first is the seat hinge which absorb the energy of a rear-end crash by translating initially and then rotating the seat back by plastically deforming an element in the mechanical linkage in a controlled manner. The other component is the fixed, high headrest, which is able to contact the occupant's head early enough in the collision

before the neck and head have chance to move differentially, preventing stresses in the neck.

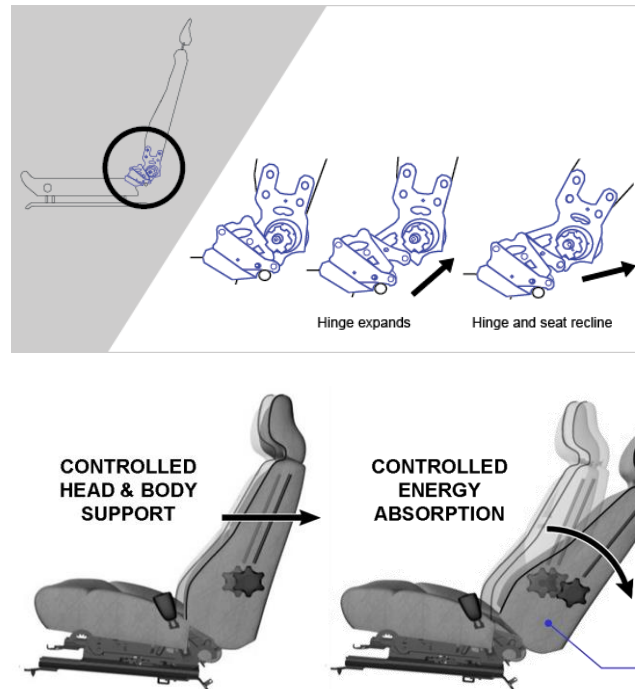


Figure 6: The WHIPS system hinge first expands and then reclines as a link plastically deforms, reducing the acceleration of the occupant relative to the car (IIHS, 1998).

The unique hinge design is made up of four-bar linkage where one of the links is designed to deform plastically causing the seat to recline due to the force applied from the occupant's torso in the seatback.

### 3.4 Passive Seat

Passive seats tend to have normal seat geometry, and no special features integrated into their mechanical design. Rather, the focus is on the material selection, in order to absorb the impact energy transferred during a collision from the occupant into the seat using special foams engineered for such a purpose. The idea is that it should allow the occupant to engage the headrest without excessive neck distortion. However, very little information is available in the public domain as to the properties of the materials used.

Although the ratings of passive seats are shown in reports as good, it should be noted that the ratings for reactive headrests and seats are generally better, thus there is opportunity and potential within the automotive industry to combine passive foam technologies with other whiplash mitigating devices to gain higher scores to mitigate whiplash further.

#### **4. CONCEPT DEVELOPMENT**

The headrest and seat should be aided by a seat damper to absorb the crash energy whilst controlling and limiting the reclining motion of the seat in conjunction with a locking mechanism to prevent rebound. The design should be reusable and add no significant weight to the vehicle and should not adversely affect the fuel economy. The chosen concept shall bear little addition to the overall cost of a standard car seat, making the device affordable for all range of cars. The concept should be designed with mass production in mind, not over complex in its design, and easy to manufacture and assemble.

A number of concepts have been generated and evaluated. For the brevity, only the selected concept is reported here. The chosen concept uniquely integrates the following reactive systems in a complete whiplash mitigating seat design.

(a) a mechanical linkage system built into the headrest to be activated by the upward motion of the link inside the seat back.

(b) a mechanical linkage system built into the seat back whereby the force of the occupant would slide a rod upwards in a controlled manner to activate the headrest.

(c) a mechanical linkage that allows the whole seat to tilt backwards in a controlled manner to reduce the differential motion between the occupant's head and torso, possibly aided by a seat damper.

All these concepts are purely mechanical and reactive in nature, operate only when the vehicle receives a rear-end collision. Mechanisms operate instantly and simultaneously when the body of the occupant begins to push against the seat back. It should be noted that the reactive seat concept requires a damper to control the motion of the seat and absorb the energy of the occupant. The design of the dampers and energy absorbing seatback foam will not be considered here, as the aim of this project is to design the mechanical systems.

##### **4.1 Headrest design**

A reactive headrest system is designed with the view to achieving a zero head-offset during a rear-end collision, in order to reduce the time in which the occupant's head makes contact with the headrest. The headrest is split into two parts, a bucket in which the four-bar parallel linkage is attached and the cushion attached to the coupler of the linkage. A slider, which moves along the lower binary link, is attached to the upper end of the activation mechanism inside the seat-back, couples the two linkage systems. The mechanical linkage concept is created using SAM 6.1 (Synthesis and Analysis of Mechanisms) software which is used for design, analysis and optimisation of mechanisms. It should be noted that the concept is shown in a simplistic two-dimensional format, to be consistent with SAM.



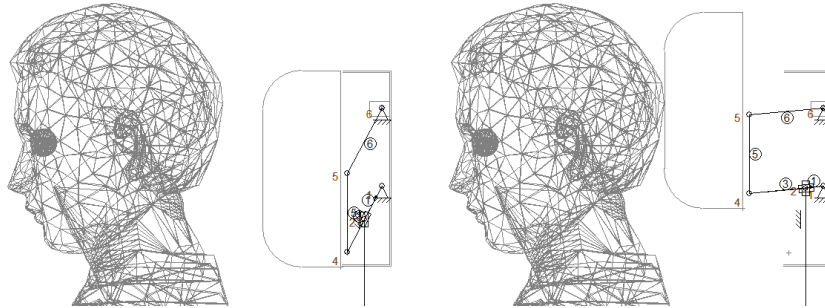


Figure 7: reactive headrest concept before and after activation.

#### 4.2 Seat back mechanism

The linkage inside the seat back is a slider crank mechanism with the slider pushing up a rod in the vertical direction when the occupant's body applies pressure on the plate at the pin joint between the crank and the connecting rod. Figure 8 shows the linkage inside the seat as generated by SAM (pressure plate is not shown). When the link in the seat-back moves upwards, reacting to the motion of the torso, it operates the parallel linkage in the headrest moving its cushion upward and forward.

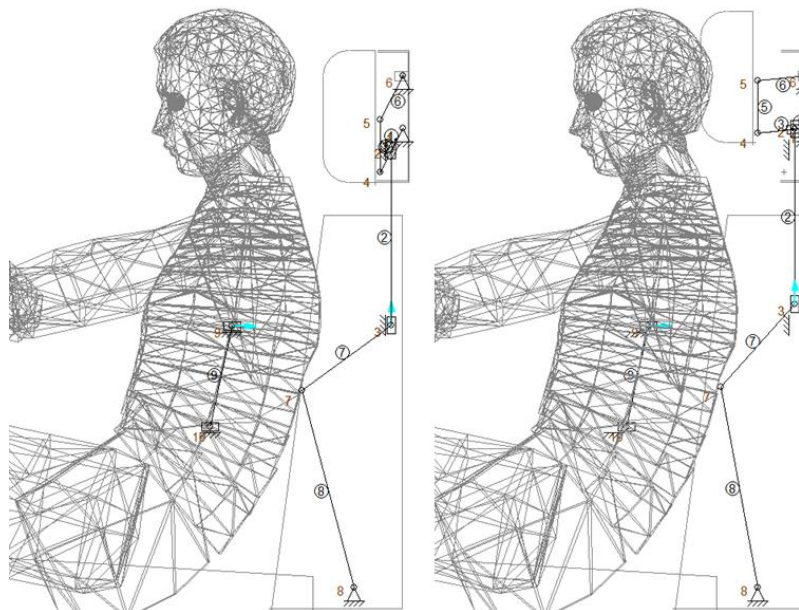


Figure 8: Reactive headrest and activation system inside the seat back.

#### 4.3 Reactive Seat Design

The purpose of a reactive seat is to reduce the differential motion between the head and torso in conjunction with a bumper to absorb the crash energy, which is not considered here. The seat should be capable of rotating rearwards in a controlled manner to achieve this. This concept works in the same way as the headrest, whereby the seat pan is attached to the

coupler of a four-bar linkage, allowing the seat to rotate rearwards as the occupant 'sinks' into the seatback.

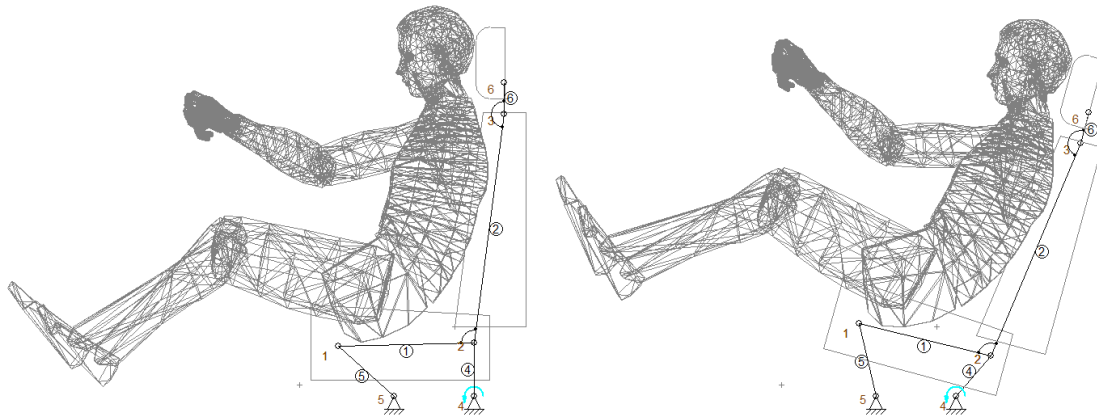


Figure 9: Reactive Seat Concept

## 5. CONCEPT MODELLING

The abilities of SAM are limited, so a separate demonstrator for the headrest and for the reclining seat has been created. It should also be noted that the human model features as a rigid body where no deformation takes place. SAM also only allows for forces to be applied as a point load at a node, it does not allow for the distributed load which would be seen in a rear-end collision.

An acceleration pulse was created for the concept model by assuming acceleration to increase linearly from 0 to 10.5g over the time period of 27 ms as per the standard EURO NCAP pulse. The acceleration input is used for the human body model in rearward direction with respect to the seat.

### 5.1 Headrest System Motion

Figure 10 shows the motion of the headrest in four steps as the body sinks into the seatback. The results from the simulation show that the human's head makes contact with the headrest within just 12ms. Figure 11 shows the relative displacement of the headrest with respect to the initial position in both the X and Y axis.

It can be seen that the headrest is capable of moving the required distance of 40 mm just as it makes contact with the human head within 12 ms, also moving upwards by more than 40 mm.

These results would suggest that the headrest concept would be capable of reducing the incurrance of whiplash, as it moves into an optimal position well before 25ms when it is believed that the whiplash phenomena will initiate as shown in Figure 2.



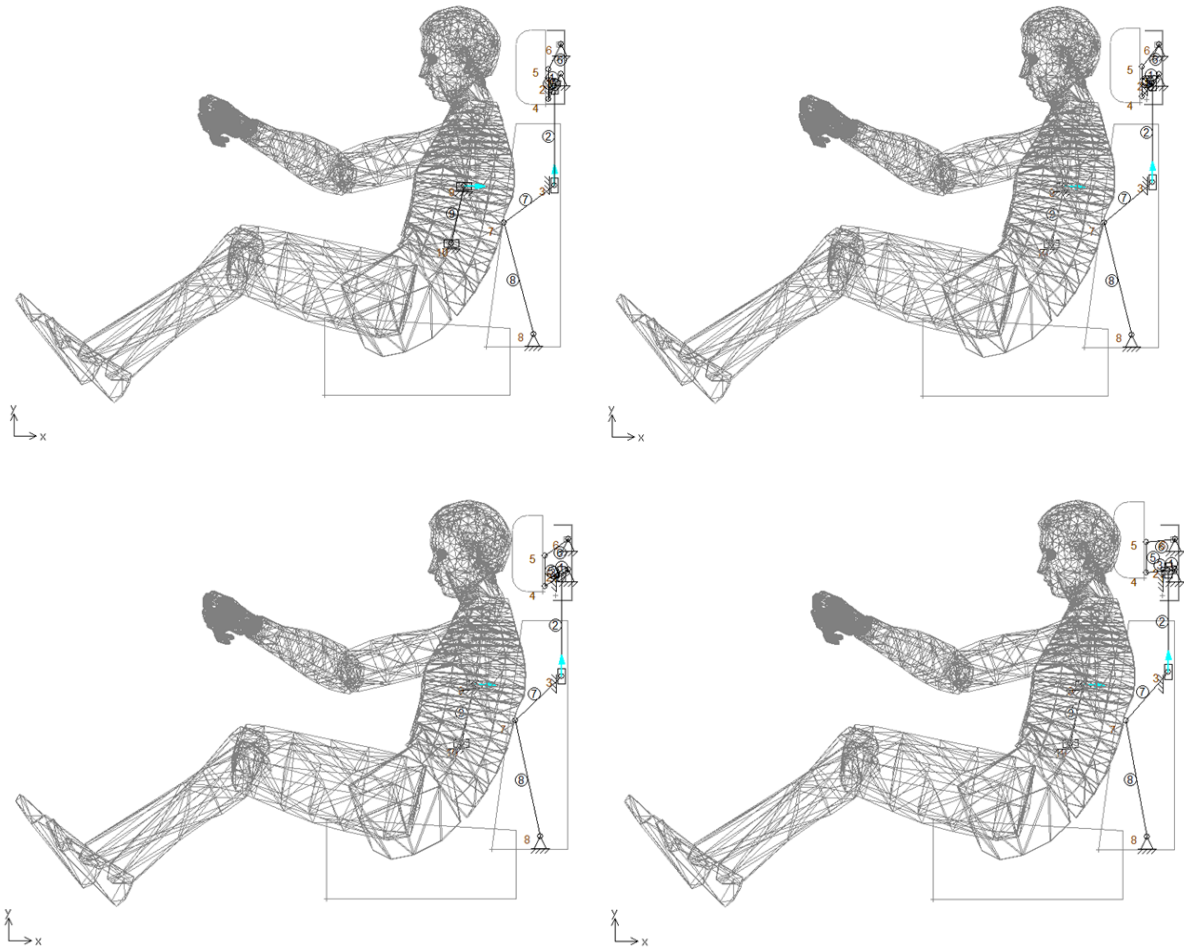


Figure 10: The motion simulation using SAM over a time period of 0-12ms showing that the headrest moves into a position reducing the distance to the occupant's head.

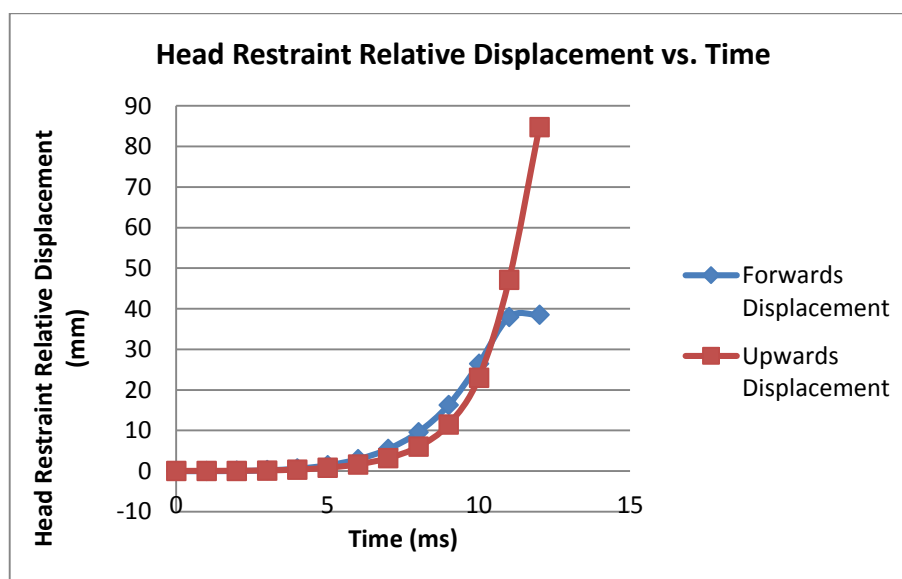


Figure 11: Headrest Relative Displacement)

## 5.2 Reactive Seat System Motion

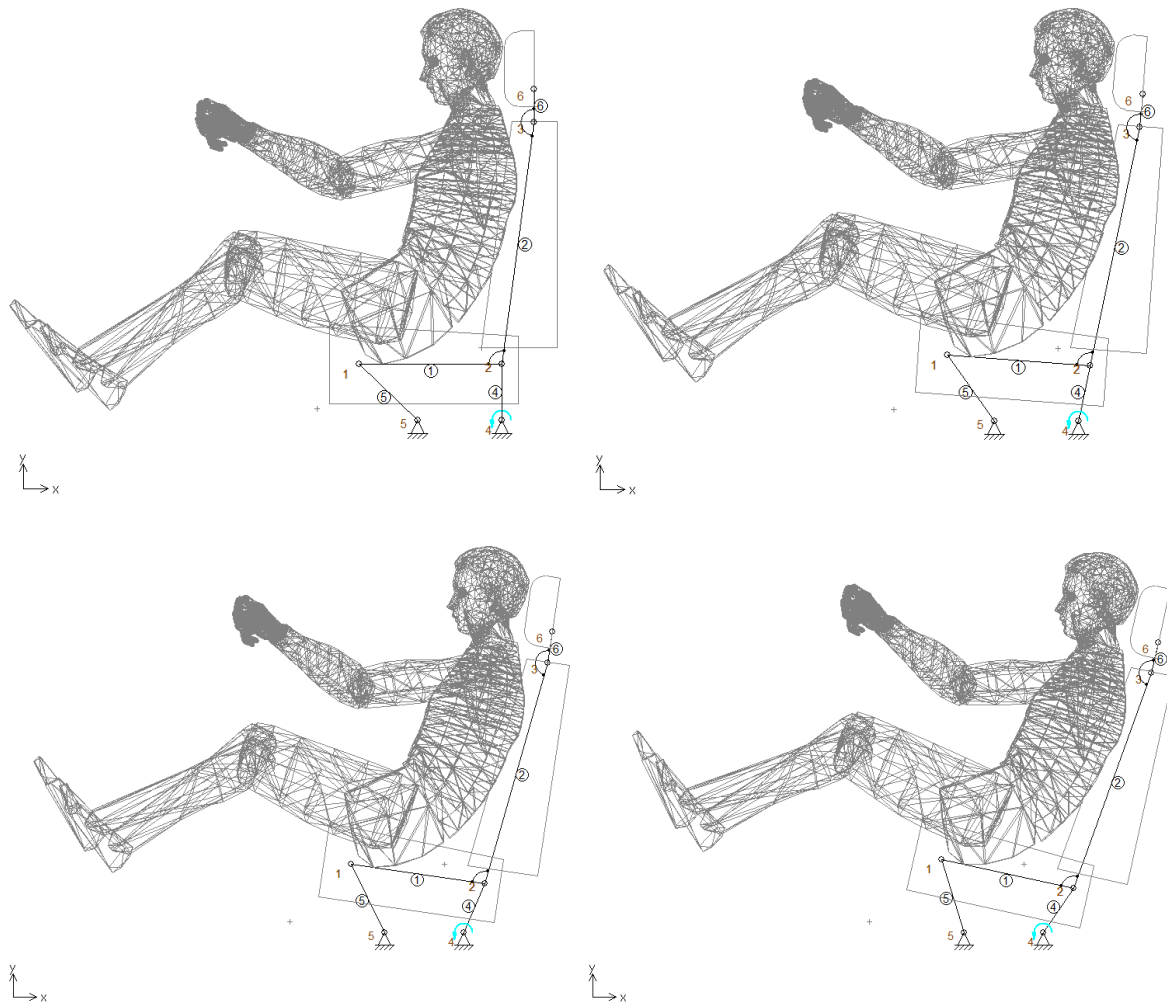


Figure12: The motion simulation of the reactive seat demonstrator using SAM over a time period of 0-25ms, showing that the whole seat reclines.

Figure 12 shows how the reactive seat concept would work, reclining backwards under the pressure from the torso to reduce the differential movement between the torso and the head. The model demonstrates a reclining motion by an angle of 15 degrees, as shown in Figure 13, matching the Volvo WHIPS, in a time of 27 ms. When this motion is combined with the forward and upward displacement of the headrest it is expected to provide an improved whiplash protection.

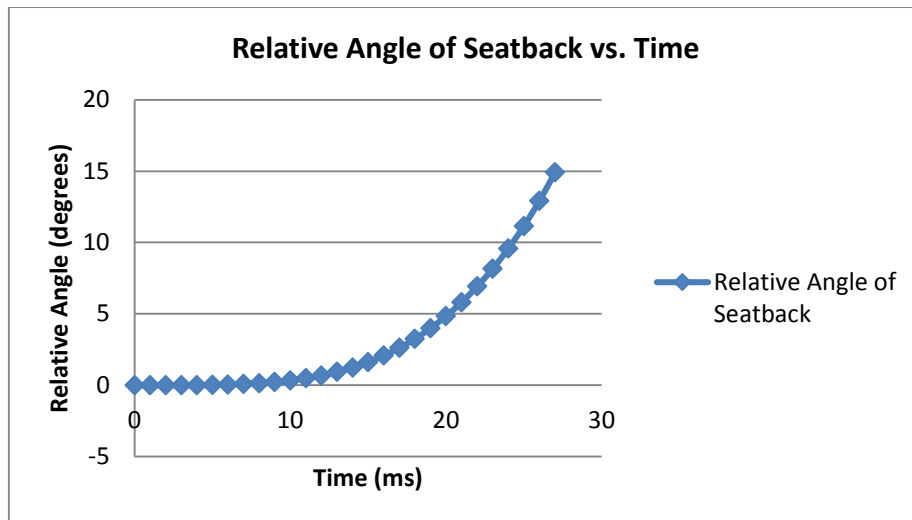


Figure 13: Relative angle of seatback

## 6. CONCLUSIONS

A novel concept that integrates a reactive headrest system with a reactive seat has been proposed. Currently, there is no product in the automotive market that integrates the two concepts. The combined system is capable of moving the headrest upwards and forwards meeting the position requirements within 12 ms well before hyperextension of the neck occurs. Hence, the likelihood of whiplash related injuries in rear-end collision could potentially be reduced with this integrated design.

The reactive seat system was designed to recline by 15 degrees, the same as the Volvo WHIPS. The seat reclines within 27ms, and thus, the chance of reducing the relative motion between the head and torso before the whiplash mechanism has time to have an effect. The seat could also be fitted with an appropriate elastomeric damper to absorb energy further reducing the effect on the occupant.

The cost of such a safety seat should be an affordable option for all manufacturers and beneficial to all consumers in the automotive industry. The concepts presented could form the basis for a prototype product for and automotive seat manufacturer to assess the potential of the concept to mitigate whiplash in rear-end collisions.

## REFERENCES

1. **Croft A.C. and Philippens M.M.G.M.**, (2007), The RID2 biofidelic rear impact dummy: a pilot study using human subjects in low speed rear impact full scale crash tests, *Accident Analysis and Prevention*, 39 (2007) 340–346
2. **Daimler, n.d. [Online]** , Available at: <https://www.daimler.com/dccom/0-5-1301676-1-1281473-1-0-0-1302066-0-0-135-0-0-0-0-0-0-0.html>, [Accessed 25 May 2014].



3. **Gunzburg, R. and Szpalski, M.**, 1998. *Whiplash Injuries Current Concepts in Prevention, Diagnosis, and Treatment of the Cervical Whiplash Syndrome*. Philadelphia, Lippincott-Raven.
4. **Insurance Institute for Highway Safety**, 1998,. *Whiplash injuries much less likely to occur in cars with new seat/head restraint combination, advanced crash tests show*. [Online] , Available at: <http://www.iihs.org>, [Accessed 25 May 2014].
5. **Memmo, S.**, 2003. *IIHS Study Touts Saab's Active Head Restraint*. [Online] Available at: <http://www.shadetree mechanic.com/saab%20active%20head%20restraint.htm> [Accessed 25 May 2014].
6. **Neck Solutions**, 2014. *Whiplash Neck Injury Is Related To Forces The Neck Is Subject To Which Commonly Happens In Rear End Car Crashes*. [Online], Available at: <http://www.necksolutions.com/whiplash-neck-injury.html>, [Accessed 25 May 2014].
7. **Prasad, P., Kim, A., Weerappuli, D., Roberts, V. et al.**, 1997, "Relationships Between Passenger Car Seat Back Strength and Occupant Injury Severity in Rear End Collisions: Field and Laboratory Studies," *SAE Technical Paper 973343*, 1997, doi:10.4271/973343
8. **Spitzer WO, Skovron ML, Salmi LR, Cassidy JD, Duranceau J, Suissa S, Zeiss E.**, 1995, Scientific Monograph of the Quebec Task Force on Whiplash Associated Disorders: Redefining "Whiplash" and its Management, *Spine*, Apr 15; 20(8 Suppl):1S-73S.



## **STRUCTURAL CRASHWORTHINESS ANALYSIS OF A PICKUP TRUCK SUBJECTED TO POLE SIDE IMPACTS**

**M. Ozan KOCABAŞ**, m.ozankocabas@hotmail.com Middle East Technical University  
– Northern Cyprus Campus, Kalkanlı, Güzelyurt, KKTC, Mersin 10, Turkey

**Eren ÜNSAL**, erenunsal1@gmail.com Middle East Technical University – Northern  
Cyprus Campus, Kalkanlı, Güzelyurt, KKTC, Mersin 10, Turkey

**Volkan ESAT**, evolkan@metu.edu.tr Middle East Technical University – Northern  
Cyprus Campus, Kalkanlı, Güzelyurt, KKTC, Mersin 10, Turkey

### **ABSTRACT**

Crashworthiness of an automobile body in side impacts depends not only on the chassis geometry and topology, but also on the design and reliability of other structural members such as B-pillar and side panels. Side impacts vary with respect to the crash partner. Barrier side impact tests are used to reconstruct vehicle-to-vehicle collisions, at least one of which is impacted laterally; whereas pole side impact test is employed to investigate an arguably more hazardous condition, where the pole impacted is stationary, possibly causing severe localized damage on the body of the vehicle. This study focuses on investigating the effects of pole side impacts on the crashworthiness of a pickup truck with a ladder frame chassis. Previous research work concentrate on the particular aspects of the structure of the vehicle to improve crash energy absorption characteristics. In this study, a finite element (FE) model is developed utilising a previously generated mesh of a pickup truck. The FE model is employed to simulate pole side crash test scenarios on the whole body of the vehicle. Total strain energies sustained by the vehicle, pole reaction forces, and equivalent von Mises stresses are presented for several proposed design improvements in order to enhance crashworthiness. Computational results yield good agreement with experimental findings.

**Keywords:** Crashworthiness, Crash energy, Finite element analysis, Pole side impact

### **1. INTRODUCTION**

Accidents are one of the main reasons of death for people across the globe. Automobile accidents are a major portion of all accidents across the globe, which result in fatalities and various injuries [Teng et al., 2008]. Crashworthiness is an engineering concept that is used to analyze the ability of vehicle structure to cover and protect passengers in



the case of an accident or impact [Jones, 1997]. This concept is used not only for automobiles but also for other types of vehicles such as planes, ships, and trains. In order to improve crashworthiness, it is necessary to analyse different factors which have effects on crash characteristics of vehicles.

There are various evaluation criteria to assess crashworthiness. Displacement and energy criterion is based on minimising the crush length of the vehicle by using modern design techniques while increasing the energy absorption potential of the automobile chassis. Crash pulse is caused by sudden deceleration gained by the impact on the vehicle as well as on the occupants. Head injury criterion (HIC) is employed to analyse the damage from crash pulse on the brain, and it should not exceed a threshold to satisfy that criterion [Newman, 1980]. Crash position is another criterion which states that the design of the car should be modernised in a way to minimize the injuries in several different crash positions such as full-frontal impact, side impact, rear impact, and rollover. Automobile compatibility criterion highlights that the chassis should also be designed in order to mitigate injuries resulting from accidents.

Crashworthiness term is used for the structure's ability to protect the occupants in the case of an impact, thus, the structure of the vehicle should be designed to satisfy some requirements. Mainly, the structure must absorb as much energy as it can sustain from an impact by plastically deforming in a controllable behaviour. The remaining amount of the impact energy can then be handled by the restraint system to protect the occupants from the consequences of the secondary impact in the vehicle. In addition, the structure should be able to maintain at least the minimum survival space to keep the injury levels at a minimum. An adequately designed vehicle should satisfy two criteria simultaneously for crashworthiness. It should be consistent with the initial design objectives such as comfort, accessibility, low weight, and reduced fuel consumption. Low weight is probably the most important design attribute in contemporary automobile industry, which is also addressed in this research. The entire design process for crashworthiness is a complex engineering problem which requires high levels of cooperation among different disciplines.

Pole Side impact is one of the most hazardous types of impact. In pole side impact crash tests, a vehicle in motion impacts a target pole from the locations of one or more of its pillars during which the kinetic energy is transformed into deformation mainly on the impacting vehicle. Test protocols are generated and standardised for two types of side impact. It may be either a vehicle impacting a non-deformable fixed body such as the pole or colliding laterally into another vehicle as a moving deformable body. In both cases, the impacting vehicle's kinetic energy is dissipated through deformation of its structure and of the crash partner's body, if any. Following the onset of the incident,



the occupant begins to move freely against the interior if not restrained, or interacts with restraint system, if restrained. The kinetic energy is then transformed into interior deformation of the structure and compression to the occupant's body. Finally, the remaining kinetic energy is dissipated as the occupant decelerates along with the vehicle. European regulations related to side impact testing [ECE R 11, 1985, ECE R 95, 2005], Euroncap [2013] pole side impact test protocol, as well as FMVSS standard 214 [2008] in the USA are the most common sources of information and test protocols for side impact tests. A snapshot from a pole side impact test is provided in Figure 1 below.



Figure 1. Pole side impact test in line with FMVSS 214 (adapted from [www.ancap.com](http://www.ancap.com))

## 2. METHODOLOGY

A finite element (FE) mesh of the 1994 Chevrolet C1500 pickup is gathered from and as a courtesy of the National Crash Analysis Center (NCAC) of the George Washington University [1997]. The mesh embodies 10500 elements, composed mainly of 4-node shell type along with a few brick type. The LS-DYNA3D and MSC.Patran are used for pre-preparation of the model files, followed by exporting into the FE modelling medium, MSC.Marc/Mentat 2010. Isometric view of the NCAC FE mesh of the vehicle is given in Figure 2.

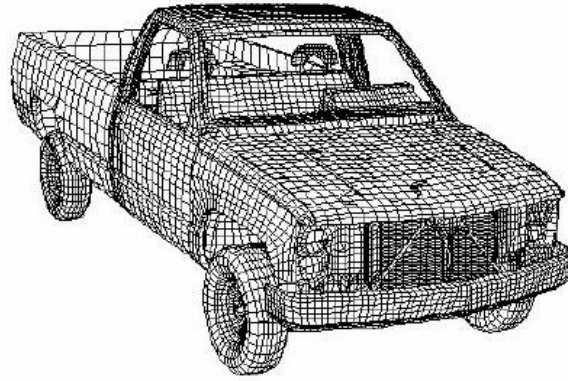


Figure 2. FE model of the 1992 model Chevrolet C1500 pickup [Zaouk et al., 1997]

In the simulations, the pole velocity is used as 29 kph in accordance with Euroncap and FMVSS 214 regulations and a typical impact duration of 120 ms is utilised. The pole is relatively narrow, so there is major penetration into the side of the car. Pole diameter is taken as 254 mm also in accordance with the test procedures.

The material for all simulations is selected to be the DP600 steel, which is frequently used in the automotive industry as the material for automobile chassis and bodies. DP600 is reported to be used for the pickup truck Chevrolet C1500 [Zaouk et al., 1997]. The elastic material properties of the DP600 are; yield stress  $\sigma_{ys} = 390$  MPa for quasi-static tension test, Young's modulus  $E = 210$  GPa, and Poisson's ratio  $\nu = 0.28$ . True stress – true strain flow curve of DP600 is reported for various strain rates [Ford Motor Company, 2012]. A midrange value corresponding to a strain rate of  $500 \text{ s}^{-1}$  is used for all analyses. The flow curve used is provided in Figure 3.

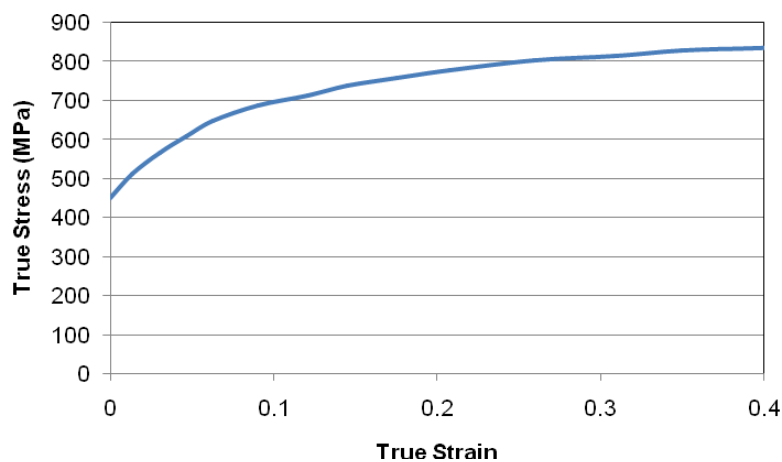


Figure 3. Flow curve of DP600 steel used in analyses

Five analyses cases are carried out to investigate the effects of improvements suggested



to enhance side impact crashworthiness.

Case 1. Changing the panel and structural element thicknesses of the entire body

Case 2. Effects of B-pillar and side doors to crashworthiness

Case 3. Variable thicknesses around the body of the truck

Case 4. Changing B-pillar cross sectional geometry

Case 5. Enhancing B-pillar with an additional support

### 3. RESULTS AND DISCUSSION

#### 3.1. Case 1: Changing the Panel and Structural Element Thicknesses of the Entire Body

In this case, a reduced model is preferred for computational reasons. The whole body is given sheet panel thickness values of 1.00 mm, 1.25 mm, and 1.50 mm. It is aimed to make a comparison between the different thicknesses and their contribution to structural crashworthiness. 1.00 mm appears to be an appropriate thickness value according to the literature [Zaouk et al., 1997, Ford Motor Company, 2012]. A snapshot taken at the full intrusion of the pillar into the vehicle with 1.00 mm body panel thickness is shown in Figure 4, depicting the von Mises stress distribution.

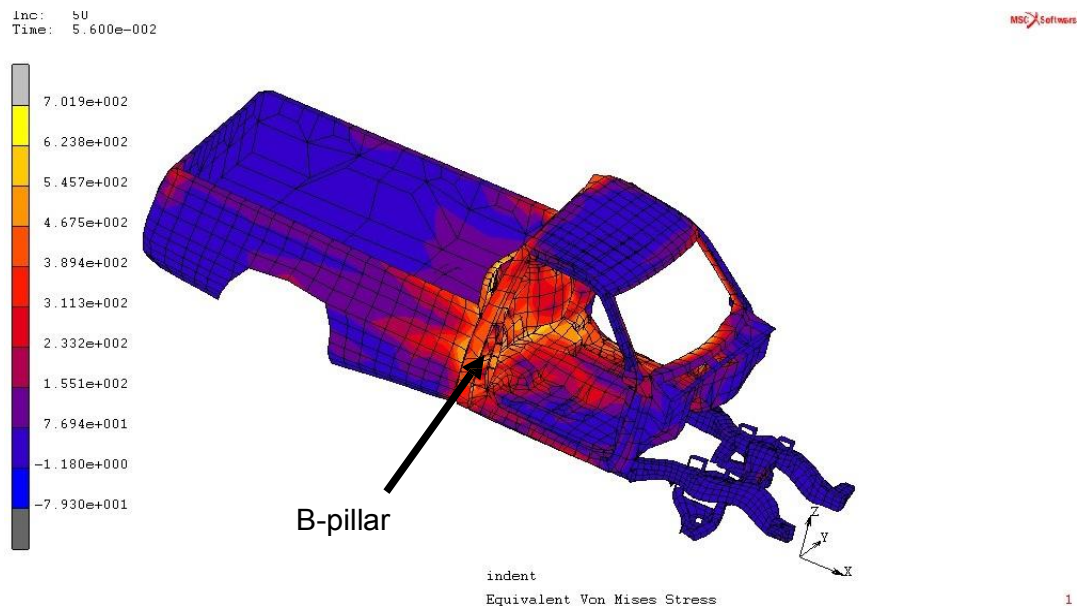


Figure 4. The von Mises stress distribution of the pickup truck with 1.00 mm body panel thickness

Total strain energies sustained by the vehicle, pole forces and equivalent von Mises

stress distributions with respect to pole intrusion are given in Figures 5-7.

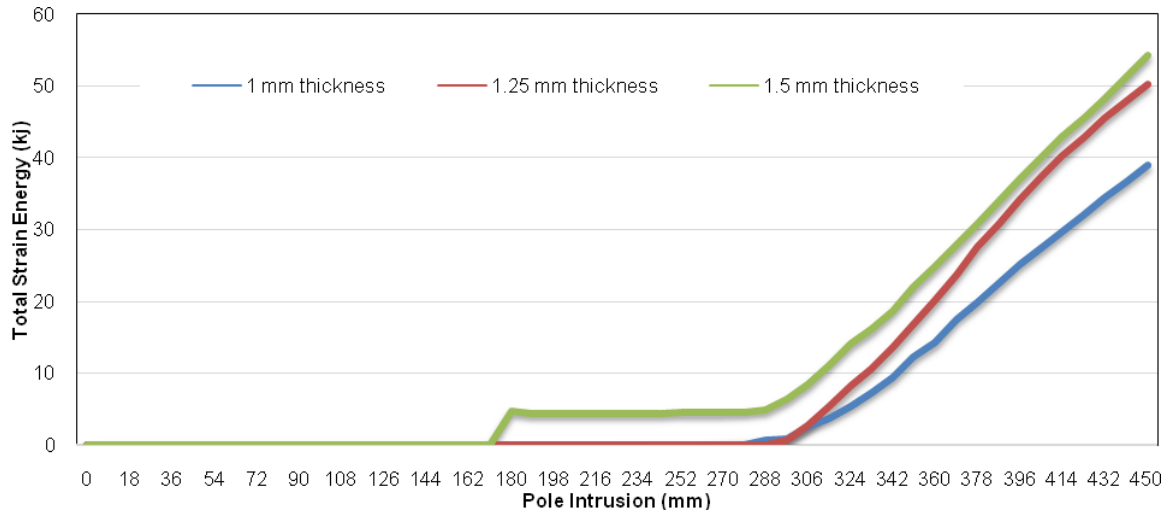


Figure 5. Total strain energies sustained by the pickup truck with different thicknesses

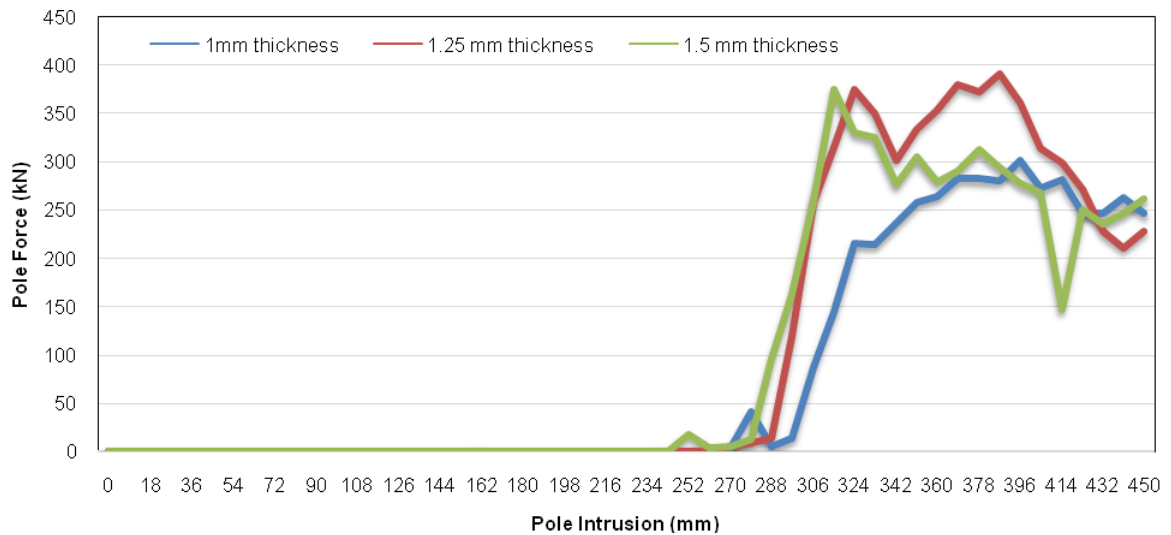


Figure 6. Pole forces with different thicknesses

Figure 4 reveals that stress concentrations and maximum equivalent von Mises stresses are accumulated mainly around the B-pillar and the transverse beam of the chassis, which highlights potential regions of support for enhanced crashworthiness. Total strain energies sustained by the truck body with 1.50 mm thickness are higher than those of 1.25 and 1.00 mm thickness bodies as seen in Figure 5. Hence, it can be concluded that structural crashworthiness of a thicker body is higher than that of thinner vehicle bodies. However, a thicker body will result in a heavier vehicle, which affects competitive advantage adversely. A trade-off might be considered by choosing the 1.25 mm

thickness as its strain energy values are close to 1.50 mm, and gives a relatively lighter vehicle when compared to 1.50 mm design. Figures 6 does not reveal a significant pattern for pole forces with respect to pole intrusion. Figure 7 shows that von Mises stresses variations are not too different from one another.

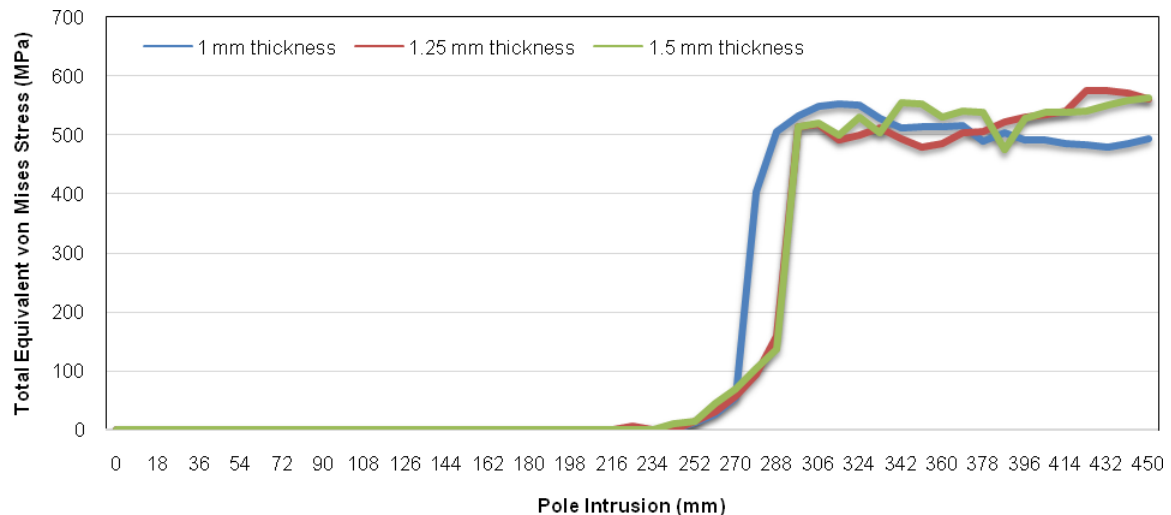


Figure 7. Equivalent von Mises stress distributions in the pickup truck with different thicknesses

### 3.2. Case 2: Effects of B-Pillar and Side Doors to Crashworthiness

Case 2 aims to show the contribution of side doors to crashworthiness of the automobile under the given impact scenario. Crash analyses are performed with the reduced body of 1mm panel thickness devoid of frontal body elements such as engine, and hood. First stage of analyses does not include side doors and wings additionally, which are included in the second stage to show their contribution to energy absorption. The second stage reduced model with side doors and wings is provided in Figure 8 showing the full intrusion of the pillar into the pickup truck. In this case the aim is to realize which part of the vehicle absorbs most of the energy. The total strain energy plots in Figure 9 exhibit that the difference in energies in both cases is not significant up to about 400 mm intrusion, revealing B-pillar is absorbing most of the energy. However, after 400 mm intrusion, meaning at a higher severity of impact, door seems to contribute more to energy absorption. Wing's contribution is observed to be less as interpreted through low von Mises stresses on the wing in Figure 8. Doors and wings are expected to be more effective in side impacts when the impact comes more directly onto them. Under the current configuration they do not add much to the crashworthiness particularly at lower impact speeds.

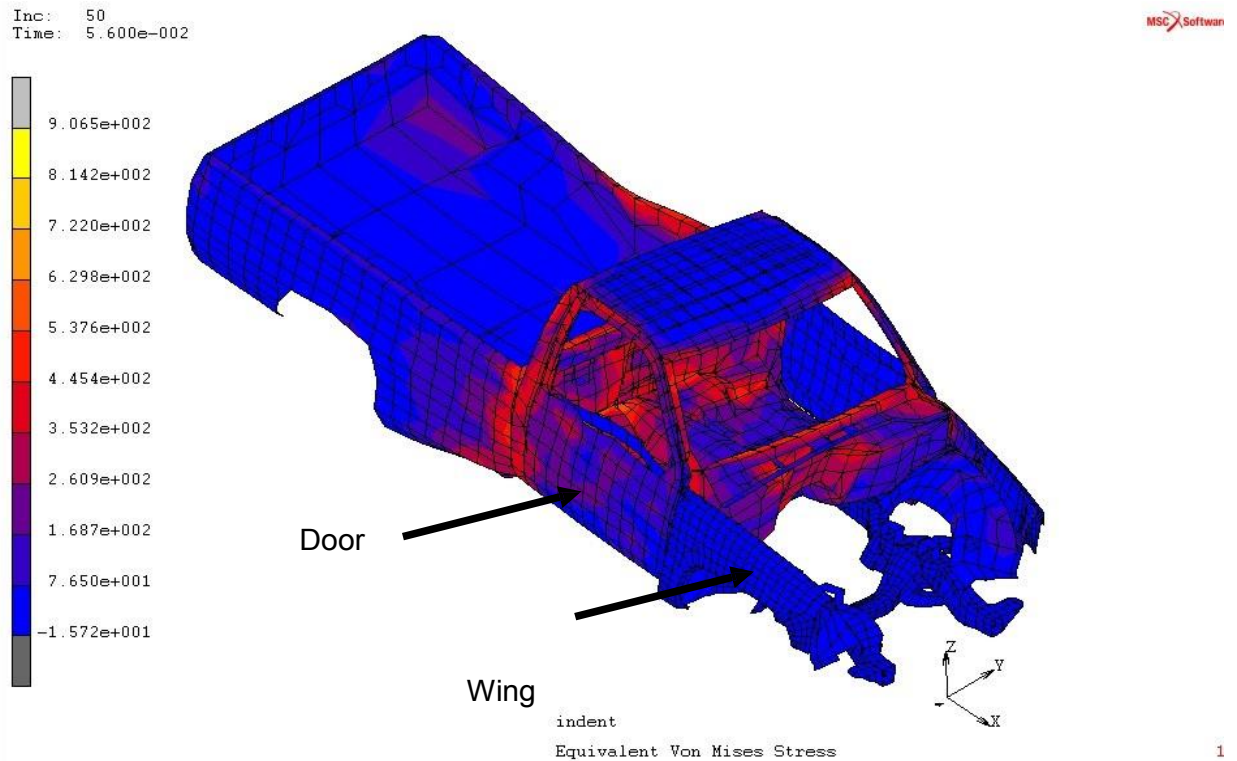


Figure 8. The von Mises stress distribution of the pickup truck reduced model with side doors and wings at full intrusion

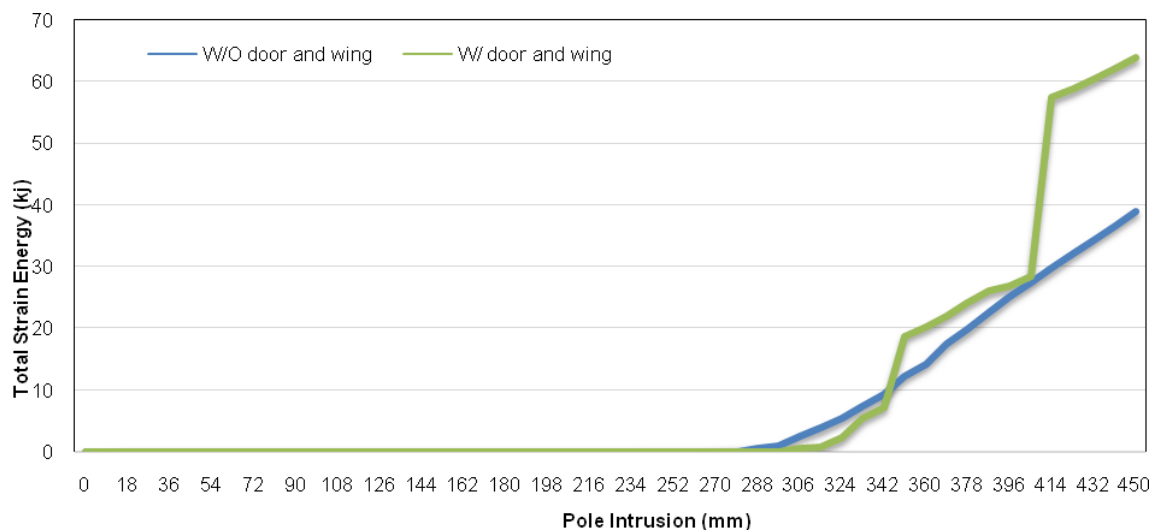


Figure 9. Total strain energies sustained by the pickup with and without the door and wing

### 3.3. Case 3: Variable Thicknesses around the Body of the Truck

In case 3, geometric properties in the form of thicknesses of the vehicle structure are varied for different parts of the body. The thicknesses of the specific parts of the body which are thought to contribute more to crashworthiness are increased, whereas for the others they are decreased to balance the changes in weight, and, if possible, to reduce

the weight. For this purpose, the thickness value of the chassis is kept as 1.00 mm whereas the thickness of the haulage is decreased from 1.00 mm to 0.75 mm. The thicknesses of the cabin panels are increased from 1.00 mm to 1.25 mm. The thickness of the roof remains the same as 1.00 mm. The results of case 3 are compared to the all around 1.00 mm thickness body case. The view at the full intrusion of the pillar into the vehicle with varying body panel thicknesses is shown in Figure 10 showing.

The primary objective of this case is to seek if reducing overall mass while increasing energy absorption values improves the crashworthiness. Results as shown in Figure 11 reveal that case 3 modifications is a possible way to increase the crashworthiness. The total strain energy values sustained are nearly 1.7 times higher than that of the initial condition (1.00 mm all around) at 450 mm pole displacement, eventually leading to an increase in vehicle's crashworthiness. However, it should be noted that weakening the haulage section of the pickup may weaken the crashworthiness during rear-end impact cases.

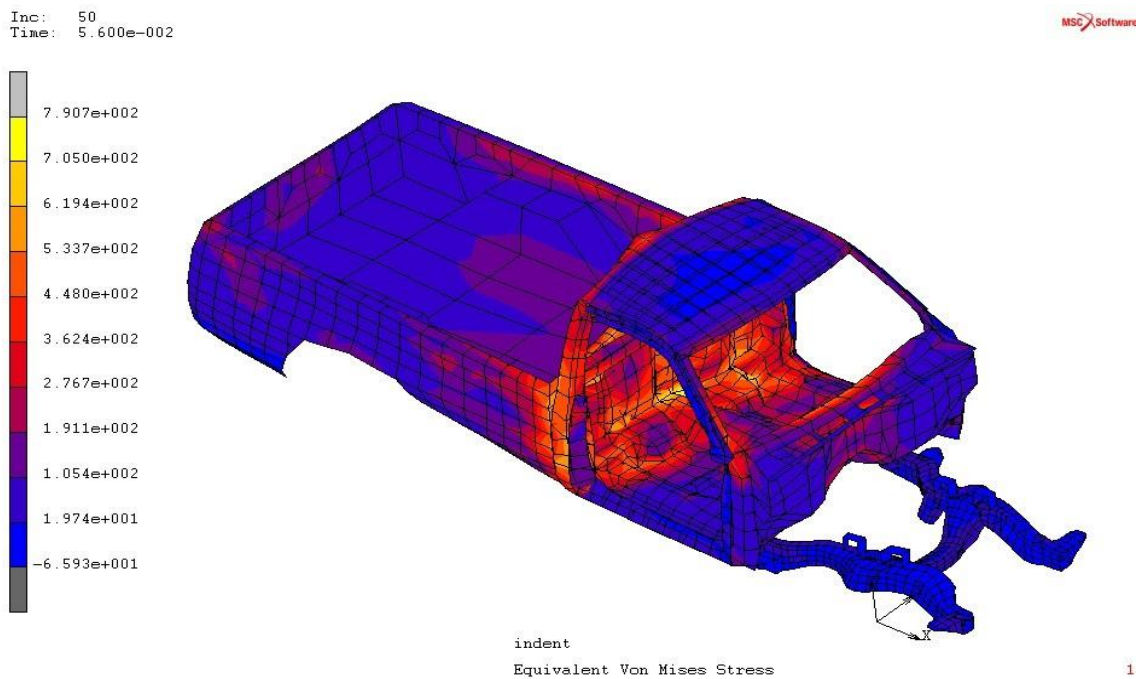


Figure 10. The von Mises stress distribution at the full intrusion of the pillar into the vehicle with varying body panel thicknesses (case 3 modifications)

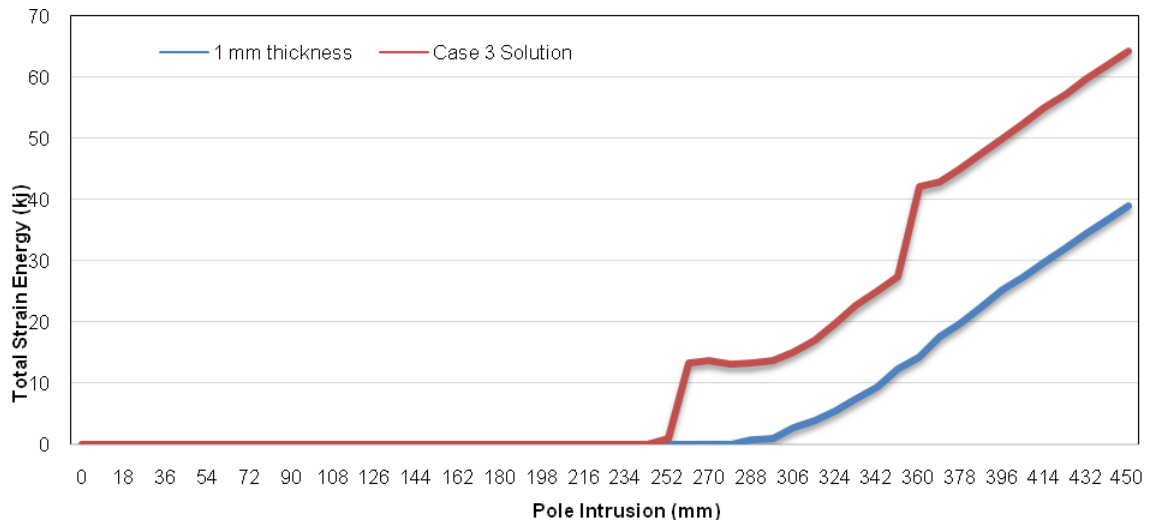


Figure 11. Total strain energies sustained by the pickup for 1.00 mm and varying thicknesses (case 3 modifications)

### 3.4. Case 4: Changing B-Pillar Cross Sectional Geometry

In case 4, the geometry of the B pillar is modified so that a longitudinal zigzag shape is used instead of a rectangular-prism-like beam. The zigzag shape results in smaller trapezoid prisms connected to each other, forming suitable locations for plastic hinges under impact load. The typical and modified B-Pillar shapes can be seen in Figure 12.

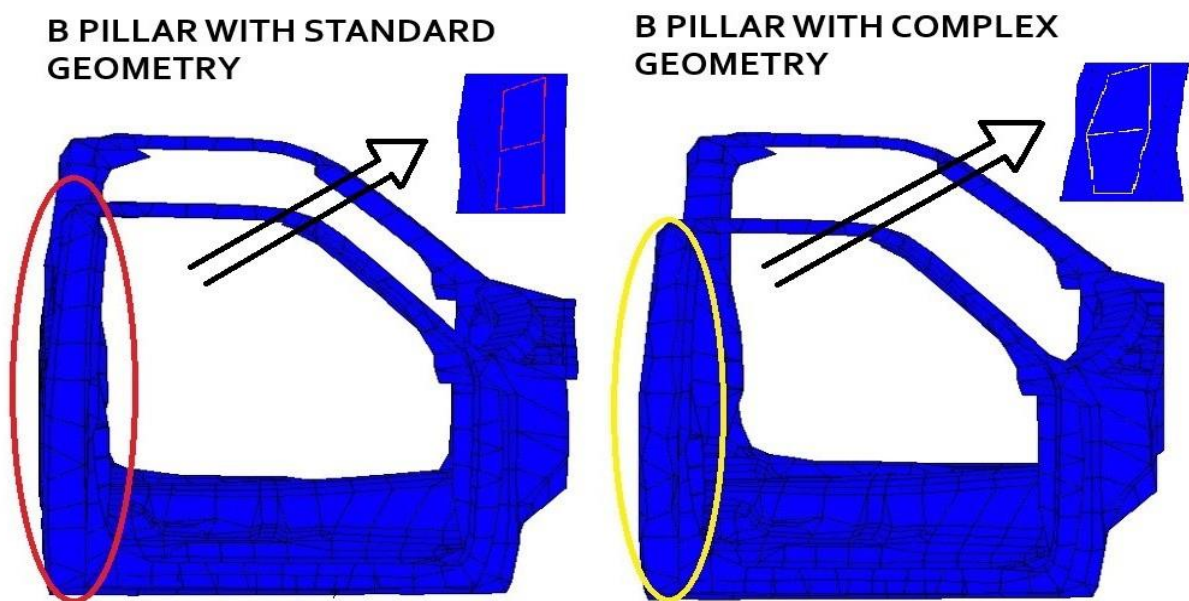


Figure 12. Typical and modified B-Pillar Shapes



Figure 13 shows that rectangular and trapezoid cross-section profiles do not have a remarkable difference in total strain energies until the very end of pole intrusion. However, at the end of the intrusion, meaning a higher severity, trapezoid cross section profile appears to sustain more energy than the ordinary rectangular profile.

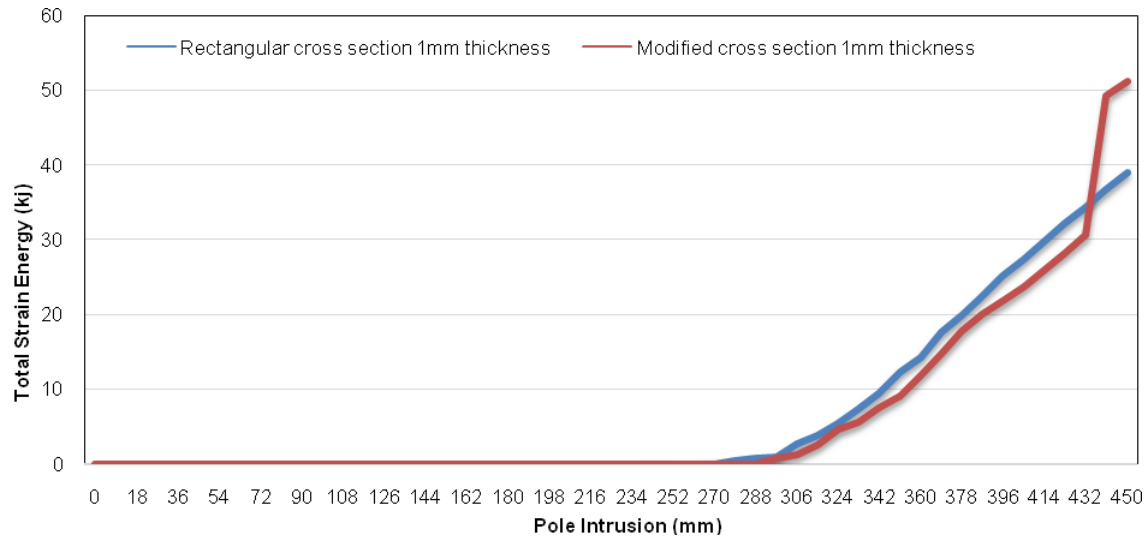


Figure 13. Total strain energies sustained by bodies with typical and modified B-pillars

### 3.5. Case 5: Enhancing B-Pillar with an Additional Support

In case 5, a support with 1.00 mm thickness is placed in the upper portion of B pillar as seen in Figure 14. An enhanced protection for occupant's head is aimed. Figure 14 exhibits that the support takes a considerable amount of stress which is believed to mitigate possible head injuries.

When energy absorption comparison is made between unsupported and supported cases, Figure 15 reveals that a significant amount of total strain energy is absorbed from the impact energy. Decreased amount of impact energy means the deceleration pulse on the occupant is less, which potentially decreases HIC values and the possibility of severe head injuries. As an additional protective strategy, the support can also be placed in lower portions of the B- pillar.

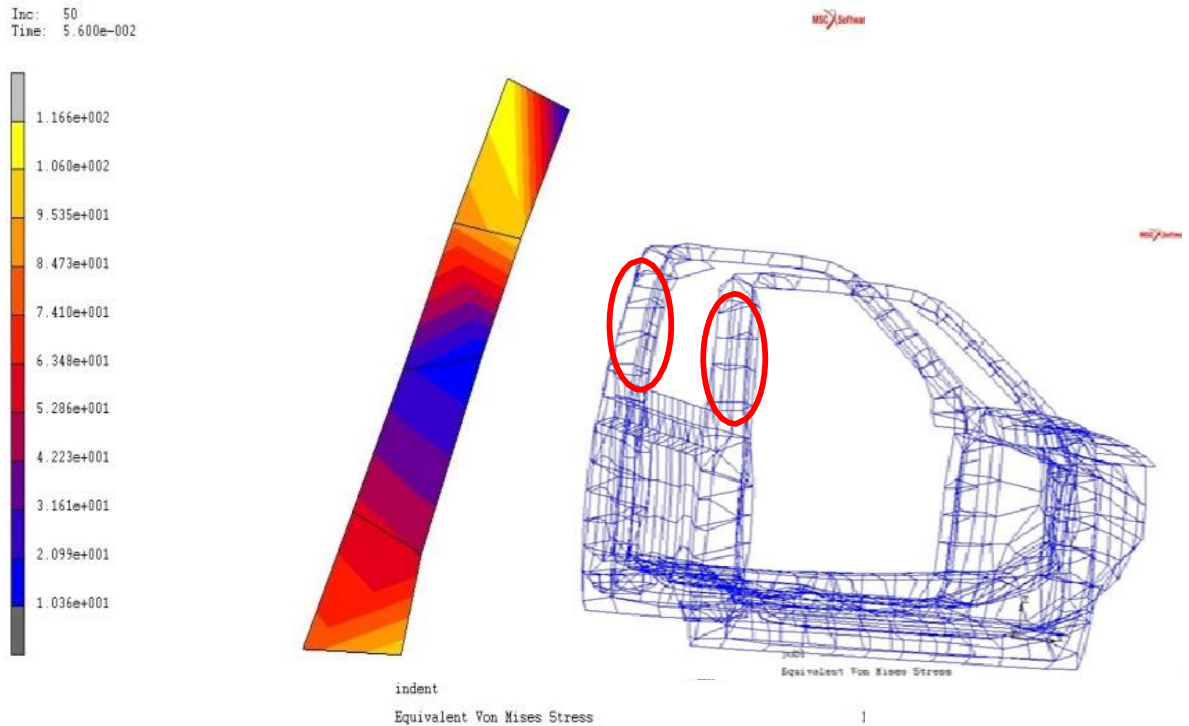


Figure 14. B-pillar support locations and von Mises stresses during impact at full intrusion

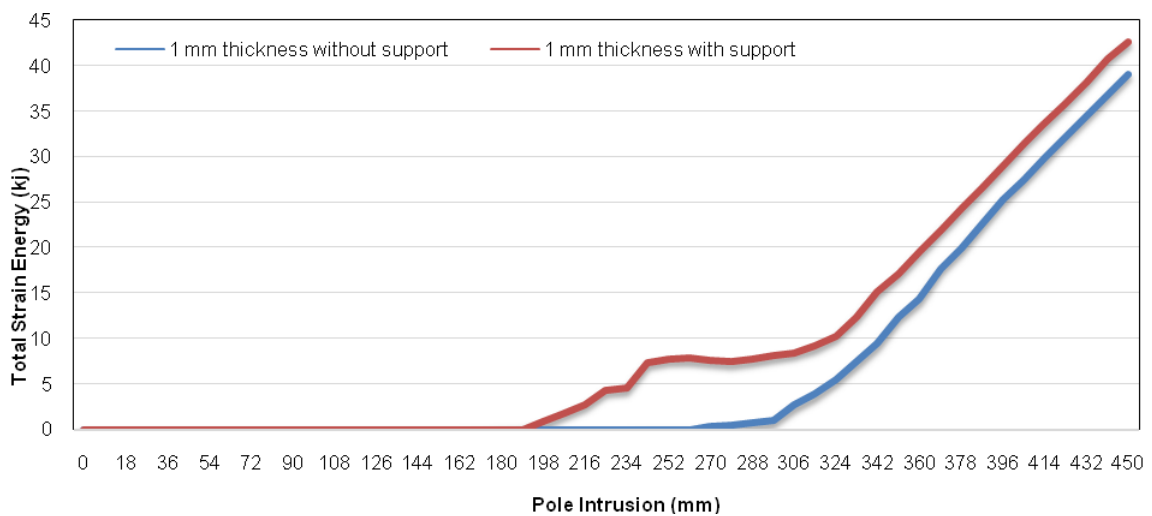


Figure 15. Energy absorption comparison between unsupported and supported cases

#### 4. CONCLUSIONS

The crashworthiness of a pickup truck subjected to pole side impact is investigated in light of various geometric structural changes and modifications conducted in the body of the vehicle.

An effort is made so that the crashworthiness and safety are improved without





compromising from performance and comfort.

For the particular case of the pickup truck investigated, an optimal solution may be achieved when cases 3, 4, and 5 are combined. This solution yields a less thick haulage, thicker cabin with trapezoid zigzag cross-section B-pillar profile with a support. Crashworthiness is anticipated to be improved greatly as none of these factors affect the other directly. In addition to that, a decrease in the weight and an increase in the crashworthiness is expected.

Crashworthiness of the vehicle can be increased by applying maximum mass reduction solutions for the energy absorption efficiency as detailed in the literature [Horstemeyer,

2009]; however, the crash test dummy is reported to be exposed to a higher lateral acceleration to the head and the spine of the dummy when energy absorption resolutions are introduced to the vehicles. Injury criteria based design combined with optimised enhanced energy absorption capabilities of the vehicle structure warrants further research to yield better solutions in terms of occupant protection in road vehicle accidents.

## REFERENCES

1. **ANCAP Safety, (2013)**, "Pole Test", <http://www.ancap.com.au/crashtesting>, accessed in December 2013.
2. **ECE R 11, (1986)**, "Uniform Provisions Concerning the Approval of Vehicles with Regard to Door Latches and Door Retention Components", [http://www.crash-network.com/Regulations/ECE\\_Regulations/ece\\_regulations.html](http://www.crash-network.com/Regulations/ECE_Regulations/ece_regulations.html), accessed in December 2013.
3. **ECE R 95, (2005)**, "Uniform Provisions Concerning the Approval of Vehicles with Regard to the Protection of the Occupants in the Event of a Lateral Collision", [http://www.crash-network.com/Regulations/ECE\\_Regulations/ece\\_regulations.html](http://www.crash-network.com/Regulations/ECE_Regulations/ece_regulations.html), accessed in December 2013.
4. **EURONCAP, (2013)**, "Pole Side Impact", <http://www.euroncap.com/Content-Web-Page/90769bbc-bb74-4129-a046-e586550c3ece/pole-side-impact.aspx>, accessed in December 2013.
5. **FMVSS 214, (2008)**, "Side Impact Protection", NHTSA, USA, <http://www.crash-network.com/Regulations/FMVSS/fmvss.html>, accessed in December 2013
6. **Ford Motor Company (2012)**, "Impact Testing and Modeling of DP600 Front Rails".



<http://www.autosteel.org/~media/Files/Autosteel/Great%20Designs%20in%20Steel/GDIS%202006/10%20%20Impact%20Testing%20and%20Modeling%20of%20DP600%20Front%20Rails.pdf>, accessed in March 2012.

7. **Horstemeyer, M. F., Ren, X. C., Fang, H., Acar, E., and Wang, P. T.**, (2009), "A comparative study of design optimisation methodologies for side-impact crashworthiness using injury-based versus energy-based criterion", *International Journal of Crashworthiness*, Vol.14, No.2, pp 125 – 138.
8. **Jones, N.**, (1997), "Structural Impact", Cambridge University Press.
9. **National Crash Analysis Center (NCAC)**, George Washington University, (1997), "C-1500 Pick-Up Truck Model". <http://www.ncac.gwu.edu/vml/models.html>, accessed in March 2012.
10. **Newman, J. A.**, (1980), "Head injury criteria in automotive crash testing", Stapp Car Crash Conference, SAE Technical Paper 801317.
11. **Teng, T. L., Chang, K. C., and Nguyen, T. H.**, (2008), "Crashworthiness evaluation of side-door beam of vehicle", *TechnischeMechanik*, Vol.28, No.3-4, pp 268 – 278.
12. **Zaouk , A. K., Bedewi, N. E., Kan, C.-D., and Marzougui, D.**, (1997), "Development and Evaluation of a C-1500 Pick-Up Truck Model for Roadside Hardware Impact Simulation", *Proceedings of FHWA Vehicle Crash Analysis Conference*, Publication No. FHWA-RD- 96-212.



## CRASHWORTHINESS OF GUARDRAIL POST EMBEDDED IN COHESIONLESS SOIL

**Sassi ABDELMONAAM**, *sassi@uwindsor.ca*, University of Windsor, Department of Civil and Environmental Engineering, Windsor, On, N9B3P4, Canada

**Faouzi GHRIB**, *fghrib@uwindsor.ca*, University of Windsor, Department of Civil and Environmental Engineering, Windsor, On, N9B3P4, Canada

### ABSTRACT

The purpose of this paper is to conduct a parametric analysis of the crashworthiness of W-beams posts. The evaluation of guardrail post's performance usually involves crash tests which consist of colliding the post with a bogie. Crashworthiness tests try to cover a range of design parameters such as the soil resistance, impact velocity and blockout crushability. When reviewing the existing various dynamic tests conducted to-date, it is apparent that the range of the considered design parameters varies widely. Because of the lack of consistency of the various test conditions, the statistical analysis of the test results is not an easy task. In this paper, the finite element method has been employed as the main tool to conduct the parametric study and generate the statistical data. A finite element model of a typical guardrail post has been developed and calibrated with the results of an impact test. A series of correlations between the different design parameters and the post reaction is established.

**Keywords:** Guardrail post, dynamic test, Finite Element Model, Cohesionless soil

### 1. INTRODUCTION

Strong post W-beam guardrail systems are widely used around the world as an essential hardware to ensure the safety of errant vehicles. Since the change of the design cycle of vehicles is much shorter than that of guardrails, it becomes urgent to review the performance of these systems. For example, in the context of North America, vehicle fleet has changed significantly over the last decades. The private vehicle automobiles' (sedans) market share decreased while Minivans, SUVs and small trucks made a significant increase to reach 25% of the vehicle fleet as of 2002, Ross et al. 2002. Statistical data collected from highway accidents show that SUVs and small trucks vehicles are more susceptible to roll in case of impact with the W-beam guardrail, Reid et al. 1997. It was argued that the increase of rollover risk is due the high impact force magnitude between the vehicle and the guardrail system as well as the higher center of gravity of SUV's when compared to sedans. Previous



research findings suggested that the crashworthiness of highway guardrail systems is dominated mainly by the soil–post interaction. Reid et al., 1997 have shown that the capacity to contain and redirect light trucks and SUVs is strongly correlated to the post stiffness and soil resistance. During impact, guardrail systems dissipate the impact energy mainly through deformations in the vehicle, the soil and the guardrail. Any Poor soil–post interaction may cause the guardrail system to fail performing the intended role and might lead to fatal accidents, Wu and Thomson, 2007. For the case of strong posts, it was found that the barrier performance begins to degrade when the reaction force reaches the level of 50 kN, Reid et al 1997.

The crash analysis of guardrail systems involves highly nonlinear material behavior associated with large deformations due to the impact load. The finite element analysis method appears to be the preferred tool that offers full control over the range of the involved parameters. The different design parameters can be evaluated through an optimization process in order to propose new guardrail design proposals or improve existing one that can reduce the risk of truck rollover, Tabiei and Wu, 2000. Consequently, a correlation of any proposed finite element model with dynamic test is fundamental to gain confidence about its capability and efficiency. Once validated, finite element models become a reliable design tool and relatively inexpensive to evaluate guardrails crashworthiness responses under a wide range of inputs, Tabiei and Wu, 2000.

Sennah et al., (2003) compared the vehicle response impacting guardrail system with different post configuration. The post cross-section and material type were the parameters of the study. A parametric study was conducted by Elmarakebi et al. (2006) to evaluate the effects of key parameters on the response of the pole embedded in soil when impacted by vehicles. These parameters included soil type (clay and sand), pole material type (steel and aluminum), embedment length of the pole, and vehicle impacting speed. This study highlighted the effect of the different parameters on the vehicle response. However, it considered only the case of small vehicles. Due to the limited amount of research conducted to evaluate the effects, the aim of the present paper is to conduct a parametric study on the major design parameters on an isolated post-soil guardrail in sandy soils. Four parameters were selected; they are (i) the impactor speed, (ii) the impactor mass, (iii) the post embedment depth and (iv) the blockout crushability. A finite element model of impactor subjected to an initial velocity impacting a guardrail post was developed and calibrated to the impact tests conducted by Coon et al. 1999. A regression analysis of the data generated by the parametric study allowed the development of series of correlations between the base design parameters and the system performances.

## 2. BASELINE MODEL DEVELOPMENT AND VALIDATION

The horizontal subgrade method was used to simulate the soil-pole interaction which consists of modeling the soil surrounding the structure by a set of nonlinear springs attached to the embedded post. Various empirical expressions are available in the literature for the identification of the modulus of subgrade reaction. However an improved simple method to calculate the subgrade model was used which defined a macro-element comprising a spring, a mass and a dashpot. The soil is decomposed into independent layers of 100 mm where the behaviour is simulated by one macro-element as shown in Figure 1. The overall soil reaction is determined as the resultant of the all the macro-elements resultant. The lumped mass represents the mass of the soil being involved during the impact. The role of the springs is to store the elastic energy and simulate the non-linear behaviour of the soil. The inclusion of dashpots is a simplistic method to account for the energy dissipation observed in crash tests. The discretization of the post-soil interface is therefore fully modeled based on the three mechanical parameters: the nonlinear stiffness, mass and damper coefficient.

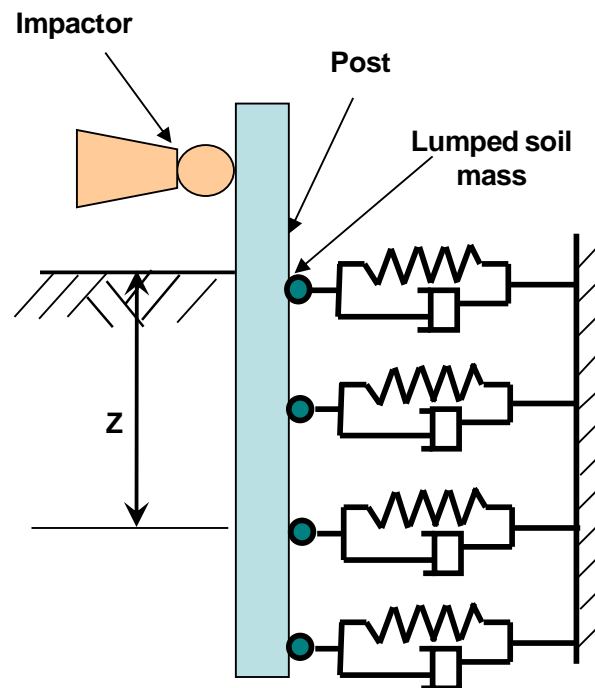


Figure 1: Proposed dynamic model for lateral post response.

To validate the proposed finite element model, the results of the dynamic tests conducted by Coon et al. 1999 are selected as baseline. These tests will be used to calibrate the added masses and dashpots' coefficients. The cart impactor consisted of a rigid nose bogie vehicle of 946 kg mass, instrumented with an accelerometer to measure the lateral deceleration during the impact. Four tests were conducted with W-beam posts, corresponding to speeds



of 4.6 m/s, 5.4 m/s, 5.9 m/s and 8.9 m/s, respectively. The soil density ranged from 1980 kg/m<sup>3</sup> to 2240 kg/m<sup>3</sup> and the tests were conducted in soils with no significant moisture. The length of the post was 1830 mm with an embedment of 1100 mm. The impact point of the bogie with the post was located at 550 mm above the ground level. The development of the baseline finite element model and its validation is presented briefly since it was covered more in details in others reference, Sassi 2011, Sassi 2014.

### Spring Stiffness Identification

The spring stiffness was calculated by the method of Habibagahi and Langer (1984). The horizontal stiffness  $K_h$ , is defined as follows:

$$K_h = N_q \frac{\sigma'}{y} \quad (1)$$

where  $\sigma'$  is the effective overburden stress,  $y$  is the lateral deflection and  $N_q$  denotes the lateral bearing capacity and it is defined as function of the deflection  $y$  and the depth  $z$ , whereas  $B$  is the width of the post and  $\varphi$  the soil friction .

$$N_q = A \left[ \frac{2}{3}(\varphi - 30) + 1 \right] \sqrt{\frac{z}{B}} \quad (2)$$

$A$  is a dimensionless parameter which depends on the deflection  $y$  is given by:

$$A = 15,276 - 14.09e^{-0.1245 y} \quad (3)$$

### Evaluation of the Lumped Mass

The lumped mass of the macro-element is defined as the mass per layer involved during the impact. To determine the size of the block activated during the impact, the results of a continuum finite element model were used. The continuum model consists of a post embedded in a soil block. The soil surrounding the post was modeled as a cylinder medium in which the post was embedded at its center. The size of the soil block used in the finite element model was 2.7 m whereas the depth of the block was 2.0 m. The soil was modeled using 8-node hexahedron and the parameters of the soil and the guardrail post were determined from the literature, Sassi 2011. The criterion defining the mass activated during the impact was based on a displacement threshold  $d_f$ . The region with a displacement higher than a given displacement  $d_f$  was assumed to be involved in the inertia reaction and it was included in the “active mass”. The contribution of the mass exhibiting lower displacement is neglected. A parametric study was conducted to determine the threshold  $d_f$ , and it was found that a displacement 2 mm produced accurate results.



### Determination of the Damping Coefficient

To determine the amount of damping coefficient,  $C_c$ , the damping is assumed viscous and expressed as a percentage of the critical value. A parametric study has been conducted to determine the damping ratio by comparing the average load, the peak load and the maximum impactor displacement of the simulation to the dynamic test results. The damping ratio,  $\xi$ , of 12% gave the optimum results matching the load deflection curve of the post and the deflection of the post with time as shown in Table 1.

Table 1: Comparison of peak load, average force and maximum deflection of dynamic test with the finite element simulation.

	Maximum Deflection (mm)			Average Force (kN)			Peak Force (kN)		
	Test	Improved Subgrade Model	Continuum method	Test	Improved Subgrade Model	Continuum method	Test	Improved Subgrade Model	Continuum method
Test #1 (4.6 m/s)	234	233	240	42.8	43.0	41.1	64.0	53.1	50.4
Test #2 (5.4 m/s)	314	296	312	43.9	45.9	42.5	66.9	57.8	51.2
Test #3 (5.9 m/s)	348	353	338	47.3	47.9	46.3	67.0	64.3	52.3
Test #4* (8.9 m/s)	Over ride	Over ride	Over ride	NA	56.3	55.3	104.7	97.2	85.2

The post used in test 4 is W150x23.5 instead of W150x13.5

### Model Correlation

As summarized in Table 1, the numerical simulations results show a good agreement to the dynamic test results. These findings demonstrate that the proposed subgrade model including an active masses and dampers predicts accurately the post behaviour during the impact while keeping the computational time reasonable.

### 3. EVALUATION OF THE IMPACTOR'S SPEED EFFECT

To study the impact speed effect on the guardrail post response, a velocity range of 3 to 10 m/s was considered. A literature survey of the experimental tests showed that the impactor

speed varies in general from 4.6 m/s, Coon et al. 1999 to 9.4 m/s Polivka et al. 2004. It is to be noted that a speed of 9 m/s represents approximately the severity of a vehicle impacting a guardrail at 100 km/h and an angle of 25°.

Results of the simulations show that the average load increases with the speed from 35.4 kN, for the lower speed of 3 m/s, to 59.6 kN, corresponding to higher speed of 10 m/s, whereas the peak load increases from 43.3 kN to 106.6 kN, respectively. The load-time history shows a first peak for all speeds that occurs between 7 and 9 ms as shown in Figure 2. This initial peak is more pronounced for speeds higher than 4 m/s. A linear regression shows that the relation of the peak and average loads are given:

$$F_{peak} = 10.795 V \quad (4)$$

$$F_{average} = 3.439 V + 26.863 \quad (5)$$

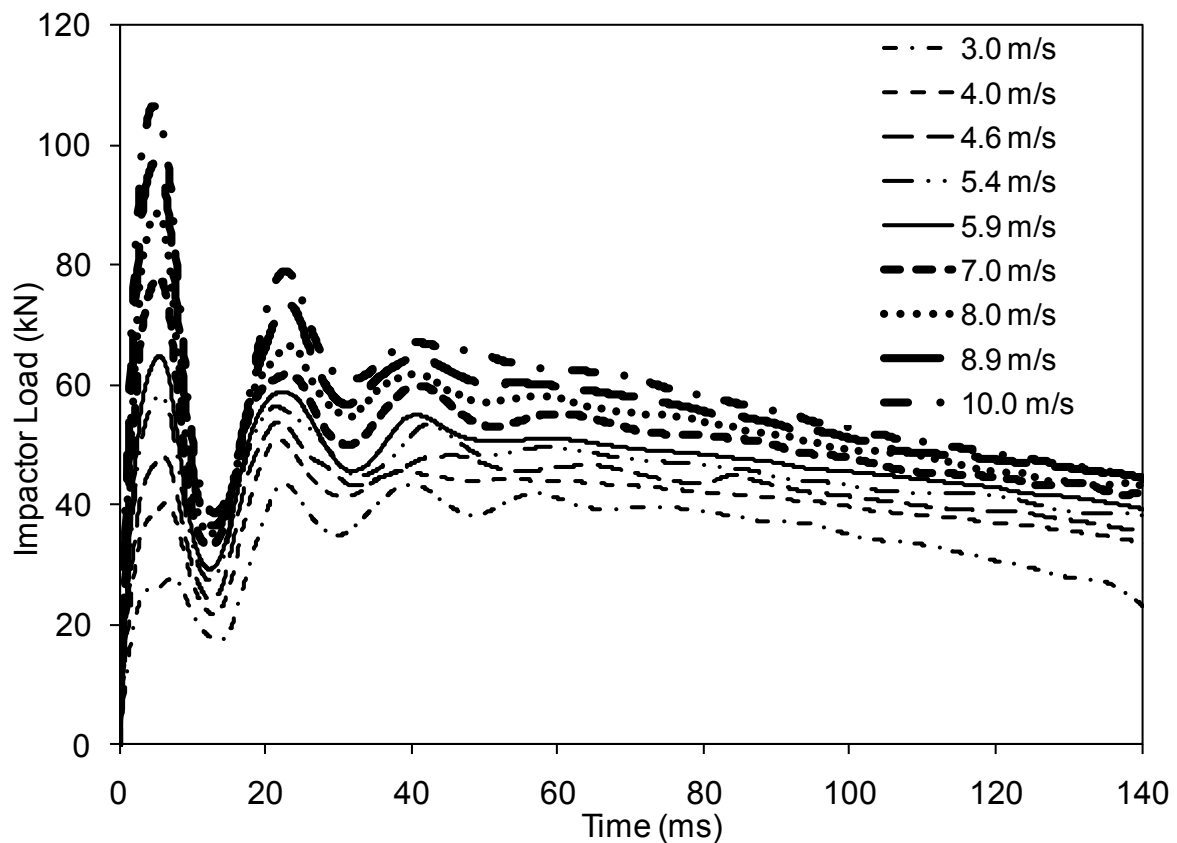


Figure 2: Time histories of the impactor load for different impact speed.



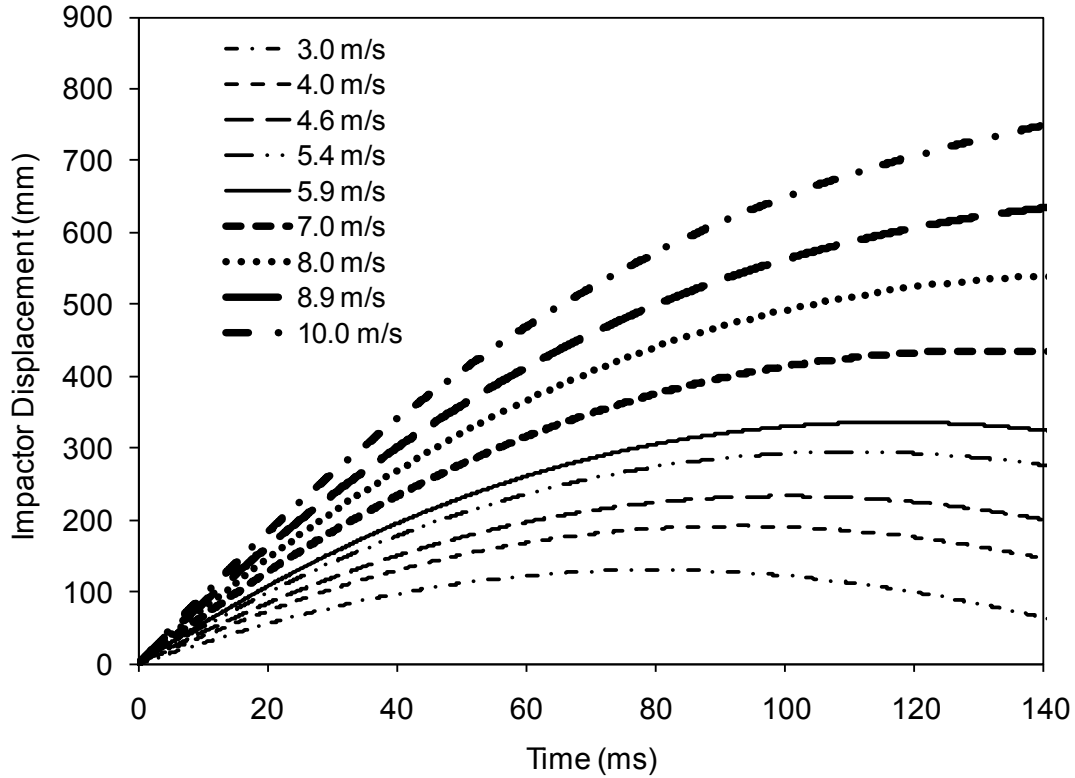


Figure 3: Variation of the impactor displacement as function of time for different impact speed.

The maximum displacement increases from 130 mm at an impact speed of 3 m/s to 796 mm at 10.0 m/s, Figure 3. For a speed higher than 9 m/s, the post was not able to stop the impactor which continued its trajectory and overrode the post. A nonlinear regression of the relationship between the maximum displacement defined in (m) and the impactor speed in (m/s) is shown in Figure 8 and given by:

$$D_{max} = 5.297 V^2 + 25.839 V \quad (6)$$

#### 4. EFFECT OF THE POST EMBEDMENT DEPTH

Simulations of the guardrail post embedded at depth ranging from 800 to 1300 mm were conducted to assess the soil reaction. Since the passive reaction applied to the post increases with the depth, the simulation used a W152x23.8 post (W6x16) instead of the W152x13.4 (W6x9) post to minimize the post yielding and to provide better comparison of the post response for the different embedment depths. Similar approach was used by Kuipers and Reid 2003 to determine the dynamic properties of soil-post at various embedment depths under different loading conditions.

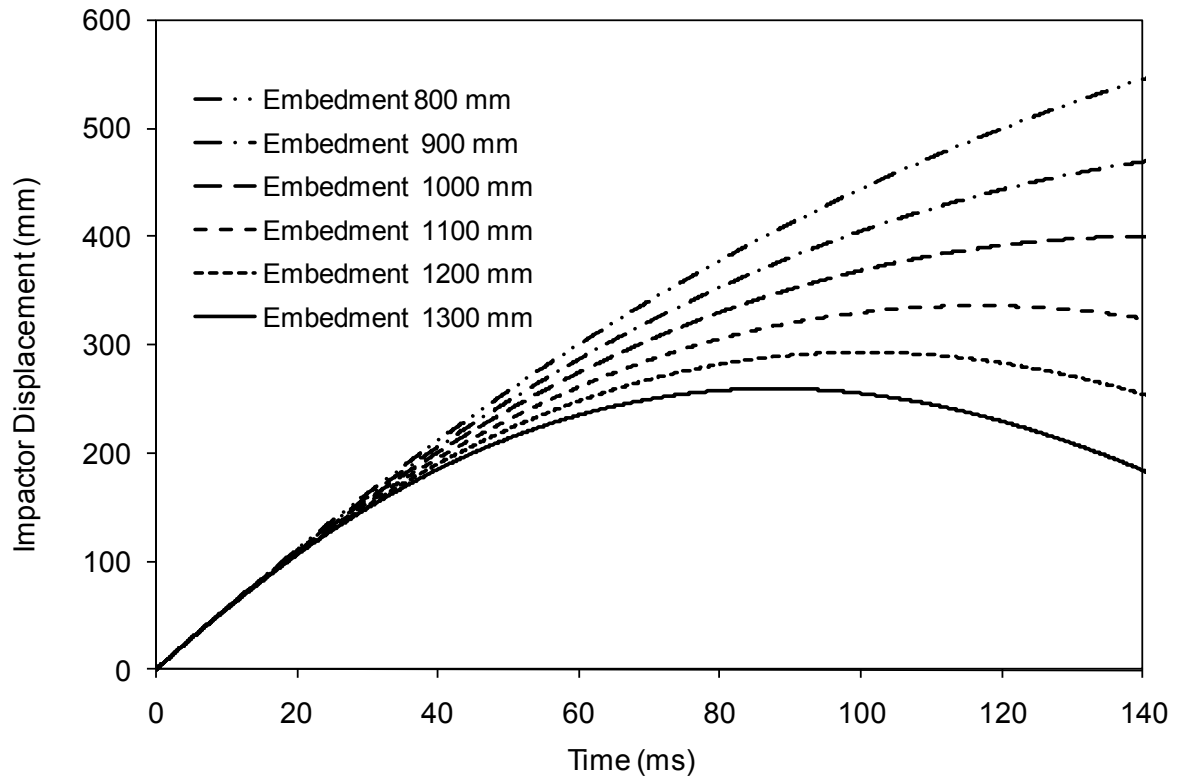


Figure 4: Variation of the impactor displacement as function time for different depth embedment.

The impactor displacement time history illustrated in Figure 4, shows that the displacement decreases with the depth from 400 mm at 1000 mm embedment to 260 mm for 1300 mm embedment. For a post embedded at 1000 mm or more in the soil, the impactor was stopped by the post-soil reaction. However, the impactor overrides the post for the embedment of 800 and 900 mm. The average load increased from 26 kN for a depth of 800 mm to 60.9 kN for 1300 mm. These simulation results are in-line with the experiments conducted by Kuipers and Reid 2003. A nonlinear regression of the maximum impactor displacement as a function of the post embedment,  $Z$ , is given by:

$$D_{max} = 0.4088 Z^{-1.833} \quad (7)$$

where  $Z$  and  $D_{max}$  are in meters.

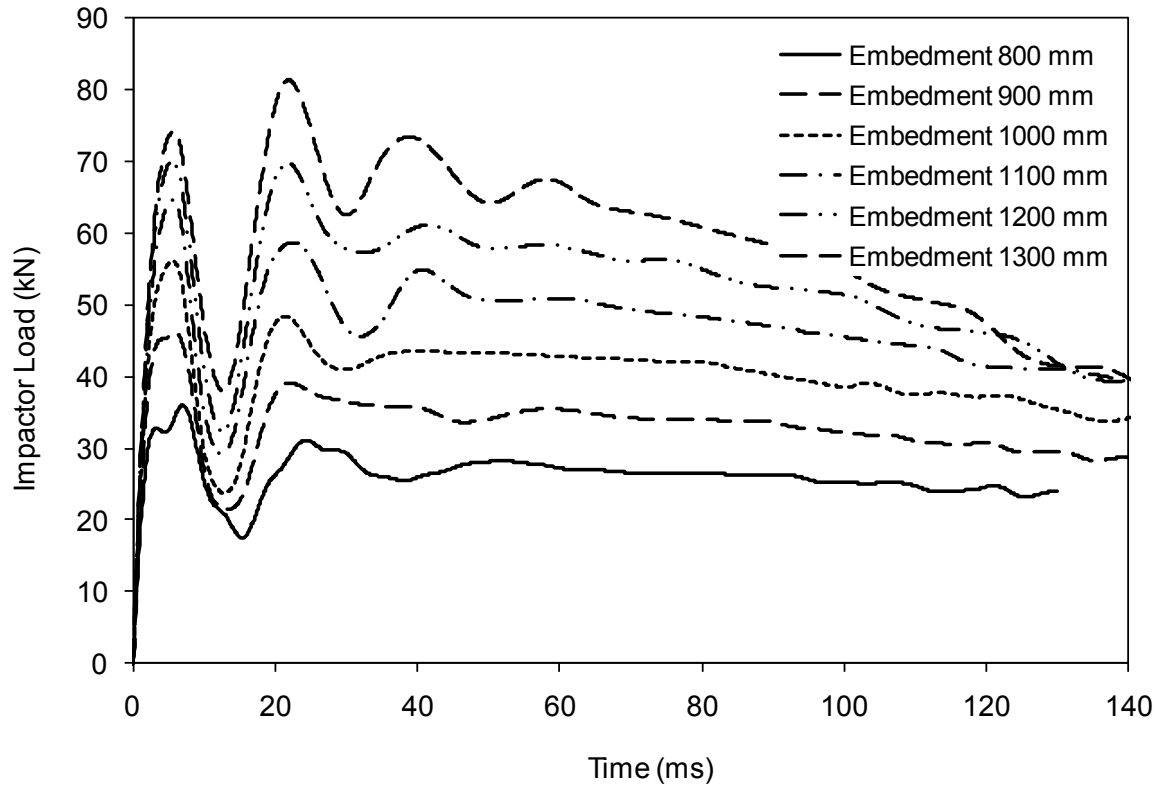


Figure 5: Variation of the impactor reaction for different depth embedment.

Figure 5 shows that the peak load increases with the depth from 64.1 kN to 81.4 kN when the embedment depth increased from 1100 mm to 1300 mm. The variations of the peak and average load as function of the depth follow a linear relationship as reported in described by:

$$P_{max} = 0.088 Z - 33.347 \quad (8)$$

$$P_{avg} = 0.0697 Z - 28.953 \quad (9)$$

## 5. EFFECT OF THE IMPACTOR MASS

To assess the effect of the impactor mass, simulations of the guardrail post embedded in the soil and impacted by a cart with different masses were conducted. The impactor mass varied from 500 to 3000 kg to cover the range of masses used in the literature. Kennedy et al., 2004 used a pendulum with a mass of 878 kg whereas Dewey (1982) used a cart of 2324 kg. The impact speed of 7 m/s remains the same for all masses.

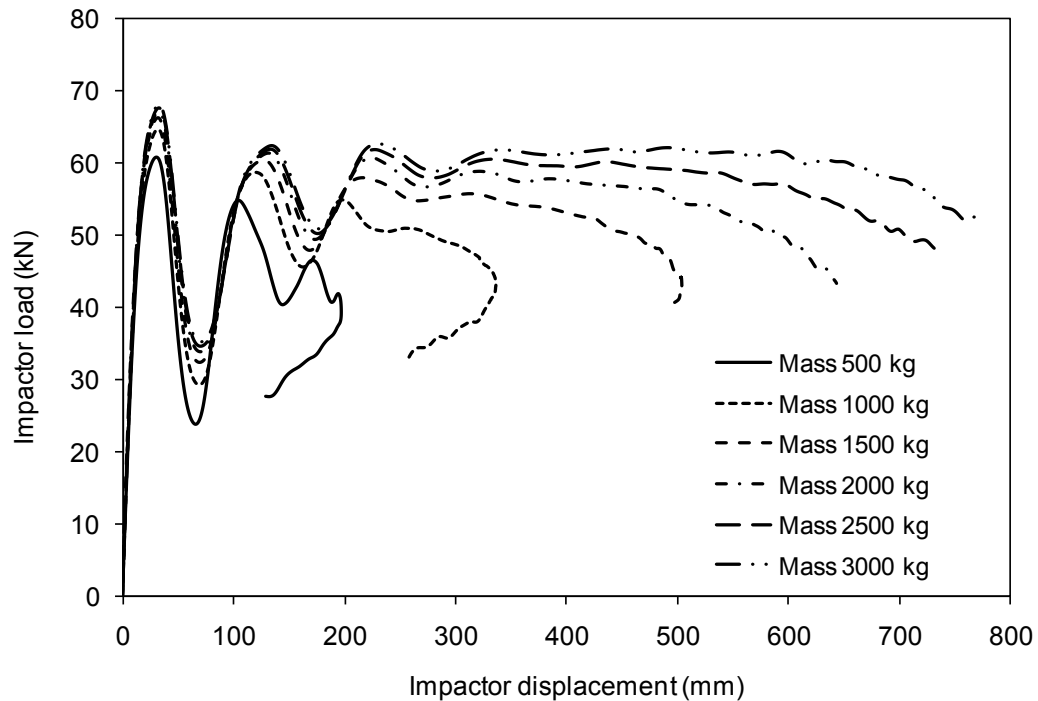


Figure 6: Effect of the impactor mass on the load-deflection of the guardrail post

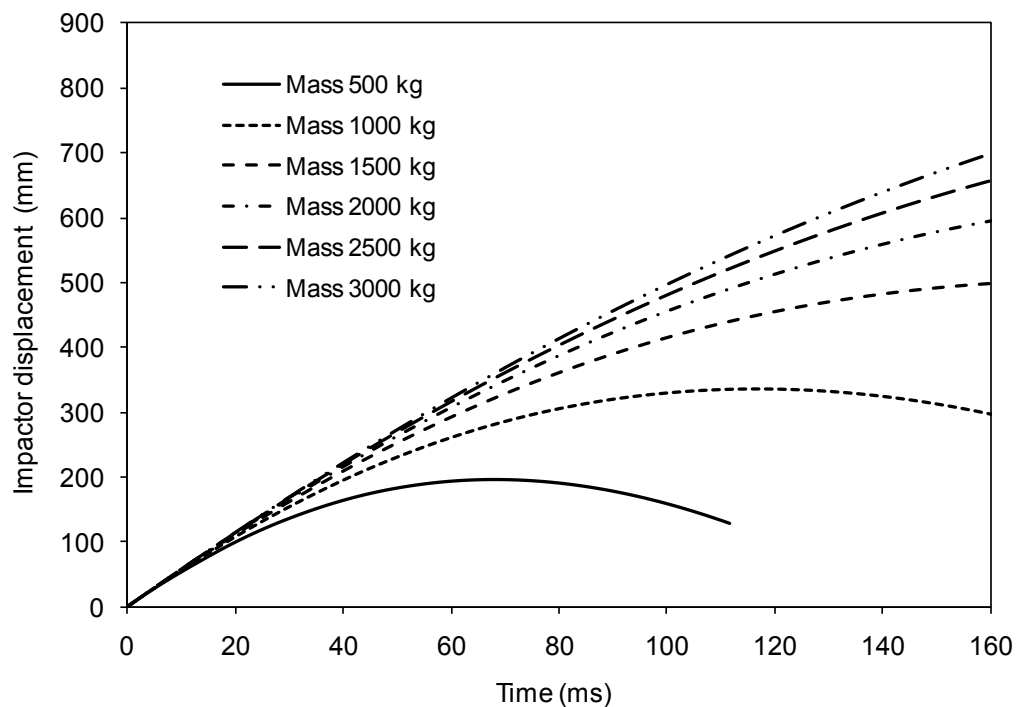


Figure 7: Variation of the impactor displacement for different mass impactor.

The load deflection responses of various impactor masses are shown in Figure 6. It can be seen that the guardrail post displacement increases with the mass. The curves show that the initial peak load is slightly sensitive to the impactor mass and occurs approximately at a

displacement of 35 mm. The maximum load increases slightly with the impactor mass from 60.7 kN for a mass of 500 kg to 68.0 kN for the heavier impactor (3000 kg). Figure 7 shows that the impactor with a mass between 500 kg to 1500 kg was stopped by the soil post reaction whereas the impactor overrides the post for a mass above 2000 kg. Linear regression of the maximum displacement as function of the impactor mass shows that the relationship is given by  $D_{\max} = 0.3494 M_{\text{impactor}}$  where  $D_{\max}$  is the maximum displacement of the impactor in (mm) and  $M_{\text{impactor}}$  is the mass of the impactor in (kg). Figure 8 reports the dissipated energy as function of the impactor displacement and shows that the dissipated energy increases linearly with the mass of the impactor. However the rate of dissipated energy appears to remain the same for all impactor masses, suggesting that the post response is independent of the impactor mass.

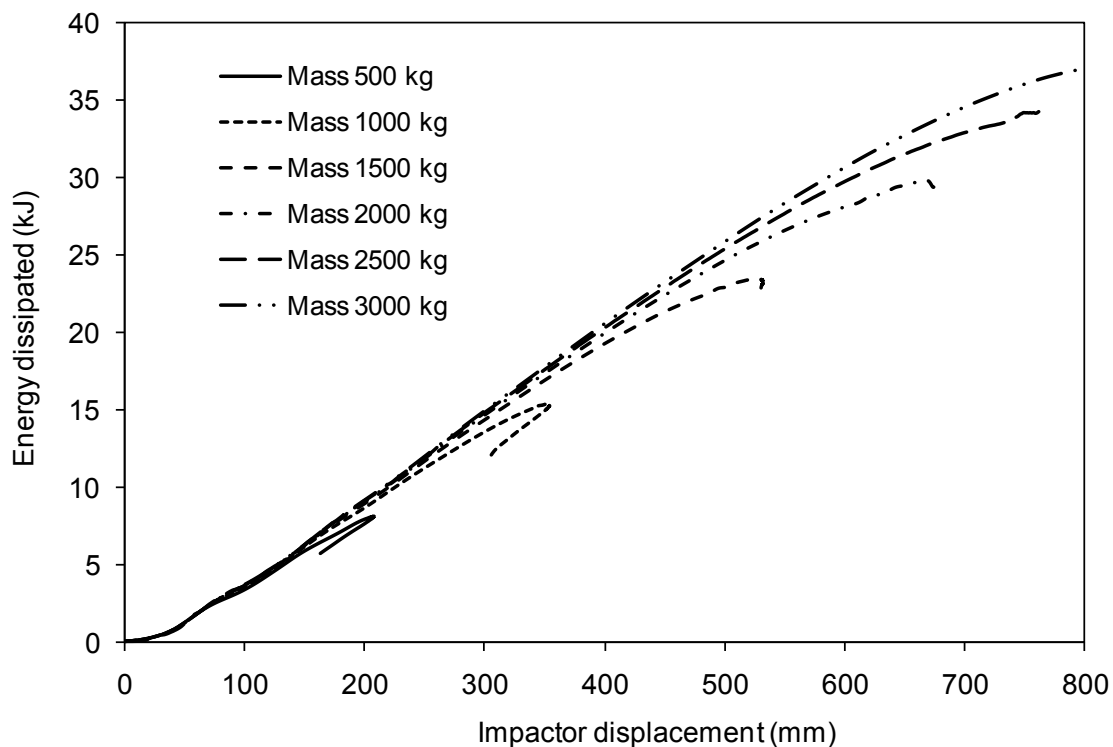


Figure 8: Energy dissipation of the guardrail post for different mass impactor.

## 6. EFFECT OF COMPRESSIBLE BLOCKOUT

During the impact, the energy could be dissipated through the soil deformation and through the post W beam structure. However it is easier to control and to maximize the energy dissipation by redesigning the blockout spacer between the post and the guardrail. For these reason, five collapsible blockout proposals with different cross sections and thicknesses were considered and integrated in the baseline guardrail post prototype as shown in Figure 9. The dimensions of these models were similar to the original rectangular wood piece

(200x150x360) and made of HSLA (High Strength Low Alloy) having a Young's modulus  $E = 205 \text{ GPa}$ , a density  $= 7850 \text{ kg/m}^3$  and a yield stress  $\sigma_0 = 615 \text{ MPa}$ . HSLA 340 which is a high strength steel commonly used in the automotive area, has been considered for all the design scenarios to fabricate the blockout system because of its good fatigue strength, its low price, its ductility and its welding capability. Five blockout components considered in this work consisted of a simplified crash box for frontal impact with a square section (Figure 11). **Blockout 1** consisted of 3 square tubes with  $80 \times 80 \text{ mm}$  cross-section and a wall thickness of  $2 \text{ mm}$ . The side length of the enclosed square section was  $150 \text{ mm}$ . The three tubes were sandwiched between two metal plates of  $2 \text{ mm}$  thickness from the same material as the square tube. **Blockout 2** was the same as blockout geometry # 1 with the exception that the wall box thickness was reduced to  $1.0 \text{ mm}$ . **Blockout 3** was similar system as blockout #1 and #2 but was pre-triggered symmetrically in both sides of the tube. **Blockout 4** was  $100 \times 200 \times 360 \text{ mm}$  rectangular tube with a wall thickness of  $3.5 \text{ mm}$  and made from the same material as systems 1 and 3. The block was attached to the post using 2 bolts simulated as springs. **Blockout 5** was similar to blockout #4 but the wall thickness was reduced to be  $2.5 \text{ mm}$ .

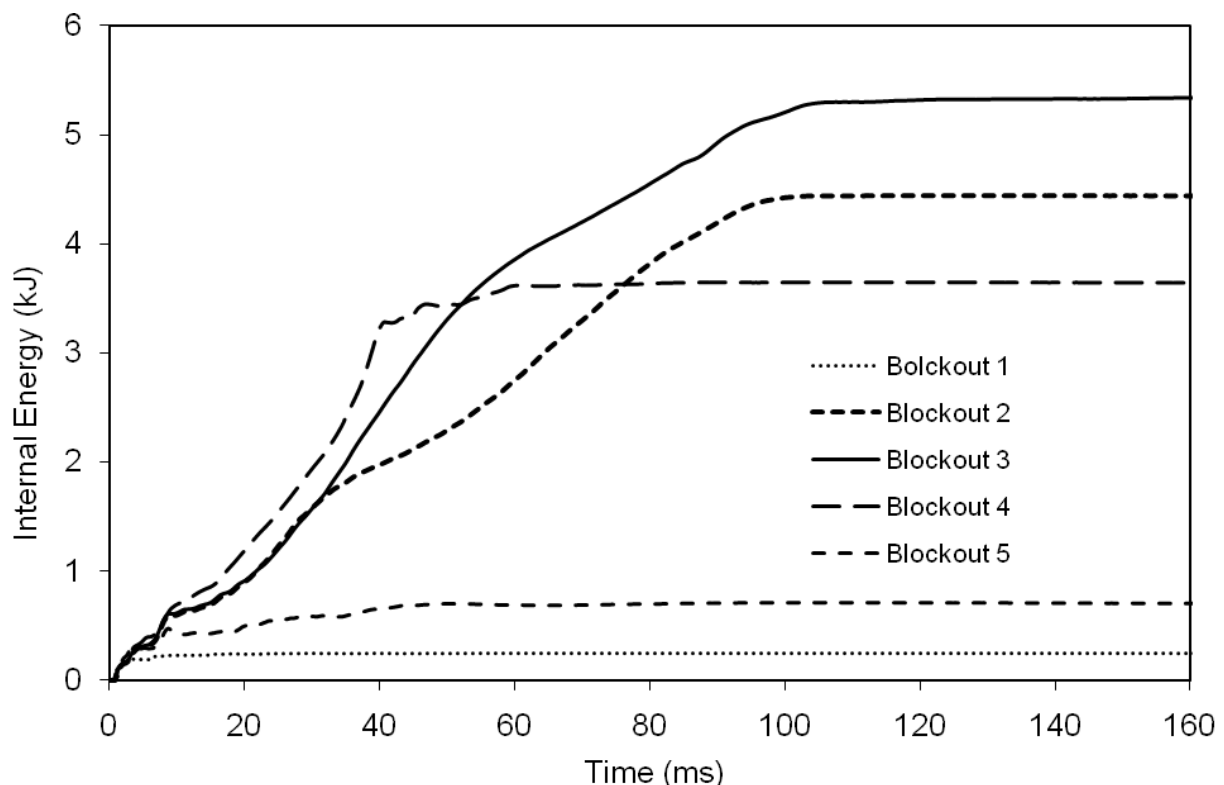


Figure 9: Internal Energy dissipation for the different crushable blockout systems.

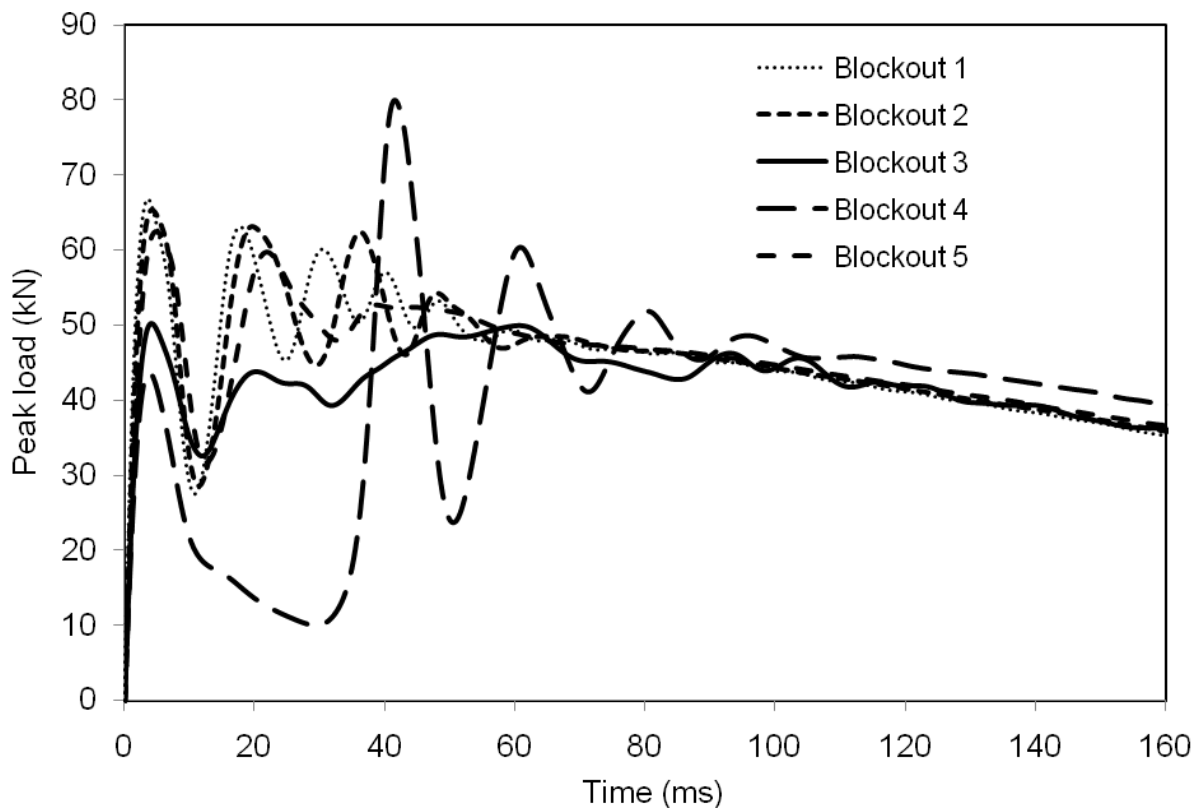


Figure 10: Variation of the Impactor load for different crushable blockout system.

Table 2: Results of the energy dissipation for different blockout designs.

Design #	Energy Dissipated (kJ)	Maximum Load (kN)	Average load (kN)	Impactor displacement (mm)
Block 1	0.25	66.8	48.4	329.8
Block 2	4.44	65.2	48.2	331.6
Block 3	5.31	50.3	43.9	378.3
Block 4	3.64	80.0	38.9	456.6
Block 5	0.71	62.5	47.9	336.3
Baseline	0	64.1	48.1	336.0



The results of the analysis are summarized in Table 2, Figures 9 and 10. It is clearly indicated that the performance of the different blackout systems is quite different. Blockout #3, designed with three longitudinal tubes and triggered on both sides, dissipated the maximum energy (5.31 kJ) whereas the same design Blockout 1 with a 2.0 mm thickness reacts as a rigid block similar to the baseline: a peak load of 66.8 kN, an average load of 48.4 kN and a maximum displacement of 330 mm. The vertical tube with a thickness of 2.5 mm (blockout 4) absorbs 3.6 kJ within the first 50 ms as shown in Figure 9, and then collapsed on the post, the peak load increased to 80 kN as shown in Figure 10. The same vertical tube of 3.5 mm thickness (blockout 5) absorbs even less energy, 0.71 kJ, because only a localized deformation was created at the lower part of the blackout as shown in Figure 11. The average load remained almost the same and the maximum impactor displacement remains similar to the baseline model (336 mm). The triggers used in blockout #3 helped the development of a stable asymmetric crushing mode, and contributed in attenuation of the first peak load from 64.1 kN to 50.3 kN



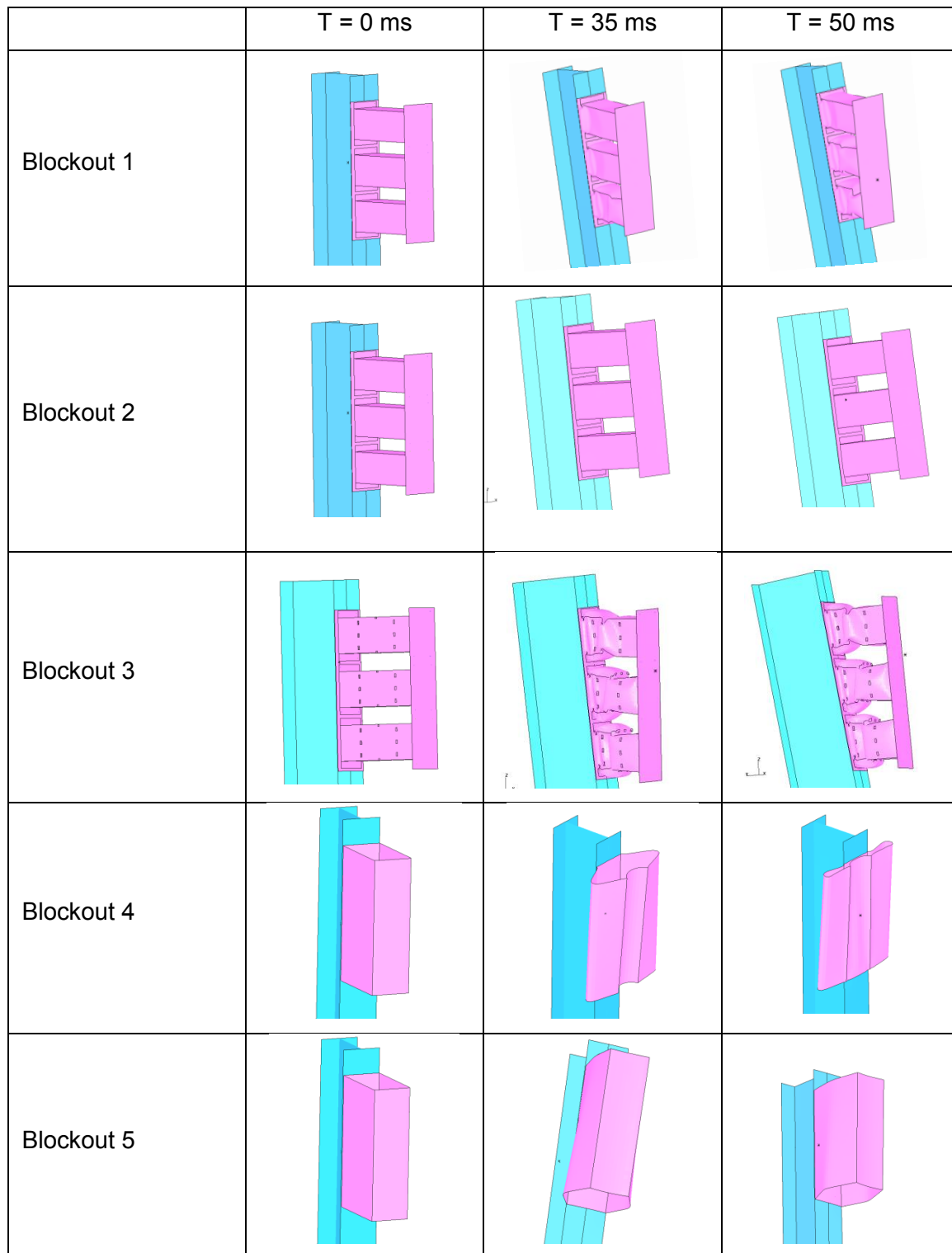


Figure 11: Behavior of the various crushable systems during the impact.

## 7. CONCLUSIONS

A macro-element comprising a spring, a mass and a dashpot was used to simulate the post-soil interaction in order to conduct an exhaustive parametric finite element study and investigate the effects of the different design parameters on guardrails post reaction. The response of the guardrail post was determined under different loading conditions and the



load deflection curve for the different parameters was determined and compared to a baseline test model. Such parameters include impactor speed and mass, post depth and the crushable blockout system.

The study shows that that the peak load and the impactor displacement increase with the speed following a linear equation. For high speeds, higher than 9 m/s, the impactor was not stopped by the post reaction. For lower speeds, lower than 3 m/s, the strain rate effect seems to be negligible.

For the current case, the peak load increases with the depth following a first-degree equation whereas the impactor displacement decreases with depth following a power function. For an embedment depth less 1000 m, the impactor was able to override the post.

The post rail undergoes higher displacement with the heavier weight impactor than with the lighter one. However, the maximum reaction remains quasi constant with the increase of the impactor mass. The maximum displacement of the impactor increases linearly with the mass and override the post for mass higher than 2000 kg. However, the rate of energy dissipation remains the same for all impactor masses.

The crushable system implemented as a replacement of the conventional rigid blockout system was able to attenuate the peak load below 50 kN and absorb more energy than the baseline. This performance suggests that the crushable blockout is able to reduce the impactor load transferred to the post during a full crash of a vehicle impacting the guardrail.

## REFERENCES

1. **Coon, B.A., Reid, J.D. and Rhode, J.R.** (1999) "Dynamic Impact Testing of Guardrail Posts Embedded in Soil" Research Report No TRP-03-77-98, Midwest Roadside Safety Facility, University of Nebraska-Lincoln, Lincoln, Nebraska.
2. **Dewey, J.F.**, (1982) "A Study of the Soil-Structure Interaction Behavior of Highway Guardrail Posts" Master thesis, Texas Transport Institute, Texas A&M University.
3. **Elmarakbi, A., Vesenjaj, M. and Sennah, K.** (2005) "Finite-element simulation of an improved traffic W-shape guardrail system in vehicle collision." Proceedings, Canadian Multidisciplinary Road Safety Conference CMRSC-XV, Fredericton, NB, pp. 1-8.
4. **Habibagahi, K and. Langer J.A.**, (1984) "Horizontal Subgrade Modulus of Granular Soils" Laterally Loaded Deep Foundations, ASTM Special Technical Publication 835, Langer Mosely and Thompson editors, American Society for Testing Materials 1984, pp. 21-34.



5. **Hampton C. E., Gabler H. C.,** (2012) "Crash Performance of Strong-Post W-beam Guardrail with Missing Blockouts" *International Journal of Crashworthiness* , Volume 17 No 1, pp 93-103.
6. **Kennedy, J.C., Plaxico, C.A. and Miele C. R.**(2004) "Design Development and Qualification of New Guardrail Post" *Transportation Research Record*, paper No. 04-2936.
7. **Kuipers B.D and Reid, J.D.** (2003) "Testing of W152x23.8 (W6x16) Steel posts-Soil embedment depth study for the Midwest guardrail system (Non-propriety guardrail system)" MwRSF Research Report No. TRP-03-136-03, Final report to the Midwest States Regional pooled fund program, Midwest roadside safety facility, University of Nebraska-Lincoln, Lincoln, Nebraska, June 12, 2003.
8. **Polivka, K.A., Faller, R.K., Sicking, D.L., Reid, J.D., Rohde, J.R., Holloway, J.C., Bielenber, B.W. and Kuipers, B.D.** (2004) "Development of the Midwest Guardrail System (MGS) for Standard and Reduced Post Spacing and in Combination with Curbs" MwRSF, Final Report 1999-2004, Research Report No. TRP-03-139-04, September 2004.
9. **Reid, J.D., Sicking, D.L. Faller R.K. and Pfeifer, B.G.** (1997) "Development of a New Guardrail System" *Transport Research Record*, 1599, TRB, National Research Council, Washington, D.C. 1997, pp. 72-80
10. **Ross, H.E., Bligh, R.P. and Mak, K.K.** (2002) "Evaluation of Roadside, Features to Accommodate Vans, Minivans, Pickup Trucks, and 4-Wheel Drive Vehicles" Report 471, Transportation Research Board, National Research Council, Washington DC, 2002.
11. **Sassi, A.,** (2014) "Effect of the blockout crushability on the response of guardrail post subjected to lateral impact" *International Journal of Crashworthiness*, Volume 19, Issue1, pages 13-26.
12. **Sassi, A.** (2011) "Analysis of W-Beam Guardrail Systems Subjected to Lateral Impact" Ph.D. dissertation, Civil Engineering, University of Windsor, Canada.
13. **Sennah, K., Samaan, M. and Elmarakbi. A.** (2003) "Impact performance of flexible guardrail systems using LS-DYNA." *Proceedings of the 4th European LS-DYNA Conference*, Ulm, Germany, pp. 1-9.
14. **Tabiei, A., and Wu, J.** (2000) "Roadmap for Crashworthiness Finite Element Simulation of Roadside Safety Structures" *International Journal Finite Elements in Analysis and Design*, Vol. 34, No. 2, pp. 145-157, 2000.
15. **Wu, W. and Thomson, R,** (2007): "A study of the Interaction Between a Guardrail post and Soil During Qquasi-static and dynamic loading" *International Journal of Impact Engineering*" Volume 34, Issue 5, May 2007, Pages 883-898.





## **EFFECTS OF CHASSIS GEOMETRY ON STRUCTURAL CRASHWORTHINESS OF A PICKUP TRUCK IN FULL-FRONTAL IMPACTS**

**Semih DAĞDEVİREN**, smhdagdeviren@gmail.com Arçelik A.Ş. –Washing Machines Divison, Altınordu Cad., No: 3, Organize Sanayi Bölgesi, Sincan, 06930, Ankara, Turkey

**Mecit YAVUZ**, mecityavuz@windowslive.com Arçelik A.Ş. –Directorate of Consumer Support & Spare Parts, Çayirova Campus, Tuzla, 34950, İstanbul, Turkey

**Volkan ESAT**, evolkan@metu.edu.tr Middle East Technical University – Northern Cyprus Campus, Kalkanlı, Güzelyurt, KKTC, Mersin 10, Turkey

### **ABSTRACT**

Automobile chassis is a major element of structural crashworthiness in road motor vehicles. Various chassis geometry and topology research studies have been conducted to improve crash energy absorption characteristics of the chassis. This study aims to contribute to the investigations on the effects of chassis geometry over crashworthiness, particularly focusing on the structure of a ladder frame chassis subjected to full-frontal collisions. Preliminary work has been conducted to evaluate the behavior of steel beam profiles under impact loading through finite element (FE) modelling, which helps understand the mechanics of the particular beams chosen as chassis elements. Another finite element (FE) model is developed utilising a previously generated mesh of a pickup truck. The FE model is employed to simulate full-frontal crash test scenarios on the isolated chassis as well as on the whole body of the vehicle. Crash energy absorption results and reaction forces are collected for different thicknesses and beam profile cross sections of the vehicle chassis. Computational results exhibit good agreement with experimental findings.

**Keywords:** Chassis geometry, Crashworthiness, Crash energy, Finite element analysis, Full- frontal impact

### **1. INTRODUCTION**

Accidents are one of the main reasons of death for people across the globe. Automobile accidents constitute about 49% of the overall accidents, which result in

fatalities as well as various injuries [Teng et al., 2008]. According to the most recent motor vehicle accident statistical analysis reports in the USA and Europe combined, more than 60,000 fatalities and millions of injuries occur on the roads due to motor vehicle accidents every year [U.S. Census Bureau, 2012a, U.S. Census Bureau, 2012b, European Commission, 2012]. Statistical data show that improving crashworthiness of road motor vehicles is vital for enhanced safety of occupants in road accidents.

Active safety (preventive or primary) systems are based on the control algorithms that engage in case of a risk of accident to increase the drivers control over the vehicle or warn the driver before the accident. On the other hand, passive (secondary) safety precautions such as material or structural improvements in the design of the vehicle body are taken to mitigate the negative consequences in case of a road accident. Passive safety systems can be divided into the two subgroups as internal safety and external safety. External safety represents all design features on the body of the car to decrease the number of injuries for the pedestrians, cyclists and motor cyclists. On the other hand, internal safety embodies all precautions to minimize the forces and accelerations which affect occupants in the vehicle. Internal safety precautions must provide enough critical volume in the car for the survival of the people during a crash. Being one of the internal passive safety precautions, deformation behaviour of the vehicle body, and particularly the chassis, plays an important role in the safety of the occupant during collisions.

The chassis of the vehicle is considered to be a major passive safety element. The chassis, which can be defined as the base frame of a motor vehicle, is known to absorb most part of the impact energy compared to other structural elements of the vehicle in frontal collisions. For most of today's family cars, the body of the vehicle and chassis are designed as an integrated unit called as monocoque body shell. Monocoque chassis may differ from vehicle to vehicle due to various design considerations. Therefore, it is relatively more complicated and less viable to consider a typical monocoque chassis for the investigation of generic chassis responses to impacts. Specific analyses may be carried out for a particular monocoque chassis chosen. The ladder frame chassis is a relatively older technology for most family segment automobiles, however still used predominantly for larger vehicles such as pickup trucks. Although frame topologies and geometries vary, the general structure of ladder frame chassis does not change significantly from vehicle to vehicle.

During a collision, chassis absorbs a significant amount of the impact energy, therefore considerably determines the behaviour of the overall vehicle structure.

The chassis absorbs the energy in some consecutive stages. Firstly, the compressive stresses in the longitudinal chassis frames begin to increase rapidly as the applied load increases. Secondly, a critical load is reached when the walls buckle on the weakest elements of the chassis showing a local collapse or folding of the beam. Then, the folded edges of the beam support the axial load through its collapsed walls. As a result of this failure mechanism, the load carrying capacity of the chassis drops as the walls continue to buckle and fold via edge yielding while the energy from the collision is being absorbed. Research studies have been conducted to enhance the energy absorbing potential of structural chassis elements during collisions. Different types of geometries are suggested for the structure to absorb the most amount of energy with stronger and lighter materials [Giess and Thomas, 1998, Yamazaki and Han, 1999]. However, effects of different cross-sectional geometries in enhancing the chassis energy absorption are not covered by the aforementioned research studies. A New Car Assessment Programme (NCAP) performance comparison is made by FORD [2012] for different geometries of the front rails of the chassis for a FORD pickup model. This study shows that geometry, material properties, forming method, manufacturing technique in the form of welding, and impact strain rate all play a role in the crashworthiness of the ladder frame chassis. Results of standard beam compression tests reveal that polygonal frame profiles such as hexagon and octagon shapes appear to yield slightly higher crush loads and absorb more impact energies when compared to traditional shapes of square, rectangular and circular cross sections. In another study, Aluminium thin-walled beams are simulated to analyse the collapse behaviour of the geometry and compared against experimental findings [Lee et al., 2008]. This paper presents the structural responses of a ladder frame automobile chassis during a full-frontal impact subjected to several modifications of cross sectional area geometry and thickness.

## **2. METHODOLOGY**

A finite element (FE) mesh of the 1994 Chevrolet C1500 pickup is obtained through and as a courtesy of the National Crash Analysis Center (NCAC) of the George Washington University [1997]. The mesh consists of 10500 elements, most of which are of the 4-node shell type along with a few solid type. The LS-DYNA3D files are imported into MSC.Patran, and then converted to a compatible file format for exporting into the FE modelling medium, MSC.Marc/Mentat 2010. Isometric view of the NCAC FE mesh of the vehicle is shown in Figure 1 [Zaouk et al., 1997].

Three phases are carried out to investigate the effects of varying cross section

geometries and thicknesses of the chassis subjected to impact loading. Preliminary work is conducted to evaluate the behaviour of steel hollow beam profiles under axial impact loading through finite element modelling, which helps understand the mechanics of the particular beams chosen as chassis elements. Secondly, a previously generated isolated mesh of the ladder frame chassis is used to compute impact forces and absorbed energy. Finally, a finite element model of the pickup truck is developed in order to investigate a series of realistic impact scenarios, results from which are compared with the isolated chassis model predictions as well as with similar findings in the literature. These three phases are:

1. Axial crush test simulations of structural beams with varying cross section geometries and thicknesses
2. Full-frontal impact simulations of the original pickup ladder frame chassis with varying cross section geometries and thicknesses
3. Full-frontal impact simulations of the whole body of the original pickup for selected cross section geometries and thicknesses

The material for all analyses within the three stages is selected to be the DP600 steel, which is a type of steel commonly used in the automotive industry as the material for automobile chassis and bodies. DP600 is reported to be used for the pickup truck Chevrolet C1500. The elastic material properties of the DP600 are; yield stress  $\sigma_{ys} = 390$  MPa for quasi-static tension test, Young's modulus  $E = 210$  GPa, and Poisson's ratio  $\nu = 0.28$ . True stress – true strain flow curve of DP600 is reported for various strain rates [Ford Motor Company, 2012]. A midrange value corresponding to a strain rate of  $500 \text{ s}^{-1}$  is used for all analyses. The flow curve employed is illustrated in Figure 2.



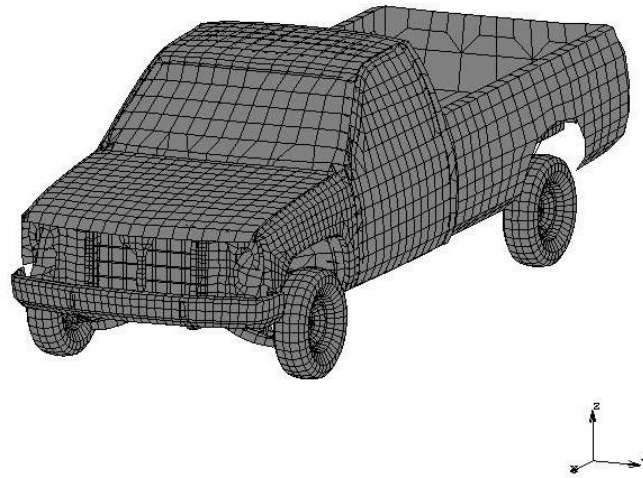


Figure 1. Isometric view of the 1992 model Chevrolet C1500 pickup model

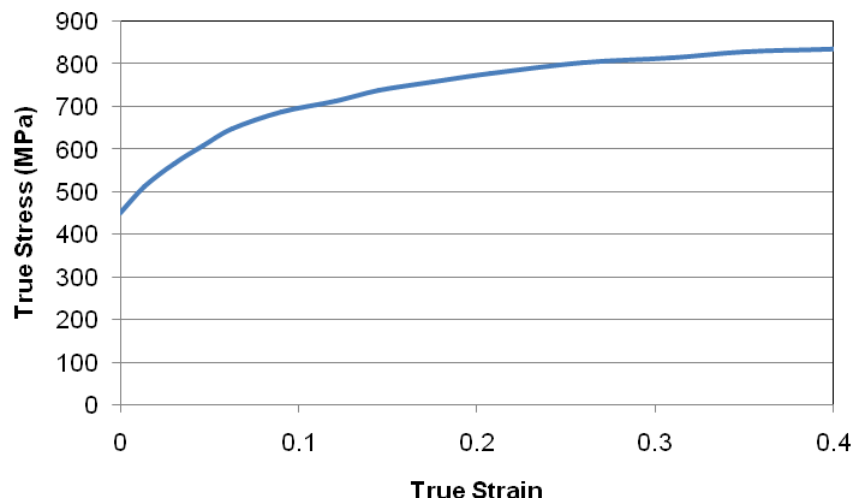


Figure 2. Flow curve of DP600 steel used in analyses

## 2.1. Modelling of the Axial Crush Tests

Axial crush (collapse) compression test simulations are carried out to have a better understanding of the typical hollow beams with various cross sectional geometries and thicknesses. A typical FE model of an axial crush test is provided in Figure 3. Three different cross-sectional shapes are selected as rectangular, square and hexagonal in line with industrial applications and previously conducted research as seen in Figure 4. Geometric parameters and areas for the selected hollow profile shapes are given in Table 1. Same cross sectional area values for the three geometries are used so that the final volume and mass of the beams are the same for comparison purposes.

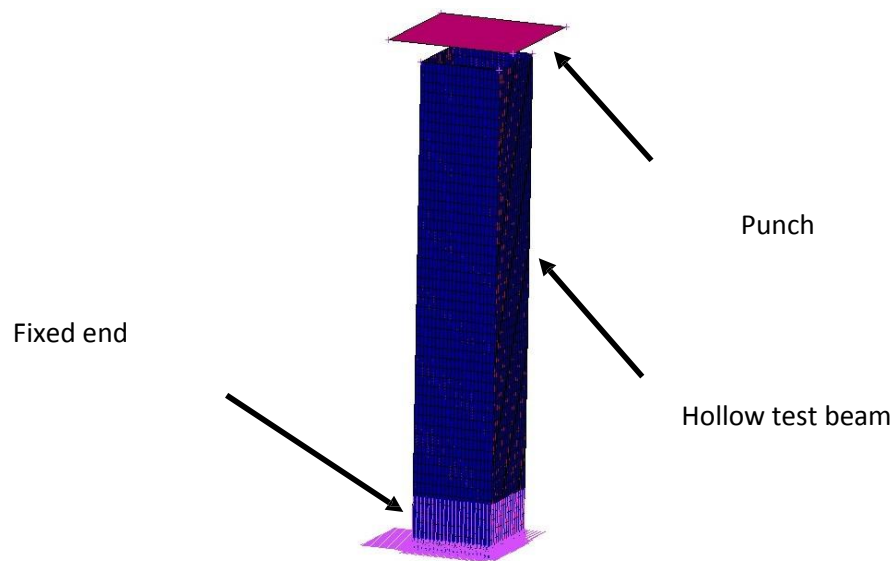


Figure 3. A typical FE model of an axial crush test

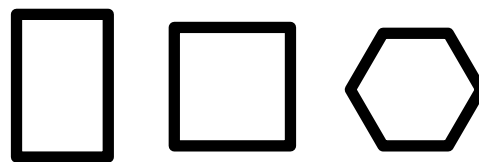


Figure 4. Schematic views of the selected cross-sectional beam shapes

Table 1. Edge lengths and areas of the selected cross-sectional shapes for a typical wall thickness,  $t$ , of 1 mm

Profile	a (mm)	b (mm)	t (mm)	Area (mm <sup>2</sup> )
Rectangular	30	38	1	132
Square	34	-	1	132
Hexagonal	23	-	1	132

## 2.2. Modelling of the Isolated Ladder Frame Chassis

The chassis of the vehicle is extracted from the complete model of the vehicle as shown in Figure 5. The amount of frontal impact force and energy absorbed by the longitudinal rails of the automobile chassis and the front bumper are investigated using this isolated FE model. The element number becomes 2410 and the run time is decreased considerably. The total element number includes a refined bumper mesh to increase the sensitivity of the analyses.

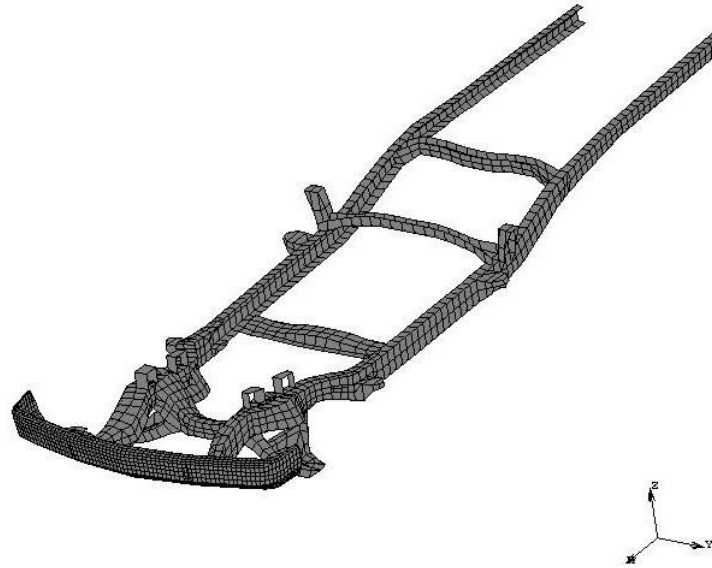


Figure 5. Isolated FE chassis model used in the analyses

A rigid non-deformable contact surface is created in order to represent the wall in the crash test, which ensures a full-frontal impact. Boundary conditions are introduced to constrain the motion of the rear of the chassis during impact. The chassis model with the wall contact surface and boundary conditions are given in Figure 6. The cross sectional areas of the front portion of the rails are varied as rectangular, square and hexagonal, as well as the thickness of the rail beams from 1.25 mm to 3.00 mm. The dimensions of the chassis rail beam cross sectional areas are chosen to be around the initial realistic values. Representative edge lengths and areas of the modified cross-sectional shapes on the ladder frame chassis for a typical wall thickness of 3 mm are tabulated in Table 2.

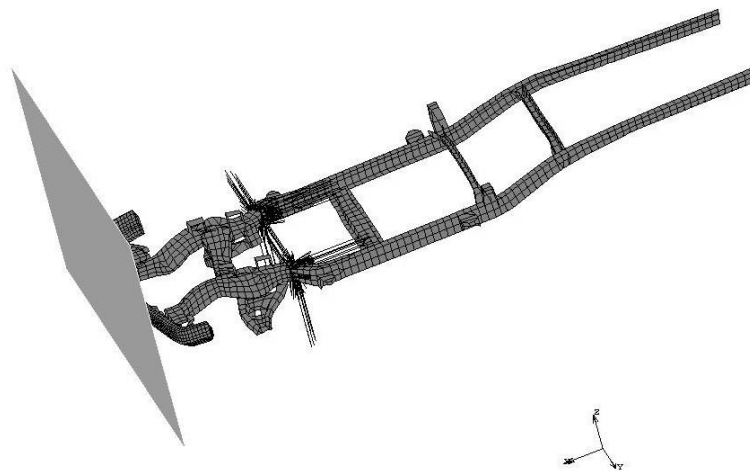


Figure 6. The chassis model with the wall contact surface and boundary conditions

Table 2. Representative edge lengths and areas of the modified cross-sectional shapes on the ladder frame chassis for a typical wall thickness,  $t$ , of 3 mm

Profile	a (mm)	b (mm)	t (mm)	Area (mm <sup>2</sup> )
Rectangular	100	120	3	1284
Square	110	-	3	1284
Hexagonal	73	-	3	1284

### 2.3. Modelling of the Whole Body

Chassis beam thickness is chosen as 2 mm for all parts of the vehicle body. Small sized elements at the corners and edges, and the tires are removed in order to decrease the element number of the model for shorter run times. The reduced model consists of 10024 shell, and 476 solid elements. In impact simulations, the hood is also removed, which causes computational problems during impact mainly due to buckling. Finite element model of the whole pickup truck divided into 21 different segments is given in different views in Figure 7.

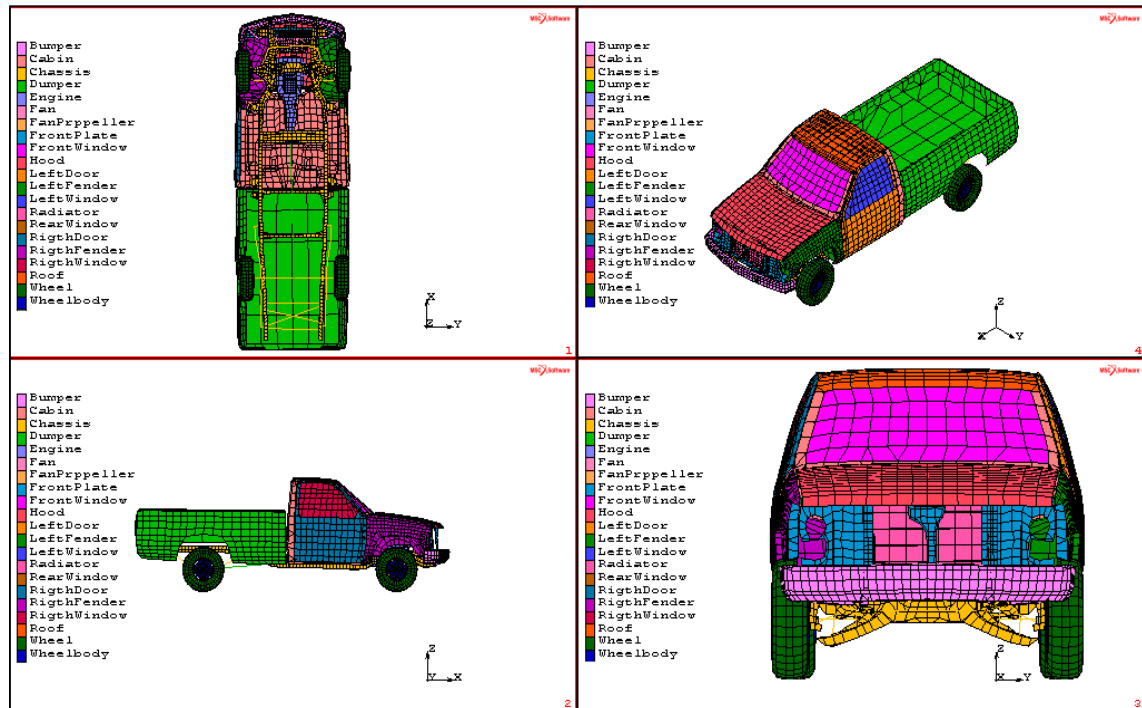


Figure 7. FE model of the whole pickup truck

### **3. RESULTS AND DISCUSSION**

#### **3.1. Simulations of the Axial Crush Test**

Total specimen length and number of elements in the mesh of the specimen are the same for all different beam models. The punch impacts the beams at a stroke of 10 mm. The reaction force of the beam increases as it resists deformation up to a point, after which collapse starts. Resistance of the material decreases because of the collapse and buckling of the material locally. The specimen again shows an increasing resistance up to a peak point, which is also followed by collapse and folding. This trend repeats itself as long as the punch moves downwards.

Crush force vs. displacement and total energy vs. displacement graphs are obtained for these beams. Figure 8 shows the simulation results compared with the predictions of a previously validated FE model (Ford Motor Company, 2012) for square and hexagonal profiles. The deformation patterns appear to be highly similar. In Figures 8c and 8d, locations highlighted in yellow colour show maximum Von Mises stress concentrations. As expected, maximum stress concentrations occur at the locations where local buckling, progressive folding and collapse occur. The crush force and the impact energy absorbed during the simulations of the tests are given in Figures 9 and 10 for all three selected cross sectional areas. Hexagonal cross sectional profile shows more resistance to impact loading and appears to provide the highest crush force and impact energy values, whereas rectangular cross section yield the lowest. Therefore, hexagonal cross-section beam as a chassis rail element may initially be considered as a more favourable choice for the structural crashworthiness of the vehicle.

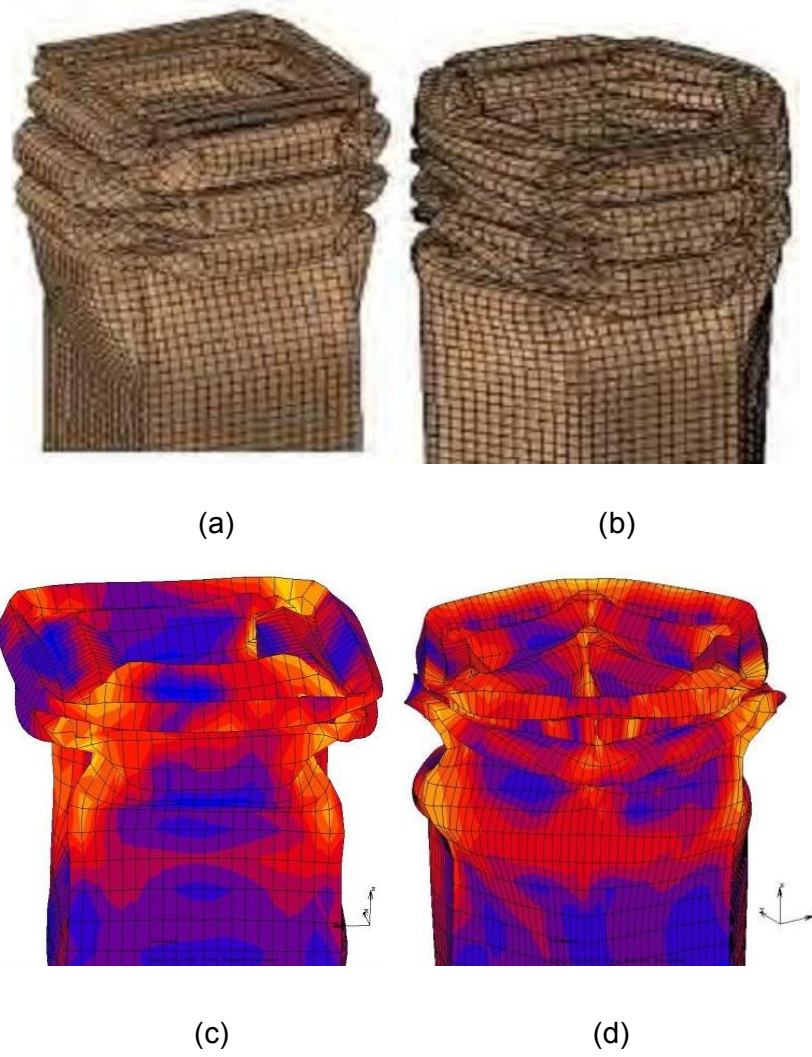


Figure 8. The predictions a previously validated FE model (a, b) (Ford Motor Company, 2012) compared with the FE simulation results (c, d) for square and hexagonal profiles

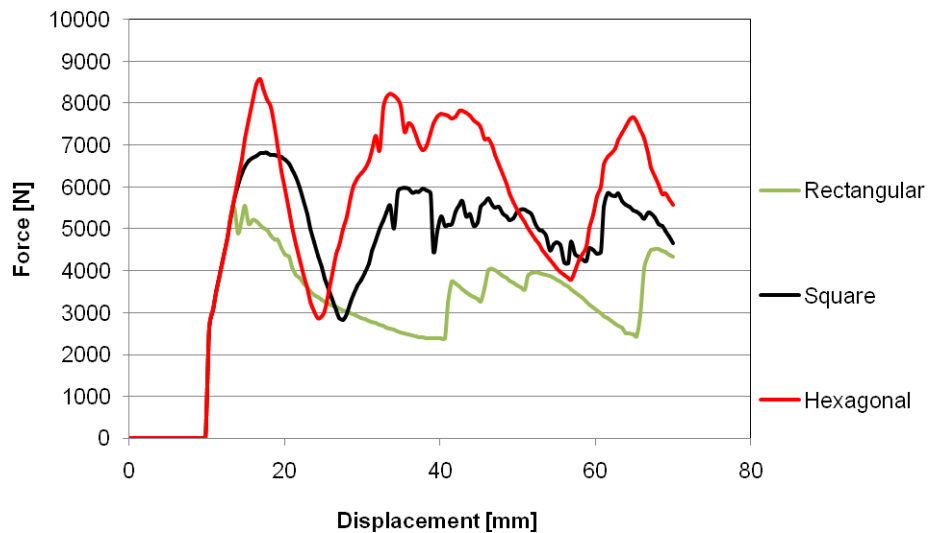


Figure 9. Crush force vs. displacement for different cross sectional profiles

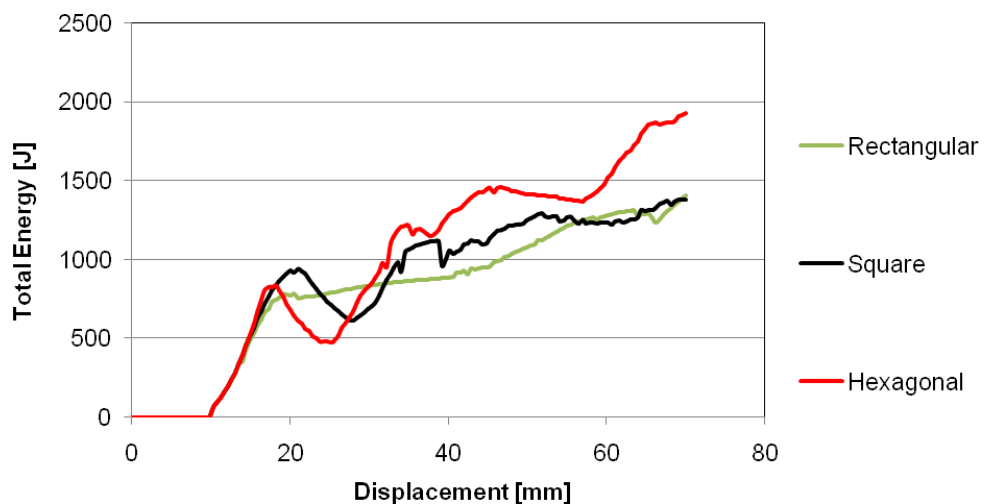


Figure 10. Total energy absorbed vs. displacement for different cross sectional profiles

### 3.2. Simulations of the Isolated Ladder Frame Chassis

The ladder frame chassis is subjected up to 700 mm of longitudinal intrusion, which corresponds to a range of impact severities. Figure 11 shows the deformation pattern and von Mises stress distributions of the isolated chassis with rectangular cross sectional area and a thickness of 3 mm. The impact force and the impact energy absorbed by the rectangular chassis of are given in Figures 12 and 13, respectively, for various thicknesses. The impact force and the impact energy absorbed by the chassis of 2 mm thickness are depicted in Figures 14 and



15, respectively, for the three cross sectional geometries.

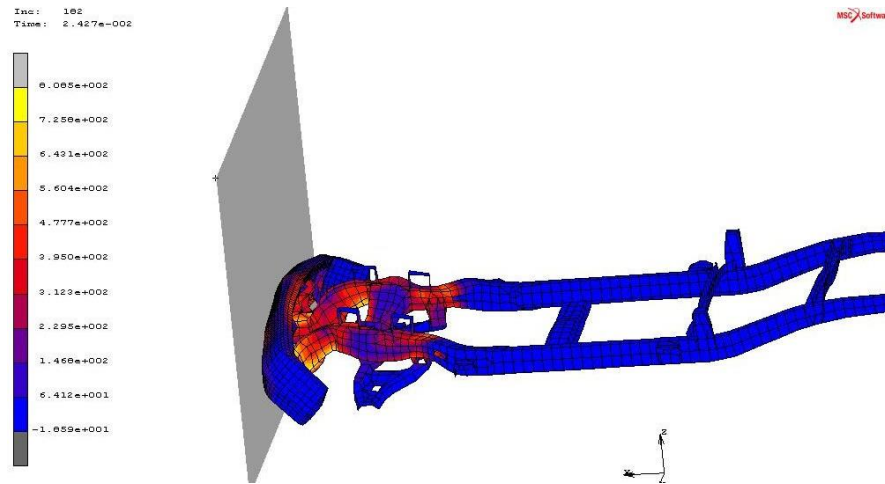


Figure 11. The deformation pattern and von Mises stress distributions of the isolated chassis with rectangular cross sectional area and a thickness of 3 mm

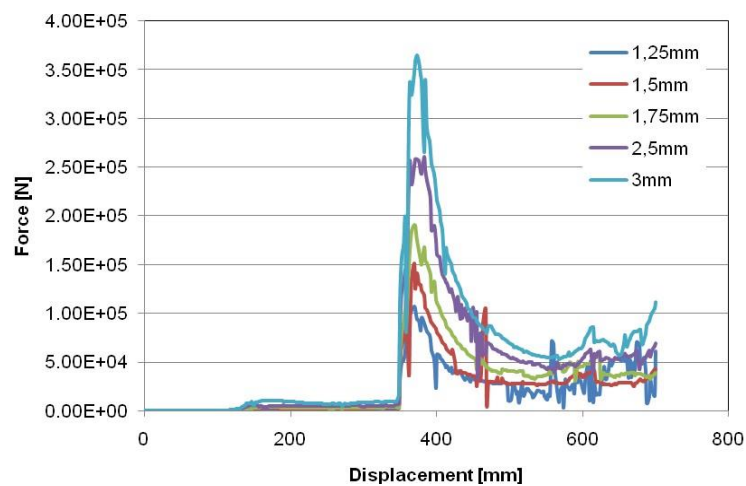


Figure 12. The impact force resisted by the rectangular chassis for various thicknesses



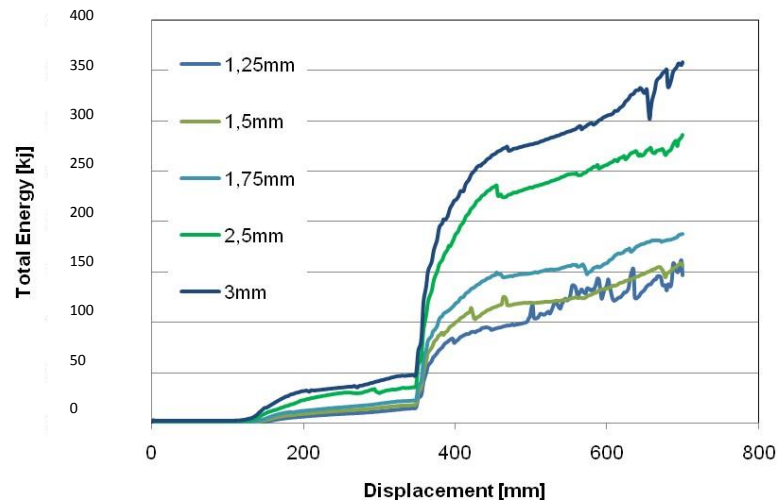


Figure 13. The impact energy absorbed by the rectangular chassis for various thicknesses

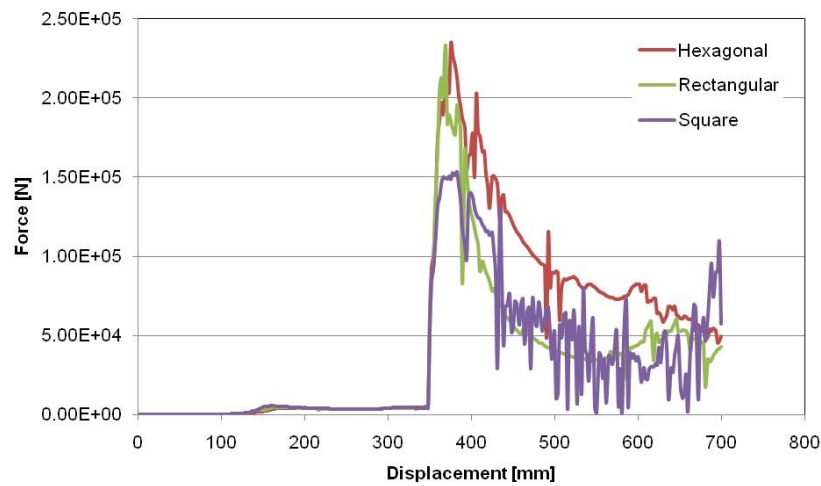


Figure 14. The impact force resisted by the chassis ( $t = 2$  mm) for various cross section profiles

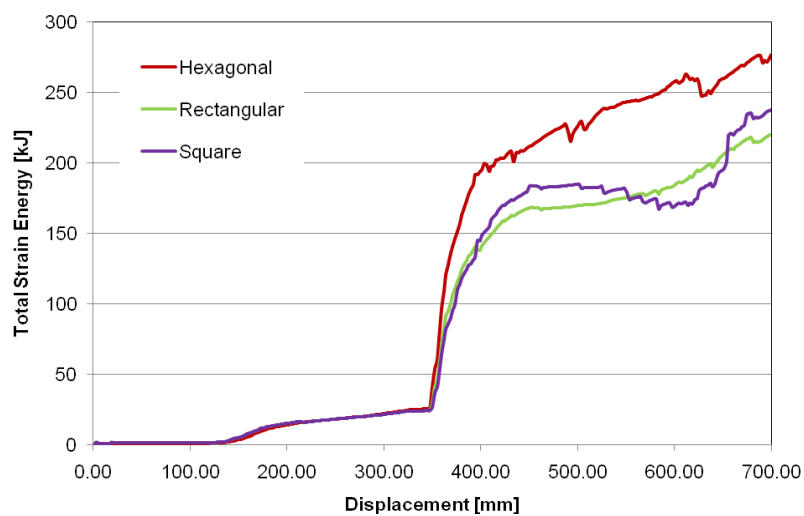


Figure 15. The impact energy absorbed by the chassis ( $t = 2$  mm) for various cross section profiles

Figure 12 exhibits that as the chassis thickness increases, total resistive force of the chassis increases as expected. The reaction forces for all thicknesses make a peak around 350 mm intrusion longitudinally as the impacting surface makes contact with the longitudinal members (rails) of the chassis; then a combination of collapse, local buckling and bending occurs in the chassis as the resistance to impact gradually drops. Similarly, Figure 13 shows that energy absorbed is a maximum for the greatest thickness of 3 mm, as the areas under F-d curves in Figure 12 should ideally give the energy absorbed, and it is a maximum for 3 mm thickness. Figures 14 and 15 reveal that the reaction force to impact and absorbed energy are a maximum for the hexagonal cross sectional shape. Rectangular and square cross sections exhibit a similar response.

### 3.3. Simulations of the Whole Body

In order to compare the impact energies absorbed by the rectangular vehicle chassis with the whole vehicle body, simulations are carried out for the whole body with an average member thickness of 2 mm. Material properties are assumed to be those of DP600. The experimental test result for a full-frontal crash test is compared with the whole vehicle body FE analysis simulation result in Figure 16. Similarities between the two deformed pickups, particularly around the chassis location and engine block space, are observed. Figure 17 exhibits the absorbed energies by the chassis and the whole vehicle. From 400 mm to 700 mm intrusion into the vehicle representing increasing crash severities, the percentage absorbed by the chassis ranges between 37% and 50%, which is in line with findings in the literature [Zaouk et al., 1997] which range between 43% - 55% for similar deformations.

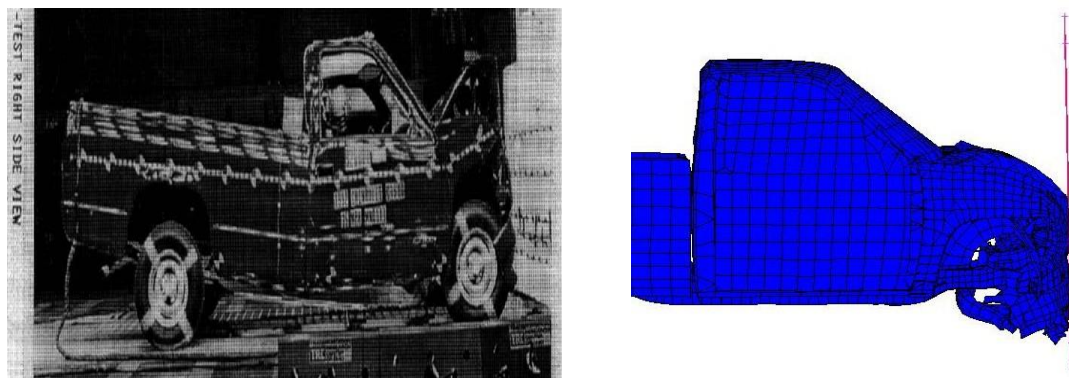


Figure 16. Experimental test vs FE simulation

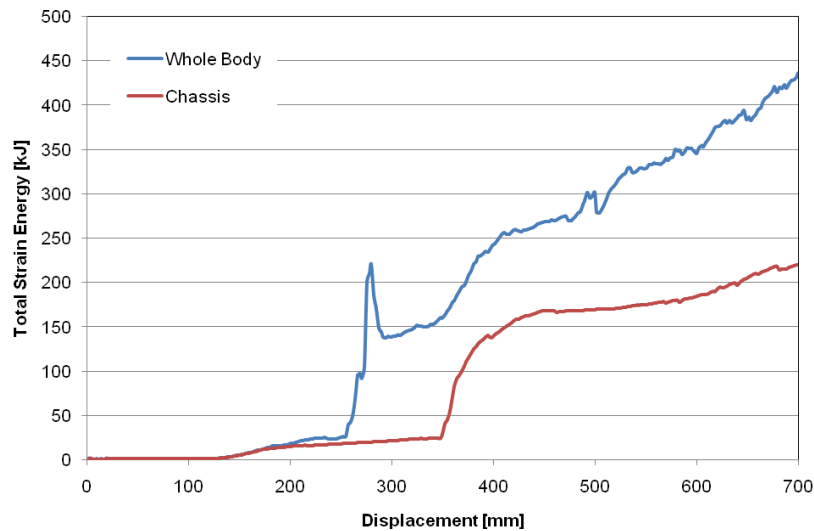


Figure 17. Absorbed energies by the rectangular chassis ( $t = 2\text{mm}$ ) and the whole vehicle

#### 4. CONCLUSIONS

Structural crashworthiness of a typical ladder frame chassis is investigated in terms of impact reaction forces and energy absorption. Results show that the chassis is the predominant energy absorbing member of the whole automobile body, capable of absorbing around 50% of the crash energy at different severities. Investigation of uniform beams under crush loads proves to provide an initial selection about which profile to select for better energy absorption. Hexagonal cross section shows better energy absorption capability when compared to traditional forms of rectangular and square profiles, which is in line with the findings of other researchers [Ford Motor Company, 2012]. However, it should be noted that the deformation mechanisms in the real life case appears to be much more complicated resulting in a 3-D stress state due to combination of compressive, buckling and bending loads.

The FE simulation predictions show that thicker the beam profiles, the higher the energy absorption. However, when the chassis profile thickness increases; the weight and cost of the vehicle, as well as its fuel consumption and emissions also increase. Therefore chassis thickness should be optimised to achieve maximum possible crashworthiness and minimum possible material mass.

#### REFERENCES

1. **European Commission, Directorate General for Mobility and Transport**, (2012), "Statistics – EU Road Fatalities", CARE EU Road Accidents Database. [http://ec.europa.eu/transport/road\\_safety/pdf/observatory/trends\\_figures.pdf](http://ec.europa.eu/transport/road_safety/pdf/observatory/trends_figures.pdf), accessed in December 2013.



2. **Ford Motor Company** (2012), “Impact Testing and Modeling of DP600 Front Rails”.  
<http://www.autosteel.org/~media/Files/Autosteel/Great%20Designs%20in%20Steel/GDIS%202006/10%20%20Impact%20Testing%20and%20Modeling%20of%20DP600%20Front%20Rails.pdf>, accessed in March 2012.
3. **Giess, M., and Tomas, J.**, (1998), “Improving Safety Performance In Frontal Collusion by Changing the Shape of Structural Components”, Proceedings of the 16th International Conference on the Enhanced Safety of Vehicles, Paper Number: 98-S I-0-07. <http://www.census.gov/compendia/statab/2012/tables/12s1105.pdf>, accessed in December 2013.
4. **Lee, K.-S., Yang, Y.-J., Kim, S.-K., and Yang, I.-Y.**, (2008), “Energy Absorption Control Characteristic of Al Thin-Walled Tubes Under Impact Load”, Acta Mechanica Solida Sinica, Vol.31, No.3, pp 383 – 388.
5. **National Crash Analysis Center** (NCAC), George Washington University, (1997), “C-1500 Pick-Up Truck Model”. <http://www.ncac.gwu.edu/vml/models.html>, accessed in March 2012.
6. **Teng, T. L., Chang, K. C., and Nguyen, T. H.**, (2008), “Crashworthiness evaluation of side-door beam of vehicle”, TechnischeMechanik, Vol.28, No.3-4, pp 268 – 278.
7. **U.S. Census Bureau**, (2012a), “Table 1105. Fatal Motor Vehicle Accidents – National Summary: 1990 – 2009.”  
<http://www.census.gov/compendia/statab/2012/tables/12s1105.pdf>, accessed in December 2013.
8. **U.S. Census Bureau**, (2012b), “Table 1106. Motor Vehicle Occupants and Non-occupants Killed and Injured: 1980 – 2009.”
9. **Yamazaki, K., and Han, J.**, (1999), “Maximization of the crushing energy absorption of cylindrical shells”, Advances in Engineering Software, Vol.31, pp 425 – 434.
10. **Zaouk , A. K., Bedewi, N. E., Kan, C.-D., and Marzougui, D.**, (1997), “Development and Evaluation of a C-1500 Pick-Up Truck Model for Roadside Hardware Impact Simulation”, Proceedings of FHWA Vehicle Crash Analysis Conference, Publication No. FHWA-RD- 96-212.



## **HYBRID RFID SYSTEM FOR DRIVER ASSISTANT AND ACTIVE ROAD ACCIDENT PREVENTION**

**Huanjia YANG**, *H.Yang@lboro.ac.uk* Loughborough University, Loughborough, UK

**Shuang-hua YANG**, *S.H.Yang@lboro.ac.uk* Loughborough University, Loughborough, UK

### **ABSTRACT**

Driver error and reaction is one of the major causes of road accidents, and having an in-vehicle driver behaviour warning system can help to prevent a significant number of road accidents. However, current technologies struggle to provide satisfactory performance for the underlying data transmission/sharing layer. In this paper we first identify the primary contributing factors to road accidents and analyse the data transmission/sharing required for tackling them based on the study of historical accident records. We then investigate the feasibility of adopting various RFID technologies as the underlying technology to address those requirements in order to support active accident prevention. Our work demonstrated the effectiveness of RFID technologies in retrieving information from roadside and other vehicles and providing reliable and affordable solutions for integrations in future driver warning systems or autonomous vehicle control systems.

**Keywords:** RFID, Data transmission, Driver assistant, Active prevention

### **1. INTRODUCTION**

Road traffic accidents is the reason of more than 2% of all death each year and remain the are the largest single cause of accidental death for people aged between 5 and 35 years. In the year of 2012 road traffic accident took nearly two thousand lives, injuring more than 165,000 just in the United Kingdom and costs an estimated £547 million [UK Department of Transport, 2013]. Most of the accidents have the drivers to blame and it is probably not surprising because they are the people who are in control or the vehicles. The major causes of accidents are usually errors or carelessness of the driver, such as speeding, poor control and proceeding without proper observation etc. An in-vehicle driver assistant system can provide drivers with useful information or warnings, especially at crucial moments with dangerous conditions, to help prevent potential accidents from occurring in an active way. Such systems could be designed to monitor and assistant various part of vehicle driving and



movement and be operating at different levels. For example, in the scenarios where drivers may make errors or bad decisions unintentionally, a system could be designed to provide information or warning signals, while in some extreme situations when intentional behaviour is detected or if there may not be enough time for warning and human reaction, it might make sense for system to engage control. However, either way it would demand that the system understands clearly about the situation around, such as speed limit, signpost, status of adjacent vehicles etc. This requires solutions with enabling technologies for the underlying data transmission/sharing layer, which needs to be a good balance between performance, cost and complexity of deployment.

In this paper, we look at the historical records of the road accidents occurred in the last three recorded years in the United Kingdom in an attempt to understand the primary contributing factors, especially those ones that led to serious/fatal accidents. We then analyse the data transmission/sharing required for tackling those factors before investigating the feasibility of adopting various Radio Frequency Identification (RFID) technologies as a stand-alone solution to address those requirements. The remainder of this paper is organized as follows: first we introduce the methodology used in this study before presenting our study of the road accident records of UK in the past few years; after that we introduce the idea of our approaches to tackle the issues identified based on the findings of the previous section before a preliminary system design is presented; a demonstration system is presented to show the feasibility of design before we discuss and conclude the current and future work.

## **2. METHODOLOGY**

### **2.1 Empirical study of historical data**

Accidents can be caused by many different reasons with various contributing factors in even a single occurrence. An active prevention system will not eliminate every single factor. However, we believe a system that can tackle the most important contributing factors can significantly reduce the number of accidents and largely improve the road safety. An analysis of the historical accidents could provide crucial understanding of the most frequent accidents, their types and causes [Darbra and Carsa, 2004]. With valuable observation in past accident records, we can identify the most important contributing factors to be targeted in our designs.

To achieve this target we conducted our study based on the accident records that come from the UK Department for Transport. In the UK all the road accidents attended by police are



recorded in the STATS19 system and since 2005 those official accident records are required to have information on contribution factors, which is what we will be focusing on in this study. The STATS19 system does not record any damage-only accident, which means the cases we are looking at will always involve at least a minor injury to at least one person involved in the accident. It should also be understood that, though almost all the accidents that leads to fatalities are reported to the police and recorded in STATS19, not all the non-fatal accidents are reported. It does mean that the case data set is not a 100% complete record of all accidents. However, it remains the most detailed and reliable information source on road accident statistics and both the Department of Transport, as the publisher, and we argue that the record is in particular a good reflection of the trends over time. Therefore the research result from studying such dataset is still valid and significant.

In order to conduct an integrated analysis of the requirement for active prevention of road accidents, the historical records in UK from 2010 to 2012 are used. We've selected the data of the last three full available years as we consider the current trend in road accident is best represented by this data set. By studying the older records we have noticed that the proportion of each contributing factor does change slowly over the years, possibly because of technology advances, improved legislations and better infrastructures. Therefore We would not want to go too far backwards in the historical data to make sure the system we design tackles the timely issues that we are currently facing. In total, 353,926 cases of road accidents have been reported in this 3-year period, of which 4780 cases are fatal. The proportion of 82 official contributing factors, which are further divided into 9 groups, are given separately. In certain cases we use a joint proportion of several similar factors when we consider that they can be grouped together from technical point of view. Based on the result we will then investigate the actively preventive information requirement of road accidents.

## **2.2 Radio Frequency Identification (RFID)**

The idea of our approach is to adopt RFID to help drivers gather data from both roadside and other vehicles on the road, which will provide an underlying data retrieval solution for possible in-car driver assistant systems that can alert the driver when dangerous situations occur or even to engage the vehicle control automatically and to record driver's behaviour when necessary. RFID is a type of the Auto-ID technologies. Auto-ID is short for automatic identification technology which is a broad term of technologies that enable the machines to identify objects. Instead of having staffs identify objects and type their information into computer manually, the key for Auto-ID technologies is their automatic data capture ability.



RFID is a generic term for technologies that use radio waves to automatically identify people or objects [Want, 2006]. Compared to the other Auto-ID technologies the RFID system has its own features: instead of typing or scanning the identification code manually, the RFID systems provide us a non-contact data transfer between the RFID tags and the interrogators without the need for a strictly obstacle-free, line-of-sight reading; tag information can be rewritable and some tags can be recycled and reused; multiple tags can be read simultaneously by a RFID reader; RFID tags are more reliable while a printed barcode is easily to be broken.

Table 1. Comparison of different RFID tags (Yang et al., 2007)

	Passive tag	Semi-active tag	Active tag
Own power for data transmission	No	No	Yes
Own power for chip	No	Yes	Yes
Communication with readers	Backscatter	Backscatter	RF transmit
Read range	short	medium	long
Tag cost	low	medium	high

The basic components of a typical RFID system include: the transponder or the tag, which is a microchip in which a unique serial code is stored and transmitted when necessary via an antenna attached; the RFID reader, which is used to receive and identify the information sent by tags; There are generally 3 types of RFID tags depending on the power source used, which are the active, passive and semi-passive/semi-active tags. Each has its own features and is suitable for certain types of applications. A brief comparison of different RFID systems is given in Table 1.

### **3. REQUIREMENT OF DRIVE BEHAVIOUR ASSISTANT FOR ACTIVE ACCIDENT PREVENTION**

#### **3.1 Historical records and contributing factors**

The contributing factors to road accidents vary largely. In the STATS19 database, some 82 contributing factors are listed under 9 sub-categories. Each accident reported by police is accompanied with several items of contributing factors. We summarized the primary factor in all the road accidents reported from 2010 to 2012 and present the result in Table 2, in which the number and percentage of accidents occurred in each sub-category as well as the three most frequent factor items in it are listed.





Table 2. Number and percentage of contributing factors of road accidents in UK (2010-2012)

Contributory factor	Fatal accidents		Serious accidents		Slight accidents		All accidents	
	Nbr	%	Nbr	%	Nbr	%	Nbr	%
<b>Road environment</b>	<b>488</b>	<b>10</b>	<b>7,030</b>	<b>13</b>	<b>43,775</b>	<b>15</b>	<b>51,293</b>	<b>14</b>
Slippery road (due to weather)	264	6	4,038	7	30,264	10	34,566	10
Road layout (eg. bend, hill, narrow road)	141	3	1,487	3	7,058	2	8,686	2
Poor or defective road surface	40	1	556	1	1,912	1	2,508	1
<b>Vehicle defects</b>	<b>124</b>	<b>3</b>	<b>1,150</b>	<b>2</b>	<b>5,191</b>	<b>2</b>	<b>6,465</b>	<b>2</b>
Tyres illegal, defective or under inflated	63	1	424	1	1,733	1	2,220	1
Defective brakes	26	1	380	1	1,897	1	2,303	1
Overloaded or poorly loaded vehicle or trailer	16	0	148	0	614	0	778	0
<b>Injudicious action</b>	<b>1,328</b>	<b>28</b>	<b>11,851</b>	<b>22</b>	<b>71,909</b>	<b>24</b>	<b>85,088</b>	<b>24</b>
Exceeding speed limit	607	13	3,315	6	12,235	4	16,157	5
Travelling too fast for conditions	589	12	4,529	8	22,235	8	27,353	8
Disobeyed 'Give Way' or 'Stop' sign or markings	90	2	1,577	3	10,535	4	12,202	3
<b>Driver/Rider error or reaction</b>	<b>3,283</b>	<b>69</b>	<b>35,548</b>	<b>65</b>	<b>214,583</b>	<b>73</b>	<b>253,414</b>	<b>72</b>
Loss of control	1,580	33	10,556	19	39,070	13	51,206	14
Failed to look properly	1,270	27	18,934	35	125,924	43	146,128	41
Failed to judge other person's path or speed	628	13	7,372	13	41,321	14	49,321	14
<b>Impairment or distraction</b>	<b>1,051</b>	<b>22</b>	<b>7,673</b>	<b>14</b>	<b>33,609</b>	<b>11</b>	<b>42,333</b>	<b>12</b>
Driver/Rider impaired by alcohol	402	8	3,404	6	11,834	4	15,640	4
Driver/Rider illness or disability, mental or physical	265	6	1,353	2	4,351	1	5,969	2
Fatigue	203	4	952	2	4,176	1	5,331	2
<b>Behaviour or inexperience</b>	<b>1,328</b>	<b>28</b>	<b>13,393</b>	<b>25</b>	<b>67,537</b>	<b>23</b>	<b>82,258</b>	<b>23</b>
Driver/Rider careless, reckless or in a hurry	878	18	9,118	17	45,982	16	55,978	16
Aggressive driving	337	7	2,214	4	8,567	3	11,118	3
Learner or inexperienced driver/rider	191	4	2,653	5	12,958	4	15,802	4
<b>Vision affected by external factors</b>	<b>378</b>	<b>8</b>	<b>5,412</b>	<b>10</b>	<b>31,823</b>	<b>11</b>	<b>37,613</b>	<b>11</b>
Dazzling sun	81	2	1,176	2	7,151	2	8,408	2
Vehicle blind spot	72	2	662	1	4,499	2	5,233	1
Road layout (eg. bend, winding road, hill crest)	67	1	651	1	3,611	1	4,329	1
<b>Pedestrian only (casualty or uninjured)</b>	<b>882</b>	<b>18</b>	<b>11,274</b>	<b>21</b>	<b>33,040</b>	<b>11</b>	<b>45,196</b>	<b>13</b>
Pedestrian failed to look properly	508	11	8,627	16	25,186	9	34,321	10
Pedestrian failed to judge vehicle's path or speed	267	6	2,747	5	8,009	3	11,023	3
Pedestrian impaired by alcohol	236	5	1,752	3	4,388	1	6,376	2
<b>Special Codes</b>	<b>292</b>	<b>6</b>	<b>2,573</b>	<b>5</b>	<b>12,634</b>	<b>4</b>	<b>15,499</b>	<b>4</b>
Other	208	4	1,584	3	7,250	2	9,042	3
Stolen vehicle	51	1	397	1	1,633	1	2,081	1
Vehicle in course of crime	26	1	248	0	1,132	0	1,406	0
<b>Total number of accidents</b>	<b>4,780</b>	<b>100</b>	<b>54,630</b>	<b>100</b>	<b>294,516</b>	<b>100</b>	<b>353,926</b>	<b>100</b>



*Fatal accidents or all accidents:* The first thing we've noticed from the summary of data was that the percentage of accidents with the same contributing factor can vary quite significantly depending on the severity of the accidents. That is to say, some contributing factors may have a much higher percentage of occurrences in fatal accidents than in the serious or slight ones, and some others could be the other way around. In an ideal world we would like to have a system that tackles all the possible contributing factors. However, while we understand that no accident is desirable, we do also realize that an electronics and communication system probably won't solve all the problems in the first instance. Hence there has to be priorities and in this study we choose to focus our work mainly on the contributing factors of the fatal accidents. Life is the most precious thing and the ultimate goal of having a driver behaviour assistant system is to save lives. Therefore in this study we are more interested in the contributing factors that are more "lethal" than the others. Looking at the percentage of contributing factors' occurrence, it is obvious that the overall percentage of occurrence of a specific factor for all accidents regardless of severity is generally a very close figure to the percentage for slight accidents. This is due to the reason that the sample number of slight accidents is much larger than that of serious accidents and outnumbered the fatal accidents even more. The percentage of occurrence in all accidents is primarily influenced by the slight accidents and therefore is not an accurate reflection of the lethality of each contributing factors. In this case we will look at the factors that contribute more to the fatal accidents. All those factors may not be the most significant ones if we look at all accidents in a whole (though most of them are still significant), but they are more likely to lead to fatalities when they do contribute to an accident, so we consider those lethal factors as the most important and with the highest priority to be tackled.

*Number of accidents or number of fatalities:* In addition, some of the factors may be more likely to contribute to accidents that have multiple fatalities, but their occurrence are only count as 1 for each accident if we are only looking at the number of accidents caused. Therefore, it makes more sense to look at the impact of the contributing factor based on the number of fatalities caused rather than the number of accident caused. Table 3 shows the summarized result of the number and percentage of fatalities of the primary contributing factors in UK from 2010 to 2012. From the result we can conclude that the trend of the number of fatalities linked to each primary contributing factor is largely associated with that of the fatal accidents but with small variations. Some of them have a higher percentage of fatalities comparing to their percentage of accidents, which means those factor are more likely to cause multiple fatalities in a single accident and therefore should be considered to have a higher importance.



Table 3 number and percentage of fatalities linked to primary contributing factors in UK

Contributing factors <sup>1</sup>	Number of fatalities	Per cent
<b>Road environment contributed</b>	<b>527</b>	<b>10</b>
<b>Vehicle defects</b>	<b>135</b>	<b>3</b>
<b>Injudicious action</b>	<b>1,446</b>	<b>28</b>
Exceeding speed limit	677	13
Travelling too fast for conditions	643	13
<b>Driver/Rider error or reaction</b>	<b>3,524</b>	<b>69</b>
Loss of control	1,728	34
Driver/Rider failed to look properly	1,318	26
Driver/Rider failed to Judge other person's path/speed	621	12
<b>Impairment or distraction</b>	<b>1,146</b>	<b>23</b>
<b>Behaviour or inexperience</b>	<b>1,421</b>	<b>28</b>
Driver/Rider careless, reckless or in a hurry	935	18
<b>Vision affected by external factors</b>	<b>387</b>	<b>8</b>
<b>Pedestrian only (casualty or uninjured)</b>	<b>885</b>	<b>17</b>
<b>Total number of casualties</b>	<b>5,092</b>	

<sup>1</sup> Please note that for the sake of simplicity only the factors that are linked to more than 10% of accidents are listed as well as the sub-categories

Category of factors and Correlation: Categorizing the contributing factors is difficult and the current categorization used in STATS19 is not designed specifically to support ICT studies. It is difficult to understand from those items listed what the real causes are from the technical point of view and how electronics and communication system can possibly help. ICT systems are more useful for solving problems when the object involved parameters related are clear. Therefore, to make more sense of the data we re-arrange the items into a few sub-categories that are directly linked to a main contributing object and a main contributing action.

Furthermore, before we finalize the result we also need to consider the correlation between different factors. As an accident can have multiple contributing factors, some of the factors listed in an accident can have a strong link to the other factors listed in the same accident. Some of the rather vague factors, such as loss of control or poor turn or manoeuvre, can be actually caused by other factors such as exceeding speed limit or careless driving. In order to understand more clearly we further improve the description of some of the items of contributing factor in an attempt to remove the correlations. By taking into consideration the percentage given in the most common pairs of factors reported together [] as well as a streamlined categorization, Table 4 shows an improved list of primary contributing factors and their percentage of fatalities caused comparing to the total fatalities. We've also removed some of the categories or items that are not directly relevant to in-car assistant system.



Table 4 Revised category and factors with percentage of accidents related

Revised contributing factors without correlation	Per cent
<b>Speed-related factors</b>	<b>26</b>
Exceeding speed limit	13
Travelling too fast for conditions	13
<b>Driver error – failed to observe</b>	<b>23</b>
Driver/Rider failed to look properly (non-speed/path related)	19
Driver/Rider failed to Judge other person's path/speed	12
<b>Driver error – failed to control</b>	<b>28</b>
Loss of control (non-speed/observation related)	28
<b>Impairment or distraction (non-vision related)</b>	<b>15</b>
<b>Behaviour or inexperience</b>	<b>16</b>
Driver/Rider careless, reckless or in a hurry (non-speed/observation related)	10
<b>Vision affected by external factors</b>	<b>8</b>

From the result we can conclude that the most significant factors in causing fatalities are speed-related factors, driver failing to observe and driver failing to control. As failing to control a vehicle is not deemed as a result of lacking real-time information, in this study we focus on the other two categories, which are more directly relevant to the demand of external warning/assistance to the driver.

### 3.2 From contributing factors to technical requirement

Speed has always been at the centre of spot light when it comes to the cause of road accident. It's not just a case in the UK as according to research by US Department of Transportation, speeding is a factor in about one-third of all fatal crashes, killing more than 1,000 people in the country every month and costing \$40 billion each year (Department of Transportation, 2009). Being partly responsible for nearly 30 percent of fatalities in road accidents in UK is significant, but probably is already lower than some have expected. Nevertheless, it is still one of the most important single parameter to be monitored and even controlled from the drive assistant system's point of view. In addition to costing lives, vehicles travelling at 80mph use 10-20% more fuel than those travelling at 70mph and an increase in vehicle speed increases the carbon emissions and generates more noise (Department for Transport, 2000). It is obvious that with growing interests in low emission strategies speeding is undesirable also for the sake of the environment.

From our study in the previous section we have learnt that there are two major contributors to speed-related road accidents: exceeding the speed limit or driving too fast for the conditions.



The former generally refers to the fixed speed limit posted on each road in general conditions while the latter mainly represents the scenario of temporary/variable speed limit enforced under various special conditions. Despite the fact that more than 80% of the European drivers state that driving too fast is a contributory factor in road accidents (Cauzard et al., 2004), many drivers still exceed the posted speed limits, both the fixed and variable ones. According to the figure from the Department for Transport (2009), 49 per cent of cars on UK motorways exceeded the 70 mph speed limit. In addition, 30 per cent of them were recorded as travelling at 80 mph or faster. The situation does not improve much off motorways, with nearly half of the vehicles exceeding the 30 mph speed limit in free flow conditions on built-up roads. While some drivers admit that they exceeded the speed limit on purpose, most of the others claim that they did so unintentionally. One reason could be that the driver is unaware of the speed limit. It may be assumed that this is an unintentional violation. This is either because a speed limit sign was absent or because the driver missed seeing it. In both cases the road characteristics are insufficiently informative about the speed limit in force. Another reason for unintentional exceeding of speed limit is underestimation. All motor vehicles have a speedometer to objectively check the driving speed. Nevertheless many drivers rely on their subjective perception or 'feeling' of their speed when it comes to determining their speed. However, human perceptual skills and limitations affect the subjective experience of speed and may lead to an underestimation of the true speed. This underestimation can easily occur in a situation where a high speed has been maintained over a long period or where drivers must reduce their speed significantly after a period of high speed driving and where there is little peripheral visual information. No matter a driver is exceeding the speeding limit intentionally or unintentionally, the road signs themselves in both cases are powerless to control the actual travelling speed of the vehicles. In this case, technologies that can alert the drivers in such situations are crucial for speed control that has the potential of preventing a significant number of accidents from happening.

On the other hand, failing to look properly is another major contributor to road accidents. This, however, is a much more vague description and can cover several different situations where the driver may have missed a road sign, missed another vehicle or have mis-judged other vehicle's path or speed. The key to an assistant system that helps prevent the first scenario actually refers back to the automatic sign post reading in the speed-related scenario, though in this case it may include road signs painted on the road surface for turning, give way or slow down etc. Missing other vehicle or mis-judging its path and speed, however, requires certain level of cooperation between the systems on both vehicles. With a



data sharing and transmission nature, such issue can potentially be addressed by network and communication technologies.

In the really world driver assistant systems can help prevent accidents from happening by providing warnings to the driver under dangerous situations, or even engaging in-vehicle automatic controllers to enforce certain control of the vehicle when the driver's behaviour is intentional or when there isn't enough time for human reaction. However, no matter which method is adopted, the system has to obtain the correct information in the first place in order to correctly understand the situation. This relies on the automatic signpost reading and vehicular network technologies that are essential for any kind of future driver behaviour warning or controlling systems. In this study, based on the result of our study of the historical accident records, we will focus on addressing the automatic speed limit reading, automatic road sign reading and automatic status sharing between adjacent vehicles using Radio Frequency Identification technology.

## **4 RFID-BASED SYSTEM – CONCEPT OF DESIGN**

### **4.1 Automatic Speed Limit and signpost Reading Technologies**

The current speed and signpost warning technologies include GPS systems, speed sign recognition based on real-time image processing as well as wireless communication technologies. GPS based technologies are usually integrated with GPS navigation systems. A GPS sensor receives satellites signal and calculates the coordinators of the vehicle. The system then locates the vehicle's position on a pre-loaded road map and indicates the corresponding speed limit or signpost information according to a database. Such technology suffers from the following shortages: 1). the map and the database are pre-loaded into the device, which means they are not updated in real-time and could contain out of date information. Temporary/variable speed limits, the changing of the road layout and signposts may cause inconsistency between the device readings and the real world information. 2). GPS localization has a limited tracking accuracy of 10 to 20 metres. GPS navigation systems use various calibration algorithms, but under certain circumstances such as in downtown environment they are still not able to ensure that the position of vehicle is correctly located, which may lead to an incorrect information reading. 3). GPS systems rely on the satellite signal which are not always reliable. This is usually due to bad weather or driving in tunnels or high-rise districts (Takahashi, 2007). Signpost recognition (Escalera et al., 2003; Kohashi et al., 2002) is a technique based on real-time image processing. Cameras are usually installed on the front of the vehicle and continuously capture images ahead of the vehicle.



Algorithms are developed to identify and read the signposts on the road by processing the images captured. Such systems have difficulty working in bad weather with decreased visibility, and are not able to provide any readings when the road signs are missing or obscured by other vehicles passing or overgrow vegetation. Even in the good weather/visibility conditions with road signs correctly displayed, the vision based algorithms still have an ineffectiveness rate of around 3%, which means approximately 3 out of 100 road signs appeared will be missed or misclassified. Such performance is robust enough to be implemented commercially, especially when the speed limit or signpost readings are expected to be used as data input to an automatic speed control systems, driver behaviour warning systems or other similar systems that may have the ability to partly engage or affect the vehicle's control.

#### **4.2 The wireless communication technologies**

Network-based: Having wireless communication between infrastructures and vehicles for control purposes is not new. However, the wireless technologies adopted are usually sophisticated and expensive to tackle specialised applications such as road robot or underwater vehicles (Wang et al., 2009). Such solutions are therefore not suitable for large scale deployment in traffic management. Vehicular Ad-hoc networks (VANET), on the other hand, are currently getting more and more focus for in-car information services. The idea is to interconnect all the vehicles on road with a communication network so that vital information for various in-car services can be retrieved or shared. The problem with the current technologies is that it requires an extensive deployment of wireless communication infrastructure to provide a network backbone that covers all the roads, which can be difficult and expensive. Also as a networked system the delay in data transmission struggles to be reduced to the level where the system could react to some crucial moments fast enough to prevent potential accidents.

RFID-based: RFID is an emerging wireless technology that provides a possible wireless communication solution that is low cost at least for one side (tag side) of the transmission. RFID is already in use in some of the transport related applications, such as vehicle parking, tolling or detection systems, where tags are attached to vehicles and readers are deployed at control points to identify the vehicles passing by. In this work we are interested in using RFID in the opposite way by locating tags at roadside and readers in vehicles. We are also interested in using RFID not only as a way of identification, but also a way of information transmission. In our study the speed limit or signpost information is stored in RFID tags





which will be embedded on signposts or certain points of road surface. Thus the RFID tags are sometimes referred as “signpost tags” in the remainder of our paper. When a vehicle passes such a signpost tag, a reader installed in the vehicle can retrieve the information from it. Such information could then be indicated on an in-car display, or be used for assistant system. As RFID provides us a non-contact data transfer between the tag and the interrogator without the need of line-of-sight data gathering, the speed limit or signpost readings of our system would be reliable in all weather conditions. Without the need to listen to satellites or base stations, the system will be suitable for all areas including tunnels and downtown areas. New road plan and temporary speed limit can be easily introduced by changing or implementing new tags. Because the in-car devices do not rely on any pre-loaded map or database, it will be simpler, cheaper and easier to maintain. In our study we investigate three application scenarios with different implementation scales, which are the permanent deployment scenario with a massive implementation scale to address speed limit and signpost reading and the temporary deployment scenario to address temporary speed limit and road sign reading as well as vehicle status sharing. We now investigate the possibility of adopting of both active and passive RFID technologies for data reading in the scenarios we identified, with RFID type chosen based mainly on the cost of the implementation and the data transmission requirements in each scenario.

Permanent deployment scenario for fixed speed limit and signpost reading: A permanent deployment scenario means deploying signpost tags as an addition or even as a replacement of the existing road signs for everyday use. Signpost tags should be deployed wherever a speed limit sign or any other signpost has been installed. The automatic signpost reading system could be operating as a standalone system with the ability to cover theoretically all the roads. In this case the system may lead to a massive implementation of signpost tags in a very large scale even the implementation is only limited to motorways, and will be even larger if it is to cover all the build-up roads. Therefore the cost of manufacture and maintenance of the signpost tags are vital for the system to be practical. As passive RFID technology was originally designed for large scale logistics applications, in which tag cost was also a vital criterion, passive RFID tag is so far the most cost efficient solution for massive deployment of the signpost tags. According to the RFID tag pricing guide published by ODIN (2010), the lowest priced UHF passive tags cost approximately 11 cents apiece. As manufacturers are still increasing production levels because of the stable market demand, tag price is expected to drop even further in the near future. Considering a normal sign post cost around \$150 the deployment of passive tags should be very feasible even taken into consideration of casing and deployment costs. For maintenance the battery powered tags



shows even more drawback, as replacing batteries regularly in all the signposts is hardly practical. The passive tags are maintenance-free devices as long as they are deployed with appropriate casing. Information changes can also be performed by remote tag writing using a reader device. In this case, we consider the passive tags as the better choice.

Temporary deployment scenario: means deploying signpost tags as supplement to existing ones. This can be useful for road work sites or congestion zones where a temporary speed limit or signpost that is different to the original one is introduced. In this case, because only a limited number of signpost tags are required, the acceptable tag cost can be much higher than the massive scale deployment. Passive technologies' low tag cost is achieved at the price of complicated and expensive reader devices, which can cost hundreds of USD each. This reader cost can be acceptable in the permanent deployment scenario as the automatic speed limit reading technology can provide a complete solution for speed limit reading at a national wide scale. However, as the automatic speed limit reading systems in temporary deployment scenario is only concerned about the temporary speed limit changing, they are more likely to operate as an integrant part in existing in-vehicle systems or navigation systems. Adopting the passive RFID readers with such a high price can hardly be acceptable for both the drivers and the car manufacturers. Active RFID readers, which can cost as little as 50 USD, are much cheaper because their hardware is in principle very similar to the active tags, which just use normal RF transceivers. In addition, the signpost tags deployed at the temporary speed limit introducing points, such as a road work site, can be expected to receive maintenance on a regular basis, thus the battery powered tags can now be a practical option. As a result, while the regular maintenance and increased tag cost become acceptable for introduction of temporary speed limits, the much cheaper reader cost makes the active RFID technologies a more appropriate choice in such scenario.

## **5 PASSIVE RFID BASED SYSTEM FOR PERMANENT DEPLOYMENT SCENARIO**

### **5.1 Location for passive signpost tag deployment**

In the adoption of passive RFID for the automatic speed limit reading system, the focus is on the location of the signpost tag deployment. Signpost tags may be placed on the existing signposts directly, mounted on overhead stands or on the road surface. While at the same time, the reader antenna may be placed on top of a vehicle pointing to various directions or underneath the vehicle pointing straight down.

**Implementing passive tags on existing signposts:** The idea of placing the passive tags on existing signposts might look straightforward. It seems simple and requires no further road

sign planning. But such an implementation has several issues, such as reading direction, reading range and on-road obstacles. **(a).** Reading direction: passive RFID reader antennas are highly directional. This means tag can be read only when reader antenna is directly facing it. This makes tagging existing signpost difficult, which have been deployed at various places on road. A RFID reader, even with sufficient read range, needs to point its antenna right towards the signposts, which is not always possible as such direction is not predictable and can change quickly when the vehicle moves. **(b).** Read range: we have tested passive UHF RFID, which have the longest reading range, and the furthest tag reading distance observed is 6m, which is insufficient for practical on road applications. According to UK Highway Agency documentation (2010) the standard lane width for motorway and dual carriage way in UK is 3.65m. The ability to read passive tag at up to 6 meters is not sufficient because only the vehicles using lane 1 is possible to have a reasonable tag reading performance. **(c).** On road obstacle: For multi-lane carriageways the reader can be blocked by other vehicles on a slower lane. The situation becomes even worse when we take into account the fact that the slower lanes are often used by large vehicles such as the HGVs. As the UHF passive RFID reading operation is very sensitive to obstacles between the tag and antenna, it is very unlikely that the signpost tag reading will be successful when obstacle vehicle are present. **Implementing passive tags overhead:** Placing tags overhead is one of the two solutions that avoid both reading confusion and on-road obstacles that we encountered in the previous section. A system that uses a similar approach and that has been implemented in Florida, USA for highway tolling and traffic control. Comparing to our approach, the difference is that the readers are implemented overhead and tags are deployed in vehicle under the windshield. And although the system is advertised as a UHF passive RFID system, the tag actually has batteries installed inside to enable it to interact with the driver when their prepaid account does not contain enough fund for paying the toll. The problem with this solution is the implementation cost, especially if considering a system that can potentially be implemented on all roads. As most of the roads do not have overhead sign stand, building such stands for all current roads can be very costly. **Implementing passive tags on road surface:** Placing passive tags on road surface is the last option. Similar to the overhead deployment there's no obstacle problem. In addition, the read range required is shorter and more controllable. Moreover, by pointing reader antennas downwards and properly controlling the readers' transmission power, the reader interference issue is controllable. It is therefore the only practical approach for passive RFID. However, the deployment in such approach is still not straightforward, especially on multi-lane roads due to tag reading speed and transmission collisions.

## 5.2 Road surface deployment – reading speed and crossover tag deployment pattern

Vehicles on road can travel at a speed of up to 70-80 mph, this means vehicles have a very short time to read tags as they pass by. This time is particularly short with road surface deployment, as reader antenna will be very close to the tags meaning that a tag will present in the antenna's RF range for a much shorter time than a tag a few meters. In this case, the application requires a lightning fast reading speed. In our experiments, we have found that passive RFID readers can achieve such reading speed but only when the reader keeps performing tag reading procedure without any anti-collision protocols. Anti-collision protocols are useful when multiple tags present in the reading area at the same time as it provides a mechanism for multiple tags to transmit their information one by one. In order to achieve satisfactory reading speed we cannot use those protocols, therefore we need to address the tag collision issue in a different way, which is by avoiding multi-tag appearance with carefully designed tag deployment pattern. In order to achieve this design objective, the tag deployment pattern has to satisfy: 1). At any on road speed limit read point, a RFID reader antenna installed under a moving vehicle is sure to pass through at least one of the tags deployed on the road surface; 2). The reader antenna has only one tag presented in its RF field at any time, or in other words avoiding the presents of multiple tags within reader field.

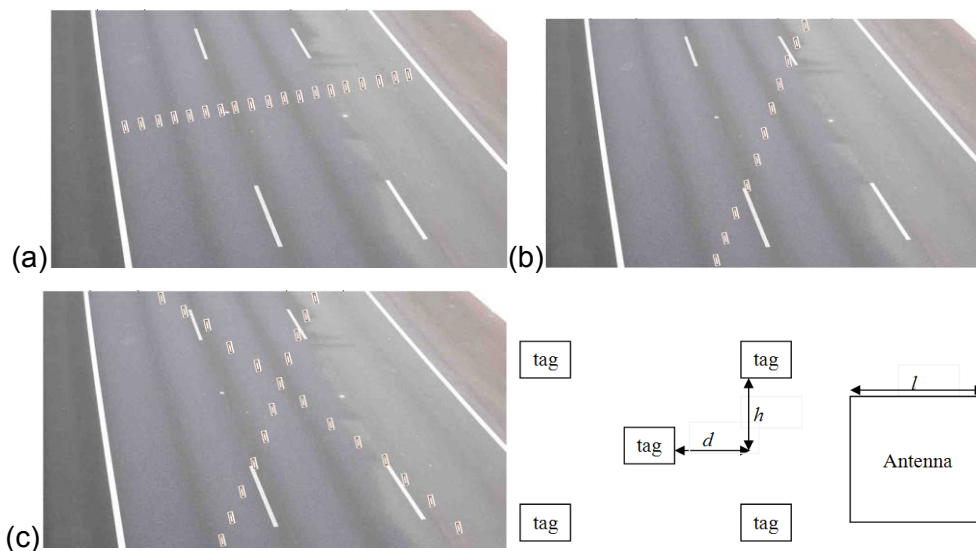


Figure 1. (a) Landscape tag deployment pattern (b) gradient tag deployment pattern

As shown in Figure 1(a), the most straightforward way is to place the tags in a landscape pattern. To ensure that the passing antenna goes over at least one tag, the distance between adjacent tags must be shorter than the antenna width. On the other hand, to ensure that only one tag presents in the antenna RF field at any time, the distance between adjacent tags

must be larger than the antenna width. Having got totally contrary conditions to satisfy, the landscape deployment pattern is obvious not practical for our application. Figure 1(b) shows a possible improved gradient pattern that has staggered tags. In this case, the antenna width needs to be larger than the horizontal distance and smaller than the vertical distance of the two adjacent tags. Those two conditions are practical in real implementation. However, for vehicles that are not moving straight, such as a vehicle that is quickly changing lane at the read point, the antenna may still miss the tags if its movement follows a track with direction  $\alpha$  as shown in figure. And with the two essential conditions to be satisfied, the direct distance between two adjacent tags cannot be less than the length of the reader antenna. This means that the reader may miss the tags. We call such reading situation a Cut-in Miss.

As the cut-in miss only happens from one direction vertical to the tag line, we add another line of tags in gradient pattern to make it a crossover pattern, so that no matter what the vehicle moving direction is, it will always follow one of the two gradient tag lines that forms the crossover pattern. As shown in Figure 1(c), our design objective in this pattern is to choose appropriate value  $d$  for the horizontal distance between adjacent tags and  $h$  for their vertical distance based on the antenna length  $l$ , so that the passing antenna will go over at least one tag, but not more than one at the same time. In this case, when the width of a passive RFID tag can be left out of account, the parameters in the crossover pattern can be determined by the following criteria: 1). To ensure that the passing antenna will go over at least one tag, the distance between adjacent tags  $d$  must satisfy  $d < l$ ; 2). To ensure that only one tag can present within the antenna RF field at any time, the distance between adjacent tags  $d$  must satisfy  $h > l$ . In our tests the crossover deployment pattern very well satisfied the two requirements we identified in the beginning of this section, and completes the design for adopting passive RFID technology for in-vehicle automatic speed limit reading.

## **6 ACTIVE RFID BASED SYSTEM FOR TEMPORARY/IN-CAR DEPLOYMENT**

Passive RFID technology shows great potential in large-scale applications where massive signposts tag implementation is required. On the other hand, for temporary and in-car deployment, passive RFID Readers cannot provide a flexible, long-range and non-directional reading performance. For temporary deployment scenarios like introducing temporary speed limit and reading status information from other vehicles, a simpler system that acts as an add-on to existing systems could be more practical. Active RFID is considered to be suitable in this case. With slightly higher tag cost and a limited but acceptable battery life, it allows the reader devices to be much simpler, cheaper and smaller, and therefore easier to for

integration with existing systems. In addition, active RFID systems have longer read range and more reliable tag reading to facilitate the tag implementation. Instead of putting tags on road surface, road workers could simply put the signpost tags on the temporary traffic signs, and vehicles can carry a tag that easily transmit its ID and status information, such as speed, direction etc. so that the vehicles adjacent could receive those information in a timely basis and use it to quickly find out whether the vehicle is in a potentially dangerous situation.

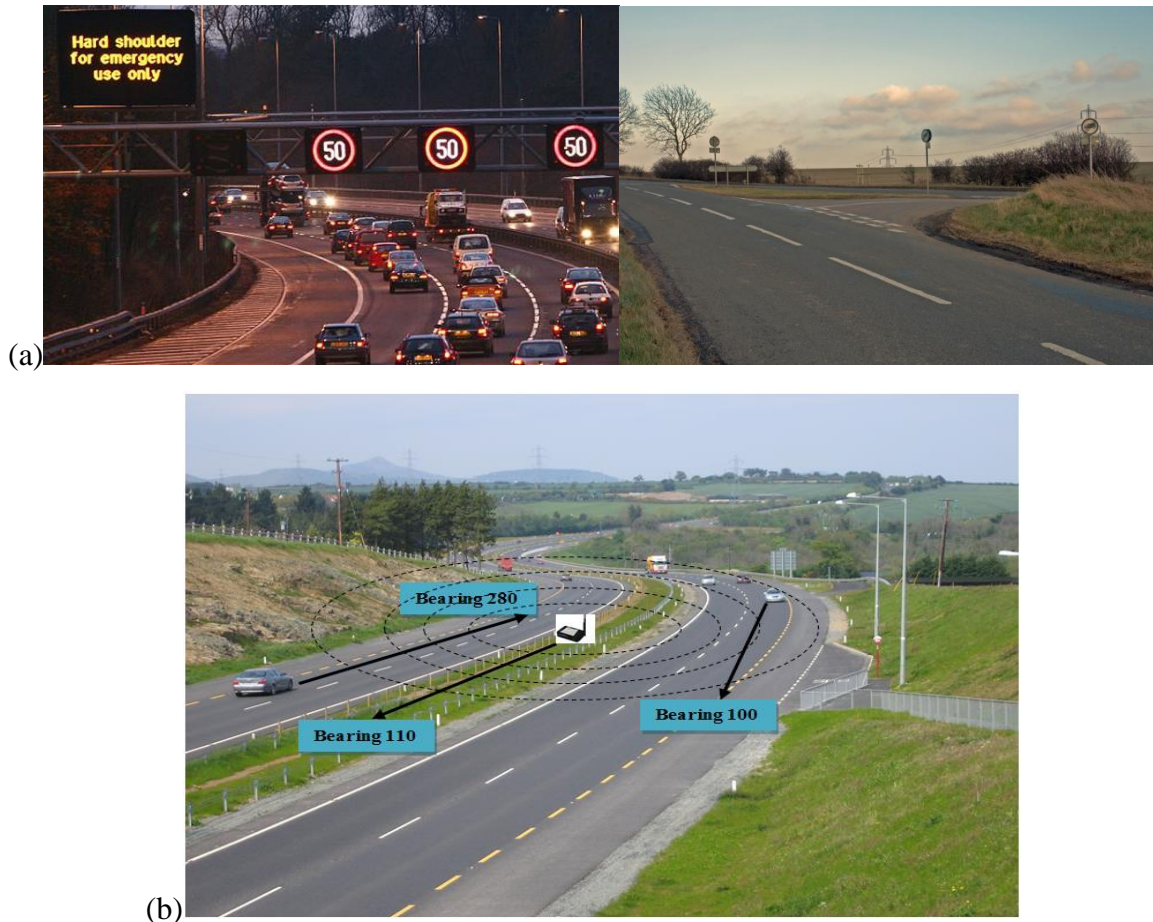


Figure 2. Active tag confusions and Design with bearing measurement module

However, there is also an issue when applying active RFID. That is to avoid tag confusion. Tag confusion happens because the RF coverage of active transmitter cannot be accurately controlled. The RF range of different active signpost tags overlap and will confuse in vehicle assistant system when multiple tags are read at the same time. Tag overlapping can happen on all roads because the two carriageways in opposite directions can have different speed limits and signposts. As shown in Figure 2a, overlapping will also happen at crossroads where the two or more roads merge or crossover. This issue is particularly important for temporary speed limit or signpost reading, while inter-vehicle information reading is probably



less affected as vehicles will be interested in others' status as long as they in a potential conflict range, regardless of the road and direction they are moving in.

In our study we propose a method of using bearing measurement to address the tag confusion issue. The idea is to let vehicle and the signpost tags identifies the traffic direction by integrating an electronic module to measure the bearing of both tag and reader devices. These modules are solid-state electronic devices built out of two or three magnetic field sensors and provide data for an on-board microprocessor. The correct bearing relative to the device is calculated using trigonometry. The bearing measurement modules are integrated with both active signpost tags and receivers. As shown in Figure 2b, by placing the signpost tags with the module board pointing in the direction of the corresponding carriageway, the module provides the tag processor with the carriage way bearing (CB). The CB is sent together with the signpost information via tag broadcasting. A receiver in the vehicles retrieves both the signpost information and the CB, and determines from its own bearing measurement module the vehicle heading (VH). It then compares the value of CB and VH to determine whether the received information is valid for the vehicle. This directional identification solution avoids the tag confusion with simple implementation, which can be done by placing the signpost tags at the roadside, with their pre-marked direction matching the traffic flow direction on the carriageway that the speed limit is to be broadcasted to.

## 7 DEMONSTRATION SYSTEM

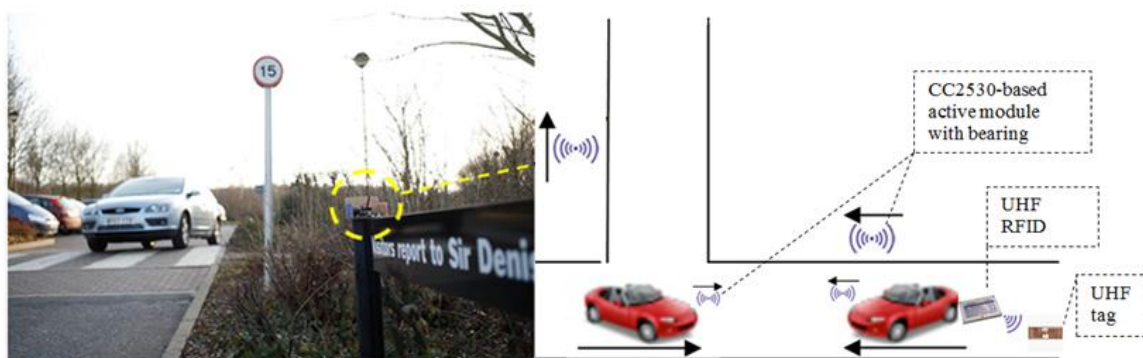


Figure 3. Demonstration system structure

We developed a test system with CAEN A528 UHF passive RFID reader, Texas Instrument CC2530 wireless system-on-chip (SOC) module as both in-vehicle active reader and active



tags and a bearing measurement module connected to the active modules to demonstrate the concept of our design. The structure of the demonstration system is shown in Figure 3, in which the arrows showing the direction that the bearing measurement modules were pointing at. The CC2530-based in-vehicle active modules queries and reads measurement modules via a standard I2C bus. In our test system the tags transmits a 20 mph speed limit. The condition for judging the validity of received speed limit is  $(VH-20) < TB < (VH+20)$ , where VH represents the vehicle heading that is measured by the reader and TB represents the tag bearing received together with the speed limit information, and the value 20 is the sweet point that we found out by experiments where opposite carriage ways and cross roads can be well identified. On the screen of the in-vehicle receiver we can consistently display the received speed limit and its TB value. The receiver then uses above judge condition to compare the TB value with its own VH value and determine whether the speed limit received is valid. The in-vehicle active module also transmit its own status, such as speed and direction, constantly via the active RF interface and the other vehicle's module receives it in the same way it receives the signpost information. For simulation purpose the system of the receiver also retrieves the vehicle's actual speed from a separate GPS module so that it could decide whether the vehicle is speeding or not. It also uses the location and both vehicles' status to find out whether the two cars are on a conflict course.

## 8 DISCUSSION AND CONCLUSION

In this paper we investigated the feasibility of adopting various RFID technologies as the underlying technology for data transmission/reading for in-vehicle driver assistant systems. By studying historical accident records we first identified the primary contributing factors to road accidents and retrieved the type of data transmission required to tackle them. We then show that RFID technologies can be used to address those requirements and are potentially better than the existing solutions. We then design the RFID solution that focuses on three application scenarios with different implementation scales, which are the permanent deployment scenario with a massive implementation scale to address speed limit and signpost reading and the temporary/in-car deployment scenario to address temporary speed limit reading and vehicle status reading. We proposed a hybrid passive and active RFID system, which uses UHF passive RFID technology with cross-over tag deployment for fixed speed limit and signpost reading, active RFID technology for inter-vehicle information sharing and active RFID with bearing measurement for temporary road sign reading. A demonstration is developed at the end as a prove-of-concept system to show the feasibility of our design. In the future we plan to extend the study to cover more sophisticated in-vehicle



parameters as well as attempt to understand more about drive control errors, which has not been tackled comprehensively in this study.

## REFERENCES

1. **Department of Transport (2013)**, “Contributory factors for reported road accidents (RAS50)”, <https://www.gov.uk/government/statistical-data-sets/ras50-contributory-factors>
2. **Want, R., (2006)**, “An Introduction to RFID Technology”. IEEE Pervasive Computing, Vol.5, No.1, pp. 25-33.
3. **Darbra, R.M., Casal, J. (2004)**, “Historical analysis of accidents in seaports”, Safety Science Vol.42, No.2, pp 85–98.
4. **Yang, H., Yao, F., and Yang, S. H., (2007)**, “Zigbee Enabled Radio Frequency Identification System”, Proceedings of the IASTED International Conference on Communication Systems, pp. 163-168, Beijing.
5. **Department for Transport, (2009)**, “Road Statistics 2008: Traffic, Speeds and Congestion”, [http://data.gov.uk/dataset/road\\_statistics-traffic\\_speeds\\_and\\_congestion](http://data.gov.uk/dataset/road_statistics-traffic_speeds_and_congestion)
6. **Department for Transport, (2000)**, “New Directions in Speed Management: A Review of Policy”, [http://webarchive.nationalarchives.gov.uk/20060213205515/http://dft.gov.uk/stellent/groups/dft\\_rdsafety/documents/pdf/dft\\_rdsafety\\_pdf\\_504682.pdf](http://webarchive.nationalarchives.gov.uk/20060213205515/http://dft.gov.uk/stellent/groups/dft_rdsafety/documents/pdf/dft_rdsafety_pdf_504682.pdf)
7. **Cauzard, J., (2004)**, “European drivers and road risk; Part 1: report on principal results”. INRETS, Paris.
8. **Takahashi, M., (2006)**, “Geographical Features of Satellite Visibility Viewed from Running Vehicles Based on GPS Signal Sensing”, Proceedings of the 64th IEEE Vehicular Technology Conference, pp. 1-5., Montreal.
9. **Escalera, A., Ma Armingol, J. and Mata, M., (2003)**, “Traffic sign recognition and analysis for intelligent vehicles”, Image and Vision Computing, Vol. 21, No. 3, pp. 247-258
10. **Kohashi, Y., Ishikawa, N. and Nakajima, M. (2002)**, “Automatic Recognition of Road signs and Traffic signs”, Proceedings of the 1st ITS Symposium 2002, pp. 321-326, Japan.
11. **Wang, W.H., Chen, X.Q., Marburg, A., Chase, J.G. and Hann, C.E., (2009)**, “Design of low-cost unmanned underwater vehicle for shallow waters”, International Journal of Advanced Mechatronic Systems, Vol. 1, No. 3, pp.194-202.
12. **Highway Agency, (2010)**, “Design Manual for Roads and Bridges (DMRB)”, <http://www.standardsforhighways.co.uk/dmrb/>





## SHAPE OPTIMIZATION OF 2D RUBBER BUSHING USING DIFFERENTIAL EVOLUTION ALGORITHM

**Necmettin KAYA**, *necmi@uludag.edu.tr*, Uludağ University, Mechanical Engineering Department, 16080, Bursa, Turkey

### ABSTRACT

The objective of this study is to design rubber bushing at desired level of stiffness characteristics in order to achieve the structural stability. A differential evolution algorithm based approach is developed to optimize the rubber bushing through integrating a finite element code running in batch mode to compute the objective function values for each generation. Two case studies were given to illustrate the application of proposed approach. Optimum shape parameters of 2D bushing model are determined by shape optimization using differential evolution algorithm.

**Keywords:** Shape optimization, differential evolution, rubber bushing, static stiffness curve

### 1. INTRODUCTION

Bushings are used in automotive industry for vibration isolation and comfort requirements. They are produced from rubber materials and their main functions are to join the elements between rigid structures, isolate vibrations through to the chassis and avoid the transmission of noise in the vehicles. Due to the increasing interest of multibody simulations of complete vehicles or subsystems, it is important to develop and effective models to represent the static stiffness of these rubber products in vehicles. During the vehicle development process, shape optimization of rubber products is also need to have target stiffness curves. Therefore trial and error method which is time consuming process must be eliminated. Many bushing manufacturers use trial and error method to meet these requirements, but optimization algorithms are the solution to this type of design problems. This research presents a simulation-based approach to optimize two dimensional rubber bushing model to meet target radial static stiffness without the need for physical prototypes.

Rubber bushings are used mostly in vehicle suspensions. The primary role of the bushings in a suspension system is to improve the ride quality of the vehicle. Their stiffness curve has



been primarily research subjects for many researchers. Blundell [1] concluded that suspension designs depend on the behavior of rubber bushings. He described the influence of rubber bushing compliance on changes in suspension geometry during vertical movement relative to the vehicle body. An experimental investigation was conducted on elastomeric bushings, which was presented by Kadlowec et al. [2,3]. The experiment reveals that the relationship between the forces and moments and their corresponding displacements and rotations is nonlinear and viscoelastic due to the nature of the elastomeric material.

Recently, the use of non-deterministic algorithms has attracted the researchers to find global optimums. Among the non-deterministic methods, the differential evolution (DE) algorithm produced good results in the literature for different applications in science and engineering.

The determination of shape parameters of a rubber product to have desired stiffness curve is an optimization problem. In this work, shape optimization is used to design a two dimensional rubber bushing model using DE algorithm to meet target stiffness curve. A Pascal (Delphi) code based DE is developed for shape optimization. Stiffness curve is obtained with the nonlinear finite element method using Abaqus software.

## **2. DIFFERENTIAL EVOLUTION ALGORITHM**

One of the main shortcoming of classical optimization methods is to stuck into local optimum instead of global optimum. Genetic Algorithm (GA) and Differential Evolution (DE) algorithms are evolutionary optimization algorithms, they were developed for finding the global optimum of the optimization problems. DE is a relatively new evolutionary optimization algorithm. It is a population-based optimization method introduced by Storn and Price. The DE algorithm's main strategy is to generate new individuals by calculating vector differences between other individuals of the population. The DE algorithm includes three important operators: mutation, crossover and selection. In the DE, a population vectors are randomly created at the start of iteration. This population is successfully improved by applying mutation, crossover and selection operators, respectively. Mutation and crossover are used to generate new vectors (trial vectors), and selection then are used to determine whether or not the new generated vectors can survive the next iteration.

Unlike simple GA that uses binary coding for representing problem parameters, DE uses real coding of floating point numbers. Among the DE's advantages are its simple structure, ease of use, speed and robustness. The key parameters of control in DE are:

NP: the population size,

CR: the crossover constant (0.0 -1.0),

F: scaling factor that controls the amplification of differential variations (0.0 – 2.0).

Several constraint handling techniques have been proposed to be used with DE algorithm. In this study, any individual which is not satisfied the constraints is removed from the population. Therefore, every individual in the population satisfies the constraints. Among the strategies in DE algorithm, DE/rand/1/bin DE strategy was used. The details of the DE algorithm can be found in literature [4].

A Pascal based DE algorithm software was developed and validated using two test cases. After validation of the developed DE optimization software, optimum shape parameters of 2D rubber model were determined using differential evolution optimization algorithm.

### 3. OPTIMIZATION OF TEST FUNCTIONS WITH DE

The developed DE software was validated using two test functions. The first test function is an unconstrained function called Rosenbrock's saddle [4]. It is a non-convex function used as a performance test problem for optimization algorithms introduced by Howard H. Rosenbrock in 1960. It is also known as Rosenbrock's valley or Rosenbrock's banana function. The global minimum is inside a long, narrow, parabolic shaped flat valley. To find the valley is trivial. To converge to the global minimum, however, is difficult with classical optimization algorithms.

The function and bound values of parameters are given as;

$$\begin{aligned} \min F(x_1, x_2) &= 100(x_1^2 - x_2)^2 + (1 - x_1)^2 \\ -2.048 &\leq x_1, x_2 \leq 2.048 \end{aligned} \quad (1)$$

It has a global minimum at  $(x_1, x_2) = (1, 1)$  where  $f(x_1, x_2) = 0$  [4]. Population size of 20, generation number of 100 and the crossover constant and scaling factor of 0.85 and 0.75 were selected. User interface of the software for test function is shown in Figure 1.

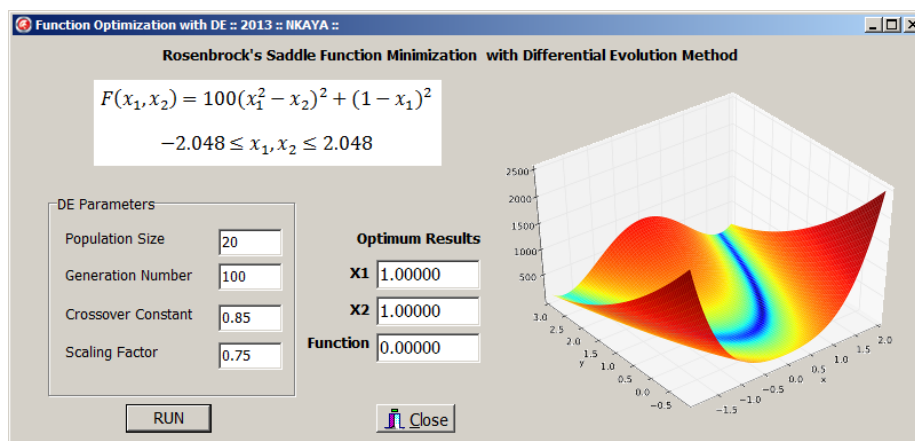


Figure 1. Optimization user interface and results for test function 1

Results were obtained as  $x_1=1$  and  $x_2=1$ , exactly. It can be seen that the DE successfully converged to the global minimum easily. It is clear from the generation history that generation number as a 40 is enough, because it converged at the 40<sup>th</sup> iteration.

After validated the first unconstrained test function, DE software was also validated using second test function. Second test function is constrained type and it is taken from reference [5]. The objective function and constraints are given as follows:

$$\min F(x_1, x_2) = (x_1 - 10)^3 + (x_2 - 20)^3 \quad (2)$$

subject to

$$g_1(x_1, x_2) = -(x_1 - 5)^2 - (x_2 - 5)^2 + 100 \leq 0$$

$$g_2(x_1, x_2) = (x_1 - 6)^2 + (x_2 - 5)^2 - 82.81 \leq 0$$

$$\text{where } 13 \leq x_1 \leq 100 \text{ and } 0 \leq x_2 \leq 100$$

This optimization problem has a global minimum at  $(x_1, x_2)=(14.095, 0.84296)$  where  $f(x_1, x_2)=-6961.8$  [5]. The DE software is also validated with the second test function, because the same results were obtained as in the literature. It is concluded that developed DE software can be used for subsequent shape optimization studies.

#### 4. FINITE ELEMENT MODELING OF RUBBER BUSHING

Rubber bushings in a vehicle suspension system can affect the stability of the vehicle. Thus, the stiffness characteristic of a rubber bushing in each direction is achieved by analyzing the vehicle performance during the design process. To design a particular rubber bushing, the stiffness in certain direction needs to meet the requirements. The purpose of this paper is to make the radial stiffness characteristic of the given 2D rubber bushing model meet the target stiffness curve by using the optimization method presented in this paper. In order to determine the stiffness curve of the bushing, nonlinear finite model were defined using Abaqus software.

##### 4.1. CAD-based design parameterization

The parametric 2D CAD model is used for design optimization. Dimensions are geometric parameters that can be varied permitting design change while preserving the basic shape or design intent of the part. Automatic model regeneration is an essential feature of dimension-driven systems. If a dimension is changed, the model should be regenerated automatically

while preserving geometric constraints and relationships. Design intent will be captured by establishing and preserving these relationships [6].

Three parameters were selected as design variables for 2D bushing model as shown in Figure 2. The guiding principle to select these design variables is to choose those parameters which influence the rubber bushing stiffness characteristics the most. Also limits and constraints were defined in order to preserve the shape. In order to undergo further parametric optimization, Python programming language was used to build the model in Abaqus software in terms of parameters such as  $R_1$ ,  $R_2$  and  $\Theta$  as shown in Figure 2.

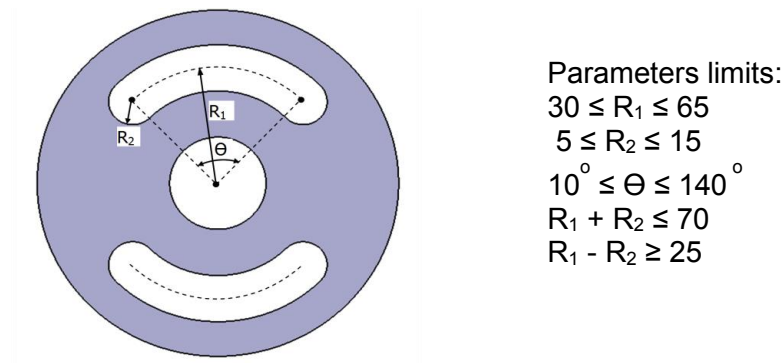


Figure 2. 2D rubber parametric model and shape parameters

#### 4.2. Material Model

The natural rubber can be considered as a hyperelastic material, showing highly nonlinear elastic isotropic behavior with incompressibility. A relationship between stress and strain in the hyperelastic material, generally characterized by strain energy potentials, is essential for the FEA of rubber components. In order to define the hyperelastic material behavior, i.e., the constitutive relation, experimental test data are required to determine material parameters in the strain energy potential. In this study, uniaxial and planar tension tests were performed at a local rubber company. Among the hyperelastic materials models, the Ogden N=5 model produces a better fit for test data. The Ogden material model appears to best capture the bushing response in the finite element study.

#### 4.3. FE Analysis of 2D rubber model

The proper element type and reasonable meshing strategy were used to model the two dimensional rubber model. The central and lower parts of the rubber component will come in contact when the slot is closed under vertical load is applied to the center of the rubber. Therefore contact interaction were defined on the finite element model. Thus, this becomes a

nonlinear large displacement contact analysis. As a whole, the initial model has about 1200 hybrid 2D elements (CPE4H) and 1340 nodes.

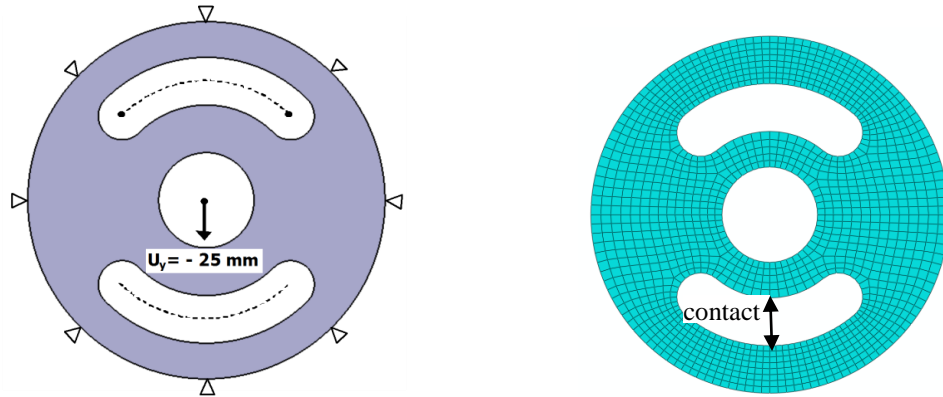


Figure 3. Boundary condition and finite element model of bushing

As shown in Figure 3, the displacement of 25 mm was applied from the center of the inner circle using rigid connection and deformed model includes self-contact. During the deformation, reaction force is stored. Outer circle is constrained with all degrees of freedom. Deformed model and radial stiffness curve are given in Figure 4.

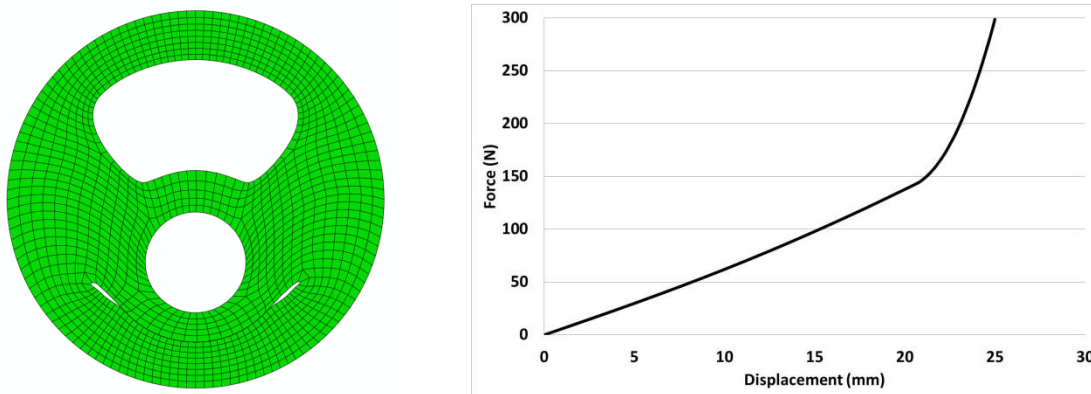


Figure 4. Deformed model and radial stiffness curve

## 5. DIFFERENTIAL EVOLUTION BASED SHAPE OPTIMIZATION

In this study, the difference between the calculated data point ( $F_{calc}$ ) and the target ( $F_{target}$ ) data point for each point in a stiffness curve is measured by a statistical term called chi-square. Fitness value (objective function) were selected as chi-square is given as follows:

$$\text{chi - square} = \sum_{i=1}^n \frac{(F_{\text{calc}} - F_{\text{target}})^2}{F_{\text{target}}} \quad (3)$$

Chi-square is a measure of the prediction error of the model, it must be as small as possible. Therefore the shape optimization problem is defined as:

objective: *min* chi-square

subject to

$$30 \leq R_1 \leq 65, \quad 5 \leq R_2 \leq 15, \quad 10^\circ \leq \Theta \leq 140^\circ$$

$$R_1 + R_2 \leq 70, \quad R_1 - R_2 \geq 25$$

Shape optimization of two dimensional bushing was implemented using software written in Pascal programming language. Displacement and forces which are required to obtain the radial static stiffness curve are calculated in Abaqus finite element analysis software. Abaqus finite element model is able to perform batch jobs when giving a parameter vector, the complete simulation, including geometric modeling, meshing and post processing of the simulation results is performed in a fully automatic manner using Python programming language. Developed software sends shape parameters to Abaqus to analysis and generate stiffness curve. After the solution is obtained, displacements and forces at the circle center are written to a text file. DE algorithm reads this file and computes the objective function. The flowchart of the proposed approach is given in Figure 5.

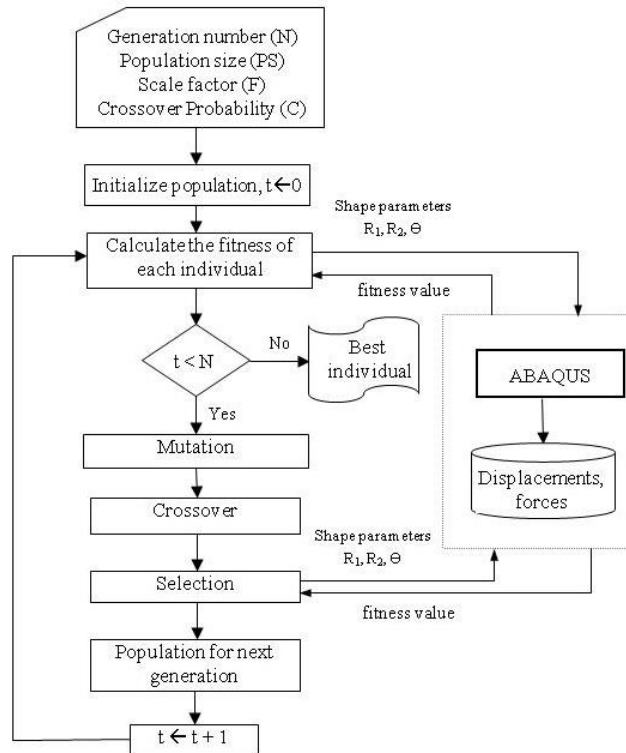


Figure 5. The flowchart of the proposed methodology and Abaqus interface

Shape optimization of the rubber bushing using proposed methodology as shown in Figure 5, two case studies were given below. In these case studies, target stiffness curves which are expected from rubber design have been defined as a polynomial form. Chi-square value was calculated using actual and target stiffness curves for objective function.

**Case Study 1:** Before setting a target stiffness curve, it should be known of limits the stiffness curves as shown in Figure 7. Target stiffness curves should remain between maximum and minimum stiffness curves. For this case study, target stiffness curve is given in Figure 6.

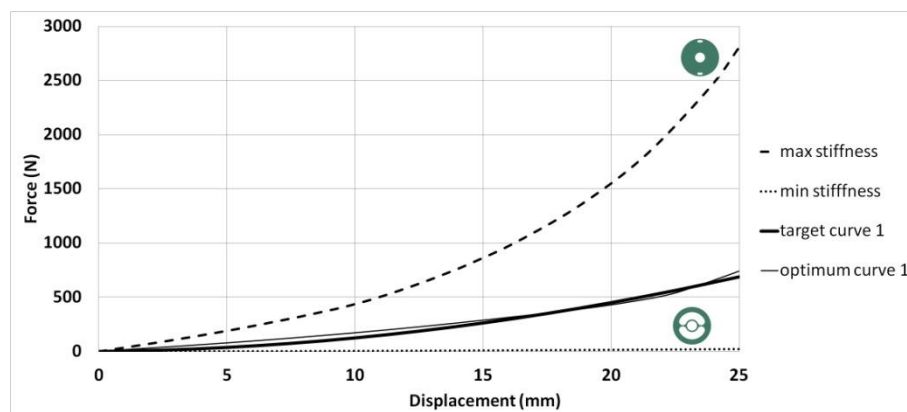


Figure 6. Optimization results for target curve 1

This optimization problem was solved by DE optimization algorithm. DE parameters were selected as; population size: 20, number of generation: 40, scale factor: 0.75, crossover rate: 0.85. After the solution phase completed, optimum shape parameters were found as  $R_1=50$ ,  $R_2=12$ ,  $\Theta=27$ . As seen in Figure 6, optimum curve is very close to target curve. DE algorithm were successfully applied to shape optimization problem in this case study. Iteration history for this case study is given in Figure 7.

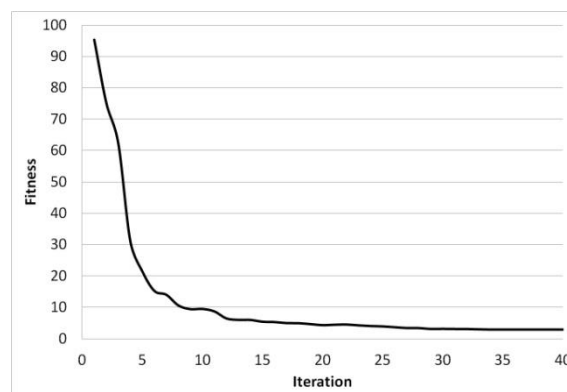


Figure 7. Iteration history for case study 1



**Case study 2:** In the second case study, stiffer rubber bushing design compared to case study 1 is expected. Target stiffness curve is shown in Figure 8.

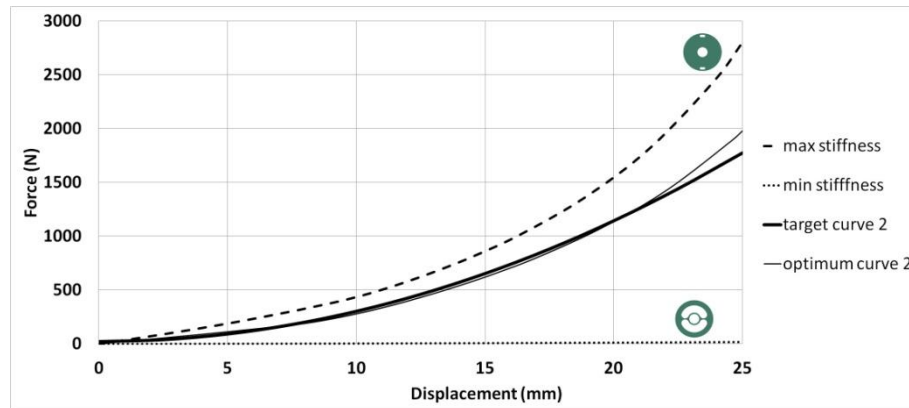


Figure 8. Optimization results for target curve 2

DE parameters are selected same as for case study 1. After solving the optimization problem with DE algorithm, optimum shape parameters were found as  $R_1=44$ ,  $R_2=5.5$ ,  $\Theta=29$ . As seen in Figure 8, optimum curve is close to target curve 2 again. In this case study, optimum curve is the best one that matches the target curve. Thus, proposed methodology was successfully applied to shape optimization problem.

## 6. CONCLUSION

In this study, a differential evolution algorithm based shape optimization is presented. A Pascal code based on DE algorithm was developed to solve shape optimization problems. DE algorithm was successfully applied to shape optimization of 2D rubber bushing to obtain target stiffness curves. Abaqus software was used for the FE calculation of objective function. It is seen that the combined DE algorithm and FE method approach seems to be powerful for finding a global optimum. The DE method is particularly suited to problems where there is no well-defined mathematical relationship between the objective function and the design variables.

**Acknowledgement:** This study has been supported by TÜBİTAK under the contract number 111M346.



## REFERENCES

1. **Blundell, M.V., (1998)**, The influence of rubber bush compliance on vehicle suspension movement, *Materials and Design* 19, 29-37.
2. **Kadlowec, J., A. Wineman, G. Hulbert, (2003)**, Elastomer bushing response: experiments and finite element modeling. *Acta Mechanica*, 163:1-2, 25-38.
3. **Kadlowec, J., D. Gerrard, H. Pearlman, (2009)**, Coupled axial–torsional behavior of cylindrical elastomer bushings, *Polymer Testing*, 28, 139–144.
4. **Storn, R., K. Price, (1997)**, Differential evolution - a simple and efficient heuristic for global optimization over continuous spaces, *Journal of Global Optimization*, 11(4), 341–359.
5. **Cai, H. L. Z., Y. Wang, (2010)**, Hybridizing particle swarm optimization with differential evolution for constrained numerical and engineering optimization, *Applied Soft Computing*, 10, 629–640.
6. **Hardee, E., K. Chang, J. Tua, K.K. Choia, I.Grindeanua, X. Yu, (1999)**, A CAD-based design parameterization for shape optimization of elastic solids, *Advances in Engineering Software*, 30, 185–199.



## STRUCTURAL OPTIMIZATION OF BLADE – DISC FIRTREE ATTACHMENT OF AN AERO-ENGINE

**Erdem ACAR**, *acar@etu.edu.tr* TOBB University of Economics & Technology, 06560, Ankara, Turkey

**Mutlu GÜNDÜZ**, *mutlu.gunduz@tei.com.tr* TEI Tusas Engine Industries, 26003, Eskişehir, Turkey

### ABSTRACT

This study describes design and optimization of turbine blade-disc attachment known as firtree attachment. Objective of the optimization is to minimize total mass of blade-disc firtree region while keeping attachment stresses below the material strength limits. Meta modeling techniques are used to identify the relations between geometrical parameters and stresses. Three different metamodelling techniques are employed in this study: polynomial response surface approximations (PRS), radial basis functions (RBF) and Kriging (KRG). Optimization of the firtree attachment is performed using these three metamodelling techniques, and three different optimum candidates are obtained for each metamodelling technique. Finally, numerical validations of optimum candidates are performed using finite element analysis.

**Keywords:** Blade-disk firtree attachment, Structural design, Optimization, Meta model

### 1. INTRODUCTION

Design of complex engineering systems (jet engines, aircrafts, automotive components etc.) are performed using high precision analysis models. Venkataraman and Haftka (2004) stated in their study that despite the significant increase in computational capacity, analysis with acceptable accuracy still takes 6-8 hours to perform. The reason is that the expectation of designers from analysis model has become more complex and accurate. It is computationally unacceptable to use these analysis models directly in optimization cycle because of excessive computational time. Besides, if a gradient based optimization method is used, convergence problems will arise because of numerical noise for calculating objective and constraint functions. Hence, substituting these slow and noisy analysis models with fast and

precise mathematical models, so called metamodels or surrogate models, have recently become a common practice.

In literature, there are several metamodeling techniques. Amongst these techniques, most popular ones are response surfaces (Myers and Montgomery 2002), radial basis functions (Buhmann 2003), Kriging (Sacks et al. 1989), neural networks (Smith 1993), support vector regression (Gunn 1997). There is no proper approach to determine which technique is suitable for a specific problem. The most popular application is to generate various types of metamodels and crosscheck their accuracy or measure test point error and determine which one is the best for the application of interest.

Metamodels are suitable for optimization studies because of their fast and accurate response prediction. In metamodel based optimization studies, it is better to perform optimization for all available metamodels if possible. If not, for a few of suitable models and obtain “candidate” optimum designs. Because the optimum obtained from the most accurate metamodel is not always guaranteed to be better than the optimums obtained from other metamodels (Acar et al., 2012).

Optimization of turbine discs and firtree attachments using metamodels in literature are as follows: Song and Keana (2005) implemented Kriging (KRG) model to a genetic algorithm optimization and performed firtree local profile optimization. Likewise, Huang et al. (2011) implemented KRG model to differential evolution program and performed turbine disc shape optimization. Lee et al. (2011) used KRG model in JPM program and performed turbine blade optimization. These studies are clear evidence that KRG models are suitable for optimization of turbine parts. The reason for this may be that KRG models are more accurate than the other mentioned modeling techniques. As mentioned before, optimum candidate obtained using most accurate metamodels may not give best optimum candidate comparing the other metamodels. Consequently in this study, besides the KRG model, PRS and RBF models are also employed. Three different optimum candidates are obtained for three different models and after validation of all three models, the candidate with the best performance is declared as optimum.

Rest of this document is structured as follows. Section 2 defines the problem of firtree attachment and formulation. Section 3 describes the details of Finite element method (FEM) analysis performed for optimization. Section 4 gives metamodeling details and accuracies of models. In section 5 optimization procedure of this study is explained. Section 6 contains further studies of firtree attachment such as additional optimization parameters and enhancement studies. Results and discussions are provided in section 7.

## 2. PROBLEM DEFINITION

Blade-disc firtree attachment is an important element, affecting the structural integrity of a jet engine. Main loadings acting on firtree attachment are the centrifugal forces caused by rotation of blade, the bending and torsion caused by aero dynamical gas loads and the thermal loads. Stresses at firtree attachment caused by the above-mentioned loads considering blade and disc contact can be calculated using FEM. Design of firtree attachment should keep the stresses below the material strength limits (proper knockdown factors should be applied).

Objective of firtree design is to minimize the mass of the attachment while keeping the stresses in a desired level. Structural design can be performed based on experiences and intuitions or can be performed modern optimization techniques. In this study, metamodel based optimization is employed.

Standard formulation of an optimization problem is given in equation (1):

$$\begin{aligned}
 &\text{Find} && \mathbf{x} = \{x_1, x_2, \dots, x_n\}^T \\
 &\text{Minimize} && f(\mathbf{x}) \\
 &\text{While} && h_j(\mathbf{x}) = 0, \quad j = 1, \dots, n_e \\
 &&& g_k(\mathbf{x}) \leq 0, \quad k = 1, \dots, n_g
 \end{aligned} \tag{1}$$

Design vector  $\mathbf{x}$  contains the design variables,  $f$  is the objective function,  $h_j$  are the equality constraints and  $g_k$  are the inequality constraints. The geometric dimensions shown in Fig. 1 are the design variables: (i) shank width, (ii) contact angle, (iii) face angle, (iv) flank angle, (v) contact length 1, (vi) contact length 2, (vii) lobe 1 radius, (viii) groove radius, (ix) lobe 2 radius.

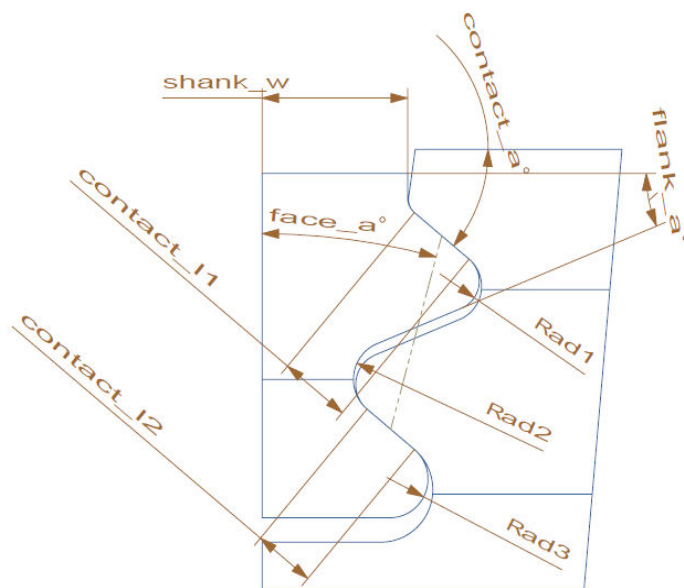


Figure 1: Blade-disc firtree attachment geometric dimensions

Objective of this study is to minimize firtree attachment mass, hence attachment mass of firtree is used for  $f(x)$  objective function in equation (1). As in many of the structural optimization applications, equality constraints are not employed in this study. Inequality constraints used in this study are determined considering the stresses in critical areas (see Fig. 2). These stresses are meant to be kept below the materials strength by using proper knockdown factor. (a) Net section average stresses should be lower than the 50% of the yield strength. (b) Peak stresses in stress concentration locations should be lower than 95% of the yield strength of material. (c) Contact stresses at contact faces of blade root and disc should be lower than 95% of the yield strength of the blade material. (d) In any case of failure, it is desired to make sure that rupture occurs at blade shank, hence *Section 1* stresses should be higher than *Section 2* stresses. (e) *Section 4* stresses should be higher than *Section 3* stresses.

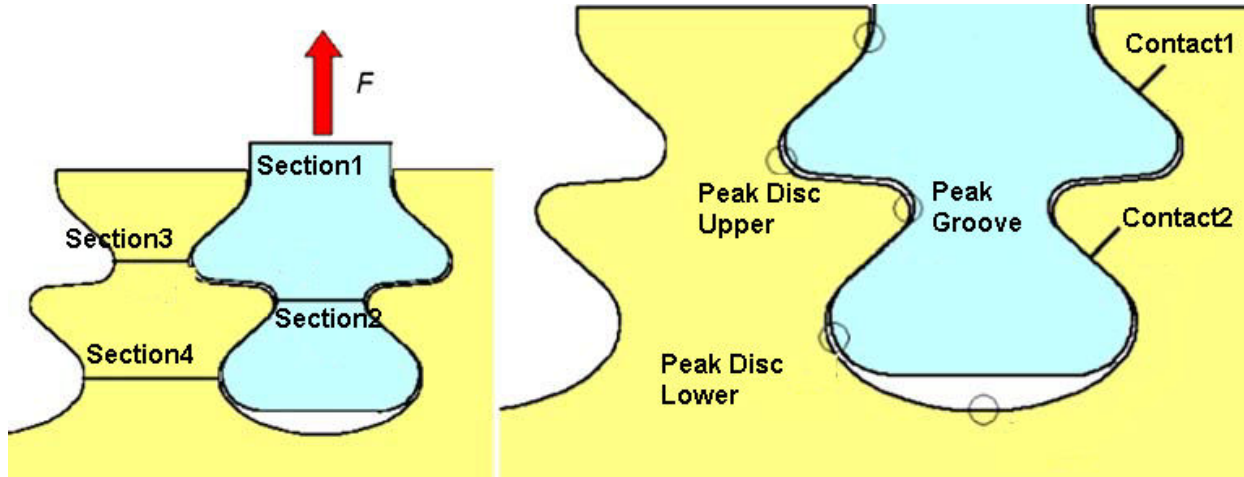


Figure 2: Firtree attachment critical stress areas

Optimization problem of blade-disc firtree structural optimization described above is formulated as follows (Eqs. (2-4)).

$$\mathbf{find} \ x = \begin{Bmatrix} \text{shank width} \\ \text{Contact angle} \\ \text{Face angle} \\ \text{Flank angle} \\ \text{Contact length 1} \\ \text{Contact length 2} \\ \text{Lobe 1 radius} \\ \text{Groove radius} \\ \text{Lobe 2 radius} \end{Bmatrix} \quad (2)$$

$$\mathbf{minimize} \ mass(x) \quad (3)$$

$$\begin{aligned}
 &\text{Section1 \& Section2 stresses} \leq 0.5 \times \text{Yield Strength} \\
 &\text{Section3 \& Section4 stresses} \leq 0.5 \times \text{Yield Strength} \\
 &\text{Upper \& Lower Contact stresses} \leq 0.95 \times \text{Yield Strength} \\
 &\text{Peak Groove Stresses} \leq 0.95 \times \text{Yield Strength} \\
 &\text{Peak disc (upper\&lower)} \leq 0.95 \times \text{Yield Strength} \\
 &1.05 \leq \frac{\text{Section1}}{\text{Section2}} \leq 1.22 \\
 &0.53 \leq \frac{\text{Section3}}{\text{Section4}} \leq 0.95
 \end{aligned}
 \tag{4}$$

**Such that**

### 3. STRESS ANALYSIS

Ansys Workbench 14.0 software is used to obtain stresses at the firtree attachment. FEM model is prepared to be basic enough to allow large number of simulations and sufficient enough to capture peak stresses at stress concentration locations. In literature there are models for firtree attachment. As mentioned before, loading on firtree region is caused by centrifugal forces, gas loads and temperature loads. Broaching angle of firtree sloths on turbine disc causes extra stress concentrations because of geometrical conditions. Witek (2006) conducted that most critical loading of firtree region is centrifugal forces. Rao (2006) made a 3D model and inspected stress concentrations in the curvatures.

Turbine blade is excluded from the FEM model and equivalent centrifugal force is applied uniformly to shank instead. Below the live rim of the disc is out of the interest of this study, hence it is excluded. Subject firtree design does not have any broaching angle, hence there is no stress concentration caused by broaching angle and every section along the thickness is the same. Because of these properties of attachment, 2D stress analysis is determined to be sufficient enough for accurate use for optimization. Since the firtree attachment is symmetrical and we aim to reduce the computational time, a half model of attachment is generated. There are similar examples of half 2D analysis of firtree attachments in literature (Abdul-Aziz et al. 1993, Meguid et al. 2000, Song et al. 2002, Keane et al Nair 2005, Maharaj et al. 2012). As depicted in Fig. 3 symmetry condition is applied both disc and blade root. Contact faces of blade root and disc are modeled as frictionless support, hence relative motion between disc and blade root is permitted. Disc is fixed from the lower end of model. Centrifugal force of blade is applied on shank uniformly. Rotation of disc and blade is simulated as rotational velocity, hence centrifugal forces due to the attachment components are modeled. Mesh sizes of elements used in the finite element model is shown in Fig. 4. Static structural analysis is performed. Centrifugal forces and rotational velocities are applied as ramp and one second is used as analysis time step. Single solution of a model is approximately 45 seconds and it takes total 90 seconds to complete an analysis of a design point with updating model parameters and remeshing. On pre-processing phase as shown in Fig. 5 average section stresses of section 1 to 4 and peak stresses are observed.



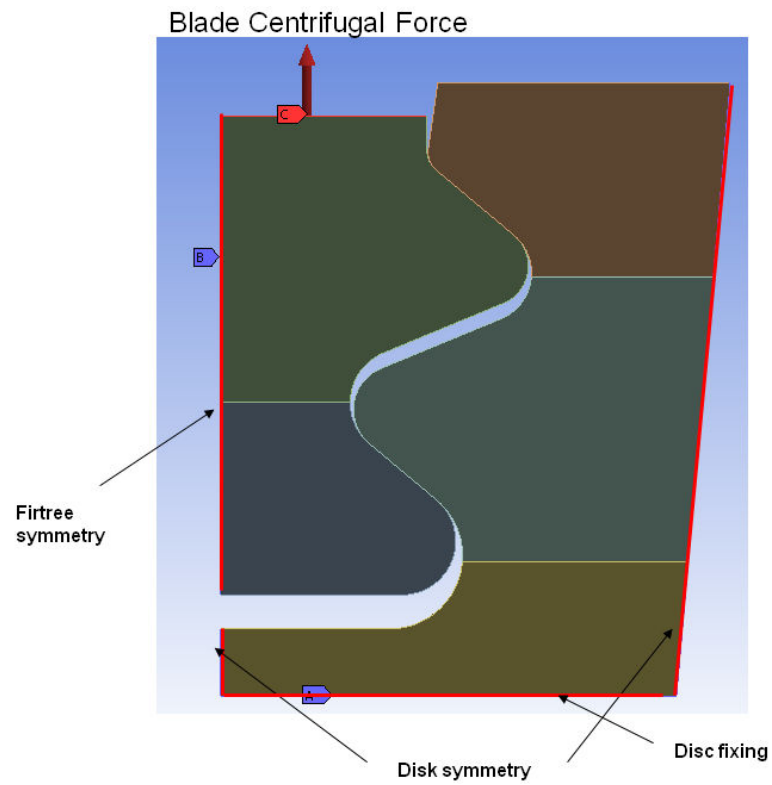


Figure3. 2D finite element model

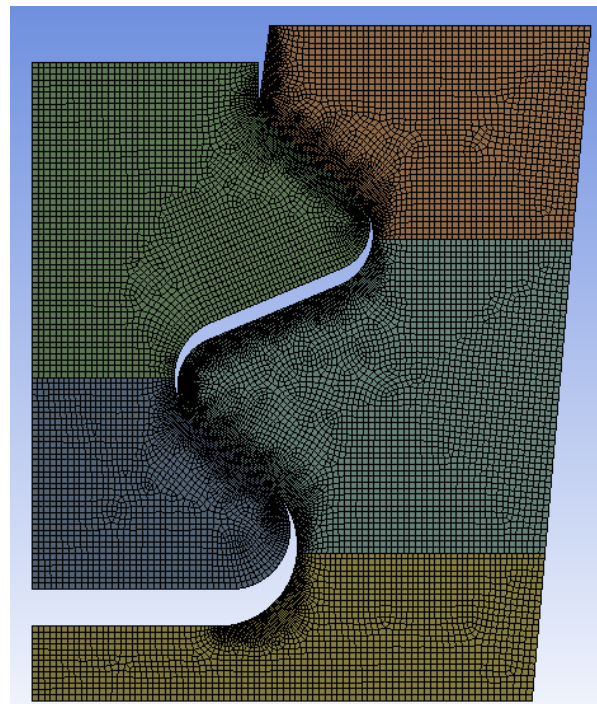


Figure 4. Mesh sizes of elements

Contact stresses are also observed, Fig. 6 shows contact stress distribution. On sections 1 to 4 and contact faces, we are interested with the average stresses, not maximum and minimum stresses.



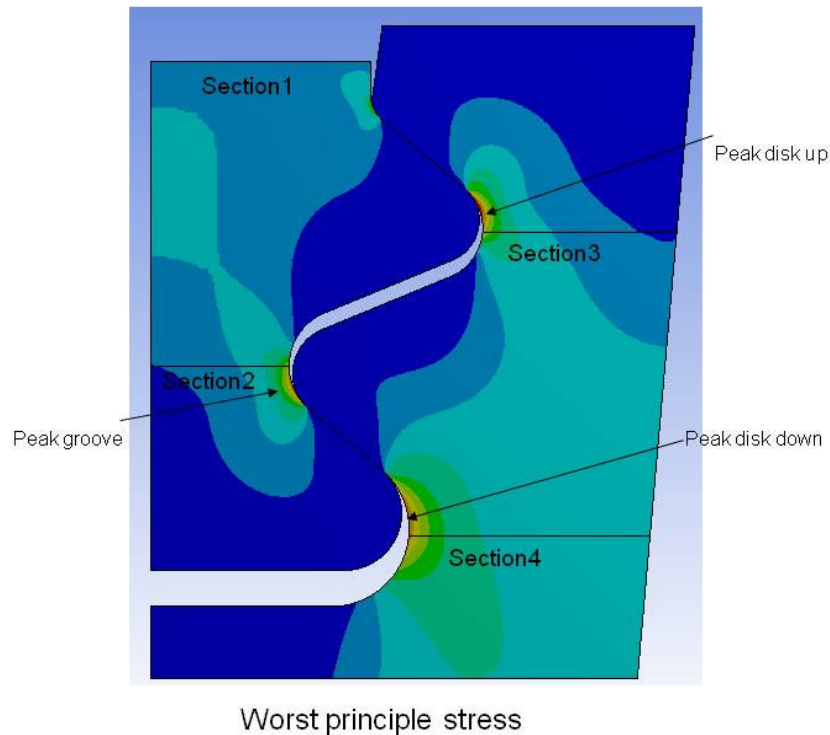


Figure 5: Stress distribution of fir tree attachment

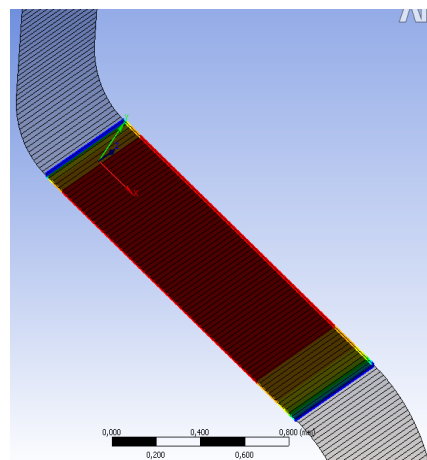


Figure 6: stress distributions on contact faces

Instead of integrating FEM model in the optimization loop directly, analysis are conducted on pre defined design of experiment (DOE) points and results are used to built metamodels. To construct metamodels, FEM analysis and evaluation of result should be performed several times. These operations are not performed manually. Ansys Workbench's parameterize properties are used. Parameters used in CAD model are introduced to Ansys and with using DOE points Ansys Workbench communicates with UG NX6 and automatically updates design according to corresponding DOE point then remeshes and solves the model. With the



help of this feature of Ansys, large numbers of analyses are performed in a short time and with less effort. DOE points and results of analysis are used to construct metamodels. Details of this procedure are provided in section 4. After obtaining optimum candidates, the performance of the candidate is easily evaluated with same method mentioned above.

#### 4. METAMODEL CONSTRUCTION

Metamodels are mathematical models that give fast responses and employed instead of time consuming analysis models, hence shorten the time of optimization procedure as noted earlier. Steps of constructing metamodels can be summarized as follows:

Step 1: Determination of input and output of metamodels. In our case, inputs of metamodels are design parameters of firtree attachment (see Fig. 1). Outputs of metamodels are stresses at critical locations of firtree attachment and mass of the attachment. Note that for each stress value, separate metamodels are constructed.

Step2: Selection of a suitable design of experiment point set according to the nature of the problem. At this point in our case physical experiments are not conducted and FEM analysis are performed. Design of experiment defines metamodel inputs, where each point is used to evaluate stress and mass individually. In our case, the combinations of geometric parameters of the firtree attachment forms the DOE, where the DOE points are determined by using Latin hypercube sampling method.

Step 3: Evaluation of every single point of DOE. In our case, performing FEM analysis for predetermined DOE points and evaluating mass and stress results. Details of analysis are given in section 4.3

Step 4: Construction of metamodels to identify relations of input and outputs. In our case PRS, KRG and RBF metamodels are employed.

Step 5: Validation of metamodels. In our case cross validation method is used. In this method, first every DOE point is temporarily erased and metamodels are constructed. Then, prediction of metamodel is calculated at the temporarily erased point and error is estimated. For every point this procedure is repeated and root mean square error is calculated for cross validation errors.

A simple illustration of a metamodel is shown in Fig. 7. Metamodel's inputs are shank width and contact angle and output is stress. It is not possible to graphically depict metamodel when inputs are more than two. In this case, there are 9 input parameters and 9 stress outputs. Including attachment mass, 10 metamodels are constructed for our problem.

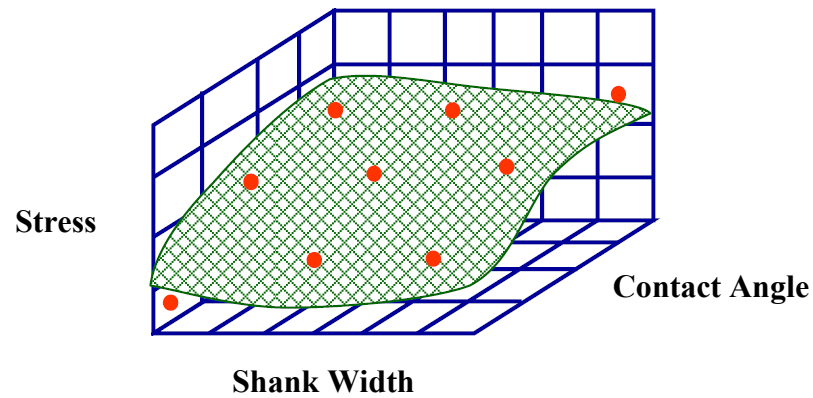


Figure 7: Example DOE and metamodel for stress prediction

If the input of the problem is 9, approximately 110 simulations are sufficient enough for metamodels. In our case 180 simulations are conducted. First 110 simulation points are used to construct metamodel and last 70 simulation is used as performance test points. With first data set, metamodels are constructed and their accuracies are determined using cross validation method (see Table 1). Then, performance of metamodels are measured using last 70 data set (see Table 2). Cross validation errors at Table 1 and test point errors at Table 2 are consistent; hence suitability of cross validation method for measuring performance is confirmed. Finally, using complete data set of 180 points is used to construct metamodels and accuracy of metamodels is measured using cross validation method (see Table 3). Cross validation errors in Table 3 are lower than cross validation errors in table 1, which means that accuracy of metamodels are increased with the increase of input points.

PRS model is the most accurate model amongst the constructed three models and has the lowest errors for all 10 problem response. It is observed that RBF error values are higher than the others. For all model types, section 2 average stress predictions have the highest error values and mass have the lowest error values. It has seen that PRS model, constructed using all 180 DOE points, has error values are mostly smaller than 5% which is sufficient enough for engineering problems.

Table 1: Cross validation errors of the metamodels constructed using first data set (110 simulations)

#	Problem Response	PRS	RBF	KRG
1	Section 1 stress	0.5	5.0	1.6
2	Section 2 stress	8.1	16.8	10.8
3	Section 3 stress	2.1	8.2	4.3
4	Section 4 stress	1.2	5.4	2.7
5	Upper Contact	1.8	6.4	2.5
6	Lower Contact	0.8	6.2	1.7
7	Peak Groove	3.7	7.6	4.3



8	Peak Disc Up	0.8	4.5	2.2
9	Peak Disc Down	0.6	4.7	2.0
10	Mass	0.1	4.6	0.4

Table 2: Test errors of metamodels constructed using first data set (110 simulations) and tested on last data set (70 simulation)

#	Problem Response	PRS	RBF	KRG
1	Section 1 stress	0.4	4.5	1.3
2	Section 2 stress	7.3	17.8	9.5
3	Section 3 stress	1.9	8.8	4.4
4	Section 4 stress	1.1	5.3	3.0
5	Upper Contact	1.4	6.2	2.0
6	Lower Contact	1.0	7.5	1.8
7	Peak Groove	3.6	9.1	4.5
8	Peak Disc Up	0.9	4.5	2.1
9	Peak Disc Down	0.6	3.8	1.7
10	Mass	0.1	5.0	0.4

Table 3: Cross validation errors of the metamodels constructed using all data set (180 simulations)

#	Problem Response	PRS	RBF	KRG
1	Section 1 stress	0.4	3.8	1.2
2	Section 2 stress	5.5	15.4	9.2
3	Section 3 stress	1.5	6.4	4.1
4	Section 4 stress	1.0	4.0	2.7
5	Upper Contact	1.4	4.6	2.0
6	Lower Contact	0.8	4.7	1.5
7	Peak Groove	2.6	6.9	3.9
8	Peak Disc Up	0.7	3.4	1.6
9	Peak Disc Down	0.5	3.2	1.8
10	Mass	0.0	3.2	0.4

## 5. OPTIMIZATION PROCESS

Constructed metamodels are used to solve the optimization problem stated in Eqs. (2-4), where *fmincon* function of MATLAB® software is used to solve optimization. *fmincon* function of MATLAB uses “*sequential quadratic programming*”. Sequential quadratic programming can stuck in local optimums. This problem can be overcome with using *multistart method*. In this method, multiple points in design space is randomly selected and every selected point is used as optimization start point. Best result of the multiple optimizations is declared as optimum. In our case, 100 starting point is used.

Common practice in metamodel based optimization is to construct many metamodels and use the most accurate model in optimization. Previous studies shows that optimum acquired

with most accurate model may not be the best solution, comparing to metamodels with less accurate ones (Acar et al., 2012). In our case, PRS, RBF and KRG metamodels are used in optimization and three candidate optimums are declared. It should be noted that these metamodels are used to predict stress values and only PRS model is used to predict mass values. Optimum candidates are validated using FEM analysis and best ones are determined. Results of optimization are shown in table 4, 5 and 6, in terms of NS (Normalized Stress, Allowable stress / Actual stress).

Table4: Performance of PRS metamodel's optimum candidate

#	Problem Response	Metamodel Prediction	FEM Results	% Error
1	Section 1 stress (NS)	2,652	2,658	-0,2%
2	Section 2 stress (NS)	2,785	2,631	5,5%
3	Section 3 stress (NS)	3,296	3,315	-0,6%
4	Section 4 stress (NS)	2,226	2,230	-0,2%
5	Upper Contact (NS)	1,398	1,378	1,4%
6	Lower Contact (NS)	1,000	0,994	0,6%
7	Peak Groove (NS)	1,000	0,967	3,3%
8	Peak Disc Up (NS)	1,000	1,006	-0,6%
9	Peak Disc Down (NS)	1,096	1,092	0,3%
10	Mass (g)	22,1	22,1	0,0%
	Section 1/ Section 2	1,05	0,99	-6,1%
	Section 3/ Section 4	0,68	0,67	-1,5%

Table 5: Performance of RBF metamodel's optimum candidate

#	Problem Response	Metamodel Prediction	FEM Results	% Error
1	Section 1 stress (NS)	3,601	3,323	7,7%
2	Section 2 stress (NS)	3,781	2,819	25,4%
3	Section 3 stress (NS)	3,597	3,542	1,5%
4	Section 4 stress (NS)	1,996	2,058	-3,1%
5	Upper Contact (NS)	1,100	1,087	1,2%
6	Lower Contact (NS)	1,000	0,971	2,9%
7	Peak Groove (NS)	1,000	0,932	6,8%
8	Peak Disc Up (NS)	1,000	0,959	4,1%
9	Peak Disc Down (NS)	1,001	1,021	-1,9%
10	Mass (g)	20,5	20,5	0,0%
	Section 1/ Section 2	1,05	0,85	-23,5%
	Section 3/ Section 4	0,55	0,58	5,2%

Table 6: Performance of KRG metamodel's optimum candidate

#	Problem Response	Metamodel Prediction	FEM Results	% Error
1	Section 1 stress (NS)	3,135	3,146	-0,4%
2	Section 2 stress (NS)	3,292	2,989	9,2%
3	Section 3 stress (NS)	3,506	3,462	1,2%

4	Section 4 stress (NS)	1,950	2,001	-2,6%
5	Upper Contact (NS)	1,180	1,131	4,2%
6	Lower Contact (NS)	1,000	0,981	1,9%
7	Peak Groove (NS)	1,000	0,988	1,2%
8	Peak Disc Up (NS)	1,000	0,972	2,8%
9	Peak Disc Down (NS)	1,000	1,016	-1,6%
10	Mass (g)	21,3	21,3	0,0%
	Section 1/ Section 2	1,05	0,95	-10,5%
	Section 3/ Section 4	0,56	0,58	3,4%

## 6. ADDITIONAL PARAMETERS AND IMPROVEMENT STUDIES

In this section, two additional parameters are introduced to metamodels and for further improvement of optimization results, stress concentrations reduction studies are performed. Shank height and disc height are taken as fixed values at the beginning of the study, but later on these parameters are introduced for better results. Figure 8 shows geometric parameters with two additional parameters included.

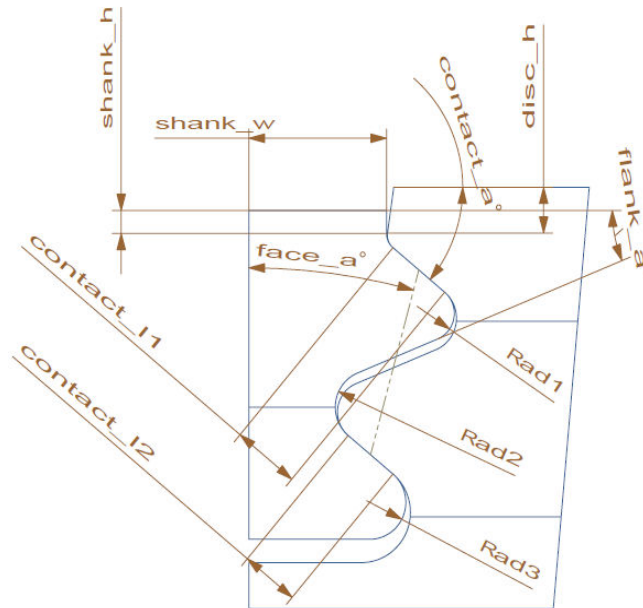


Figure 8: Blade-disc firtree attachment updated geometric dimensions

To improve low cycle fatigue life of firtree attachment, peak stresses at stress concentration locations shown in Fig. 2 are reduced using spline curves instead of using single fillet radii. Similar studies are presented in literature by Song et.al. (2002, 2005).

### 6.1 Disc Upper Stress Concentration Reduction

In this section, it is aimed to reduce stress concentrations on disc upper curvature. Spline curves are used instead of single fillet radius. Spline curvatures are applied to the optimum designs obtained with single fillet radius. Control points of spline are used as optimization

parameters. B-spline method is used to generate spline curves and Figure 9 shows modeling of curvatures with splines.

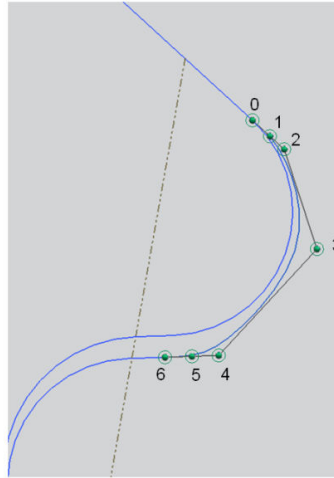


Figure 9: Spline modeling of disc upper curvature

Points shown in Fig. 9 are control points of bspline. Number 0 and 6 control points are start and end points of the radius, obtained from previous optimization studies. There is no change in the attachment geometry except single fillet disc upper curvature here. Control points 1 and 2 are on the same line with the upper contact face to obtain smoother transition and reduced parameters for optimization. Control points 4 and 5 has similar situation. As optimization parameters; 0-1 distance, 0-2 distance, 0-3 horizontal distance, 0-3 vertical distance, 5-6 distance and 4-6 distances are used.

Modeling and optimization procedures mentioned in section 3 and 4 are performed again. Table 7, 8 and 9 shows performance of disc upper stress concentration reduction optimization.

Table 7: Performance of PRS metamodel's optimum candidate for disc upper stress concentration reduction

#	Problem Response	Metamodel Prediction	FEM Results	% Error
1	Section 1 stress (NS)	2,221	2,221	0,0%
2	Section 2 stress (NS)	2,332	2,333	0,0%
3	Section 3 stress (NS)	3,404	3,399	0,2%
4	Section 4 stress (NS)	2,223	2,223	0,0%
5	Upper Contact (NS)	1,272	1,272	0,0%
6	Lower Contact (NS)	1,191	1,191	0,0%
7	Peak Groove (NS)	1,101	1,102	0,0%
8	Peak Disc Up (NS)	1,267	1,244	1,8%
9	Peak Disc Down (NS)	1,123	1,123	0,0%
10	Mass (g)	23,7	23,7	0,0%
	Section 1/ Section 2	1,05	1,05	0,0%
	Section 3/ Section 4	0,65	0,65	0,0%

Table 8: Performance of RTF metamodel's optimum candidate for disc upper stress concentration reduction

#	Problem Response	Metamodel Prediction	FEM Results	% Error
1	Section 1 stress (NS)	2,637	2,221	15,8%
2	Section 2 stress (NS)	2,964	2,301	22,4%
3	Section 3 stress (NS)	4,707	3,346	28,9%
4	Section 4 stress (NS)	2,630	2,224	15,4%
5	Upper Contact (NS)	1,458	1,283	12,0%
6	Lower Contact (NS)	1,483	1,179	20,5%
7	Peak Groove (NS)	1,389	1,088	21,7%
8	Peak Disc Up (NS)	1,583	1,111	29,8%
9	Peak Disc Down (NS)	1,325	1,122	15,3%
10	Mass [g]	23,7	23,7	0,0%
	Section 1/ Section 2	1,0	1,1	9,1%
	Section 3/ Section 4	0,7	0,6	-16,7%

Table 9: Performance of KRG metamodel's optimum candidate for disc upper stress concentration reduction

#	Problem Response	Metamodel Prediction	FEM Results	% Error
1	Section 1 stress (NS)	2,221	2,221	0,0%
2	Section 2 stress (NS)	2,343	2,340	0,1%
3	Section 3 stress (NS)	3,454	3,407	1,4%
4	Section 4 stress (NS)	2,223	2,223	0,0%
5	Upper Contact (NS)	1,268	1,269	-0,1%
6	Lower Contact (NS)	1,194	1,194	0,0%
7	Peak Groove (NS)	1,106	1,105	0,1%
8	Peak Disc Up (NS)	1,267	1,249	1,4%
9	Peak Disc Down (NS)	1,123	1,124	0,0%
10	Mass (g)	23,7	23,7	0,0%
	Section 1/ Section 2	1,1	1,1	0,0%
	Section 3/ Section 4	0,7	0,6	-16,7%

## 6.2 Disc Lower Stress Concentration Reduction

In this section, it is aimed to reduce stress concentrations on disc lower curvature similar to section 5.1. Spline curves are used instead of single fillet radius. Control points of spline are used as optimization parameters. Bspline method is used to generate spline curves and Figure 10 shows modeling of curvatures with splines.

Points shown in Figure 10 are control points of bspline. Number 0 and 6 control points are start and end points of the radius, obtained from previous optimization studies. There is no change in the attachment geometry except single fillet disc lower curvature here. Control



points 1 and 2 are on the same line with the lower contact face in order to obtain smoother transition and reduced parameters for optimization.

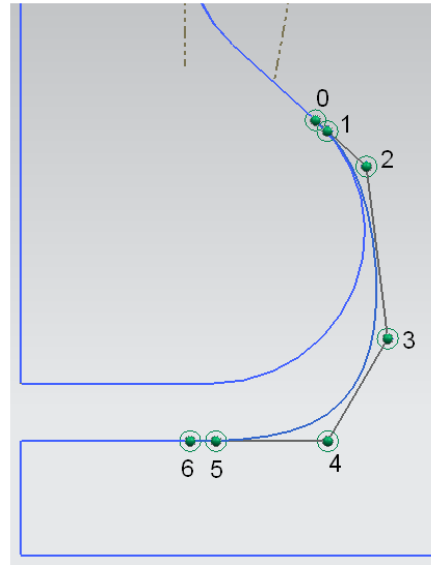


Figure 10: Spline modeling of disc lower curvature

Control points 4 and 5 has similar situation. As optimization parameters; 0-1 distance, 0-2 distance, 0-3 horizontal distance, 0-3 vertical distance, 5-6 distance and 4-6 distances are used.

Modeling and optimization procedures mentioned in section 3 and 4 are performed again. Table 10,11 and 12 shows the performance of disc lower stress concentration reduction optimization study.

Table 10: Performance of PRS metamodel's optimum candidate for disc lower stress concentration reduction

#	Problem Response	Metamodel Prediction	FEM Results	% Error
1	Section 1 stress (NS)	2,221	2,221	0,0%
2	Section 2 stress (NS)	2,349	2,349	0,0%
3	Section 3 stress (NS)	3,374	3,376	0,0%
4	Section 4 stress (NS)	2,244	2,257	-0,6%
5	Upper Contact (NS)	1,266	1,266	0,0%
6	Lower Contact (NS)	1,135	1,132	0,2%
7	Peak Groove (NS)	1,106	1,106	0,0%
8	Peak Disc Up (NS)	1,245	1,246	0,0%
9	Peak Disc Down (NS)	1,301	1,303	-0,1%
10	Mass (g)	23,7	23,7	0,0%
	Section 1/ Section 2	1,1	1,1	0,0%
	Section 3/ Section 4	0,7	0,7	0,0%



Table 11: Performance of RBF metamodel's optimum candidate for disc lower stress concentration reduction

#	Problem Response	Metamodel Prediction	FEM Results	% Error
1	Section 1 stress (NS)	4,970	2,221	55,3%
2	Section 2 stress (NS)	5,644	2,392	57,6%
3	Section 3 stress (NS)	7,297	3,348	54,1%
4	Section 4 stress (NS)	3,868	2,079	46,2%
5	Upper Contact (NS)	2,716	1,252	53,9%
6	Lower Contact (NS)	2,556	1,129	55,8%
7	Peak Groove (NS)	2,600	1,125	56,7%
8	Peak Disc Up (NS)	2,644	1,228	53,5%
9	Peak Disc Down (NS)	2,440	1,098	55,0%
10	Mass (g)	23,5	23,5	0,0%
	Section 1/ Section 2	1,1	1,1	0,0%
	Section 3/ Section 4	0,6	0,5	-20,0%

Table 12: Performance of KRG metamodel's optimum candidate for disc lower stress concentration reduction

#	Problem Response	Metamodel Prediction	FEM Results	% Error
1	Section 1 stress (NS)	2,221	2,221	0,0%
2	Section 2 stress (NS)	2,350	2,265	3,6%
3	Section 3 stress (NS)	3,374	3,415	-1,2%
4	Section 4 stress (NS)	2,226	2,138	3,9%
5	Upper Contact (NS)	1,266	1,292	-2,1%
6	Lower Contact (NS)	1,123	1,427	-27,1%
7	Peak Groove (NS)	1,107	1,048	5,3%
8	Peak Disc Up (NS)	1,245	1,272	-2,1%
9	Peak Disc Down (NS)	1,357	1,034	23,8%
10	Mass (g)	23,7	23,7	0,0%
	Section 1/ Section 2	1,1	1,0	-10,0%
	Section 3/ Section 4	0,6	0,7	14,3%

## 7. RESULTS AND DISCUSSIONS

In this study, design of blade-disc firtree attachment of an aero-engine is optimized. Objective of the optimization is minimization of attachment mass while stress values and stress ratios are used as constraints. Stresses are evaluated using ANSYS workbench software. Design parameters of firtree attachment are used as input, stress values and mass value of attachment are used as output for metamodeling. PRS, RBF and KRG metamodels are employed for predicting of stress values and PRS metamodel is used for predicting mass values. Considering metamodel's accuracies following results are obtained:

- PRS metamodel shows best performance modeling firtree attachment's stress values and RBF has maximum error values.
- Predicting of section 2 stresses has maximum error in metamodels and mass prediction has minimum prediction error.
- PRS metamodels cross validation errors for all problem responses are within 0.0% and 5.5 %. Errors at these levels are acceptable for engineering problems.

For each metamodel an optimum candidate is obtained. Validation of these optimum candidate designs are performed using FEM analysis. Results of the validation are as follows:

- Amongst the 3 metamodels PRS shows the best performance and RBF shows worst performance.
- Optimum candidates do not violate any of the constraints.
- At peak stresses at stress concentration locations, stress reduction is achieved up to %25
- Distribution of section stresses are managed in a desired manner.
- Mass of the attachment is increased but considering stress reductions it is an acceptable increase
- Stress values are kept lower than the material's acceptable limits considering 2D FEM analysis in this study and there may be differences in 3D due to non-uniform distribution of centrifugal load.

Table 13 shows comparison of initial geometry and final optimization results with additional parameters and improvement studies.

Table 13: Firtree optimization results

	Initial Geometry	Final Geometry	Final vs Original
Section 1 stress (NS)	2,775	2,219	20,1%
Section 2 stress (NS)	2,186	2,345	-7,3%
Section 3 stress (NS)	3,667	3,370	8,1%
Section 4 stress (NS)	2,197	2,257	-2,7%
Upper Contact (NS)	1,411	1,267	10,3%
Lower Contact (NS)	1,267	1,133	10,6%
Peak Groove (NS)	0,840	1,106	-31,6%
Peak Disc Up (NS)	0,931	1,245	-33,7%
Peak Disc Down (NS)	0,999	1,302	-30,3%
Mass (g)	20,3	23,7	14,4%
Section 1/ Section 2	0,79	1,06	Improved
Section 3/ Section 4	0,60	0,67	Improved



## REFERENCES

1. **Abdul-Aziz A., (1993)**, "Assessment of crack growth in a space shuttle main engine first-stage, high-pressure fuel turbopump blade" Lewis Research Center Group, Brook Park, Ohio.
2. **Acar, E., Guler, M.A., Gerçeker, B., Cerit, M.E., and Bayram, B., (2011)**, "Multi-objective crashworthiness optimization of tapered thin-walled tubes with axisymmetric indentations," Thin-Walled Structures, Vol. 49, No. 1, pp. 94-105.
3. **Brujic D., Ristic M., Mattone M., Maggiore P., De Poli G.P., (2009)**, "CAD based shape optimization for gas turbine component design" Structural and Multidisciplinary Optimization, Vol. 41, pp. 647-659.
4. **Buhmann, M.D., (2003)**, "Radial Basis Functions: Theory and Implementations," Cambridge University Press, New York, NY.
5. **Gunn, S.R., (1997)**, "Support Vector Machines for classification and regression," Technical Report, Image Speech and Intelligent Systems Research Group, University of Southampton, UK.
6. **Huang, Z., Wang, C., Chen, J., Tian, H., (2011)**, "Optimal design of aeroengine turbine disc based on kriging surrogate models," Computers and Structures, Vol. pp. 27–37.
7. **Keane A.J., Nair P.B, (2005)**, "Turbine blade design (II) fir-tree root geometry" Computational Approaches for Aerospace Design: The pursuit of excellence, Wiley, Southampton, UK.
8. **Lee, K-K, Lee, K-H, Han, S-H, (2011)**, " Use of an orthogonal array based on the Kriging model to maximize the fatigue life of a turbine blade," International Journal of Structural Integrity, Vol. 2 No. 3, pp. 303-313.
9. **Maharaj C., Morris A., Dear J.P., (2012)**, "Modeling of creep in Inconel 706 turbine disc fir-tree", Materials Science & Engineering, Vol. 558, pp.412-421.
10. **Meguid S.A., Kanth P.S., Czekanski A., (2000)**, "Finite element analysis of fir-tree region in turbine discs", Finite Elements in Analysis and Design, Vol.35, pp. 305-317.
11. **Myers, R.H., Montgomery, D.C., (2002)**, "Response Surface Methodology: process and product optimization using designed experiments," Wiley, New York, NY.



12. **Papanikos P., Meguid S.A., Stjepanovic Z., (1998)**, "Three-dimensional nonlinear finite element analysis of dovetail joints in aeroengine discs" *Finite Elements in Analysis and Design*, Vol.29, pp. 173-186.
13. **Rao J.S., Suresh S., (2006)**, "Blade root shape optimization", *Altair CAE users conference*, Bangalore.
14. **Sacks, J., Welch, W. J., Mitchell, T. J. Wynn, H. P., (1989)**, "Design and Analysis of Computer Experiments," *Statistical Science*, Vol. 4, No. 4, pp. 409-435.
15. **Simpson, T.W., Peplinski, J.D., Koch, P.N., Allen, J.K., (2001)**, "Metamodels for computer based engineering design: survey and recommendations," *Engineering with Computers*, Vol. 17, pp. 129-150.
16. **Smith, M., (1993)**, "Neural networks for statistical modeling," *Von Nostrand Reinhold*, New York, NY.
17. **Song, W., Keane, A.J., (2005)**, "An efficient evolutionary optimisation framework applied to turbine blade fir-tree root local profiles," *Structural and Multidisciplinary Optimization*, Vol. 29, pp. 382–390.
18. **Song W., Keane A., Rees J., Bhaskar A., Bagnall S., (2002)**, "Turbine blade fir-tree root design optimization using intelligent CAD and finite element analysis" *Computers and Structures*, Vol. 80, pp. 1853-1867.
19. **Venkataraman, S., Haftka, R.T., (2004)**, "Structural optimization complexity: what has Moore's law done for us?" *Structural and Multidisciplinary Optimization*, Vol. 28, pp. 375–387.
20. **Witek, L., (2006)**, "Failure analysis of turbine disc of an aero engine," *Engineering Failure Analysis*, Vol.13,pp. 9-17.

## APPENDIX

### DESCRIPTION OF SELECTED METAMODELING TECHNIQUES

#### Polynomial Response Surface (PRS)

The most commonly used PRS model is the second-order model in the form of a second-degree algebraic polynomial function as

$$\hat{f}(x) = b_0 + \sum_{i=1}^L b_i x_i + \sum_{i=1}^L b_{ii} x_i^2 + \sum_{i=1}^{L-1} \sum_{j=i+1}^L b_{ij} x_i x_j \quad (\text{E1.1})$$

where  $\hat{f}$  is the response surface approximation of the actual response function,  $f$ ,  $L$  is the number of variables in the input vector  $\mathbf{x}$ , and  $b_0$ ,  $b_i$ ,  $b_{ii}$ ,  $b_{ij}$  are the unknown coefficients to be determined by the least squares technique.

#### Radial Basis Function (RBF)

RBF methods were originally developed to approximate multivariate functions based on scattered data. For a dataset consisting of the values of input variables and response values at  $n$  sampling points, the true function  $y(x)$  can be approximated as

$$\hat{y}(x) = \sum_{i=1}^n \lambda_i \phi(\|x - x_i\|) \quad (\text{E1.2})$$

Where  $\hat{y}(\mathbf{x})$  is the prediction of RBF of response function  $y(\mathbf{x})$ ,  $\lambda_i$  interpolation coefficients,  $n$  sampling point number and  $\phi$  is defining the radial basis function. Euclidian norm used in radial basis function,  $\|x - x_i\|$ , represents the radial distance,  $r$  from design point  $\mathbf{x}$  to the sampling point or center  $\mathbf{x}_i$ .

$$r = \|x - x_i\| = \sqrt{(x - x_i)^T (x - x_i)} \quad (\text{E1.3})$$

Unknown interpolation coefficients ( $\lambda_i$ ) are found by minimizing the residual or the sum of the squares of the deviations. In matrix form:

$$[\mathbf{A}]\{\lambda\} = \{\mathbf{y}\} \quad (\text{E1.4})$$

Where,  $[\mathbf{A}] = [\phi\|x_j - x_i\|]$ ,  $i, j = 1, \dots, n$ ,  $\{\lambda\}^T = \{\lambda_1, \lambda_2, \dots, \lambda_n\}^T$  and  $\{\mathbf{y}\}^T = \{y(x_1), y(x_2), \dots, y(x_n)\}^T$ .

Unknown coefficients  $\lambda$  can be found by solving Equation (E1.4).

Some of the most commonly used RBF formulations include: thin-plate-spline, Gaussian and multi-quadratic equations. In this study, multi-quadratic equation (Equation 1.5) is used. Where  $c$  is a constant. Where, sampling points are normalized between 0 and 1 than  $c$  becomes  $0 < c \leq 1$ . The choice of  $c = 1$  is found to be suitable for most function approximations.

$$\phi(r) = \sqrt{r^2 + c^2} \quad (\text{E1.5})$$

#### Kriging (KRG)

Kriging model combines trend of the data used and probabilistic distributions. Response function  $y(\mathbf{x})$  can be expressed as follows:

$$\hat{y}(\mathbf{x}) = p(\mathbf{x}) + Z(\mathbf{x}) \quad (\text{E1.6})$$

Where  $\hat{y}(\mathbf{x})$  is the prediction of RBF of response function  $y(\mathbf{x})$ ,  $p(\mathbf{x})$  is a known polynomial that globally approximates the response,  $Z(x)$  is the stochastic component that generates deviations such that the Kriging model interpolates the sampled response data. Figure E1 shows an example of kriging model, trend, stochastic deviations and sample points for single dimension function.

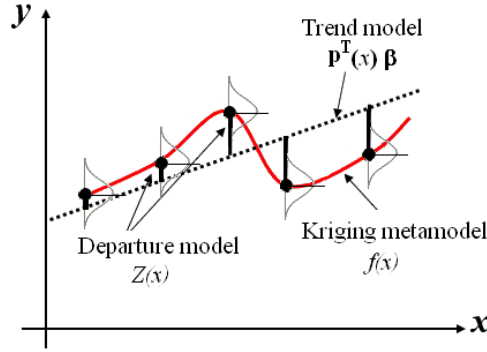


**Figure E1: Response approximation via Kriging metamodel**

The stochastic component has a mean value of zero and covariance of ;

$$COV[Z(x_i), Z(x_j)] = \sigma^2 \mathbf{R}[R(x_i, x_j)] \quad (E1.7)$$

where  $\mathbf{R}$  is  $N \times N$  correlation matrix if  $N$  is the number of data points,  $R(x_i, x_j)$  is correlation function between the two data points  $x_i$  and  $x_j$ . Mostly, the correlation function is chosen as Gaussian, that is,

$$R(\theta) = \prod_{k=1}^L \exp(-\theta_k d_k^2) \quad (E1.8)$$

where  $L$  is the number of variables,  $d_k = x_k^i - x_k^j$  is the distance between the  $k$ th components of the two data points  $x^i$  and  $x^j$  and  $\theta_k$  are the unknown parameters to be determined. Besides Gaussian correlation function, exponential and linear correlation functions can also be used.

Once the correlation function has been selected, the response  $f$  is predicted as;

$$\hat{y}(\mathbf{x}) = \hat{\beta} + \mathbf{r}^T(\mathbf{x}) \mathbf{R}^{-1}(\mathbf{f} - \hat{\beta} \mathbf{p}) \quad (E1.9)$$

where  $\mathbf{r}^T(\mathbf{x})$  is the correlation vector between prediction point  $\mathbf{x}$  and sampling points.  $\mathbf{f}$  represents the responses at sampling points and  $\mathbf{p}$  is an  $L$  vector of ones. The vector  $\mathbf{r}$  and scalar  $\hat{\beta}$  are given as follows:

$$\mathbf{r}^T(\mathbf{x}) = [R(x, x^1), R(x, x^2), \dots, R(x, x^n)]^T, \quad \hat{\beta} = (\mathbf{p}^T \mathbf{R}^{-1} \mathbf{p})^{-1} \mathbf{p}^T \mathbf{R}^{-1} \mathbf{f} \quad (E1.10)$$

Variance of the metamodel can be estimated as;

$$\hat{\sigma}^2 = \frac{(\mathbf{f} - \hat{\beta} \mathbf{p})^T \mathbf{R}^{-1} (\mathbf{f} - \hat{\beta} \mathbf{p})}{n} \quad (E1.11)$$

The unknown parameters  $\theta_k$  can be estimated by solving the following constrained maximization problem (Simpson et al. 2001)

$$\begin{aligned} \text{Max } \Phi(\Theta) &= \frac{-[N \ln(\hat{\sigma}^2) + \ln|\mathbf{R}|]}{2} \\ \text{s.t. } \Theta &> 0 \end{aligned} \quad (E1.12)$$

Where,  $\Theta$  is the vector of unknown parameters  $\theta_k$  and both  $\mathbf{R}$  and  $\hat{\sigma}$  are functions of  $\Theta$ .





## DEVELOPMENT OF NEW CRASH BOXES FOR AUTOMOTIVE INDUSTRY

**Emre DEMİRCİ**, *emre.demirci@btu.edu.tr*, Bursa Teknik Üniversitesi, 16190, Bursa

**Ali Rıza YILDIZ**, *aliriza.yildiz@btu.edu.tr*, Bursa Teknik Üniversitesi, 16190, Bursa

**Fehim SEMERCİ**, *fsemerci@toksanotomotiv.com*, Toksan R&D Center, Bursa

### ABSTRACT

Nowadays, a lot of research works have been conducted in the field of crashworthiness in order to define crash performance of vehicles and crash boxes. In this study, new crash box designs are developed for frontal impact of vehicles. Numerical studies include determination of energy absorption characteristics of different geometries of crash boxes. In addition, these studies include making changes in existing profiles with wall thickness of crash boxes, changing the positions of some of the profiles and adding new profiles.

**Keywords:** Crash box, Frontal Impact, Vehicle design

### 1. INTRODUCTION

The design of new vehicles is driven by many competing criteria, such as improved safety, energy efficiency, lower cost, and increased style flexibility. Especially vehicle crashworthiness, lightweight design, energy economy and environmental protection are vital tasks need to be solved urgently in the automotive industry all over the world in the twenty-first century. Vehicle weight reduction is an important way to realize energy savings and oil economy [1,2]. To make vehicles lighter with a good rating in crashworthiness give an automaker a strong argument for sales. Increased traffic intensity and growing concern of the public have made vehicle safety one of the major research areas in automotive engineering. In vehicle safety, crash boxes have important tasks. Energy absorption capabilities of the crash boxes has been subject of different research works in the literature [3-7]. Crash boxes have been commonly used as energy absorber for their efficient energy absorption capacity in automotive industry. The main aim in crash box design is to control the kinetic energy of the car during impact while preventing the peak force. The specific issue of this research is to design a new crash box structure that substitutes the conventional energy absorber in a frontal vehicle structure.

## 2. NEW CRASH BOX DESIGNS

The crash boxes are used to convert the kinetic energy to plastic deformation in automotive industry. Other purpose of the crash boxes is to reduce the peak force to protect occupants from serious damages while subjected to impact load.

In this work, firstly, an initial crash box is developed. In order to increase energy absorption amount and to reduce peak force of the initial design, new designs are developed as surface. In design works, the geometry of the initial design is changed and triggers are used in new designs. Additionally, the components of the energy absorber and thickness values are modified. In new designs, number of the spot welds and locations are changed. In figure 2.1, and in figure 2.2, initial design and alternative crash box designs are shown.

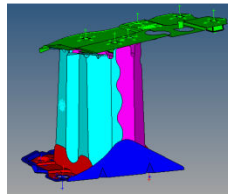
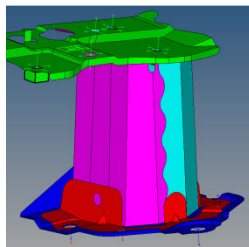
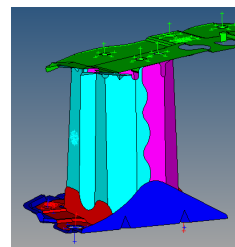


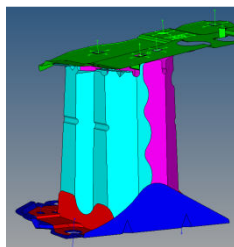
Figure 2.1 Initial design



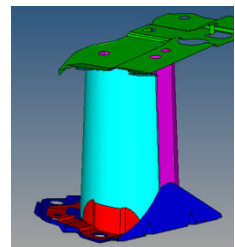
D1



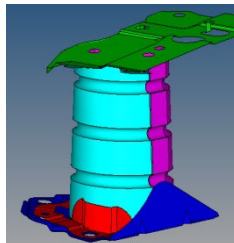
D 2



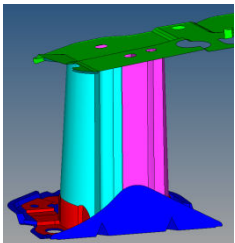
D 3



D 4



D 5



D 6

Figure 2.2 New crash box designs

## 2.1 FE model and material properties

The developed crash box geometries are imported into Hypermesh. Meshing of the components of the crash boxes is carried out using shell elements of size 3mm x 3mm. In this research work, SPC 400 steel is used as material. Material model card selected for SPC 400 is MAT 24 in Is-dyna, known as Piecewise linear isotropic plasticity. Material properties are given as below.

Density = 7850 kg/m<sup>3</sup>

Elasticity modulus, E = 206 GPa

Poisson ratio, PR=0.3

Shear stress, SIGY= 318 MPa

True stress-strain values for used material are given in Table 2.1.

Table 2.1 True stress-strain values for SPC 400 steel

$\sigma$ [MPa]	318,02	363,49	435,39	478,47	508,29	532,10	551,66	564,68
$\epsilon$	0	0,0212	0,0506	0,0814	0,1134	0,1479	0,1841	0,2255

In table 2.2, component number, thickness, number of the spot welds, mass values are given for new designs.

Table 2.2. Properties of the crash boxes developed in this study

	Thickness (mm)	Number of Components	Number of spot welds	Mass	Mass (%)
<b>Initial design</b>	1,2	6	23	1069,09	-
<b>D1</b>	1,3	6	23	1014,8	-5,078
<b>D 2</b>	1,2	6	23	1068,63	-0.043
<b>D3</b>	1,25	5	23	1049,11	-1,869
<b>D 4</b>	1,5	5	21	1003,05	-6,177
<b>D 5</b>	1,6	5	20	1071,26	0,203
<b>D 6</b>	1,2	5	21	1077,22	0,761

In this work, a rigid wall modeled as 80 kg and moved at a speed of 15.6 m/s. The boundary conditions and other definitions are shown in Fig 2.3 The crash analysis of the all design are done in Ls dyna.

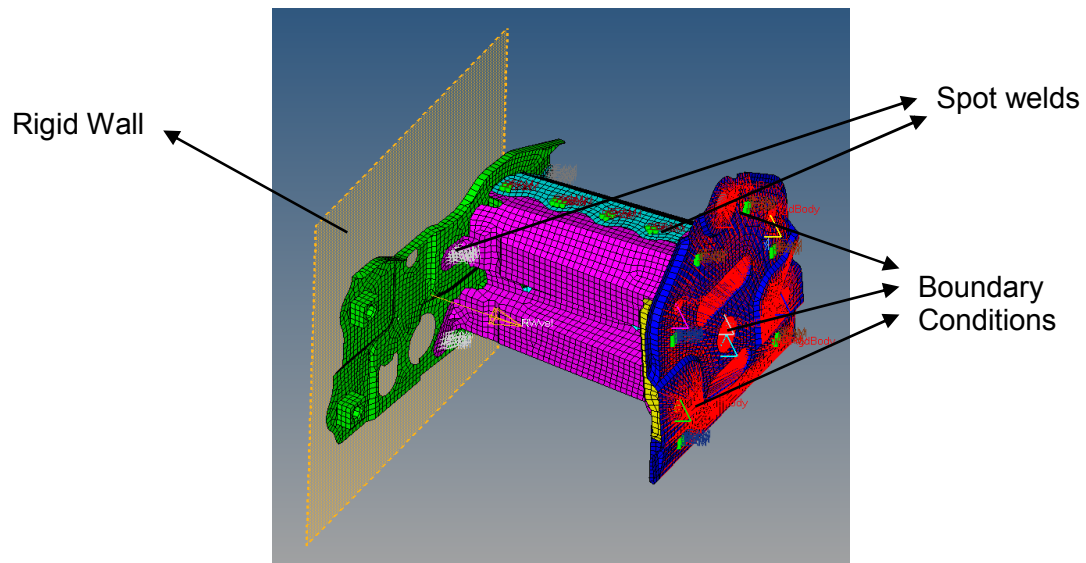


Figure 2.3 Rigid wall, spot welds and boundary conditions

### 3. CONCLUSIONS

The amount of the energy absorption and peak force versus displacement for all designs are shown in fig 3.1 and 3.2.

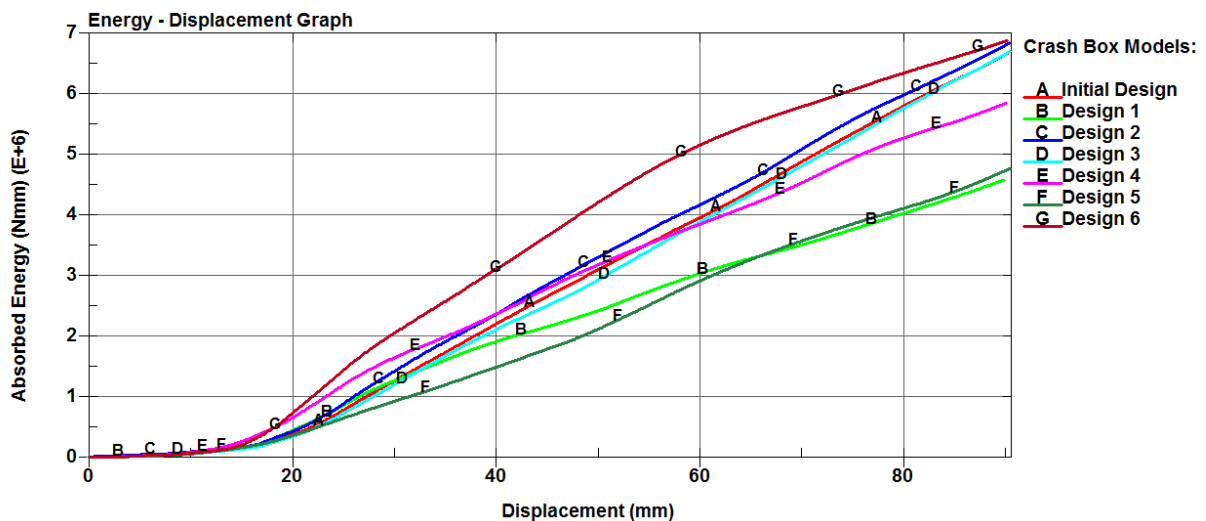


Figure 3.1 Energy absorption-displacement graph for all designs

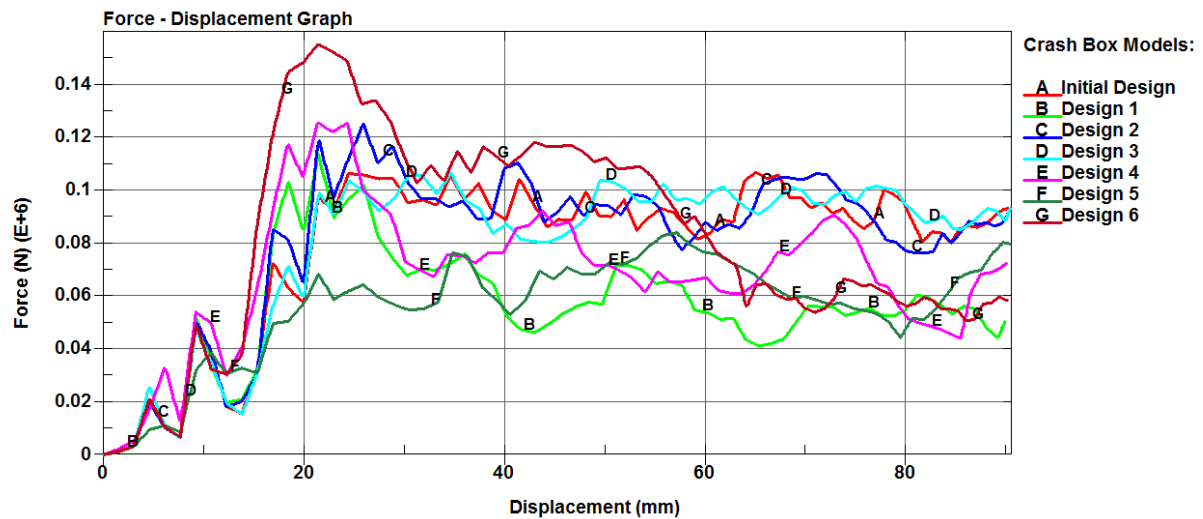


Figure 3.2 Force- displacementgraph for all designs

The figures show that energy absorption and peak force are related to the thickness of the crash boxes, triggers and cross-section. The energy absorption and peak force values of the all designs are given inTable3.1.

Table 3.1 Results of the crash analysis

	Energy absorption (kJ)	Peak force (kN)	Force efficiency (%)
<b>Initial design</b>	6,66	107	62
<b>D 1</b>	4,57	113,86	40,14
<b>D 2</b>	6,83	125,33	54,50
<b>D3</b>	6,7	106,80	62,71
<b>D4</b>	5,84	125,81	46,42
<b>D 5</b>	4,76	84,15	56,57
<b>D 6</b>	6,87	155,45	44,19

As can be seen fromTable 2.2 ve Table 3.1, design 3 has better performance as initial design. Additionally, mass, number of the components and cost are reduced.The all designs presented in this work will be tested using Instron Drop tower in Bursa Technical University.

## **Acknowledgments**

This study is funded by the Turkish Ministry of Science, Industry and Technology and TOKSAN R&D Center within the scope of the SAN-TEZ project 01348.STZ.2012-1.

## **REFERENCES**

1. **Yildiz, A.R. , Solanki, K.** (2012), Multi-objective optimization of vehicle crashworthiness using a new particle swarm based approach", International Journal of Advanced Manufacturing Technology, Vol: 59(1-4):pp.367-376.
2. **Acar E., Güler, M.A., Gerçeker, B., Cerit, M.E., Bayram, B., (2011)**, Multi-objective crashworthiness optimization of tapered thin-walled tubes with axisymmetric indentations, Thin wall Struct, 49, 94-105.
3. **Langseth, M., (2003)**, "Crashworthiness of Light-weight Automotive Structures 2001-2006", NorLight Conference, Tron
4. **Nagel, G., (2005)**, "Impact and Energy Absorption of Straight and Tapered Rectangular Tubes", PhD Thesis, The School of Civil Engineering Queensland University, Queensland.
5. **Alghamdi, A.A.A., (2001)**, "Collapsible Impact Energy Absorbers: an overview ", Thin-Walled Structures, Vol. 39, pp. 189-213.
6. **Chathbai, A., (2007)**, "Parametric Study of Energy Absorption Characteristic of a Rectangular Aluminum Tube Wrapped With E-Glass/Epoxy", Master Thesis, Wichita State University, **Mechanical Engineering Department, Kansas, USA.**
7. **Jin, S.Y., Altenhof, W., (2007)**, "Comparison of the Load/Displacement and Energy Absorption Performance of Round and Square Aa6061-T6 Extrusions Under a Cutting Deformation Mode", International Journal of Crashworthiness, 12(3), 265- 278.



## INVESTIGATING THE EFFECTS OF VARIABLE FEED RATE ON TOOL LIFE IN TURNING

**Ali ORAL**, *alioral@balikesir.edu.tr* Balikesir University, 10145 Balikesir, Turkey

**M. Cemal ÇAKIR**, *cemal@uludag.edu.tr* Uludag University, 16100 Bursa, Turkey

**Demet GÖNEN**, *dgonen@balikesir.edu.tr* Balikesir University, 10145 Balikesir, Turkey

**A. Deniz KARAOĞLAN**, *deniz@balikesir.edu.tr* Balikesir University, 10145 Balikesir, Turkey

### ABSTRACT

The life of a tool is affected by many factors such as cutting speed, depth of cut, chip thickness, tool geometry, workpiece material or the cutting fluid and rigidity of machine tool. In this paper, an innovative turning strategy, variable feed turning, was introduced and a thorough investigation has been carried out to study the effect of gradual feed rate on tool life at constant depth of cut and cutting speed with no cooling fluid. Turning experiments with both constant and variable feed rates were conducted and comparisons were made to show the significant influence of variable feed rate. Feed rate was increased twice gradually in every millimeter at the beginning of turning and kept constant for the rest of the cut. Apart from the reduction in initial wear, the new turning strategy produced very successful results regarding the tool wear in moderate wear zone and considerable increase of 42% in tool life was achieved. Besides, the new strategy provided a longer tool life (upto 47% increase) along the entire life of tool.

**Keywords:** Tool life, Initial wear, variable feed rate

### 1. INTRODUCTION

Among the metal cutting methods, turning is one of the widely used material removal method in industry. Chips removed from the material surface frictionally slide on the surface once they are deformed due to high normal stresses and shearing tensions. As a result, tool wear occurs [Xavior\_2009, Kophac\_1998].

Tool wear is a time dependent process and is a result of complicated physical, chemical, and thermo-mechanical phenomena. Because different “simple” mechanisms of wear (adhesion, abrasion, diffusion, oxidation, etc.) act simultaneously with predominant influence of one or more of them in different situations, identification of the dominant mechanism is far

from simple actions. As cutting proceeds and the cutting temperature increases, the amount of tool wear increases gradually.

Tool wear is generally considered to be a result of mechanical (thermo-dynamic wear, mostly abrasion) and chemical (thermo-chemical wear, diffusion) interactions between the tool and workpiece [Dahu Z., Xiaoming Z., Han D.\_2013, Jianwen H., Chou K.Y.\_2007]. Primary tool wears are classified as flank wear, crater wear and nose wear, are important wears which will affect the smoothness of the product, cost of operation and performance (Figure 1).

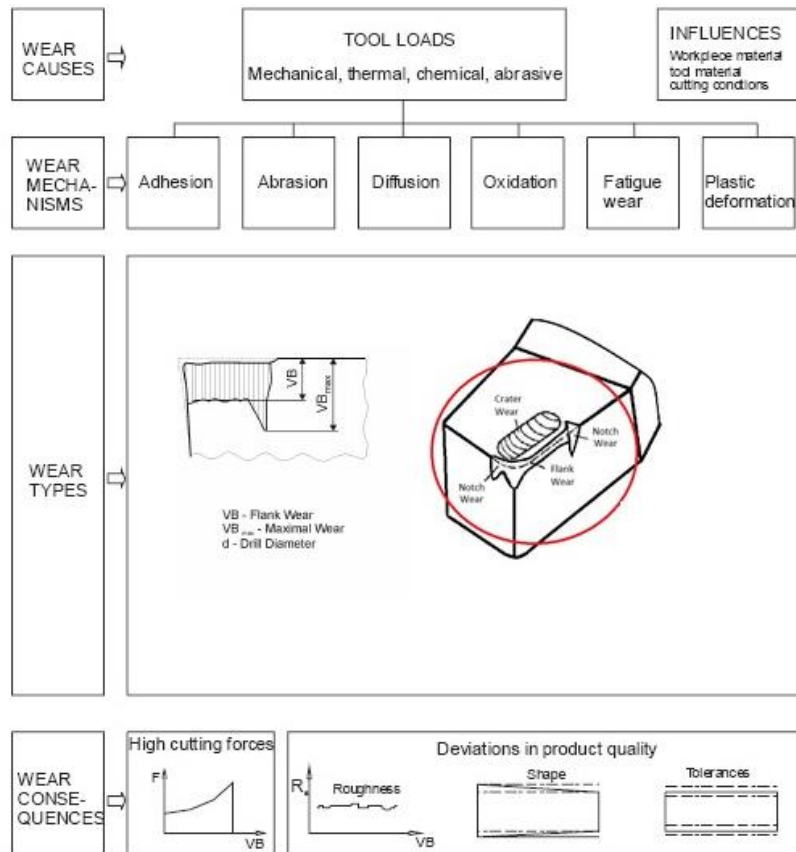


Figure 1. Types of Wear [Grzesik\_2001]

The correlation of  $V_B$  versus cutting time (so-called wear curve) is shown in Figure 2. Wear curve that has a straight line in its central part, whereas the terminal fragments are presented by curved lines consists of three zones: initial wear, steady wear (so called moderate wear) and accelerated wear [Mehrban\_2008, Grzymkowski and Kapinski\_1972, Janecki and Hebda\_1969, Dmochowski\_1978]. Tool wear shows a rapid increase at the very beginning of the cut (initial wear). Following this rapid increase, wear rate slows down and keeps climbing up with a linear increase. As the tool life comes to an end, wear rate accelerates, and therefore, the tool life expires as the cutting operation continues [Özdemir\_2003].



Various studies have been conducted about the representation of wear curve. Kaczmarek presented the wear curve in the form of three connected line segments (Fig. 3) showing the dependence of the wear land height ( $h_p$ ) on the cutting time  $t$  [Kaczmarek\_1970].

Hryniewicz and Pluta presented a model of the entire wear curve, covering all of its characteristic segments relating to the cutting process from the beginning to its end [Hryniewicz T., Pluta Z.\_2012]. In their novel model they represented the wear curve in four periods of time (first, without any detectable wear; second, initial wear; third, moderate wear; fourth, accelerated wear). In their model they assumed that the first period of the curve has not always been determined univocally; due to the fact that the measurements of parameter of the tool edge wear begin after extended machining time, which does not allow characterization of geometric changes of the edge during the first period of its operation (Figure 4).

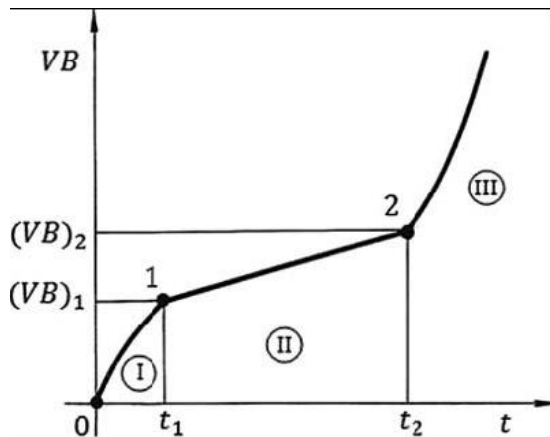


Figure 2. Wear curve [Mehrban\_2008]

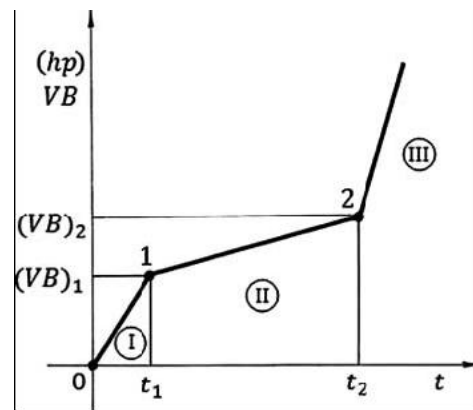


Figure 3. Linearized wear curve (Kaczmarek\_1970)

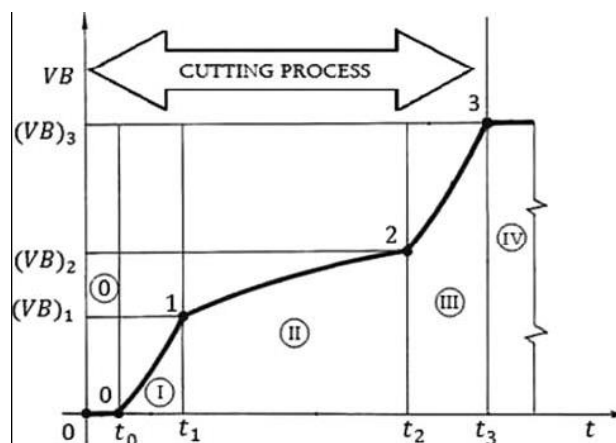


Figure 4. A novel model for the wear curve (Hryniewicz T., Pluta Z.\_2012)

Özdemir et al. investigated the factors that affect initial wear and found out that the most important factor is the feed rate [Özdemir\_2009]. Oral et al. indicated that an essential part of

initial wear zone is caused by extreme cutting forces generated on first contact between the tool and the workpiece [Oral\_2010]. Suggesting that the initial wear increases due to the increase of cutting forces at the first contact, it is assumed that the initial wear will decrease if the forces are reduced [Oral\_2013].

Sikdar and Chen presented the experimental results and discussed the use polynomial equations to express the relationship between cutting forces and flank wear areas in their studies [Sikdar S.K. and Chen M., 2002]. Yuefeng et al, performed a turning operation for a period of 2 minutes using different cutting inserts from various tool manufacturers and he suggested that it is possible to establish a correlation between initial wear and uniform wear [Yuefeng\_2010].

The most widely used tool life equation is the Taylor tool life equation [Taylor\_1907], which relates the tool life to the cutting speed  $V$  through an empirical tool life constant,  $C_t$ :

$$VT^n = C_t \quad (1)$$

When  $T$  is specified in minutes,  $C_t$  is the cutting speed which yields one minute tool life. The exponent  $n$  determines the slope of the tool life curve. Although Taylor's equation reflects the dominant influence of the cutting speed on the tool life, it does not account for the smaller but the significant effects of the feed rate and depth of the cut. For this reason extended Taylor equation [Woldman and Gibbons\_1951], is often used.

$$VT^n f^a d^b = K_t \quad (2)$$

Values of  $K_t$ ,  $n$ ,  $a$  and  $b$  for specific tool grades and common work materials are sometimes tabulated in tooling catalogues.

As can be observed from the literature, many research studies have been conducted on cutting parameters - tool life relations in turning operations. However, no study has been reported in the literature about the reduction of wear, especially initial wear by variable feed rate. In this study, a group of machining test was conducted in order to evaluate the effects of variable feed onto the tool life in both initial and moderate wear zones.

## 2. EXPERIMENTAL PROCEDURES

AISI 1050 was the workpiece material and TiN coated KORLOY CNMG-120408 (NC3020) was the cutting insert used in the machining tests. The chemical composition of workpiece material is given in Table 1. Machining tests were conducted on cylindrical samples ( $\varnothing 80 \times 200$ ) in dry conditions on Goodway-GS-200 CNC lathe (Figure 5). An Otto-Welpert DIA

TESTOR 2 RC S microscope with a sensitivity of 0.001 mm was used for wear measurements. In accordance with Standard ISO 3685, flank wear ( $V_B$ ) was used as a criterion for tool wear. Cutting parameters used in experiments are given in Table 2 and Table 3. In this study, two groups of flank wear values were acquired, for constant feed and variable feed, respectively. The aim of the study was to investigate the effect of variable feed rate onto the tool life, therefore cutting speed and the depth of cut kept constant.

Table 1. Chemical composition of AISI 1050

C	Mn	Si	P	S
0.52	0.80	0.25	0.035	0.035



Figure 5. CNC lathe used in the experiments

Table 2. Cutting parameters for constant feed turning operation

Cutting speed (m/min)	Feed (mm/rev)	Depth of cut (mm)
280	0.25	3

Table 3. Cutting parameters for variable feed turning operation

Cutting speed (m/min)	Feed (mm/rev)	Depth of cut (mm)
280	$f_1=0.15$ for the first 1 mm; $f_2=0.20$ for the next 1 mm; $f_3=0.25$ for the rest	3

### 3. RESULTS AND DISCUSSION

In this study, influences of variable feed on initial and moderate wear zones have been investigated. Hence, flank wear was measured and evaluated first, in every 2 seconds of turning with a constant feed rate.

As the next step, same process was repeated for the variable feed that was increased from 0.15 mm/rev to 0.20 mm/rev in every millimeter and kept constant at 0.25 mm/rev for the rest of the cut. Initial tool wear results for both constant and variable feed are listed in Table 4 and their comparison is illustrated in Figure 6. Brand new insert was used in each machining test.

Table 4. Initial tool wear results for the first 10 seconds

a) Constant feed rate

Time (s)	Feed (mm/rev)	Flank wear VB - (mm)
2	0.25	0.0215
4		0.0265
6		0.0250
8		0.0275
10		0.0290

b) Variable feed rate

Time (s)	Feed (mm/rev)	Flank wear VB - (mm)
2	f <sub>1</sub> =0.15 for first 1 mm; f <sub>2</sub> =0.20 for next 1 mm; f <sub>3</sub> =0.25 for the rest	0.013
4		0.016
6		0.016
8		0.021
10		0.019

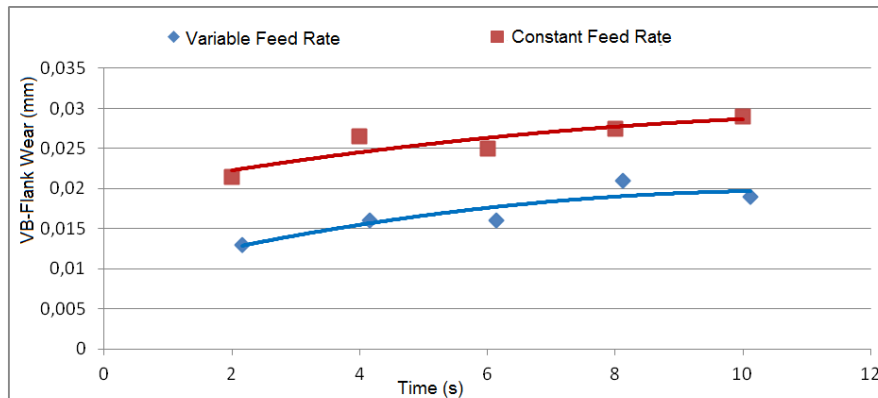


Figure 6: Variable vs constant feed rate

Cutting forces measured in machining tests are illustrated in Figure 7. In Figure 7a, as a result of constant feed rate, cutting force was constant (0.25 mm/rev). However, gradual increase in cutting force was observed as the feed increased gradually from 0.15 to 0.25 mm/rev with an increment of 0.05 mm/rev (Figure 7b). Cutting forces increased proportionally with the increase in feed rate and the initial wear was significantly altered based on the magnitude of these cutting forces.

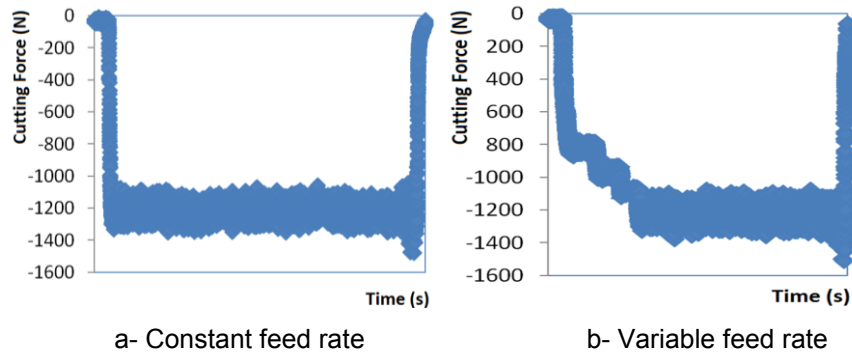


Figure 7. Cutting forces for constant and variable feed turning.

In the present work, in order to investigate the effects of variable feed in moderate wear zone, the tool wear was observed for 120 seconds of machining and comparisons between constant and variable feed rates were made. Thus, a volume of 436404.9 mm<sup>3</sup> was turned at three cutting depths during this period with a constant feed rate first. The wear curve for 120 seconds is given in Figure 8 and tool wear values in Table 5. Flank wear in variable feed was realized to be the half of the wear in constant feed.

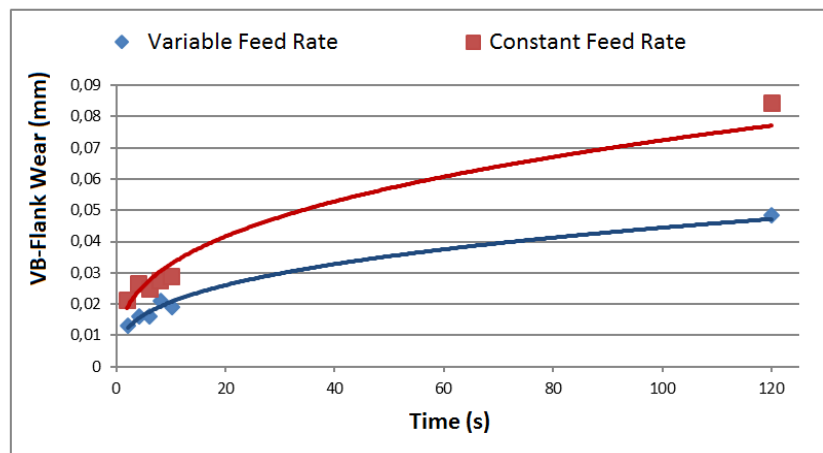


Figure 8. Wear curve for 120 seconds of machining

Next, the same amount of material (436404.9 mm<sup>3</sup>) was machined using variable feed rate for each depth of cut (see Table 5). This time, the machining process was completed in 120.7 seconds which means although the wear was halved, there was 0.7 seconds of extra machining time that had to be eliminated. Thus, the feed at the last part of turning was increased to 0.26 mm/rev. Consequently, machining process was completed in 116.1 seconds removing the same amount of material. Tool wear resulted from the increment in feed is given in Table 6. Wear values for the first 120 seconds are illustrated in Figure 9.

Table 5. Tool wear values for the first 120 seconds

	Cutting speed (m/min)	Depth of cut (mm)	Feed (mm/rev)	Flank wear $V_B$ - (mm)
Constant feed	280	3	0.25	0.0845
Variable feed	280	3	$f_1=0.15$ first 1 mm	0.0485
			$f_2=0.20$ next 1 mm	
			$f_3=0.25$ for the rest	

Table 6. Tool wear after the feed was increased to 0.26 mm/rev (variable feed 2)

Cutting speed (m/min)	Depth of cut (mm)	Feed (mm/rev)	Flank wear $V_B$ - (mm)
280	3	$f_1=0.15$	0.0573
		$f_2=0.20$	
		$f_3=0.26$	

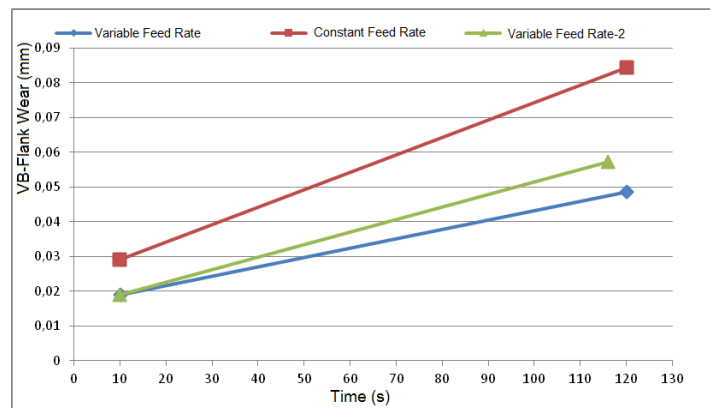


Figure 9. Variations in tool wear for constant and variable feeds

In the second group experiments for moderate wear zone, machining tests were carried on until the flank wear reached a maximum value of 0.20 mm which took 368.7 and 545.4 seconds, for the constant feed and the variable feed, respectively. According to the test results, the difference between the cutting tool lives is 47%. Wear curves of these machining processes are given in Figure 10.

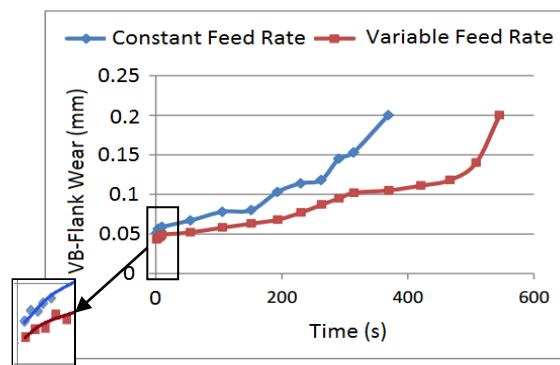


Figure 10. Wear development for entire tool life



#### 4. CONCLUSIONS

In this paper, a new approach for turning operations, variable feed turning, was introduced. Machining tests were performed using variable feed in order to emphasize the difference in both initial and moderate wears from the values obtained at constant feed. In machining tests, cutting speed and depth of cut kept constant and only the effect of variable feed rate was taken into consideration. Consequently, it was concluded that gradual increase of feed rate had a substantial effect in both wear stages owing to the lower cutting forces due to lower feeds at the access of workpiece.

Apart from the reduction in initial wear, the new turning strategy produced very successful results regarding the tool wear in moderate wear zone and considerable increase of 42% in tool life. In order to compensate the 0.58% of increase in machining time resulting from the variable feed, feed rate was increased by a small amount (4%) at the last part of machining. This results not only significant reduction in wear (32%), but reduction in machining time (%3) as well. Besides, the new strategy provided a longer tool life (upto 47% increase) along the entire life of tool.

At last but not least, some more research is intended to be done in order to include the variable feed rate into CAM softwares.

#### REFERENCES

1. **Xavior M.A, Adithan M, (2009)**, “Determining the influence of cutting fluids on tool wear and surface roughness during turning of ASSI 304 austenitic stainless steel”, Journal of Materials Processing Technology, Vol. 209, No.2, 900-909.
2. **Kophac J., (1998)**, “Influence Of Cutting Material And Coating on Tool Quality and Tool Life”, Journal of Materials Processing Technology Vol.78, No.1-3, 95-103.
3. **Dahu Z., Xiaoming Z., Han D. (2013)**, “Tool wear characteristics in machining of nickel-based superalloys”, International Journal of Machine Tools & Manufacture, Vol. 64, 60-77.
4. **Jianwen H., Chou K.Y. (2007)**, “Characterizations of cutting tool flank wear-land contact”, Wear 263, 1454–1458.
- 5 **Grzesik W. (2001)**, “An Investigation of the Thermal Effects in Orthogonal Cutting Associated with Multilayer Coatings”, Annals of the CIRP 50, 53-56.



- 6. Özdemir U., Erten M., (2003),** “Talaşlı İmalat Sırasında Kesici Takımda Meydana Gelen Hasar Mekanizmaları Ve Takım Hasarını Azaltma Yöntemleri”, Havacılık ve Uzay Teknolojileri Dergisi, Vol.1, No.1, 37-50.
- 7. Kaczmarek, J. (1970),** “Fundamentals of Cutting, Abrasive, and Erosive Machining”, WNT: Warsaw, Poland.
- 8. Grzymkowski, M. and Kapinski, S. (1976),** “Friction and Lubrication in the Processes of Sheet Forming,” Mechanik, 2, 69–72.
- 9. Janecki, J. and Hebda, M. (1969),** Friction, Lubrication and Wear of Machine Parts, WNT: Warsaw, Poland.
- 10. Dmochowski, J. (1978),** Fundamentals of Cutting Treatment, PWN: Warsaw, Poland.
- 11. Hyrnewicz T., Pluta Z. (2012),** “Novel Modeling of Tool Edge Wear”, Tribology Transactions, 55, 230-236.
- 12. Özdemir K., Oral A., Çakır M.C., (2009),** "Kesme Parametrelerinin Başlangıç Aşınmasına Etkisinin Deneysel Olarak İncelenmesi", 1. Ulusal Talaşlı İmalat Sempozyumu, Yıldız Teknik Üniversitesi, İstanbul, 84-93.
- 13. Oral A., Çakır M.C., Göktepe M., Türkmen T., (2013),** “Tornalama İşlemlerinde Yeni Bir İşleme Stratejisi-Değişken İlerlemeli Tornalama”, 4. Ulusal Talaşlı İmalat Sempozyumu, Kuşadası, 479-486.
- 14. Merhban M., Naderi D., Panahizadeh V., Naeini H. M., (2008),** “Modelling of Tool Life in Turning Process Using Experimental Method”, International Journal of Metallic Forming, Vol.1, 559-562.
- 15. Sikdar, S.K., Chen, M. (2002),** Relationship Between Tool Flank Wear Area And Component Forces In Single Point Turning”, Journal of material Processing Technology, 128, 2002, 210-215.
- 16. Yuefeng Y., Wuyi C., Liansheng G. (2010),** “Tool Materials Rapid Selection Based on Initial Wear”, Chinese Journal of Aeronautics, Vol.23, 386-392.
- 17. Taylor F.W. (1907),** “On the Art of Metal Cutting”, Transactions of the ASME, 28, 31–35.
- 18. Woldman N.E., Gibbons R.C. (1951),** “Machinability and Machining of Metals”, McGraw-Hill, New York, 47-53.





## EXPERIMENTAL INVESTIGATION OF DOUBLE POINT ANGLE POLYCRYSTALLINE DIAMOND DRILL GEOMETRIES

Yiğit KARPAT, *ykarpat@bilkent.edu.tr* Bilkent University, 06800, Ankara, Turkey

Onur BAHTİYAR, *obahtiyar@tai.com.tr* TUSAŞ-Turkish Aerospace Industries, Ankara, Turkey

### ABSTRACT

Carbon fiber reinforced plastics (CFRPs) possess desirable material properties that make them preferable for the aerospace industry such as high strength to weight ratio, high resistance to corrosion, and low thermal expansion. Drilling of CFRPs has been studied extensively in the literature in recent years, where the influence of process parameters and drill geometry on delamination and tool wear were considered. In this study, three different double point angle polycrystalline diamond (PCD) drills were investigated using a mechanistic approach where the goal is to reveal the influence of drill geometry on the drilling forces and torques and delamination. A generalized drilling force and torque model for double point angle PCD drills is proposed and validated with experiment data. It is shown that proposed model can be used in drill design optimization studies.

**Keywords:** Machining, Drilling, Carbon fiber reinforced plastics, Polycrystalline Diamond

### 1. INTRODUCTION

CFRPs are difficult-to-cut materials due to the abrasive nature of carbon fibers and low thermal conductivity of the polymer matrix. Rapid tool wear is common while machining CFRPs which in turn increases drilling forces and high thrust forces at the hole exits lead to delamination. Many studies have shown that feed and tool geometry are the two most important drilling input parameters. In order to obtain delamination-free holes, it has been recommended to set feed low and rotational speed high [Rawat and Attia , 2009, Karpat et al. 2012].

Polycrystalline diamond (PCD) is a commonly used tool material in drills used for drilling CFRPs due to their high abrasion resistance, thermal conductivity, hardness, and impact toughness. PCD drills usually have a double point angle geometry with various edge lengths and angles which are selected depending on the CFRP drilling operation in hand. It is known that, CFRP material properties change drastically depending on the carbon fiber diameter, length of carbon fibers, type of resin used in the laminate, etc. Therefore, it is not a

straightforward task to select a suitable PCD drill geometry for a given CFRP laminate. In addition, tool manufacturers introduce new drill geometries to the market. The number of studies in the literature on drilling CFRPs with PCD drills are limited despite of their widespread use in industry [Park et al. ,2012, Karpal et al., 2014].

Modeling of CFRP drilling operation is important in order to be able to understand the influence of drill geometry on drilling process outputs such as forces, torques, and hole exit quality [Schulze et al, 2011]. This paper investigates the drilling of CFRPs with double point angle PCD tools. A mechanistic modeling approach is used to understand the drilling characteristics of three PCD drills having different geometries. Experimental thrust force and torque measurements are used to identify cutting force and edge coefficients for each drill. Identified cutting force coefficients are then used to obtain a generalized formulation to predict drilling forces and torques for a given double point angle drill design.

## 2. EXPERIMENTAL PROCEDURE

All the experimental work in this study was conducted under industrial conditions using a five-axis machining center which is specifically designed for machining carbon fiber composites. Experiments were performed under wet conditions by using an emulsion type coolant. An aluminum plate with 8 mm diameter holes was placed under the CFRP laminate to support the hole exits. A Kistler 9123 rotating dynamometer was used to measure the drilling forces and torques. Intermediate modulus UD-CFRP laminates of 8 mm thickness, with equal fiber directions repeating in a sequence of  $0^\circ/45^\circ/90^\circ/135^\circ$  with two layers of  $45^\circ$  and  $135^\circ$  laminates on the top and bottom surfaces, are produced for drilling tests. The intermediate modulus carbon fiber reinforce epoxy resin unidirectional tape used in this study has 59% fiber volume with 2690 MPa tensile strength. Figure 1 shows the CFRP plate and aluminum back plate used in the experiments.

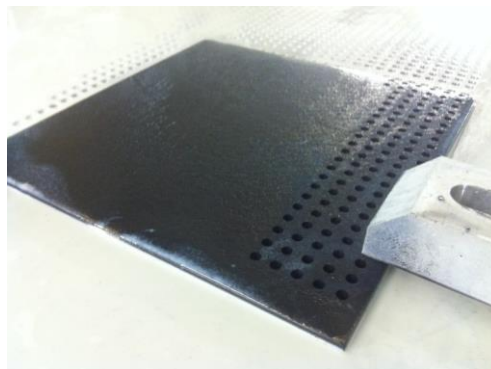


Figure 1. The CFRP plate used in drilling experiments and the aluminum back plate

The double point angle PCD geometries used in this study are shown in Figure 2a, 2b, and 2c. Three different PCD drills with different edge lengths were custom fabricated by the tool manufacturer. Drills are named as D1, D2, and D3.

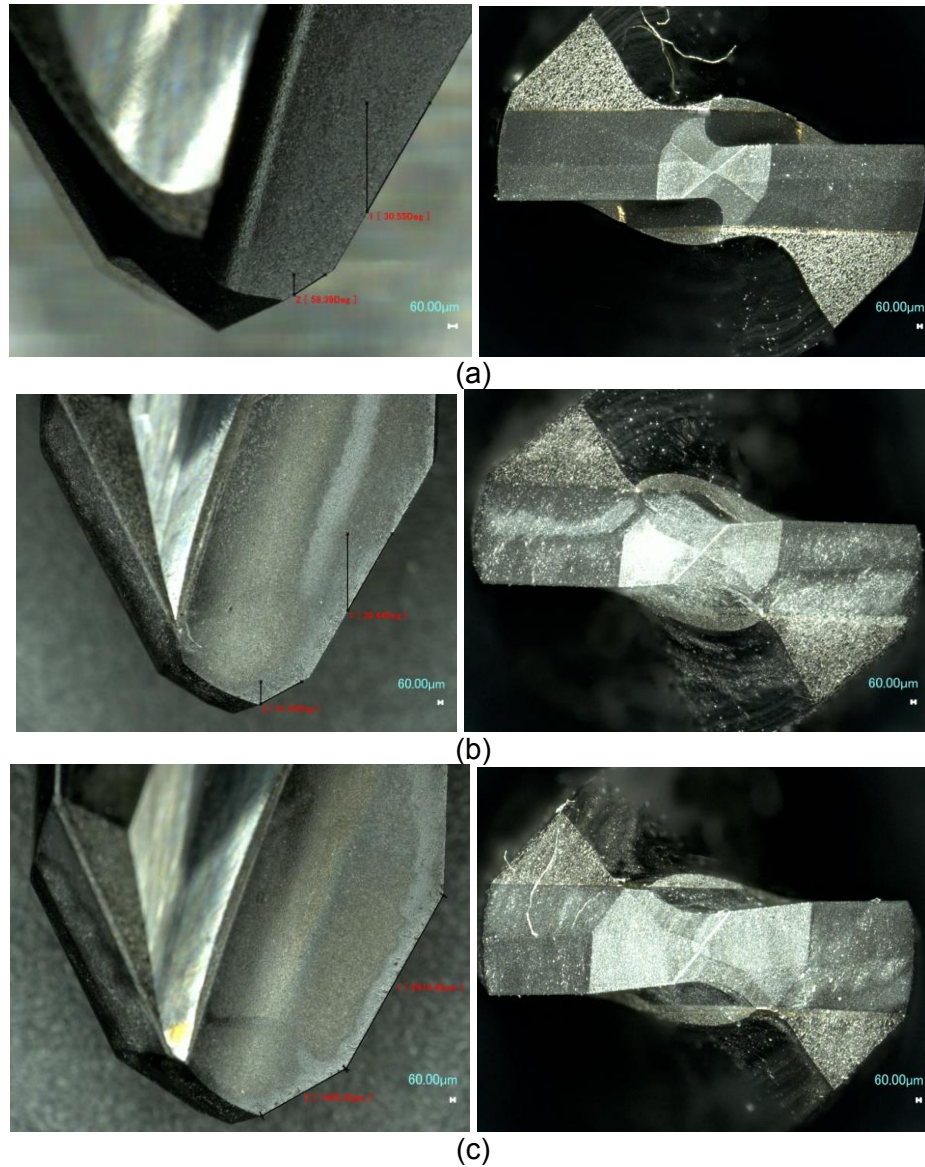


Figure 2. Double point angle drill geometries. (a) D1, b) D2, c) D3

The PCD grade of 2 µm grain size were used in all of the drills. The drills are fabricated to have the same chisel edge length. The edge radius of all the drills are measured to be 10 µm. Figure 3 shows the profile of the cutting edge measured by laser scanning microscope (Keyence VKX 110).

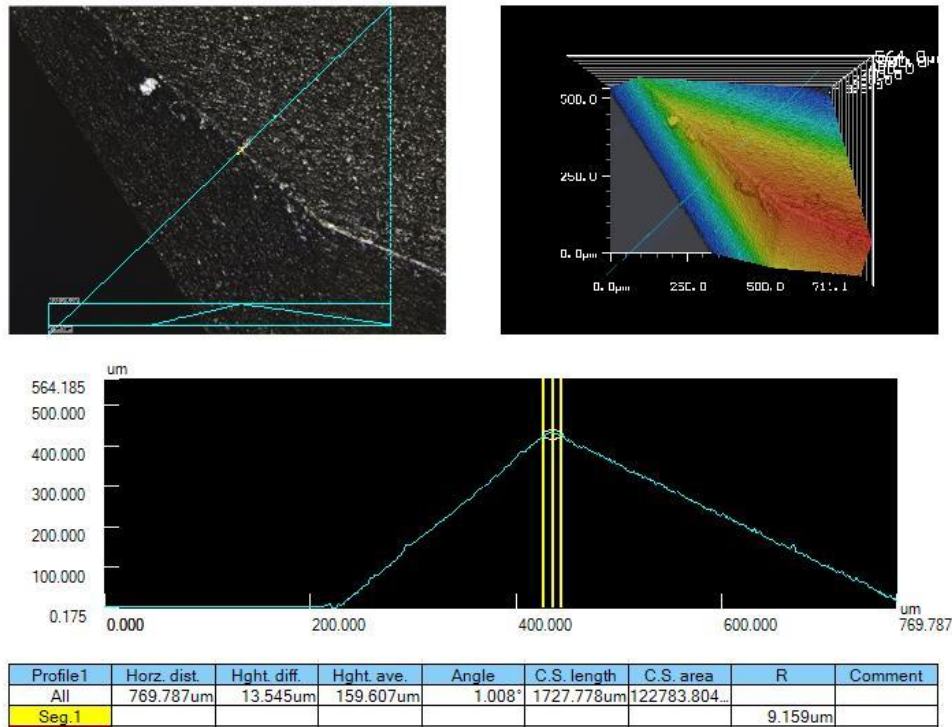


Figure 3. Edge radius of the PCD drills.

### 3. GENERALIZED DOUBLE POINT ANGLE DRILL GEOMETRY

Based on the drill designs shown in Figure 2, a generalized double point angle tool geometry can be developed as shown in Figure 4. In this figure;  $O'-O$  represents the chisel edge region,  $OA$  shows the primary drilling region,  $AB$  shows the secondary drilling region and  $BC$  shows the tertiary drilling region. The length and angle of the chisel edge are represented with  $L$  and  $\gamma$ , respectively.

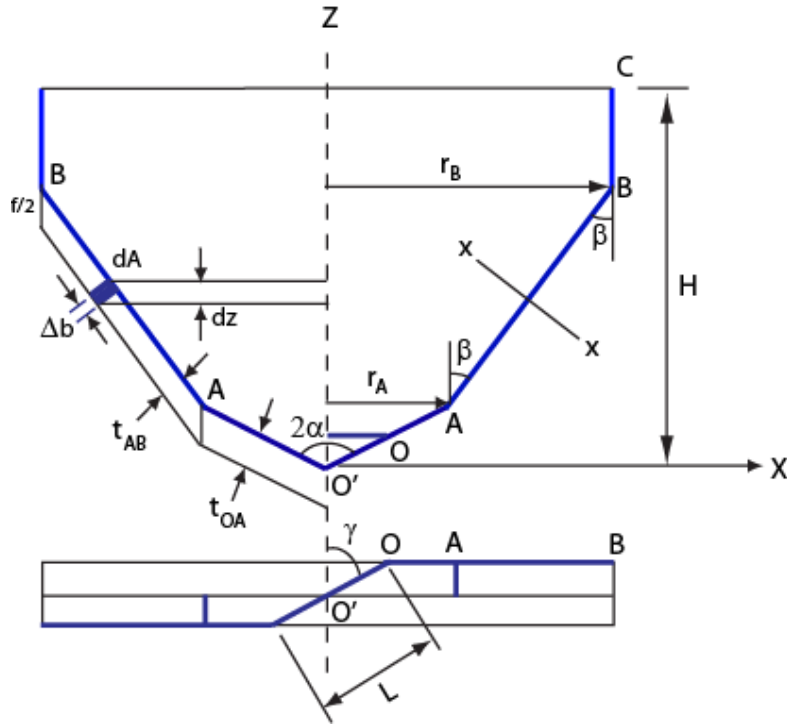


Figure 4. Generalized double tip point angle PCD drill geometry.

The tool tip angles corresponding to primary and secondary drilling regions are shown with  $\alpha$  ( $60^\circ$ ) and  $\beta$  ( $30^\circ$ ). The drill has zero helix angle. Uncut chip thicknesses  $t_{AB}$  and  $t_{OA}$  are different due to double point angle design, and they can be calculated as a function of feed ( $f$ ) per edge as shown in Equation 1. It is seen that uncut chip thickness in secondary drilling edge is less than the primary drilling edge.

$$\begin{aligned} t_{OA} &= (f/2) \sin \alpha \\ t_{OB} &= (f/2) \sin \beta \end{aligned} \quad (1)$$

Assuming that in hole diameters are standardized in aerospace industry and for known tool angles, primary edge length, and PCD tip height ( $H$ ), the length of the secondary and tertiary drilling regions ( $L_{AB}$ ) and ( $L_{BC}$ ) can be calculated as dependent variables by using Equations 2 and 3.

$$L_{AB} = \frac{1}{\sin \beta} \left( r_B - L_{OA} \sin \alpha - \frac{L \sin \gamma}{2} \right) \quad (2)$$

$$L_{BC} = H - L_{AB} \cos \beta - L_{OA} \cos \alpha - \left( \frac{L \cos \alpha}{2} \right) \quad (3)$$

Table 1 summarizes the actual tool geometry measurements. The tool tip measurements were performed using Keyence VHX 1000 digital microscope. There are some slight discrepancies in the chisel edge length and angle which are related to drill fabrication process.

Table 1. Tool geometry measurements.

Drill	OA ( $\mu\text{m}$ )	AB ( $\mu\text{m}$ )	$\alpha$	$\beta$	L ( $\mu\text{m}$ )	$\gamma$
D1	448	4407	58	30	1275	50
D2	915	3883	61	30	1216	42
D3	1455	2914	61	30	1345	42

#### 4. THRUST FORCE and TORQUE CHARACTERISTICS of DRILLING with DOUBLE POINT ANGLE PCD DRILLS

Measurements of thrust force and torque during drilling reveal important information about the influence of tool geometry [Langella et al., 2005]. Figure 5 illustrates a drilling cycle with the double point angle PCD drill used in this study, and seven distinct drilling phases (I-VII) are identified above the figure. The point (I) and (II) corresponds to the chisel edge and the primary cutting edge (OA) entering the hole, respectively. The thrust force increases rapidly in this region but the increase in torque is small. When the secondary drilling zone enters the hole (AB), the rate of increase in thrust force is lower due to chip thinning as a result of lower drill angle ( $\beta$ ). Peak thrust force (III) is reached at the end of the secondary drilling zone. The region BC does not carry any thrust force, but the torque reaches its peak value here. As the length of the tertiary drilling zone increases, the peak value of torque also increases due to rubbing of a larger area on the CFRP material. The thrust force decreases from III to IV due to decreasing stiffness of the material as drilling progresses. Thrust force decreases rapidly with a similar rate observed at the hole entry as soon as the chisel edge (IV-V) and primary drilling edge (V-VI) leave the cut. The torque stays almost the same between IV and VI since the secondary and tertiary cutting edges are still in contact with the material. The thrust force and torque decrease continuously between VI-VII until the drill completely leaves the cut.



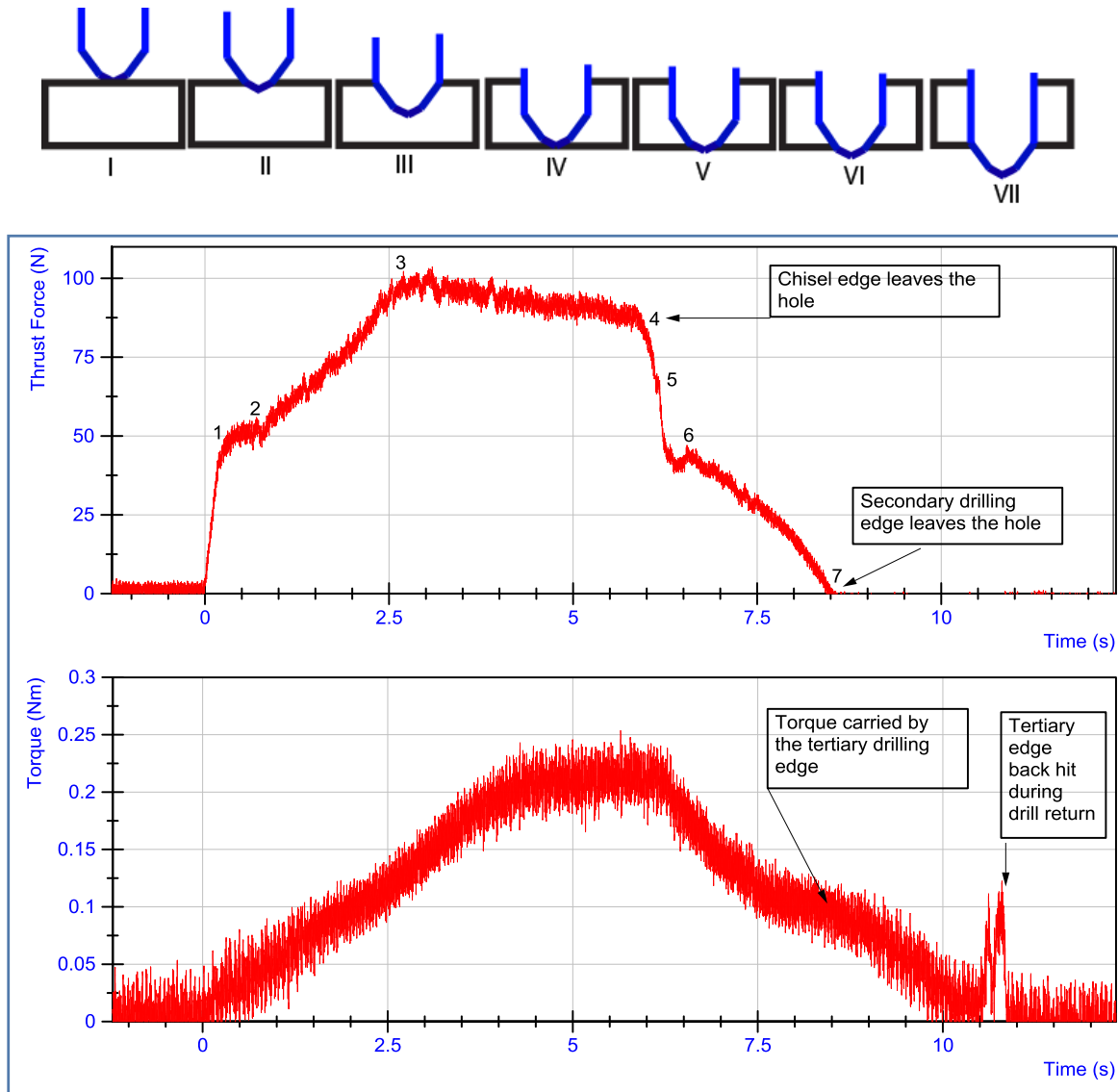
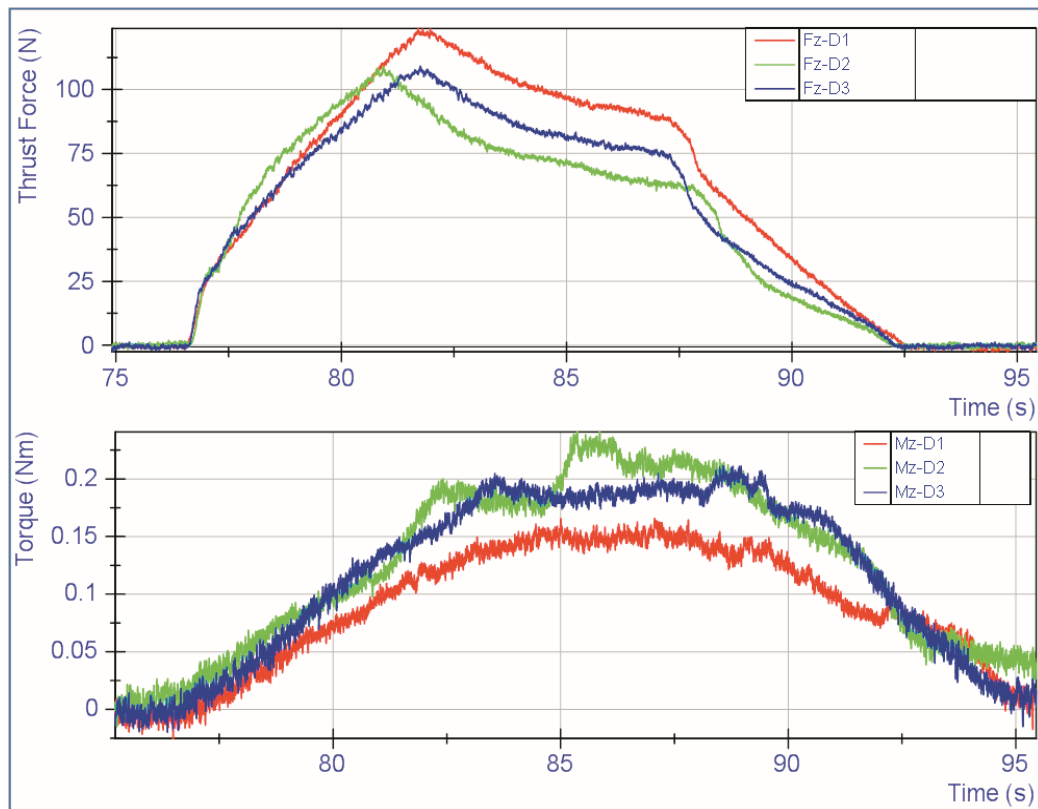
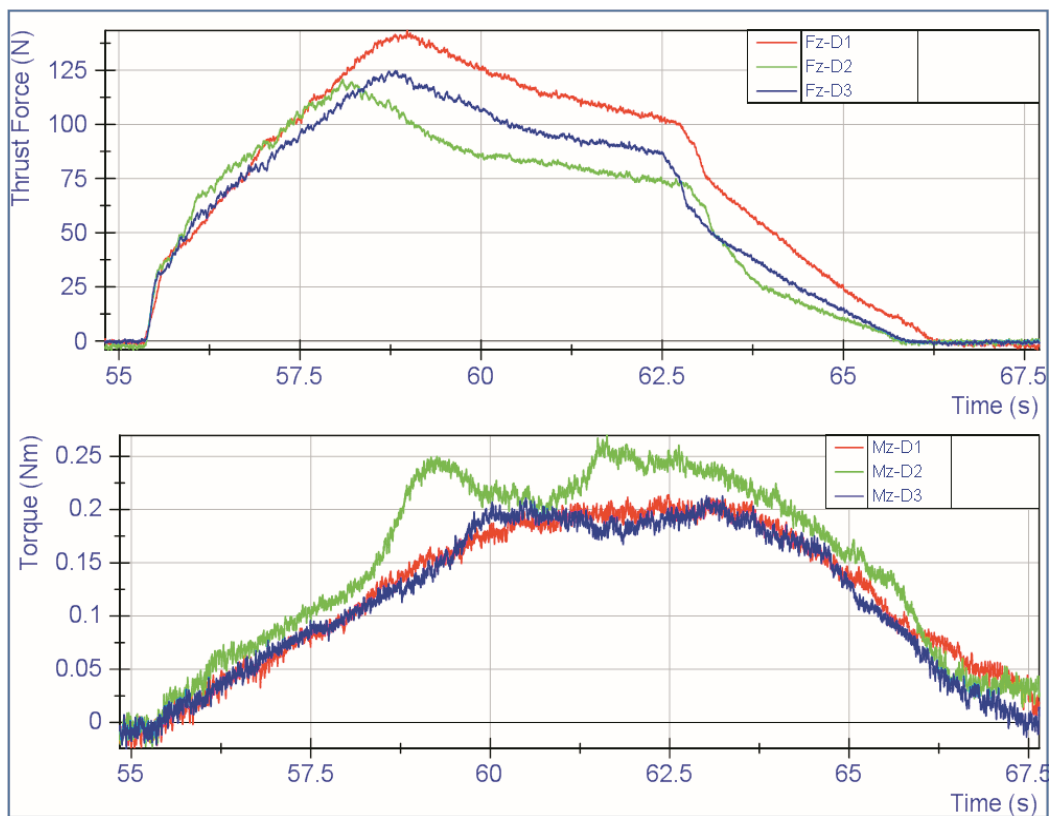


Figure 5. Thrust force and torque measurements with a double point angle PCD drill at 5000 rpm and 0.02 mm/rev feed [Karpat et al., 2014].

Figure 6a, 6b, and 6c show the thrust force and torque measurements for drills D1, D2, and D3 under various feed rates at 5000 rpm rotational speed. Based on these thrust force and torque measurements, drill D1 yielded higher thrust force and but lower torque than drills D2 and D3. Drill D3 yielded lower thrust forces but higher torques at all feeds tested in this study. The chisel edge forces are measured to be similar as intended. The trade off in drill designs in terms of thrust force and torque measurements can be clearly seen in Figure 6.

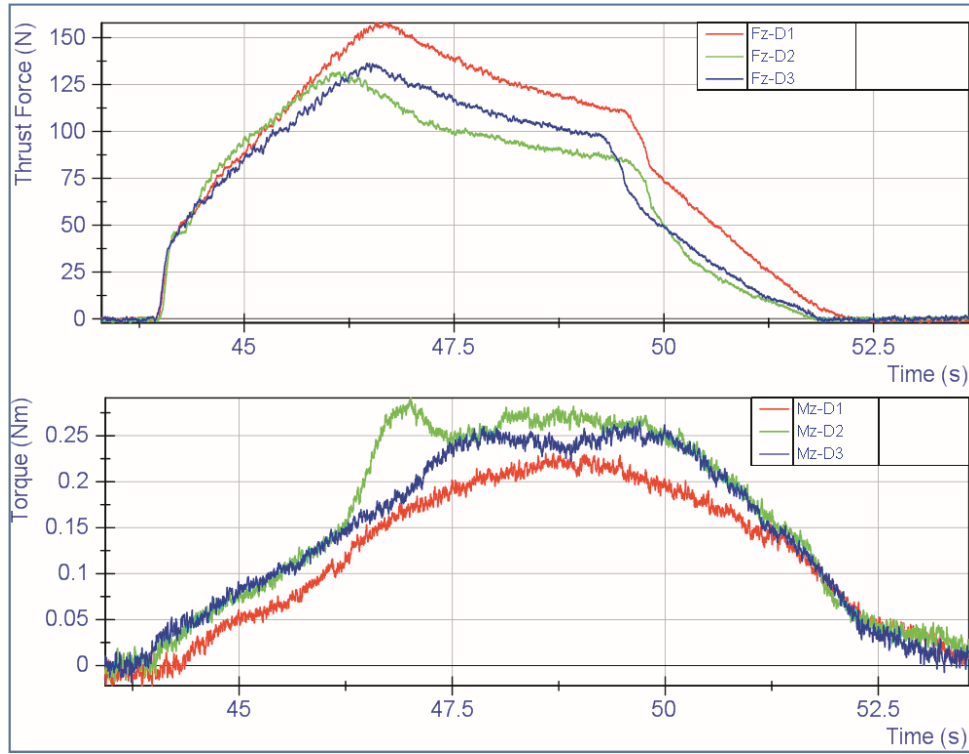


(a)



(b)





(c)

Figure 6. Thrust force and torque measurements with drills D1, D2, and D3 at feeds: a) 50 mm/min, b) 75 mm/min, b) 100 mm/min (at 5000 rpm).

## 5. MECHANISTIC MODELING OF DRILLING THRUST FORCE and TORQUE

The total thrust force ( $F_z$ ) and torque acting on the tool can be represented with Equation 4. The first term ( $F_{z\_ch}$ ) represents the influence of the chisel edge, the second term ( $F_{z\_OA}$ ) represents the influence on the primary drilling edge, and the last term ( $F_{z\_AB}$ ) represents the influence of the secondary drilling edge. The effect of the BC region on the thrust forces is neglected. A similar equation can also be written for total drilling torque ( $T$ ) also shown in Equation 4 where the effect of chisel edge on the torque is neglected based on measurements given above.

$$\Sigma F_z = F_{z\_ch} + F_{z\_OA} + F_{z\_AB} \quad (4)$$

$$\Sigma T = T_{OA} + T_{AB} + T_{BC}$$

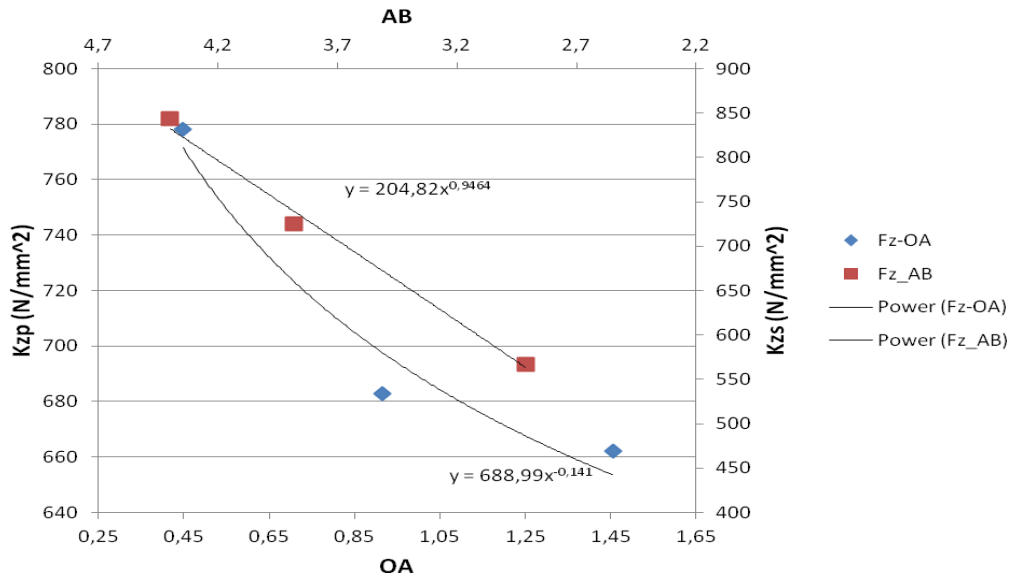
A mechanistic force modeling approach has been used to model drilling thrust forces and torques where machining forces and torques are related to the uncut chip area [Pirtini and Lazoğlu, 2005, Roukema and Altintas, 2007]. Average force and edge coefficients represent the influences of drills' cutting edge and material properties on the forces. Equation 5 represents the mechanistic force modeling (thrust and cutting force per edge) adapted to

drilling with a double point angle tool. The subscript  $p$  represents primary (OA) and subscript  $s$  represents secondary (AB) drilling regions. The thrust and cutting forces can be calculated for known values of average force and edge coefficients through Equations 4 and 5.

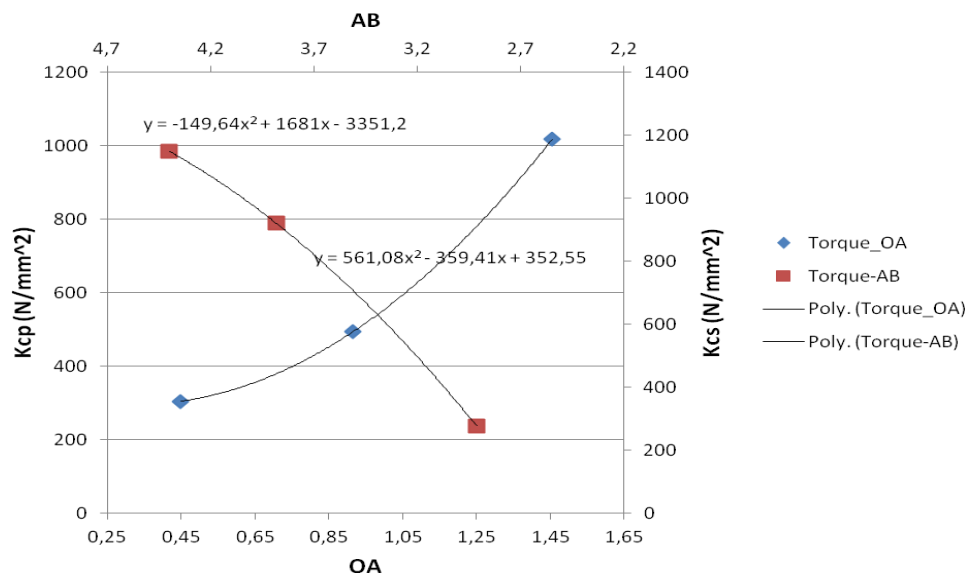
$$\begin{aligned}
 F_{zp} &= OA \left( \bar{K}_{zp} \frac{f}{2} \sin \alpha + \bar{K}_{zep} \right) \\
 F_{zs} &= AB \left( \bar{K}_{zs} \frac{f}{2} \sin \beta + \bar{K}_{zes} \right) \\
 T_{OA} &= F_{cp} \cdot \bar{r}_{OA} = OA \left( \bar{K}_{cp} \frac{f}{2} \sin \alpha + \bar{K}_{cep} \right) \\
 T_{AB} &= F_{cs} \cdot \bar{r}_{AB} = AB \left( \bar{K}_{cs} \frac{f}{2} \sin \beta + \bar{K}_{ces} \right) \\
 T_{BC} &= F_{BC} \cdot r_{BC} = BC(\bar{K}_p)
 \end{aligned} \tag{5}$$

Drilling tests can be used to calculate the average values of thrust and cutting force ( $K_{zp}$ ,  $K_{cp}$ ,  $K_{zs}$ ,  $K_{cs}$ ) and edge ( $K_{zep}$ ,  $K_{cep}$ ,  $K_{zes}$ ,  $K_{ces}$ ,  $K_p$ ) coefficients in reverse fashion using characteristic thrust forces and torques. More details on this calculation procedure can be found in [Karpat et al, 2014]. The chisel edge forces can be represented as a function feed using a linear fit.

Figure 7 shows the identified primary and secondary edge force coefficients as a function of primary edge length. As mentioned earlier, for a given primary edge length, the length of the secondary edge can be calculated as a dependent variable. The corresponding length of secondary edge is also shown in the figure. The results in Figure 7(a) show that as primary edge length increases, force coefficients for thrust force decrease. Longer secondary drilling edge results in larger total thrust forces. Figure 7(b) shows the force coefficients related to torque where an inverse relationship is observed. As the primary edge length increases, more torque is carried on the secondary and tertiary drilling edge. The edge coefficients are also calculated but no such trend was identified. The edge coefficients for primary and secondary drilling edges are assumed to have an average value of 7 N/mm. Calculated force coefficients as a function of primary edge lengths are represented with nonlinear equations as shown in Figure 7.



(a)



(b)

Figure 7. Identified force coefficients as a function of primary drilling edge length.

Another important observation in Figure 6 is that, the decrease in thrust forces between III and IV changes as a function of drill geometry. As feed increases, the ratio of  $F_{z_{IV}}/F_{z_{III}}$  remains almost constant for each drill design. A simple relationship can be obtained as shown in Figure 8, where ratio of primary and secondary drilling edge lengths are plotted against the thrust force ratio. It reveals that as primary edge length increases the decrease in thrust force increases.

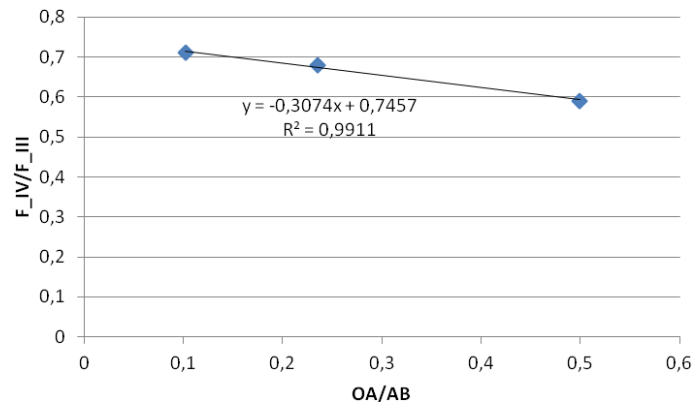


Figure 8. The relationship between thrust force decrease and edge length ratio.

The characteristic thrust force at point IV is important. In literature, it is defined as critical thrust force after which delamination initiates [König et al, 1985]. Therefore, the prediction of the critical thrust force is important in terms of selecting drilling operational parameters. Thrust force and torque for a given drill design at a given drilling condition can be predicted using the procedure described in this paper. Figure 9 shows the prediction of drilling thrust forces and torques for the drilling case of 100 mm/min feed rate with drill D1. The prediction agrees well with the experimental measurements.

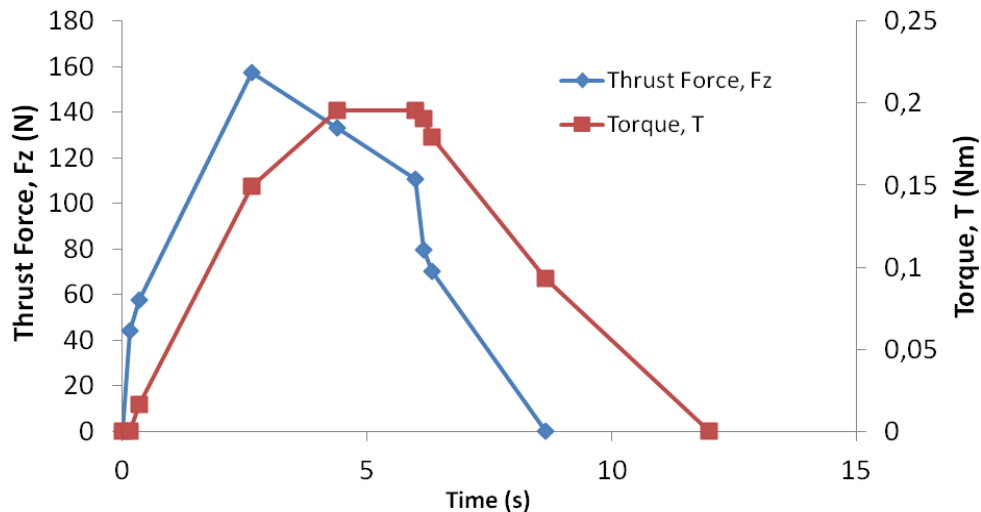


Figure 9. Drilling thrust force and torque predictions at 100 mm/min feed rate at 5000 rpm.

In order to investigate the influence of primary drilling edge length on the critical thrust force, some simulations are performed. Two different cases are considered where the critical thrust forces are fixed at 60 N and 75 N. The maximum allowable feed rate as a function of primary drilling edge are calculated as a function feed for various primary edge lengths. The results can be seen in Figure 10. The critical thrust force is assumed to be specific to CFRP material

properties and its thickness. The use of back plate also affects the critical thrust force. Therefore, it needs to be measured experimentally.

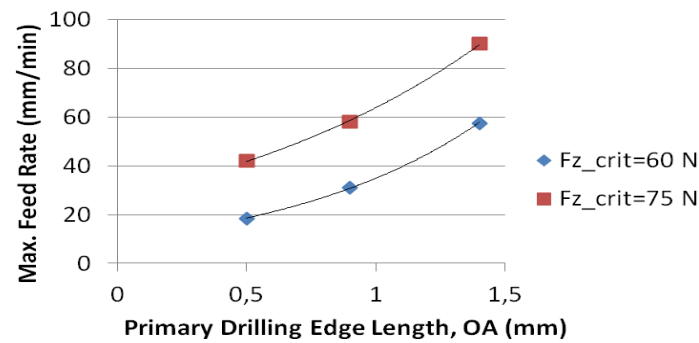


Figure 10. Maximum allowable feed rate as a function of primary drilling edge.

Figure 11 shows the hole exits as a function of increasing feed per revolution. It can be seen that drills D2 and D3 performs better than D1 as expected from analysis. However, there is not much performance difference between D2 and D3.

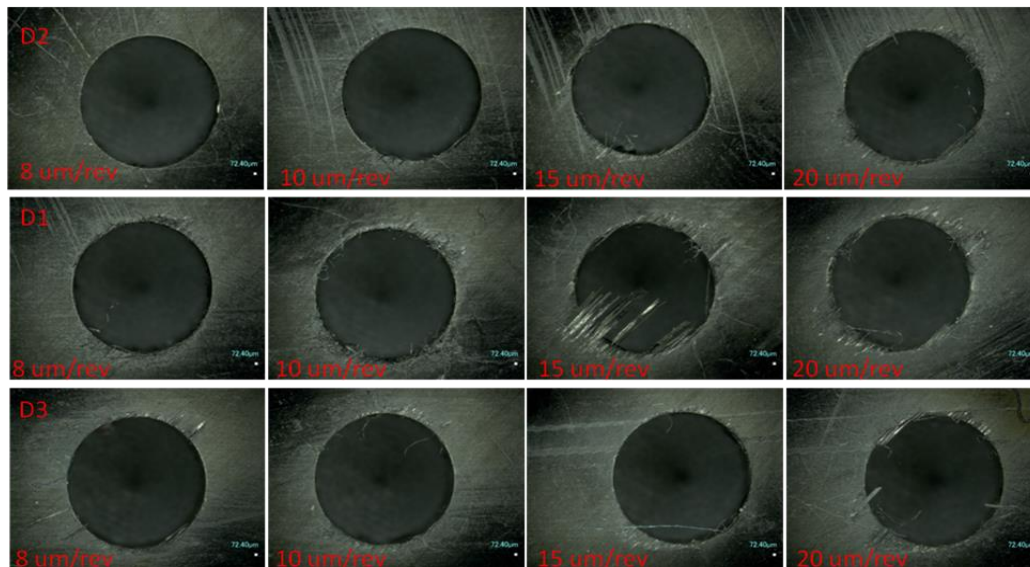


Figure 11. First drilled hole exits as a function of drill geometry and feed per edge.

It must be noted that, above given analysis is valid for unworn drills and only the influence of thrust forces are considered on the drill performance. Due to abrasive nature of CFRPs, tool wear is abrupt while drilling CFRPs. From experimental studies, it is known that tool wear is also a function of drill geometry and it is closely related to the torque distribution between drilling edges. Therefore, for a more robust drilling optimization study, the tool wear rate information as a function of drill geometry must be included in the analysis.



## CONCLUSIONS

In this study, a mechanistic based drilling thrust force and torque prediction model has been proposed for double point angle PCD drills. Identified force and edge coefficients are used to predict the critical thrust forces at the hole exits. It is shown that proposed methodology can be used in drilling optimization studies when combined with a tool wear analysis.

## ACKNOWLEDGEMENT

The authors would like to thank The Scientific and Technological Research Council of Turkey TÜBİTAK-TEYDEB and ODAGEM A.Ş for the financial support for the project.

## REFERENCES

1. **Rawat, S., Attia, H.** (2009), "Characterization of the dry high speed drilling process of woven composites using Machinability Maps approach", *CIRP Annals - Manufacturing Technology*, Vol 58, pp 105–108.
2. **Karpat, Y., Değer, B., Bahtiyar, O.** (2012), "Drilling thick fabric woven CFRP laminates with double point angle drills", *Journal of Materials Processing Technology*, 212(10) 2117-2127.
3. **Schulze, V., Becke, C., Pabst, R.** (2011), "Specific machining forces and resultant force vectors for machining of reinforced plastics", *CIRP Annals - Manufacturing Technology*, 60(1) 69-72.
4. **Park, K. Beal, A., Kim, D., Kwon, P., Lantrip, J.** (2011), "Tool wear in drilling of composite/titanium stacks using carbide and polycrystalline diamond tools". *Wear*, 271(11–12), , 2826-2835.
5. **Karpat, Y., Değer, B., Bahtiyar, O.,** (2014), "Experimental Evaluation of Polycrystalline Diamond Tool Geometries while Drilling Carbon Fiber Reinforced Plastics", *International Journal of Advanced Manufacturing Technology*, Volume 71, Issue 5, 1295-1307.
6. **Langella, A., Nele, L., Maio, A.,** (2005), "A torque and thrust force prediction model for drilling of composite materials", *Composites Part A: Applied Science and Manufacturing*, 36 83-93.
7. **Pirtini, M., Lazoglu, I.,** (2005), "Forces and hole quality in drilling". *International Journal of Machine Tools and Manufacture*, 45(11) 1271-1281.
8. **Roukema, J.C., Altintas, Y.,** (2007), "Generalized Modeling of Drilling Vibrations, Part I: Time Domain Model of Drilling Kinematics, Dynamics and Hole Formation", *International Journal of Machine Tools and Manufacture*, Vol. 47/9, pp. 1455-1473.
9. **König, W., Wulf, Ch., Graß, P., Willerscheid, H.,** (1985), "Machining of Fibre Reinforced Plastics", *CIRP Annals - Manufacturing Technology*. 34(2) 537-548.



## EXPERIMENTAL INVESTIGATION OF CGI DRILLING ADAPTED WITH EXTERNAL MQL SYSTEM

**A. Taner KUZU**, *kuzua@itu.edu.tr* Istanbul Technical University, 34437, Istanbul, Turkey

**U. Alican ALMA**, *alma@boun.edu.tr*, Boğaziçi University, 34342, Istanbul, Turkey

**Kaveh RAHIMZADEH BERENJI**, *rahimzadehberen@itu.edu.tr* Istanbul Technical University, 34437, Istanbul, Turkey

**Mustafa BAKKAL**, *bakkalmu@itu.edu.tr* Istanbul Technical University, 34437, Istanbul, Turkey

### ABSTRACT

As automotive industry tries to meet the expectations of the user demands for a long time, they also try to respond the scope of expanding environmental protection laws. Because of the low emission laws, engine designers are forced to improve technology in order to have more effective combustion process in engines. For this purpose CGI is used instead of gray cast iron due to the higher mechanical properties, corrosion and wear resistance. Thus it provides more efficient combustion environment. Moreover, in recent years, MQL attracted researchers' attention due to its eco-friendly and cost wise efficiency properties. Besides these advantageous, MQL can enhance the machining performance. Therefore, during drilling operation MQL systems have been used for lubrication, cooling and chip removal aspects. Throughout the study over and above, the proper cutting parameters were determined for a longer tool life and efficient machinability with MQL.

**Keywords:** CGI drilling, MQL, Wear

### 1. INTRODUCTION

Emissions legislation and the demand for higher performance from smaller engines have together driven the development of diesel engine technology over the past ten years [1]. It is today thought to use a compact graphite cast iron (CGI) for especially diesel engine bodies, exhaust manifold and cylinder heads instead of gray cast iron used in the past due to better mechanical properties of CGI. The higher peak firing pressures provide more efficient combustion, improved performance, reduced emissions and quieter engine operation. At the same time, the increased firing pressures place increased mechanical loads on the main bearing region of the cylinder block, potentially resulting in premature fatigue failures. With at least 75% increase in ultimate tensile strength, 35-40% increase in elastic modulus and approximately double the fatigue strength of gray cast iron, compacted graphite iron is ideally





suited to meet the current and future requirements of diesel engine design [1]. In addition, another advantage of compact graphite iron can provide fine mechanical properties with lighter weight.

Compacted graphite iron (CGI) characteristic combination of double the ultimate strength, intermediate thermal conductivity, higher modulus of elasticity, and superior crack initiation and propagation resistances compared to gray cast iron (GCI), as well as better thermal conductivity and greater resistance to thermal distortion compared to nodular graphite iron [2,3]. While additional alloy elements which are magnesium, titanium and chromium improve the mechanical properties of compact graphite cast iron, these alloy elements negatively affects the machinability of compact graphite cast iron. Aside from the absence of the protective and lubricating layer of manganese sulfide (MnS) in CGI machining, the presence of titanium in CGI poses a quite severe effect on tool wear. Large amounts of titanium (0.1–0.25%) is commonly used to control the formation of compacted graphite particles by increasing the stable range of magnesium in CGI production [4]. Higher percentage of titanium in compacted graphite iron (CGI) promotes the formation of titanium carbonitride (TiCN) inclusions which are harder than tungsten carbide leading to more tool wear. It was found that a slight increase of trace level of titanium from 0.01 to 0.02% was sufficient to reduce the tool life by about 50% [5]. The main drawback of using CGI for engine blocks is its poor machinability, as compared to gray cast iron, leading to higher production costs [6]. Good machinability is significant factor to achieve economic manufacturing conditions. In general, the three available avenues for optimizing the machinability of CGI include: improving the robustness of the insert materials; improving the machining techniques; and, improving the CGI itself [7]. To reach good machinability conditions, determination of the cutting parameters and the reduction of tool wearing are the first steps to be taken in this regard. Factors that increase the amount of tool wear are high temperature at cutting zone due to friction and unbroken chips. In particular, engine cooling holes and lubrication holes are getting harder for deep hole drilling applications. To improve hole drilling applications in critic areas, variations and temperature distribution during the cutting process, cooling and lubrication method, selection of the optimal cutting parameters are very important in terms of improving the machinability characteristics.

Minimum quantity lubrication (MQL) systems commonly used in the production of automotive driveline system. This system reduces the costs of manufacturing and more environmentally than their equivalents. MQL system applies very small amount of oil with pressured air to the area in contact with the tool and the workpiece. Several investigations have been performed on effect of MQL on tool life, wear behavior, surface roughness and cutting performance in different machining operations. Results show that MQL increases tool life by decreasing flank wear and reducing condition for build-up edge development and cutting edge micro-chipping



[12]. Generally speaking, there are three functions of MQL system which are lubrication, cooling and chip removal, but cooling rate of MQL is less than traditional wet cutting system. Especially, deep hole drilling is such a high power consumed application that can cause some problems such as thermal distortion and missing tight geometric tolerances due to reaching high heat level.

In this project, previously machinability tests were performed to apply efficient hole drilling process on the compact graphite cast iron.

## 2. EXPERIMENTAL PROCEDURE

The CGI workpiece material was prepared for tool wear tests with 150 mm x 300 mm x 24 mm dimensions. Nital 2 was used as an etchant in order to investigate the microstructure of the workpiece. The workpiece microstructural composition was mixture of pearlite and graphite phases which is clearly shown in the optical micrograph in Figure 1. The shape of graphite in the workpiece material was both worm, indicated as B, and nodular shape, indicated as A in Figure 1 [8]. According to the literature, being randomly oriented and elongated, thicker and round edges of graphite particles, makes CGI more resistant to crack initiation and propagation even works as crack arrestors [9]. Pearlite was the main phase of CGI workpiece material which provides high hardness and good strength on matrix structure.

Table 1. Mechanical properties of CGI

Yield Strength (MPa)	Tensile Strength (MPa)	Elongation (%)	Hardness (HB)
350	460	1,6	190-210

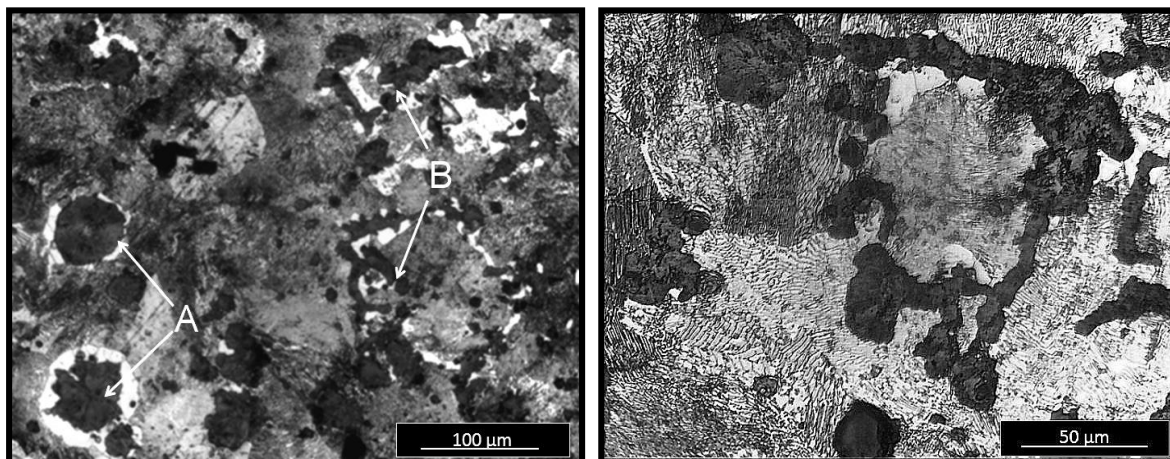


Figure 1. Microstructures of workpiece material

The mechanical properties of CGI workpiece are shown in Table 1, which was determined with standard uniaxial tensile test as regard of ASTM E8M. The drilling tests were conducted with a Spinner VC 650 CNC vertical machining center with a maximum spindle speed of 8000 rpm.

The machine was implemented with SKF LubriLean Vario MQL system and 4-axis dynamometer Kistler 9272. The mixture of compressed air and lubricant sprayed as micro droplets of oil to the cutting zone via two nozzles. The MQL flow rate was kept constant throughout the machinability experiment. 50 ml/h cutting fluid was supplied from MQL system to cutting zone with 6 bar air. The position of MQL nozzle and drill is given in Figure 2.

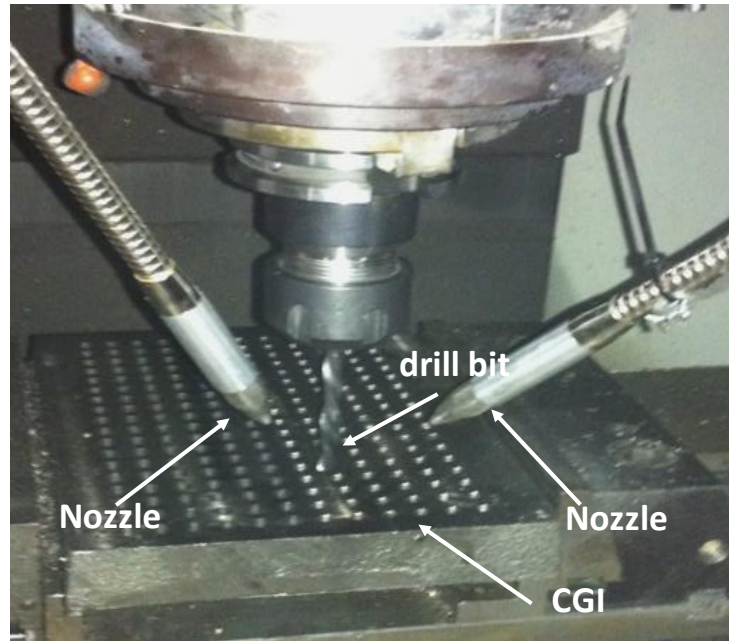


Figure 2. Experimental setup

The AlCrN coated Sandvik Corodril R842 model drill was used in this study. The diameter of drill was 6.1 mm. The selected cutting parameters are given in Table 2.

Table 2. Design of experiments

Cutting Speed, $V_c$ [m/min]	60, 80, 100
Feed, $f$ [mm/rev]	0.16, 0.2, 0.27
Cutting condition	DRY, MQL

NIKON SMZ800 stereo-optical microscope was used to investigate the flank wear. At the end of the every 54 holes, the tool wear tests were interrupted and tool wear measurement was performed.

### 3. RESULTS AND DISCUSSION

#### 3.1 Thrust force and torque in drilling

Force and torque values were investigated with a cutting speed of 60, 80, and 100 m/min and at feed rates of 0.16, 0.2, 0.27 mm/rev. Thrust force and torque distributions are given in Figure 4a and 4b for both machining conditions. The thrust force values linearly increase with feed

rate values because of the higher chip load at high feed rates as expected. The thrust forces during MQL drilling were approximately 6% lower than dry cutting conditions due to the better lubrication effect of MQL. The effects of cutting speed on thrust forces at high feed rate values were more significant. The high cutting speed creates higher cutting temperatures and this causes the workpiece softening. Therefore, measured thrust force values were lower at higher cutting speed condition. Similar observations were seen for torque values. Effect of MQL in torque value of CGI drilling is clear and MQL used tests causes less torque values during all trials.

Cutting force components in time domain for both cutting conditions are given in Figure 3. As shown in Figure 3, MQL significantly decreases the cutting forces. MQL usage also decreases cutting temperature and it causes more consistent workpiece strength during cutting. However, dry cutting condition workpiece is softer than the one under MQL condition, because of the higher friction and hence created higher temperature at the cutting zone. Furthermore, MQL leads to reduction in friction coefficient between tool and chip interface. Depends on this attitude, cutting forces decreasing is expected. These two conflicting behavior compensate each other so it is hard to understand effect of MQL on thrust forces.

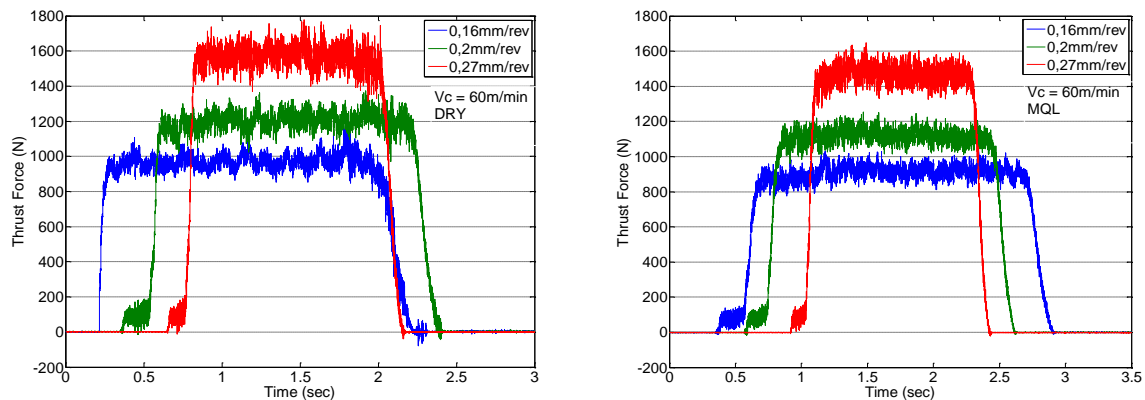


Figure 3. Representation of measured forces in dry and MQL cooling conditions

Specific cutting pressure was calculated by the following equations [16]

$$K_s = 8.M_z/f.d^2 \quad (1)$$

Where  $M_z$  is the torque in N.m,  $f$  is feed in mm/rev and  $d$  is the diameter of the drill in mm. Specific cutting pressure are shown in Fig 4c. General trend in all experiments, the specific cutting pressure value decrease with increasing cutting speed. According to Davim et. al. at lower cutting velocities, the tool would have tendency to plough on the work material, resulting in higher order specific cutting pressure. As the cutting velocity increases, the tool would cut better without ploughing, resulting in a drop in specific cutting pressure. Since the MQL

prevents the effects of ploughing, the specific cutting pressure will be lower than the ones in dry cutting conditions. In drilling cutting power was calculated by

$$P = M_z \cdot \omega \quad (2)$$

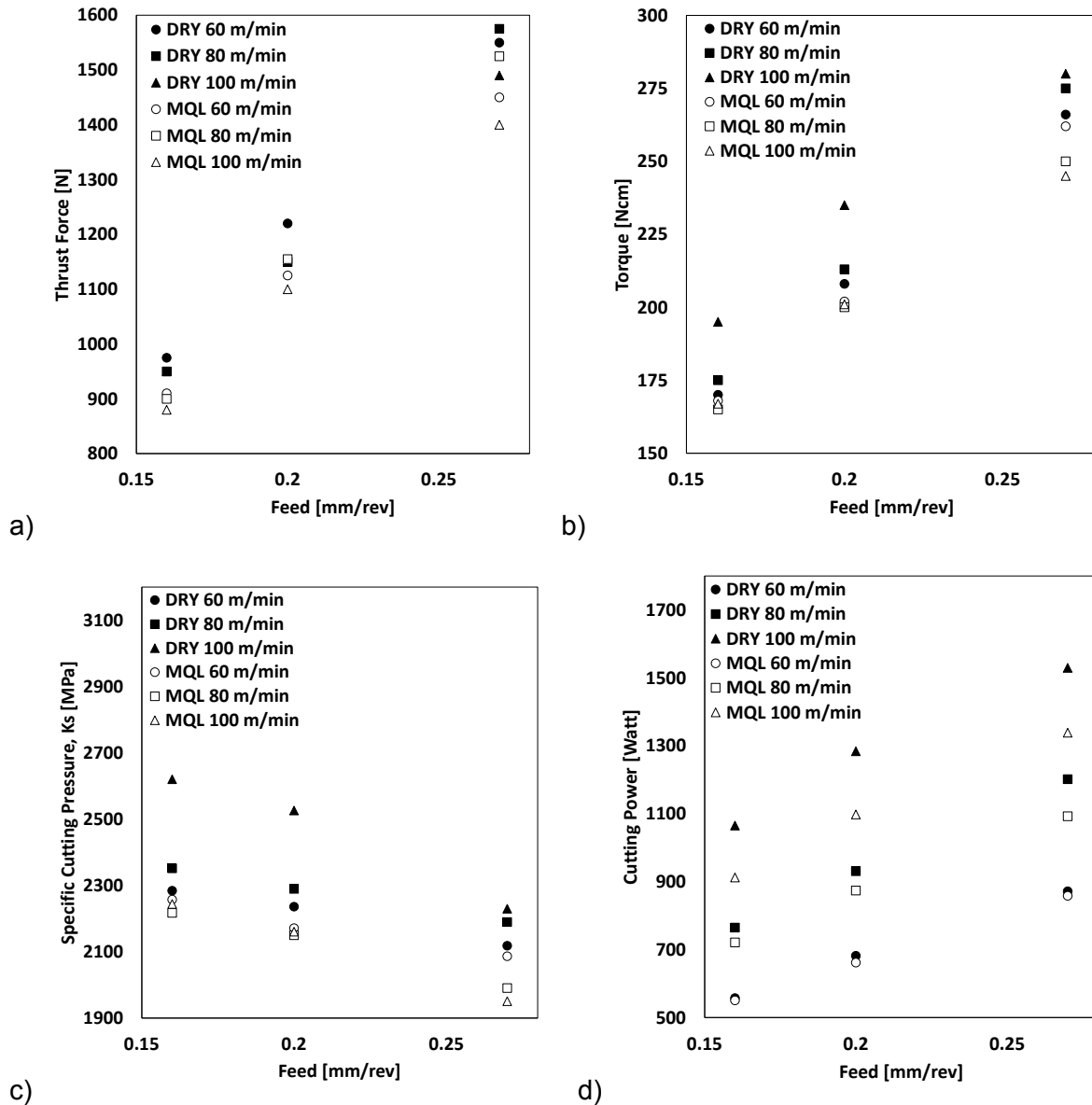


Figure 4. a) Measured thrust force, b) Measured torque, c) Calculated specific cutting pressure, d) Calculated cutting power

where  $\omega$  is the rotation in  $\text{rad.s}^{-1}$ . Calculated cutting powers in drilling tests are given in Figure 4d. For all cases cutting power increases with feed rates. It is notably seen in the graph MQL usage decreases consumed power during process.

### 3.2 Tool wear

In order to produce parts with desired surface finish and dimensional tolerances, the cutting edges of tools must be in favorable life cycle with monitoring the tool wear and breakage. When

the quality of cutting edge is lost because of wear, it means the tool reaches its life limit and it should be replaced with new one [11]. Tool wear is mostly related to cutting parameters, tool and workpiece materials and coolant circumstances. Because of importance of wear behavior in mass production and directly relation to manufacturing costs, understanding the wear mechanisms with longer tool life achievement is needed during the machining operations. In this study, tool wear of CGI was measured in order to comprehend the influence of MQL on tool life. Drilling tests for MQL and DRY machining was conducted in order to observe effect of MQL on tool wear during drilling CGI blocks. In order to determine the tool wear and monitor the tool life, flank wear on the drill bit has been investigated. Xavier reported that the adhesion and abrasion are the two main parameters of wear mechanisms in machining CGI [9]. The interaction between two materials under high pressure and high temperature will result an effect, which called welding, or adhesion [10]. Whereas, abrasion is related with mechanical wearing due to hard particles. These phenomena could be decreased by the means of lubricant and its main role in friction coefficient minimization. Because of the effective role of MQL in this attitude, it has been growingly popular.

The cutting parameter were selected depend on the constant material removal rate which are 24400 mm<sup>3</sup>/min (MRR). These parameters designations are presented in Table 3.

Table 3. Cutting parameters for wear tests with designations

Designation	MRR (mm <sup>3</sup> /min)	V <sub>c</sub> (m/min)	f (mm/rev)	Coolant
CC1_DRY	24400	100	0,16	DRY
CC2_DRY	24400	80	0,20	DRY
CC3_DRY	24400	60	0,27	DRY
CC1_MQL	24400	100	0,16	MQL
CC2_MQL	24400	80	0,20	MQL
CC3_MQL	24400	60	0,27	MQL

Figure 5 shows the wear behavior on flank surface against number of hole for both machining conditions. The experiments conducted at equal material removal rate value, however, the corresponding feed rates and cutting speeds are different for each case as explained earlier. Note that the experiments conducted up to wear rate of 150 µm due to the comparison purpose. Figure 5 obviously represents the advantage of utilizing MQL at machining operations especially in drilling process even in external application. As can be seen in the figure 5, performing external minimum quantity lubrication in drilling decreases the wear rate significantly. A remarkable increase in tool life observed at CC1 where by using MQL the tool can cut 30-40% more in comparison with the dry condition. For instance, at the cutting condition CC1 where the cutting speed is 100m/min, after 1000<sup>th</sup> hole there is about 25%

decrease in wear rate in a certain number of hole in MQL method. Similarly, in a definite wear rate we can reach up to 40% more holes when using MQL cooling strategy. Furthermore, for the CC3 case which the cutting speed is 60 m/min, it is able to cut 40% more during MQL in comparison with dry condition to reach a particular wear rate, where at a definite number of hole the wear rate during using MQL is 40% lower than dry condition. This can be related to the fact that using MQL increases the cooling and lubrication effects at tool-chip and tool-workpiece interface which cause an increase in tool life by reducing condition for built-up edge development, micro chipping at cutting edges and flank wear [12].

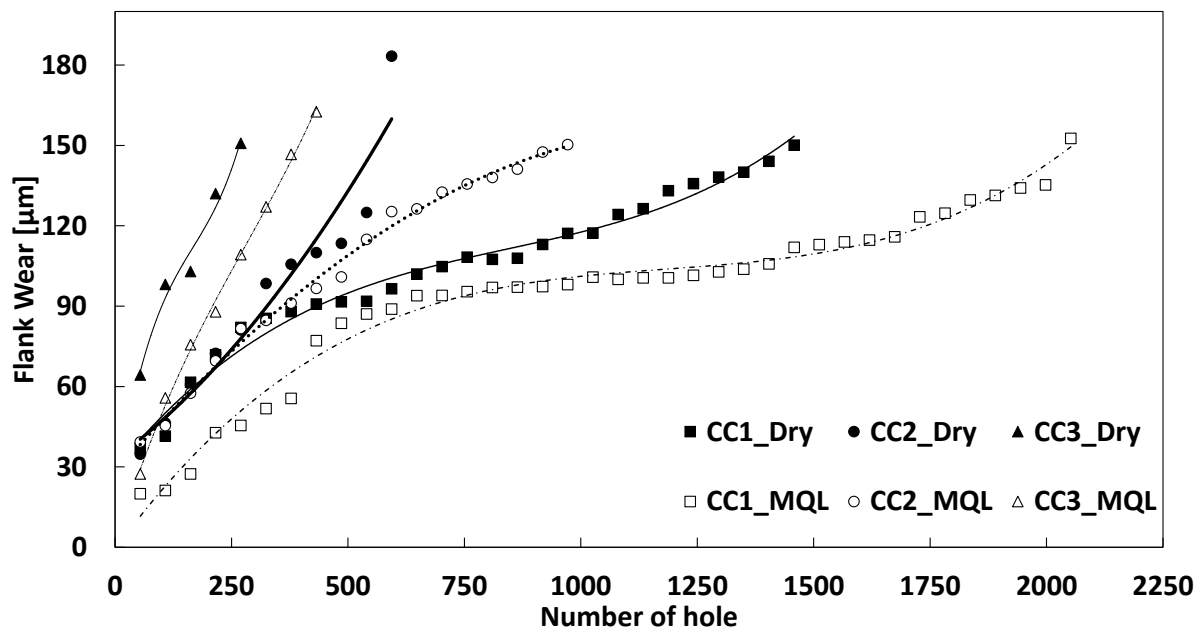
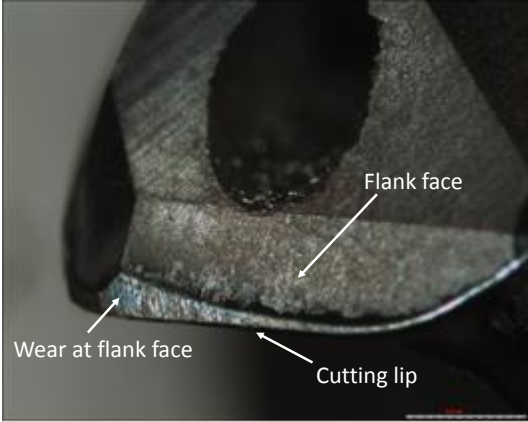
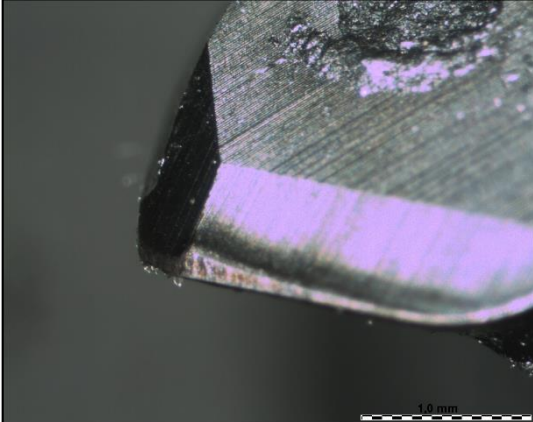
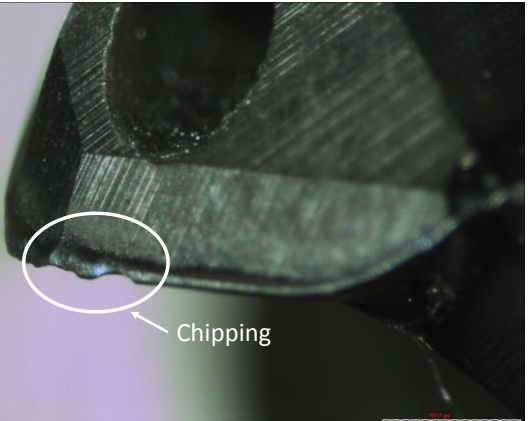
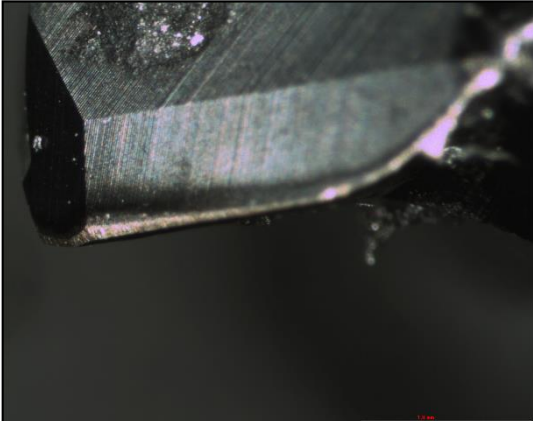
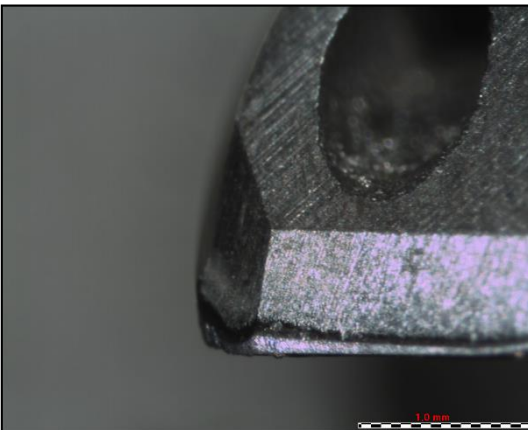
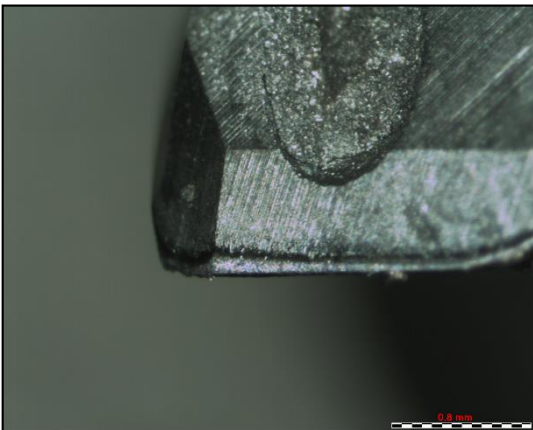


Figure 5. Flank wear of drill bit

In this regard, oil mist supplied from MQL nozzle generates a thin film at tool-workpiece interface, this can significantly affect the thermal and frictional behavior of cutting operation. The thin film of lubrication generated by MQL will decrease the sliding friction coefficient, which cause reduction in heat generation and adhesion [13]. This phenomenon can be relate to the lubricating effects of MQL, however, since the MQL acts as an coolant, this cause chip up-curling which decrease the total contact length on tool's rake face [14]. Moreover, the cooling aspect of MQL results temperature reduction in both tool and chip will prevent high diffusion rate of carbide tool into the work material, leading to the hastened of tool wear and rapid tool failure [15]. It was observed that in all ranges of cutting speeds, MQL produces a lower tool wear and high tool life in comparison with dry cutting.



Table 4. Cutting parameters for wear tests with codes

	DRY	MQL
$V_c = 100$ m/min $f = 0.16$ mm/re $v$ at 540. hole		
$V_c = 80$ m/min $f = 0.2$ mm/re $v$ at 648. hole		
$V_c = 60$ m/min $f = 0.27$ mm/re $v$ at 1458. hole		

However, we can deduce that the wear rate in CC1 is lower than the CC2 and CC3 because of low feed rate. In addition, chipping was observed at the condition coded CC2\_DRY which can be seen both in Figure 5 and Table 4. The chipping occurred at 648<sup>th</sup> hole where in the same cutting parameters but using MQL, not only the chipping was not seen but also the tool life enhanced and the determined wear rate occurred at 1026<sup>th</sup> hole. As like, it can be observed from Figure 5 that, using MQL and CC2 case, increased the tool life up to 20% besides preventing chipping. This can be due to the fact the cooling-lubricating effects of MQL



decreases the adhesion or welding of parts at tool which can cause breakage and chipping at cutting edges.

## CONCLUSION

- Using MQL results a reduction about 10-15% in both thrust force and torque during the drilling operation which can be related to the lubrication effect of MQL in tool-workpiece interface.
- Specific cutting pressure decreased about 15% during using MQL due the lubrication effects of MQL which decreases the friction and prevents high ploughing effect.
- Cutting power decreased about 10-15% due the reduction in cutting forces which shows the costly efficiency of MQL.
- Using MQL during drilling operation will decrease the wear rate in high cutting speeds and high feed rates in comparison to dry cutting.
- The tool life enhances by utilizing MQL system even at external supply due to the generated thin film of lubricant at tool-workpiece-chip interface which provides an easy sliding of chip and tool.
- MQL decreases wear rate 20-30% by applying both cooling and lubrication effect which prevents sticking by decreasing sliding friction coefficient and adhesion by decreasing the tool temperature.
- Applying MQL can prevent occurring chipping during cutting operation which has a significant effect on tool wear progress.

## ACKNOWLEDGEMENT

The authors would like to thank The Scientific and Technological Research Council of Turkey (TÜBİTAK) for funding the research project 112M335.

## REFERENCES

1. **Guesser, T. Schroeder, S. Dawson (2001)**, "Production Experience With Compacted Graphite Iron Automotive Components" SinterCast Technologies AB, Katrineholm, Sweden
2. **Dryden, J. R., & Purdy, G. R. (1989)**. "The effect of graphite on the mechanical properties of cast irons". *Acta Metallurgica*, 37(7), 1999-2006.
3. **S.V. Subramanian, D.A.R. Kay, G.R. Purdy (1982)**, "Compacted Graphite Morphology Control" *Transactions of the American Foundrymen's Society Proceedings of the 86th Annual Meeting*, AFS, Chicago, IL, USA, pp. 589–603





4. **Walid M. Mohammed, E. Ng, M.A. Elbestawi (2012)**, “Modeling the effect of compacted graphite iron microstructure on cutting forces and tool wear”, CIRP Journal of Manufacturing Science and Technology, Volume 5, Issue 2, Pages 87-101, ISSN 1755-5817
5. **S. Dawson, I. Hollinger, M. Robbins, J. Daeth, U. Reuter, Schults (2001)**, “The Effect of Metallurgical Variables on the Machinability of Compacted Graphite Iron” SAE Technical Paper Series
6. **F. Mocellini; E. Melleras; W. L. Guesser; L. Boehs (2004)**, “Study of the machinability of compacted graphite iron for drilling process”, J. Braz. Soc. Mech. Sci. & Eng. vol.26 no.1 Rio de Janeiro Jan./Mar
7. **Dawson, S., Hollinger, I., Robbins, M., Daeth, J., Reuter, U., & Schulz, H. (2001)** “The effect of metallurgical variables on the machinability of compacted graphite iron”. SAE Transactions: Journal of Materials & Manufacturing, 110, 334-352.
8. **Mohammed, W., M., Ng, E., Elbestawi, M.a., (2012)**, “Modeling the effect of compacted graphite iron microstructure on cutting forces and tool wear”, CIRP Journal of Manufacturing Science and Technology 5, 87-101.
9. **Alves, S. M., Schroeter, R. B., Bossardi, J. C. D. S., & Andrade, C. L. F. D. (2011)**. “Influence of EP additive on tool wear in drilling of compacted graphite iron”. Journal of the Brazilian Society of Mechanical Sciences and Engineering, 33(2), 197-202.
10. **Groover, M., P., (2010)**, “Fundamentals of Modern Manufacturing: Materials, Processes, and Systems”, 4th Edition, Wiley & Sons
11. **Altintas, Y., (2012)**, “Manufacturing automation: metal cutting mechanics, machine tool vibrations, and CNC design”, Cambridge University Press, Cambridge
12. **R. Dhar, M. Kamruzzaman, Mahiuddin Ahmed (2006)**, “Effect of minimum quantity lubrication (MQL) on tool wear and surface roughness in turning AISI-4340 steel” , Journal of Materials Processing Technology, Volume 172, Issue 2, Pages 299-304, ISSN 0924-0136
13. **Faverjon, P., Rech, J., & Leroy, R. (2013)**. “Influence of Minimum Quantity Lubrication on Friction Coefficient and Work-Material Adhesion During Machining of Cast Aluminum With Various Cutting Tool Substrates Made of Polycrystalline Diamond, High Speed Steel, and Carbides”. Journal of Tribology, 135(4), 041602
14. **B. Tisdelen, H. Thordenberg, D. Olofsson (2008)**, An experimental investigation on contact length during minimum quantity lubrication (MQL) machining, Journal of Materials Processing Technology, Volume 203, Issues 1–3, Pages 221-231, ISSN 0924-0136
15. **E.A. Rahim, H. Sasahara (2011)**, A study of the effect of palm oil as MQL lubricant on high speed drilling of titanium alloys, Tribology International, Volume 44, Issue 3, Pages 309-317, ISSN 0301-679X



16. **J.P. Davim, P. Reis (2003)**, Drilling carbon fiber reinforced plastics manufactured by autoclave—experimental and statistical study, *Materials & Design*, Volume 24, Issue 5, August 2003, Pages 315-324, ISSN 0261-3069



## PERFORMANCE OF NOVEL $\alpha/\beta$ -SiAlON-TiN CERAMIC COMPOSITES ON HIGH SPEED MILLING OF INCONEL 625

**Ali ÇELİK**, *acelik1@anadolu.edu.tr* MDA Advanced Ceramics Ltd., 26110, Eskisehir, Turkey

**Melike SERT ALAGAÇ**, *mseret@alp.com.tr* Alp Aviation Co., 26110, Eskisehir, Turkey

**Uğur Evrensel YILMAZ**, *uyilmaz@alp.com.tr* Alp Aviation Co., 26110, Eskisehir, Turkey

**Alpagut KARA**, *akara@anadolu.edu.tr* Anadolu University, Department of Materials Science and Engineering, 26480, Eskisehir, Turkey.

**Servet TURAN**, *sturan@anadolu.edu.tr* Anadolu University, Department of Materials Science and Engineering, 26480, Eskisehir, Turkey.

**Ferhat KARA**, *fkara@anadolu.edu.tr* Anadolu University, Department of Materials Science and Engineering, 26480, Eskisehir, Turkey.

### ABSTRACT

In this study, aim was to produce a novel  $\alpha/\beta$ -SiAlON-TiN ceramic milling cutter and to investigate its performance on high speed machining of Inconel 625 superalloy. Micro-chipping was found to be the main wear mechanism at the early stage of the cutting where the temperature is lower than the softening temperature of the Inconel part. After a few revolution in contact with the work-piece, the wear mode turned into diffusion dominant due to the increase in temperature above 1000°C. Despite the fact that the mechanical properties was improved by the addition of TiN, it reduces the chemical stability of the ceramic at aggressive machining conditions ( $T > 1000^\circ\text{C}$ ).

**Key words:** SiAlON, milling, superalloys, diffusion wear

### 1. INTRODUCTION

Nickel-based superalloys, having high thermal and corrosion resistance, ability to retain mechanical properties at elevated temperatures over 700°C, are the most widely used materials (50 wt. % of total materials) especially in gas turbine compartment of an aerospace engine [Ezugwu et al., 2003, Balazinski et al., 1995]. However, these materials are classified



as difficult to machine due to their high shear strength, work-hardening tendency, highly abrasive carbide particles in the microstructure, strong tendency to form built up edge (BUE), and low thermal conductivity [Natural and Yamaha, 1993, Alauddin et al., 1996]. Therefore, the rapid cutting tool wear occurs on all machining processes and there is always a strong demand for a new high wear resistant cutting tool material.

Nickel-based superalloys can be machined with WC-Co based cermets with a cutting speed in the order of 50 m/min. [Li et al., 2002]. However, carbide tools have poor thermochemical stability and diffusion of the atoms of tool and work-piece between each other during turning at speeds in excess of 30 m/min. In that case, the temperature at the tool-work piece interface can exceeds 1000°C and results to failure of the tool with a plastic deformation [Kramer, 1987]. Tungsten-based carbides can be used in high feed-rate and severe interrupted cutting due to their high fracture resistance, but they cannot be used at high speeds because of their thermochemical instability. [Choudhury and El-Baradie, 1998]. As suggested by [Jindal et al., 1999], tool life can be extended by the coating of WC-Co substrate with different hard coating materials such as TiN, TiAlN, TiCN. They stated that the coatings increase wear resistance and may reduce cutting forces and temperatures at the tool edge and thereby indirectly affect the deformation and fracture behavior of the tool. [Devillez et al., 2007] also compared the performance of TiAlN and AlTiN coated carbide tools on turning operation of Inconel 718, and observed that AlTiN coating is the most suitable coating material for the carbide substrates against to chemical and mechanical wear.

Ceramics are another class of cutting materials used for turning and milling of Ni-based superalloys in insert form at 2-3 times higher cutting speeds than that of carbides due to their excellent thermo-mechanical properties and chemical durability at high temperatures. SiC whisker reinforced  $\text{Al}_2\text{O}_3$  composite ( $\text{Al}_2\text{O}_3\text{-SiC}_w$ ) is one of the most successful tool material owing to the high fracture toughness promoted by the whisker shaped SiC phase. However, SiC is less stable at high temperatures in comparison to  $\text{Al}_2\text{O}_3$  matrix and limits the use of these materials at the cutting speeds in the range of 200-750 m/min [Whitney, 1974]. Alternatively,  $\alpha/\beta$ -SiAlONs, having hard  $\alpha$  and tough  $\beta$  phases, are promising tool materials with a unique combination of mechanical, thermal and chemical properties. The possibility of varying the  $\alpha/\beta$  phase ratio enables one to prepare SiAlON ceramics with desired properties. Due to the advances in wheel grinding technology and ease of gas pressure sintering (GPS) technique which gives the possibility to sinter fully dense SiAlON ceramics in complex shapes, SiAlONs are the potential materials to be used as solid milling cutters with complex geometry for the machining of Ni-based superalloys at high speeds (400-1000 m/min). It was highlighted that the carbides cannot be utilized for the high speed machining of superalloys because of the insufficient chemical wear resistance [Liao et al., 2008]. Therefore, SiAlONs, with the

superior high temperature properties in comparison to the carbide counterparts, can be a solution for the high speed machining of superalloys with a reasonable cost. In this work, a novel  $\alpha:\beta$ -SiAlON-TiN composite milling cutters were manufactured in two different geometries and tested on peripheral and end milling operations. Wear behavior of the tools were investigated.

## 2. EXPERIMENTATION

### Preparation of Ceramic Composites

In the present study,  $\text{Si}_3\text{N}_4$  (UBE-SE10/Germany),  $\text{AlN}$  (Tokuyama/Japan),  $\text{Al}_2\text{O}_3$  (Sumitomo/Japan),  $\text{Y}_2\text{O}_3$  (Treibacher/ Austria),  $\text{Sm}_2\text{O}_3$  (Treibacher/Austria) and  $\text{CaO}$  (in the form of  $\text{CaCO}_3$ ) were used in the starting SiAlON batch, which was charged to an attrition mill (Union Process/USA). The mixture with 60 wt.% of solid loading was milled for 2 hours in aqueous medium for particle size reduction and uniformity. TiN powder (HC-Starck-Grade C/Germany) and the organic additives (mixture of polyethylene glycol, acrylic emulsion binder and wax based lubricant) were then mixed with the SiAlON slurry for the subsequent powder consolidation. The slurry was dried in a spray dryer (Nubilos/Germany) to obtain nearly spherical granules with an average particle size of 100  $\mu\text{m}$  for good flowability. SiAlON granules were cold isostatic pressed (MSE-CIP200/Turkey) into cylindrical rod shape ( $\varnothing 15 \text{ mm} \times 100 \text{ mm}$ ) in a flexible polyurethane die under 200MPa pressure. After shaping, binder burn-out process was carried out in Ar atmosphere in order to prevent thermal oxidation of TiN particles at 650°C. Subsequently, the compacts were sintered in a gas pressure sintering furnace (FCT-Anlagenbau GmbH, Germany) at 1900°C of maximum temperature for 1.5 h under 100 bar  $\text{N}_2$  gas pressure.

### Production of Milling Cutters

Sintered SiAlON-TiN cylindrical rods were ground into 2 different geometries by CNC controlled grinding centre (Anca-TX7/Australia) and the wheels (Wendt-D45/Germany) attached to the machine. The pictures of the milling cutters after grinding is given in Fig.1. The rake, clearance and helix angles are 35°, 11° and 30° for G-1, and 0°, 25° and 0° for G-2, respectively.

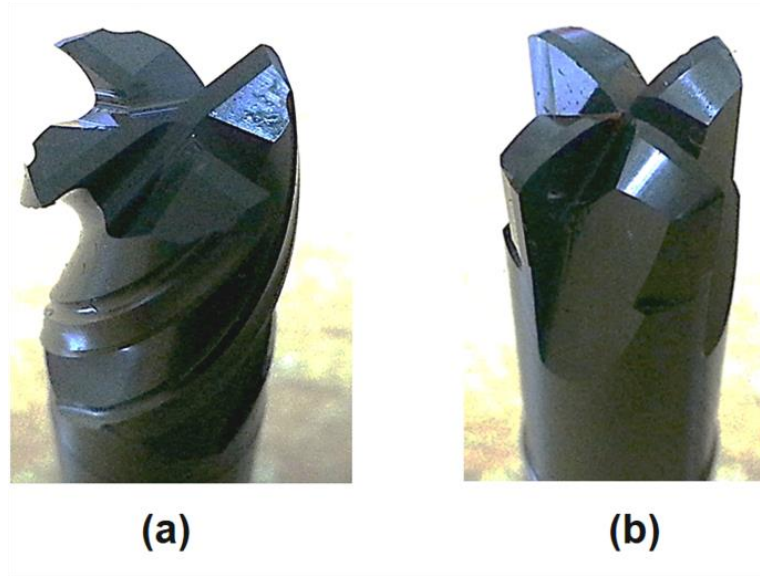


**Fig. 1.** The SiAlON-TiN milling cutters in a) G-1 and b) G-2 geometries. ( $\varnothing$ : 12 mm)

### Machining Tests

Milling tests were performed on (Makino-GF8/Japan) 5-axis CNC machining center at maximum rotational speed of 15000 rpm. The work-piece material used in milling tests was Inconel 625 super alloy part in a composition of 62% Ni, 20% Cr, 9% Mo, 3.6% Nb. The superalloy part was in a complex geometry of a chopper engine. Three different milling operations, summarized in Table 1, were carried out with SiAlON-TiN ceramic milling cutters. In the first operation, G-1 was used for peripheral milling (edge trimming), so the part was machined by the periphery of the cutting edges. In other two operations, G-2 was used for end milling of Inconel 625 part in different machining path.

**Table 1.** Details of the milling operations performed by  $\alpha/\beta$ -SiAlON-TiN ceramic milling cutters

	Operation 1	Operation 2	Operation 3
<b>Milling cutter</b>	G-1	G-2	G-2
<b>Spindle speed (rpm)</b>	15000	15000	15000
<b>Radial depth of cut (mm)</b>	0.762	7.2	5.08
<b>Axial depth of cut (mm)</b>	6.35	0.508	0.508
<b>Feed rate (mm/min)</b>	1270	1270	1270
<b>Chip volume (cm<sup>3</sup>)</b>	3.563	16.4	15.148

## Characterization

The density of the SiAlON composite was measured according to Archimedes method. Phase identification of the sample was performed by X-ray diffractometer (Rigaku Rint 2200/Japan). Indentation hardness and fracture toughness were measured by applying the load of 98 N for 10 seconds with a diamond indenter. The hardness and the fracture toughness values were obtained from the formulas given in Eq. 1 and 2 [Evans and Charles, 1976].

$$HV10 = 0,47 \times \frac{F}{a^2} \quad (1)$$

$$K_{1C} = 0.16 \left(\frac{c}{a}\right)^{-1.5} \left(HV10 \times a^{\frac{1}{2}}\right) \quad (2)$$

where  $HV10$  is hardness,  $K_{1C}$  is the fracture toughness,  $F$  is indentation load and  $a$  and  $c$  are the half length of the diagonal and the crack, respectively.

Microstructure of the SiAlON-TiN ceramic composite, worn surfaces of the milling cutters and the chips produced during machining tests were examined by a scanning electron microscope (Zeiss-Supra 50 VP/Germany) equipped with an energy dispersive X-ray spectrometer (EDX). In order to simulate the cutting environment during milling operation, a piece of Inconel 625 superalloy (5 mm×5 mm×1 mm), was sandwiched between two slices of SiAlON-TiN ceramics. This layered ceramic-Inconel structure was heated between  $Al_2O_3$  pistons of a creep test machine (Instron/UK) up to 1200°C under a constant load of 120N and kept 2 hours to let the diffusion takes place between the ceramic and the superalloy. After that, the sample was cut from the cross-section by a precise wire cutting machine and mirror polished for subsequent microstructural characterization.

## 3. RESULTS AND DISCUSSION

### Properties of the SiAlON-TiN Ceramic Composite

Machining of nickel based superalloys is a challenging process which requires high mechanical, thermal and chemical wear resistance from cutting tool material. The final properties of the material strongly dependent on the microstructural development and phases in the composite material. In Fig 2a and b, back-scattered SEM image and XRD spectrum are given, respectively. It is clearly seen that the composite contains four main distinct phases: TiN, with a particle size between 0.5 to 3  $\mu m$  seen as white equiaxed particles, light gray equiaxed  $\alpha$ -SiAlON and dark gray elongated  $\beta$ -SiAlON grains as well as the inter-granular phase seen as small dots all around the grains (Fig. 2a). The amount of  $\alpha$ -SiAlON phase was calculated from the XRD spectrum (Fig. 2b) as 35 %. The physical and mechanical properties



of the  $\alpha/\beta$ -SiAlON-TiN composite are summarized in Table 2. It was stated that the hardness, oxidation and thermal shock resistance is proportional with the  $\alpha$ -SiAlON phase content. [Ekström and Nygren, 1999]. On the other hand, fracture toughness of the composite ceramic is controlled by the elongated  $\beta$ -SiAlON grains and the TiN particles. The measured fracture toughness of the composite is quite high ( $6.14 \text{ MPam}^{1/2}$ ) for an  $\alpha/\beta$ -SiAlON ceramic containing 35% of alpha phase due to the presence of TiN particles.

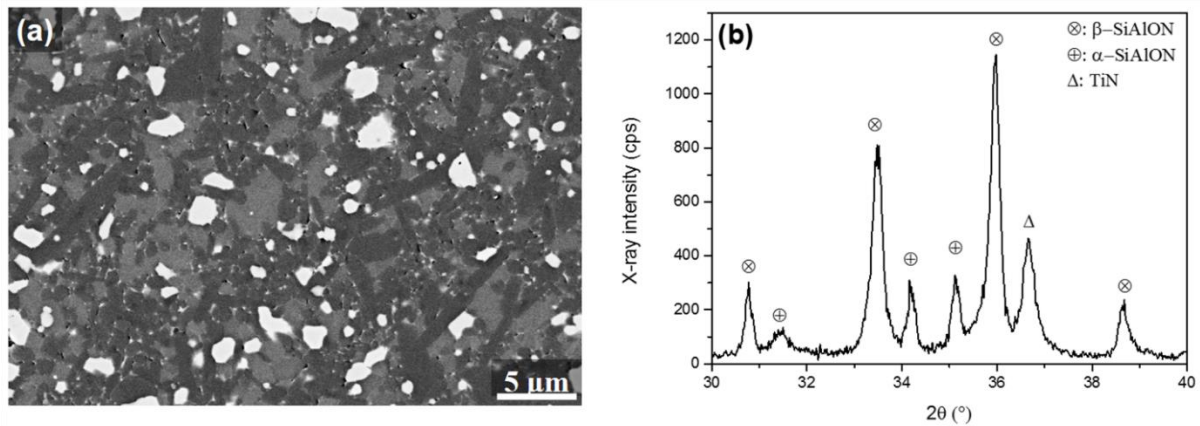


**Fig. 2.** a) Back-scattered SEM micrograph and b) XRD spectrum of  $\alpha/\beta$ -SiAlON-TiN composite.

**Table 2.** Properties of  $\alpha/\beta$ -SiAlON-TiN composite.

<b>Density (<math>\text{g/cm}^3</math>)</b>	3.44
<b>HV10 (GPa)</b>	17.34
<b><math>K_{1C}</math> (<math>\text{MPam}^{1/2}</math>)</b>	6.14



## Milling Performance of SiAlON-TiN Composites

### Side milling:

The secondary cutting edge of the G-1 milling cutter after side milling test is given in Fig 3. As soon as the cutting edge approaches to the work-piece, micro-chipping occurs due to the high shear forces at the cutting zone (Fig 3a). Even for the WC-Co tools with relatively higher fracture toughness in comparison to the ceramics, the micro-chipping is one of the main tool wear mechanism at especially low cutting speeds when machining of heat resistant superalloys which shows surface hardening as a function of deformation as explained by [Kear et al., 1970]. After a few revolution, it was understood from the welding of the work-piece onto the cutting edge that the temperature at the contact zone exceeds 1000°C due to very high deformation rate of the work-piece. Therefore, the diffusion wear at the cutting edge becomes dominant under such aggressive conditions. A stable diffusion layer created by the migration of the atoms from the tool and the work-piece through the interface is seen in Fig 3b. The branched micro-cracks on this layer indicate the thermal mismatch between this layer and substrate during rapid cooling from the cutting temperature.

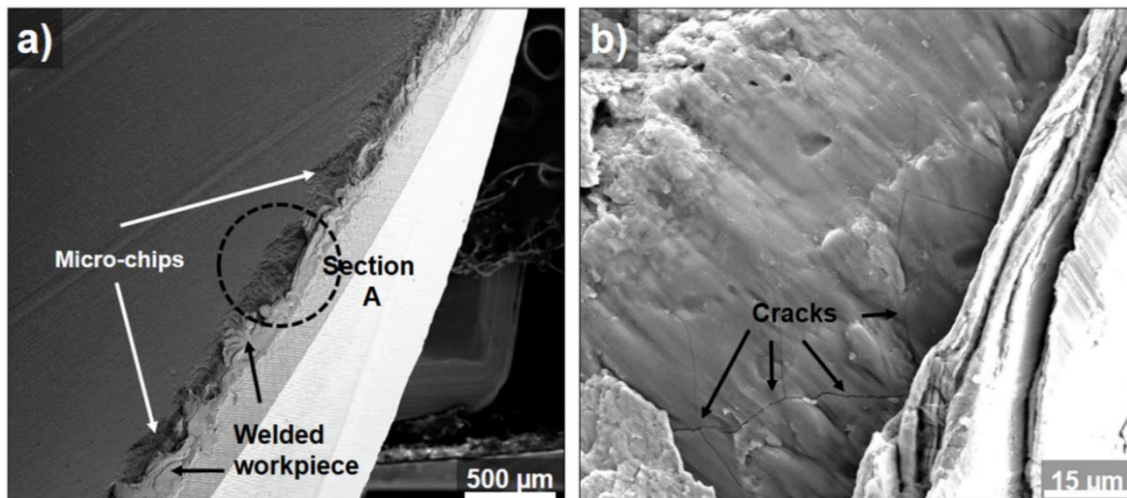


**Fig. 3. a)** SEM macrograph of the periphery of the G-1 milling cutter and **b)** magnified image of the Section A

In order to characterize the diffusion layer in depth, ceramic-superalloy diffusion couple was prepared and the distribution of the atoms at the interface was visualized by the mapping mode of the EDX analysis (Fig. 4). In the back-scattered SEM image, a diffusion layer (indicated in white dashed line) was formed at the interface. This layer is mainly composed of oxygen, chromium, aluminum, titanium and little amount of nickel elements in order of concentration.

Quantitative results also proved that the diffusion layer contains 21 wt.% of Cr, 12 wt.% of Al, 10 wt.% of Ti, 1.5 wt.% of Ni and the balance of O. Ti and Al elements are available in both Inconel 625 and SiAlON-TiN ceramic structures. While the concentration of Al is higher at the SiAlON-TiN side, the concentration of Ti is comparatively high at the diffusion layer except in the TiN grains. This indicates that the Ti migrated from the tool material through the interface, and joined to the diffusion layer due to its high diffusion rate at the cutting temperature. The diffusion of Ti atoms through the surface as a function of temperature was explained in detail by [Çelik et al., 2012], previously. Consequently, while the mechanical properties of the SiAlON matrix was improved by the TiN phase, its presence deteriorates the chemical stability of the tool material at high temperatures.

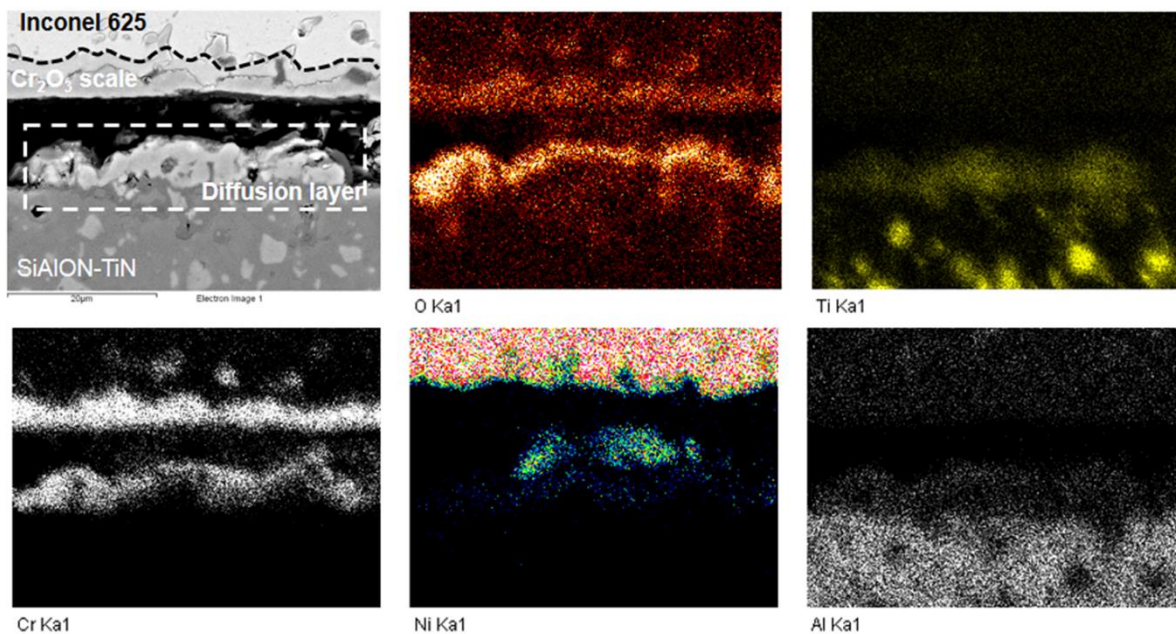


**Fig. 4.** Mapping analysis of the cross-section of the SiAlON-Inconel 625 diffusion couple.

### **End milling:**

SiAlON-TiN ceramic milling cutter in G-2 geometry was used for end-milling of Inconel 625 work-piece in two different operations in which the volume of the chips evacuated from the work-piece are about five times higher than that of side milling (Table 1). In Fig. 5, the primary cutting edges of the ceramic end mills after the tests are given. As stated by [Ezugwu et al., 2003], the primary wear mechanism for the ceramic tools is diffusion wear due to the high operating temperature resulted by the high cutting speed. Similar to the peripheral milling results, there is again the diffusion layer at the flank face of the end mills tested in Operation 2 (Fig. 5a and b) and Operation 3 (Fig. 5c and d). In addition to these stable BUE regions, there are also the cavities available on the worn surfaces seen clearly in magnified SEM images (Fig. 5c and d). These cavities are believed to be resulted by the partial removal of the

BUE layer. Since the temperature at the cutting zone was increased gradually with the continuous high speed cutting of work-piece in high volumes, the diffusion rate of the atoms increases with the temperature exponentially according to the Arrhenius law as follows:

$$D = D_0 e^{-E/RT} \quad (3)$$

where  $E$  is activation energy,  $D_0$  is pre-exponential factor. After a critical saturation level, the BUE layer became unstable and was removed from the edge by the high cutting forces. Therefore, it was expected that the tool life would be determined by the development of these cavities resulted by the diffusion wear.

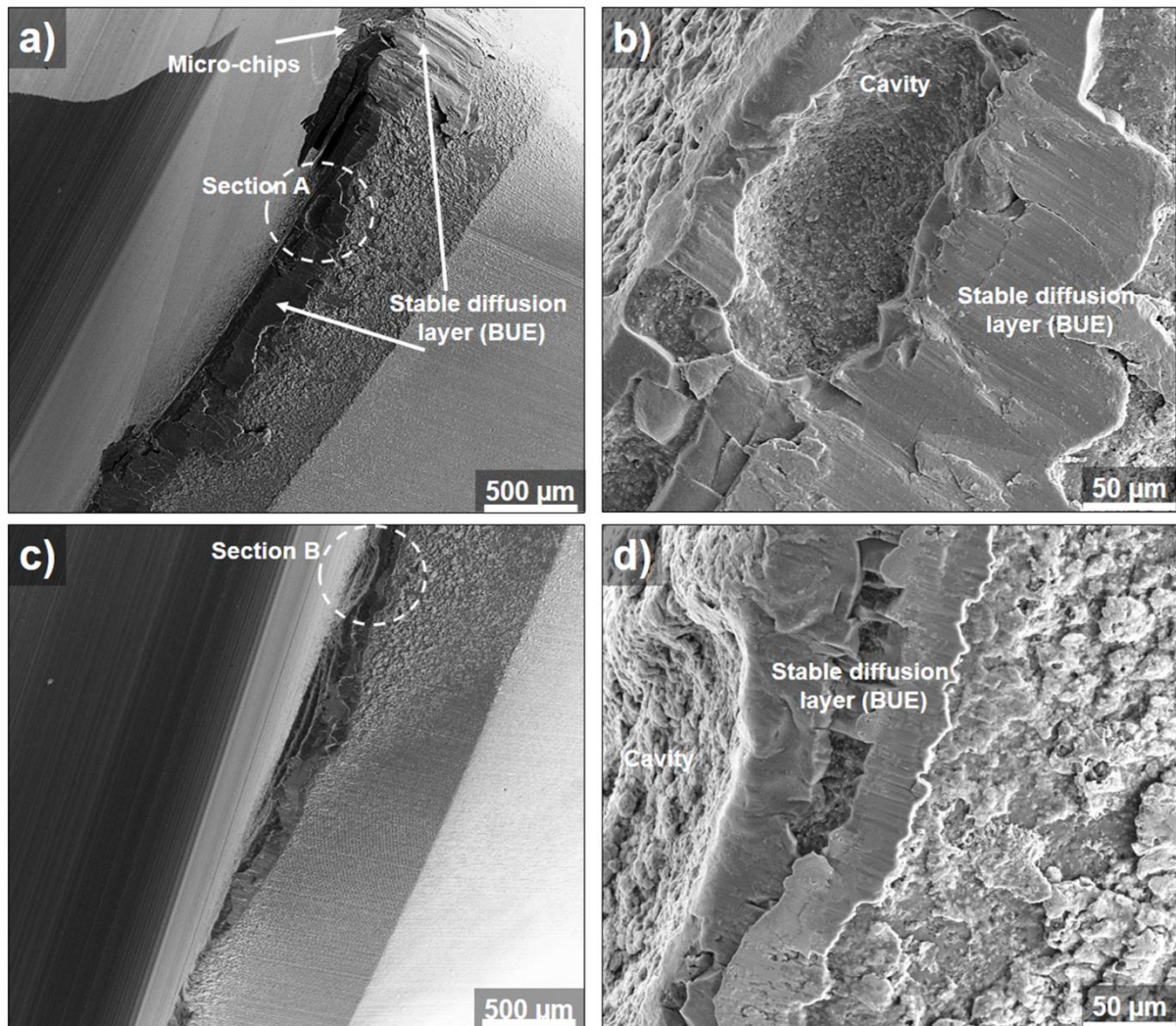


**Fig. 5.** a) SEM micrograph of the primary cutting edge of the milling cutter tested in operation 2, b) magnified image of section A, c) SEM micrograph of the primary cutting edge of the milling cutter tested in operation 3 and d) magnified image of section B.



In Fig. 6, the chip morphologies after end milling of Inconel 625 with SiAlON-TiN (Fig. 6 a) and WC-Co (Fig. 6 b) tools are given, comparatively. While the chips produced by the SiAlON-TiN tool were serrated and fragmented in shapes due to the very high cutting speed, they were continuous for the carbide milling cutter, which was operated at much lower cutting speed (15 m/min). It is obvious that the plastic deformation of the chip was increased considerably with the cutting speed. Because of the insufficient thermal conductivity of Inconel 625, the heat generated by the friction between tool and work-piece cannot be dispatched and the softening of the work-piece at the interface becomes evident. However, a thermal gradient occurs at the cutting zone as a result of the plastic deformation, and some parts of the work-piece stay unsoften state which shifts the shear zone away from the tool tip. Therefore, an oscillatory state occurs at the cutting zone which corresponds to the formation of a discontinuous chips [Davies et al. 1997]. The increase in fragmentation of the chips with increasing cutting speed also showed by [Zheng et al., 2013].

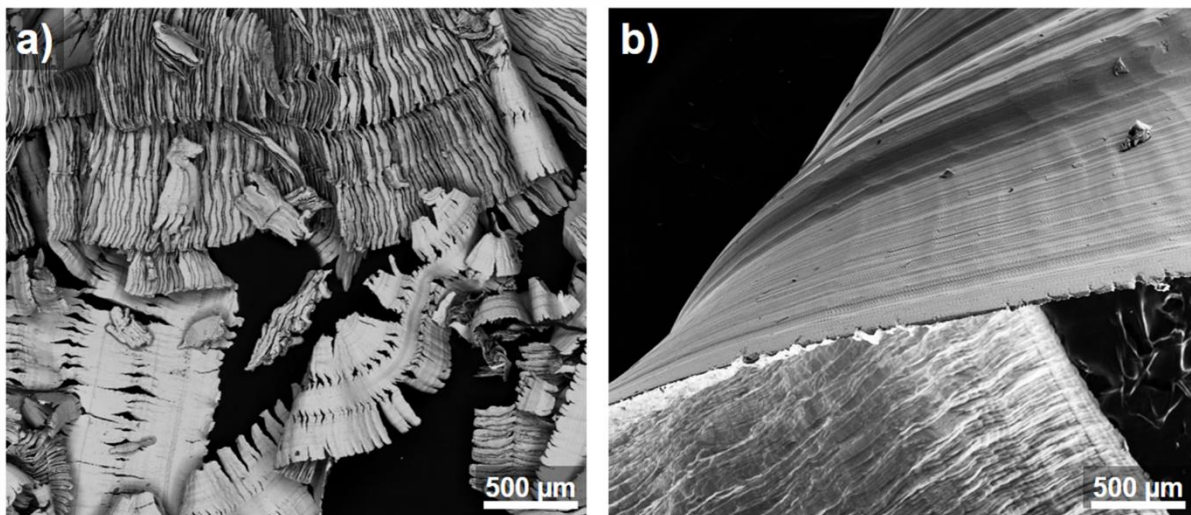


**Fig. 6.** SEM micrograph of the chips produced by **a)** SiAlON-TiN and **b)** WC-Co tools

#### 4. CONCLUSIONS

In this study, a novel SiAlON-TiN solid ceramic milling cutter was developed in order to machine superalloys at ultra-high speeds (400-1000m/min). The ceramic milling cutters were tested in 3 different milling operations of Inconel 625 superalloy part. The microstructural investigation of the worn cutting edges of the tools and the chips were performed. Accordingly, the following conclusions were obtained:

- At the first stage of the milling, micro-chipping was occurred due to the high strain hardening property of the work-piece. At this stage, cutting edge geometry and the surface finish of the ceramic tool should be improved in order to reduce micro-chipping.



- After a few revolution, owing to the high cutting speed and absence of a coolant, the temperature at the cutting zone exceeds 1000°C. After this point, diffusion wear becomes dominant. Cr, Al, Ti and Ni atoms migrate and form a complex oxide layer at the interface of the tool and the work-piece.
- Although TiN improves the mechanical properties of the  $\alpha/\beta$ -SiAlON composite, it weakens the chemical durability of the composite because of the high tendency to diffusion at high temperatures. Therefore, it is believed that the improved tool life would be obtained by using monolithic  $\alpha/\beta$ -SiAlON ceramics instead of TiN reinforced one.
- Inconel 625 can be successfully machined by SiAlON-based ceramics at 5-10 times higher cutting speeds compared to WC-Co based counterparts without any coolant.

## REFERENCES

- Alauddin, M., El-Baradie, M.A., Hashmi, M.S.J., (1996),** “End milling machinability of Inconel 718, J. Eng. Manuf., Vol. 210, pp. 11-23.
- Balazinski, M., Songmene, V., (1995),** “Improvement of tool life through variable feed milling of Inconel 600”, Ann. CIRP, Vol. 44, pp. 55-58.
- Choudhury, I.A., El-Baradie, M.A., (1998),** “Machinability of nickel-base superalloys: a general review”, J. Mater. Process. Tech., Vol. 77, pp. 278-284.
- Çelik, A., Ayas, E., Halil, E., Kara, A., (2012),** “Oxidation behavior of electrically conductive  $\alpha/\beta$ -SiAlON composites with segregated network of TiCN”, J. Euro. Ceram. Soc., Vol. 32, pp.1395-1403.
- Davies, M.A., Burns, T.J., Evans, C.J., (1997),** “On the dynamics of chip formation in machining hard metals”, Ann. CIRP, Vol. 46, pp. 25-30.
- Devillez, A., Schneider, F., Dominiak, S., Dudzinski, D., Larrouquere, D., (2007),** “Cutting forces and wear in dry machining of Inconel 718 with coated carbide tools”, Wear, Vol. 262, pp. 931-42.
- Ekström, T., Nygren, M., (1992),** “SiAlON ceramics”, J. Am. Ceram. Soc., Vol. 75, pp. 259-276.
- Evans A. G. and Charles E. A., (1976),** “Fracture toughness determination by indentation”, J. Am. Ceram. Soc., Vol. 59, pp. 371-372.
- Ezugwu, E.O., Bonney, J., Yamane, Y., (2003),** “An overview of the machinability of aeroengine alloys”, J. Mat. Process. Tech., Vol. 134, pp. 233-53.



**Jindal, P.C., Santhanam, A.T., Schleinkofer, Shuster A.F., (1999)**, “Performance of PVD TiN, TiCN and TiAlN coated cemented carbide tools in turning”, *Int. J. Refract. Metals Hard Mater.*, Vol. 17, pp. 163-170.

**Kear, B.H., Oblak, J.M., Giami, A.F., (1970)**, “Stacking faults in gamma prime precipitation hardened nickel-base alloys”, *Metal. Tran.*, Vol. 1, pp. 2477-86.

**Kramer, B.M., (1987)**, “On tool materials for high speed machining”, *J. Eng. Ind.*, Vol. 109, pp. 87-91.

**Li, L., He, N., Wang, M., Wang, Z.G., (2002)**, “High speed cutting of Inconel 718 with coated carbide and ceramic inserts”, Vol. 129, pp. 127-130.

**Liao, Y.S., Lin, H.M., Wang, J.H., (2008)**, “Behaviors of end milling Inconel 718 super alloy by cemented carbide tools”, *J. Mater. Process. Tech.*, Vol. 201, pp. 460-465.

**Natural, N., Yamaha, Y., (1993)**, “High speed machining of Inconel 718 with ceramic tools”, *Ann. CIRP*, Vol. 42, pp. 103-106.

**Whitney, E.D., (1974)**, “Ceramic cutting tools”, *Powder Met. Int.*, Vol. 6, pp. 73-76.

**Zheng, G., Zhao, J., Zhou, Y., Li, A., Cui, X., Tian, X., (2013)**, “Performance of graded nano-composite ceramic tools in ultra-high speed milling of Inconel 718”, *Int. J. Adv. Manuf. Tehnol*, Vol. 67, pp. 2799-2810.



## HIGH EFFICIENCY ELLIPTICAL VIBRATION CUTTING OF HARDENED STEEL WITH LARGE NOSE RADIUS SINGLE CRYSTAL DIAMOND TOOL

**Yilong WANG**, *wang@upr.mech.nagoya-u.ac.jp* Nagoya University, 464-8603, Nagoya, Japan

**Eiji SHAMOTO**, *shamoto@mech.nagoya-u.ac.jp* Nagoya University, 464-8603, Nagoya, Japan

### ABSTRACT

Elliptical Vibration Cutting of hardened steel with large nose radius single crystal diamond tool is proposed in this paper. Experimental findings revealed that the proposed machining method has great potential to realize the high efficiency ultra-precision diamond machining of steel. However, it was found that ploughing phenomenon significantly affects the finished surface quality. An analytical model was developed for the optimization of machining conditions to minimize the ploughing effect. The analytical model was then validated in a qualitative manner with experimental tests using steel workpieces.

**Keywords:** Elliptical Vibration Cutting, Hardened steel, Single crystal diamond tool, Minimum uncut chip thickness

### 1. INTRODUCTION

Requirement for high dimensional precision and optical quality surface as well as a decrease in cost and cycle time in molds and dies manufacturing is rapidly increasing. Molds and dies manufacturing represents a significant link in the entire production chain. Nearly all mass produced discrete parts are made by utilizing molds and dies [1, 2]. Therefore, the quality of the molds and dies directly affects the quality of the produced parts. High speed machining (HSM) is a cost effective method of machining hardened steels for various molds and dies [3, 4]. Today nearly all dies and molds makers use HSM to achieve dimensional precision requirement in an efficient way. However, the use of conventional cutting tools (e.g. tungsten carbide or fine carbide with various and multiple coatings) makes it difficult to achieve optical quality surface by the conventional HSM method. In order to achieve optical quality surface, the grinding, polishing or lapping process is generally required. However, these processes



are not only time and cost consuming but also inclined to pose a high risk of shape deterioration and subsurface damage. Moreover, complex surface structure is difficult to be produced by these processes. On the other hand, nickel-plated steel molds [5] with high shape precision and surface roughness have long been used for the injection molding of plastic optics. Established process for nickel-plated steel molds consists of high speed machining of steel mold shape, electroless nickel coating and diamond cutting of the nickel layer [6]. However, the nickel plating is very time and cost consuming. Moreover, the disadvantages, such as low hardness and thus short life time, low temperature stability and thus cannot be used for hot pressing of glass, severely limit the use of nickel-plated steel molds in modern optics application.

As a promising machining method, ultrasonic Elliptical Vibration Cutting has been proposed to ultra-precision machine hardened steel with submicron-scale shape accuracy and nano-scale surface roughness. Up to now, the superior machining performance of this technology has been verified in both experimental and theoretical ways [7-9]. Now, this ultrasonic Elliptical Vibration Cutting technology is being increasingly expected to be one of the possible next-generation steel molds and dies manufacturing techniques for the ultra-precision fabrication of complex/micro structure with arbitrary shape and/or freeform surface. However, this machining technology is currently limited to the relatively small-size workpiece machining due to the extremely demanding requirements of machining conditions. If it is used to machine large size workpiece, the machining time and cumulative cutting distance (or tool wear) will be remarkably increased which in turn dramatically increase the machining cost and cycle time. To overcome this problem and apply this emerging machining technology effectively in industrial application, Elliptical Vibration Cutting with large nose radius single crystal diamond tool is proposed to realize the ultra-precision machining of large size steel molds and dies in this paper.

## **2. BASIC IDEA OF HIGH EFFICIENCY ELLIPTICAL VIBRATION CUTTING OF STEEL WITH LARGE NOSE RADIUS DIAMOND TOOL**

During Elliptical Vibration Cutting, two-directional vibration at an ultrasonic frequency is superimposed on the cutting feed motion of the diamond tool, therefore, the cutting process can be considered as interrupted cutting, with the interruption occurring at an ultrasonic frequency. This periodic tool-workpiece separation not only reduces heat transfer from the chip to the tool but also provides a chance for the ambient air and lubricant molecules to penetrate the tool-work interface, hence preventing the chemical reaction and diffusion wear between the newly formed surface and the diamond tool. Though Elliptical Vibration Cutting works effectively in suppressing diamond tool wear, the tool wear would be still very severe if



it is used for large size steel workpiece machining due to the extremely long cumulative cutting distance. In diamond machining, the cumulative cutting distance  $L$  (m) can be estimated by:

$$L \approx \frac{A}{f} \quad (1)$$

Where  $A$  is area of the total machined surface (mm<sup>2</sup>);  $f$  is the feed rate (μm in planing and μm/rev in turning). For a given workpiece, the cumulative cutting distance can be shortened by increasing the feed rate  $f$ . Moreover, the increase of feed rate will further shorten the total machining time. However, the feed rate  $f$  directly related to the surface roughness  $SR$  (nm) which can be theoretically determined by:

$$SR = R - \sqrt{R^2 - \left(\frac{f}{2}\right)^2} \approx \frac{f^2}{8R} \quad (2)$$

Where  $R$  is tool nose radius (mm). It can be seen that, the increase of feed rate  $f$  results in an increase of surface roughness  $SR$ .

Equations (1) and (2) suggest that, the cumulative cutting distance and the total machining time as well as the theoretical surface roughness are functions of feed rate. For a given diamond tool it is unrealistic to shorten the cumulative cutting distance while still maintain the same good surface roughness by increasing the feed rate. On the other hand, from Equation (2), it can be seen that, the theoretical surface roughness is inversely proportional to the tool nose radius of  $R$ , a shorter cumulative cutting distance and the same good surface roughness can be achieved by increasing both the feed rate and the tool nose radius. In this study, diamond tool with large nose radius of 50 mm is proposed to realize the ultra-precision but high efficiency machining of steel.

### 3. EXPERIMENTAL DETAILS

The cutting experiments were carried out on a five-axis ultra-precision machine tool (NACHI, ASP01UPX) equipped with an Elliptical Vibration Cutting device (Taga Electric Co., Ltd., EL-50 Σ). Fig.1 shows a photograph of the main section of the experimental setup. The machine tool consists of three slide-guides on the XYZ axes, two rotary index tables on the B and C axes and a five-axis control system. During machining, the depth of cut, pick feed and cutting speed can be achieved through the motion along Z-, Y- and X-axes, respectively. Typical hardened die steel (Stavax) was used as workpiece. Single crystal diamond tool with a nose radius of 50 mm was used as cutting tool in the experiments (as shown in Fig.2). Detailed machining conditions are shown in Table 1.

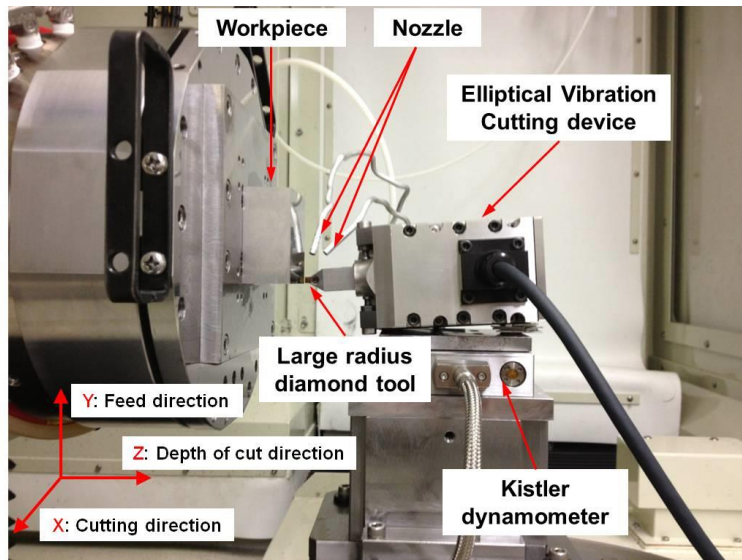


Fig.1 Photograph of the main section of the experimental setup

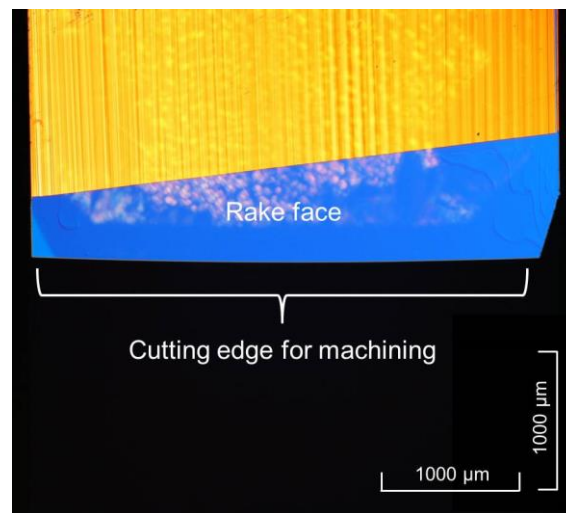


Fig.2 Photograph of the large nose radius diamond tool

Table 1 Machining conditions

Workpiece	Material: hardened die steel (Stavax) with a hardness of 53-54HRC Size: 50x50mm
Diamond tool	Tool radius (mm): 50 Rake angle: 0° Flank angle: 10°
Vibration conditions	Frequency (kHz): 41 Amplitude in cutting and depth of cut directions, respectively ( $\mu\text{m}_{p-p}$ ): 4, 4
Cutting conditions	Depth of cut ( $\mu\text{m}$ ): 4 Pick feed ( $\mu\text{m}$ ): 80 (20,60,100,160) Cutting speed (mm/min): 1000 Cutting fluid: Oil mist (PS – No. 12, Palace Chemical Co. Ltd.)

#### 4. EXPERIMENTAL RESULTS AND DISCUSSION

Fig.3 shows a photograph of the machined surface taken with a differential interference microscope. As shown, the finished surface is very smooth and there are no discontinuous cutting traces. Moreover, no apparent tool wear marks are observed.

Fig.4 shows the variation of surface roughness  $R_z$  and  $R_a$  (sample points were achieved along the feed direction) with respect to cutting distance. It is evident that the surface roughness  $R_z$  and  $R_a$  maintained a relatively low level of better than 60 nm and 10 nm respectively throughout the cutting process although several small fluctuations can be observed.

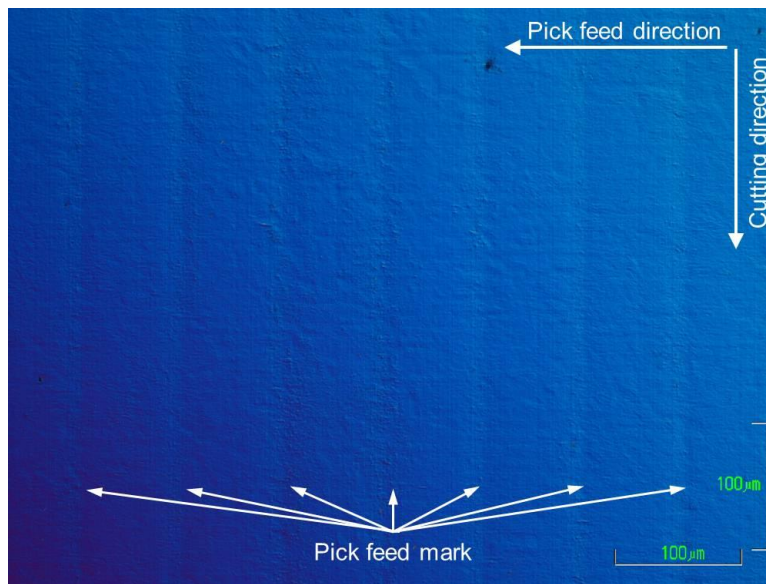


Fig.3 Photograph of the machined surface taken with differential interference microscope

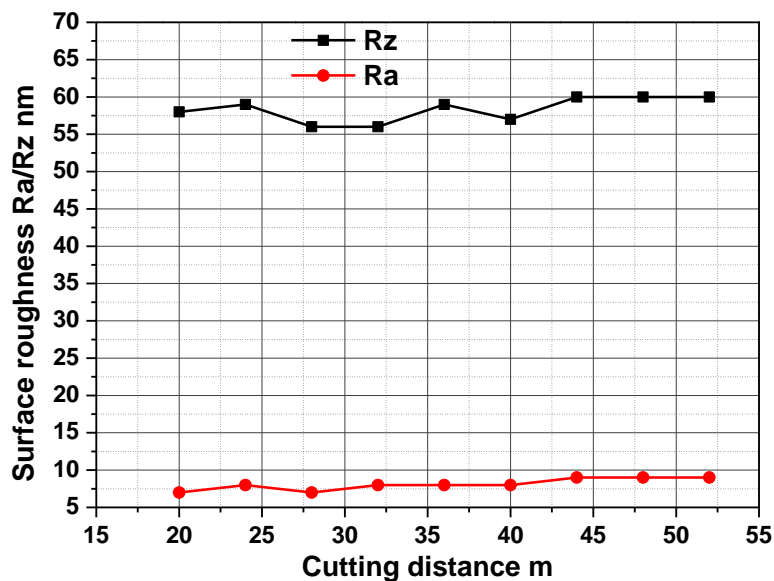


Fig.4 Surface roughness variation as a function of cutting distance

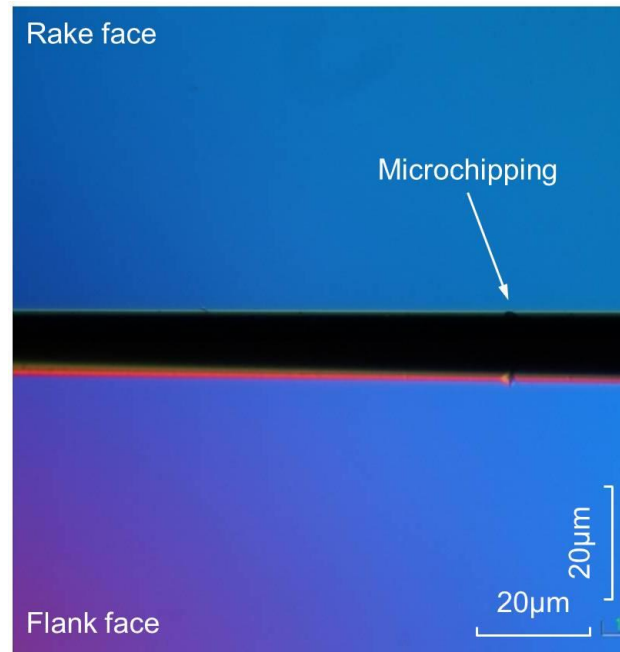


Fig.5 Photograph of the cutting edge after machining taken with differential interference microscope

Table 2 Machining performance comparison

	EVC with R50mm diamond tool	EVC with R1mm diamond tool
Workpiece	Hardened steel (Stavax, Size: 50x50mm)	
Depth of cut ( $\mu\text{m}$ )	4	4
Pick feed ( $\mu\text{m}$ )	80	20
Cutting speed (mm/min)	1000	1000
Actual machined surface roughness (nm)	Rz: 50-60 Ra: <10	Rz: 40-50 Ra <10
Cutting distance (m)	31.3	125
Machining time (min)	57.3	229.2

Fig.5 shows a photograph of the cutting edge after machining, which was taken with a differential interference microscope, too. It is evident that, although microchipping was observed, the tool wear pattern around the main cutting area of the cutting edge did not represent severe deterioration.

The above results suggest that, ultra-precision machining of steel (with optical quality surface) can be realized by using the proposed method. Moreover, the machining efficiency can be significantly improved as compared with that of diamond machining with normal cutting tool (nose radius is typically in the range of 1-2 mm). A comparison between the proposed method and Elliptical Vibration Cutting with normal diamond tool is summarized in

Table 2. Here, it should be noted that, the only difference between the two diamond tools is the nose radius; other parameters are the same with each other. It is evident that, the machining distance and time was significantly shortened by using large nose radius diamond tool.

Although high efficiency ultra-precision machining was achieved by using large nose radius diamond tool, ploughing marks were observed in the region between the successive pick feed pitches on the machined surface, as shown in Fig.6. In this study, the ploughing marks observed on the machined surface were considered to result from the excessive small uncut chip thickness. In ultra-precision diamond machining, the uncut chip thickness is comparable or even less than the tool edge radius and as a result ploughing will occur if the uncut chip thickness is less than a critical value which is defined as the minimum uncut chip thickness. Below this critical value, the material flows downward without any chip formation and the process performs as ploughing. Above this critical value, the material flow up and forms as chips and the process performs as shearing [10]. The minimum uncut chip thickness thereby significantly affects the machining performance in terms of chip formation, machined surface roughness, burr formation, surface integrity, etc. [10, 11]. Therefore, the influence of the minimum uncut chip thickness on material removal behavior during diamond machining is of great scientific interest and needs to be understood to minimize the ploughing effect. Several investigations have resorted to experimentation, molecular dynamic simulation, and microstructure level finite element simulation to estimate the minimum uncut chip thickness which can be roughly estimated as [10, 11]:

$$d_m = \rho(1 - \cos(\theta)) \quad (3)$$

Where  $d_m$  is the minimum uncut chip thickness,  $\rho$  is the edge radius of the diamond tool and  $\theta$  is the friction angle.

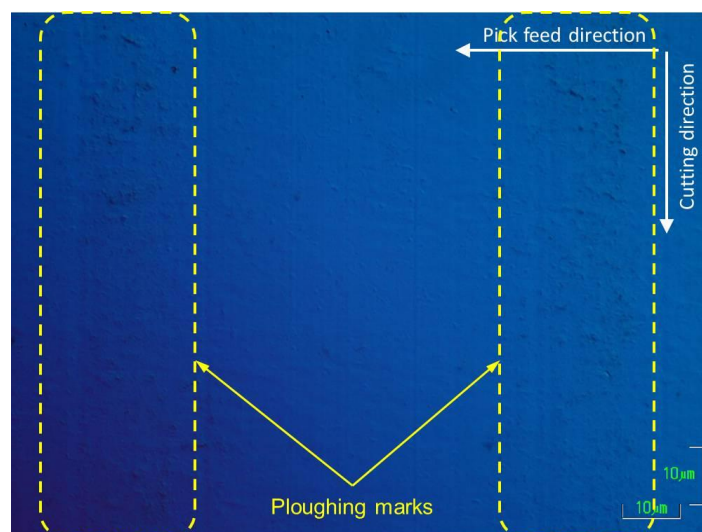


Fig.6 Ploughing marks on the machined surface

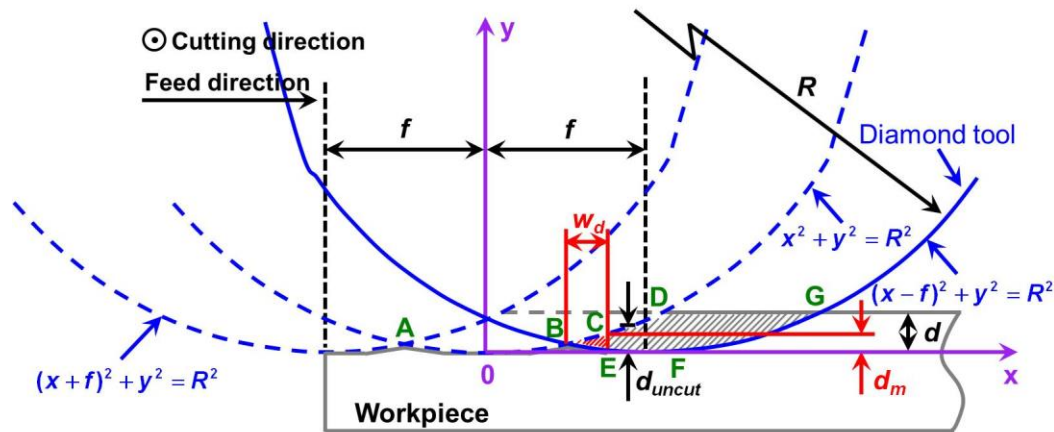


Fig.7 Schematic of the relationship among the uncut chip thickness, the nose radius, the depth of cut, the pick feed and the width of ploughing

Equation (3) suggests that, for a given work material the minimum uncut chip thickness is strongly affected by the edge radius of the diamond tool. However, in addition to the edge radius, the minimum uncut chip thickness, the tool nose radius, the machining conditions (especially the pick feed) and final machined surface quality should be considered as a whole to study the process mechanism in diamond machining of steel. Fig.7 illustrates a schematic of the relationship among the uncut chip thickness  $d_{uncut}$ , the nose radius  $R$ , the depth of cut  $d$ , the pick feed  $f$  and the width of ploughing  $W_d$ . Suppose the machined surface after the previous cutting was conducted over the region  $ABCD$ , then during the current cutting pass the cutting edge starts to engage the work material at point  $B$  with uncut chip thickness  $d_{uncut}=0$ . Since the R-shaped diamond tool is used, the uncut chip thickness  $d_{uncut}$  gradually increases along cutting edge profile  $BEF$  and the cutting process performs as ploughing until the uncut chip thickness  $d_{uncut}$  exceeds the minimum uncut chip thickness  $d_m$  at point  $E$ . After point  $E$  a chip starts to generate and the cutting process performs as shearing, then new machined surface after point  $E$  will follow the cutting edge profile of  $EFG$ . However, the work material in the red shaded area of  $BCE$  will not be removed because the uncut chip thickness is less than the minimum uncut chip thickness and as a result ploughing marks will be left on the machined surface.

From the geometrical schematic of Fig.7, the uncut chip thickness  $d_{uncut}$  can be approximately estimated as:

$$d_{uncut} = \left| \sqrt{R^2 - x^2} - \sqrt{R^2 - (x-f)^2} \right| \quad (4)$$

Then the width of ploughing  $W_d$  can be obtained where  $d_{uncut}=d_m$ :

$$w_d = x_m - (f / 2) \quad (d_{\text{uncut}} = d_m) \quad (5)$$

Where  $x_m$  is the distance in horizontal direction between point  $E$  and point  $O$ . Here,  $d_m$  can be readily computed from Equation (3).



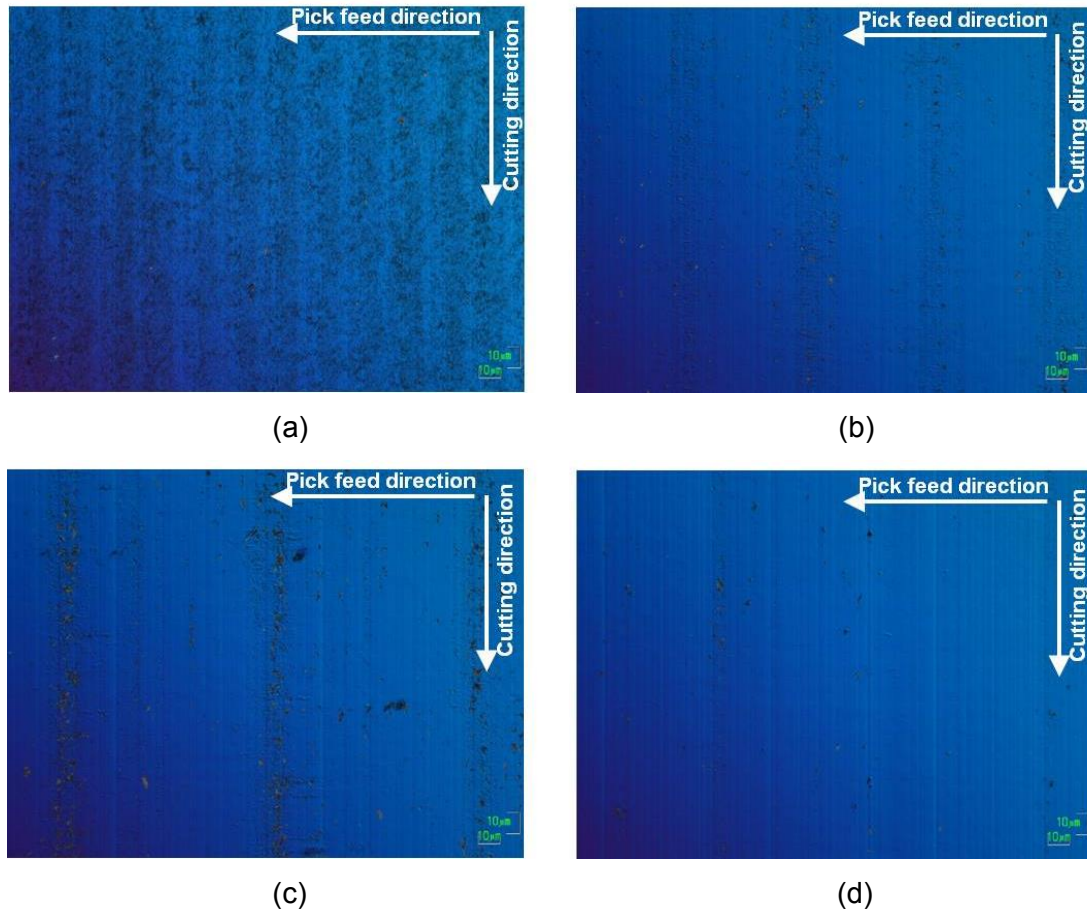


Fig.8 Effect of pick feed on ploughing behavior (a) pick feed is 20  $\mu\text{m}$  (b) pick feed is 60  $\mu\text{m}$  (c) pick feed is 100  $\mu\text{m}$  (d) pick feed is 160  $\mu\text{m}$

Equations (4) and (5) suggest that, for a given diamond tool, ploughing can be minimized by optimizing the pick feed. Hence, it is desirable to investigate the effect of pick feed on ploughing behavior. In view of this, cutting experiments with different pick feeds were carried out. Fig.8 summarizes an easy-to-see correlation between the pick feed and the ploughing marks. It is clearly seen that, for a given diamond tool the ploughing marks that left on the machined surface are strongly dependent on the pick feed. As the pick feed decreases the width and ratio of ploughing increase (for example the entire machined surface is covered with ploughing marks when the pick feed decreases to 20  $\mu\text{m}$ ). On the contrary, as the pick feed increases the width of ploughing decreases and the ploughing marks are almost unobservable when the pick feed increases to 160  $\mu\text{m}$ . These experimental results clearly show that, ploughing can be minimized by optimizing the pick feed in ultra-precision diamond machining. Moreover, it is evident that, the analytical model developed in this study can be applied for the optimization of pick feed to minimize ploughing. However, it should be noted that, here the deterioration of the edge radius of the diamond tool is not considered, as the diamond tool develops tool wear (results in large edge radius) during machining the minimum



uncut chip thickness will keep increasing. Therefore, the pick feed needs to increase for the worn tool to avoid severe ploughing.

## 5. CONCLUSIONS

A high efficiency ultra-precision machining method with large nose radius single crystal diamond tool was proposed in this study. And an analytical model with considering the tool edge radius, the tool nose radius, the machining conditions and the minimum uncut chip thickness was developed for the optimization of machining conditions to minimize ploughing effect. The following conclusions can be drawn from this paper:

- (1) Optical quality surface can be achieved by using the diamond tool with large nose radius at a relatively high machining efficiency;
- (2) The tool wear pattern around the main cutting area of the cutting edge did not represent severe deterioration under the present machining conditions, therefore, it has great potential to realize the high efficiency machining of large size steel workpiece;
- (3) Ploughing marks were observed in the proposed machining with large nose radius which may slightly deteriorate the quality of the finished surface. It was found that, for a given diamond tool, the ploughing behavior in Elliptical Vibration Cutting of steel is strongly dependent on the pick feed. An analytical model was developed for the optimization of pick feed to minimize the ploughing effect. The model was validated through a series of cutting experiments and it was found that ploughing effect becomes less as the pick feed increases, and vice versa.

The present work clearly showed that, the proposed method has great potential to realize the high efficiency ultra-precision machining of hardened steel molds and dies for the replication of structured optical quality elements. It is expected that the proposed research will enable the low cost but high efficiency fabrication of high precision molds and dies for use in photonics, telecommunication and automotive applications, etc.

## REFERENCES

- [1] **Altan, T., Lilly, B., Yen, Y.C., (2001)**, "Manufacturing of Dies and Molds", CIRP Annals - Manufacturing Technology, Vol.50, No.2, pp 404-422.
- [2] **Altan, T., Lilly, B.W., Kruth, J.P., König, W., Tönshoff, H.K., Lutervelt van, C.A., Khairy A.B., (1993)**, "Advanced Techniques for Die and Mold Manufacturing", CIRP Annals - Manufacturing Technology, Vol.42, No.2, pp 707-716.
- [3] **Vivancos, J., Luis, C.J., Costa, L., Ortiz, J.A., (2004)**, "Optimal Machining Parameters Selection in High Speed Milling of Hardened Steels for Injection Moulds", Journal of





Materials Processing Technology, Vol.155-156, pp 1505-1512.

- [4] **Krajnik, P., Kopac, J., (2004)**, "Modern machining of die and mold tools", Journal of Materials Processing Technology, Vol.157-158, pp 543-552.
- [5] **Ozyilmaz, A.T., Kardas, G., Erbil, M., Yazıcı, B., (2005)**, "The Corrosion Performance of Polyaniline on Nickel Plated Mild Steel", Applied Surface Science, Vol.242, No.1-2, pp 97-106.
- [6] **Pramanik, A., Neo, K.S., Rahman, M., Li, X.P., Sawa, M., Maeda, Y., (2003)**, "Cutting performance of diamond tools during ultra-precision turning of electroless-nickel plated die materials", Journal of Materials Processing Technology, Vol.140, No.1-3, pp 308-313.
- [7] **Wang, Y., Suzuki, N., Shamoto, E., Zhao, Q., (2011)**, "Investigation of Tool Wear Suppression in Ultra-precision Diamond Machining of Hardened Steel", Precision Engineering, Vol.35, No.4, pp 677-685.
- [8] **Suzuki, N., Yokoi, H., Shamoto, E., (2011)**, "Micro/nano Sculpturing of Hardened Steel by Controlling Vibration Amplitude in Elliptical Vibration Cutting", Precision Engineering Vol.35, No.1, pp 44-50.
- [9] **Shamoto, E., Moriwaki, T., (1999)**, "Ultraprecision diamond cutting of hardened steel by applying elliptical vibration cutting", CIRP Annals - Manufacturing Technology, Vol.48, No.1, pp 441-444.
- [10] **Malekian, M., Mostofa, M.G., Park, S.S., Jun, M.B.G., (2012)**, "Modeling of minimum uncut chip thickness in micro machining of aluminum", Journal of Materials Processing Technology, Vol.212, No.3, pp 553-559.
- [11] **Yuan, Z.J., Zhou, M., Dong, S., (1996)**, "Effect of diamond tool sharpness on minimum cutting thickness and cutting surface integrity in ultraprecision machining", Journal of Materials Processing Technology, Vol.62, No.4, pp 327-330.





## VERIFICATION OF CONE FRUSTUM ACCURACY TEST OF FIVE-AXIS MACHINING CENTER

**Toru TAJIMA**, *m1m13412@st.oit.ac.jp* Osaka Institute of Technology, 535-8585, Osaka, Japan

**Tomohiro KUBO**, *e140057@st.oit.ac.jp* Osaka Institute of Technology, 535-8585, Osaka, Japan

**Yukitoshi IHARA**, *ihara@med.oit.ac.jp* Osaka Institute of Technology, 535-8585, Osaka, Japan

### ABSTRACT

The motion accuracy evaluation method of five-axis machining centers (5-axis MC) is not fixed enough though their demand has increased now. There is NAS979 made as National Aerospace Standard in 1969 for an accuracy test method, and the cone frustum cutting test by endmill exists. However, this method assumes large scale 5-axis MCs for making aircraft parts with rotary axes on the spindle side, and then it is necessary to misinterpret the test method suitably to apply for a lot of 5-axis MC. Nevertheless, it is still used because there is no other test method of five-axis machining center that takes the place of NAS979. The discussion about the ISO standard concerning the accuracy test method of 5-axis MC started in 2006. In the discussion, the cone frustum cutting test in NAS979 is improved as five-axis simultaneous interpolation motion described in ISO10791-7 "Accuracy of a finished test piece", and similar test using ball bar is also described in ISO10791-6 "Accuracy of interpolation motion test". These two standards are DIS stage in 2013, and they are scheduled to be issued as International Standards by the end of 2014. In this report, the cone frustum tests that are scheduled to be adopted for ISO10791-6 and ISO10791-7 are outlined. Next, the results of the accuracy test of interpolation motion by the ball bar that are actually measured on several 5-axis MCs are shown, and the kind of error source of the machine appeared with this test method is also shown. Moreover, the feasibility of the evaluation test method is discussed. In addition, the offset of the rotary axes that is mainly caused by the thermal deformation and that is appeared to the measurement results is discussed.

**Keywords:** Five-axis machining center, Motion accuracy, Test standard, Ball bar



## 1. INTRODUCTION

Five-axis machining center (5-axis MC) is a machine tool with two rotary axes in addition to three linear orthogonal axes. Two rotary axes change the orientation of the tool against the workpiece and it is possible to make complex shape parts without using a special jig. Therefore, the demand for 5-axis MC has been increased. However, both users and manufacturers cannot evaluate the accuracy of 5-axis MC because there is no active standard of accuracy test of 5-axis MC.

NAS979 is a standard enacted in 1969 made as National Aerospace Standard, in which there is a test method by cutting a truncated cone using an endmill to evaluate the accuracy on 5-axis MCs. However, it is difficult to apply this test method to current 5-axis MCs because this test is assumed for machines with two rotary axes in the spindle head. Nevertheless, this standard is still used because there is no alternative accuracy test method that takes the place of NAS 979. The accuracy test standard on 5-axis MC has been discussed in the subcommittee of ISO since 2006, and then it is described also as a test method in ISO10791-6 [2] using a measuring instrument called a ball bar that is capable of measuring machine's motion accuracy without cutting, as well as in ISO10791-7 [1] that deals with the accuracy of finished test piece.

In this report, the actual test results of the interpolation motion accuracy on several five-axis MCs are shown first, and the error sources appearing on the results are shown. In addition, the working problems on this test method and the evaluation method were examined. Furthermore, the influence on the measurement result, caused by the positional change of the center of rotary axes by thermal deformation of the machine etc., and the gap between two rotary axes, are discussed.

## 2. CONE FRUSTUM TESTS IN THE NEW STANDARD

### 2.1 Accuracy of Finished Test Piece

ISO10791-7 is a standard to test the accuracy of finished test piece such as cylindricity, straightness, squareness, parallelism and positioning of the rotary axis on various cutting conditions of the machine tool. In this standard, test items are not classified by the structure of the 5-axis MC such as ISO10791-6. Figure 1 shows a setting condition of the cone frustum cutting test named as M3 test in ISO/DIS10791-7.  $\theta$  is the half apex angle of the truncated cone,  $t$  is the thickness of the test piece,  $D$  is the diameter of the base,  $\beta$  is the degree of inclination setting and  $d$  is the offset between the center of the truncated cone base and the center of the table. A test condition includes two kinds of test piece shape with a common condition of  $D=80\text{mm}$ ,  $d=$  (25% of the diameter the table).

$$(1) \theta = 15^\circ, t = 20\text{mm}, \beta = 10^\circ$$

$$(2) \theta = 45^\circ, t = 15\text{mm}, \beta = 30^\circ$$

Simultaneous five-axis interpolation is necessary since the cone frustum is installed with the inclination to the table.

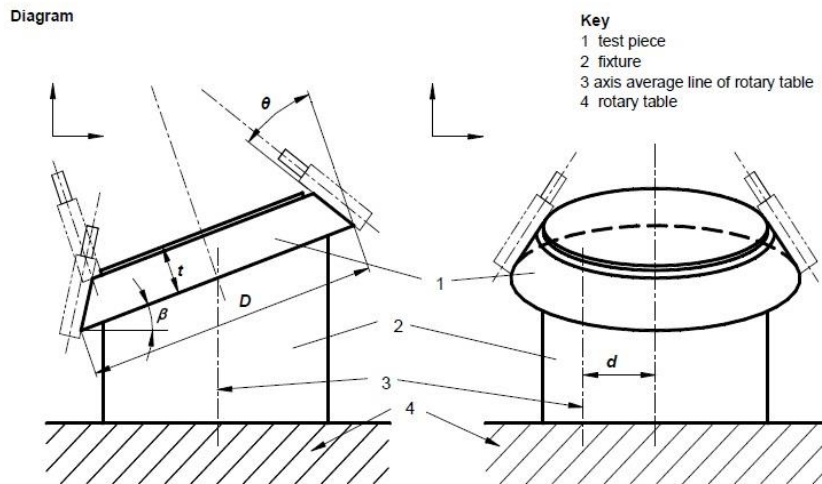


Figure 1. Diagrams of workpiece of cone frustum cutting.

## 2.2 Accuracy of Interpolation Motion

ISO 10791-6 is a standard to test the accuracy of feed speed, spindle speed and interpolation motion of the machine tool. In this standard, 5-axis MC tests are described in the normative annex, and are classified by the structure of the 5-axis MC: the one which has two rotary axes in the spindle head is type A, the one which has two rotary axes in the workpiece side is type B and the one which has a swivel head and a rotary table is type C. In this report, since 5-axis MCs having two rotary axes in the workpiece side were measured, BK3 test in ISO/DIS10791-6 was considered as an accuracy test of interpolation motion simulating the truncated cone cutting. Figure 2 shows the setting conditions of BK3, in which half apex angle and inclination angle of the virtual truncated cone are the same as those of ISO/DIS10791-7 M3. Offset to the bottom center of the truncated cone from the center of the table is 10% of the table diameter. The feed speed on the circle is 1000mm/min. NC program to be used is made by using spreadsheet software. A set of measurement was done in both clockwise direction and counter clockwise direction. A ball bar instrument used is shown in the next clause.

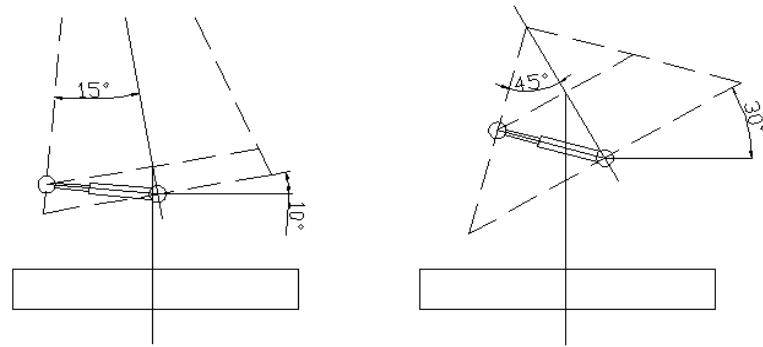


Figure 2. Setting condition of half apex angle 15° and 45°.

### 3. EXPERIMENTAL APPARATUS AND MEASUREMENT METHOD

#### 3.1 Measuring Object and Measuring Instrument

In this report, three 5-axis MCs having two rotary axes in the workpiece side were measured. Table 1 shows the motion range of each rotary axis of them. The axis configuration of the machine A is shown in Fig. 3.

Table 1. Moving range of rotary axis

Machine	Axis	range
A	B-axis	160° ~ -180°
	C-axis	360°
B	A-axis	30° ~ -120°
	C-axis	360°
C	A-axis	360°
	B-axis	-20° ~ 110°

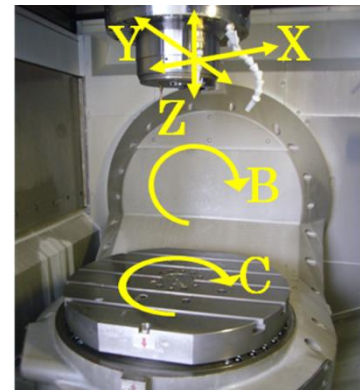


Figure 3. Axis configuration

The measuring instrument used in this experiment is QC20-W (ball bar) made by RENISHAW as shown in Fig. 4. The ball bar is the device which has two balls and a telescoping bar. Each ball is installed in the spindle and table side, and they are connected by a bar with a build-in displacement sensor. It is possible to measure the accuracy of the interpolation motion of 5-axis MC by making NC program of a circle so as to keep a constant distance of two spheres.

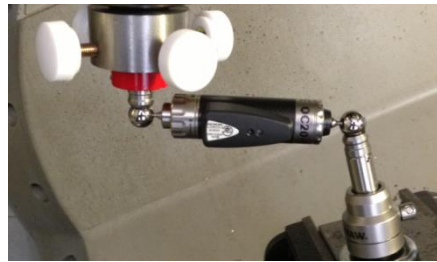


Figure 4. QC20-W ball bar system is made by RENISHAW

### 3.2 Tool Center Position Control

Tool center position control (TCP) is a function of controlling the trajectory of the tool tip, including the motion of the rotary axis of 5-axis MC. By using this feature, it's possible to adjust the position of the tool tip automatically in synchronization with the movement of rotary axes, to keep the position of the workpiece and the tool tip constant. When making an NC program, it's not necessary to convert the coordinates of the orthogonal axes X, Y, and Z to follow the rotating of the rotary axis, and then the program becomes simpler. TCP refers to the parameter of the center position coordinate of a rotary axis stored in NC.

### 3.3 Method for Measurement without the TCP Control

Ball Center of the ball bar which is attached to the spindle and the center of the spindle do not coincide in normal case, however, without TCP control, it is possible to perform measurement by centering the center positions of the ball and C-axis as shown in Fig. 5, and making the program by controlling a relative position using an incremental mode (G91).

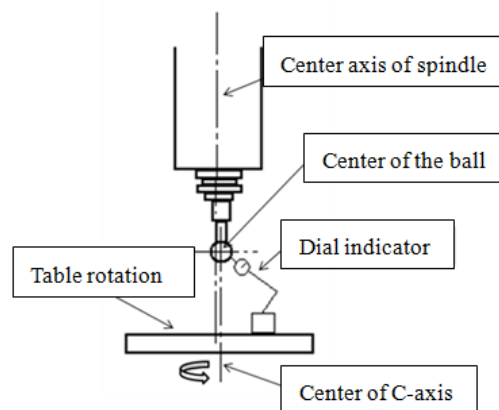


Figure 5. Centering method

### 3.4 Measurement Method Using the TCP Control

In case of the measurement using the TCP control, the result has some influence when the center of the ball is matched to C-axis center, because the position of the tool center point is automatically adjusted synchronizing with the rotation as described by section 3.2. Therefore,



it is necessary to match the center of the spindle to the center of the ball as shown in Fig. 6. Moreover, because the center coordinates of two rotary axes stored in NC are used when the TCP control is used, those exact center coordinates are needed. In this research, the dial gauge is touched to the ball installed on the table as shown in Fig. 7, the table is rotated, and the center of C-axis is matched to the center of the ball. The dial gauge installed in the spindle is touched to the ball and the spindle is rotated, and next, the center of the spindle and the center of the ball are adjusted, and then center coordinates of C-axis are obtained by reading the spindle position. X coordinates of B-axis center is used 18 $\mu$ m away from X coordinates at C-axis center, and it is not possible to measure Z coordinates of B-axis accurately. Therefore, original coordinates as a machine parameter is used.

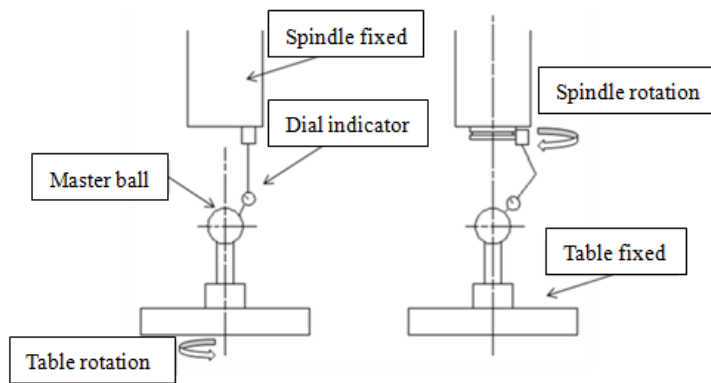


Figure 6. Centering method of C-axis rotary center

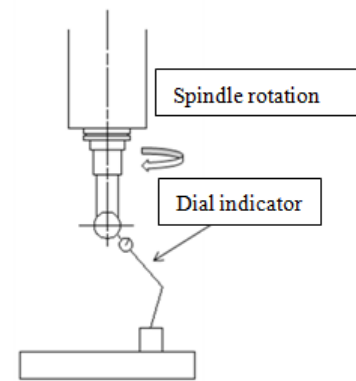
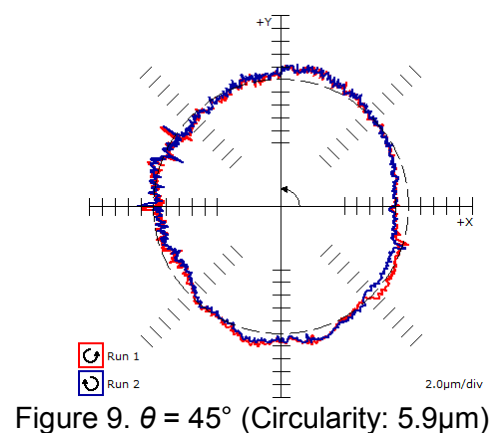
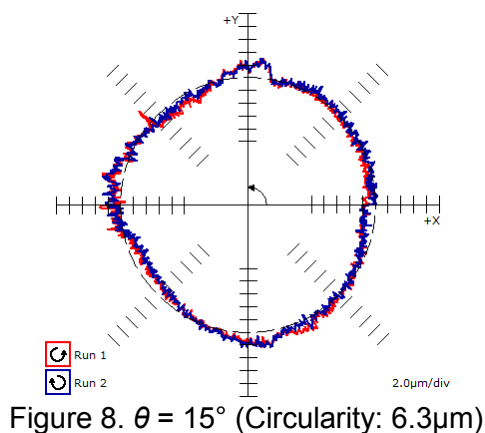


Figure 7. Centering method using TCP

#### 4. RESULT OF INTERPOLATION MOTION ACCURACY TEST

##### 4.1. Difference in the Result by Using TCP Control or not

Figure 8 and 9 show the best results that were measured under the conditions of half apex angle 15° and 45° without using the TCP control.



There is a large step around 80° at 15° half apex angle. The step of the similar tendency was observed at the position of 280°, which is the opposite side against X-axis, but it is not clear. It is thought that the positive side of B-axis is deteriorated because of heavy usage as compared to the negative side of the B-axis. Those two steps are caused by an error motion of B-axis when B-axis goes along 19°. There can be seen many projections. The projections around 160° and around 280° supposed to be caused by the reversal motion of the Y-axis. The projections around 140° and around 300° supposed to be caused by the reversal motion of the X -axis.

In the test condition of half apex angle 45°, as shown in Fig. 9, the projections around 140° and 340° are caused by the reversal motion of X-axis, and those around 150° and 280° by the reversal motion of Y-axis. The overall shape is in a portrait oval and a little uneven. The results of measurements without TCP control are not shown here, however, those look similar with TCP control in both conditions of a half apex angle 15° and 45°. It is thought that there is no big difference in the motion of the machine in the presence of the TCP control.

#### 4.2 Effect of the Displacement of the Center Coordinates of the Rotary Axis

It is thought to influence the measurement result when there is a displacement of the center position of C-axis from the setting value that is stored in NC by the thermal deformation etc. of the machine. Then, the influence on the shape of the circle on C-axis center position shift was examined. First of all, under the test condition of a half apex angle 15°, when the  $\pm 20\mu\text{m}$  displacement in X-axis direction is given based on the result of measurement in Fig. 8, the measurement results are shown in Fig. 10 and Fig. 11.

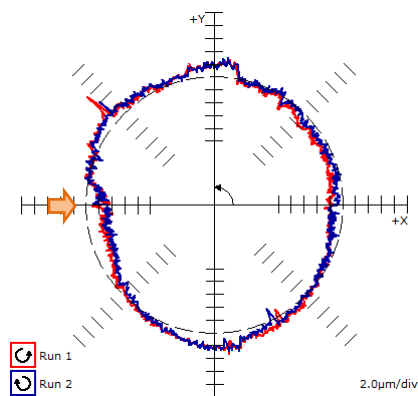


Figure 10. +X axis direction  
(Circularity: 10.4 $\mu\text{m}$ )

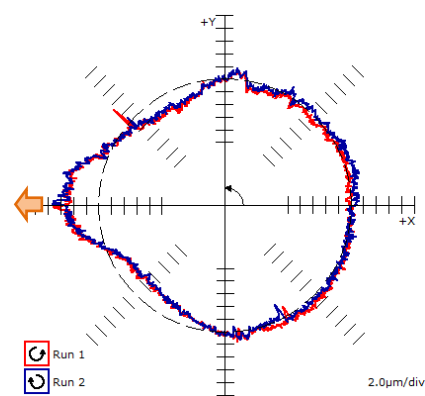


Figure 11. -X axis direction  
(Circularity: 11.3 $\mu\text{m}$ )

If the positive displace is given in the X-axis direction, there is a dent around 180°. Oppositely, if the negative displace is given in the X-axis direction, there is a swell around 180° has swelled out. Secondly, when the  $\pm 10\mu\text{m}$  displacement in Y-axis direction is given, the measurement results are shown in Fig. 12 and Fig. 13.

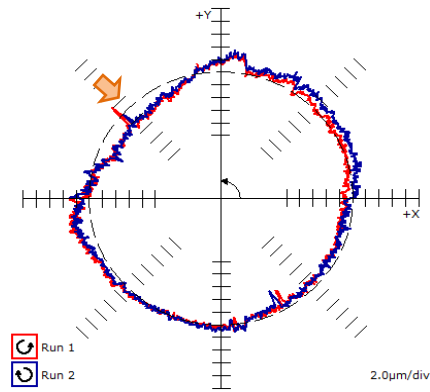


Figure 12. +Y axis direction  
(Circularity: 7.5µm)

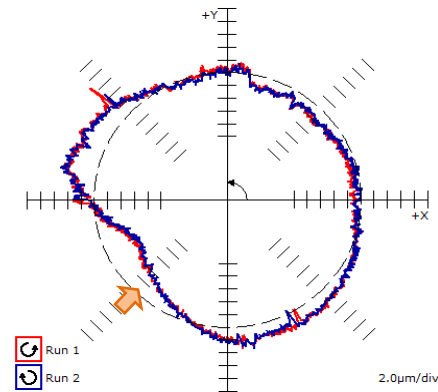


Figure 13. -Y axis direction  
(Circularity: 12.8µm)

If the positive displace is given in the Y-axis direction, there is a dent around 135°. If the negative displace is given in the Y-axis direction, there is a dent around 225°.

Finally, even if the  $\pm 40\mu\text{m}$  displacement in the Z-axis direction is given, little change is observed both in the shape of the circle and value of circularity. It is thought that this test method is not sensitive to the Z-axis position of the rotary axes. The same experiment in the condition of 45° half apex angle were performed, however, the similar result was observed as the 15° half apex angle.

#### 4.3 Influence the Position Deviation between Two Rotary Axes

The rotary axes have not intersected strictly through manufacturing and assembly, although two rotary axes of most five-axis MCs have intersected in the design. Therefore, as there is 18µm gap between B-axis and C-axis in machine A used in this study, this positional deviation saved in the NC unit is taken into consideration when the TCP control is used. It doesn't intersect actually though it is set to C-axis center that B-axis center has intersected in the NC unit when positional deviation is not considered. Then, the influence of this gap exerted on the result of a measurement was examined. On the condition of a half apex angle 15°, the result with gap consideration is shown in Fig. 14, while the result without gap consideration is shown in Fig. 15.

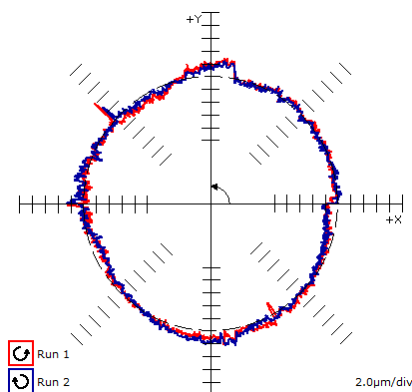


Figure 14. Gap enabled (Circularity: 6.7µm)

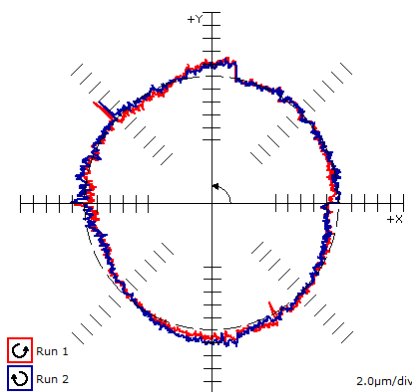


Figure 15. Gap disabled (Circularity: 7.4µm)

On the condition of a half apex angle  $15^\circ$ , when both are compared, the shape of the circle is not changed so much. Figure 16 and 17 show the similar test result done under the condition of  $45^\circ$  half apex angle.

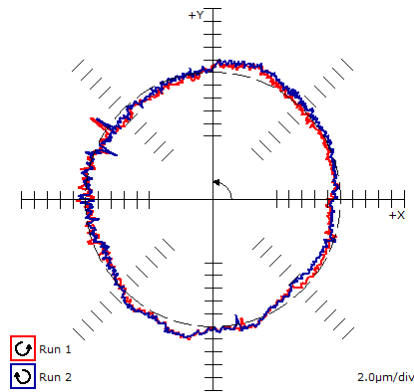


Figure 16. Gap enabled (Circularity:  $6.5\mu\text{m}$ )

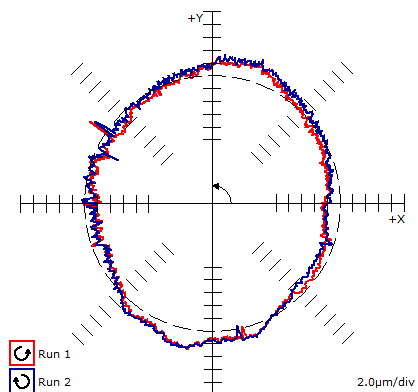


Figure 17. Gap disabled (Circularity:  $7.7\mu\text{m}$ )

Without considering the gap, the circularity is  $1.2\mu\text{m}$  larger than that the gap is considered. On the condition of larger half apex angle, the shape change is visible and the circle looks like a portrait oval. It is thought that the condition of half apex angle  $45^\circ$  was greatly influenced because B-axis was greatly moved compared with the condition of half apex angle  $15^\circ$ . Next, when the set value of the gap between two rotary axes is changed, whether a clear influence was caused on the shape of the circle or not was examined. The interval between B-axis and C-axis was set to  $\pm 100\mu\text{m}$ , and measured on the condition of half apex angle  $45^\circ$ . The measured results are shown in Fig. 18 and 19.

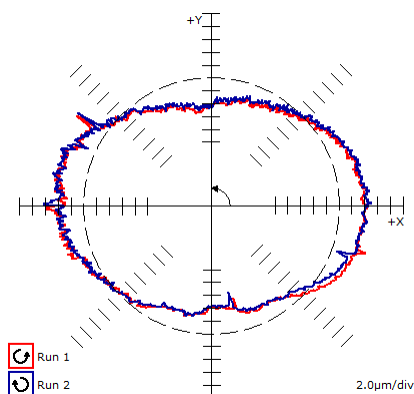


Figure 18. Gap  $+100\mu\text{m}$  (Circularity:  $12.5\mu\text{m}$ )

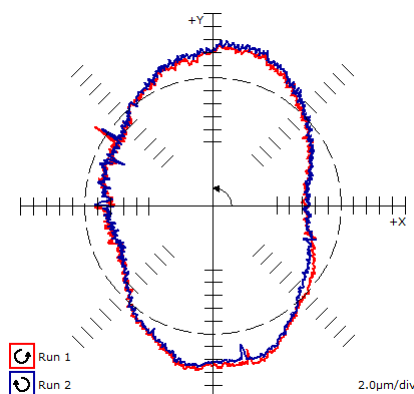


Figure 19. Gap  $-100\mu\text{m}$  (Circularity:  $12.2\mu\text{m}$ )

The shape became an oblong oval when the interval was  $+100\mu\text{m}$ , and the shape became a portrait oval when the interval was  $-100\mu\text{m}$ .

#### 4.4 Measurements in Negative Angle of B-axis

In the test condition prescribed in draft ISO standard, B-axis rotates  $5^\circ - 25^\circ$  for half apex angle  $15^\circ$  and  $15^\circ - 75^\circ$  for half apex angle  $45^\circ$  during the measurement. Because most trunnion type 5-axis machine has small rotation range, it cannot measure the other side of B-axis. However, because B-axis turns to  $160^\circ \sim -180^\circ$  in machine A as shown in Table 1, even if the virtual cone frustum is set up oppositely, it is possible to be measured. Then, the virtual cone frustum was set up oppositely against the ZX plane, and the measurements were done. The measurement results on the condition of a half apex angle  $15^\circ$  without the TCP control is shown in Fig. 20 and the one with TCP control is shown in Fig. 21. Although the value of circularity is growing by the influence of the projection, the shape of the circle is more beautiful than that of the previous result by a half apex angle  $15^\circ$ . There is a small step at  $105^\circ$  and also at  $255^\circ$  of the other side of X-axis. It is thought that motion error of B-axis is a cause as well as the previous measurement of a half apex angle  $15^\circ$ . The steps in the previous measurement results are much larger because it is thought that positive angle side of B-axis was deteriorated during the heavier use than negative angle side of B-axis.

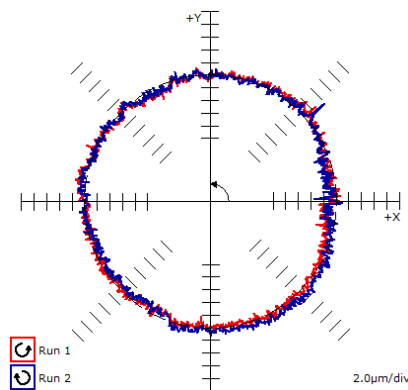


Figure 20. Without TCP (Circularity: 7.5µm)

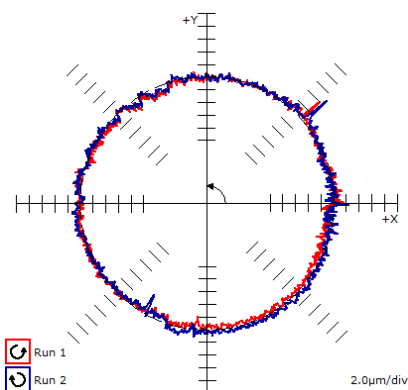


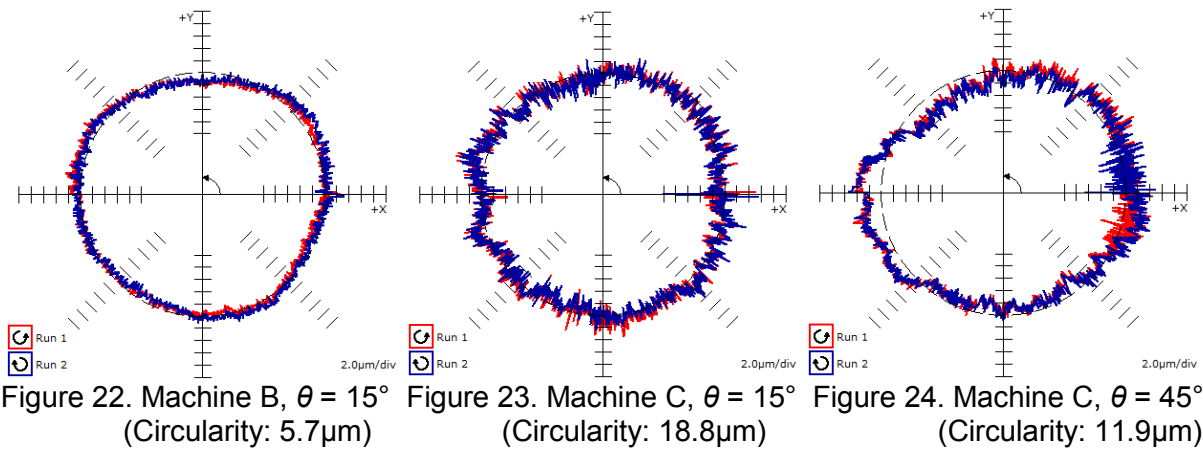
Figure 21. With TCP (Circularity: 8.3µm)

#### 4.5 Measurement of other 5-axis MC.

The measurement result on machine B is shown in Fig. 22, on the condition of a half apex angle  $15^\circ$ . The TCP control was not used on this machine.

The influence of the projection by the moving direction change in A-axis is seen around  $0^\circ$ , although the influence of the projection by the moving direction change in the linear axes is small. Moreover, the shape is an oblong oval since it doesn't consider 39µm gap between two rotary axes.

Next, the measurement results on machine C is shown in Fig. 23 and 24, on the condition of a half apex angle  $15^\circ$  and  $45^\circ$  respectively. The TCP control was not used on this machine either. A-axis of this machine could be rotated by  $360^\circ$  as shown in Table 1, and at this measurement A-axis was turned to a vertical position, and then it was set to the base position.



The high frequency vibration is observed although the shape is overall near circle on the condition of a half apex angle  $15^\circ$ . The projection can be seen in  $0^\circ$  by the influence of the reversal motion in B-axis. On the results on the condition of a half apex angle  $45^\circ$ , the high frequency vibration is observed as well as on the condition of a half apex angle  $15^\circ$ , and the projection  $0^\circ$  can be seen by the influence of reversal motion in B-axis. The projection on latter condition is smaller because the direction of the ball bar has become less sensitive against the error motion.

## 5. CONCLUSIONS

In the study, the followings were achieved as the results of testing the interpolation motion accuracy of three 5-axis MCs by imitating the cone frustum cutting test by using the ball bar.

- (1) The setup procedure and the measurement results, depending on the presence of the TCP control, were confirmed.
- (2) The influence on the measurement result was confirmed when a center position of a rotary axis was changed.
- (3) The influence of the incorrect gap setting between two rotary axes on the measurement result was confirmed.

## ACKNOWLEDGEMENTS

We would like to express our gratitude to Machine Tools Technologies Research Foundation (MTTRF) for renting the machining center used in the experiments.

## REFERENCES

1. ISO/DIS 10791-7 (2012), "Machine Tools — Test conditions for machining centres — Part 7: Accuracy of finished test piece".
2. ISO/DIS 10791-6 (2012), "Machine Tools — Test conditions for machining centres — Part 6: Accuracy of speeds and interpolations".



3. **Matano, M., Ihara, Y.** (2007), "Ball bar measurement of five-axis conical movement", *Laser Metrology and Machine Performance*, VIII, pp.34-43.
4. **Senda, O.** (2012), "Technology for Intelligent Machine Tools and Machining Example", *Journal of Japanese Society for Precision Engineering*, Vol.78, No.9, 748-751 (In Japanese).
5. **Kato, N., Tsutsumi, M., Chen, Y.** (2013), "Error evaluation by geometry deviation on five-axis controlled machining center that imitates cone frustum cutting", *Proc. of Spring meeting of JSPE*, pp 703-704 (In Japanese).
6. **Ibaraki, S., Nakino, Y., Akai, T., Takayama, N., Yamaji, I., Ogawa, K.** (2010), "Identification of Motion Error Sources on Five-axis Machine Tools by Ball-bar Measurements", *Precision Engineering*, Vol. 76, No. 3, pp 333-337.



## EFFECT OF JOINT STIFFNESS ON THE DYNAMIC PERFORMANCE OF THE MACHINE TOOL

**Chih Chung, Faby FENG**, *faby@g-tech-inst.com*, G-TECH Instrument, Taichung, Taiwan (R.O.C.)

**Robert J. BENJAMIN**, *bob@benstone.com*, Benstone Instrument, St. Paul, Minnesota, USA

### ABSTRACT

Machine Tool performance has many influencing factors from feed rate, spindle rotation, various system that turn on and off during the machining operation, thermal coefficients, and the stiffness of the machine tool and more. Joint stiffness is one factor that is typically overlooked in evaluating the performance of machine tools. This paper presents the effect of the joint stiffness on the dynamic performance of the machine tool by using the frequency response function (FRF) of the tool-spindle system, structure, and measurement of vibration (power spectrum) during heavy milling, and analysis using the stability lobe diagrams (SLD). These methods of measurement show how non-uniformed scraped surfaces and improper threaded holes are the cause for weak joint stiffness and poor machine tool performance.

**Keywords:** Milling, Chatter, Modal analysis, Joint stiffness, Scraping

### 1. MACHINE TOOL CHATTER PROBLEM

Machine tool manufacturers typically perform in-house test (Fig.1) that increases the amount of material removal beyond normal specifications to investigate the shape and surface accuracy on work-piece to determine if the machine tool is working properly prior to shipping. The bridge type machine tool (Fig.2) in our case study is designed with a high material removal rate (MRR) but exhibits chatter in the work-piece. The milling chatter occurs when the spindle head is at the position ( $Z = -800\text{mm}$ ) and only in one feed direction ( $-X$ ). The specifications of the machine tool and the milling conditions are listed below.

#### Machine tool main specifications:

X/ Y/ Z travel: 2200/ 2300/ 920 mm

Spindle: Gear type/ BT50 (6,000 RPM)/ 22KW

#### Milling conditions:

Feed rate:  $F = 1500\text{mm/min}$ ,  $F_t = 0.375\text{ mm/flute}$

Tool: Sandvik R200-140Q40-20M  $\phi 160\text{mm}$ , RCKT2006M0-PH4240 with 8 flutes

Work-piece material: S45C,

Axial depth of cut (DOC): 5 mm,



Radial width of cut (WOC): 100mm,  
Z axis position: -800mm

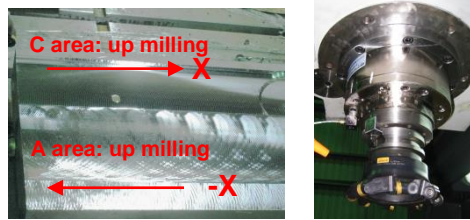


Fig. 1 Tool marks generated on the work-piece are from the tool itself and two different feed directions.



Fig. 2 Bridge type machine tool. (Courtesy of Vision Wide Tech Co., Ltd.)

## 2. FRF TEST ON SPINDLE AND STRUCTURE

Equipment used: 1-axis accelerometer (Endevco 27AM1-10), 3-axis accelerometer (Kistler 8762A50), small modal impact hammer (Kistler 9726A5000), big modal impact hammer (Kistler 9728A20000) and 4 channel real time FFT analyzer (Benstone Instruments' impaq Elite). The FRF of the tool-spindle system is measured by the 1-axis accelerometer which is placed directly on the tool itself and the small modal hammer strikes the tool tip on the opposite side. The measured results of the FRF as displayed in the graph (Fig.3) shows that the tool-spindle system has high natural frequency at 609Hz (X), 591Hz (Y), and 308Hz (Z).

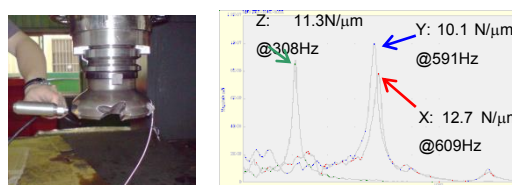


Fig.3 FRF of the tool-spindle system.

The FRF of the structure is then measured by using the 3-axis accelerometer, a big impact hammer and Benstone Instruments' FFT analyzer. The 3-axis accelerometer is placed directly on the spindle housing and the modal hammer strikes the spindle housing on the

opposite side. The measured results of the FRF as displayed in the graph (Fig.4) shows that the structural stiffness of X-direction is lower than the Y-direction or Z-direction.

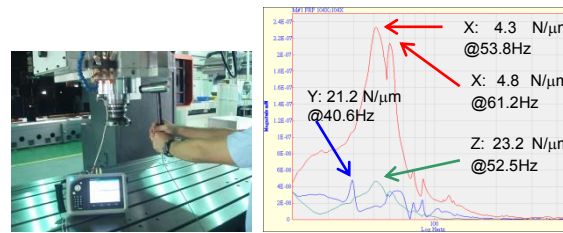


Fig.4 FRF of the structure at Z=-800mm.

The spindle position is then moved from Z= -800 mm to Z= -700 mm, and Z= -650 mm, and the test repeated. The X-axis first natural frequency of FRF changes from 53.8Hz to 54.1Hz and 56.3Hz respectively. The dynamic stiffness ( $2k\zeta(1-\zeta^2)^{1/2}$ ) and the damping ratio changes dramatically, indicating that the dynamic stiffness of the structure is sensitive to the Z axis position (Fig.5). The X-axis dynamic stiffness of the first natural frequency is 4.3 N/μm at Z= -800mm (Fig.4).

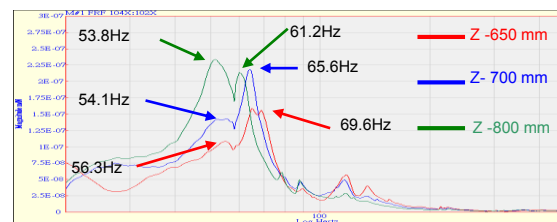


Fig.5 X-axis FRF of machine tool structure at Z= -650mm, Z= -700mm, Z= -800mm.

### 3. STABILITY LOBE DIAGRAM (SLD)

The stability expression was first obtained by [Tlustý and Poláček, 1963]. [Tobias and Fishwick, 1958] presented a similar solution. [Altintas, 2000] did much more detailed research in the field. Stability lobe diagrams show the maximum depth of cut that you can expect from the machine tool. The SLD and cutting force graphs are obtained by using [CUTPRO V10, 2013] software (by Manufacturing Automation Laboratory Inc.) by inputting the measured FRF readings. For high speed machining or heavy machining, if the dynamic stiffness of the structure is higher than the tool-spindle, then the cutting chatter is dominated by the tool-spindle dynamic stiffness, called regenerative chatter. So, we consider firstly the tool-spindle system FRF for evaluation using the SLD.

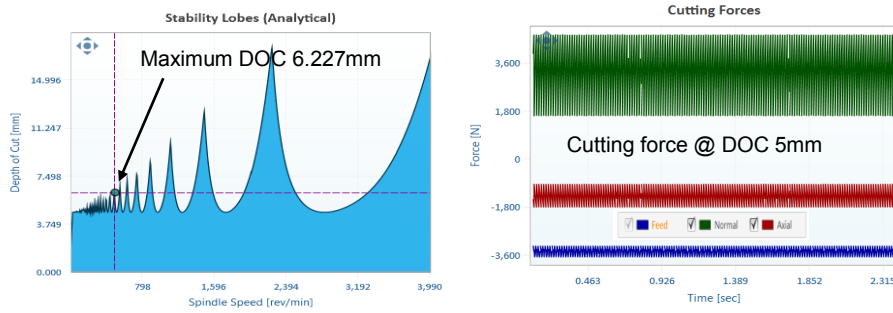


Fig.6 SLD of the tool-spindle system FRF only -- showing expected DOC of 6.227mm and milling force of 5 mm DOC milling (no chatter) [6]

A machine tool very often has structural stiffness greater than 50N/ $\mu$ m. However, our results show a weak structural dynamic stiffness. When we add the structural dynamic stiffness together with the tool-spindle FRF to create a new SLD, it shows the expected maximum depth of cut to be reduced to 3.138 mm (Fig.7).

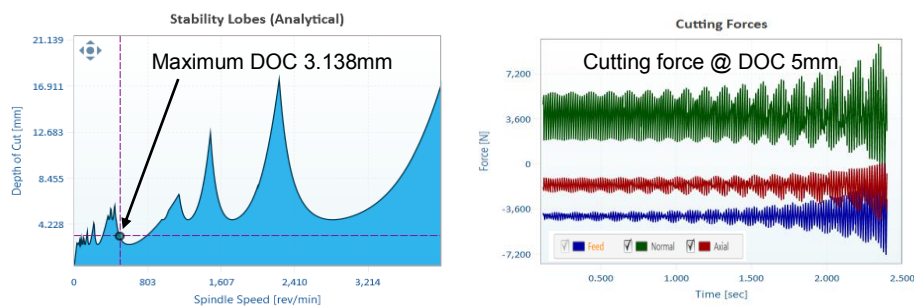


Fig.7 SLD of 3.138 mm of the structure and spindle. Simulated chatter observed at 5 mm DOC cutting force [CUTPRO V10, 2013]

This tool-spindle system is estimated to be capable of milling a 6.227 mm DOC without chatter, but we cannot achieve this depth of cut. The estimated maximum DOC is only 3.138 mm for the structure (Fig.7). Our conclusion is based on the SLD and FRF analysis that the chatter problem is a result from the structural dynamic weakness, not from the spindle.

#### 4. MILLING AND VIBRATION TEST

To perform the vibration spectrum measurement, a 3-axis accelerometer is placed on the spindle head with a 5 mm depth of cut and 100 mm width of cut milling, and the results recorded. A tooth passing frequency is observed of (66.7Hz) and a chatter frequency of (51Hz) which is excited when the chatter vibration occurs in the A area (up milling).

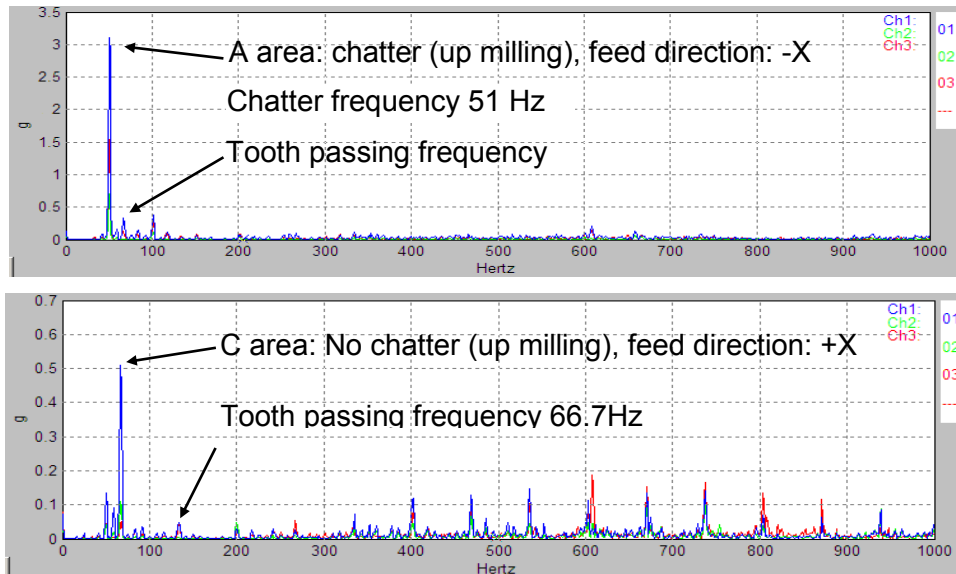


Fig.8 Vibration spectrum as milling test with 5 mm DOC & 100 mm WOC.

Notice that there is no chatter in the C area. The vibration power spectrum shows the tooth passing harmonic frequencies (Fig.8). The milling force is the same in these two areas. But the force direction acting on the spindle is opposite (Fig.9), which means the direction of force changes the structure dynamic stiffness. This is another indication of a weak structure.

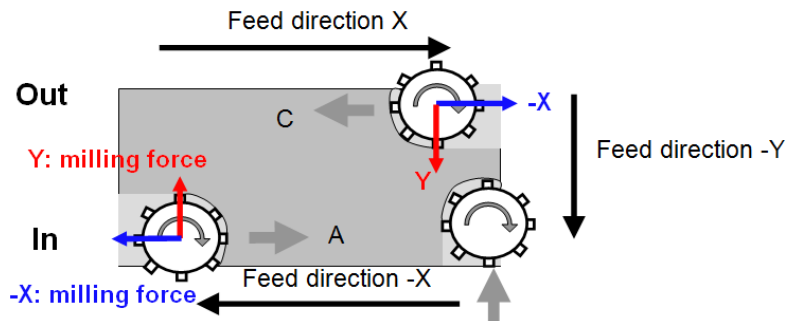


Fig.9 Milling force and direction acts on the spindle. (A area: milling-force pulls the spindle out from structure, C area: milling-force pushes the spindle into the structure.)

## 5. MODAL TESTING

Modal testing is a proven method to find the location of the mode shapes on the machine tool. The input force and the model are shown in Fig.10. The FRF data is shown in Fig.11.

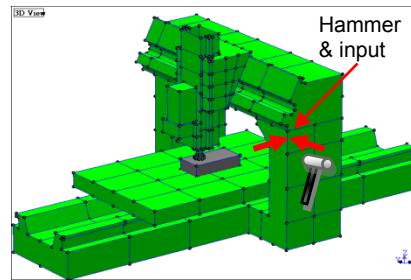


Fig.10 The measuring points and force input of modal testing. [ME'scopeVES]

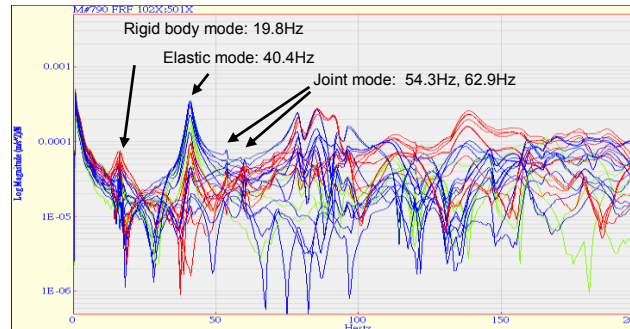


Fig.11 The FRF and joint mode frequencies as shown on the plot.

The natural frequency, damping ratio and mode shapes are estimated by using [ME'scopeVES] based on the modal values obtained from the Benstone Instruments' Impaq elite analyzer. They are listed in Table 1.

Table 1 The natural frequencies and damping ratios

Mode	1	2	3	4	5	6	7
Frequency (Hz)	19.8	40.4	54.3	62.9	78.9	85.6	92.5
Damping ratio (%)	2.1	1.8	13.1	7.7	1.5	1.6	1.4

The 1<sup>st</sup> mode (19.8 Hz) is rigid body motion. The 2<sup>nd</sup> mode (40.4 Hz) is an elastic mode. The double columns twist in this mode. The 3<sup>rd</sup> mode (54.3Hz) and 4<sup>th</sup> modes which have high damping ratio (13.1%) are joint separation motion (Fig.12). The damping ratio is normally below 5% for the structure of a machine tool. The 3<sup>rd</sup> mode (54.3Hz) is the cause of milling chatter in this case study (very close to 53.8 Hz as measured with FRF and vibration power spectrum 51 Hz). Opposite direction of milling force causes the joint to be stiffer or softer. That motion also changes the dynamic performance, the FRF and the SLD.

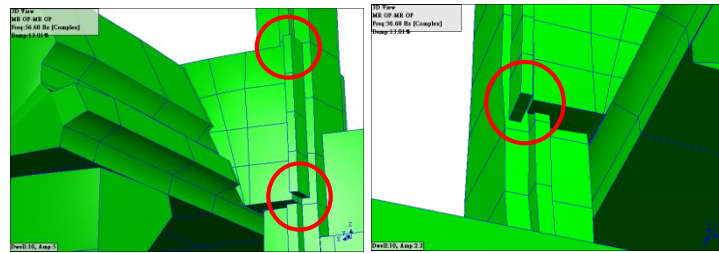


Fig.12 Mode 3 (54.3Hz, damping ratio 13.1%) is the joint separation motion between the spindle head and the saddle [ME'scopeVES]

## 6. DISCUSSION

The spindle head is installed into the hard rail of the saddle. The joint interface includes the bolt, thread, and the scraped surface of the hard rail. If the scraped surface is not uniform or is configured with inadequate contact points, plastic deformation will occur in the contact points when force is applied during machining. Therefore, joint stiffness and heavy milling ability are reduced. The weak joint stiffness is sensitive to the amplitude of milling force. Because the contact area is not uniform a crater lip is formed near the thread upon tightening and milling force (Fig.13).

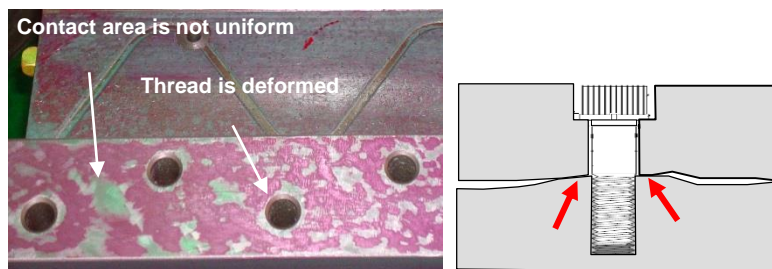


Fig.13 The scraping surface is not uniform and the tightening force form a crater lip.

To correct this problem, threads are redesigned to start a distance below the surface to avoid forming a crater lip upon bolt tightening and during milling force. Both surfaces of the saddle are finely re-scraped to achieve a more uniform surface and thus proper contact points. The rule of scraping and bolt joint are presented by [Moore, 1970] and [Slocum, 1992].

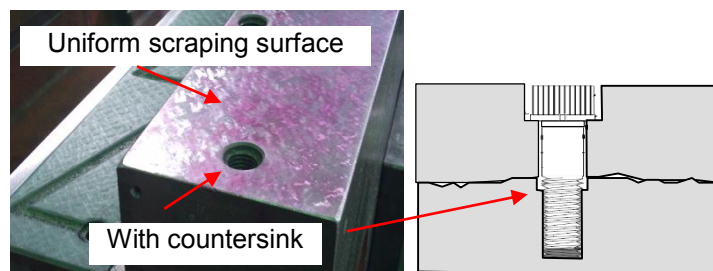


Fig.14 Rebuild the scraping surface and the countersink to get a stiffer joint.

The FRF of the rebuilt joint has a much higher dynamic stiffness (Fig.15). The dynamic performance is also improved in SLD (Fig.16).

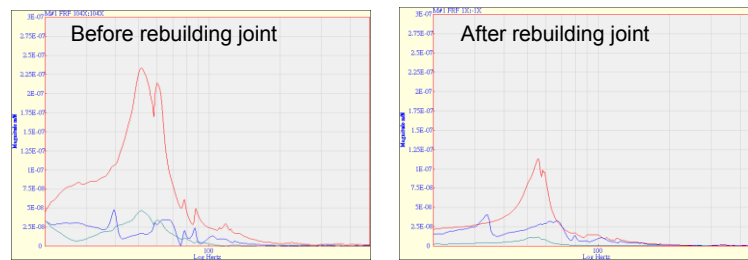


Fig.15 The new FRF is stiffer than the previous one.

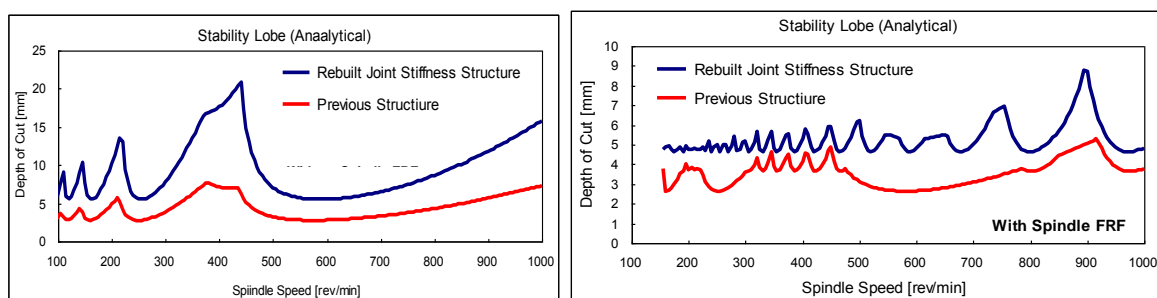


Fig.16 The SLD of the rebuilt joint structure shows a higher depth of cut. [CUTPROV10, 2013]

## 7. CONCLUSION

This paper describes the approach of using frequency response function (FRF), power spectrum measurements and stability lobe diagrams (SLD) to clearly identify weak joint stiffness that contribute to machine tool performance during machining. Using these techniques also help understand the amount of improvement achieved after correcting the discovered problems.

## ACKNOWLEDGEMENT

In accomplishing this work, we acknowledge the helpful support of Dr. Yusuf Altintas (UBC, Canada) and the Vision Wide Tech Co., Ltd. of Taiwan (R.O.C.)

## REFERENCES

1. **TIUSTY, J., POLACEK, M. (1963).** "The Stability of the Machine Tool Against Self Excited Vibration in Machining." International Research in Production Engineering, ASME.
2. **Tobias, S.A., Fishwick, W (1958).** "Theory of Regenerative Machine Tool Chatter." The Engineer (London).





3. **Altintas, Y. (2000).** “Manufacturing Automation-Metal Cutting Mechanics, Machine Tool Vibration, and CNC Design.” Cambridge University Press.
4. **CUTPRO (2013).** Advanced Machining Process Simulation Software, Manufacturing Automation Laboratories Inc., [www.malinc.com](http://www.malinc.com)
5. **Moore, W.R. (1970).** “Foundations of Mechanical Accuracy.” The Moore Tool Company, Inc.
6. **Slocum, A.H. (1992).** ”Precision Machine Design.”
7. **ME’scopeVES,** Modal Analysis Software, Vibrant Technology, Inc, [www.vibetech.com](http://www.vibetech.com)







## THE EFFECT OF TOOL ORIENTATION ON FIVE AXIS BALL END MILLING OF Ti6Al4V

**S. Ehsan LAYEGH K.**, *slayegh@ku.edu.tr* Koc University, 34450, Istanbul, Turkey

**I. E. YİĞİT**, *iyigit13@ku.edu.tr* Koc University, 34450, Istanbul, Turkey

**Ismail LAZOĞLU**, *ilazoglu@ku.edu.tr* Koc University, 34450, Istanbul, Turkey

### ABSTRACT

Five-axis sculptured surface milling is one of the most common machining processes in high-tech industries such as aerospace, automotive, and biomedical industries. Lead and Tilt angles are among the parameters that critically influence the efficiency of five axis milling in many respects, e.g., dissipated energy in cutting, tool deflection, and surface quality. Up to now, most of the investigations on the effects of lead and tilt angles are regarded to consider the geometrical optimization and gouge-free machining only. Effects of lead and tilt angles on mechanics of the process and dissipated energy have been studied very little. In this paper, firstly the process of five-axis sculptured surface milling is mechanically modeled. Then for the same removed material volume, the effects of lead and tilt angle on the cutting forces are investigated. It will be shown that by selecting the appropriate lead and tilt angles resultant cutting force and the force component perpendicular to the machined surface can be reduced in an optimum way. Finally, the simulation result are validated with the conducted experimental tests.

**Keywords:** 5-axis milling, Lead and tilt angle, Optimization

### 1. INTRODUCTION

Ti6Al4V is an advanced engineering alloy with a wide range of applications. The main characteristics of this alloy are high strength, corrosion and fatigue resistance at elevated temperatures which make Ti6Al4V as a superior alloy. Ti6Al4V is being used in various industries such as aerospace, nuclear energy generation plants, food processing machinery, biomedical product and implant manufacturing.

The problems during the machining of this alloy are the increase in manufacturing costs, decrease of product quality and efficiency. Within this perspective, studies aiming to optimize machining process are becoming more important. Many researchers have studied about machining of Ti6Al4V. Generally, the effects of tool wear, coating performance, chip



formation, temperature effects and work hardening in turning and flat end milling of Ti6Al4V have been studied widely in the literature.

However, ball end milling of Titanium alloy has not been investigated widely. One of the few researches in this field was conducted by [Ozturk, E., Tunc, L.T. and Budak, E., 2009]. They developed an approach to avoid the tip of tool from cutting and reduce the indentation and ploughing effect. [Ng, E.-G. et al., 2000] conducted some experiments to investigate the effects of cutter orientation, tool coating and cutting environment on tool life, tool wear mechanisms, cutting forces, chip formation, cutting temperature and workpiece surface roughness. In this study, rough cutting is considered during horizontal downward orientation of cutter with using high pressure cutting fluid. According to this research the tool life can be increased up to 15 m cut length which is two times longer than dry cutting. Also, it is concluded that machining at a workpiece angle of 45°, horizontal downwards cutter orientation generated the longest length cut.

Surface integrity in ball end milling of Titanium alloys has been studied by [Mhamdi, M.-B., Boujelbene, M., Bayraktar, E. and Zghal, A., 2012] and [Sonawane, H.A. and Joshi, S.S., 2012]. Based on those researches the root mean square roughness (Sq) increases from 2.9 micron to 4.8 micron by increasing the feed speed from 300 mm/min to 900 mm/min for ball end milling of Titanium alloys. It is also declared that the tool positioning can affect the Sq up to 50%.

The effect of tool orientation in ball end milling of Titanium alloys is investigated even less. [Daymi, A. et al., 2009] considered the influence of workpiece inclination angle on the surface roughness in high speed finish ball end milling of Ti6Al4V. They developed a mathematical model based on the cutting speed, feed and radial depth of cut and tried to optimize the surface quality by changing the workpiece inclination. According to their mathematical model, an increase in either the feed or the radial depth of cut increases the surface roughness, while an increase in cutting speed decreases it. The radial depth of cut is the most significant parameter in their model. They showed the improvement of the surface roughness quality when it was machined with a workpiece inclination angle of 25°.

Despite all of the above mentioned studies, the effects of tool orientation in five axis ball end milling of super alloys has not been investigated comprehensively. Due to the complexity of calculation of engagement between the cutter and workpiece in machining of free form surfaces, simulation of the process and predicting the optimum tool orientation is still unknown.

In order to investigate the effects of tool orientation on five axis ball end milling of Titanium alloy, the first step is simulation of the cutting forces. By knowing the magnitude and trend of cutting forces, it is possible to estimate the surface quality, dimensional error, tool deflection,



tool life etc. To fulfill this goal, the cutting coefficient have been calculated accurately for each segment of the tool using an efficient experimental setup. Using a solid modeler kernel, Parasolid, the engagement between the tool and the workpiece is calculated for different orientation of tool. During the change of tool orientation, the material removal rate kept constant by updating the tool position using a postprocessor. This way, the depth of cut and width of cut kept constant and the effect of tool orientation was investigated while the other cutting parameters were same for all cases. Using a developed force model [Boz, Y., Layegh, S.E., Lazoglu, I. and Erdim, H., 2012] the effect of lead and tilt angles of the tool during the cutting were investigated thoroughly. It was shown that the resultant cutting force and the force component perpendicular to the machined surface can be reduced by selecting appropriate tool orientation.

## 2. MECHANISTIC IDENTIFICATION OF CUTTING FORCES

Gradišek et al. introduced a general approach to calculate the cutting constants for general end mills using mechanistic calibration method [Gradišek, J., Kalveram, M. and Weinert, K., 2004]. This method was modified experimentally to consider the contribution of each segment of tool individually. This modification is necessary because during the five axis ball end milling, tool is engaged with the workpiece partially. However, in the model developed by Gradišek the calibration test was conducted for constant depth of cut.

The geometry of ball end mill is briefly represented in Figure 1. Since the local geometric parameters such as radius, immersion angle and helix angle change along the tool axis, the cutting coefficients are not constant. In this figure  $dF$  is the force component,  $\psi(z)$  is the zenith angle and  $R$  is the tool radius, respectively.

In order to estimate the cutting coefficients tool is divided into thin disks. The disks are selected as thin as possible to have almost constant geometric parameters. In order to measure the contribution of each disk element in cutting force, only that disk should be in contact with the workpiece. Figure 2 demonstrates the configuration of experimental setup that was used to measure average edge and cutting forces. The thickness of disk elements in spherical part of the tool was set as 1 mm. The thickness of machining region on workpiece was 1 mm as well. In order to prevent the unwanted vibrations and chatter, some shoulders were created using slot cutting.

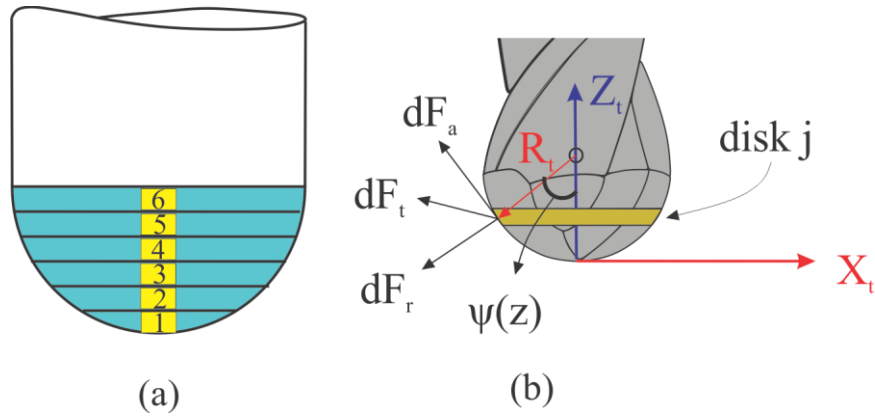


Figure 1. Disk numbers and geometry of ball end mill tool

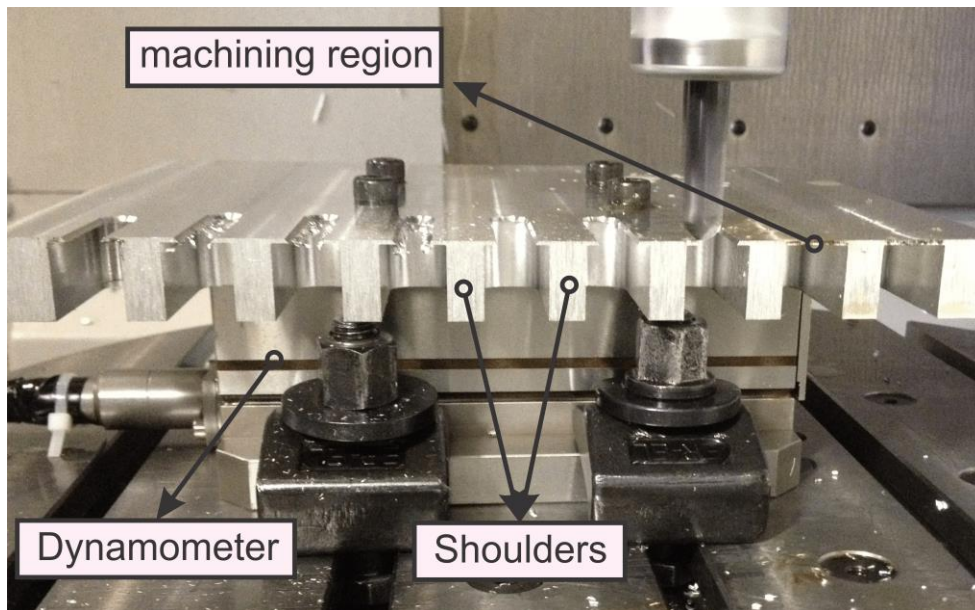


Figure 2. Experimental setup

### 3. ENGAGEMENT MODELING

Despite of 3-axis milling, in five-axis milling, tool axis can have an inclination angle with respect to the normal vector of the XY plane. As it is shown in Figure 3, this inclination angle can be represented by tilt and lead angles. In this figure,  $X_w Y_w Z_w$  is the workpiece coordinate frame and  $Z_t$  is the tool axis. Considering the feed direction,  $\alpha$  and  $\beta$  are lead and tilt angles, respectively.

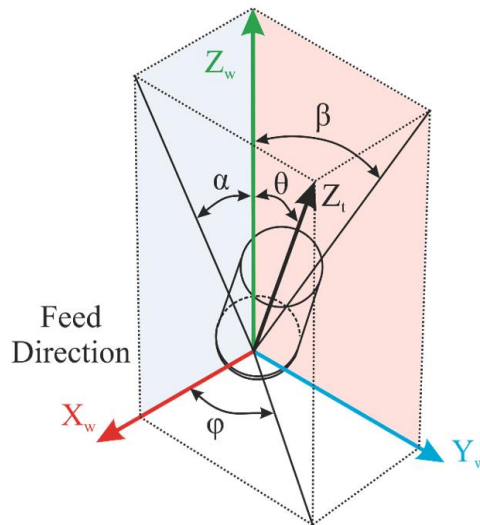


Figure 3. Definition of lead ( $\alpha$ ) and tilt ( $\beta$ ) angles in five axis milling

Another difficulty in simulation of cutting process in five axis ball end milling is predicting the engagement between the tool and workpiece. In order to model the engagement map, an algorithm is developed using Parasolid which is a solid modeler kernel. The engagement is calculated by modeling the swept volume of tool motion and subtracting it from the in-process workpiece which is going to be updated after each subtraction feature. As it is presented in Figure 4, the tool is divided into some elemental disk and the engagement points are extracted using an efficient algorithm in C#.

When the engagement points are extracted, the entrance and exit angles are calculated with respect to the cross feed direction. This process is shown in Figure 5. The entrance and exit angles are going to be used in the force modeling algorithm to estimate the cutting forces at each cutter location position.

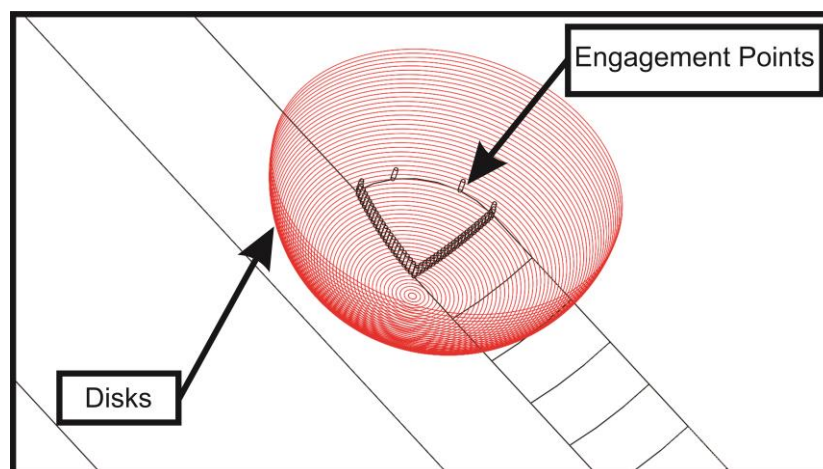


Figure 4 – Engagement points extracted from Parasolid for each elemental disk

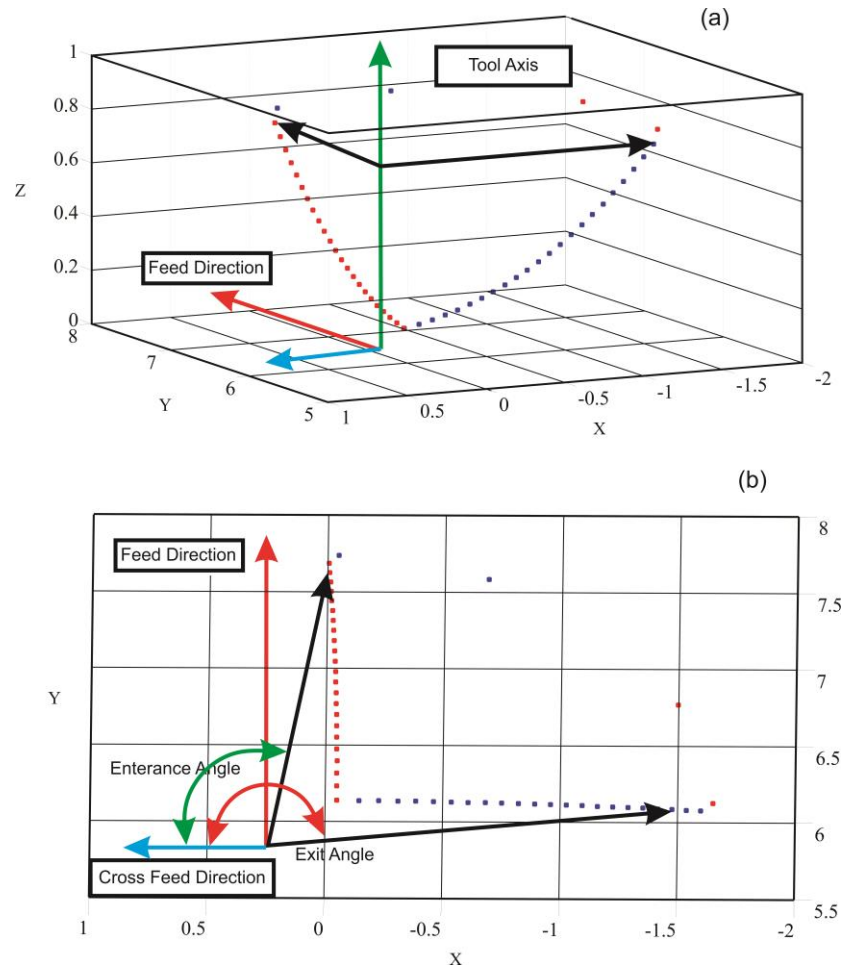


Figure 5 – (a) 3D engagement map for tool (b) Top view of 3D engagement map

## 5. SIMULATION AND EXPERIMENTAL RESULTS

By knowing the cutting coefficients, engagement condition and kinematic of the process, a mechanistic force model is developed to estimate the cutting forces [Layegh K., S.E., Erdim, H. and Lazoglu, I., 2012]. Table 1 presents the cutting conditions and tool specifications in the simulation and the experiment.

Table 1 - Cutting Conditions

Tool Diameter	6 [mm]
Over hang	30 [mm]
Number of flutes	2
Spindle Speed	7700 [rpm]
Feedrate	1540 [mm/min]
Depth of cut	0.5 [mm]
Step over	0.5 [mm]



Figure 6 and Figure 7 illustrate the simulated and measured cutting forces. In all of the cases a very good agreement can be observed between the simulated cutting forces and measured forces. However, in z direction the maximum estimation error of 10% is observed. The source of this error is mainly the ploughing and size effect phenomena during the ball end milling.

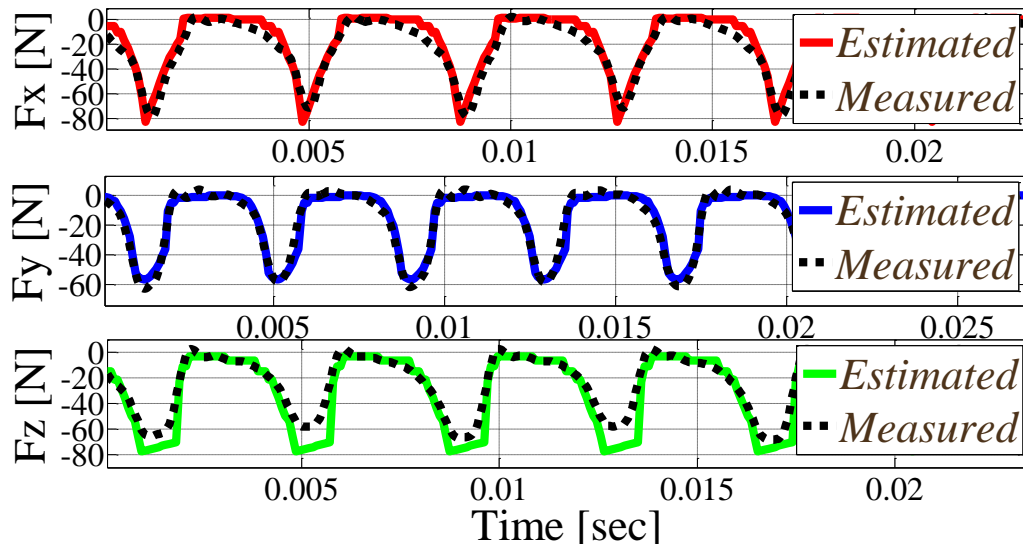


Figure 6- Cutting Forces for Lead = 1.5 [deg] and tilt = 3.7 [deg]

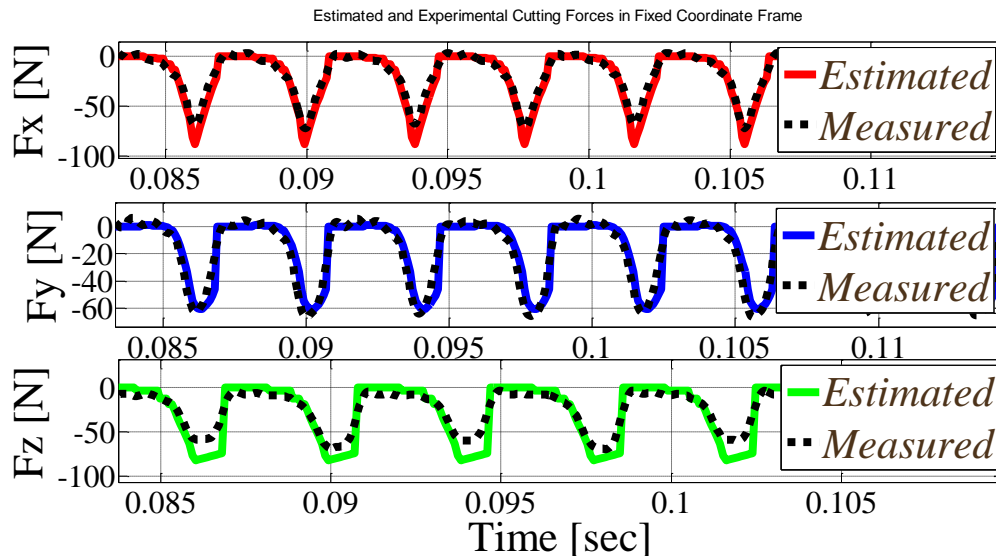


Figure 7 - Cutting Forces for Lead = 0 [deg] and tilt = 4 [deg]

## 6. RESULTS AND DISCUSSION

In order to investigate the effect of lead and tilt angle, series of tests were conducted with different lead and tilt angles. The average of the resultant cutting force and the normal component of the cutting force with respect to the machined surface are considered and illustrated as 3D plots for up and down milling operations.



Figure 8 and Figure 9 represent the average of resultant cutting force for different lead and tilt angles. It can be inferred from those figures that the maximum average resultant force occurs at zero lead and tilt angle for down milling. In contrast, the maximum resultant cutting force for up milling happens in zero lead angle and higher negative tilt values.

It can be concluded From Figure 8 that in order to have lower amount of resultant cutting force in down milling operation, the optimum tilt angle should be around  $4^\circ$  and the lead angle should be selected more than  $8^\circ$ . For the up milling case, however, the optimum tilt angle is zero and the lead angle should be selected higher than  $8^\circ$ .

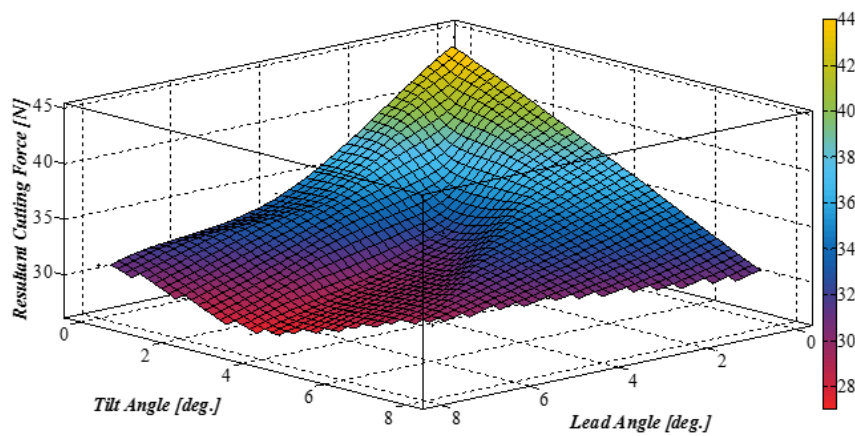


Figure 8 - Average resultant cutting force in down milling operation

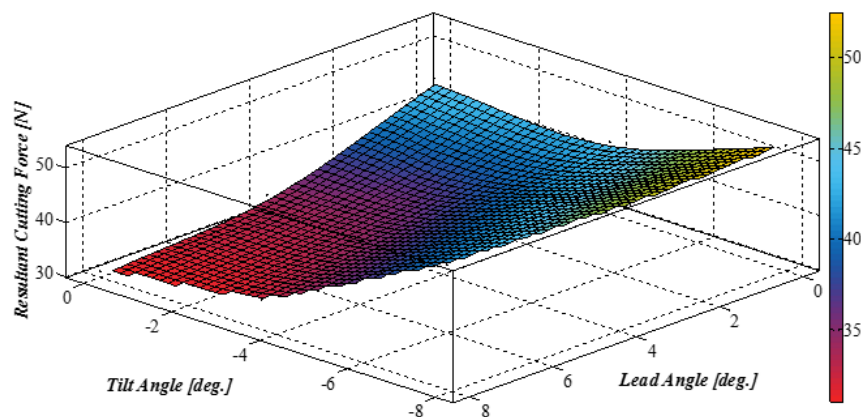


Figure 9 - Average resultant cutting force in up milling operation

The surface integrity of finished workpiece is highly dependent on the component of machining force which is normal to final surface. Since the normal component force with respect to the machined surface change with respect to the lead and tilt angle, it would be

necessary to find the optimum orientation in which lower cutting force is exerted on workpiece. Figure 10 and Figure 11 show the contour plot in which the optimum tool orientation can be chosen. According to Figure 11, the maximum average of normal cutting force occurs at zero lead and tilt angles. However, for the up milling case, the highest normal force happens at zero lead and higher negative values of tilt angle. The optimum lead and tilt angles are defined with red color in Figure 10 and Figure 11. Obviously, the selection of optimum lead and tilt angle should be based on the geometry of the process as well. There should always be checking criteria to make sure that the selected lead and tilt angle is feasible from geometrical point of view. This literally means to check for having collision free machining operation.

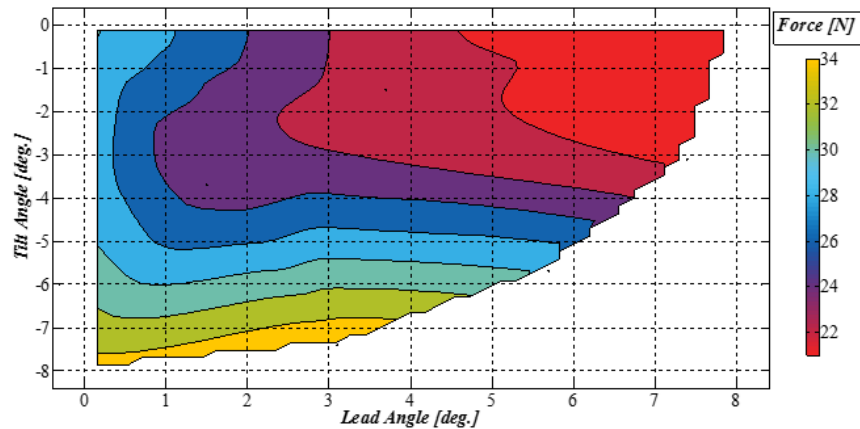


Figure 10 - Average of cutting force normal to machined surface for down milling operation

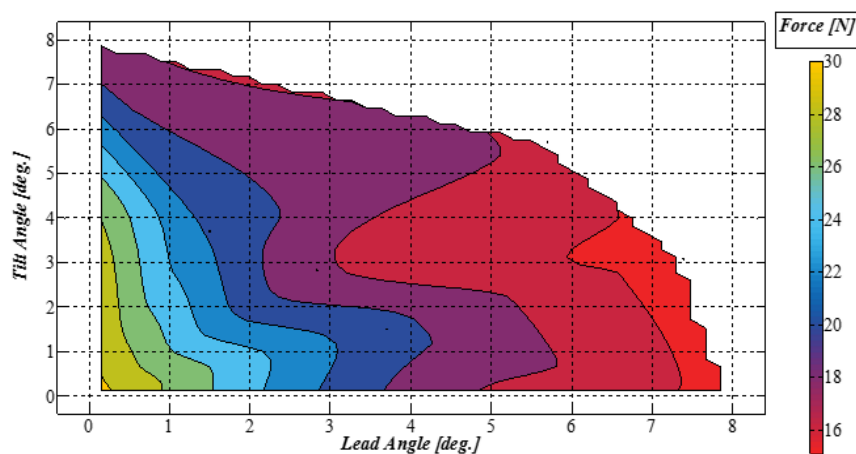


Figure 11 - Average of cutting force normal to machined surface for up milling operation



## 7. CONCLUSION

The mechanics of ball end milling for five axis machining of Ti6Al4V was investigated for various lead and tilt angles. The engagement between tool and workpiece was calculated using a developed algorithm in C# and employing Parasolid as a solid modeler kernel. Cutting forces were simulated and measured experimentally for different tool orientation. It was shown that the orientation of the tool plays a critical role in mechanics of the five axis ball end milling process. It is possible to optimize the tool orientation to minimize the cutting forces, which in turn will increase the integrity and quality of the finished surface. It is also possible to find an optimum condition in which the cutting torque and consumed energy is minimum.

## REFERENCES

1. **Ozturk, E., Tunc, L.T. and Budak, E., (2009)**, "Investigation of lead and tilt angle effects in 5-axis ball-end milling processes", *Int. J. Mach. Tools Manuf.*, Vol. 49, No. 14, pp 1053–1062.
2. **Ng, E.-G. et al., (2000)**, "High Speed Ball Nose End Milling of Inconel 718", *CIRP Ann. - Manuf. Technol.*, Vol. 49, No. 1, pp 41–46.
3. **Mhamdi, M.-B., Boujelbene, M., Bayraktar, E. and Zghal, A., (2012)**, "Surface Integrity of Titanium Alloy Ti-6Al-4V in Ball end Milling", *Phys. Procedia*, Vol. 25, pp 355–362.
4. **Sonawane, H.A. and Joshi, S.S., (2012)**, "Analysis of machined surface quality in a single-pass of ball-end milling on Inconel 718", *J. Manuf. Process.*, Vol. 14, No. 3, pp 257–268.
5. **Daymi, A. et al., (2009)**, "Influence of workpiece inclination angle on the surface roughness in ball end milling of the titanium alloy Ti-6Al-4V", *J. Achiev. Mater. Manuf. Eng.*, Vol. 35, No. 1, pp 79–86.
6. **Boz, Y., Layegh, S.E., Lazoglu, I. and Erdim, H., (2012)**, "High performance of five axis milling of complex sculptured surfaces." *Davim, J. P., Ed., Chapter: 3*, pp67–125, Springer.
7. **Gradišek, J., Kalveram, M. and Weinert, K., (2004)**, "Mechanistic identification of specific force coefficients for a general end mill", *Int. J. Mach. Tools Manuf.*, Vol. 44, No. 4, pp 401–414.
8. **Layegh K., S.E., Erdim, H. and Lazoglu, I., (2012)**, "Offline Force Control and Feedrate Scheduling for Complex Free Form Surfaces in 5-Axis Milling", *Procedia CIRP*, Vol. 1, pp 96–101.



## A STUDY OF A POSTPROCESSOR SYSTEM FOR A HYBRID PARALLEL-SERIAL FIVE-AXIS MACHINE TOOL

**Yuan-Lung LAI**, *lyllaiber@cc.ncue.edu.tw*, Department of Industrial Education and Technology, National Changhua University of Education, Changhua, Taiwan, R.O.C.

**Hsiao-Ying CHAN**, *gm30121@outlook.com*, Department of Industrial Education and Technology, National Changhua University of Education, Changhua, Taiwan, R.O.C.

**Tzuo-Liang LO**, *TzuoLiangLo@itri.org.tw*, Intelligent Machine Tool Technology Center, Industrial Technology Research Institute, Taichung, Taiwan, R.O.C.

### ABSTRACT

This paper proposes a general postprocessor initially aimed to translate CC path for CNC controllers. Five-axis machine tools have become the most important role in modern production systems. The complicate frames of the machine tools lead to an inaccuracy at the tool tip caused by kinematics parameter deviation resulting from manufacturing errors, assembly errors or quasi-static errors. The rotary axis in a common 5-axis machine tool is driven by a single motor that holds the platform for the axial rotation. However, with different weights of work pieces and the motor loaded, the rotating speed should be in reverse proportion to the weight. As a result, the axis-to-axis synchronization is poor, resulting in dramatic decrease in machining precision. Therefore, a 2PRP planar parallel platform is designed by connecting the two PRP connectors and moving table with a round bar. The motor drives ball screws and propels these PRP connectors. The two parallel ball screws acquire both effects on movement or rotation by generating different displacements of these two connectors. Thus the simulation of the rotating table on a 5-axis machine tool is achieved. In order to explore the error origins of these machine tools it is necessary to have a suitable mathematical model of the machine tools. The model can be not only used for developing postprocessors but also compensating the errors mentioned previously. The diagnosed errors could be taken under consideration only by the precise description of the actual kinematics of the machine tools.

**Keywords:** Five-axis, D-H transformation matrix, Kinematic model, Postprocessor.



## 1. INTROUCTION

Recently, precision machining heading to a high quality and complication level has become a trend. The machined pieces must meet the requirement of a machine tool that completes all or part of the work pieces with minimal number of clamping operations. For this, multi-axial structure has become the tendency of precision machining. CNC machining has evolved from the automated machine tools of the 1960s to the modern multi-axis machining centres. In parallel to the advances in hardware design, the programming requirements of the machines have increased in complexity and a nimity of computer aided systems collectively are now utilized to manufacture extremely complex components on the machines.

Compared with serial kinematic machine tools, parallel structured machine tools have many advantages. Parallel kinematic architectures are commonly claimed to offer several advantages over their serial counterpart, as widely claimed:

- Compact structure, higher structural rigidity
- Higher load-bearing capacity
- Structures are not easily bent
- Lower dynamic errors, Avoiding of accumulated error, High precision
- Less inertia, simple structure and modular design easily
- Short flow of force
- Reduced effect of thermal expansion with symmetry structure
- Easy to find inverse kinematic solution

Parallel mechanisms are often said to be more precise than serial robots because they do not suffer from error accumulation. While this might be true in theory [1], the real reason is that parallel robots can be built to be stiffer without being more massive. Most precision positioning prototypes based on planar parallel mechanisms count on the use of flexures [2]. Between the few existing planar 3-DOF parallel mechanism prototypes that do not employ flexures, one is based on a symmetric 3-PRP architecture, where the base actuators form an equilateral triangle and the platform linear guides form a star. This robot has a very limited work space though. In contrast, the 3-RRP mechanism of which a new prototype was proposed in [3], offers unlimited rotation in addition to excellent stiffness in the vertical direction [4].

Generally mechanical kinematics is divided into two categories, direct kinematics and inverse kinematics. Inverse kinematics the location of the end-effector is given and the target is to

find the joint variables. In the direct kinematics the joint variables are given and the problem is to calculate the position of the end-effector [5-9].

Owing to the simultaneous interpolation movement both with the linear and rotary axes on a five-axis machine, the derivation of the five-axis feeding path is more complex than that of the three-axis feeding path. Therefore a postprocessor must be utilized to transfer the cutter location (CL) data from the CAM system into the machine control data. Although the advanced controllers can accept the CL data to machine the working piece in real-time without the need of postprocessor [10], they are relatively expensive and only used in some specific works. According to the researches from the papers published, the methods of developing multi-axis postprocessors can be mainly divided into three categories, graphical [11], numerical iterative [12] and coordinate transformation [13-15]. Whereas the coordinate transformation method leads to the analytical equation of NC data most efficiently, it has been used regularly in recent work. Therefore, almost all of these methods involve postprocessor methods for five-axis machine tools with orthogonal rotary axes. Sorby [16] has stated a closed-form solution for a table tilting type five-axis machine tool with a nutating table. Only few studies have addressed non-orthogonal configuration for translate or rotary axes. Another example is the spindle-tilting type five-axis machine tool with a nutating head [17].

## 2. HYBRID FIVE-AXIS MACHINE TOOL

Simplified the structure, a machine tool may be regarded as a set of links joined in a set of connectors. Standard definition of five-axis machine coordinate frame consists of the X, Y and Z axes in right-hand rectangular coordinates. The rotary axes are defined as A axis, B axis and C axis which rotate about the X axis, Y axis and Z axis respectively. Common configuration for five-axis machine tools can be classified into three basic types [18]: (1) Double Rotary Table: this type with two rotations on the table as shown in Fig.1(a), (2) Double Pivot Spindle Head: this type with two rotations on the spindle as shown in Fig.1(b), and (3) Rotary Table and Pivoting Spindle Head: this type with one rotation each on the table and spindle as shown in Fig.1(c). Tools can be designated according to rotary axes features, such as AB, AC and BB types. Each type has two appropriate cutter orientations to support the five-axis machining function. Basically, the cutter orientation is defined as the Z axis, the five-axis machine tools can be classified as AB type, AC type and BC type.

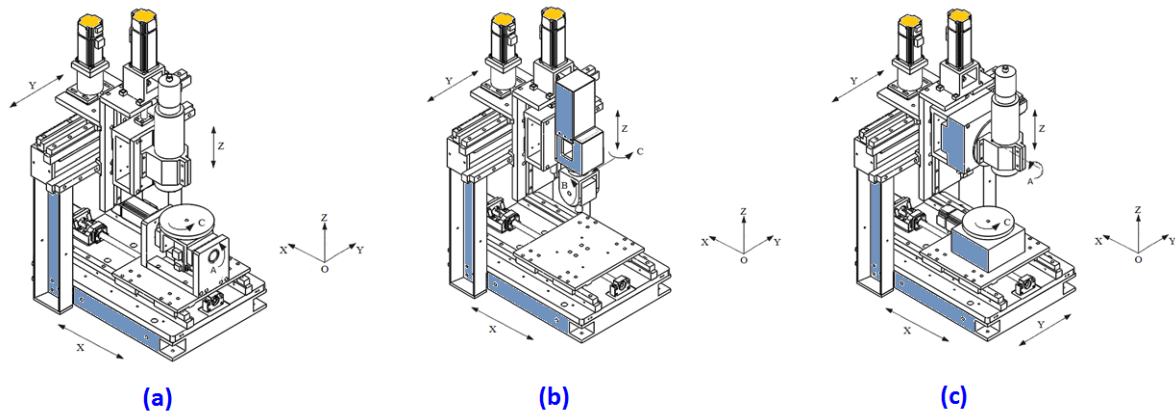


Fig. 1 Three main different types of five-axis machine tools.

The mechanical model of the proposed five-axis machine tool considered in this paper as shown in Fig.2, is the basic option of the planned reconfigurable multi-axis machining system for HSC-milling of aluminum, epoxy tooling board as well as small size model making, plastic and foam machining. The machine has a two-DOF structure of parallel type to execute one translational motion and rotational motion on working table. Compare with the previous discussion, the proposed machine is similar to the type of Rotary Table and Pivoting Spindle Head.

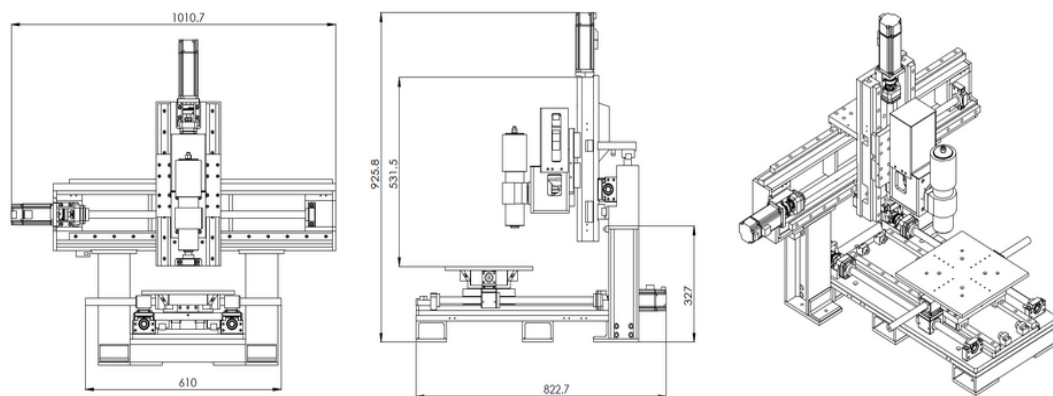


Fig. 2 The proposed hybrid parallel-serial five-axis machine tool.

### 3. MODIFIED D-H REPRESENTATION FOR FIVE-AXIS MACHINE TOOL

To implement the position and orientation of the cutting tool and the machine tool, the relationship of the coordinate system between the adjacent links and joint should be built. The widely used parametric representation for spatial mechanisms is the Denavit-Hartenberg (D-H) representation [18 19]. In this representation a spatial mechanism is formulated in terms of four parameters for each link in the linkage. These parameters are termed the link-



length, link angle, link-offset, and twist-angle. Under normal situation a mechanism with revolute, prismatic and cylindrical joints, depending upon the type of joint, the link-lengths and twist-angles typically remain static during operation, and the link-angles and link-offsets vary. Deficiently, the Denavit-Hartenberg representation presents insufficient number for error analysis when mechanisms have parallel or nearly parallel joint axes. Small variations in the D-H parameters result in large errors in the output function. For this paper we adopt the representation of [26 20] that adds an extra link-length for next link, resulting in a better representation of the link shape as shown in Fig. 3. The extra parameter will not affect anything to the kinematic description of the mechanism but is beneficial for error analysis. Denavit and Hartenberg proposed a systematic notation for assigning classic orthogonal coordinate frames. A modified D-H notation proposed by Lin and Chen is used in this paper. The added fifth parameter  $l_i$  can ensure that the joint is located on the link. That means the adjacent two links can be assembled on correct locations by the transformation matrix. The transformation matrix between adjacent coordinate frames for the modified D-H notation changes as follows:

$${}^{i-1}H_i = Trans(0,0,b_i)Rot(z,\theta_i)Trans(a_i,0,0)Rot(x,\alpha_i)Trans(0,0,\lambda_i)$$

$$= \begin{bmatrix} \cos \theta_i & -\sin \theta_i \cos \alpha_i & \sin \theta_i \sin \alpha_i & \lambda_i \sin \theta_i \sin \alpha_i + a_i \cos \theta_i \\ \sin \theta_i & \cos \theta_i \cos \alpha_i & -\cos \theta_i \sin \alpha_i & -\lambda_i \cos \theta_i \sin \alpha_i + a_i \sin \theta_i \\ 0 & \sin \alpha_i & \cos \alpha_i & \lambda_i \cos \alpha_i + b_i \\ 0 & 0 & 0 & 1 \end{bmatrix} \quad (1)$$

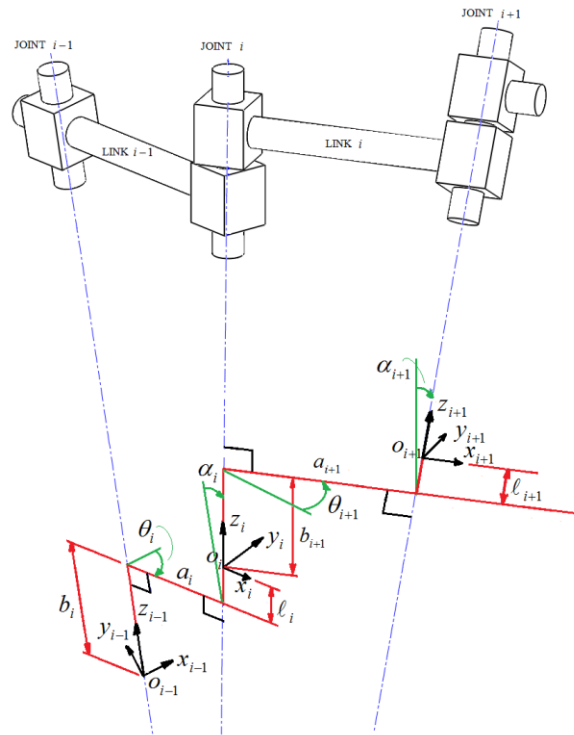


Fig. 3 Modified D-H representation for spatial linkages.





As shown in Fig. 3, the coordinate systems  $O_i$  and  $O_{i+1}$  are defined as follows. The origin  $O_i$  is located on  $Z_i$  of the  $i^{th}$  link and the common normal to both  $i^{th}$  and  $(i+1)^{th}$  joint axis, the  $Z_i$ -axis is coincident with the  $i^{th}$  joint axis, the  $X_i$ -axis is along the common normal to both  $i^{th}$  and  $(i+1)^{th}$  joint axis, and the  $Y_i$ -axis is determined by the cross product of the  $Z_i$ -axis and  $X_i$ -axis. Summarize the procedure based on the modified D-H convention in the following algorithm for deriving the forward kinematics for any manipulator.

- 1: Give the definition for  $i^{th}$  link.
- 2: Locate and label the joints  $i$  and  $i+1$ .
- 3: Establish the base frame. Set the  $Z_i$ -axis,  $Z_i$  is the linear moving axis for translation movement,  $Z_i$  is the rotary axis for rotation movement.
- 4: Locate the origin  $O_i$  between link  $i-1$  and  $i$ . The  $X_i$  and  $Y_i$  axes are chosen conveniently to form a right-hand frame.
- 5: Establish  $X_i$ -axis along the common normal between  $Z_{i-1}$ -axis and  $Z_i$ -axis,  $X_i$ -axis pass through  $O_i$  and perpendicular to  $Z_i$ -axis.  $\hat{p}_i = \pm(\hat{z}_{i-1} \times \hat{z}_i) / \|\hat{z}_{i-1} \times \hat{z}_i\|$ .
- 6: Establish  $Y_i$ -axis to complete a right-hand frame.  $\hat{y}_i = \pm(\hat{z}_i \times \hat{x}_i) / \|\hat{z}_i \times \hat{x}_i\|$
- 7: Create a table of link parameters  $b_i, \theta_i, a_i, \alpha_i, l_i$ .
- 8: Form the homogeneous transformation matrices  ${}^{i-1}H_i$  by substitution the previous parameters into Eq. 1.
- 9: Form  ${}^0H_6 = {}^0H_1 {}^1H_2 {}^2H_3 {}^3H_4 {}^4H_5 {}^5H_6$ . Thus then finds the position and orientation of the tool frame expressed in base coordinates.

After the coordinate system is defined, the D-H parameters can be obtained as:

- $b_i$ : the distance from point  $O_{i-1}$  to the common normal along  $Z_{i-1}$ -axis,
- $\theta_i$ : the angle between the  $X_{i-1}$ -axis and the  $X_i$ -axis measured about the  $Z_{i-1}$ -axis,
- $a_i$ : the distance between  $Z_{i-1}$ -axis and  $Z_i$ -axis along the common normal,
- $\alpha_i$ : the angle between the  $Z_{i-1}$ -axis and the  $Z_i$ -axis measured about the  $X_i$ -axis,
- $l_i$ : the distance from the common normal to point  $O_{i-1}$  along  $Z_i$ -axis.

The geometric parameters for the example machine tool shown in Fig. 4 are listed in Table 1. Link 0 and link1 implement a rotary variable. Link 1 and link 2, link 2 and link 3, link 3 and link 4 all implement translate variables. Link 4 and link 5 implement another rotary variable. Finally, link 5 and link 6 employ the cutting tool length.

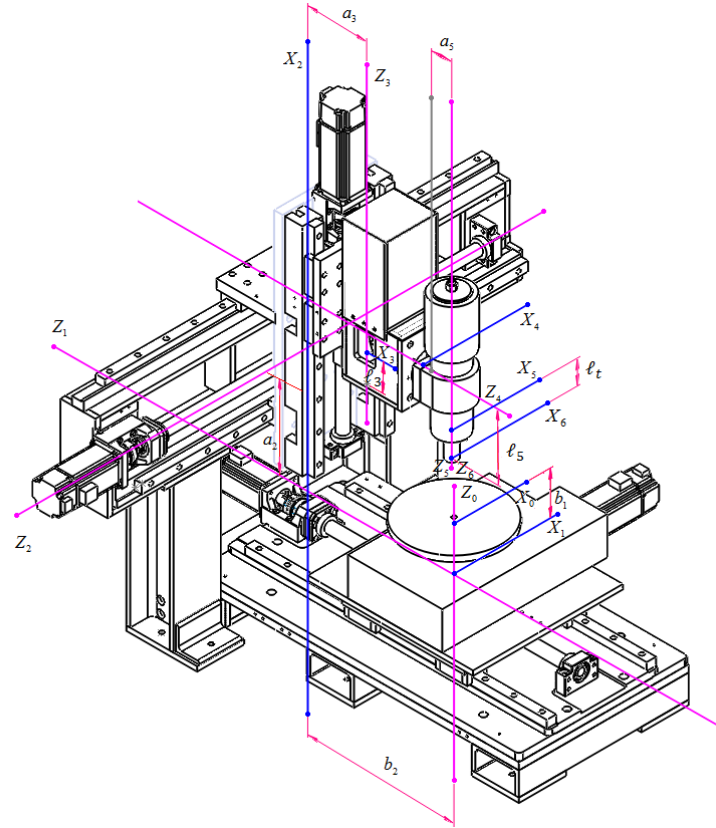


Fig. 4 Example of five-degree-of freedom machine tool.

Table 1 Geometric parameters of the example serial chain manipulator in Fig. 4.

Link	$b_i$	$\theta_i$	$a_i$	$\alpha_i$	$\ell_i$
0/1	$-b_1$	$\theta_1$	0	$-\pi/2$	0
1/2	$b_2$	$-\pi/2$	$a_2$	$\pi/2$	0
2/3	$b_3$	$-\pi/2$	$a_3$	$-\pi/2$	$\ell_3$
3/4	$b_4$	$\pi/2$	0	$\pi/2$	$\ell_4$
4/5	$b_5$	$\theta_2$	0	$\pi/2$	$\ell_5$
5/6	0	0	0	0	$\ell_t$

#### 4. KINEMATIC MODEL ON PARALLEL CONSTRUCTED TABLE

Three examples will be studied in order to illustrate the proposed geometric approach for the hybrid parallel-serial machine tool. In Fig. 5,  $q_i$  are the active-joint variables standing for directed distances, defined as follows. For 3PRP/1PRP, PreXYT and 3PRP alignment stages,  $q_1$  is the directed distance from the base y-axis to point  $P_1$ , while  $q_2$  and  $q_3$  are the directed distances from the base x-axis to points  $P_2$  and  $P_3$ , respectively.

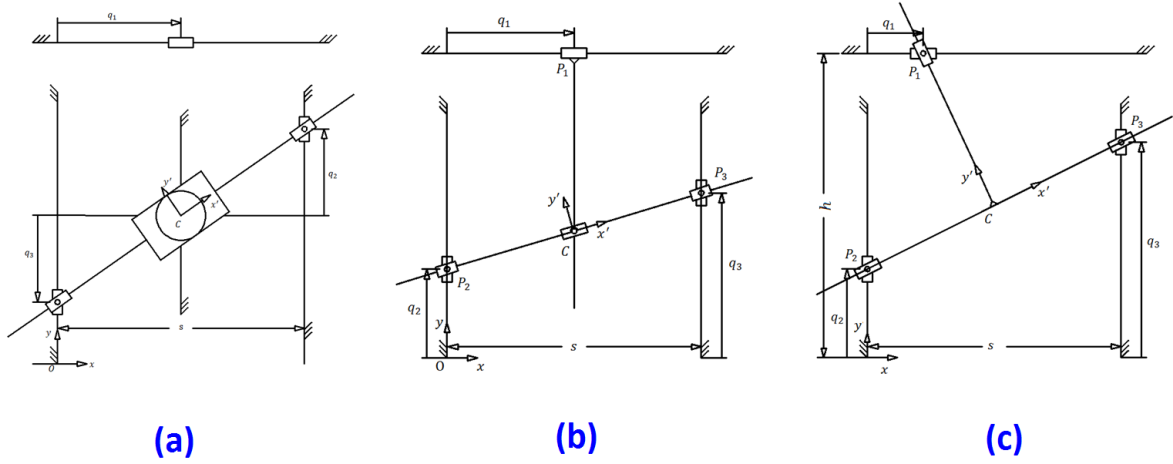


Fig. 5 Schematics of (a) 2PRP/1PRP (b) PreXYT (c) 3PRP parallel table.

##### 4.1 DIRECT KINEMATIC MODELING

For direct kinematic modeling, given the active-joint variables, it is straightforward to uniquely define the position and orientation of the mobile platform. The orientation angle, position of the mobile table are easily obtained as

2PRP/1PRP parallel actuated table

$$\phi = \tan^{-1} \left( \frac{q_3 - q_2}{s} \right) \quad (2)$$

$$x = q_1 \quad (3)$$

$$y = q_2 + \left( \frac{q_3 - q_2}{2} \right) \quad (4)$$

PreXYT parallel actuated table

$$\phi = \tan^{-1} \left( \frac{q_3 - q_2}{s} \right) \quad (5)$$

$$x = q_1 \quad (6)$$

$$y = q_2 + q_1 \left( \frac{q_3 - q_2}{s} \right) \quad (7)$$

3PRP parallel actuated table

$$x = \frac{s(q_1 s + (h - q_2)(q_3 - q_2))}{s^2 + (q_3 - q_2)^2} \quad (8)$$



$$y = \frac{s^2 q_2 + h(q_3 - q_2)^2 + s q_1 (q_3 - q_2)}{s^2 + (q_3 - q_2)^2} \quad (9)$$

## 4.2 INVERSE KINEMATIC MODELING

From the structure of the movable platform shown in Fig. 5, as one can observe, the direct kinematics of 2PRP/1PRP and PreXYT are relatively simple and partially decoupled while 3PRP parallel robot is more complex and highly coupled. The inverse kinematic analysis is also trivial. Given the position and orientation of the mobile platform, the active-joint variables are obtained as;

2PRP/1PRP parallel actuated table

$$q_1 = x \quad (10)$$

$$q_2 = y - \frac{s}{2} \tan \phi \quad (11)$$

$$q_3 = y + \frac{s}{2} \tan \phi \quad (12)$$

PreXYT parallel actuated table

$$q_1 = x \quad (13)$$

$$q_2 = y - x \tan \phi \quad (14)$$

$$q_3 = y + (s - x) \tan \phi \quad (15)$$

3PPR parallel actuated table

$$q_1 = x - (h - y) \tan \phi \quad (16)$$

$$q_2 = y - x \tan \theta \quad (17)$$

$$q_3 = y + (s - x) \tan \phi \quad (18)$$

## 5. POSTPROCESSOR FOR A HYBRID PARALLEL-SERIAL FIVE-AXIS MACHINE



Fig. 6 Relationship between CAM, postprocessor and CNC.

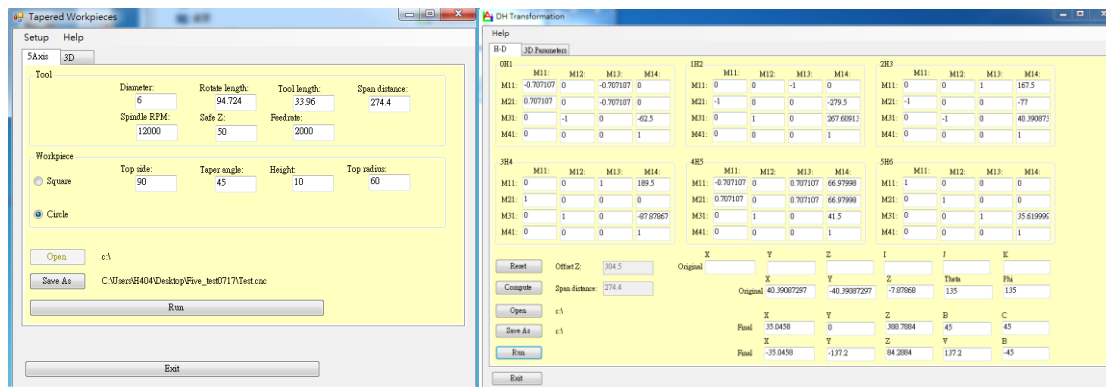


Fig. 7 Dialog of the developed five-axis postprocessor.

A postprocessor is utilized to transform the data from the model spatial space in CAM to the machine spatial space in the CNC. The corresponding file will be transferred to the controller and will be used to machine the work piece. As a postprocessor is a unidirectional translator, the completeness of the data transferred to the machine will be compromised as soon as any modifications are made in the information at the controller on the shop floor. As mentioned above, inverse kinematics is used to determine the set of axis variables  $X$ ,  $Y$ ,  $Z$ ,  $B$ , and  $V$  that will produce the desired CL information given in the CL data file. Postprocessing primarily utilizes the inverse kinematics. The direct kinematics is used to calculate the CL from the machine axis variables. This is used in postprocessors for checking tool path accuracy in the linearization algorithm. To verify the effectiveness of the proposed

methodology, a window-based postprocessor software has been developed under the Windows7 environment with programming language. Fig. 6 shows the role of the postprocessor system, Fig. 7 indicating the generalized kinematics model including transfer the virtual rotary  $C$ -axis to real translate  $Y$ -axis and  $V$ -axis on the working piece table and the spindle for the proposed five-axis machine tool. The user first selects cutting tool and the corresponding cutting shapes. The system will automatically create the NC codes of the configured machine tool.

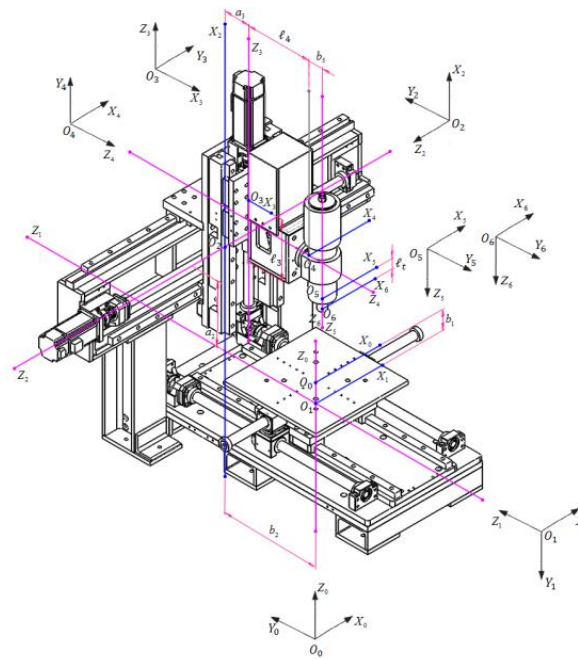


Fig. 8 Hybrid parallel-serial five-axis machine tool.

Table 2 Modified D-H parameters of the proposed five-axis machine tool.

Link	$b_i$	$\theta_i$	$a_i$	$\alpha_i$	$l_i$
0/1	-62.5	0+C	0	$-\pi/2$	0
1/2	308+Y	$-\pi/2$	279.5	$\pi/2$	0
2/3	0+X	$-\pi/2$	77	$-\pi/2$	167.5
3/4	-80+Z	$\pi/2$	0	$\pi/2$	189.5
4/5	41.5	0+B	0	$\pi/2$	94.724
5/6	0	0	0	0	35.62

According to Fig. 8, as the kinematics model has been configured completely, the user enter the relevant parameters, as shown in Table 2, for NC machining, e.g. the offset vector from

the program origin to the centre of the virtual rotary table, the offset vector from the centre of the virtual rotary table to the centre of the  $Y$ -axis, and then  $X$ -axis, and then  $Z$ -axis. Finally, the offset vector from the centre of the rotary spindle to the centre of the tool tip vector. Follow the procedure, the target CL data are captured and the NC data will be generated accordingly. Moreover, since the presented system is a generalized postprocessor, the corresponding CL data can also be transformed if the user opens the NC data for the configured machine tool. In addition, to confirm the feasibility of the proposed algorithm, a typical configurations, namely the hybrid parallel-serial type, is tested. Eq. 18 shows the calculated value of the distance from tool tip to table top is 174.156mm.

$${}^0H_6 = \begin{bmatrix} 1 & 0 & 0 & 0 \\ 0 & 0 & 1 & 0 \\ 0 & -1 & 0 & -62.5 \\ 0 & 0 & 0 & 1 \end{bmatrix} \begin{bmatrix} 0 & 0 & -1 & 0 \\ -1 & 0 & 0 & -279.5 \\ 0 & 1 & 0 & 308 \\ 0 & 0 & 0 & 1 \end{bmatrix} \begin{bmatrix} 0 & 0 & 1 & 167.5 \\ -1 & 0 & 0 & -77 \\ 0 & -1 & 0 & 0 \\ 0 & 0 & 0 & 1 \end{bmatrix} \quad (18)$$

$$\begin{bmatrix} 0 & 0 & 1 & 189.5 \\ 1 & 0 & 0 & 0 \\ 0 & 1 & 0 & -80 \\ 0 & 0 & 0 & 1 \end{bmatrix} \begin{bmatrix} 1 & 0 & 0 & 0 \\ 0 & 0 & -1 & -94.724 \\ 0 & 1 & 0 & 41.5 \\ 0 & 0 & 0 & 1 \end{bmatrix} \begin{bmatrix} 1 & 0 & 0 & 0 \\ 0 & 1 & 0 & 0 \\ 0 & 0 & 1 & 35.62 \\ 0 & 0 & 0 & 1 \end{bmatrix} = \begin{bmatrix} 1 & 0 & 0 & 0 \\ 0 & -1 & 0 & 0 \\ 0 & 0 & -1 & 174.156 \\ 0 & 0 & 0 & 1 \end{bmatrix}$$

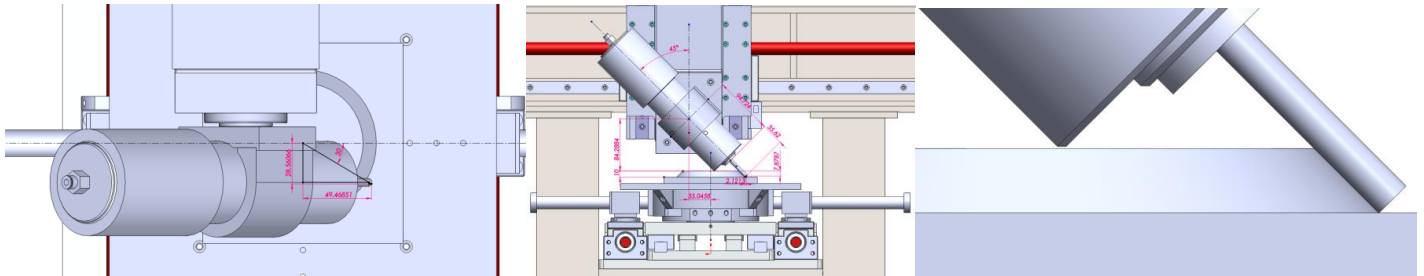


Fig. 9 Hybrid parallel-serial five-axis machine tool.

In the following, a test will show a cutter contact point is transformed to cutter location position. Given a point with initial control points as follows: (X49.47、Y-28.56、Z-7.88、 $\theta 150$ 、 $\phi 135$ ). First the solution is meet the virtual  $C$ -axis coordinate system: (X35.0458、Y0、Z388.7884、B45、C30). Next these corresponding data regenerate to  $Y/V$ -axis coordinate system: (X-35.0458、Y-79.2125、Z84.2884、V79.2125、B-45). The graphic user interface for the transformation information from CC point to CL position is shown in Fig. 10.



Joint	M11	M12	M13	M14
0B1	-0.866025	0	-0.5	0
1B2	0	0	-1	0
2B3	0	0	1	167.5
3B4	0	0	1	189.5
4B5	-0.707107	0	0.707107	66.97998
5B6	1	0	0	0

Offset Z: 304.5  
Spine distance: 274.4

Original X: 49.4685, Y: -28.56066, Z: -7.87868  
Final X: 35.0458, Y: -35.0458, Z: -79.2125

Joint Angles: I=150, J=135, K=45, Theta=30, Phi=-45

Fig. 10 Dialog of the transformation from CC to CL.

## 6. CONCLUSIONS

In order to machine the designed surface correctly, the position and orientation of the working piece and the cutter must be implemented adequately according to the appropriate NC codes. The NC codes are generated by the postprocessor from the corresponding CL data. Essentially, the NC machine requires its own special postprocessor which is designed according to the kinematic model of that NC machine. This paper has proposed a methodology based on the generalized kinematics model for a hybrid parallel-serial five-axis postprocessor. The analytical equations of NC data for various five-axis machine tools with three orthogonal linear axes and two orthogonal rotational axes can be explicitly expressed in terms of CL data. Moreover, the NC data for the specific virtual *C-axis* machine tool can be transformed to the hybrid parallel-serial five-axis machine tool configuration using the derived analytical equations so that the portability of the NC data can be greatly promoted. The results presented in the paper are useful when a fast and robust calculation of the inverse kinematics is necessary, for example in real-time postprocessing of CL data on hybrid parallel-serial five-axis machine tool control units. The presented methodology shows a general procedure that can make the generation of hybrid parallel-serial five-axis postprocessors more systematically and efficiently.

## ACKNOWLEDGMENT

The authors gratefully acknowledge the supports of the National Science Council in Taiwan through project number NSC 101-2221-E-212-018-.





## REFERENCE

1. **Briot, S. and Bonev, I.A., (2007)**, "Are parallel robots more accurate than serial robots", Transactions of the Canadian Society for Mechanical Engineering, Vol.31, No.4, pp 445–455.
2. **Zhang, Z., Mills, J.K. and Cleghorn, W.L., (2010)**, " Multi-mode vibration control and position error analysis of parallel manipulator with multiple flexible links", Transactions of the Canadian Society for Mechanical Engineering, Vol.34, No.2, pp 197–213.
3. **Lotfi, B., Zhong, Z.W. and Khoo, L.P., (2010)**, "A novel algorithm to generate backlash-free motions", Mechanism and Machine Theory, Vol.45, No.8, pp 1171–1184.
4. **Joubair, A., Slamani, M. and Bonev, I.A., (2012)**, "A novel XY-Theta precision table and a geometric procedure for its kinematic calibration", Robotics and Computer-Integrated Manufacturing, Vol.28, No.1, pp 57–65.
5. **Radavelli L., Simoni R., De Pieri E. and Martins D., (2012)**, " A COMPARATIVE STUDY OF THE KINEMATICS OF ROBOTS MANIPULATORS BY DENAVIT-HARTENBERG AND DUAL QUATERNION ", Mecánica Computacional, Vol.XXXI, pp 2833–2848.
6. **Sahul, S., Biswall, B. B. and Subudhi, B., (2008)**, "A novel method for representing robot kinematics using quaternion theory", IEEE sponsored conference on computational intelligence, control and computer vision in robotics & automation.
7. **Sariyildiz, E., Cakiray, E. and Temeltas, H., (2011)**, "A comparative study of three inverse kinematic methods of serial industrial robot manipulators in the screw theory framework", International Journal of Advanced Robotic Systems, Vol. 8, No. 5, pp 9–24.
8. **Sariyildiz, E. and Temeltas, H., (2009)**, "Solution of inverse kinematic problem for serial robot using dual quaternions and plucker coordinates", IEEE, pp 338–343.
9. **Shoham, M. and Ben-Horin, P., (2009)**, "Application of grassmann-cayley algebra to geometrical interpretation of parallel robot singularities", International Journal of Robotics Research, Vol. 28, No. 1, pp 127–141.
10. **Affouard, A., Duc, E., Lartigue, C., Langeron, J-M. and Bourdet, P., (2004)**, " Avoiding 5-axis singularities using tool path deformation", International Journal of Machine Tools and Manufacture, Vol. 44, pp 415–425.
11. **Fauvel, O. R., Vaidyanathan, J. and Norrie, D.H., (1990)**, "An analysis of linearization errors in multi-axis APT-based programming systems", Journal of Manufacturing Systems, Vol. 9, No. 4, pp 353–362.
12. **Nagasaka, M. and Takeuchi, Y., (1996)**, "Generalized post-processor for 5-axis control machining based on form shape function", Journal of the Japan Society for Precision Engineering, Vol. 62, No. 11, pp 1607–1611.



13. **Lee, R.S. and She, C.H., (1997)**, "Developing a postprocessor for three types of five-axis machine tools", *International Journal of Advanced Manufacturing Technology*, Vol. 13, No. 9, pp 658–665.
14. **She, C.H. and Lee, R.S., (2000)**, "A postprocessor based on the kinematics model for general five-axis machine tools", *SME Journal of Manufacturing Processes*, Vol. 2, No. 2, pp 131–141.
15. **Bohez, E., Makhanov, S.S. and Sonthipermpon, K., (2000)**, "Adaptive nonlinear tool path optimization for five-axis machining", *International Journal of Production Research*, Vol. 38, No. 17, pp 4329–4343.
16. **Sorby, K., (2007)**, "Inverse kinematics of five-axis machines near singular configurations", *International Journal of Machine Tools and Manufacture*, Vol. 47, No. 2, pp 299–306.
17. **She, C.H. and Chang, C.C., (2007)**, "Development of a five-axis postprocessor system with a nutating head", *Journal of Materials Processing Technology*, Vol. 187–188, pp 60–64.
18. **She, C.H. and Chang, C.C., (2007)**, "Design of a generic five-axis postprocessor based on generalized kinematics model of machine tool", *International Journal of Machine Tools & Manufacture*, Vol. 47, No. 3-4, pp 537–545.
19. **Denavit, J. and Hartenberg, R.S., (1955)**, "A Kinematic Notation for Low-pair Mechanisms Based on Matrices", *ASME Journal of Applied Mechanics*, Vol. 22, pp 215–221.
20. **Lin, P.D. and Chen, J.F., (1994)**, "Analysis of Error in Precision for Closed Loop Mechanisms", *Journal of Mechanical Design*, Vol. 116, pp 197–203.





## MODELLING OF TURN MILLING PROCESSES FOR INCREASED PRODUCTIVITY

**Umut KARAGÜZEL**, *karaguzelu@itu.edu.tr* Istanbul Technical University, Istanbul, Turkey

**Emre UYSAL**, *emreuysal@sabanciuniv.edu* Sabanci University, Istanbul, Turkey

**Erhan BUDAK**, *ebudak@sabanciuniv.edu* Sabanci University, Istanbul, Turkey

**Mustafa BAKKAL**, *bakkalmu@itu.edu.tr* Istanbul Technical University, Istanbul, Turkey

### ABSTRACT

This paper presents mathematical models and experimental data for the turn milling process which combines conventional turning and milling. Turning with a milling tool offers the advantage of intermittent cutting which allows higher productivity by increased cutting speeds and improved tool life. In this paper, models for turn milling process geometry and chip formation including eccentricity effects are presented. Furthermore, circularity, cusp height and surface roughness are investigated, and cutting forces are simulated. Predictions are verified by experimental results. Tool wear tests performed on hard-to-machine materials to demonstrate substantially increased tool life in turn milling.

**Keywords:** Modelling, Wear, Turn Milling

### 1. INTRODUCTION

Turn-milling is a relatively new concept offering increased productivity. Basically, turn-milling is a turning operation with a milling tool. As a result, turning operation becomes interrupted consisting of contact and non-contact periods which allows tool to cool down reducing cutting temperatures compared to continuous cutting [1]. Thus, increased productivity can be achieved by turn-milling for difficult-to-machine materials such as high temperature alloys as well as parts with large diameters which cannot be rotated at high speeds.

Academic studies on turn-milling have started in 1990 by Schulz et al. [2]. Schulz described the turn-milling operations in two categories: orthogonal and co-axial. In the study a set of experiments were conducted to show the advantages of turn-milling from productivity and part quality point of views.



Recent studies on turn-milling have mostly focused on experimental investigation of the surface quality. Choudhury and Mangrulkar [3] carried out a series of orthogonal turn-milling experiments and compared the surface roughness with those obtained by conventional turning. They found that the surface quality obtained by orthogonal turn-milling is 10 times better than those obtained by conventional turning. In a later study, Choudhury et al. [4] studied the surface roughness in orthogonal turn-milling, this time comparing the results with those obtained by conventional milling where the surface roughness is also predicted by experimental design. They indicated that the surface roughness in turn-milling mainly depends on the rotational speed of the workpiece. Another possible configuration in turn-milling is the tangential one. Savas et al. [5] performed series of experiments using different cutting conditions and analysed the surface roughness achieving surface quality which is comparable to grinding. Kopac and Pogacnik [6] investigated the effect of eccentricity on surface quality in turn-milling and obtained much better surface roughness compared to centric turn-milling. Yuan and Zheng [7] geometrically defined the surface morphology and emphasized the effect of eccentricity on surface roughness.

Geometry and kinematics of turn-milling are complicated due to rotational motions of both workpiece and tool. In order to describe the process, Neagu et al. [8] analysed orthogonal turn-milling from kinematics, cutting forces, roundness, cutting speed and tool geometry points of view. As a conclusion they claimed that turn-milling can achieve up to 20 times higher productivity than turning in roughing of straight shafts. Filho [9] conducted orthogonal turn-milling experiments on a five axis machining center, measured cutting forces and compared them with the analytical model predictions for plunge turn-milling. Jiang [10] defined different surface textures obtained during tangential turn-milling which can be predicted by analytical expressions. Similarly, Zhu et al. [11] described surface topography in orthogonal turn-milling, and proposed to increase number of cutting teeth for higher productivity. They also mentioned that turn-milling could be an alternative to conventional turning especially for machining of large and heavy workpieces.

The objective of this study is analytical and experimental investigation of turn-milling in order to determine the conditions which yield increased productivity and quality compared to conventional turning. For this purpose, process geometry, chip formation, and machined part quality were formulated including eccentricity effects and verified experimentally. In addition, tool life tests were conducted on hard-to-machine materials and compared with those in conventional turning. Finally, advantageous of turn-milling were summarized with suggestions on selection of process conditions.

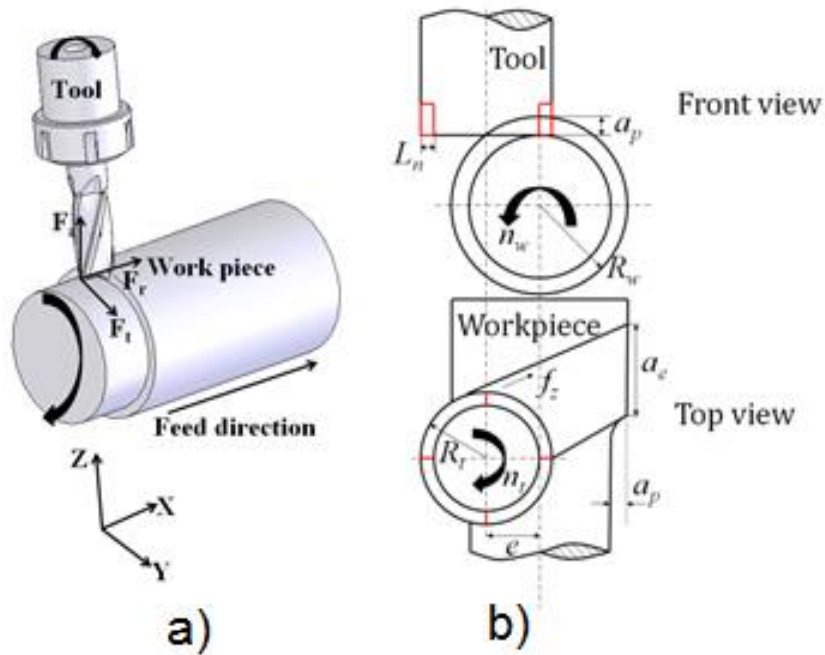


Figure 1. a) Turn-milling process geometry b) Parameters in turn-milling.

## 2. PROCESS KINEMATICS AND UNCUT CHIP GEOMETRY

Turn-milling has a complex geometry due to rotational motions of both cutting tool and workpiece. Figure 1a illustrates the geometry of orthogonal turn-milling and the parameters in the process. As shown in Figure 1b tool and workpiece rotate with speeds of  $n_t$  and  $n_w$ , respectively where their ratio,  $n_t/n_w$ , is defined as  $r_n$ . In addition, there are two different feeds in turn-milling;  $f_z$  is the feed per tooth which is in the circumferential direction, whereas  $a_e$  is the feed per revolution in the axial direction.

In Figure 2a, uncut chip geometry evaluation procedure is shown. It should be noted that both bottom and side of the tool are in cutting action due to the rotation of the workpiece. Figure 2b illustrates uncut chip cross section in orthogonal turn-milling. The parameters used to describe uncut chip geometry can be seen in Figure 2b.

Interrupted characteristics of turn-milling cause facets on the workpiece. The angle between these facets according to the workpiece axis is represented by  $\theta$  angle and formulated as given formula:

$$\theta = \frac{360}{z r_n} \quad (1)$$

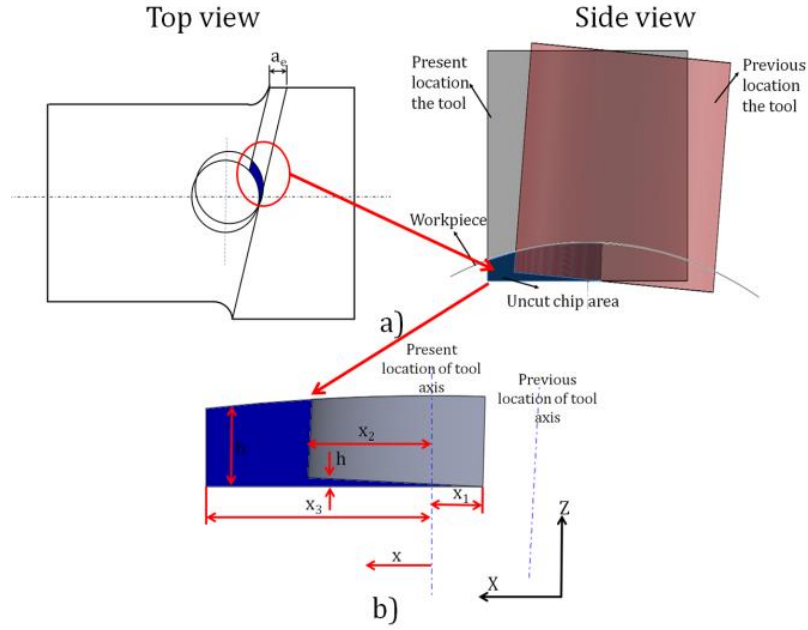


Figure 2. Uncut chip cross section in orthogonal turn-milling.

The uncut area can be found by using  $\theta$  angle and other process parameters. First, the positions of points 1, 2 and 3 shown in Figure 2b must be known, which are used to determine the boundaries of the uncut area:

$$x_1 = (R_w - a_p) \tan\left(\frac{\theta}{2}\right)$$

$$x_2 = R_t - ((R_w - a_p) \tan \theta \tan\left(\frac{\theta}{2}\right) + (R_w - a_p)) \sin \theta \quad (2)$$

$$x_3 = R_t$$

where  $R_w$  and  $R_t$  are the radii of the workpiece and the tool, respectively, and  $a_p$  is the depth of cut.

The points defined above determine the boundaries of the uncut chip geometry. The chip area can be found by using  $h$ , which is the height in  $Z$  direction (Figure 2) with respect to the incremental length on the  $X$  axis. In the first region, which is limited by lines 1-2 and 1-3, height,  $h$ , can be represented as follows:

$$h(x) = \tan(\theta) * x + (R_w - a_p) \tan \theta \tan\left(\frac{\theta}{2}\right) \quad (3)$$

In the second region which is limited by curve 2'-3' and line 1-3,  $h$  can be defined as

$$h(x) = \sqrt{R_w^2 - x^2} - (R_w - a_p) \quad (4)$$



Finally, start and exit angles of the cutting edges in orthogonal turn-milling can be summarized as shown in Table 1.

Table 1. Start and exit angles in orthogonal turn-milling.

	Up-milling	Down-milling
$\varphi_{st}$	0	$\pi/2 + \arcsin((R_t - a_e)/R_t)$
$\varphi_{ex}$	$a \cos((R_t - a_e)/R_t)$	$\pi$

## 2.1. Effect of Eccentricity on Uncut Chip Geometry

Eccentricity in orthogonal turn-milling  $e$ , is defined as the offset of the tool axis from the workpiece axis as shown in Figure 1. Eccentricity changes engagement boundaries and the chip thickness... Analysis of the chip formation including eccentricity effects show that chip formation can be separated into three cases due to the amount of material cut by the bottom of the tool.

Figure 2 shows the cross section of uncut chip for Case 1, which represents the configuration where presence of a piece of uncut chip beyond the tool axis. As eccentricity increases the area between the tool axis and point  $x_2$ , decreases. Beyond a certain eccentricity, chip is formed only by the side of the cutting tool. Table 2 summarizes all three cases and governing equations for  $h$ .

## 2.2. Cutting Speed

Cutting speed in turn-milling is a function of both tool and workpiece rotational speeds. The cutting speed in orthogonal turn-milling can be expressed as follows:

$$\begin{aligned} \text{Relative Velocity} &= \overline{V_2} - \overline{V_1} \\ &= V_2 + V_1 \cos(90 - \varphi) \end{aligned} \quad (5)$$

$$V_1 = 2\pi(R_w - a_p)n_w$$

$$V_2 = 2\pi R_t n_t$$

where  $V_1$  is the speed of workpiece,  $V_2$  is the speed of tool and  $\varphi$  is the rotation angle.



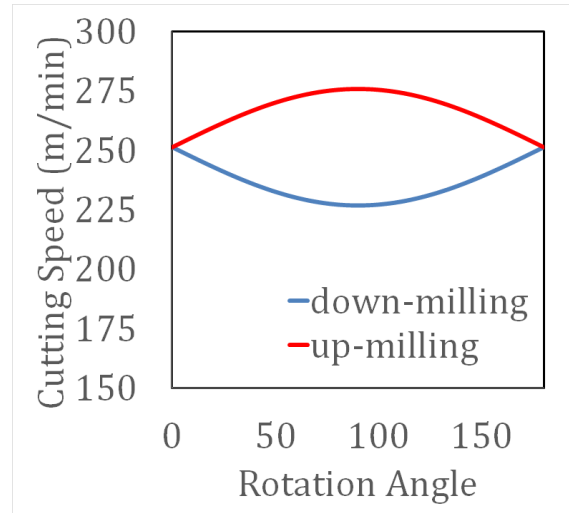


Figure 3. Cutting speed in turn-milling.

Figure 3 presents a comparison for an arbitrary condition between up- and down-milling from the cutting speed point of view. It can be seen that the cutting speed varies during turn-milling process.

### 3. CUTTING FORCES

Cutting forces in turn-milling including eccentricity effects are simulated by oblique transformation of orthogonal cutting data and the chip thickness expressions developed in Section 2 [12, 13]. For the orthogonal data used in the force coefficient calculations, true values of cutting conditions, such as local chip thickness and instantaneous cutting speed, are used in the calculations. Then, the turn-milling forces can be determined by dividing the uncut chip into elements within the cutting zone. The elemental cutting forces can be expressed as follows:

$$\begin{aligned} dF_{t,j(\varphi,z)} &= [K_{tc}h_j(\varphi_j(z)) + K_{te}]dz \\ dF_{r,j(\varphi,z)} &= [K_{rc}h_j(\varphi_j(z)) + K_{re}]dz \\ dF_{a,j(\varphi,z)} &= [K_{ac}h_j(\varphi_j(z)) + K_{ae}]dz \end{aligned} \quad (6)$$

Table 2. The value of  $h$  in Z direction including eccentricity effect for different cases.

	$0 < x < x_2$	$x_2 < x < x_3$
Case 1	$h = \tan(\theta) * x + ((R_w - a_p) * \tan(\theta/2) - e) * \tan(\theta)$	$h = \sqrt{R_w^2 - (x - e)^2} - (R_w - a_p)$
Case 2	$h = \tan(\theta) * (x - (e - (R_w - a_p) * \tan(\theta/2)))$	$h = \sqrt{R_w^2 - (x - e)^2} - (R_w - a_p)$
Case 3	None	$h = \sqrt{R_w^2 - (x - e)^2} - (R_w - a_p)$

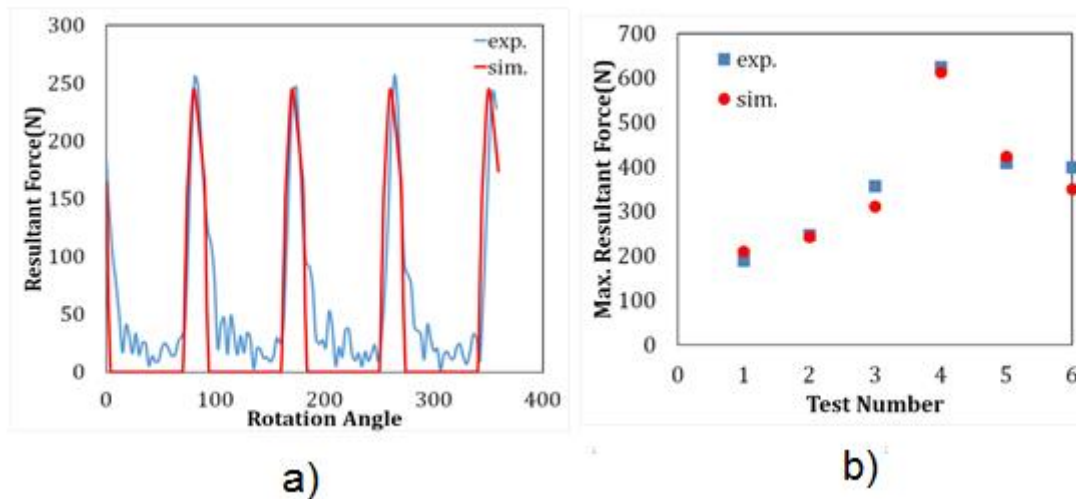


Figure 4. Measured and simulated cutting forces in turn-milling. a) Periodic forces in turn-milling b) Peak resultant forces for different cutting conditions.

The elemental forces are integrated within the engagement zone to obtain the total cutting forces. In order to verify the proposed model, cutting experiments were performed. Cutting tool was a 10 mm diameter solid carbide end mill with 4 teeth. Due to interrupted cutting, periodic forces occur in turn-milling. Figure 4a shows experimental and simulation results of orthogonal turn-milling of 1040 steel. The test parameters were as follows for Figure 4a;  $n_t=2000$  rpm,  $n_w=20$  rpm,  $a_p=0.5$  mm and  $a_e=0.3$  mm/rev.

In order to determine the effects of cutting parameters on turn-milling forces, cutting tests and simulations were performed using different values of  $r_n$ ,  $a_p$  and  $a_e$ .

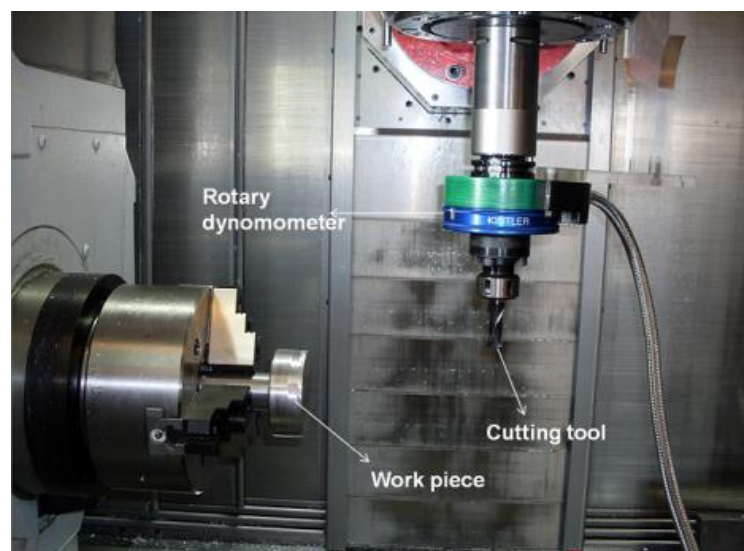


Figure 5 Experimental setup for cutting force measurement

Table 3 summarizes parameters used in the tests. . The experimental setup can be seen in Figure 5 for cutting force measurements. The measured and simulated cutting forces for the conditions given in Table 3 are shown in Figure 4. It can be observed that there is a good

match between experimental and simulation results. In generally speaking cutting forces increase with the values of  $a_e$  and  $a_p$ , and decrease with  $r_n$  ratio.

**Table 3. Cutting conditions used in turn-milling tests.**

Test No	$R_w$	$R_t$	$n_t$	$n_w$	$r_n$	$a_p$	$a_e$
1	45	5	3000	20	150	0.5	0.3
2	45	5	2000	20	100	0.5	0.3
3	45	5	2000	20	100	0.5	0.6
4	45	5	2000	20	100	1	0.6
5	45	5	4000	20	200	1	0.6
6	45	5	4000	20	200	1	0.3

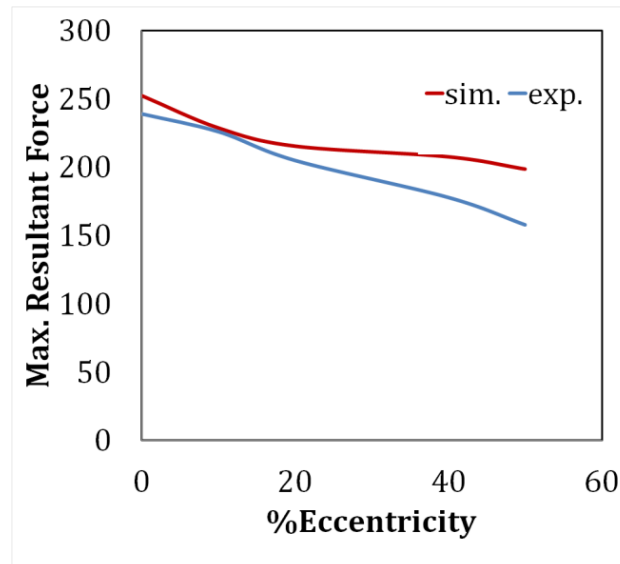


Figure 6. Peak cutting forces in turn milling including eccentricity effects.

Figure 6 shows the effect of eccentricity on cutting forces. In eccentricity tests  $r_n$  was 250 where  $a_p=0.5\text{mm}$  and  $a_e=0.5\text{mm/rev}$  and 5 different eccentricity values were selected %0, 10, 20, 40 and 50 of tool diameter. From Figure 6, one can see that cutting forces decrease with increasing eccentricity. With increasing eccentricity, the region that is cut by the tool bottom, decreases. Beyond a certain value eccentricity, the chip is formed only by the tool side which results in lower cutting forces.

#### 4. MACHINED SURFACE QUALITY

Figure 7 shows the surface quality problems in turn-milling operation. Two different problems are illustrated in Figure 7; namely circularity and cusp height.

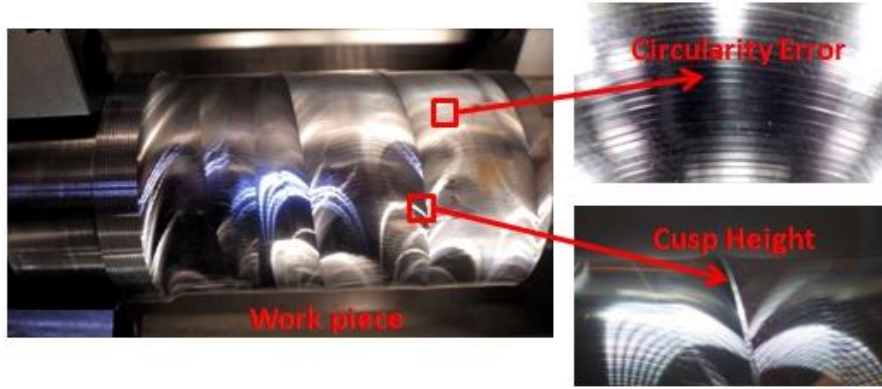


Figure 7. Form errors in turn-milling.

Circularity error is a result of interrupted cutting and simultaneous rotation of milling tool and workpiece, so that the final cross section of machined part in turn-milling is a polygon. The difference between polygon and the corner of the polygon is defined as circularity error and formulated as:

$$circ = (R_w - a_p) \left( \frac{1}{\cos \frac{\theta}{2}} - 1 \right) \quad (7)$$

As given by Eq. 1,  $\theta$  angle depends on only circular distance between subsequent cutting teeth and  $r_n$ . In addition, Eq. 6 illustrates that  $R_w$  and  $a_p$  effects circularity error and where eccentricity has no effect. The optimal eccentricity is  $e=R_t-L_n$  where  $L_n$  is the length of minor cutting edge of cutting tool as it is represented in Figure 1b. If  $a_e$  is defined as higher than the maximum contact zone length, cusp height form error can be observed on machined workpiece surface and that is geometrically defined as:

$$ch = \sqrt{(R_w - a_p)^2 + \left( \left[ e + \left[ (R_w - a_p) x \tan \left( \frac{180^\circ}{z x r_n} \right) \right] \right] - \left[ \sqrt{(R_t)^2 - \left( \frac{a_e}{2} \right)^2} \right] \right)^2} - (R_w - a_p) \quad (8)$$

As it can be seen from Eq. 7, the cusp height ( $ch$ ) depends on many parameters. The formulation of cusp height geometry is first derived in the present work, while previous studies considered circularity as the only form error in turn-milling. The analytical formulation predicts that unlike the circularity form error, cusp height is an avoidable case. By using cusp height formulation, MRR and productivity can be increased without sacrificing the any surface quality. When  $e$  equals the optimal value and  $a_e$  equals to the maximum cutting zone length, maximum MRR with zero cusp can be obtained.

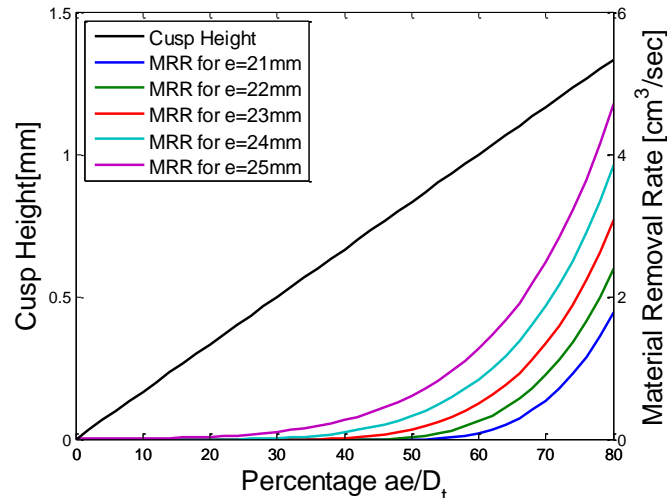


Figure 8. Process parameters effect on both cusp height and MRR.

Figure 8 illustrates the  $a_e$  and eccentricity effect on both cusp height and MRR. Process parameters which are used in simulation can be summarized as follows;  $R_w=50$ mm,  $R_f=25$  mm,  $r_n=200$ ,  $z=4$ ,  $L_n=4$  mm and  $f_z=0.2$  mm/rev-teeth. Increasing the amount of eccentricity results in higher cusp height value for the same  $a_e$ . Moreover, MRR increases in reaction to increasing  $a_e$ . Thus, this can be called as an optimization problem because while increasing  $a_e$  affects surface roughness negatively it affects productivity in a positive way. As a result,  $a_e$  is the main parameter which must be defined at first in order to obtain an acceptable cusp height.

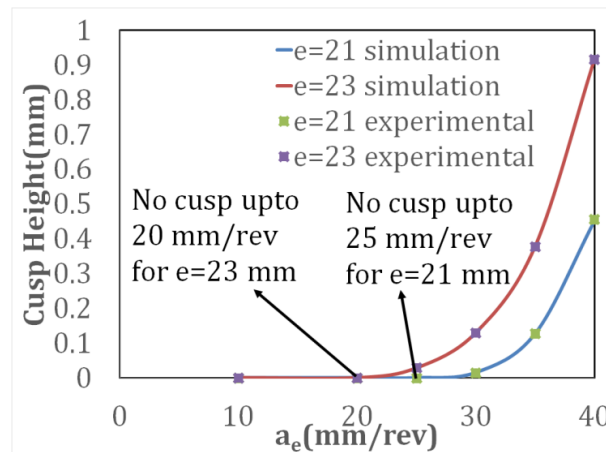


Figure 9. Cusp height with respect to  $a_e$  and  $e$ .

Feed per workpiece revolution and eccentricity effects on cusp height are shown Figure 9. In addition to the analytical model predictions, the figure also contains several experimental results. The cutting parameters in the experiment are as follows;  $a_p=1$ mm,  $R_w=48.5$  mm,  $R_f=25$ mm,  $z=4$ ,  $n_f=2000$  rpm,  $n_w=4$  rpm,  $f_z=0.12$ mm/rev-teeth. One can interpret from the graph that up to a certain value of  $a_e$  there is no cusp which increases with eccentricity  $e$ . For optimal eccentricity value ( $e=21$ mm),  $a_e$  can be increased up to 25 mm/rev without any cusp.

## 5. TOOL WEAR

A turn-milling cycle includes cutting and non-cutting periods which allow cutting tool to cool down reducing the tool wear. This aspect of turn-milling is particularly important for machining of difficult-to-cut materials such as high temperature alloys. In order to investigate tool life in turn-milling, tool wear experiments were conducted on Mori Seiki NTX2000 multi-tasking machine. A 32 mm diameter Seco Micro Turbo 217.69-03 milling tool with three cutting teeth was used in the experiments. The inserts were F40M grade which is recommended for machining of superalloys by Seco. The work piece materials used in the tests were Inconel 718, Waspaloy and Ti6Al4V. The cutting parameters were as follows:  $V_c=45\text{m/min}$ ,  $f_z=0.4\text{ mm/rev}$ ,  $a_p=0.2\text{ mm}$  and  $a_e=8\text{ mm}$ . The cutting tests were repeated under dry, with fluid and with MQL conditions. Figure 10 presents Mori Seiki NTX 2000 machine tool on which the tool wear experiments were conducted and the experimental setup. In addition tool wear measurement via Nanofocus  $\mu\text{surf}$  can be seen in Figure 11.

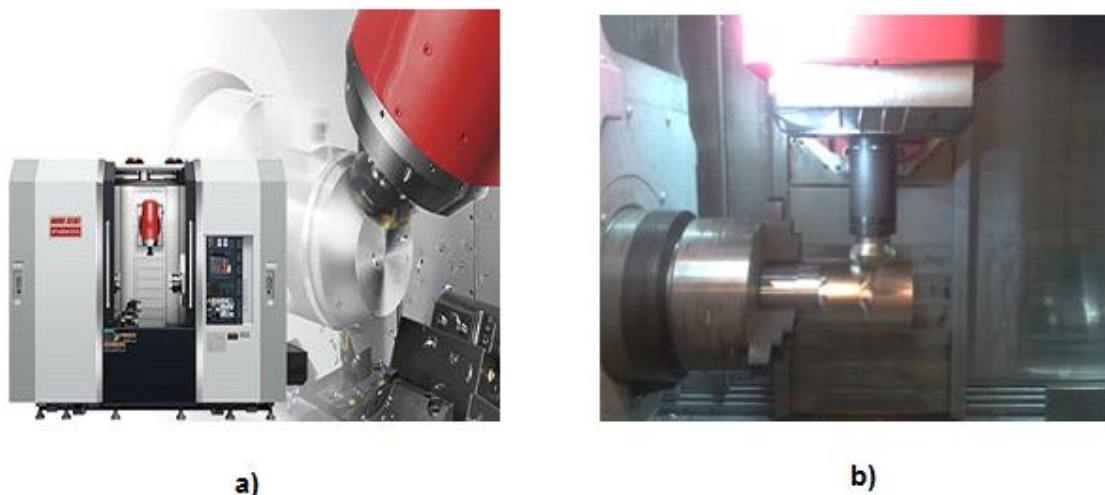


Figure 10 a) Mori Seiki mill-turn machine tool b) Tool wear experiment setup

Figure 12 presents the whole results of tool wear tests. The results are normalized to one tooth by dividing the cutting time by 3 in order to compare the results with conventional turning data which were obtained using the same cutting speed and MRR. Results show that turn-milling has 3 to 40 times better tool life under similar cutting conditions for different workpiece materials. In particular MQL provides the best result for Inconel in terms of tool life. As it is also shown in Figure 12 **Error! Reference source not found.**, turn-milling with MQL provides two times longer tool life compared to dry turn-milling whereas dry turn-milling results in almost 3 times better tool life compared to dry conventional turning. Tool life for Waspaloy is improved more than 20 times by turn-milling with cutting fluid in comparison to dry conventional turning under the same cutting conditions. In addition, dry turn-milling



results are three times better than the dry conventional turning. Although dry turn-milling result in shortest tool life for Ti6Al4V compared to the other cooling conditions, it is almost 40 times longer with respect to the dry conventional turning. It can be concluded from presented data that turn-milling provides a clear advantage in terms of tool life in machining of hard-to-cut materials.

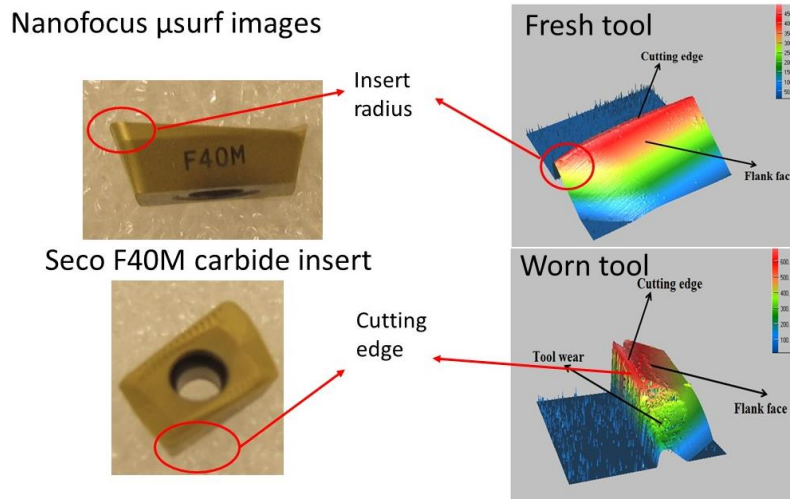


Figure 11 Tool insert and wear measurement on Nanofocus

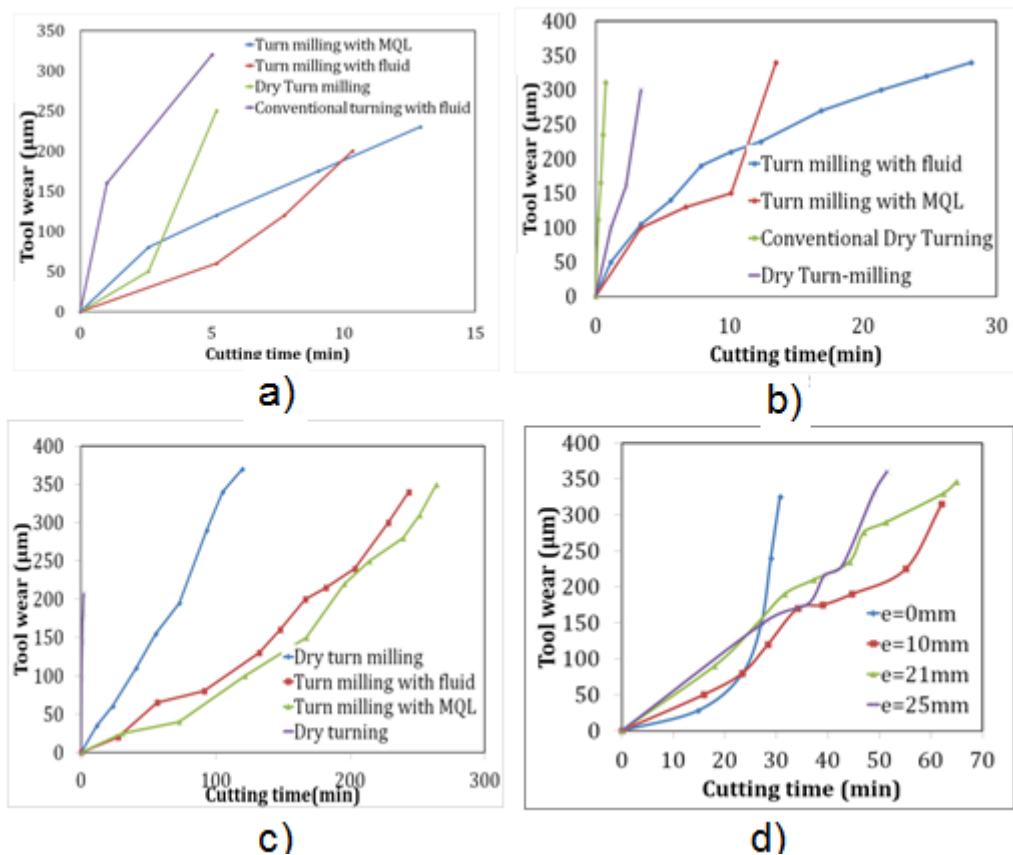


Figure 12. Tool wear results for a) Inconel 718, b) Waspaloy, c) Ti6Al4V and d) effect of eccentricity.



## 5. CONCLUSIONS

In this paper turn-milling process is examined through part quality, tool wear and cutting forces. Developed process models show that productivity of turn-milling can be improved by optimization of cutting parameters. Cusp height and circularity are main quality problems in turn-milling. It is shown that cusp height is correlated with the eccentricity and there is no cusp under a certain value of feed per workpiece revolution. In addition to the machined part quality, tool wear tests in cutting of hard-to-cut materials are also performed and it is demonstrated that turn-milling could be a favorable alternative to turning process in order to increase productivity and tool life. It is experimentally observed that 3 times better tool life for Inconel 718 is possible by turn-milling whereas it is 20 times for Waspaloy and 40 times for Ti6Al4V. Cutting forces in turn-milling were also simulated and experimentally verified. The speed ratio has a significant effect on cutting forces which decrease dramatically with the speed ratio.

## ACKNOWLEDGEMENTS

The supports from TUBITAK (Project 110M522), Mori Seiki and Pratt and Whitney Canada are appreciated by the authors.

## REFERENCES

1. **Armendia M, Garay A, Villar A, Davies M A, Arrazola P J** (2010) High Bandwidth Temperature Measurement in Interrupted Cutting of Difficult to Machine Materials. CIRP Ann Manuf Technol 59/1:97-100.
2. **Schulz G, Spur G** (1990) High Speed Turn-milling—a New Precision Manufacturing Technology for the Machining of Rotationally Symmetrical Workpieces. CIRP Ann Manuf Technol 39/1:107–109.
3. **Choudhury SK, Mangrulkar KS** (2000) Investigation of Orthogonal Turn-milling for the Machining of Rotationally Symmetrical Workpieces. J Mater Process Technol 99:120–128.
4. **Choudhury SK, Bajpai JB** (2004) Investigation in Orthogonal Turn-milling Towards Better Surface Finish. J Mater Process Technol 170: 487-493.
5. **Savas V, Ozay C** (2007) Analysis of the Surface Roughness of Tangential Turn-milling for Machining with End Milling Cutter. J Mater Process Technol 186:279–283.
6. **Kopac J, Pogacnik M** (1995) Theory and Practice of Achieving Quality Surface in Turn Milling. Int. J. Mach. Tools Manufact. 37/5:709-715.





7. **Yuan S, Zheng W** (2012) The Surface Roughness Modeling on Turn-milling Process and Analysis of Influencing Factors. *Applied Mechanics and Materials* 117-119:1614-1620.
8. **Neagu C, Gheorghe M, Dumitrescu A** (2005) Fundamentals on Face Milling Processing of Straight Shafts. *J Mater Process Technol* 166:337–344.
9. **Filho J** (2012) Prediction of Cutting Forces in Mill Turning Through Process Simulation Using a Five-axis Machining Center. *The International Journal of Advanced Manufacturing Technology*, 58:71-80.
10. **Jiang Z, Liu X, Deng X** (2012) Modeling and Simulation on Surface Texture of Workpiece Machined by Tangential Turn-milling Based on Matlab. *2nd International Conference on Artificial Intelligence, Management Science and Electronic Commerce (AIMSEC)*, 4072-4075.
11. **Zhu L, Li H, Wang W** (2013) Research on Rotary Surface Topography by Orthogonal Turn-milling. *Int J Adv Manuf Technol*, 69:2279-2292.
12. **Budak E, Altintas Y, Armarego E** (1996) Prediction of Milling Force Coefficients from Orthogonal Cutting Data. *Journal of Engineering for Industry*, 118:216-224.
13. **Altintas Y** (2000) *Manufacturing Automation*. Cambridge University Press.



## MECHATRONIC SPINDLE HEAD FOR CHATTER SUPPRESSION IN HEAVY DUTY OPERATIONS

**Iker MANCISIDOR**, *imancisidor@ideko.es*, IK4-IDEKO, DanobatGroup, Elgoibar, Basque Country, Spain

**Jokin MUNOA**, *jmunoa@ideko.es*, IK4-IDEKO, DanobatGroup, Elgoibar, Basque Country, Spain

**Rafael BARCENA**, *rafa.barcena@ehu.es*, University of the Basque Country (UPV-EHU), Bilbao, Basque Country, Spain.

**Xabier MENDIZABAL**, *xmendizabal@soraluce.com*, Soraluce, DanobatGroup, Bergara, Basque Country, Spain

### ABSTRACT

A new concept of spindle head for heavy roughing operations has been developed integrating an inertial actuator and an accelerometers in a heavy duty spindle head. With this head is possible to introduce active damping using the inertial drive, and improve the dynamic stability of the machine. A novel mechatronic milling model is employed for designing the actuator, where the effect of cutting process and inertial actuators can be simulated. The validation tests of the new actuator are shown and all mechatronic system is completely integrated on the machine. Finally, experimental cutting tests are performed, showing that material removal rate is doubled with this new spindle head.

**Keywords:** Stability, Milling, Chatter, Active Control.

### 1. INTRODUCTION

Actually, self-excited vibrations known as chatter are one of the most important restrictions in cutting processes. These vibrations are principally due to the regenerative effect [Tlustý and Polacek, 1957; Tobias and Fishwick, 1958] and are the cause of unacceptable surface finishes, tool breakages and timelife reduction of different mechanic elements.

Probably one of the most employed solutions for increasing the stability is to add a tuned mass damper to the structure [Sims et al., 2005; Yang et al., 2010]. This is not a novel technique and it has been widely employed [Den Hartog, 1956]. However, the use of passive dampers is not feasible in many cutting processes where the dynamics of the system may vary during the process.



Active dampers can overcome these limitations by means of their adaptability to variable conditions. These actuators are based on performing a reaction force onto the main structure, controlled by a control algorithm.

The development of active dampers had its origin in the aeronautical industry. In 1968 Bies and Yang reported that the problems presented by passive absorbers could be solved by means of adding an active element. In 1970, Cowley and Boyle proposed to use an electromagnetic inertial actuator with an accelerometer in order to introduce active damping onto the structure of a machine tool.

The combination of active devices and sensors makes up an advanced mechatronic solution, whose behaviour is comparable to a smart material, such as piezoelectric actuators. In fact, inertial actuators have better performance for improving the dynamic behaviour of machine tool in heavy duty operations [Ehmann and Nordmann, 2002].

Piezoelectric actuators are usually located inside the machine in serial way due to their characteristics. It means that they are inside the force path of the machine, and therefore a big stiffness is required to transmit cutting forces. However, inertial actuators tend to locate in parallel way maintaining the original stiffness of the machine [Ehmann and Nordmann, 2002; Loix and Verschueren, 2004]. During the last years, the introduction of inertial actuators in heavy duty machines has been studied. For instance, Ehmann and Nordmann (2002) recommended the introduction of inertial actuators for big dimension machines.

In order to build an inertial actuator, some authors have employed hydraulic technology. Brecher et al. (2005) developed an electrohydraulic actuator for testing different control strategies in chatter problems. The hydraulic technology is interesting because it offers high forces and strokes. However it exhibit big disadvantages such as maintenance problems, non-linearities or delays.

From an energetic point of view, the piezo actuators merely need power to change their state. In contrast, the electromagnetic actuator need to continuously overcome resistor losses. Nevertheless, the cost for piezoelectric systems exceeds those of the electromagnetic actuator systems roughly by a factor of 3-4. Moreover, the electromagnetic actuators present another advantage of not having physical contact between the moving and fixed parts, so they are widely used in vibration applications.

Among electromagnetic devices, reluctance or attraction force actuators offer large forces, but this force is proportional to the current squared and inversely proportional to the air gap squared. Hence, they are difficult to control and are not usually employed in precision applications. Lorentz force actuators can produce less force, but their linearity makes them a good option for vibration control. In this case, the force is proportional to the strength of the magnetic field, and if a proper design with permanent magnets is selected, the force is strictly



proportional to the applied current. Several authors have applied inertial electromagnetic actuators based on Lorentz forces for avoiding chatter on machine tools [Loix and Verschueren, 2004, Bilbao-Guillerna et al., 2012].

In recent years, actuators where both reluctance and Lorentz forces are combined have been developed and patented [Claeyssen et al., 2008]. These actuators, known as MICA, are reported as devices that offer higher forces but require a very accurate guiding system. This work presents the development of a new spindle head, where an electromagnetic inertial actuator is integrated for active control of vibrations. The active devices have to be located close to the cutting tool, where machine tools offer reduced space for them. In this case, the design of a new spindle head provides the possibility of introducing a small inertial actuator inside it. The paper shows the design of the actuator by means of a mechatronic model and its validation test. Finally, the experimental cutting tests show the great improvement obtained by this new spindle head.

## **2. DYNAMIC CHARACTERISTICS OF A RAM TYPE TRAVELLING COLUMN MILLING MACHINE**

Chatter vibrations appear in many different ways in the milling process. The prediction and suppression techniques vary depending on the process [Munoa et al., 2005]. For example, in high speed aluminium rough milling, the modes limiting the stability are associated to the tool and the toolholder, or to the spindle (the chatter frequency is roughly between 300 and 3000 Hz) [Mancisidor et al., 2011]. However in steel roughing the critical modes are related to the whole machine tool structure (the chatter frequency is roughly between 15 and 100 Hz).

The ram type machine tools have some special characteristics defined mostly by the ram. Basically, the ram is a special cantilever beam with a big mass in form of a spindle in its tip. The ram can change its overhang using one of the drives of the machine. This machine concept introduces flexibility in two axes (X and Y in our case) related to bending directions and maintains high stiffness in the axial direction (Z in our case). The overhang of the ram varies depending on the working position and this produces big variations in the dynamic stiffness of the machine.



Figure 1. Ram type Moving Column Milling Machine

The overhang of the ram has a capital influence, because the bending and the rotation of the ram are directly involved in the critical modes. These modes change their properties inside the workspace, produce displacements in the two bending planes and can have similar frequencies. Generally speaking, chatter is always generated by modes with important displacements in the tool tip.

In the present study a prototype of a SORALUCE milling machine (see Figure 1) has been selected for integrating the new active spindle head. First of all, a complete dynamic study was carried out including a complete modal analysis (see Table 1).

Considering the dynamical characteristics of ram type machine tools, the optimum damper should have an active behavior to adapt to dynamical variations inside the workspace and it should be placed close to the tool tip. In this work, it will be located on the top of the spindle head (point  $q$ ), and the original stiffness of the machine will be maintained since it will be located in a parallel way as a suspended mass.

**Table 1** Results of the modal analysis of a ram type milling machine (ram overhang=1000mm)

Natural Frequency ( $\omega_n$ )	Damp- ing ratio ( $\xi$ )	Modal Stiffness ( $k$ )	Modal vector [Q]	
			Tool ( $p$ )	Spindle Head ( $q$ )
1 33.6Hz	5.5%	27.9 N/ $\mu$ m	(-0.70, 0.61, -0.38)	(-0.59, 0.54, -0.22)
2 51.2Hz	2%	145 N/ $\mu$ m	(-0.99, 0.05, 0.06)	(-0.80, 0.06, 0.11)
3 193Hz	1.5%	639 N/ $\mu$ m	(0.70,-0.56, 0.43)	(0.2, 0.04, 0.06)

### 3. MILLING MECHATRONIC MODEL

In the state of art, the need of design guidelines of inertial actuators is reflected, in order to assure certain stability to a certain machine. Some authors analyzed the integration of active devices in machine tools by means of simulations [Zaeh et al., 2009; Sajedipour et al., 2010]. However, no one verified their results experimentally and the different control parameters and limitations of actuators were not taken into consideration. Therefore, a mechatronic model has been developed in order to provide guidelines in the design of inertial actuators. This model simulates the behaviour of a milling machine in time domain considering the cutting process and the behaviour of the actuator at the same time. This way, the stability of the system can be studied. The model provides the option of introducing different limitations of the actuator. The most important limitation is usually the maximum force of the inertial device.

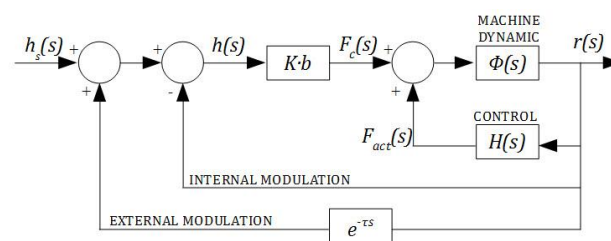


Figure 2. Closed loops taken into account in the mechatronic model.

### 3.1. Mathematical formulation

The simulation is characterized by two closed loop systems (Figure 2). Normally, it is not possible to measure and act directly in the tool. Therefore, different points and their relation have to be taken into account (see points  $p$  and  $q$  in Figure 1 and Table 1).

The first loop calculates the regenerative cutting force  $F_c$  on the tool tip (point  $p$ ) following the formulation proposed by Altintas (2012). The tangential ( $F_t$ ), radial ( $F_r$ ) and axial ( $F_a$ ) forces for each tooth  $j$  are calculated by the next equation:

$$\begin{Bmatrix} F_{t,j} \\ F_{r,j} \\ F_{a,j} \end{Bmatrix} = \begin{Bmatrix} K_{tc} \\ K_{rc} \\ K_{ac} \end{Bmatrix} h(\phi_j, \kappa) b + \begin{Bmatrix} K_{te} \\ K_{re} \\ K_{ae} \end{Bmatrix} S g(\phi_j), \quad (1)$$

where  $K_{tc}$ ,  $K_{rc}$  and  $K_{ac}$  are cutting coefficients, and  $K_{te}$ ,  $K_{re}$  and  $K_{ae}$  are the edge coefficients.  $b$  is the depth of cut of the tool and  $S$  is referred to the length of the flute. The immersion angle  $\phi_j$  defines if the tool  $j$  is cutting and is defined as

$$g(\phi_j) = \begin{cases} 1 & \phi_s < \phi_j < \phi_e \\ 0 & \phi_j > \phi_e \text{ and } \phi_j < \phi_s \end{cases} \quad (2)$$

where  $\phi_s$  and  $\phi_e$  are the cutter entry and exit angles, respectively.

The chip thickness ( $h$ ), consists of a static part ( $h_s$ ), which depends on the feed per teeth  $f_z$ , and a dynamic component ( $h_d$ ), affected by the vibration ( $r$ ) on the point  $p$ :

$$\begin{aligned} h(\phi_j, \kappa) &= h_s(\phi_j, \kappa) + h_d(\phi_j, \kappa) \\ h_s(\phi_j, \kappa) &= f_z \sin(\phi_j) \sin \kappa \\ h_d(\phi_j, \kappa) &= \{ \sin(\phi_j) \sin \kappa \quad \cos(\phi_j) \sin \kappa \quad -\cos \kappa \} \{ \Delta r(t) \}_p \end{aligned} \quad (3)$$

where  $\Delta r(t) = r(t) - r(t - \tau)$ , being  $\tau$  the tooth passing period and  $\kappa$  is the lead angle.

Finally, adding the cutting forces contributed by all teeth, where  $Z$  is the number of teeth and projecting onto the  $xyz$  Cartesian axes,

$$\{F_c(t)\}_p = \begin{Bmatrix} F_x(t) \\ F_y(t) \\ F_z(t) \end{Bmatrix}_p = \sum_{j=0}^{Z-1} \begin{bmatrix} -\cos(\phi_j) & -\sin(\phi_j) & 0 \\ \sin(\phi_j) & -\cos(\phi_j) & 0 \\ 0 & 0 & 1 \end{bmatrix} \begin{Bmatrix} F_{t,j} \\ F_{r,j} \\ F_{a,j} \end{Bmatrix}_p \quad (4)$$

On the other hand, the second loop is due to the active control of the inertial actuator. In this way, the actuator force  $\{F_{act}\}_q$  is calculated depending on the chosen control law and the actuator location  $q$ .

The behaviour of the system is described by a matrix equation defined considering the Cartesian coordinates of both points  $p$  and  $q$ , where  $[M]$ ,  $[C]$  and  $[K]$  are the mass, damping and stiffness matrices respectively.

$$[M]\left\{\ddot{r}(t)\right\} + [C]\left\{\dot{r}(t)\right\} + [K]\{r(t)\} = \{F(t)\} \quad (5)$$

where,

$$\{r(t)\} = \begin{Bmatrix} \{r(t)\}_p \\ \{r(t)\}_q \\ \{r(t)\}_m \end{Bmatrix} \text{ and } \{F(t)\} = \begin{Bmatrix} \{F_c(t)\} \\ \{F_{act}(t)\} \\ 0 \end{Bmatrix}.$$

A modal transformation is performed using a modal vector matrix  $[Q]$ . Each column of this matrix coincides with the modal displacement  $\eta$  of each mode in points  $p$  and  $q$ , where  $n$  modes are considered. Therefore:

$$[Q]^T [M] [Q] \{\ddot{\eta}(t)\} + [Q]^T [C] [Q] \{\dot{\eta}(t)\} + [Q]^T [K] [Q] \{\eta(t)\} = [Q]^T \{F(t)\} \quad (6)$$

Considering proportional damping the matrix equation is diagonalised and decoupled:

$$\ddot{\eta}_i(t) + 2\xi_i \omega_{n,i} \dot{\eta}_i(t) + \omega_{n,i}^2 \eta_i(t) = \frac{P_i(t)}{m_i} \quad (7)$$

where  $m_i$ ,  $\omega_{n,i}$  and  $\xi_i$  are the modal mass, the natural frequency and the damping of the  $i$ th mode of the structure respectively.  $P_i$  is the modal force which is calculated by the sum of modal milling force and modal actuator force:

$$P_i(t) = [Q_p^i]^T \{F_c(t)\}_p + [Q_q^i]^T \{F_{act}(t)\}_q \quad (8)$$

Modal displacements are calculated using the numerical integration proposed in [Bediaga et al., 2009], based on state space model:

$$\begin{Bmatrix} \dot{\eta}_i(t) \\ \dot{\eta}_i(t) \end{Bmatrix} = \begin{bmatrix} 0 & 1 \\ -\omega_{n,i}^2 & -2\xi_i \omega_{n,i} \end{bmatrix} \begin{Bmatrix} \eta_i(t) \\ \dot{\eta}_i(t) \end{Bmatrix} + \begin{bmatrix} 0 \\ 1 \end{bmatrix} \frac{P_i(t)}{m_i} \quad (9)$$



$$\begin{Bmatrix} \eta_i(t_{k+1}) \\ \dot{\eta}_i(t_{k+1}) \end{Bmatrix} = \begin{bmatrix} A_{11,i} & A_{12,i} \\ A_{21,i} & A_{22,i} \end{bmatrix} \begin{Bmatrix} \eta_i(t_k) \\ \dot{\eta}_i(t_k) \end{Bmatrix} + \begin{bmatrix} \frac{\Delta t^2}{2} \\ \Delta t - \xi_i \omega_{n,i} \Delta t^2 \end{bmatrix} \frac{P_i(t_k)}{m_i} \quad (10)$$

Then, the Cartesian displacements of each point are calculated by modal vectors and they will be used in the calculation of the next forces.

$$\{r(t_{k+1})\} = \begin{Bmatrix} \{r(t_{k+1})\}_p \\ \{r(t_{k+1})\}_q \end{Bmatrix} = [Q]^T \{\eta(t_{k+1})\} \quad (11)$$

### 3.2. Control law

Several control laws for suppression of chatter vibrations have been presented in the literature [Brecher and Schulz, 2004; Huyanan and Sims, 2007; Bilbao-Guillerna et al., 2010]. In this work the direct velocity feedback (DVF) strategy is employed, since it is the most common law for this application. It is based on the measurement of vibration velocity and its negative feedback is multiplied by a gain  $G$ . In this way, the control forces appear as viscous damping and the stability lobes increase their limit depth of cut [Munoa et al., 2013].

$$\{F_{act}(t)\}_q = G \cdot \{\dot{x}(t)\}_q \quad (12)$$

In this way, DVF can actuate over all vibrations measured and thus it does not need any model of the system. So, such technique is widely used for its simplicity and leads to very good results. However, when a DVF is used, a high-pass filter should be added in the control loop in order to minimize the effects of low frequency dynamics of the actuator. In the study presented by this paper, a low-pass filter has been also added in order to neglect the high frequency noise. In addition, the closed-loop can easily become unstable for sufficiently large values of the feedback gain. For this reason, sometimes it is necessary to introduce more filters in order not to consuming significant energy trying to reduce the whole frequency range including regions with no contribution to chatter. This work proposes the utilization of a notch filter to avoid the spindle tooth passing frequency, when it is located far from the frequencies of interest. Finally, the force is limited by a saturation block, since actuators cannot perform more than a certain force.

### 3.3. Mechatronic model results

In this work, the mechatronic model has been used in order to design the electromagnetic inertial actuator for the proposed milling machine. In the design of the new spindle head, a

space for the inertial actuator was provided on the top of the head. Taking into account the available space, different possible designs has been simulated over the machine dynamics. As demonstrated by Munoa et al. (2013), a biaxial actuator is very efficient in ram type travelling column machines in order to act in the two flexible directions of the ram. However, the reduced space of the spindle head makes the design of different alternatives necessary. After the first design of the electromagnetic part by means of a magnetic finite element model (Flux), two alternatives were considered for the same space. On the one hand, a biaxial actuator was calculated, which was capable of performing a maximum of 350N in each direction. On the other hand, a single axis actuator was designed for the same space. Since the space could be optimized better, a capability of 1000N was calculated for this actuator. Using the modal parameters defined in Table 1, the stability results of each actuator were obtained (Figure 3). It can be observed that better results can be obtained by a 1000N single axis actuator around the minimum stability zone, although the biaxial actuator also improves the stability considerably. Therefore, in this case a higher force capability is preferred than a biaxial performance.

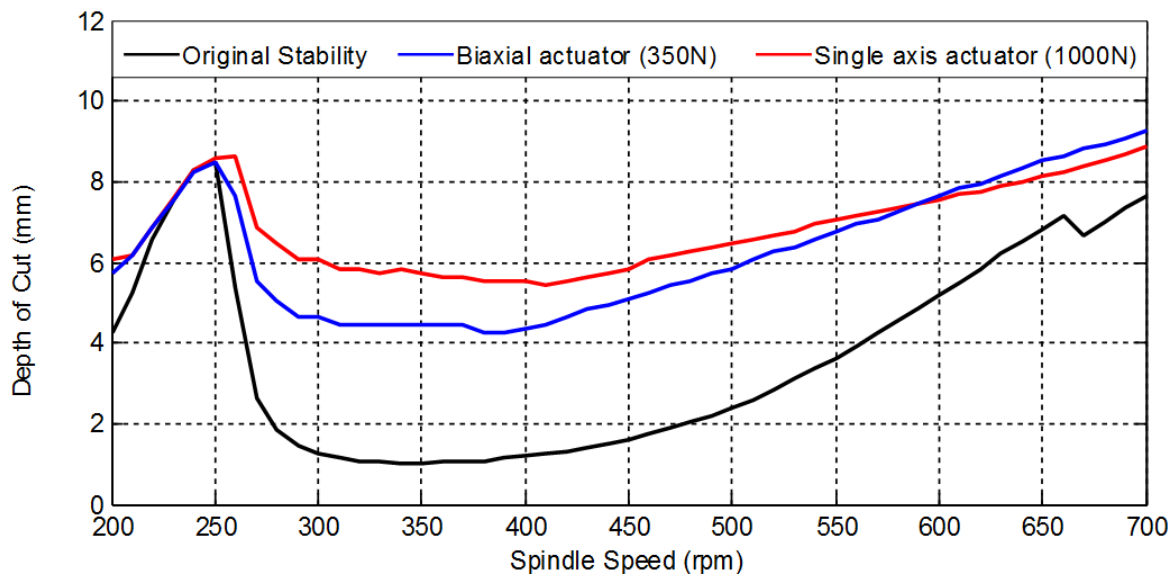


Figure 3. The comparison of the stability improvement by the two proposed inertial actuators.

#### 4. DEVELOPMENT OF THE NEW SPINDLE HEAD

##### 4.1. Introduction

The main objective is to develop an active spindle head with an integrated accelerometer and an electromagnetic actuator. The new device will be able to provide active damping to an ordinary milling machine.

SORALUCE has selected the H210 spindle head to be the base of the brand new spindle head with integrated sensors and actuator. It is a Huré type universal head and it is one of the most widely used spindle head.

The idea has been to design a spindle head able to provide a power of 32kW and a torque of 1200Nm. The maximum speed has been defined around 5000 rpm.

A new inertial actuator with 1000N has to be integrated inside the spindle head without any additional limitation or collision in the travel of the machine. This means that the actuator cannot be higher than 120mm.

#### 4.2. Design of the inertial actuator

Once the single axis actuator is chosen, the challenge is to design in detail and develop the actuator capable of providing 1000N in the available space. The electromagnetic design is based on an alternative of linear motor with limited stroke. A sinusoidal current with the desired frequency is introduced in the static coils. In this way, due to Lorentz force, a linear displacement force is performed on the moving mass where neodymium permanent magnets are located. The magnetic flux density of the permanent magnets is 1.2 T, while each coil consists of 380 turns where a maximum of 3 A current is introduced.

The optimization of the space has been obtained by locating four parallel rows of permanent magnets and coils, which have been sized by magnetic finite element software (Flux), calculating the theoretical force obtained with the design. Figure 4 shows the finite element model and the magnetic flux obtained.

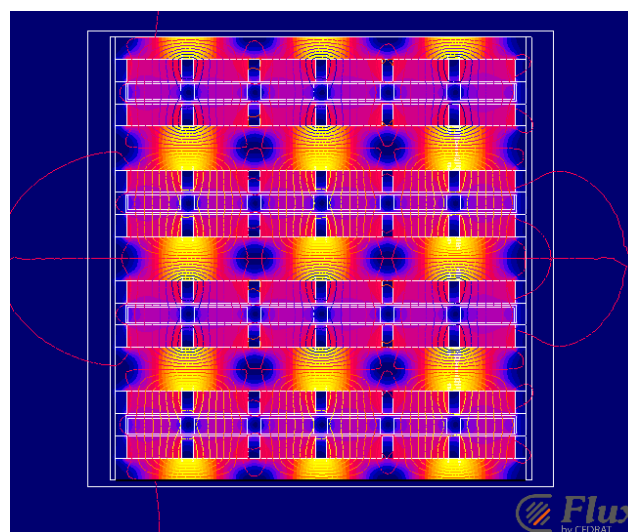


Figure 4. Magnetic finite element model built by Flux.

A simple flexure has been designed for the guiding system to endure the magnetic forces. In order to dimensioning this flexure, two simulations have been performed by finite element method (NX I-deas). On one hand, a fatigue simulation has been carried out to check the reliability of the flexure. The flexure has to be sufficiently stiff to assure that the displacement of the moving part is not too high. On the other hand, the dynamic behaviour of the flexure has been analysed. In this type of applications, the suspension mode of the actuator may occur at low frequency for not affecting the operating range of the active control. Therefore, this objective requires having a low stiffness without fatigue problems. Another option is to increase the moving mass, but it would require more space. Finally, the final design of the double flexure will be capable of enduring theoretically the forces and will have 17.5Hz suspension mode considering a 20kg moving mass.

Once the device is developed, the energy has to be provided to the actuator to generate sinusoidal current signals and obtain the required force. In this case the command voltage is converted onto current by ELMO TUBA servo amplifier. The digital controller is a National Instruments CompactRIO with a 50 kHz sample frequency.

#### **4.3. Validation of the inertial actuator**

The validation of the manufactured actuator (Figure 5) has been performed by 3 tests. The first test analyses the dynamic behaviour of the actuator and the linearity that it offers according to the force level. The second test studies the maximum force level that the actuator does. After these two tests, the thermal behaviour of the actuator is tested.

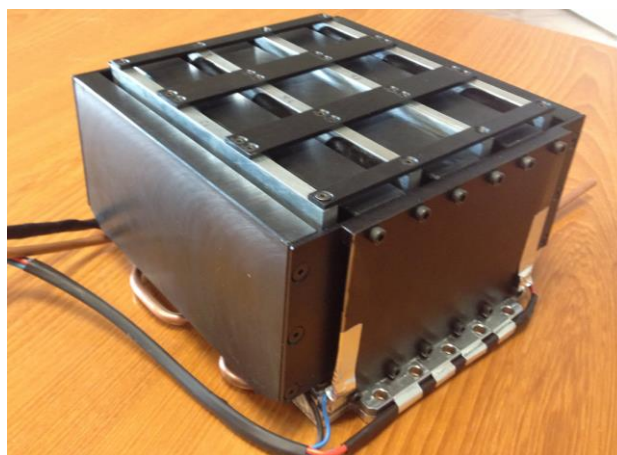


Figure 5. Electromagnetic actuator developed for the new spindle head.

In order to analyse the ratio between input voltage and force obtained, a chirp excitation signal with constant amplitude is commanded to the servo amplifier and force is measured by

means of a dynamometric plate. In this way the frequency response function (FRF) between the generated force and applied voltage input is obtained (Figure 6). The suspension frequency is located at 17.1 Hz, as predicted by the finite element method, and it has a 3.51 % damping ratio. On the other hand, the actuator shows a linear behaviour, since the relation  $N/V$  is maintained in a wide frequency band.

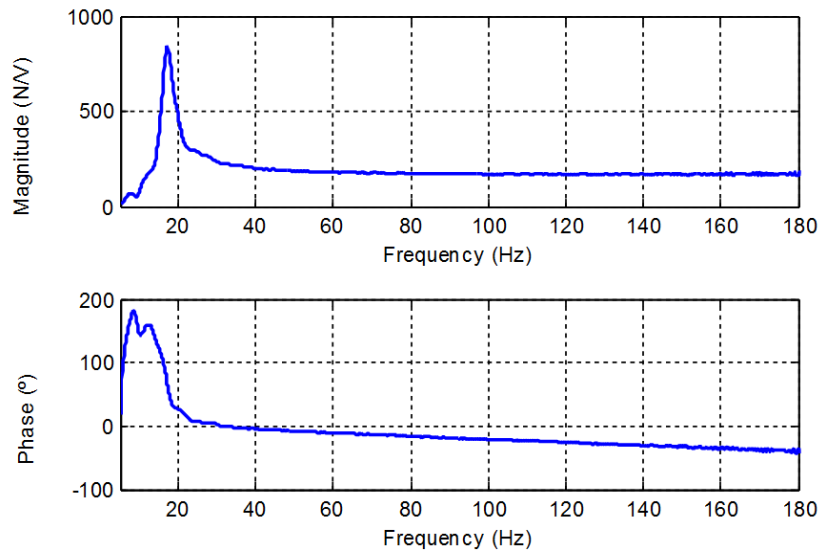


Figure 6. Force/Voltage ratio.

The force done by the actuator with different input amplitudes has been measured. A sinusoidal excitation has been introduced and as well as the previous test, the force has been measured by the dynamometric plate. In these tests, three frequencies close to the typical chatter frequencies have been selected.

Table 2: Measured force for different input voltage and frequencies.

Input voltage	Measured force		
	30 Hz	60 Hz	80 Hz
1 V	260 N	184 N	176 N
2 V	510 N	365 N	350 N
3 V	750 N	540 N	520 N
4 V	985 N	725 N	710 N
5 V	1200 N	900 N	875 N
6 V	1420 N	1070 N	1040 N

As shown in table 2, the actuator is capable of performing 1000N. Moreover, in some frequencies this capability is considerably increased due to the proximity of the suspension mode.

Finally, the evolution of the temperature inside the actuator has been analysed. The thermal test is a fundamental test for validating the actuator. When the current is introduced into the coils, they warm up due to their resistance. If this heating were very high, the permanent magnets could lose their properties and the force level would reduce considerably. In this actuator the maximum limit temperature has been established at 100°C, introducing a safety margin before the apparition of commented possible problems.

In the tests, the actuator has been excited with sinusoidal signals of 2 different amplitudes and the temperature evolution has been measured by temperature sensors. The frequency of the signals is set to 60Hz.

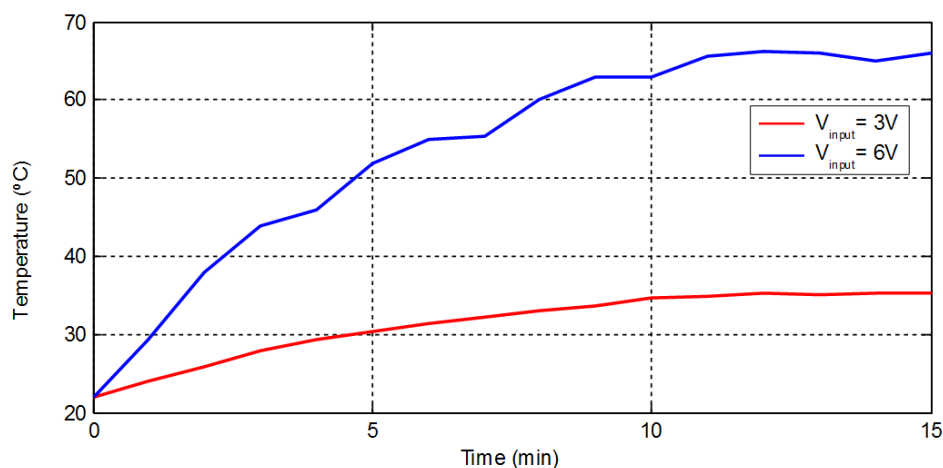


Figure 7. Thermal evolution of the actuator.

Figure 7 shows that the temperature is stabilized within the first 15 minutes and they are far from the limit. However, a water cooling system has been introduced to prevent the possible heating problems and thermic distortions. This systems works as a thermic barrier between the actuator and the spindle head.

#### 4.4. Final design

SORALUCE has experience introducing small electric motors in this spindle head. The idea was to redesign basically one of the parts to have more space to introduce the actuator and use the connections of the H210 spindle head to provide the required power to the inertial actuator and send the signal of the accelerometer to the control cabinet of the machine.

The controller (NI CompactRIO) and the power electronics (ELMO Tuba) have been integrated in the electronic cabinet of the machine and all cables have been connected. A new part was designed and manufactured in cast iron to place the new actuator and the accelerometer. Finally, the new spindle head was assembled and mounted in a SORALUCE FL6000 milling machine (Figure 8).

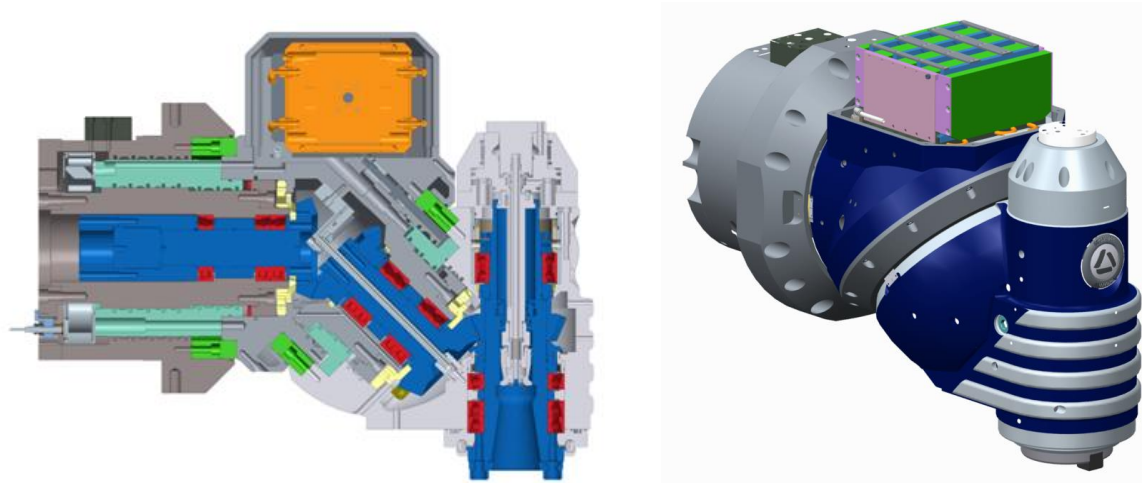


Figure 8. Integration of the inertial actuator over the new spindle speed.

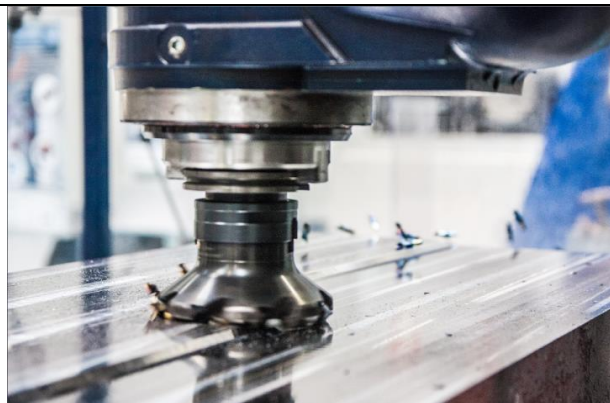
## 5. EXPERIMENTAL RESULTS

Finally, the stability of the machine with the new spindle speed has been verified by experimental cutting tests. Table 3 describes the cutting tool, the cutting conditions and the cutting coefficients employed in these tests. In this way, different ram overhangs have been studied and the improvement due to the integration of the inertial actuator is analysed in Figure 9.





Table 3. Description of cutting tool, cutting conditions and cutting coefficients.



---

**Cutting tool**

---

Reference	SANDVIK R245-125Q40-12M
Diameter	125 mm
Number of teeth	8
Z	
Inserts	SANDVIK R245-12
reference	T3 M-PM 4030
Lead angle $\kappa$	45°

---

**Cutting conditions**

---

Spindle Speed	440 rpm
Feed per tooth	0.15 mm/z
Radial engagement	100 mm (downmilling)
Workpiece material	F1140 Steel (C45)

---

**Cutting coefficients**

---

Specific tangential $K_{tc}$	1883 N/mm
Specific radial $K_{rc}$	0.38
Specific axial $K_{ac}$	-0.25

---



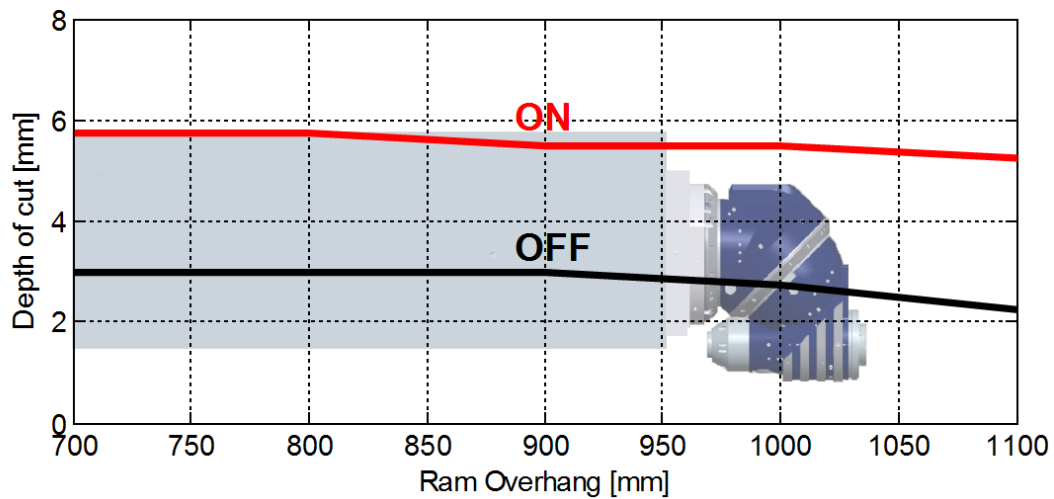


Figure 9: Stability improvement obtained by the new active spindle head.

The results show that the new spindle head with the active damper can double the cutting capability of the machine. The 1000 N actuator is capable of reducing the cutting forces from around 20000N (when the process is unstable) to around 7000N (when the process is stable). The effect of the actuator in machine vibrations is clear if the actuator is deactivated during the cutting process (Figure 10). The surface finishing shows the benefits of these results as well.

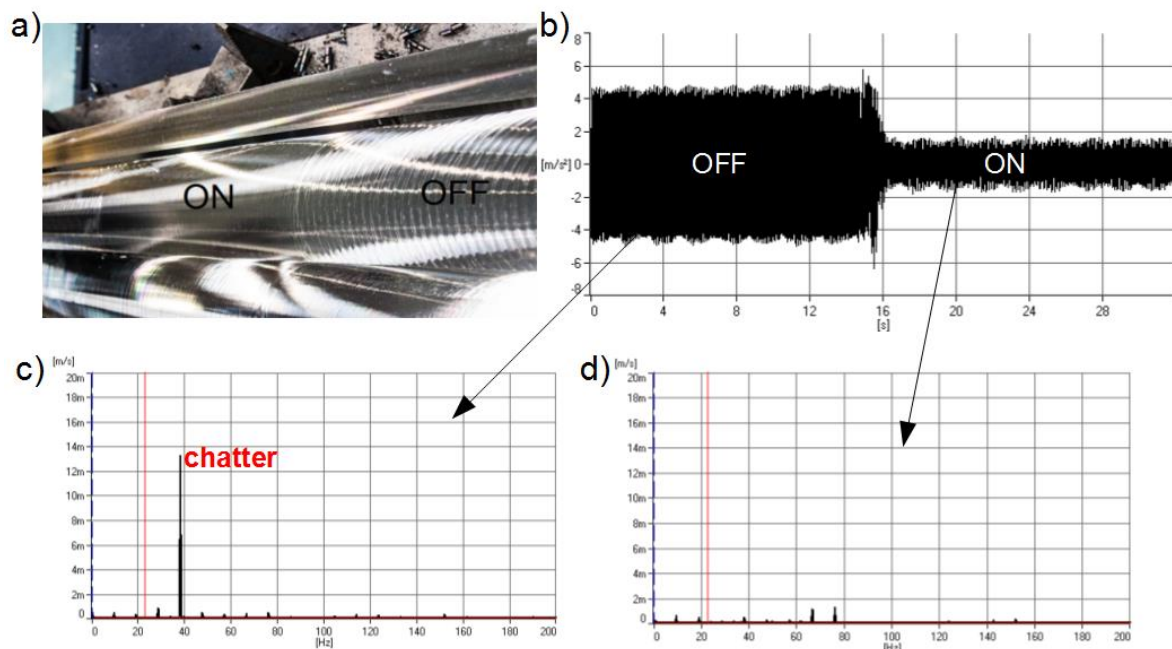


Figure 10: Cutting test (ram overhang 1000 mm, spindle speed of 440 rpm and 5.5 mm depth of cut), with and without active damping; a) Surface finishing; b) Time domain signal of machine acceleration; c) and d) Vibration spectrum with actuator deactivated and activated, respectively.



Nevertheless, it should be commented that when the maximum force is required during a long time, the actuator is heated. The performance of the actuator does not change while higher temperatures than 100°C are not achieved, so the cooling system employment is strongly recommended for these cases. In reference to mechanical behavior, it remains constant, but a revision of the guiding system is recommended after a long operating time. Sometimes, a dynamic response measurement of the actuator can be sufficient for proving that it remains fine.

## 5. CONCLUSIONS

The work presents the development of a new concept of spindle head for heavy roughing operations. It is based on the integration of an electromagnetic inertial actuator inside the spindle head and overcomes the flexibility limitations of this type of milling machines.

A mechatronic model, where the effect of inertial actuator control loop is simulated including the regenerative effect of milling process, is employed for evaluating different actuator designs. The model has provided the design guidelines for the active device and control parameters.

In this way, a new single axis electromagnetic actuator with 1000 N force capability has been developed and validated by different experimental tests. Then it has been completely integrated on the spindle head and SORALUCE FL6000 milling machine.

Finally, experimental cutting tests are presented, where the machine with the new integrated actuator has been able to double its cutting capability, achieving the design objective.

## ACKNOWLEDGEMENTS

This research was partially supported by the EU FP7 DYNXPERS (260073/FP7-2010-NMP-ICT-FoF) and by the PAINT ETORGAI project (ER-2012/00019) funded by the Basque Government.

## REFERENCES

1. **Altintas, Y. (2012).** “**Manufacturing Automation**”. *Cambridge University Press*, 2<sup>nd</sup> edition, New York, USA.
2. **Bediaga, I.; Zatarain, M.; Munoa, J.; Zelaieta, O. (2009).** “Analysis of Stability of Structural Modes in Milling Processes”. *5<sup>th</sup> CIRP International Conference and Exhibition on Design and Production of Machines and Dies/Molds*, Kusadasi, Turkey.
3. **Brecher, C.; Schulz, A. (2004).** “Active Auxiliary Mass Damper”. *Proceedings of ISMA 2004 – International Conference on Noise and Vibration Engineering*, Leuven, Belgium.



4. **Brecher, C.; Schulz, A.; Week, M. (2005).** “Electrohydraulic Active Damping System”. *CIRP Annals – Manufacturing Technology*, vol. 54, no. 1, pp. 389-392.
5. **Bies, D.A.; Yang, T.M. (1968).** “Hybrid Vibration Isolation System for Helicopters”. *Shock and Vibration Bulletin*.
6. **Bilbao-Guillerna, A.; Barrios, A.; Mancisidor, I.; Loix, N.; Munoa, J. (2010).** “Control laws for chatter suppression in milling using an inertial actuator”. *Proceedings of ISMA 2010 – International Conference on Noise and Vibration Engineering*, Leuven, Belgium.
7. **Bilbao-Guillerna, A.; Azpeitia, I.; Luyckx, S.; Loix, N.; Munoa, J. (2012).** “Low Frequency Chatter Suppression using an Inertial Actuator”. *9th CIRP International Conference on High Speed Machining*, San Sebastian, Spain.
8. **Claeyssen, F.; Magnac, G.; Sosnicki, O. (2008).** “Moving Iron Controllable Actuators”. *Actuator 2008 – 11<sup>th</sup> International Conference on New Actuators*, Bremen, Germany.
9. **Cowley, A.; Boyle, A. (1970).** “Active Dampers for Machine Tools”. *CIRP Annals – Manufacturing Technology*, vol. 18, no. 1, pp. 213-222.
10. **Den Hartog, J.P. (1985).** “Mechanical Vibrations”. *McGraw-Hill*, 4<sup>th</sup> edition, New York.
11. **Ehmann, C.; Nordmann, R. (2002).** “Low Cost Actuator for Active Damping of Large Machines”. *IFAC Conference on Mechatronics Systems*, Berkeley, USA.
12. **Huyanan, S.; Sims, N.D. (2007).** “Vibration Control Strategies for Proof-Mass Actuators”. *Journal of Vibration and Control*, vol. 13, no. 12, pp. 1785-1806.
13. **Loix, N.; Verschueren, J.P. (2004).** “Stand Alone Active Damping Device”. *Actuator 2004 – 9<sup>th</sup> International Conference on New Actuators*, Bremen, Germany.
14. **Mancisidor, I.; Zatarain, M.; Munoa, J.; Dombovari, Z. (2011).** “Fixed Boundaries Receptance Coupling Substructure Analysis for Tool Point Dynamics Prediction”. *Proceedings of 13<sup>th</sup> CIRP Conference on Modelling of Machining Operations*, Sintra-Lisbon, Portugal.
15. **Munoa, J.; Zatarain, M.; Bediaga, I.; Lizarralde, R. (2005).** “Optimization of Hard Material Roughing by means of Stability Model”. *Proceedings of the 8<sup>th</sup> CIRP Conference on Modelling of Machining Operations*, Chemnitz, Germany.
16. **Munoa, J.; Mancisidor, I.; Loix, N.; Uriarte, L.G.; Barcena, R.; Zatarain, M. (2013).** “Chatter suppression in ram type travelling column milling machines using a biaxial inertial actuator”. *CIRP Annals – Manufacturing Technology*, vol. 62, pp. 407-410.
17. **Sajedipour, D.; Behbahani, S.; Tabatabaei, S.M.K. (2010).** “Mechatronic Modeling and Control of a Lathe Machine Equipped with a MR Damper for Chatter Suppression”. *Proceedings of 8<sup>th</sup> IEEE International Conference on Control and Automation*, Xiamen, China.



18. **Sims, N.D. (2007).** "Vibration Absorbers for Chatter Suppression: A New Analytical Tuning Methodology". *Journal of Sound and Vibration*, vol. 301, pp. 592-607.
19. **Tlustý, J.; Polacek, M. (1957).** "Beispiele der behandlung der selbsterregten Schwingung der Werkzeugmaschinen FoKoMa". *Hanser Verlag*, Munchen, Germany, pp. 47-56.
20. **Tobias, S.A.; Fishwick, W. (1958).** "Theory of regenerative machine tool chatter". *The Engineer*, vol. 205.
21. **Yang, Y.; Munoa, J.; Altintas, Y. (2010).** "Optimization of Multiple Tuned Mass Dampers to Suppress Machine Tool Chatter". *International Journal of Machine Tools & Manufacture*, vol. 50, no. 9, pp. 834-852.
22. **Zaeh, M.F.; Waibel, M.; Baur, M. (2009).** "A Computational Approach to the Integration of Adaptronic Structures in Machine Tools". *Computational Structural Engineering*, pp. 1017-1028.





## INFLUENCE OF THE SPACER CLEARANCE ON THE DYNAMIC CHARACTERISTICS OF A SPINDLE TOOL

**Jui-Pin Hung**, *hungjp@ncut.edu.tw*, Institute of Precision Manufacturing, National Chin-Yi University of Technology, Taichung, Taiwan, R.O.C.

**Kung-Da Wu**, *ffi85236@hotmail.com*, Department of Mechanical Engineering, National Chin-Yi University of Technology, Taichung, Taiwan, R.O.C.

**Chun-Wei Lin**, *oo781114@yahoo.com.tw*, Department of Mechanical Engineering, National Chin-Yi University of Technology, Taichung, Taiwan, R.O.C.

**Bing-Jie Peng**, *posa.posa@msa.hinet.net*, POSA Precision Spindle Co., Ltd., Taichung, Taiwan, R.O.C.

### ABSTRACT

This study was aimed to identify the influence of the spacer clearance on the dynamic characteristics of a spindle tool through the finite element and experimental approaches. The correlations between the spacer clearance and modal parameters were first examined by conducting vibration tests on physical spindle units. Experimental measurements show that the dynamic stiffness and damping ratio associated with the dominating modes were affected to vary negatively with bearing preload. When the spacer clearance was adjusted from 2 to 32  $\mu\text{m}$ , the bearing preload increased from 73 to 636 N. This in turn enhances the bearing stiffness and natural frequency of the spindle unit, but the dynamic compliance was found to increase from 0.217 to 0.452  $\mu\text{m}/\text{N}$ . Besides, comparisons of simulations and experimental measurements clearly show the accuracy of the finite element modeling of a spindle tool unit presented in this study. It is believed that the developed analysis model associated with the experimental measurements on the preloading spacer can help the machine tool designer to accurately simulate and optimize the machining performance of the machine tool at design stage.

**Keywords:** Bearing preload, Dynamic compliance, Spacer clearance.

### 1. INTRODUCTION

The spindle tool system is the most important component for a machine tool executing the machining operation. For various application areas, a wide variety of spindles of different designs have been developed [Abele et al. 2010, Weck et al.1993]. In machine tool spindle

system, angular contact ball bearings are most commonly used due to their low-friction properties and ability to withstand external loads in both axial and radial directions. In addition, the bearing groups could be adequately preloaded to increase the rigidity of spindle unit. For the machining of large frames in auto industry, spindles were designed with high power and high rigidity, which requires a heavy preload applied to the bearings. However, several studies [Harsha et al. 2003, Cao et al. 2007, Alfares et al. 2003, Spiewak et al. 2001, Gunduz et al. 2012] have revealed that the dynamic behavior of a spindle tool system is significantly affected by the preload state of the supporting bearings.

Recently, in order to meet requirements for machining precision in airplane and semiconductor industries, spindles with high speed and high precision are developed. But occurrence of chatter vibration during machining was a fatal problem for a machine tool toward high performance. Studies [Tlustý et al. 1963, 1986, Koenisberger et al. 1967, Tobias et al. 1958] reported that chattering is caused by the dynamic interaction between the cutting tool and the workpiece during the chip generation process. Also the machining stability is greatly determined by the dynamic characteristics of the spindle tool system. Therefore, for the design of spindle with high machining performance, the machining stability over a wide operation range should be taken into consideration. Under this condition, the setting amount of preload to the bearings is of importance to ensure the spindle with enough dynamic stiffness and damping capability.

On the other hand, for different machining application with better efficiency, the dynamic performance should be adjusted by applying appropriate preload to the bearing groups during assemblage of a spindle unit. Basically, two preloading methods are commonly adopted, that is, constant pressure preload (spring preload) and position preload (fixed preload). The latter is the most common preload arrangement, which can be easily arranged using spacers with proper size between two bearing sets. As shown in Fig.1, the axial preload is determined by the clearances (a) between the inner spacer and inner ring of bearing and clearance (b) between the outer spacer and outer ring of bearing. Reducing the inner ring spacer can increase preload, while reducing the outer ring spacer decreases the preload. For example, as suggested in the bearing user guidelines [NSK Technologies Company 2003], if the preload of the 7914 angular contact bearing needed to be changed from light to medium, the inner ring spacer length would need to be reduced by adequate size, about several micrometers. However, as discussed in studies [Ozturk et al. 2012, Lin et al. 2007, Jiang et al. 2010], increasing the bearing preload can increase the bearing stiffness, but also reduces the damping ratio of the bearings. This would be unfavorable for suppression of the chattering in high speed machining. Although the effect of preload on natural frequencies and dynamic stiffness are demonstrated previously in the literatures,



quantifications of the effects with the adjustment of the preload on the modal parameters associated with spindle frequency responses is worthy of further study.

This study was aimed to identify how the changing of spacer clearance affects the dynamic characteristics of a spindle tool. In particular, we intended to examine the correlations between the spacer clearance and modal parameters by experimental approaches. The results are expected to provide a reference for tuning the dynamic characteristics of the spindle. In addition, we employed the finite element method to modeling the dynamic behavior of the spindle with different preloaded spacer. With experimental measurements as a validation, the proposed model can be applied for further development of the whole machine tool integrated with the spindle tool and the machine frame structure model. It is believed that the developed analysis model associated with the experimental measurements on the preloading spacer can help the machine tool designer to accurately simulate and optimize the machining performance of the machine tool at design stage.

## 2. EXPERIMENTAL APPROACH

### 2.1 Adjustment of bearing preload

In this study, the high speed spindle (DDS BT-30) was employed for tests, in which the front and rear bearing sets coded NSK-7008C were mounted in DBB arrangement for higher stiffness. Each spindle unit was respectively preloaded at different amounts by using the spacers with different clearance, as shown in Fig. 2. The clearance is determined by the difference of axial length between the outer and inner spacers, irrespective to the clearance in radial direction. The spacer clearance can be set at different amount to preload the bearings in axial direction at different amounts. Here, according to the manufacturer, six inner spacers were made with a clearance of 2, 7, 12, 17, 22, 27 and 32  $\mu\text{m}$ , differed by 5  $\mu\text{m}$ , with respect to the outer spacer, They were respectively assembled in the spindle for test.

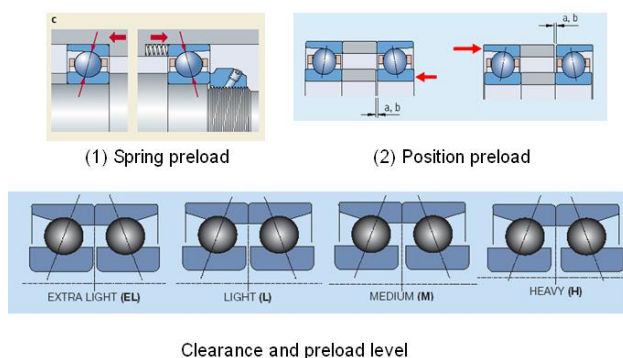


Fig.2 Bearing spacers and configuration of vibration test.



## 2.2 Experimental configuration

Fig. 2 illustrates the experimental configuration of the spindle unit with a tool holder (BT30). Each spindle was assembled with specific spacer between the front and rear bearing groups. It was then suspended by two wire ropes for test. The accelerometer was mounted on the tool holder tail to measure the vibration signal excited by the impact hammer at the opposite side of tool holder. The dynamic response was then extracted from the recorded FFT spectrum. The modal parameters such as damping ratio and dynamic stiffness associated with the dominant vibration modes were extracted from the measured FRFs.

## 2.3 Dynamic characteristics of spindle unit

The measured vibration responses of the spindle units with different spacer clearances are illustrated in Fig.3 for comparison, which are expressed in terms of the compliance varying with frequency. It is found from Fig. 3 that the spindle tool with standard preload behaves three fundamental modes at about 780, 1350 and 2751 Hz. The three modes could be identified as the bending vibrations of the spindle shaft according to finite element modeling of the spindle system in later section. In addition, the first and second modes show great vibration amplitude, which can be considered as the possible modes dominating the compliance of the spindle tool. From this figure, we can also find the difference in the vibration frequency and dynamic compliance among the spindles with different spacer clearances. This clearly demonstrates the influence of the bearing preload produced by the spacer with different clearances on the dynamic characteristics of the spindle.

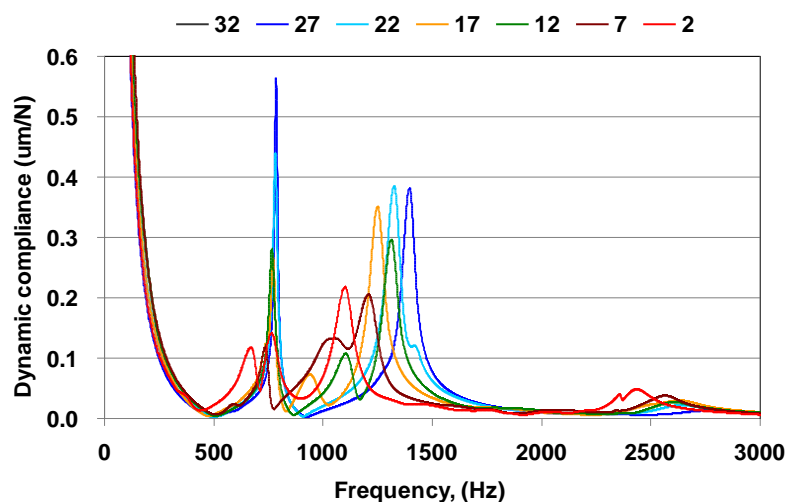


Fig. 3 Frequency response functions (FRFs) measured at end of tool holder for spindles with different preloads, which were produced by different spacers.

## 2.4 Variations of modal parameters

The modal damping ratios and dynamic compliances corresponding to the four fundamental modes were extracted from the measured FRFs. The influence of the spacer clearance on the modal frequency, damping and compliance are demonstrated in Fig. 4, 5 and 6 respectively. Fig. 4 shows that the natural frequencies of the spindle shaft increase with the increasing of the spacer clearance from 2  $\mu\text{m}$  to 32  $\mu\text{m}$ . Significant positive correlations are found for the four vibration modes between these different spindles. This also implies that the spacers with larger clearance produced more preload to bearings and hence increased the natural frequencies of the spindle. To the contrary, a small clearance reduced the bearing preload and the spindle natural frequency. Fig. 5 shows that the modal damping ratios associated with the first two modes decrease with the adjustment of the spacer from small clearance to larger clearance, with significant correlations between them. However, the modal damping ratios of third mode was affected to decrease with the increasing bearing preload. Fig. 6 shows the variations of the dynamic compliance with the change of spacer clearance. As can be seen in Fig.6, the compliances occurring at mode 1 and 2 are positively affected to increase with the increasing spacer clearance. However, the spacer clearance shows a negative influence on the modal compliance of mode 3. This can be ascribed to the fact that the larger spacer clearance in spindle bearing groups produces greater preload to the bearings, but it also lessens the damping ratio of the rolling interface, which in turn reduces the dynamic stiffness of the spindle tool.

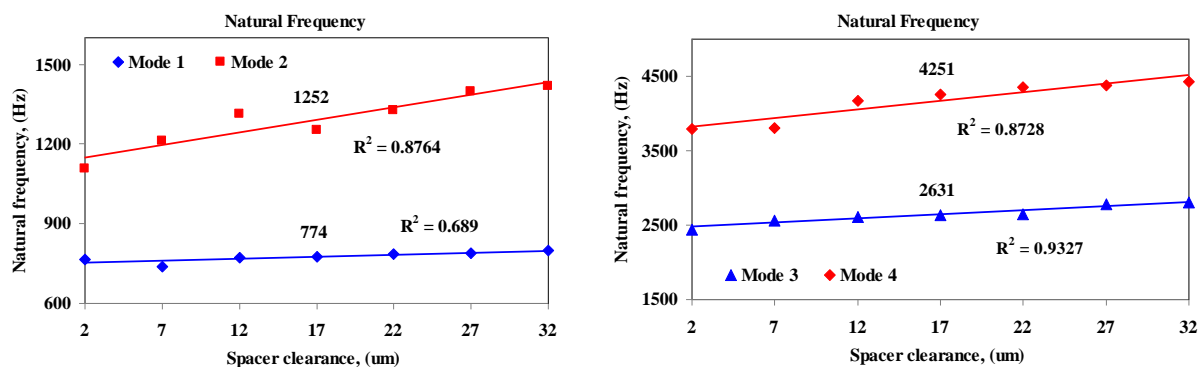


Fig. 4 Variations of the natural frequencies of spindle with the change of spacer clearance.

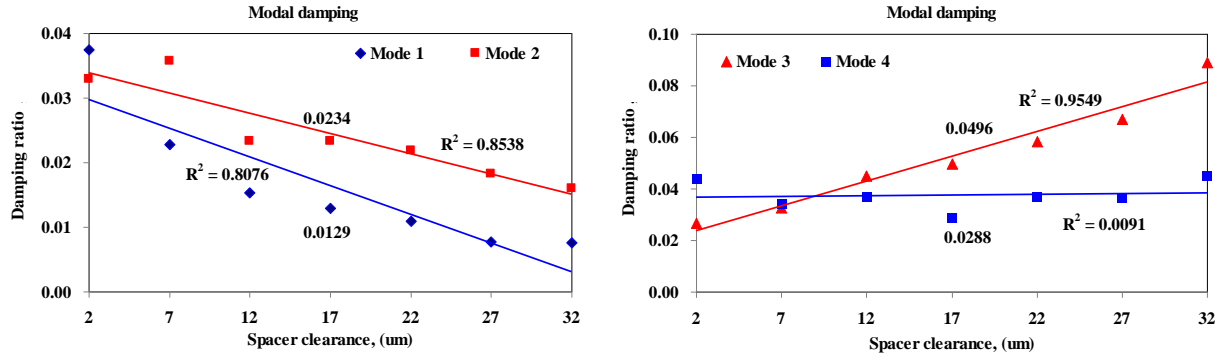


Fig. 5 Variations of the modal damping ratios with the change of spacer clearance.

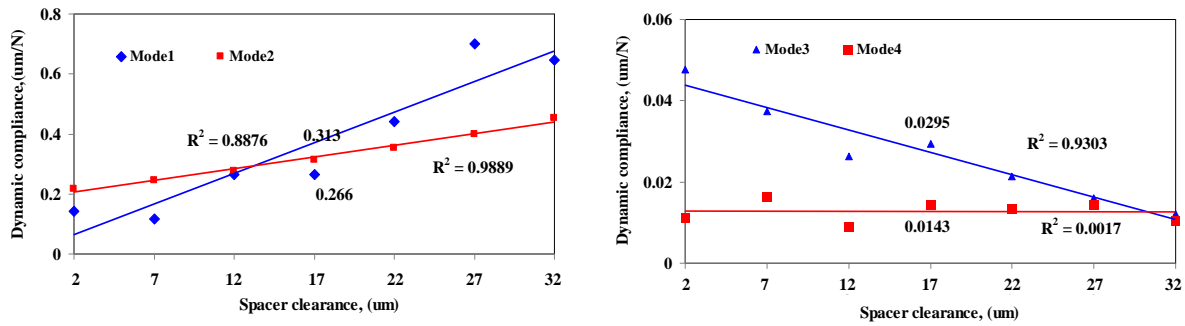


Fig. 6 Variations of the tool dynamic compliances with the change of spacer clearance.

### 3. FINITE ELEMENT MODELING

#### 3.1 Contact stiffness of ball bearing

In a spindle tool unit, there exist rolling interfaces in bearing between rolling balls and raceways, which primarily contributes to the dynamic characteristics of spindle tool. Therefore, modeling of the rolling interface is the prerequisite for the creation of the analysis model and for accurate evaluation of the dynamic characteristics of the spindle tool.

Fig. 7 (a) shows a typical angular contact ball bearing used for high speed spindle unit, which can provide the capabilities to withstand external loads from both radial and axial directions when it is properly preloaded. The contact force between the rolling ball and the raceway can be related to the local deformation of contact point by the Hertzian expression [Johnson 1985] as follows:

$$Q = K_h \delta^{3/2} \quad (1)$$

where  $Q$  denotes the contact force and  $\delta$  is the elastic deformation at the contact point.  $K_h$  represents the Hertz constant, which is determined by the contact geometry of the ball groove or raceway and the material properties of the contacting components. Details are

available in the literature [Brewer et al. 1997]. The normal stiffness at a specific preload can then be obtained as

$$K_n = \frac{dQ}{d\delta} = \frac{3}{2} K_h \delta^{1/2} = \frac{3}{2} K_h^{2/3} Q^{1/3} \quad (2)$$

$$Q = F_a / N \cdot \sin \alpha \quad (3)$$

It is noticed that the contact stiffness in the normal direction varies nonlinearly with the contact force  $Q$ . While the contact force, as given in Eq (3), is essentially determined by the axial preload acting on the bearings and the contact angle of the rolling balls to the ball groove.

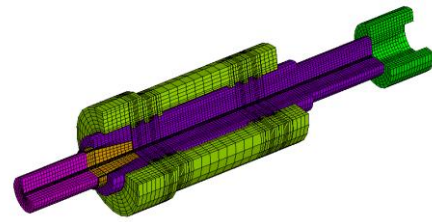
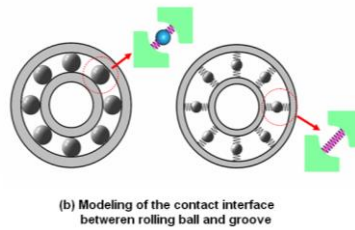
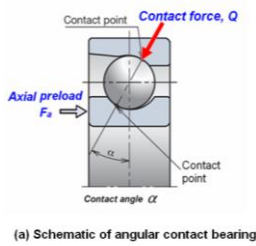


Fig. 7 Typical angular contact ball bearing.

Fig. 8 Finite element model of spindle tool unit.

### 3.2 FE model of spindle unit

To investigate the dynamic behavior of the spindle, a solid model of the spindle bearing system including the rotating shaft and the spindle housing was created and meshed with hexahedron elements (see Fig. 8). To reduce the complexity in model creation and mesh generation of the motion components, such as the ball bearing, the contact configuration between rolling ball and the raceway is modeled as two-point contact mode. For the supporting bearings, the outer and inner rings were respectively simplified as a part of the spindle shaft and housing in geometry, respectively. The inner and outer rings are directly connected using a series of spring elements by neglecting the effect of rolling balls, as shown in Fig. 7. For finite element analysis, all the metal components have the following material properties of carbon steel: elastic modulus  $E = 200\text{GPa}$ , Poisson's ratio  $\mu = 0.3$ , and density  $\rho = 7800\text{Kg/m}^3$ .

For subsequent analysis, the finite element model was validated by comparing the results of the modal analysis with the experimental measurements. For this, the vibration test was conducted on the physical spindle unit, which was rated at standard preload of 290N by assembling a standard spacer of clearance of  $17\mu\text{m}$  between bearing groups according to

the technology guidelines [NSK 2003]. In the finite element model of the tested spindle, the overall contact stiffness of each bearing was calculated as 264 N/ $\mu$ m according the equations (1)-(3). The stiffness of each bearing is distributed on the spring elements circumferentially surrounding the spindle shaft created in the FE model. For other spindle units assembled with different spacer clearances, the preloads produced in bearings were estimated following the method proposed in [NSK 2003], and the overall stiffness of each bearing preloaded at different amount was then calculated and listed in Table 1.

Table 1 Preload and contact stiffness of bearing under different spacer clearances.

Clearance ( $\mu$ m)	2	7	12	17	22	27	32
Preload (N)	73	132	204	290	391	506	636
Contact angle (degree)	15.53	15.77	16.01	16.25	16.5	16.75	17.00
Contact stiffness (N/ $\mu$ m)	192	224	244	264	284	304	336

### 3.3 Dynamic characteristics of the spindle unit

The fundamental vibration modes of the spindle unit were assessed under free-free boundary conditions, as depicted in Fig.9. It is found that the fundamental modes are associated with the bending vibrations of the spindle shaft. In addition, the bending vibration induces a maximum displacement at the spindle tail, which is likely to affect the machining accuracy. The natural frequencies corresponding to the first four vibration modes are 771, 1321, 2751 and 4079 Hz, respectively, agreeing well with the experimental measurements (778, 1315, 2669 and 4230 Hz).

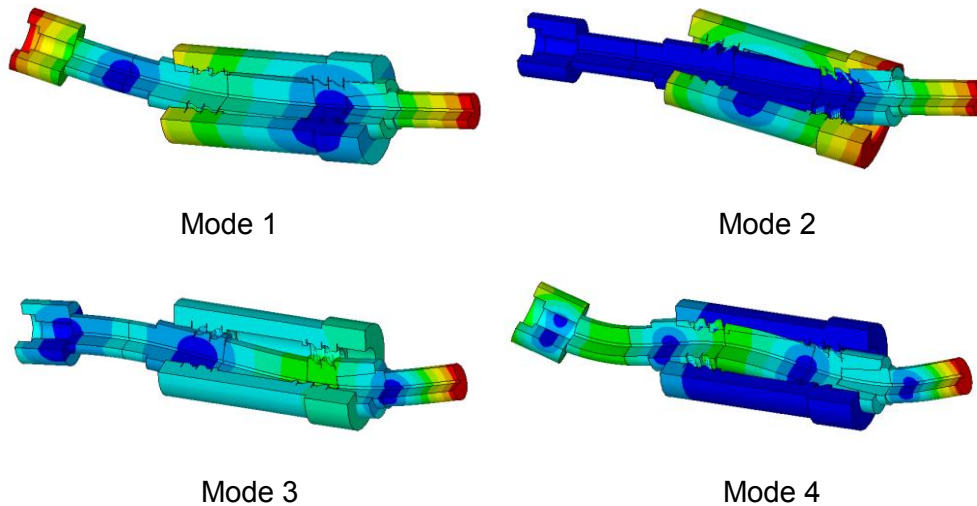


Fig. 9 Fundamental vibration modes of spindle tool unit.

The harmonic analysis was performed to assess the dynamic response of the spindle tool under unit force at the tool holder. The frequency response function predicted at end of tool holder was also illustrated in Fig. 10 for the comparison with the measurement, which clearly verifies that the spindle tool model behaves a dynamic behavior comparable to that measured in physical spindle. Again, the spindle unit was found to become more compliant when the first and second bending modes were excited. For spindle with spacer clearance of 22 $\mu\text{m}$ , the dynamic compliance at second mode was predicted as 0.331  $\mu\text{m}/\text{N}$  at frequency of 1346 Hz, while the measured value was 0.354  $\mu\text{m}/\text{N}$  at 1327Hz. For spindle with spacer clearance of 12 $\mu\text{m}$ , the corresponding dynamic compliance was predicted as 0.331  $\mu\text{m}/\text{N}$  at frequency of 1346 Hz and was measured as 0.27  $\mu\text{m}/\text{N}$  at 1314 Hz.

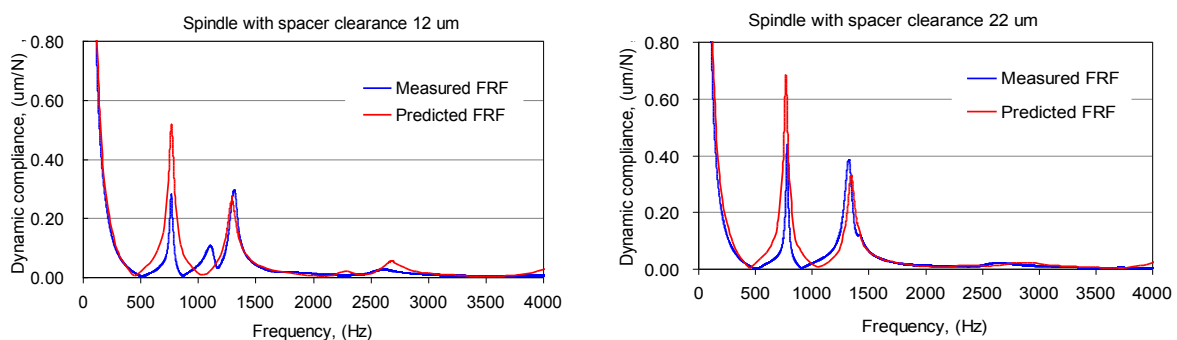


Fig.10 Comparisons of the predicted and measured frequency response functions of spindle with different preloads.

Table 2 summarizes the predicted and measured compliances for spindle with various preloads. It is noticed that the differences between the predicted results and experimental measurements are approximately around 6%. This addresses that the proposed analysis model of the spindle can appropriately predict the dynamic behavior of the spindle tool system. The influence of the bearing preload also can be accurately analyzed with the modeling of the rolling interface into the solid finite element model. However, it is worthy of notice that the predicted values are lower than the measured values. This can be ascribed to fact that in the analysis model the tool holder was assumed to be perfectly mounted in the spindle tail, which indeed overestimate the stiffness of the spindle tool unit. According to the study [Cao et al. 2003], the interface characteristics between spindle nose and tool holder also plays an important role on the dynamic behavior of the spindle tool system. To be a more realistic model for further development of the whole machine tooling system, the proposed spindle tool model will be adequately modified with the introduction of the tool holder interface and then integrated with the machine frame structure model.

Table 2 Comparisons of the 2<sup>nd</sup> modal compliances predicted by finite element analysis and experimental measurements.

Clearance ( $\mu\text{m}$ )	2	7	12	17	22	27	32
Measured compliance	0.452	0.400	0.354	0.313	0.277	0.245	0.217
(frequency)	1419	1397	1327	1252	1314	1210	1108
Predicted compliance	0.425	0.375	0.331	0.292	0.259	0.231	0.211
(frequency)	1401	1369	1346	1321	1293	1261	1203

#### 4. CONCLUSIONS

The study has investigated the influence of the bearing preload on the dynamic characteristics of a spindle tool. The bearing preload was produced by the spacer with proper clearance mounted between the front and rear bearings in spindle. The vibration tests were conducted on the spindle unit with different spacers. The modal parameters such as the frequency, damping ratio and compliance were extracted from the measured frequency response functions, which were correlated to the spacer clearance. On the other hand, the finite element model of the spindle was created to predict the dynamic characteristics of the spindle tool system. Based on the results, the following conclusions are presented:

1. The adjustment of spacer clearance from a smaller to larger value produce a negative influence on the dynamic stiffness and damping ratio associated with the dominated



modes of a spindle tool. The bearing preloads and modal damping ratios are related to the spacer clearance in a nonlinear way.

2. A spacer with smaller clearance produces a lower bearing stiffness, but it increases the damping ability and the dynamic stiffness of the dominated vibration mode, which may enable the spindle tool to be favorable for high speed and precision machining with stability. To the contrary, a spacer with larger clearance can increase the bearing stiffness and the rigidity of the spindle tool, which is appropriate to application in heavy machining.
3. The influence of the spacer clearance on the dynamic characteristics of the spindle can also be investigated through the finite element model proposed in this study. The prediction accuracy is determined by the modeling of the rolling interface of ball bearings in spindles, in which the bearing preload and contact stiffness can be calculated based on the Hertz contact theory and the results of the vibration tests of a physical spindle.

**ACKNOWLEDGMENT:** The authors gratefully acknowledge the supports of the National Science Council in Taiwan through project number NSC101-2622-E-167-022-CC3 and POSA Precision Spindle Co., Ltd.

## REFERENCE

1. **Abele, E., Altintas, Y., Brecher, C., (2010)**, "Machine Tool Spindle Units", CIRP Annals-Manufacturing Technology, Vol.59, No.2, pp 781-802.
2. **Weck, M., and Koch, A., (1993)**, "Spindle-Bearing Systems for High-Speed Applications in Machine Tools", CIRP Annals-Manufacturing Technology, Vol.42, No.1, pp 445-448.
3. **Harsha, S. P., Sandeep, L., Prakash, R. E., (2003)**, "Effects of Preload and Number of Balls on Nonlinear Dynamic Behaviors of Ball Bearing System", International Journal of Nonlinear Science and Numerical Simulation, Vol.4, No.3, pp 265-278.
4. **Cao, Y., Altintas, Y., (2007)**, "Modeling of Spindle-Bearing and Machine Tool Systems for Virtual Simulation of Milling Operations", International Journal of Machine Tools and Manufacturing, Vol.47, No.9, pp 1342-1350.
5. **Alfares, M. A., Elsharkawy, A. A., (2003)**, "Effects of Axial Preloading of Angular Contact Ball Bearings on the Dynamics of a Grinding Machine Spindle System", Journal of Materials Processing Technology, Vol.136, No.1-3, pp 48-59.
6. **Spiewak, S.A., and Nickel, T., (2001)**, "Vibration Based Preload Estimation in Machine Tool Spindles", International Journal of Machine Tools & Manufacture,





Vol.41, No.4, pp 567-588.

7. **Gunduz, A., Dreyer, J. T., and Singh, R., (2012)**, "Effect of Bearing Preloads on the Modal Characteristics of a Shaft-Bearing Assembly: Experiments on Double Row Angular Contact Ball Bearings", *Mechanical Systems and Signal Processing*, Vol.31, pp 176-195.
8. **Tlustý, J., and Poláček, M., (1963)**, "The Stability of Machine Tools Against Self-Excited Vibrations in Machining", *International research in production engineering*, ASME, pp 465-474.
9. **Tlustý, J., (1986)**, "Dynamics of High-Speed Milling", *Trans. ASME, Journal of Engineering for Industry*, Vol. 108, No. 2, pp 59-67.
10. **Koenisberger, F., and Tlustý, J., (1967)**, "Machine Tool Structures—Vol. I: Stability Against Chatter", Pergamon Press.
11. **Tobias, S.A., and Fishwick, W., (1958)**, "The Chatter of Lathe Tools under Orthogonal Cutting Conditions", *Trans. ASME, Journal of Engineering for Industry*, Vol.80, pp 1079-1088.
12. **NSK Technologies Company. (2003)**, "NSK super precision bearings Part 5: Technical guides", <http://www.nsk.com/products/spb/>
13. **Ozturk, E., Kumar, U., Turner, S., Schmitz, T., (2012)**, "Investigation of Spindle Bearing Preload on Dynamics and Stability Limit in Milling", *CIRP Annals-Manufacturing Technology*, Vol. 61, No.1, pp 343-346.
14. **Lin, C.W., and Tu, J.F., (2007)**, "Model-Based Design of Motorized Spindle Systems to Improve Dynamic Performance at High Speeds", *Journal of Manufacturing Processes*, Vol.9, No.2, pp 94-108.
15. **Jiang, S., and Mao, H., (2010)**, "Investigation of Variable Optimum Preload for a Machine Tool Spindle", *International Journal of Machine Tools and Manufacture*, Vol.50, No.1, pp 19-28.
16. **Johnson, K.J., (1985)**, "Contact Mechanics", Cambridge University Press.
17. **Brewe, D.E, and Hamrock, B.J., (1997)**, "Simplified Solution for Elliptical-Contact Deformation between Two Elastic Solid". *Journal of Lubrication Technology*, Vol.99, pp 485-487.



## COMPARISON OF DAMPING PROPERTIES OF SPINDLE BEARINGS

**C. BRECHER**, *c.brecher@wzl.rwth-aachen.de* Laboratory for Machine Tools and Production Engineering, 52074, Aachen, Germany

**M. FEY**, *m.fey@wzl.rwth-aachen.de* Laboratory for Machine Tools and Production Engineering, 52074, Aachen, Germany

**R. HABERMANN**, *r.habermann@wzl.rwth-aachen.de* Laboratory for Machine Tools and Production Engineering, 52074, Aachen, Germany

### ABSTRACT

The calculation of frequency response functions for machine tools helps to predict the dynamic behavior during the design phase of machine tools. While the calculation of static stiffness and eigen frequencies can be considered state of the art, the prediction of damping ratios is not possible without detailed damping models. This paper determines and compares local damping properties of spindle bearing packages of a single size but different physical properties for three preload classes. A simulation model is used to isolate the test bench damping. The validity of two different damping models is studied under changed dynamic boundary conditions.

**Keywords:** Manuscripts, Preparation guide

### 1. INTRODUCTION

The demand for machining of high strength materials requires an in-depth consideration of the dynamic behavior of machine tools. The overall productivity is in many cases not limited by the performance of the machine tool, but by regenerative chatter vibrations [Quintana, 2011]. Chatter vibration are caused by an interaction of process forces and the dynamic behavior of the machine tool structure [Altintas, 2004]. To anticipate the dynamic behavior in the design phase in a feasible way, simulation models have to be enabled to predict the frequency response function (FRF). While the calculation itself is considered state of the art and stiffness and inertia parameters of materials and machine elements in the force flux are obtainable from the manufacturers, damping parameters of machine elements are often unknown [Altintas, 2005]. The focus of this paper thus lies in the identification of damping parameters of spindle bearing packages as an important source of damping in a spindle and thus of the whole machine tool structure.

## State of the art

The damping of ball bearings in general, from which spindle bearings are a subcategory, is being analyzed by different authors since the 1980s. Stone gave a summary of the state of art in the 1980s and described the influence of temperature, preload and rotational speed [Stone, 1982]. Ophey researched the influence of lubricants on the stiffness and damping properties of angular contact ball bearings, which are predecessors of spindle bearings, under the influence of rotational speed [Ophey, 1986]. In the 1990s, Dietl and Zeilinger examined different ball bearings, among other angular contact ball bearings. Higher computational power enabled them to use the finite-elements-analysis (FEA) instead of analytical models used before to determine local damping parameters [Zeilinger, 1995], [Dietl, 1997].

Wijnant analyzed the stiffness and damping for elastohydrodynamic contacts based on the evaluation of the dynamic response using a full dynamic simulation of contact forces [Wijnant, 1998]. These results were applied and validated on ball bearings by Wensing [Wensing, 1998].

A recent study from Jacobs investigated the stiffness, damping and electrical conductivity properties of a deep groove ball bearing. He used an analytical method to extract local bearing properties, and additionally used a reference dummy to validate the matched stiffness parameter [Jacobs, 2014]. A comparison of the test benches of the mentioned authors are shown in Figure 1.

While many bearing types were investigated in the past, this was only done for individual bearing types. Every researcher used his own test bench and his own method, which makes a comparison of the different damping properties difficult. Spindle bearings in particular are high precision bearings made specifically for machine tool spindles and are available in different configurations. The stiffness of these bearings is well analyzed and understood, but their damping behavior is mostly unknown. Therefore in this paper five different spindle bearing packages of the same size but different physical properties are examined for three preload classes in the same test bench and with the same methodology.

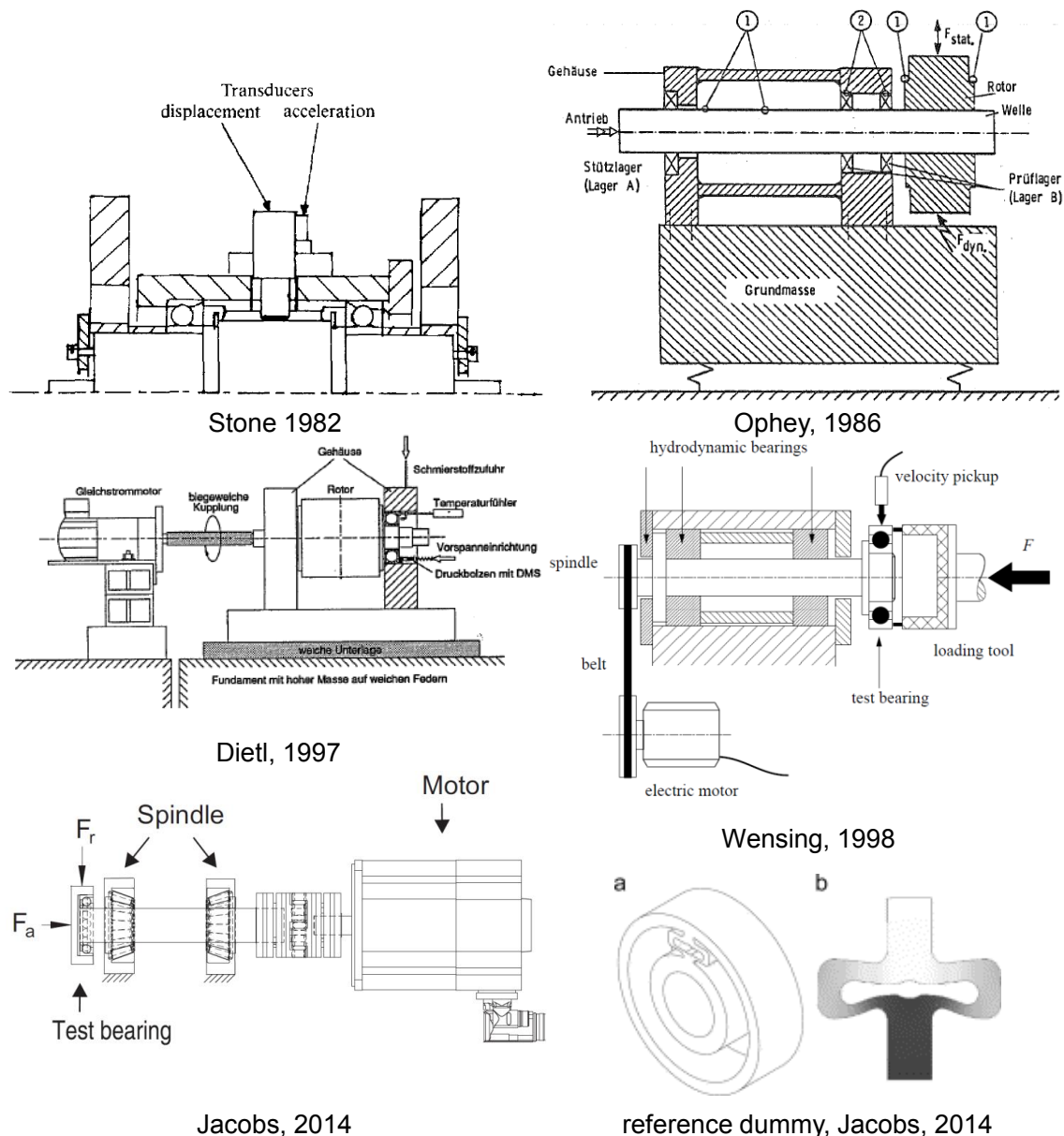


Figure 1. Test bench comparison.

## Methodology

Mechanical damping manifests only in relative motion, so the measurement of damping effects has to be conducted under dynamic loading. This is achieved by exciting a resonant system and recording both the excitation and the response of the system. For example, in order to measure the damping properties of a machine element directly, the excitation force and the displacement response directly at the component can be captured. [VDI, 2005]

Because bearings have to be preloaded in axial and radial direction and thus need to be assembled, a direct measurement cannot be achieved easily. To overcome the difficulties of a direct measurement, an indirect approach is often used in research. With this approach, the test object, in this case the spindle bearing package, is used as the structural weakest link in an otherwise much stiffer system. The test bench is then excited with an external force

and responses with a free oscillation. To prevent an influence of the surroundings, the system has to be decoupled by means of a mechanical low pass. This can be achieved by mounting the test bench on soft springs [VDI, 2005].

Through the design of the test bench, its eigen modes can be configured in a way that the resulting FRF shows clearly separated resonance peaks and the corresponding mode shapes are characterized mainly by rigid body motions, with the spindle bearings being stressed by the oscillations. The FRF can then be analyzed to determine the damping ratio of the resonance peaks, e.g. with the 3db-method. The advantage of this approach is that the bearings are mounted exactly as they are in a main spindle. A significant fraction of the oscillation takes place in the bearings, so they act as main source of damping.

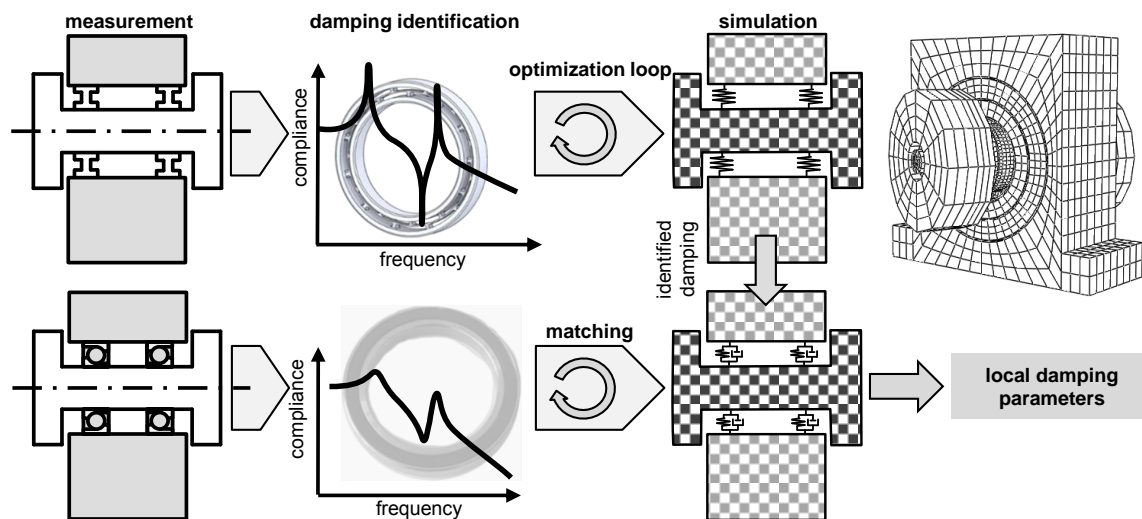


Figure 2. Methodology of the science group.

To extract local damping properties from the global damping ratio, the method shown in Figure 2 is used. In a first step shown in the upper half of the figure, the test bench is fitted with reference dummies. These dummies have the same interfaces and a similar stiffness compared to the actual bearings, but are manufactured as a solid steel part. Consequently they exhibit only material damping, which is small in comparison to the damping of the spindle bearings and thus can be neglected. The eigen frequencies and mode shapes however are similar to these of the test bench with bearings, so the measurements are comparable [Brecher, 2012a].

The measurement of the reference dummy system results in global damping values for the test bench structure, which are used as optimization criteria to model the damping effects for a simulation model of the test bench. Parameters in this test bench are the material damping and the gap damping between the different structural parts. Because these

parameters remain constant when using spindle bearings, the extrinsic damping of the test bench is considered in the simulation model.

The measurement of the bearings in the test bench, shown in Figure 2 in the lower half, again yields global damping ratios. The simulation model is used to extract local damping parameters. Different model abstractions can be used as long as they use linear spring-damper combinations. An optimization loop is used to match the calculated global damping ratios to the measured ones.

## **2. Test bench and measurements**

In this chapter the design of the test bench is described and measurements of the reference dummy as well as measurements with different bearing setups are presented.

### **Design of the test bench**

The design of the test bench has to fulfill different criterions: It must incorporate the bearings in a way that they have their required preload, its structure must allow defined oscillations and its mass distribution has to be chosen in accordance to the stiffness of the bearings to enable eigen frequencies in a practical and meaningful range. Up to about 30 Hz rigid body movements of the whole test bench on its mounting springs take place. Above about 1500 Hz structural eigen modes in which the parts itself are oscillating are found. Therefore the test bench is designed in a way that the resulting eigen frequencies of the system are located in a target range between 100 Hz and 1000 Hz to ensure unaffected measurements [VDI, 2005]. The spindle package is assembled between two modules sharing a common center of masses. One module consists of a shaft with two masses, the other module is the pillow block with an adapter bushing, shown in Figure 3. The masses on the shaft are used to adjust the frequency range.

Additional spacers separate the bearings. The bearing package is tightened in axial direction with a locknut, ensuring that the axial preload, which depends on the fit of the spacers, is achieved. Four springs decouple the test bench from the environment. The z-axis is in direction of the shaft and is called axial, the x-axis is horizontal while the y-axis is vertical. Both axes are in radial direction in relation to the shaft.

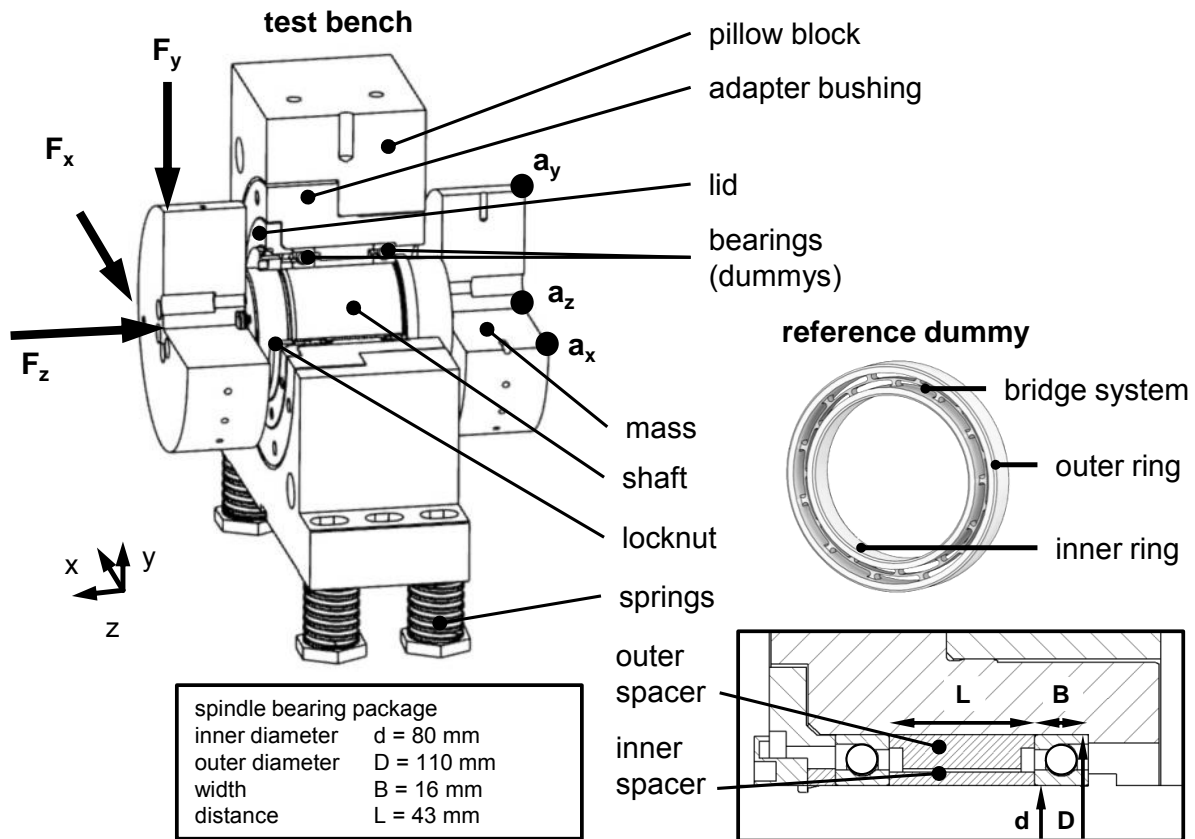


Figure 3. Test bench with reference dummies.

The used bearings have the dimensions shown in Figure 3. Their designation is 71916C for a contact angle of  $15^\circ$  and 71916D for a contact angle of  $25^\circ$  [DIN 628-6, 1993]. The norm does not define the inner structure of the bearing, and different configurations are available. There are two sizes of the rolling elements available, hereinafter called small (diameter ca. 6.5 mm) and large (diameter ca. 9.5 mm). They are available as steel or ceramic parts. Further selection have to be made, for example the used lubricant (oil or grease) and the presence of lip seals. The employed bearings are all grease lubricated with lip seals keeping the grease contained. Only the bearings with large steel rolling elements have no lip seals in order to demonstrate the lowest damping properties possible.

The reference dummy has inner and outer ring similar to the original bearings. A bridge system between these rings acts as a static connection, its stiffness is adjusted by the placement of connecting struts.

### Measurement of the reference dummy and dynamic of the test bench

A measurement with reference dummies, shown in Figure 4, shows the basic dynamic behavior of the test bench. The test bench is excited with a manual impact hammer at the points shown in Figure 3 marked with F and its acceleration is measured with piezo transducers, marked with a. In the frequency range between 100 Hz and 1000 Hz, there are



five distinct eigen modes, resulting in resonance peaks in the FRF. Below 100 Hz there are eigen modes caused by the mounting springs. The five eigen modes are dominated by rigid body motions of the two modules with the reference dummies acting as springs. One mode oscillates in the z-direction, characterized by an axial movement of the shaft, called mode Z. The other four modes are distributed in two modes in x- and two modes in y-direction. The lower modes X1 and Y1 manifest as a tilting of the shaft in each direction while the upper modes X2 and Y2 appear as a radial translation of the shaft. So X2, Y2 and Z are purely translational oscillations, while the lower radial modes X1 and Y1 combine rotational and translational movements.

Because the resonance peaks are clearly separated and exhibit very linear behavior, the 3db method is used to identify the damping ratios. All modes have very low damping ratios, a spread between 0.0013 and 0.0024 with only minor deviation between individual measurements is found. In a preliminary paper, different mountings were examined, but their influences were negligible [Brecher, 2012b].

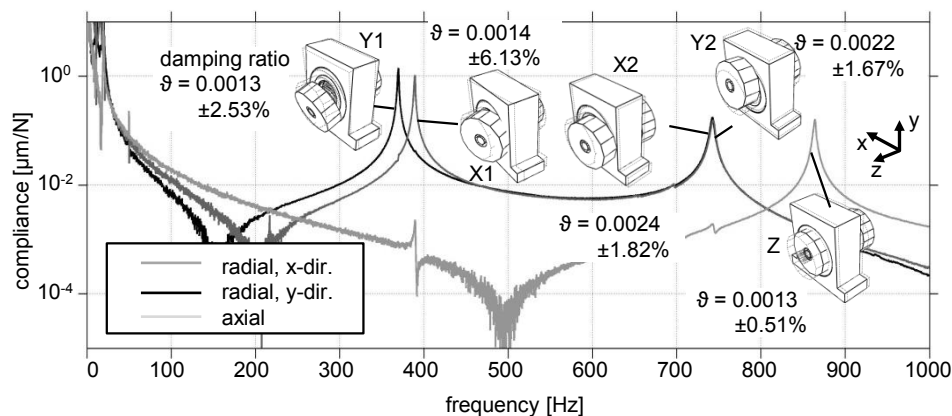


Figure 4. Measurement of the test bench with reference dummies.

### Measurements of the spindle bearings

The measurements of the spindle bearings are realized by assembling the spindle bearings instead of the reference dummies in the test bench, using otherwise the same components. To adjust the axial preload of the spindle bearings, they are mounted on the shaft with specific spacers and a specific torque on the locknut. The clearance of the spacers is calculated before depending on the type of spindle bearing and the required preload. The measurements show the same behavior as shown in Figure 4 with a slightly higher tendency for nonlinear behavior, nevertheless the 3db-method is still applicable.

Initial tests on the test bench to determine the scatter range of the measurements are conducted with the bearings with large ceramic balls under medium preload. Firstly, the



number of necessary measurements for the statistical evaluation is determined. A measurement with 75 repetitions in x-direction is used as a reference. The Kolmogorov-Smirnov test shows that the frequency and the damping ratio distribution of both modes in x-direction are normally distributed. As a next test, only the first five repetitions were used for the determination of the mean, the standard deviation  $\sigma$  and the relative standard deviation (%RSD). The comparison shows only little deviation between both methods. Hence, only five repetitions are used throughout this paper.

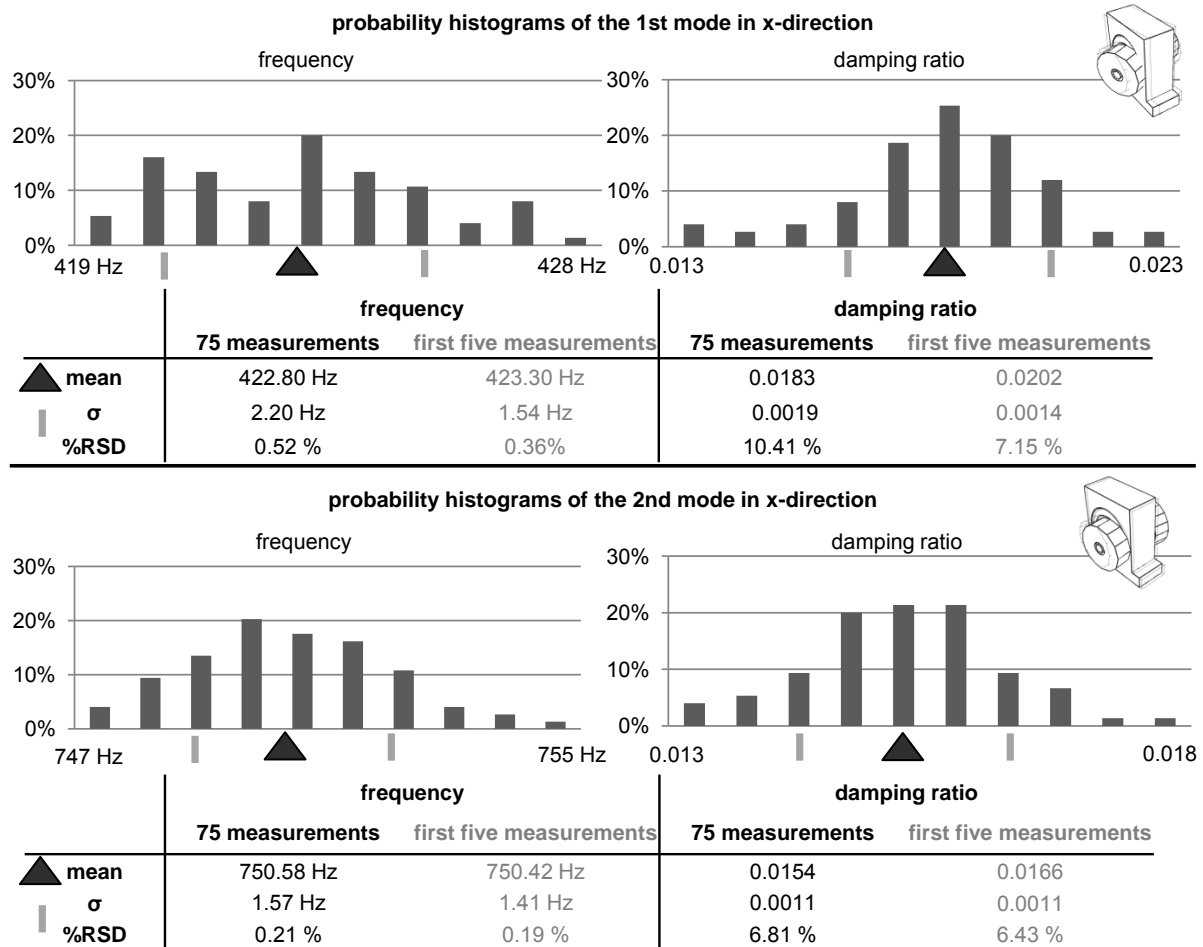


Figure 5. Probability distributions.

Lastly, the setup is assembled three times. This includes removing and assembling the spindle bearings from the shaft. Altogether only the adapter bushing is left in the pillow block. The result is depicted in Table 1. The relative standard deviation in the frequency repeatability is higher in comparison to a single assembly setup, caused by slightly different preloads in the different assemblies, even when direct-reading torque wrenches are used. The damping repeatability is only in one case higher than 12%, in axial direction it is even

remarkably low. This means that the found damping ratios are consistent over different setup conditions.

Table 1. Repeatability of the test bench setup.

Mod	Frequency repeatability				Damping ratio repeatability			
	Setup 1 [Hz]	Setup 2 [Hz]	Setup 3 [Hz]	%RSD	Setup 1 [-]	Setup 2 [-]	Setup 3 [-]	%RSD
X1	421.8	383.6	384.2	<b>5.5%</b>	0.01806	0.01672	0.01899	<b>6.4%</b>
Y2	745.7	675.3	691.3	<b>5.2%</b>	0.01824	0.01894	0.02264	<b>11.9%</b>
Y1	410.0	354.0	399.7	<b>7.7%</b>	0.01593	0.01946	0.01615	<b>11.5%</b>
Y2	776.1	707.5	628.9	<b>10.5%</b>	0.01811	0.01459	0.02313	<b>23.0%</b>
Z	537.9	477.6	508.3	<b>5.9%</b>	0.02699	0.02834	0.02907	<b>3.7%</b>

The measured eigen frequencies and damping ratios of the spindle bearing packages are shown in Figure 6. All measurements were taken without shaft rotation. The used spindle types are marked in the headline of each diagram, showcasing the used rolling element size and material and the contact angle. The horizontal axis shows the eigen frequencies of the modes while the vertical axis show the damping ratios. For both axes, the same limits are used throughout the figure to enable comparison.

The %RSD of every measurement is shown, with the frequency deviation being too small to be visible. The %RSD of the damping ratios are higher, spanning from as low as 0.4% to as high as 14%. The different preload classes, L for light, M for medium and H for heavy are shown in the diagrams as well. Because the resulting pressure in the bearing rings produced by the contact of the rolling elements is the limiting factor for the preload force, different forces are specified for the different bearing types. Larger rolling elements allow for a higher force, while ceramic rolling elements, because of its higher Young's modulus, require a lower force.

Regardless of the configuration, a trend is visible for all bearing types. With a growing preload the measured eigen frequencies are increasing as well, while the damping ratio is decreasing. This fits with the modeling concept that the damping is mainly generated in the contact areas of the rolling elements and less damping is generated under higher contact pressure.

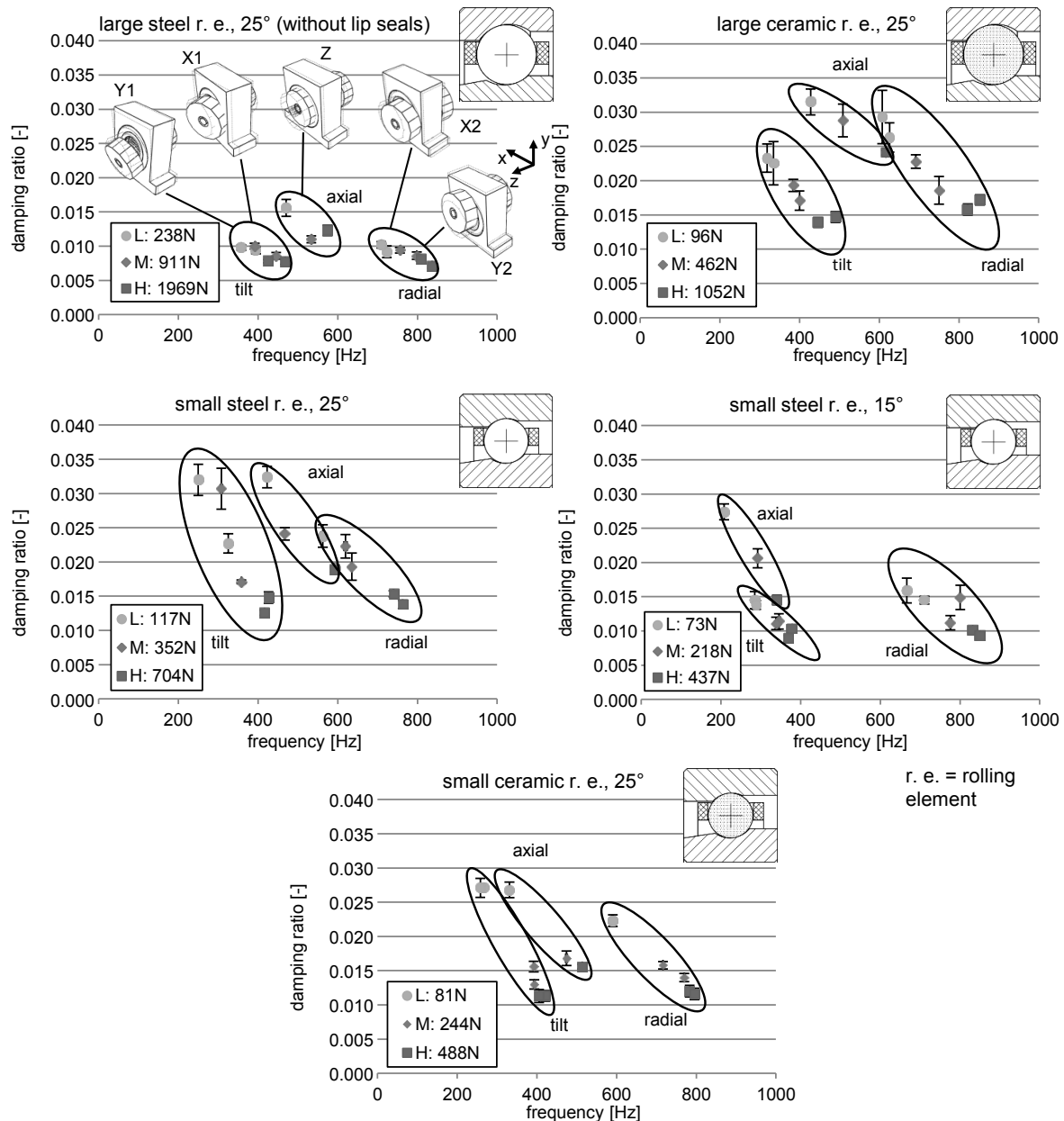


Figure 6. Measurement of the spindle bearings.

The comparison between the bearing types shows that the damping of the bearing packages with large ceramic rolling elements and small steel rolling elements and a contact angle of 25° have the highest damping, followed by the bearings with small ceramic rolling elements. The bearings with small steel rolling elements and a contact angle of 15° have, except for the axial mode, considerable lower damping. The lowest overall damping is exhibited by the bearings with large steel rolling elements. As observed in the overall trend that with rising preload the damping ratios are decreasing, the spindle bearing type with the highest absolute preload forces have the lowest damping, reinforcing the model of damping generated in the contact areas.



The comparison between the bearings with small steel rolling elements shows the effect of the contact angle on the frequency and therefore on the stiffness, as the axial mode frequency is much lower for the bearings with a contact angle of 15°.

### **3. Local parameter extraction**

In this chapter, the local damping parameter determination is presented. A finite-elements model of the test bench with matched local damping properties is used.

#### **Simulation model of the test bench**

The FEA was chosen to determine local damping parameters instead of using analytical models. The test bench is modeled as an assembly of three dimensional parts which are abstracted, simplified and meshed with hexagonal elements. The gaps between the parts are modeled with contact definitions, using three different sets for their stiffness and damping properties in relation to the gap position and preload. The mounting of the test bench on four springs is also considered and modeled as linear spring elements.

The bearings are abstracted further. Only the inner and outer ring are modeled as actual parts, the interaction is each modeled with a spring-damper bushing. The used FEA software supports two linear local damping models simultaneously in its modal simulations, viscous damping, which velocity proportional, and structural is damping, which is proportional to the displacement. The effect of viscous damping depends on the frequency, while structural damping is frequency independent. The used algorithm calculates the undamped eigen frequencies of a system and projects the full viscous and structural damping matrices onto these modes. In following steps, a FRF can be calculated using these fully populated damping matrices.

The material damping of all parts of the test bench is modeled with structural damping, because measurements show the independence of material damping from frequency. The gaps between the parts are modeled with viscous damping. The damping of the bearings are modeled with viscous and with structural damping.

#### **Matching of the reference dummy setup**

The reference dummies are modeled using only stiffness parameters for the bushing because their damping is negligible. These stiffness parameters are determined using an optimization routine with the eigen frequencies as an optimization goal. The optimization routine makes use of the dependency of the eigen frequency of the axial mode from the stiffness of the reference dummy in axial direction as well as both radial modes in both radial directions. Together with using starting values the algorithm converges very fast.

The damping property of steel is relatively well researched. But the gap damping, which has a much greater contribution to the overall system damping, is not known in advance. Instead, the damping ratios of the reference dummy setup are used as an optimization goal for a matching procedure of the gaps' damping properties in the FE-model.

### Matching of the spindle bearings

The spindle bearings are basically modeled like the reference dummy. Additionally, there are two different linear damping models, viscous and structural damping, available. These models use three stiffness parameters and three damping parameters. The stiffness parameters are matched in a first step, analogue to the dummy matching process. The results for the spindle bearing with large ceramic rolling element is shown in Figure 7 in comparison to three differently predicted stiffness values. Catalog values from the manufacturer, two software calculated stiffness values and the matched parameters are compared, using the manufacturers software and a software developed at the WZL of the RWTH Aachen University, WinLager. The comparison shows a good consistence between all methods, indicating the successful determination of stiffness parameters through the methodology.

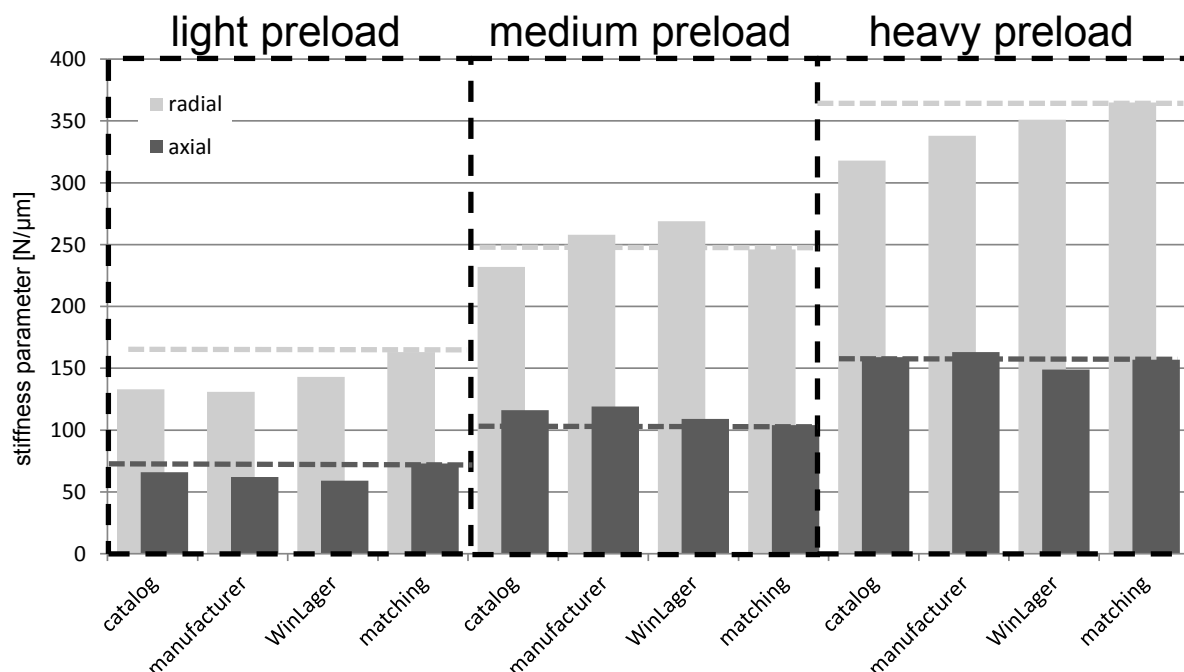


Figure 7. Comparison of stiffness properties for a spindle bearing.

Since the damping of the test bench is already matched, all additional damping in the bearing measurements has to originate from the bearings. Because there is a correlation between the damping ratios and local damping parameter, proceeding from the clearly separated

eigen modes, an easier and faster algorithm is utilized to match them. The results for all five bearing types and their preload classes are shown for both the viscous damping model and the structural damping model in Figure 8.

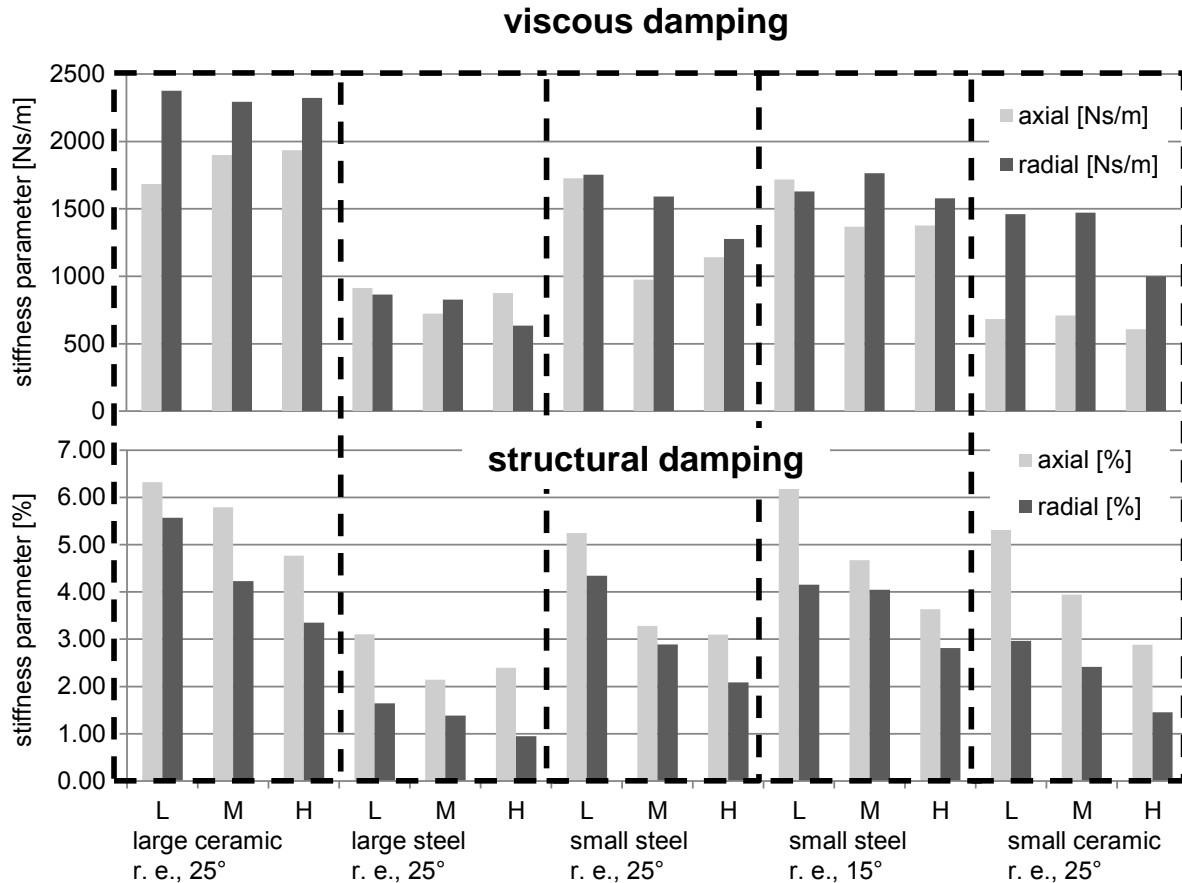


Figure 8. Local damping properties of spindle bearings.

The viscous damping parameter seems to be mostly independent from the preload for most bearing types with the exception of the bearing with small steel rolling elements and 25° contact angle, while the structural damping parameter has a strong tendency for decreasing values with rising preload classes. The local damping values are highest for the bearings with large ceramic rolling elements and lowest for bearings with large steel rolling elements as could be expected from the measurement of the damping ratios. The remaining three bearing types are similar to each other in the case of viscous damping with the exception of the radial damping for the bearings with small ceramic rolling elements. The parameters for the structural damping model show more scattering without a clear trend.

#### 4. Validation

As stated before, the determination of damping properties was carried out under specified dynamic conditions. To validate the extracted local damping parameters, these conditions

have to be changed, so the damping models operate at new resonance frequencies. Under these new conditions, the two damping model will yield different damping ratios caused by their different frequency dependencies.

To change the dynamic behavior, one of the two masses on the test bench shaft is removed in a first step and the FRF is measured using the large ceramic rolling elements bearings with medium preload. This changes the eigen modes, as shown in Figure 9, so that only two radial modes, X and Y, and the axial mode Z remain, but with higher eigen frequencies. To change the dynamic behavior even further, the second mass was also removed. In this setup, only the axial mode Z was present in the evaluated frequency range.

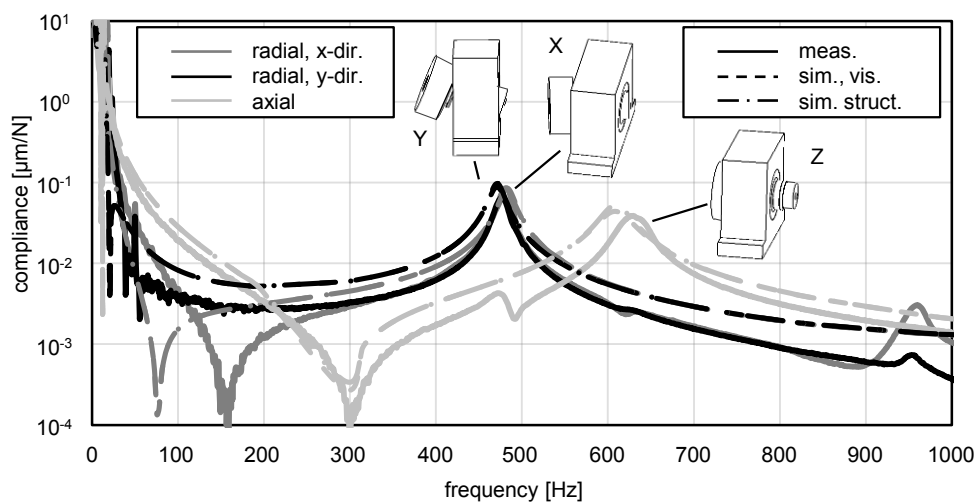


Figure 9. Validation of the parameter extraction.

The comparison between measurement and simulation shown in Figure 9 is realized after a completely new assembly in order to test the parameter extraction process under realistic conditions. Because the simulations of both damping models appear very similar in Figure 9, the resulting frequencies and damping ratios are compared in Table 2. The direct comparison shows that the simulated eigen frequencies, which are independent of the used damping model, have very little deviation in comparison to the measurements. The damping ratio comparison reveals that the damping ratios predicted by the viscous model are too high, up to 134% for the setup without both masses. The structural damping model on the other hand gives very good predictions, with the highest deviation being 27% for the setup without masses.

In conclusion, the structural damping model seems to be a good fit to model the damping effects of these spindle bearing packages even under subsequent assembly setups and changed dynamic conditions.

Table 2. Comparison of the prognoses.

		frequency prognosis			damping ratio prognosis				
	mode	meas. [Hz]	sim. [Hz]	diff.	meas. [-]	viscous [-]	struct. [-]	diff. viscous	diff struct.
one mass	X	483.6	482.9	-0.1%	0.0150	0.0196	0.0174	30%	16%
	Y	477.0	471.2	-1.2%	0.0169	0.0192	0.0174	13%	3%
	Z	630.1	608.7	-3.4%	0.0265	0.0345	0.0288	30%	9%
zero mass	Z	942.8	924.1	-2.0%	0.0227	0.0530	0.0287	134%	27%

## 5. Summary

A method to extract local damping parameters of spindle bearing packages from global damping ratios with the help of a simulation model and a reference measurement was presented. An appropriate test bench for dynamic measurements was designed and introduced. Five different spindle bearing types were measured with this test bench and their eigen frequencies and damping ratios for three preload classes were analyzed. A simulation model was built up and its damping was matched with the measurement of a reference setup using an optimization algorithm. Subsequently local damping parameters were identified and compared. Finally, the damping models were validated using the example of one spindle bearing package.

Future studies will examine the damping behavior under a wider variety of conditions, e.g. different dimensions, different arrangements, different lubricants and particularly under rotation of the shaft.

## 6. ACKNOWLEDGMENTS

This work was supported by the German Research Foundation (DFG) within the research unit FOR-1087 "Damping effects in Machine Tools".

## REFERENCES

1. **Quintana, G. (2011)**, "Productivity improvement through chatter-free milling in workshops", Proceedings of the Institution of Mechanical Engineers, Part B: Journal of Engineering Manufacture, July 2011, vol. 225, no. 7, pp 1163-1174.
2. **Altintas, Y. and Weck, M. (2004)**, "Virtual Machine Tools", CIRP Annals - Manufacturing Technology, Volume 53, Issue 2, 2004, pp 619–642.





3. **Altintas, Y.; Brecher, C and Weck, M. (2005)**, "Chatter Stability of Metal Cutting and Grinding", CIRP Annals - Manufacturing Technology, Volume 54, Issue 2, 2004, pp 115–138.
4. **Stone, B.J. (1982)**, "The State of the Art in the Measurement of the Stiffness and Damping of Rolling Element Bearings", CIRP Annals - Manufacturing Technology, Volume 31, Issue 2, 2004, pp 529–538.
5. **Ophey, L. (1986)**, "Dämpfungs- und Steifigkeitseigenschaften vorgespannter Schrägkugellager", Verein Deutscher Ingenieure: [Fortschrittberichte VDI / 1] Fortschrittberichte VDI: Reihe 1, Konstruktionstechnik, Maschinenelemente; Nr. 138.
6. **Zeilinger, R. (1995)**, "Zum Dämpfungsvermögen von Wälzlagern und Wälzlagerverbindungen", Dissertation, Technische Universität Wien, Fakultät für Maschinenbau, Wien, Austria.
7. **Dietl, P. (1997)**, "Damping and Stiffness Characteristics of Rolling Element Bearings – Theory and Experiment", Dissertation, Technische Universität Wien, Fakultät für Maschinenbau, Wien, Austria.
8. **Wijnant, Y. H. (1998)**, "Contact Dynamics in the Field of Elastohydrodynamic Lubrication", Dissertation, University of Twente, Enschede, the Netherlands
9. **Wensing, J.A. (1998)**, "On the Dynamics of Ball Bearings", Dissertation, University of Twente, Enschede, the Netherlands
10. **Jacobs, W. (2014)**, "The influence of the lubricant film on the stiffness and damping characteristics of a deep groove ball bearing", Mechanical Systems and Signal Processing, Volume 42, Issues 1–2, January 2014, pp 335–350.
11. **VDI (2005)**, „Damping of materials and members“, VDI 3830, Part 5, Düsseldorf.
12. **Brecher, C. (2012a)**, „Identification method for damping parameters of roller linear guides“, Production Engineering, Volume 6, Issue 4-5, pp 505-512.
13. **DIN 628-6. (1999)**, "Rolling bearings – Angular contact radial ball bearings – Part 6: Single row, contact angle 15° and 25°", Beuth Verlag GmbH, Berlin
14. **Brecher, C. (2012b)** "Damping behavior of spindle bearings", MM Science Journal, Special Issue, MATAR 2012



## ACTIVE DAMPING OF HEAVY DUTY MILLING OPERATIONS

**Robin KLEINWORT**, *Robin.Kleinwort@iwb.de* Technische Universitaet Muenchen, Germany

**Yusuf ALTINTAS**, *Altintas@mail.ubc.ca* University of British Columbia, Vancouver, Canada

**Michael F. ZAEH**, *Michael.Zaeh@iwb.de* Technische Universitaet Muenchen, Germany

### ABSTRACT

The material removal rate of a machine tool is often restricted by its chatter stability limits. If the axial depth of cut is too high, the cutting process becomes unstable and chatter vibrations occur. The critical depth of cut can be increased using active methods to damp the structural modes which cause chatter. In this paper a methodology is introduced on how to implement an active damping system on milling machines to improve their productivity. A new control strategy for active damping is presented, which was tested on a commercial milling machine. It is demonstrated experimentally that 33% productivity increase has been achieved with the proposed method.

**Keywords:** Active damping, Chatter, Stability, Milling

### 1. INTRODUCTION

Chatter causes a poor surface of the workpiece and large dynamic loads for the machine, which also increases the tool wear. For cutting processes at high spindle speeds, spindle speed selection can be used to change the spindle speed towards a stability pocket [Smith & Tlustý, 1992]. Heavy duty milling operations run at low spindle speeds where this method is not applicable. As the critical depth of cut, which forms the stability lobes, is a function of the receptance at the tool center point (TCP) [Altintas & Budak, 1995], the dominant eigenmodes of the TCP need to be damped. In general, there is a distinction between passive and active damping methods. Passive dampers improve the stability by minimizing the magnitude of the FRF's negative real part of the critical mode. Even though [Yang et al., 2010] introduced a multiple tuned mass damper, which allows to damp more than one eigenfrequency, the main disadvantage of passive dampers - inflexibility concerning the adaption to changing dynamics - remains. Active strategies are more flexible than passive dampers and meet the requirements posed by dynamic machine tools [Simnofske et al., 2009].

[Zulaika et al., 2011] present a new lightweight design strategy and combine it with an active damping system embedded in a lightweight machine ram. [Simnofske et al., 2009] follow the same idea to increase the dynamic and static stiffness of a grinding machine. But their focus is on the design process of the adaptronic parts. A computational approach to the integration

of adaptronic structures in machine tools is introduced by [Zaeh et al., 2009]. Apart from the actuator placement, an adaptive controller is presented and tested in an integrated simulation model containing the structural dynamics of a portal milling machine, the cutting process and an analytical model of the adaptronic active damping system. [Brecher et al., 2010a] provide a new approach for an active compensation of static and dynamic deformations.

However, past studies were restricted to experimental machine tools. This paper provides a new cost-effective methodology to improve the productivity of already-in-use heavy duty milling machines. Therefore a commercial shaker of type *Micromega Dynamics S.A.* with a seismic mass of 2.2 Kg is used that can be attached to the machine structure without an external anchor. In a bandwidth from 20 to 2000 Hz this actuator has a maximum force output of 45 N. Furthermore, a new control strategy is presented that shows a better performance than the commonly-used direct velocity feedback (DVF) controller. There are several publications that concentrate on the control design like [Locatelli, 2001] and [Ehmann & Nordmann, 2004].

Hence, the paper is organized as follows. In Section 2 the methodology of finding the optimum actuator placement is explained and applied on a commercial milling machine. A new control strategy for active damping is presented in Section 3. The simulation results from Section 4 are verified by experiments in Section 5 and the paper is concluded in Section 6.

## 2. ACTUATOR PLACEMENT

The optimum actuator placement is found in 4 steps: First the direct frequency response functions (FRF) in the most flexible directions are measured at the tool center point (TCP). In a second step the most dominant eigenfrequencies, which may cause chatter, are extracted from the measured FRFs. It is important to consider that at low spindle speeds chatter occurs more likely at the first eigenfrequencies, because higher eigenmodes are damped by process damping. After the critical eigenfrequency is found, a modal analysis is carried out in the third step in order to plot the mode shapes of this eigenmode. In the last step the mode shapes are evaluated. The optimum actuator placement is as close to an antinode as possible. In Figure 1 the actuator placement methodology is visualized.

### Application

As an example the explained methodology was applied to a commercial 5-axis milling machine of type *Mori Seiki NMV5000*. To predict chatter, the direct FRFs at the TCP in feed and in normal direction are required.



Figure 1: Methodology for actuator placement

The stability limit is inversely proportional to the negative real part of the FRF. For the used face mill the dynamic cutting forces in Z-direction are negligible. Figure 2 presents the real part of the direct FRFs in X- and Y-direction. The measurements show two dominant modes at 75 Hz in Y-direction and around 790 Hz in both directions. Because of process damping the excitation amplitude of the eigenmode at 790 Hz will be damped at low spindle speeds. Hence, the eigenfrequency at 75 Hz is the most critical mode which will most likely cause chatter. Therefore, the following investigations focus on clamping the actuator in Y-direction. In the third step a modal analysis was carried out. Instead of measuring the complete machine tool, which can be a very extensive task, it is more productive to look only at the parts of interest. Often it is sufficient to measure a few points in proximity to the TCP to plot the mode shapes. Analyzing the mode shape of the 75 Hz mode in Figure 3 leads to the conclusion that this is the first global bending mode of the Z-slide in Y-direction. Therefore, the maximum magnitude of the mode shape is at the TCP and - concerning the methodology - the optimum actuator position is at an antinode of the mode, because at this point the actuator force shows the highest effect on a displacement at the TCP. According to Figure 3(a), the magnitude at the 75 Hz mode decreases with the distance to the TCP. Taking into account that the clamping magnets of the actuator require a plane surface, only the Z-slide provides a practicable mounting position as shown in Figure 3(b). Besides the mode at 75 Hz there might be other modes at which chatter occurs at certain spindle speeds. Considering these cases, the direct FRF at the TCP is compared with the cross FRFs in Figure 4. The continuous black line symbolizes the direct FRF at the TCP.

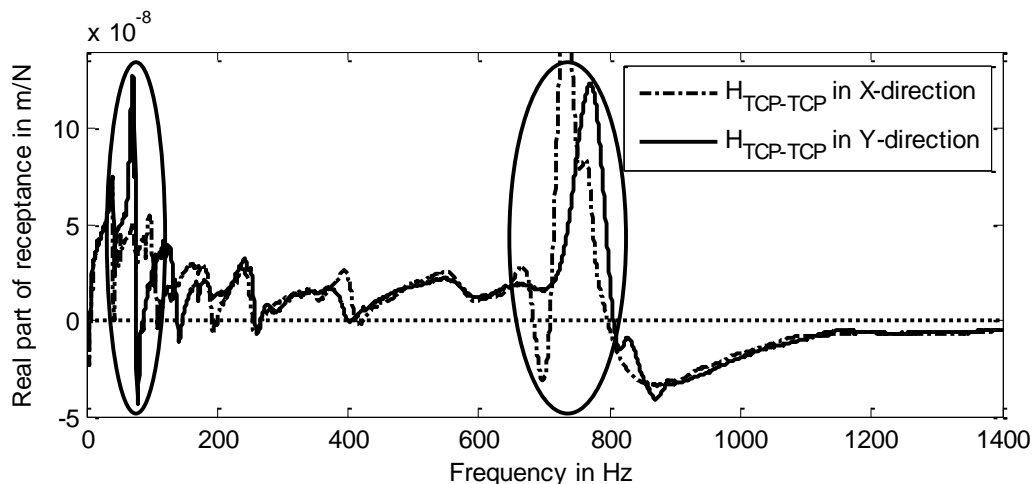


Figure 2: Direct FRF at the TCP – X- and Y-direction

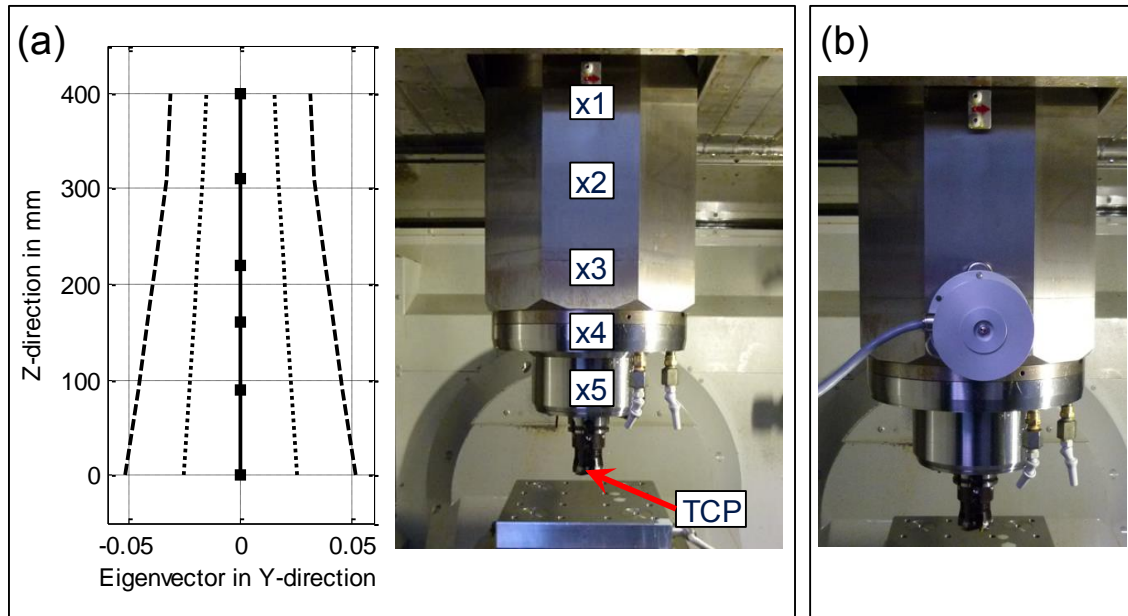


Figure 3: (a) mode shape of the 75 Hz mode, (b) mounting position of the actuator

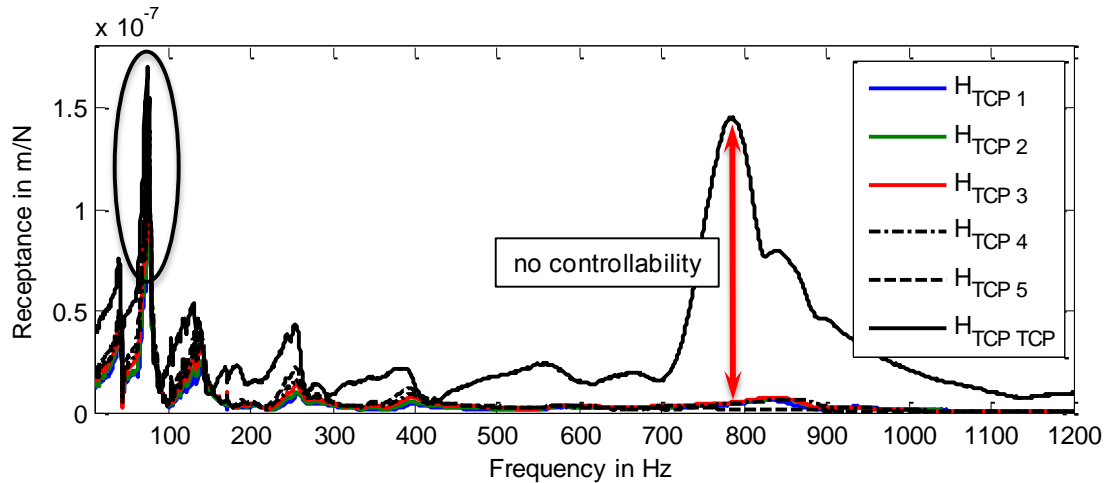


Figure 4: Direct FRF and cross FRFs at TCP – Y-direction

The other curves are the cross FRFs distributed along the Z-Slide, where  $H_{TCP\ 1}$  refers to the cross FRF between the TCP and the highest measurement point at the Z-slide. Now it is obvious that the other dominant mode around 790 Hz is a local mode, which belongs to the spindle and only occurs at the TCP. This local spindle mode could only be damped, if the actuator was mounted directly at the TCP, which is not possible. Hence, this mode cannot be damped.

### 3. CONTROL DESIGN

#### Direct Velocity Feedback Control

The most commonly used collocated controller for active damping of machine tools is the *Direct Velocity Feedback* (DVF) controller. Compared to other collocated control strategies it shows

the best performance [Munoa et al., 2013], [Ehmann & Nordmann, 2004]. Collocation between the actuator and the sensor leads to higher stability of the control loop [Preumont, 2002]. Therefore, only a collocated actuator-sensor configuration was used in this research. The controller acts as viscous damper by applying an actuator force  $F_{act}$  proportional to the measured velocity signal to the system:

$$F_{act} = -K_C \dot{x} \quad (1)$$

The gain  $K_C$  is the only variable, which has to be adapted in a way that the controller remains stable. Assuming a single degree of freedom system, the equation of motion can be written as

$$m\ddot{x} + c\dot{x} + kx = F_D + F_{act} , \quad (2)$$

where  $F_D$  is the disturbance force, respectively cutting force. Inserting Equation (1)) into Equation (2) shows how the damping ratio is increased:

$$m\ddot{x} + (c + K_C)\dot{x} + kx = F_D \quad (3)$$

However, the structure of a machine tool is not a single degree of freedom system, but shows several significant eigenfrequencies (cf. Figure 2). The DVF controller damps all eigenfrequencies instead of focussing on damping only the critical eigenfrequency, which causes chatter. Therefore, a new control strategy is presented in the following section, which counteracts this disadvantage.

### Model-based Velocity Feedback Control

Compared to the DVF controller, which does not need any plant model, the *Model-based Velocity Feedback* (MbVF) controller takes the cross transfer function between the TCP and the mounting position of the actuator as well as the direct transfer function  $P(s)$  at the TCP into account. The transfer functions of the actuator and the amplifier are combined with the cross FRF to the secondary-path transfer function  $S(s)$ . The controller  $C(s)$  consists of a gain with an integrator for the velocity feedback and the inverse of the estimated secondary-path transfer function  $\hat{S}(s)$  multiplied with the estimated direct FRF  $\hat{P}(s)$ :

$$C(s) = \frac{K_C}{s} \cdot \hat{S}(s)^{-1} \cdot \hat{P}(s) \quad (4)$$

Assuming that the estimations for  $P(s)$  and  $S(s)$  are exact, this controller would be equal to a DVF controller. The advantage of the MbVF controller is the possibility to tune it in a way so

that only certain modes are damped. This can be done very easily by restricting the estimation of the direct FRF  $\hat{P}(s)$  to the modes that are to be damped. To show how the controller works in theory, the closed-loop transfer function is calculated:

$$\frac{\ddot{X}_R(s)}{F_D(s)} = \frac{P(s)}{1 + C(s) \cdot S(s)} = \frac{P(s)}{1 + \frac{K_C}{s} \cdot \hat{S}(s)^{-1} \cdot \hat{P}(s) \cdot S(s)} \quad (5)$$

where  $\ddot{X}_R$  is the acceleration at the TCP, which results from the subtraction between  $\ddot{X}_{Act}$  and  $\ddot{X}_D$ . The acceleration at the TCP that is caused by the disturbance force  $F_D$  is described through  $\ddot{X}_D$ , while  $\ddot{X}_{Act}$  refers to the acceleration at the TCP that is caused by the actuator.

For the following example, the controller is tuned to damp the first eigenfrequency  $\omega_{n,1}$ . Hence,  $\hat{P}(s)$  contains only this eigenmode. Assuming that the estimation of the secondary-path transfer function is exact, the inverse of the estimated and the real secondary-path transfer function cancel out each other. Also  $P(s)$  and  $\hat{P}(s)$  can be expressed with modal parameters so that Equation (5) can be rewritten as:

$$\frac{\ddot{X}_R(s)}{F_D(s)} = \frac{P(s)}{1 + \frac{K_C}{s} \cdot \hat{P}(s)} = \frac{\sum_{i=1}^{\infty} \frac{1/m_i \cdot s^2}{s^2 + 2\zeta_i \omega_{n,i} s + \omega_{n,i}^2}}{1 + \frac{K_C}{s} \cdot \left( \frac{1/m_1 \cdot s^2}{s^2 + 2\zeta_1 \omega_{n,1} s + \omega_{n,1}^2} \right)} \quad (6)$$

Splitting up the fraction into two summands with one only containing the first mode and the other containing all left-over modes of  $P(s)$  leads to:

$$\begin{aligned} \frac{\ddot{X}_R(s)}{F_D(s)} &= \frac{\frac{1/m_1 \cdot s^2}{s^2 + 2\zeta_1 \omega_{n,1} s + \omega_{n,1}^2}}{1 + \frac{K_C}{s} \cdot \left( \frac{1/m_1 \cdot s^2}{s^2 + 2\zeta_1 \omega_{n,1} s + \omega_{n,1}^2} \right)} + \frac{\sum_{i=2}^{\infty} \frac{1/m_i \cdot s^2}{s^2 + 2\zeta_i \omega_{n,i} s + \omega_{n,i}^2}}{1 + \frac{K_C}{s} \cdot \left( \frac{1/m_1 \cdot s^2}{s^2 + 2\zeta_1 \omega_{n,1} s + \omega_{n,1}^2} \right)} = \\ &= \frac{s^2}{m_1 \cdot (s^2 + 2\zeta_1 \omega_{n,1} s + \omega_{n,1}^2) + K_C \cdot s} + \frac{\sum_{i=2}^{\infty} \frac{1/m_i \cdot s^2}{s^2 + 2\zeta_i \omega_{n,i} s + \omega_{n,i}^2}}{1 + \frac{K_C}{s} \cdot \left( \frac{1/m_1 \cdot s^2}{s^2 + 2\zeta_1 \omega_{n,1} s + \omega_{n,1}^2} \right)} \end{aligned} \quad (7)$$

For frequencies above  $\omega_{n,1}$  the estimation of the direct FRF  $\hat{P}(s)$  is assumed to be zero. Therefore, the denominator of the second summand becomes one. Hence, Equation (7) can be simplified to:



(8)

$$\frac{\ddot{X}_R(s)}{F_D(s)} \cong \frac{s^2}{m_1 s^2 + (c_1 + K_C) \cdot s + k_1} + \sum_{i=2}^{\infty} \frac{1/m_i \cdot s^2}{s^2 + 2\zeta_i \omega_{n,i} s + \omega_{n,i}^2}$$

A block diagram of the control strategy is shown in Figure 5.

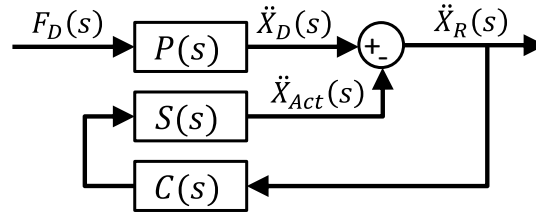


Figure 5: Block diagram of the MbVF controller in continuous time

It is obvious that damping is only increased for the first mode. For all other modes the standard equation for accelerance is obtained. In the next section the performance of this control strategy is compared with the performance of the DVF controller in simulation.

#### 4. SIMULATION

##### Simulation Environment

The main purpose of this simulation is to investigate how much the damping can be increased at the TCP. For this purpose, the structural dynamics of the machine tool as well as the adaptronic active damping system have to be simulated. The simulation is run in time domain using SIMULINK<sup>®</sup>. With the help of MATLAB<sup>®</sup> the results are also analyzed in the frequency domain. To simulate the dynamic behavior of the whole system, only the transfer functions of the structure are needed as information. Taking all FRFs from the modal analysis into account, a state space model is formed. Not all the active components are simulated. The amplifier is only modeled as a single gain, assuming that the amplification gain is constant inside the bandwidth. The sensor and its noise are not modeled.

The following results are specific for the milling machine used in this research (*Mori Seiki NMV5000*). The dynamics of the *NMV5000* do not change significantly in X- and Y-direction. Therefore, position dependent dynamics are not investigated in this paper. Only in Z-direction position dependent dynamics can be observed as the length of the ram changes. However, the cutting tests were carried out at nearly the same Z-position, so that changing dynamics can be neglected anyway. Not the whole structure of the *NMV5000* has to be modeled, but only the dynamics of the Z-slide, the tool-holder and the tool. The simulation model is shown in a block diagram in Figure 6.



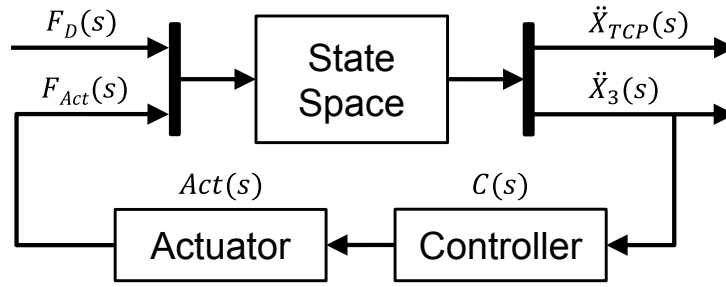


Figure 6: Simulation model in state space representation

A disturbance  $F_D(s)$ , typically coming from cutting forces at the TCP, causes a vibration at the TCP as well as at the actuator and sensor mounting position, which is called position '3' in the following. The controller processes the acceleration feedback and the output signal drives the actuator, which leads to the second input of the state space model, the actuator force  $F_{Act}$ . For evaluating the performance, the acceleration at the TCP is scoped. To compare different control strategies, only the controller block has to be modified. The state space model and the actuator block always stay the same. Five modes were identified for derivation of the state space model (cf. Table 1). The transfer function of the DVF controller consists of an integrator multiplied with a gain  $K_C$ :

$$C(s) = \frac{K_C}{s} \quad (9)$$

For the MbVF controller, the transfer function is found through Equation (4):

$$C(s) = \frac{K_C}{s} \cdot \hat{S}(s)^{-1} \cdot \hat{P}(s) = \frac{K_C}{s} \cdot \left( \frac{\hat{H}_{3-TCP,75}}{\hat{H}_{TCP-TCP,75}} \cdot \hat{H}_{3-TCP} \right)^{-1} \cdot \hat{H}_{TCP-TCP,75} \quad (10)$$

The estimated transfer functions  $\hat{H}_{3-TCP,75}$  and  $\hat{H}_{TCP-TCP,75}$  only consider one mode at 75 Hz. Hence, the ratio of the two transfer functions becomes a scalar. The estimation of the direct FRF focuses the controller on damping only the 75 Hz mode.

In the simulation, the estimated transfer functions use the same modal parameters as the state space model, which assumes that the estimation matches perfectly with the simulated system.

## Simulation Results

The performance of the different control strategies are compared with a simulated direct FRF at the TCP. As an input disturbance signal a single pulse is used, which simulates the impulse of a hammer. To calculate the direct FRF, the vibration response at the TCP and the input force signal are needed. Additionally the actuator force was monitored, which helps to understand the working principle of the controllers.

Table 1: Modal parameters of the state space model

Mode	$f_m$	$\zeta_m$	$\phi_{1m}$	$\phi_{2m}$	$\phi_{3m}$	$\phi_{4m}$	$\phi_{5m}$
1	41 Hz	0.0380	0.0168	0.0540	0.0633	0.0786	0.4950
2	74.5 Hz	0.0400	0.0117	0.0459	0.0481	0.0435	0.0051
3	134 Hz	0.0540	0.0113	0.0387	0.0381	0.0254	0.0258
4	252 Hz	0.0300	0.0111	0.0331	0.0307	0.0194	0.0250
5	811 Hz	0.0325	0.0118	0.0341	0.0275	0.0170	0.0211

One disadvantage of the Direct Velocity Feedback controller is that all modes, which are captured by the accelerometer, are damped and not only the 75 Hz mode. Figure 7 shows a Fast Fourier Transformation (FFT) of the actuator force signal for the DVF and the MbVF controller. Besides the mode of interest at 75 Hz, the other four simulated modes are also visible in the actuator force signal of the DVF controller. For the MbVF controller the actuator vibrates at only one frequency (75 Hz). Thus, the whole actuator force is concentrated on only damping this single mode.

To compare the performance of both control strategies, the gain  $K_C$  has to be arranged in a way that the actuator does not saturate. In Figure 8 the measured FRF at the TCP for the undamped case is compared to simulation results achieved with the DVF controller and the MbVF controller. Over the whole bandwidth both controllers seem to show the same behaviour except for the mode of interest at 75 Hz. As the stability limit is inversely proportional to the negative real part of the FRF, it is reasonable to analyze the Nyquist plot of the 75 Hz mode in Figure 8, too. Using the MbVF controller, a further decrease of the magnitude of the negative real part of 29% compared to the DVF controller was achieved. Another way to evaluate the performance of both controllers is to look at the increase of damping. From [Ewins, 1984] the damping ratio in resonance can be calculated with some simplifications as follows:

$$|\hat{G}| = \frac{\phi^2}{2 \cdot \zeta \cdot \omega_n^2} \rightarrow \zeta = \frac{\phi^2}{2 \cdot \omega_n^2 \cdot |\hat{G}|}, \quad (11)$$

where  $\phi$  is the eigenvector,  $\omega_n$  the eigenfrequency,  $|\hat{G}|$  the magnitude of the mode and  $\zeta$  the damping ratio. The results for both controllers are presented in Table 2.

Table 2: Damping ratio achieved simulating impulse response

	Magnitude $ \hat{H} $	Decrease of $ \hat{G} $	$\zeta$	Increase of $\zeta$	Controller gain $K_C$
Undamped (measured)	1.70e-7 m/N	-	4.0%	-	-
DVF controller	1.59e-7 m/N	6.47%	4.33%	8.25%	4000
MbVF controller	1.26e-7 m/N	25.88%	5.53%	38.25%	4700

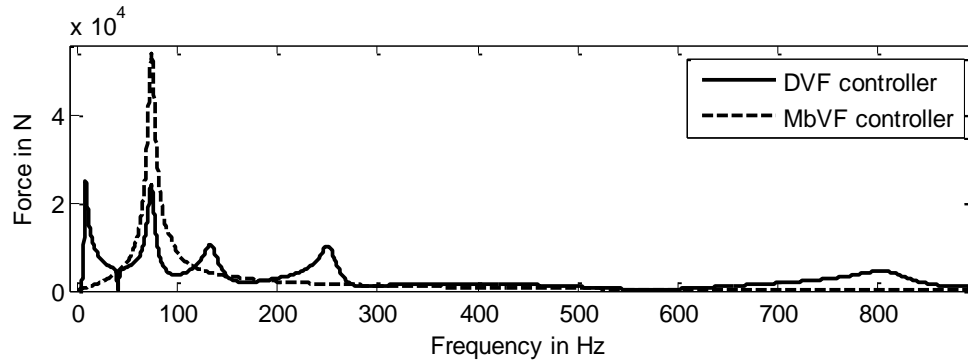


Figure 7: FFT of the actuator force – DVF controller & MbVF controller

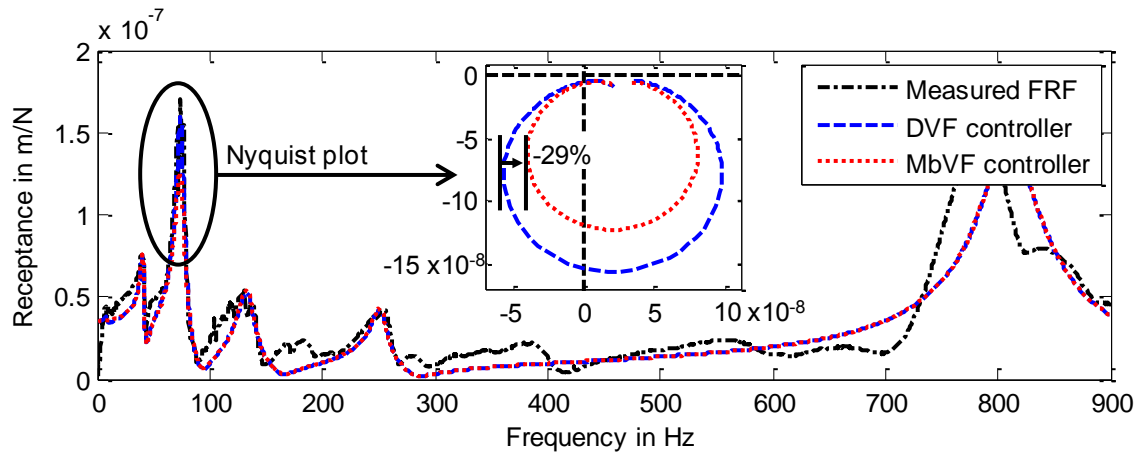


Figure 8: Comparison of DVF & MbVF controller– magnitude and Nyquist plot

## 5. EXPERIMENTAL VERIFICATION

In this section the simulation results are verified by experiments carried out on the *Mori Seiki NMV5000*. First the measurement equipment and the hardware of the active damping system is presented. Then the achievable damping ratios as well as the Nyquist plots, that can both be obtained from the direct FRFs at the TCP, are compared for the DVF and the MbVF controller. Finally, chatter stability tests were conducted to demonstrate the increase of stability.

### Experimental Setup

The measurement setup is shown in Figure 9. The actuator is clamped with three magnets on the Z-slide. The direct FRF was measured using an input/output device from National Instruments, an impulse hammer, a laser vibrometer and the software tool CUTPRO<sup>®</sup>. All measured data were exported and plotted in MATLAB<sup>®</sup>. The acceleration signal coming from the external accelerometer was amplified by a power supply coupler and fed into a dSpace<sup>®</sup> AD (analog to digital) channel as shown in Figure 10. The controller was designed in SIMULINK<sup>®</sup> and implemented on a real time computer through dSpace<sup>®</sup>.

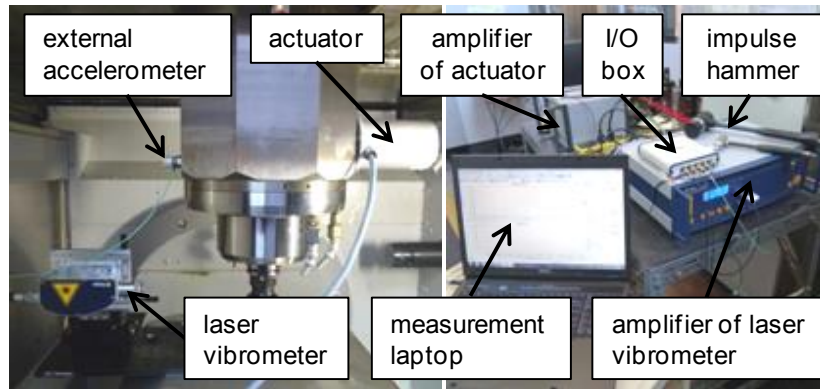


Figure 9: Measurement setup – machine tool

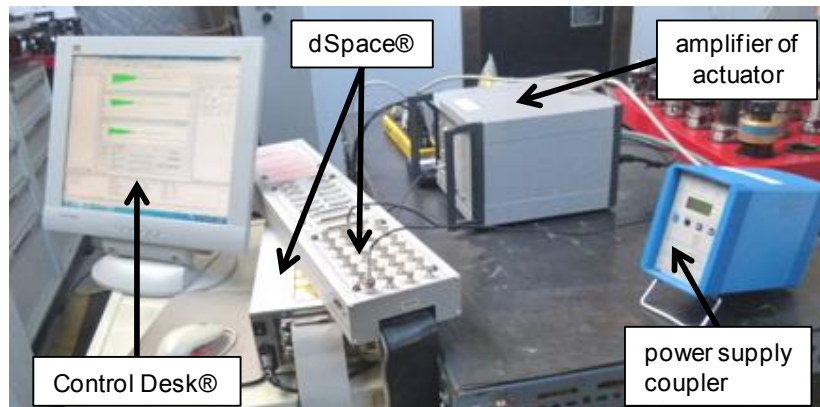


Figure 10: dSpace system for implementing a SIMULINK® controller

The controller output goes from a dSpace® DA (digital to analog) channel to the amplifier of the actuator.

### Modal Testing

Both controllers were tested at the maximum gain setting, where the controller output does not saturate. To cut-off high frequency content above the bandwidth of the actuator, a 2<sup>nd</sup> order low-pass filter was implemented. The DC offset was reduced by a 2<sup>nd</sup> order high-pass filter. Figure 11 shows a cut-out of the Nyquist plot of the critical mode at 75 Hz. Even though the MbVF controller reduces the negative real part further than the DVF controller, the results are a bit below the expected improvements. One reason might be the high level of noise that occurs, when the machine is turned on. In simulation, noise was completely neglected. Nevertheless with the new MbVF controller a significant increase of damping is achieved. The results for both controllers are summarized in Table 3. By using more advanced filters, such as 4<sup>th</sup> order high-pass and low-pass filters the effectiveness of the DVF and the MbVF controller can be further increased by sharpening the transition area and reducing the phase shift.

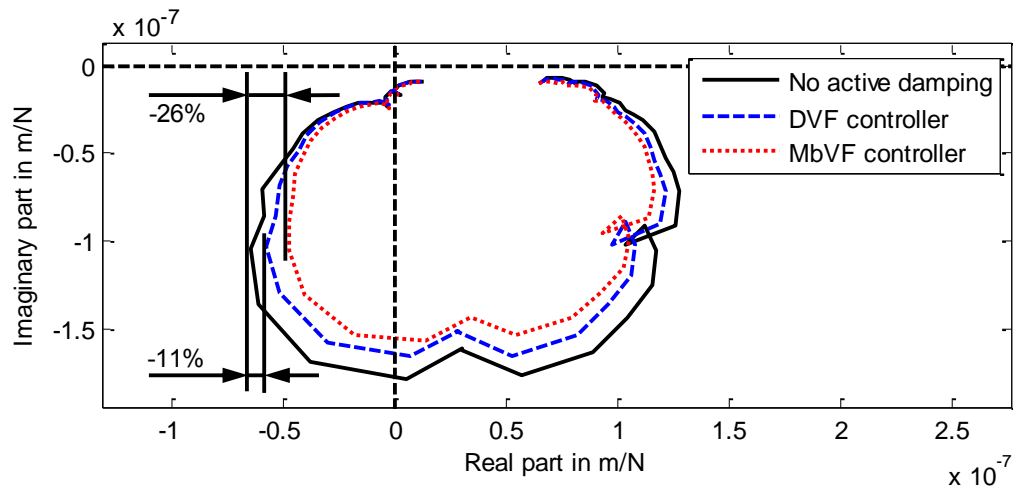


Figure 11: Influence of the DVF and the MbVF controller on the direct FRF at the TCP

Table 3: Damping ratio achieved in experiments during tap tests

	Magnitude $ \hat{H} $	Decrease of $ \hat{G} $	$\zeta$	Increase of $\zeta$	Controller gain $K_C$
No active damping	1.86e-7 m/N	-	4.00%	-	-
DVF controller	1.74e-7 m/N	-6.5%	4.28%	7.0%	4000
MbVF controller	1.64e-7 m/N	-12.0%	4.54%	13.5%	4700

Furthermore, applying notch filters the electrical power frequency component and the tooth-passing frequency as well as its dominant harmonics can be canceled out. The design principles of the filters mentioned above are explained in [Zumbahlen, 2008]. The parameters of all filters used in this paper are summarized in Table 4. The 2nd and 4th order filters were both implemented with the same parameters. Figure 12 shows the results for the MbVF controller at higher gain settings, where the controller output starts saturating. The magnitude of the negative real part is reduced by 50%.

### Chatter Stability Tests

In total six cutting tests at different depths of cut and spindle speeds were carried out. For each cutting test, the first half of the way was cut without active damping and during the second half the MbVF controller was turned on. The calculated stability lobes using the theory of [Altintas & Budak, 1995] show a stability limit of 3.5 mm at 1300 rpm. Chatter test results in Figure 13 show that at 3.5 mm light chatter already occurs. If the controller is switched on, the stability limit increases from 3 mm to 4 mm. Therefore, a productivity increase of 33% is achieved. This result is reasonable taking into account, that the negative real part of the 75 Hz mode is reduced by 26% for gain settings  $K_C$  at which the actuator does not saturate. Evaluating the

cutting forces at 4 mm depth of cut, the FFT shows a dominant chatter frequency at 76 Hz without active damping, which disappears when the MbVF controller is turned on. At higher depths of cut, the actuator saturates and is not able to damp the chatter vibrations anymore.

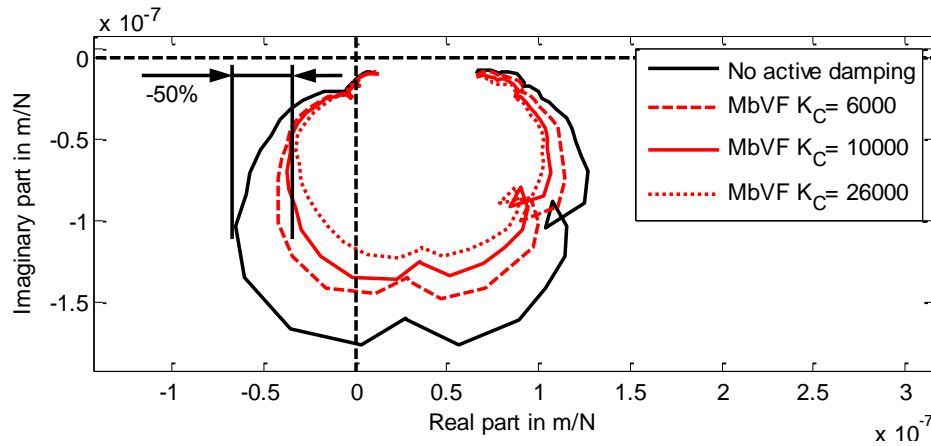


Figure 12: Nyquist plot of the MbVF controller with advanced filters at higher gain settings

Table 4: Filter parameters of all filters used in this paper

	High-pass filter	Low-pass filter	Notch filter 1	Notch filter 2
Cut-off frequency	5 Hz	2000 Hz	60 Hz	108.3 Hz-
Quality factor	0.707	0.707	7.5	5.0

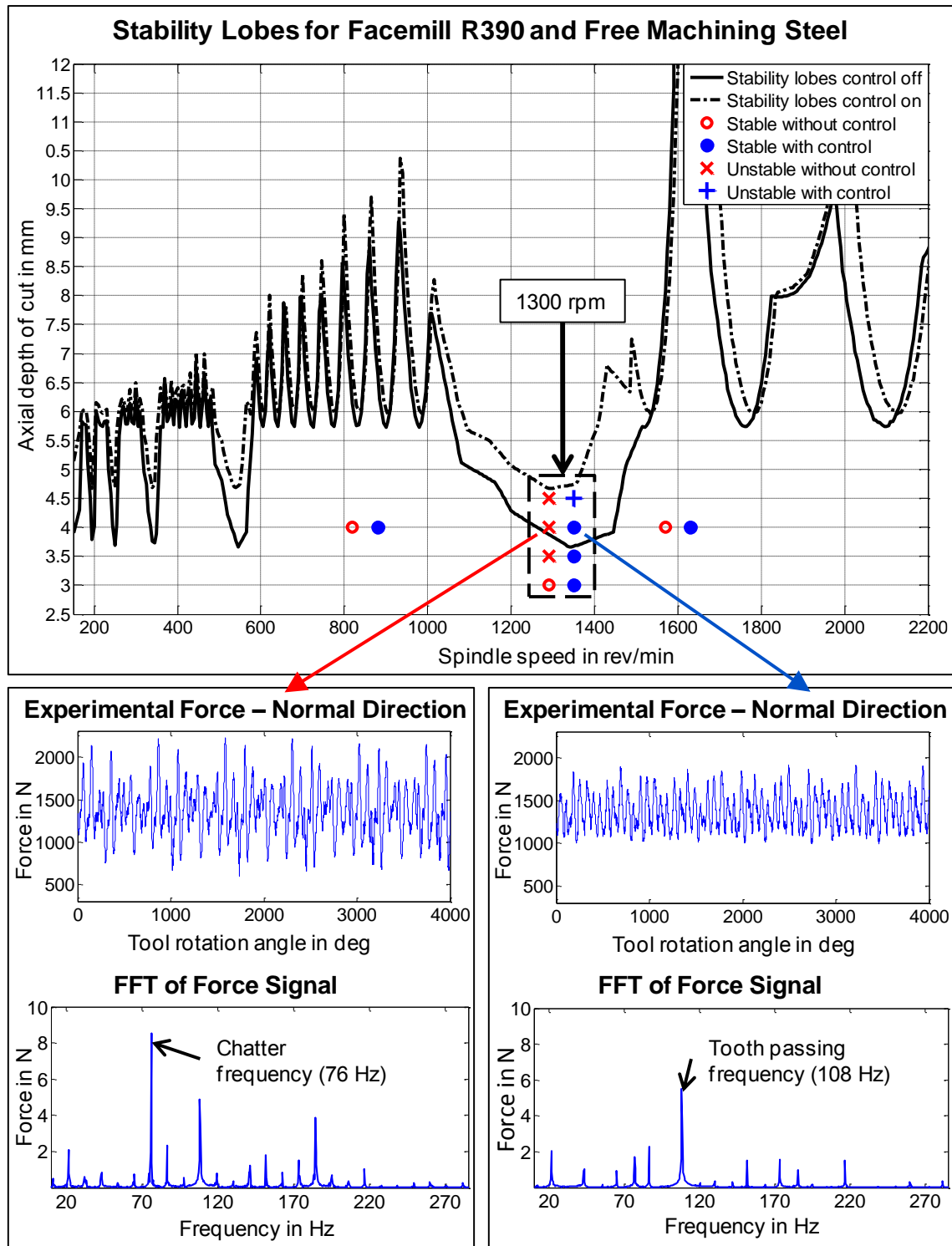


Figure 13: Analytically predicted stability lobes of a facemill with five inserts for control on and off; the feedrate is  $f = 0.12$  mm/tooth – experimental results

## 6. CONCLUSIONS

For milling machines the material removal rate is often limited by an insufficient stability of the machine. Active damping can be used to improve the stability limits of milling machines in order to increase the productivity. In this paper an efficient method was presented, how to setup an



adaptronic system for active damping on an existing machine tool used for heavy-duty milling operations. Besides of a methodology for positioning the actuator, a new control strategy was introduced, which shows a significantly higher performance than the commonly-used direct velocity feedback (DVF) controller. For the machine used in this research the new control strategy shows a 29% higher reduction of the negative real part of the critical eigenmode in simulation compared to a DVF controller. Analytically predicted stability lobes were calculated and verified by chatter tests. In total an increase of 33% in productivity was achieved.

## ACKNOWLEDGEMENT

The results presented in this paper were accomplished during a scholarship of Robin Kleinwort at the Manufacturing Automation Laboratory (MAL) in Vancouver/Canada. At the MAL this work was supervised by Prof. Dr. Yusuf Altintas, whereas Prof. Dr.-Ing. Michael F. Zaeh was the supervisor at the Institute for Machine Tools and Industrial Management (*iwb*) at the Technische Universität München (TUM), Germany. Financial support was provided through the PROMOS-Program by the German Academic Exchange Service (DAAD).

## REFERENCES

1. **Smith, S. and Tlustý, J., (1992)** "Stabilizing Chatter by Automatic Spindle Speed Regulation", CIRP Annals - Manufacturing Technology, Vol.41, No.1, pp. 433–436.
2. **Altintas, Y. and Budak, E., (1995)** "Analytical Prediction of Stability Lobes in Milling", CIRP Annals - Manufacturing Technology, Vol.44, No.1, pp. 357–362.
3. **Yang, Y.; Muñoz, J.; Altintas, Y (2010)** "Optimization of multiple tuned mass dampers to suppress machine tool chatter", International Journal of Machine Tools & Manufacture, Vol.50, No.9, pp. 834–842.
4. **Simnofske, M.; Raatz, A.; Hesselbach, J. (2009)** "Design process for adaptronic machine tools", Production Engineering, Vol.3, No.4-5, pp. 461–468.
5. **Zulaika, J.; Campa, F.; Lopez de Lacalle, L.N. (2011)** "An integrated process-machine approach for designing productive and lightweight milling machines", International Journal of Machine Tools & Manufacture, Vol.51, pp. 591–604.
6. **Zaeh, M. F.; Waibel, M.; Baur, M. (2009)** "A Computational Approach to the Integration of Adaptronic Structures in Machine Tools", Computational Structural Engineering, pp. 1017–1028.
7. **Brecher, C.; Manoharan, D.; Klein, W. (2010)** "Active compensation for portal machines", Production Engineering Vol.4, No.2-3, pp. 255–260.
8. **Locatelli, G. (2001)** "Piezo-actuated adaptive structures for vibration damping and shape control - modeling and testing", PhD-thesis, TU Munich Mech. Eng. Dept., Munich.





9. **Ehmann, C.; Nordmann, R. (2004)** „Gegenueberstellung von Reglerstrategien zur aktiven Schwingungsdaempfung am Beispiel einer Werkzeugmaschine“, Proceedings of Adaptronic Congress, Hildesheim.
10. **Munoa, J.; Mancisidor, I.; Loix, N.; Uriarte, L.; Barcena, R.; Zatarain, M. (2013)** “Chatter suppression in ram type travelling column milling machines using a biaxial inertial actuator”, CIRP Annals - Manufacturing Technology, Vol.62, pp. 407–410.
11. **Preumont, A. (2002)** Vibration control of active structures. 2nd ed., Dordrecht, Boston. Kluwer Academic Publishers, ISBN: 1402004966.
12. **Ewins, D. J. (1984)** Modal testing. 2nd ed., New York. Research Studies Press; Wiley, Letchworth, Hertfordshire, England, ISBN: 978-0-8638-0218-8.
13. **Zumbahlen, H. (2008)** Linear circuit design handbook, Amsterdam, Boston. Elsevier/Newnes Press, ISBN: 978-0-7506-8703-4



## A MODEL OF TOOL POINT DYNAMICS CONSIDERING EFFECTS OF BI-DISTRIBUTED JOINT INTERFACES

**Yun YANG**, *yunyang@mail.nwpu.edu.cn* Northwestern Polytechnical University, 710072 Xi'an, P.R. China

**Min WAN**, *m.wan@nwpu.edu.cn* Northwestern Polytechnical University, 710072 Xi'an, P.R. China

**Weihong ZHANG**, *zhangwh@nwpu.edu.cn* Northwestern Polytechnical University, 710072 Xi'an, P.R. China

### ABSTRACT

This paper investigates the dynamics of cutting tool point by modeling tool-collet and collet-holder joint interfaces as two zero-thickness damped-elastic layers with variant stiffness along the cutter's axis. The tool-collet assembly is considered to rest on the resilient support provided by the spindle-holder assembly. Dynamics of the tool and the collet was modeled using Euler-Bernoulli beam theory. Properties of the joint interfaces were identified by minimizing the difference between the measured and predicted frequency response functions. Tool point dynamics of tool mounted in different holders was predicted by the proposed model. Experimental results showed that the model is valid for different spindle-holder-tool combinations.

**Keywords:** Tool point dynamics, Frequency response function (FRF), Receptance coupling, Euler-Bernoulli beam, Stability lobe diagram

### 1. INTRODUCTION

Frequency response function (FRF) of the tool point is important for the prediction of stability lobe diagram (SLD), from which chatter-free process parameters, such as feed, depth of cut and spindle speed can be selected properly to avoid tool breakage and poor machining accuracy. Determinations of tool point FRFs are usually based on direct impact modal tests [Tlustý & Ismail, 1981; Altintas & Budak, 1995; Bayly et al., 2003; and Insperger & Stepan, 2004] and analytical means supported by beam theory [Schmitz & Donaldson, 2000; and Albertelli et al., 2013]. Experimental measurement has the advantage of high accuracy but its application is limited by the repeated and time-consuming measurements as holder and tool

vary. To overcome this drawback, many researchers performed computational methods in the past.

[Schmitz & Donaldson, 2000] applied receptance coupling substructure analysis (RCSA) of structural dynamics to calculate tool point FRFs by treating the spindle-holder-tool assembly as two substructures, i.e., spindle-holder and overhung tool. Much attention was paid to improving the model. For example, [Park et al., 2003] pointed out the importance of both rotational dynamics at the joints and the rotational dynamic response of the spindle-holder substructure for the accurate prediction of FRF. [Kivanc & Budak, 2004] investigated the effects of contact length and clamping torque on the holder-tool joint parameters. [Park & Chae, 2008] emphasized the effect of joint dynamics of modular tools on tool point receptances and presented a method for identification of the joint dynamics. [Albertelli et al., 2013] used a finite difference method to overcome the drawbacks in the estimation of the receptances of the spindle-holder. Later, [Schmitz and Duncan, 2005] proposed the second-generation RCSA method, in which the spindle-holder-tool assembly is divided into three substructures: the spindle-holder base subassembly, the extended holder component and the overhung tool component. [Ertürk et al., 2006] enriched the RCSA by analytically modeling the spindle-holder-tool dynamics using Timoshenko beam theory. [Bediz et al., 2012] presented new results for modeling three-dimensional dynamic behavior of milling tools by the spectral-Tchebyshev technique considering the actual fluted geometry.

It is worth noting that the above works were conducted with the assumption of lumped joint locating at the junction between the portions of the tool inside and outside the holder. To consider the dynamical interactions between tool-holder joint interfaces, [Schmitz et al., 2007] developed the third generation RCSA method by including multiple connections between the tool and holder. [Movahhedy & Gerami, 2006] used two linear joint elements to equivalently simulate the rotational stiffness of the joint. [Ahmadi & Ahmadian, 2007] considered the tool-holder interface as a single distributed damped-elastic interface layer with variable stiffness.

This paper proposed a bi-distributed interfaces model to analyze the tool point dynamics for collet chuck holder. The changes of stiffness along the tool-collet and holder-collet joint interfaces were taken into account separately. The tool was considered to partly rest on the collet via a distributed damped-elastic tool-collet interface while the collet rests on the resilient support provided by the spindle-holder assembly via a distributed damped-elastic tool-collet interface. Tool point dynamics of tool mounted in different holders was predicted by the proposed model. The model was also experimentally verified for different spindle-holder-tool assemblies.

## 2. METHODOLOGY

As shown in Fig. 1, the joint of collet chuck holder was modelled separately as a distributed tool-collet and a holder-collet joint interface. Both joint interfaces were regarded as zero-thickness damped-elastic layers, which were denoted by nonuniform stiffness coefficients  $K_1(x)$  and  $K_2(x)$ , respectively. The collet was modelled as a continuous beam with variable cross section resting on a flexible support via the holder-collet joint interface. The tool was considered as a continuous step beam with two cross sections (the inserted and overhung parts) partly resting on the collet via the tool-collet joint interface. The dynamics of both the tool and collet were modeled by using Euler-Bernoulli beam [Ahmadi & Ahmadian, 2007; and Rao, 2011]:

$$E_1 I_1 \frac{\partial^4 U_1(x,t)}{\partial x^4} + m_1 \frac{\partial^2 U_1(x,t)}{\partial t^2} = K_1(x) [U_2(x,t) - U_1(x,t)], \quad 0 \leq x < L_1 \quad (1)$$

$$\begin{aligned} & \frac{\partial^2}{\partial x^2} \left[ E_2 I_2(x) \frac{\partial^2 U_2(x,t)}{\partial x^2} \right] + m_2(x) \frac{\partial^2 U_2(x,t)}{\partial t^2} \\ & = K_2(x) [V(x,t) - U_2(x,t)] - K_1(x) [U_2(x,t) - U_1(x,t)], \quad 0 \leq x < L_1, \end{aligned} \quad (1.b)$$

$$E_3 I_3 \frac{\partial^4 U_3(x,t)}{\partial x^4} + m_3 \frac{\partial^2 U_3(x,t)}{\partial t^2} = 0, \quad L_1 \leq x < L, \quad (1.c)$$

where  $V(x,t)$  and  $U_s(x,t)$  ( $s=1,2,3$ ) are the lateral displacements of the holder, inserted part, collet and overhung part.  $L_1$  and  $L$  are the length of the tool inserted part and the whole tool.  $E_1$ ,  $E_2$ ,  $E_3$  are the Young's moduli of the material of the inserted part, collet and the overhung part.  $I_1$ ,  $I_2(x)$ ,  $I_3$  are the area moments of inertia of the inserted part, collet and the overhung part.  $m_1$ ,  $m_2(x)$  and  $m_3$  are the mass per unit length of the inserted part, collet and the overhung part.  $K_1(x)$  and  $K_2(x)$  are the stiffness coefficients of the tool-collet and holder-collet interface elastic layers, respectively. They were assumed to vary along the interface layers and identified by matching the calculated responses with the measured ones. In this paper, they were approximated as polynomial forms [Ahmadi & Ahmadian, 2007; and Eisenberger, 1994]. Note that  $I_2(x)$  and  $m_2(x)$  are functions of  $x$  due to the variable cross section of the collet.

Under the harmonic excitation, the steady-state solutions  $U_s(x,t)$  ( $s=1,2,3$ ) for the governing Eqs. (1) can be expressed as the product of shape functions  $W_s(x)$  ( $s=1,2,3$ ) and time-term  $e^{i\omega t}$ , where  $W_s(x)$  ( $s=1,2,3$ ) are complex shape functions due to the non-

proportional damping mechanism of the system. Similarly, the lateral displacement of the holder at arbitrary point can be approximated as the following polynomials:

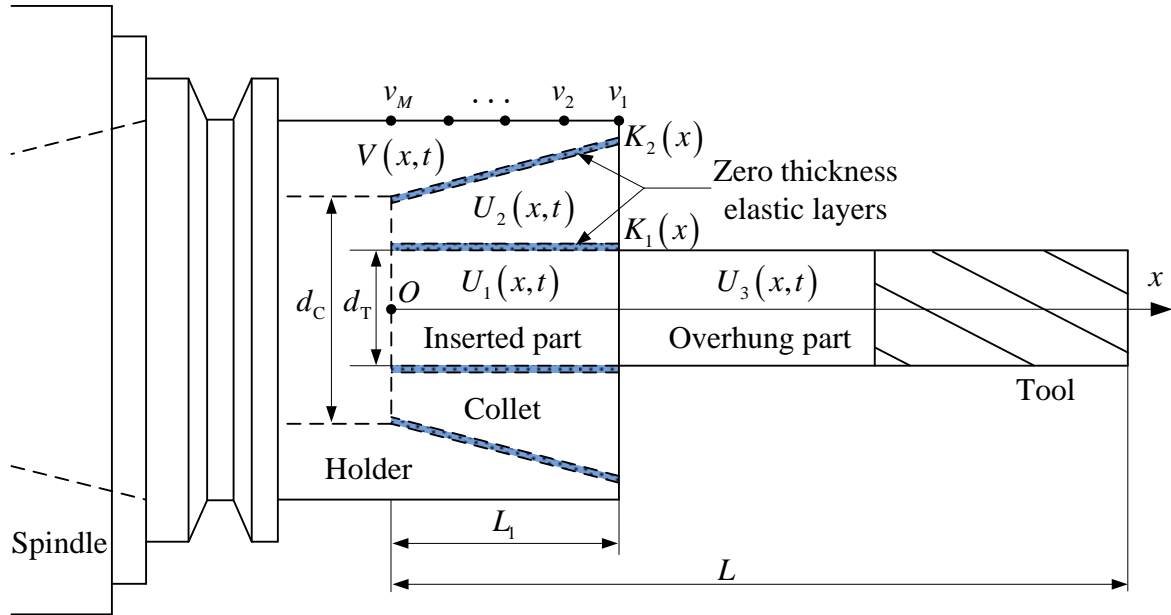


Fig. 1 The tool-spindle-holder assembly.

$$V(x,t) = v(x)e^{i\omega t} = [p_1(x)v_1 + p_2(x)v_2 + \dots + p_M(x)v_M]e^{i\omega t} = \mathbf{p}^T \mathbf{v}e^{i\omega t} \quad (2)$$

By substituting  $U_s(x,t)$  ( $s=1,2,3$ ) and  $V(x,t)$  into Eq. (1), the variables, i.e.  $x$  and  $t$ , in the partial differential eq. (1) can be separated, and ordinary differential equations are derived.

In order to obtain displacement-to-force receptance, the boundary conditions at the tool tip were a unit harmonic shear force with frequency  $\omega$  and zero moment. Whereas, boundary conditions on the other end of the tool included both zero shear force and zero moment. Under the compatibility, boundary conditions corresponding to the inserted and overhung parts of the tool included the equality of the displacement, the slope, the shear force and the moment. Besides, boundary conditions were both zero shear force and zero moment on each end of the collet, respectively.

The lateral displacement vector  $\mathbf{v}$  in Eq. (2) can be expressed as the relation between lateral displacements and shear forces, i.e. receptance, multiplied by shear forces.

$$\mathbf{v} = \mathbf{H}(\omega)\mathbf{f} \quad (3)$$

where  $\mathbf{H}(\omega)$  contains measured direct and cross displacement-to-force receptances at different points on spindle-holder assembly. The distributed force  $\mathbf{f}$  can be expressed as:

$$\mathbf{f} = (f_1, f_2, \dots, f_M)^T = \int_0^L \mathbf{p}K_2(x) [\Phi_2(x) - v(x)] dx$$

Finally, the tool point receptance is expressed as

$$H_T(\omega) = \frac{W_3(L)e^{i\omega t}}{e^{i\omega t}} = C_1 e^{i\lambda L} + C_2 e^{-i\lambda L} + C_3 e^{\lambda L} + C_4 e^{-\lambda L} \quad (4)$$

where the coefficients  $C_1, C_2, C_3, C_4$  can be determined by solving the partial differential equations above, and  $\lambda^4 = \frac{m_3 \omega^2}{E_3 I_3}$ .

### 3. EXPERIMENTAL VERIFICATION

Fig. 2 shows the procedure for the prediction of tool point dynamics. Two holders, i.e., long BT40-ER32-100 and short BT40-ER32-70 holders, are used to measure the spindle-holder subassembly receptances  $\mathbf{H}(\omega)$  required in Eq. (3). As shown in Fig. 3 (a) and (b), direct and cross receptances of spindle-holder were measured at some discretized points by standard impact tests, and results are shown in Fig. 3 (c) and (d).

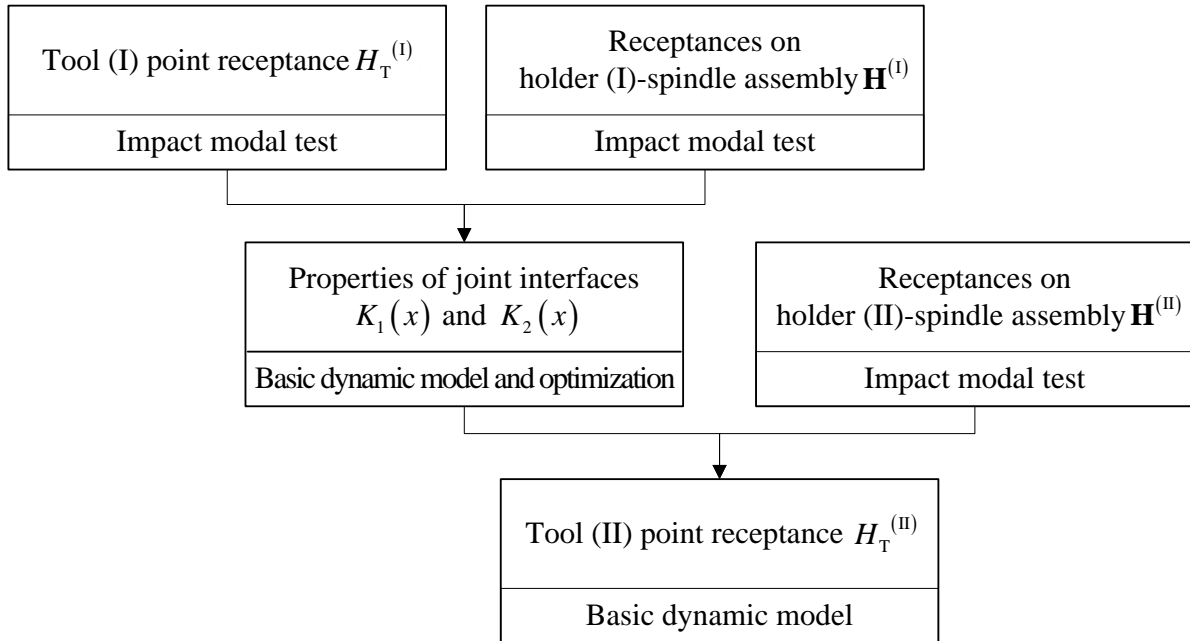
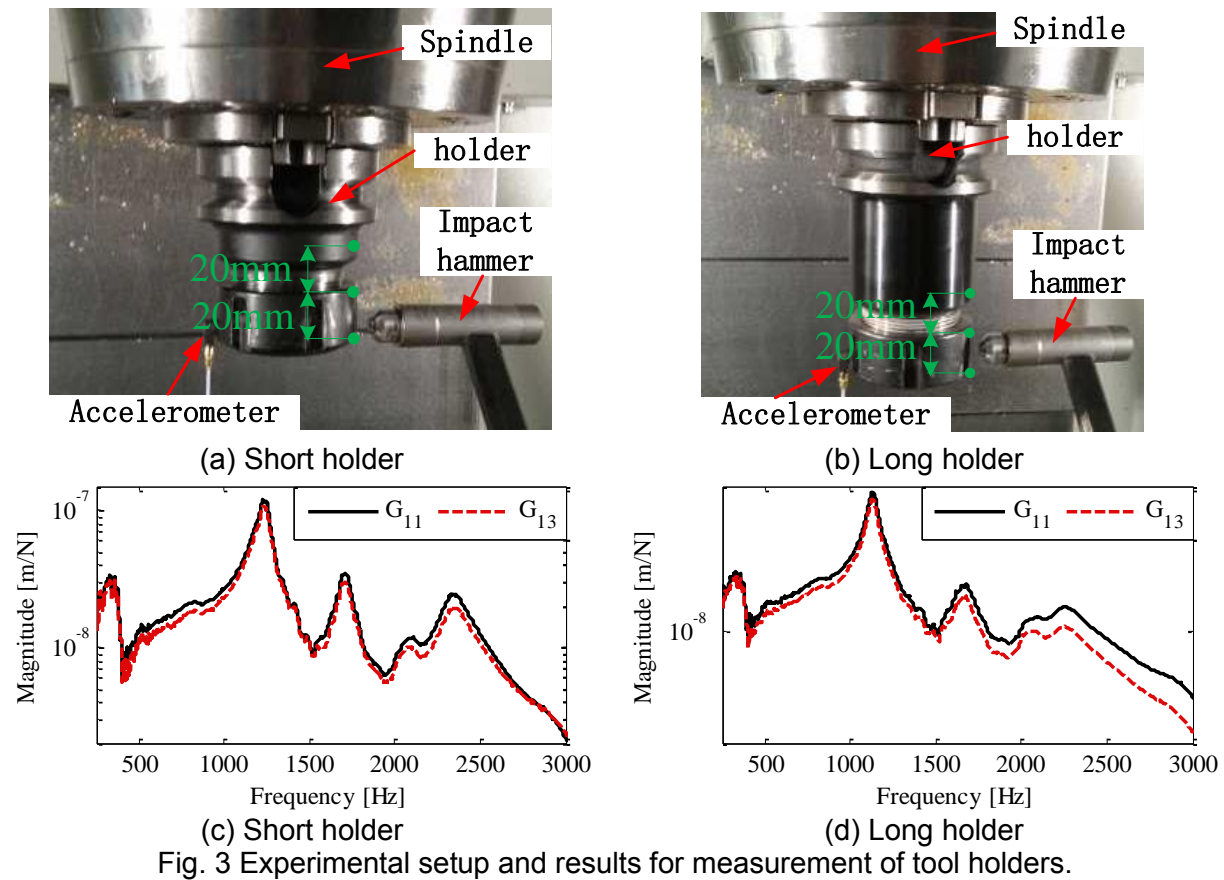


Fig. 2 Prediction procedure of tool point FRFs.

The stiffness properties of the joint interfaces were optimally identified by minimizing the difference between the predicted tool point FRF and the measured one from impact modal test on a tool blank mounted in long holder (see Fig. 4 (a)). Geometry and material properties of the blank tool are listed in Table 1. Table 2 shows the identified properties of joint interfaces, with which the predicted tool point FRF for tool blank was compared with the

measured one in Fig. 4 (b). Percentage difference between measured and predicted dominant natural frequency was 0.74%.



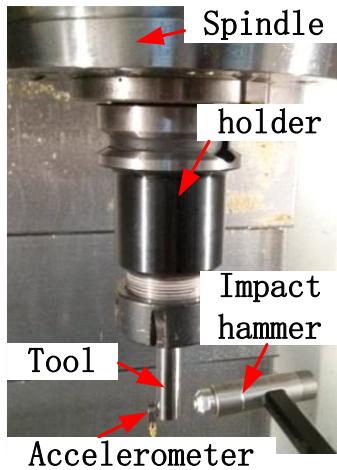
Further verification was also carried out by the following two set-ups. First, the tool blank in the long holder was replaced by the Tool 2, whose parameters are also shown in Table 2. Second, Tool 2 was mounted in the short holder. The properties of joint interfaces identified from the blank were directly adopted to predict the tool point FRFs. Comparisons of measured and predicted tool point receptances in different holders shown in Fig. 5 indicate that there were good agreements between measurements and predictions although the set-up is changed. This phenomenon suggested that the properties of joint interfaces are independent of the holder geometries, such as its length and diameter.

Table 1 Tool blank's geometry and material properties.

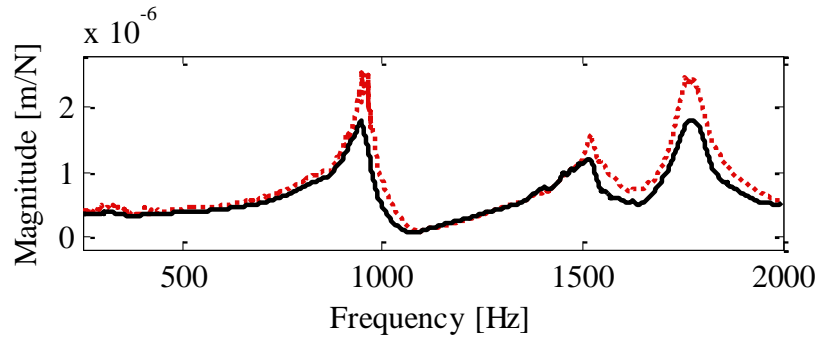
Tool No.	Diameter $d_T$ (mm)	Total length L (mm)	Tooth length (mm)	Young's Modulus (N/m <sup>2</sup> )	Density (kg/m <sup>3</sup> )	Damping
1	12	110	Blank, no tooth	$5.58 \times 10^{11}$	14500	0.0015
2	12	83	27			

Table 2 The identified properties of joint interfaces.

$\kappa_{A,0}$ (N/m <sup>2</sup> )	$\kappa_{A,1}$ (N/m <sup>3</sup> )	$\eta_A$	$\kappa_{B,0}$ (N/m <sup>2</sup> )	$\kappa_{B,1}$ (N/m <sup>3</sup> )	$\eta_B$
1.420×10 <sup>11</sup>	-6.878×10 <sup>11</sup>	1.010×10 <sup>-3</sup>	2.889×10 <sup>10</sup>	-1.007×10 <sup>12</sup>	7.661×10 <sup>-2</sup>

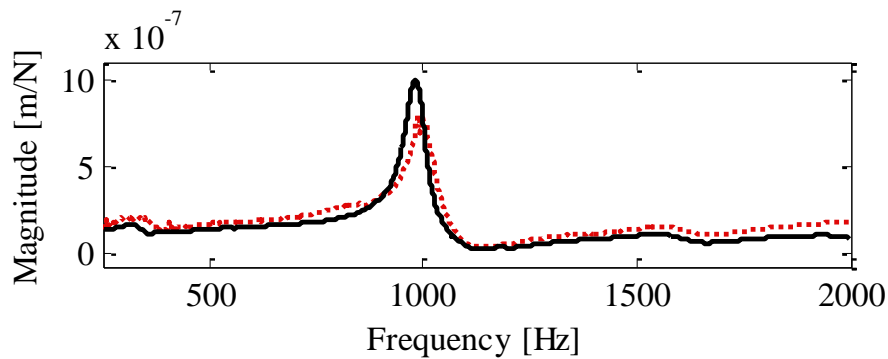


(a) Experimental setup

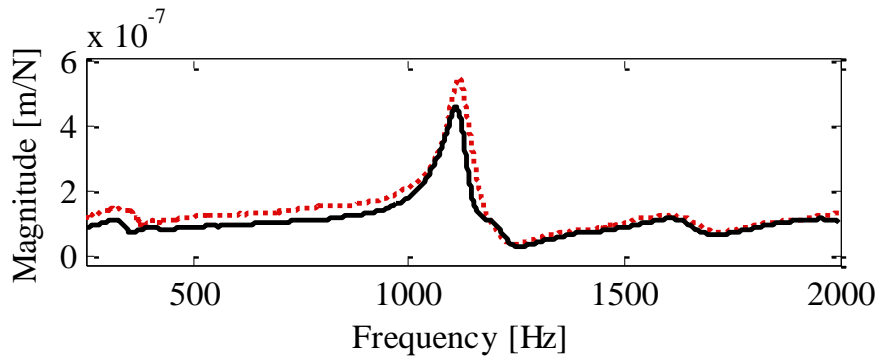


(b) Comparison of measured (solid line) and predicted (dashed line) tool point receptances

Fig. 4 Identification of properties of the joint interfaces.



(a) Tool point FRF in long holder



(b) Tool point FRF in short holder

Fig. 5 Comparison of measured (solid line) and predicted (dashed line) tool point receptances in different holders.





#### 4. CONCLUSIONS

A model was proposed for the prediction of dynamics of the tool mounted in collet chuck. The interfaces between tool-collet and collet-holder joints were regarded as two distributed damped-elastic layers. The properties of interfaces were determined by optimization method. Experiments showed that the properties of joint interfaces can be used to predict tool point dynamics of different tool-holder set-ups. The model is valid for different tool-holders such as shrink fit and hydraulic holders.

#### 5. ACKNOWLEDGEMENT

This research has been supported by the National Natural Science Foundation of China under Grant No. 11272261, the Program for New Century Excellent Talents in University under Grant No. NCET-12-0467, the NPU Foundation for Fundamental Research under grant No. JC20110251 and 111 Project under Grant No. B07050.

#### REFERENCES

1. **Tlustý J., Ismail F., (1981)**, "Basic nonlinearity in machining chatter", CIRP Ann., Vol.30, pp 299-304.
2. **Altintas Y., Budak E., (1995)**, "Analytical Prediction of Stability Lobes in Milling", CIRP Ann., Vol.44, pp 357-362.
3. **Bayly P.V., Halley J.E., Mann B.P., Davies M.A., (2003)**, "Stability of interrupted cutting by temporal finite element analysis", Trans. ASME, J. Manuf. Sci. E., Vol.125 pp 220-225.
4. **Inspurger T., Stepan G., (2004)**, "Updated semi-discretization method for periodic delay-differential equations with discrete delay", Int. J. Numer. Meth. Eng., Vol.61 pp 117-141.
5. **Schmitz T., Donaldson R., (2000)**, "Predicting High-Speed Machining Dynamics by Substructure Analysis", CIRP Ann., Manuf. Techn., Vol.49 pp 303-308.
6. **Albertelli P., Goletti M., Monno M., (2013)**, "A new receptance coupling substructure analysis methodology to improve chatter free cutting conditions prediction", Int. J. Mach. Tools. Manuf., Vol.72 pp 16-24.
7. **Park S.S., Altintas Y., Movahhedy M., (2003)**, "Receptance coupling for end mills", Int. J. Mach. Tools. Manuf., Vol.43 pp 889-896.
8. **Kivanc E., Budak E., (2004)**, "Structural modeling of end mills for form error and stability analysis", Int. J. Mach. Tools. Manuf., Vol.44 pp 1151-1161.
9. **Park S.S., Chae J., (2008)**, "Joint identification of modular tools using a novel receptance coupling method", Int. J. Adv. Manuf. Technol., Vol.35 pp 1251-1262.



10. **Schmitz T.L., Duncan G.S., (2005)**, “Three-Component Receptance Coupling Substructure Analysis for Tool Point Dynamics Prediction”, Trans. ASME, J. Manuf. Sci. E., Vol.127 pp 781-790.
11. **Ertürk A., Özgüven H.N., Budak E., (2006)**, “Analytical modeling of spindle-tool dynamics on machine tools using Timoshenko beam model and receptance coupling for the prediction of tool point FRF”, Int. J. Mach. Tools. Manuf., Vol.46 pp 1901-1912.
12. **Bediz B., Kumar U., Schmitz T.L., Ozdoganlar O.B., (2012)**, “Modeling and experimentation for three-dimensional dynamics of end mills”, Int. J. Mach. Tools. Manuf., Vol.53 pp 39-50.
13. **Schmitz T.L., Powell K., Won D., Duncan G.S., Sawyer W.G., Ziegert J.C., (2007)**, “Shrink fit tool holder connection stiffness/damping modeling for frequency response prediction in milling”, Int. J. Mach. Tools. Manuf., Vol.47 pp 1368-1380.
14. **Movahhedy M.R., Gerami J.M., (2006)**, “Prediction of spindle dynamics in milling by sub-structure coupling”, Int. J. Mach. Tools. Manuf., Vol.46 pp 243-251.
15. **Ahmadi K., Ahmadian H., (2007)**, “Modelling machine tool dynamics using a distributed parameter tool-holder joint interface”, Int. J. Mach. Tools. Manuf., Vol.47 pp 1916-1928.
16. **Rao S.S., (2011)**, Mechanical Vibrations, 5th ed., Prentice Hall, Upper Saddle River, N.J..
17. **Eisenberger M., (1994)**, Vibration frequencies for beams on variable one- and two-parameter elastic foundations, J. Sound Vib., Vol.176 pp 577-584.





## MECHANICS AND DYNAMICS OF MULTI-FUNCTIONAL TOOLS

**Min WAN**, *m.wan@nwpu.edu.cn*, School of Mechanical Engineering, Northwestern Polytechnical University, 710072 Xi'An, Shaanxi, People's Republic of China.

**Z. Murat KILIÇ**, *kilic@alumni.ubc.ca*, Manufacturing Automation Laboratory, University of British Columbia, V6T1Z4, Vancouver, Canada

**Yusuf ALTINTAŞ**, *altintas@mech.ubc.ca*, Manufacturing Automation Laboratory, University of British Columbia, V6T1Z4, Vancouver, Canada

### ABSTRACT

The multi-functional tools are frequently used in the industry because of their advantage of combining drilling, boring and chamfering holes in one operation. In this study, we developed a mechanics/dynamics model to predict cutting forces and torque, and stability of the operation. General cutting mechanics is applied to analytically predict the oblique cutting forces along the arbitrary cutting edge of the cutter. The regenerative effect of lateral and torsional/axial vibrations is included in the model. Dynamic chip thickness is modeled with multiple delays due to distribution of cutting edges on the cutter body. The lateral and torsional/axial chatter stability of the complete hole making operation is simulated in semi-discrete time domain. The proposed static cutting force and chatter stability prediction models are experimentally validated with a multi-functional tool for drilling Aluminum Al7050.

**Keywords:** Chatter; multi-functional tools; multiple delays; cutting force

### 1. INTRODUCTION

Holes with large diameter, chamfers and steps were traditionally machined by a sequence of operations with dedicated but different tools in the past. There have been many proposed models which predict the mechanics and dynamics of individual operations such as drilling, boring and chamfering (Altintas, 2012). Hole-making operations with multiple tools have long machining cycle time due to the interruption of tool change process. But, this is not desirable in production. Recent trend is to complete the hole-making with single tool with multiple cutting functions. For example, multi-functional tools shown in Fig.1 can open a pilot hole, drill, enlarge and chamfer a hole in one step. These tools reduce the machining cycle time and costs significantly. However the tool and process must be designed to keep the cutting torque, cutting forces and static deflection within tolerable limits. Excessive chatter vibrations

must be avoided as well. This paper presents the combined mechanics and dynamics of making stepped holes with multi-functional tools.

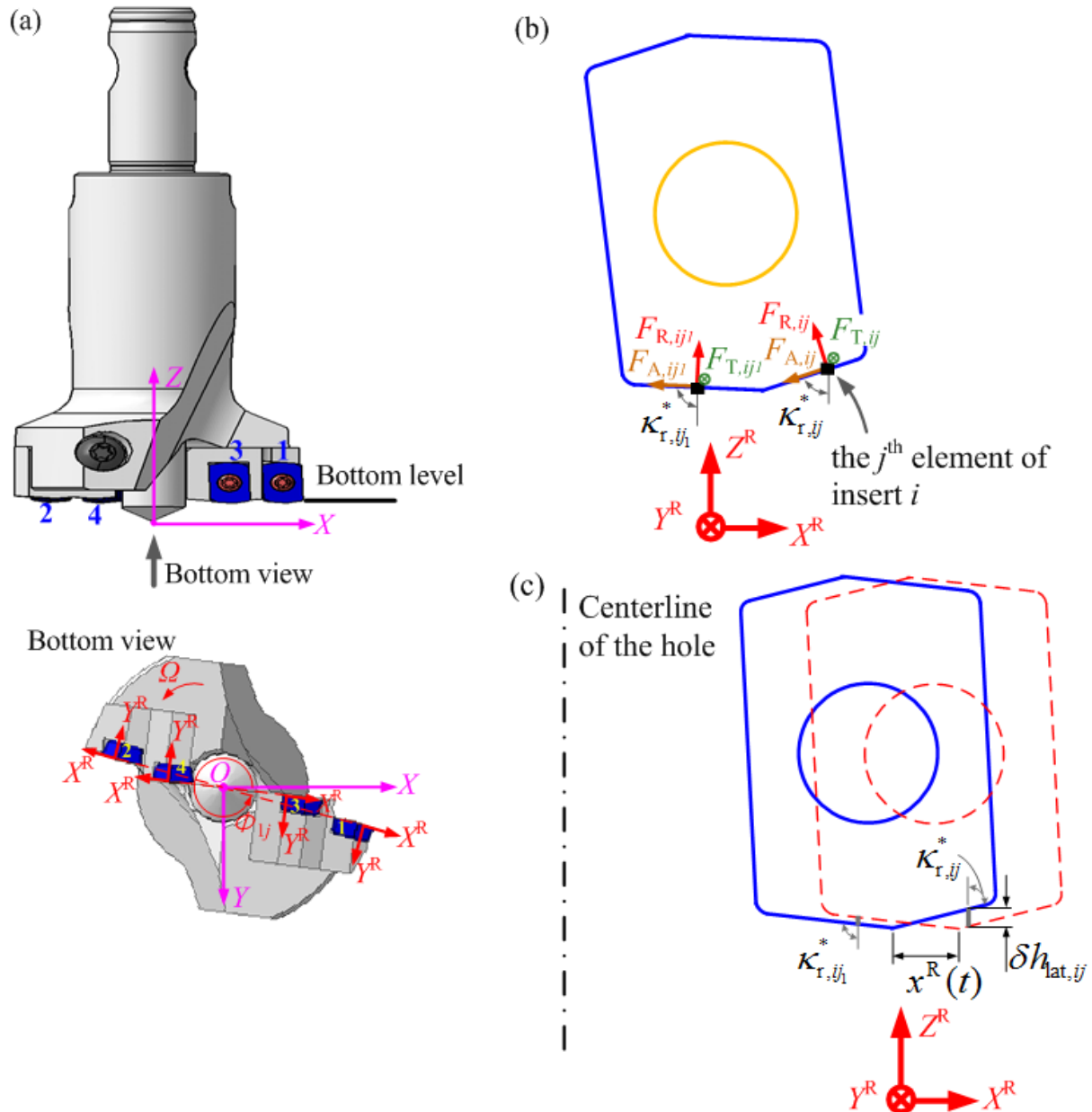


Fig.1 Geometry, coordinates and cutting forces of three multi-functional tools. (a) Kennametal drill with multiple inserts (XYZ is the Cartesian coordinate system); (b) Cutting forces related to the cutting edge elements  $j$  and  $j_1$  of insert  $i$ ; (c) Chip thickness variation contributed by lateral deflections.

The past literature has mainly been on the modeling of mechanics and dynamics of individual operations with dedicated tools. For example, the mechanics of drilling has been widely studied to predict cutting forces and torque (Chandrasekharan et al., 1995; Roukema and Altintas, 2007a; Sambhav et al., 2013; Strenkowski et al., 2004). (Roukema & Altintas, 2007a)



used orthogonal to oblique cutting transformation (of (Budak et al. 1996)) material's shear stress, shear angle and friction coefficient.

The mechanistic methods identify the relationship between the chip area and cutting forces by empirically predicting the cutting force coefficients from a set of experimental measurements. (Chandrasekharan et al., 1996) expressed the specific normal and tangential cutting force coefficients as a function of feed, cutting speed and normal rake angle for conical drills for machining non-isotropic, fiber reinforced composite materials.

Considerable research has also been conducted on the modeling of forced and chatter vibrations of drilling. (Pirtini and Lazoglu, 2005) predicted the effect of forced vibrations on the quality of holes by neglecting the regeneration of chip thickness, hence chatter. Flexible drills experience torsional, axial and lateral vibrations which regenerates the chip thickness, and cause chatter (Roukema and Altintas, 2007a). Chatter stability of machining operations are studied numerically in time domain, or analytically in discrete time and frequency domains (Altintas and Weck, 2004). (Ema et al., 1988) modeled the lateral chatter stability of drilling to explain the mechanism behind whirling, which leads to noncircular holes. (Bayly et al., 2002) developed a frequency domain solution for torsional-axial chatter including edge rubbing, and showed that backward whirling modes of the drill occurs at the odd integer of spindle speeds. (Filiz and Ozdoganlar, 2010) derived a unified dynamics model for both macro- and micro- drills using spectral-Tchebychev technique. They pointed out that the model's efficiency can be increased by considering the tool's circular cross-section (shank, extension, and tapered sections) as a one-dimensional beam while considering the fluted portion as a three-dimensional beam. Roukema and Altintas also presented both numerical (Roukema and Altintas, 2007a) and frequency (Roukema and Altintas, 2007b) domain prediction of hole shape, vibrations and chatter stability of drilling by including lateral, torsional and axial vibrations. However, the past chatter stability models showed poor agreement with experimental results due to un-modelled process damping mechanism. (Ahmadi and Altintas, 2013) proposed a model to predict the drilling stability chart by including the lateral, torsional and axial vibrations with process damping which led to improved accuracy in predicting chatter stability limits.

The previous studies did not consider the dynamics of multi-functional tools which have layers of simultaneously cutting edges with different geometry, varying stiffness and multiple delays. This paper presents a model that predicts the cutting forces and chatter stability of multifunctional tools which open stepped holes in one operation.

The paper is organized as follows. The geometric model of inserts, that are distributed at the bottom, around the periphery of the tool, is presented in Section 2. The geometric model is used to identify the location of discretized cutting edges with the corresponding axial rake,

radial rake and cutting edge angles which are used in orthogonal to oblique cutting transformations. The predicted cutting coefficients vary along the cutting edge due to changing cutting edge geometry and speed. The differential forces along the cutting edge are summed and projected at the Cartesian coordinates of the tool to predict the static cutting forces. The dynamics of the multi-functional tool is presented in Section 3. The effect of torsional, axial and lateral vibrations on the regenerative chip thickness is modeled. The effect of flank wear and cutting edge radius is included in the velocity dependent process damping forces. The dynamic cutting process is transformed into semi-discrete time domain which leads to the prediction of chatter stability. The prediction of cutting forces and chatter stability models are experimentally validated in Section 4 in machining Al7050 Aluminum alloy.

## 2. MECHANICS OF MULTI-FUNCTIONAL TOOLS

The multi-functional tool of Fig.1 demonstrates the modeling process. It has a twist drill at the center to open a pilot hole, and four identical inserts on its two flutes. Each insert is divided into  $m$  number of differential cutting edge elements having three differential cutting forces in tangential ( $F_{T,ij}$ ), radial ( $F_{R,ij}$ ) and axial ( $F_{A,ij}$ ) directions as shown in Fig.1, where  $i$  and  $j$  correspond to insert and differential cutting edge element indices, respectively. Since the geometry of each insert varies along its cutting edge, the cutting force coefficients are evaluated by applying oblique transformation of shear stress, shear angle and friction coefficient (Altintas, 2012). The radial rake angle ( $\gamma_r$ ), axial rake angle ( $\gamma_p$ ) and insert cutting edge angle ( $\kappa_r$ ), which are required in oblique transformation, are evaluated from the tool geometry as described in (Kaymakci et al. 2012). The number pattern of inserts is shown in Fig.1, and cutting edge element  $j$  of each insert ( $i$ ) is numbered in sequence that begins with 1 from the end close to the cutter's outer periphery.

The cutting forces contributed by the cutting edge element  $j$  of insert  $i$  is defined in cutting edge coordinate (RTA coordinate system) as follows (Kaymakci et al., 2012):

$$\begin{aligned} F_{R,ij} &= K_{Rc,ij} b_{ij} h_{ij} + K_{Re,ij} c_{ij} \\ F_{T,ij} &= K_{Tc,ij} b_{ij} h_{ij} + K_{Te,ij} c_{ij} \\ F_{A,ij} &= K_{Ac,ij} b_{ij} h_{ij} + K_{Ae,ij} c_{ij} \end{aligned} \quad (1)$$

where  $h_{ij}$  and  $b_{ij}$  are the instantaneous uncut chip thickness and width of the cutting edge element.  $h_{ij}$  is measured in spindle axis direction (Z) whereas  $b_{ij}$  is defined in the direction normal to Z axis.  $c_{ij}$  is the width of the cutting edge.  $K_{Rc,ij}$ ,  $K_{Tc,ij}$  and  $K_{Ac,ij}$  are cutting force coefficients contributed by the chip shearing, and  $K_{Re,ij}$ ,  $K_{Te,ij}$  and  $K_{Ae,ij}$  are cutting force

coefficients contributed by the edge ploughing (Altintas, 2012). The cutting force coefficients are evaluated from an orthogonal cutting database using the generalized transformations (Kaymakci et al., 2012), and the coordinate transformations from the rake face to cutting edge are briefly summarized as follows.

$$\begin{aligned} [K_{Rc,ij}, K_{Tc,ij}, K_{Ac,ij}]^T &= \mathbf{T}_{IU} [K_{uc,ij}, K_{vc,ij}]^T \\ [K_{Re,ij}, K_{Te,ij}, K_{Ae,ij}]^T &= \mathbf{T}_{IU} [K_{ue,ij}, K_{ve,ij}]^T \end{aligned} \quad (2)$$

with

$$\mathbf{T}_{IU} = \begin{bmatrix} \cos \gamma_{n,ij} \cos \eta_{ij} & -\sin \gamma_{n,ij} \\ \sin \lambda_{s,ij} \cos \eta_{ij} + \cos \lambda_{s,ij} \sin \gamma_{n,ij} \cos \eta_{ij} & \cos \lambda_{s,ij} \cos \gamma_{n,ij} \\ -\cos \lambda_{s,ij} \sin \eta_{ij} + \sin \lambda_{s,ij} \sin \gamma_{n,ij} \cos \eta_{ij} & \sin \lambda_{s,ij} \cos \gamma_{n,ij} \end{bmatrix} \quad (3)$$

where  $\lambda_{s,ij}$ ,  $\gamma_{n,ij}$  and  $\eta_{ij}$  are the oblique, normal rake and chip flow angles associated with the cutting edge element  $j$  of insert  $i$ .

Based on the geometric relationship shown in and Eq.(1), the cutting forces in X, Y and Z directions and the torque in torsional direction can be evaluated as follows.

$$[F_{X,ij}, F_{Y,ij}, F_{Z,ij}, T_{c,ij}]^T = \mathbf{T}_{OR} \mathbf{T}_{R1} [F_{R,ij}, F_{T,ij}, F_{A,ij}, F_{T,ij} R_{ij}]^T \quad (4)$$

where  $R_{ij}$  is the local radius of the cutting edge element  $j$  of insert  $i$ . Transformation matrices  $\mathbf{T}_{OR}$  and  $\mathbf{T}_{R1}$  are functions of true cutting edge angle  $\kappa_{r,ij}^*$  and position angle  $\phi_{ij}$  as illustrated in Fig.1. Total cutting forces ( $F_X$ ,  $F_Y$ ,  $F_Z$ ) and torque ( $T_c$ ) acting on the whole tool are evaluated by summing the contribution of elemental cutting forces of all edges:

$$[F_X, F_Y, F_Z, T_c]^T = [F_{X,In}, F_{Y,In}, F_{Z,In}, T_{c,In}]^T + [F_{X,Ce}, F_{Y,Ce}, F_{Z,Ce}, T_{c,Ce}]^T \quad (5)$$

where  $[F_{X,In}, F_{Y,In}, F_{Z,In}, T_{c,In}]^T = [\sum_{i,j} F_{X,ij}, \sum_{i,j} F_{Y,ij}, \sum_{i,j} F_{Z,ij}, \sum_{i,j} T_{c,ij}]^T$  is the total cutting forces/torque vector contributed by inserts, and  $[F_{X,Ce}, F_{Y,Ce}, F_{Z,Ce}, T_{c,Ce}]^T$  is the forces/torque vector contributed by the central twist drill.

### 3. DYNAMICS OF MULTI-FUNCTIONAL TOOLS

The dynamics of the cutting process is presented by modeling the regenerative chip thickness, time delays caused by the distribution of inserts and semi-discrete time domain stability of the system with torsional/axial and lateral vibrations as follows.

**1. Dynamic Chip Thickness:** Since the static chip thickness does not contribute to the chatter stability of machining, only the regenerative chip generated by the lateral, axial and torsional vibrations of the tool is considered. If the time delay is  $\tau$  between the current and previously cut surface locations of the cutting edge element  $j$  of insert  $i$ , the dynamic chip



load at time  $t$  is evaluated by considering the axial ( $Z$ ), lateral ( $X, Y$ ) and torsional ( $\theta$ ) vibrations as follows (Fig.1c):

$$\Delta h_{ij} = \Delta h_{Z,ij} + \Delta h_{\theta,ij} + \Delta h_{lat,ij} \quad (6)$$

**2. Dynamics of the Multi-Functional Tools:** The general dynamic model of multifunctional tool in modal space is:

$$\ddot{\mathbf{P}}(t) + 2\xi\omega\dot{\mathbf{P}}(t) + \omega^2\mathbf{\Gamma}(t) = \mathbf{U}^T\mathbf{H}\mathbf{U}\mathbf{F}(t) - \sum_{l=1}^{N_d} [\mathbf{U}^T\mathbf{H}_l\mathbf{U}\mathbf{F}(t - \tau_l)] + \mathbf{U}^T\mathbf{H}_d\mathbf{U}\mathbf{F}(t), \quad \mathbf{H} = \sum_{l=1}^{N_d} \mathbf{H}_l \quad (7)$$

where  $\xi$  and  $\omega$  are the diagonal damping ratio and natural frequency matrices with the size  $N_m \times N_m$ , respectively.  $\mathbf{\Gamma}(t)$ ,  $\dot{\mathbf{P}}(t)$ ,  $\ddot{\mathbf{P}}(t)$  are the modal displacement, velocity and acceleration vectors, in time domain.  $\mathbf{H}_l$  and  $\mathbf{H}_d$  are directional coefficient matrices relating chip geometry to cutting force and relating process damping to cutting force, respectively.  $\mathbf{U}$  is the mass normalized mode shape and  $N_m$  is the number of dominant modes.  $N_d$  is the total number of delay items, and  $N_d = 4$  for the tool in this study.

The chatter stability of hole making process can be analyzed separately for lateral and torsional/axial vibrations since they have uncoupled dynamics in regeneration mechanism.

**3. Torsional-axial stability:** The torsional and axial deflections of the drill are assumed dominating, and the lateral forces and vibrations are neglected. If there is a single delay ( $N_d = 1$ ), the stability of Eq.(7) has been well reported for standard twist drills in Refs.(Altintas, 2012)(Arvaje and Ismail, 2006)(Arvaje and Ismail, 2006b)(Roukema and Altintas, 2007b). Here, the dynamics of multi-functional drill is represented by a set of differential equations (DDE) with multiple delays, and analyzed with an extended semi-discretization method of (Insperger and Stépán, 2004) as follows.

Eq.(7) can be rewritten in the following compact format form.

$$\ddot{\mathbf{Y}}(t) = \mathbf{A}\mathbf{Y}(t) + \sum_{l=1}^{N_d} \mathbf{B}_l\mathbf{Y}(t - \tau_l) \quad (8)$$

If the spindle period ( $T$ ) is divided into  $\varsigma$  uniform discrete time intervals with length  $\Delta t = T / \varsigma$ , the solution of Eq.(8) at discrete time interval ( $a+1$ ) can be approximated as:

$$\mathbf{Y}_{a+1} = \mathbf{P}_a\mathbf{Y}_a + \sum_{l=1}^{N_d} (w_{l,1}\mathbf{V}_{l,a}\mathbf{Y}_{a-q_l+1} + w_{l,2}\mathbf{V}_{l,a}\mathbf{Y}_{a-q_l}) \quad (9)$$

where  $\mathbf{Y}_a$  stands for the system's state  $\mathbf{Y}(t_a)$  at discrete time  $t_a = a\Delta t$ .  $q_l$  is the number of intervals covering the delay period  $\tau_l$ . The system's delayed state,  $\mathbf{Y}(t_a - \tau_l)$  during the discrete interval  $a$  is calculated by  $w_{l,1}\mathbf{V}_{l,a}\mathbf{Y}_{a-q_l+1} + w_{l,2}\mathbf{V}_{l,a}\mathbf{Y}_{a-q_l}$  with weighted factors

$w_{l,1} = w_{l,2} = 0.5$  which relate  $Y(t - \tau_l)$  with the state values at the two ends of the delayed interval  $[t_{a-q_s}, t_{a-q_s+1}]$  (Wan et al. 2010). Eq.(9) can be rewritten as the following the discrete map form:

$$\Theta_{a+1} = \Phi_a \Theta_a \quad (10)$$

where  $\Theta_a$  is the state vector

$$\Theta_a = [Y_a^T, Y_{a-1}^T, \dots, Y_{a-q_1}^T, \dots, Y_{a-q_2}^T, \dots, Y_{a-q_{N_d}}^T]^T \quad (11)$$

The transition matrix  $\Phi_a$  obtained from is time invariant and constant for a specified radial depth of cut, feed per tooth and speed. If all the eigenvalues of  $\Phi_a$  at each spindle speed and radial depth of cut are less than unity, the system is asymptotically stable. Otherwise, if any one of the eigenvalues is outside the unit circle, the process is unstable. The critical stability occurs when the eigenvalues lie on the unit circle. By repeating the eigenvalue evaluation at the interested range of spindle speeds and radial depths of cut, the stability lobes can be constructed. Note that when the system is dominated by one mode ( $N_m = 1$ ), the dimension of the transition matrix is reduced, so as the computation time.

#### 4. SIMULATIONS AND EXPERIMENTAL RESULTS

A series of cutting tests have been conducted on a 5-axis Mori Seiki NMV5000 machining center with the multi-functional tool. The workpiece material is Aluminum 7050-T7451. The cutting forces in X, Y and Z directions have been measured with a Kistler table dynamometer 9255B.

Impact modal tests were conducted to measure frequency response function (FRF) and modal parameters. The direct and cross frequency response functions (FRF) of the tools in axial and torsional directions (Z and  $\theta$ ) are measured as illustrated in Fig.2. Accelerometer allocated at S1 is used to capture the axial (Z) vibrations. Accelerometer S2, which is placed on the front surface of the insert, is used to measure torsional vibrations.

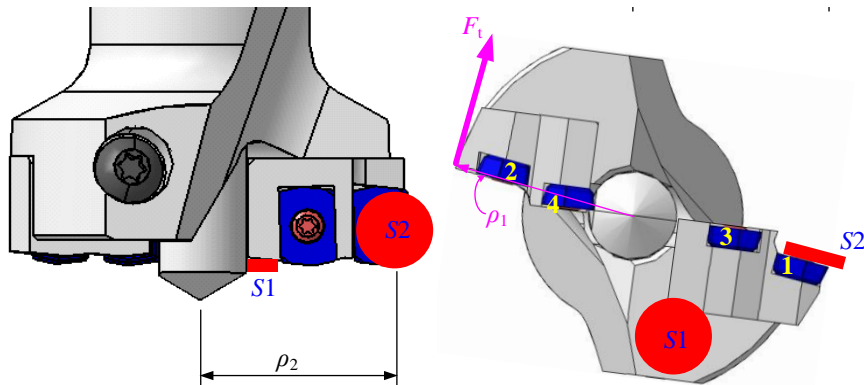


Fig.2 Schematic setup for measuring torsional-axial transfer function.

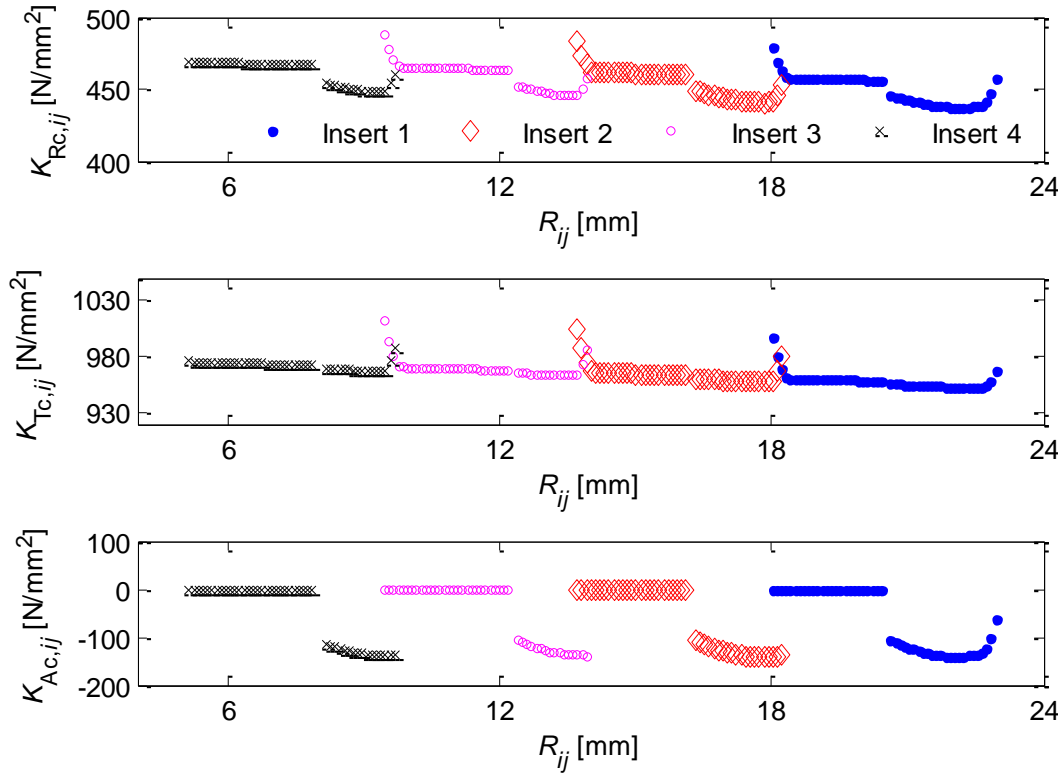


Fig.3 Distribution of cutting force coefficients along the radius of the cutting tools. Aluminum

7050-T7451.  $K_{uc} = 21.4$  [N/mm],  $K_{vc} = 33.2$  [N/mm]

The impact force ( $F_z$ ) is applied in axial direction to find the direct and cross FRFs as follows:

$$\psi_{ZZ}(\omega) = \frac{F_z}{S_1} \quad ; \quad \psi_{\theta Z}(\omega) = \frac{F_z}{S_2 / \rho_2} \quad (12)$$

where  $S_1$  and  $S_2$  represent the measured displacements,  $\rho_2$  is the distance between S2 and the cutter axis.

By applying a tangential impact force  $F_t$  on the periphery of the tool as shown in Fig.2, the direct and cross FRFs of the torsional and axial responses due to cutting torque are evaluated as:

$$\psi_{\theta\theta}(\omega) = \frac{F_t \times \rho_1}{S_2 / \rho_2} \quad ; \quad \psi_{Z\theta}(\omega) = \frac{F_t \times \rho_1}{S_1} \quad (13)$$

where  $\rho_1$  is the distance between torque arm. The modal parameters of the two tools are identified with (CutPro, 2000) Modal module. Modal parameters for the torsional-axial mode are: Natural frequency 3677-Hz, damping ratio 0.51%, mass normalized mode shape vector

$$\mathbf{U} = \begin{bmatrix} u_{Z,1,1} \\ u_{\theta,1,1} \end{bmatrix} = \begin{bmatrix} 0.1761 (1/\sqrt{\text{kg}}) \\ 188.4 (1/\sqrt{\text{kg m}^2}) \end{bmatrix}.$$

**1. Validation of the Static Cutting Force Model:** The cutting force coefficients obtained through orthogonal to oblique cutting transformation are mapped along the cutting edges as shown in Fig.3. The orthogonal parameters of Aluminum 7050-T7451 are given by (Kaymakci et al., 2012). The predicted and measured cutting forces are in agreement as shown in Fig.4 for various cutting conditions for both tools. The radial depth of cut  $a_p$  is measured as the difference between the radius of the desired hole and that of the pre-drilled pilot hole.

**2. Validation of the Stability Model:** The predicted stability limits with process damping effects have been experimentally verified as shown in Fig.5 for cutting Aluminum 7050-T7451. Since new tool was used in the experiments, flank wear land of  $20\text{-}\mu\text{m}$ , which is close to the edge radius of tools, is assumed for all inserts. The indentation force coefficient of Aluminum 7050-T7451 identified as  $K_{sp} = 1.5 \times 10^5 \text{ -N/mm}^3$ . The simulated stability results related to torsional-axial mode are plotted in Fig.5. Most of the experimental observations agree with the predicted stability borders. A series of unstable islands can be observed at the spindle speed range of 3000 to 5000 rev/min. There is hardly any stability pocket at the 10.5-mm depth of cut, and torsional-axial mode chatters at the spindle speed range of 500 to 2500-rev/min, although some points close to the critical limit are predicted to be stable. The process is highly stable under 5000-rev/min spindle speed due to process damping. The discrepancies are attributed to changes on the cutting edge geometry, inaccuracies in FRF measurements, and variations in the boundary conditions of the system when tool penetrates into the hole.

The chatter stability limits are identified from the force and sound measurements and their spectra. When the spectra of the measured signals are dominated by the spindle speed and/or tooth passing frequencies, the process is stable. The unstable processes are dominated by the tools' torsional, axial and lateral natural frequencies.

The measured cutting forces, sound and their spectra for three sample tests are shown in Fig.6 for the torsional-axial chatter condition. It can be seen that the spectra of  $F_Y$  and  $F_Z$  are dominated by torsional/axial mode ( $\sim 3545\text{-Hz}$ ). The forces grow exponentially and the sun-rise pattern can be observed at the finished bottom of the hole which is typical for torsional-axial chatter phenomenon in drilling (Ahmadi and Altintas, 2013; Roukema and Altintas, 2007b).

## 5. CONCLUSIONS

Mechanics and dynamics of multi-functional tools with multiple inserts are presented to predict cutting forces and chatter free cutting conditions to open stepped holes in one

operation. Since the inserts have varying geometry with arbitrary placements on the tool body, the cutting force coefficients are best estimated from orthogonal to oblique cutting transformation. The chatter stability may also depend on the distribution of the dynamic forces; hence the semi-discrete time domain stability solution that considers the varying directional factors, process damping and multiple time delays is advantageous over frequency domain solutions for multi-functional tools. The research is currently extended to cover the unified mechanics and dynamics of turning, drilling, boring and milling with a generalized solution.

## 6. ACKNOWLEDGEMENT

This research has been supported by the National Natural Science Foundation of China under Grant No. 11272261, the Program for New Century Excellent Talents in University under Grant No. NCET-12-0467, and National Sciences and Engineering Research Council of Canada (NSERC) under CANRIMT and NSERC—Pratt & Whitney Canada Research Chair Grants. Kennametal provided the tool.

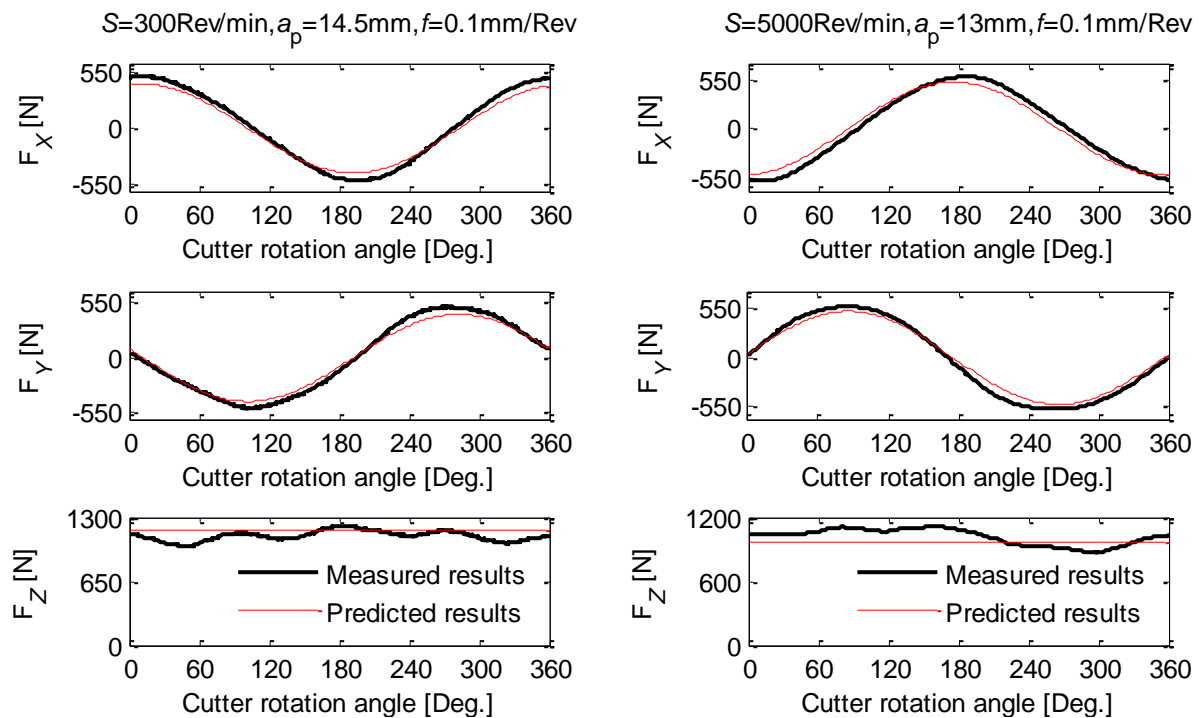


Fig.4 Comparisons of predicted and measured cutting forces. Aluminum 7050-T7451

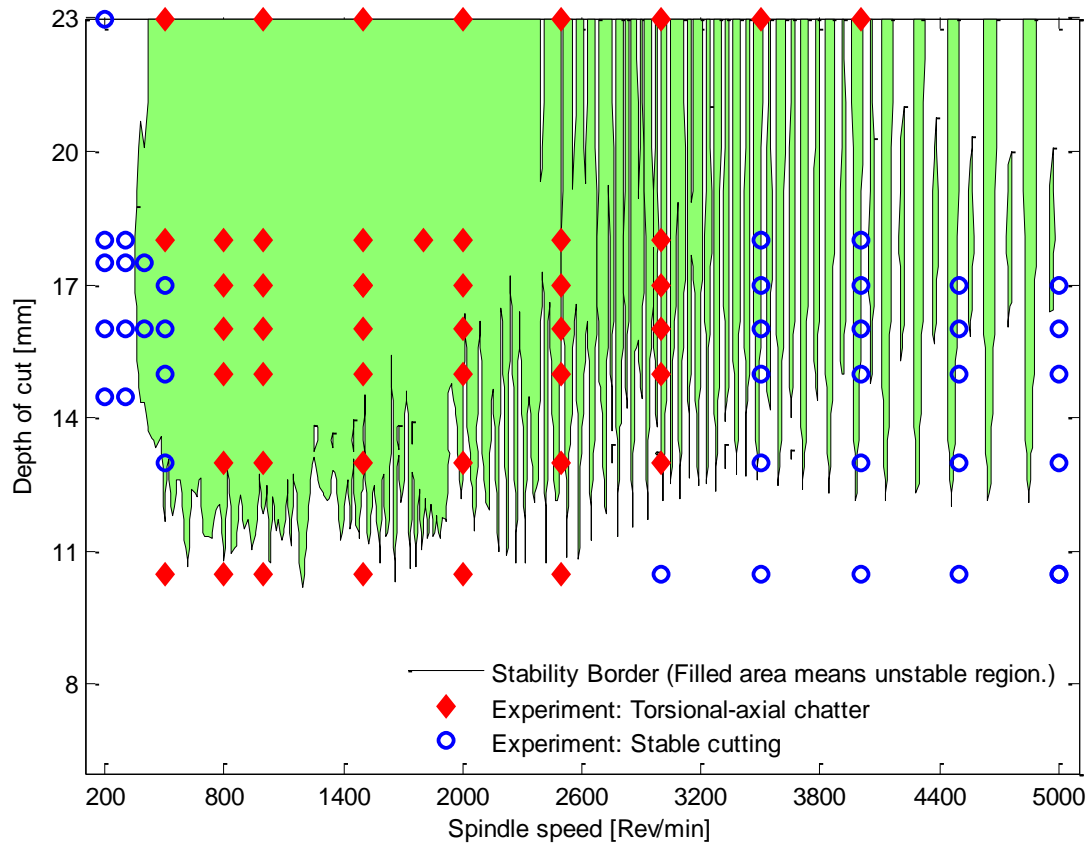


Fig.5 Comparison of predicted (Torsional-axial stability lobes) and experimentally measured stability limits. Material: Aluminum 7050-T7451. Feedrate: 0.1-mm/rev/tooth.

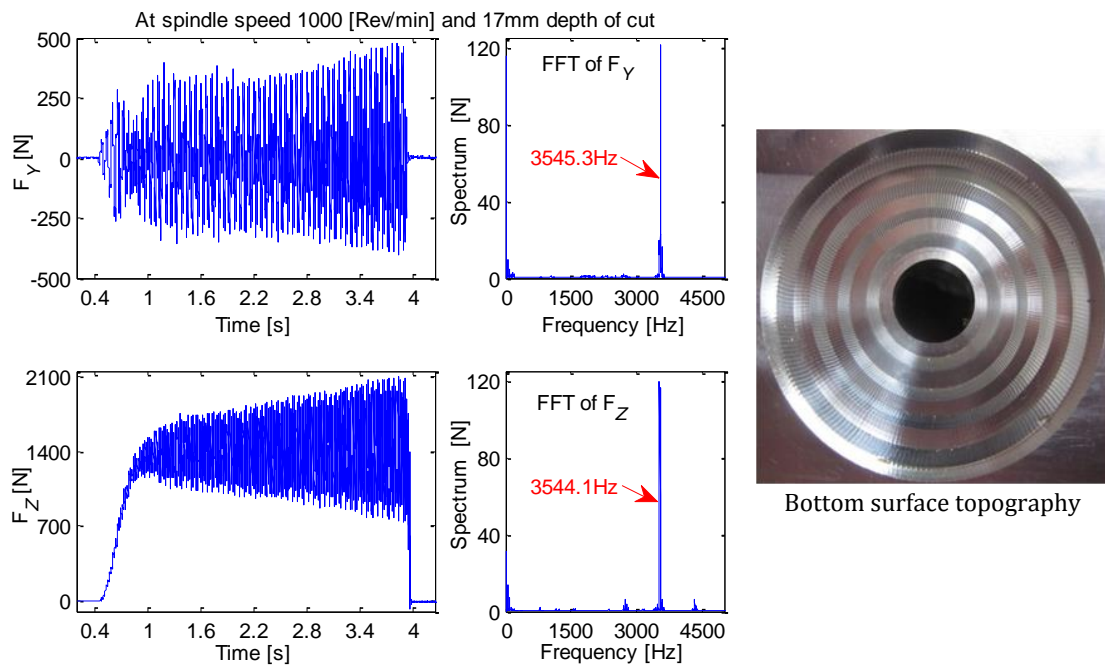


Fig.6 Measured cutting forces and sound along with the photograph of hole shape for sample experiment at chatter condition. Spindle speed 1000-rev/min, radial depth of cut=17-mm, feedrate=0.1-mm/rev. Material: Aluminum 7050-T7451.



## 7. REFERENCES

1. **Ahmadi, K., and Altintas, Y. (2013).** Stability of lateral, torsional and axial vibrations in drilling. *Int.J.Mach.Tool.Manu.*, 68, 63–74.
2. **Altintas, Y. (2012).** *Manufacturing Automation: Principles of Metal Cutting Mechanics, Machine Tool Vibrations, and CNC Design.* Cambridge University Press.
3. **Altintas, Y., and Weck, M. (2004).** Chatter stability of metal cutting and grinding. *CIRP Annals-Manufacturing Technology*, 53(2), 619–642.
4. **Arvajah, T., and Ismail, F. (2006a).** “Machining stability in high speed drilling—Part 2: Time domain simulation of a bending–torsional model and experimental validations.” *Int.J.Mach.Tool.Manu.*, 46(12-13), 1573–1581.
5. **Arvajah, T., and Ismail, F. (2006b).** “Machining stability in high-speed drilling—Part 1: Modeling vibration stability in bending.” *Int.J.Mach.Tool.Manu.*, 46(12-13), 1563–1572.
6. **Bayly, P.V., Lamar, M.T., and Calvert, S.G. (2002).** “Low-Frequency Regenerative Vibration and the Formation of Lobed Holes in Drilling.” *ASME J.Manuf.Sci.Eng.*, 124(2), 275.
7. **Budak, E., Altintas, Y., and Armarego, E.J.A. (1996).** “Prediction of milling force coefficients from orthogonal cutting data.” *ASME J.Manuf.Sci.Eng.*, 118(2), 216.
8. **Chandrasekharan, V., Kapoor, S.G., and DeVor, R.E. (1995).** “A mechanistic approach to predicting the cutting forces in drilling: with application to fiber-reinforced composite materials.” *ASME J.Eng.Ind.*, 117, 559–570.
9. **Chandrasekharan, V., Kapoor, S.G., and Devor, R.E. (1996).** “A Mechanistic Model to Predict the Cutting Force System for Arbitrary Drill Point Geometry.” *ASME J.Manuf.Sci.Eng.*, 120(3), 563–570.
10. **CutPro. (2000).** *Advanced Machining Simulation System*, MAL, Inc., Vancouver, Canada. [www.malinc.com](http://www.malinc.com)
11. **Ema, S., Fujii, H., and Marui, E. (1988).** “Chatter Vibration in Drilling.” *ASME J.Eng.Ind.*, 110, 309–314.
12. **Filiz, S., and Ozdoganlar, O.B. (2010).** “A Model for Bending, Torsional, and Axial Vibrations of Micro- and Macro-Drills Including Actual Drill Geometry—Part I: Model Development and Numerical Solution.” *ASME J.Manu.Sci.Eng.*, 132(4), 041017.
13. **Insperger, T., and Stépán, G. (2004).** “Updated Semi-Discretization Method for Periodic Delay-Differential Equations with Discrete Delay.” *Int. J. Numer. Math. Engng.*, 61, 117–141.
14. **Kaymakci, M., Kilic, Z.M., and Altintas, Y. (2012).** “Unified cutting force model for turning, boring, drilling and milling operations.” *Int.J.Mach.Tool.Manu.*, 54-55, 34–45.
15. **Pirtini, M., and Lazoglu, I. (2005).** “Forces and hole quality in drilling.” *Int.J.Mach.Tool.Manu.*, 45(11), 1271–1281.



16. **Roukema, J.C., and Altintas, Y. (2007a).** “Generalized modeling of drilling vibrations. Part I: Time domain model of drilling kinematics, dynamics and hole formation.” *Int.J.Mach.Tool.Manu.*, 47(9), 1455–1473.
17. **Roukema, J.C., and Altintas, Y. (2007b).** “Generalized modeling of drilling vibrations. Part II: Chatter stability in frequency domain.” *Int.J.Mach.Tool.Manu.*, 47(9), 1474–1485.
18. **Sambhav, K., Tandon, P., Kapoor, S.G., and Dhande, S.G. (2013).** “Mathematical Modeling of Cutting Forces in Microdrilling.” *ASME J.Manu.Sci.Eng.*, 135(1), 014501.
19. **Strenkowski, J., Hsieh, C., and Shih, A. (2004).** “An analytical finite element technique for predicting thrust force and torque in drilling.” *Int.J.Mach.Tool.Manu.*, 44(12-13), 1413–1421.
20. **Wan, M., Zhang, W.-H., Dang, J.-W., and Yang, Y. (2010).** “A unified stability prediction method for milling process with multiple delays.” *Int.J.Mach.Tool.Manu.*, 50(1), 29–41.







## THE MECHANICS OF DOUBLE-SIDED MILLING OPERATION

**Z. Murat KILIÇ**, *kilic@alumni.ubc.ca*, Manufacturing Automation Laboratory, University of British Columbia, V6T1Z4, Vancouver, Canada

**Yusuf ALTINTAŞ**, *altintas@mech.ubc.ca*, Manufacturing Automation Laboratory, University of British Columbia, V6T1Z4, Vancouver, Canada

### ABSTRACT

Double-sided milling operations are becoming more popular for producing guides for elevator rails, railways and drives of machine tools. Traditional single-sided milling application may cause problem due to deflection of flexible workpiece. One solution to that is to have zero net force in axial direction of the cutter. Thus, double-sided milling can be applied to have equal forces from both sides of flexible workpiece. This paper introduces the mechanics model for the double-sided milling operation. Cutting forces are predicted using a general milling model. Cutting coefficients are calculated using material database. The model is validated through experiments. Predicted cutting forces are within 11% accuracy, and forces in axial direction are reduced significantly.

**Keywords:** Cutting forces, double-sided milling, parallel milling.

### 1. INTRODUCTION

Parallel milling processes are becoming more popular due to its higher efficiency and vibration stabilization effects. (Comak and Budak 2012) and (Ozturk and Budak 2010) analyzed multi-tasking, dual-spindle machine tools, and find predicted the stable cutting conditions. A special application of parallel milling is the double-sided milling. It is used for machining flexible plates, or constant cross section workpieces. Some examples for the workpieces could be elevator guide rails, railway tracks and machine tool drive guide rails. Double-sided cutting has the advantage of force cancellation in the flexible direction of the workpiece. (Mori et al., 2011) designed a dual-spindle system with synchronized angular locations of cutting edges. This way they successfully stabilized the vibrations by cancelling the axial cutting forces. Single-tooth cutters give high surface quality and ensure the force cancellation if the cutting edges are synchronized. For multiple-insert cutters, both force stabilization and good surface quality is harder to achieve. This is because of the high radial and axial runouts of the indexable cutters.

Although using advanced mechatronics can ensure synchronized cutting edge, it may be hard to apply and maintain such systems. Additionally, many machine tools have single

spindles. We used single-spindle system with multiple-teeth and brazed inserts. Double-sided cutter ensures the synchronous location of cutting edges, by using keyways. Brazed inserts ensures the minimum axial and radial runout. Thus, the feed speed can be increased to high values while keeping the forces cancelled.

We present the mechanics model which includes effects of angular location of each cutting edge, unequal pitch angle and radial runout. Instead of doing separate cutting coefficient identification the cutting forces are estimated based on orthogonal cutting database of the work material (Budak et al., 1996). The generated cutting forces on the rake face are correlated to the cutting speed, normal rake and inclination angle (Kaymakci et al., 2012). Predicted forces are within 11% of the measured forces. Since this cutter design is still at improvement stage, surface finish and smoothness of cutting force are not considered.

Both cutter and workpiece are kept rigid, thus vibrations are negligible and have no effect on the cutting forces. Dynamics modeling and stability/vibration simulation will be completed during future research. As state-of-art, (Shamoto et al. 2013) give a comprehensive dynamics frequency-domain model for dual-spindle cutting.

## 2. MODELING OF MECHANICS

The cutter has two components (as seen in Fig.3 and Fig.4): Left-side (subscript  $L$ ) and right-side (subscript  $R$ ). Each cutting edge segment of these cutters ( $s_{jk,L}$  and  $s_{jk,R}$ ) are located in angular ( $\phi_{j,L}(t)$  and  $\phi_{j,R}(t)$ ), radial ( $R_l(kdz)$ ) and depth-of-cut ( $kdz$ ) directions.

Angular positions ( $\phi_{j,L}(t)$  and  $\phi_{j,R}(t)$ ) are determined by cutter rotation speed ( $\Omega$  [rev/min]) and relative location angle ( $\psi_{j,L}$  and  $\psi_{j,R}$ ). From

Fig.3, position angle of the edge of the  $j$ -th insert is:

$$\phi_{j,x}(t) = \left( \Omega \frac{2\pi}{60} \right) \cdot t + \psi_{j,x} \quad (1)$$

Where, for left-side cutter,  $x = L$ , and for right-side cutter,  $x = R$ . Relative location angle can be described easier with the help of the pitch angle:

$$\phi_{p,j,x} = \begin{cases} \phi_{1,x} - \phi_{N,x} & \text{if } j = 1 \\ \phi_{j,x} - \phi_{j-1,x} & \text{if } 2 \leq j \leq N \end{cases} \quad (2)$$

Where,  $N$  is the number of inserts on the cutter (equal for left and right-side cutters).

The in-cut or out-of-cut condition can be determined by checking angular position with respect to local entry and exit angles,

$$g_{1,x}(\phi_j(t)) = \begin{cases} 1 & \text{if } \phi_{st}(kdz) < \phi_{j,x}(t, kdz) < \phi_{ex}(kdz) \\ 0 & \text{otherwise} \end{cases} \quad (3)$$

Each cutting edge segment is located at different diameter along the cutter. Thus, radial entry angle ( $\phi_{st}(kdz)$ ) and exit angle ( $\phi_{ex}(kdz)$ ) of the cutter depend on the axial location on the insert edge (Fig.1).

Since the inserts of the cutter have 0-deg axial rake, the cutting action is orthogonal in this study. Also, radial rake is 0-deg, thus normal rake is 0-deg. The inserts assumed to have negligible nose radius, i.e. cutting edge angle is constant for all inserts:  $\kappa_{rj} = 15\text{-deg}$  (0.262-rad). Since both radial and axial rake angles are 0-deg, the cutting edge angle is equal to the true cutting edge angle:  $\kappa_{ij}^* = \kappa_{rj}$  (Kaymakci et al., 2012).

Static (st) cutting edge forces (x, y, z and torque) are geometrically transformed (Altintas and Kilic 2013) into the machine coordinates (

Fig.3):

$$d\mathbf{F}_{xyz0,j,x}^{st}(t) = \begin{bmatrix} \mathbf{T}_{0R,j,x}(t) \cdot \mathbf{T}_{RI,j,x} \\ 0 \quad R_t(kdz) \quad 0 \end{bmatrix} \cdot d\mathbf{F}_{rta,j,x}^{st}(t) \quad (4)$$

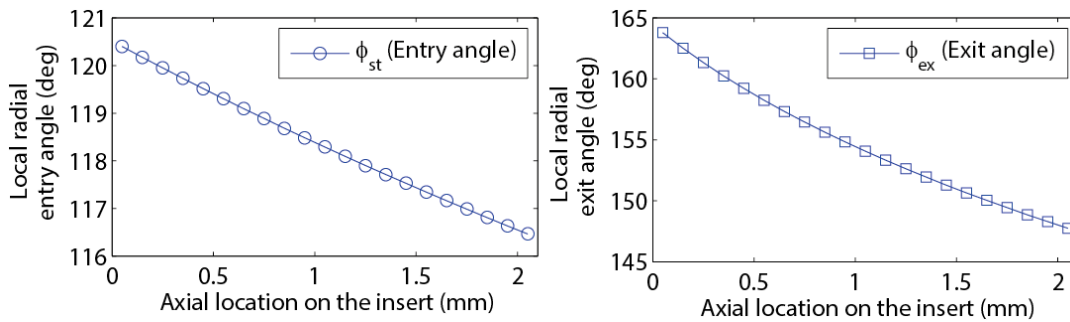


Fig.1 Local radial entry (left) and radial exit (right) angles.

Where, transformation from cutting edge (RTA) to local insert coordinates ( $X_R Y_R Z_R$ ) for left and right-side cutters are denoted by  $\mathbf{T}_{RI,j,L}$  and  $\mathbf{T}_{RI,j,R}$ .

transformation from local insert coordinates ( $X_R Y_R Z_R$ ) to machine coordinates (XYZ) for left and right-side cutters  $\mathbf{T}_{0R,j,L}(t)$  and  $\mathbf{T}_{0R,j,R}(t)$ .

$R_t(kdz)$  is the local radius of the cutting edge segment. In Eqn.(4), forces on cutting edge are related to chip thickness:

$$d\mathbf{F}_{rta,j,x}^{st}(t, kdz) = \mathbf{K}_{rta,j}^c(kdz) h_{e,j,x}(t, kdz) dS_j + \mathbf{K}_{rta,j}^e(kdz) dS_j \quad (5)$$

Where cutting coefficients in radial, tangential and axial directions are in vector form:

$$\mathbf{K}_{rta,j}^c(kdz) = \begin{bmatrix} K_{r,j}^c(kdz); K_{t,j}^c(kdz); K_{a,j}^c(kdz) \end{bmatrix}. \text{ Similar for edge coefficients:}$$

$\mathbf{K}_{ta,j}^c(kdz) = [\mathbf{K}_{r,j}^c(kdz); \mathbf{K}_{t,j}^c(kdz); \mathbf{K}_{a,j}^c(kdz)]$ . Cutting coefficients along the insert edge are plotted in Fig.2.

In Eqn.(5), the chip length at cutting edge of the insert is  $dS_j = dz / \sin \kappa_{tj}^*$ . The effective chip thickness  $h_{e,j,x}(t)$  is calculated with runout effect included (Eksioglu, Kilic, and Altintas 2012).

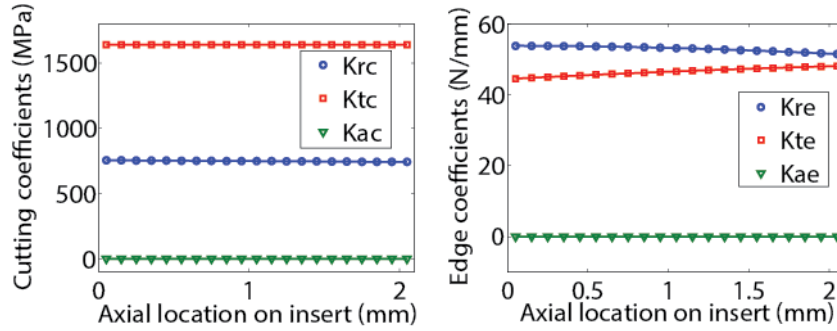


Fig.2 Cutting and edge coefficients along the edge of the insert.  $\kappa_r^* = 15$ -deg cutting edge angle; 0-deg normal rake angle; 0-deg inclination angle. Material database of AISI 1045 steel from (CutPro 2000). Average values for 0.5-mm depth of cut:

$$[\mathbf{K}_{r,j}^c; \mathbf{K}_{t,j}^c; \mathbf{K}_{a,j}^c] = [753; 1641; 0] \text{ -MPa} ; [\mathbf{K}_{r,j}^e; \mathbf{K}_{t,j}^e; \mathbf{K}_{a,j}^e] = [54; 45; 0] \text{ -N/mm} .$$

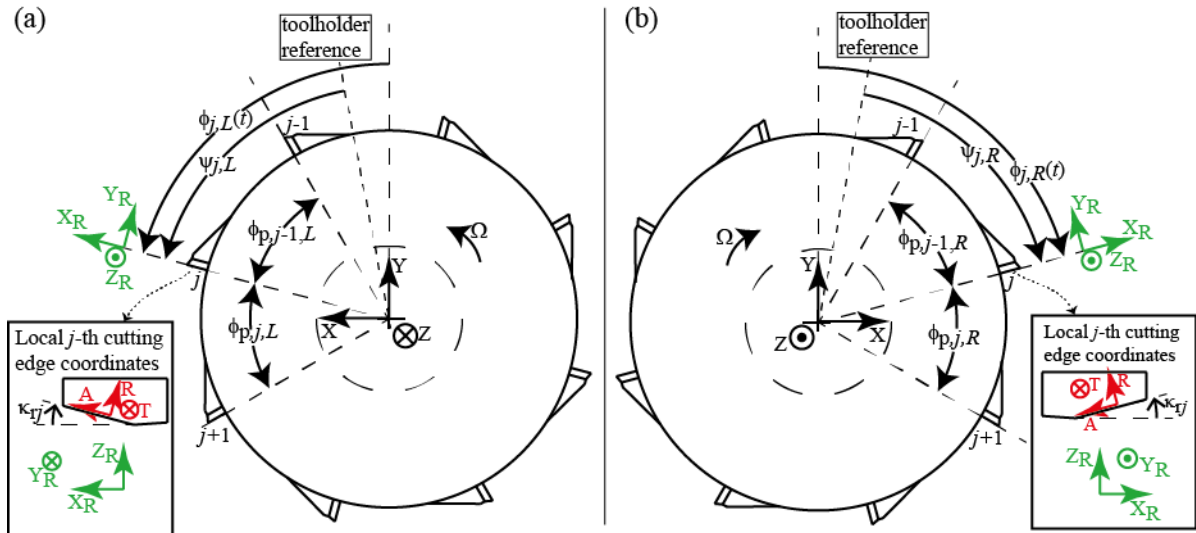


Fig.3 Coordinate systems of (a) left-side cutter, and (b) right-side cutter.

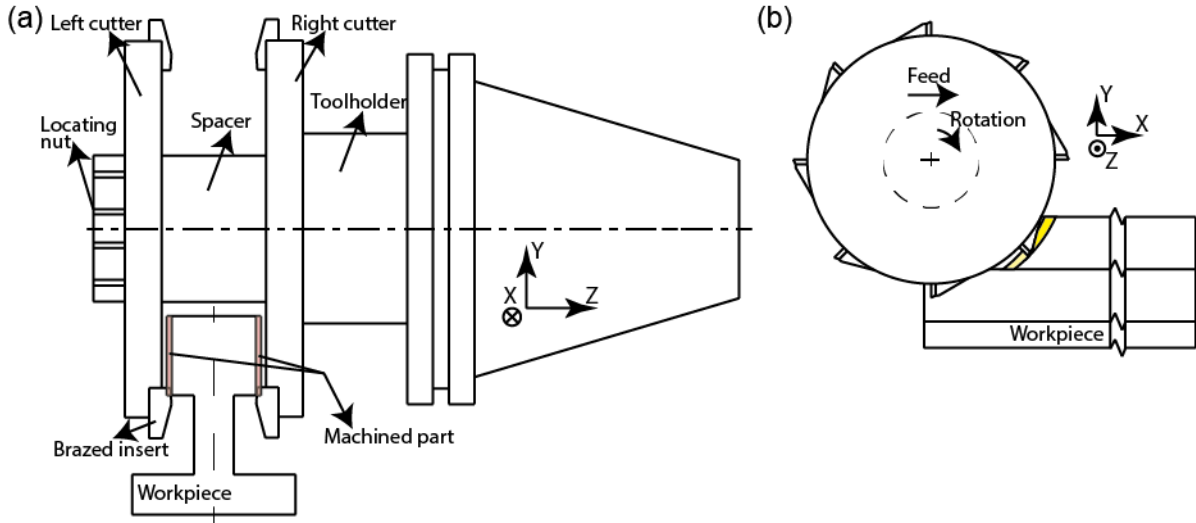


Fig.4 (a) Components of double-sided cutter; (b) down milling (about 20% radial immersion) cutting.

From Eqn.(3) and Eqn.(5), the total force of left- and right-side cutters are:

$$F(t) = \sum_{j=1}^N \sum_{k=1}^q g_1(t, kdz) \left[ d\mathbf{F}_{j,L}^{st}(t, kdz) + d\mathbf{F}_{j,R}^{st}(t, kdz) \right] \quad (6)$$

The static (st) cutting forces are composed of cutting (cs) and ploughing (es) parts:

$$\begin{aligned} d\mathbf{F}_{j,x}^{st}(t, kdz) &= d\mathbf{F}_{j,x}^{cs}(t, kdz) + d\mathbf{F}_{j,x}^{es}(t, kdz); \\ d\mathbf{F}_{j,x}^{cs}(t, kdz) &= \begin{bmatrix} \mathbf{T}_{0R,j,x}(t) \cdot \mathbf{T}_{RI,j,x} \\ 0 & R_t(kdz) & 0 \end{bmatrix} \cdot \mathbf{K}_{rtaj}^c(kdz) \frac{h_{ej,x}(t, kdz)}{\sin \kappa_{tj}^*} dz \\ d\mathbf{F}_{j,x}^{es}(t, kdz) &= \begin{bmatrix} \mathbf{T}_{0R,j,x}(t) \cdot \mathbf{T}_{RI,j,x} \\ 0 & R_t(kdz) & 0 \end{bmatrix} \cdot \mathbf{K}_{rtaj}^e(kdz) \frac{1}{\sin \kappa_{tj}^*} dz \end{aligned} \quad (7)$$

### 3. EXPERIMENTAL VALIDATION

KOVA cutter company (Taiwan) produced the custom double-sided cutter for the experiments. Fig.4 shows the cutter schematics. Left-side cutter (KOVA D125-20L-D109.7-8T) and right-side cutter (KOVA D125-20R-D109.7-8T) have non-detachable, brazed inserts. The radial and axial runout of inserts are minimized by grinding the insert edges to size, after brazing on the cutter. The inserts have  $\kappa_r^* = 15$ -deg cutting edge angle; 0-deg normal rake angle; 0-deg inclination angle. The cutters are installed on keyways of the shank of the custom toolholder. The toolholder has BT-50 spindle connection interface. Machine-tool is DIXI DJC-350 from Switzerland.

General view of experiment setup is shown in Fig.5. Cutting forces are measured by Kistler9257BA dynamometer. The AISI1045 steel workpiece (170-mm length) is mounted on the dynamometer using an adapter plate and 6 clamps (with M8 screws).

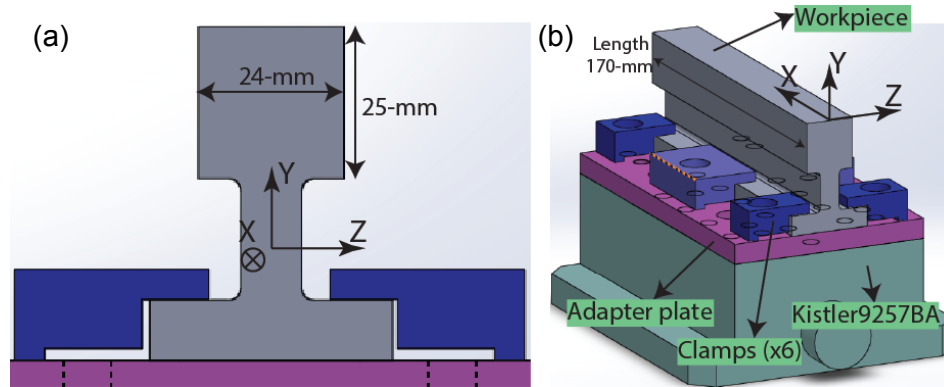
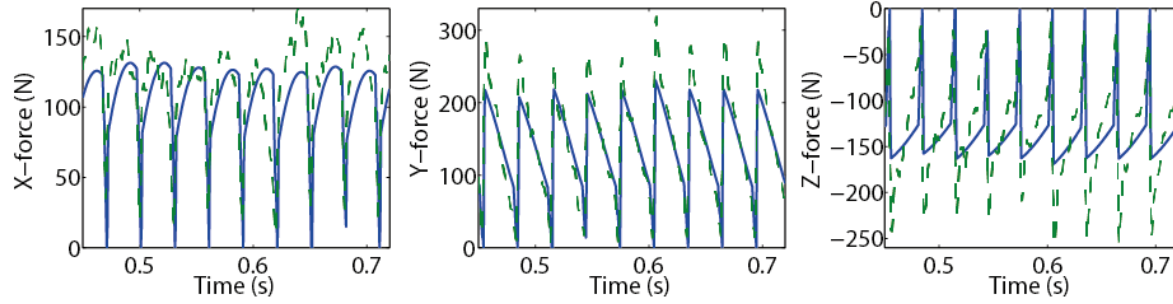


Fig.5 Experiment setup: (a) Front view showing workpiece cross section; (b) general view. The AISI 1045 steel workpiece is fixed on Kistler9257BA force dynamometer, using 6 clamps.

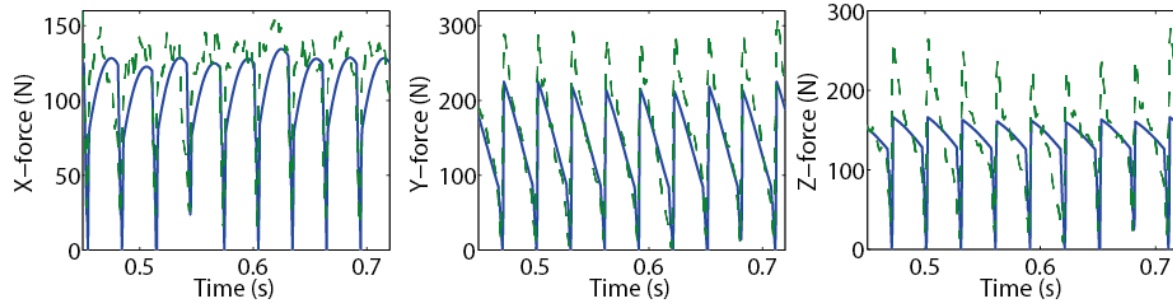
Table 1 Measured angular location (with respect to toolholder reference in Fig.3), pitch angle and radial runout of the left and right-side cutters.

Insert no.	Relative angular location (deg)		Pitch angle (deg)		Radial runout (mm)	
	Left cutter $\psi_{j,L}$	Right cutter $\psi_{j,R}$	Left cutter $\phi_{p,j,L}$	Right cutter $\phi_{p,j,R}$	Left cutter $\varepsilon_{j,L}$	Right cutter $\varepsilon_{j,R}$
1	-8	-9	44.5	45	0	0.018
2	36.5	36	45.5	45	0.006	0.018
3	82	81	45.5	45	0.006	0.009
4	127.5	126	45	44.5	0.022	0
5	172.5	170.5	44.5	45.5	0.021	0.004
6	217	216	45	45.5	0.017	0.004
7	262	261.5	45	45	0.017	0.014
8	307	306.5	45	44.5	0	0.016

(a) Left-side cutting forces



(b) Right-side cutting forces



(c) Double-sided cutting forces

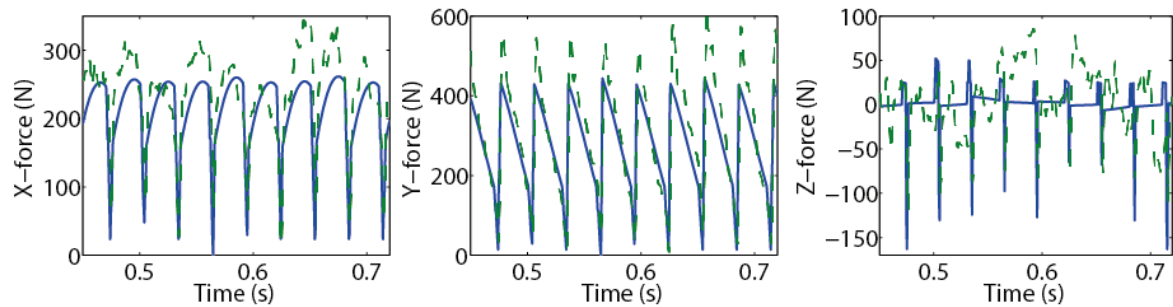


Fig.6 Predicted (solid line) and experimental (dashed line) X-Y-Z cutting forces: (a) Left-side cutting; (b) right-side cutting; (c) double-sided cutting.  $N = 8$ -teeth ;  $\Omega = 250$ -rev/min spindle speed;  $f = 0.2$ -mm/tooth/rev feed; dry cutting (with no cutting fluid);  $\kappa_r^* = 15$ -deg cutting edge angle; 0-deg normal rake angle; 0-deg inclination angle; 0.5-mm axial depth of cut from each side;  $dz = 0.1$ -mm axial segment height ( $q = 5$ -segments ); Simulation sample time: 0.6-ms.

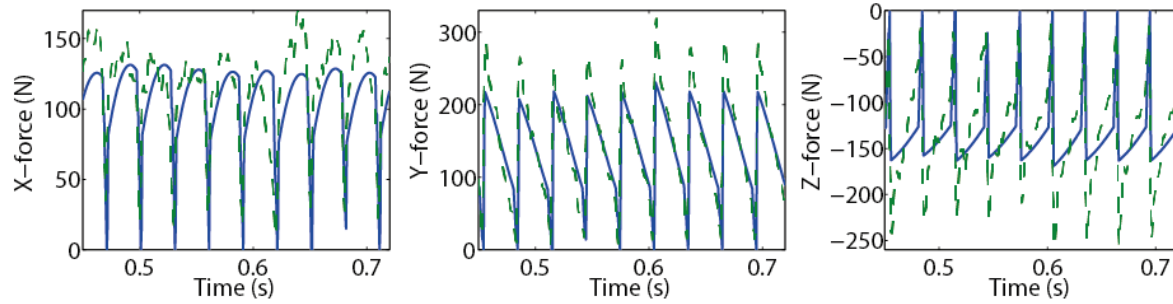
Radial entry and exit angles from Fig.1. Cutting and edge coefficients from Fig.2. Angular location, pitch angle and radial runout from Table 1.

Relative angular location and radial runout values are measured for both cutters (given in Table 1). Three cutting tests are done: Only left-side cutting, only right-side cutting and

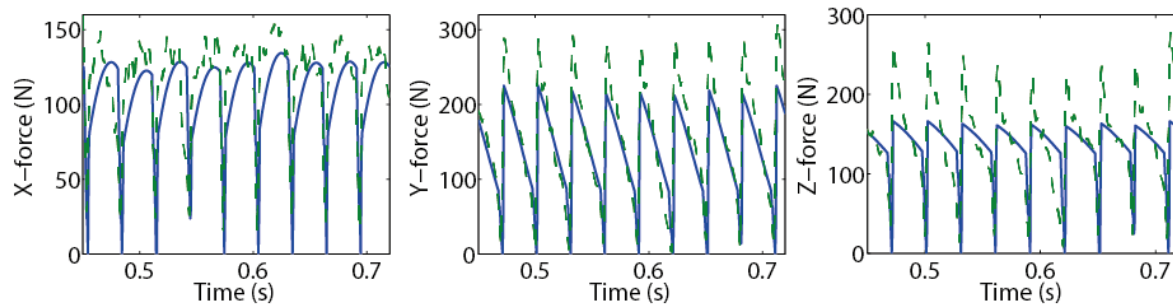


double-sided cutting. The predictions and experiment results for all tests are given in Fig.6.

(a) Left-side cutting forces



(b) Right-side cutting forces



(c) Double-sided cutting forces

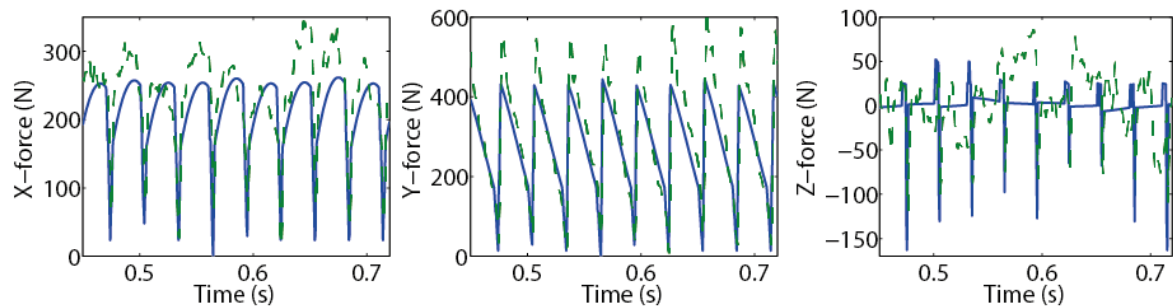


Fig.6 Predicted (solid line) and experimental (dashed line) X-Y-Z cutting forces: (a) Left-side cutting; (b) right-side cutting; (c) double-sided cutting.  $N = 8$ -teeth;  $\Omega = 250$ -rev/min spindle speed;  $f = 0.2$ -mm/tooth/rev feed; dry cutting (with no cutting fluid);  $\kappa_r^* = 15$ -deg cutting edge angle; 0-deg normal rake angle; 0-deg inclination angle; 0.5-mm axial depth of cut from each side;  $dz = 0.1$ -mm axial segment height ( $q = 5$ -segments); Simulation sample time: 0.6-ms. Radial entry and exit angles from Fig.1. Cutting and edge coefficients from Fig.2. Angular location, pitch angle and radial runout from Table 1.

compares the average cutting forces from theory and experiments.

#### 4. DISCUSSION AND CONCLUSION

The cutting forces (X,Y,Z) of double-sided cutting are simulated. Effects of angular mismatch of left and right-side cutters, unequal pitch angles, and radial runout of insert edges are included. Cutting coefficients are calculated analytically, using the material database.



Table 2 Average forces from experiment and theory. Single-sided cutting forces are within 11% error. Z force accuracy of double-sided cutting is low due to the geometrical differences of left and right-side cutters.

	Average theoretical force (N)	Average experiment force (N)	% Prediction error ((The-Exp)/Exp*100)
Left-side X-force	105	118	-11 %
Left-side Y-force	138	147	-6.1 %
Left-side Z-force	-133	-132	-0.75 %
Right-side X-force	105	116	-9.4 %
Right-side Y-force	138	153	-9.8 %
Right-side Z-force	133	141	-5.6 %
Double-sided X-force	211	240	-12 %
Double-sided Y-force	276	305	-9.5 %
Double-sided Z-force	0.11	6.1	-98 %

The average forces of single sided cutting are predicted accurately, whereas the peak amplitudes do not match precisely. It is assumed that there is no burr formation at the edge of the workpiece, at the exit side of the cutter. If additional burr formation at exit (increased radial exit distance) is considered, peak amplitudes could be captured.

The edge geometry of the insert has a custom chamfer. This could affect especially the edge coefficients. The difference in the peaks and the average forces might be explained with this fact.

Another reason for the nonmatching peaks might be the electrical noise. 250-rev/min spindle speed and 8-teeth cutter has 33-Hz tooth-passing frequency. Due to the electrical noise at 60-Hz, the second harmonic at 66-Hz frequency may add fluctuation to the measured dynamometer forces.

The surface quality of the workpiece is bad after the operation. One other reason for nonmatching peaks of forces might be more material removal due to the bad surface finish, i.e. the cutter tends to recut the same surface at the backside.

The future study will be the experiment for the simulation of vibrations during double-sided cutting operation.



## 5. ACKNOWLEDGMENT

Authors would like to acknowledge the technical and funding support of ITRI-Intelligent Machine Tool Technology Center (Taiwan) and HITACHI (Japan). KOVA (Taiwan) produced the custom double-sided cutter. Mr.Faby Feng helped during the experiments. Dr.Ming-Chyuan Lu from National Chung Hsing University loaned the dynamometer.

## 6. REFERENCES

1. **Altintas, Y., and Kilic, Z.M. (2013).** "Generalized Dynamic Model of Metal Cutting Operations." *CIRP Annals - Manufacturing Technology* 7–10.
2. **Budak, E., Altintas, Y., and Armarego, E.J.A. (1996).** "Prediction of Milling Force Coefficients from Orthogonal Cutting Data." *Journal of Manufacturing Science and Engineering* 118(2):216.
3. **Comak, A., and Budak, E. (2012).** "Chatter Stability of Parallel Milling Operations." in 15. Uluslararası Makina Tasarım ve Imalat Kongresi (UMTIK 2012). Pamukkale, Denizli, Turkey.
4. **CUTPRO (2000).** "CUTPRO (C) UBC Advanced Machining Simulation System.", [www.malinc.com](http://www.malinc.com)
5. **Eksioglu, C., Kilic, Z.M. and Altintas, Y. (2012).** "Discrete-Time Prediction of Chatter Stability, Cutting Forces and Surface Location Errors in Flexible Milling Systems." *Journal of Manufacturing Science and Engineering* 134(6).
6. **Kaymakci, M., Kilic, Z.M. and Altintas, Y.. (2012).** "Unified Cutting Force Model for Turning, Boring, Drilling and Milling Operations." *International Journal of Machine Tools and Manufacture* 54-55:34–45.
7. **Mori, T., Hiramatsu, T., and Shamoto, E. (2011).** "Simultaneous Double-Sided Milling of Flexible Plates with High Accuracy and High efficiency—Suppression of Forced Chatter Vibration with Synchronized Single-Tooth Cutters." *Precision Engineering* 35(3):416–23.
8. **Ozturk, E., and Budak, E. (2010).** "Modeling Dynamics of Parallel Milling Processes in Time-Domain." in *CIRP PMI*. Vancouver.
9. **Shamoto, E., Mori, T., Sencer, B., Suzuki, N., and Hino, R. (2013).** "Suppression of Regenerative Chatter Vibration in Multiple Milling Utilizing Speed Difference Method - Analysis of Double-Sided Milling and Its Generalization to Multiple Milling Operations." *Precision Engineering* 1–10.



## WORKPIECE SURFACE BURN DETECTION BY FORCE AND TEMPERATURE MODELING FOR GRINDING OPERATIONS

**Deniz ASLAN**, *denizaslan@sabanciuniv.edu*, Manufacturing Research Laboratory, Sabanci University, 34956, Istanbul, Turkey

**Erhan BUDAK**, *ebudak@sabanciuniv.edu*, Manufacturing Research Laboratory, Sabanci University, 34956, Istanbul, Turkey

### ABSTRACT

This paper presents a methodology to detect whether grinding temperatures will cause a surface burn over workpiece material or not by process modeling. Based on the triangular heat flux model, grinding wheel is represented as a moving heat source along the surface where the heat distribution over workpiece is investigated. Predicted temperatures are experimentally validated by using the measurements from the embedded thermocouples in the workpiece. In addition, using the previously developed semi-analytical grinding force model, the calculated shear stress and shear angle per abrasive grits are used in the primary and secondary zone energy equations in order to determine the chip temperatures. When the burning of the workpiece is initiated, there is a trend of growth of metallic particle adhesion in the abrasive grains of the wheel, having as consequence the increase of the grinding forces which agrees with the visible burn threshold as well. In this study, both force monitoring and visual inspection are used to detect surface burn and burn threshold results agree with the literature. Predicted and measured temperatures agree within approximately 11-14%, hence surface burn occurrence can be predicted by the presented model with an acceptable level of confidence.

**Keywords:** Surface Grinding, Force Model, Temperature Model, Surface Burn

### 1. INTRODUCTION

Grinding is a machining process in which the energy required to remove a unit volume chip from workpiece is high compared to other operations such as turning or milling. It is generally assumed that all this energy is converted to heat in the grinding zone where the wheel interacts with the workpiece, causing very high temperatures [7]. These high temperature values cause thermal damages to the workpiece, such as surface burn, metallurgical phase transformations and undesired residual tensile stresses. Thermal damage risk is the main constraint for the grinding operations as it limits the production rates drastically. Therefore, it is crucial to understand cutting mechanism for abrasive grits on the wheel and predict process



temperatures in order to prevent thermal damages to the workpiece [7]. Developments of the abrasive technology, rigid machine tools and need for super abrasive machining on difficult to cut materials led to a considerable increase for research related to abrasive processes. The classical moving heat source model for sliding contacts was first studied by Jaeger [1]. Outwater and Shaw [2], used Jaeger's model for grinding operations for the first time by assuming that the contact zone between grinding wheel and the workpiece is moving along the surface of the workpiece material.

Research focusing on abrasive grit-workpiece interaction helped understanding; chip formation and shearing mechanisms for the grinding operations better [6]. Therefore, grinding process temperatures can be predicted by calculating temperatures on the shear plane by adequate heat transfer models. Malkin and Guo [7] presented an extensive literature review on modeling of workpiece surface temperatures for dry grinding.

There are several works on grain scale grinding force and heat transfer modeling [4, 10, 16]. Lavine [13] combined the micro and macro scale analysis for temperature modeling where grinding fluid was considered to be a solid moving at the wheel speed. Shen et al. [12] presented a heat transfer model based on finite difference method considering convection heat transfer on the workpiece surface in wet grinding. Later, Shen et al. [11] expanded that work by explaining their thermocouple fixation method into the workpiece, presenting their experimental results for dry, wet and MQL grinding conditions. Apart from thermocouple fixation method, Mohamed et al. [13] used infrared camera to measure process temperature for surface grinding operations and calculated the heat flux based on average measured power. Tahlivian et al. [14] used both embedded thermocouple and high speed camera to measure total process temperature and chip thickness per abrasive grain, respectively, for robotic grinding process. Temperature distribution in the workpiece is simulated with a 3D transient thermal finite element code.

In this paper, a methodology is proposed to detect whether there will be a surface burn over workpiece material or not by process modeling. Instead of investigating grinding wheel in a macro scale as often done in the literature [11,12,13], abrasive grains are examined individually and energy generated per grain on primary and secondary shear zones as well as third deformation zone are identified. Hence, heat flux into the workpiece and energy that is thrown out by chip can be predicted more accurately. For the model, the first step is to measure and obtain adequate data on abrasive wheel topography and average grit properties such as rake angle, height, width and edge radius. Afterwards, cutting forces, shear stress and friction coefficients are calculated for each operation by previously developed semi analytical force model. Forces are needed for the calculation of the process energy, thus temperature in the cutting zone. Last step is to calculate total energy that is produced during the operation and



use it for the semi-analytical temperature model. Following this procedure, it is possible to predict surface burn occurrence before the operation.

### Nomenclature

$a$	Axial depth of cut (mm)
$b$	Radial depth of cut (mm)
$feed$	Workpiece velocity (mm/s)
$feed_r$	Workpiece velocity per revolution (mm/rev)
$h$	Instantaneous uncut chip thickness (mm)
$V_c$	Cutting velocity (m/s)
$V_s$	Shearing velocity (m/s)
$\Theta$	Grain position angle (degrees)
$K_{tc}$	Tangential cutting force coefficient (Mpa)
$K_{nc}$	Normal cutting force coefficient (Mpa)
$K_{tp}$	Tangential ploughing force coefficient (Mpa)
$K_{np}$	Normal ploughing force coefficient (Mpa)
$l_c$	Length of cutting zone (mm)
$l_{c-area}$	Area of cutting zone (mm <sup>2</sup> )
$D$	Diameter of the grinding wheel (mm)
$R$	Radius of the grinding wheel (mm)
$W$	Width of the grinding wheel (mm)
$C$	Grain number per mm <sup>2</sup>
$W_{area}$	Area of grinding wheel surface (mm <sup>2</sup> )
$T_{grains}$	Total number of grains on the grinding wheel
$A_g$	Active grain number
$\alpha$	Grit rake angle (degrees)
$r$	Grit edge radius
$F_{tc}$	Force in tangential direction (N)
$F_{nc}$	Force in normal direction (N)
$F_{tp}$	Ploughing force in tangential direction (N)
$F_{np}$	Ploughing force in normal direction (N)
$F_{tc-g}$	Force per grain in tangential direction (N)
$F_{nc-g}$	Force per grain in normal direction (N)
$F_{tp-g}$	Ploughing force per grain in tangential direction (N)
$F_{np-g}$	Ploughing force per grain in normal direction (N)
$F_f$	Frictional force (N)
$F_s$	Shear Force (N)
$MRR$	Material removal rate (mm <sup>3</sup> /s)
$\phi_s$	Shear Angle (degrees)
$\beta$	Friction Angle (degrees)
$\tau$	Shear Stress (Mpa)
$\chi$	Proportion of the shearing heat entering into the workpiece
$a_{diff}$	Thermal diffusivity (m <sup>2</sup> /s)
$k$	Thermal conductivity (W/(m*K))
$\rho$	Workpiece material density (kg/m <sup>3</sup> )
$c_p$	Specific heat capacity (J/(kg*K))
$R_t$	Thermal number



## 2. ABRASIVE WHEEL TOPOGRAPHY

It is essential to identify the wheel topography in order to model mechanics and dynamics of the grinding process. There are numerous methodologies to scan abrasive wheel surfaces and obtain abrasive grains' geometric properties [4]. In this study, a camera system with a special lens is utilized to measure the abrasive grain number per mm<sup>2</sup> on the abrasive wheel. Afterwards, a special areal confocal 3D measurement system is used for determining geometric properties of the abrasive grains such as rake angle, edge radius and their distribution. In Figure 1, it can be seen how grain numbers per mm<sup>2</sup>, which is named as “C” parameter in the literature [5], for alumina and silicon carbide wheels are obtained.

C is measured as 5 and 6 for alumina and silicon carbide grinding wheels, respectively. Field of views of 1x1 mm for alumina and 0.5x0.5 mm for silicon carbide wheel were used due to the focusing properties of the camera system. C parameter is crucial since it is used to determine the number of active grains performing cutting action in the contact zone (Ic-area) between the abrasive wheel and the workpiece. C is not constant for all abrasive wheels; therefore it should be measured carefully for each wheel as a first step.

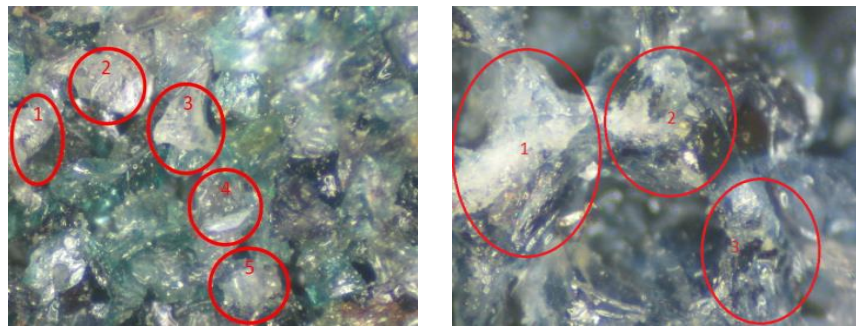


Figure 1 - (a) Alumina and (b) SiC wheel grain per mm<sup>2</sup>

After determining the C number, in order to obtain average rake angle, edge radius and distribution of abrasive grains on the wheel, a special areal confocal 3D measurement system is used. Sufficient number of grains is scanned; this was 100 grains for both the Silicon Carbide wheel used in this paper and alumina wheel. A sample for these measurements can be seen in Figure 2.

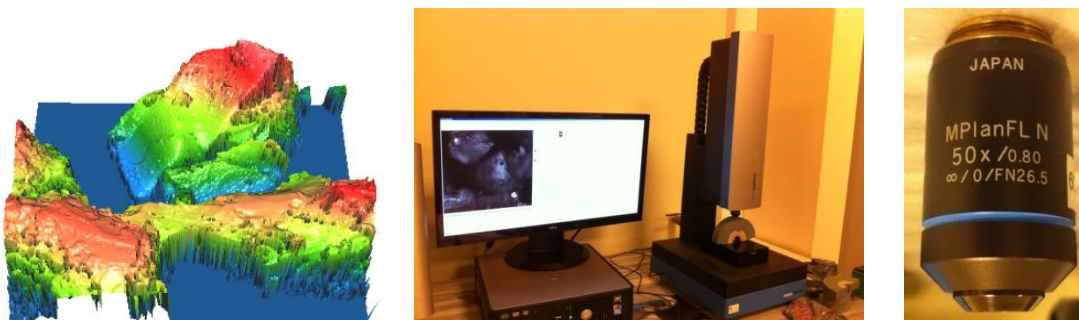


Figure 2 - Sample for a scanned grain and

From the scans and by considering the cutting direction, rake angle and edge radius of that particular grain can be measured via 3D measurement tool. These values are used in semi-analytical force and temperature models explained in the following sections. Each abrasive grain is treated as a micro milling tool tooth where Merchant's metal cutting model adapted to abrasive machining by certain modifications [15]. In Figure 3, measured average rake angles and edge radii for abrasive grains are presented as  $-21.52^\circ$  and  $4 \mu\text{m}$ , respectively. Standard deviation for the rake angle is  $4.58^\circ$  and for the edge radius it is  $1 \mu\text{m}$ .

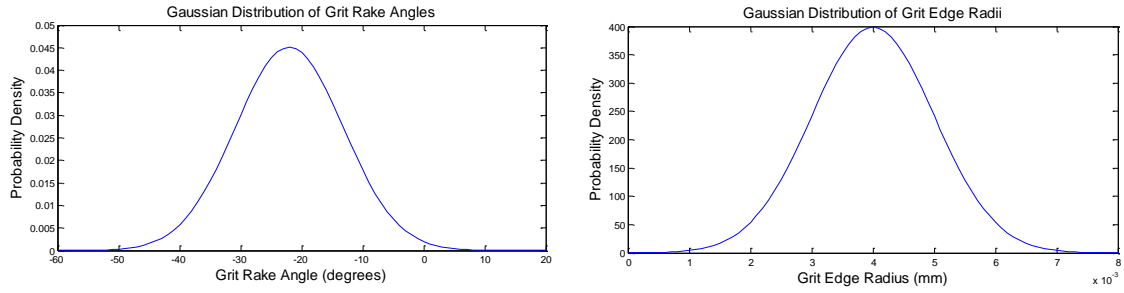


Figure 3 - Grit rake angle and edge radius distribution

### 3. SEMI ANALYTICAL FORCE MODEL

Micro-milling analogy is used for the force modeling and milling force equations are used with some modifications.

$$\begin{aligned} F_{t-grain} &= K_{tc} \times f \times \sin(\theta) \times b + K_{tp} \times b \\ F_{n-grain} &= K_{nc} \times f \times \sin(\theta) \times b + K_{np} \times b \end{aligned} \quad (1)$$

In these equations,  $K_{tc}$ ,  $K_{tp}$ ,  $K_{nc}$  and  $K_{np}$  are cutting coefficients to be identified empirically but can be used for other cases with the same abrasive wheel and workpiece pair.  $K_{tc}$  and  $K_{nc}$  are for chip formation, whereas  $K_{tp}$  and  $K_{np}$  are for ploughing forces. Ploughing forces are obtained by linear regression analysis and subtracted from the total forces in order to identify the average chip formation force per grain [18]. Finally; cutting coefficients for both chip formation and ploughing components are obtained. It requires a few calibration experiments to identify these coefficients. However; once they are determined, it is possible to predict forces for other operations performed with the same abrasive type-workpiece pair.

Expressions for other geometrical parameters, i.e. contact length, wheel surface area, total number of abrasive grits, number of active cutting grains and contact area are given below in order [18].

$$l_c = \sqrt{D \times a} \quad (2)$$

$$W_{area} = 2 \times \pi \times (D/2) \times w \quad (3)$$



$$T_{grains} = W_{area} \times C \quad (4)$$

$$A_g = l_{real-area} \times C \quad (5)$$

$$l_{c-area} = l_c \times b \quad (6)$$

Contact length is straightforward to derive from geometry where the wheel surface is the perimeter times the width of the wheel. Since C was identified beforehand, it can be multiplied with the wheel area to determine the total number of abrasive grains on the grinding wheel. Number of active grains,  $A_g$ , on the other hand, is obtained by multiplying C with the contact area. Using the position of a grain in the cutting zone, the corresponding chip thickness at each time increment can be determined and used in force per grain calculation. Once the force per grain and active grain numbers are known, it is possible to calculate total forces by integration as shown in equation 7.

$$F_{t-total} = \int_{i=1}^{A_g} F_{t-activegrain(i)} \quad (7)$$

$$F_{n-total} = \int_{i=1}^{A_g} F_{n-activegrain(i)}$$

Each abrasive grain performs cutting action similar to a milling operation, but in a micro scale. However; in a macro scale, abrasive wheel moves along the workpiece and in order to calculate the total force or temperature, transformation from micro to macro scale should be performed via integration or geometrical manipulations.

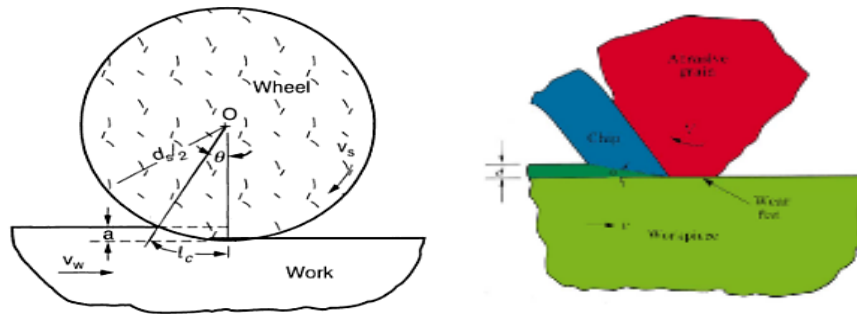


Figure 4 - (a) wheel-workpiece (b) grain-workpiece interaction [13]

One single grain's workpiece engagement region is divided into small sections to investigate the local cutting edge angle and forces. At the edge of the grain, edge angle changes with the edge radius in each section as it can be seen in Figure 5 - b [5].

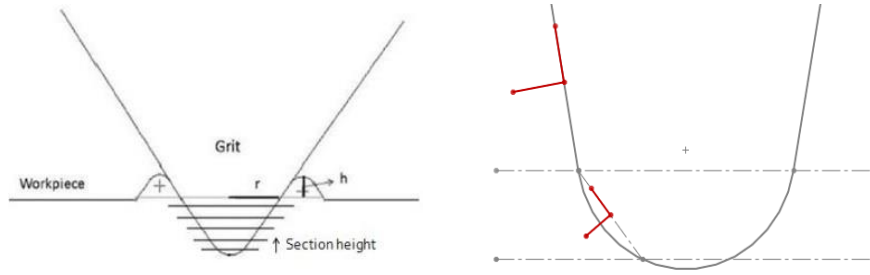


Figure 5 - (a) engagement section and division into sections (b) force direction variation

#### 4. TEMPERATURE MODEL

Surface burn and metallurgical damages on workpiece material due to high temperatures can be considered as a major drawback for abrasive machining. However; by using process models and obtaining optimum process parameters, it may be possible to avoid such undesirable outcomes. In this study, triangular heat flux model is used where abrasive wheel is represented as a 2D moving heat source along the surface and used to determine heat distribution over the workpiece.

Total process energy and power are obtained from the semi-analytical force model [18]. The total heat generated during the operation is calculated as follows:

$$q_{total} = Q_{primary} + Q_{secondary} + Q_{workpiece-rubbing} \quad (8)$$

where  $Q_{primary}$  and  $Q_{secondary}$  are heat generated per unit depth in the primary and secondary shear zones, respectively.  $Q_{workpiece-rubbing}$  is the contribution of the third deformation zone and investigated separately. The total heat generated during the operation is evacuated in four ways: through the chip ( $q_{ch}$ ), grinding fluid ( $q_f$ ), grinding wheel ( $q_{gw}$ ) and the workpiece ( $q_w$ ) as follows:

$$q_{total} = q_{ch} + q_f + q_{tool} + q_w \quad (9)$$

Since hundreds of interactions between abrasive grains and workpiece occur simultaneously along the contact length, some assumptions should be made in order to investigate the process better. As the geometrical properties of abrasive grains on the wheel differ, their chip formation mechanism, hence energy generation is not identical, either. Therefore, average geometrical properties that are obtained through optical measurements as presented in Section 2 are used. The total heat generated during the process can be calculated by Eq. 9, however;  $q_w$  should be determined in order to investigate the surface burn or other metallurgical damages on the workpiece. Energy partition is a crucial factor for calculating process temperatures and can be defined as the fraction of the total energy transported as heat to the workpiece at the grinding zone. There are estimations for determining heat partition ratio into the workpiece [7], in this

study; heat partition is calibrated through some initial experiments. Once it is identified; it can then be used for different cases involving the same workpiece and abrasive type however with different arrangements. Heat flux into the workpiece is  $q_{total}$  times the heat partition ratio ( $\varepsilon$ ) [7].

$$q_w = q_{total} * \varepsilon = q_{total} - q_{ch} - q_f - q_{tool} = \frac{F_t * v_c}{l_c * b} * \varepsilon \quad (10)$$

#### 4.1 Heat Generated in the Primary and Secondary Shear Zones

Heat generated in the primary shear zone is mainly due to plastic deformation. In the classical machining theory, the rate of heat generated is the product of the shear plane component,  $F_s$ , of the resultant force and shear velocity,  $V_s$ . The shear energy is almost completely converted into heat. Due to the complexity of the plastic deformation, contribution from the secondary shear zone to the heat generation is often ignored in the literature [8]. In this study, it is assumed that the process has orthogonal geometry and there is no inclination angle for the abrasive grains. Heat generated per unit depth in the primary and secondary zones are given as follows in the order [9];

$$Q_{primary} = F_s * V_s = \frac{\tau * h * V_w * \cos(\alpha_n)}{\sin(\phi_n) * \cos(\phi_n - \alpha_n)}, \quad Q_{secondary} = F_f * V_c = \frac{\tau * h * V_w * \sin(\beta_n)}{\cos(\phi_n + \beta_n - \alpha_n) * \sin(\phi_n - \alpha_n)} \quad (11)$$

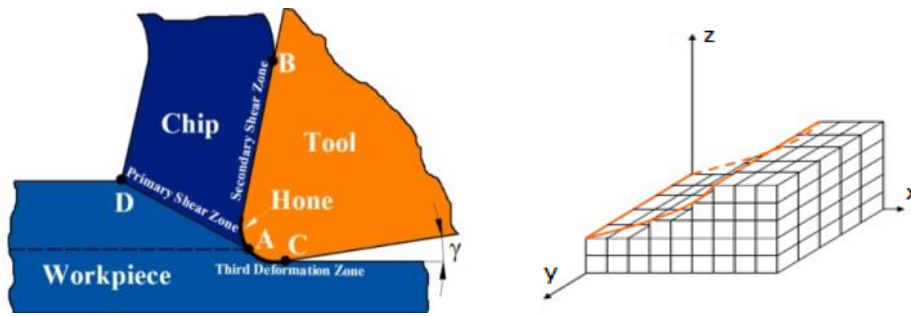


Figure 6 - (a) orthogonal cutting schematic (b) scanning the contact zone between wheel and workpiece

As it can be seen in Figure 6-b, the contact length is scanned and each abrasive grain's position, corresponding chip thickness and width of cut is calculated. Chip is investigated per unit depth of cut and the average temperature for each element due to shearing is obtained by Oxley's energy partition function [9].

$$\Delta \bar{T} = Q'_{primary} * \frac{1 - \chi}{p * c_c * h * V_w} \quad (12)$$

In this equation,  $p$  and  $c_c$  are the mass density and specific heat capacity of the chip, respectively.  $\mathcal{X}$  is the proportion of the shearing flux that goes into the workpiece material. It is defined by [9];

$$\begin{aligned} \mathcal{X} &= 0.5 - 0.35 \log(R_t \cdot \tan(\phi_n)) & \text{for } 0.004 \leq R_t \cdot \tan(\phi_n) \leq 10 \\ \mathcal{X} &= 0.3 - 0.15 \log(R_t \cdot \tan(\phi_n)) & \text{for } R_t \cdot \tan(\phi_n) \geq 10 \end{aligned} \quad (13)$$

$R_t$  is the thermal number and defined as  $R_t = \frac{h \cdot V_w}{a_{diff}}$ ,  $a_{diff} = \frac{k_c}{p \cdot c_c}$  [9]. Shear plane is assumed to have a zero thickness and the average temperature rise on the shear plane is used as a boundary condition for the start point of the contact length ( $l_c$ ). Primary and secondary zones are used as heat sources in solving the temperature distribution. They are calculated for all active abrasive grains and then integrated in order to obtain the total heat generation.  $Q_{chip}$  and  $q_{tool}$  are calculated via presented primary and secondary zone investigations and subtracted from  $q_{total}$  in order to determine  $q_w$  for dry grinding condition. If it is wet or MQL grinding conditions,  $q_f$  should be taken into account as well.  $q_f$  is estimated via calibration tests as explained in results and discussions section.

#### 4.2 Heat Transferred into the Workpiece Material

Heat generated in the third deformation zone is due to the frictional rubbing phenomena between tool and workpiece. In Figure 6 – (a), between A and C points, tool and workpiece are in contact, however; there is no cutting action. As it is stated earlier, the third deformation zone forces (ploughing forces) are identified via linear regression analysis and subtracted from the total measured process forces in order to obtain the chip formation portion of them [18].

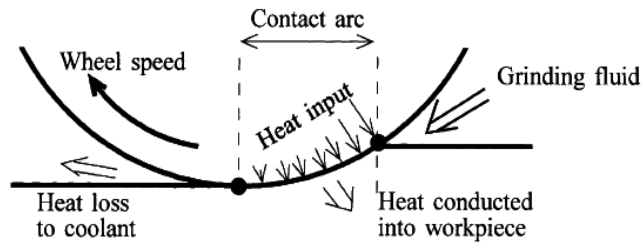


Figure 7 - Contact length heat input [8]

Abrasive wheel is modeled as a moving heat source on workpiece which has a triangular shape. The 2D heat transfer governing equation is [9]:

$$\frac{\partial^2 T}{\partial x^2} + \frac{\partial^2 T}{\partial y^2} = \frac{1}{a_{diff}} \frac{\partial T}{\partial t} \quad (14)$$

where  $a_{diff}$  is the thermal diffusivity of the workpiece material and calculated by Eq. 15 [9];

$$a_{diff} = \frac{k}{c_p * \rho} \quad (15)$$

In Figure 8,  $l_{chip}$  is the maximum chip thickness and  $\phi_n$  is the nominal shear angle.  $\phi$  is the angle between the triangular heat source's line of motion and the plane of the band source, as shown in Figure 8 [10];

$$\phi = \sin^{-1} \sqrt{\frac{a}{d}} \quad (16)$$

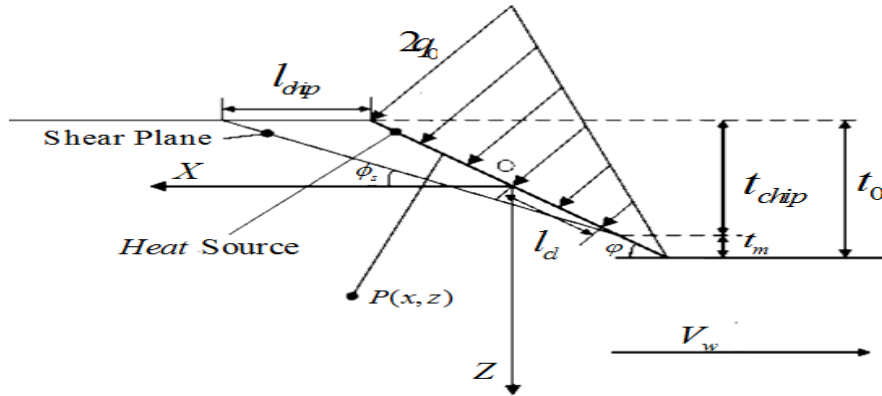


Figure 8 - Contact zone between wheel and workpiece

By considering Jaeger's moving heat source model, equation for the moving triangular band heat source is derived as [10];

$$T(x, z) = \frac{R_w}{\pi * k} * \int_{-\frac{l_c}{2}}^{\frac{l_c}{2}} q_{l_c} * e^{-\frac{V_w * (x + a_{diff} * \cos \phi)}{2 * a}} * K_0 \left\{ \frac{V_w * [(x + a * \cos \phi)^2 + (z - a * \sin \phi)^2]^{1/2}}{2 * a_{diff}} \right\} da_{diff} \quad (17)$$

where  $K_0$  is the second kind modified Bessel function and  $R_w$  is the heat partition ratio to the workpiece.

## 5. SIMULATION AND EXPERIMENT RESULTS

### 5.1 Measured and Predicted Forces

In order to validate the calculated forces and temperatures by the presented models, experiments have been conducted with different process parameters on TOS\_FNK 2 NC milling machine tool. AISI 1050 steel and 150\*25\*20 SiC 80 M grinding wheel are used as workpiece and cutting tool respectively. Single point diamond dresser with 2 carat grade is used for dressing the wheel. Four different axial depth of cuts at 0.03, 0.06, 0.1 and 0.15 mm and three feed values at 0.06, 0.11 and 0.18 mm per revolution with one cutting velocity (1600 rpm - 12.57 m/s) have been used in the experiments as it can be seen in Table 1 ( results are for dry case).



Table 1 - Experiment Parameters and Calculated Shear Stresses

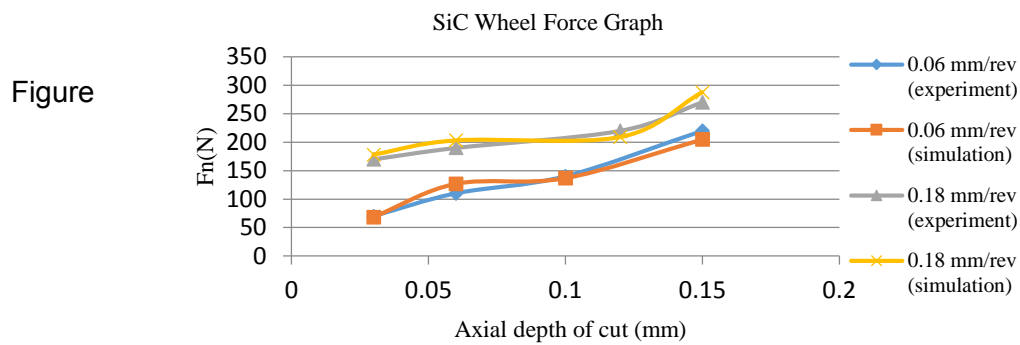
Test no	Feed (mm/rev)	axial depth (mm)	F <sub>x</sub> (average) (experiment)	F <sub>z</sub> (average) (experiment)	Shear Area(mm)	Shear Angle	Shear Stress (Mpa)
1	0,06	0,03	35	70	0,01285	33,19	2797,28
2	0,06	0,06	40	110	0,01774	34,10	1844,73
3	0,06	0,1	80	140	0,02578	29,87	1278,74
4	0,06	0,15	100	220	0,03049	31,05	1277,95
5	0,11	0,03	30	85	0,02192	35,28	1839,75
6	0,11	0,06	55	125	0,03276	33,13	1448,81
7	0,11	0,1	75	140	0,04500	30,91	990,03
8	0,11	0,15	110	180	0,05788	29,29	763,16
9	0,18	0,03	50	170	0,03287	36,81	2859,22
10	0,18	0,06	70	190	0,04870	34,89	1799,65
11	0,18	0,1	85	220	0,06965	34,44	1358,43
12	0,18	0,15	100	270	0,07709	34,84	1272,87

Sample experimental and simulation force graph is given in Figure 10. Forces are measured via Kistler 3 axis dynamometer which is placed under the workpiece. Total grain number on the abrasive wheel is determined via optical surface measurements as 47123. Active grain number differs for each operation and presented in Table 3.



Figure 9 -

Experimental Setup (a) during operation (b) thermocouple junction with the w.p



Figure

10 -

#### Comparison of the experimental and simulation results

Average error between simulation and experimental results is 8%. Forces that are measured from calibration tests are plugged into the Equation 1 and cutting coefficients ( $K_{tc}$  and  $K_{nc}$ ) are identified as presented in Table 2.

Cutting Coeff./feedr	0.06 (mm/rev)	0.11 (mm/rev)	0.18 (mm/rev)
$K_{tc}$ (Mpa)	2800	1350	1428
$K_{nc}$ (Mpa)	5600	3777	4857

Third zone (ploughing) forces are identified through linear regression analysis. These force values are mostly used for the calculation of the heat transferred into the workpiece material.

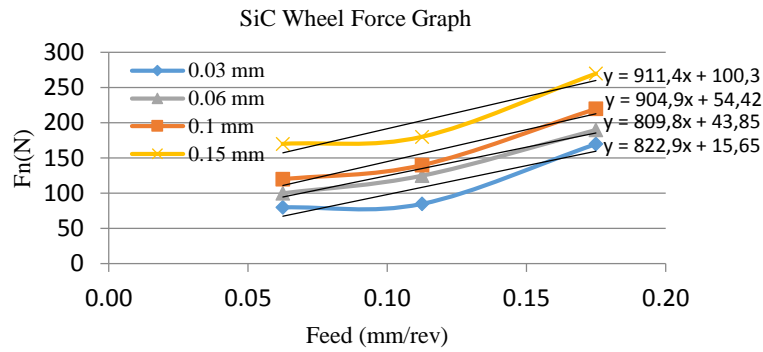


Figure 11- Ploughing force identification

Ploughing forces are identified as 15.65, 43.85, 54.42, 100.30 N for 0.03, 0.06, 0.1 and 0.15 mm axial depth of cut values, respectively. Shear area (mm<sup>2</sup>), shear angle (degrees) and shear stresses are calculated via Merchant's theory [15] for each operation and presented in Table 1.

Table 3 - Active grain number, Teeth Number and Feed per grain

Test No.	feed (mm/rev)	Axial depth(mm)	Active grain #	Total teeth	Feed per grain (mm)	lc(mm)	lc_area(mm <sup>2</sup> )
1	0,06	0,03	212	222	0,0002813	2,12	53,03
2	0,06	0,06	300	157	0,0003979	3,00	75,00
3	0,06	0,1	387	122	0,0005137	3,87	96,82
4	0,06	0,15	474	99	0,0006291	4,74	118,59
5	0,11	0,03	212	222	0,0005064	2,12	53,03
6	0,11	0,06	300	157	0,0007162	3,00	75,00
7	0,11	0,1	387	122	0,0009246	3,87	96,82
8	0,11	0,15	474	99	0,0011324	4,74	118,59
9	0,18	0,03	212	222	0,0007878	2,12	53,03
10	0,18	0,06	300	157	0,0011141	3,00	75,00
11	0,18	0,1	424	111	0,0015756	4,24	106,07
12	0,18	0,15	474	99	0,0017615	4,74	118,59

## 5.2 Measured and Calculated Temperatures

### 5.2.1 Measurement of Grinding Temperature

Temperature experiments are conducted simultaneously with the force measurement experiments. In each operation, dynamometer is used to measure forces and a thermocouple embedded into the workpiece material is utilized to measure the temperature in the contact



zone. K type thermocouple with a 0.8 mm diameter is used in the experiments. It is embedded into the workpiece with epoxy in a 0.1 mm diameter blind hole opened by wire EDM. The hole is blind because when grinding wheel reaches to the thermocouple, thermocouple smears with the workpiece which ensures full contact between them [8]. Temperature measurements are done via taking continuous data from the contact zone. For being able to measure or collect the data correctly, the data acquisition device should have sufficient sampling rate and measurement capability. As it is stated earlier, each active abrasive grain cluster is modeled as a milling tool tooth; therefore minimum time that takes one tooth to engage with workpiece and then leave is 0.17 seconds in our experiment set, maximum time is 0.38 seconds for 0.03 and 0.15 mm axial depth of cut, respectively. Hence, a data logging device which can take measurements with 0.1 second intervals is used.

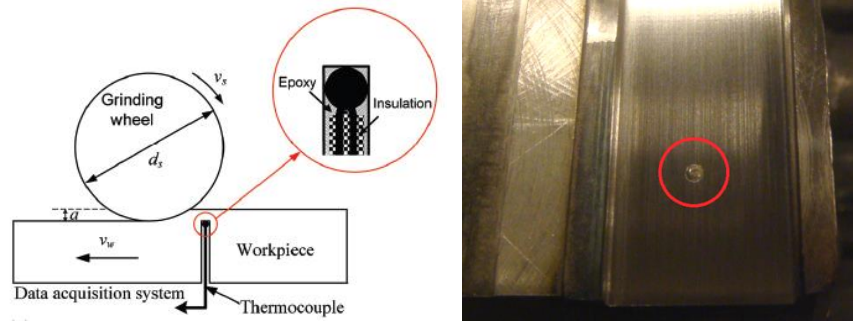
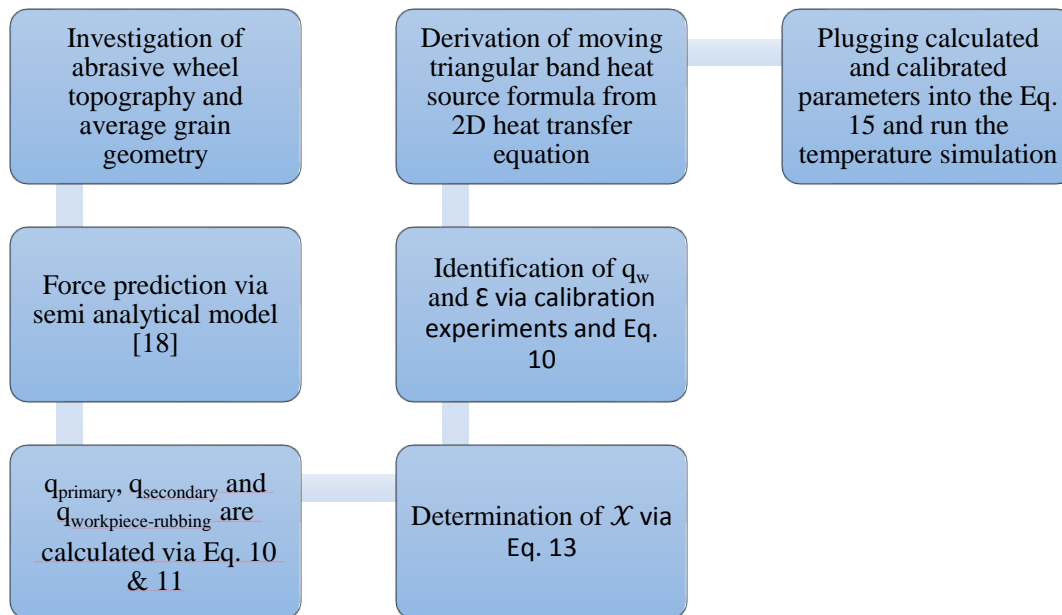


Figure 12 - (a) Thermocouple fixation diagram (b) Exposed thermocouple junction after an operation

### 5.2.2 Simulation of Grinding Temperature

Grinding temperatures are predicted via presented semi-analytical model that is explained in Section 4. Flowchart for the simulation procedure can be seen in Table 4.

Table 4 - Temperature simulation methodology



It is crucial to predict process forces correctly in order to be able to calculate the heat flux into the workpiece accurately. Once  $F_{tc}$  and  $F_{nc}$  are calculated by semi analytical force model [18], heat generated in the primary and secondary shear zones can be calculated by Equation 11. Proportion of the shearing flux ( $X$ ) that goes into the workpiece material is identified via Equation 13 and plugged into the Equation 12 to determine the heat generated due to shearing. Heat partition ratio ( $\epsilon$ ) that is identified via calibration tests are used to calculate the total heat flux into the workpiece. Equation for the moving triangular band heat source is derived from the classical 2D heat transfer equation and simulated via MATLAB in time domain.

Total power used for the primary shear zone and the third deformation zone are calculated by Eq. 11 and 17 and subtracted from total power to find secondary shear zone's power. Once the power for secondary shear zone is known,  $F_f$ , which is the frictional force between tool rake face and the chip contact zone, can be calculated.  $F_f$  values are presented in Table 6 and can be used to calculate temperature on the abrasive wheel in the future studies. Chip temperature is calculated via Eq. 12 which gives the average temperature rise of the chip due to shearing [Table 6]. In addition, contribution from secondary shear zone is considered as well by evaluating the energy input from frictional force between tool rake face and the chip contact zone. Note that chip temperature rises with the axial depth of cut, which means more heat is removed from the contact zone by chips. That phenomenon is the main reason behind non-linear temperature behavior with the cutting parameters, increasing the feed rate and axial depth of cut does not make sure that the temperature on workpiece surface will be higher. It

depends on the chip temperature which is going out from the contact zone and increasing  $l_c$  area (thus lower energy input per unit area) due to higher axial depth of cut or feed rate values.

### 5.2.3 Results for Measured and Calculated Temperatures

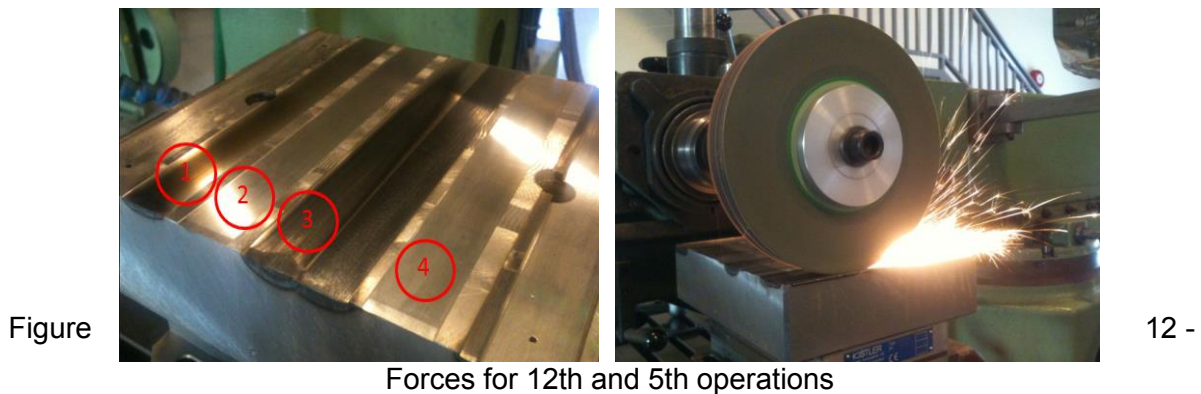
Measured and simulated maximum (peak) temperatures for dry, wet and MQL cases are presented in Table 5. Friction coefficient ( $\mu$ ) is identified via Merchant's theory [15] for each operation. Note that  $\mu$  is smallest in MQL cases which is the main advantage of using minimum quantity lubrication. Average  $\mu$  values are 0.62, 0.55, 0.45 and heat partition values are 72.27%, 25.11% and 61.52% for dry, wet and MQL cases, respectively. In Figure 15 and 16; 0.18 mm/rev feed and 0.15 mm axial depth of cut case results for dry and wet conditions are presented respectively. Since temperatures for MQL case are quite similar to those in dry operations, they are not illustrated.

Table 5 - Temperature and  $\mu$  results

			Temperature (°C) Dry			Temperature (°C) Wet			Temperature (°C) MQL		
Test No.	feed (mm/rev)	a (mm)	Experiment	Simulation	$\mu$	Experiment	Simulation	$\mu$	Experiment	Simulation	$\mu$
1	0,06	0,03	610	671	0,62	197	217	0,52	481	573	0,43
2	0,06	0,06	693	743	0,60	256	240	0,55	547	634	0,45
3	0,06	0,1	785	874	0,69	309	282	0,53	619	746	0,43
4	0,06	0,15	1051	1159	0,66	322	374	0,53	829	990	0,44
5	0,11	0,03	510	571	0,57	147	184	0,60	402	488	0,48
6	0,11	0,06	623	706	0,62	227	228	0,58	491	603	0,47
7	0,11	0,1	897	1009	0,67	289	364	0,58	707	862	0,47
8	0,11	0,15	964	1058	0,70	281	342	0,59	761	904	0,48
9	0,18	0,03	495	586	0,53	160	189	0,51	390	501	0,42
10	0,18	0,06	605	690	0,58	270	223	0,51	477	589	0,43
11	0,18	0,1	732	820	0,59	292	265	0,55	577	700	0,45
12	0,18	0,15	854	921	0,58	360	330	0,56	674	872	0,46

For wet grinding, the water based Boron Oil coolant at 4 vol. % with flow rate 2000 ml/min, for the MQL grinding, the Werte 2000 with 5 ml/min flow rate were used. Surface burn is detected in 3, 4, 7, 8 and 12th operations given in Table 4. When process temperature exceeds the burn threshold and burning of the workpiece is initiated, metallic particle adhesion in the abrasive

grains of the wheel increases, having as consequence the increase of the grinding forces. In this study, both force monitoring and visual inspection are used to detect surface burn and burn threshold results agree with the literature. Wojtas et al. [17] claimed that burn threshold for AISI 1050 steel is identified as 750°C by using the Magnetic Barkhausen Method. Experiments show that temperature and force measurements fairly agree with the 750°C threshold value. Forces increase as burning of the workpiece is initiated which corresponds to temperatures above 720-750°C. In Figure 13, measured forces are illustrated for 12th (burn) and 5th (burn-free) operations [see Table1] respectively.



As it can be seen from the Figure 13, forces have increasing trend in burn-observed operations whereas they are almost constant for burn-free cases. This behavior is always observed for burn and burn-free operations throughout the experiments. Visual inspection of the final workpiece surface also agrees with the force measurements and determined burn threshold.

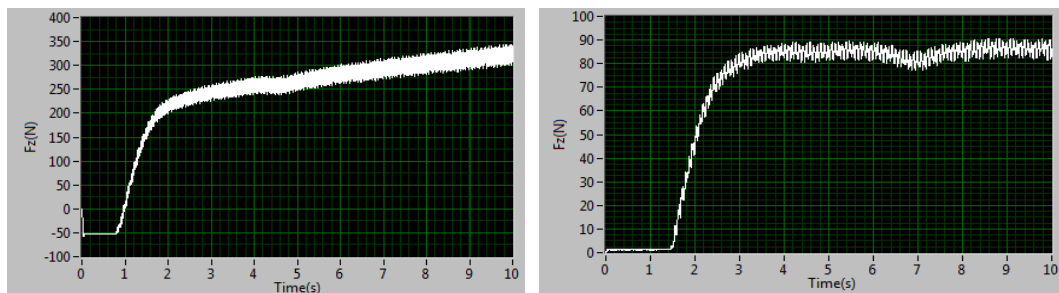


Figure 13 - (a) workpiece surface inspection (b) surface 3 observed operation

In Figure 14, 2nd and 1st surfaces are results for coolant used cut with 0.1 mm axial depth of cut & 0.11 mm/rev feed parameters and dry case with same parameters, respectively. 3rd surface is the result of 0.15 mm axial depth of cut with 0.11 mm/rev feed without coolant and 4th surface is for coolant used case with same parameters..

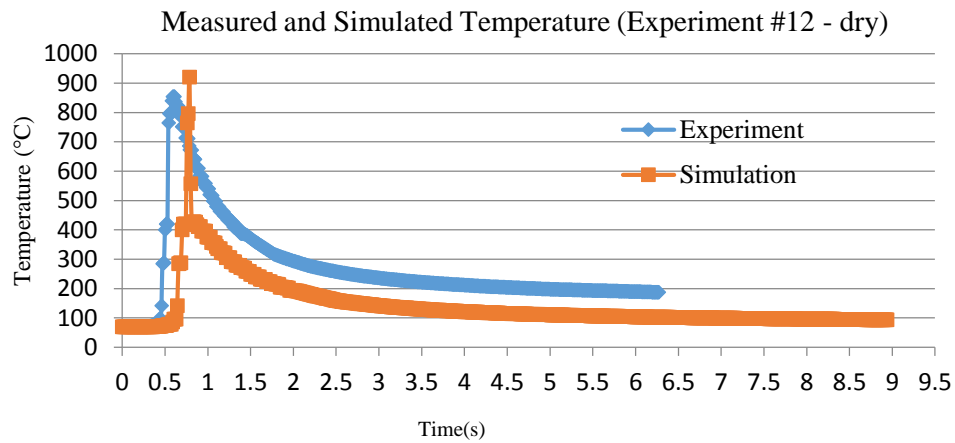


Figure 15 - (a) experiment (b) simulation result for test 12 (dry)

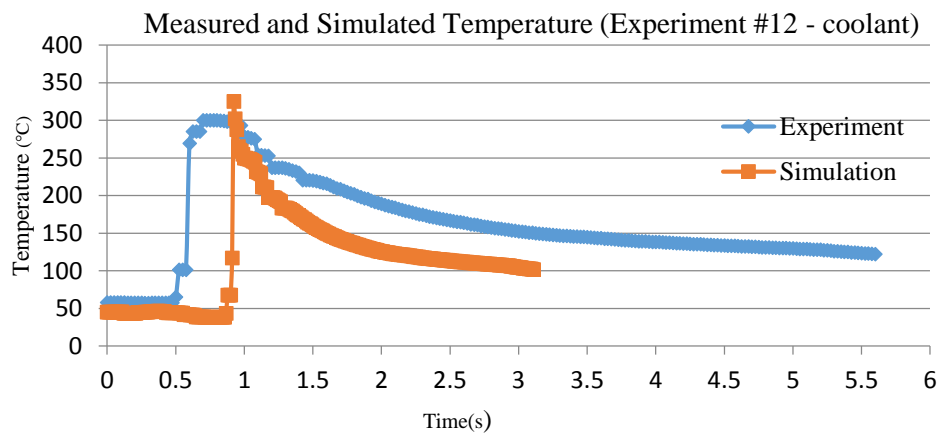


Figure 16 - (a) experiment (b) simulation result for test 12 (wet)

Table 6- Frictional force calculation between tool & chip

Test No.	feed (mm/rev)	Axial depth(mm)	Q_primary (W)	Q_secondary (W)	Total Power (W)	Ff (N)	Chip Temperature (°C)
1	0,06	0,03	674,64	330,67	1005,31	26,31	164
2	0,06	0,06	626,36	630,28	1256,64	50,16	206
3	0,06	0,1	579,57	928,39	1507,96	73,88	241
4	0,06	0,15	692,69	1443,60	2136,28	114,88	347



5	0,11	0,03	792,14	276,00	1068,14	21,96	105
6	0,11	0,06	889,79	681,00	1570,80	54,19	153
7	0,11	0,1	798,69	960,60	1759,29	76,44	170
8	0,11	0,15	757,43	1504,52	2261,95	119,73	218
9	0,18	0,03	1912,74	223,54	2136,28	17,79	143
10	0,18	0,06	1706,28	681,33	2387,61	54,22	159
11	0,18	0,1	1824,03	940,57	2764,60	74,85	184
12	0,18	0,15	1908,43	1484,49	3392,92	118,13	226

## 6. CONCLUSION

In this paper; a methodology is presented to detect whether the temperature values during grinding operation will cause a surface burn over workpiece material or not by process modeling. Achieved or explored items are listed as;

- A semi-analytical force model is presented and used for determination of the total power.
- Based on the triangular heat flux model, wheel is modeled as a moving heat source along the workpiece surface and semi-analytical temperature model is utilized.
- Calculated force and temperature values are experimentally validated by an average error of 8% and 14% respectively.
- Energy partition value is identified for dry, wet and minimum quantity lubrication (MQL) grinding conditions as 72,27%, 25,11% and 61,52% respectively.
- Chip temperature is calculated which led to a more accurate prediction of surface burn.
- It has been observed that there is a non-linear temperature behavior with the cutting parameters, increasing the feed rate and axial depth of cut does not make sure that the temperature on workpiece surface will be higher.
- It has been showed that abrasive grain scaled analysis is an adequate approach to predict force and temperatures for grinding operations.



## 7. REFERENCES

1. **Jaeger, J.C.**, (1942), Moving Sources of Heat and the Temperature at Sliding Contacts, Journal and Proceedings of the Royal Society of New South Wales, Vol. 76, 203-224.
2. **Outwater, J. O., and Shaw, M. C.**, (1952), Surface Temperatures in Grinding, Transactions of ASME, Vol. 74, pp. 73–86.
3. **Shaw, M. C.**, (1990), A Simplified Approach to Workpiece Temperature in Fine Grinding, CIRP Ann., Vol. 39, pp. 345–347.
4. **Hecker, R., Ramoneda, I., Liang, S.**, (2003), Analysis of Wheel Topography and Grit Force for Grinding Process Modeling, Journal of Manufacturing Processes, Vol. 5, pp. 13-23.
5. **Durgumahanti, U., Singh, V., Rao, P.**, (2010), A New Model for Grinding Force Prediction and Analysis, International Journal of Machine Tools & Manufacture, Vol. 40, pp. 231-240.
6. **S C., Salmon.**, (1992), Modern grinding process technology. New York. McGraw-Hill.
7. **Malkin, S., and Guo, C.**, (2007), Thermal Analysis of Grinding, CIRP Ann., Vol. 56, pp. 760-782.
8. **Augustine, U., and Olisaemeka, N.**, (2013), Evaluation of Tool and Chip Temperature during Machining Process Using Numerical Method, The International Journal of Engineering and Science, Vol. 2, 66-79.
9. **Lazoglu, I., and Altintas, Y.**, (2002), Prediction of Tool and Chip Temperature in Continuous and Interrupted Machining, International Journal of Machine Tools & Manufacture, Vol. 42, 1011-1022.
10. **Park, H. W., Liang, S. Y.**, (2009), Force Modeling of Microscale Grinding Process Incorporating Thermal Effects, International Journal of Advanced Manufacturing Technology, Vol. 44, 476-486.
11. **Shen, B., Xiao, G.**, (2008), Thermocouple Fixation Method for Grinding Temperature Measurement, Journal of Manufacturing Science and Engineering, Vol. 130, pp. 1-8.
12. **Shen, B., Xiao, G.**, (2011), A Heat Transfer Model Based on Finite Difference Method for Grinding, Journal of Manufacturing Science and Engineering, Vol. 133, pp. 1-10.
13. **Mohamed, O., Warkentin, A., Bauer, R.**, (2012), Variable heat flux in numerical simulation of grinding temperatures, International Journal of Advanced Manufacturing Technology, Vol. 63, 549-554.
14. **Tahlvian, A.M., Champlaud, H., Liu, Z., Hazel, B.**, (2013), Study of Workpiece Temperature Distribution in the Contact Zone During Robotic Grinding Process Using Finite Element Analysis, 8th CIRP Conference on Intelligent Computation in Manufacturing Engineering, Procedia CIRP, Vol. 12, 205-210.



- 15. Merchant, E.,** (1945), Mechanics of the Metal Cutting Process, Journal of Applied Physics, Vol. 16, pp. 207.
- 16. Hadad, M., and Sadeghi, B.,** (2012), Thermal Analysis of Minimum Quantity Lubrication (MQL) Grinding Process, International Journal of Machine Tools & Manufacture, Vol. 63, pp. 1-15.
- 17. Wojtas, A., Suominen, L., Shaw, B.,** (1998), Detection of Thermal Damage in Steel Components After Grinding Using the Magnetic Barkhausen Noise Method, Proceedings of 7th European Conference on Non-destructive Testing, Vol. 3, No.9, Copenhagen.
- 18. Aslan, D., Budak, E.,** (2014), Semi-analytical Force Model for Grinding Operations, 6th CIRP Conference on High Performance Cutting, Procedia CIRP.







## FORCE MODEL FOR MICRO MILLING OF FREE FORM SURFACES

**Ali MAMEDOV**, *amamedov@ku.edu.tr*, Koç University, 34450, Istanbul, Turkey

**İ. E. YİĞİT**, *iyigit13@ku.edu.tr*, Koç University, 34450, Istanbul, Turkey

**Ismail LAZOĞLU**, *ilazoglu@ku.edu.tr*, Koç University, 34450, Istanbul, Turkey

### ABSTRACT

This paper presents a new model for estimating instantaneous machining forces with shearing and plowing mechanisms in micro ball end milling of free form surfaces. The analysis of cutting forces in micro milling plays an important role for the investigation of mechanics and dynamics of the cutting process. Force analysis is preliminary step to estimate the surface quality of machined miniature parts. Presented force model calculates instantaneous chip thickness by considering trajectory of the tool tip while tool rotates and moves ahead continuously. The model also takes into consideration the plowing force component which is important in micro milling and relates it to elastic recovery based on interference volume between micro tool and workpiece. The mathematical model is used to determine the force distribution on the micro milling tools. Presented force model is validated on Ti-6Al-4V grade Titanium Alloy, through micro ball end milling experiments for a wide range of cutting conditions using micro dynamometer.

**Keywords:** Micro milling; force model; Titanium Ti-6Al-4V;

### 1. INTRODUCTION

Ti-6Al-4V is an advanced engineering alloy finding wider application areas day by day. High strength, corrosion and fatigue resistance at elevated temperatures are among the superior properties of this alloy. Ti-6Al-4V is used in various industries such as aeronautics, nuclear energy generation plants, food processing machinery, and implant manufacturing. The reason that this alloy is widely used in aeronautics is the superior characteristics that make it suitable to be used in extreme working conditions such as jet engines. Although a lot of research has been conducted on flat end milling, ball end milling of Titanium alloy has not been investigated widely. The ball end milling operation is used extensively in manufacturing of free form surfaces in hi-tech industries. Due to the different cutting speed along the tool axis, ball end milling operation is extremely depended upon the cutting parameters such as feedrate, tool orientation, spindle speed, etc.

Due to the low thermal conductivity of these alloys higher portion of the temperature generated during cutting process flows into the cutting tool which causes excessive wear and premature failure of micro tools. Several groups of researchers are working on micro milling of Titanium to understand process kinematics, improve machinability and decrease tool wear during cutting process. The most effective method to decrease tool wear is coating of micro tools. The prior research on wear mechanisms of polycrystalline diamond (PCD), cubic crystalline boron nitride (cBN) and TiB<sub>2</sub> coated carbide tools during high performance machining of Ti-6Al-4V titanium alloy is done by [Corduan & Himbet, 2003]. Later [Aramcharoen, Mativenga, Yang, Cooke, & Teer, 2008] compared different coatings like TiN, TiCN, TiAlN, CrN and CrTiAlN and their effect on flank wear, chipping, edge radius wear, burr size and machined surface quality. [Özel, Sima, Srivastava, & Kaftanoglu, 2010] investigated effects of CBN, TiAlN and TiAlN+cBN coatings on wear rate distribution and cutting forces formed during micro milling process. [Thepsonthi & Özel, 2013] investigated the effect of cBN coating on cutting temperature and stated that the tool temperature and wear rate increase by increasing the cutting speed and feed rate.

The critical factor in micro milling is to manufacture high precision parts within a tight surface and form tolerances. It is known that portion of dimensional, surface and form errors are induced by deflections of micro tool caused by cutting forces. Due to this reason many researchers worked on modeling of kinematics of the micro milling cutting process. In foregoing research [Vogler, Kapoor, & DeVor, 2004] and [Waldorf, DeVor, & Kapoor, 1998] have developed shear plane plasticity model. Based on these studies [Jun, Liu, DeVor, & Kapoor, 2006] and [Fang, 2003] have developed more complex plasticity models, which covers elastic recovery of plowed material. [Fang & Jawahir, 2002] proposed a generalized slip-line field model to predict shearing and plowing forces. [Rodríguez & Labarga, 2013] developed an analytical force model for micro end milling considering the size effect and eccentric deviation of the tool path. [Jin & Altintas, 2011] presented a slip-line field model, which considers the stress variation in shear zones and relates it to temperature and tool edge radius effect. A mechanistic force model proposed by [Park & Malekian, 2009] considers both the shearing and plowing dominant cutting regimes and relates plowed area to volume of the plowed material due to the effect of tool edge radius. All the presented work above is done for flat end milling.

In this research mechanical effects of machining parameters in ball end milling and a new mathematical model to predict cutting forces during micro milling with ball end mill processes are presented. Estimated cutting forces are presented as a function of cutting coefficients. A comprehensive chip thickness model developed by [Li, Lai, Li, & Ni, 2007] for micro milling is used for precise estimation of cutting forces. The predicted micro milling forces are validated by the experimental tests and some of the results are shared in this paper.

## 2. KINEMATICS OF THE PROCESS

Modeling of micro milling forces is a key factor to improve machining quality, control and understand kinematics of cutting process. From the prior research, it is now clear that micro milling is different from conventional machining operations and besides scaling down of the process presence of specific phenomena was found. The most frequent phenomenon faced during micro milling is the size effect. The size effect occurs because the edge radius of the micro tool is in the same range with uncut chip thickness. This phenomenon results in plowing of workpiece material where no chip formation occurs because the chip thickness is less than minimum chip thickness which depends on material of machined part.

A new methodology for modeling cutting forces for ball end mill is proposed in this paper. The ball end mill is discretized to finite number of flat end mills according to local radius as shown in Figure 1 and forces calculated at each disk are integrated to calculated total cutting force in x and y directions.

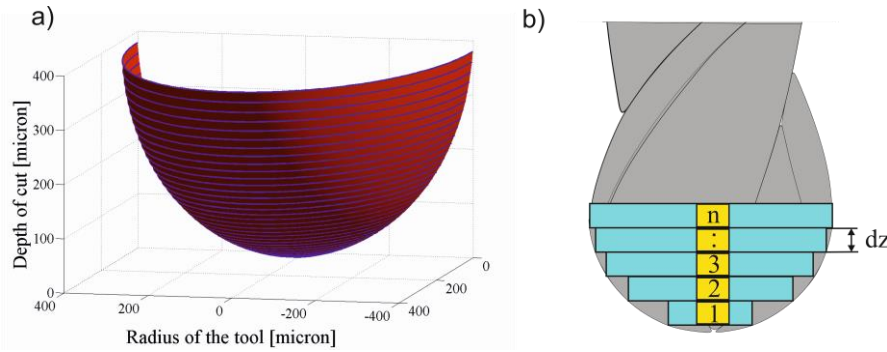


Figure 1. a) Discretization of ball end mill, b) Schematic view of discretization

From the prior research, it is clear that chip thickness is the primary input for estimating cutting forces. The expression of the chip thickness for conventional milling was proposed by [Martellotti, 1941], but this equation is not valid for micro milling, where the ratio of feed per tooth to tool radius is higher than in conventional milling. Several research groups developed chip thickness models for micro milling. The chip thickness models proposed by [Martellotti, 1941], [Bao, 2000], [Kang & Zheng, 2013] and [Li et al., 2007] were compared. During cutting force estimation it was seen that chip thickness model developed by Li has the best match with experimental results. The same chip thickness model is utilized in the developed force prediction model. The proposed chip thickness model is given below,

$$(h)_k = R \cdot \left[ 1 - \sqrt{1 - \frac{2t_x \sin \theta}{R + \frac{Nt_x}{2\pi} \cos \theta} - \frac{t_x^2 \cos(2\theta)}{(R + \frac{Nt_x}{2\pi} \cos \theta)^2} - \frac{t_x^3 \sin \theta \cos^2 \theta}{(R + \frac{Nt_x}{2\pi} \cos \theta)^3}} \right] \quad (1)$$



where  $(h)_k$  is chip thickness,  $R$  is the local radius of the tool,  $N$  is number of flutes,  $t_x$  is feed per tooth and  $\theta$  is rotational angle. Force model for predicting forces during the micro milling process with ball end mill was established using mentioned chip thickness model.

The instantaneous chip load for  $k^{th}$  disk can be written as following:

$$dA_c = (h)_k \cdot (dz)_k \quad (2)$$

Formation of the chip during the cutting process depends on the uncut chip thickness. Plowing is observed when actual uncut chip thickness is less than minimum uncut chip thickness. No chip formation occurs during plowing, however, if actual uncut chip thickness is greater than minimum uncut chip cutting process becomes shear dominant.

During the shear dominant regime the differential cutting forces in tangential and radial directions  $(t, r)$  for each disk are estimated using following model;

$$\begin{bmatrix} dF_t \\ dF_r \end{bmatrix} = \begin{bmatrix} K_{tc} dA_c \\ K_{rc} dA_c \end{bmatrix} + \begin{bmatrix} K_{te} dz \\ K_{re} dz \end{bmatrix} \quad (3)$$

where  $dF_t$  and  $dF_r$  are differential forces in tangential and radial directions shown in Figure 2 and  $K_{tc}$  and  $K_{rc}$  are cutting force coefficients,  $K_{te}$  and  $K_{re}$  are cutting edge coefficients.

During the plowing dominant regime generated forces are related to the volume of the plowed material and are estimated using following model [Jun, Goo, Malekian, & Park, 2012];

$$\begin{bmatrix} dF_t \\ dF_r \end{bmatrix} = \begin{bmatrix} K_{tp} A_p dz \\ K_{rp} A_p dz \end{bmatrix} \quad (4)$$

above  $dF_t$  and  $dF_r$  are differential forces in tangential and radial directions,  $K_{tp}$  and  $K_{rp}$  are plowing coefficients and  $A_p$  is plowed area which depends on height of elastically recovered material  $(h_e)$ , edge radius of the tool  $(r_e)$  and clearance angle  $(\psi_e)$ . The detailed calculation of plowed area  $(A_p)$  is described in [Malekian, Park, & Jun, 2009] paper. Cutting force and edge coefficients vary along tool axis direction and are determined by calibration procedure described in [Lazoglu, Boz, & Erdim, 2011].

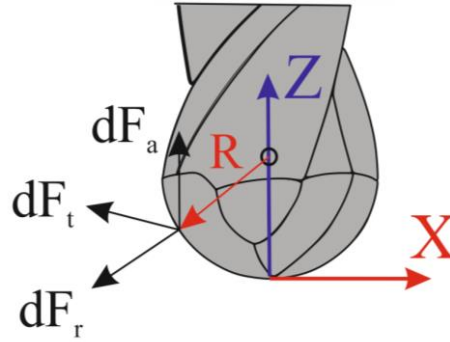


Figure 2. Cutting force components

$$T = \begin{bmatrix} \cos(\theta) & \sin(\theta) \\ -\sin(\theta) & \cos(\theta) \end{bmatrix} \quad (5)$$

By using transformation matrix  $T$  given in Equation 5 tangential and radial forces for each disk are transformed to forces in Cartesian directions – X and Y as following:

$$\begin{bmatrix} dF_x \\ dF_y \end{bmatrix} = [T] \times \begin{bmatrix} dF_t \\ dF_r \end{bmatrix} \quad (6)$$

## 2.1 Cutter-Workpiece Engagement Calculation

Cutter workpiece engagement calculation is extremely critical aspect in modeling of kinematics of the cutting process, because chip load and force calculations are based on it. In this paper solid modeler based cutter workpiece calculation method is employed. Swept volume of cutting tool is calculated according to cutter location file and later is subtracted from blank workpiece. After contact surface between tool and workpiece is calculated at each cutter location point, entrance and exit angles of each discrete disc located on tool are calculated. These entrance and exit angles are forming engagement domain, which is used as an input for force model. The resulting contact region for sample cutter location point #4009 and final machined part are illustrated in Figure 3.

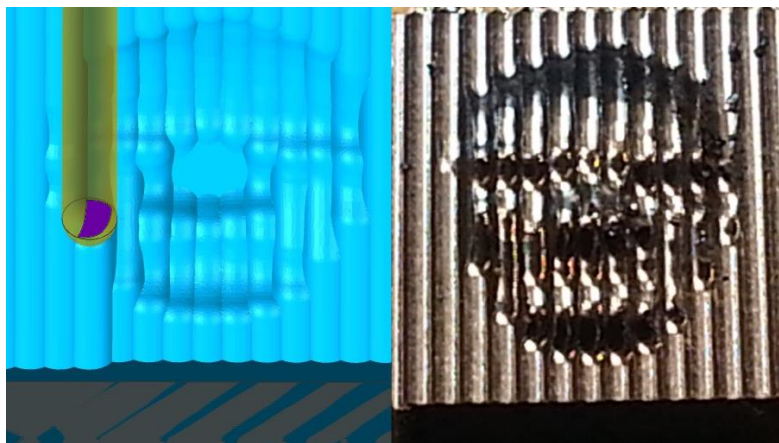


Figure 3. The contact region for CL #4009 and machined part

### 3. SIMULATION AND EXPERIMENTAL RESULTS

Experiments are performed on Ti-6Al-4V grade titanium alloy using 800  $\mu\text{m}$  diameter two fluted Tungsten Carbide micro end mill on Mori Seiki NMV5000DCG 5-axis CNC milling machine and cutting forces are measured with table type mini dynamometer. The experimental setup used for validation of force model for micro ball end milling on free form surfaces is shown below in Figure 4.



Figure 4. Experimental setup

Cutting experiments were performed on Ti-6Al-4V grade Titanium alloy at 10.000 rpm spindle speed with the feed per tooth values of 5 microns. Run out of the tool was measured as 2  $\mu\text{m}$  and was considered during simulations of cutting forces. Table 1 presents the cutting conditions and tool specifications used in the simulation and the experiments for micro milling.

Table 1. Cutting conditions and tool specifications

Tool Diameter	800 [ $\mu\text{m}$ ]
Number of flutes	2
Edge radius	2 [ $\mu\text{m}$ ]
Measured helix angle	25.2°
Spindle Speed	10000 rpm
Feedrate	100 mm/min

In order to validate cutting force model experimental force measurements are done. In Figure 5 and Figure 6 simulated and experimental forces in x and y directions for single tool path (layer-2, path-13) are presented. Simulated and experimental forces in x and y direction shown in Figure 7 and Figure 8 show prediction accuracy of cutting force model. Estimated

forces in z direction showed difference with experimental results due to high amount of plowing, presented model is being developed in order to consider this phenomenon.

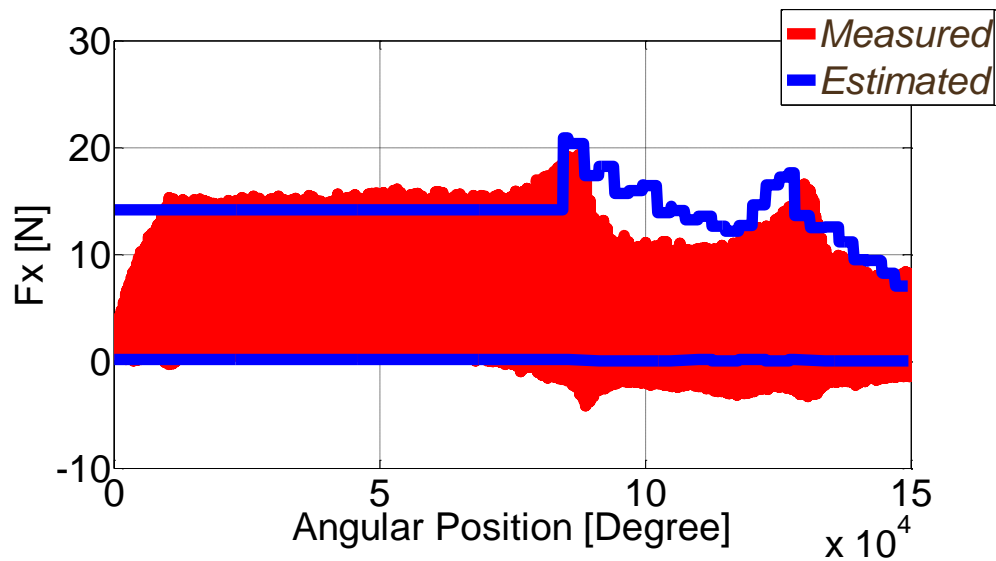


Figure 5. Cutting forces in x-direction for single path

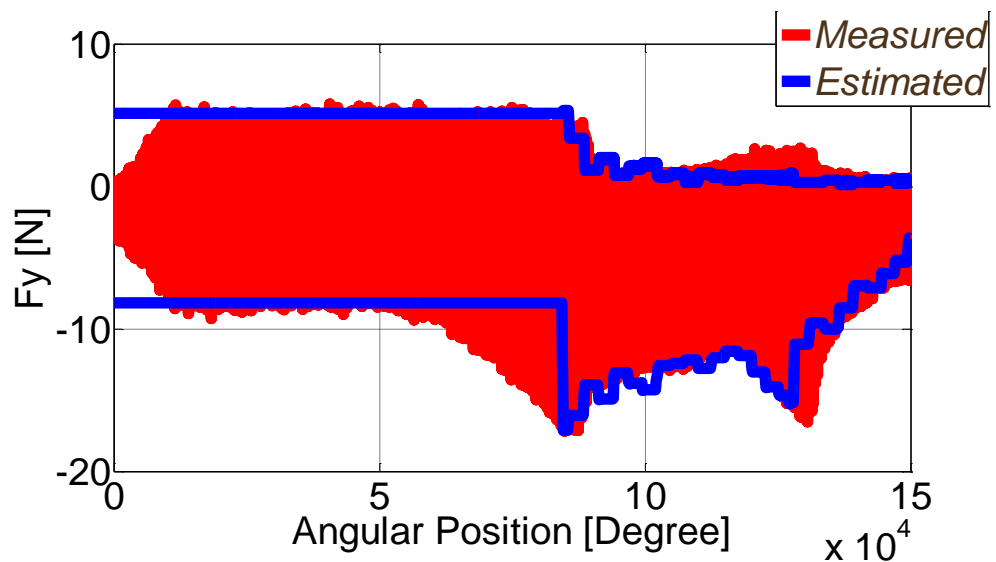


Figure 6. Cutting forces in y-direction for single path



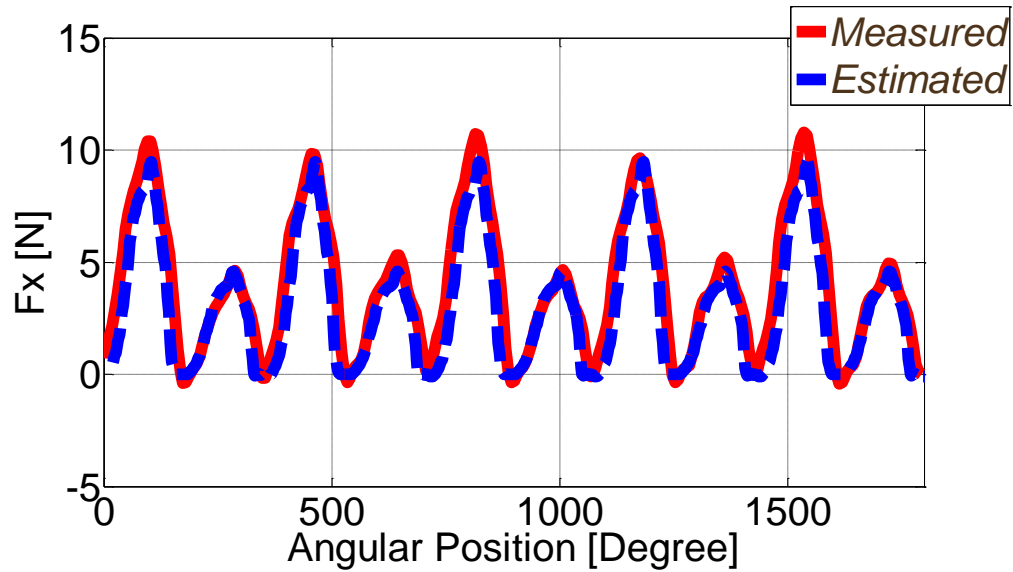


Figure 7. Cutting forces in x-direction

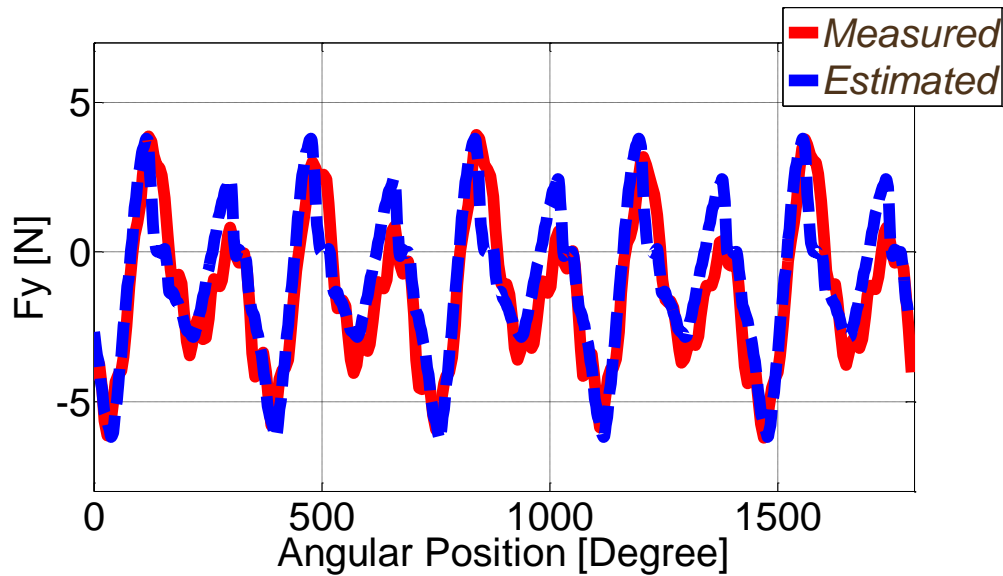


Figure 8. Cutting forces in y-direction

#### 4. CONCLUSION

In this paper, new analytical model for predicting micro milling cutting forces for ball end milling of free form surfaces was presented. The presented cutting force model is a function of cutting force coefficients, micro chip thickness model and tool edge geometry. This model precisely estimates micro milling cutting forces formed by both shearing and plowing cutting mechanisms. Through the sets of the experiments, it was seen that force model showed good agreement with experimental data.



## REFERENCES

1. **Corduan, N., & Himbet, T. (2003).** "Wear Mechanisms of New Tool Materials for TiBAI4V High Performance Machining". *CIRP Annals - Manufacturing Technology*, 51, 73–76.
2. **Aramcharoen, A., Mativenga, P., Yang, S., Cooke, K., & Teer, D. (2008).** "Evaluation and selection of hard coatings for micro milling of hardened tool steel". *International Journal of Machine Tools and Manufacture*, 48, 1578–1584.
3. **Özel, T., Sima, M., Srivastava, a. K., & Kaftanoglu, B. (2010).** "Investigations on the effects of multi-layered coated inserts in machining Ti–6Al–4V alloy with experiments and finite element simulations". *CIRP Annals - Manufacturing Technology*, 59, 77–82.
4. **Thepsonthi, T., & Özel, T. (2013).** "Experimental and finite element simulation based investigations on micro-milling Ti-6Al-4V titanium alloy: Effects of cBN coating on tool wear". *Journal of Materials Processing Technology*, 213, 532–542.
5. **Vogler, M., Kapoor, S., & DeVor, R. (2004).** "On the Modeling and Analysis of Machining Performance in Micro-End milling, Part II: Cutting Force Prediction". *Trans. ASME Journal of Manufacturing Science and Engineering*, 126, 695–705.
6. **Waldorf, D. J., DeVor, R., & Kapoor, S. (1998).** "Slip-Line Field for Ploughing During Orthogonal Cutting". *Trans. ASME Journal of Manufacturing Science and Engineering*, 120, 693–698.
7. **Jun, M. B. G., Liu, X., DeVor, R. E., & Kapoor, S. G. (2006).** "Investigation of the Dynamics of Microend Milling—Part I: Model Development". *Journal of Manufacturing Science and Engineering*, 128, 893–900.
8. **Fang, N. (2003).** "Slip-line modeling of machining with a rounded-edge tool—Part I: new model and theory". *Journal of the Mechanics and Physics of Solids*, 51, 715–742.
9. **Fang, N., & Jawahir, I. S. (2002).** "An Analytical Predictive Model and Experimental Validation for Machining with Grooved Tools Incorporating the Effects of Strains, Strain-rates, and Temperatures". *CIRP Annals - Manufacturing Technology*, 51, 83–86.
10. **Rodríguez, P., & Labarga, J. E. (2013).** "A new model for the prediction of cutting forces in micro-end-milling operations". *Journal of Materials Processing Technology*, 213, 261–268.
11. **Jin, X., & Altintas, Y. (2011).** "Slip-line field model of micro-cutting process with round tool edge effect". *Journal of Materials Processing Technology*, 211, 339–355.
12. **Park, S. S., & Malekian, M. (2009).** "Mechanistic modeling and accurate measurement of micro end milling forces". *CIRP Annals - Manufacturing Technology*, 58, 49–52.
13. **Li, C., Lai, X., Li, H., & Ni, J. (2007).** "Modeling of three-dimensional cutting forces in micro-end-milling". *Journal of Micromechanics and Microengineering*, 17, 671–678.
14. **Martellotti, M. (1941).** "An Analysis of Milling Process". *Trans. ASME Journal of Manufacturing Science and Engineering*, 63, 677–700.



15. **Bao, W. (2000).** "Modeling micro-end-milling operations. Part I: analytical cutting force model". *International Journal of Machine Tools and Manufacture*, 40, 2155–2173.
16. **Kang, Y. H., & Zheng, C. M. (2013).** "Mathematical modelling of chip thickness in micro-end- milling: A Fourier modelling". *Applied Mathematical Modelling*, 37, 4208–4223.
17. **Jun, M. B. G., Goo, C., Malekian, M., & Park, S. (2012).** "A New Mechanistic Approach for Micro End Milling Force Modeling". *Journal of Manufacturing Science and Engineering*, 134, 1–9.
18. **Malekian, M., Park, S. S., & Jun, M. B. G. (2009).** "Modeling of dynamic micro-milling cutting forces". *International Journal of Machine Tools & Manufacture*, 49, 586–598.
19. **Lazoglu, I., Boz, Y., & Erdim, H. (2011).** "Five-axis milling mechanics for complex free form surfaces". *CIRP Annals - Manufacturing Technology*, 60, 117–120.



## **SINGLE GRIT SCRATCH TESTS TO EXPLORE THE MATERIAL REMOVAL MECHANISM IN GRINDING AT MICRO SCALE**

**Tahsin T. ÖPÖZ**, *t.t.opoz@ljmu.ac.uk* Liverpool John Moores University, L3 3AF, Liverpool, UK

**Xun CHEN**, *x.chen@ljmu.ac.uk* Liverpool John Moores University, L3 3AF, Liverpool, UK

### **ABSTRACT**

This paper presents the material removal mechanism in relation to the pile up ratio of material removal and the change of a grit cutting edge during single grit grinding. Investigation was carried out by utilizing single grit scratch tests on Inconel 718 material with a CBN grit of 40/50 mesh size. The concept of pile up ratio was introduced to determine material removal behaviour considering ploughing and cutting actions. The pile up ratio was calculated at the cross sections of scratches with various depths of cut and also along a scratch path to show the longitudinal behaviour of the material removal. The experimental results showed that material removal mechanism during single grit action was highly dependent on the shape change of grit cutting edge and the depth of cut.

**Keywords:** Single grit scratch, Grinding, Pile up ratio, Material removal, Inconel 718

### **1. INTRODUCTION**

High material removal rate and high surface quality are fundamental requirements of most grinding operations. The material removal ability of abrasive grits is of great interest in order to understand the grinding behaviour and its influence on the ground surface creation, particularly at the micro scale. With the entire grinding wheel-workpiece interaction (Kannappan and Malkin, 1972; Zhong and Venkatesh, 2009), it is difficult to evaluate an individual grit contribution to material removal and difficult to observe the effects of abrasive grit geometrical parameters, such as cutting edge shape, size, and depth of cut on the ground surface.

It was postulated that there could exist three stages of material removal in grinding, namely, rubbing, ploughing and cutting, to ultimately remove the material from the workpiece surface in the form of tiny chips (Hahn, 1962). As an abrasive grit slides on the workpiece surface for a small distance at the initial stage, the grit-workpiece interaction does not cause any permanent change on the surface topography, where the interaction only occurs in the

elastic range and recovers due to elastic spring back effect after the interaction ends. This stage in the process is called rubbing. The ploughing stage is initiated with increasing penetration of the grit into the workpiece while the abrasive grit travels forward simultaneously. At this stage, the interaction occurs in both the elastic and plastic regions but no real material removal occurs. When the shearing stresses increase beyond the tearing stresses, the ploughed material in front of the grit is finally removed from the workpiece material in the form of chips. This stage is known as cutting. Among these stages, rubbing has negligible contribution to material removal, while ploughing plays a crucial role influencing energy consumption, surface roughness characterization, surface creation, and overall efficiency of the grinding process. In order to improve material removal efficiency, effective cutting should be maximized while rubbing and ploughing should be minimized because they consume energy without much contributing to the material removal (Ghosh et al., 2008).

To investigate single abrasive grit – workpiece interaction at the micro scale down to the submicron scale as well as the material removal characteristics at that range, single grit scratching tests have been utilized by many researchers (Takenaka, 1966; Doyle, 1973; Matsuo et al., 1989; Subhash and Zhang, 2002; Ghosh et al., 2010; Anderson et al., 2011; Öpöz and Chen, 2012). Albeit, there are a substantial amount of tests performed by using a shaped abrasive grit or shaped cutting tool (known geometry) such as a diamond indenter or stylus (Subhash and Zhang, 2002; Komanduri et al., 2010; Gu et al., 2011), spherical tool (Anderson et al., 2011), or negative raked cutter (Barge et al., 2008) to reduce shape factor influence during material removal, some experimental works also exist with the actual abrasive grits (Takenaka, 1966; Doyle, 1973; Matsuo et al., 1989; Brinksmeler and Glwierzew, 2003; Öpöz and Chen, 2012). Shaped tools are good for experiments because they make easy comparisons with computational models (Barge et al., 2003; Liang et al., 2005; Doman et al., 2009; Doman et al., 2009; Kermouche et al., 2010; Anderson et al., 2011; Öpöz and Chen, 2011). Besides, the shaped tools make parametric investigation easy to study the effect of speed, depth of cut, and hardness of materials on the material removal mechanisms by keeping the tool geometry stable. However, scratches with shaped tools diverge from the reality of actual grinding because the shapes of grit cutting edges continuously alter due to grit wear and fracture occurring during grinding process. Takenaka (Takenaka, 1966) performed one of the earliest scratch tests and observed that a chip was produced even at a small depth of cut (lower than 0.5  $\mu\text{m}$ ) in the form of torn leaves from the workpiece surface although the rubbing and ploughing phases are also prominent in that range of depth cuts. Material removal was found mainly by the cutting process when the depth of cut is higher than 1  $\mu\text{m}$ . Komanduri (Komanduri, 1971) investigated the grinding mechanism by using a highly negative rake angled diamond tool and observed chip

formation up to a rake angle of  $-75^\circ$ . Shaw (Shaw, 1996) described the material removal process during single grit-workpiece interaction as an extrusion-like mechanism. Wang et al (Wang et al., 2001) performed single grit scratching test with a conical diamond tool on pure titanium to characterize the material removal mechanism. The scratches depth of the tests was around  $60\text{ }\mu\text{m}$  with a cutting speed of  $0.54\text{ m/s}$ . They observed that there exist four zones in the interaction region, namely, a stagnant zone, a lamella zone with shear bands, a hardened sublayer zone, and a propagating zone during front ridge development in scratching test.

In the literature, the effect of cutting speed was studied mainly using shaped abrasive grits in order to minimize the influence of grit shape alteration during scratching test (Patnaik Durgumahanti et al., 2010; Anderson et al., 2011; Anderson et al., 2011). The majority of the research show that lower cutting speed and depth of cut increase the proportion of ploughing and make cutting less efficient (Brinksmeler and Glwerzew, 2003; Park et al., 2007; Patnaik Durgumahanti et al., 2010). The influence of cutting speed may not be captured appropriately when the grit profile changes significantly due to grit wear and fracture on the cutting edges. Thus, in this research, the effect of cutting speed was not discussed due to significant alteration in the grit profile during scratching. Rather, this paper is mainly focused on morphological alteration in aspects of ploughing and cutting during scratching. Extended version of this paper will be available in reference (Öpöz and Chen, 2014).

## **2. EXPERIMENTAL SETUP AND METHODOLOGY**

Single grit scratching tests were conducted on a Nanoform 250 Ultragrind machine centre. In order to accommodate a single grit scratching test, a test setup was designed and manufactured as shown in Figure 1. The workpiece was mounted on a Kistler 3 axis piezoelectric force sensor. In addition, an acoustic emission (AE) sensor was mounted near the workpiece to detect the contact between the grit and the workpiece.

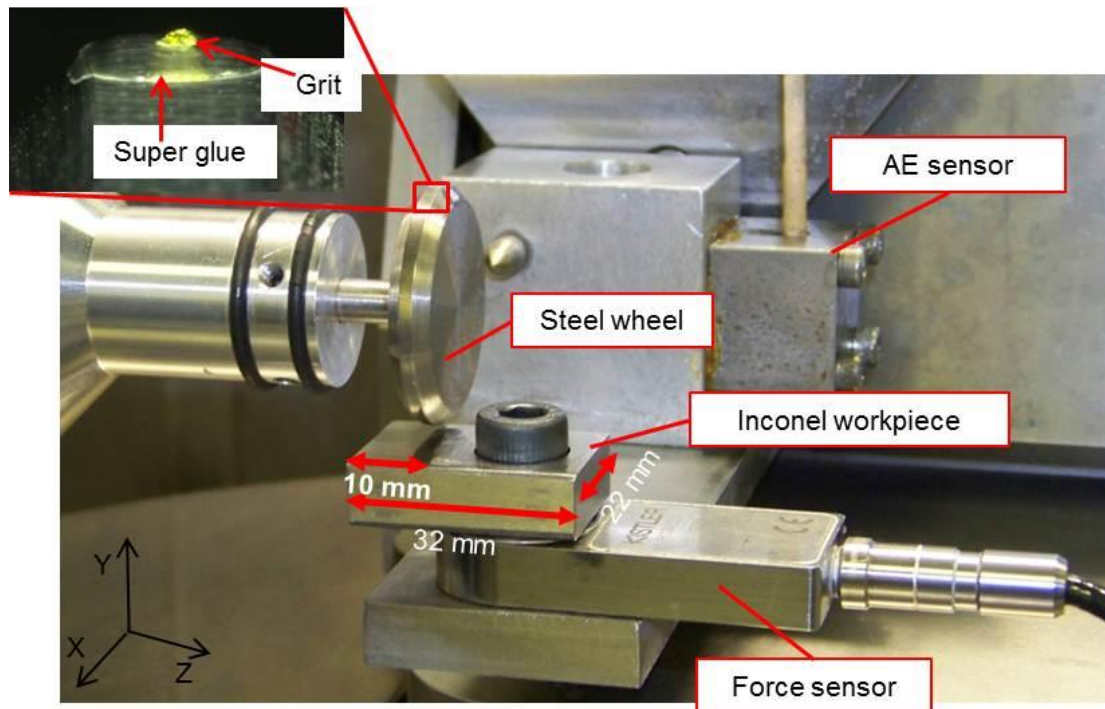


Figure 1. Single grit scratch test setup.

A Cubic Boron Nitride (CBN) grit of 40/50 mesh size was used for the scratching tests. Inconel 718 with a hardness of 355 HV at a 1 kg load was used as a workpiece. The workpiece surface was ground and polished prior to the scratching tests. The polished average surface roughness  $R_a$  was around  $0.04 \mu\text{m}$  throughout the scratching surface. The diameter of the steel wheel was measured as 34.8 mm after grinding the circumferential surface of the steel wheel by using a high speed spindle (rotational speed  $N = 20000 \text{ rpm}$  or peripheral speed  $V_c = 8.37 \text{ m/s}$ ). The steel wheel provided a run-out error less than  $1 \mu\text{m}$ . A CBN grit was glued onto the circumferential surface of the steel wheel by using Loctite super glue as shown in Figure 1. The same grit was used during the experiment as long as the grit stayed on the wheel surface. In case of the grit dropped off from the steel wheel, a new grit would be reinstalled to continue the experiment. Throughout the single grit grinding experiments, the same grit was used without experiencing the grit dropping off the steel wheel. A traverse scratching method was used to generate scratches at various depths of cut. Figure 2 shows the schematic of this traverse scratching method. More about description of the scratching process and the traverse scratching method were given in previous publications (Öpöz and Chen, 2012).



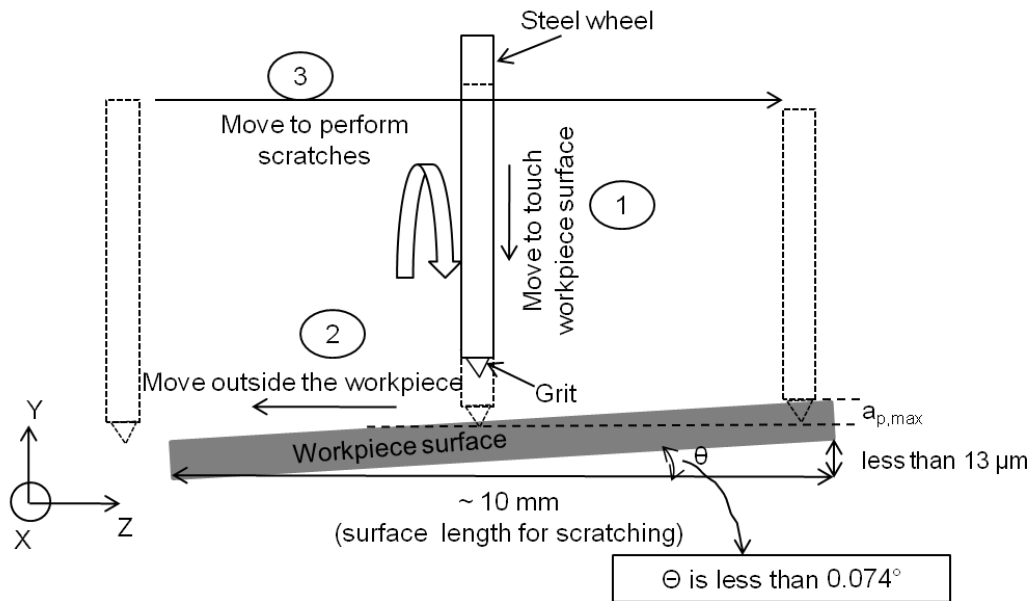


Figure 2. Scratching test methodology on a tilted surface ( $a_{p,max}$ : Maximum depth of cut).

A microscopic view of some single grit scratches on an Inconel workpiece with increasing depth of cut is shown in Figure 3. It can be seen that some scratches are less than 100  $\mu\text{m}$  in length and less than 1  $\mu\text{m}$  in groove depth. The scratch profiles of the samples were measured by using a Talysurf CCI 3000 white light interferometer. A sample of the resulting 3D profile measurement is shown in Figure 4, where the gouging features can be clearly seen. After 3D profiles of the scratches were obtained, 2D profile sections were extracted from the deepest point of the scratches to measure the groove depth, groove area, and pile-up area. Figure 5 shows the 2D profile of the scratches at the deepest point, from which the total pile-up and groove area sections will be used for analyses.

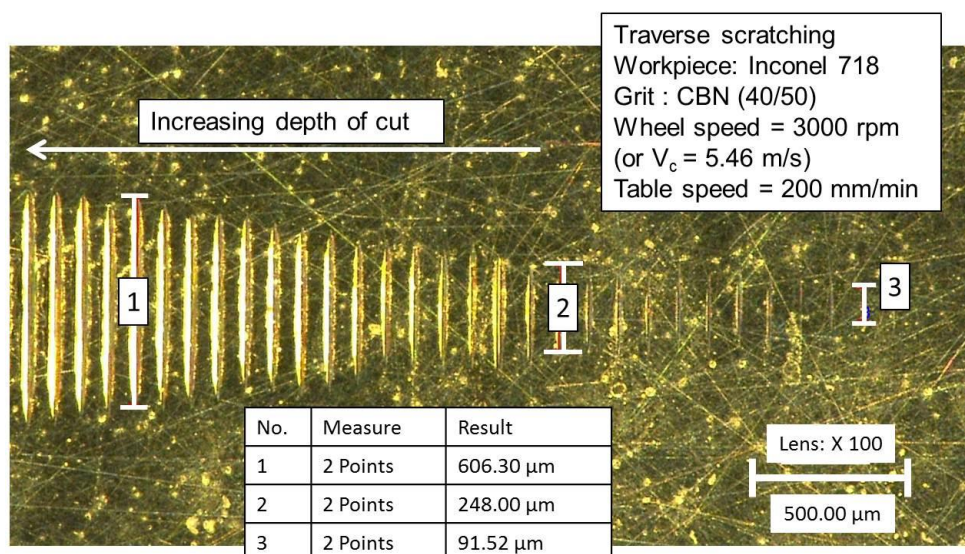


Figure 3. A view of scratches with increasing depths of cut.



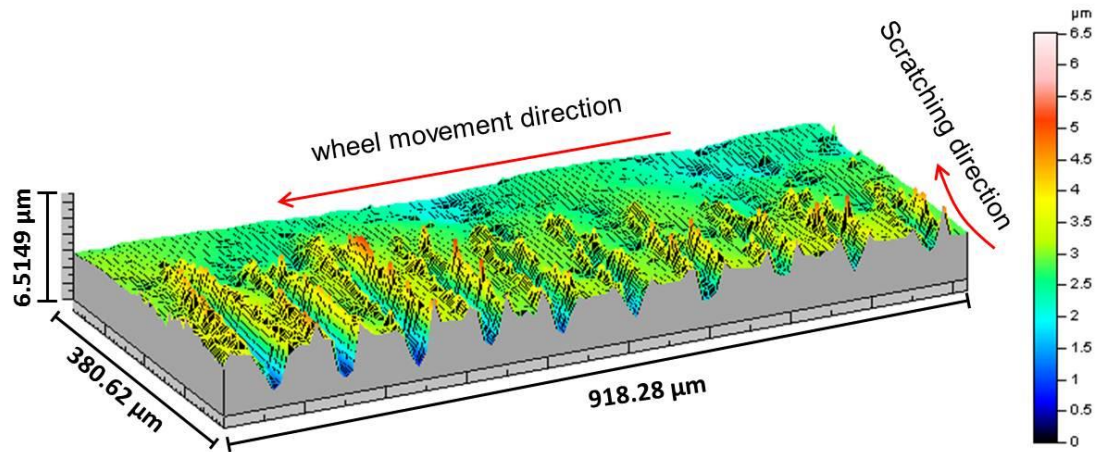


Figure 4. Example of 3D profile of scratches on the Inconel 718 workpiece.

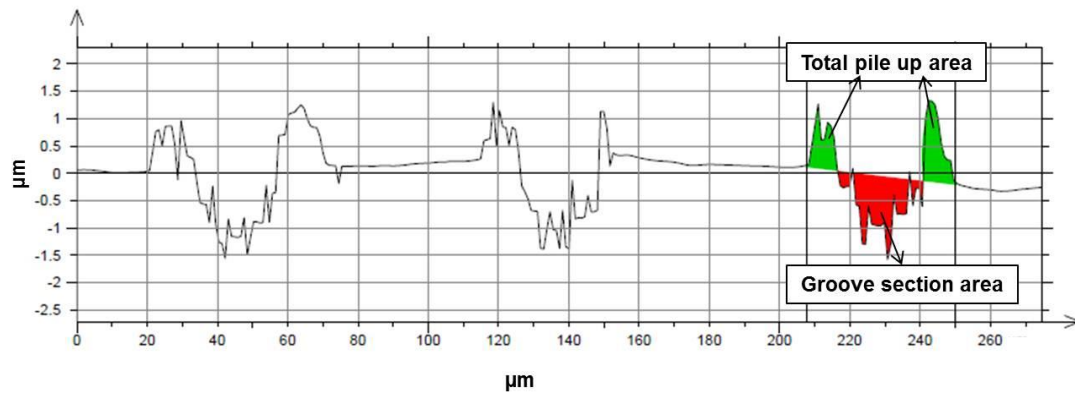


Figure 5. Scratch cross sectional profile, pile-up area and groove section area demonstration.

The profile of the scratches shows that the shape of the scratched grooves is altering at every consecutive scratch generation due to alteration of the cutting edge shape of the grit. With increasing numbers of scratch generation, the grit wear will present itself in the profile of the scratches. The alteration of the grit cutting edge occurs mainly due to wear flat generation and fracture of the grit. Ultimately, grit fracture leads to new cutting edges, which will maintain sharp cutting edges throughout the scratching. This phenomenon is also known as a self-sharpening during grinding process (Chen et al., 1998). In some circumstances, the grit fracture could be very influential in creating multiple grit edges which would therefore generate multiple edge scratches. The multiple edge scratches due to grit fracture sometimes will be either in the form of adjacent scratches (Öpöz and Chen, 2012) (Figure 6-a) or in the form of distinctly separated scratches (Figure 6-b). In the former one, the ploughed material at the adjacent side edge was squeezed together, which reinforced the

ploughing function and made the cutting mechanism less efficient by increasing the ploughing portion and decreasing cutting portion of the material removal during scratching. In the latter one, separate scratches due to separate cutting edges on the grit do not contribute to each other removal mechanisms due to the distance between them, thus, dissimilar to the former one where the adjacent cutting edges causes higher ploughing (or pile up) resulting in less actual material removal (i.e. less efficient in cutting); the efficiency of cutting mechanism is strongly dependent on the grit cutting edge shape and other factors (such as, grit cutting edge sharpness, bluntness, and depth of cut). Two scratches with different profiles were generated by two different cutting edges, assuming the actual grit cutting edge have similar profile which may present its shape into the scratch's cross section profile. The efficiency of the material removal in terms of the cutting and ploughing processes will be analysed through the paper by introducing a concept of pile up ratio.

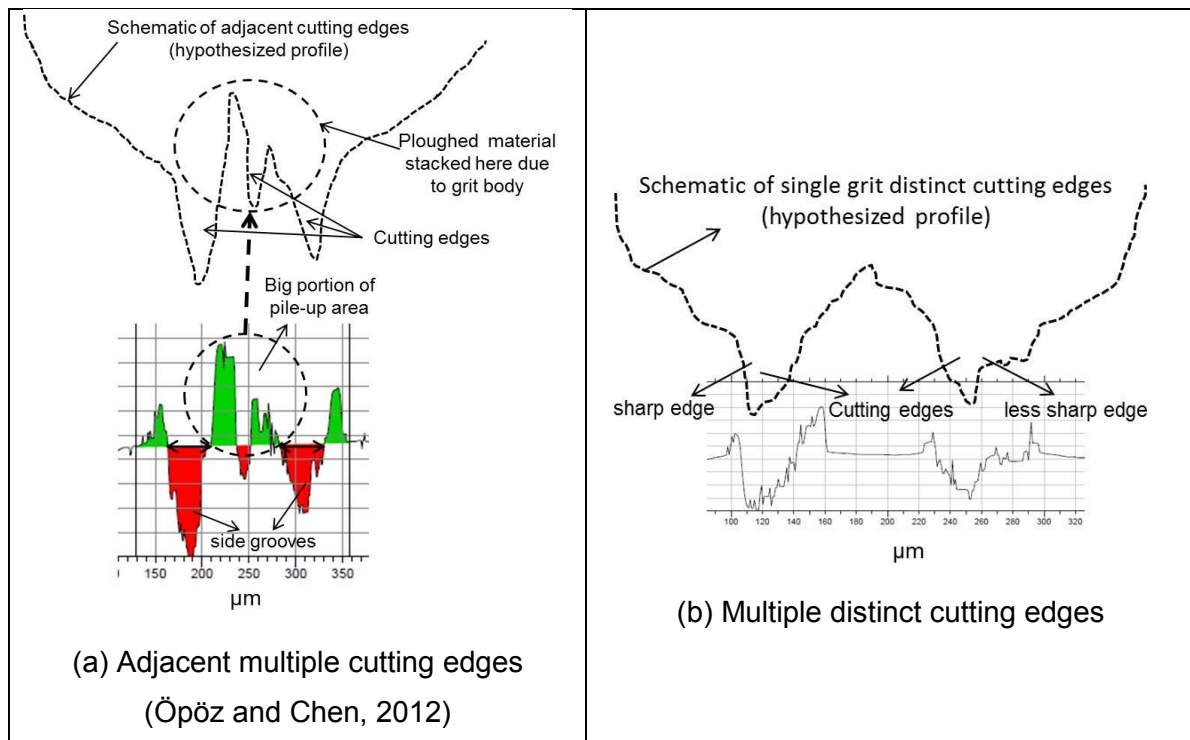


Figure 6. Schematic illustration of a multiple cutting edges

In the scope of this work, the investigation of material removal mechanism during single grit scratching on the Inconel workpiece takes account of the grit cutting edge shape alteration in the ploughing and cutting mechanism analysis. Prominent material removal mechanism is decided using a measure of pile up ratio, which is defined as the ratio of total pile up area to total groove section area in the cross section under the consideration. The pile up areas was calculated at the deepest point of scratches by using Mountains software (TalyMap universal

version 3.1.9), which is software built for the surface measurement on Talysurf CCI 3000 interferometer.

### 3. EXPERIMENTAL RESULTS

#### Material Removal at the Middle of Scratch Path

The relations between the pile-up ratio and the depth of cut at the middle of scratch paths was investigated by applying multiple scratches on Inconel 718 workpiece with various depth of cut ranged from around 0.5  $\mu\text{m}$  to 6  $\mu\text{m}$ . Figure 7 shows the pile-up ratio against depth of cut, where a steep decreasing trend of pile-up ratio with the increase of depth of cut presents when the depth of cut is less than 1.5  $\mu\text{m}$ . When the depth of cut is greater than about 1.5  $\mu\text{m}$ , the decreasing of pile-up ratio becomes less significant.

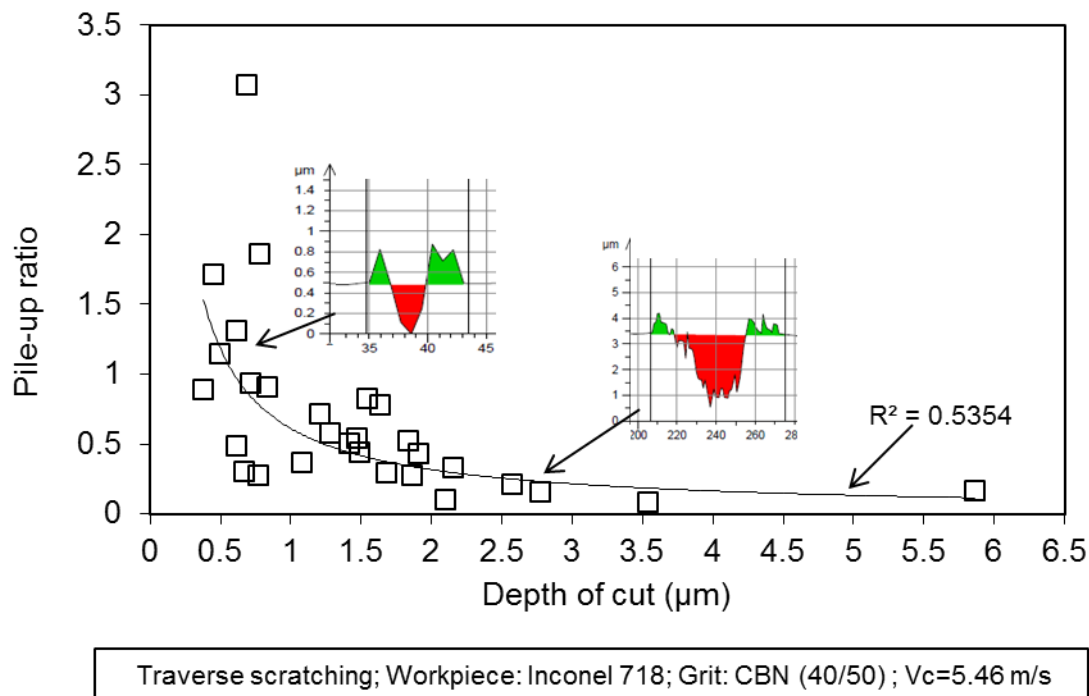


Figure 7. Pile-up ratio variation with depth of cut.

It should be pointed out that the pile-up ratio can have a value larger than unity when the depth of cut is very small (e.g.  $< 1$   $\mu\text{m}$ ) as shown in Figure 7, this can be attributed to ploughing action. It shows less efficient cutting actions at small depth of cut, where material ploughing is more prominent. At small depths of cut, materials were deformed plastically and pushed forward creating ridges in both sides of groove. Cutting might exist with a very small proportion compared to that exists at a higher depth of cut. When cutting action is not significant at small depths of cut, the pile-up ratio becomes larger than one. Hence, the larger pile-up ratio can be attributed to not only the smaller depth of cut makes cutting inefficient but

also the grit pushes materials forward leading to residual material accumulation at the different position along the scratch path.

Figure 8 shows the variation of pile-up ratio with depth of cut in a test with a grit that has two cutting edges interacting with the work sample and generates two distinct scratches having different profiles. The trend line looks generally similar to previous graph for the single edge grit, but the pile-up ratio looks to be highly scattered (lower coefficient of determination  $R^2$ ). Large variation in this test is due to the generation of two different scratches by two different cutting edge profiles. The cross section profiles of different scratches given in Figure 8 can be considered as the reflection of the two different cutting edges profile. In Figure 8, at a depth of cut of about 1.5  $\mu\text{m}$  it can be seen that the scratch profile above the trend line is sharper than the one below the trend line. Thus, scratches are clustered into two groups according to their cross section profile: scratches with sharp cutting edges and scratches with less sharp cutting edges. The former scratches are mainly placed above the trend line and have higher pile up ratio while the later scratches are mainly placed below the trend line and have less pile up ratio. However, some scratches generated with less sharp cutting edge are also placed at above the trend line and result in high pile up ratio (e.g. with pile up ratio of 1.5 at 1.05  $\mu\text{m}$  depth, see on Figure 8). That means pile up ratio variation with depth of cut represent highly scattered distribution when two different scratch profiles are created due to multiple cutting edges on a grit body.

Similarly, Figure 9 shows the variation of pile up ratio with depth of cut for a different test. The scratches in this test also present two different scratch profiles created by two different cutting edges. Two cutting edges interact with the workpiece at each pass of the grit. One of the cutting edges was sharper while the other was less sharp. As shown in the right side of Figure 9, the sharper cutting edge has a narrower width compared to the less sharp one. Thus, the sharper the grit cutting edge (narrower the width) gives higher pile-up ratio, while wider the cutting edges (less sharp) results in a lower pile-up ratio. This result is also consisting with previous graphs in Figure 8.

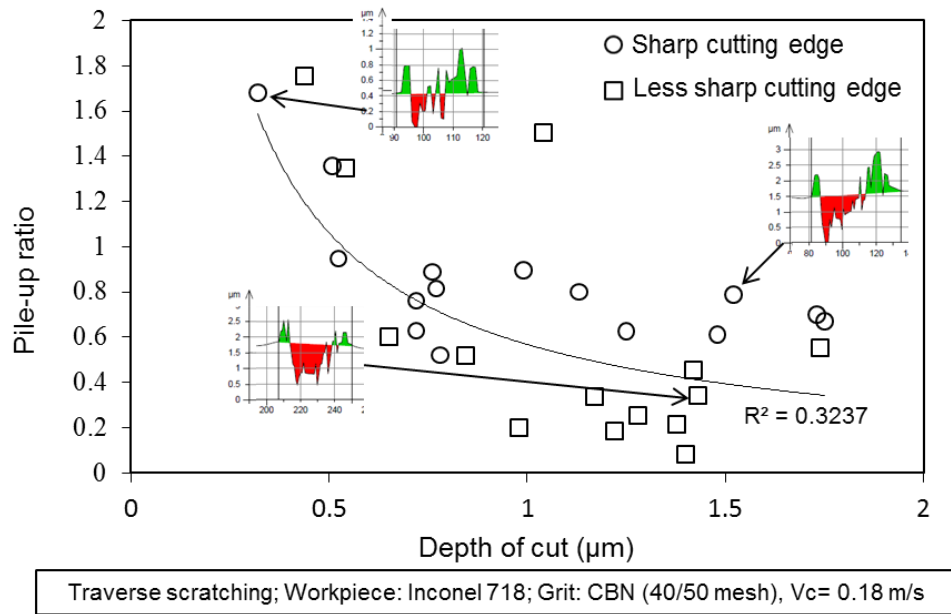


Figure 8. Pile-up ratio versus depth of cut (two scratches at every grit-workpiece interaction).

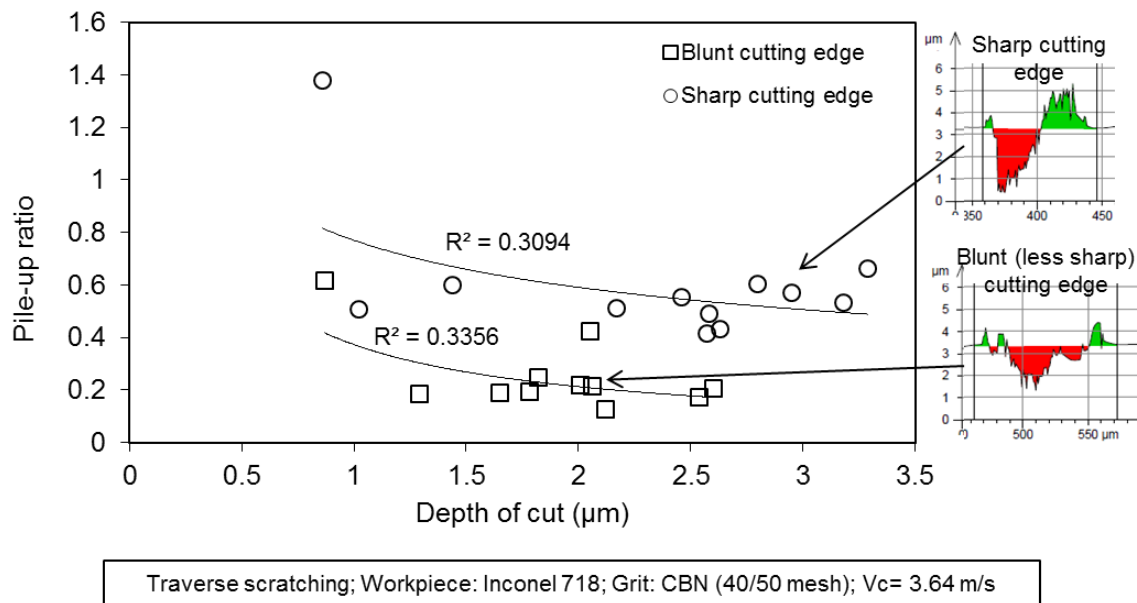


Figure 9. Pile-up ratio versus depth of cut (two scratches at every grit-workpiece interaction).

### Material Removal Mechanism along Scratch Path

In previous section, measurements were done in the deepest point of the scratches. Material removal mechanism along a scratch path cannot be represented by a cross section obtained only at deepest point of a scratch. So, the longitudinal and lateral cross-sections along the scratch path on Inconel 718, as shown in Figure 10, were also investigated to reveal the fundamental material removal characteristics along the scratch path. Figure 11 shows variation of pile-up ratio along the length of the scratch beginning from the initial grit-

workpiece interaction and continuing to the end of scratch. The pile-up ratio is relatively smaller in the first half of the scratch than that obtained in the second half of the scratch, as shown in Figure 11. At the initial stage of scratch in Figure 11, few spikes points for the pile up ratio represent material removal mechanism dominantly exist as a material swelling up without notable cutting because of very shallow cutting depth in that region. Once remarkable cutting action began, pile up ratio dropped down to around 0.5, after than it is continuously rising with fluctuating trend towards the end of scratch. The reason of increasing pile up ratio towards the end of scratch could be partly attributed to ploughed material accumulation in front of the grit while the grit moves toward the end of scratch. At the end of the scratch, very high pile up ratio ( $\sim 4$  to 5) were measured with almost no cutting action. Grit pushed forward material towards the end of the scratch and material accumulation become very high at the exit side of the scratch. In that region, scratched groove by the grit is above the workpiece surface level that means grit cut the accumulated material rather than work surface. Similarly, little material swelling up above the surface level at the entrance of the scratch was observed but this cannot be attributed to material accumulation at this stage, it seems the grit squeezed some material up around two side of it without cutting action when it started penetrating into the workpiece. Micro break and wear could take place on the grit cutting edges during single scratch generation and this will change the cutting edge geometry. Sudden change in cutting edge geometry resulted in uneven scratch depth profile. It can also be claimed that the cutting ability of the grit is better at the entrance side of the scratch than that at the exit side of the scratch.

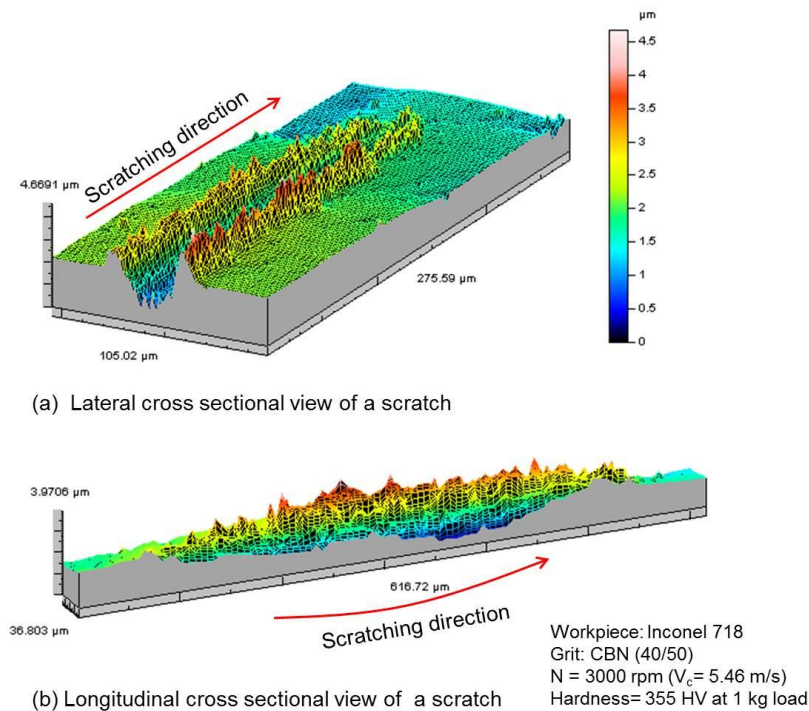


Figure 10. 3D view of single scratch (a) lateral cross-section, (b) longitudinal cross-section.



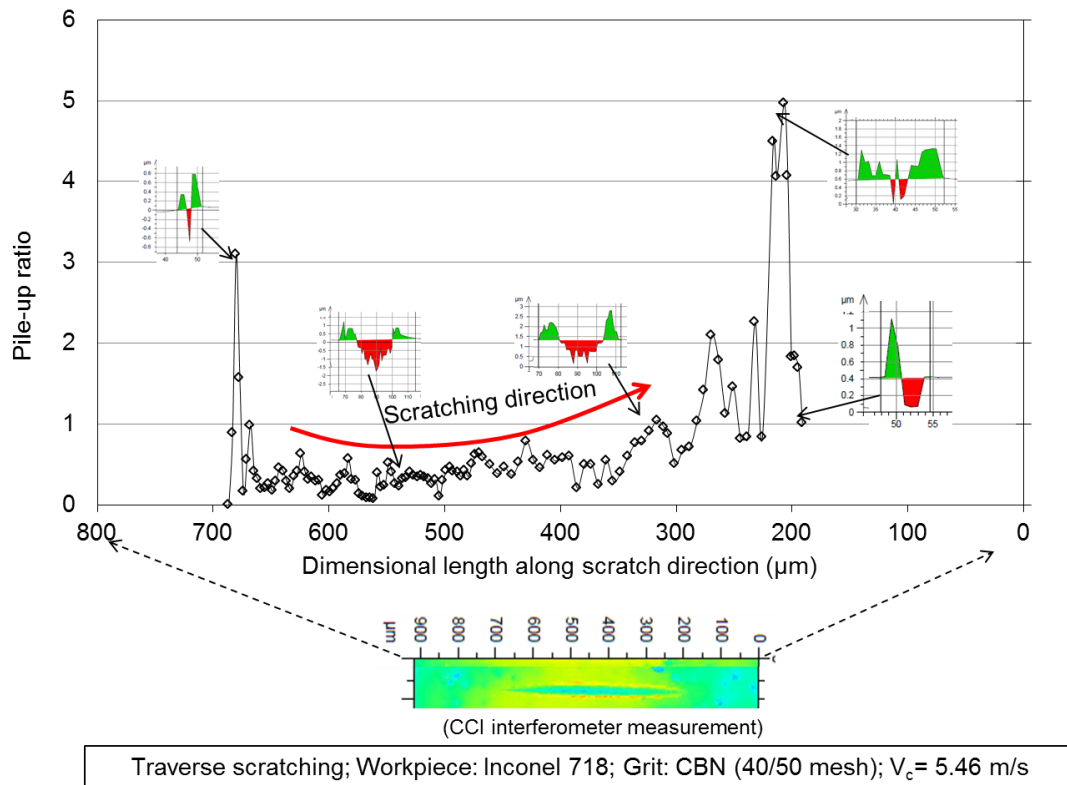


Figure 11. Variation of pile-up ratio along scratch path.

## SUMMARY

The cutting ability of a CBN grit on an Inconel 718 material sample was studied by utilizing single grit scratching tests. It was found that abrasive grit cutting edge profile changes during the scratching test are similar to that in the actual grinding process. Experiments showed that the shape alteration of cutting edges on the grit during scratching process is one of the most influential parameters to determine prominent material removal mechanism in terms of rubbing, ploughing and cutting. Pile up ratio was used as a measure to represent the material removal mechanism. Single cutting edge and multiple cutting edge scratches were generated, which demonstrated that different material removal mechanism can exist simultaneously due to the change of cutting edges presented on the abrasive grit. The pile up ratio decreases with increasing the depth of cut albeit it is highly dependent on the grit cutting edge shape. Sharp cutting edge resulted in higher pile up ratio compared to that found in less sharp cutting edge.

Material removal mechanism along the scratch length was also investigated. It was found that the cutting ability of the grit was better at the entrance side of the scratch than that at the exit side of the scratch. The accumulation of ploughed material increases towards the end of scratch in the second half the scratch. Thus, the pile up ratio was found dramatically higher



at the exit side of scratch compared to that found at the entrance side of the scratch. Knowing this behaviour of material removal with a single grit grinding will help people to understand grinding mechanism at micro scale.

## REFERENCES

1. **Anderson, D., Warkentin, A. and Bauer, R., (2011)**, "Experimental and numerical investigations of single abrasive-grain cutting." *International Journal of Machine Tools and Manufacture*, Vol.51, No. 12, pp. 898-910.
2. **Anderson, D., Warkentin, A. and Bauer, R., (2011)**, "Novel Experimental Method to Determine the Cutting Effectiveness of Grinding Grits." *Experimental mechanics*, Vol.51, No. 9, pp. 1535-1543.
3. **Barge, M., Kermouche, G., Gilles, P. and Bergheau, J. M., (2003)**, "Experimental and numerical study of the ploughing part of abrasive wear." *Wear*, Vol.255, No., pp. 30-37.
4. **Barge, M., Rech, J., Hamdi, H. and Bergheau, J. M., (2008)**, "Experimental study of abrasive process." *Wear*, Vol.264, No. 5-6, pp. 382-388.
5. **Brinksmeler, E. and Glwerzew, A., (2003)**, "Chip formation mechanisms in grinding at low speeds." *CIRP Annals-Manufacturing Technology*, Vol.52, No. 1, pp. 253-258.
6. **Chen, X., Rowe, W. B., Mills, B. and Allanson, D., (1998)**, "Analysis and simulation of the grinding process. Part IV: Effects of wheel wear." *International Journal of Machine Tools and Manufacture*, Vol.38, No. 1, pp. 41-49.
7. **Doman, D. A., Bauer, R. and Warkentin, A., (2009)**, "Experimentally validated finite element model of the rubbing and ploughing phases in scratch tests." *Proceedings of the Institution of Mechanical Engineers, Part B: Journal of Engineering Manufacture*, Vol.223, No. 12, pp. 1519-1527.
8. **Doman, D. A., Warkentin, A. and Bauer, R., (2009)**, "Finite element modeling approaches in grinding." *International Journal of Machine Tools and Manufacture*, Vol.49, No. 2, pp. 109-116.
9. **Doyle, E. D., (1973)**, "On the formation of a quick-stop chip during single grit grinding." *Wear*, Vol.24, No. 2, pp. 249-253.
10. **Ghosh, S., Chattopadhyay, A. B. and Paul, S., (2008)**, "Modelling of specific energy requirement during high-efficiency deep grinding." *International Journal of Machine Tools and Manufacture*, Vol.48, No. 11, pp. 1242-1253.
11. **Ghosh, S., Chattopadhyay, A. B. and Paul, S., (2010)**, "Study of grinding mechanics by single grit grinding test." *International Journal of Precision Technology*, Vol.1, No. 3, pp. 356-367.





12. **Gu, W., Yao, Z. and Liang, X., (2011)**, "Material removal of optical glass BK7 during single and double scratch tests." *Wear*, Vol.270, No. 3, pp. 241-246.
13. **Hahn, R. S. (1962)**, On the nature of the grinding process. Proceedings of the 3rd International Machine Tool Design & Research Conference, Manchester.
14. **Kannappan, S. and Malkin, S., (1972)**, "Effects of grain size and operating parameters on the mechanics of grinding." *Journal of Engineering for Industry - Transaction of the ASME*, Vol.94, No. 3, pp. 833-842.
15. **Kermouche, G., Rech, J., Hamdi, H. and Bergheau, J. M., (2010)**, "On the residual stress field induced by a scratching round abrasive grain." *Wear*, Vol.269, No. 1, pp. 86-92.
16. **Komanduri, R., (1971)**, "Some aspects of machining with negative rake tools simulating grinding." *International journal of machine tool design and research*, Vol.11, No. 3, pp. 223-233.
17. **Komanduri, R., Varghese, S. and Chandrasekaran, N., (2010)**, "On the mechanism of material removal at the nanoscale by cutting." *Wear*, Vol.269, No. 3, pp. 224-228.
18. **Liang, F., Qihong, C., Kun, S., Weiming, L., Xiaofeng, Z. and Zhifu, H., (2005)**, "FEM computation of groove ridge and Monte Carlo simulation in two-body abrasive wear." *Wear*, Vol.258, No. 1-4, pp. 265-274.
19. **Matsuo, T., Toyoura, S., Oshima, E. and Ohbuchi, Y., (1989)**, "Effect of grain shape on cutting force in superabrasive single-grit tests." *CIRP Annals-Manufacturing Technology*, Vol.38, No. 1, pp. 323-326.
20. **Öpöz, T. T. and Chen, X. (2011)**, Single Grit Grinding Simulation by Using Finite Element Analysis. In: *Advances in Materials and Processing Technologies Conference*, Paris (France), 24-27 October 2010. (Published in American Institute of Physics conference proceedings 1315, pp.1467–1472, 2011)
21. **Öpöz, T. T. and Chen, X., (2012)**, "Experimental investigation of material removal mechanism in single grit grinding." *International Journal of Machine Tools and Manufacture*, Vol.63, No. 1, pp. 32-40.
22. **Park, H. W., Liang, S. Y. and Chen, R., (2007)**, "Microgrinding force predictive modelling based on microscale single grain interaction analysis." *International Journal of Manufacturing Technology and Management*, Vol.12, No. 1, pp. 25-38.
23. **Patnaik Durgumahanti, U. S., Singh, V. and Venkateswara Rao, P., (2010)**, "A new model for grinding force prediction and analysis." *International Journal of Machine Tools and Manufacture*, Vol.50, No. 3, pp. 231-240.
24. **Shaw, M. C. (1996)**. Principles of abrasive processing, Clarendon Press Oxford.
25. **Subhash, G. and Zhang, W., (2002)**, "Investigation of the overall friction coefficient in single-pass scratch test." *Wear*, Vol.252, No. 1-2, pp. 123-134.



26. **Takenaka, N., (1966)**, "A study on the grinding action by single grit." Ann. CIRP, Vol.13, No. 1, pp. 183-190.
27. **Wang, H., Subhash, G. and Chandra, A., (2001)**, "Characteristics of single-grit rotating scratch with a conical tool on pure titanium." Wear, Vol.249, No. 7, pp. 566-581.
28. **Zhong, Z. W. and Venkatesh, V. C., (2009)**, "Recent developments in grinding of advanced materials." The International Journal of Advanced Manufacturing Technology, Vol.41, No. 5, pp. 468-480.
29. **Öpöz, T. T. and Chen, X., (2014)**, "Experimental study on single grit grinding of Inconel 718." Proc IMechE Part B: Journal of Engineering Manufacture (in print).





## A DECISION SUPPORT SYSTEM FOR SELECTION OF BIO-MATERIALS

**M. Alper SOFUOGLU**, *asofuoglu@ogu.edu.tr*, Eskisehir Osmangazi University, 26480 Eskisehir, Turkey

**Sezan ORAK**, *sorak@ogu.edu.tr*, Eskisehir Osmangazi University, 26480 Eskisehir, Turkey

### ABSTRACT

With the availability of more various materials, selecting the most suitable material is a challenging task. In this article, a bio-material selection decision support system, namely BIOSEL has been developed to help decision makers in their selection of bio-materials. It has been written in Visual Basic 6.0 program and tested with a literature example. The developed selection program eliminates unsuitable materials in two steps. In the first elimination step, the decision maker obtains the proper bio-materials by entering limit values of the bio-compatibility and cost requirements. BIOSEL, then, uses different decision making methods to rank the materials. The application of BIOSEL shows that it is useful and easy to use.

**Keywords:** Decision support system, bio-material selection, decision making methods

### 1. INTRODUCTION AND LITERATURE REVIEW

Materials are developing faster nowadays than in the past. The challenges have emerged and the opportunities have increased in materials industry. Because of the large amount of materials, a systematic procedure should exist for making a right choice for materials [1]. In recent years, there has been an increasing interest in selection of materials using different methods.

Bio-materials are used in the biomedical industry to replace or repair the parts of human bodies. A growing number of scientists and engineers are interested in fabrication and research of bio-materials. Bio-material engineering includes the development of new materials capable of interacting with biological systems. For bio-medical designs, it is possible to compare the properties of manufactured materials and biological tissues and fluids. Therefore, it should be decided which material is the best during biological repair/replacement. Also, interactions between the material and human body are an important issue [2].



A considerable amount of literature has been published on different material selection techniques. A number of studies have found that Decision Support Systems (DSS) and Multiple Criteria Decision Making (MCDM) methods are good ways to choose appropriate materials. There are a limited number of bio-material selection studies and most of the studies in selection of bio-materials have only been carried out in a small number of areas. A recent study by Jahan and Edwards [3] involved a MCDM model. In their study, the target criterion has been taken into account. Also, the strategy of dependent weightings has been used and an alternative method has been proposed to incorporate the correlation, objective, and subjective weightings to help inexperienced designers. This method has been validated using two biomedical applications, amalgam tooth filling and hip joint prosthesis material selection. It gives good results and it is applicable for the further studies. Enab and Bondok [4] have investigated total knee replacement (TKR) with aseptic loosening. MCDM approach has been developed to select the best material among the alternatives for femoral component of TKR. VIKOR method has been used to find the feasible materials. Porous and Ni-Ti shape memory alloys has been chosen as the appropriate materials. A longitudinal study of orthopedic materials by Guven [5] gives information about the mechanical properties and bio-compatibility of bio-materials. He has reviewed orthopedic materials and its properties. He has pointed out that bio-materials must satisfy their characteristics under different conditions. Patel and Gohil [6] have reviewed the types of bio-materials which are commonly used nowadays and their evaluation and selection for the human body. They have suggested that the bio-material compatibility to human body in the long term must be satisfied. Kumar and Mathew [7] have developed Finite Element Model (FEM) for various aortic valve stent designs to find the best design and bio-material under different conditions. Four stent models have been generated to compare the performances when subjected to the physiological pressures. Three bio-materials and different loads ranging from 10 665.8 N/m<sup>2</sup> to 26 664 N/m<sup>2</sup> have been used. Paez et al. [8] have described a selection procedure based on mechanical and morphological criteria for the calf pericardium used in the construction of cardiac valve leaflets. 180 pairs of tissue samples have been used. A decrease in tensile strength at rupture has been obtained for the sutured samples when compared with unsutured samples. Jadid [9] has focused on automating the material selection process using Web-based DSS. The system consists building material database and decision support components. Quantitative methods have been used and cost and environment effects have been taken into account for the construction process. Jahan and Bahraminasab [10] have studied the material selection for femoral component of total knee replacement via VIKOR method. A systematic procedure for sensitivity of weights has been proposed to select the

optimum material. Porous and Ni-Ti shape memory alloys have been chosen first and second respectively.

This study contributes to bio-material selection literature by developing a decision support system (DSS), namely BIOmaterial SElection (BIOSEL), to perform bio-material selection decisions for decision makers. In making the selection decisions, BIOSEL DSS will require physical and mechanical properties of materials as inputs and then eliminates and ranks for specific bio-material applications and determine the candidate materials.

## 2. DEVELOPMENT OF BIOSEL

As a first step in the development of BIOSEL, a flow chart has been created using a two-stage approach. The first stage aims to obtain the candidate materials and the last stage ranks the bio-materials and offers the most suitable material (Figure 1).

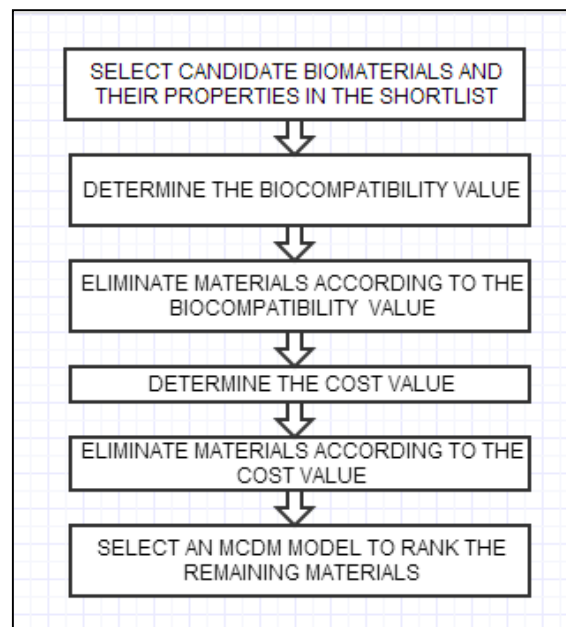


**Figure 1.** Flow chart of BIOSEL

In the first stage, materials have been eliminated according to bio-compatibility and cost criteria. Bio-materials should be bio-compatible and have low cost. Decision maker should decide bio-compatibility and cost limit values and enter these in the program. Therefore, a shortlist of candidate materials is determined. In the second stage, different decision-making models are developed. Decision makers can choose any of the model among different MCDM models and make comparisons between these models. Mechanical and physical properties of the materials are used while decision-making. Decision-making models used in the program are given in Table 1. The material property data is stored in Visual Basic 6.0



program. The data for material properties has been compiled from a bio-material handbook [11] and Cambridge Engineering Selector (CES) program.

**Table 1.** Decision-making models in BIOSEL

Models
AHP
Fuzzy AHP
ELECTRE-I
ELECTRE-III
PROMETHEE
WSA
MAPPAC
ORESTE
OBJECTIVE TREE
PUGH
DOMINIC

### 2.1. AHP Method (Analytic Hierarchy Process)

AHP was proposed by Saaty in 1977. The human behavior is taken into consideration and it is a subjective decision making procedure. It can be summarized below [12].

*Step 1:* Hierarchical system is defined and constructed.

*Step 2:* Relative weights for each alternative is determined.

*Step 3:* Performance scores are calculated for each alternative.

*Step 4:* The alternatives are ranked according to the performance scores.

### 2.2. Fuzzy AHP

Takahagi [13] has showed  $\lambda$  fuzzy measure and fuzzy integral method (Fig. 2).

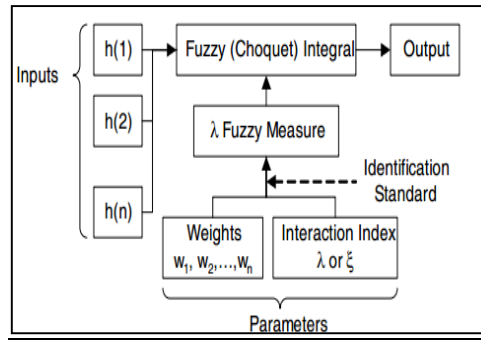


**Figure 2.**  $\lambda$  fuzzy measure and fuzzy integral [13]

The steps are given below.

*Step 1:* Make pair wise comparison.

*Step 2:* Choose interaction degree identification method.

*Step 3:* Choose fuzzy measure identification standard.

*Step 4:* Calculate Choquet Integrated values.

### 2.3. Pugh Method

Pugh method is a qualitative comparison to a reference alternative. The steps of the method are given below [14].

*Step 1:* Alternatives are listed in a matrix.

*Step 2:* One alternative is selected as a reference.

*Step 3:* The other alternatives are filled with better (+), worse (-) or the same (S) symbols in the matrix.

*Step 4:* The number of these symbols are summed.

### 2.4. Dominic Method

It is a quantitative method and includes criteria weighting factors. Alternatives are evaluated using excellent, good, fair, poor and unacceptable ratings. Criteria are rated as high priority, moderate, priority and low priority. The matrix is completed by ranking each criterion [14].





## **2.5. Objective Tree Method**

It is a quantitative method and uses weighted criteria. Criteria are weighted numerically and created as a hierarchy tree. Weights are multiplied and summed from above to below of the hierarchy tree [14].

## **2.6. MAPPAC Method (Multicriterion Analysis of Preferences by Means of Pairwise Actions and Criterion Comparisons)**

It was introduced by Matarazzo in 1986. It requires pair wise comparison of alternatives relative to each pair of criteria using two relations, preference and indifference. A variety of relations on feasible actions is obtained [15].

## **2.7. ORESTE Method (Organization, Rangement Et Synthese De Données Relationnelles)**

It was introduced by Roubens in 1982. The alternatives are ranked according to the criterion and the criteria are ranked according to their importance. It deals with the ranking of alternatives and criteria and uses ordinal data. The aim is to find a global preference structure on alternatives. It doesn't require detailed information compared to the other MCDM methods [15].

## **2.8. WSA Method (Weighting Sum Approach)**

It is a simple decision making method and uses weighted criteria. Weights are established for each criterion that gives influence of attributes. Total alternative scores are determined using the weights [16].

## **2.9. PROMETHEE Method (The Preference Ranking Organization Method for Enrichment of Evaluations)**

It is proposed as an outranking method by Brans in 1984. Preference functions and weights of criteria are used. PROMETHEE-I gives partial ranking of alternatives, while PROMETHEE-II gives complete ranking of alternatives. PROMETHEE-III is used to set up an interval order where the set of feasible solutions is finite, whereas PROMETHEE-IV is used for the case where the set of feasible solutions is continuous [12].

## 2.10 ELECTRE-I Method (Elimination and Choice Translating Reality English)

The model was developed by Roy in 1968. Concordance and discordance indexes are used. The indexes measure the strength of relation between objects [12].

## 2.11. ELECTRE-III Method

It was proposed by Roy in 1977. Solution steps are given in the Figure 3.  $q(g)$  and  $p(g)$  represent the indifference and preference threshold [12].

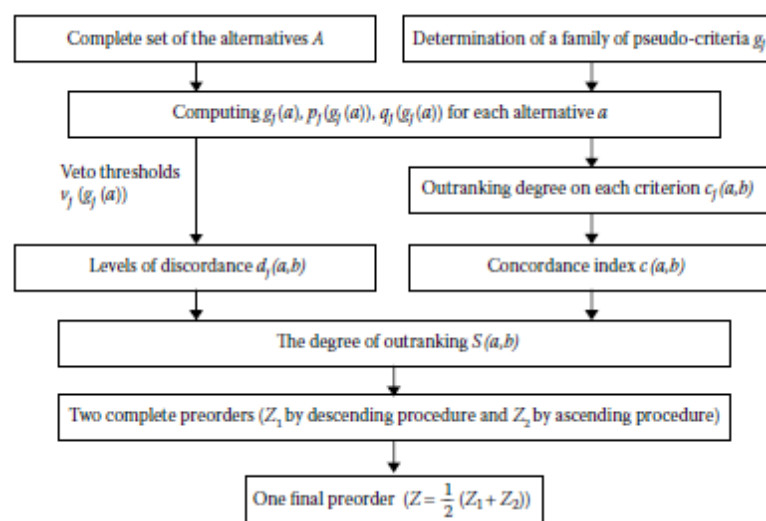


**Figure 3.** Solution steps of ELECTRE [12].

## 3. THE OPERATION OF BIOSEL

In the operation of BIOSEL, the window, in which the values from the handbook and program are entered, comes to the screen. On the window, there are toolboxes to select the bio-materials and its properties. Also, there are toolbars to enter the values for bio-compatibility and cost/unit volume. Bio-materials are classified into four categories: Metal and alloys, ceramics, polymeric and bio-composite materials. Metals are divided into four subgroups: Stainless steel, Co-Cr, Ti and alloys, dental metals. Properties are divided into five categories: Metal and alloys, bio-composite materials, polymer materials, ceramic material and others properties. First four properties are determined according to the materials categories. The others category includes cost and bio-compatibility criterions. Decision maker selects the suitable materials and their properties for the given application according to past studies, experience and applications. Materials and their properties are added to list boxes using command buttons. After determining materials and properties, limit values are

entered to the program for cost and bio-compatibility criteria. First, materials are eliminated according to bio-compatibility criteria. Then, cost criterion is used to find the suitable materials. The remaining materials are ranked using different MCDM methods. Criterion weights and limit values are determined according to experience and applications. The methods are shown using different command buttons. AHP, fuzzy AHP, ELECTRE, PROMETHEE, MAPPAC, WSA and ORESTE models are integrated with Microsoft Excel Documents (VBasic-MS Excel integration), whereas OBJECTIVE TREE, PUGH, DOMINIC models include the algorithm code in the program. As a result, final ranking results are obtained.

#### 4. CASE STUDY

BIOSEL DSS is successfully tested on the material selection of tooth filling. A literature study has presented below (Table-2).

**Table-2.** Tooth filling materials and their properties [16]

Properties/ Materials	Amalgam (Ag-Sn)	Ni-Cr alloys	Co-Cr alloys	Au-Pt alloys	Composite resin
Strength (MPa)	200 (10p)	500 (7p)	500 (7p)	400 (8p)	400 (8p)
Thermal strength (MPa)	200 (10p)	500 (7p)	500 (7p)	400 (8p)	200 (10p)
The ability to be shaped	10p	10p	8p	8p	8p
Corrosion resistance	10p	10p	10p	10p	10p
Bio-compatibility	10p	10p	10p	10p	7p
Cost/unit volume (Mg/m <sup>3</sup> )	800 (5p)	150 (9p)	300 (8p)	1200 (1p)	30 (10p)

The desired properties of material for tooth filling are given below [16].

1. Strength of materials is the ability to resist an external load without failure. The material shouldn't have low or high strength. The strength of material should be moderate.



2. The material shouldn't have low or high thermal strength. Thermal strength should be moderate.
3. The material should be easy to shape.
4. Corrosion resistance is the resistant of the materials to the destruction by different reactions with its environment. Corrosion resistance should be high.
5. Bio-compatibility is the ability of materials to perform suitable response in different situations. The material should be bio-compatible.
6. The material should be cheap

#### 4.1. First Stage

As shown in the figures below, the materials which have higher bio-compatibility value (Bio-compatibility > 8p) have been chosen. Composite resin has been eliminated. The remaining materials are Amalgam, Ni-Cr alloys, Co-Cr alloys and Au-Pt alloys (Fig. 4 and 5).

The screenshot shows the 'Form1' software interface. It has a top menu bar with 'Form1' and a window control button. Below the menu bar are several tabs: 'Metals and alloys', 'Ceramics', 'Polymeric biomaterials', 'Biocomposite materials', and 'Properties'. The 'Biocomposite materials' tab is selected, showing a dropdown menu with 'Composite resin'. The 'Properties' tab is also visible, showing dropdown menus for 'Metals and alloys' and 'Biocomposite materials'. On the left side, there are four dropdown menus labeled 'Stainless steel:', 'Co-Cr:', 'Ti and alloys:', and 'Dental metals:'. Below these is a 'CHOOSE MATERIAL' button. In the center, there is a list of materials: 'Ag-Sn', 'Ni-Cr', 'Co-Cr', 'Au-Pt', and 'Composite resin'. Below this list are 'REMOVE MATERIALS' and 'REMOVE PROPERTIES' buttons. On the right side, there are 'OPEN PROPERTY BOOK' and 'OPEN CES' buttons. A 'Project1' dialog box is open in the center, with the text 'Enter 1 1 criteria-alternative value' and a text input field containing '10'. The dialog box has 'OK' and 'Cancel' buttons.

**Figure 4.** The input window for bio-compatibility criterion



The screenshot shows the 'Form1' software interface. At the top, there are tabs for 'Metals and alloys', 'Ceramics', 'Polymeric biomaterials', and 'Biocomposite materials'. Below these are dropdown menus for 'Stainless steel', 'Co-Cr', 'Ti and alloys', and 'Dental metals'. A 'CHOOSE MATERIAL' button is present. In the center, there are lists for 'Materials' (Ag-Sn, Ni-Cr, Co-Cr, Au-Pt, Composite resin) and 'Properties' (Compressive strength, Thermal strength, The ability to be shaped, Corrosion resistance, Biocompatibility, Cost/unit volume). A 'REMOVE MATERIALS' button is located below the materials list. On the right, there are more dropdown menus for 'Metals and alloys', 'Biocomposite materials', 'Polymeric biomaterials', 'Ceramics', and 'Others' (Cost/unit volume). There are also buttons for 'OPEN PROPERTY BOOK' and 'OPEN CES'. At the bottom, there are sections for 'Criteria' (6), 'Alternatives' (5), '1-Bio-compatibility', '2-Cost', and '3-Decision making procedure'. A dialog box titled 'Project1' is open in the center, displaying the message '5. alternative has been eliminated' and a 'Tamam' button.

**Figure 5.** Elimination according to the bio-compatibility criteria

In Fig. 6, the materials which have lower cost/unit volume (cost/unit volume < 850 Mg/m<sup>3</sup>) have been selected. The remaining materials are Amalgam, Ni-Cr alloys and Co-Cr alloys.

The screenshot shows the 'Form1' software interface. At the top, there are tabs for 'Metals and alloys', 'Ceramics', 'Polymeric biomaterials', and 'Biocomposite materials'. Below these are dropdown menus for 'Stainless steel', 'Co-Cr', 'Ti and alloys', and 'Dental metals'. A 'CHOOSE MATERIAL' button is present. In the center, there are lists for 'Materials' (Ag-Sn, Ni-Cr, Co-Cr, Au-Pt, Composite resin) and 'Properties' (Compressive strength, Thermal strength, The ability to be shaped, Corrosion resistance, Biocompatibility, Cost/unit volume). A 'REMOVE MATERIALS' button is located below the materials list. On the right, there are more dropdown menus for 'Metals and alloys', 'Biocomposite materials', 'Polymeric biomaterials', 'Ceramics', and 'Others' (Cost/unit volume). There are also buttons for 'OPEN PROPERTY BOOK' and 'OPEN CES'. At the bottom, there are sections for 'Criteria' (6), 'Alternatives' (4), '1-Bio-compatibility', '2-Cost', and '3-Decision making procedure'. A dialog box titled 'Project1' is open in the center, displaying the message '4. alternative has been eliminated' and a 'Tamam' button.

**Figure 6.** Elimination according to the cost criteria

#### 4.2. Second step

WSA method has been selected (Figure 7 and 8) as an example model. Criterion weights are chosen equal from the literature [16]. Corrosion resistances are the same for the all materials and can be eliminated. The results show that amalgam material is more appropriate than the other materials. Ni-Cr and Co-Cr materials are good alternatives according to their points.



Figure 7. The input window for WSA method

Figure 8. The results window.

These results are consistent with Findik's study [16]. Findik [16] has found that amalgam is the most appropriate material. He has also found that Ni-Cr, Co-Cr and composite resins good alternatives. These results show that BIOSEL is compatible to make decisions in bio-material selection.

## 5. CONCLUSIONS

The bio-material selection problem requires extensive knowledge and experience with many different applications. It may be difficult to accumulate all the necessary information for a bio-



material selector. This article proposes a bio-material selection program (BIOSEL). BIOSEL identifies the feasible bio-materials and selects the one with the lowest cost per unit and bio-compatible. The applications provided the cost-effective and bio-compatible materials. It can be considered that BIOSEL is useful and it will help users to take right decisions in bio-material selection.

## NOMENCLATURE

**Mg** Milligram

**VIKOR** VlseKriterijumska Optimizacija I Kompromisno Resenje  
(Multicriteria Optimization and Compromise Solution)

## REFERENCES

1. **Ashby, Michael F. (2011)**, Materials Selection in Mechanical Design. 4th edition. Elsevier Ltd., 1-5. eBook.
2. **Chu, Paul K., and Xuanyong Liu (2008)**, Biomaterials Fabrication and Processing Handbook. USA: CRC Press (Taylor-Francis Group), 4-5. eBook.
3. **Jahan, A. & Edwards, K. L. (2013)**, "Weighting of dependent and target-based criteria for optimal decision-making in materials selection process: Biomedical applications." Materials & Design 49, 1000–1008.
4. **Enab, T. A. & Bondok, N. E. (2013)**, "Material selection in the design of the tibia tray component of cemented artificial knee using finite element method." Materials & Design 44, 454–460.
5. **Guven S.A. (2010)**, "Ortopedik malzemelerin biyouyumlulukları ve mekanik özelliklerine göre seçimi", 2nd National Design and Manufacturing Congress, Balıkesir, 472–484.
6. **Patel, N. R. & Gohil, P. P. (2012)**, "A Review on Biomaterials: Scope, Applications & Human Anatomy Significance.", International Journal of Emerging Technology and Advanced Engineering, 2, 91-101.
7. **Kumar, G. P. & Mathew, L. (2011)**, "Stent biomaterial and design selection using finite element analysis for percutaneous aortic valve replacement." Artificial organs 35, 166–775.



8. **Páez, J. M. G. et al. (2001)**, “Influence of the Selection of the Suture Material on the Mechanical Behavior of a Biomaterial to be Employed in the Construction of Implants. Part 1: Calf Pericardium.” *Journal of Biomaterials Applications* 16, 47–67.
9. **Jadid, M. N. (2013)**, “Development of a web-based decision support system.” *International Journal of Civil Engineering and Technology*, 4, 177–188.
10. **Bahraminasab, M. & Jahan, A. (2011)**, “Material selection for femoral component of total knee replacement using comprehensive VIKOR.” *Materials & Design* 32, 4471–4477.
11. **Black, J. & Hastings, G. (1998)**, *Handbook of Biomaterial Properties* 1st edition, Chapman&Hall, 135-363, eBook.
12. **Tzeng, G. and Huang, J. (2011)**, *Multi Attribute Decision Making: Methods and Applications*, CRC Press, USA, 15-29, 81-103.
13. **Takahagi, Eiichiro (2005)**, “ $\lambda$  Fuzzy Measure Identification Methods Using  $\lambda$  and Weights  $\lambda$  Fuzzy Measure.” 1, 1–5
14. ***Materials Selection and Design (1997)***, ASM Handbooks, USA, Vol.20, 667-680.
15. **Dincer S. (2011)**, “The Structural Analysis of Key Indicators of Turkish Manufacturing Industry: ORESTE and MAPPAC Applications”, *European Journal of Scientific Research* Vol.60, No 1, 6-18.
16. **Quinn, A. et al. (2007)**, “Classification for Accuracy and Insights: A weighted sum approach” *AusDM'07 Proceeding of sixth Australasian Conference on Data Mining*, 203-208.
17. **Findik, F. (2010)**, *Malzeme ve Tasarım Bilgisi*. 1st edition. Ankara: Seckin Publishing, 239-241







## EXTENDED MODELS FOR SUPPORTING CAPP-MES INTEGRATION IN DISCRETE PRODUCTION SYSTEMS

**Tibor TÓTH**, *toth@ait.iit.uni-miskolc.hu* University of Miskolc, 3515 Miskolc, Hungary

**Gyula KULCSÁR**, *iitkgy@uni-miskolc.hu* University of Miskolc, 3515 Miskolc, Hungary

**Ferenc ERDÉLYI**, *ef@ait.iit.uni-miskolc.hu* University of Miskolc, 3515 Miskolc, Hungary

**Mónika KULCSÁRNÉ FORRAI**, *aitkfm@uni-miskolc.hu* University of Miskolc, 3515 Miskolc, Hungary

**Péter BIKFALVI**, *bikfalvi@uni-miskolc.hu* University of Miskolc, 3515 Miskolc, Hungary

### ABSTRACT

Production Information Engineering faces big challenges in developing integrated computer support both for manufacturing control and for technology process planning. The two sets of software applications are located on different hierarchy levels of the enterprise functional model. In the field of discrete manufacturing, hierarchical structuring of engineering and management functions is the only utilizable “framework”. For integration purposes, only solving of term coherence problems is not enough, there is also a need for solving problems originating from the differences between the models used at the two levels. The paper shows the role of robust technological parameters concept as well as of the extended scheduling models in IT based integration and in realizing flexible and robust manufacturing control.

**Keywords:** Integration, Process Planning, Production Planning and Control, Detailed Scheduling, Manufacturing Execution System.

### 1. INTRODUCTION

In the field of discrete manufacturing, along with efficient and profitable production, the service level of customer's requirements is becoming of ever greater importance [Askin, 1993]. Flexible and agile manufacturing is a term applied to manufacturers that have production processes able to respond quickly to customers' needs and market changes. Agile manufacturers have to take also into consideration that the high-level of readiness for delivery is the most important part of measuring enterprise performance [Lee, 2001].



Today, the dynamic and structural complexity of manufacturing systems makes traditional production planning and control (PPC) activities increasingly difficult, and the methods and models used are often insufficient to face the dynamic changes of the global market. Moreover, the cumulative nature of production processes over time, the increasing intensity of production processes as well as the importance of customer demands and deadlines, emphasize the outstanding role of PPC, and also, the role of computer-integrated solutions.

Production planning typically runs according to the rolling time horizon principle. That is, a candidate plan is created for the actual time horizon and decisions of the first few time periods of this horizon are executed accordingly. Then, the candidate plan is revised and re-planned, if necessary. Revision/re-planning is due to the uncertainties and unpredicted events that may occur in the demand list and – often – in the production processes.

The control tasks of complex and complicated processes require hierarchical architecture and feedback control loops. Feedback control calls for the measuring of specific quantities (of physical processes) at the production execution level, and needs aggregated, cumulated or more generally derived indicators, called Key Performance Indicators (KPIs), to measure the abstract “performance” of production processes at different managerial levels.

Manufacturing Execution Systems (MES) are dedicated software applications that support manufacturing operations management functions. The main purpose of the MES is to create and execute a detailed and near-optimal schedule to meet the master production plan defined at the Enterprise Resource Planning (ERP) level.

Discrete manufacturing processes present a large variety of diverse and very distinct technologies that claim for specific models when designing their efficient control systems. In this respect, there is a particular demand for accurate modelling, formulation and solving of scheduling problems. However, most scheduling problems are complex and hard to solve.

Unfortunately, most of production models use only one performance measure [Choi, 2006], [Quadt, 2007], and only few models deal with multi-objective criteria that are more important in flexible and agile manufacturing [Loukil, 2005], [Shen, 2006]. Moreover, the existing models often disregard machine processing abilities, alternative process plans, robust operation plans, limited machine availability time frames, job travelling times, machine eligibility and other characteristics. That is, improvements and extensions of the scheduling models are required [Kulcsár, 2009], [Kulcsár, 2013], [Kulcsárné, 2013].

Computer aided process planning (CAPP), as an important activity between design (CAD) and manufacturing (CAM), is an essential component of a computer aided engineering (CAE) system. The goal of CAPP is to create and optimize the process and operation plans for the component parts and the final product to be manufactured and/or assembled economically.



This paper deals with two components of possible improvement of the CAPP-MES integration. The first considers the role of robust technology parameters in determining the actual most robust technology parameter alternatives, while the second deals with extended fine scheduling and rescheduling issues.

## **2. SHORT REVIEW ON INTEGRATION OF PROCESS PLANNING AND SCHEDULING**

Many researchers have addressed the need for integration of process planning and scheduling (IPPS) to facilitate flexibility and for improving production processes. Comprehensive reviews on the IPPS have been provided by [Tan, 2000] and [Li, 2010]. A detailed and remarkable state-of-the-art review on IPPS is presented in [Phanden, 2011]. Next, only some approaches are discussed with their relative advantages/disadvantages.

### **Non-linear approach**

In the non-linear approach (NLA), possible process plans (multiple, flexible, or alternative process plans) are created for each component part and each product before manufacturing or assembly on the shop floor. Generation of non-linear process plans (NLPPs) is based on the possibility of performing an operation on different machines, on the possibility of interchanging the sequence in which required production operations are performed, and on the possibility of producing the same object with different operations or sequence of operations. In general, the NLA approach uses a directed one-way information flow from process planning to production scheduling. For solving this problem, many researchers have developed and proposed different decision-making approaches. For example, a schedule improvement method [Sundaran, 1988], a negotiations and simulation-based method [Joo, 2001], a predictive (off-line) scheduling method [Rajkumar, 2010], a simulation-based genetic algorithm [Lee, 2001], a feature-based multiple-alternative process planning with scheduling verification [Usher, 1996], a genetic algorithm-based method [Choi, 2006], a simulated annealing based method [Leung, 2010], a multi-objective adaptive search procedure [Rajkumar, 2010], an alternative formulation and evolutionary based model [Li, 2012], an agent-based ant colony optimization algorithm [Leung, 2010], an active learning genetic algorithm [Li, 2012], a hybrid genetic algorithm [Naseri, 2012], and a constraint programming procedure [Zhang, 2012] can be found in the literature.

### **Closed-loop approach**

In the closed-loop approach (CLA), process planning attempts to take into account dynamic resource availability and shop floor status information. CLA is also referred to as real-time or dynamic process planning, because of the fact that process plans are created based on the dynamic feedback from the production scheduling or production control modules.

One of the CLA categories is the two-phased (or layered) integration architecture. Typically, static (off-line) planning and dynamic (on-line) planning phases are distinguished. The first phase generates alternative macro-level plans and predictive schedules. In the second phase, the system considers the changes in the production conditions (i.e. actual utilization and availability of resources), and modifies or regenerates alternative process plans and shop floor schedules [Mamalis, 1996], [Usher, 1996].

Different proposed architectures can also be found in the literature, which integrate the PPS functions by using feedback loops [Joo, 2001], [Yang, 2001]. The closed-loop solution includes production constraints and objective functions as the feedback from the on-line scheduling module to the off-line process planning module to facilitate planning or re-planning of existing solutions.

Agent-based and holonic approaches based on negotiations protocol have been also developed for IPPS [Wang, 2003], [Shen, 2006], [Zhao, 2007], [Shrestha, 2008].

### **Distributed approach**

Distributed approach (DA) reduces the complexity of the CLA by subdividing integrated process planning and production scheduling decisions into multiple decision phases. Process planning and scheduling tasks are often divided into two phases: preplanning and final planning. The preplanning phase analyzes the product types of the jobs to be executed. The product features and their relationships are recognized, the suitable production processes are determined and the required machine/workforce capabilities are estimated. The final planning phase assigns the operations to the available resources and defines the specific characteristics of the job execution. Interactions between process planning and scheduling take place in both phases. For example, in [Wang, 2003] two-level decision-making for supervisory planning and operation planning architecture is presented for an IPPS evolving reconfigurable manufacturing system.

There are also approaches in which the integrated process planning and scheduling tasks are separated into three levels or phases. Huang et al. [Huang, 1995] separates the integration problem into the following three phases: (1) preplanning, (2) pairing planning, and (3) final planning. The preplanning is a technical analysis of the product to identify requirements and constraints in its realization. This task is executed in an early stage, as soon as the product design is finished. Pairing planning matches the required job operations with the operation capabilities of the available production resources. This method is executed when, for example, a manufacturing order has been released. The final planning prepares the detailed manufacturing plans of the product for the selected equipment and it is realized just before the execution.

### 3. A NEW CONCEPT FOR INTEGRATING CAPP AND MES

Computer integration has already achieved considerable successes. However there are still a lot of unsolved problems in the integration of process-near PAC and MES functions. CAPP-MES integration proves to be efficient, because it increases the robustness of technology process planning and makes possible introduction of new approaches in optimization of operations. The realization of such integration reacts upon the algorithms and services of the functional components, and it sets new requirements, as for example: generating the alternatives of assembly components; generating prefabricated alternatives; creating alternative new routings; planning and applying flexible and robust operations; using multi-purpose machining centers and tool systems; dynamic generation of lot sizes in job planning; elaborating alternative schedules adapted to several goals at the same time; using adaptive re-scheduling functions; real-time decision-support based on process monitoring and KPIs.

Determination of the technology parameters for manufacturing operations is a multi-level and multi-objective optimization task, which can only be solved in a satisfactory manner by means of a “robust” approach. Traditionally, technology process planning focused mainly on planning of individual operations and their models were defined on the basis of the “operation cost” approach. However, at MES level, the technology parameters become the parameters of a new model (used for fine scheduling of the prevailing manufacturing system). At this level, the average amount of running jobs ( $\bar{N}$ ) is a function of the average rate of operations ( $\bar{q}_{i,j}$ ), the average utilization rate of machines ( $\bar{u}_j$ ), and the average flow time of jobs ( $\bar{T}_i$ ), where  $i$  and  $j$  are the running indices for operations and machines, respectively.

Based on the above considerations, the following relations can be written [Bikfalvi, 2013]:

$$\bar{N} = F(\bar{q}_{i,j}, \bar{u}_j, \bar{T}_i), \quad (1)$$

$$\bar{q}_{i,j} = \frac{m \cdot n}{\sum_{i=1}^n \sum_{j=1}^m \tau_{i,j}}, \quad (2)$$

where in equation (2)  $n$  is the number of jobs,  $m$  is the number of machines (workplaces),  $\tau_{i,j}$  is the technology operation time of job  $i$  on machine  $j$ .

The rate of operations (i.e. number of performed operations over a time unit) has a significant impact on product quality, on the waste product proportion and on the tool utilization. All these demand for knowledge of alternative sets of allowed and still efficient technology parameters in the multi-objective sense. Such a set of the technology parameters can rightly be named “robust” because their utilization is efficient both in creating of the Master Plan at the higher ERP/MRP level and in detailed scheduling at the lower MES level.

The followings describe a possible ERP-CAPP and CAPP-MES integration concept:

- The ERP-MRP planning level sends top-down rules and special data characterizing the “priority rates” of the prevailing orders to the technology process planning. To perform this action, the ERP-MRP level uses partly the Master Plan, partly the Data Center. The rules are related to the priority of operation planning objectives (Figure 1).
- Operation planning determines the domains of technology parameter values that belong to the manufacturing strategy, following from the rules. Based on these, alternative and parameterized operation plans can be elaborated, and NC programs can be generated.
- The alternative operation plans of CAPP (and/or CAD/CAM) will be updated by the detailed scheduling function of MES for the jobs created on the basis of the Master Plan. It assumes that the fine scheduling system is able to manage, by means of AI methods, the numerous allowed alternatives for job release, for lot sizes, for operations sequence, for machines and routings, as well as for the different combinations of technology parameter values. The monitoring function of MES observes the status of the jobs and resources by means of the real-time supervising of manufacturing processes and determines the actual values of the Key Performance Indices (KPIs). If required, the dispatcher makes real-time decisions to change the status of jobs and resources, as well as to re-schedule the processes. Re-scheduling considers the allowed (robust) alternatives of the main parameters of the operations, too.
- Suppliers, on the basis of aggregated and detailed production plans, and of daily call-downs, have to update their MRP-CAPP and MES systems database. Coherent planning makes possible the harmonic synchronization of supplying lead times, central component part manufacturing times, purchasing and final assembly activities in this manner.

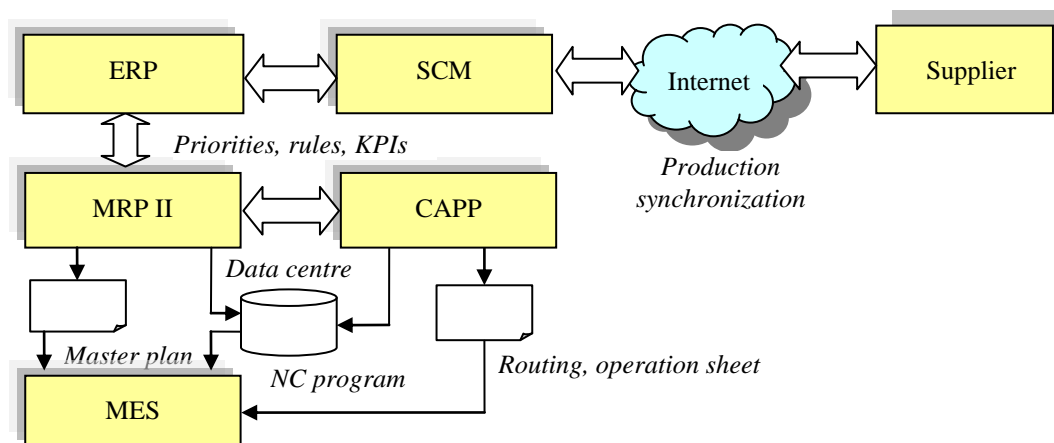


Figure 1. Integrated CAPP-MES functions in an extended CIM system

Integration of CAPP applications can support the advantageous realization of the complete functional activities outlined above. The service-oriented cooperation of applications can be provided by network-based application systems, safe data centers and servers.

In the field of discrete part manufacturing the robust technology parameter alternatives can be allocated to the following objectives and their combinations, respectively: Optimal technology parameter values in respect to the operation costs (minimizing); Optimal technology parameter values for assuring the imposed production rate level (maximizing); Data for optimal usage of tools (edges) and of auxiliary resources (constraints); Data for optimal energy usage (constraints); Data for high level quality assurance; etc.

As example, in case of cutting operations, the Material Removal Rate represents an important element, as a technological parameter to be optimized. It makes the work of the Master Plan planner, job originator, technology process planner, as well as the fine scheduler and of the manufacturing execution manager (dispatcher) more comprehensive and reliable.

When elaborating the Master Plan (at the ERP/MRP level) and in the course of making the detailed schedule (at MES level) different objective functions are used. At ERP/MRP level, the produced quantities (according to the product types), the aggregated production costs, the return of production assets (i.e. capacity utilization), and meeting of the market demands are the main goals. As regards the MES level, here the work in progress (WIP) level, the stable process and balanced loading of the resources with special focus on bottlenecks, and the readiness for delivery (i.e. the due dates) are important. For example, in the case of make-to-order (MTO), compliance with the due dates of the orders means continuous supervision of the so-called customer service level indices. The ERP system calculates the production costs not only through the summing up of the operation costs but on the basis of the utilization of resources and of other means, too. Hence, the models of planning technology processes, of creating Master Plans and manufacturing schedules are focusing on different performance criteria. One of the consequences is that the scheduler is firstly interested in the maximum of production rate ( $q_{i,j}^* = q_{i,j} \rightarrow \max$ ) allowed in creating the production schedules. This rate has to take into consideration the valid constraints, and has to be considered primarily for the workplaces in which bottlenecks form. However, in many cases there are operations  $o_{i,j}$  where the operation time  $\tau_{i,j}$  can be increased without a change in flow times  $\tau_i$  of some jobs. In these cases, the material removal rate  $Q$  can be decreased, which results in decreasing the tool wear and the risk of rejected products.

The tasks of PPS and that of technology process planning link to each other with a big number of threads. The relatively independent functional planning units and software applications can use these interconnections effectively in the case of an integrated system.



#### 4. EXTENDED SCHEDULING AND RESCHEDULING MODELS FOR SUPPORTING CAPP-MES INTEGRATION

A scheduling system with increased capabilities for supporting CAPP-MES integration has been recently developed. In this section of the paper, this integrated, advanced, simulation-based fine scheduling approach is summarized. The focus is set to the fine (detailed) scheduling function of the MES. The main purpose of the fine scheduler is to create a detailed and near-optimal schedule to meet the master plan defined at the ERP level.

The scheduler is able to get the actual data of dependent (internal) production orders, products, resource environment, process plans and additional constraints. The shop floor management configures the actual production goals and their priorities. The scheduler has to provide a feasible schedule meeting the managerial goals. The resulting fine schedule declares the releasing sequence and execution time data of the jobs and their operations, assigns all the necessary resources to them and proposes the starting time of activities. The computation time is also an important issue, especially when large number of internal orders, jobs, operations, resources, technological variants and constraints are considered.

A new Extended Flexible Job Shop (EFJS) model was defined in order to extend the set of jobs, operation execution characteristics and alternative technological process plans. From the operation execution point of view, in the flexible job shop (FJS) model, there are choices to be made in solving the scheduling problem from among alternative parallel machines on which an operation can be performed. In our new EFJS model, alternative technological process plans can be assigned to each job, where a particular process plan specifies the number and sequence of operations to be performed. The problem is NP-hard to solve.

In order to formulate the new EFJS class of scheduling problems, the well-known formal specification  $\alpha|\beta|\gamma$  is used, where  $\alpha$  denotes machine environment descriptors,  $\beta$  denotes processing characteristics and constraints, and  $\gamma$  denotes the list of objective functions. The EFJS scheduling model can be described as follows:

$$FJ, M_g, Q_{i,m}, Set_{i,j,m}, Cal_m / R_i, D_i, Exe_i, A_{i,g} / f_1, f_2, \dots, f_K, \quad (3)$$

where the symbols are as follows:  $FJ$  - flexible job shop environment,  $M_g$  - group of multi-purpose parallel machines, which can execute one or more operations in a given sequence,  $Q_{i,m}$  - unrelated parallel machines with job dependent production rates,  $Set_{i,j,m}$  - job sequence and machine dependent setup times,  $Cal_m$  - machine dependent availability time intervals,  $R_i$  - job dependent release time,  $D_i$  - job dependent due date,  $Exe_i$  - required type and sequence of technological steps for jobs,  $A_{i,g}$  - available set of suitable machines in groups for jobs,  $f_1, f_2, \dots, f_K$  - objective functions to be minimized (criteria of multi-objective optimization).

The numerical result of a specific objective function expresses the quality of the generated solution (fine schedule). In a real manufacturing environment, production management may require various objective functions. Therefore, our focus was directed towards general multi-objective scheduling approaches in order to obtain flexible and adaptive methods for supporting shop floor scheduling. Some examples of considered typical objective functions were:  $C_{max}$  - completion time of last job (makespan),  $T_{max}$  - maximum tardiness,  $\sum F_i$  - sum of throughput times,  $\sum T_i$  - sum of tardiness,  $\sum U_i$  - number of tardy jobs,  $\sum W_m$  - sum of machine blocking times,  $N_{WIP}$  - average number of work in process,  $N_{SET}$  - number of setups,  $\sum T_{SET}$  - sum of setup times to be minimized.

In general, production scheduling consists of batching, assigning, sequencing and timing. An integrated approach is proposed to solve all these sub-problems as a whole without decomposition (Figure 2). According to it, all the issues are answered simultaneously, because the integrated scheduling approach combines model building, decision making, simulation and evaluation processes.

In the presented approach, the job plays the role of the basic scheduling unit (containing one or more pieces with execution steps required). Each internal production order consists of jobs (individual units). In order to create the detailed schedule of each production order in the considered EFJS environment, it is necessary for each job:

- (1) to assign it to one of the suitable routes (technological process plans),
- (2) to assign it to one of the suitable machines at each possible machine group according to the chosen route,
- (3) to fix its position in the queue of each chosen machine,
- (4) and to pre-set its starting time on each chosen machine.

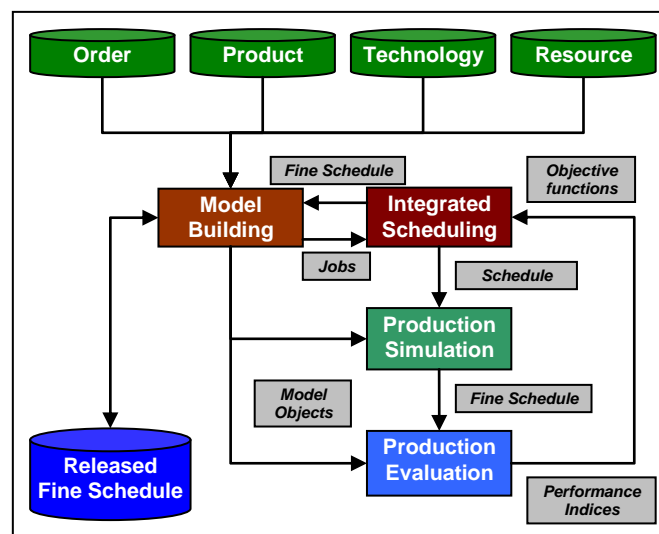


Figure 2. Integrated production scheduling

Taking decisions in the last step (4) is very complicated. The main idea of our approach is a problem space transformation and reduction based on simulation. We use the sequence of job-machine assignments on each machine to represent a candidate schedule as a solution. The decision variables of this reduced problem space form a simple schedule, which is extended to a fine schedule by using simulation. The fast, execution-driven simulation answers the remaining issue concerning the starting time data of the execution steps. Consequently, the simple schedule determines the fine schedule. The jobs move alone on the shop environment and have got owner time data. Sizes of production batches are formed dynamically by scheduling and executing the jobs on machines. Before scheduling, a builder method creates the full indexed data model, which includes the valid technological and resource constraints and possible alternatives.

The core of the scheduler engine uses a multi-objective and multi-operator searching algorithm. Our searching algorithm variant iteratively moves in the feasible solution space from an actual schedule  $s_0$  to a candidate schedule  $s$  in the neighborhood of  $s_0$  until the stop criterion is satisfied. To reach and to examine the unexplored regions of the search space, the method modifies the neighborhood structure of each schedule as the search progresses.

A taboo list containing the schedules that have been visited in the recent past is used to escape from a local optimum, since they are excluded when searching neighbors of the actual solution. The neighbors of the current schedule are generated randomly by modifying process plans, resource allocations, job sequences (decision variables) according to the problem space characteristics. The objective functions concerning candidate schedules are evaluated by simulation. Overloaded relational operator is used to compare the generated schedules according to multiple objective functions. The definition of the overloaded relational operator is described in [Kulcsár, 2007].

In practice, generating of a high quality predictive schedule according to multi-objective functions is usually not enough because many unexpected events require the revision and modification of the released schedule. Rescheduling is a process of updating an existing production schedule in response to disruptions or creating a new one if the current schedule has become infeasible. There are different unpredicted events that may occur: machine failure, missing/delay of materials, underestimated processing time, due date changes, etc.

In order to solve the manufacturing rescheduling problem, the predictive scheduling method was over developed and it was extended to new directions to meet additional demands. The aim of rescheduling is to find a feasible schedule which (1) considers the modified circumstances, (2) is near-optimal according to predefined criterion and (3) is as close as possible to the original schedule.

The last released schedule appears as a new input element of the rescheduling system. It is very important to preserve this initially released schedule as much as possible in order to maintain the system stability. For this purpose, new qualitative indices (e.g. related to process plans, machine changeover/setup time and job due date) are to be defined for supporting comparison of schedule changes. For example, such indices could be: 1) Number of jobs having modified execution route; 2) Number of jobs having at least one modified parallel machine; 3) Number of jobs having late status deviation; 4) Number of newly late jobs; 5) Number of production orders that have at least one job with modified execution route; 6) Number of production orders that have at least one job with at least one modified parallel machine; 7) Number of production orders having late status deviation; 8) Number of newly late production orders; 9) Number of machines with changeover or setup deviation; 10) Number of machines with new changeover or setup.

The listed measures focus on decreasing the distance of the candidate schedule from the original schedule. Such KPIs can be considered as extra objective functions of rescheduling and they can be used in multi-objective searching methods. The integrated scheduling model is able to cover the objective functions of performance and scheduling distance measures, too. Input parameters have been designed in order to support the decision maker in calibrating the actual priority for each objective function independently.

In order to satisfy additional demands, rescheduling has also to consider lots of special constraints. For example, some of these constraints are as follows: 1) All the jobs which are already finished when the rescheduling process starts are not changeable but can affect the other jobs and orders. 2) The manufacturing tasks of jobs running at the starting time of the rescheduling process must not be interrupted and their possible execution route and parallel machines (other alternatives) can differ from the original possibilities. 3) All the production orders starting after the rescheduling process can be considered in their original status.

To satisfy such comprehensive constraints freezing techniques can be used. The main classes of these techniques are as follows: (1) to freeze jobs, (2) to freeze production orders and (3) to freeze machines (or production line/group). Using these techniques the priority controlled neighboring operators of the searching algorithms can work effectively without violation of the rescheduling constraints.

Before starting the rescheduling process the model must be rebuilt in order to update the resource environment, job characteristics, constraints and objective functions with their priorities. The rescheduling problem can be solved effectively by applying multi-objective searching algorithms with the proposed extensions.



## 5. CONCLUSIONS

Integration of CAPP and MES in flexible manufacturing environments enables effective support of the up-to-date production paradigms. As the manufacturing companies have to continuously improve their product design, process plans, job creating, supply processes, quality assurance, manufacturing systems and indoor logistics, they must continuously increase their ability to respond quickly to customers' special requests. This important requirement depends on the ability to rapidly create or modify technological process plans and alternative operation plans. In addition, rapid adaptation to customers' needs calls for fast generation of production fine schedules according to the current load of the shop floor, the status of manufacturing, assembly and logistical resources and the availability of raw materials. In order to effectively support such capabilities, it is necessary to fill the gap between CAPP and MES through the development of integrated process planning and detailed scheduling. The proposed CAPP-MES integrated solution concepts are able to: (1) significantly improve the performance indicators (e.g. shorter lead times and minimized tardiness, increased resource utilization, etc.), (2) produce enhanced coordination between customers and suppliers, and (3) effectively help in handling changes and managing uncertainty and disturbances of manufacturing systems.

## ACKNOWLEDGMENTS

This research was partially carried out in the framework of the TÁMOP-4.1.1.C-12/1/KONV-2012-0002: "Cooperation between higher education, research institutes and automotive industry". The Project is supported by the Hungarian Government and co-financed by the European Social Fund.

## REFERENCES

1. **Askin R. G., Standridge C. R., (1993)**, "Modeling and Analysis of Manufacturing Systems", J. Wiley Inc., New York.
2. **Baker K., (1974)**, "Introduction to Sequencing and Scheduling", John Wiley & Sons, Canada.
3. **Bikfalvi P., Erdélyi F., Kulcsár Gy., Tóth T., Kulcsárné F. M., (2013)**, "On Some Functions of the MES Applications Supporting Production Operations Management", Topics in Intelligent Engineering and Informatics, Vol. 7, Applied Information Science, Engineering and Technology, Springer, pp. 103-129.



4. **Choi H., Park B., (2006)**, “Integration of process planning and job shop scheduling using genetic algorithm”, Proceedings of 6th WSEAS international conference on simulation, modelling and optimization, 22–24 September Lisbon, Portugal, pp. 13–18.
5. **Defersha F. M., Chen M., (2012)**, “A parallel genetic algorithm for a flexible job-shop scheduling problem with sequence dependent setups”, International Journal of Advanced Manufacturing Technology, 49 (1), pp. 263-279.
6. **Erdélyi F., Tóth T., Kulcsár Gy., Bikfalvi P., (2012)**, “Some new considerations for applying MES models to improve the effectiveness of production operations management in discrete manufacturing”, Proceedings of the 14th International Conference on Modern Information Technology in the Innovation Processes of the Industrial Enterprises - MITIP 2012, Budapest, Hungary, pp. 391-400.
7. **Huang S. H., Zhang H. C., Smith M. L., (1995)**, “A progressive approach for the integration of process planning and scheduling”, IEE Trans., 27 (4), pp. 456–464.
8. **Joo J., Park S., Cho H., (2001)**, “Adaptive and dynamic process planning using neural networks”, International Journal of Production Research, 39 (13), pp. 2923–2946.
9. **Kulcsár Gy., (2011)**, “A practice-oriented approach for solving production scheduling problems”, Proceedings of the XXV microCAD International Scientific Conference, Miskolc, Hungary, pp. 61-66.
10. **Kulcsár Gy., Bikfalvi P., Erdélyi F., Tóth, T., (2012)**, “A new simulation-based approach to production planning and control”, Proceedings of the 37th International MATADOR Conference, Manchester, GB, 25th – 27th July, 2012, pp. 251-254.
11. **Kulcsár Gy., Erdélyi F., (2007)**, “A new approach to solve multi-objective scheduling and rescheduling tasks”, International Journal of Computational Intelligence Research, 3 (4), pp. 343-351.
12. **Kulcsár Gy., Kulcsárné F. M., (2009)**, “Solving multi-objective production scheduling problems using a new approach”, Production Systems and Information Engineering, A Publication of the University of Miskolc, Vol. 5, pp. 81-94.
13. **Kulcsár Gy., Kulcsárné F. M., (2013)**, “Detailed production scheduling based on multi-objective search and simulation”, Production Systems and Information Engineering, A Publication of the University of Miskolc, Vol. 6, pp. 41-56.
14. **Kulcsárné F. M., Erdélyi F., Kulcsár Gy. (2013)**, “A new extended model for solving flexible job shop scheduling problems”, Proceeding of the International Conference on Innovative Technologies, IN-TECH 2013, Budapest, Hungary, 2013.09.10-2013.09.12. pp. 325-328.



15. **Lee H., Kim S., (2001)**, “Integration of process planning and scheduling using simulation based genetic algorithms”, *International Journal of Advanced Manufacturing Technology*, 18, 586–590.
16. **Leung C. W., Wong T. N., Mak K. L., Fung R. Y. K., (2010)**, “Integrated process planning and scheduling by an agent-based ant colony optimization”, *Computers and Industrial Engineering*, 59 (1), pp. 166–180.
17. **Li X., Gao L., Shao X., (2012)**, “An active learning genetic algorithm for integrated process planning and scheduling”, *Expert Systems with Applications*, 39 (8), pp. 6683–6691.
18. **Li X., Gao L., Shao X., Zhang C., Wang C., (2010)**, “Mathematical modeling and evolutionary algorithm-based approach for integrated process planning and scheduling”, *Computers and Operations Research*, 37 (4), pp. 656–667.
19. **Loukil T., Teghem J., Tuytens D., (2005)**, “Solving multi-objective production scheduling problems using metaheuristics”, *European Journal of Operational Research*, 161, pp. 42-61.
20. **Mamalis A. G., Malagardis I., Kanbouris K., (1996)**, “Online integration of process planning module with production scheduling”, *International Journal of Advanced Manufacturing Technology*, 12 (5), pp. 330–338.
21. **Naseri M. R. A., Afshari A. J., (2012)**, “A hybrid genetic algorithm for integrated process planning and scheduling problem with precedence constraints”, *The International Journal of Advanced Manufacturing Technology*, 59, 273–287.
22. **Phanden R. K., Jain A., Verma R., (2011)**, “Integration of process planning and scheduling: a state-of-the-art review”, *International Journal of Computer Integrated Manufacturing*, 24 (6), pp. 517–534.
23. **Quadt D., Kuhn H., (2007)**, “A taxonomy of flexible flow line scheduling procedures”, *European Journal of Operational Research*, Volume 178, pp. 686-698.
24. **Rajkumar M., Asokan P., Page T., Arunachalam S., (2010)**, “A GRASP algorithm for the integration of process planning and scheduling in a flexible job-shop”, *International Journal of Manufacturing Research*, 5 (2), pp. 230–251.
25. **Shen W., Wang L., Hao Q., (2006)**, “Agent-based distributed manufacturing process planning and scheduling: a state-of-the-art survey”, *IEEE Transactions on Systems, Man, and Cybernetics, Part C: Applications and Reviews*, 36 (4), pp. 563–577.
26. **Shrestha R., Takemoto T., Ichinose K., Sugimura N., (2008)**, “A study on integration of process planning and scheduling system for holonic manufacturing with modification of





process plans”, *International Journal of Manufacturing Technology and Management*, 14 (3–4), pp. 359–378.

27. **Sundaram R. M., Fu S. S., (1988)**, “Process planning and scheduling”, *Computer and Industrial Engineering*, Vol. 15, pp. 296–307.

28. **Tan W., Khoshnevis B., (2000)**, “Integration of process planning and scheduling - a review”, *Journal of Intelligent Manufacturing*, 11, pp. 51-63.

29. **Tóth T, Erdélyi F, Kulcsár Gy, (2008)**, “Decision supporting of production planning and control by means of key production performance measuring indicators”, *Proceedings of Seventh International Symposium on Tools and Methods of Competitive Engineering – TMCE 2008*, Imre Horváth (ed.), Vol. 2, Delft University of Technology, Delft, pp. 1201-1215.

30. **Usher J., Fernandes K., (1996)**, “Dynamic process planning – the static phase”, *Journal of Materials Processing Technology*, 61, pp. 53–58.

31. **Wang L. Shen W., (2003)**, “DPP: an agent-based approach for distributed process planning”, *Journal of Intelligent Manufacturing*, 14 (5), pp. 429–439.

32. **Wong T. N., Leung C. W., Mak K. L., Fung R. Y. K., (2006)**, “An agent-based negotiation approach to integrate process planning and scheduling”, *International Journal of Production Research*, 44 (7), pp. 1331–1351.

33. **Yang Y. N., Parsaei H. R., Leep H. R., (2001)**, “A prototype of a feature-based multiple-alternative process planning system with scheduling verification”, *Computers and Industrial Engineering*, 39, pp. 109–124.

34. **Zhang L., Wong T. N., (2012)**, “Solving integrated process planning and scheduling problem with constraint programming”, *Proceedings of the Asia Pacific Industrial Engineering & Management Systems Conference 2012*, pp. 1525-1532.

35. **Zhang Y., Saravanan A., Fuh J., (2003)**, “Integration of process planning and scheduling by exploring the flexibility of process planning”, *International Journal of Production Research*, 41 (3), pp. 611–628.

36. **Zhao F., Honga Y., Yua D., Yang Y., Zhanga Q., (2010)**, “A hybrid particle swarm optimisation algorithm and fuzzy logic for process planning and production scheduling integration in holonic manufacturing systems”, *International Journal of Computer Integrated Manufacturing*, 23 (1), pp. 20–39.







## CONCEPTUALIZATION OF A WEB-BASED SOFTWARE PLATFORM THAT ENABLES CLEANER PRODUCTION AND INDUSTRIAL SYMBIOSIS

**Tuna Çağlar GÜMÜŞ**, *tgumus@etu.edu.tr*, TOBB University of Economics and Technology, 06560, Ankara, Turkey

**Christoph HUGI**, *christoph.hugi@fhnw.ch*, University of Applied Sciences and Arts Northwestern Switzerland

**Dirk HENGVOSS**, *dirk.hengevoss@fhnw.ch*, University of Applied Sciences and Arts Northwestern Switzerland

**Sadık Engin KILIÇ**, *engin.kilic@atilim.edu.tr*, Atılım University, 06830, Ankara, Turkey

**Guillaume MASSARD**, *guillaume.massard@sofiesonline.com*, SOFIES SA, Switzerland

**Murat ÖZBAYOĞLU**, *mozbayoglu@etu.edu.tr*, TOBB University of Economics and Technology, 06560, Ankara, Turkey

**Hakkı Özgür ÜNVER**, *hounver@etu.edu.tr*, TOBB University of Economics and Technology, 06560, Ankara, Turkey

### ABSTRACT

In this project the concept of a web-based service platform for Resource Efficient and Cleaner Production, as well as Industrial Symbiosis (CPIS) measures for individual or for groups of factories is presented. The platform allows to link companies with specialized consultants and provides functionalities to conduct CPIS projects. It includes data collection, analyzing and managing of material and energy flows, knowledge transfer, identification of CPIS improvement potentials and determining best optimal environmental and financial solutions for improving the overall resource efficiency.

**Keywords:** Cleaner Production, Industrial Symbiosis, Service Oriented Architecture

### 1. INTRODUCTION

In the 27 European Union member states (EU-27) 2'570 million tons of wastes were generated in 2010. The European statistic database reports<sup>1</sup> 31 distinct waste streams which are generated in 18 economic sectors and households. By far the largest waste stream, amounting to 33.3%, is generated by the construction sector. Mining and quarrying generate 28.3%, the manufacturing industry 10.9% (280 million tons) and the households

---

<sup>1</sup> [http://epp.eurostat.ec.europa.eu/statistics\\_explained/index.php/Waste\\_statistics/de](http://epp.eurostat.ec.europa.eu/statistics_explained/index.php/Waste_statistics/de)



contribute with 8.6%. One reason for the enormous amount of industrial waste are today's concepts of industrial management which are mainly one-way along the classic value chain of products and services. This linear input and output thinking inside a company's boundaries is simpler to manage but often generates higher costs and inefficient solutions.

Input materials, e.g. raw and auxiliary materials, water and energy, are transformed into products and by-products, but also waste streams and emissions. The input in this concept is based largely on geogenic resources. As a consequence, the system demands large quantities of these primary, non-renewable resources and produces emissions and waste flows. Source and sink limitations became an urgent issue in the last decades due to such concepts that will ultimately run out of new geogenic resources. There is an overall understanding that resource consumption in production must be drastically reduced by a factor 5 to 10 until 2050 to keep our planet a worth living place.

## 2. BACKGROUND

Even if waste prevention initiatives such as the promotion of Cleaner Production (see box) and integrated technologies (e.g. Cleantech) contribute to the prevention and reduction of waste still large amounts are generated in manufacturing processes. Waste disposal does not belong to the core business of manufacturing companies. Therefore emissions and wastes will in general be costly treated with end of pipe technologies to the regulatory limits.

The general principles of waste management are embodied in the so-called waste management hierarchy [1]. Beside prevention, reuse of waste material has in general the lowest environmental impact but is still not very common compared to recycling, co-processing, incineration, or even land filling. But these latter waste management methods often are

**Cleaner Production (CP)** is defined as the continuous use of industrial processes and products to prevent the pollution of air, water and land, to reduce wastes at source, and to minimize risks to the human population and the environment. Cleaner Production focuses on improving the efficiency of production processes across individual enterprise: improving resource management, production processes, product design, substitution of raw materials (toxic and hazardous materials) and local reuse of by-products. Its goal is to improve the efficiency of production processes and "end-of-pipe" treatment of waste.

energy intensive and are sources of emissions, which must be controlled. Because of the limitation and finite availability of non-renewable resources, new concepts based on a closed loop paradigm which in most cases needs to go beyond companies' boundaries are needed to increase overall resource efficiency. Options must be identified to realize a better use of surplus heat and waste by considering the waste management hierarchy.

Incentives, management attention and capacity building are needed to optimize these flows outside the own factory's boundaries as in general improvement of resource efficiency.

Beside the economic and ecological assessment of the material and energy flows, the main challenge is to improve the communication and information exchange between factories, which have to be encouraged to succeed with such a systemic concepts. However, this also requires open and transparent communication between factories that supply and those that utilize the residues so that the quality of the outgoing waste material satisfies the requirements of the receiving companies.

**Industrial Ecology (IE)** is a broader field that studies “the flows of materials and energy in industrial and consumer activities, of the effects of these flows on the environment, and of the influences of economic, political, regulatory and social factors on the flow, use, and transformation of resources”. As one of the prominent subsets within IE, **Industrial Symbioses (IS)** seek to create new collaborations among economic players with the goal of exchanging information, raw materials, and waste directly among area businesses, and to step up the potential pooling of services and infrastructure among neighbouring companies.

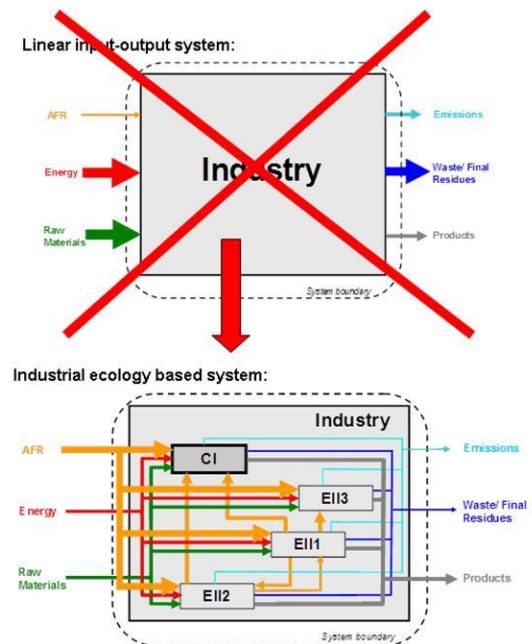


Figure 1. Linear input-output system<sup>2</sup> replaced by Industrial Ecology (Mutz, Hengevoss, & all)

The challenge is to ensure that these exports and imports are effectively co-ordinated between the different industrial sectors and involved companies. When this concept is implemented it can be expected that both the overall energy and material inputs required by an industrial region and the flows of emissions and final residues (waste) produced can be reduced significantly.

In some larger industries the concept of Industrial Ecology (IE) is known since the beginning of the 90' and was applied successfully, e.g. in the cement industry [2] or the chemical industry. The Kalundborg cluster in Denmark for example comprises of five core partners: a coal fired power station, a refinery, a plasterboard factory, an international biotechnological company and the city of Kalundborg which supplies district heating to about 20'000 residents. Over the last 20 years, these partners developed bilateral exchanges of waste materials which also include a number of other companies [3].

To address the demand of industry managers, there is a need to merge CP and Industrial Symbioses (IS) approaches (see box) and propose methodologies and tools that support

<sup>2</sup> EII: Energy intensive industry, CI: Cement industry, AFR: Alternative fuel and raw material



them in their efforts to globally optimize resource use and waste flows inside and outside of companies. By developing an assessment framework that evaluates these opportunities from a technical, legal, economic, and environmental standpoint, it is possible to determine which industrial symbioses are technically feasible and pertinent in a given context, and under what circumstances they would represent real added value compared to the current use of the resource and to existing systems for collecting and reusing waste streams.

A recent survey on eco-innovation parks has provided an overview of spatially located eco-innovation initiatives for selected European and Non-European countries [4]. The statistical analysis of eco-criteria appears as an efficient tool to foster a move from a linear industrial system to a closed-loop system mimicking biological ecosystems. The results show that the eco-criterion material flow is strongly linked with energy efficiency, water and waste management as industrial symbiosis encompasses these dimensions. There is a huge need to gain community and private sector support to foster this new paradigm of eco-innovation parks, such as Kalundborg in Denmark, Kwinana in Australia [5] or Kawasaki in Japan [6].

Closing waste streams of individual industrial processes will contribute to minimize both input and output of energy and material flows for manufacturing companies as main economic and resources consuming players. This will support closing further the resource cycle within the factories, an industrial park or a cluster of factories. To support this processes the development of software based facilitator platform has to consider inter-industrial communication/information needs and has to focus on the two primary principles of the waste hierarchy: waste avoidance and reuse of materials. With the inter-industrial assessment of economic and environmental benefits and a transparent communication the management of companies within an industrial park or a cluster shall be motivated to participate.

Several tools have already been developed around these topics [7] but none has link CP and IS to the authors' knowledge. Thus the present project aspires to develop a universal reproducible tool for decision support integrating the existing experience and methodologies of both CP and IS concepts into a single CPIS-tool, with the following five main goals:

1. **In-house CP:** Implement cleaner production within the factories through waste avoidance, minimization reuse and recycling, the identification of cleantech alternatives, energy efficiency measures etc.;
2. **Knowledge Transfer:** Exchange of information and experiences on good practices in the field of resource management and material flow;
3. **Supply-Demand-Match-Making-Network:** Creation of exchange networks of co-products (materials, water, energy) for reuse - recovery of waste by another company;

4. **Input-Output-Symbiosis:** Sharing certain services such as supply of raw materials and manufactured goods and waste collection;
5. **Infrastructure Symbiosis:** Sharing of infrastructure for the operation of certain renewable resources endogenous or centralized processing of certain flows, and the recovery of specific waste streams.

Within the frame of a LEAD ERA “Ecomanindustry” project founded by TUBITAK, Turkey and the Swiss Federal Office for the Environment (FOEN) a consortium consisting of FHNW University of Applied Sciences and Arts Northwestern Switzerland (project coordination), TOBB University of Economics and Technology (software development), ODAGEM A.S (Implementation), SOFIES SA (Implementation), UNIL University of Lausanne (Concept and user platform development) is currently developing the so called CPIS software platform.

### 3. CPIS Software Platform

A software based CPIS-platform to facilitate inter-industrial assessments and communication for waste avoidance and reuse of materials will be developed based on the Software as a Service (SaaS) principles (Figure 2) and Service-oriented architecture (SOA). The license free software aims at facilitating and providing decision support for the options mentioned above to improve the industrial sustainability of a cluster or region. Data from a Geo Information System (GIS) will be integrated as a module in order to optimize transportation aspects such as costs and environmental impacts.

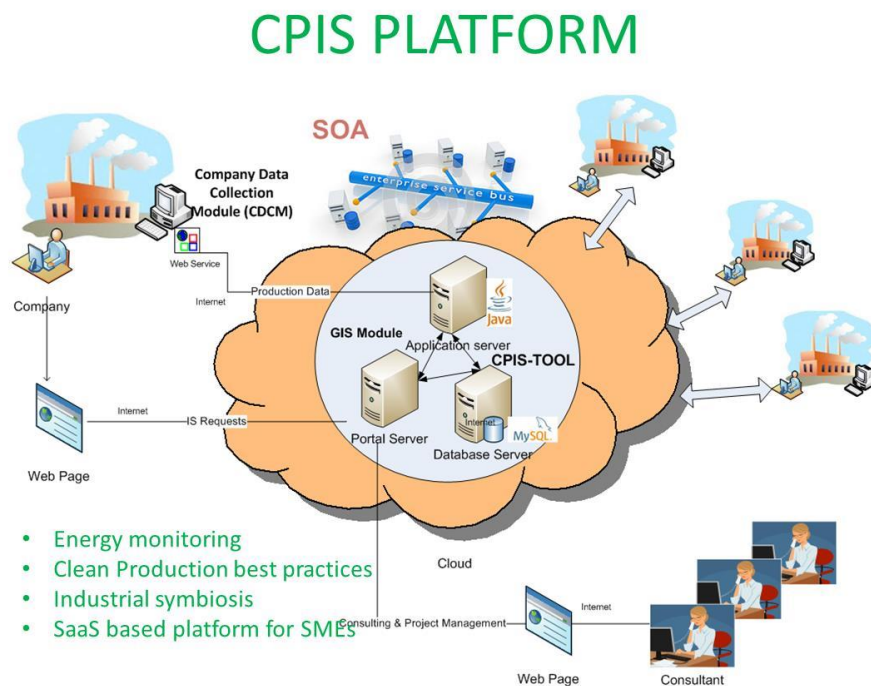


Figure 2. CPIS Software Platform



The software functionalities will allow the storage of the company location, the production activities, waste generation and energy consumption data that are collected from the companies and process this data for monitoring, visualization in order to support effective decision making by production managers, supervisors and meso-level decision supporters. In order to generate actionable key performance indicators (KPIs) for different industry sectors, the system will be designed flexible and easily configurable.

SOA involves a collection of standardized, self-contained services that are available throughout the enterprise or to external parties and that can be used individually or in a composed manner. With SOA, developers can model processes gain insight from these models, and use it to increase quality, agility, and resilience of the projects. SOA services can be available through platform-neutral interfaces and communication protocols [8].

Software as a Service (SaaS) is a cloud based delivery of software application that runs on a local area network, internet, or personal computer. SaaS now is used in different business tasks like computerized billing, human resource and document management, financial issues, collaboration, etc. Core characteristics of the SaaS model are:

- Ease of access to and manageable network based software
- Ease of access remotely to applications through the Web
- Providing software as an application from one central delivery system to multiple customers based on special pricing and management systems.
- Capable to be integrated to other networks or to be a plug-in to a platform as a service.

#### **4. CONCLUSION**

Merging Cleaner Production (CP) and Industrial Symbiosis (IS) should be understood as a holistic approach to support identification and implementation of the most ecological and economic sound resource efficiency measures within a factory's boundary or a cluster of factories. The SaaS and SOA based CPIS platform as multi-purpose vehicle to manage resource efficiency projects allow companies to transform their linear waste intensive input and output material flow management to a closed loop system with benefits for all involved parties. A first generic version of the platform is planned to be available for a pilot testing in Turkey and Switzerland by the end of this year.





## REFERENCES

1. **Kijak, R., & Moy, D. (2004).** A Decision Support Framework for Sustainable Waste Management. *Journal of Industrial Ecology*, 8(3): 33 - 50.
2. **Massard, G., Jacquat, O., Wagner, L., & Zürcher, D. (2012).** International survey on eco-innovation parks - Learning's from experiences on the spatial dimension of eco-innovation. *Bundesamt für Umwelt BAFU, Swiss Confederation*, 295 .
3. **Jacobsen, N. B. (2006).** Industrial Symbiosis in Kalundborg, Denmark: A Quantitative Assessment of Economic and Environmental Aspects. *Journal of Industrial Ecology*, 10(1 - 2): 239 - 255.
4. **Massard, G., Jacquat, O., Wagner, L., & Zürcher, D. (2012).** International survey on eco-innovation parks - Learning's from experiences on the spatial dimension of eco-innovation. *Bundesamt für Umwelt BAFU Swiss Confederation*, 295.
5. **van Beers, D., Corder, G., & al., e. (2007).** Industrial Symbiosis in the Australian Minerals Industry: The Cases of Kwinana and Gladstone. *Journal of Industrial Ecology*, 11(1): 55-72.
6. **van Berkel, R., Fujita, T., & al., e. (2009).** Quantitative Assessment of Urban and Industrial Symbiosis in Kawasaki, Japan. *Environmental Science & Technology*, 43(5): 1271-1281.
7. **Grant, G. S. (2010).** *Information and communication technology for industrial symbiosis.* Journal of Industrial Ecology.
8. **Dreibelbis, A., Hechler, E., Milman, I., Oberhofer, M., Run, P. v., & Wolfson, D. (2008).** *Enterprise Master Data Management, An SOA Approach to Managing Core Information.* Boston: IBM Press.







## **INVESTIGATION OF FREE-FORM SURFACE RECONSTRUCTION TECHNIQUES FOR REVERSE ENGINEERING OF WORN-OUT GAS TURBINE BLADES: A CASE STUDY**

**Özgür POYRAZ**, Ozgur.Poyraz@tei.com.tr, Tusaş Engine Industries, 26003, Eskişehir, Turkey

**Oğuzhan YILMAZ**, oyilmaz@gantep.edu.tr, University of Gaziantep, 27310, Gaziantep, Turkey

**Evren YASA**, evren.yasa@tei.com.tr, Tusaş Engine Industries, 26003, Eskişehir, Turkey

### **ABSTRACT**

Harsh working conditions of gas turbine blades lead to various types of unexpected failures which result in a worn-out or broken blade. Besides replacement by a new blade, the repair of worn-out blades may be preferred as a low-cost solution. The adaptive repair of worn-out blades needs reverse engineering of the actual blade shape since the nominal CAD model may not be available or it may not fit to actual one because of distortions. Besides, each damaged blade is considered as a unique geometry. At this point the point cloud of damaged blade is needed to obtain actual blade geometry and damage analysis. The point cloud of an airfoil can be quickly obtained by using an optical measurement system; such as structured light or laser. Different surface generation techniques have been developed and implemented to commercial software platforms which offer auto surfacing from point cloud, or from splines which are extracted section curves of point cloud. In the repair of turbine blades the worn-out or damaged surfaces must be reconstructed with minimum deviation in order to be effectively used in further repair stages, i.e. deposition and machining. This work presents a brief investigation of different free-form surface reconstruction techniques and an adaptive surface reconstruction method was developed for part-to-part variation. Virtual experiments were conducted on a high pressure compressor (HPC) blade data with commercial CAD software. The deviation of point cloud to generated surface in the original region and the deviation point cloud to extended surface in the worn-out area showed the method's accuracy for surface reconstruction.

**Keywords:** Adaptive blade repair, reverse engineering, optical measurement

## 1. INTRODUCTION

Gas turbine engines use different type of blades in compressor and turbine sections. All of these blades are subjected to high stresses and high vibration in their working environment due to centrifugal forces generated by rotational motion. In addition to these, HPC and high pressure turbine (HPT) blades are exposed to high pressure and high temperature gases because they are located close to combustion chamber. Foreign object damage (FOD) incidents like bird strike, runway debris, ingestion of rocks or volcanic ash are other factors make the working conditions worse for compressor blades. These working conditions cause different types of failures like fracture, yielding, creep, fatigue and corrosion which result into a worn-out or broken blade. Blade fractures in different regions of the blades are shown in Figure 1 [Poursaeidi et al., 2013].



Figure 1. Gas turbine blade fractures [Poursaeidi et al., 2013].

Repair of worn-out blades offers a low-cost solution instead of replacing them with the new ones. It has been estimated that about 70% of defective airfoils in the first stage and 97% of those in the fourth stage of a gas turbine are amenable to repair as opposed to being replaced [Antony and Goward, 1988]. Manual repair of the used gas turbine blades is not desirable since it requires higher labor times and skilled operators. Automated repair processes include consecutive steps like 3D measurement and digitizing of the used blade, build-up process for the worn-out or broken area and machining of the additional material around the blades [Qi et.al.(2010), Grossman et.al.(2012), Wu et.al. (2013)]. All these steps are interrelated to each other. For example, CNC machining operations and toolpaths depend on the actual blade shape which is obtained in the first step as a result of 3D



measurement and digitization. Most of the time, it is not possible to use original design data since the nominal CAD model may not be available or it may not fit to actual one because of distortions.

3D measurement of the blade is performed to obtain a point cloud indicating the coordinates of the blade exterior surface. The point cloud of an airfoil can be quickly obtained by an optical measurement system; using structured light or laser. The airfoil geometry can also be obtained with a coordinate measuring machine (CMM) as well, but optical measurement systems get higher number of points in shorter times than tactile probing systems. Digitizing of the blade geometry requires reverse engineering following the measurement. Due to the fact that some of the commercial computer aided manufacturing (CAM) software does not support toolpath generation on point clouds while others result with rough toolpaths which lead to poor machining quality on the blade surfaces.

Reverse engineering process includes reconstruction of surfaces from point clouds. Different surface generation techniques [Li et.al. (2010), Babu et.al. (2011)] have been developed and implemented to commercial software platforms which offer auto surfacing from point cloud, or from splines which are extracted section curves of point cloud. Reconstructed surface should ensure various features like minimum deviation and smoothness within original point cloud region, minimum deviation and smoothness around extended areas which has no point data due to wear or fixture contact on the blade. This work presents a brief investigation of different free-form surface reconstruction techniques and an adaptive surface reconstruction method was developed for part-to-part variation.

## **2. RELATED WORK**

Curve fitting and surface reconstruction methods are of great interest for engineering discipline in different functions like design, manufacturing, prototyping and repair. Specific studies on geometry reconstruction for the repair of gas turbine components are increasing in the last decade. A template-based optimal profile fitting method is developed to generate optimal profiles for robotic surface finishing of repairing turbine vane parts. Original design profile is used as a 2D template and it is carried to a position where its deviation to measurement points is at minimum. 3D airfoil surface is generated from all of the sectional profile curves which are fitted by the proposed method [Gong et al., 2000]. In the “Robust Profile Reconstruction Algorithm” method [Ng et al., 2004] a reference template is obtained from the new unused turbine blade to provide sectional information. Then the neutral line is obtained with the algorithm which is defined as the group of points on each layer at the equal distance from the profiles of the points on the convex and concave sides. The projection of the deformation on the used blade is taken with the analysis of two layers of sectional profile

comparing to unused one. As a result the used blade is re-constructed on the referenced data of unused blade. The strategy for the worn area modeling for automating the repair of turbine blades [Zheng et al., 2006] included four aspects: point-to-surface best fitting, worn boundary extraction, geometric model representation of the worn boundary and generation of the new STL file. Adaptive restoration of complex geometry parts through reverse engineering application [Gao et al., 2006] is proposed in the following research activities. A defects-free model and a worn part model are created and aligned together to determine maximum repair error. At last the repair profile and patch is extracted for the use of cladding and machining. Sectional Gauss Map concept is applied to generate a series of Prominent Cross Sections (PCS) along the longitudinal axis of a digitally acquired defective airfoil [Piya et al., 2011]. The model is firstly developed on a hyperboloid along its central axis as the sweep direction. Then the experimental set-up is tested on an airfoil. Surface error analysis on PCS with uniformly re-sampled points showed a deviation within the range of  $\pm 0.5\text{mm}$ . Surface error analysis for the other option on PCS without uniformly re-sampled points resulted to a deviation of  $\pm 0.2\text{mm}$ . Finally Yurong and Xu (2013) developed a deformable template based approach to recovering the surface of blade from the cross-sectional profiles. Proposed method can automatically transform and deform the template curve to best fit the cross-sectional points which come from the measurement data of the worn blade. According to these reconstructed sectional profiles, the actual blade surface is reconstructed by surface skinning operations.

Most of the research activity on surface reconstruction was carried out using template or reference shapes which come from original design data or new unused blade. One of consequences of using a template shape is that, the method cannot function if there is none. Other consequence is that, the fitting may not be possible for every blade shape due the complexity of fitting operation.

### **3. DESCRIPTION OF THE REPAIR SYSTEM**

In this study, a repair system is used for the repair of a worn-out stage 2 demonstrator compressor blade. The system includes a worn-out part and a part fixture, an optical measurement system (GOM ATOS II Triple Scan) and data pre-processing system (GOM Inspect), commercial CAD/CAM software (Siemens PLM / Unigraphics NX), reverse engineering methodology and a CNC laser cladding machine (HUFFMAN HC-245ACC).

#### **3.1. Geometrical Features of Gas Turbine Blades**

The principles of gas turbine blade geometry design play an important rule during surface reconstruction for repair process. A blade is a turbo machinery component which is designed to add work to or remove work from air. Its design, material and usage may vary according to

many constraints. For example, a HPT blade is desired to have a nickel based alloy with a thicker section for the geometry where a HPC blade may have a titanium based alloy with a thinner section for the geometry. However, simplification of the geometrical features of gas turbine blades helps for a clearer understanding during surface reconstruction. Figure 2 shows the common geometrical features of gas turbine blades and section profiles.

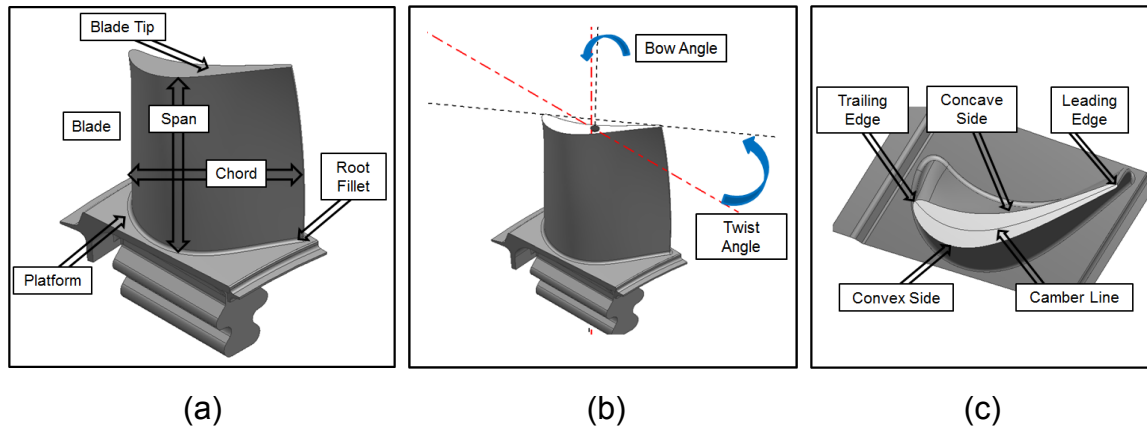


Figure 2. Blade geometrical features (a), blade angles (b), section profile geometrical features (c).

Common geometrical features of gas turbine blades can differ according to the engine section where the blade functions. For example, some blades have a curved profile along stacking axis while the others have a straight profile. It is possible to define straight blades with sectional profiles along one direction, but curved blades need to be defined with sectional profiles in more than one direction. This distinction becomes more important during surface reconstruction of worn-out blades. Figure 3 shows different type of blades, construction curves and the deviation between them.

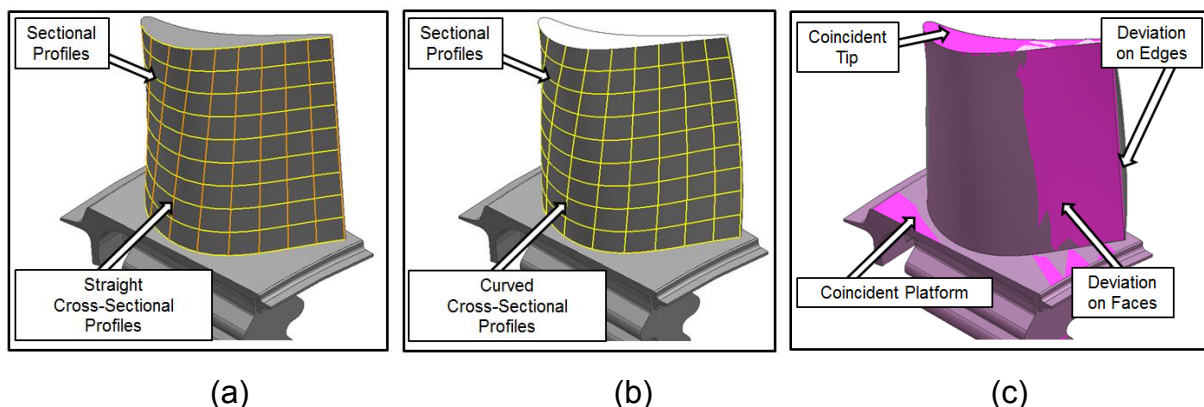


Figure 3. Straight blade with construction curves (a), curved blade with construction curves (b), deviation between straight and curved blades which use coincident platform and tip sections (c).



### 3.2. Overview of 3D Measurement Techniques

Coordinate measuring machines, special gauges and standard measurement devices are used for verification of geometrical & dimensional tolerances. On the other hand tactile probes are getting inadequate for the requirement of faster inspection or complex geometries [Voltan, 2010]. Nowadays optical measurement systems such as laser and structured light scanners are getting more important for industries due to reverse engineering studies and quick inspection times.

Structured light scanners use fringe projection method and have at least one projection unit and one Charged Coupled Device (CCD) camera. Different fringe patterns are projected on to the object surface and pictures are captured by camera(s) shown in Figure 4 [Luhmann et al., 2000]. After gathering all pictures, images are processed and stored via the computer. TWhite light is the first color for projection unit. Blue light and green light were later on developed due to the need to satisfy harsh working conditions and especially scanning ability of shiny surfaces. Yet, some studies prove there is not a significant difference for shiny or mat surfaces using between white or colored light [Yasa et al., 2013].

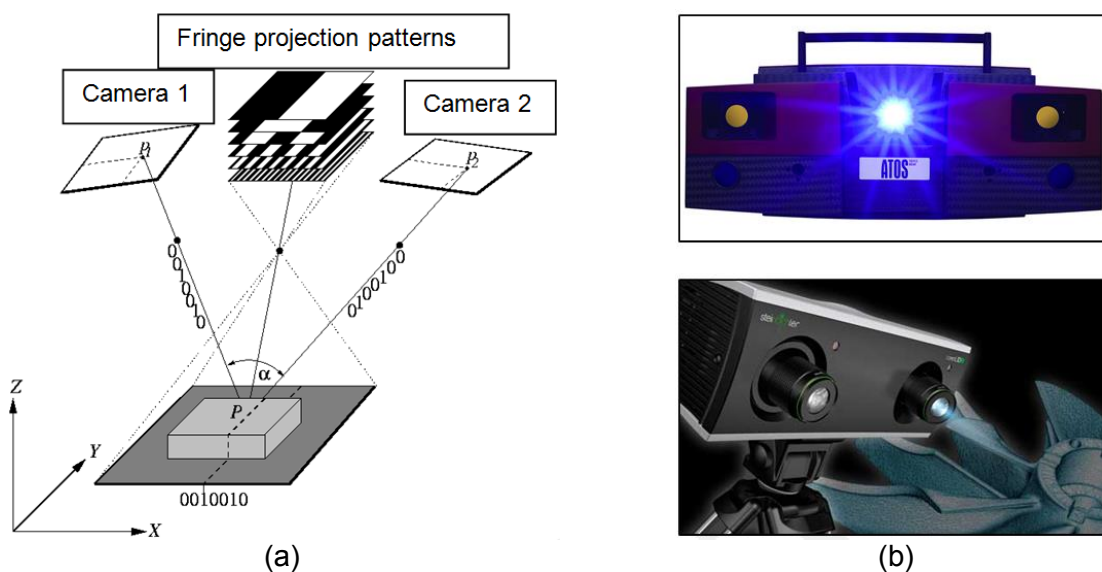


Figure 4. Basic working principle of structured light scanners (a), Sample structured light scanners (b)

Laser scanners use laser triangulation method and have one laser source and at least one CCD camera shown in Figure 5. Laser source reflects a laser line or laser point onto the object, reflection of laser dot(s) is exploited by camera. In consequence, the distance between the laser dot and camera are calculated and the location of the object is found. The name of the method called as laser triangulation comes from the triangle between the laser source, laser dot on the object and camera [Voltan, 2010]. There are various types of laser scanners depending on installation, for example; laser scanners which can be mounted on a

CMM like a probe and hand-held scanners. As expected, a CMM with a laser scanner is more accurate than the hand-held laser scanners. On the contrary, hand-held scanners provide mobility and flexibility. Thus, selection of scanner type depends on the application. Thus in this study an optical measurement system using structured light is preferred.

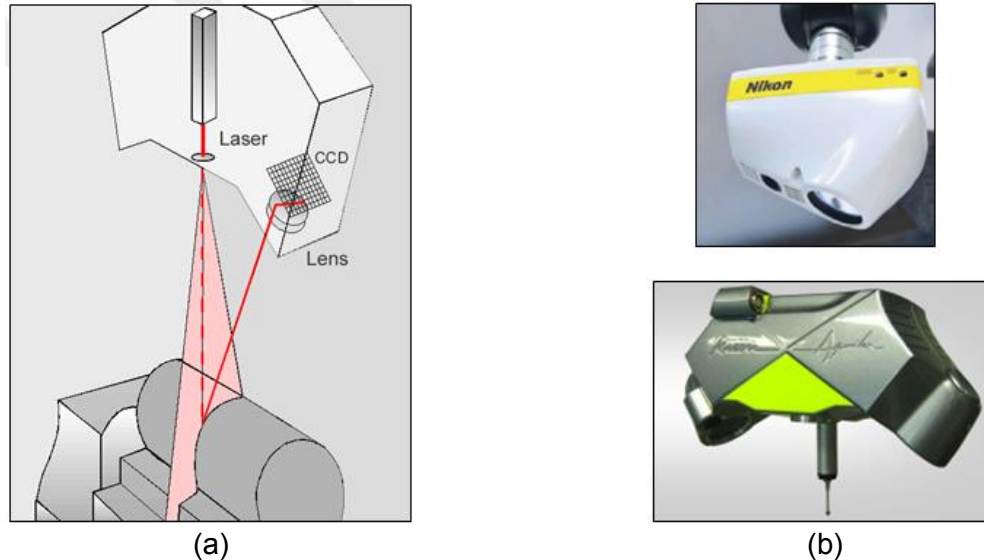


Figure 5. Laser triangulation method (a), Sample laser scanners (b).

### 3.3. Part Setup and Fixture Conditions

Good understanding of part setup and fixture conditions is essential. There are various part setup and fixture concepts used in the automated repair of gas turbine blades. Single part and fixture setup is used in consecutive steps like measurement, cladding and machining. This gives the advantage of a precise changeover between different steps of the repair process by using planar and/or cylindrical fixture faces as reference for measurement, cladding and machining. Apart from this, the position changes and misalignment of the blade inside the fixture is another risk. In addition to these, milling of thin walls has the possibility of lateral vibration of them in some cutting conditions and at some stages of machining [Bravo et al., 2005]. Different fixture designs are developed because of all these reasons. Specially designed pin fixtures maintain the blade position precisely and are adjustable to different surface shape and can thus be used for clamping different blades adaptively [Gao et al., 2008]. Figure 6 shows two types of fixture concepts applied on the sample blade. On the other hand, new technological developments allow repair techniques to use adaptive machine vision systems to adapt the cladding/welding procedure according to the part's actual geometry [Yilmaz et.al. 2010].



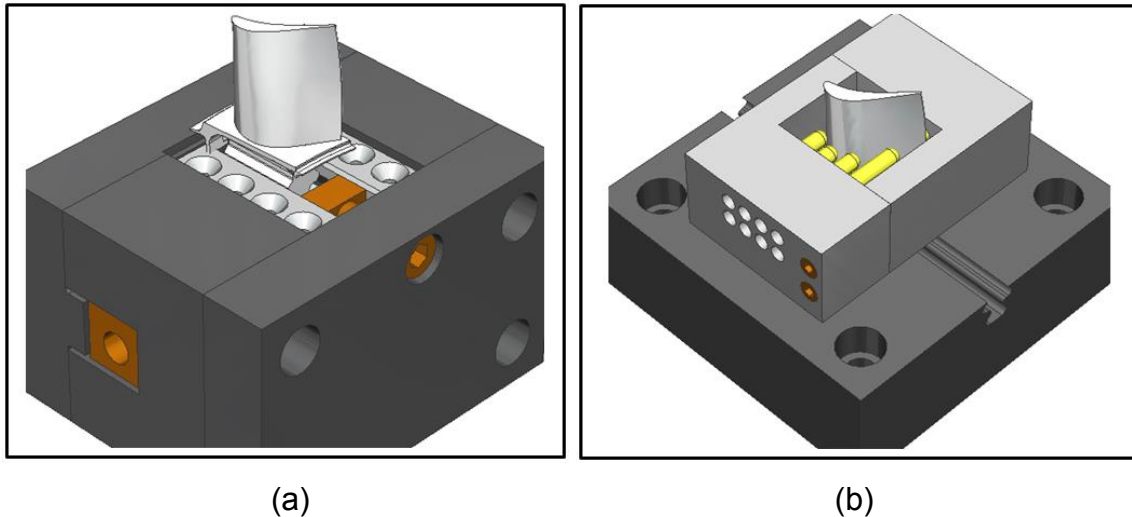


Figure 6. Blade fixture concept holding dovetail section (a), adaptive blade fixture concept with adjustable pins (b).

#### 4. FREE-FORM SURFACE RECONSTRUCTION

Adaptive repair process of worn-out blades focuses on determinate regions on the parts' surface which do not have regular shape. Blade tip, edges, pressure or suction sides are the regions which do not have a regular geometry because of defects after a certain service time. Repair operation is followed with a machining process and it requires having a smooth surface model in order to create smooth toolpaths. The used method for free-form surface reconstruction must provide this smooth surface. Free-form surfaces can be constructed with encoded algorithms in programming languages and with commercially available CAD software. With the recent advances in software technology, many CAD packages offer auto-surfacing and Non-Uniform Rational B-Spline surfaces (NURBS) options at the same time.

##### 4.1. Auto-surfacing Options Offered by Commercial Software

Auto-surfacing options offered by commercial CAD or Reverse Engineering packages have different terms and command structure but they function similarly. Free-form surfaces are generated around either the point cloud or a pre-selected region of the point cloud. It is possible to adjust various attributes of reconstructed surface like the node tolerance, smoothness, degree and segments of non-rational spline elements of surface, and the number of patches (single patch or multiple is available). Besides, automatically construction of the surface inhibits the balancing of different attributes. For instance, Figure 7 shows the consequence of using auto-surfacing option. In this figure, the compressor blade has a worn-out area on the convex side and near trailing edge. A rectangular region is selected, staying out of the fixture, and surface reconstruction is completed using auto-surfacing option and %100 smoothing correction. The reconstructed surface is a single patch surface which has a deviation less than 0.1 mm with the point cloud. However, the reflection analysis showed that

the surface is wrinkled and both the surface normal and the radius of curvature are irregular. As a result of this wrinkled surface, five axes toolpaths are fluctuating.

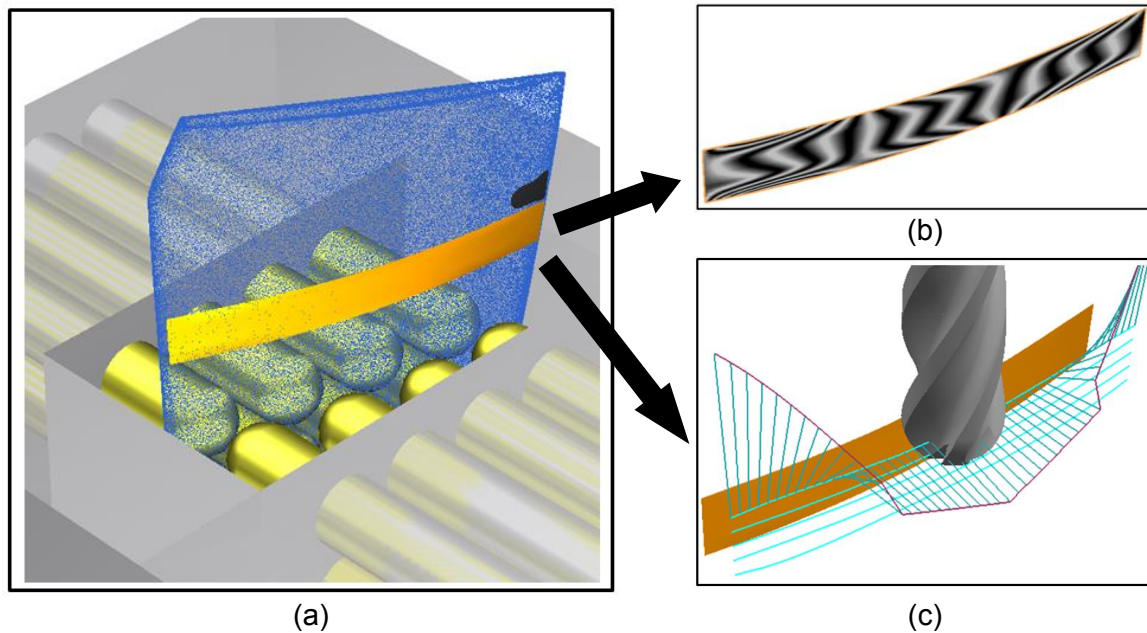
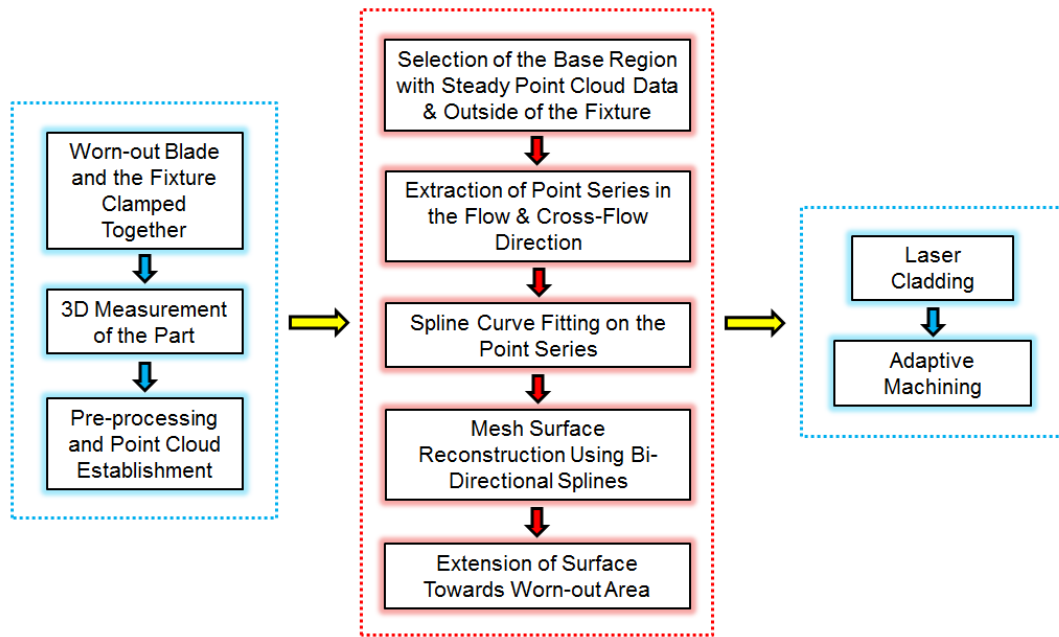


Figure 7. Adaptive blade fixture, HPC blade point cloud, reconstructed surface (a), reflection analysis of reconstructed surface (b), five axes toolpaths on reconstructed surface (c).

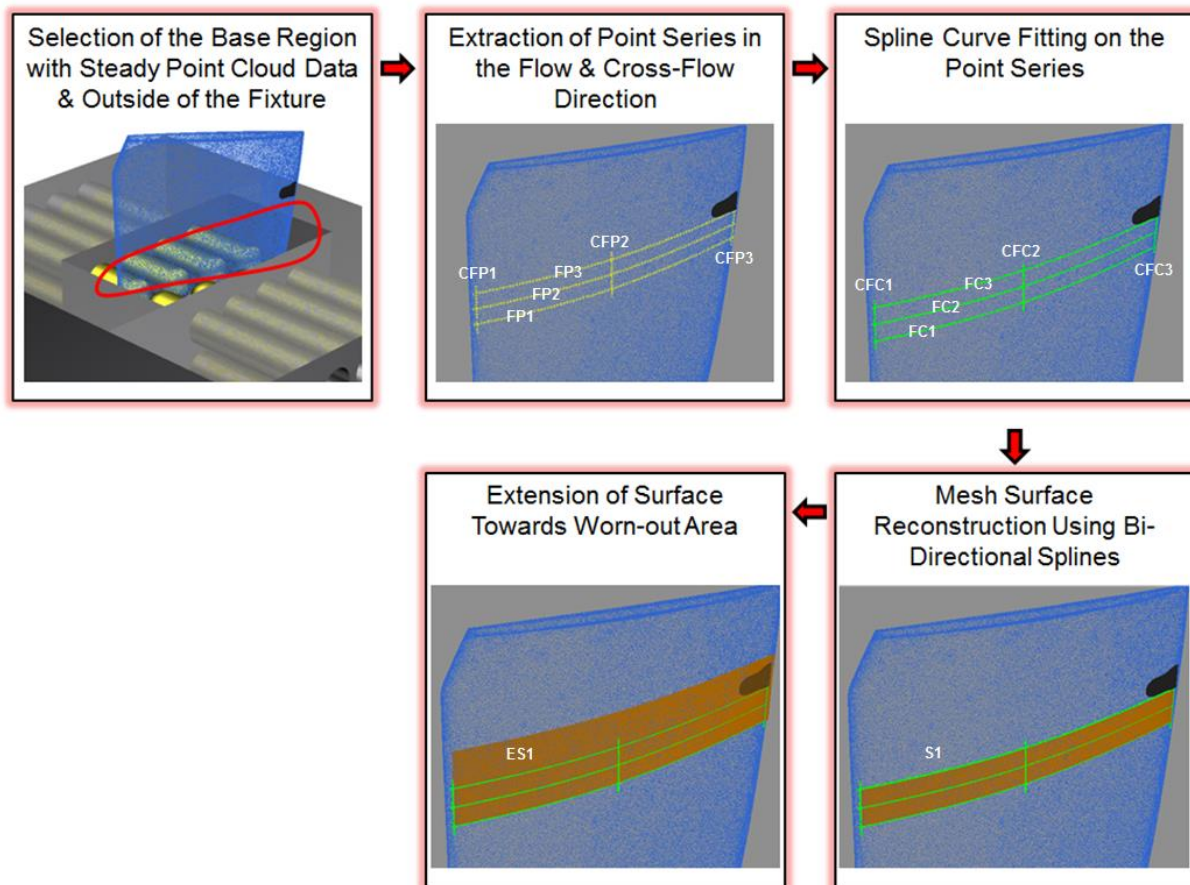
Auto-surfacing presents a rapid surface reconstruction option with less deviation and thus can be used for visual applications. Outside of this, it is not possible to use that option automatically for the applications which will lead to manufacturing issues.

#### 4.2. Surface Reconstruction Using Splines

Surface generation techniques using splines are included in most of the commercially available CAD packages with different options like sweep along guide, swept, loft, and ruled, through curves and through curve mesh. These options vary according to use of curves and they can be single directional sections, bi-directional sections and cross sections, or bi-directional sections and guides. However, surface reconstruction with bi-directional sections and cross sections in the flow and cross-flow directions will cover design intent of the blade both for straight and curved blades. Figure 8 illustrates the related process steps. General repair procedure is indicated with the proposed method for reverse engineering highlighted in the middle. Surface reconstruction using splines is given with graphical details in each step.



(a)



(b)

Figure 8. General repair procedure (a) and the proposed method for reverse engineering (b).

Siemens PLM NX (formerly Unigraphics) has been chosen for this study among the available CAD software which offer miscellaneous curve and surface modeling options. Detailed descriptions of the steps of Figure 8 (b) are given below:

**Step 1:** A region of the point cloud is determined which has steady point data and stays close to worn-out area and out of the fixture so it can be reached during surface reconstruction.

**Step 2:** Point series are extracted from the point cloud in the determined region. Three equidistant planes are used to extract point series in the flow direction (FP1, FP2, FP3) and three in the cross-flow direction (CFP1, CFP2, CFP3).

**Step 3:** Spline curves are fitted on these point series in the flow direction (FC1, FC2, FC3) and in the cross-flow direction (CFC1, CFC2, CFC3) using a distance tolerance of 0.001 mm.

**Step 4:** Mesh type NURBS surface (S1) constructed using six fitted spline curves. Flow curves (FC1, FC2, FC3) are selected as primary curves and the cross-flow curves (CFC1, CFC2, CFC3) are selected as cross curves for the construction of the surface (S1).

**Step 5:** Reconstructed surface are extended towards the worn-out area (ES1) to cover that region. The extension (ES1) is done by keeping the tangency and curvature of the original surface (S1).

## 5. COMPARISON RESULTS AND VERIFICATION

It is important to demonstrate functionality of the proposed method in areas showing different geometrical characteristics in order to ensure that the method offers an adaptive solution for surface reconstruction. It is possible to perform these experiments on different type of blades and/or different regions of the same blade. For this reason, virtual surface reconstruction experiments are carried-out on different regions of the demonstrator compressor blade. Table 1 gives the results of the experiments. In Table 1, the deviation values with reflection analysis are given. Five different regions are determined to use in the experiments. These regions are blade tip, convex side, concave side, leading edge and trailing edge. Auto-surfacing is used first in these regions with a tolerance of 0.001 mm from the point cloud in order to form a foundation for deviation analysis. Surface reconstruction with the proposed method is performed in the same regions following to auto-surfacing. Face-to-face deviation analysis is carried-out with 50 equidistant control points in  $u$  and  $v$  direction. Maximum deviation values obtained are exhibited in the table with millimeter unit format. Designer's profile tolerance values are also exhibited to indicate the status of the reconstructed surface. Reflection analysis is also performed in order to show the smoothness of the new reconstructed surfaces.







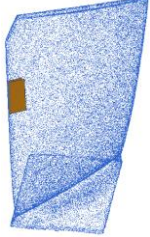



Region	Reconstructed Surface and Point Cloud	Maximum Deviation of Reconstructed Surface	Manufacturer Tolerance for Blade Profile	Reflection Analysis of Reconstructed Surface	Status
Blade Tip		0.056 mm	$\pm 0.125$ mm		Conforms
Convex Side		0.033 mm	$\pm 0.125$ mm		Conforms
Concave Side		0.027 mm	$\pm 0.125$ mm		Conforms
Leading Edge		0.093 mm	$\pm 0.100$ mm		Conforms
Trailing Edge		0.116 mm	$\pm 0.125$ mm		Conforms

Table 1: Surface reconstruction experiments and results.

## 6. DISCUSSIONS AND CONCLUSION

A surface reconstruction methodology is proposed based on NURBS surface generation using spline curves. Point series along flow and cross-flow directions are extracted from a selected region of point cloud staying outside of the fixture. Spline curves are fitted on these point series and mesh surface construction is completed using these spline curves. Finally constructed surface is extended to cover worn-out area of the blade. Proposed method is tested for the sample blade in virtual platform using commercial CAD software. The tests are





carried-out in different regions of the blade like blade tip, convex face, concave face, leading edge and trailing edge. These experiments in different regions showed the method's ability of adaptation for different geometrical features. Surface reconstruction with the proposed method converged to original data better on the blade faces than the blade tip, leading edge and trailing edge. Still the method offered conforming results in all the regions comparing manufacturer's blade profile tolerances. Surface quality is verified using reflection analysis and it showed smoother results comparing to automatic surface reconstruction options.

## ACKNOWLEDGEMENT

The authors would like to acknowledge Scientific and Technical Research Council of Turkey (TUBITAK) for its support in this research given in TEYDEB 3120541 project.

## REFERENCES

1. **Antony, K.C. and Goward, G.W., (1988)**, "Aircraft gas turbine blade and vane repair in superalloys", Proceedings of 6<sup>th</sup> Superalloys Symposium, Pennsylvania, pp. 745-754.
2. **Babu, T.S. and Thumbanga, R.D., (2011)**, "Reverse Engineering, CAD\CAM & pattern less process applications in casting-A case study", INTERNATIONAL JOURNAL OF MECHANICS, (1-5), pp. 40-47.
3. **Bravo, U., Altuzarra, O., Lopez de Lacalle, L.N., Sanchez, J.A. and Campa, F.J., (2005)**, " Stability limits of milling considering the flexibility of the workpiece and the machine", International Journal of Machine Tools & Manufacture, (45), pp. 1669-1680.
4. **Gao, J., Chen, X., Yilmaz, O. and Gindy, N., (2008)**, "An integrated adaptive repair solution for complex aerospace components through geometry reconstruction", International Journal of Advanced Manufacturing Technology, (36), pp. 1170-1179.
5. **Gao, J., Chen, X., Zheng, D., Yilmaz, O. and Gindy, N., (2006)**, "Adaptive restoration of complex geometry parts through reverse engineering application", Advances in Engineering Software, (37), pp. 592-600.
6. **Gong, Z., Chen, X.Q. and Huang, H., (2000)**, "Optimal Profile Generation in Distorted Surface Finishing", Proceedings of the IEEE International Conference on Robotics & Automation, California, pp. 1557-1562.
7. **Grossman, D. and Jüttler, B., (2012)**, "Volumetric Geometry Reconstruction of Turbine Blades for Aircraft Engines", Lecture Notes in Computer Science, (6920), pp. 280-295.



8. **Li, J., Yao, F., Liu, Y. and Wu, Y., (2010)**, "Reconstruction of Broken Blade Geometry Model Based on Reverse Engineering", Proceedings of the Third International Conference on Intelligent Networks and Intelligent Systems, Shenyang, pp. 680-682
9. **Luhmann, T., Wendt, K., (2000)**, "Recommendations for an Acceptance and Verification Test of Optical 3-D Measurement Systems", International Archives of Photogrammetry and Remote Sensing, Vol. 33, Part B5, pp. 493-500.
10. **Ng, B.T-J., Lin, W-J., Chen, X., Gong, Z. and Zhang, J.B., (2004)**, "Intelligent System for Turbine Blade Overhaul Using Robust Profile Re-Construction Algorithm", Proceedings of the 8<sup>th</sup> International Conference on Control, Automation, Robotics and Vision, Kunming, pp. 178-183.
11. **Piya, C., Wilson, J.M., Murugappan, S., Shin, Y. and Ramani, K., (2011)**, "Virtual Repair: Geometric Reconstruction for Remanufacturing Gas Turbine Blades", Proceedings of the ASME 2011 International Design Engineering Technical Conferences & Design for Manufacturing and the Life Cycle Conference, Washington.
12. **Poursaeidi, E., Arablu, M., Yahya Meymandi, M. A., and Mohammadi Arhani, M. R., (2013)**, "Investigation of Choking and Combustion Products' Swirling Frequency Effects on Gas Turbine Compressor Blade Fractures", Journal of Fluids Engineering, Vol.135, Issue 6.
13. **Qi, H., Azer, M. and Singh, P., (2010)**, "Adaptive toolpath deposition method for laser net shape manufacturing and repair of turbine compressor airfoils", International Journal of Advanced Manufacturing Technology, (48), pp. 121-131.
14. **Voltan, A., (2010)**, "Metrological Performance Verification of Optical Coordinate Measuring Systems", Ph. D. Thesis, University of Padova Department of Mechanical and Innovation Management (DIMEG), Padua.
15. **Wu, H., Gao, J., Li, Si., Zhang, Y. and Zheng, D., (2013)**, "A Review of Geometric Reconstruction Algorithm and Repairing Methodologies for Gas Turbine Components", TELKOMNIKA, (11-3), pp. 1609-1618.
16. **Yasa, E., Ören, S., Uğur Solakoğlu, E., Poyraz, Ö., Akbulut, G., Pilatin, S., (2013)**, "Havacılık sektöründe optik ölçüm yöntemlerinin yeri ve karşılaştırmalı değerlendirilmesi üzerine bir çalışma", Proceedings of VIII. Ulusal Ölçübilim Kongresi ve Sergisi, Kocaeli.



17. **Yilmaz, O., Gindy, N. and Gao, J., (2010)**, "A repair and overhaul methodology for aeroengine components", *Robotics and Computer Integrated Manufacturing*, (26), pp. 190-201.
18. **Yurong, Xu, J. and Sun, Y., (2013)**, "A surface reconstruction strategy based on deformable template for repairing damaged turbine blades", *Proceedings of the Institution of Mechanical Engineers, Part G: Journal of Aerospace Engineering*.
19. **Zheng, J., Li, Z. and Chen, X., (2006)**, "Worn area modeling for automating the repair of turbine blades", *International Journal of Advanced Manufacturing Technology*, (29), pp. 1062-1067.







## EVALUATION OF A SCANNING TECHNIQUE USED FOR MEDICAL DESIGN APPLICATIONS

**Octavian CIOBANU**, *oct.ciobanu@gmail.com* “Grigore T. Popa” University of Medicine and Pharmacy, Iasi, 700115, Romania

**Gabriela CIOBANU**, *gciobanu03@yahoo.co.uk* “Gheorghe Asachi” Technical University Iasi, 700050, Romania

### ABSTRACT

The reverse engineering processes involve measuring an object and then reconstructing it as a 3D model. Any physical object can be measured using 3D scanning technologies like laser scanners, structured light digitizers, photogrammetry etc. The medical industry and medical bioengineers use detailed models of organs or of anatomic surfaces in order to design customized prostheses and orthoses. Also medical personnel need 3D models in order to perform different medical interventions. Paper approaches different typical objects and anatomic surfaces by photogrammetric scanning technique and 3D reconstruction using commercial software. Reconstructed objects are discussed and the quality of mesh models, shaded models and textured models are compared. The aim is to give users recommendations, which object or body part are suited for this type of scanning, or even if a combination of photogrammetry and another 3D scanning technique is advisable. Comments like possible applications, quality of the results are to be considered.

**Keywords:** 3D modeling, photogrammetry, 3D reconstruction, medical applications

### 1. INTRODUCTION

Technological advances in recent years have enabled a lot of studies to reveal more detailed information about the body's internal or external anatomic surfaces. Computer tomography (CT), magnetic resonance imaging (MRI), ultrasound, 3D laser, structured light devices have revolutionized the capacity to scan and to reconstruct the human anatomy in order to aid in the diagnosis, surgical planning, biomechanics, simulation and design of prostheses and orthoses [Jin et al 2006], [Venkatesh, 2012], [Wilson et al, 2007].



3D scanning is becoming increasingly important besides medical sciences in industry, architecture, archeology etc. [Curless, 2000], [Strobl et al, 2011], [Ciobanu et al, 2013]. There are a lot of classifications for 3D scanning and 3D geometry reconstruction of objects, and they can be classified into surface and in depth analysis. CT, magnetic resonance imaging (MRI), and ultrasound are in depth 3D scanners, being able to reveal tissues under the skin including details of the bone tissues. Surface methods do not reveal tissues under the skin. 3D laser, structured light and other photogrammetric devices are used to extract the shape and process stereo triangulation for pairs of images of anatomic surfaces.

Three-dimensional surface body scanners use several technologies, including photogrammetry, laser-based scanning, structured light and radio-wave devices.

### **1.1. Photogrammetry**

Photogrammetry is the technique of obtaining information about objects and the environment by recording, measuring, and processing photographic images. The operation of taking photographs is a process that transforms the 3D real objects into flat 2D images. In this case, the photo camera is the device that transforms 3D objects to 2D objects.

Photogrammetry may be considered the reverse of the normal photographic process transforming the 2D images into 3D models.

Photogrammetry can be classified after camera position during photography. On this classification there are:

- Close-range photogrammetry (used in this paper).
- Aerial photogrammetry (or remote sensing).

### **1.2 Structured light based scanners**

These 3D scanners project patterns of light on the body. A video projector produces the pattern and the cameras record the distorted pattern. The scanners may have one or several pairs of cameras, with the images sent to software that calculates the visual disparities between corresponding points in each pair of images. The 3D geometry of objects is obtained using stereoscopy.

Scanners projecting light patterns on objects are based on conventional video cameras.

### **1.3 Laser based scanners**

This type of 3D scanner uses harmless, invisible laser beams to measure the body. The scanners are based on the principle of triangulation, projecting points or lines onto the object, and using a video camera offset from the laser source to register the laser beam on the object being scanned.

Laser range scanners are based on an array of depth sensors. These sensors send a laser beam on the surface of the object and measure the direction of the reflected ray to calculate



the distance between the sensor lens and the measured surface. Knowing the position and orientation of the sensor from the scanner's construction and calibration, it is possible to calculate the spatial coordinates of the point.

#### **1.4 Millimeter waves scanners**

The millimeter waves scanners use different radio-wave technology to scan a subject's body, and the waves can pass through clothing. The system contains small antennas that send and receive low-power radio waves. The signals pass through the person's clothing, but reflect off the skin, which contains water.

A number of surface scanning systems with the ability to quickly and easily obtain 3D digital representations of the anatomic surfaces are now commercially available. This paper aims to present an evaluation of the feasibility of the use of photogrammetric technique in medical engineering. A usual commercial digital camera was used (Cannon SX 200 IS) together with a photogrammetric software (3DSOM) in order to reconstruct different 3D models. In this study, some objects and some anatomic surfaces were scanned, reconstructed and discussed in order to evaluate the feasibility of the application of this technique in medical engineering.

## **2. METHOD**

In this study, a photogrammetric technique was approached using a single camera, known as the photo-based technique. The photo-based technique includes software capable to calibrate cameras and to determine the position of the camera when shooting photos. This scanning method is able to digitize objects with any digital photo camera. When shooting an object, the number of required shots should be about between 20 and 40 and the surfaces should be permanently in focus and lit with diffuse illumination.

After taking photos, computer programs (known as scanning software) are used to perform the 3D digital reconstruction. The main goals of the 3D scanning software are to import the photos from the digital camera and to transform 2D photos to 3D digital model.

The scanning software compares photos patch by patch to find the matches and when these matches are found, the position data of the photographs is used to assemble the patches in 3D space.

Some algorithms can exploit other information about the object allowing the 3D reconstructions of 3D coordinates from only one camera position. They often fail in the presence of subsurface scattering [Mark et al, 2013], [El-Hakim, 2000].

In this study a digital camera was used (Cannon SX 200 IS) together with a photogrammetric software in order to test the feasibility of the method in medical applications.

### 3. RESULTS

First, some objects with simple geometry were scanned and reconstructed and finally the fingers of a limb and the human head were scanned and reconstructed and the results were discussed. The simple objects studied had holes, blind holes and thread (equivalent to helicoidal indentations) and offered details about the reconstruction of this type of peculiar geometrical shapes.

#### 3.1 Holes reconstruction

A cylindrical object with a cylindrical hole (Figure 1) was scanned and reconstructed in three solutions: 3D mesh model (left in Figure 2), 3D shaded model (center in Figure 2) and textured model (right in Figure 2). A calibration mask was placed around the object according to 3DSOM software instructions.

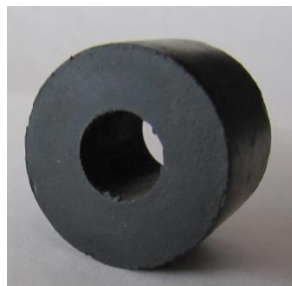


Figure 1. Object with cylindrical hole

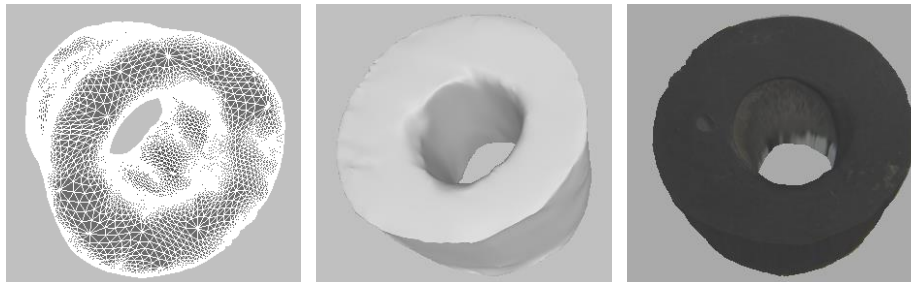


Figure 2. The 3D mesh (left) shaded (center) and textured models (right)

#### 3.2 Hexagonal blind holes and screw thread



Figure 3. Object with hexagonal blind hole and thread

An object with hexagonal blind hole and thread was scanned (Figure 3) and reconstructed as 3D mesh model (left), shaded model (center) and textured model (right in Figure 4)

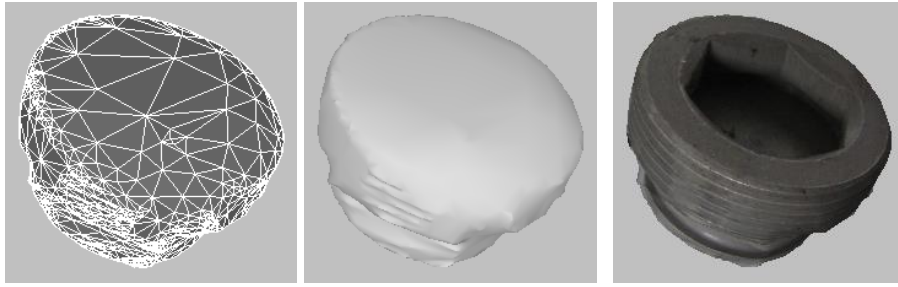


Figure 4. The 3D mesh (left) shaded (center) and textured models (right)

### 3.3 Rectangular blind holes

An object with a deep rectangular blind hole and sharp edges (Figure 5) was scanned and reconstructed in three solutions (Figure 6) to understand how the 3D reconstruction works.



Figure 5. Object with deep rectangular blind hole

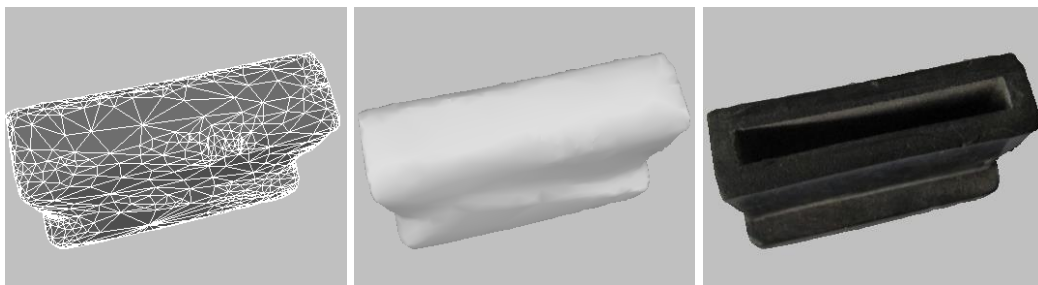


Figure 6. The 3D mesh (left) shaded (center) and textured models (right)

### 3.4 Anatomic surfaces- the leg and the human head

A first anatomic surface was the human leg (Figure 7) reconstructed in order to observe the 3D mesh model, the 3D shaded model and the 3D textured model (Figure 8). A calibration mask according to software indications was used around anatomic surfaces.



Figure 7. Human leg



Figure 8. The 3D mesh (left) shaded (center) and textured models (right)

The human head (Figure 9) was scanned and reconstructed to observe the details of the 3D mesh model, 3D shaded model and the 3D textured model (Figure10).



Figure 9. Human head

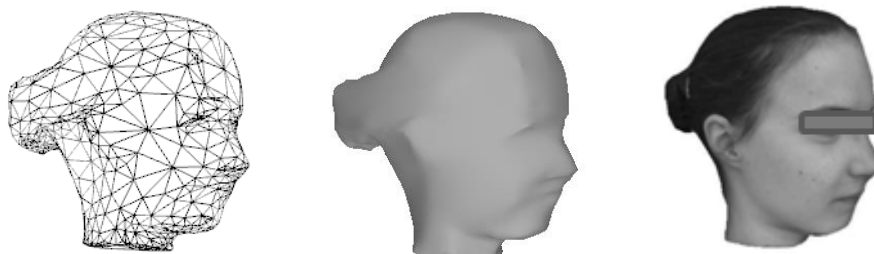


Figure 10. The 3D mesh (left) shaded (center) and textured models (right)

#### 4. DISCUSSION

Each 3D scanning technique has its advantages, limitations, and costs. According to some scientific papers [Van Den Heuvel, 2000], [Ngan, 2000] photogrammetry has advantages and

disadvantages in the kind of objects that can be digitized and in some features. Photogrammetric software are capable to automatically calibrate the photo camera and to determine the lens distortion. During scanning, the object was fix and camera was mobile making circles around object.

The results of this study on small objects show that the cylindrical hole studied in Figure 1 is well determined and revealed with about 1-0.5 mm error. The reconstructed 3D mesh and the shaded model have some minor imperfections (as in Figure 2 left and center) but the 3D textured model (Figure 2 right) look impressive being very close to the real model.

Blind holes studied in Figure 3, Figure 4, Figure 5 and Figure 6 are impossible to be revealed directly. The reconstructed 3D meshes show no blind holes. Also the 3D shaded models show no blind holes. But the 3D textured models show the blind holes being very close to real model. In this case, the texture creates the illusion of the presence of the blind holes. Also the raised helical rib going around a screw in Figure 3 is revealed only in the textured reconstruction (Figure 4 right).

Anatomic surfaces approached in Figures 7 and 8 show that the spaces between the fingers of the leg are impossible to be revealed directly. The 3D mesh model and the shaded model (Figures 8 left and center) have no such spaces for fingers. Only the textured model (Figure 8 right) creates this illusion. There are necessary some image processing, eventually with other 3D software to create the existing indentations.

A very important 3D reconstruction application in medical engineering is in connection with the human head (Figure 9). The 3D reconstruction with texture (Figure 10 right) creates the illusion that the reconstructed face is exactly like in reality. But the 3D mesh model and the shaded model (Figure 10 left and center) show that there are a lot of approximations in the reconstruction of face shapes. As a result, the there are some imperfections in the 3D model:

1. The corner between eye, nose and forehead (1 in Figure 11)
2. The intersection line between nose and face (2 in Figure 11)
3. The inner space of nose (3 in Figure 11);
4. The real shape of ear (4 in Figure 11).

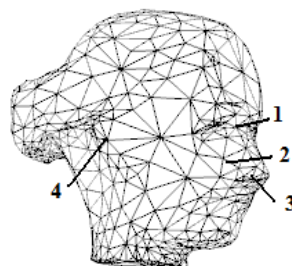


Figure 11. Imperfections of the 3D photo-based model





If these details are not important, the photo-based technique may be used in a lot of medical applications including the design and fabrication of prostheses and orthoses with CAD/CAM or Rapid Prototyping technologies, and in the planning of surgical interventions.

## 5. CONCLUSIONS

Photogrammetric scanning technique became one of the most cost-effective solutions for the 3D modeling of small objects and of some types of anatomic surfaces. During 3D reconstruction, there been observed some difficulties in reproducing the exact details: some blind holes and indentations will not appear on the 3D model. Also, shiny, mirroring, transparent or moving objects are very difficult to be reconstructed.

A lot of photo-based software has a number of manual and automatic tools to modify and to improve the 3D model. Using these tools or other software for editing it is possible to move parts of surfaces inwards in order to create an indentation or to pull the surface out to create a bump.

All these supplementary tools or additional processing software have as effect the extent of reconstruction duration and the cost of 3D modeling. Despite these disadvantages, the photo-based scanning technique with its low cost, noninvasive character and ease of use make it useful for different medical applications and especially in prosthetics and orthotics.

## REFERENCES

1. **Jin, G., Lee, S.J., Hahn, J.K. et al. (2006)**, “3D surface reconstruction and registration for image guided medialization laryngoplasty”, *Advances in Visual Computing: Lecture Notes in Computer Science* 2006; 4291: 761-7.
2. **Venkatesh, S., Ganeshkar, S.V., Ajmera, S. (2012)**, “Image-based modelling: A simple and economical technique to create 3-D models of the face”. *Int J Health Sci Res* 2012; 93-9.
3. **Ciobanu, O., Ciobanu, G., Rotariu, M. (2013)**, “Photogrammetric Scanning Technique and Rapid Prototyping Used for Prostheses and Orthoses Fabrication”, *Applied Mechanics and Materials* Vol. 371, pp 230-234.
4. **Curless, B. (2000)**, "From Range Scans to 3D Models", *ACM SIGGRAPH Computer Graphics* 33 (4): 38–41.
5. **Strobl, K. H., Mair, E., Hirzinger, G. (2011)**, "Image-Based Pose Estimation for 3-D Modeling in Rapid Hand-Held Motion", *Proceedings of the IEEE International Conference on Robotics and Automation (ICRA 2011)*, Shanghai, China. pp. 2593-2600.



6. **Aguilera, D.G. and Lahoz, J.G. (2010)**, “Virtual Archaeological Sites Modelling Through Low-Cost Methodology”, *Survey Review*, Volume 42, Number 317, July 2010, pp. 300-315(16).
7. **Mark, S., Erickson, J., Bauer, J.J., Hayes, W.C. (2013)**, “The Accuracy of Photo-Based Three-Dimensional Scanning for Collision Reconstruction Using 123D Catch”, *SAE International - 2013 World Congress – Under press*
8. **El-Hakim, S., (2000)**, “A practical approach to creating precise and detailed 3D models from single and multiple views”. *ISPRS Congress*, July 16-23, 2000, Amsterdam. *IAPRS Vol. XXXIII, Part 5*, pp. 203-211.
9. **Van Den Heuvel, F. (2000)**, “Trends in CAD-Based photogrammetric measurement”. *ISPRS Congress*, July 16-23, 2000, Amsterdam. *IAPRS Vol. XXXIII, Part 5*, pp. 852-863.
10. **Wai Kit Addy Ngan (2003)**, “Image-based 3D Scanning System using Opacity Hulls”, *Doc. thesis*, Massachusetts Institute of Technology, 2003.





## BIOINSPIRED TRANSFORMATION FOR DESIGN OF BIOROBOTS

**Aylin KONEZ EROĞLU**, *akonez@atilim.edu.tr* ATILIM University, 06838, Ankara, Turkey

**Zuhal ERDEN**, *zuhal@atilim.edu.tr* ATILIM University, 06838, Ankara, Turkey

**Abdulkadir ERDEN**, *aerden@atilim.edu.tr* ATILIM University, 06838, Ankara, Turkey

### ABSTRACT

Bioinspired Design (BID) process, the use of nature to inspire, is based on analogical reasoning. Two key steps of this process are “biological system analysis” and “bioinspired transformation”. While biological systems are represented in the first step, the second step exhibits analogical translation. The main aim of this paper is to present the “bioinspired transformation” step of a developed bioinspired conceptual design (BICD) process of jointed-leg biorobots. During the studies, four biorobot case studies are implemented. Experimental results show that the transformation provides an easy and systematic mapping between biological and engineering domains. In this paper, one of the case studies, bioinspired dog robot (BioDog) is described for the bioinspired transformation step.

**Keywords:** Bioinspiration, Biomimetic, Bioinspired Design, Analogical Reasoning, Bioinspired Transformation, Biorobots

### 1. INTRODUCTION

Bioinspiration or Biomimetics which are dated back 27th century B.C. are used to indicate sophistication, robustness, and adaptability of biological systems, conducted by natural evolution, to develop creative and innovative software and hardware systems [Floreano and Mattiussi, 2008]. Velcro [Wilson et al., 2010], Gecko-like adhesive tape [BioTrue, 2013, Hargroves and Smith, 2006, Vukusic, 2010], and BigDog [Dynamics, 2012] are well known products of bioinspired engineering. Beijing National Stadium [Narahara, 2013], exohand [FESTO, 2012] or smart bird [FESTO, 2011] of Festo, Biotrue eye solution [BioTrue, 2013], self-cleaning paint inspired from lotus [Vukusic, 2010] and shark skin-like coating of A-340 aircrafts [Burns and Pook, 2010] are other design examples of products designed using Bioinspired Design (BID) process.

BID process uses biological phenomena to inspire solutions to engineering problems [Glier, McAdams and Linsey, 2011, Helms, Vattam and Goel, 2009]. Comprehensive studies performed on the literature reveal some drawbacks of the existing BID processes. The main reason of the drawbacks depends on the technology transfer problems [Helms et al., 2009, Project, 2008, Vincent and Mann, 2002], so the link between biological domain and engineering domain is still ad-hoc [Glier et al., 2011]. This drawback prevents an effective knowledge transfer from biological domain to engineering domain. The study presented in this paper focuses on developing a realistic, reliable and systematic analogical translation step, called bioinspired transformation. The bioinspired transformation is one of the key step of developed Bioinspired Conceptual Design (BICD) process generated for jointed-leg biorobots.

Within the context of the paper, background required for bioinspired transformation step is given in Section 2. Bioinspired Transformation is detailed in Section 3 where required knowledge about the investigated biological system and the biorobot is represented. In Section 4, Bioinspired Dog Robot (BioDog) is presented as a case study. Finally, bioinspired transformation step and its implementation on the BioDog are discussed.

## 2. BACKGROUND

BID is a technique in which analogical reasoning [Helms et al., 2009, Mak and Shu, 2004, Nelson, Wilson and Yen, 2009, Tsujimoto et al., 2008, Wilson, 2008] is used to create novel engineering design products in engineering domain by drawing upon solutions and patterns in biological domain [Glier et al., 2011, Yen et al., 2011]. The analogical reasoning of the BID can be provided into four key areas as given in Figure 1.

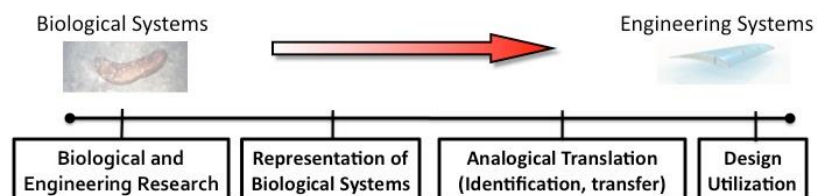


Figure 1. Current research on BID and four key areas of the BID [Wilson, 2008]

Two key steps of a BID process are representation of biological system and analogical translation. These two steps;



1. Representation of biological systems: In the existing BID approaches, several decomposition models such as function-behavior-structure (FBS) [Gero and Kannengiesser, 2007] or SBF [Vattam, Helms and Goel, 2007] are used to provide information about biological systems. However, these models do not provide required “correct” knowledge about biological systems.
2. Analogical translation: This step represents a link between biological domain and engineering domain. In literature, this link is supported by several databases, such as Biomimicry Guild Database [Project, 2008], Biologists at the Design Table (BaDTs) [Project, 2008], BioTRIZ [Glier et al., 2011, Mak and Shu, 2004, Wilson, 2008], WordNet [Chiu and Shu, 2004, Helms et al., 2009, Mak and Shu, 2004], SAPPHIRE [Chakrabarti, 2007, Helms et al., 2009, Wilson, 2008]. However, most of these databases work as a keyword translators and required knowledge about the engineering problem is not clear.

The development of BID process including steps of representation of biological systems and analogical translation is still challenging steps because of the current limitations of existing processes.

A BICD process including systematic and clear analogical reasoning is developed at the Atılım University, Department of Mechatronics Engineering. The analogical reasoning considering in the proposed BICD process is constructed by a well-defined step- biological systems analysis- in which biological systems are represented and a clear mapping step- bioinspired transformation- which provides a link between biological and engineering domains as analogical translation.

The developed BICD process is constructed with a combination of standard engineering design steps and approaches coming from existing BID studies. The BICD process as given in Figure 2 from customer needs to concept of a biorobot is composed of the following steps:

- Task Clarification: This step transfers customer’s needs to a design/engineering problem which covers required functions and essential constraints of the design.
- Biological System Selection: A biological system or biological systems are selected from the literature based on the clarified functions and constraints in this step.

- **Biological System Analysis:** In this stage, the selected biological system(s) is/are analyzed to collect required knowledge in terms of morphology, function and behavior. Literature and/or experimental research can be used to collect the data.
- **Bioinspired Transformation:** The collected and synthesized knowledge is transformed from biological domain into engineering domain during the stage of “Bioinspired Transformation”.
- **Engineering Structures Generation:** Alternatives of engineering materials, structures and components for each knowledge about a biorobot are generated in this stage.
- **Engineering Structures Selection.** In this step, concept variants are developed for the biorobot. A concept of the biorobot is selected among these variants at the end of the process.

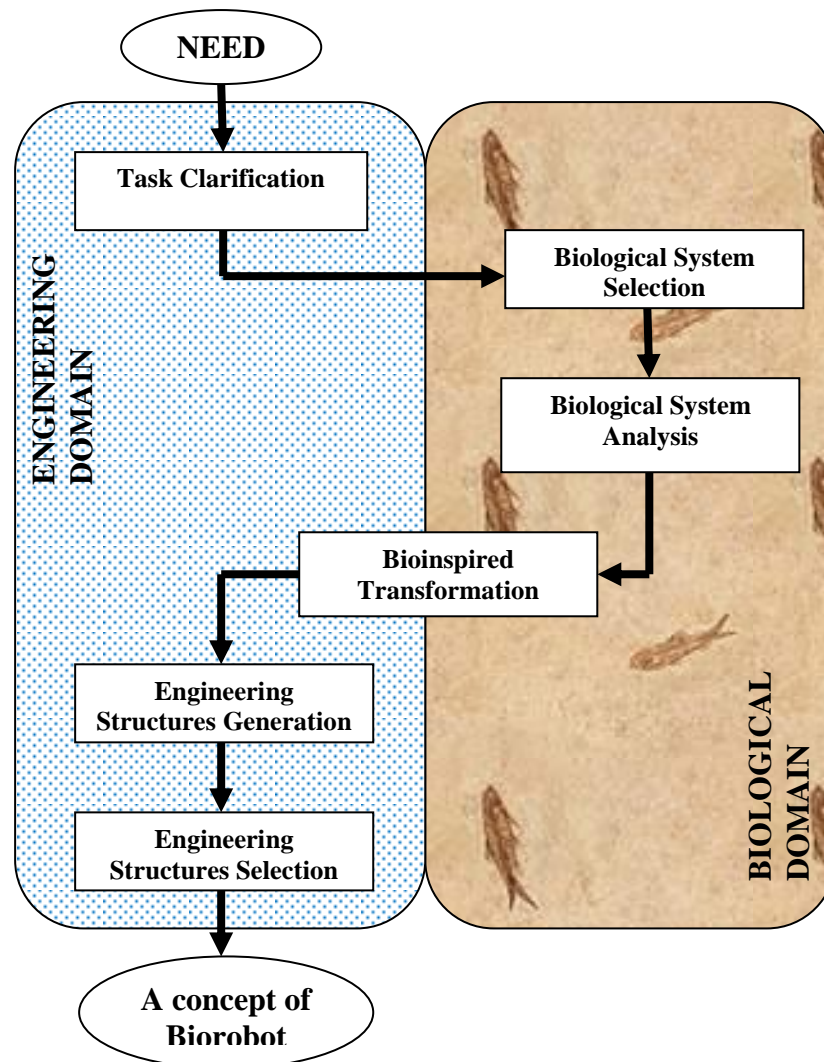


Figure 2. Steps of the developed BICD process

Within the concept of the paper, a step of BICD process, bioinspired transformation is considered in the next section.

### 3. BIOINSPIRED TRANSFORMATION

Sartori and Chakrabarti [Sartori, Pal and Chakrabarti, 2010] states that “Even a well-known biological solution can trigger innovative solutions in engineering if the knowledge is available at the right time and in the right form, a common language with which the functionality of both biological and engineered systems could be expressed.” It is known that analysis of biological systems is used to collect “correct” knowledge which should be transformed from biological to engineering domain. Thus, an important question arises; “What is the required knowledge which represents biological systems?” and “How can the knowledge is transferred from biological domain to engineering domain?”. Possible answers of the questions are given in the next two parts of Section 3.

#### **Knowledge about a Biological System and Knowledge about a Biorobot:**

In order to answer the question about required knowledge, two approaches are used in this study [Eroglu, Erden and Erden, 2011]. Firstly, the definition of “biorobot” is investigated so that the requirements of biorobots inspired from biological systems are determined. Secondly, existing case studies on biorobots are studied to collect properties of biological systems which are used for inspiration. Details about these studies are given in [Eroglu, 2013]. At the end of the studies on biorobots and case studies, a semantic network is structured to categorize the terms about bioinspiration of biorobots and to show relationships between these terms. The network is given in Figure 3.

The network shows that motion and forces are related with the function which performs a task. Form and structure are parts of morphology, which includes the anatomy of a biological system. Behavior of a biological system affected by changes in the environment can implement different functions [Kitamura, Koji and Mizoguchi, 2006]. Therefore, “function”, “morphology”, and “behavior” features can be used to represent a biological system to design a biorobot which includes energy, material, and information inputs and outputs as a system. The morphological information includes dimensions (length, shape, etc.), weight and body structure details (the number of links, joint details, etc). The function covers function types and mathematical models for desired kinematic data. The behavior gives information about how the biological system achieves the desired function.



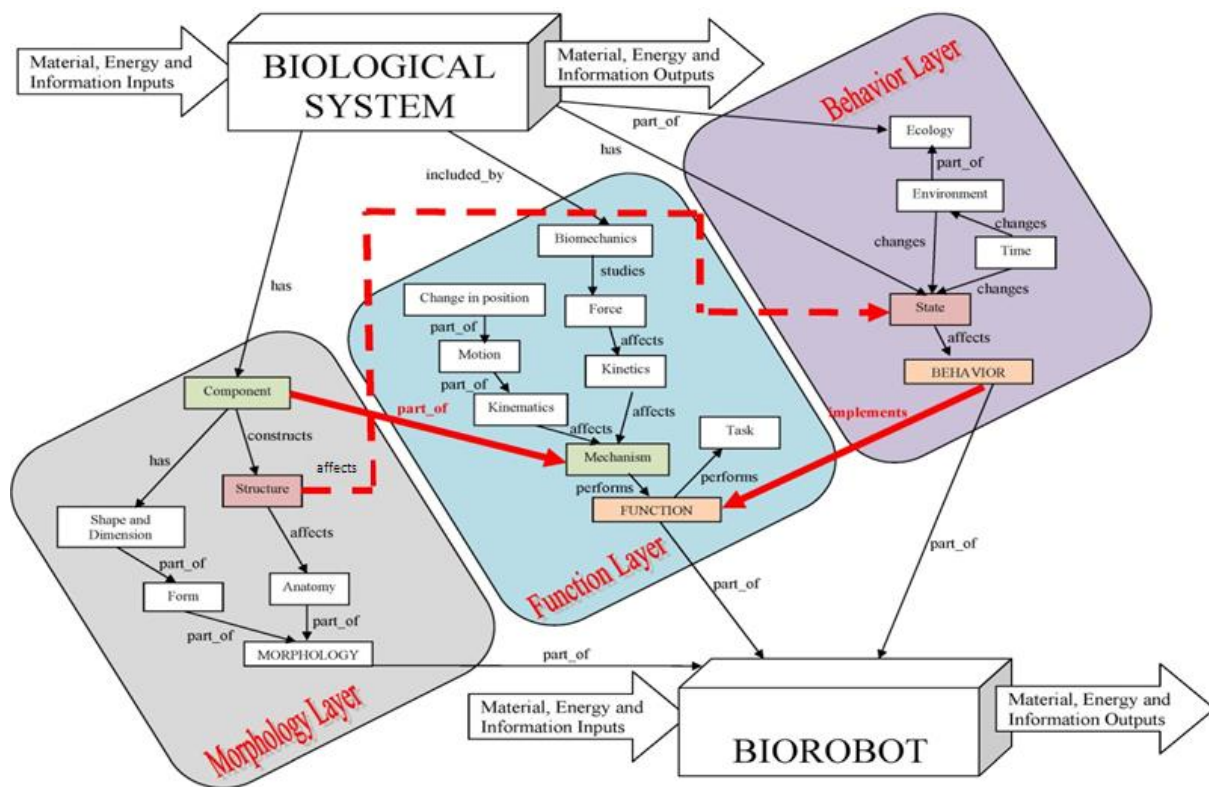


Figure 3. A semantic network representation of concepts for biological systems and biorobots

According to Figure 3, combination of “morphology”, “function”, and “behavior” represents required knowledge about a biological system (BS) and a biorobot (BR) in the BICD process. The links between the knowledge about a BS and a BR can be provided Bioinspired Design step.

### Bioinspired Transformation Step:

Bioinspired Transformation step transforms knowledge about the selected and investigated biological system into knowledge about the desired biorobot. In this step, creative and innovative design ideas can be transferred from biological domain to engineering domain with four activities: matching, separating, modeling and synchronizing.

In “matching”, required morphology of BS are matched with the existing engineering forms and structures. “Separating” is to clarify the locomotion cycle of a biorobot. In “modeling”, the collected data of the biological system for a locomotion cycle is linearized for the BR. Finally, in “synchronizing”, all legs and their combinations are considered for the expected function



and behavior of the BR. The output of this stage can be represented as a set of Knowledge about Biorobot (KBR). The KBR is given in Equation 1.

$$\text{KBR} = \{\text{MorBR}, \text{FuBR}, \text{BeBR}\} \quad (1)$$

In Equation 1, *MorBR* represents to **M**orphology of the **B**io**R**obot as given in Equation 2.

$$\text{MorBR} = \{\text{NuL}, \text{PaL}, \text{LoL}, \text{FoLb}, \text{JoL}, \text{ToJo}\} \quad (2)$$

where

- *NuL*- the **N**umber of **L**egs,
- *PaL*- the **P**aired **L**egs according to anatomic structure,
- *LoL*- the **L**imbs of each paired **L**egs,
- *FoLb*- the **F**orms of **L**imbs,
- *JoL*- the **J**oint of each paired **L**egs,
- *ToJo*- the **T**ypes of **J**oints, and

In Equation 1, *FuBR* and *BeBR* represent **F**unction of the **B**io**R**obot and **B**ehavior of the **B**io**R**obot. *FuBR* includes expected function, kinematic data and joint angles during the locomotion cycle. *BeBR* covers leg combinations during the cycle.

Implementations of the BICD process and its key step- bioinspired transformation are applied on different case studies. One of the studies is a bioinspired dog-like robot (BioDog). Within the context of studies on the BICD process, BioDog is designed and its initial prototype is manufactured. In the next section, bioinspired transformation step of BioDog is detailed.

#### 4. BIODOG

The conceptual design of a BioDog is started with a customer need and completed with a concept of the BioDog. In this study, the customer need is stated as, “I need a robot which can walk and trot on an indoor smooth surface like a dog. It looks like a small dog. The robot should be light and compact. I have some servo motors and an Arduino platform; we can use them in its prototype....”. According to the customer need, function of the BioDog is clarified as walking and trotting. A Terrier dog is selected as an inspiration source. Selected dog is analyzed in the “biological system analysis” step and KBS is developed for the dog. Generated KBS including morphology, function, and behavior about the dog is an input of the “bioinspired transformation” step. In this paper, bioinspired transformation step is given in detail.

The first activity of the step is “matching” in which Terrier dog’s joint structures (Table 1) and forms of links; humerus, radius and ulna, forepaw, femur, tibia and fibula, and hindpaw are matched with known engineering structures and forms.

Table 1. The matched joint structures of the Terrier dog

Legs	Joint name	Joint type	
		Biological	Engineering
Front Legs	Shoulder	Glenohumeral Joint	Ball and Socket
	Elbow	Ginglymus	Hinge Joint
	Wrist	distal radioulnar articulation (inferior radioulnar joint)	Pivot Joint
Hind legs	Hips	Acetabulofemoral Joint	Ball and Socket
	Knee	Compound Joint	Hinge Joint
	Ankle	Talocrural Joint (Synovial)	Hinge Joint

In the “matching”, some major assumptions are considered:

1. All joints of the dog legs are assumed as hinge joints because of the negligible angular changes in the third dimension.
2. The scapula is fixed in the body, so the joint of scapula is neglected.
3. Radius and Ulna are designed together as a link.
4. Tibia and Fibula are designed together as a link.

In “separating”, a locomotion cycle of BioDog is determined. This cycle covers a stance (contact with the ground) and swing (no contact with the ground) phases and each leg repeats its own cycle. Figure 4 and Figure 5 shows joint angles versus time graphs for, respectively, the walking and trotting where the “stance” and “swing” phases are considered for the left legs.

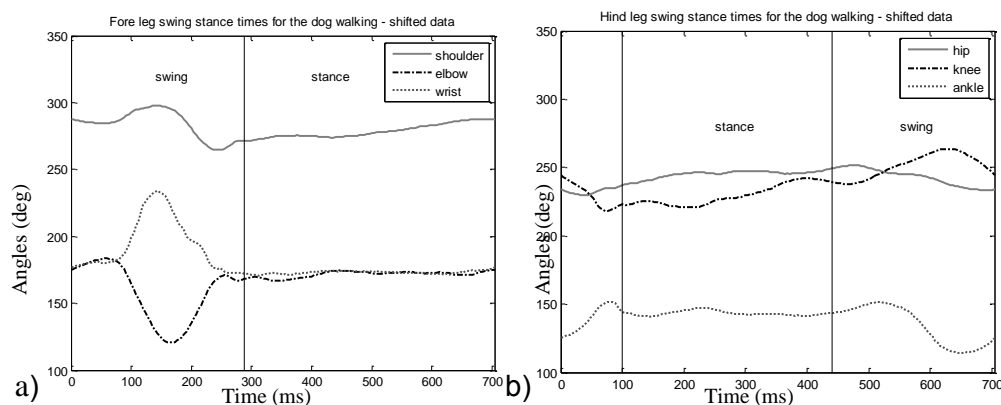


Figure 4. Walking locomotion cycle of the BioDog for a) fore leg b) hind leg.

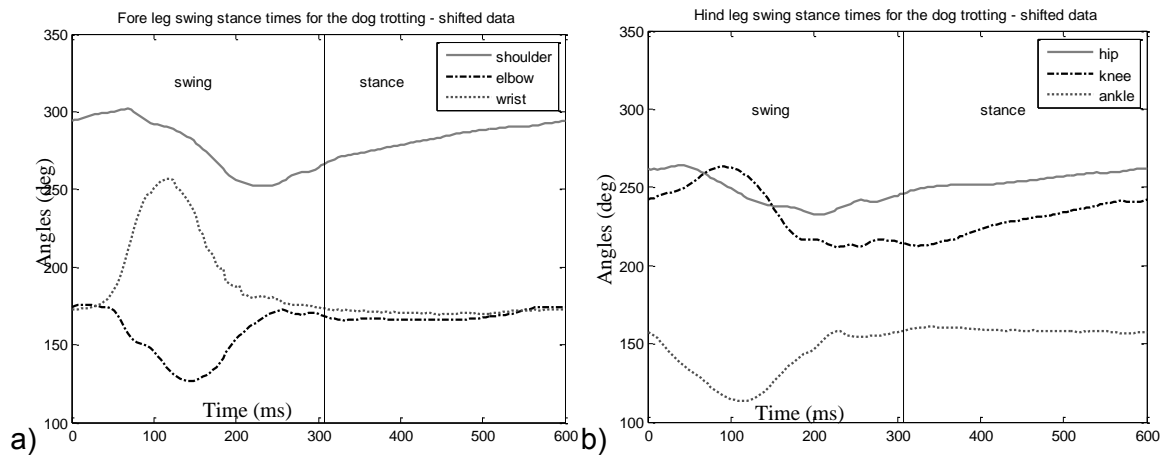


Figure 5. Trotting locomotion cycle of the BioDog for a) fore leg b) hind leg.

Biological systems are flexible systems, so they do not actually follow a locomotion cycle. In “modeling” sub-state, joint angles are switched linearly around the initial angle in order to complete the repeatable locomotion cycle for the BioDog. Thus, a synchronous motion is developed for the biorobot. Figure 4 and Figure 5 demonstrate the shifted joint angles.

If mathematical models for joint angles are required, curve fitting methods could be applied. In this case study, discrete data sets are used to drive the servo motors with an Arduino platform, so mathematical models of joint angles are not derived.

The “modeling” gives the behavior of the Terrier dog during the locomotion cycles of walking and trotting. The walking and trotting behavior in a locomotion cycle are shown in Figure 6 and Figure 7 where R and L show right and left legs and 1 and 2 symbolize fore and hind legs. Stance phases of each leg are represented by black ellipses.

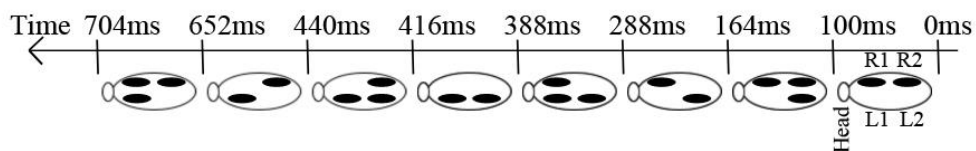


Figure 6 A walking cycle for the BioDog

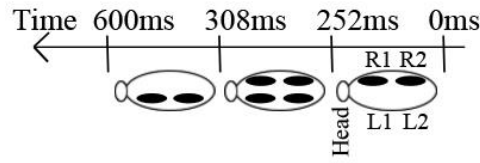


Figure 7 A trotting cycle for the BioDog

When the designer completes “modeling” sub-state, s/he starts “synchronizing”. In “synchronizing”, the left leg joint data set of the locomotion cycle is synchronized with the right legs, so the two-dimensional (2D) locomotion model is transformed into a three-dimensional (3D) model.

The first component of the output- *KBR* is *MorBR* as given in Equation 2 whose elements are given from Equation 3 to Equation 9. In Equation 7, *Fo* represents the form of a limb and the forms/structures of the BioDog.

$$\text{NuL} = \{4\} \quad (3)$$

$$\text{PaL} = \{\text{fore, hind}\} \quad (4)$$

$$\text{LoL}_{\text{fore}} = \{\text{humerus, radius, paw}\} \quad (5)$$

$$\text{LoL}_{\text{hind}} = \{\text{femur, tibia, paw}\} \quad (6)$$

$$\text{FoLb} = \{\text{Fo}_{\text{humerus}}, \text{Fo}_{\text{radius}}, \text{Fo}_{\text{forepaw}}, \text{Fo}_{\text{femur}}, \text{Fo}_{\text{tibia}}, \text{Fo}_{\text{hindpaw}}\} \quad (7)$$

$$\text{JoL} = \{\text{shoulder, elbow, wrist, hips, knee, ankle}\} \quad (8)$$

$$\text{ToJo} = \{\text{joints} = \text{hinge joints}\} \quad (9)$$

The second component of the *KBR* is *FuBR*. In the equation of the *FuBR* (Equation 10), dynamic models are based on joint angles for a locomotion cycle and they were given in Figure 4 and Figure 5.

$$\text{FuBR} = \{\text{walking} = 1 \text{ km/h speed, trotting} = 2 \text{ km/h,} \quad (10)$$

$$\text{dynamic model of walking, dynamic model of trotting}\}$$

*BeBR* is the last component of the *KBR*. *BeBR* is represented in Equation 11 where terms of leg combinations represent the swing and stance time combinations of the dog performed walking and trotting locomotion illustrated in Figure 6 and Figure 7.

BeBR = {no matching legs for walking, legs are matched and right legs  
are matched for trotting, walking leg combination, trotting leg  
combination} (11)

“Bioinspired transformation” step is implemented in six days. In twenty nine days, the concept design of the BioDog is completed. According to the concept of the biorobot (CBR), an initial prototype is produced to demonstrate the system feasibility. The BioDog prototype shown in Figure 8 simulates the walking and trotting behavior of a dog and these two modes can be switched with a remote control.

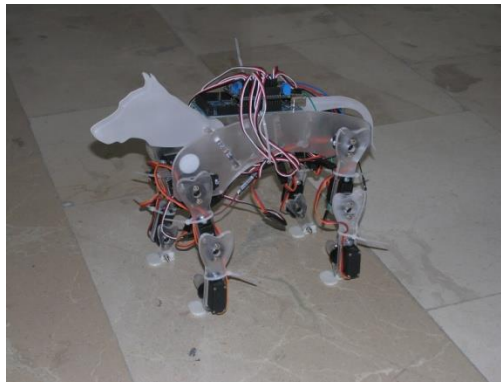


Figure 8. A view of the initial prototype of the BioDog

The BioDog was designed and a prototype robot is manufactured following the stated bioinspired transformation steps. The procedural details of the process are omitted in the manuscript. Testing of the robot to understand the scope and success of the bioinspired transformation and its discussion are left for further research.

## DISCUSSIONS AND CONCLUSIONS

Bioinspired Design (BID) is not a new process but it is a newly developed concept that underlines the necessity for powerful interaction between different fields of engineering and biology. The studies on BID raise especially two important key points; realistic representation of biological systems and clarified and well-planned analogical translation. In this paper, a suitable method for the analogical translation in between biological systems and biorobots is proposed. The translation is a key step of a new Bioinspired Conceptual Design (BICD) and it is called as bioinspired transformation. In the bioinspired transformation, knowledge about a biological system (KBS) is transformed into knowledge about a biorobot (KBR). Morphology, function and behavior are components of the knowledge. These components of



biological systems and biorobots are matched. This activity is supported by mathematical models. Thus, a clear and well-defined mapping in between biological and engineering domain is provided.

Envisaged future studies are;

- Systematic “scaling” is not considered in the transformation. The “scaling” for biorobots can be considered as a future work.
- If sufficient numbers of biological systems are analyzed and the knowledge about biological systems can be transformed into the engineering domain, a database about biological systems in the engineering domain can be created. Thus, without analyzing the biological systems, biorobots can be designed by use of the database.

## REFERENCES

1. **BioTrue, (2013)**, "An innovation in lens care inspired by the eye itself". <http://solution.biotrue.com/>, (Download Date: 19.11.2013).
2. **Burns, L. and Pook, M. D., (2010)**, "Tree joints: biomimetic insights for aerospace composite joints" In Proceedings of the 27th International Congress of the Aeronautical Sciences.
3. **Chakrabarti, A., (2007)**, "Research in Eng Design Creativity-Some Recent Findings" In Design Creativity Workshop for ICED 2007.
4. **Chiu, I. and Shu, L. H., (2004)**, "Natural language analysis for biomimetic design" In ASME 2004 International Design Engineering Technical Conferences and Computers and Information in Engineering Conference, pp. 99-107.
5. **Dynamics, B., (2012)**, "Changing Your Idea of What Robots Can Do". <http://www.bostondynamics.com>, (Download Date: 03.10.2012).
6. **Eroglu, A. K., (2013)**, "A Bioinspired Conceptual Design Methodology for Biorobots", in Modeling and Design of Engineering Systems (MODES) Ph.D. Program, ATILIM University, Ankara, Turkey.
7. **Eroglu, A. K., Erden, Z. and Erden, A., (2011)**, "Biological System Analysis in Bioinspired Conceptual Design (BICD) for Bioinspired Robots", Journal of Control Engineering and Applied Informatics, vol. 13, pp. 81-86.
8. **FESTO, (2011)**, "SmartBird- bird flight deciphered". [http://www.festo.com/cms/en\\_corp/11369.htm](http://www.festo.com/cms/en_corp/11369.htm), (Download Date: 21.02.2014).





9. **FESTO, (2012)**, "ExoHand – human-machine interaction".  
[http://www.festo.com/cms/en\\_corp/12713.htm](http://www.festo.com/cms/en_corp/12713.htm), (Download Date: 21.02.2014).
10. **Floreano, D. and Mattiussi, C., (2008)**, "Bio-inspired artificial intelligence: theories, methods, and technologies" The MIT Press.
11. **Gero, J. S. and Kannengiesser, U., (2007)**, "A function-behavior-structure ontology of processes", AI EDAM, vol. 21, pp. 379-391.
12. **Glier, M. W., McAdams, D. A. and Linsey, J. S., (2011)**, "Concepts in Biomimetic Design: Methods and Tools to Incorporate Into a Biomimetic Design Course", IDETC.
13. **Hargroves, K. and Smith, M., (2006)**, "Innovation inspired by nature: Biomimicry", Ecos 2006, pp. 27-29.
14. **Helms, M., Vattam, S. S. and Goel, A. K., (2009)**, "Biologically inspired design: process and products", Design Studies, vol. 30, pp. 606-622.
15. **Kitamura, Y., Koji, Y. and Mizoguchi, R., (2006)**, "An ontological model of device function: industrial deployment and lessons learned", Applied Ontology, vol. 1, pp. 237-262.
16. **Mak, T. and Shu, L., (2004)**, "Abstraction of biological analogies for design", CIRP Annals-Manufacturing Technology, vol. 53, pp. 117-120.
17. **Narahara, T., (2013)**, "Computer as a Tool for Creative Adaptation: Biologically Inspired Simulation for Architecture and Urban Design", Computation for Humanity: Information Technology to Advance Society, vol. 67.
18. **Nelson, B., Wilson, J. and Yen, J., (2009)**, "A study of biologically-inspired design as a context for enhancing student innovation" In Frontiers in Education Conference, 2009. FIE'09. 39th IEEE, pp. 1-5.
19. **Project, T. N. E., (2008)**, "Unit 3 - Biomimicry/Green Chemistry; Lecture 9: Biomimicry - Design Inspired by The nature". <http://www.naturaledgeproject.net/ESSPCLP-Principles and Practices in SD-Preliminaries3.aspx>, (Download Date: 26.02.2010).
20. **Sartori, J., Pal, U. and Chakrabarti, A., (2010)**, "A methodology for supporting "transfer" in biomimetic design", AI EDAM, vol. 24, pp. 483-506.
21. **Tsujimoto, K., Miura, S., Tsumaya, A., Nagai, Y., Chakrabarti, A. and Taura, T., (2008)**, "A method for creative behavioral design based on analogy and blending from natural things" In ASME 2008 International Design Engineering Technical Conferences and Computers and Information in Engineering Conference, pp. 801-810.





22. **Vattam, S., Helms, M. E. and Goel, A. K., (2007)**, "Biologically-inspired innovation in engineering design: a cognitive study". <http://hdl.handle.net/1853/14346>.
23. **Vincent, J. F. and Mann, D. L., (2002)**, "Systematic technology transfer from biology to engineering", Philosophical Transactions of the Royal Society of London. Series A: Mathematical, Physical and Engineering Sciences, vol. 360, pp. 159-173.
24. **Vukusic, P., (2010)**, "An Introduction to Bio-Inspired Design". [www.clspectrum.com/articleviewer.aspx?articleid=104164](http://www.clspectrum.com/articleviewer.aspx?articleid=104164), (Download Date: 29.05.2012).
25. **Wilson, J. O., (2008)**, "A Systematic Approach to Bio-Inspired Conceptual Design", in Mechanical Engineering, Georgia Institute of Technology.
26. **Wilson, J. O., Rosen, D., Nelson, B. A. and Yen, J., (2010)**, "The effects of biological examples in idea generation", Design Studies, vol. 31, pp. 169-186.
27. **Yen, J., Weissburg, M., Helms, M. and Goel, A., (2011)**, Biologically inspired design: a tool for interdisciplinary education, In Biomimetics: Nature-Based Innovation, ed. Bar-Cohen, Y., 332-360. New York: CRC Press/Taylor & Francis.



## DEVELOPMENT OF AN AUTONOMOUS LAWN MOWER

**Serkan ÇİÇEK**, *serkancicek@gmail.com*, Middle East Technical University, 06531, Ankara, Turkey

**E. İlhan KONUKSEVEN**, *konuk@metu.edu.tr*, Middle East Technical University, 06531, Ankara, Turkey

**A. Buğra KOKU**, *kbugra@metu.edu.tr*, Middle East Technical University, 06531, Ankara, Turkey

### ABSTRACT

Starting from early 2000's domestic robots have been taking their place in our daily lives. Today, numerous products are globally available on the domestic robotics market. Among many domestic robot types, robotic cleaners and lawn mowers take the lead in this competition, with their success for reducing undesired house chores. It is becoming more and more crucial for developers to offer best navigation performance with the lowest price in the market.

In this study, a differentially driven Autonomous Lawn Mower (ALM) with an enhanced position correction technique is developed. In this technique, odometric error compensation is applied, based on the identification of mowed and non-mowed lawn areas.

After completion of the design, manufacturing and system integration tasks, performance tests have also been performed. These physical indoor and outdoor tests have been performed on different terrains with various coverage patterns.

**Keywords:** Autonomous Lawn Mower, Product Development, Industrial Design, Odometric Error Compensation, Coverage Performance

### 1. INTRODUCTION

Until today, million units of domestic robots have already been sold in the market. One of the most popular products in house chores is ALM. ALMs take the second biggest share after autonomous vacuum cleaners globally. Approximately 10 main ALM manufacturers, with more than 25 products, are available on the global market today.



All of these commercial ALMs are internal battery powered. Almost all of them have 2 DC motors for differential drive and 2 additional castor wheels for balance. In order to lower the manufacturing costs, almost all of the body components are made by plastic materials with injection molding or vacuum forming processes. Furthermore, all of the products use mulching technique for lawn mowing. On contrary to the conventional man-powered lawn mowers, most of the ALMs do not have a single large cutting blade. Instead, they use multiple smaller blades for this purpose. The cutting height is manually adjustable in all ALMs. In average, lawn height can be kept around 20-100 mm, depending on the ALM model.

The navigation techniques of all the commercial ALMs are quite similar. They all have a charging station from where they start their operations. They have no expensive visionary sensors like LIDARs or cameras to inspect the environment. Even though some of them use inertial sensors (i.e. accelerometers or digital gyroscopes) to make the localization more accurate, they all operate “blind” with their odometric wheel encoders (i.e. they count encoder ticks for calculating traveled distances). This lack of “wisdom” causes the robots to operate mainly on random patterns instead of operating on predefined geometrical patterns.

In order to work within the desired area, all of the commercial ALMs use the same type of method. This method consists of a perimeter wire and an inductive sensor. A perimeter wire is simply a harmless low-current passing wire. The user connects both ends of this wire to the charging station to obtain a closed current loop. The wire is buried only a few millimeters deep in the ground along the perimeter of the desired area. During their operations, robots sense the borders with the aid of the inductive sensors located at the bottom of their body.

Static or dynamic obstacle avoidance is achieved by using ultrasonic (US) sensors or bumper switches in all commercial products.

ALM technology has proceeded within the last decade, but there’s still a lot to do in order to make these robots more intelligent and more affordable.

## **2. SYSTEM DEVELOPMENT**

This study mainly presents the design, development, manufacturing and test phases for a real ALM. All these design phases are completed and a physical working prototype is obtained, which has a potential to be turned into a commercial product after some modifications.

A real product must satisfy the real environmental and economic considerations within the sector. Generally, seven main properties can be expected from an ALM in a customer’s perspective. These properties can be listed in the order of priority: an ALM must mow efficiently with high quality cutting, be mobile, be autonomous, be affordable, move in the desired area,



avoid obstacles, and visually has to be attractive. These properties are the requirements and considered as the design criteria in this study.

Mowing efficiently with quality and being visually attractive are comparably easy-to-do tasks. The remaining requirements can be combined and defined as affordable autonomous mobility. The main evaluation metric for autonomous mobility is the navigation performance. Consequently, the primary problem in this work can be defined as autonomous outdoor navigation.

### **Concept Selection**

Lawn Mowing Technique: All of the commercial ALMs use mulching technique, which is an agricultural term for lawn mowing. In mulching, the grass is cut into very small clippings that are buried in the roots of the lawn. They decompose and act like a natural fertilizer in time. This technique results in a healthier and better-looking lawn. The major advantage of this technique is that it eliminates the need to collect and remove the lawn clippings.

In a conventional man-powered lawn mower that does not use mulching, lawn clippings are collected in a basket. The volume of a conventional basket is about 40 L. It can carry the clippings of an approximately 50 m<sup>2</sup> lawn yard. After mowing this area, the user must empty the basket. The mass of a basket full of lawn clippings is about 6 kg. It is found inconvenient for an ALM to collect lawn clippings since they add extra weight to the system, which means a decrease on the operation time inefficiently. Moreover, the main idea of autonomous lawn mowing is regaining the time spent on lawn mowing to the user. This goal cannot be achieved if the user periodically empties the lawn basket of a robot.

Therefore, mulching technique is selected for lawn mowing in this study. For grass cutting, a single cutting blade with multiple cutting edges is used for energy efficiency and easy-cleaning purposes.

Mobility: Most of the conventional lawn mowers use internal combustion engines (ICE) for their cutting systems. ICEs can create large amounts of energy, however they are inefficient and they have high running costs for this type of relatively-low-power-required applications. The user must also refill the fuel almost before every operation, which is an undesired task.

Man-powered lawn mowers that use electricity for “mower motor” usually do not use internal batteries. Electric is supplied from an external source by using a power cable. This cable always rambles to the mower or to the user, which is also undesired.

Considering mobility, using an internal source of energy is almost compulsory. Since the desired mowing area is limited, internal batteries are decided to be used in the proposed design. Given that the mowing system will be electrically powered, the driving mechanism is

also preferred to be fed by the same source. Ni-Mh batteries are used since they are affordable compared to LI-ION or LI-PO batteries.

Autonomous Outdoor Navigation Technique: Almost all the commercial ALMs in the market operate randomly. The major disadvantage of operating with random patterns is that the robot's coverage performance is random. Considering ALMs, a randomly operating type robot may not be able to mow some specific regions of the garden even if the garden is geometrically too simple to cover. Operating with this type of a coverage algorithm is not energy-efficient. Regarding these disadvantages, instant localization is found to be compulsory, even if the robot operates randomly.

Considering GPS as a localization technique, it is relatively inaccurate. Since some improved techniques like dGPS and dGPS-RTK can locate the position of the receiver accurately, they are extremely expensive for such a product. Satellite navigation is also found to be disadvantageous and expensive for such a system.

Another trilateration/multilateration technique, beacon localization can be considered, which performs well indoors. However, it is not suitable for outdoor applications due to the complexity of the application of this system for comparably large regions. It is inconvenient to install beacons for every garden, even if the required number of beacons is low. This means the method becomes more expensive and besides needs too much effort. Consequently, beacon localization has certain disadvantages.

Landmark-Based navigation brings some difficulties with itself inherently. For sole localization, exact positions of the external references must be known. It is almost impossible to apply this method to every single garden. LIDARs can be very useful for such an application, however commercial LIDARs are extremely expensive.

Path guidance methods are also found useless, since it is nearly impossible to create prior paths for every garden.

In this study, in order to maintain the simplicity, odometric dead-reckoning method is used for localization. Although the odometric dead-reckoning method is vulnerable to inevitable slippage-based error deposition, it is cheap and simple. In our case, coverage performance is more important than localization accuracy. In order to increase the coverage performance of the robot, a novel enhancement technique for position correction is proposed. The key idea in this method is to determine the mowed and non-mowed areas using IR switch sensors.

Bordering Technique: Considering the gardens as the field of operation, all of them are unique regarding their geometry and fencing. Therefore, it is found to be necessary to utilize a generic bordering technique for the ALM operation. Using the perimeter wire seems to be logical in this manner. In this technique, a low current passing wire is buried only a few millimeters deep in

the ground. The current (i.e. the magnetic field) on the wire can be detected by the inductive sensors located at the bottom of the robot. This technique is decided to be used for bordering unknown environments (i.e. operation fields) in this work.

**Obstacle Avoidance Technique:** Every single garden may have many static or dynamic obstacles. In order not to collide with these obstacles, some “sensing” equipment such as infrared (IR) sensors, US sensors, LIDARs, RADARs, etc. can be used. LIDAR and RADAR sensors are highly accurate, but they are extremely expensive for our purpose. IR sensors are quite cheap but they are incapable of detecting transparent obstacles, since the infrared beams can pass through and cannot be reflected back from the medium. In this study, ultrasonic sensors, which detect transparent and non-transparent mediums, are decided to be used for obstacle avoidance.

**Visual Attraction:** All commercial ALMs are machine-looking robots that many people can find unattractive. In this study, esthetic concerns played an important role in the design procedure. It is aimed to produce a visually appealing and attractive robot. Since the ALM is planned to be operate mainly in domestic gardens, a pet-like shape is given to the robot. In order to emphasize its fast operation, and due to its best fitting to a grass area, the robot is decided to be rabbit-shaped.

## Hardware Architecture

Selection of major hardware components of the ALM and their selection criteria are briefly presented in this section. These selections are important since they directly affect all design phases and the resultant performance of the system. Functionality, availability and price are chosen as the main considerations for all hardware selections.

**Drive Motors:** It has been stated that two differentially driven DC motors are decided to be used for robot’s motion. For selection of these “drive motors”; torque, power and speed requirements have been calculated in advance. Figure 1 represents the free body diagram of the system.

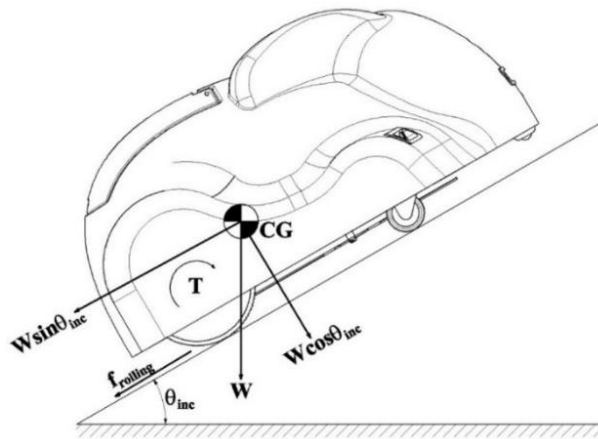


Figure 1. Free Body Diagram of the Autonomous Lawn Mower

Assuming that there is no slippage at the beginning of the motion, the following calculations are made for a single wheel to satisfy the requirements considering the two-wheeled system.

Table 1. Parameters Used for Drive Motor Selection

Parameter	Value
Mass, $m$ [kg]	30.0
Rolling Resistance, $C_r$	0.1
Maximum Robot Velocity for Inclined Surface, $V_{max,flat}$ [km/h]	3.6
Maximum Inclination, $\theta_{inc}$ [deg]	10.0
Drive Wheel Diameter, $D$ [mm]	155.0

For the given parameters in Table 1; the minimum torque, power, and angular velocity requirements are calculated as;

$$T_{min} = 3.1 \text{ Nm} \quad (1)$$

$$P_{min} = 33.37 \text{ W} \quad (2)$$

$$\omega_{min} = 123.28 \text{ rpm} \quad (3)$$

Due to relatively high torque requirement, a gear-motor is decided to be used for the driveline. The selected gear-motor (Intecno EC035.240 + P42\_2\_25) has a rated power of 35 W, a rated torque of 3.38 Nm, and a rotational speed of 140 rpm. It uses 24 V DC power, and allows 4 A peak current with 2.6 A rated. Also, it has a 1:25 ratio planetary gearbox on its head.

**Mower Motor:** It is hard to determine the required power and torque for a lawn mowing process since the shear strength of a grassy area depends on various parameters. For that purpose, some product comparisons have been made on both conventional and autonomous lawn mowers. At the end, it is concluded that a minimum rotational speed of 2500 rpm is sufficient for lawn mowing operation.

Selected “mower motor” (Kormas 671-143-23) has a rated power of 140 W, and a rotational speed of 2800 rpm. It uses 24 V DC power, and allows 7 A peak current with 3 A rated.

**Motor Drivers:** Two “drive motors” and one “mower motor” with their drivers are used in the system. The selected 24 V DC “drive motors” can consume up to 4 A per motor. A sophisticated and cheap driver is chosen to drive both “drive motors”. Similarly, a reliable, low cost motor driver has been chosen to drive the “mower motor”.

The selected “drive motor” driver (Dimension Engineering Sabertooth 2x12A) uses 6 - 24 V DC power, and allows continuous output current up to 12 A per motor. Selected “mower motor” driver (Pololu 24v12) uses 24 V DC, and allows continuous output current up to 12 A.

**Batteries:** The desired operation time for an ALM is thought to be about 1 hour. Except the “drive” and “mower” motors, the power consumption is found to be negligible for the





determination of the power budget. 12 V Ni-Mh type battery (Yuasa NP 7-12) with continuous output current 7 A is selected.

Encoders: One of the major reasons for the selection of specified “drive motor” is its integrated encoder, which is used for odometric calculations. Two identical optical, hollow-shaft type, quadrature wheel encoders (Intecno SE22) are used in the system. The selected encoder has a resolution of 300 counts per revolution (CPR).

Ultrasonic Sensors: For obstacle avoidance, US sensor is used since it is relatively inexpensive and accurate. The selected sensor (Parallax PING) is a US distance sensor, which provides precise, non-contact distance measurements from about 2 cm to 3 m. The PING sensor works by transmitting an ultrasonic burst and providing an output pulse that corresponds to the time required for the burst echo to return to the sensor. By measuring the echo pulse width, the distance to target can easily be calculated. It is very easy to connect to microcontrollers requiring only one I/O pin for both TX and RX.

Infrared Sensors: Infrared sensors are decided to be used for the fall-off and the tilt-over detection. For this purpose, Sharp GP2Y0D810Z0F model IR sensor is chosen. It is a distance measuring sensor unit composed of an integrated combination of PD (photo diode), IRED (infrared emitting diode) and signal processing circuits. Its range is 5-100 mm.

Infrared Switches: IR switches are decided to be used for identification of mowed and non-mowed areas within the garden. For this purpose the SHARP GP1A57HRJ00F model IR switch sensor is chosen. It is a standard transmissive photo-interrupter with an opposing emitter and detector, providing non-contact sensing. The emitter and detectors are inserted in a case, resulting in a through-hole design, which is suitable for this type of application.

Controllers: The entire control algorithm developed for this prototype robot is run on the Arduino Due. Arduino is a single-board microcontroller used for building electronics projects. It consists of a physical programmable circuit board and an Integrated Development Environment (IDE), used to write and upload the code to the physical board.

Using a single controller, both timer and encoder interrupts are handled, however it is realized that nested interrupts occur in the system which cause missing ticks from the encoders. The software architecture needs a main timer interrupt routine for all the process to run successfully. Therefore, it is planned to handle encoder tick -hardware- interrupts by a separate controller.

## **Mechanical Design**

This section of the study reveals the mechanical design, which is finalized after numerous revisions. The key components and subsystems are explained in detail below.



**Overview and General Dimensions:** Functionality and visual perfection are the main considerations taken during the mechanical design process of the ALM. It is also intended to minimize bounding box as much as possible without affecting the desired functionality and visibility.

As a result, the outer skin, which acts as a cover for the main body and interior components, is designed as a rabbit shape. All the outer dimensions of the ALM are intended to be kept lower from the rivals. The finalized mechanical design overview and the major dimensions are given in Figure 2 and Figure 3, respectively.



Figure 2. Overview of the Mechanical Design

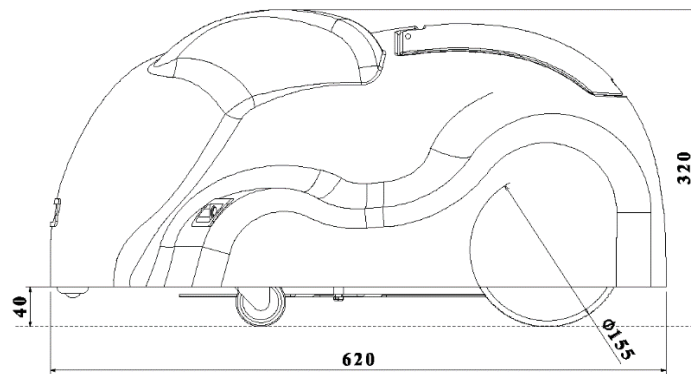


Figure 3. Main Dimensions

**External Design and Layout:** The external view of the ALM is intended to be kept as lean as possible. The layout of external components can be seen in Figure 4.

The outer cover mainly acts as a water and dust proof cover for internal components. In order to lower the manufacturing costs, this cover is decided to be made via vacuum forming process using polyethylene (PE) plastic material. Therefore, no negative slopes exist in any curvature of the design.

The US sensors are assembled on the outer cover using their own enclosures. Also a hinged rear-cap is designed to protect the robot-human physical interface from water and dust. Rear-cap and US sensor enclosures are made by a lightweight plastic, Delrin.

**Wheel Design:** The wheel diameter plays an important role for the trade-off between torque and drive speed to satisfy the desired design requirements. The outer diameter for the drive wheels is chosen as 155 mm, which satisfies both requirements at the same time.

The main threat for an odometry-based robot is the slippage. In order to decrease the potential slippage, drive wheels are coated with a synthetic rubber material, which increases the friction coefficient between wheels and the ground.

In order to balance the weight distribution, two standard castor wheels are placed in front of the robot. Moreover, a spherical wheel is placed in front of the robot in order to provide robot's first ground contact through this wheel.

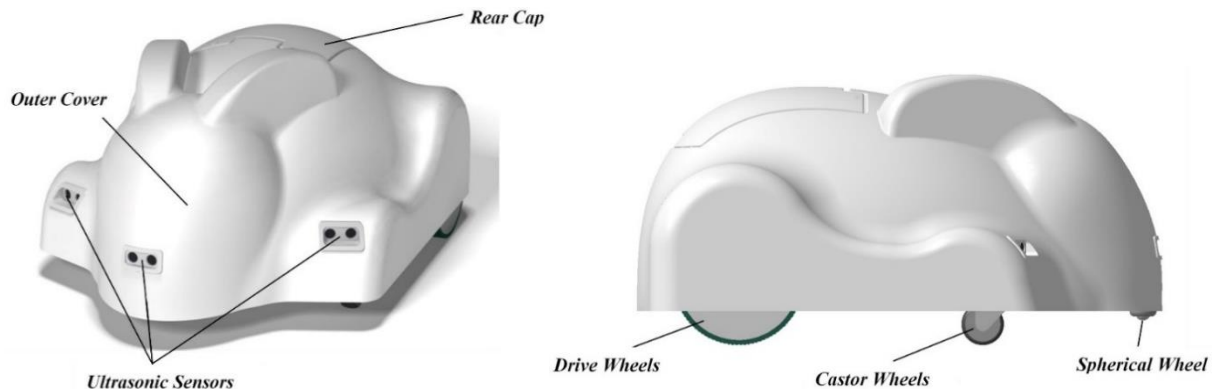


Figure 4. External Layout (Left) and Wheel Design (Right)

Internal Design and Layout: The gear-motors are assembled using a bracket, which is placed on the rear of the main body and attached to the drive wheels without any additional transmission. Sheet metal wheel covers have also been placed on both wheels in order to prevent the particles to enter the robot interior. Both of the wheel covers and “drive motor” brackets are designed to be aluminum.

All electronics are located on the plate above the “drive motors” in order to use this dead-volume efficiently. An enclosure with a cap is designed to protect electronics from dust.

“Mower motor” and the cutting blades are placed as close as possible to the front region of the main body to make the mowing operation more efficient.

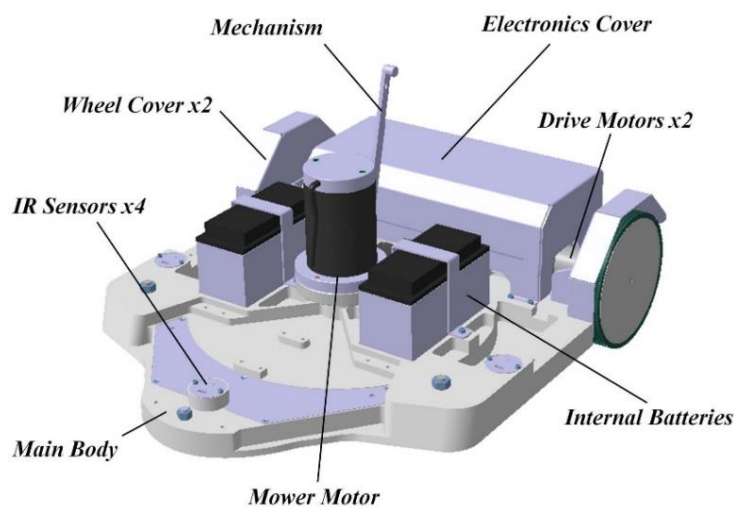


Figure 5. Internal Layout

In order to move the center of mass to the rear side of the robot the internal Ni-Mh batteries are placed besides the "mower motor" using aluminum brackets.

Mowing System Design: The design of the mowing system and its components is critical since the actual purpose of the robot is lawn mowing. Mowing system design is given in Figure 6.

The mowing system is mainly composed of a "mower motor" and a cutting blade. A comparably bigger, single blade has been decided to be used. The cutting blade has four cutting edges sharpened from both sides. Steel (St37) is chosen as the blade material for strength purposes.

There is no reduction or transmission between the "mower motor" and the cutting blade since the torque requirement is negligible compared to the angular velocity requirement. The motor and the blade is aligned by using a shaft. This blade shaft is mounted in a motor holder by using a ball bearing and a linear bearing. The blade shaft material is chosen as stainless steel.

The reason for using linear bearing comes from the requirement of cutting height adjustment for lawn mowers, whether they are autonomous or not. As given in Figure 6, a lever arm is designed and hinged onto the "mower motor" holder to position whole mowing mechanism to the desired cutting height. An existing housing for the lever arm is assembled on the outer cover.

It is intended to move whole height adjustment mechanism by a finger movement. Therefore a finger handle is designed and mounted on the top of the lever arm. It actually stays out of the outer cover, inside the rear cap. Also a balance arm and torsion bars have been designed for distributing mowing system weights evenly, so that the required pulling force is decreased. The mechanism parts are made of aluminum.

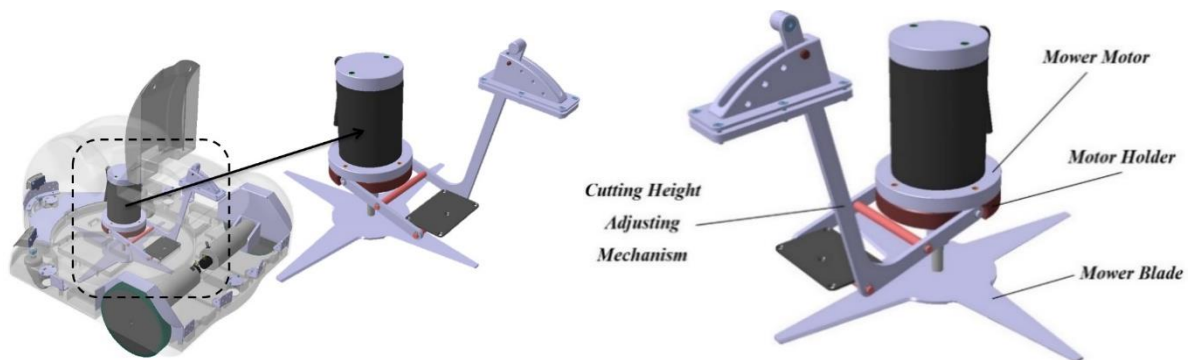


Figure 6. Overview (Left) and Detailed View of Mowing System (Right)

With the help of the finger handle and the mechanism, the cutting height (i.e. the height between the cutting blade and the ground surface) can be adjusted from 30 mm to 60 mm. Adjustable cutting height range (30 mm) is divided into 4 segments. The use of finger handle for adjusting the mechanism has an important necessity i.e. the whole mechanism must be designed in such a way that a standard user can easily generate the amount of force required



to pull the handle by his/her finger. For this requirement, a Multi Body Dynamics analysis was performed. It is calculated that a minimum of 22.3 N pulling force can trigger the mechanism and 27.9 N is required to lift whole mowing system 30 mm above (i.e. to insert the lock-pin to the last hole). Finally, it was concluded that 27.9 N force can easily be generated by a standard user's finger and thereby the mowing system mechanical design was successfully completed.

### **3. MANUFACTURING AND SYSTEM INTEGRATION**

#### **Manufacturing**

The external cover of the ALM is designed to be made by vacuum forming process. Vacuum forming is a specific form of thermoforming, in which a plastic sheet is heated to the forming temperature and stretched over a concave (female) or convex (male) mold. Afterwards, the air between the mold and the sheet is vacuumed onto the surface of the mold to shape the plastic precisely. In this study, a wooden mold was manufactured by conventional 3-axis CNC milling for this purpose.

Except for the outer cover, all of the mechanical components of the ALM are produced by conventional manufacturing methods for this first prototype. The main body, rear cap and US sensor enclosures are produced by Delrin plastic material, by 3-axis CNC milling.

All of the solid aluminum components are also produced by CNC milling and/or turning. The sheet metal aluminum parts have been laser machined, press-formed and corner welded. Besides aluminum sheet metal parts, welding is not used for assembling any of the system components. Therefore, all mechanical components are modular as desired.

After manufacturing, all aluminum parts are coated with white colored eloxal-coating. Drive wheels and cutting blades are protected from oxidation by hot dip galvanization.

#### **System Integration**

After the completion of manufacturing processes, the mechanical body is assembled first. Necessary electromechanical hardware is placed on the body in advance. "Drive motors", drive wheels, idle wheels, "mower motor", cutting height adjustment mechanism, IR sensors and necessary covers are mounted onto the main body by using bolted connections.

The external components of the cutting height adjustment mechanism are mounted onto the outer cover afterwards. Then, US sensors are placed to their locations on the outer cover.



Figure 7. Final Assembly

After the completion of the integration of mechanical subsystems and sensors, the outer cover is bolted to the main body. Afterwards, the cutting blade is assembled and fixed by using its particular lock-pin. Integration of all electronic components have been completed by using a reasonable harness structure for a prototype. The final assembly of the product with all components is presented in Figure 7.

#### 4. TESTING

Before all performance tests, both unit and system level functionality tests have been completed. The functionality of all hardware and software are proved.

##### Test Scenarios and Aspects

The main aspect of physical testing is to determine coverage performance of the ALM for different geometrical patterns and for different terrain conditions. For this purpose, some major geometrical patterns like rectangular inward spiral, parallel swath and random patterns have been executed on different terrain configurations for indoor and outdoor tests.

In indoor tests, it is mainly aimed to determine the deviation from the desired trajectory, amount of slippage and corresponding coverage percentage for the ALM. Indoor tests are also divided into two subgroups. They are performed on flat parquet floor and on flat synthetic grass. For each coverage patterns, operation completion time and coverage percentage is calculated and compared.

After determining response characteristics of the ALM for different terrains and patterns in indoor environment, the last set of tests are executed on outdoor grass terrain. Although synthetic grass terrain simulates the real grass terrain behavior closely, outdoor environment tests reveal the actual operational behavior of the robot.



The crucial part of the testing procedure is also done on outdoor grass terrain, in which the sole odometric navigation and integrated position correction techniques are compared. The inner swaths start after many rotations in rectangular inward spiral pattern in which rotation errors depose cumulatively. Therefore, for this comparison, only the parallel swath pattern is found logical. These outdoor comparisons are made lengthwise and widthwise of mowing areas.

### **Test Setup**

In order to evaluate the performance of the robot, navigating with different techniques for varying environments, a basic, generic test setup has been built. Simply, a camera was placed at the top-center of the test areas for both indoor and outdoor tests. Its maximum field of view dimensions have been taken as the borders of mowing area. The dimensions of borders are 295 x 162.5 cm<sup>2</sup>, which corresponds to an area of approximately 5 m<sup>2</sup>.

### **Data Acquisition and Post Processing**

More than 30 tests were accomplished for indoor and outdoor environments. Within these tests, the odometric data of encoders are collected from the controller's serial port and from the robot motion recorded by a camera. Since the camera naturally has an optical distortion, post processing has also been made to make raw video data meaningful. By using an available software, recordings are optically compensated to obtain the actual trajectory.

Finally, the actual trajectories are stroked by the width of the cutting blade. The coverage percentage is calculated by determination of the ratio of mowed and non-mowed areas.

### **Tests**

Indoor tests are done for flat parquet and synthetic grass terrains with predefined patterns; Rectangular Inward Spiral, Widthwise and Lengthwise Parallel Swaths, and Random.

In outdoor tests, it is only aimed to reveal the differences in autonomous navigation behavior of sole odometry and proposed enhancement technique. In order to determine odometric navigation enhancement, two sets of tests are performed. On a decent grass terrain, Widthwise and Lengthwise Parallel Swath Pattern coverage operations are performed several times with and without IR position correction mechanism.

### **Results**

In the physical testing phase of the development procedure; actual response of the robot, its possible improvements and overall design success are investigated by indoor and outdoor tests. The operation completion time and coverage percentage results for indoor and outdoor tests, sorted according to terrain and coverage pattern types are given in Table 2 and Table 3.





Table 2. Indoor Test Results

Indoor Tests		Operation Completion Time	Coverage Percentage
Parquet Flat Floor Tests	Rec. Inw. Spiral	2 min	99.18 %
	Wid. Par. Swath	2 min 30 sec	98.03 %
	Len. Par. Swath	2 min	99.53 %
	Random (Ave.)	2 min 30 sec (Terminated)	64.04 %
Synthetic Grass Tests	Rec. Inw. Spiral	2 min 5 sec	89.25 %
	Wid. Par. Swath	2 min 37 sec	89.40 %
	Len. Par. Swath	2 min	69.35 %
	Random (Ave.)	2 min 37 sec (Terminated)	58.26 %

Table 3. Outdoor Test Results

Indoor Tests		Operation Completion Time	Coverage Percentage
Sole Odometry	Wid. Par. Swath	2 min 34 sec	90.26 %
	Len. Par. Swath	2 min	70.75 %
Enhanced Technique	Wid. Par. Swath	2 min 36 sec	92.43 %
	Len. Par. Swath	2 min 1 sec	82.03 %

## 5. CONCLUSION

In this study, it is mainly aimed to build an affordable ALM, which can assure the necessities expected from a commercial product. Major objectives of an ALM can be stated as leanness and simplicity, while assuring the quality and performance. With these requirements, an ALM was sketched, designed, optimized, manufactured and assembled. All mechanical design, software development and system integration tasks are completed from scratch.

Functionality, reliability and visual quality are determined as primary aspects for the mechanical design of the ALM. An unconventional mowing method, mulching is selected in order to cohere with the concept of autonomy and for energy efficiency. In addition, differential drive steering system for the robot is found to be advantageous for mowing outdoors.

In order to reduce the overall cost of the system, navigation techniques which require expensive hardware and high computational power are avoided. Instead, it is shown that a minimalist approach with limited hardware can also provide adequate results for outdoor navigation. Although it is vulnerable to the inevitable slippage-based error deposition, odometric dead-reckoning method is selected since it is cheap and simple.

The major enhancement made for increasing the outdoor navigation performance is to utilize IR switches, which are mounted at the bottom of the robot. The slippage-based error deposition is aimed to be compensated by the identification of mowed and non-mowed lawn areas.

After manufacturing and system integration, many indoor and outdoor tests are performed in order to determine navigation characteristics of the robot. The functionality and the success of



the control architecture of the robot are proved by indoor tests. Moreover, various coverage patterns are tested and their superiorities are revealed.

The proposed enhancement is tested in outdoor grass terrain. It is proved that the proposed position correction technique improves the outdoor coverage performance up to 16%. The overall coverage with this technique is calculated above 80% for lengthwise parallel swath pattern. Coverage percentages above 80% are generally considered as a successful operation for ALMs. It can be concluded that the developed ALM accomplished its mission.

Additionally, it has been shown that the major performance criterion for an ALM -coverage performance- can be satisfied with a low cost hardware. Two IR switches cost below 10 USD, which is negligible when compared to sophisticated sensors.

As a future work, mechanic and electronic hardware can be further developed. The body and the mowing system designs can be improved to sustain coverage performance over more rugged and slippery terrains. Also, the position correction method which uses IR switches may be improved by considering different types of sensors as a future work.

In conclusion, the mechanical, electrical and software designs of the ALM is succeeded for both indoor and outdoor terrains.

## REFERENCES

1. **Çiçek, S., (2014)**, "Development of an Autonomous Lawn Mower with Minimalist Hardware Approach", M.Sc. Thesis, METU Mech. Eng. Dept., Ankara.
2. **Arkin, R. C., (1998)**, Behavior Based Robotics, MIT Press, Cambridge, MA.
3. **Borenstein, J., (1995)**, "Internal Correction of Dead-reckoning Errors with A Dual-drive Compliant Linkage Mobile Robot", Journal of Robotic Systems, Vol.12, No.4, pp 257-273.
4. **Etkin, B., (1971)**, "Dynamics of Atmospheric Flight, Stability and Control", Wiley, pp 117-118.
5. **Everett, H. R., (1995)**, "Sensors for Mobile Robots", A K Peters Ltd., Wellesley, MA.
6. **Borenstein, J., Feng, L. (1996)**, "Measurement and Correction of Systematic Odometry Errors in Mobile Robots", IEEE Transactions Robotics and Automation, Vol.12, pp 869-880.
7. **Borenstein, J., Everett, H., Feng, L., Wehe, D., (1997)**, "Mobile Robot Positioning: Sensors and Techniques", Journal of Robotic Systems 14(4): pp 231-249.





8. **Borenstein, J., Koren, Y., (1987)**, “Motion Control Analysis of a Mobile Robot”, Transactions of ASME, Journal of Dynamics, Measurement and Control, Vol.109, No.2, pp 73-79.
9. **Kuhnert, K. D., Seemann, W., (2007)**, “Design and Realization of the Highly Modular and Robust Autonomous Mobile Outdoor Robot Amor”, Robotics and Applications and Telematics
10. **Martinelli, A., (2002)**, “The Odometry Error of a Mobile Robot with a Synchronous Drive System”, IEEE Transactions on Robotics and Automation, pp 399-405.
11. **Spyridon, M. G., Eleftheria, M., (2012)**, “Classification of Domestic Robots”
12. **Nilsson, N. J., (1984)**, “Shakey the Robot”, Technical Note 323. AI Center, SRI International, 333 Ravenswood Ave., Menlo Park, CA 94025
13. **Siegwart, R., Nourbakhsh, I. R., (2004)**, “Introduction to Autonomous Mobile Robots”, MIT Press, pp 90-114.
14. **Ogata K., (2009)**, “Modern Control Engineering”, Prentice Hall



## DESIGN OF A HUMANOID ROBOT SPINE CONSTRUCTED OF ASYMMETRIC PARALLEL MECHANISM MODULES

**Ekim YURTSEVER**, *ekimyurtsever@gmail.com* Istanbul Technical University, 34437, Istanbul, Turkey

**Şeniz ERTUĞRUL**, *seniz@itu.edu.tr* Istanbul Technical University, 34437, Istanbul, Turkey

### ABSTRACT

Conventional mechanical applications in humanoid robots cause non-human-like and discontinuous motion. In this work, to create human-like motions, a modular structure where every module can move relative to the preceding or the following module has been suggested. A novel parallel mechanism as a module has been designed for this purpose. Parallel mechanisms are attached to each other as modules to constitute the spine. In addition to the continuous movement, the mechanism is able to maintain its position when the motors cease to work, which makes the system mechanically stable. In simulations, the new concept design achieved to mimic human spine movements successfully. The modular spine like mechanism is designed as a part of a master thesis to be applied for an ongoing humanoid project in Istanbul Technical University, Faculty of Mechanical Engineering, System Dynamics and Control Laboratory.

**Keywords:** Humanoid trunk and spine design, Modular parallel mechanisms, asymmetric parallel mechanism

### 1. INTRODUCTION

In recent decades, various types of humanoid robots with the goal of acting like human beings have been developed by many research groups. The earlier humanoids which resemble the human form were constructed as biped walkers with limbs as legs and arms and a torso to carry the loads and components required for robot operations. The conventional solutions for limb and body structures consist of dedicated motors for each degree of freedom axis, which establishes a serial open loop kinematic chain. While a simple approach like this enabled the control of the robot as an achievable task, the lack of fluidity in the motions caused by low degree of freedoms and serial kinematic chains made the movements of the robots discontinuous and not human-like. Until recent years the

importance of the mechanical aspect of mimicking human skeletal and muscular structures has been neglected. However, robots like Robota [Roos, Guenter, Guignard and Billard, 2006], Kotaro [Mizuuchi et al., 2006], Kojiro [Mizuuchi et al., 2007] and Kenzoh [Osada, Ito, Nakanishi, and Inaba, 2010] introduced new approaches to mechanical design of limbs and body. Furthermore, the works of these researchers showed the validity of the applications of human-like artificial skeletal and muscular structures in robotics.

In this paper, the design of a torso will be discussed, as the motion of the torso is a crucial element to achieve human-like movements in robots and also the trunk is the main part where all other limbs are connected. The design requirements of the torso may summarized as below:

- 1) The design must allow fluid, human-like motions
- 2) Nonlinear behavior characteristics must be avoided in order to achieve the model and controllability of the system in future works
- 3) The structure must be able to hold its position in any given state without help from motors
- 4) The structure should provide space and carry equipments for other parts

Conventional designs like Honda's ASIMO [Sakagami et al., 2002] fail to create human-like motions while the mentioned Kojiro and Kenzoh achieves this criteria but fails to avoid nonlinear behavior and maintain mechanical stability.

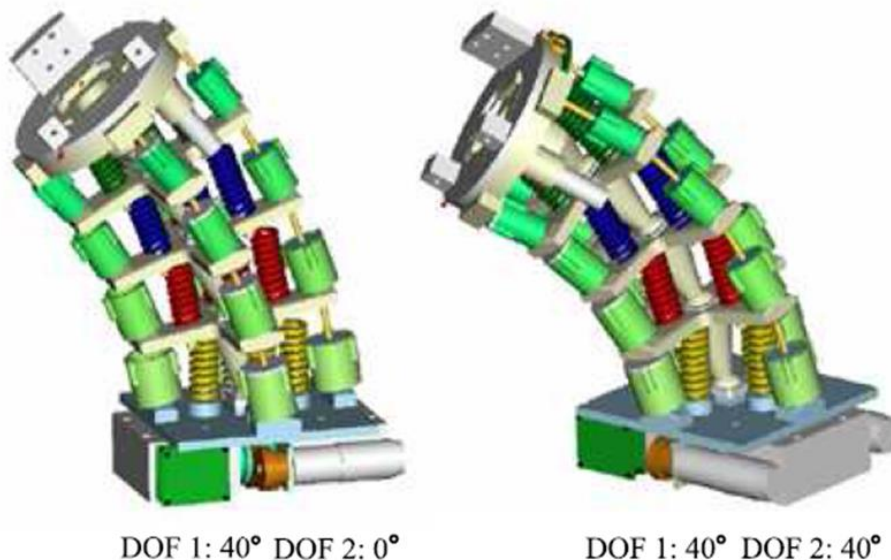


Figure 1. Spine structure of ROBOTA [Roos et al, 2006]

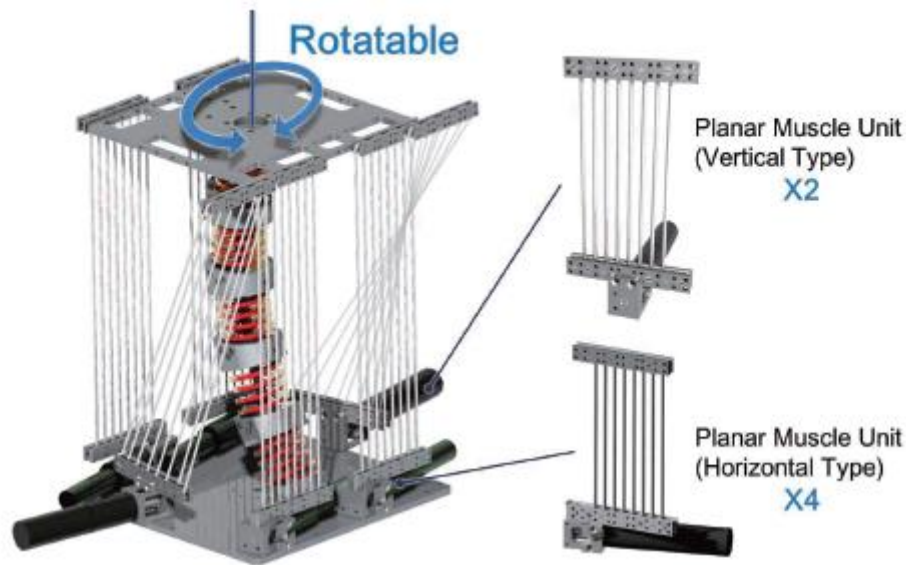


Figure 2. Artificial Spine with planar muscle units [Osada et al, 2011]

These structures shown in Figure 1 and Figure 2 consist of components which show nonlinear behaviors. We believe that parallel mechanisms could be used to achieve the first criteria and that every moving part of the structure must be of a rigid mechanical constitution for fulfilling the second criteria. For the third criteria, the structure must have components that have the property of self position maintaining.

## 2. HUMAN SPINE PROPERTIES AND REDUCED PLANAR SPINE MODEL

First the kinematic specifications of human trunk will be investigated. The trunk part of the human body is from neck to hip. As given in Table 1, neck can roll and pitch, waist can yaw and hip can yaw, pitch and roll [Yussof, Yamano, Nasu and Ohka, 2006].

Table 1. DOF's of Human hip to neck [Yussof, Yamano, Nasu and Ohka, 2006]

Axis	Degree
Neck (roll and pitch)	-90 to 90
Waist (yaw)	-45 to 45
Hip (yaw)	-90 to 60 and -60 to 90
Hip (roll)	-60 to 45 and -45 to 60
Hip (pitch)	-130 to 45

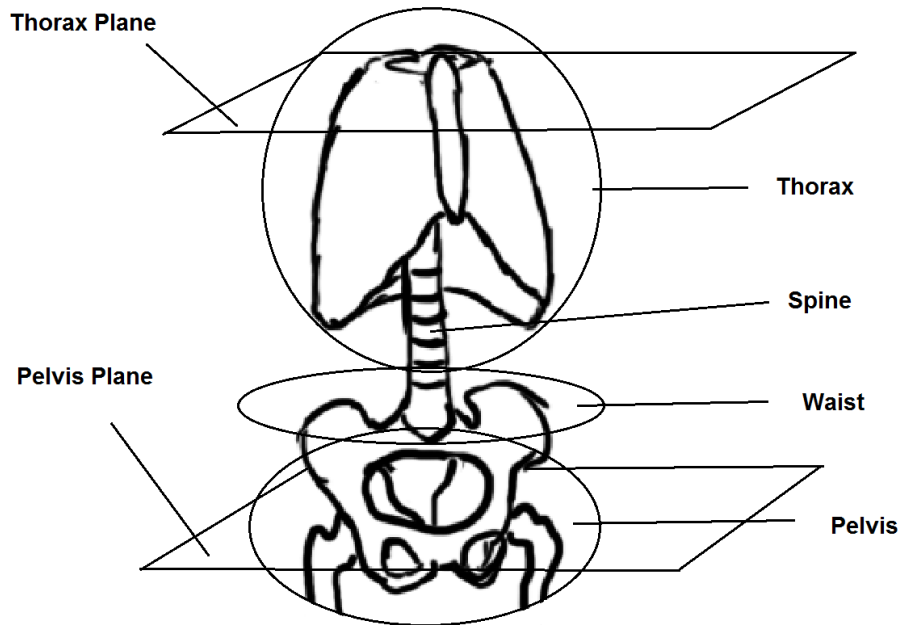


Figure 3. Main parts of the trunk

Main parts of the trunk, shown in Figure 3, are thorax, waist and pelvis. Thorax plate can yaw, pitch and roll relative to pelvis plate. Thorax plate is connected to pelvis plate through the spine. Spine consists of 33 vertebrae in 5 main zones; cervical, thoracic, lumbar, sacral and coccyx, coccyx is attached to Sacrum [Bullough and Boachie-Adje, 1988]. Due to the lack of the motion of sacral group, only cervical, thoracic and lumbar parts of the spine will be considered in our work.

Spine is divided into four main groups [Bullough and Boachie-Adje, 1988] shown in Figure 4 (a). Human spine is reduced to four planes in our design. These planes are shown in Figure 4 (b).

Plane D is the end of sacral group and start of the lumbar group. Plane C is the end of lumbar group and start of thoracic group. Plane B is the end of thoracic group and start of cervical group. Plane A is the terminus of cervical group.

Movement capabilities of human spine will be recreated through these four planes. When the longitudinal axis of the spine is accepted as Z axis, we believe that in order to achieve continuous motion of the body, each plane must be able to; Pitch, yaw and move in X,Y and Z directions. However, with the consideration of human spine restrains, the transitional displacement in X and Y axis must be constrained.

These planes will be the end actuators of the each parallel mechanism as shown in Figure 4 (c). The artificial spine will be constructed with the serial connection of these parallel mechanisms.

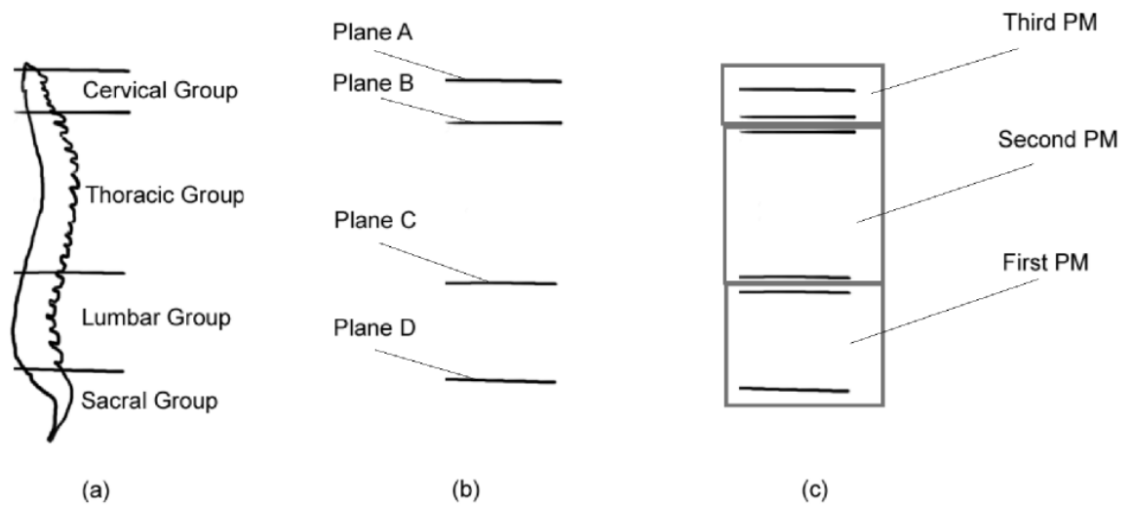


Figure 4. (a) Main zones of human spine [Bullough and Boachie-Adje, 1988] (b) Reduced spine planes (c) Orientation of parallel mechanisms

### 3. KINEMATIC DESIGN OF THE SPINE MODULE

Parallel mechanisms are closed kinematic chains with high degree of freedoms. They have many advantages over serial kinematic chains as being stiffer, accurate construction with a low moment of inertia [Merlet, 2000].

In the previous chapter, desired degrees of freedom were given. To achieve these degrees of freedom a novel 5 DOF RRURR/RRUCR asymmetric parallel mechanism is suggested as shown in Figure 5. Where, R stands for one directional rotation (Rotation), C for one directional rotation and linear displacement at the same axis of rotation (Cylindrical), U for two degree of freedom universal joint (Cardan coupling). Also two screw joints are used but since the DOF is identical to R it is shown with the symbol R3.

One, two or three of this module can be used together to obtain any desired degree of freedom as shown in Figure 6. It should be noted that this is still an ongoing research and the design will be refined after a set of analysis.

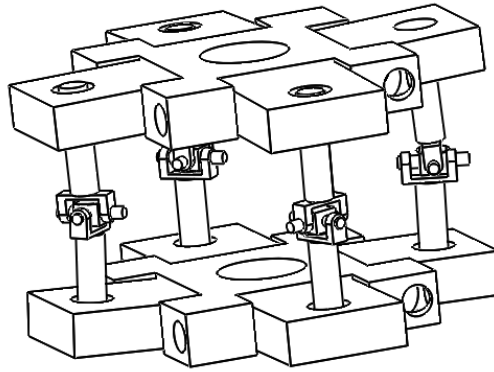


Figure 5. Spine module: The suggested design for parallel mechanism

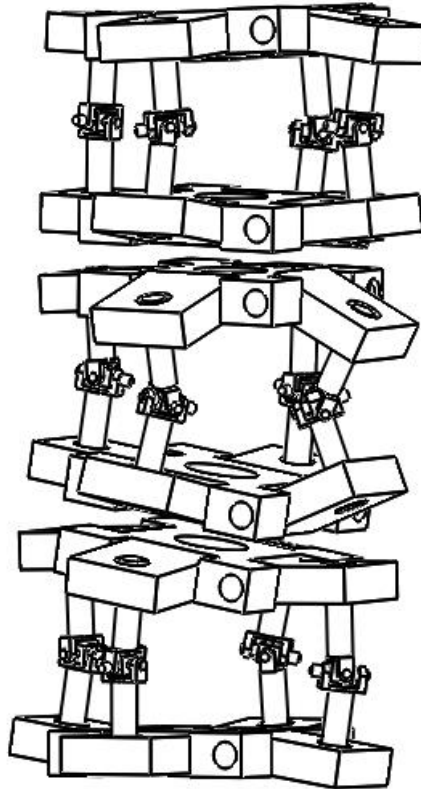


Figure 6. Spine structure constructed with three modules

The degree of freedoms can be evaluated from the Grübler formula (1).

$$F = 6(n - 1) - \sum_1^i (6 - f_i) - Fid \quad (1)$$

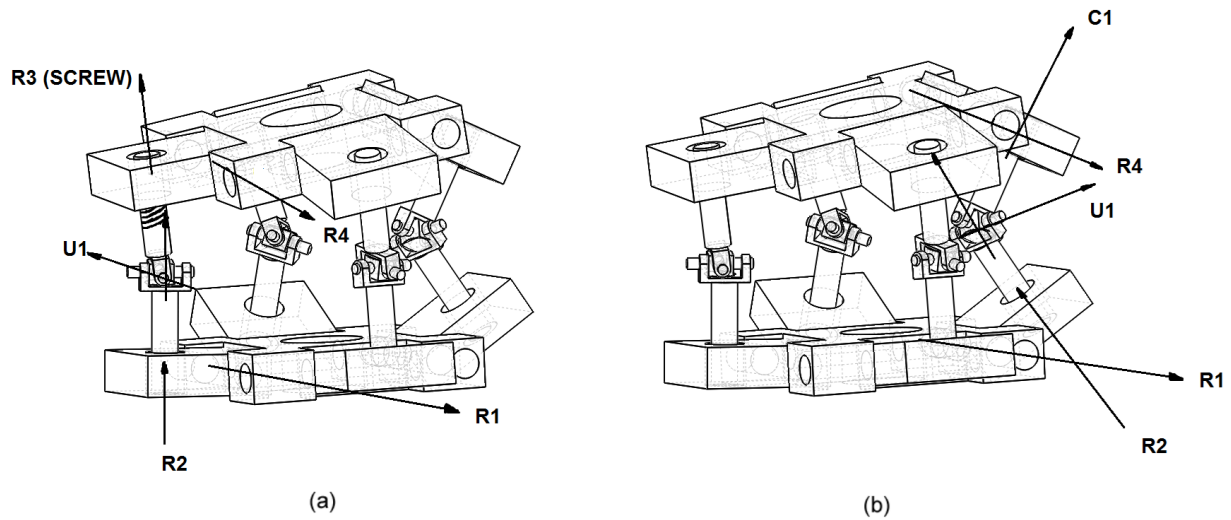


Figure 7. Joint orientations; RRURR (a), RRUCR (b)

Where  $F$  is the total DOF of the mechanism,  $n$  is the number of independent rigid parts,  $f_i$  is the DOF of corresponding joint and  $F_{id}$  is the idle movements. There are 18 independent parts in the mechanism. The joint distribution and axis of rotations are shown in Figure 7. There are two pairs of limps. The joint orientation of RRURR pair is shown in Figure 7 (a) and RRUCR pair is shown in (b), one limp per pair is shown in the figure.

Calculation of the  $\sum_i (6 - f_i)$  term is shown in Table 2.  $F_{id}$  is 3 in our mechanism. Now with all variables known equation becomes;

$$F = 6 * (18 - 1) - 94 - 3 = 5 \quad (2)$$

Table 2. DOF of joints

Type of the joint	Number of joints	DOF	(NoJ) x (6-DOF)
U	4	2	16
R	12	1	60
C	2	2	8
R3(Screw)	2	1	10
<b>SUM</b>			<b>94</b>





From Equation (2), it can be seen that 5 degree of freedom can be achieved with the suggested mechanism.

#### **4. RESULTS**

The CAD model of the suggested spine module has been created in SOLIDWORKS. Parts are mated together as explained in kinematic design process. With using SOLIDWORKS motion add in yaw, pitch and transitional X,Y,Z motions have been simulated. Bottom plane is fixed in the simulations. Position of the top plane has been changed with various inputs. Results are shown in Figure 8.

The spine structure is also modeled in SOLIDWORKS. With using motion add in, motion of the spine structure has been observed, results are shown in Figure 9.

Strength related finite element and a through dynamical analysis yet to be done as a part of the work. The main goal of the study at this stage is to develop a novel approach to humanoid torso/spine concept rather than producing a finished mechanical design. However, the mentioned analyses will be done and an improved final design is going to be presented.

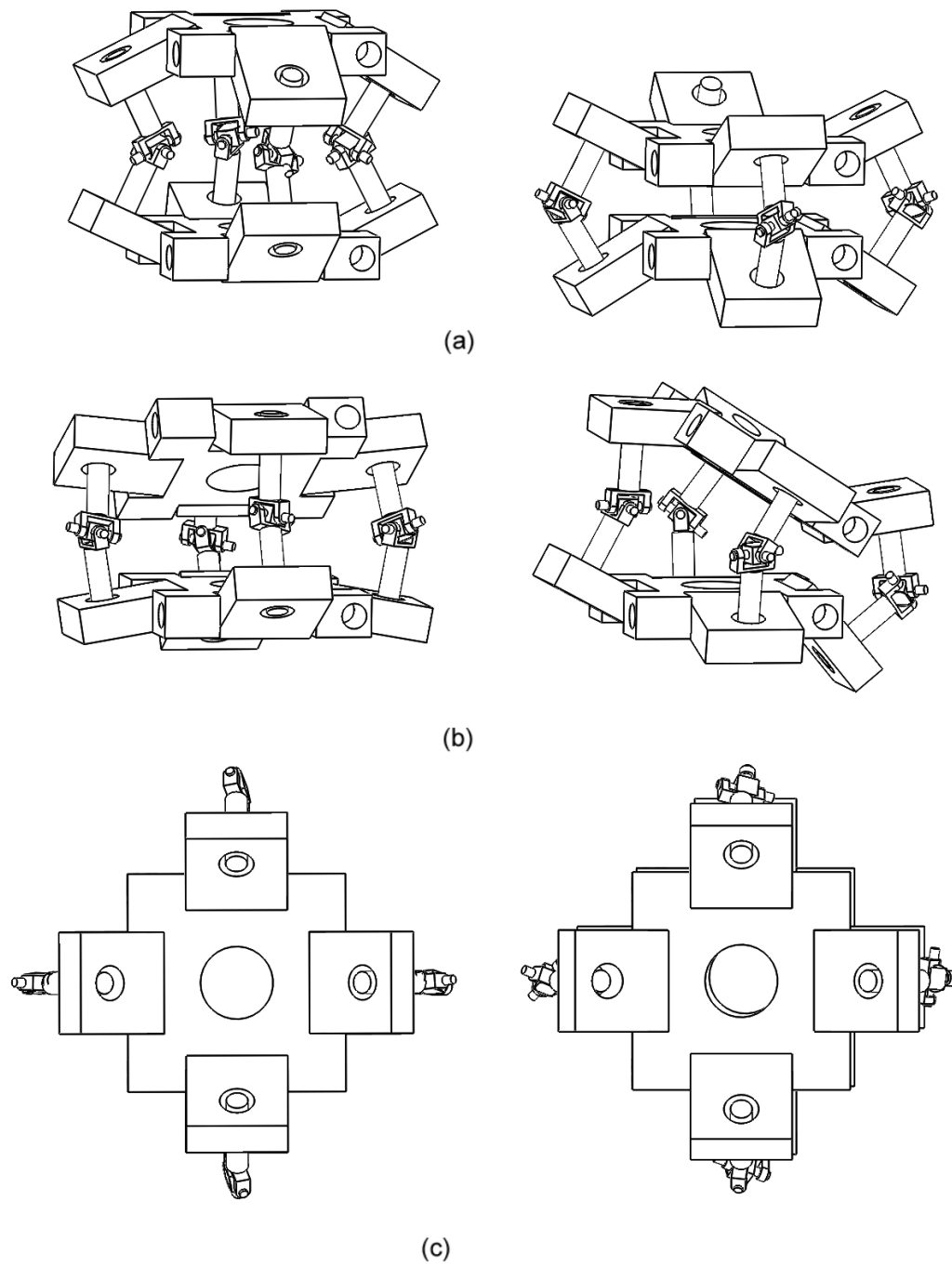


Figure 8. Transitional Z (a) Roll and Pitch (b) Transitional X and Y (c)

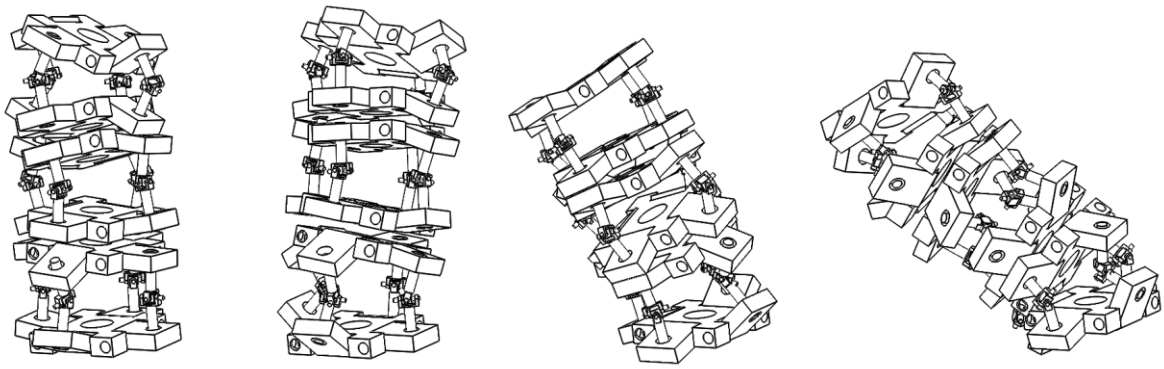


Figure 9. Various orientations of Spine

## 5. FUTURE WORKS

First of all, the design will be improved and a prototype will be manufactured. Kinematic and inverse kinematics of the mechanism will be solved and known control methods will be applied. The spine structure will be combined with a humanoid arm design which is also an undergoing project, to analyze stability and overcome singularity problems.

Human spine movements during various predetermined action cycles using motion capture techniques can be observed and categorized in future. By using data obtained from the motion capture, certain behavior models can be developed. The ultimate goal is, of course, to achieve certain action cycles with human-like grace.

## REFERENCES

1. **Roos, L., Guenter, F., Guignard, A. and Billard, A.G., (2006)**, “Design of a Biomimetic Spine for the Humanoid Robot Robota”, IEEE / RAS-EMBS International Conference on Biomedical Robotics and Biomechatronics, Pisa, Italy, pp. 329 – 334.
2. **Mizuuchi, I., Yoshikai, T., Sodeyama, Y., Nakanishi, Y., Miyadera, A., Yamamoto, T., Niemela, T., Hayashi, M., Urata, J., Namiki, Y., Nishino, T. and Inaba, M., (2006)**, “Development of musculoskeletal humanoid Kotaro”, Proceedings of The 2006 IEEE International Conference on Robotics and Automation, pp. 82–87.
3. **Mizuuchi, I., Nakanishi, Y., Sodeyama, Y., Namiki, Y., Nishino, T., Muramatsu, N., Urata, J., Hongo, K., Yoshikai, T. and Inaba, M., (2007)** “An advanced musculoskeletal humanoid Kojiro”, Proceedings of the 2007 IEEE-RAS International Conference on Humanoid Robots (Humanoids 2007), pp. 294 – 299.



4. **Osada, M., Ito, N., Nakanishi, Y. and Inaba, M., (2010)**, “Stiffness readout in musculo-skeletal humanoid robot by using rotary potentiometer”, Proceedings of the 9th Annual IEEE International Conference on Sensors, pp. 2329–2333.
5. **Y. Sakagami, R. Watanabe, C. Aoyama, S. Matsunaga, N. Higaki and K. Fujimura, (2002)**, “The intelligent ASIMO: system overview and integration”, Proc. IEEE/RSJ Int. Conf. on Intelligent Robots and Systems, Lausanne, pp. 2478–2483.
6. **Osada, M., Mizoguchi, H., Asano, Y., Kozuki, T., Urata, J., Nakanishi, Y., Okada, K. and Inaba, M., (2011)**, “Design of Humanoid Body Trunk with Multiple Spine Structure and Planar-muscle-driven System for Achievement of Humanlike Powerful and Lithe Motion”, Proceedings of the 2011 IEEE International Conference on Robotics and Biomimetics, Phuket, Thailand, pp. 2217 – 2222.
7. **Yussof, H., Yamano, M., Nasu, Y. and Ohka, M., (2006)**, “Design of a 21-DOF Humanoid Robot to Attain Flexibility in Human-Like Motion”, The 15<sup>th</sup> IEEE International Symposium on Robot and Human Interactive Communication, Hatfield, UK, pp. 202-207.
8. **Bullough, P. G. and Boachie-Adjei, O., (1988)**, Atlas of Spinal Diseases, JB Lippincott, Philadelphia.
9. **Merlet, J., (2000)**, Parallel Robots, Kluwer Academic Publishers, Norwell, MA.





## DEFECTS AND REMEDIES IN ADVANCED HIGH STRENGTH STEELS STAMPING

**Ilyas KACAR**, *ikacar@gmail.com* Nigde University, Nigde, Turkey

**Fahrettin OZTURK**, *fozturk@pi.ac.ae* The Petroleum Institute, Abu Dhabi, UAE

**Firas JARRAR**, *fjarrar@pi.ac.ae* The Petroleum Institute, Abu Dhabi, UAE

### ABSTRACT

In recent years, the use of advanced high strength steel (AHSS) in the automotive industry has been increased due to their role in increasing fuel economy and reducing carbon dioxide emissions. The lightweight AHSS structures would be the optimum choice for many applications; however, there are many defects to overcome in their stamping. In this present study, different types of defects and remedies of AHSS stampings are presented.

**Keywords:** Advanced high strength steel, Failure analysis, Damage behavior of multiphase steels, Failure prediction

### 1. INTRODUCTION

After the oil crisis in the 1970s, the steel industries have started to develop the dual-phase steels (ferritic-martensitic) in order to increase fuel economy and reduce carbon dioxide emissions. Lightweight metals are widely used in motor vehicles, aircrafts, electronics, and sports equipment. New materials such as ultra-lightweight high-strength steels, metal foam, Al, Mg, and Ti alloys, ceramic products, and polymer composites are very common in automobile manufacturing. AHSS have been used for the production of critical parts, such as the passenger compartments to reduce automotive weight. Examples of some AHSS and their mechanical properties are shown in Table 1.

Table 1 The mechanical characteristics of some AHSS materials.

Grade	Yield Stress $R_p$ (MPa)	Tensile Strength $R_m$ (MPa)	Elongation (%) min
TM1400 [Rehrl, et al., 2014]	1287	1431	4.7 ( $A_{50}$ )
CP800 GI [Steel, 2013]	600-750	780-950	$\geq 10$ ( $A_{80}$ )
DOCOL 1400 [SSAB, 2007]	1150	1400-1600	$\geq 3$ ( $A_{80}$ )

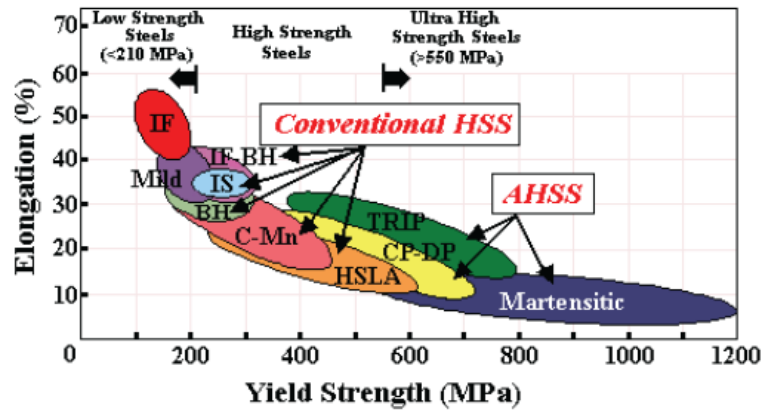


Figure 1 Comparison of the elongation and yield strength of different grades of steels [Baosteel, 2013, Kawahito, et al., 2014].

Low carbon steels have excellent formability (e.g. for deep drawing) and high strength steels (HSS) offer a good balance of strength, formability, energy absorption, and durability. On the other hand, AHSS have the advantage of offering relatively high strength. Lower density materials (such as Al and Mg alloys) can be used, however, in these cases thicker parts are required to compensate for their lower strength. In addition, there are difficulties in forming such low density alloys. Therefore, weight reduction is not efficient every time. It is required to obtain a balance among material cost, performance, and production techniques. AHSS that offers up to five times the strength relative to the mild steels is a viable alternative to satisfy this balance. Advanced high strength steel tubes are principally applied as side impact door beams, seat structures, and instrument panel beams in automobiles. The cross-sectional shapes of these tubes and beams may be circular, square, oval, and tapered.

Figure 1 compares the elongation and yield strength values of different grades of steel. The AHSS are classified as ultra-high strength steels. Steels in the AHSS family are under continuous development and include Dual-Phase (DP), TRansformation Induced Plasticity (TRIP), High Strength Low Alloyed (HSLA), and Complex-Phase (CP) steels.

Dual Phase (DP) steels are characterized by their microstructure where hard martensite grains are dispersed. Martensite grains provide high strength in the soft and ductile structure of the ferritic matrix. The strength is adjusted by the amount of martensite and C content. DP steels exhibit a high hardening exponent, low and constant yield strength, and a high tensile strength. In addition, their energy absorption capability is relatively good.



High Strength Low Alloyed (HSLA) steels are characterized by specific mechanical properties. Because carbon content is lower than in classical mild steel, their formability and weldability are relatively good. Other alloying elements, such as copper, niobium, vanadium, titanium, are present in the small quantities and are used for strengthening purposes. These elements create change in the ferrite-pearlite microstructure of carbon steels to offer a very fine dispersion of alloy carbides in an almost pure ferrite matrix.

Transformation Induced Plasticity (TRIP) steels are characterized by a good combination of strength and ductility and have a microstructure containing retained austenite in a ferrite matrix and hard phases like bainite and martensite.

Complex Phase (CP) steels are considered as a transition from DP to ultra-high strength steels.

## **2. FORMING OF ADVANCED HIGH STRENGTH STEEL SHEETS**

While mild steels have excellent formability (e.g. for deep drawing), HSS have a good balance among strength, formability, energy absorption and durability, and AHSS have high strength. DP steels, which constitute a considerable portion of the AHSS applications, may generally be preferable for parts required to absorb energy in case of a car crash. Martensitic steels (MS) or UHSS are typically used to provide collision protection through minimizing the deformation from a side impact. DP steels have enough ductility for forming and part strength although they have large work hardening properties. DP steels are preferable for stamping processes because of these features. The hot stamping of boron-alloyed steel is better than that in conventional cold stamping.

Automotive steel parts are subjected to dynamic loading from road conditions. The current trend is to resist cracking under cyclic loading through the development of new materials, manufacturing techniques, and easy to use designs for complex part requirements. To successfully form complex parts for automotive body panels from sheet materials, deep drawing is often used. A press machine for stamping is seen in Figure 2. AISI 109, 430Ti, AHSS, such as DP, TRIP, HSLA have being increasingly used in automobile structural components such as floor panels and the trunk lid due to their corrosion resistance, toughness, and high resistance to impact. However, it should be taken into consideration that carbon (C) and nitrogen (N) alloying elements decrease the deep drawability of such steels.



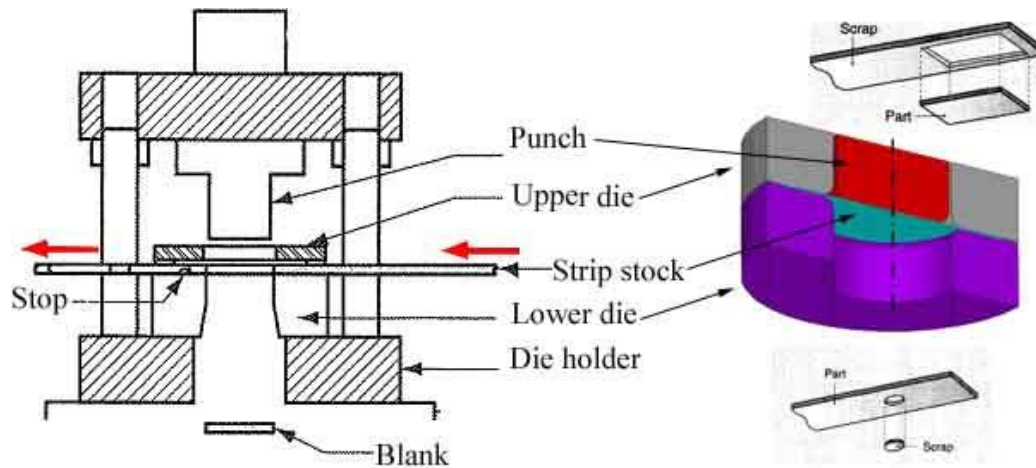


Figure 2 A typical stamping press and deep drawing die

There have been numerous studies on transformation induced plasticity (TRIP) [Han, et al., 2005], Al-alloyed TRIP [Xia, et al., 2008], HSLA300, DP600, M900, DP980 [Xia, et al., 2007], and M1310 [Bratt and Noel, 2004, Zhao, et al., 2013] both experimentally and numerically. While forming methods are available for high-strength low-alloy steels, it is more difficult to form AHSS with higher carbon and alloy percentages.

Tests on the sample from material to be evaluated are very helpful for designers. Scanning Electronic Microscopy (SEM) is used for the determination of the microstructures, the chemical composition and grain size. Tensile tests are used to compare the strain hardening behavior (stress-strain and instantaneous  $n$  value), and anisotropy coefficients of different materials. Hardening values provide the Aging Index (AI) to determine the natural aging behavior. Paint-baking heat treatment gives the work hardening value (WH) and the bake hardening value (BH). The Erichsen test is used for stretching simulation. The limiting drawing ratio (LDR) test is used to compare the drawability of different materials. The hole expansion test is used to evaluate the flangeability of the steels. The forming limit curves (FLCs) are also used to simulate this forming mode and determine the workability of the materials.

### 3. DEFECT TYPES and REMEDIES

In this section, the failures are examined because “Defect” causes lack of perfection and “Failure” causes loss of success. Of course, as it is mentioned before, almost all parameters are dependent to each other, one affects the others. There are lots of AHSS materials, forming processes, and defect types. These all issues are beyond the topic of the present work. So we focused on the defects for only HSLA, DP, and TRIP AHSS grades. The first part of this research, present results have been determined from literature. Low formability,

high springback are main concerns in AHSS forming. Yield stress,  $n$ -value and Young's modulus change with deformation (strain). Inconsistency is present in causes of the stamping defects.

Some simple shaped AHSS parts (such as side impact beams) can be formed by cold stamping up to 1200 MPa [Altan, 2006]. There are no heating and cooling costs in cold forming but these steels have limited formability and significant **springback** at room temperature and warm forming conditions. This causes improper fit, which creates serious problems during assembly of the parts. In addition, it is inevitable to use more straightened materials than 1200 MPa and complex shape for some parts such as roof reinforcements, pillars, side members, tunnel reinforcements, and rear rails.

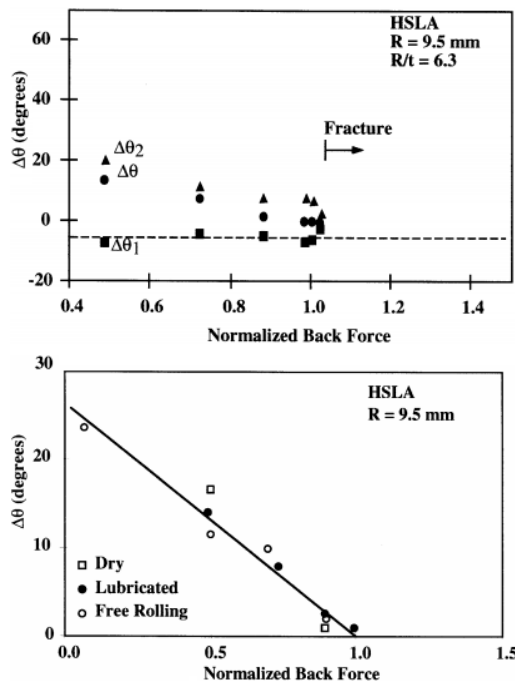
**Splitting (tearing)** is another defect present in the forming of AHSS from necking that stems from critical levels of strain. **Wrinkling** is also a type of defect which occurs in the forming of AHSS from folding which is due to insufficient constraints. **Earing** in a drawn steel cup is caused by the planar anisotropy (the resistance to thinning) of the sheet metal.

While these types of defects can be predicted using forming limit diagrams (FLD) for most metals, defect prediction is not so easy for AHSS. Although, recent developments and challenges in stamping of AHSS are satisfactory in terms of strength and formability, the fracture mode known as **shear fractures** have still been a more general failure mechanism. These types of failures occur while bending and tension exist together such as in stretching and sometimes they happen without localized necking. There are a number of factors leading to shear fractures in AHSS materials. The ratio of the punch radius to the material thickness, called the "r/t ratio" could be one of the factors. While a value of that ratio which is sufficient in pure bending case, may be too small for bending + tension. For AHSS materials in general, FLDs may be used to predict the failure for bending + tension cases because it is known that the failure is either on the sidewall of the sample or at the punch nose radius. Another factor may be due to the microstructure of the AHSS. For example, failure behavior in multiphase materials is not predictable, because of its complex phase behavior. In DP steel stampings, homogeneity in microstructure provides more resistance to failure occurrences. There are many numerical simulation and optimization studies on the failure prediction of these fractures but none of them consider general stamping conditions. Furthermore, if there is no localized necking, it is almost impossible to predict these fractures. Strain distribution at the transition zone was investigated for HSS and UHSS [Groche, et al., 2008]. A multi-stand roll forming simulation was developed for a large cross-section of a channel by using a method based on Lagrange method in the deformable bodies mechanics [Han, et al., 2002].

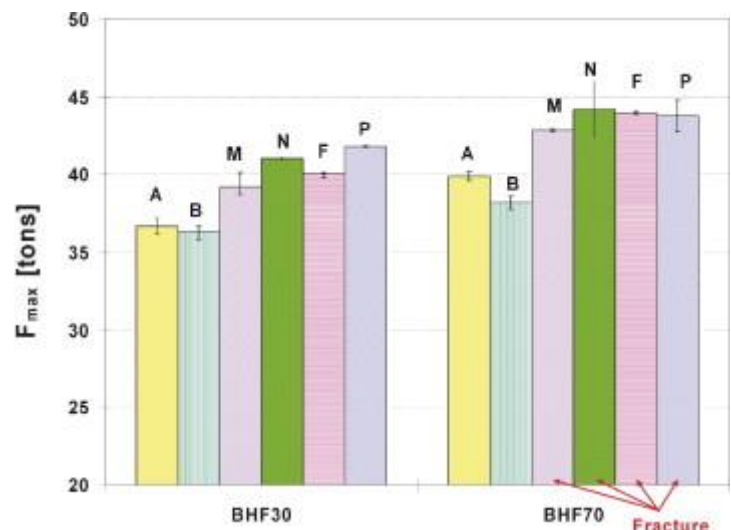
Table 2 Constitutive relations of some DP, TRIP, and HSLA steels

Material	Constitutive equation	Anisotropy
DP600 [Iriondo, et al., 2013]	$\sigma = 1008\varepsilon^{0.169}$ (MPa)	$r_0^\circ = 0.73$ ; $r_{45^\circ} = 0.9$ ; $r_{90^\circ} = 0.93$
TRIP780 [Nasser, et al., 2010]	From tensile test $\sigma = 1444\varepsilon^{0.208}$ (MPa) From bulge test $\sigma = 1554\varepsilon^{0.183}$ (MPa)	$r_0^\circ = 0.802$ ; $r_{45^\circ} = 0.9$ ; $r_{90^\circ} = 0.874$ [Amin E. Al-Nasser, 2009]
DP-1000 [Ingarao, et al., 2009]	$\sigma = 1521\varepsilon^{0.09}$ (MPa)	$r_0^\circ = 0.75$ ; $r_{45^\circ} = 0.9$ ; $r_{90^\circ} = 0.77$
HSLA 350/450 [Ingarao, et al., 2009]	$\sigma = 807\varepsilon^{0.14}$ (MPa)	$r_0^\circ = 1.1$
TRIP 450/800	$\sigma = 1690\varepsilon^{0.24}$ (MPa)	$r_0^\circ = 0.9$
HSLA 410 [Schaeffler, 2005]	$\sigma = 592[0.686 + 1.044\varepsilon - (1 - 109000\varepsilon^2)e^{-995\varepsilon}]$	$r_0^\circ = 0.559$ [Ferreira, et al., 2008]

The constitutive equation that models the materials' mechanical behavior establishes the relationship between the most relevant state variables characterizing the continuum conditions. The formation process response window is governed by the process conditions, and the plastic modulus of the materials flow curve. BHF is main parameter on springback. Max value is achieved at 1.0 normalized BHF (32021 N) for HSLA 410 in edge bending. It is seen fracture beyond that force values as seen in Figure 3. Role off variouse lubricants over total springback is determined too. Reducing springback is possible by using very small tool radii. Fracture in Figure 3 (b) is caused by the failure of lubricant film under high contact pressure.



(a) Fracture occurrences in case of excess BHF [Carden, et al., 2002]



(b) Deep Drawing Tests for DP590 with different lubricants [Kim, et al., 2008]

Figure 3 Fracture occurrences and boundaries.



(a) HSLA



(b) DP790 Underbody structural part and DP980 B-pillar inner [Chen, et al., 2005]

Figure 4 Defects shapes for over BHF in deep drawing for HSLA and DP steels.

When the fracture shapes are examined it is seen that the most cracks become in MODE 1 type as seen in Figure 4. Local formability is a primary issue for AHSS in automotive applications due to unpredicted failures during forming especially, in stretch bending and flanging. The hole expansion test is used to evaluate flanging. Local failures are common and these do not correlate to  $n$ -value,  $R$ -value or elongation. Brittleness and cracking can occur in steels when C content is greater than 0.3%C (0.4%C equivalent). In Figure 5, AHSS edge formability and defects are shown. Machined and punched surfaces are compared in Figure 6.

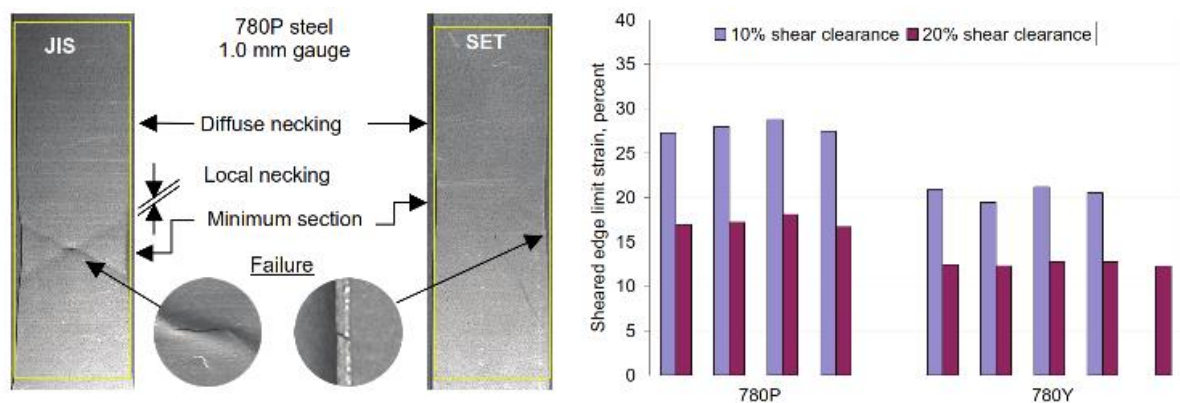


Figure 5 Edge defects and limit strains for TRIP780 steels [Wang, et al., 2008].

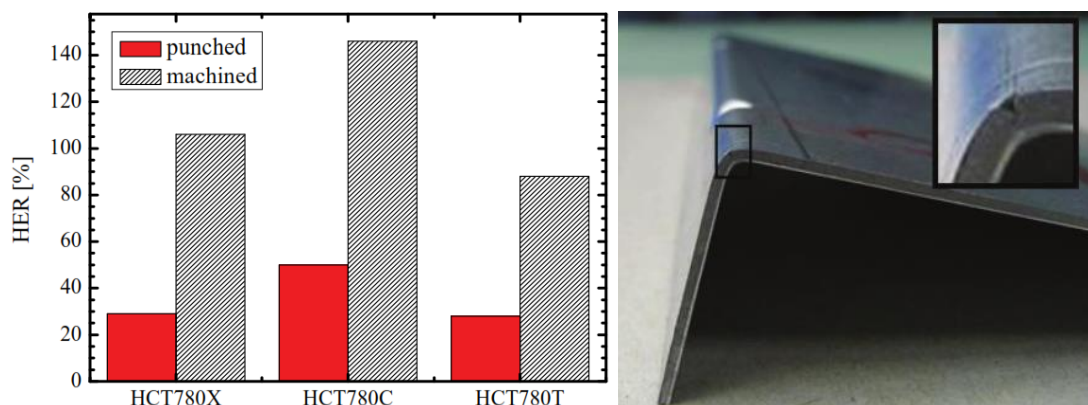


Figure 6 Hole expansion ratio (HER) for a DP 780 (HCT780X), CP 780 (HCT780C) and TRIP 780 (HCT780T) grade [Spenger, et al., 2008, Fekete, et al., 2008].

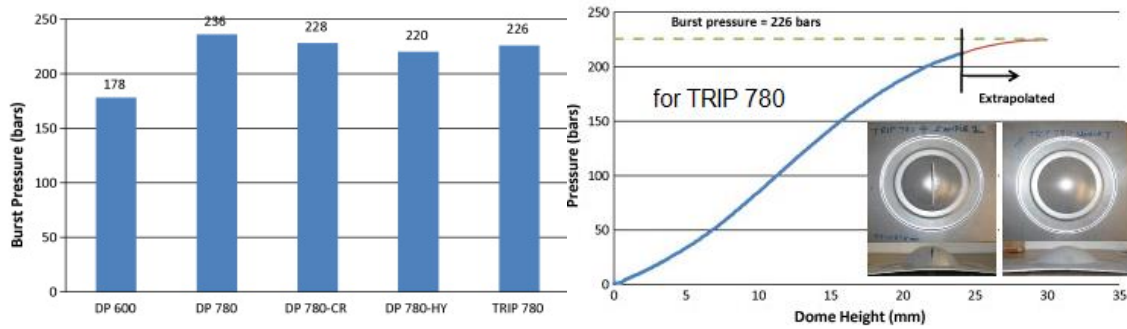
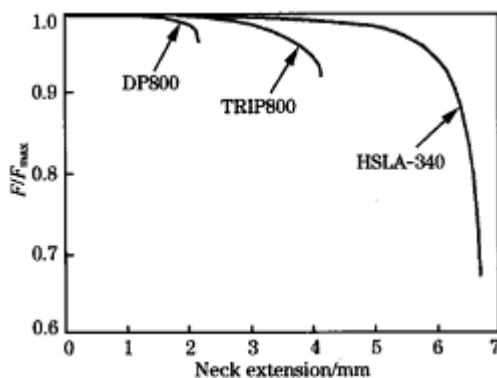
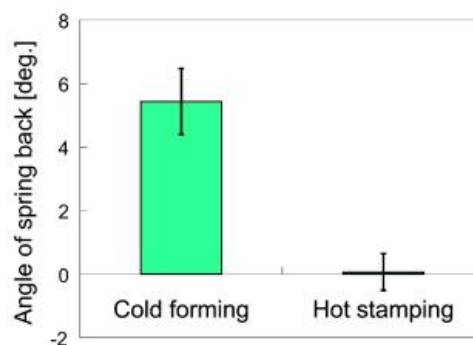


Figure 7 Burst pressure of the five AHSS materials in bulge tested [Nasser, et al., 2010]

Tension test is not enough. Elongation in bending does not correlate to elongation in tension test. Bulge (VPB) test is more reliable. While a material in tensile test fails at 15% elongation, 40% elongation in bending. The dome height at fracture (bursting) in the VPB test can be used as a measure of formability as seen in Figure 7. The post-uniform deformation capability of the material is important factor in bottoming technic to overcome to springback. HSLA 340 has more post-uniform deformation capability than others as seen in Figure 8 (a). For the same deformation condition, springback increases with decreasing the modulus of elasticity,  $E$ , and increasing the yield strength  $Y$  of a material. Overforming (makes compensation), bottoming (makes reduction in the stress distribution on bended section) and heating (makes decreasing of yield point). Neither overforming nor bottoming is needed in *hot stamping* processes to eliminate the springback. Deformation above recrystallization temperature lets the material crystallize again during forming. Springback disappears due to the fact that the material's yield point is decreased. If AHSS stampings are formed using hot processes, springback can be eliminated as seen in Figure 8 (b).



(a) The post-uniform deformation capability [Ozturk, et al., 2013]



(b) Heat effect [Ikeuchi and Yanagimoto, 2011]

Figure 8 The post-uniform deformation capability and hot-cold deformation condition.



Also hot stamping of boron alloyed steels is getting more and more important, especially for the production of body parts with high crash performance [Kouadri-David, 2014]. In hot forming, shielding gases like Argon should be used to avoid the scale layer, or oxidation which causes a more stiff and fragile layer causing a worsening of the mechanical properties. Shielding gases prevent the contact between material and air in the atmosphere. In addition, protective coating can be applied before heating like Al-Si coating on 22MnB5.

Wrinkle is a main indicator for evaluating the formation quality of stampings especially hot stamped parts. The height of wrinkle, microstructure analysis, and tensile tests can be considered as an evaluation criteria. Bursting is useful to determine the defect parameters. When end feed pressure's effects are investigated, at 1.5 YS end feed level, mild wrinkles were produced, while 2 YS resulted in severe wrinkling of the tube as seen in Figure 9.

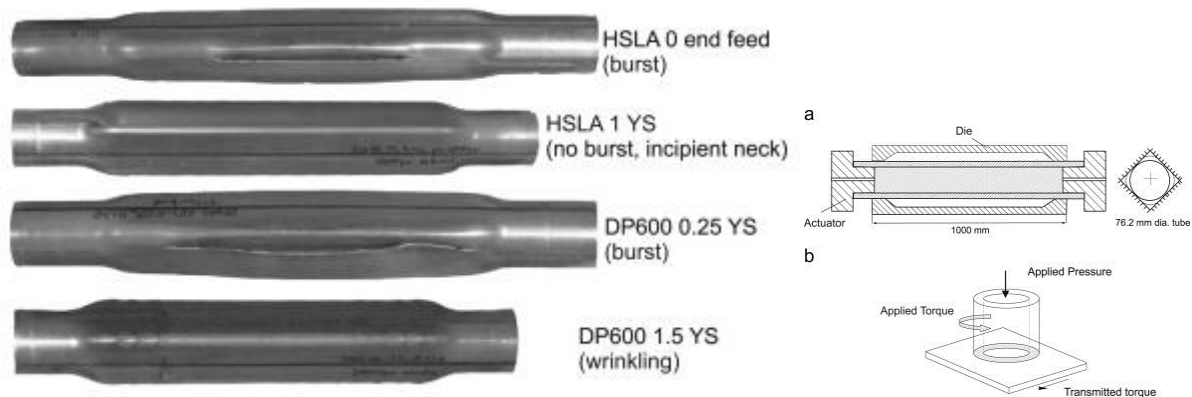


Figure 9 End feed pressure's effects on failure for HSLA and DP steels [Sorine, et al., 2008].

When the locations and heights of draw beads are not designed properly, deformation restriction on the hemispherical punch head is not sufficient to provide the required stretching. While the blank in front of the punch is pulled towards the die line, compressive stresses are created in the circumferential direction due to the circumference reduction and the tensile stresses in the axial direction. These excessive compressive stresses cause wrinkling.

Blank holder force and stand movements are the main factors affecting the occurrence of wrinkling and tearing in sheet metal parts. Improvements on defects are based on the *control of material flow* during forming. Force and stand movement controlling techniques are often used to change the restraining force locally and to control uncertain material flow that may lead to failures (such as wrinkling, tearing, fracture, surface distortion, and springback) that occur due to excessive or insufficient restraining of the roll formed part.

Erichsen cupping test involves biaxial stretching of a constrained test specimen. Ideally, no draw-in of flange metal from under the hold-down occurs. The sheet metal test specimen is bulged at a specified rate until the load drops or until either necking or fracture occurs; the test is then terminated. Ball punch (penetrator) movement to drop in-load or necking or fracture is the test result as seen in Figure 10. It is known that test results may vary with hold-down force, lubrication, and criterion for determining the end point of the test.

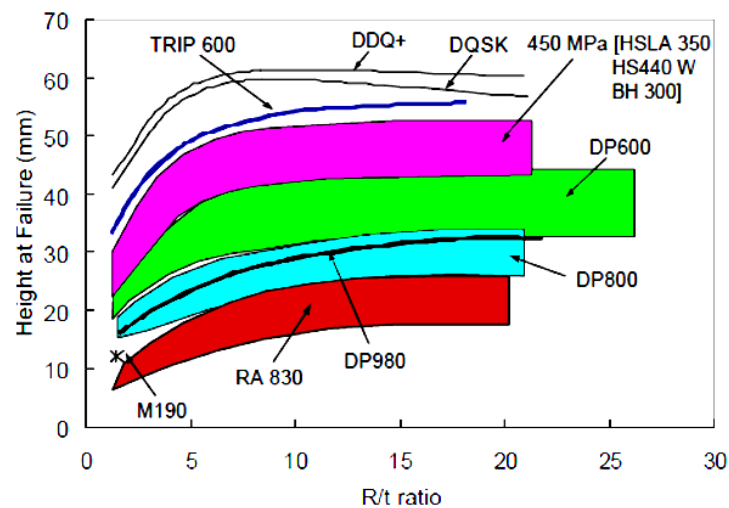


Figure 10 Erichsen cupping test to evaluate the fracture limits of some AHSS materials [Wu, et al., 2006].

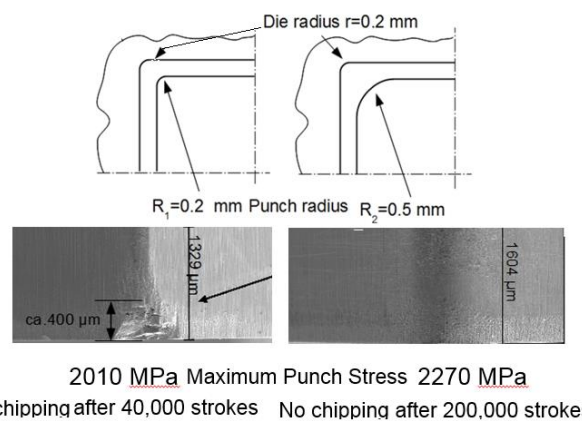


Figure 11 Wearing on die-punches [Högman, 2004].

Wearing on die-punches is other parameters to effect on stamping failures. Design considerations make serious improvements as seen in Figure 11. Various parameters are like sheet material and thickness, punch material and coating, punch-die clearance and punch velocity, and punch/die corner radii influence punch-die life. Coating provides 10 times longer than uncoated tools as seen in Figure 12 and applied on cutting tools and tooling with CVD, PVD generally.

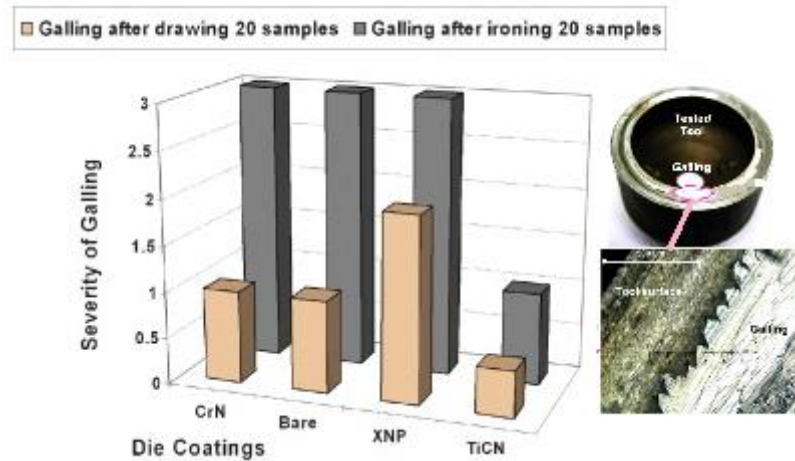


Figure 12 Galling on die and effects of coatings [Kim, et al., 2008].

It is seen that tearing has been occurred when the strain ratio for the critical point is about 0.35 for DP600 as seen in Figure 13.

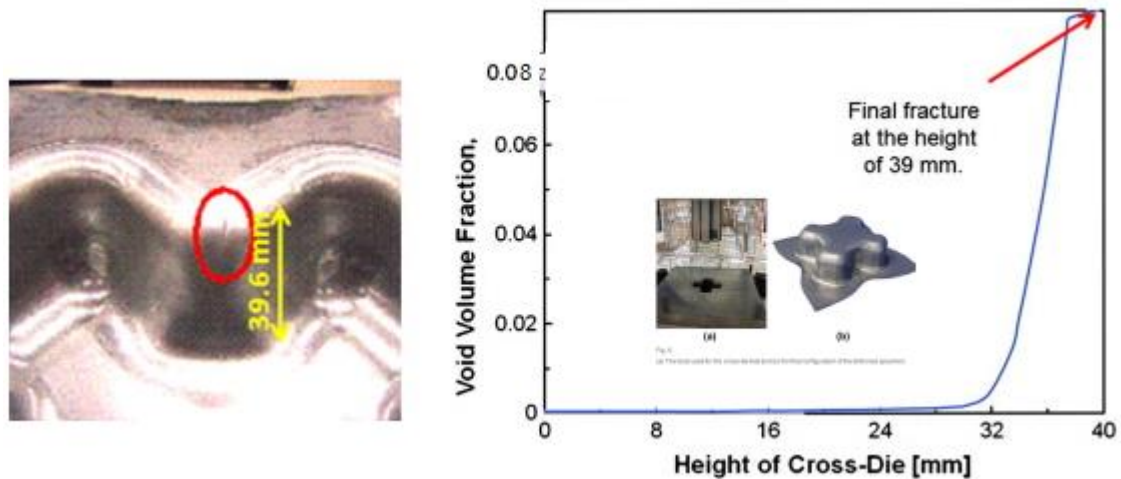


Figure 13 Tearing at DP600 [Ramazani, et al., 2012]

Tearing and wrinkling are a concept related to each other. Different BHF's are a solution on tearing and wrinkling. In the Figure 14, the wrinkle is avoided totally with the BHF approaching 1.62 MPa from BR1500HS [Baosteel, 2013]. While BHF is more than 1.62 MPa, for example 1.80 MPa, crack occurs which affects the hot formation quality.



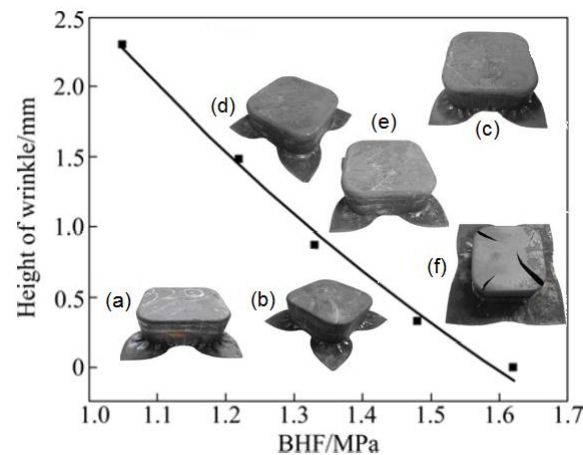
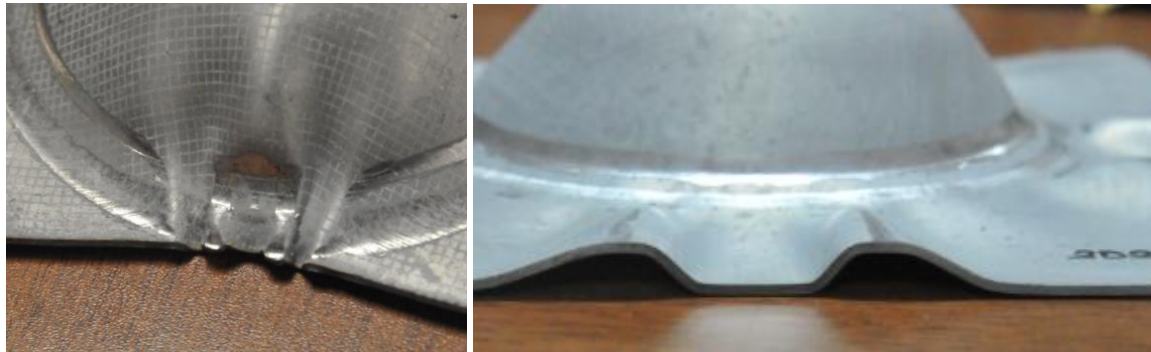


Figure 14 Height of wrinkle becomes bigger when the applied BHF decreases from 1.62 MPa to 1.05 MPa. (a) 1.05 MPa; (b) 1.22 MPa; (c) 1.33 MPa; (d) 1.48 MPa; (e) 1.62 MPa; (f) 1.80 MPa [Liu, et al., 2012]

Why the crack position in hot stamping is located in the across corner flange of square-box-shaped part is that the material is softened during hot stamping. The BHF used in hot stamping is smaller due to the fact that the material is softened at elevated temperature and the force requirements decrease to become wrinkle smaller.

#### 4. CONCLUSION

In this study, defect types encountered during forming of AHSS were reviewed. Remedies for defects eliminations were presented for springback, wrinkling, splitting, and shear fractures. These are critical manufacturing defects in the forming of UHSS and advanced UHSS. Nowadays the applications of AHSS in automobile body have become common and a wider range of their usage is projected in the future.

#### REFERENCES

1. Rehrl, J., Mraczek, K., Pichler, A., and Werner, E., (2014), "Mechanical properties and fracture behavior of hydrogen charged AHSS/UHSS grades at high- and low strain rate tests", *Materials Science and Engineering: A* 590, 360-367.



2. **Steel, T., (2013),** "CP800 GI, Highly bendable roll forming steel", In NLAMLTDS:750/ENG:11/2013, T.S.E. Limited, ed. (The Netherlands: Tata Steel Automotive Commercial Headquarters 7H-04 PO Box 10000 1970 CA IJmuiden The Netherlands).
3. **SSAB, (2007),** "Docol 1400", In DATA SHEET: 12-11-07 GB8207 DOCOL D.H.S. Steel, ed. (SSAB EMEA AB SE-781 84 Borlänge Sweden), p. 4.
4. **Baosteel, (2013),** "BaoSteel Automotive Advanced High Strength Steels", B.A. SHEETS, ed. (Printed in Shanghai China).
5. **Kawahito, Y., Niwa, Y., and Katayama, S., (2014),** "Laser direct joining between stainless steel and polyethylene terephthalate plastic and reliability evaluation of joints", *Welding International* 28, 107-113.
6. **Han, T.K., Park, S.S., Kim, K.H., Kang, C.Y., Woo, I.S., and Lee, J.B., (2005),** "CO<sub>2</sub> laser welding characteristics of 800 MPa class TRIP steel", *Isij Int* 45, 60-65.
7. **Xia, M., Tian, Z., Zhao, L., and Zhou, Y.N., (2008),** "Fusion zone microstructure evolution of Al-alloyed TRIP steel in diode laser welding", *Mater Trans* 49, 746-753.
8. **Xia, M., Sreenivasan, N., Lawson, S., Zhou, Y., and Tian, Z., (2007),** "A comparative study of formability of diode laser welds in DP980 and HSLA steels", *Journal of Engineering Materials and Technology, Transactions of the ASME* 129, 446-452.
9. **Bratt, C., and Noel, J., (2004),** "Laser hybrid welding of advanced high strength steels for potential automotive applications (201)". (San Francisco, CA).
10. **Zhao, Y.Y., Zhang, Y.S., and Hu, W., (2013),** "Effect of welding speed on microstructure, hardness and tensile properties in laser welding of advanced high strength steel", *Sci Technol Weld Joi* 18, 581-590.
11. **Altan, T., (2006),** "Hot-stamping boron-alloyed steels for automotive parts. Part I: Process methods and uses", *Stamping Journal* An FMA Publication, 40-41.
12. **Groche, P., Henkelmann, M., Gotz, P., and Berner, S., (2008),** "Cold rolled profiles for vehicle construction", *Arch Civ Mech Eng* 8, 31-38.
13. **Han, Z.W., Liu, C., Lu, W.P., and Ren, L.Q., (2002),** "Simulation of a multi-stand roll-forming process for thick channel section", *Journal of Materials Processing Technology* 127, 382-387.
14. **Iriondo, E., Alcaraz, J.L., Daehn, G.S., Gutiérrez, M.A., and Jimbert, P., (2013),** "Shape calibration of high strength metal sheets by electromagnetic forming", *Journal of Manufacturing Processes* 15, 183-193.
15. **Nasser, A., Yadav, A., Pathak, P., and Altan, T., (2010),** "Determination of the flow stress of five AHSS sheet materials (DP 600, DP 780, DP 780-CR, DP 780-HY and



- TRIP 780) using the uniaxial tensile and the biaxial Viscous Pressure Bulge (VPB) tests", *Journal of Materials Processing Technology* 210, 429-436.
16. **Amin E. Al-Nasser, B.E., (2009)**, "Characterization of Sheet Materials for Stamping and Finite Element Simulation of Sheet Hydroforming ", In *The Graduate School of the Ohio State University, Volume The Ohio State University (The Ohio State University The Ohio State University )*, p. 132.
  17. **Ingarao, G., Lorenzo, R.D., and Micari, F., (2009)**, "Analysis of stamping performances of dual phase steels: A multi-objective approach to reduce springback and thinning failure", *Mater Design* 30, 4421-4433.
  18. **Schaeffler, D.J., (2005)**, "Introduction to advanced high-strength steels - Part I", *STAMPING JOURNAL®*.
  19. **Ferreira, J.L., Tepedino, J.O.A., and Melo, T.M.F., (2008)**, "Formability of a 590 MPa Dual Phase Steel Compared to Two HSLA Steels with Similar Yield and Tensile Strengths", (Associaion for Iron & Steel Technology).
  20. **Carden, W.D., Geng, L.M., Matlock, D.K., and Wagoner, R.H., (2002)**, "Measurement of springback", *Int J Mech Sci* 44, 79-101.
  21. **Kim, H., Han, S., Yan, Q., and Altan, T., (2008)**, "Evaluation of tool materials, coatings and lubricants in forming galvanized advanced high strength steels (AHSS)", *CIRP Annals - Manufacturing Technology* 57, 299-304.
  22. **Chen, X.M., Shi, M.F., Chen, G., Kamura, M., Watanabe, K., and Omiya, Y., (2005)**, "Crash Performances of Advanced High Strength Steels of DP780, TRIP780 and DP980", *SAE Technical Paper*.
  23. **Wang, J., Link, T.M., and Merwin, M.J., (2008)**, "AHSS Edge Formability in Sheared-Edge Tension", (Associaion for Iron & Steel Technology).
  24. **Spenger, F., Hebesberger, T., Pichler, A., Krempaszky, C., and Werner, E.A., (2008)**, "AHSS Steel Grades: Strain Hardening and Damage as Material Design Criteria", (Associaion for Iron & Steel Technology).
  25. **Fekete, J.R., Hall, J.N., Meuleman, D.J., and Rupp, M., (2008)**, "Progress in Implementation of Advanced High-Strength Steels into Vehicle Structures", (Associaion for Iron & Steel Technology).
  26. **Ozturk, F., Polat, A., Toros, S., and Picu, R.C., (2013)**, "Strain Hardening and Strain Rate Sensitivity Behaviors of Advanced High Strength Steels", *J Iron Steel Res Int* 20, 68-74.
  27. **Ikeuchi, K., and Yanagimoto, J., (2011)**, "Valuation method for effects of hot stamping process parameters on product properties using hot forming simulator", *Journal of Materials Processing Technology* 211, 1441-1447.



28. **Kouadri-David, A., (2014)**, "Study of metallurgic and mechanical properties of laser welded heterogeneous joints between DP600 galvanised steel and aluminium 6082", *Materials and Design* 54, 184-195.
29. **Sorine, M., Simha, C.H.M., van Riemsdijk, I., and Worswick, M.J., (2008)**, "Prediction of necking of high strength steel tubes during hydroforming—multi-axial loading", *Int J Mech Sci* 50, 1411-1422.
30. **Wu, J., Zhou, D., Zhang, L., Zhou, Y., Du, C.Q., and Shi, M.F., (2006)**, "A Failure Criterion for Stretch Bendability of Advanced High Strength Steels", *SAE Technical Paper 2006-01-0349*.
31. **Högman, (2004)**, "Punching tests of Ahs- and uhs- steel sheet", In *Proceedings of the International Conference on Recent Advances in Manufacture & Use of Tools & Dies and Stamping of Steel Sheets: October 5-6, 2004, Olofström, Sweden*. (Olofström, Sweden: Volvo).
32. **Ramazani, A., Abbasi, M., Prah, U., and Bleck, W., (2012)**, "Failure analysis of DP600 steel during the cross-die test", *Comp Mater Sci* 64, 101-105.
33. **Liu, H.S., Xing, Z.W., and Lei, C.X., (2012)**, "Hot formation quality of high strength steel BR1500HS for hot stamping without cooling system", *T Nonferr Metal Soc* 22, S542-S547.





## RECENT TRENDS OF APPLICATION OF ADVANCED HIGH-STRENGTH STEELS IN AUTOMOTIVE INDUSTRY TO ENHANCE SUSTAINABILITY

**Suleyman KILIC**, *suleymankilic@gmail.com* Ahi Evran University, 40200, Kirsehir, Turkey

**Fahrettin OZTURK**, *fozturk@pi.ac.ae* The Petroleum Institute, PO BOX 2533, Abu Dhabi, UAE

### ABSTRACT

In recent years, vehicle weight reduction projects have brought significant improvements to fuel economy, with a concomitant reduction in carbon dioxide emissions. Lightening of a vehicle, without sacrificing the strength, performance, and comfort is the main target of the automotive industry; it is a major success when these parameters are improved. The lightening is usually accomplished by using thinner Advanced High Strength Steels (AHSS). In the present study, the use of AHSS in automotive industry is discussed. The advantages and disadvantages of these steels are evaluated.

**Keywords:** Advanced High Strength Steels, AHSS, DP, TRIP, CP, MS, TWIP

### 1. LIGHTENING EFFORTS

Weight reduction of a vehicle without sacrificing, or perhaps even while increasing the strength, performance, and comfort is the main target of the automotive industry. High oil prices, environmental pollution, and corrosion issues have intensified materials research in the automotive industry. Lightweight materials in automotive industry consist mainly of aluminum-magnesium alloys, plastics, and advanced high-strength steels (AHSS). The most widely used steels in AHSS group are dual phase (DP), transformation-induced plasticity (TRIP), and twinning-induced plasticity (TWIP) steels. Lightening is performed by the use of advanced high strength steel in reduced thickness.

During recent years, a tremendous amount of effort has put forth on steel research. Basically, the research projects have been focused on two distinct areas: Advanced High Strength Steels and Ultra-Light Steel Program (ULSP). ThyssenKrupp AG and ArcelorMittal are the largest iron and steel companies leading world steel research under the name of

"Advanced Technology Products Steel" group. ULSP group consists of companies, manufacturing under the name of "Ultra-Light Steel". That is divided into four sub-programs, shown in Fig.1 [Ruifrok, 2012, AHSS Guidelines].



Fig.1. Ultra-light steel team workspace [Ruifrok, 2012, AHSS Guidelines].

Ultra-Light Automotive Body Steel (ULSAB) program's purpose is to reduce automotive body weight minimum 25% without losing strength, performance, and comfort. The program aims to develop lightness and impact modifier properties in door and panel parts approximately 25% with 30% percent. The purpose of the Ultra-Lightweight Steel Automotive Suspension (ULSAB) program is supplying lightening between approximately 25% with 34%. UltraLight Steel Auto Body – Advanced Vehicle Technology (ULSAB-AVC) "Enhanced Ultra-Light Car Concept" program's aim is to increase safety and reduce fuel economy.

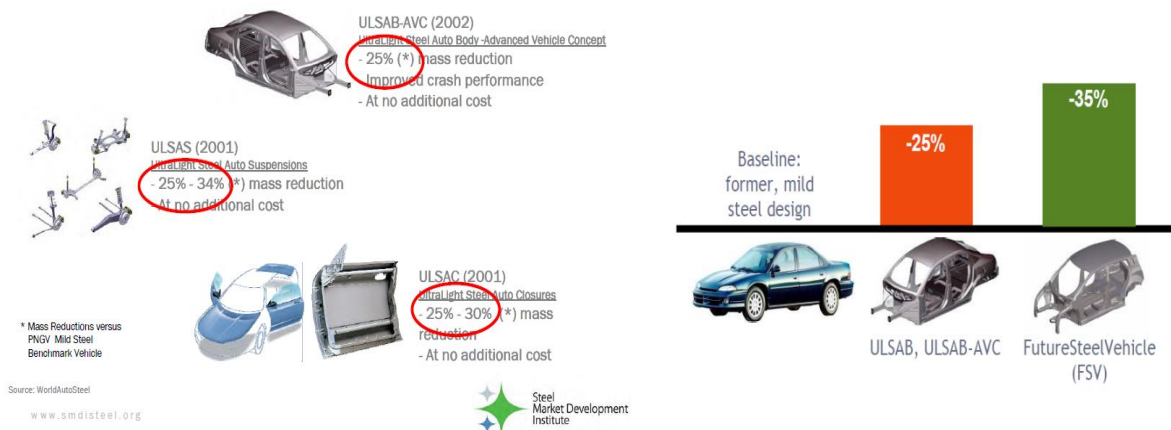


Fig. 2. Steel research groups and their targets [Ruifrok, 2012, AHSS 101].

The purpose of ULSAB-AVC group is to produce safe, efficient, low-weight, and inexpensive automobile. One way of achieving this is to use advanced high strength steel structural parts. Parts manufactured from the advanced high strength steel are thin which makes the parts lighter and they have higher strength than those fabricated from conventional steels. ULSP team's working targets are shown in Fig. 2 [Ruifrok, 2012, AHSS 101].



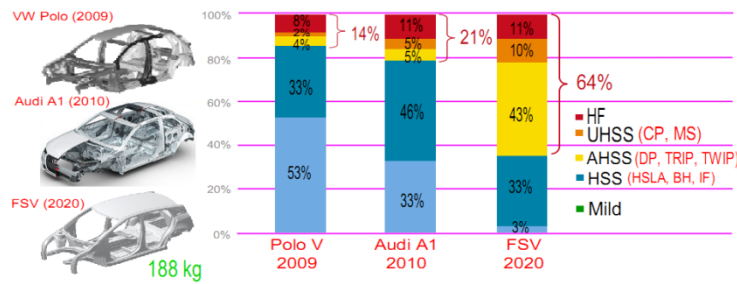


Fig. 3 Materials used in some automotive models [Ruifrok, 2012].

Fig. 3 presents information for 2009 model VW Polo, 2010 model Audi A1. The graph indicates that a lightening of 188 kg, without losing of strength, is foreseen [Ruifrok, 2012].

## 1.2. ADVANCED HIGH STRENGTH STEELS (AHSS)

High strength steels can help reduce energy efficiency and greenhouse gas by providing lower fuel consumption through reducing the weight without sacrificing the safety. For automotive applications, there are several factors in the selection of materials such as: safety, fuel efficiency, manufacturability, durability, and quality. In a highly competitive industry, both cost and material selection is extremely important. The steel use in North America in 2007 and future predictions are graphed in Fig.4. [AHSS Guidelines]. It is clearly seen that a significant increase the use of AHSS in automotive industry will be expected in near future.

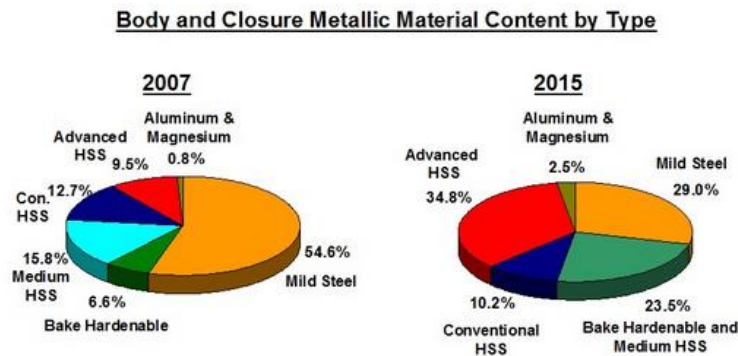


Fig. 4. The use of steel in 2007 and future forecast [AHSS Guidelines].

Tensile strength vs. elongation is shown in Fig. 5 [AHSS 101]. It is very obvious that new generation steels have a lot of advantages, compared to traditional steels. With a good combination of tensile strength vs. elongation, it is possible to produce very complex and structurally important parts. Besides, the high strength to weight ratio contributes the weight reduction significantly.



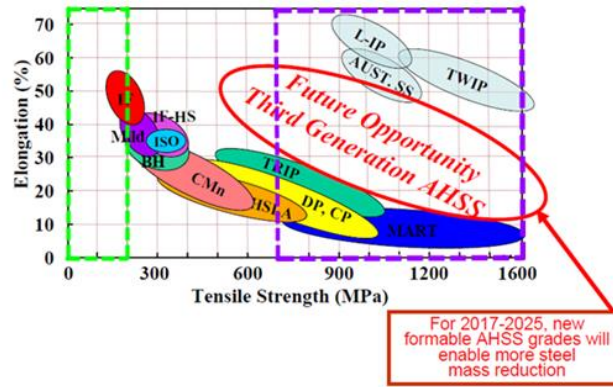


Fig. 5 Tensile strength vs. elongation [AHSS 101].

Mechanical properties of various steels which are widely used in a car is given in Table 1. Table 1 clearly indicates that material properties of AHSS have greater advantages, compared to traditional low carbon steels.

Table 1. Mechanical properties of various steels [AHSS Guidelines].

Steel Grade	YS (MPa)	UTS (MPa)	Total Elongation (%)
HSLA 350/450	350	450	23-27
DP 300/500	300	500	30-34
DP 350/600	350	600	24-30
DP 500/800	500	800	14-20
DP700/1000	700	1000	12-17
CP 700/800	700	800	10-15
TRIP 450/800	450	800	26-32
MS 1250/1520	1250	1520	4-6

### 1.2.1. DUAL PHASE STEELS (DP)

Dual phase steels have a microstructure consisting of a martensite and ferrite. They have a very high energy absorption capability, high-strength values, and good isotropic properties.

(a)



(b)



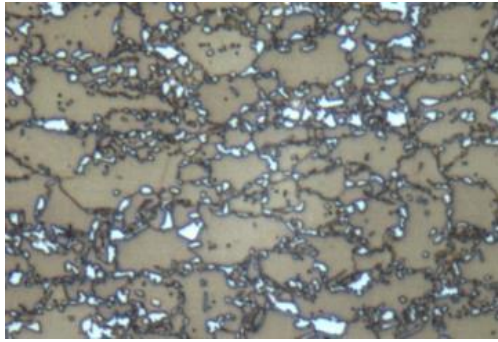
(c)



Fig. 13. (a) Bumper from DP 1180, (b) Wheel web from hot rolled DP 600, (c) B-pillar reinforcement from DP 980 [ArcelorMittal].

Fig. 13 illustrates the auto parts produced from DP steels. The microstructures and FLD graphs of DP steels are shown in Fig. 14 [ArcelorMittal].

(a)



(b)

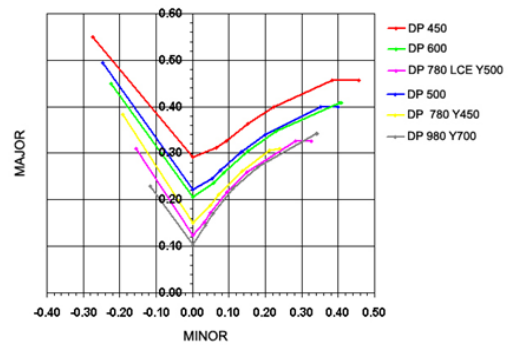


Fig. 14. DP600 steel microstructures, (b) FLDs of various DP steels [ArcelorMittal].

### 1.2.2. TRIP STEELS (TRANSFORMATION INDUCED PLASTICITY)

The microstructure of this steel is composed of bainite and retained austenite grains contained in a soft ferrite. This retained austenite can transform into martensite during deformation, so that these steels show excellent formability at high elongation. High impact energy and long fatigue life are important for the automotive industry.

(a)



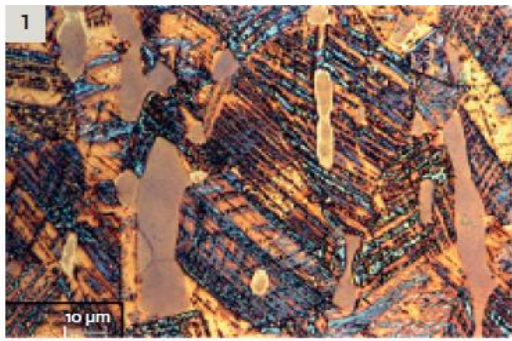
(b)



Fig. 15(a) B-pillar reinforcement in TRIP 780, (b) Bumper cross member in TRIP 780 [ArcelorMittal].

The auto parts produced from TRIP steels is displayed in Fig.15. The microstructures and FLDs of TRIP steels are shown in Fig. 16 [ArcelorMittal]. The graphs clearly reveal that the formability of TRIP steel is better than DP steel.

(a)



(b)

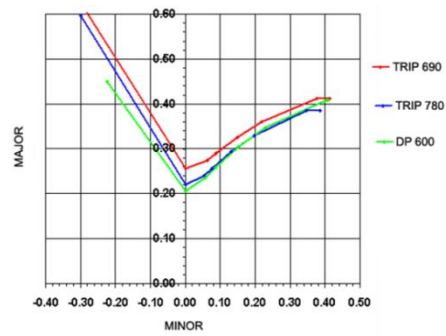


Fig. 16(a) TRIP steel microstructures [www.mpg.de], (b) Comparisons of the FLDs [ArcelorMittal]

As seen from Fig.17, the while limited increasing strain hardening exponent in DP steel, TRIP steel has higher  $n$  values as a results of the formation of new martensite [AHSS Guidelines].

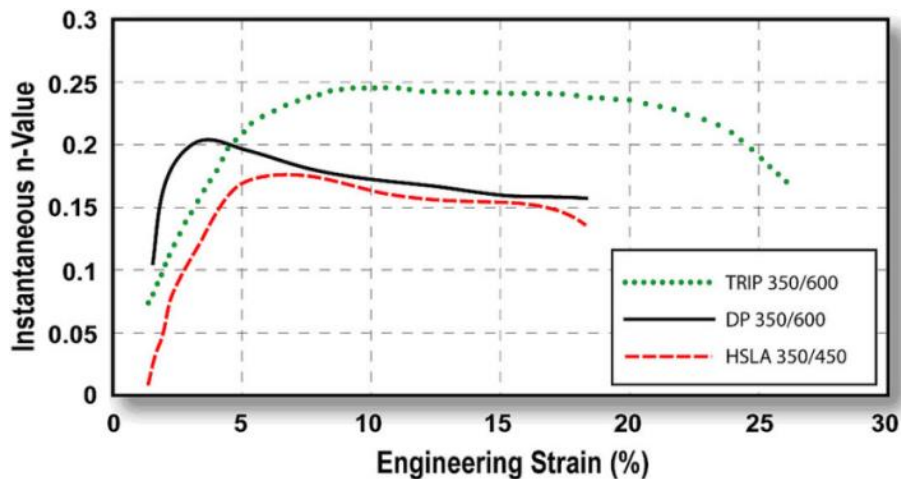


Fig. 17 Relationships of strain hardening exponents with engineering strains in TRIP, DP, and HSLA steels [AHSS Guidelines].

### 1.2.3. COMPLEX PHASE (CP) STEELS

Complex-Phase (CP) steels are contain more phases, and the yield point of them can be a minimum of 360 MPa, and the tensile strength is about 1130 MPa. Alloying elements are the same as same as those for DP and TRIP steels.

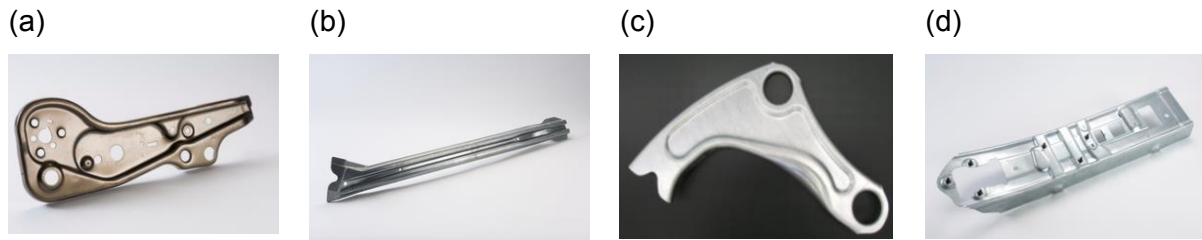


Fig. 18. (a) Seat flange in Complex Phase 600, (b) Door bar in Complex Phase 1000, (c) Suspension arm in Complex Phase 800, (d) Tunnel stiffener in Complex Phase 800 [ArcelorMittal].

Some automotive parts manufactured from CP steels are shown In Fig.18 [ArcelorMittal]. Fig.19 shows microstructure that belongs to the CP steel and FLDs of various CP steels. Microstructure consists of ferrite, bainite, and martensite phases. It is seen that the CP steel, formability is decreased with increasing yield strength.



Fig. 19.(a) CP800 steel microstructures, b-) FLDs of various CP steels [ArcelorMittal].

#### 1.2.4. MARTENSITIC STEELS (MS-MART)

Microstructure of martensitic steel consists of a full martensite phase [Zeytin, 2012], and as shown in Fig.20, tensile strength is between 700 to 1700 MPa, the total elongation is maximum 15%. It is used chassis components in automobiles, in fuel lines, exhaust systems, vehicle accessories, etc. [AHSS Guidelines].

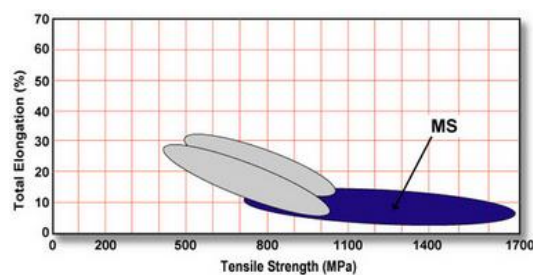


Fig. 20. Strength vs. elongation for MS steel

## 2. RECENT DEVELOPMENTS

TWIP, TRIP, and TRIPLEX steels have recently been developed for the automotive industry. These steels have 1000-1200 MPa tensile strength and elongations up to 70%.

### 2.1. TWIP STEELS (TWINNING INDUCED PLASTICITY)

TWIP steel contains high manganese in the austenite phase [Schumann, 1972]. Unlike other high-strength steels, TWIP steels contain deformation mechanism with slip dislocation and also twinning [Grassel, et al., 2000, Jung, et al., 2008]. High strength ( $> 800$  MPa) in TWIP steels is provided by the twinning mechanism. Also due to higher strain hardening, necking is delayed and occurs later. So higher elongation values ( $> 40\%$ ) are obtained. However, TWIP steels have higher springback [Lee, et al., 2005]. This is the disadvantage of the steel.

Factors in plastic deformation of metals are slip, grain boundary slip, twinning, and creep. Plastic deformation with twinning occurs when crystal structure doesn't shift. Structure formed by twinning is symmetric case according to the plane is called the twin plane of structure in the initial state. As shown in Figure 21, sliding varies in the adjacent atoms, in the case of twinned, adjacent atoms are unchanged.

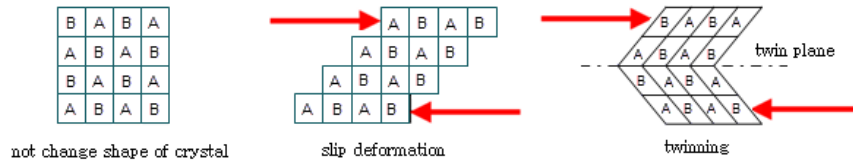


Fig. 21 The crystal structure of plastic deformation.

Akbari et al. studied the stacking fault energy (SFE) exchange by manganese and carbon content, as seen in Fig. 22. According to this study, at a proportion of 20% Mn and 0.6% C, 20 mJ/m<sup>2</sup> SFE energy is seen in TWIP steel [Akbari, 2009].

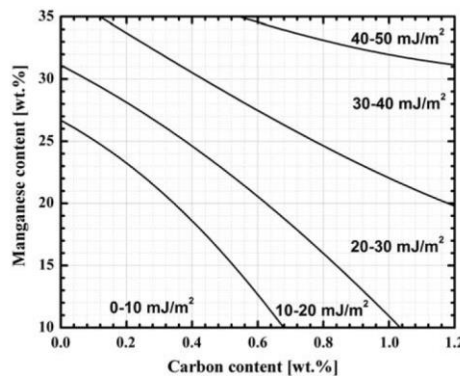


Fig.22. SFE energy based on manganese and carbon content (wt. %) [Akbari, 2009].





True stress vs. strain curves of the AHSS and TWIP steel are shown in Fig. 23 [Ferrando, 2011]. In TWIP steels, the effects of twinning are to increase the strength and elongation. Strain hardening coefficient is higher than the other AHSS.

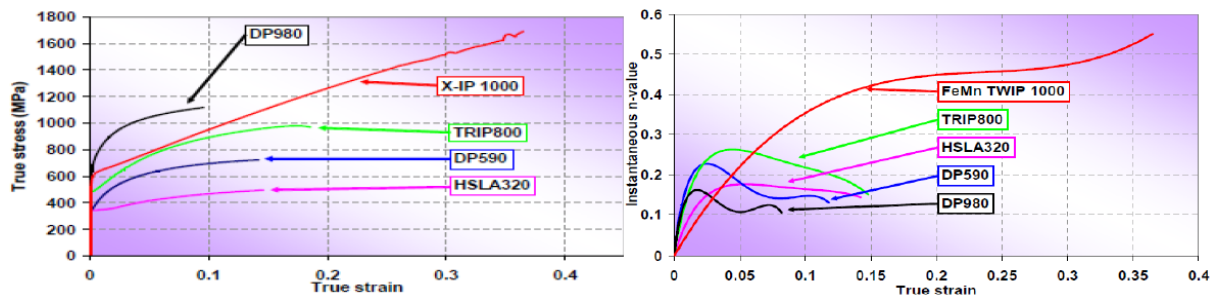


Fig. 23 TWIP (X-IP 1000) and true stress- true strain curves and strain hardening exponent changes for various steels [Ferrando, 2011].

### 3. THE LATEST PROGRESS IN AUTOMOTIVE INDUSTRY

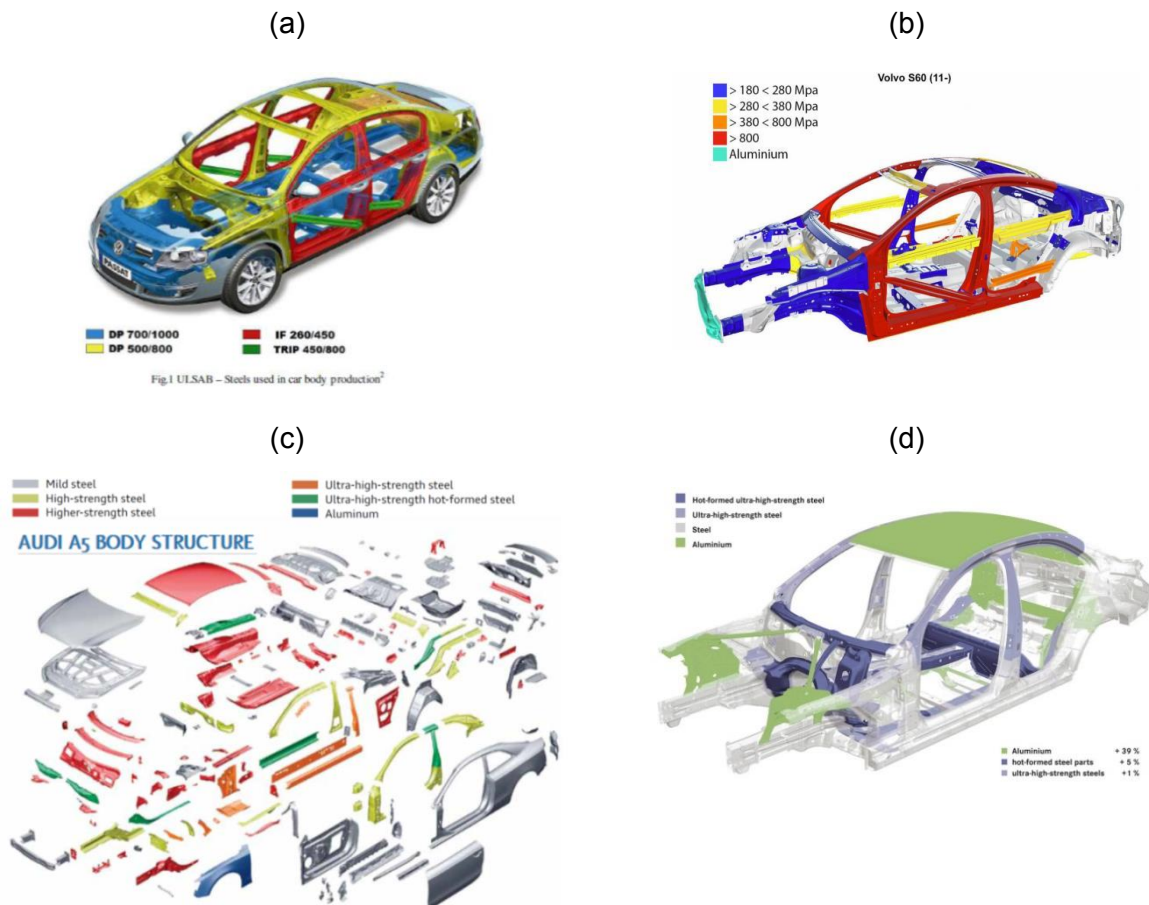


Fig. 24. The latest progress in car body materials [boronextrication.com].



#### 4. CONCLUSION

This study reveals that lightening of car structures is being performed by replacing traditional materials with advanced high strength steel thin sheet materials. AHSS, especially TWIP steel, has been the fastest growing material in automotive industry, is expected to be widespread, and attractive due to perfect uniform elongation corresponding to ultra-high strength values. The use of AHSS in car structure has been increasing gradually. New steel development is increasingly continued.

#### ACKNOWLEDGMENT

This work is part of Suleyman Kilic's PhD thesis and supported by Ahi Evran University. The university support is profoundly acknowledged.

#### REFERENCES

1. **Ruifrok, R., (2012)** "Light Weight Steel Solutions in Automotive Design", Volume 22. [http://www.han.nl/onderzoek/nieuws/more-weight-to-lightweigh/\\_attachments/presentatie\\_tata\\_steel\\_han\\_automotive\\_symposium\\_22-11-12.pdf](http://www.han.nl/onderzoek/nieuws/more-weight-to-lightweigh/_attachments/presentatie_tata_steel_han_automotive_symposium_22-11-12.pdf)
2. **Grassel, O., Kruger, L., Frommeyer, G., and Meyer, L.W., (2000)**, "High strength Fe-Mn-(Al, Si) TRIP/TWIP steels development - properties - application", Int J Plasticity 16, 1391-1409.
3. *AHSS Guidelines*, <http://www.worldautosteel.org>
4. AHSS 101: The Evolving Use of Advanced High-Strength Steels for Automotive Applications, [www.autosteel.org](http://www.autosteel.org)
5. [http://www.arcelormittal.com/automotive/saturnus/sheets/catalogue.pl?id\\_sheet=G&language=EN](http://www.arcelormittal.com/automotive/saturnus/sheets/catalogue.pl?id_sheet=G&language=EN)
6. **Havva KAZDAL ZEYTİN, G.G., Banu BERME, (02-04 April 2012)**, "İleri Teknoloji Ürünü Otomotiv Çelikler", In International Iron & Steel Symposium. (Karabük, Türkiye).
7. **Schumann, V.H., (1972)**, "Martensitische Umwandlung in austenitischen Mangan-Kohlenstoff-Stählen", Neue Hütte 17, 605-609.
8. **Grassel, O., Kruger, L., Frommeyer, G., and Meyer, L.W., (2000)**, "High strength Fe-Mn-(Al, Si) TRIP/TWIP steels development - properties - application", Int J Plasticity 16, 1391-1409.



9. **Jung, J.K., Lee, O.Y., Park, Y.K., Kim, D.E., Jin, K.C., Kim, S.K., and Song, K.H., (2008)**, "Microstructure and Mechanical Properties of High Mn TWIP Steels", *J Korean Inst Met Ma* 46, 627-633.
10. **Lee MG, Kim D, Kim C, Wenner ML, Chung K, (2005)**, "Spring-back Evaluation of Automotive Sheets Based on Isotropic-Kinematic Hardening Laws and Non-Quadratic Anisotropic Yield Functions, Part III: Applications", *Int. J. Plasticity*, 21 (5), 915-953.
11. **Akbari, A.S., Imlau, J., Prahl, U., Bleck, W., (2009)**, "Derivation and Variation in Composition-Dependent Stacking Fault Energy Maps Based on Subregular Solution Model in High-Manganese Steels", The Minerals, Metals & Materials Society and ASM International.
12. **R. Pla-Ferrando S. Sánchez-Caballero, M.A.S., A.V. Martínez-Sanz, (2011)**, "TWIP/TRIP steels. Future trends in automotive industries", *Fascicle of Management and Technological Engineering Volume X (XX)*.
13. *<http://boronextrication.com>*
14. *<http://www.mpg.de>*







## NOISE IN HYDRAULIC SYSTEMS AND PREVENTION METHODS

**H.Sevil ERGUR**, *hsergur@ogu.edu.tr* Eskişehir Osmangazi University, 26480, Eskişehir

**Yasar PANCAR**, *ypancar@ogu.edu.tr* Eskişehir Osmangazi University, 26480–Eskişehir

### ABSTRACT

This document presents the noise phenomena and prevention methods in hydraulic systems. Sound that is unwanted or disrupts one's quality of life is called as noise. It is also form of waste energy. When there is a lot of noise in the environment, it is termed as noise pollution. Noise is a broad and complex subject that is generally caused by pressure waves in the fluid stream. In hydraulic systems, there are three main forms of noise, such as air borne, fluid borne and structure borne. Fluid borne noise is one of the main components of hydraulic systems and its attenuation has a significant effect on the cost of systems. The noise level of a system is dependent on the complex interaction of a large number of components. The most common source of noise in hydraulic systems is the sound produced by the fluid itself. When the noise level created in the piping system exceeds the background noise level in any audible frequency band, it may become objectionable. When the created levels exceed 90 dB(A), permanent hearing damage can occur and a necessity of preventing erosion of the system components. Noise problems in liquid systems are comparatively low due to the flowrates in most piping systems are limited to reduce pressure drop. Noise emission by hydraulic system machinery has become a serious problem for fluid power equipment manufacturers and operators. Since the pumps are the largest component of sound power in hydraulic system, much more attention has to be given on these elements. Noise levels generally depend on mounting method and present conditions of hydraulic circuit in which the pump is used. Due to for their high level of noise, hydraulic power systems may cause frequent complaints. Besides limiting the application of fluid power, these problems may also compel the designers to replace it with other methods of power transmission.

**Keywords:** Noise, sound power, fluid power, pressure waves, pressure drop, filter selection, hydraulic system.

### 1. INTRODUCTION

The best definition of noise is “unwanted sound” “[Wang, 2008]”. It is obvious that high levels of noise are extremely harmful to people's health, that's why it is the most important reason to



control it. Exposure to a high level of noise could cause immediate, noticeable temporary and permanent hearing loss of a person exposed with a noise environment above a certain level. Since the Walsh–Healthy Act of 1969 was amended by adding restrictions on the workers, most industries and governments are motivated strongly to find some effective and economical methods to reduce the noise produced by machines. Thereby, noise control which has developed rapidly in the last few years, is a very important subject and is likely to have a promising development in the future "[Wang, 2008, Concha, Campbell and Steenland, 2004]".

Sound is a physical occurrence. It is caused by instantaneous pressure variation that are transmitted by wave motion. Noise generation and increase of intensity is proportional with the operation pressure. In general, hydraulic pump is the source of noise and its type is effective on noise creation. Noise by rotating elements is considered secondly. Prevention methods, design and applications of manufacturers are important from the noise level point of view. Since noise created from the industrial equipment is rather serious matter "[Wang, 2008]", there are various methods for cutting down and controlling it. So, it won't be hazardous to operators. Employers stay away from this matter because, methods need skilfull crew and extra cost. Noise reduction is warranted by constructive measures. Besides these, noise at pumps can be absorbed by hydraulic muffler.

As with any occupational hazard, control technology should aim at reducing noise to acceptable levels by action on the work environment. Such action involves the implementation of any measure that will reduce noise being generated, and/or will reduce the noise transmission through "[Concha, Campbell and Steenland, 2004; Skaistis, 1988]" the air or through the structure of the workplace. Such measures include modifications of the machinery, the workplace operations and the layout of the workroom. In fact, the best approach for noise hazard control in the work environment is to eliminate or reduce the hazard at its source of generation, either by direct action on the source or by its confinement. Practical considerations must not be overlooked; it is often unfeasible to implement a global control program all at once. The most urgent problems have to be solved first, then the priorities have to be set up. In certain cases, the solution may be found in a combination of measures which by themselves would not be enough, for example, to achieve part of the required reduction through environmental measures and to complement them with personal measures "[Skaistis, 1988]".

## **2. NOISE AND EFFECT ON HUMANITY**

Noise in everydaylife conscious struggle is in the foreground, this is because the noise threatens the human health. Noise problem imposes responsibility so, necessary precaution must be taken by employer "[Concha, Campbell and Steenland, 2004]". The effect of noise on human health is investigated under two headings. They are namely negative effects on hearing



sensation and psychological discomfort. Chronic hearing loss can be seen on human who are under the effect of noise for a long duration which are not hazardous in short periods. High intensity level noise is hazardous to feathers in hearing organ. A human under the high level noise effect will have hearing loss for a while, but situation "[NTIS,1974; Eaton–Vickers, 2002]" is temporary and is go away in certain period. However, the actual important point is permanent hearing loss. Investigations show that, while some of the operators working at 100 dB(A) and higher values can bear high level noise without any problem, but some have very little response. In continual operations in noisy medium, the level of deafness will increase. Ringing in ear is the indicator of decrease in hearing sense and precautions must be taken.

**2.1 Formation of Noise in Hydraulic Systems:** Although technological developments has prevented the fluid loss, most of the designers accept the hydraulic losses due to their nature as noise sources. Noise can not be foreclosed, however with the aid of several methods level of, it can be reduced to acceptable values. Long studies, efforts and investments may satisfy bonifications "[Wang, 2008, Concha, Campbell and Steenland, 2004]". Hydraulic power systems are well known for their high levels of noise. By the 1950's hydraulic powered machine noise had eached levels that caused frequent complaints "[Skaistis,1988]". These problems can not only limit the application of fluid power, but also compel the designers to replace it with other methods of power transmissions as electrical systems "[NTIS, 1974]". Thereby the commercial benefit of hydraulic systems is greatly affected. For hydraulic machinery, more than 95% of noise comes from the pumps and motors. Valves are another noise source, but they cause fewer problems in industry because of the masking noise from other predominating sources "[Skaistis,1988; Şahin, 2003]". As known all hydraulic pumps are responsible for transporting the sucked fluid and operate on the principle of compressing fluid from big to small volumes. Pressure variations in pump body will cause vibrations. Reason for noise is these vibrations then, this noise is transmitted to pump body and piping system. As a result of these vibrations, secondary noise sources occur due to resonance. Vibration may also be fluid borne. Pressure and discharge variations also cause vibrations and spread all around the piping systems and hydraulic equipments "[Tazawa and Spon, 2004; Moser, 2009]".

Noise at valves, regulators and control equipment is temporary and dependable on turbulence level and cavitation. Actually, in some designs and conditions, elements of hydraulic system cause vibration and noise. That's why, general analysis is rather difficult for this matter, due to design. Noise level of this tools are dependable to design, fluid velocity and response time. Main source of noise in piping systems is transmission of vibration to walls and rijid joints of vibration at pump, fluid and the other elements' vibration. Sufficient supports at certain intervals will warrant for decrease of noise level. Flexible pipe bracelets will transfer the vibration in fluid to surface directly "[Ortwig, 2005]". Periodic and developed noise types in the operation of hydraulic pumps are classified in three ways.



1. Body Borne–Noise: It is due to variable pressures in pump body.
2. Fluid Borne–Noise: It is due to vibrations developed by pressure and discharge.
3. Fluid Noise: Generally it arises at valves and piping system, specially at contraction sections. It is also called cavitation noise. This kind of noise is analysed in two group items.
  - a) Impulse Noises: They are due to valve position changes.
  - b) Mechanical Noises: Noises by movable concentric part "[Eaton–Vickers, 2002]".

**2.2 Pump Noise** : Pump noise is caused by pressure fluctuations which are developed by rotating and sliding parts such as blades, pistons, rotors, gears, etc. Metal bodies are a part of hydraulic pump or electrical motor which do not have any precaution in preventing noise transmitting out. Coupling noise is produced by improperly ejected shaft. If pump–motor group works in fluid media, fluid will serve as a cushion, so noise will not be transferred outlet "[Concha, Camphell and Steenland, 2004]". Generally, pump is responsible from noise in hydraulic system. Also the piston, vane and gear pumps operate noisy. Since the pumps are major noise source, there are so many studies going on this subject. Noise level measured by manufacturers is more satisfactory, this is because noise at operation point may be affected by environmental conditions. However, this may be not safe guidance, because there is not any method for measuring pump noise directly "[Tazawa and Spon, 2004; Eaton–Vickers, 2002; Şahin, 2003; Jensen and Jokel, 1978]".

In hydraulic system desing, selection of pump must done according to noise level. Movable parts, forms and efficiency are directly dependable to vibration. Besides all these parameters, pump type, control conditions, flow characteristics at suction and discharge sides, revolution and pressure rises have important influences on noise and vibration occurance. These characteristics will lead to one more classification. The another matter is assembly type which is also effective too. Inapropriate assembly will increase present noise level "[Ortwig, 2005]". Since screw pumps are the quietest ones, than the internal–annular gears, an exclusive constructive gear pumps and vane pumps are adviced to be treated. At the end, we will come accross to piston pumps.

Nowadays more constructional development is possible for piston pumps. If such situation occurs, then secondary care has to be taken. Displacement, pressure and revolution are operational conditions and they are impressive on noise generation. In variable discharge, the noise level of axial piston pumps increase with the driving power "[Eaton–Vickers, 2002]". Pump noise is the form of either fluid borne or mechanic sources. Fluid borne noise is due to flow shocks which create pressure waves and is decreased at the source or minimized by changing the hydraulic design. At the design of gear pumps by changing the gear forms, pressure waves is decreased or fluid movement is changed by compressed fluid between the



teeth. Suction construction is also effective for noise level. If fluid velocity is decreased, pressure rising time prolongs and so, pump vibration is minimized.

**2.3 Motor Noise** : Noise comes from bearings, the rotor and stator assembly (the characteristic hum), and especially the fan. A standard electric motor contains a fan with blades designed to provide cooling whether the motor shaft rotates clockwise or counter-clockwise. A fan designed for rotation in only one direction will generate less noise, so the expense of this option may be warranted if the application demands quiet operation "[Eaton–Vickers, 2002]".

**2.4 Valve Noise:** Generally, high level noise occurs while fluid is entering the valve and pressure drops seriously. This because of dissolved air in fluid. When the valve's gate is not seated properly, this kind of noises arises. All of these noises can be eliminated by good design or adding damping features in a valve. Anyhow, electrovalves are in use and "[Tazawa and Spon, 2004]" noise level is not a problem. Valves are also used to meter flow and to control pressure in systems. As a rule, noise increases exponentially with the amount of restriction of flow and pressure. As a rule of thumb, noise is proportional to approximately the fourth power of low restriction and square of pressure increase. When flow is restricted to less than 20 to 25 percent of maximum, noise often becomes a problem. The extreme turbulence generated at the restrictions produces substantial and vibratory energy.

Noise has occurred in cabs of construction and other mobile equipment for years. Often, a high-frequency occurs noise randomly when fluid traveling at high velocity through the valve, undergoes a rapid and severe drop in pressure "[Concha, Campbell and Steenland, 2004; Ver and Beranek, 2006]". This causes air dissolved in the fluid to form bubbles when they collapse, generate noise. Other types of noise such as chattering, squealing or buzzing is generated when poppet-type valves do not seat properly. Fortunately, most of these problems can be eliminated through better system design or by incorporating cushioning features into valves. A current trend replaces direct-operated valves with joystick-controlled remote "[Şahin, 2003; Crook and Heron, 1977]" electrohydraulic valves. This process of removing the hydraulics from the equipment cab offers other advantages beyond providing a quieter workplace environment. However, decrease in discharge and the velocity also causes the decrease of energy converted to noise. Due to diminishing of velocity also the reason for high percentage of material wear.

**2.5 Piping Noises:** Pressure pulsations in plumbing can distribute noise over a large area. They can shake hose and tubing, causing rattling and eventual leakage. Although reducing fluid-borne noise can be complicated, many manufacturers suggest rules of thumb to help reduce noise. Terminating a long run of metal tubing with a section of hose at each end helps isolate noise sources, One might be tempted to simplify the design by instead specifying a single section of hose. Hose, however, is very sensitive to pressure pulsations, so in long

sections it can be a greater source of noise than metal tubing or pipe. Securing tubing to framework with resilient clamps eliminates rattling and banging noise. However, care should be taken not to confine tubing too tightly "[Lyle, 2003; Crocker, 2008]" because lines may need to undergo thermal expansion. On the other hand, allowing a tube to fit too loosely could cause wear as the tube constantly rubs against a metal clamp surface. Likewise, resilient grommets should be used when a hose or tube passes through a hole in framework, covers, etc. Actuators, especially hydraulic motors also generate noise as well, sometimes are considered to generate noise equivalent to that of pumps. In any case, hydraulic motors often operate at relatively slow speeds, so motors generally operate much quieter than pumps. Although decrease of noise level is rather complex, there are few practical methods for eliminating fluid borne noise. For example, as shown in (Fig. 1), renewed both nebs of hose ends with metal piping may help in reducing noise level.

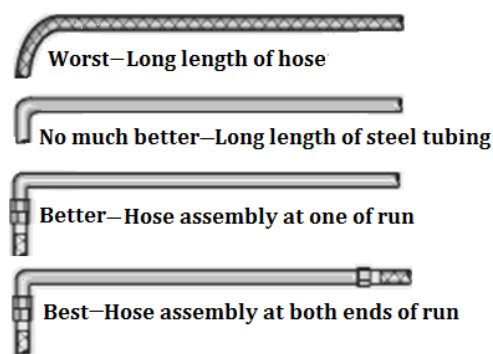


**Fig. 1** Hose Replacements in Piping Systems "[Eaton–Vickers, 2002]".

Hose is very sensitive to pressure borne vibrations. That's long, ones may produce more noise than metal tubing and hoses. Flexible bracelets are very usable in reducing tickle and shock noises. In the same manner, if hose and piping get through the holes of the body, "[Eaton–Vickers, 2002, Bies and Hansen, 2009]" flexible stuffing must not be used for sealing

### 3. NOISE LEVEL

In general, noise level is calculated with the evaluated data obtained by noise level meter and noise dose meter. Identified total power and revolution per minute "[Ortwig, 2005]" will help the prediction of theoretical noise level. The level of sound expressed in dB(A) via reasonable measure of the loudness of that sound. Different sounds having the same dB(A) level generally sound about equally as loud, although the character of noise also place apart in its perceived loudness.

**3.1. Determination The Level of Theoretical Noise Power** : The method for determination of noise power level of a machine differs according to the machine types. In anyway, certain



amount of total power is converted to noise. Usually, the level of noise power ( $W$ ) is approximately determined by

$$W = f \cdot W_m \quad (1)$$

In equation (1) the machine conversion factor and the machine total power are notated as  $f$  and  $W_m$  respectively.

$$f_{min} = \frac{10 \log(W_{enk})}{10^{-12}} \quad (2)$$

$$f_{max} = \frac{10 \log(W_{enb})}{10^{-12}} \quad (3)$$

The definition of lower and upper limits of conversion factors are also calculated by using equation (2) and (3). In these equations, lower limit of conversion factor is indicated as  $W_{enb}$ , likewise the upper limit is also remarked as  $W_{enk}$ . With the aid of these equations, the minimum and maximum power levels can be predicted easily.

**3.2. Calculation of Pump Noise Power Level:** Pumps generally create wide frequency band over 3000 Hz. This is because of cavitation and high flow velocity. The basic notation for pumping frequency is  $F$ . The other parameters composing the frequency are notated as  $n$  and  $m$ . These parameters are determined as the pump operation speed (rpm) and the conversion constant of pump pressure per revolution respectively.

$$F = \frac{n \cdot m}{60} \text{ (Hz)} \quad (4)$$

Especially for big pumps, at basic pumping frequency, pure noise is dominant. If manufacturer does not confer the noise level, the below equation is used. In equation (5), the pump efficiency as signed with  $\eta_e$ ,  $K_p$  and  $N_e$  refers the noise power constant and effective power that is consigned the pump type respectively "[Ortwig, 2005]".

$$W = 10 \log N_e \left( 1 - \frac{\eta_e}{2} \right) + K_p \quad (5)$$

#### 4. ENGINEERING NOISE CONTROL

Any noise problem may be described in terms of a source, a transmission path and a receiver. Noise control may take the form of altering any one or all of these elements. The noise source is where the vibratory mechanical energy originates, as a result of a physical phenomena, such as mechanical shock, impacts, friction or turbulent airflow "[Moser, 2009]". With regard to the noise produced by a particular machine or process, experience strongly suggests that, when control takes the form of understanding the noise-producing mechanism and changing it to produce a quieter process. As opposed to the use of a barrier for control of the transmission path, the unit cost per decibel reduction is of the order of one tenth of the latter cost.

Clearly, the best controls are those implemented in the original design. It has also been found that, when noise control is considered in the initial design of a new machine, advantages manifest themselves resulting in a better machine overall "[Jensen and Jokel, 1978; Ver and Beranek, 2006]". These unexpected advantages then provide the economic incentive for implementation and noise control becomes an incidental benefit. Unfortunately, in most industries, occupational hygienists are seldom in the position of being able to make fundamental design changes to noisy equipment. In fact, there may be a multiplicity of paths, both in air and in solid structures. The total path which contains all possible avenues along which noise may reach the ear, has to be considered. In existing facilities, controls may be required in response to specific complaints from within the workplace and excessive noise levels may be quantified by suitable measurements as described previously "[Ortwig, 2005]".

In proposed new installations, possible complaints must be anticipated and expected excessive noise levels must be estimated by some procedures. As it is not possible to entirely eliminate unwanted noise, minimum acceptable levels of noise must be formulated and these levels constitute the criteria for acceptability which are generally established with reference to appropriate regulations in the workplace.

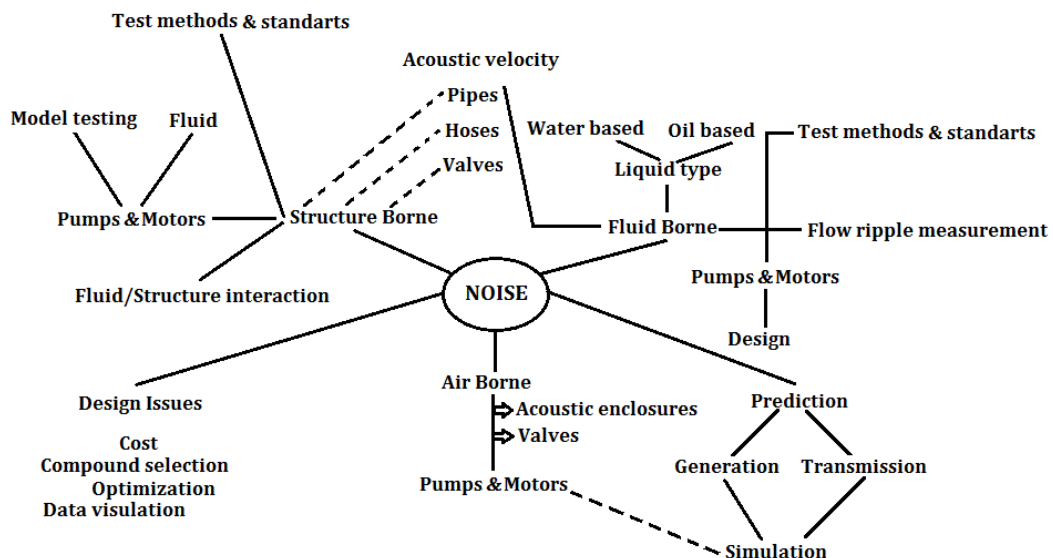


**Fig.2** Parameters of Noise in Hydraulic System

In both existing and proposed new installations, an important part of the process is to identify noise sources and to rank order them in terms of contributions to excessive noise. When the requirements for noise control have been quantified "[Cheremisinoff, 2004; Moser, 2009; Ver and Beranek, 2006]" and sources firstly identified and ranked, it is possible to consider the various options for control and finally to determine the cost effectiveness of the various options. The cost of enclosing a noise source is generally much greater than modifying the source or process producing the noise as detailed in Fig. 2.



**4.1. Control of Noise at the Source** : Main rule is to control the noise level at source. In this way, all environment is prevented from the noise and is the most effective method. General fundamentals of controlling the noise at sources are, the control of noise with planning and maintenance, alteration of noise operation conditions, selection of less noisy procedures, change of operation point, using mufflers, isolation of vibration, absorbing the vibration and isolation of noise source "[Jensen and Jokel, 1978; Lyle, 2003]".

**4.2. Noise Control between the Source and Receiver**: As to the area is convenient, the control of noise level at extension area can be done by adjustment of gap between the machines, mounting noise absorbent on all kinds of surfaces and barriers. The control noise at the source, it is first necessary to determine the cause of the noise and secondly to decide on what can be done to reduce it. Modification of the energy source to reduce the noise generated often provides the best means of noise control.

**4.3. Noise Control at Receivers** : If noise is not controlled at source and extension area, operator can use protective clothing. These measures can be outlined as isolation human from noise, control with administrative precautions, decrease the duration of noise effects, operation rotationally at noisy media and using ear protectors "[Şahin, 2003]". In new installations, quantification of the noise problem at the design stage may range from simple to difficult but never impossible. At the design stage, the problems are the same as for existing installations; they are identification of the source or sources, determination of the transmission paths of the noise from the source to the receivers, rank ordering of the various contributors to the problem and finally, determination of acceptable solutions [Şahin, 2003; Ver and Beranek, 2006].

## **5. NOISE CONTROL AT HYDRAULIC SYSTEMS**

**5.1. Proposed Methods in Controlling Noise Level** : Noise pollution is one of the important issue for human health arising from technological products and machines. Noise and vibration that increase the noise pollution are also caused hazardous effects on human body. These handicaps can be diminished by achieving the acoustic comfort and improving operation conditions "[Rusko, Bilova and Lumnitzer, 2011, Cheremisinoff, 2004]". Undesirable noises and damage on human can decrease by using various noise isolation methods. One of the main design problem for noise, control engineers is to search methods for low cost with noise absorbent properties. In noise isolation technology, there are so many basic factors. They are outlined as determination of noise kind, material type, selection of area for isolation and environmental conditions. Mounting method of pump group into hydraulic tank is also effective on noise. Noise sources of hydraulic systems are classified as structure borne, air borne and fluid borne "[Şahin, 2003; Jensen and Jokel, 1978]" mentioned in section 4. Basic structure of borne noise is from pump group. Pumps and motors must be mounted on noise absorbent plates. For decreasing the noise level, precautions given below are advisable.



- a. Pump must be coupled directly to driver.
- b. Pump–driver to be mounted on noise absorbent wedges.
  - b<sub>1</sub>. Pump plate must not get in resonance with pump frequency.
  - b<sub>2</sub>. For preventing the extension area of noise diffusion, pump and driver contact surfaces must be as little as possible.
  - b<sub>3</sub>. Pump–driver must be made of noise absorbent material (GG 14–18 etc.).
  - b<sub>4</sub>. Users must get advices for elastic couplings from manufacturers.
  - b<sub>5</sub>. All rotating parts must be dynamically balanced.
  - b<sub>6</sub>. Eccentricity must be controlled for shaft and coupling.
  - b<sub>7</sub>. Thrust bearing must be preferred instead of ball bearing.

Pump and motor noise can be controlled by isolation "[NTIS,1974; Ver and Beranek, 2006]". Effective solution for vibration at pump inlet and discharge line is to use hose instead of metal piping. But this kind of precaution can not prevent noise from piping systems to hydraulic systems. Although tank seems absorbent, it is not useful for decreasing the noise level. By-pass must be avoided in isolation precautions. For high level control, surrounding of pump–motor group is enclosed by acoustic materials. In all this kind of precautions may prevent cooling, so heating might be the ascending problem "[NTIS,1974]". Precautions for controlling the noise in piping systems are outlined as following,

- i. Metal pipes is preferred for short and long piping systems. (In metal pipes, fluids borne noise level is low but air borne noise level may be high). In compact systems between the hoses and very short metal pipes are preferable for noise level decrease.
- ii. Metal piping must be mounted on concrete base near to machine body and bracelets are used for holding the pipes in right position, not advisable to mount bracelets on flexible bodies.
- iii. It is advisable to avoid using sharp elbows in steel piping systems. Otherwise, pressure waves will not be unavoidable "[Lyle, 2003, Crook and Heron, 1977]".

**5.2. Noise Control by Constructive Methods:** Control panel mounted on hydraulic tank may spread noise increasingly. So, mounting on some separated surface is advisable for decreasing noise level. Since, covered coupling between pump and motor group is not sufficient for decreasing noise level, using pressed hard rubber between two absorbent plates will good sollution. Hydraulic power units are mounted on main body of hydraulic presses and machining. Noise on power units will spread all around the body. Therefore, power unit is mounted on either on concrete floor or on vibration absorbent plates. Moreover, rubber hose and vibration absorbent can used at discharge side of the pump. Succesfully mounted support on piping systems will decrease noise level considerably. Steel waved rubber hose are used at the inlet elbows for increasing the noise piping systems. For cavitation and decreasing noise

level at valve outlet due to sudden pressure rise, pressure reducing elements are used for reducing pressure step by step.

Although all kinds of precautions, if noise is present then power unit is used away from human, airy and noise isolated room "[Ortwig, 2005; Crook and Heron, 1977]". Noise control is an active or passive means of reducing sound emissions, often for personal comfort, environmental considerations or legal compliance. Active and passive noise controls are the kind of sound reduction methods. For controlling the active noise, a power source is used. However, noise-isolating materials such as insulation, sound-absorbing tiles or a muffler are preferred rather than a power source in passive noise control. Active noise canceling is best suited for low frequencies. For higher frequencies, the spacing requirements for free space and zone of silence techniques become prohibitive. In acoustic cavity and duct based systems, the number of modes grows rapidly with increasing frequency, which quickly makes active noise control techniques unmanageable "[Ver and Beranek, 2006]".

## 6. ACOUSTIC PROPERTIES OF NEW EQUIPMENT ACCORDING TO NOISE POLICY

Noise policy is a testimony which designates general rules for noise problems and related organisations. One of the most important topic of them is noise which causes constant hearing loss. It is not only a threat for hearing loss, also the noise control target must be specified due to cause of many other problems. On the other hand, noise policy of enterprises are to be show the duty and responsibilities of the workers. Noise usually measured at operators nearby, however "[Bies and Hansen, 2009; Crocker, 2008]" surrounding of a machine is the place too, where the level of noise be controlled. Low levels of unwanted sound are closely associated with the notions such as comfort, luxury, wealth and quality. Wealthy people tend to live in quiet areas to work in quiet environments and to purchase products and services with optimized acoustic comfort. The World's mightiest decision makers tend to prefer noiseless interiors and exteriors. Wealthy as well as less wealthy people, mighty as well as less mighty decision makers, nonetheless have in common that they often make their decisions regarding products' and services' acoustic aspects unconsciously.

**6.1. Acceptable Noise Level:** Target noise level and acceptable maximum noise level must be assessed. In order to keep the surroundings of the machine at certain points, noise level in all parts of the machine must also be kept under predicted value. Flowchart shown in Figure 3 is used for determining the acceptable noise level. Assessment of the acceptability of an environmental noise is necessary to judge if complaints about an existing noise source are justified or if a proposed development can proceed with or without mitigation methods.

**Table 1.** Guide to Reactions for Different Levels of Noise Intrusion

Noise Intrusion	Likely Reaction
-----------------	-----------------



0–5 dB	Marginal
5–15 dB	Great concern
15–20 dB	Serious concern
20–25 dB	Extreme action

One approach involves comparison with background noise levels and is more applicable for assessment of industrial, commercial or neighbour noise than for transportation. A general guide to the expected reactions to noise intrusion is given in Table 1 "[Crocker, 2008]". The aim is to limit the intrusiveness of the noise. This approach to assessment requires measurement of the noise level in the area before the proposed development or if it is in response to a complaint with the noise considered to be offensive turned off. If it is not possible to turn the noise source off, the background noise measurements can be made in a similar type of area. The background noise can vary during different times of the day so, the measurements must be made during the time intervals, the noise may be considered to be annoying. After the background level of noise is determined, the adjusted measured or predicted noise level compared with the background noise level with an excess of (+)5dB(A) considered acceptable. This is based on the assumption that such small increases in noise level are not likely to cause a long-term significant raise in annoyance. A 5dB(A) increase is also often used to determine whether a full environmental impact statement needs to be prepared.

## **6.2. Responsibility and Liability of Noise Managers and Production Engineers:**

Production engineer determines new equipment necessity, disputes or not noiseless process be effective in supplying the new machines. Noise policy application program, budget planning nad organization "[Rusko, Bilova and Lumnitzer, 2011; Cheremisinoff, 2004]" and maintenance are coordinated by the noise manager. The Health and Safety at Work Act (HSWA) which is firstly formed in 1974 governs the provisions necessary for securing the health, safety and welfare of people at work including controlling the storage and use of dangerous substances. The HSWA imposes general duties on employers. All employers must provide and maintain a safe place of employment with adequate facilities for their employees' welfare by implementing all necessary procedures, training for the safe use and handling of dangerous articles. Under the management of HSWA regulations that is constituted in 1992, an employer is required to assess risks to health and safety which arises in connection with his work and take any necessary preventative measures. As well as this legal responsibility, the employers also have an implied responsibility to take reasonable steps as far as they are able to ensure the health and safety of their employees is not put at risk. So an employer might be found liable for his actions or failure to act even if these are not written in law "[Rusko, Bilova and Lumnitzer, 2011; Bies and Hansen, 2009]". Fig.3 outlines a procedure, step-by-step for calculating the maximum acceptable noise level for a given installation site.



- (a) In Box 1 enter the noise exposure goal that the organisation has set for working areas.
- (b) In Box 2 enter the present noise exposure level at what will be the operator position of the new machine, measured when the machine to replace is not running. If the value in Box 1 exceeds the value in Box 2, use the *subtracting decibels table* on the flowchart to subtract the level in Box 2 from the level in Box 1 and enter the result in Box 4.
- (c) For example, if the level in Box 1 is 85 dB(A) and the level in Box 2 is 80 dB(A), by using the *subtracting decibels table*, the level to be entered in box 4 is 82 dB(A). If the value in Box 2 exceeds the value in Box 1, the present noise in the area is above the goal and therefore needs to be reduced. Estimate the level that will exist in the area after feasible engineering controls have been installed and insert this value in Box 3.
- (d) If the value in Box 3 is lower than the value in Box 1 (that is, anticipated engineering controls will reduce the noise in the area below the goal), use the *subtracting decibels table* to subtract the value in Box 3 from the value in Box 1 and enter the result in Box 4. The result is the maximum noise exposure level that can be introduced into the treated noise environment without causing the noise goal to be exceeded.
- (e) If the value in Box 3 is higher than the value in Box 1 (that is, after the installation of feasible controls the noise in the area will still exceed the goal) then, reduce the value in Box 3 by 10 dB(A) and enter the result in Box 4. This will ensure that after feasible controls have been introduced, installation of new equipment will have a minimal effect (the increase will be less than 0.5 dB(A)) on the noise of exposure level in the area. Subtract 0.3 or 5 dB(A) from the value in Box 4 depending on whether 1, 2 or 3 or more machines respectively will be installed either now or in the future and enter the result in Box 5. This correction allows for the additive effects of noise from adjacent sources. The value in Box 5 is the maximum level that can be tolerated from an individual machine over its working lifetime. Since the noise emitted by a machine normally increases with wear and tear, it is desirable to specify for a new machine, a somewhat lower limit than the calculated maximum acceptable value. A correction of 2 dB(A) allows a small margin for wear and tear and produces the final result in Box 6. This is the maximum acceptable noise level to specify for a new machine.

**6.3. Usage of Suppliers Noise Data:** Design and construct such machinery so that it can be operated, adjusted and maintained without putting people at risk and, for noise, reduce risks from noise emissions to the lowest level taking account of technical progress and the availability of means of reducing noise, in particular at source. Standard methods are now available for measuring the noise emission of industrial machines. Measurements made according to other procedures may, however, be acceptable if performed by a competent operator with a clearly defined procedure. International standards are used for measuring and definition of noise emissions. Flowchart in Figure 4 is used the prediction of noise level. This flowchart presents a method for using supplier's noise information to estimate the amount of





noise for a given machine will be introduced into the workplace "[Tazawa and Spon, 2004; Rusko, Bilova and Lumnitzer, 2011]".

- (a) Enter the supplier's noise measurements result in Box 1.
- (b) Refer to the supplier's noise information sheet to determine whether the noise was measured as a sound pressure level or a sound power level.
- (c) If measured as a sound pressure level, make no adjustment. However, if supplier's sound pressure level data are for positions at larger distances than the operator's location, seek expert advice.
- (d) If measured as a sound power level, subtract 8 dB(A) from the value in Box 1 and enter the result in Box 2.
- (e) Refer to the supplier's noise information sheet for a description of the conditions under which the noise measurement was made.
- (f) If the test conditions appear to have been representative of typical working conditions (for example, machines are installed in reverberant surroundings, have suffered some wear and tear and are run fully loaded), no adjustment is necessary.
- (d) If the test conditions are not representative (for example, the test machine is in new condition and is run on less than full load in non-reverberant surroundings) add a 6 dB(A) correction to the value in Box 2 and enter the result in Box 3. If the test conditions are partially, but not fully, representative of the working conditions, select an appropriate correction between 0 and 6 dB(A).
- (e) The value in Box 3 is the estimated noise level, the machine will introduce into the area in which it is installed. This value is an estimate and that variations of 5 dB(A) are possible.
- (f) The noise introduced by the new machine will combine with the noise already present in the area. To calculate the new noise level in the area, enter the present noise level in the installation area in Box 4, then use the *adding decibels table* to combine the levels in Boxes 3 and 4. For example, if a machine with a noise level of 78 dB(A) is introduced into an area where the existing noise level is 80 dB(A), by using the *adding decibels table*, the new noise level in the area will be 82 dB(A).

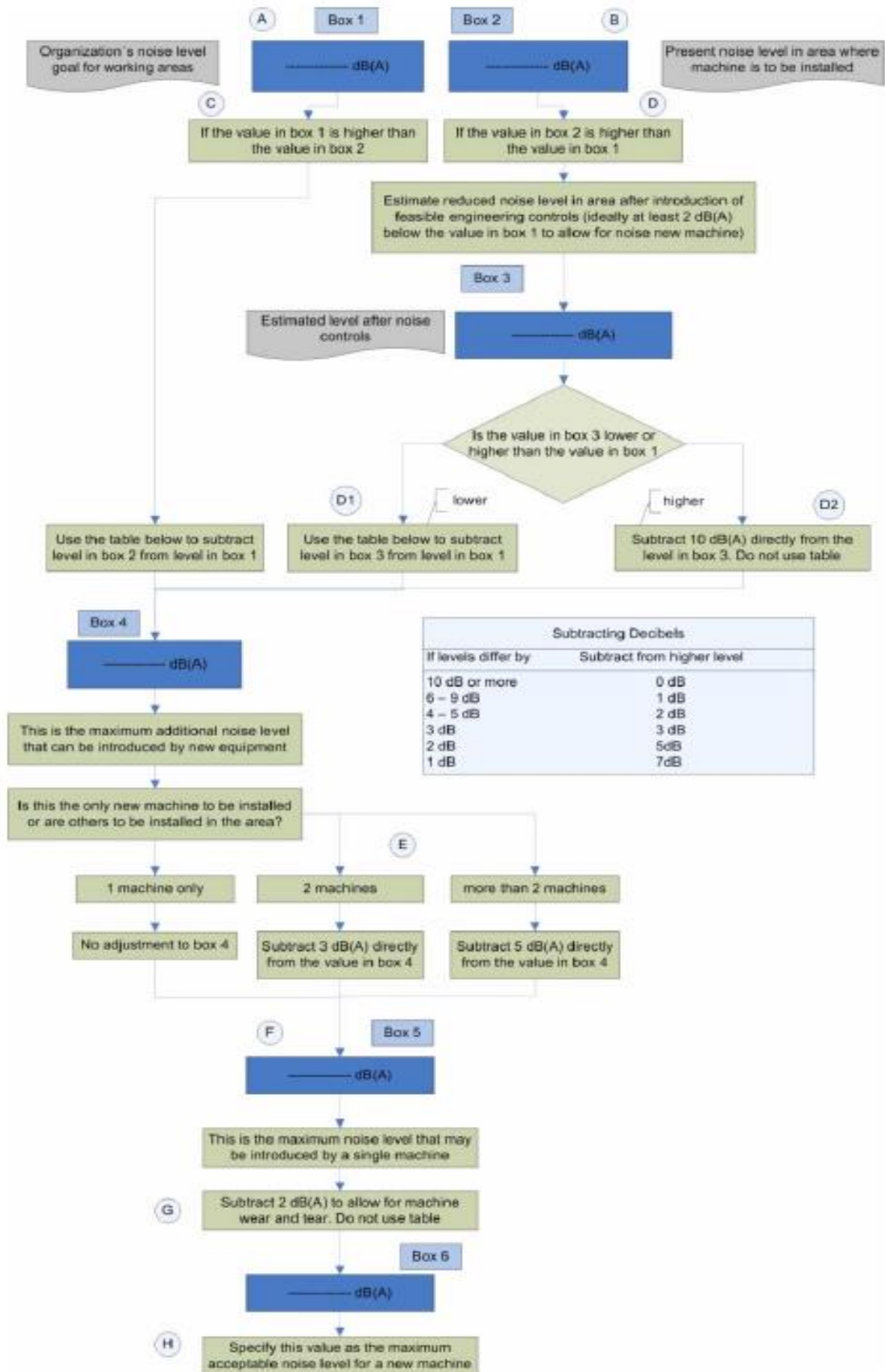
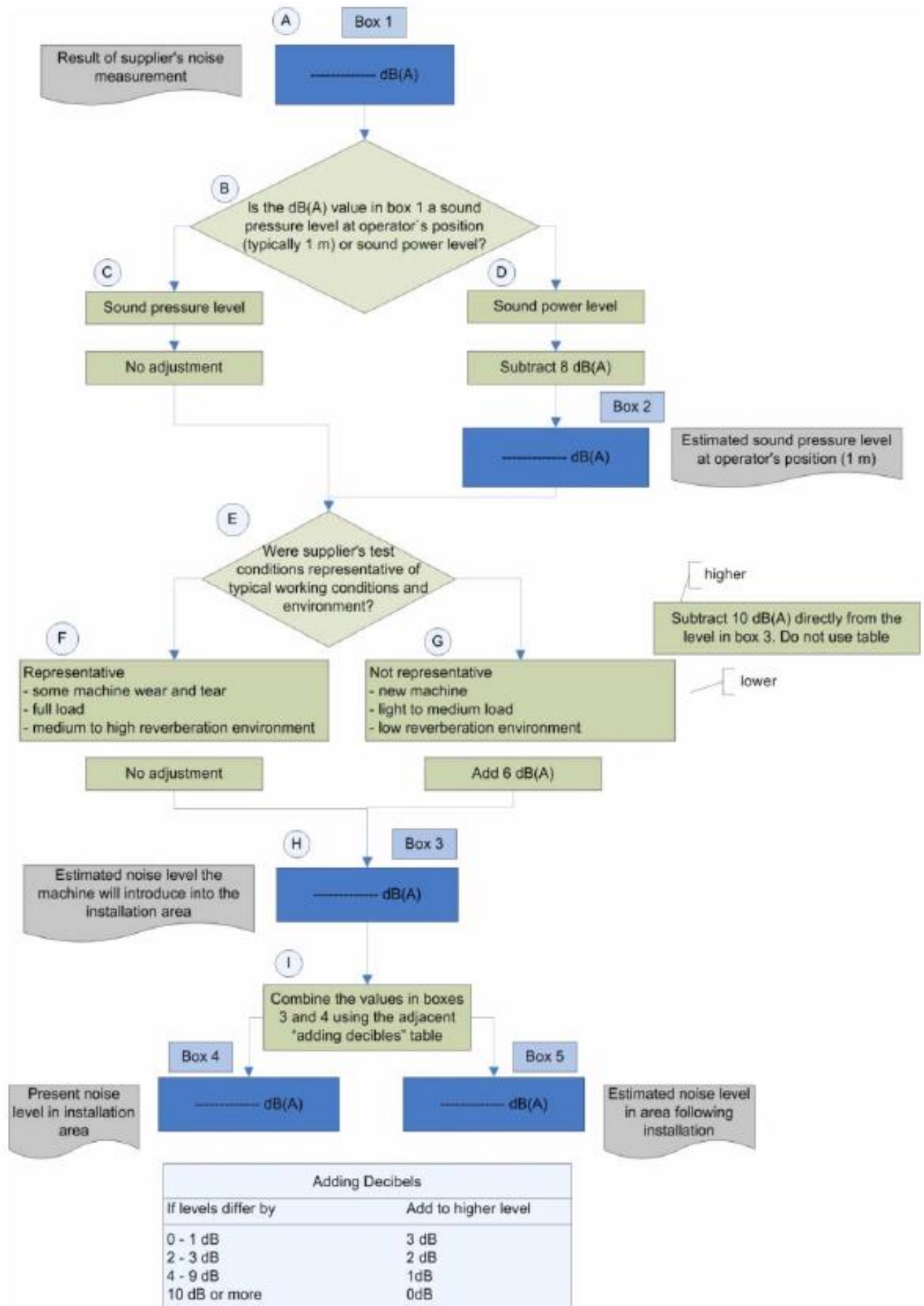


Fig. 3 Prediction of Acceptable Maximum Noise Level "[Rusko, Bilova and Lumnitzer, 2011]"



**Fig. 4** Usage of Suppliers Noise Data "[Rusko, Bilova and Lumnitzer, 2011]"



## 7. CONCLUSIONS

A large number of people work in industrial plants, where the noise level found consistently high, and the exposure takes place regularly for about 8–10 hours a day, year after year, the effects cease to be temporary and even permanent hearing loss, rather than leading to significant adverse physiological effects. Studies on human working in noisy environments have reported an increased incidence of heart disease, accident at work, inefficiency, feeling of annoyance, irritation, speech and work interference, sleep disturbance, cancer, headache, tension, digestive, respiratory, nervous problems and so many psychological effects on human system.

There is fairly consistent evidence that prolonged exposure to noise levels at or above 90 dB(A) cause deafness. However, noise is more often a major problem in terms of quality of human life in specific localities. Much of the work is being done all over the world to limit high level environmental and occupational noise levels within the comfortable limits. But in developing countries, little work being done in this regard. Also due to lack of regulatory laws to limit high level noise and general unawareness of workers about ill-effects of noise, the owners of the plants pay negligible attention to provide health and safety measures to their workers against high level noise. Noise occurring during the operation of hydraulic systems will not only lead to various ill-effects, but also the noise pollution will spread to surroundings. That's why so many precautions must be taken in order to control the noise level. Main or primary source in hydraulic systems is pump-motor group. Valve noise is the secondary one. Then, piping noise, fluid borne noise will follow these. These noises can be eliminated with several precautions such as mounting muffler at pump discharge, preferring rubber hose with metal ends, etc.

International Noise Emission Standards are designed to control the noise emitted by specific machines, such as hydraulic systems in aircraft, cars or industrial equipment. Environmental noise exposure standards and legislation are, on the other hand, normally devised by national or local authorities to provide an acceptable noise environment for their specific conditions. Whether affiliated with major component manufacturers or engineering laboratories, application engineers possess a wealth of knowledge that includes solutions to noise problems very similar to those experienced by applications. Process engineers and noise managers are also responsible for the duty of noise struggle. Therefore, at the design stage of hydraulic systems, high importance shall be given for more quieter operation. So, during the lifetime of the system, operators will be in non hazardous working area. Not only can manufacturers provide specifications on components, but they may also have useful literature containing more information on noise control of hydraulic systems.



## REFERENCES

1. **Wang, L., (2008)**, "Active Control of Fluid-Borne Noise", Ph.D. Thesis, University of Bath, Mech.Eng.Dept., G.Britain.
2. **Concha, M., Campbell, D. and Steenland, K., (2004)**, "Occupational Noise", Environmental Burden of Disease Series, No.9, Geneva, pp 1–41.
3. **Skaistis, S., (1988)**, "Noise Control of Hydraulic Machinery", Marcel Dekker Inc. NewYork.
4. **NTIS, (1974)**, "Hydraulic System Noise Study", Fluid Power Research Center, Oklahoma, U.S.A., pp 1–71.
5. **Tazawa, E. and Spon, F.N., (2004)**, "Noise Control in Industry", Sound Research Laboratories Ltd., Taylor & Francis, U.S.A., p.430.
6. **Ortwig, H., (2005)**, "Experimental and Analytical Vibration Analysis in Fluid Power Systems", International Journal of Solids and Structures, Vol. 42, No. 21–22, pp 5821–5830.
7. **Eaton–Vickers, (2002)**, "Noise Control in Hydraulic Systems", U.S.A., pp 1–16.
8. **Şahin, E., (2003)**, "Noise Control Methods–An Application", Gazi University, Eng.Faculty Magazine, Vol.18, No.4, Ankara, pp 67–80.
9. **Jensen, P. and Jokel, C. R., (1978)**, "Industrial Noise Control Manual", NIOSH Technical Report Revised Ed., No.94231, U.S.A.
10. **Rusko, M., Bilova, M. and Lumnitzer, E., (2011)**, "Acoustical Specification of New Equipment With Respect to Noise Policy", Research Paper, Vol.19, No. 30, 2011, pp. 73–82.
11. **Cheremisinoff, N. P., (2004)**, "Noise Control in Industry, A Practical Guide", Nyes Publications, No.79–117, Washington D.C., U.S., pp 1–101.
12. **Moser, M., (2009)**, "Engineering Acoustics–An Introduction to Noise Control", Springer, Berlin, Germany, p.539.
13. **Ver, L. I. and Beranek, L. L., (2006)**, "Noise and Vibration Control Engineering, Principles and Applications", John Wiley & Sons. Inc., New York, U.S.
14. **Lyle, F.Y., (2003)**, "Noise Control in Plumbing Systems, HPAC Engineering", Career and Technical Education, Vol.75 No. 4, pp.46–52.
15. **Crook, A., Heron, R.A., (1977)**, "Airborne Noise from Hydraulic Lines due to Liquid Borne Noise", I.Mech.E., Seminar, London.
16. **Bies, A.D., and Hansen, H.C., (2009)**, "Engineering Noise Control, Theory and Practice", 4th Ed., Spon Pres, Taylor & Francis, U.S.A.
17. **Crocker, M. J., (2008)**, "Handbook of Noise and Vibration Control", John Wiley & Sons, Inc., New York, U.S.



## CONTAMINATION PHENOMENA AND PREVENTION METHODS IN HYDRAULIC SYSTEMS

**H.Sevil ERGUR**, *hsergur@ogu.edu.tr* Eskişehir Osmangazi University, 26480, Eskişehir

### ABSTRACT

This paper presents the contamination phenomena and prevention methods related with fluid cleanliness in hydraulic systems. Fluid power is one of the most reliable and repeatable forms of power and motion control. In hydraulic fluid systems, power is transmitted through a liquid under certain amount of pressure. Many factors can reduce the service life of hydraulic components. One of these factors is the contamination of hydraulic fluid by insoluble particles. In order to prevent the aging process, the hydraulic fluid cleanliness must be first defined and then maintained on a continuous basis. It is widely accepted that, particle contamination reduces the service life of hydraulic components. Fact is, some level of particle contamination is always present in hydraulic fluid, even in new fluid. The level of contamination or conversely, the level of cleanliness considered acceptable, depends on the type of hydraulic system. The presence of solid contaminants in the hydraulic fluid interferes with the ability of fluid to lubricate and causes wear to the system elements. That's why, it is necessary to control the solid contaminants which has direct performance of the system. Typical types of contamination that can threaten hydraulic systems include particulates, water, gases and bacteria. Combined with these contaminants, conditions of elevated temperatures and flow can lead to further chemical and physical degradation of hydraulic fluids. About 75% of all hydraulic systems degrade due to contaminated hydraulic fluids. Contamination will cause aging, degradation of fluids and failure of hydraulic systems or a number of different reasons. While hydraulic system contaminants can be either solid particles or liquids, water is the most common. In general, solid particles contaminate by chemically reacting with the fluid. Contamination with liquids other than water can occur both miscible and immiscible fluids.

**Keywords:** Particle contamination, contamination standarts, filtration, cleanliness, fluid power, operation life, hydraulic system.



## 1. INTRODUCTION

Contamination is defined as an additive of all kinds of solids, fluids and gas particles excluding the base fluid and its additives. Contamination can be the form of solid particles, froth, gas or water which is locked into fluid and soft materials "[Ozkurkcü, Kurt, and Caglayan, 1999]". Taking in consideration of all these materials, the contamination types in hydraulic systems are classified in Fig.1.

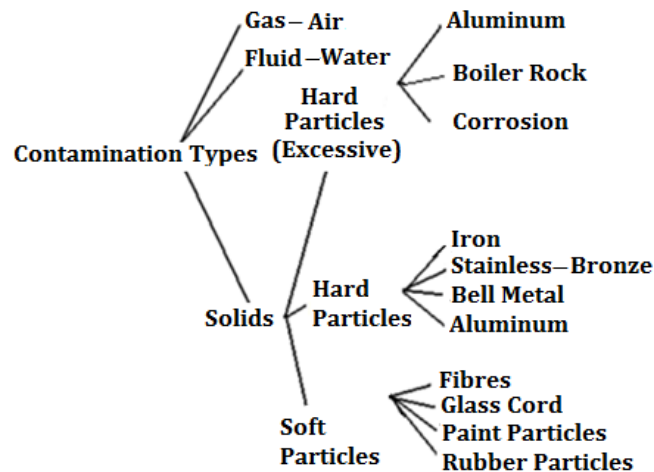


**Fig. 1** Contamination Types "[Busch and Fischer, 2003]"

Filters are frequently considered as a necessary evil and are added to a system as an after thought instead of a valuable asset. Proper filter selection and sizing can provide years of reliable equipment operation and save money that is commonly lost battling contamination related failures. Approximately 75% of all hydraulic component failures are attributed to surface degradation caused by contamination and corrosion. This is the percentage of breakdown reasons in hydraulic systems due to contamination and decrepit the fluid. The cost of installing and maintaining suitable filtration is estimated to be 3% of the cost associated with contamination related issues, the tip of the iceberg. Hidden costs of runaway contamination include; unplanned downtime, component replacement or repair expenses, fluid replacement, disposal, maintenance labour hours, troubleshooting time and energy waste. Although soft ones are ready for damage, hard particles may cause wear and also damage if cleaned after a while. With sufficient intervention measures, entrance quantity of contamination to system may be decreased "[Busch and Fischer, 2003; Hydac, 2010]".

Besides the hardness of particles, quantity and dispersal of contamination are also so important. Granularity in new system will differ from the old one. In the systems, filtering and contamination dimensions can be lessen and so, contamination shall be decreased. After few operations, particles are to be minimized "[Busch and Fischer, 2003]" as invisible



distribution. As shown in Figure 2, the contamination level with and without contamination methodology in a system is more important than the other factors which has sufficient methodology.

With the aid of ISO 4406, contamination measurement is set easily. For the definition of particle numbers, a special code is developed. This code uses two numbers is noted with "slash mark (division)" index, a/b. "a" means particle number,  $5\mu$  in 1 ml fluid, "b" means particle number  $15\mu$  or bigger in 1 ml fluid. As an example, If ISO contamination code 20/16, it means in 1 ml fluid, there are 5000–10000,  $2\mu$  or  $5\mu$  particles and there are 320–640,  $15\mu$  particles respectively. For  $2\mu$ ,  $5\mu$  and  $15\mu$ ; a/b/c notation is also used. Most common one is a/b "[Ozkurkcu, Kurt, and Caglayan, 1999; Busch and Fischer, 2003]". Contamination will cause breakdowns for various reasons such as, decayed and worn fluid. Due to decrease in discharge and pressure level, contamination creates waste energy and low efficiency. Contamination sources are production process, hydraulic fluid, environment effects, component wear and protective maintenance.

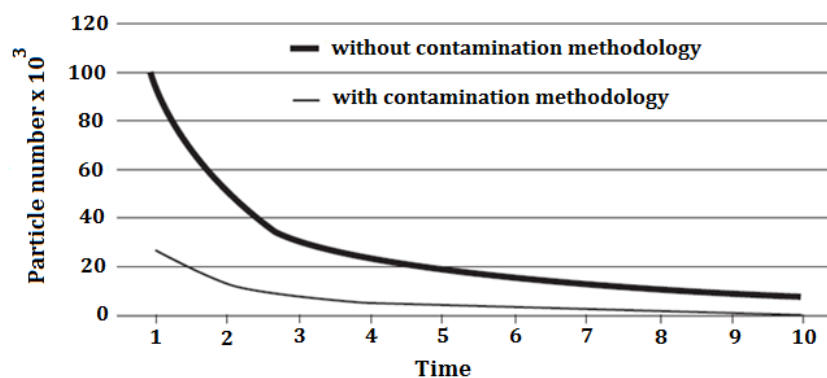


**Fig. 2** Decontamination of Hydraulic System with and without Contamination Methodology  
"[Hydac, 2010]"

Basic assignments of hydraulic fluids are, energy transfer, fluidization and sealing of moving parts. Production losses and blocking will occur, if one of the above matters substantiates. Blockage of orifices, chemical decay of fluid, wear and corrosion of parts, specification losses of additives, failure of viscosity shall terminate the mission of hydraulic fluid. This fact is contamination and simply, it is fluid contamination. As a result, hydraulic system with contamination "[Hydac, 2010]" will not achieve to required performance.

## 2. CAUSES OF CONTAMINATIONS

The troubles in hydraulic systems are because of fluid contamination and decay. Contaminated fluid in system leads to production loss, cost increase in spare part exchange, decrease the time for fluid exchange and increase in percentage of waste. Besides these,



contamination also causes losses in energy transfer, lubrication of moving parts, heat transfer and sealing in the hydraulic system. Due to the reasons mentioned above, loss of time means labour loss. Predictive maintenance eliminates or decreases the losses. Hydraulic system contaminants may originate from solid particles or fluids and the most common one is water. When solid particles react chemically with fluid, deposition will allow the contamination. Behaviour of water as a contaminant differs from system to system "[Hydac, 2010; Hydac, 2009]". Water may form emulsion or may not mix partially. Design errors, maintenance, production and fluid cause entrance of water to the system. Handling of open-top tanks and insufficient fluid transfer are the reason of serious contamination problems. Contaminants enter to the systems through aeration holes and with contaminated and changed equipments. Environmental contaminants enter via suction line and can be prevented by sealed tanks, safety valve and highly efficient aeration filters. With proper handling flees the contamination.

Humidity is also hazardous for hydraulic systems. Periodic control of sealing, the accumulation of water on top of the bins may be prevented "[Hydac, 2009; Mahle, 2009]". Contaminants cause wear on moving part surface and then failure of hydraulic systems. These failures "[Donaldson, 2012]" have been formed by particle contamination (dust, sand, dirt, rust, fiber, elastomer, paint and swarf), metal wear, silicon and excessive additives (aluminum, chrome, copper, iron, lead, tin, sodium, zinc, barium, phosphorus), water, sealing material (paste, band), mud, oxidation-other corrosion products, acids and other chemicals. Contamination dimensions generally are measured in micrometer scale. Human eye sight capacity is minimum  $40\mu$  and particles which cause contamination are smaller than  $40\mu$ . That's why it is impossible to observe them by naked eye "[Mahle, 2009]". Contamination will be the reason clogging of orifices, wear at parts, dust and oxidation, chemical composition, decay of solid substances and biological confusion. Furthermore, friction between the moving parts is minimized with liquid film that is formed by hydraulic fluid. Liquid film must fill the cavities. If the film thickness decreases then, the life of the system components ends gradually with avoiding the wear at surfaces.

**2.1 Contamination Types and Sources:** Free or dissolved water in hydraulic system acts like intense particle contaminant, so it must be removed away from the system. Water saturation points of some special fluids must be defined for hydraulic fluids. The acceptable level of value is 300 ppm (0.03%). Apart from this point, hydraulic fluid can hold up excessive water and so fleeing of water will cause dimming in hydraulic fluid. In the operation, water handling capacity increases with temperature rise. As a result of this, system temperature will rise with water effect "[Donaldson, 2012]". Water corrodes the contacted surfaces and ice crystals formed blocks the valves, wear speed rise, decrease the filter and bearing life.

Decrease in fluid film thickness "[Mraz, 2001]" will lead to tearing and then metal contact and excessive wear

Contamination in fluids usually is defined inaccurately. Sometimes darkened fluid are called to be contaminated, but often feeling of particles in fluid kept between the fingers can be taken as contamination dimension. To the above mentioned approach, there is a little reality, but these definitions might be faulty. In general, the range for contamination of particles is between  $0.5\mu$  and  $10\mu$ . However, the acceptable values are  $>2\mu$  and  $>50\mu$  "[Donaldson, 2012; Mraz, 2001]".

**2.2 Stages for Measurement of Contamination:** Wear will occur when the liquid film is torn. Wrong fluid, storing the bins in contaminated circumstances are evident and easily preventable contamination causes. If film layer between the surfaces is kept undisturbed, then operation will carry on without wear "[Totten, 2000]".

Argument 1: To prolong the machine operation life, decrease the number of breakdowns.

There is a serious relation between the machine operation life and fluid contamination.

Argument 2: In order to control the filtering system's efficiency.

In general, filtration systems for machines are designed deficiently. This is because of ignorance of contamination level.

Argument 3: To control the doubt of breakdown filtering systems.

In most hydraulic systems, exchanging depends on the operation time. Pressure transducers are preferred in advanced systems.

Argument 4: To detect the failure at the beginning of progress phase.

Decaying of fluid, bearing, gearbox, pump, motor, piston and cylinder failures and corrosion cause the formation of contamination into the fluid.

Argument 5: To decide the filter exchange.

Filter contamination indicator operates with the pressure difference. The relation between the pressure and the contamination percentage is shown in Figure 3. This phenomena supported with the measurement of contamination levels.

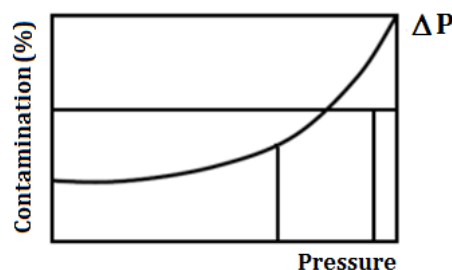


**Fig. 3** The Variation on Accumulation of Contaminants with The Pressure Difference



**Table 1.** Characteristic particle distribution in hydraulic system "[Totten, 2000]".

Particle dimension intervals ( $\mu$ )	Particle number (mg/l) – industrial systems
<5	none
5–15	2.000 000
15–25	300 000
25–50	100 000
50–100	5 000
>100	500
Weight reversed	100

Therefore, the best way is to change the pressure difference "[Ozkurkcu, Kurt, and Caglayan, 1999; Totten, 2006]" by observing the contaminant quantity. The usage of dirty bin and wrong filter will also cause contamination. When the size of contaminants is equal to or bigger than  $40\mu$ , then they must be filtered before transferring into the system. In Table 1, dimensions and concentration of particle contaminants are given. The loss of operator and lack of education about the contamination will increase the possibility of getting the contaminants "[Totten, 2006; Jarrett, 1914]" in the system.

**2.3 Particle Contamination Standards:** NAS and ISO 4406 standards are used for definition of contamination. These standards denote the contamination with the numbers of 1–12 and 1–30 respectively. ISO 4406 is very accurate, however NAS is used in most of the industrial enterprises in general. R, Ranj number in ISO 4406 which is used for counting contaminants has number between 1 and 30 and particle number in 100 ml fluid specimen has such relation,  $2^R$ . Before ISO standard was defined with two numbers for  $>5\mu$  and  $>15\mu$  particles in 1 ml fluid, 19/14. But according to renewal of standard three codes, standard is defined with  $>2\mu$ ;  $>5\mu$  and  $>15\mu$  (21/19/14). With the aid of this definition "[Lloyd, Akers, Scarlett, Stenhous, and Ward, 1971]" in 1 ml 10000–20000 particles for  $2\mu$ , 2500–5000 particles for  $5\mu$  and 80–160 particles for  $15\mu$ .



**Table 2.** ISO4406 Ranj number and particles number in 1 ml "[Mráz, 2001]"

Ranj number (R)	Particles number in 1 ml	
	Lower Limit	Upper Limit
24	80 000	160 000
23	40 000	80 000
22	20 000	40 000
21	10 000	20 000
20	5 000	10 000
19	2500	5000
18	1300	2500
17	640	1300
16	320	640
15	160	320
14	80	160
13	40	80
12	20	40
11	10	20
10	5	10
09	2.5	5
08	1.3	2.5
07	0.64	1.3

NAS 1638 standard was put to use in 1968 and it is rough comparing with ISO standards. It does not match with ISO. An interval accepted in NAS standard with only one number is defined with two numbers in ISO standards. Illustration for NAS standards are given in Table 2. The other method for understanding the water content is usage of filter tests. In this test, certain amount of fluid which are passed through the paper filter and then colour changes are observed. Although this method is not accurate as particle counting, but still can remedy "[Mráz, 2001; Lloyd, Akers, Scarlett, Stenhous, and Ward, 1971]" for instant problems.

**2.4 Cleanliness Standards:** After the detection of problems, contamination reference scale is used for solution. On the analysis period, the most common method is particle counting. To reduce the measurement errors, highly-accurated optical equipment is used for counting. Equipment can easily classify, according to the particle dimensions during counting.

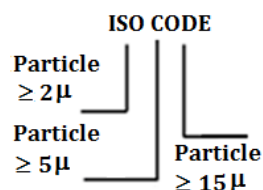


**Fig. 4** The Levels of ISO Coding System



ISO 4406 standards are accepted almost in every kind of industrial enterprises. It has very large uses and variable versions. Generally, particles in 1 ml or 100 ml which are bigger than  $2.5\mu$  and  $15\mu$  are selected as a reference.

**Table 3.** NAS1638 Contamination code and comparison values with ISO 4406 "[Mraz, 2001]"

NAS1638	> $5\mu$ m	> $15\mu$ m	ISO 4406
–	640 000	80 000	26/23
–	320 000	80 000	25/23
–	80 000	10 000	23/20
12	20 000	2500	21/18
–	10 000	2500	20/18
11	10 000	1300	20/17
–	10 000	640	20/16
10	5 000	640	19/16
9	2500	320	18/15
8	1300	160	17/14
7	640	80	16/13
6	320	40	15/12
–	160	40	14/12
5	160	20	14/11
4	80	10	13/10
3	40	5	12/9

Familiarity of fluid's cleanliness level is essential for control measurements. As to ISO coding system that is indicated in Fig. 4, the level of coding index does not increase with particle dimension as given in Table 3. There is an explanation for definition of standards that is edited for understanding the contamination level easily and quickly. Each class number has a double value of the one before "[Totten, 2000]". Machine and hydraulic equipment manufacturers designate their ISO standard for cleanliness level in order to achieve the optimum standard performance of hydraulic system.

### 3. THE MATERIAL TYPES OF FILTER ELEMENT AND PERFORMANCES

Main part of the filter is the contamination capturing section. Filter element generally is manufactured in twisted layers. Layers increase the filtering capacity and decrease the pressure difference. In some designs, multi layer element and enforced network used in order to achieve the required performance criteria "[Totten, 2006; Totten 2000]".

**3.1. Comprehensive Filter Element:** In this kind of filters, fluid acts indirectly due to the construction of filter. There is labyrinth which traps the contaminants. So, this kind of structure helps catching in big capacities rather bigger particles, this is because of dimensional difference distribution.

**Table 4.** Comparison of filter elements with general parameters "[Park,1997]"

Material	Capture efficiency	Holding capacity	Pressure drop	Life in system	Initial cost
Fiberglass	High	High	Medium	High	Medium
Cellulose	Medium	Medium	High	Medium	Low
Wire electric	Low	Low	Low	Low	High

In Table 4, the comparison of filter elements according to certain criterias and main parameters such as, type of material, capture efficiency, holding capacity, pressure drop, life in system and initial costs in a simple line "[Jarrett, 1914; Park, 1997]". In filtration life, because of the nature of filtration elements and contamination loading process, there are millions of pores in each filter element.

**3.2 Surface Filter Element:** In this type of elements, fluid flow in filter is parallel with piping flow. Contaminants are caught on element's flow surface. They are generally made of curly weaves. At the beginning of production process, curly wire is inspected very carefully and "[Lloyd, Akers, Scarlett, Stenhous, and Ward, 1971; Totten, 2000]" made sure that pores are equal.

**3.3. Multipass Test:** In order to determine the filter element performance, according to the principle of test process as shown in Fig. 5, ISO 4572 multipass test procedure has been used in filter industry.

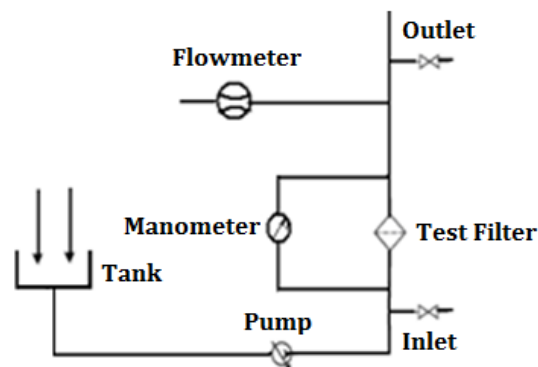


**Fig. 5** Multipass Test Circuit [Briggs, 1969]

This procedure is also approved by American National Standards Institute (ANSI) and National Fire Protection Association (NFPA). During the multipass test, fluid passes through very well controlled and observed circuit. Pressure drop is recorded regularly and certain amount of contaminants are injected to the clean fluid. As result of this measurements, beta ratio is extracted. There are three very important results concerning the performance characteristics of elements after the multipass test "[Briggs, 1969]" such as, the capacity of element in catching the contaminant, pressure drop and filtration efficiency defined as beta ratio.





**3.4 Beta Ratio:** Up to know, there has not been any universally accepted test method to measure and describe the media pore size or the size of particles captured and holded by a filter media. Fortunately, now a test procedure called *multi-pass testing* or *beta ratio testing* is a universally accepted test method that yields readily comparable test results. It was introduced with the object of giving both filter manufacturer and user for an accurate and representative comparison "[Briggs, 1969]" amongst filter media. Multi-pass testing uses a specified contaminate, of known sizes, added regularly in measured quantities to the fluid which is pumped continuously through the filter. Measured samples of the fluid are taken at time intervals from both the downstream and the upstream of the filter simultaneously, then particles are measured and counted by electronic means using automatic particles counters. From these measurements, a beta ratio is formulated by dividing the number of particles of a particular sizes in the upstream flow "[Briggs, 1969, Hannifin, 2006]" by the number of particles of the same size in the downstream flow. In the below equation,

$$\beta = \frac{N_u}{N_d} \quad (1)$$

$$E_x = \left( \frac{\beta_x - 1}{x} \right) \cdot 100 \quad (2)$$

where  $\beta_x$  is the beta ratio for contaminant larger than  $x$ ,  $N_u$  is the number of particles larger than  $x$  per unit of volume upstream,  $N_d$  is the number of particles larger than  $x$  per unit of volume downstream. Therefore, filters with a higher beta ratio retain more particles and have higher efficiency. Efficiency for a given particle size ( $E_x$ ) can be derived directly from the beta ratio by the equation (1) and (2).

**Table 5.** Some selected beta ratios and the correspondent efficiencies

b value to x (mm)	Cumulate efficieny for particles x (mm)
b x	for particles x (mm)
0	0.00
1.50	33.00
2.00	50.00
10.00	90.00
20.00	95.00
50.00	98.00
75.00	98.70
100.00	99.00
200.00	99.50
1000.00	99.90
10000.00	99.99

The beta ratio is an indicator of how well a filter controls particulate. If one out of every two particles in the fluid pass through the filter, the beta ratio at  $x$  is 2, if one out of every 200 of

the particles pass through the filter, the beta ratio is 200. In Table 5, some beta ratios and the correspondent efficiencies are given.

#### 4. EFFECTS OF FILTER ELEMENTS ON TOTAL AND OPERATION LIFE PROFILE

**4.1 The Effect of Filter Element on Total Life Profile:** At the beginning contamination loading, pressure difference grows slowly, but when the element approaches to the end of life, growing will increase rapidly "[Mahle, 2009; The OilGear Company, 1994]". The best way to avert the contamination is mounting the filter system on line. Filter decreases the efficiency due to the flow passing through it. If filter is not designed or dimensioned properly, pressure difference will decrease efficiency considerably. So, energy increases and heat problems will arise. Besides these, if invalid filter is used, performance of system and process speed decrease and the quality of product will rapidly fall down "[The OilGear Company, 1994]". That's why periodic cleaning and exchange is necessary for all filters.

**4.2 The Effect of Filter Element on Operation Life Profile:** All filters have pressure alternation characteristic depending on contamination loading. This is defined as *filter element operation life profile*. Real life profile is affected directly from the process conditions. The effect of changes on discharge and fluid viscosity, pressure difference on real life profile has been illustrated clearly. It is very difficult to evaluate the life profile in real operation conditions. Idle time during operation, heavy operation conditions, operation under changeable contaminated environment will affect the life profile.

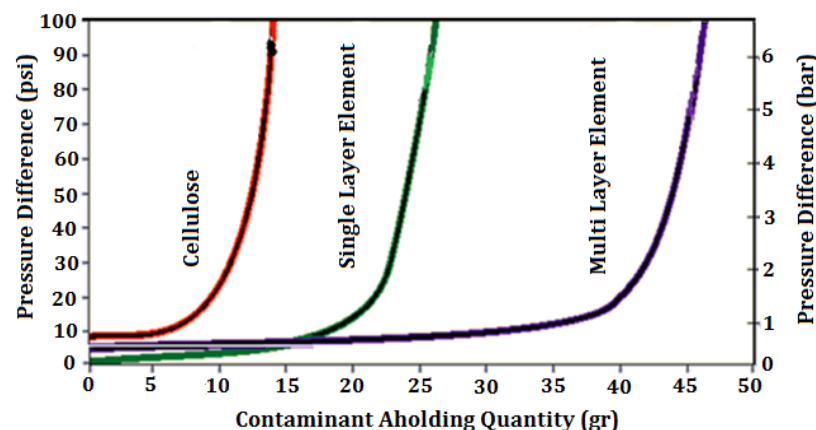


**Fig. 6.** Comparison of Life Profile with Various Filter "[Hannifin, 2006]"

Multipass test data was quite useful for defining the filter element life profile and development of correlation of contamination loading and pressure increase. For healthy comparison of life profiles, process conditions must be the same and the dimensions of filter elements must be equal. Since filter elements are made of cellulose, single layer fiberglass and multi layer fiberglass, they have various life profiles. Life profiles by the comparison of holding contaminants with various filters are shown in Fig. 4. As shown in the figure, multi layer

fiberglass element's life "[Mahle, 2009; Donaldson, 2012; Hannifin, 2006]" profile stands out considerably.

## 5. SELECTION OF FILTER BODY AND FILTER DESIGN

Filter body is the name of a container who holds the filter element. Although the hydraulic fluid flows through a relatively closed system, hydraulic filters are extremely important. The nature of most hydraulic machinery entails the regular creation of damaging metal chips and filings and the hydraulic filter is responsible for removing these objects. Other internal contaminants include plastic and rubber particles generated by abraded seals and bearings. These functions are integral to the consistent operation of any hydraulic-powered device and unfiltered hydraulic fluid "[Totten, 2000]" will lead to increased leakage, decreased efficiency. Sensitive hydraulic circuits are vulnerable to a variety of contaminants that result in inefficiency, downtime and excessive repair costs. It is important to remember that, protecting and maintaining the most sensitive components within a circuit will result in effective contamination control. Follow the below recommendation steps to identify the correct filter and parts required for efficient contamination control.

1. Determine the system operating pressure and flow rate
2. Select the filter housing model
3. Consider application factors when selecting the filter
4. Choose the appropriate line and reservoir accessories
5. On-going contamination control practices

**5.1 By-Pass Valve:** By-pass valves are important in any system through which hydraulic fluid is pumped to maintain an even pressure and keep the system operating. Construction equipment in particular relies on by-pass valves to relieve pressure build-up. With nowhere to flow, the oil could create too much pressure, leading to a stalled engine or an explosion. But before that happens, the by-pass valve opens to vent the pressure and divert the oil back to the reservoir. Always consider the worst case scenario which will occur when the entire flow goes over the by-pass valve. It is imperative that, you consider the maximum pressure drop at the maximum flow across the by-pass valve as shown in Fig.5.

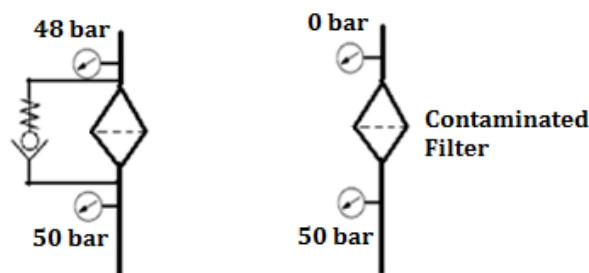


**Fig. 7** Contamination Operation with By-Pass Valve and without By-Pass Valve



If you locate a filter in a return line and the full flow through by-pass valve, pressure drop were to be 50 bar or higher than. In this position, one must make sure all the components upstream of filter will not be affected. It is used for collapsing and detonation when excessive contamination occurs. As contamination increases then pressure difference increases and so, by-pass valve cracks. In some designs, by-pass valve is connected directly to hydraulic tank. If cracking pressure of a by-pass valve is selected highly, "[Hannifin, 2006; Madhavan, 2000]" then valve will have long operation life.

**5.2 Element Case Indicator:** Element case indicator gives a signal for cleaning and exchanging time. Calibration indication appears when by-pass valve of filter element opens. Indicator is connected to either to by-pass valve or pressure difference measuring device. By-pass valve generally gives signal at 5–25% under cracking pressure.

**5.3 Filter Body and Element Dimensioning :** Ratio of by-pass valve cracking pressure to pressure difference of submerged filter element body into clean fluid is 2:1. However, for long operation life, the ratio is 3:1 or higher, but this means high cost for the system. Pressure difference which is very effective on the operation determined easily, if viscosity is known. Maximum flow value at filter must be determined carefully. Otherwise, excessive flow originating fluid wave will bypass through the valve "[The OilGear Company, 1994]". This is specially considerable in return line filters and instead of pump discharge, the flow from cylinder must be taken into account. Pressure difference in filter element increases when it is blocked by contaminants up to by-pass valve cracks. Standard value "[Madhavan, 2000]" for common by-pass valves ranges from 1.7 to 6.9 bar depending on the system capacity.

**5.4 Filter Design:** From the design point of view, filter design affects the pressure drop in it. Main consuming element is the filter material and it is generally fiberglass. Proper oil cleanliness levels are critical clearances on components in the hydraulic fluid stream. Filtration performs multi-pass, pressure-drop, flow-fatigue and hydrostatic burst testing on all hydraulic elements to ensure product reliability and top performance "[Hannifin, 2006]". Filters which catch smaller particles cost more and have less operation life. Pressure drop in a system is dependable on material type and suitable material area. Different filter materials have various contamination catching capacity "[Madhavan, 2000]".

**5.5 Filter Selection:** Generally, filter cost is consisted of purchasing, transport cost and renewal of filter elements. Residuary fluid cost and operation of equipment include energy costs according to the losses for filter exchange. Some of these features changes the filter operation life. If water contamination is a real fact, then dampering elements are mounted. These elements have moisture absorption units and so, water is caught easily. But, thoroughly dissolved water in fluid is taken "[Madhavan, 2000]" away by vacuum dehydration system.

## 6 FILTER TYPES AND MOUNTING PATTERNS

**6.1 Suction and Discharge (Pressure) Filters:** Suction filters shown in Fig. 6.1a helps in preventing contaminants entering pump and mounted to the system before the pump. Commonly, it is in the fluid but sometimes it may be fixed externally. Its maintenance is easy. It has an effect on the cavitation, either increasing or decreasing energy loss. So, it is necessary for pump protection.

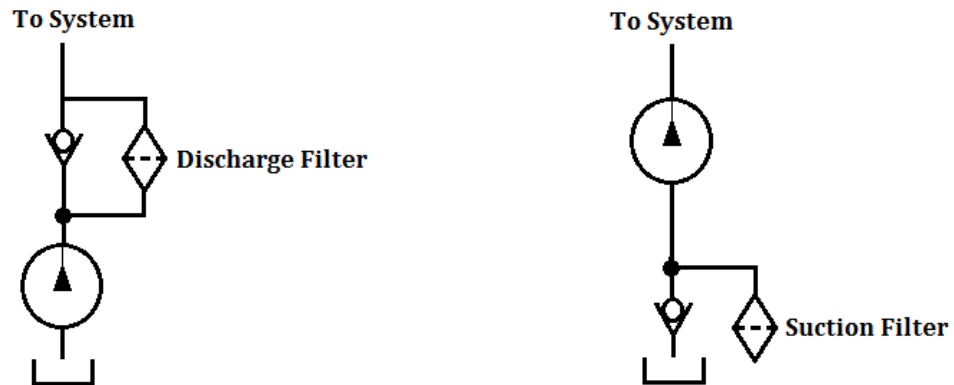


Figure 8 (a) Suction filter line

(b) Discharge filter line

On the other hand, they have some disadvantages as not suitable for variable discharge pumps, not protect against worn parts, high costed and the necessity of big dimension at low pressures. Consequently, some manufacturers do not advise suction filters for these causes. Suction filters are defined as *mesh* dimension, such as 60 mesh=238 $\mu$ , 100 mesh=149 $\mu$ , 200 mesh=74 $\mu$ , etc. In modern filtering systems "[Mahle, 2009; Lloyd, Akers, Scarlett, Stenhous, and Ward, 1971, Madhavan, 2000]", suction filter is not preferred.

Pressure filters are mounted just after the pump outlet and designed according to the pressure and discharge in order to control the system more efficiently. They protect the system equipments, help to adjust the contamination level as shown in Fig. 6.1b. They also provide efficient–good filtering. Contaminants from pump are caught by this filter, then the whole system is protected "[Hannifin, 2006, Eaton, 2002]". The pressure filters also known as discharge filters are expensive elements, although they can not catch all the contaminants from the equipments.

**6.2 Return Filters:** Pump is very accurate and high–costed equipment so, it is advisable to use return filter is the best solution for protecting the pump. Return filter is the last equipment of the sample return line circuit in Fig. 6.2, before the fluid returns to the tank.

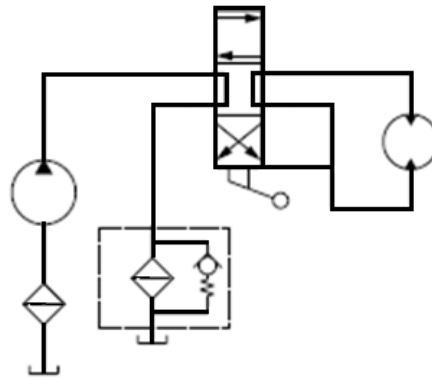


**Fig. 9** Sample Return Line Circuit

Worn particles and sealing elements are caught by the filter easily. It prevents the whole system from the contaminants of cylinders and its worn elements. This filter can not protect the system against worn elements of the circuit. Besides, pressure pulsations will reduce the filter performance.

**6.3 Off-Line Filtration:** Off-line filtration can not protect the whole equipment, so it is called auxiliary filtration. This kind of filtration demonstrated by Figure 6.3 has to be used before system blocks and operating with cooling system. Main pump operates independently from the hydraulic system. This system requires extra space for mounting so, its initial cost is very high.

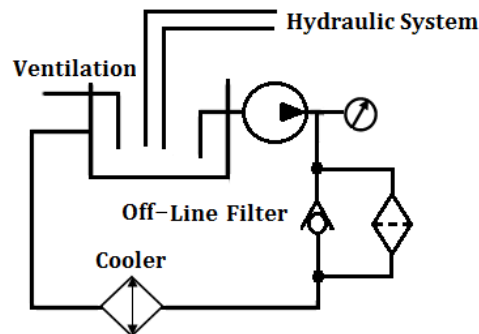


**Fig. 6.3** Off-Line Filtration System

The main parts of an off-line filtration systems are pump, filter, driving motor and fittings. All these equipments are mounted separately from the main circuit. Sometimes heat exchanger is used too "[Eaton, 2002]". In off-line filtration, pump discharge consists of 15–20 % tank volume.

## 7. CONCLUSIONS

The effects of contamination typically begin with the hydraulic fluid, extend into the system, can even continuously worsen in a closed or sealed system. Particle contamination for hydraulic system performance is very important. Losses are very costly due to solid particle,



water and air contamination in hydraulic systems. Additionally, water, other liquids and even purposely added additives can cause solids or slime to accumulate in the system, gradually reducing the performance of tight-tolerance components. Contamination causes aging/degradation of fluids and ultimate failure of hydraulic systems for a number of different reasons. In addition to increasing internal leakage, it also decreases the ability of valves to control flow and pressure accurately, thus wasting horsepower and generating excess heat. Furthermore, it causes parts to stick due to sludge or silting, or they can seize when large amounts of contaminants accumulate in the clearances.

In order to solve the contamination problem, contamination analysis is first needed to identify the type and concentration of the contaminant. Methods for gauging solid particle contamination involve counting, sizing, and/or weighing of the particles contained in a given volume of fluid. The presence of solid contaminant particles in the liquid interferes with the ability of the hydraulic fluid to lubricate and causes wear to the components. The extent of contamination in the fluid has a direct bearing on the performance and reliability of the system and it is necessary to control solid contaminant particles to levels that are considered appropriate for the system concerned.

Necessary and careful precautions must be taken in order to avoid and prevent contaminations. Generally ISO 4406 standard is taken as a base matter for hydraulic fluid cleanliness in European countries. The importance of filtering must be explained in details to hydraulic system operators. Effective filtration for high performance in hydraulic systems means understanding the valve design, setting and maintaining cleanliness objectives, appropriate filtration for the environment, no short cuts with filter quality or replacement elements, regular monitoring and service.

## REFERENCES

1. **Ozkurkcu, Y., Kurt, R. and Caglayan, I.H., (1999)**, "The Importance of Contamination for Hydraulic and Fluidizing", I. National Hydraulic and Pneumatic Congress, İzmir, pp.15–227.
2. **Busch A. and Fischer E., (2003)**, "Practical Contamination Management From Processing to Delivery", Hydac, Germany, pp 1–49.
3. **Hydac, (2010)**, "Filtration Handbook", HYDAC International, U.S.A., pp 1–22.
4. **Hydac, (2009)**, "Hydraulic & Lube Oil Filters–Housings, Elements, Indicators, Sizing", U.S.A., pp 1–248.





5. **Mahle, (2009)**, "Filtration in Hydraulic and Lubrication Circuits–Know-how for More Efficiency and Profitability", MAHLE Industrial Filters, Germany, pp 1–52.
6. **Donaldson, (2012)**, "Filtration Technical Reference", Filtration Solutions, Minneapolis, U.S.A., pp 1–28.
7. **Mráz S., (2001)**, "Contamination: Hydraulic System Enemy No.1", Machine Design, Sep.13.
8. **Totten E. G., (2006)**, "Handbook of Lubrication and Tribology, Application and Maintenance", Vol.1, 2<sup>nd</sup> ed., Taylor & Francis Group.
9. **Lloyd, P.J., Akers, R.J., Scarlett, B., Stenhouse, J.I.T. and Ward, A.S., (1971)**, "Particle Contamination in Hydraulic Systems", AFFDL–TR–71–73, England.
10. **Totten E. G., (2000)**, "Handbook of Hydraulic Fluid Technology", Marcel Dekker Inc., U.S.A.
11. **Jarrett H.V., (1914)**, "Practical Ways to Control Hydraulic System Contamination", Farm Machinery Fact Sheet FM–20, Utah State University, Logan, Utah, pp 1–2.
12. **Park R.W., (1997)**, "Contamination Control–A Hydraulic OEM Perspective", Workshop on Total Contamination Control Centre for Machine Condition Monitoring, Monash University, Moog Australia, pp 1–18.
13. **Briggs A.J., (1969)**, "Determining Contamination Levels in Hydraulic Systems", 24<sup>th</sup> ASLE Annual Meeting, May 5–9, Philadelphia, pp 148–155.
14. **The OilGear Company, (1994)**, "Contamination Evaluation Guide for Rating Hydraulic Fluids" USA, pp 1–6.
15. **Hannifin P., (2006)**, "Hydraulic Filtration Handbook, Parker Hannifin Corporation, Hydraulic Filter Division Europe, pp 1–40.
16. **Madhavan P., (2000)**, "Control Contamination to Extend Fluid's Service Life", Hydraulics & Pneumatics, Washington, pp 35–38.
17. **Eaton, (2002)**, "The Systemic Approach to Contamination Control–A Complete Guide for Maximum System Performance", Vickers, U.S.A., pp 1–33.





## DESIGN AND VALIDATION OF A THREE-AXIS HIGH-PRECISION POSITIONING SYSTEM FROM MECHATRONICALLY MODULAR COMPONENTS

**Erva ULU**, *erva@bilkent.edu.tr*, Bilkent University, 06800, Ankara, Turkey

**Nurcan GECER-ULU**, *ulu@bilkent.edu.tr*, Bilkent University, 06800, Ankara, Turkey

**Melih ÇAKMAKCI**, *melihc@bilkent.edu.tr*, Bilkent University, 06800, Ankara, Turkey

### ABSTRACT

Precision positioning devices are used for almost every operation in micro/nano-scale applications. The positioning device introduced here is built from mechatronically modular single axis sliders and can also be reconfigured for a specific application without changing its mechanical or control software design. The sliders are modular due to their deliberate mechanical design, adaptive feature of encoder interpolation technique and structure of learning based cross-coupled control algorithm. Moreover, the sensitivity of the system is also reconfigurable by changing the encoder resolution for a specific application so that optimum velocity vs resolution trade offs can be fully utilized. Performance of the overall three axis positioning system with its mechanical design, encoder signal interpolation and position control algorithm is shown through validation and experiments. The integrated precision positioning system achieves nanometer level tracking and contouring performance utilizing a modular but axis coupled control algorithm.

**Keywords:** Modularity, nano-positioning

### 1. INTRODUCTION

Precision positioning is required in many industrial applications including micro/nano-scale manufacturing and assembly, optical component alignment systems, scanning microscopy applications, and cell/tissue engineering [2, 5]. Precision positioning devices are used for almost every operation in micro/nano-scale applications. Performance characteristics of these devices are measured by comparing their positioning accuracy, maximum velocity and acceleration that they can operate reliably.

The performance characteristics are primarily determined by the main components of the system: the actuator that provides the force for motion, the feedback sensor, which supplies the position information, and the controller that manages the system operation. Typical actuators used for micro/nano-positioning systems are piezoelectric actuators [1], ballscrew

mechanisms [5, 6] and permanent magnet linear motors (PMLM) [6, 17]. Linear motors are gaining popularity for precision positioning applications due to their superior characteristics. Since there is no contact between the stationary and moving parts of PMLMs, the backlash or wear is not concern and nonlinear effects due to the contact is not experienced. With the linear motors, high acceleration and velocity values can be achieved in long ranges (greater than). High-resolution displacement sensors are used in micro/nano-positioning systems in order to satisfy high-precision. Commonly used sensors are laser interferometers, capacitive sensors and optical encoders [17, 4]. Measurement ranges of linear optical encoders are in hundreds of millimeters but their resolutions are usually in micrometer level. However, signal processing techniques for interpolation of the available encoder signals serves further improvement of the encoder resolution by deriving intermediate position values out of the original sinusoidal encoder signals. Although it is possible to achieve high resolution values using various kinds of interpolation techniques [7, 8, 3], both hardware and software interpolation methods require ideal encoder signals with a quadrature phase difference between them. Hence, in order to obtain high-resolution position information, original encoder signals containing some noise and errors are to be corrected before the interpolation process. In [9], an adaptive modular interpolation technique which is suitable for multi-axis positioning systems is presented by the authors.

For most applications, precision positioning require both high contour and tracking accuracy. In tracking control, the objective is moving a certain pre-determined point in the system along a desired trajectory. Although almost all systems employ feedback as a part of tracking control, substantial improvement of tracking accuracy is achieved by addition of feed-forward control. Several feed forward control schemes are developed in literature to improve tracking accuracy such as zero phase error tracking control (ZPETC) [18, 13, 16], feed forward friction compensation [19, 20] and iterative learning control (ILC) [17, 10]. Generally, improving tracking accuracy of an individual axis also increases contouring accuracy of the multi-axis system. However, in some cases, decreasing the tracking error may not decrease the contour error; it may even deteriorate the contouring performance [15]. Hence, the control structure should be designed considering not only the tracking error but also the contour error in order to achieve high accuracy for both. Koren [14] proposed the cross-coupled control (CCC) structure that focuses on eliminating the error in contouring rather than tracking in individual axes. Since the introduction of CCC, it has been modified and combined with different control techniques [20, 10, 11]. In [12], a learning based cross coupled control algorithm suitable for multi-axis positioning applications is also presented.

In this paper, control design and validation of a three-axis precision positioning device is presented based on the modular methods developed in [9] and [12]. The results of this paper show the modularity and performance of the methods are still valid even though the dynamics of the axis implemented have significant changes such as the gravitational effects in the z-axis and its coupled effect to x and y axis control. To the best of our knowledge, this is the first time design of a multi-axis high precision positioning system that can achieve nanometer level positioning in long ranges is explained with the employed encoder signal interpolation and control techniques. The rest of this paper is structured as follows: In Section II, system design, encoder resolution improvement method and the control algorithm for the 3-axis system is presented. Validation and experimental results are given in Section III. Conclusions and future work is discussed in Section IV.

## 2. SYSTEM DESIGN

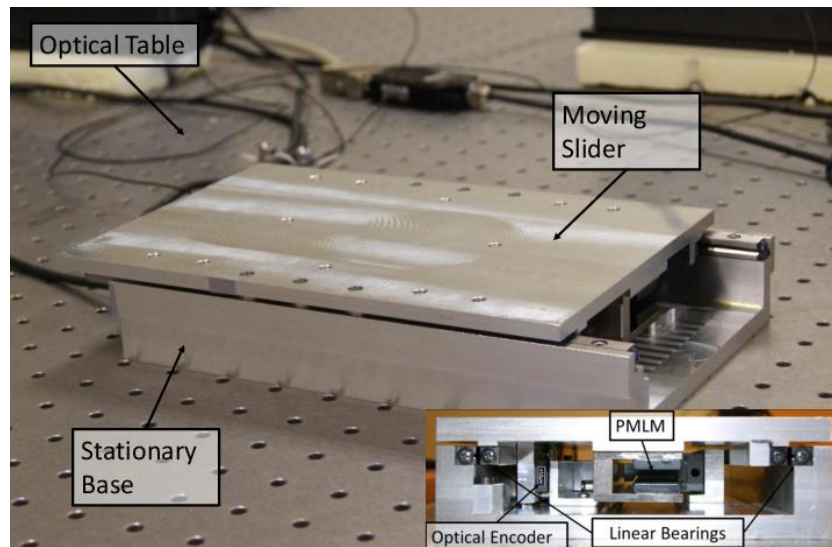


Figure 1: Single-axis slider

For the research project discussed in this paper, a specific three-axis micro/nano-positioning device with  $120mm \times 120mm \times 120mm$  operation space is developed. This device is constructed by assembling three of the same modular single-axis sliders (shown in Fig. 1) perpendicularly as shown in Fig. 2. As a first step to develop this system, a modular single-axis slider that can achieve micro/nano-meter level positioning over  $120mm$  operation range is built.

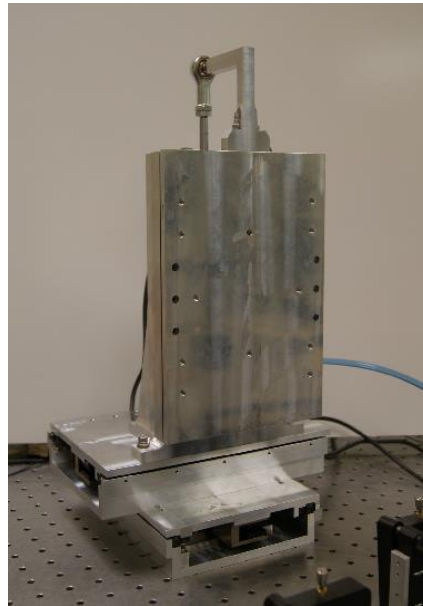


Figure 2: Assembled Three-axis micro/nano-positioning system

Performance of a micro/nano-positioning device can be evaluated by its working range, maximum velocity and acceleration, positioning resolution and positioning accuracy values. Components of the single axis slider shown in Fig. 1 are chosen considering these performance characteristics. In this design, stationary base and the moving slider are connected via low-friction precision cross-roller linear bearings. Due to its outstanding characteristics in precision positioning applications, a permanent magnet linear motor is used as the actuator. The position feedback is taken from a linear optical encoder. This encoder has  $4\mu m$  scale grating in pitch satisfying  $1\mu m$  original measurement resolution. However, this resolution is increased up to  $25nm$  using the original encoder interpolation technique explained in Section 2.2. As illustrated in Fig. 3, designed system is composed of an actuator, an optical encoder and a controller which includes encoder interpolation and position control algorithms. In the system, an adaptive encoder resolution improvement approach is used to achieve nanometer level position information. A modular learning based control algorithm is developed for position control of the system.

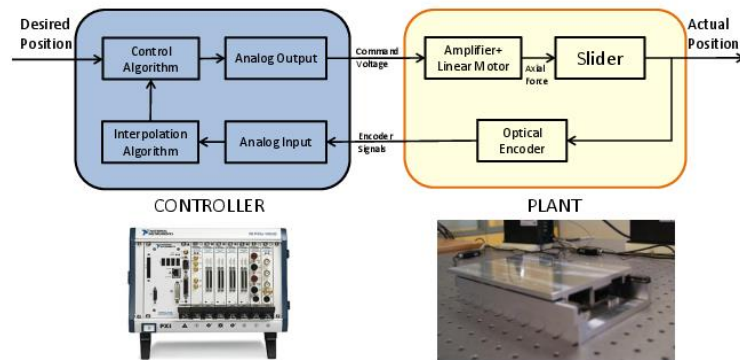


Figure 3: Control setup of the precision positioning system

## 2.1 Modularity of the Sliders

In addition to typical off-the shelf components, several mechanical components designed and manufactured for the single axis slider such as the base part, the slider and the sensor housing. While designing these parts, main concerns are ease of assembly, compactness and modularity. Moreover, geometrical properties of these parts are designed to keep their rigidity during the manufacturing processes. The mechatronic (hardware and software) modularity of the sliders helps for easy reconfigurability for a specific application. Modularity of the system provided from mechanical design, adaptive feature of encoder interpolation technique and modular structure of control algorithm. Moreover, the sensitivity of the system is reconfigurable in the sense that the encoder resolution can be adjusted for a specific application so that optimum velocity and resolution combinations can be achieved.

For modularity purposes, each part of the single axis slider is designed so that one of them can be assembled on another one in various configurations to build single, two or three axis systems for different applications. Here, any of the configurations can be built without making any modifications in the single axis slider. By assembling the single axis sliders in different forms, systems with various reachable operation areas can be obtained for many specific applications. In Fig. 4, several possible assembly configurations for single, two and three axis systems are illustrated. For example, assembling two single axis sliders obliquely, a rectangular working area can be obtained when it is required. Although maximum three number of sliders are used in the illustrations in Fig. 4, it is possible to built different systems by assembling several single axis sliders to satisfy specific applications.



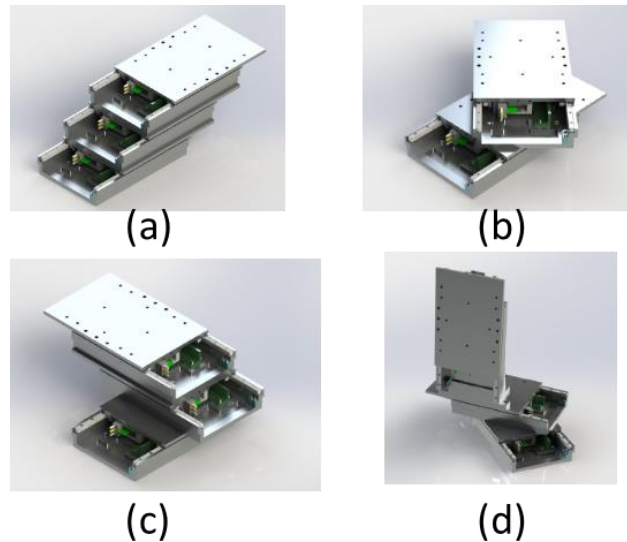


Figure 4: Possible assembly configurations of single-axis sliders: (a) Range extension by cascaded assembly, (b) Oblique assembly due to range and rigidity concerns, (c) Range extension in one axis, (d) Three dimensional oblique assembly

Although there are various possible assembly configurations as summarized in this section, the main focus of interest of this paper is the specific three-axis configuration shown in Fig. 2. In this design, a counter balance subsystem is used as an adapter for single-axis slider to be assembled in vertical position. It is composed of two main parts: an L shaped beam structure and an air piston. The purpose of the L shaped beam is to support the slider in vertical position. On the other hand, air piston is used to compensate the weight of the sliding part so that similar control inputs can be used in both directions in vertical for high precision positioning.

## 2.2 Encoder Resolution Improvement:

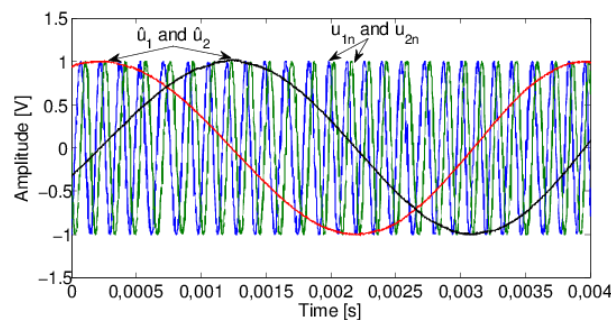


Figure 5: Interpolation results for  $n = 25$

As mentioned previously, presented micro/nano-positioning system includes linear optical encoders as feedback sensors to obtain position information. However, measurement

resolution of the encoder used in the system is  $1\mu m$ . Hence, in order to achieve nanometer level positioning performance with the overall system, it is crucial to increase the resolution of the encoders. Basic idea behind the implemented encoder resolution improvement technique is to generate high-order quadrature sinusoids from original encoder signals so that any deviations or distortions in these signals can be tolerated. For this purpose, an adaptive signal conditioning step to obtain ideal sinusoids with quadrature phase difference is applied before the interpolation process. Then, a quick access look-up table accomplishes mapping of the first-order signals to higher-order ones. In Fig. 5, first-order sinusoidal signals,  $\hat{u}_1$  and  $\hat{u}_2$ , and higher-order sinusoids,  $u_{1n}$  and  $u_{2n}$ , obtained as a result of an example interpolation process. Defining the ideal encoder signals as first order sinusoids with quadrature phase difference, relation between real ( $u_1$  and  $u_2$ ) and ideal encoder signals ( $u_{1i}$  and  $u_{2i}$ ) can be written as shown in (1).

$$\begin{aligned} u_1 &= u_{1i} + m_1 \\ u_2 &= \frac{1}{R}(A_1 \cos(\alpha - \phi)) + m_2 \end{aligned} \quad (1)$$

where  $m_1$  and  $m_2$  are mean offset values and  $\phi$  is the quadrature phase shift error. In (1),  $R$  is the gain ratio ( $A_1/A_2$ ) where  $A_1$  and  $A_2$  are amplitudes of actual encoder signals. A recursive least squares (RLS) with exponential forgetting and resetting method is used to correct these errors online. After the correction and interpolation processes are accomplished, high-order sinusoids are converted into binary pulses so that the position information can be derived by counting the zero crossings. Details of the correction and interpolation method explained in this section and its experiment results in single axis can be found in [9].

### 2.3 Three Axis Control Implementation

In this section, first, a mathematical model of the positioning system is derived through its dynamics. Then, the modular learning based cross-coupled control algorithm that is used for controlling the system is explained.

Mechanical and electronic components of the single-axis linear stage are introduced in Section II-A. The same dynamic model can be used for horizontal and vertical configurations of the sliders due to the counterbalance system used for vertical cases. An ideal dynamic model of a single-axes linear stage is given in Fig. 6 where  $R$  is the linear motor resistance,  $L$  is the linear motor inductance,  $K_{BEMF}$  is the back electromotive force constant,  $K_{force}$  is

the force constant,  $m$  is the sliding mass,  $b$  is the viscous friction,  $e_m$  is the linear motor input voltage,  $K_{amp}$  is the amplifier gain and  $i$  is the linear motor current. In the dynamic model, ripple forces of the permanent magnet linear motor are neglected and linear bearings are modeled as a viscous friction component. The dynamic model, the transfer function relating the displacement  $X(s)$  to applied voltage  $E(s)$  for the linear stage is found as in (2).

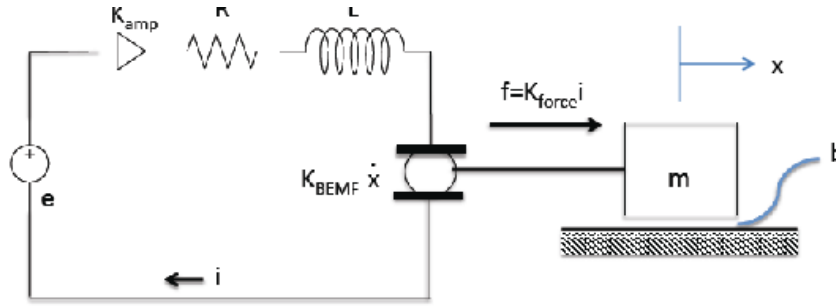


Figure 6: Dynamic model of a single-axis system

$$P(s) = \frac{X(s)}{E_m(s)}$$

$$= \frac{K_{amp} K_{force}}{s[Lms^2 + (Rm + bL)s + (Rb + K_{BEMF} K_{force})]} \quad (2)$$

For most positioning applications, designing a modular control framework with high tracking and contouring performance is desirable. Our three-axis positioning system is designed such that three modular single-axis stages will be assembled on top of each other to build it. In this section, the modular learning based cross-coupled controller is explained. The control system is intended to be modular so that the stages can be interchanged without changing the control system. For modularity reasons, ILC is chosen to improve tracking performance since controller structure does not change with alterations in plant model structure and parameters. Moreover, the use of ILC is beneficial for modular systems to compensate for changes after the assembly through learning process. For example, when a modular stage is assembled on top of another, weight of the sliding mass changes. ILC via zero-phase filtering is chosen to be integrated into the modular learning based controller due to its practical implementation. Moreover, CCC which considers the effects between axes is used for contouring control. In CCC, axial position errors are combined into one contour error and then, this contour error is fed to the cross-coupled controller. When CCC is used, there is a need for contour error construction approach since calculating the exact contour error is very

complex for nonlinear contours. For the modular learning based cross-coupled control algorithm, contouring error vector method [21] is chosen to use with CCC since it is computationally more efficient. The encoders of the positioning system have been interpolated to achieve nanometer resolution. This procedure is accomplished without any extra hardware. Due to this fact, there is a trade of between the resolution of the encoders and the computational effort in the control loop. Therefore, it is important to minimize computational effort in the control loop to maximize encoder resolution. Using the contouring error vector technique also makes the control method more suitable to implement on three-axis systems and to work with arbitrary nonlinear contours.

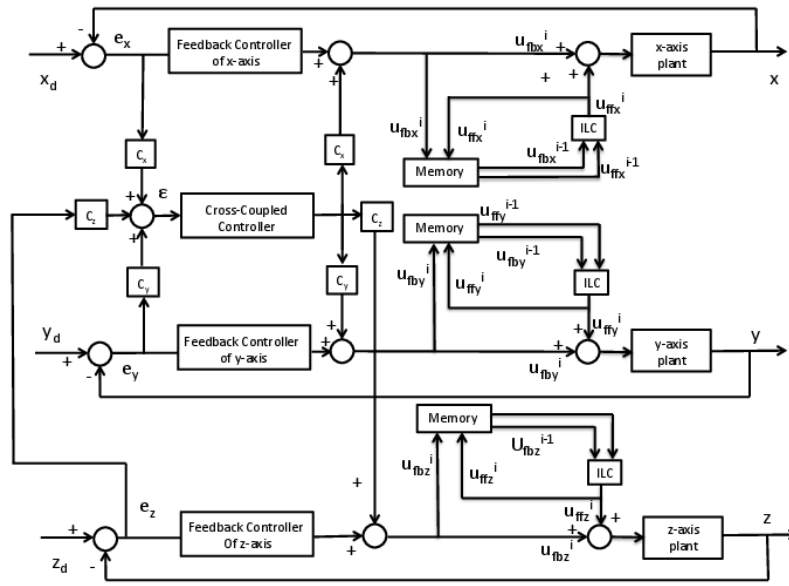


Figure 7: Block diagram for the learning based cross-coupled control method

Block diagram of the presented control for three-axis systems is given in Fig. 7. In the control algorithm, desired input trajectories are given to the system as the  $x_d$ ,  $y_d$ ,  $z_d$  for each axis. Then, the axial tracking errors are found as the  $e_x$ ,  $e_y$ ,  $e_z$  and sent to the feedback controllers. Also, the contour error,  $\varepsilon$  is calculated multiplying the axial position errors with coupling gains,  $C_x$ ,  $C_y$  and  $C_z$  as shown in (3).

$$\varepsilon = C_x e_x + C_y e_y + C_z e_z \quad (3)$$

Contour error is sent to the cross-coupled controller and the output is multiplied by coupling gains to find the cross-coupled control input for each axis. After adding the cross-coupled control signal to the feedback control signal, the combined signals,  $u_{fbx}^i$ ,  $u_{fby}^i$ ,  $u_{fbz}^i$ , are stored in memory. In these combined signal symbols,  $i$  stands for the iteration number.

Then, the feed-forward control signals,  $u_{ffx}^i$ ,  $u_{ffy}^i$ ,  $u_{ffz}^i$ , are calculated using the feed-forward signals,  $u_{ffx}^{i-1}$ ,  $u_{ffy}^{i-1}$ ,  $u_{ffz}^{i-1}$ , and combined signals,  $u_{fbx}^{i-1}$ ,  $u_{fby}^{i-1}$ ,  $u_{fbz}^{i-1}$ , stored in the memory as shown in (4) without axis subscripts for simplicity using  $k$  is the time index,  $\gamma$  is the learning gain and  $M$  is the length index of zero phase filter.

$$u_{ff}^i(k) = u_{ff}^{i-1}(k) + \frac{\gamma}{2M+1} \sum_{j=-M}^M u_{fb}^{i-1}(k+j) \quad (4)$$

Moreover, the feed-forward control signals are added to the combined signals and given to the plants. Therefore, the expected benefits of the method described here is good tracking performance (due to ILC features) and good contouring performance (due to the application of CCC) with low computational effort, which is applicable to systems with any number axis. Although this paper focuses on control of three-axis system, control scheme presented in this section is applicable to multi-axis systems with any number of axes. Detailed explanation of the control algorithm and its experimental test results on the two-axis version of the precision positioning system can be found in [12].

### 3. VALIDATION AND EXPERIMENTS

In order to express the performance of the encoder resolution improvement method numerically, an external validation is required before the experiments. For this purpose, a two-arm laser vibrometer with adjustable resolution is used as an external measurement device.

In the validation experiments, the aim is to compare the displacement values obtained using the linear encoder and the vibrometer. Calculating the RMS error levels by taking the vibrometer readings as reference, a numerical expression for performance of the encoder resolution improvement method is obtained. In order to show the performance clearly, validation experiments are conducted for the maximum interpolation number ( $n=100$ ) for each axis. Here, a Polytech OFV-552 two-arm laser vibrometer with  $3nm$  measurement resolution is used as an external measurement device. For the validation experiments, one of the laser arms is directed to the stationary base of the slider as the reference and the other arm is positioned to point at the moving slider of the system. Hence, the measured vibrometer reading is differential and free from undesired common vibrations. Moreover, the whole system including the sliders and laser arm mounts is mounted on an optical table to obtain noise-free displacement measurements. Measurement range of this vibrometer is limited to  $200\mu m$ . However, in order to illustrate the validation results clearly, displacements

with couple of micrometers are given in Fig. 8. In this figure, displacement measurements obtained with the vibrometer and the linear encoder with interpolation are given for interpolation number of  $n=100$  leading  $10nm$  resolution. For all axes, interpolation results match with the displacements measured with laser vibrometer. Root mean square (RMS) of measurement difference between the vibrometer and linear encoder with interpolation are obtained as  $7.2nm$ ,  $7.9nm$  and  $7.1nm$  for x, y and z axis, respectively. Since these values are below the intended measurement resolution ( $10nm$ ) achieved with the application of the interpolation method on linear encoder, it can be concluded that the proposed method is validated successfully.

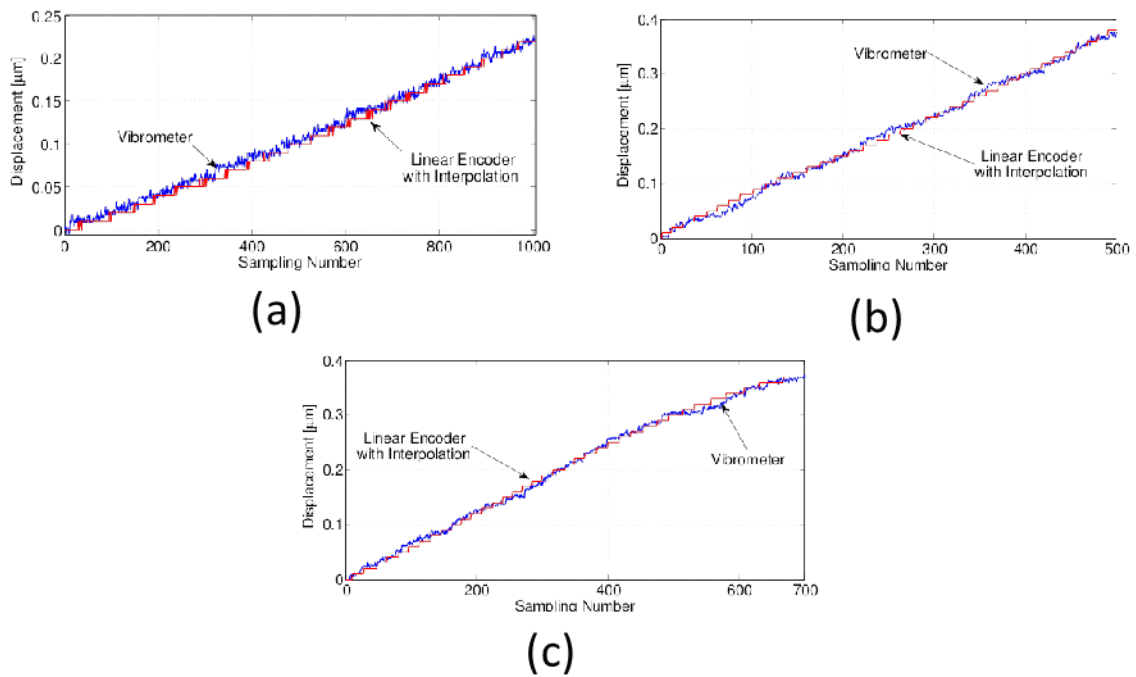


Figure 8: Validation results on (a)x- (b)y- and (c)z-axis sliders for interpolation number of  $n=100$  resulting  $10nm$  measurement resolution

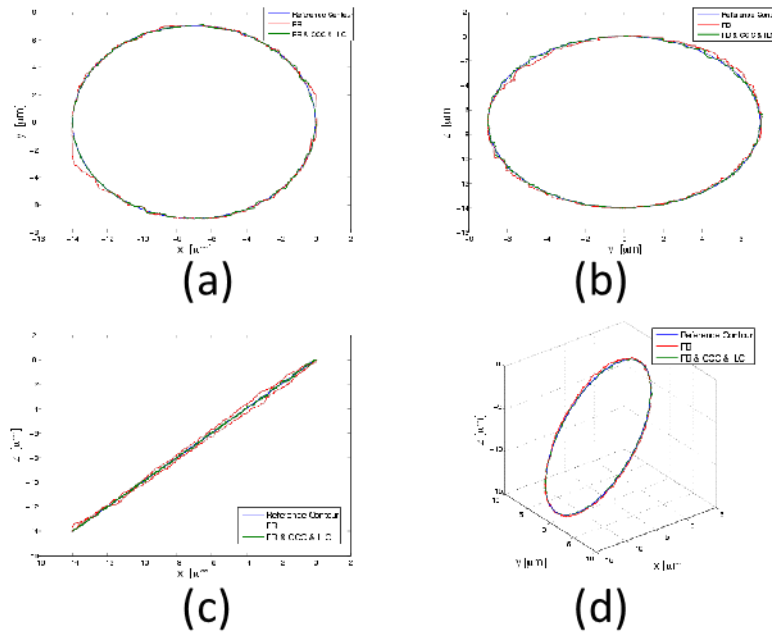


Figure 9: (a) x-y plane, (b) y-z plane, (c) x-z plane and (d) 3 dimensional experimental results of three-axis system for the nonlinear contour

Table 1: Three-axis system experiment - RMS error values for the nonlinear contour

RMS Error	x-axis	y-axis	z-axis	contour
	[nm]	[nm]	[nm]	[nm]
FB	135.16	99.97	213.43	137.95
FB CCC	70.71	86.56	229.72	74.04
FB ILC	72.56	81.60	34.90	57.45
FB CCC ILC	53.55	76.86	34.41	43.61

Performance of the three-axis positioning system is tested through some experiments. Moreover, performance of the employed learning based cross-coupled controller is compared with feedback control (FB), feedback control with iterative learning control (FB ILC), feedback control with cross-coupled control (FB CCC). Learning based controller is mentioned as feedback control with cross-coupled control and iterative learning control (FB CCC ILC). A reference contour of  $45^\circ$  inclined circle with  $7\mu m$  radius is fed to the system using S-curve trajectory planning. Using the contour error vector approach, coupling gains have been found without too much computational effort. FB ILC and FB CCC ILC experimental results are recorded after 20 iterations since after 20 iterations improvements are not obvious as before. Variation of RMS single-axis position errors and RMS contour error with the different control schemes is given in Table 1. Looking at Table 1, it can be



observed that FB CCC system decreases contour error significantly whereas axial error for z-axis increases a little bit. This is acceptable since cross-couples control promises to improve contour error while axial tracking may deteriorate. Also, contouring performance is the important criteria for multi-axis systems rather than axial-tracking errors. Similarly, FB ILC system decreases axial tracking errors more effectively than contour error as expected. Best tracking and contouring performance is obtained for FB CCC ILC system. Therefore, the modular learning based cross-coupled control algorithm performs very well for the three-axis precision positioning system. Moreover, having maximum RMS error as  $76.86nm$  is fairly good for a system with  $25nm$  encoder resolution.

In Fig. 9, contour tracking of the system is given for x-y plane projection, y-z plane projection, x-z plane projection and x-y-z three dimensional view. Looking at these figures, performance of the overall high precision positioning system with the learning based cross-coupled control and the adaptive encoder interpolation technique is shown to be successful.

#### 4. CONCLUSIONS

In this paper, development of a three-axis high precision positioning system is explained. Modularity of the positioning system was the major criteria in both mechanical design and control algorithm development. In order to obtain nanometer level positioning, measurement resolution of the linear optical encoders is increased using an adaptive encoder resolution improvement method. Since this is a software based method, resolution of the encoders can be adjusted according to the application requirements. In order to support the modular characteristics of the system, a learning based cross-coupled controller is developed. With the implementation of this controller and encoder interpolation method on three-axis positioning system, nanometer level positioning performance is achieved in the experiments. Validation of the encoder resolution improvement method under a more challenging environment (more axis equals to more electrical interference on the signals) is also provided. In future, other modular positioning system configurations can be tested. Moreover, decreasing the electrical noise in the system is one of the most important future plans. This way, encoder resolution could further be increased resulting in better tracking and contouring performance. In order to make the most of adjustable encoder resolution feature, a study on optimization between encoder resolution and maximum operation velocity could be carried out.

#### ACKNOWLEDGMENT

The authors would like to thanks undergraduate students Oytun Ugurel and Ersun Sozen for their support on computer aided design of the positioning system. Authors would also like to



thank Dr. Sinan Filiz for sharing his experience in precision positioning systems. This work was supported by Scientific and Technical Research Council of Turkey (TUBITAK) through Project No: 110M251.

## REFERENCES

1. **S. S. Aphale, S. Devasia, and S. O. R. Moheimani**, (2001), "High-bandwidth control of a piezoelectric nanopositioning stage in the presence of plant uncertainties," *Nanotechnology*, vol. 19, no. 12, p. 125503.
2. **S. Devasia, E. E. Eleftheriou, and R. Moheimani**, (2007), "A survey of control issues in nanopositioning," *IEEE Transactions on Control Systems Technology*, vol. 15, no. 15, pp. 802–823.
3. **H. V. Hoang and J. W. Jeon**, (2011), "An efficient approach to correct the signals and generate high-resolution quadrature pulses for magnetic encoders," *IEEE Transactions on Industrial Electronics*, vol. 58, no. 8.
4. **W. Kim and S. Verma**, (2007), "Multiaxis maglev positioner with nanometer resolution over extended travel range," *ASME Journal of Dynamic Systems, Measurement, and Control*, vol. 129, pp. 777–785.
5. **L. Lihua, L. Yingchun, G. Yongfeng, and S. Akira**, (2010) "Design and testing of a nanometer positioning system," *Journal of Dynamic Systems, Measurement, and Control*, vol. 132, no. 2, pp. 021 011–6.
6. **N. Sclater and N. Chironis**, (2006), "*Mechanisms and Mechanical Devices Sourcebook*", fourth edition, McGraw-Hill Professional.
7. **K. K. Tan, H. X. Zhou, and T. H. Lee**, (2002), "New interpolation method for quadrature encoder signals," *IEEE Transactions on Instrumentation and Measurement*, vol. 51, no. 5, pp. 1073–1079.
8. **K. K. Tan and K. Z. Tang**, (2005), "Adaptive online correction and interpolation of quadrature encoder signals using radial basis functions," *IEEE Transactions on Control Systems Technology*, vol. 13, no. 3, pp. 370–377.
9. **E. Ulu, N. Gecer-Ulu, and M. Cakmakci**, (2014), "Adaptive correction and look-up table based interpolation of quadrature encoder signals," *ASME Journal of Dynamic Systems Measurement and Controls*, May 2014.
10. **K. L. Barton and A. G. Alleyne**, (2008), "A cross-coupled iterative learning control design for precision motion control," *IEEE Transactions on Control System Technology*, vol. 16, no. 6, pp. 1218–1231.
11. **H. Y. Chuang and C. H. Liu**, (1990), "A model referenced adaptive control strategy for improving contour accuracy of multi-axis machine tools," in *Conference Record of the 1990 IEEE Industry Applications Society Annual Meeting*, 2, Ed., pp. 1539–1544.



12. **N. Gecer-Ulu, E. Ulu, and M. Cakmakci**, (2012), "Learning based cross-coupled control for multi-axis high precision positioning systems," *Proc. ASME Dynamic Systems and Control Conference*, Ft. Lauderdale, FL.
13. **P. Hsu, Y. Houn, and S. Yeh**, (2001), "Design of an optimal unknown unknown input observer for load compensation in motion systems," *Asian Journal of Control*, vol. 3, no. 3, pp. 204–215, 2001.
14. **Y. Koren**, (1980), "Cross-coupled biaxial computer control for manufacturing systems," *Journal of Dynamic Systems, Measurement and Control*, vol. 102, no. 4, pp. 265–272, 1980.
15. **Y. Koren and C. C. Lo**, (1991), "Variable-gain cross-coupling controller for contouring," *CIRP Annals-Manufacturing Technology*, vol. 40, no. 1, pp. 371–374, 1991.
16. **L. Qing, W. Tai-yong, D. Ying-chuan, J. Yong-xiang, and L. Bo**, (2010), "Applications of position controller for cnc machines based on state observer and cross-coupled controller," in *International Conference on Computer Mechatronics, Control and Electronic Engineering(CMCE), IEEE*, pp. 593–596.
17. **K. K. Tan, H. Dou, Y. Chen, and T. H. Lee**, (2001), "High precision linear motor control via zero-phase filtering," *IEEE Transactions on Control Systems Technology*, vol. 9, no. 2, pp. 244–253.
18. **M. Tomizuka**, (1987), "Zero phase error tracking algorithm for digital control," *Journal of Dynamic Systems, Measurement and Control*, vol. 109, no. 1, pp. 65–68.
19. **R. Sato, M. Tsutsumi**, (2007), "Friction compensator for feed drive systems consisting of ball screw and linear ball guide," in *Proc. of the 35th International MATADOR Conference*, pp. 311–314.
20. **L. Wang, S. Lin, and H. Zeng**, (2011), "Precision contour control of XY table based on LuGre model friction compensation," in *2nd International Conference on Intelligent Control and Information Processing (ICICIP), IEEE*, pp. 1124–1128.
21. **S. S. Yeh and P. L. Hsu**, (2002), "Estimation of contouring error vector for the cross-coupled control design," *IEEE/ASME Transaction on Mechatronics*, vol. 7, no. 1, pp. 44–51.



## **AUTHORS INDEX**

Author	Paper No (Page Number )
ABDELMONAAM, Sassi	SA6 (181)
ACAR, B. Serpil	SA1 (101)
ACAR, Erdem	EA2 (245)
ACAR, Memis	SA1 (101), SA4 (153)
AKSAL, Ahmed	85 (908)
AKSUNGUR, D. Kıvanç	46 (1032)
AL KHAWASHKİ, Hazem	8 (1012)
ALAGAÇ, Melike Sert	MD14 (309)
AL-AHMARİ, A. M.	8 (1012)
ALİEW, Fuad	85 (908)
ALKASASBEH, Jihad A. S.	3 (934)
ALMA, U. Alican	MD13 (297)
ALNIAK, M. Oktay	77 (1104)
ALQAWABAH, Safwan M. A.	3 (934), 5 (948), 62(1076)
ALTINTAŞ, Yusuf	Keynote (1), MD34 (443), MD42 (483), 47 (804)
APAK, Serhat	25 (1246)
ARDIÇ, Halil	82 (888)
ARIKAN, Kutluk Bilge	44 (788), 85 (908)
ARIKAN, R. Güçlü	6 (1212)

Author	Paper No (Page Number )
ASCROFT, Helen	Keynote (29)
ASLAN, Deniz	MD43 (493)
ATTARI, Sanaz	78 (1184)
AZİZ, T.	8 (1012)
BAHTİYAR, Onur	MD12 (283), 41 (1396)
BAKKAL, Mustafa	MD13 (297), MD25(381)
BARCENA, Rafael	MD31 (395)
BARNES, Stuart	Keynote (29)
BENJAMIN, Robert J.	MD22 (345)
BEWSHER, S.R.	SA4 (153)
BHUDWANNACHAI, Pipat	Keynote (29)
BIKFALVI, Péter	53 (555)
BOUZAKİS, E.	Keynote (13)
BOUZAKİS, K.-D.	Keynote (13)
BRECHER, C.	MD33 (427)
BUDAK, Erhan	MD25(381), MD43 (493)
BÜYÜKKOÇAK, Süleyman	43 (840)
ÇAKIR, Ayşegül	41 (1396)
ÇAKIR, M. Cemal	MD11 (273), 84 (774), 21 (1368), 23 (1380)



Author	Paper No (Page Number )
ÇAKMAKCI, Melih	18 (711)
ÇALIŞKAN, Halil	56 (762)
CAN DEDE, M. İ.	50 (810)
CAPUTO, Francesco	SA2 (115)
ÇELİK, Ali	MD14 (309)
CENG, Wei-Kai	35 (824)
ÇETİN, Barbaros	43 (840)
CHAIRLADIES, W. M.	61 (1060)
CHAN, Hsiao-Ying	MD24 (365)
CHARALAMPOUS, P.	Keynote (13)
CHAWLA, Anoop	SA3 (131)
CHEN, C. H.	16 (984)
CHEN, Shao-Hsien	39 (752)
CHEN, Tsung-Chia	35 (824)
CHEN, Xun	MD45 (525)
CHIANG, J. H.	16 (984)
CHOUPANI, Naghdali	33 (1162)
CHUNG, Chih	MD22 (345)
ÇİÇEK, Serkan	72 (619)

Author	Paper No (Page Number )
CİĞEROĞLU, Ender	27 (1116)
CIOBANU, Gabriela	17 (595)
CIOBANU, Octavian	17 (595)
ÇOĞUN, Can	12 (976), 15 (1322)
ÇÖKER, Demirkan	81 (1049)
DAĞDEVİREN, Semih	SA7 (199)
DAHNEL, Aishah Najiah	Keynote (29)
DALKIRAN, Tugce Aydil	69 (1094)
DARWİSH, S. Saied	8 (1012)
DEMİR, Ali Gökhan	70 (850)
DEMİR, Hakan	9 (1226)
DEMİRCİ, Emre	EA3 (267)
DERE, Mustafa	55 (998)
DUDÁS, László	51 (874)
DURGUN, İsmail	83 (860)
ERDAL, Merve	69 (1094)
ERDÉLYI, Ferenc	53 (555)
ERDEN, Abdulkadir	22 (605)
ERDEN, Zuhail	YM4 (87), 22 (605)

Author	Paper No (Page Number )
ERDOĞAN, Bilgehan	82 (888)
ERDÖL, Muhammet	24 (1272)
ERGUR, H.Sevil	20 (675), 80 (693)
ERKEN, Uğur	28 (1338)
EROĞLU, Aylin Konez	22 (605)
EROL, Fulya	82 (888)
ERTUĞRUL, Şeniz	74 (635)
ESAT, Volkan	SA5 (167), SA7 (199)
ESENER, Emre	FO1 (1314)
ES'HAGİ OSKUİ , Abuzar	33 (1162)
FENG, Faby	MD22 (345)
FEY, M.	MD33 (427)
FİLİZ, İ. Hüseyin	55 (998), 67 (1150)
FIRAT, Mehmet	FO1 (1314)
FORRAI, Mónika Kulcsárné	53 (555)
GECER-ULU, Nurcan	18 (711)
GEZGİN, Erkin	50 (810)
GHRIB, Faouzi	SA6 (181)
GOEHLICH, Dietmar	SA3 (131)

Author	Paper No (Page Number )
GOLMOHAMMADZADEH, M.Hassan	44 (788)
GÖNEN, Demet	MD11 (273)
GÜMÜŞ, Tuna Çağlar	65 (571)
GÜNDÜZ, Mutlu	EA2 (245)
GUPTA, Aniruddha	Keynote (29)
GÜRSAKAL, Necmi	21 (1368)
HABERMANN, R.	MD33 (427)
HAMAMCI, Mustafa	57 (1412)
HARMAN, Hasan Erdem	28 (1338)
HASAN, Muhammad A.	55 (998)
HEMEIMAT, Raghad S.	2 (920)
HENGEOSS, Dirk	65 (571)
HOSHINO, Y.	YM2 (61)
HUGİ, Christoph	65 (571)
HUNG, Jui-Pin	MD32 (415)
HUSSEIN, A. A.	61 (1060)
IHARA, Yukitoshi	MD21 (333)
İRFANOĞLU, Bülent	44 (788)
IŞIK, Yahya	84 (774)

Author	Paper No (Page Number )
ISMAEL, Sh. M.	60 (1132)
JARRAR, Firas	FO3 (647)
KACAR, Ilyas	FO3 (647)
KAMIYA, Kei	YM3 (75)
KANAZAWA, Shuji	YM1 (49)
KARA, Alpagut	MD14 (309)
KARA, Ferhat	MD14 (309)
KARADOĞAN, Celalettin	46 (1032)
KARAGÜZEL, Umut	MD25(381)
KARAOĞLAN, A. Deniz	MD11 (273)
KARPAT, Yiğit	MD12 (283)
KASMAN, Şefika	29 (1354)
KATİRTZOGLU, G.	Keynote (13)
KATO, T.	YM2 (61)
KAYA, Necmettin	EA1 (235)
KEÇECİ, Emin Faruk	28 (1338)
KHAIR-ALDIEN, W. M.	60 (1132)
KHALIL A. A.	61 (1060), 60 (1132)
KILIÇ, Sadık Engin	65 (571)

Author	Paper No (Page Number )
KILIÇ, Suleyman	FO4 (663)
KILIÇ, Z. Murat	MD41 (469), MD42 (483), 47 (804)
KILINÇEL, Mert	73 (1174), 86 (1196)
KİPER, Gökhan	50 (810)
KITO, Akira	YM3 (75)
KLEINWORT, Robin	MD34 (443)
KOCA, Selim	23 (1380)
KOCABAŞ, M. Ozan	SA5 (167)
KOKU, A. Buğra	72 (619)
KONUKSEVEN, E. İlhan	72 (619)
KUBO, Tomohiro	MD21 (333)
KULCSÁR, Gyula	53 (555)
KURTARAN, Hasan	24 (1272)
KUŞ, Abdil	84 (774)
KUSUNOKI, Yuma	YM3 (75)
KUZU, A. Taner	MD13 (297)
LAI, Yuan-Lung	MD24 (365)
LAMANNA, Giuseppe	SA2 (115)
LAYEGH K., S. Ehsan	MD23 (355)

<b>Author</b>	<b>Paper No (Page Number )</b>
LAZOĞLU, Ismail	MD23 (355), MD44 (515), 83 (860)
LEBLOND, Jean-Baptiste	78 (1184)
LIAO, Chien-Chih	47 (804)
LIN, Chun-Wei	MD32 (415)
LO, Tzuo-Liang	MD24 (365)
LUO, Tzuo-Liang	47 (804)
MAKRIMALLAKIS, S.	Keynote (13)
MAMEDOV, Ali	MD44 (515)
MANCISIDOR, Iker	MD31 (395)
MASTAR, Ercan	50 (810)
MATSUOKA, Yoshiyuki	YM1 (49), YM3 (75)
MELHEM, Hebah B.	13 (962)
MENDIZABAL, Xabier	MD31 (395)
MERIC, Moustafa	SA1 (101)
MUKHERJEE, Sudipto	SA3 (131)
MUNOA, Jokin	MD31 (395)
MURAT, Dilek	21 (1368)
NASSER, A. A.	61 (1060), 60 (1132)
OLGUNER, Sadik	67 (1150)

Author	Paper No (Page Number )
ÖPÖZ, Tahsin T.	MD45 (525)
ORAK, Sezan	48 (541)
ORAL, Ali	MD11 (273), 21 (1368)
ÖZBAYOĞLU, Murat	65 (571)
ÖZDEN, Ersel	6 (1212)
ÖZER, M. Bülent	43 (840)
ÖZGEN, Barış	83 (860)
ÖZGEN, Gökhan O.	82 (888)
ÖZKAN, S. Samet	82 (888)
ÖZTÜRK, Fahrettin	FO3 (647), FO4 (663)
ÖZUĞUR, Burhan	25 (1246)
PANCAR, Yasar	20 (675)
PARDOEN, Thomas	78 (1184)
PENG, Bing-Jie	MD32 (415)
POLAT, Fikret	73 (1174), 86 (1196)
POYRAZ, Özgür	79 (579)
PREVITALI, Barbara	70 (850)
RAHIMZADEH BERENJI, Kaveh	MD13 (297)
RAJIHAMED, Babak	81 (1049)



Author	Paper No (Page Number )
SAKAE, Yuma	YM1 (49)
SAKLAKOĞLU, İ.Etem	29 (1354)
SAMANDARI, Hamed	27 (1116)
ŞANSVEREN, M. Fatih	32 (1284)
SARUHAN, Hamit	73 (1174), 86 (1196)
SATO, Koichiro	YM1 (49), YM3 (75)
SEÇKİN, Serdar	28 (1338)
ŞEKER, Ulvi	41 (1396)
SEMERÇİ, Fehim	EA3 (267)
SHAMOTO, Eiji	MD15 (321)
SİĞİRTMAÇ, Tayfun	50 (810), 9 (1226)
ŞİMŞEK, Ülke	15 (1322)
SKORDARİS, G.	Keynote (13)
SOFUOĞLU, M. Alper	48 (541)
SOGA, T.	YM2 (61)
SOLTANPOUR KHAMNEH, Morteza	33 (1162)
SUBRAMANIAN, Hariharan S.	SA3 (131)
TAJIMA, Toru	MD21 (333)
TAKANO, Shuji	YM1 (49)

Author	Paper No (Page Number )
TANABI, Hamed	69 (1094)
TAŞGETİREN, Süleyman	37 (1296)
TAŞKIN, Ebru	6 (1212)
TEKOĞLU, Cihan	78 (1184)
TOPAL, E. Sabri	57 (1412)
TOPÇU, Muzaffer	37 (1296)
TÓTH, Tibor	53 (555)
TSAİ, M. Y.	16 (984)
TUĞRUL, H. Onat	46 (1032)
TURAN, Servet	MD14 (309)
ULU, Erva	18 (711)
ULUKÖY, Arzum	37 (1296)
ÜNSAL, Eren	SA5 (167)
ÜNVER, Hakkı Özgür	65 (571)
USAL, M.R.	45 (1258)
UYSAL, Emre	MD25(381)
UZUNOĞLU, Emre	50 (810)
WAN, Min	MD35 (459), MD41 (469)
WANG, C. C.	30 (726)

Author	Paper No (Page Number )
WANG, Yilong	MD15 (321)
WU, Kung-Da	MD32 (415)
YAMAN, Kemal	12 (976)
YAMAN, Mustafa	32 (1284)
YANG, Huanjia	SA8 (215)
YANG, Shuang-Hua	SA8 (215)
YANG, Yun	MD35 (459)
YASA, Evren	79 (579)
YAU, H. T.	30 (726)
YAVUZ, Mecit	SA7 (199)
YİĞİT, Alparslan	32 (1284)
YİĞİT, İ. E.	MD23 (355), MD44 (515)
YILDIRAN, H. Orhan	36 (736)
YILDIZ, Ali Rıza	EA3 (267)
YILMAZ, D.	45 (1258)
YILMAZ, Oğuzhan	79 (579)
YILMAZ, Uğur Evrensel	MD14 (309)
YÖNTEM, Orçun	6 (1212)
YURTSEVER, Ekim	74 (635)

Author	Paper No (Page Number )
ZAEH, Michael F.	MD34 ( <b>443</b> )
ZAID, Adnan I. O.	2 ( <b>920</b> ), 3 (934), 5 ( <b>948</b> ), 13 ( <b>962</b> ), 62( <b>1076</b> )
ZEİNALİ, Soheila	43 ( <b>840</b> )
ZHANG, Weihong	MD35 ( <b>459</b> )